Transactions of the ASME®

HEAT TRANSFER DIVISION
Chair, S. M. CHO
Vice Chair, O. A. PLUMB
Secretary, R. A. NELSON, JR.
Treasurer, W. A. FIVELAND
Technical Editor, J. R. HOWELL (2000)

Associate Technical Editors,
T. L. BERGMAN (1998)
R. D. BOYD (1999)
S. H. CHAN (1997)
M. KAVIANY (1999)
M. D. KELLEHER (1999)
A. S. LAVINE (1998)
T. J. RABAS (1997)
S. RAMADHYANI (1998)
P. G. SIMPKINS (1998)
M. S. SOHAL (1998)
T. TONG (1999)
K. VAFAI (1997)
B. W. WEBB (1997)

BOARD ON COMMUNICATIONS
Chairman and Vice President
R. MATES

OFFICERS OF THE ASME
President, R. J. GOLDSTEIN
Executive Director,
D. L. BELDEN
Treasurer,
J. A. MASON

PUBLISHING STAFF
Managing Director, Engineering
CHARLES W. BEARDSLEY
Director, Technical Publishing
PHILIP DI VIETRO
Managing Editor, Technical Publishing
CYNTHIA B. CLARK
Managing Editor, Transactions
CORNELIA MONAHAN
Production Coordinator
VALERIE WINTERS
Production Assistant
MARISOL ANDINO

Transactions of the ASME, Journal of Heat Transfer (ISSN 0022-1481) is published quarterly (Feb., May, Aug., Nov.) for $220.00 per year by The American Society of Mechanical Engineers, 345 East 47th Street, New York, NY 10017. Periodicals postage paid at New York, NY and additional mailing offices. POSTMASTER: Send address changes to Transactions of the ASME, Journal of Heat Transfer, c/o THE AMERICAN SOCIETY OF MECHANICAL ENGINEERS, 22 Law Drive, Box 2300, Fairfield, NJ 07007-2300.
CHANGES OF ADDRESS must be received at Society headquarters seven weeks before they are to be effective. Please send old label and new address. **PRICES:** To members, $40.00, annually: to nonmembers, $220.00. Add $30.00 for postage to countries outside the United States and Canada.
STATEMENT from By-Laws. The Society shall not be responsible for statements or opinions advanced in papers or . . . printed in its publications (B7.1, Para. 3), **COPYRIGHT** © **1996** by The American Society of Mechanical Engineers. Authorization to photocopy material for internal or personal use under circumstances not falling within the fair use provisions of the Copyright Act is granted by ASME to libraries and other users registered with the Copyright Clearance Center (CCC) Transactional Reporting Service provided that the base fee of $3.00 per article is paid directly to CCC, 222 Rosewood Drive, Danvers, MA 01923. Request for special permission or bulk copying should be addressed to Reprints/Permission Department. **INDEXED** by Applied Mechanics Reviews and Engineering Information, Inc. Canadian Goods & Services Tax Registration #126148048.

Journal of Heat Transfer

Published Quarterly by The American Society of Mechanical Engineers

VOLUME 118 • NUMBER 3 • AUGUST 1996

TECHNICAL PAPERS

1995 Max Jakob Lecture

518 In Search of Two-Phase Flow
G. F. Hewitt

Analytical and Experimental Techniques

528 An Evolutionary-Genetic Approach to Heat Transfer Analysis
R. V. Davalos and B. Rubinsky

532 Design of Experiments Using Uncertainty Information
A. F. Emery and T. D. Fadale

Heat Conduction

539 Nonlocal and Nonequilibrium Heat Conduction in the Vicinity of Nanoparticles
G. Chen

546 Inverse Determination of Boundary Conditions and Sources in Steady Heat Conduction With Heat Generation
T. J. Martin and G. S. Dulikravich

Forced Convection

555 Experimental Investigation of the Laminar Flow Heat Transfer Enhancement in a Small-Scale Square Duct With Aqueous Carbopol Solutions
Cheng-Xian Lin, Shao-Yen Ko, and F. K. Tsou

562 Prediction of Jet Impingement Heat Transfer Using a Hybrid Wall Treatment With Different Turbulent Prandtl Number Functions
G. K. Morris, S. V. Garimella, and R. S. Amano

570 Optimal Spacing Between Pin Fins With Impinging Flow
G. Ledezma, A. M. Morega, and A. Bejan

578 Local Heat Transfer in Rotating Smooth and Ribbed Two-Pass Square Channels With Three Channel Orientations
S. Dutta and J.-C. Han

585 Unsteady Heat Transfer in Baffled Channels
G. Wang, K. Stone, and S. P. Vanka

592 Oscillatory Heat Transfer in a Pipe Subjected to a Laminar Reciprocating Flow
T. S. Zhao and P. Cheng

Natural and Mixed Convection

598 Natural Convection Heat Transfer in Horizontal Rod-Bundle Enclosures
M. Keyhani and T. Dalton

606 Flow and Mixed Convection Heat Transfer in a Divergent Heated Vertical Channel
C. Gau, T. M. Huang, and W. Aung

Falling Film Heat Transfer

616 The Intertube Falling Film: Part 1—Flow Characteristics, Mode Transitions, and Hysteresis
X. Hu and A. M. Jacobi

626 The Intertube Falling Film: Part 2—Mode Effects on Sensible Heat Transfer to a Falling Liquid Film
X. Hu and A. M. Jacobi

634 Correlations for Film Regeneration and Air Dehumidification for a Falling Desiccant Film With Air in Crossflow
M. Park, J. R. Howell, and G. C. Vliet

Radiative Transfer

642 A Multi-objective Optimization of Radiative Fin Array Systems in a Fuzzy Environment
B. T. F. Chung, B. X. Zhang, and E. T. Lee

650 An Alternative Formulation of the S-N Discrete Ordinates for Predicting Radiative Transfer in Nongray Gases
A. B. De Miranda and J. F. Sacadura

Downloaded 04 Feb 2011 to 194.85.80.107. Redistribution subject to ASME license or copyright; see http://www.asme.org/terms/Terms_Use.cfm

(Contents continued)

Boiling and Condensation

654 Transition Boiling Curves in Saturated Pool Boiling From Horizontal Cylinders
E. K. Ungar and R. Eichhorn

662 Gas-Saturated Pool Boiling Heat Transfer From Smooth and Microporous Surfaces in FC-72
J. P. O'Connor, S. M. You, and J. Y. Chang

668 Nucleate Boiling Heat Transfer in Spray Cooling
J. Yang, L. C. Chow, and M. R. Pais

672 Optimizing and Predicting CHF in Spray Cooling of a Square Surface
I. Mudawar and K. A. Estes

680 Study on Critical Heat Flux in Rectangular Channels Heated From One or Both Sides at Pressures Ranging From 0.1 to 14 MPa
Y. Sudo

689 A New Model for Forced-Convection Condensation on Integral-Fin Tubes
A. Cavallini, L. Doretti, G. A. Longo, and L. Rossetto

Phase-Change and Multiphase Heat Transfer

694 Study on Sublimation Phenomenon of Horizontal Frost Layer Exposed to Forced Convection Air Flow and Radiant Heat
H. Inaba and S. Imai

702 Transient Temperature During the Vaporization of Liquid on a Pulsed Laser-Heated Solid Surface
H. K. Park, X. Zhang, C. P. Grigoropoulos, C. C. Poon, and A. C. Tam

709 The Onset of Flow Instability for Downward Flow in Vertical Channels
R. Stelling, E. V. McAssey, Jr., T. Dougherty, and B. W. Yang

715 Mechanism and Effects of Predominant Parameters Regarding Limitation of Falling Water in Vertical Countercurrent Two-Phase Flow
Y. Sudo

725 Fluid Flow Effects in Evaporation From Liquid–Vapor Meniscus
D. Khrustalev and A. Faghri

Heat Pipes

731 Theoretical Analysis of the Maximum Heat Transport in Triangular Grooves: A Study of Idealized Micro Heat Pipes
G. P. Peterson and H. B. Ma

740 Experimental Investigation of the Maximum Heat Transport in Triangular Grooves
H. B. Ma and G. P. Peterson

747 The Interline Heat Transfer of Evaporating Thin Films Along a Micro Grooved Surface
J. M. Ha and G. P. Peterson

Porous Media

756 A Numerical Study of Thermal Dispersion in Porous Media
F. Kuwahara, A. Nakayama, and H. Koyama

Heat Transfer in Manufacturing

762 Transport Phenomena During Resistance Spot Welding
P. S. Wei, S. C. Wang, and M. S. Lin

774 Transient Model for CW and Pulsed Laser Machining of Ablating/Decomposing Materials—Approximate Analysis
M. F. Modest

781 Anomalous Diffusion in Short-Pulse Laser Interactions With Random Media
M. C. Hipwell and C.-L. Tien

TECHNICAL NOTES

787 Correlation for Opposing Flow, Mixed Convection Heat Transfer in a Vertical Tube With Constant Wall Temperature
D. D. Joye

789 Integrals Involving Bickley and Bessel Functions in Radiative Transfer, and Generalized Exponential Integral Functions
Z. Altaç

792 Nucleate Pool Boiling on Micro Graphite–Copper Composite Surfaces
Gai-Wai Yang, Hsing-Sheng Liang, Wen-Jei Yang, and Daniel Leroy Vrable

797 Laminar Film Condensation on a Horizontal Surface With Surface Tension Effect
J. S. Chiou, T. B. Chang, and C. K. Chen

799 Fundamental Study on Latent Cold Heat Storage by Means of Direct-Contact-Freezing Between Oil Droplets and Cold Water Solution
H. Inaba and K. Sato

(Contents continued on p. 538)

Downloaded 04 Feb 2011 to 194.85.80.107. Redistribution subject to ASME license or copyright; see http://www.asme.org/terms/Terms_Use.cfm

(Contents continued)

803 The Effect of Temperature-Dependent Viscosity on the Onset of Convection in a Saturated Porous Medium
D. A. Nield

805 A Thermodynamic Method for the Comparison of Plate-Fin Heat Exchanger Performance
L. Tagliafico and G. Tanda

ANNOUNCEMENTS

531 Announcement for authors

561 Change of address form for subscribers

584 Announcement: Heat Transfer Memorial Award

810 Announcement and call for papers: Engineering Foundation Conference on Compact Heat Exchangers for the Process Industries

811 Call for photographs: Visualization of Thermal Phenomena

811 Call for papers: 1997 National Heat Transfer Conference

812 Information for authors

Downloaded 04 Feb 2011 to 194.85.80.107. Redistribution subject to ASME license or copyright; see http://www.asme.org/terms/Terms_Use.cfm

1995 Max Jakob Award Lecture

G. F. Hewitt
Imperial College,
London, United Kingdom

In Search of Two-Phase Flow

1 Introduction

The objective I have set myself for this lecture is to take an overview of progress in the search for knowledge in two-phase flow over the past three and half decades, and to try to draw conclusions about future directions from this historical perspective. The famous English historian A. J. P. Taylor was fond of stating that history was purely for entertainment and that nobody ever drew any lessons from it. Nevertheless, this has not prevented many people from trying to draw such lessons, and I feel some trepidation in joining this throng!

Two-phase gas–liquid flow is of considerable importance in a whole range of applications. Starting in the 1950s, intensive studies of this area were made in the context of the nuclear industry. Although the nuclear industry work has declined, there is still a strong driving force with respect to other applications: for instance, the growing use of multiphase flow systems in offshore oil recovery. Two-phase flow is also important in heat and mass transfer systems, for example boilers and condensers, and thus finds its applications in the process and chemical industries, in refrigeration, air conditioning, and gas liquefaction. All of these industrial applications have led to research work in the area being widely supported and many tens of thousands of papers have been published. However, a generalized solution methodology for two-phase flow problems has remained an elusive goal, mainly because gas–liquid flow systems combine the complexities of turbulence with those of deformable interfaces. Some simplification of the problems can be obtained by dealing with specific flow regimes (bubble flow, slug flow, annular flow, etc.) but, even within a given regime, the flow behavior is complex and not susceptible to direct calculation. This has led to a variety of phenomenological models, which have been applied with varying degrees of success.

In the past three and half decades, I have been involved (directly or indirectly) in a very wide range of studies in two-phase flow and heat transfer. Rather than to try to cover the whole of this range of topics, I thought it best to select only two for examination, namely *flooding* and *disturbance waves in annular flow*. I have been involved in work on these two topics almost continuously over the past three and half decades; in neither case is the understanding of the phenomena complete and in both cases, work will be expected to continue into the far future. The subject of flooding is addressed in Section 2, and that of disturbance waves in Section 3. At the end of the lecture, in Section 4, I attempt to take an overview of the subject area, in the particular context of *predictions* I made in giving the DQ Kern Award Lecture at the 1981 US National Heat Transfer Conference.

2 Flooding

The phenomenon of flooding is illustrated in Fig. 1. Liquid is introduced around the periphery of a tube in which gas is flowing upward. At low gas flow rates, the liquid falls down as a thin film on the channel wall and the flow is *counter-current*. As the gas flow rate is increased, liquid begins to be carried above the injection point (Fig. 1(*b*)), and this is known as the *flooding point*. Beyond the flooding point, liquid is flowing upward above the injector in *co-current* flow while counter-current flow still occurs below the injector. At a high enough gas flow rate, all of the flow is upward co-current (Fig. 1(*e*)). If the gas flow is now decreased, then a point is reached (Fig. 1(*g*)) at which liquid begins for fall below the injector. This latter point is often referred to as the *flow reversal* condition.

Flooding is of considerable technological importance; it is a limiting condition for the operation of reflux condensers, it is a controlling mechanism for critical heat flux in closed-end channels, it limits the ingress of water in postulated loss-of-coolant accidents in nuclear reactors and, from a more fundamental point of view, it is the phenomenon that governs transition between slug and churn flows.

I did my first experiments on flooding in the early 1960s together with Graham Wallis, now at Dartmouth College (Hewitt and Wallis, 1963). The experiments were conducted with low-pressure air–water flow in a vertical 31.75 mm (1.25 inch) tube and the apparatus used is shown in Fig. 2. The air flowed through a long calming length before meeting the falling water film, which was introduced through a porous wall section and was extracted also through a similar section as shown. Thus, the experiments represented an attempt to have smoothest possible entrance and exit. Wallis (1961) had developed the following equation for the correlation of flooding:

$$\sqrt{U_G^*} + \sqrt{U_L^*} = C \tag{1}$$

where

$$U_G^* = U_G \sqrt{\frac{\rho_G}{gD(\rho_L - \rho_G)}} \tag{2}$$

$$U_L^* = U_L \sqrt{\frac{\rho_L}{gD(\rho_G - \rho_L)}} \tag{3}$$

In Eqs. (1)–(3), U_G and U_L are the superficial velocities of the gas and the liquid phases, ρ_G and ρ_L their densities, g the acceleration due to gravity and D the tube diameter. The constant C has values in the range 0.75–1. The data obtained using the apparatus shown in Fig. 2 are shown in Fig. 3. At high liquid flow rates, the correlation fitted the data with $C = 1$ and at lower liquid flow rates, the data were fitted with $C = 0.88$ with the points for decreasing flow at higher liquid flow rates also falling on this line.

The Wallis correlation (Eq. (1)) is perhaps the most widely used method of predicting flooding. However, when the data for flooding are plotted in terms of this correlation, there is a large scatter, as is indicated in Fig. 4, obtained by McQuillan (1985). Obviously, something is wrong! The main reason for the scatter is that of differences due to end conditions. Figure 5 shows a comparison of data obtained between two alternative

Contributed by the Heat Transfer Division and presented at the 30th National Heat Transfer Conference, Portland, Oregon, August 5–9, 1995. Manuscript received by the Heat Transfer Division August 28, 1995; revision received May 14, 1996. Keywords: Flow Instability, Multiphase Flows, Thin Film Flow. Associate Technical Editor: J. R. Howell.

Copyright © 1996 by ASME
Downloaded 11 Dec 2010 to 193.140.21.150. Redistribution subject to ASME license or copyright; see http://www.asme.org/terms/Terms_Use.cfm

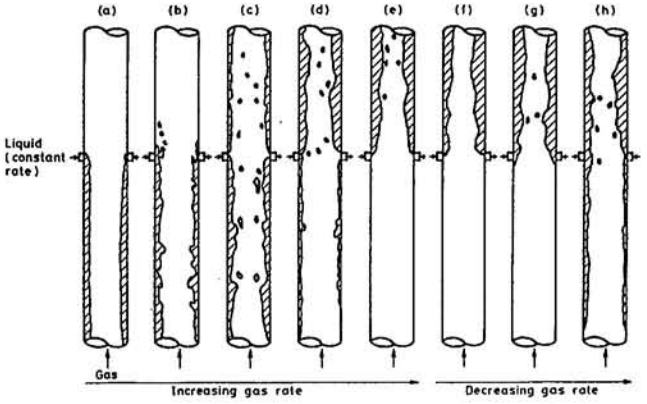


Fig. 1 Flooding and flow reversal in a tube

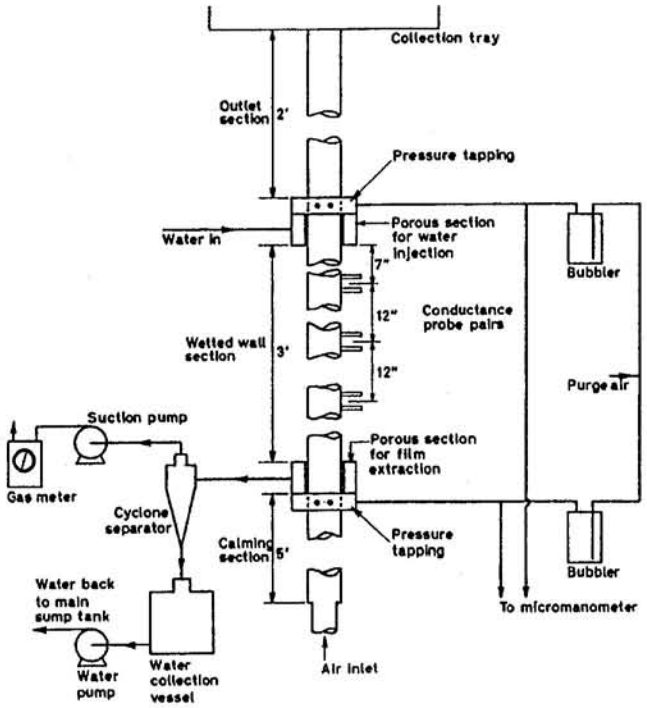


Fig. 2 Apparatus for studying flooding in a vertical 31.75 mm tube (Hewitt and Wallis, 1963)

end conditions. In Case 1, the conditions are similar to those shown in Fig. 2, where the water is introduced through a porous wall section and taken out through a similar section, with fully developed air flow at the point where the two phases meet. In Case 2 (Hewitt, 1977), there is a sharp end to the tube and the air enters from a plenum as shown in Fig. 5. The flooding

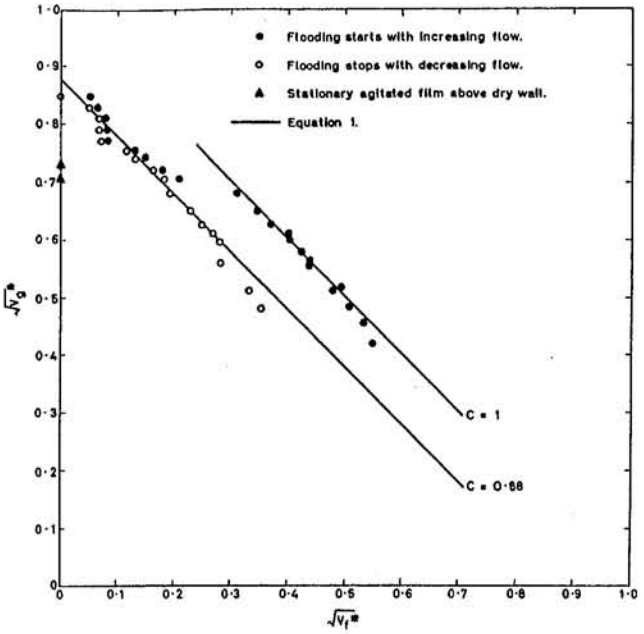


Fig. 3 Dimensionless plot of results obtained for flooding by Hewitt and Wallis (1963)

velocities for Case 1 are much higher than for Case 2 and decrease with increasing length (Hewitt et al., 1965). For Case 2, the flooding velocities are much lower but are not sensitive to the length of the tube (see Fig. 5).

The importance of the flooding phenomenon has led to a considerable body of fundamental work on the mechanisms for its occurrance. Visualization studies of the flooding process are reported, for instance, by McQuillan et al. (1985) who used two alternative techniques of visualization:

1 The multicolor axial view system shown in Fig. 6. Here, the porous wall in/porous wall out system was used (see Fig. 2) and various colored plastic material was wrapped around the (transparent) tube, which was illuminated both by axial view and also by side illumination. Briefly, the axial view gives information on the motions of the liquid in the cross-sectional plane and the side illumination gives an indication of the location of a particular liquid element (wave or drop) in the axial direction.

2 Side view visualization in a converging–diverging channel. Here, the test section was in the form of an annulus (Fig. 7) with the falling liquid film formed on the inner surface and with the outer surface shaped such that the gas accelerates and then decelerates in its flow over the liquid film. This allows the occurrence of the flooding mechanism to be observed at a position remote from the ends.

These visualization methods gave similar results, as illustrated in Figs. 8 and 9, respectively. Toward the liquid outlet

Nomenclature

a = constant in Eq. (7), volt^2
b = constant in Eq. (7), volts^2/(N/m^2)
C = constant in Eq. (1)
D = tube diameter, m
g = acceleration due to gravity, m^2/s
Ku_G = Kutateladse number for gas phase (Eq. (4))
Ku_L = Kutateladse number for liquid phase (Eq. (6))
U_G = gas phase superficial velocity, m/s
U_{GK} = gas velocity for flooding calculated from Eq. (5), m/s
U_{GWT} = gas velocity required for upward wave transport, m/s
U_G^* = gas phase dimensionless velocity (Eq. (2))
U_L = liquid phase superficial velocity, m/s
U_L^* = liquid phase dimensionless velocity (Eq. (3))
γ_o = wall shear stress, N/m^2
ρ_G = gas phase density, kg/m^3
ρ_L = liquid phase density, kg/m^3
σ = surface tension, N/m

Downloaded 11 Dec 2010 to 193.140.21.150. Redistribution subject to ASME license or copyright; see http://www.asme.org/terms/Terms_Use.cfm

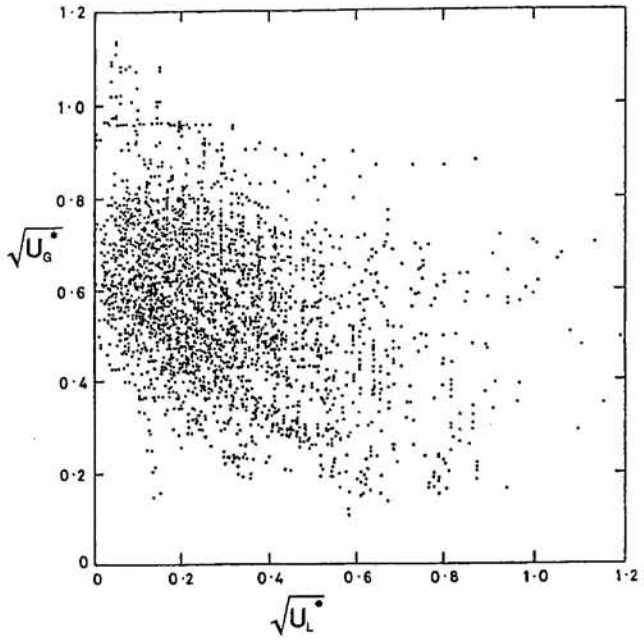


Fig. 4 Literature data on flooding plotted in terms of the Wallis parameter (McQuillan, 1963)

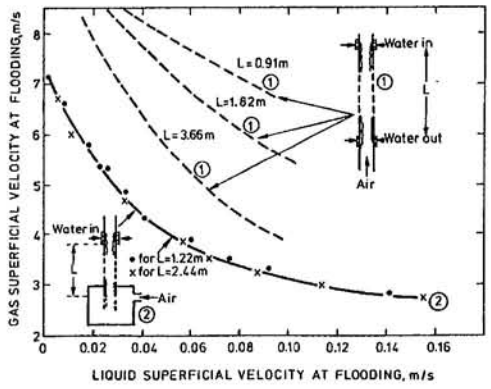


Fig. 5 Effect of end conditions on flooding velocity

end of the test section, large waves begin to grow on the falling film as the flooding point is approached. Ultimately, one of these large waves is arrested by the gas flow and then grows

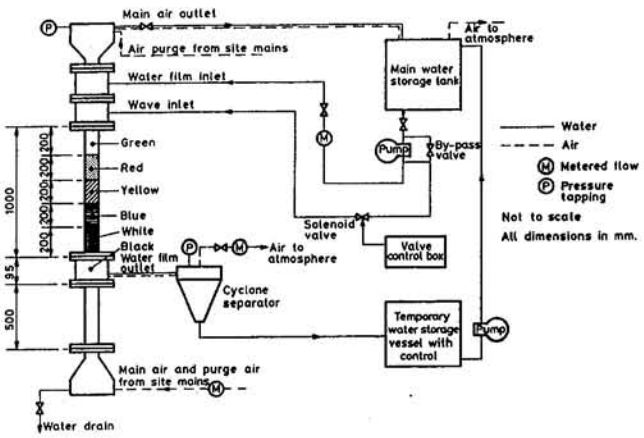


Fig. 6 Axial view with combined axial and side illumination for the visualization of flooding (McQuillan et al., 1985)

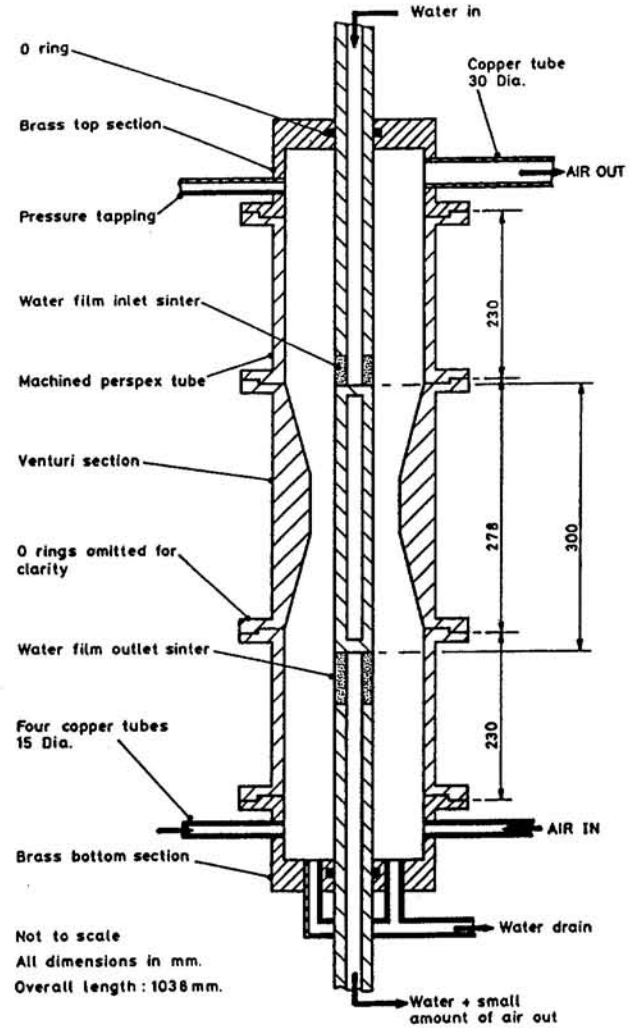


Fig. 7 Converging, diverging annular channel used in visualization of flooding (McQuillan et al., 1985)

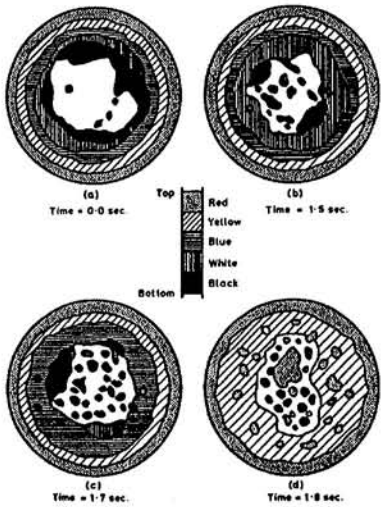


Fig. 8 Sequence of events observed in axial view visualization of flooding (McQuillan et al., 1985)

Downloaded 11 Dec 2010 to 193.140.21.150. Redistribution subject to ASME license or copyright; see http://www.asme.org/terms/Terms_Use.cfm

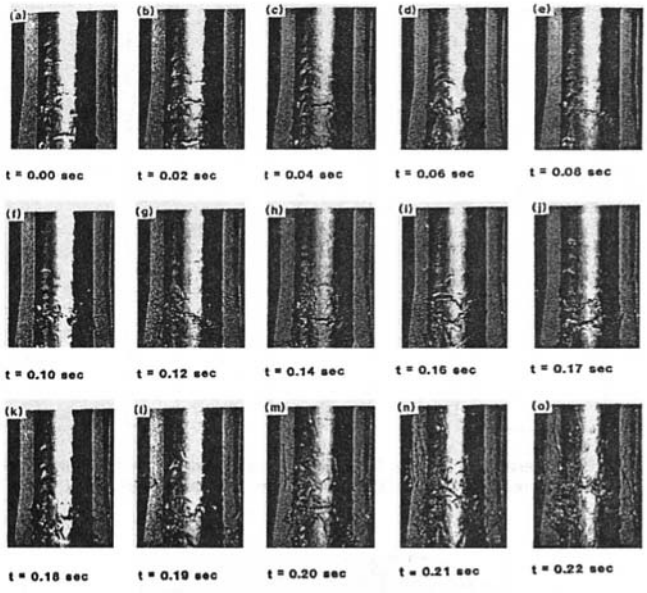


Fig. 9 Sequence of event observed in visualization of flooding in a converging/diverging channel (McQuillan et al., 1985)

rapidly by accretion of other waves falling into it. The wave is then transported upward beyond the liquid injector, this being a manifestation of the flooding event.

In the late 1970s and 1980s, a quite different view of the flooding phenomena was beginning to be developed by Prof. Abe Dukler and co-workers at the University of Houston (Dukler and Smith, 1979; Dukler et al., 1984; Zabaras and Dukler, 1988). Incidentally, I had known of Prof. Dukler's work during my Ph.D. studies in 1957 and, later, became a friend when I got to know him in the early 1960s and when he came to the Harwell Laboratory in England for a sabbatical year in 1967. His untimely death on 12th February 1994 was a great sadness to me and to many people; he was a very enthusiastic and inspiring person, always deeply interested in multiphase flow and always stimulating and inventive. Prof. Dukler and his team took careful measurements of the interfacial wave structure and concluded that the waves continued to flow downward after flooding and that there was no sign of the wave reversal effect discussed above. Rather, they concluded that the flooding event was manifested by droplet entrainment from the lower part of the tube, the droplets penetrating above the injector and wetting the wall there. In the experiments at Houston, the gas entry (liquid exit) was via a bell-mouth section and this, of course, is different in form to that used in the Harwell experiments where a porous extraction system was used at the exit, allowing the gas flow to be fully developed before it met the liquid. In order to elucidate the mechanisms, we carried out a series of experiments in which we compared bell-mouthed, sharp-edged, and porous exits (Govan, 1990; Govan et al., 1991). The results are shown in Fig. 10. As will be seen, the results for the bell-mouthed gas entrance (liquid exit) lie well below those for the porous wall system, but higher than those for a square-edged outlet. It was concluded, therefore, that the Houston experiments were a special case and the only differences could be ascribed to end effects. The matter seemed to be closed!

The anomaly in interpretation of the flooding mechanism appeared again, however, as a result of some experiments carried out at the Centre d'Etudes Nucleaires de Grenoble (Biage, 1989; Biage et al., 1989). Experiments were carried out in a two-dimensional channel as illustrated in Fig. 11. Here, a falling film was formed on one wall of a 25 × 250 mm cross-sectional channel and porous wall injection and extraction was employed.

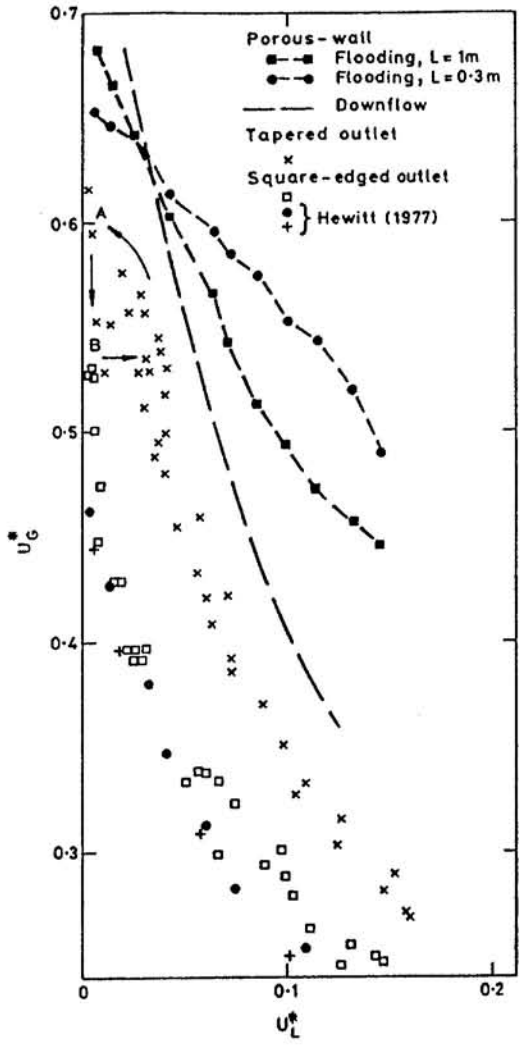


Fig. 10 Comparison of bell-mouth and porous wall and sharp-edge inlet for flooding (Govan, 1990; Govan et al., 1991)

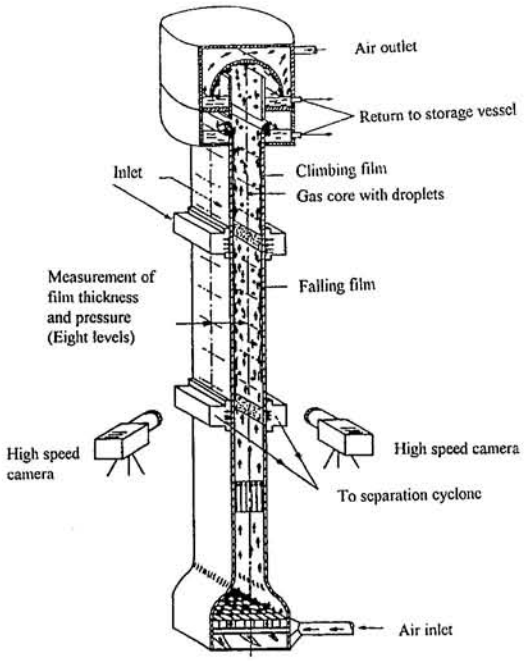


Fig. 11 Experimental rig used in flooding experiments of Biage (1989)

Downloaded 11 Dec 2010 to 193.140.21.150. Redistribution subject to ASME license or copyright; see http://www.asme.org/terms/Terms_Use.cfm

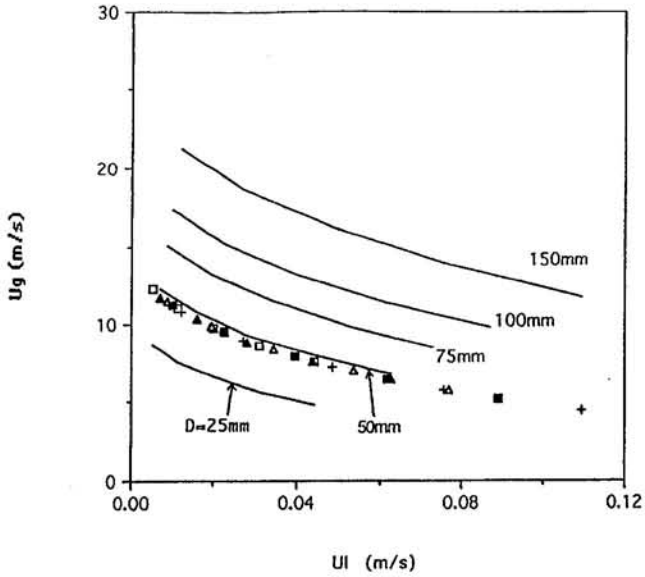


Fig. 12 Comparison of flooding velocities predicted from Eq. (1) (lines) and Eq. (5) (points) for a range of tube diameters (Jayanti et al., 1994)

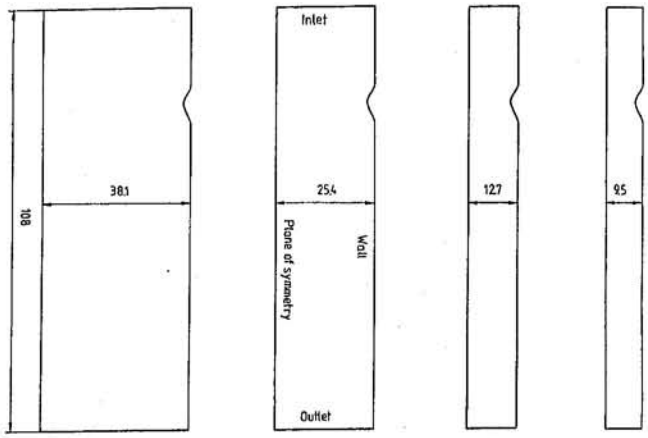


Fig. 13 Interaction of gas flow and flooding wave: two-dimensional channel geometries used in CFD calculation (Jayanti et al., 1994)

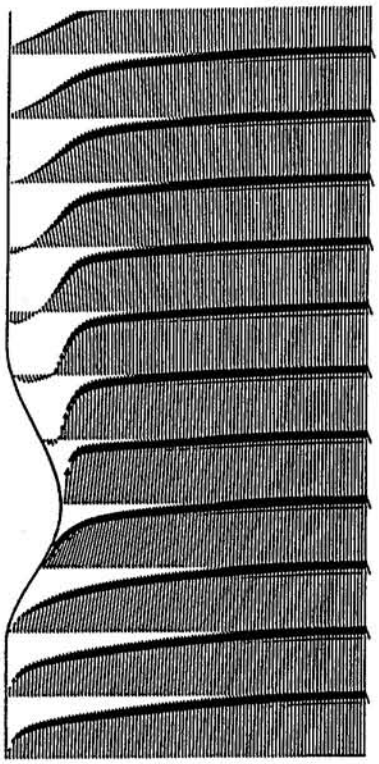


Fig. 14 Velocity vectors in flow over a flooding wave (Jayanti et al., 1994)

It was found that, in these experiments, flooding was not associated with single wave transport and that droplet entrainment from standing waves near the inlet occurred before such transport, consistent with the finding from the Houston experiments! Thus, the anomaly continued!

Some clue as to the explanation for the anomaly actually appears by comparing some correlations for flooding, which appeared in the earlier literature. Pushkina and Sorokin (1969) suggested that flooding should be correlated in terms of the Kutateladse number (Ku_G) for the gas phase as follows:

$$Ku_G = U_G \rho_G^{1/2} [g\sigma(\rho_L - \rho_G)]^{-1/4} = 3.2 \qquad (4)$$

where σ is the surface tension. The use of the Kutateladse number has been further developed by Sun (1979), Bradford and Simpson (1987), and Kokkenen and Tuomisto (1990).

More recent correlations take account of the effect of the liquid phase through equations of the form:

$$\sqrt{Ku_G} + \sqrt{Ku_L} = 1.79 \qquad (5)$$

where

$$Ku_L = U_L \rho_L^{1/2} [g\sigma(\rho_L - \rho_G)]^{-1/4} \qquad (6)$$

Equation (5) reduces to Eq. (4) for zero liquid flow rate.

It will be noted that the tube diameter is included in Eq. (1) and not in Eq. (5). Figure 12 shows a comparison of predictions from the two equations for air–water flows over a range of diameters from 25 to 150 mm. As will be seen, the Wallis equation predicts that the gas velocity required for flooding will increase continuously with tube diameter at a constant liquid velocity. Equation (5), on the other hand, predicts no change with diameter, the two equations giving around the same values for tubes of 50 mm diameter. Thus, we see that there may be a change in behavior at around this diameter and this has led us to investigate gas–liquid interactions using computational fluid dynamics (CFD). Using information about the shape of the standing wave formed prior to flooding (Shearer and Davidson, 1965), the flow over such waves was simulated using the CFDS-FLOW3D code. The simulation was two dimensional with various channel half-widths as illustrated in Fig. 13. Details are given by Jayanti et al. (1994). Figure 14 shows a typical set of velocity contours calculated, indicating the recirculation behind the wave as expected.

The forces on the wave comprise shear forces summed over the interface (shear is enhanced as a result of the presence of the wave) and body forces, which arise from the resolved component of the normal stress (pressure) over the wave. The wave can be levitated when the sum of these forces exceeds the gravitational force on the wave. Table 1 shows the results

Table 1 Forces on flooding wave (Jayanti et al., 1994)

Channel height 2h (mm)	Gas velocity U (m/s)	Pressure force on wave (N/m)	Shear force on wave (N/m)	Total force (Fg) on wave (N/m)
19	9.3	0.0727	0.0183	0.0910
25.4	9.3	0.0597	0.0169	0.0766
25.4	6.3	0.0268	0.0083	0.0351
50.8	6.3	0.0173	0.0077	0.0250
76.2	6.3	0.0155	0.0069	0.0224

Downloaded 11 Dec 2010 to 193.140.21.150. Redistribution subject to ASME license or copyright; see http://www.asme.org/terms/Terms_Use.cfm

Table 2 Comparison of gas velocity required for wave transport (U_{GWT}) with gas velocity (U_{GK}) calculated from Eq. (5)

	U_{GWT} / U_{GK}			
	Channel half-width			
U_L^*	0.25	0.50	0.75	0.10
0.15	0.52	0.78	1.05	1.19
0.2	0.67	1.07	1.33	1.67
0.25	0.85	1.33	1.67	2.07

of the calculation; as will be seen, the pressure force is much greater than the shear force but the force decreases with channel size for a given gas velocity. One can see, therefore, that there are essentially two alternative mechanisms for gas–liquid interaction:

1 Wave transport. Here, the force on the wave exceeds the gravity force on the wave.
2 Breakup of the standing waves near the bottom of the channel leading to droplet entrainment and droplet transport beyond the injector.

The first mechanism would be favored by small-diameter channels whereas the second mechanism would occur in larger diameter channels. If we regard Eq. (5) as giving an indication of the velocities required for the second mechanism, we can calculate the ratio of this velocity (U_{GK}) with that calculated to be necessary to transport the waves as a result of the forces exerted on them (U_{GWT}).

Table 2 shows the results as a function of U_L^* and channel half-width. The ratio begins to exceed unity as the channel width increases and as U_L^* increases. The results are consistent with the experimental observations.

Thus, we see that *both* main suggested mechanisms for flooding are feasible, one operating for small-diameter pipes and the other for large-diameter pipes. Although the CFD calculations would not necessarily give accurate answers, this example illustrates the usefulness of CFD in elucidating mechanisms.

3 Disturbance Waves in Annular Flow

Disturbance waves are the most predominant feature of annular two-phase gas–liquid flow. Visually, they appear as "milky" regions, which progress along the channel at a constant velocity and whose extent is of the order of the channel diameter (see Fig. 15).

These waves have a dominant role in friction and heat transfer in the channel and are the source of entrained droplets. Thus, understanding the behavior of the waves is a key to understanding the annular flow region, which itself is very important in most commercial evaporators and condensers and in many other applications of two-phase flow.



Fig. 15 Disturbance waves in annular flow (Hewitt and Lovegrove, 1969)

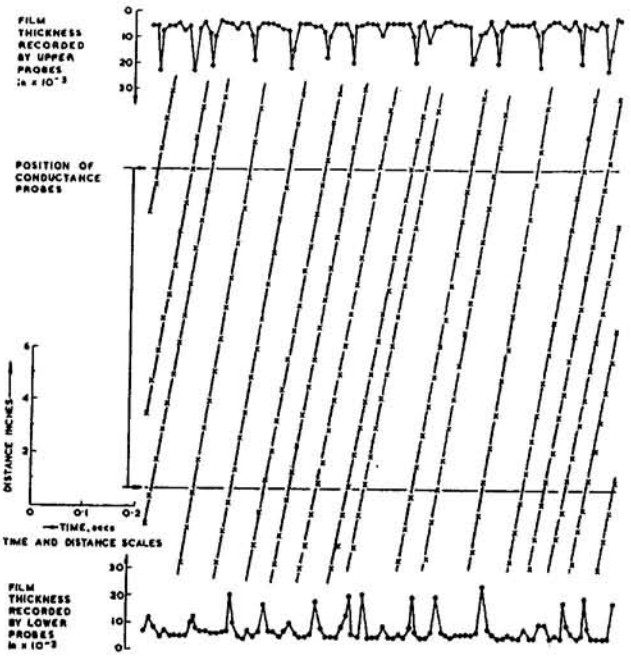


Fig. 16 Tracks of disturbance waves in air–water annular flow (Hewitt and Lovegrove, 1969)

Starting in the early 1960s (Hall-Taylor and Hewitt, 1962), a great deal of effort at Harwell and elsewhere was put into determining the characteristics of disturbance waves (velocities, frequencies, etc.). Commonly, visual methods (high-speed photography) were employed coupled with film thickness measurements made by flush-mounted conductance probes and other devices. Figure 16 shows plots of position (taken from high-speed cine film) and of conductance probe responses for the waves. As will be seen, the waves are characterized by a peak in the liquid film thickness and have a continuous existence along the channel. Their spacing is apparently random. The conductance probe method is incapable of making highly localized measurements and, to obtain an indication of the true shape of the wave, it is better to use the fluorescence method (Hewitt et al., 1965), which is illustrated in Fig. 17. Blue light from a mercury vapor lamp excites a green glow in a fluorescene dye-

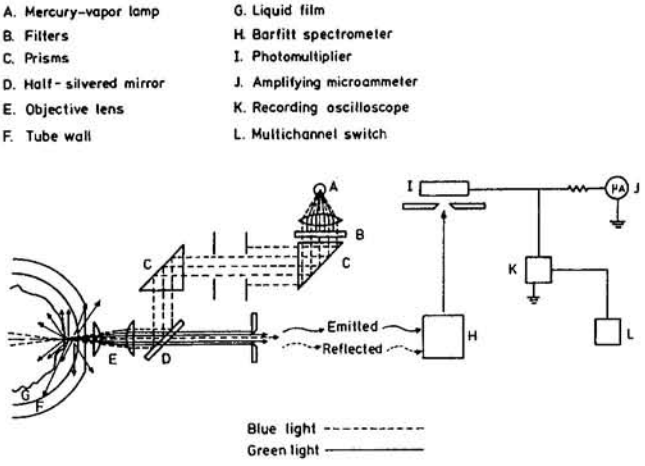


Fig. 17 Fluorescence method for measurement of liquid film thickness (Hewitt et al., 1969)

Downloaded 11 Dec 2010 to 193.140.21.150. Redistribution subject to ASME license or copyright; see http://www.asme.org/terms/Terms_Use.cfm

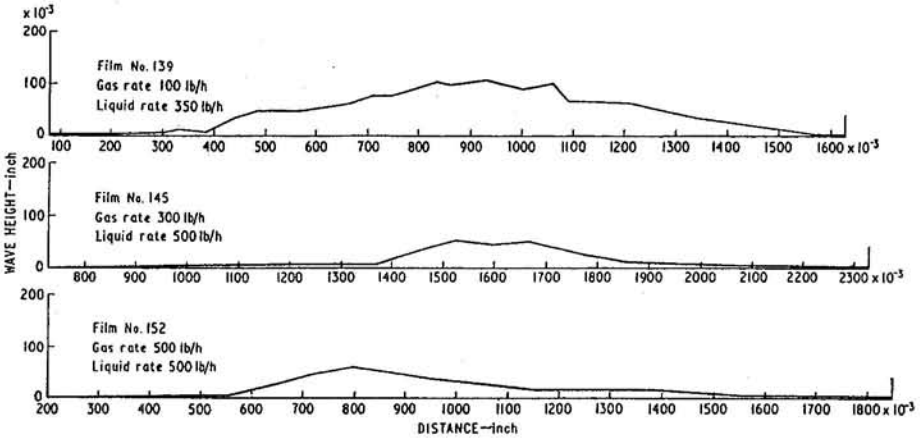


Fig. 18 Typical shapes of disturbance waves in a 31.7 mm tube (Hewitt and Nicholls, 1969)

stuff dissolved in the liquid film. The intensity of the glow is a function of the film thickness. By making point film thickness measurements using the fluorescence technique and coupling this with measurements of velocity, the shapes of the waves may be determined and typical results are shown in Fig. 18. The disturbance waves are around five times the mean film thickness in height.

The link between disturbance waves and liquid entrainment can be established using a variety of techniques, perhaps the most graphic one being the use of axial view photography. A system for using a parallel laser beam passing through the tube is illustrated in Fig. 19 (Hewitt and Whalley, 1980).

Using such techniques, it is possible to observe the breakup of the disturbance waves into droplets; basically, there are two forms of breakup, namely *ligament breakup* and *bag breakup.* In ligament breakup, ligaments are torn from the tips of the disturbance waves and break up into small droplets in the gas core. In bag breakup, the disturbance waves are undercut forming large open-ended bubbles near the wall. These bubbles break up, with their rim being the source of large droplets with rapid radial motion.

For such an interesting phenomenon, it is perhaps surprising that our knowledge of its precise source is somewhat obscure. In annular flows close to the transition to churn flows, the waves occur over the full range of liquid velocities and are probably related to the flooding waves referred to in Section 2 above. However, when the gas flow is high enough, the waves only exist above a certain critical liquid flow rate or liquid film Reynolds number. Below this critical value, any waves artificially introduced into the system are damped out. Figure 20 shows the results obtained by Hall-Taylor and Hewitt (1962) for these various regions.

The fact there appears to be a critical Reynolds number for the onset of disturbance waves suggests a link between such

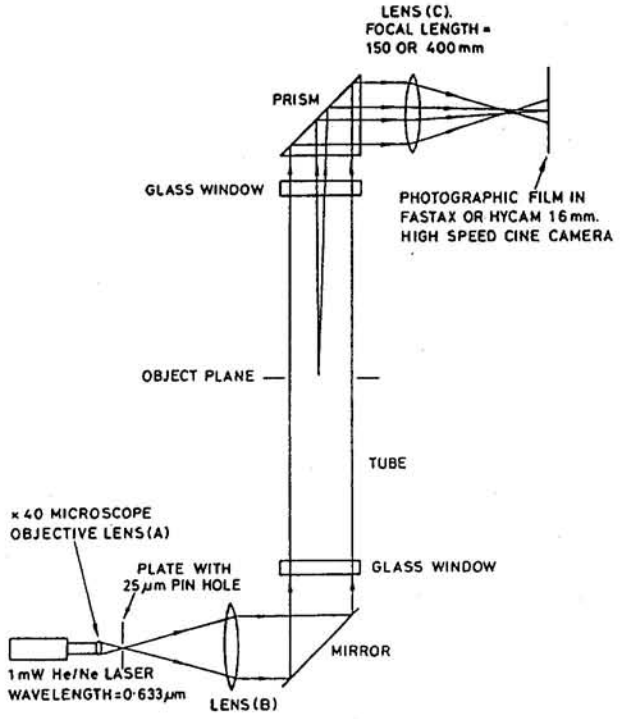


Fig. 19 Laser axial view system for annular flow (Hewitt and Whalley, 1980)

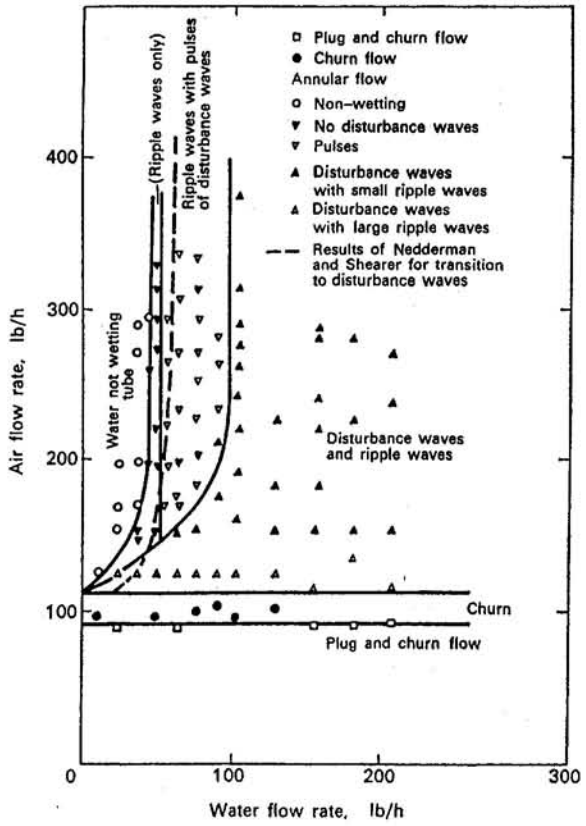


Fig. 20 Regions of occurrence of disturbance waves (Hall-Taylor and Hewitt, 1962)

Downloaded 11 Dec 2010 to 193.140.21.150. Redistribution subject to ASME license or copyright; see http://www.asme.org/terms/Terms_Use.cfm

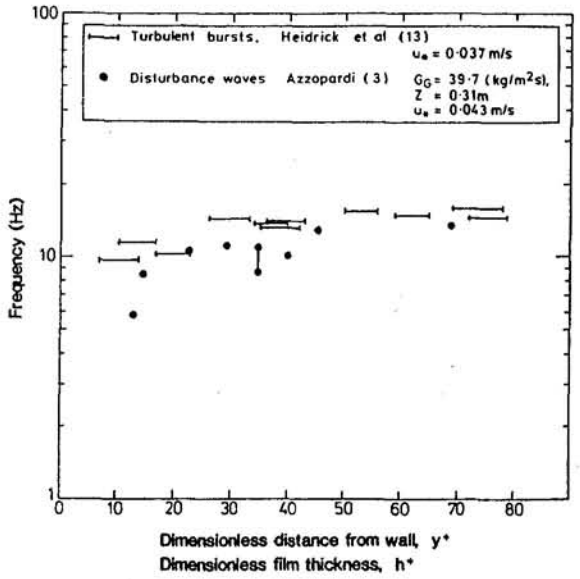


Fig. 21 Comparison of initial disturbance wave frequencies with turbulent burst frequency data of Heidrick et al. (1977) and Martin and Azzopardi (1985)

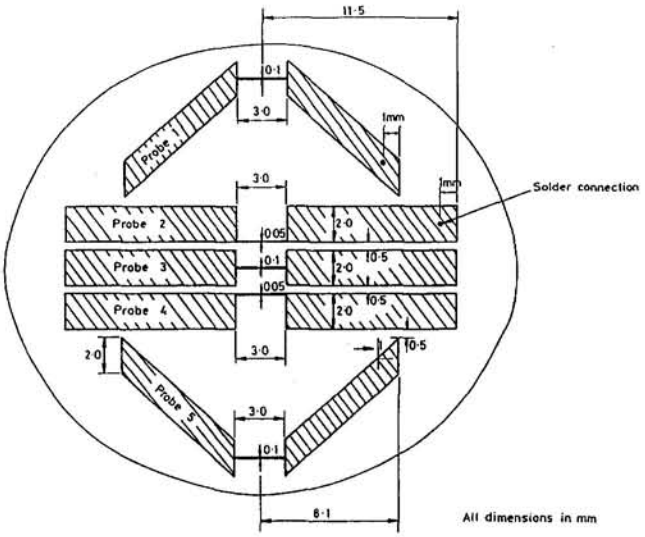


Fig. 23 Hot-film probes for measurement of wall shear stress (Martin, 1982)

waves and turbulence. Some intriguing evidence relating to this possible link was obtained by Martin and Azzopardi (1985) and is shown in Figs. 21 and 22. The *initial* wave frequency (i.e., just above the liquid injection point) seems to be close to the frequency of turbulent bursts measured in a liquid flow at the same value of dimensionless distance from the wall (y^+) (Fig. 21). From this initial frequency, the disturbance waves coalesce to some extent and reach an asymptotic frequency, which is much lower (Fig. 22). This turbulence mechanism for the onset of the disturbance waves needs much further investigation.

As was mentioned above, there is a strong link between disturbance waves and the wall friction. This can be demonstrated by making measurements of instantaneous wall shear stress using the hot film technique. This was done at Harwell by Martin (1982) using the vapor-deposited probe system shown in Fig. 23.

The central probe (probe 3) is maintained at a constant temperature using a standard hot-wire anemometer circuit. The voltage (V) applied to the probe is then related to wall shear stress (τ_o) by the equation:

$$V^2 = a + b\tau_o^{1/3} \tag{7}$$

where the constants a and b are determined by calibration. The system shown in Fig. 23 could be used for measuring the direction of flow near the wall by employing probes 4 and 2 as temperature sensors, sensing the hot fluid arising from the hot-film probe. This was particularly useful in studying flows where there were flow reversals such as vertical pipe flow. Results for wall shear stress measurements are shown in Fig. 24. Simultaneous local measurements were made of film thickness using a conductance probe and it will be seen that the wall shear stress and the film thickness are strongly coupled, indicating the very large effect of disturbance waves on the shear stress and, thus, wall friction. In very recent experiments by Wolf (1995) at

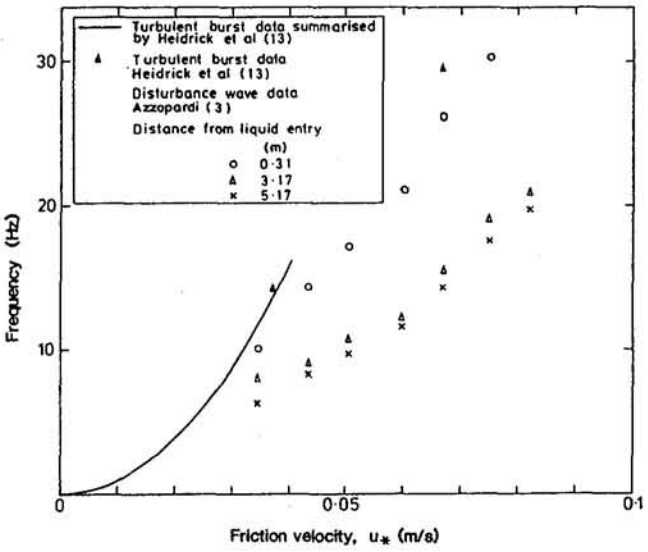


Fig. 22 Development of disturbance wave frequency downstream of injector (Martin and Azzopardi, 1985)

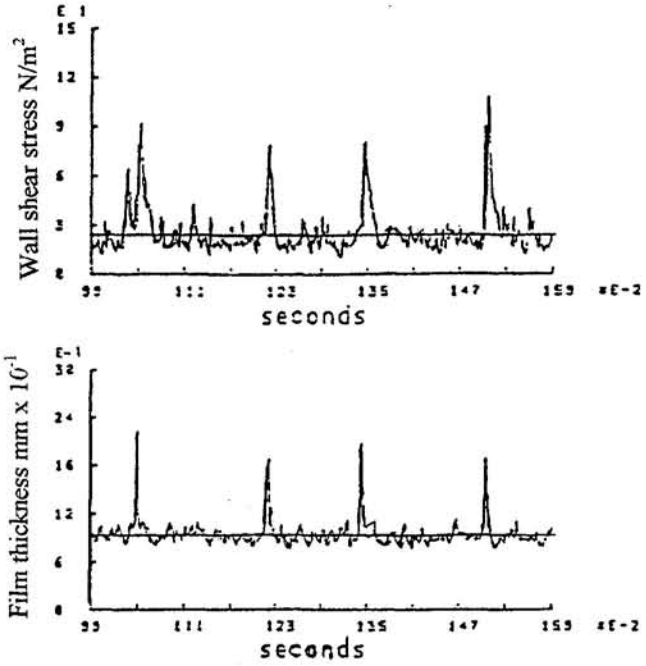


Fig. 24 Simultaneous film thickness and wall shear stress measurements (Martin, 1982)

Downloaded 11 Dec 2010 to 193.140.21.150. Redistribution subject to ASME license or copyright; see http://www.asme.org/terms/Terms_Use.cfm

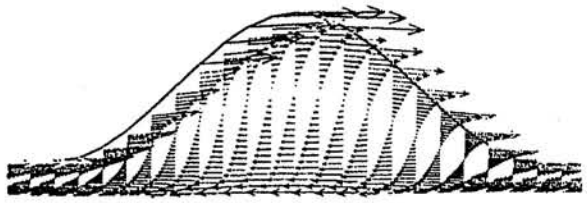


Fig. 25 Predicted velocity vectors in wave using low Reynolds number $k-\epsilon$ model (Jayanti and Hewitt, 1994)

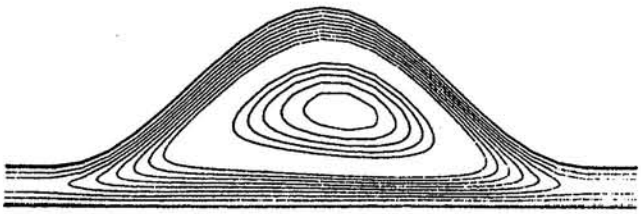


Fig. 26 Turbulent viscosity distribution in disturbance wave calculated using standard $k-\epsilon$ model (Jayanti and Hewitt, 1994)

Imperial College, it has been shown that a small but significant lag between the peak of shear stress and the peak of film thickness occurs in this system.

Some insight into the behavior of the disturbance waves may be obtained using CFD methods; work in this direction is reported by Jayanti and Hewitt (1994). A typical disturbance wave was chosen for study that had a disturbance wave region of 20 mm followed by a substrate film region of 80 mm in length. The disturbance wave was assumed to be of sinusoidal shape in its region of influence with a maximum amplitude of 0.75 mm, namely five times the assumed substrate thickness of 0.15 mm. The gas velocity was assumed to be 50 m/s and the shear stress in the disturbance wave region was calculated by making the assumption (consistent with data) that the interfacial roughness in this region was five times the film thickness. In the substrate region, the correlation of Shearer and Nedderman (1965) for subcritical films (i.e., those without disturbance waves) was employed to give an interfacial friction factor and hence an interfacial shear stress. Two forms of turbulence model were used, namely the standard $k-\epsilon$ model and a low-Reynolds-number $k-\epsilon$ model due to Jones and Launder (1972). The latter can take account of damping of the turbulence in the near-wall and near-interface regions.

Figure 25 shows the predicted velocity vectors within the disturbance wave (note that, for convenience, the longitudinal scale has been relatively foreshortened!). As will be seen, the disturbance wave region is one of a recirculatory flow. Figures 26 and 27 show the turbulent viscosity distributions calculated using the standard and low-Reynolds-number $k-\epsilon$ models, respectively. With the latter model, the turbulence is restricted to the wave region, the substrate being essential laminar. Thus, one can picture the disturbance waves as being circulating zones of turbulence traveling over a laminar substrate film.

Heat transfer is clearly strongly influenced by the disturbance waves and Fig. 26 shows calculations of the temperature distribution in the disturbance wave for a fixed heat flux and a fixed interface temperature. Note how the isotherms are distorted by the presence of the circulation within the wave. Figure 28 shows values of temperature difference and shear stress, respectively, obtained from the CFD calculations. As expected, the heat transfer is improved during the passage of the disturbance wave (ΔT falls) and the shear stress increases. The mean heat transfer coefficient for the low-Reynolds-number $k-\epsilon$ model is around 30 percent higher than that for laminar flow and around a factor of 6 lower than that calculated using the standard $k-\epsilon$ model, which does not include interface damping. If one takes average shear stress at the interface and uses a one-dimensional analysis, again without damping, then the heat transfer coefficients calculated are around two and half times that estimated from the low-Reynolds-number $k-\epsilon$ model but are in themselves around 50 percent higher than the experimental values, which are more consistent with the predictions from the low-Reynolds-number $k-\epsilon$ model.

Although one should not claim that such calculations can achieve a high degree of accuracy at the present time, at least they give an indication of the flow mechanism and are producing results for heat transfer coefficient that are in reasonable agreement with the observations.

It will be seen, therefore, that, gradually, a picture of disturbance waves is beginning to emerge that is reasonably consistent with experimental observations on both hydrodynamics and heat transfer. Again, the availability of modern CFD tools has been extremely valuable in elucidating the mechanisms.

4 Overview and Conclusions

I was invited to give the Donald Q. Kern Lecture at the 1981 US National Heat Transfer Conference (see Hewitt, 1982). The lecture was concerned with the prospects for understanding and modeling multiphase systems and I made a number of predictions about what might happen in the years to come! This is always a dangerous exercise, but I thought it might be interesting, in concluding this present lecture, to see how well (or how badly!) I did in predicting the future! My predictions and my current estimate of their outcome are given as follows:

1 *"There will be an increase in detailed observation and measurement of local parameters using modern instrumentation techniques."* The effort peaked in the 1980s and then decreased but has, fortunately, continued as a smaller activity in a number of groups. The decrease reflected the reduction in funding from the nuclear industry but the continuing importance of the two-phase flow area is leading to continued funding at a lower level. It would certainly not be good to reduce the effort in this area further and perhaps international collaboration would be the best way forward.

2 *". . . more and better phenomenological models will be developed."* It is true that this has happened, but *generalized* constitutive relationships (e.g., for interfacial friction and mass transfer) have proved an elusive goal.

3 *"Increasingly, the improved models will be applied in the design process."* Actually, the penetration has been less than

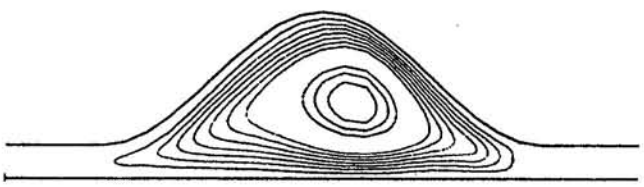


Fig. 27 Turbulent viscosity distribution in disturbance wave calculated using low-Reynolds-number $k-\epsilon$ model (Jayanti and Hewitt, 1994)

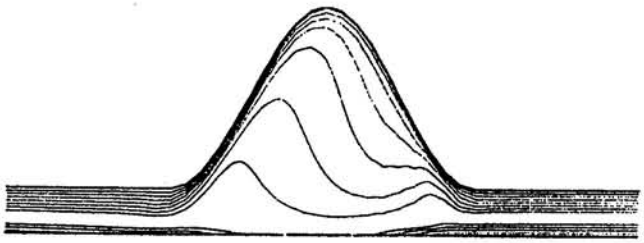


Fig. 28 Temperature contours in a disturbance wave calculated using the low-Reynolds-number $k-\epsilon$ model (Jayanti and Hewitt, 1994)

Downloaded 11 Dec 2010 to 193.140.21.150. Redistribution subject to ASME license or copyright; see http://www.asme.org/terms/Terms_Use.cfm

I would have anticipated (even taking account of the research worker's undying optimism) though there are some good examples of the use of more phenomenological modeling, particularly in the oil industry.

4 *"There will be a gradual phasing out of the empirical approach, though, if we are realistic, this is likely to take many years, and perhaps tens of years."* Empirical models are still the norm in industry and one would have been right to be realistic!

5 *"There will be a consolidation of the analytical and phenomenological approaches."* This has certainly been true to some extent. The most important change in the field is the availability of computational fluid dynamics (CFD) methods. These methods are extremely useful in developing *understanding* of the phenomena.

Thus, my overall conclusions are as follows:

1 Two-phase flow remains a fascinating subject with many surprises.
2 CFD techniques provide new means of addressing phenomenological issues, which should not yet be taken too literally as a predictive tool.
3 Good experimental design and modern instrumentation will make an increasing impact.
4 The search goes on!

References

Biage, M., 1989, "Structure de la surface libre d'un film liquide ruisselant sur une plaque plane verticale et soumis à un contrecourant de gaz; transition vers l'écoulement cocourant ascendant," Ph.D. Thesis, Institut National Polytechnique de Grenoble, Grenoble, France.

Biage, M., Delhaye, J. M., and Vernier, Ph., 1989, "The Flooding Transition: a Detailed Experimental Investigation of the Liquid Film Before the Flooding Point," *Proc. ANS. National Heat Transfer Conference,* pp. 53–60.

Bradford, A. M., and Simpson, H. C., 1987, "Penetration Effects Arising From Simulated Hot-Leg Injection in a 1/10 Scale PWR Test Facility," presented at the European Two-Phase Flow Group Meeting, Trondheim, Norway, Paper No. A4.

Dukler, A. E., and Smith, L., 1979, "Two-Phase Flow Interaction in Countercurrent Flow: Studies of the Flooding Mechanism," Annual Report, Nov. 1985–Oct. 1986, US Nuclear Regulatory Commission, Washington. Report NUREG/CR-0617.

Dukler, A. E., Smith, L., and Copra, A., 1984, "Flooding and Upward Film Flow in Tubes. I. Experimental Studies," *Int. J. Multiphase Flow,* Vol. 10, pp. 585–597.

Govan, A. H., 1990, "Modelling of Vertical Annular and Dispersed Two-Phase Flows," Ph.D. Thesis, University of London.

Govan, A. H., Hewitt, G. F., Richter, H. J., and Scott, A., 1991, "Flooding and Churn Flow in Vertical Pipes," *Int. J. Multiphase Flow,* Vol. 17, pp. 27–44.

Hall-Taylor, N., and Hewitt, G. F., 1962, "The Motion and Frequency of Large Disturbance Waves in Annular Two-Phase Flow of Air–Water Mixtures," UKAEA Report No. AERE-R3952.

Heidrick, T. R., Banerjee, S., and Azad, R. S., 1977, "Experiments on the Structure of Turbulence in Fully Developed Pipe Flow. Part 2. A Statistical Procedure for Identifying "Bursts" in the Wall Layers and Some Characteristics of Flow During Bursting Periods," *J. Fluid Mech.,* Vol. 82, p. 705.

Hewitt, G. F., and Wallis, G. B., 1963, "Flooding and Associated Phenomena in Falling Film Flow in a Tube," UKAEA Report No. AERE-R4022.

Hewitt, G. F., Lacey, P. M. C., and Nicholls, B., 1965, "Transitions in Film Flow in a Vertical Tube," presented at Symposium on Two-Phase Flow, Exeter, June 1965 (*Proceedings,* Vol. 2, paper B4); see also UKAEA Report No. AERE-R4616.

Hewitt, G. F., and Lovegrove, P. C., 1969, "Frequency and Velocity Measurements of Disturbance Waves in Annular Two-Phase Flow," UKAEA Report No. AERE-R4304.

Hewitt, G. F., 1977, "Influence of End Conditions, Tube Inclination and Fluid Physical Properties on Flooding in Gas-Liquid Flows," UKAEA Report No. HTFS-RS222.

Hewitt, G. F., and Whalley, P. B., 1980, "Advanced Optical Instrumentation Methods," *Int. J. Multiphase Flow,* Vol. 6, pp. 139–156.

Hewitt, G. F., 1982, "Applications of Two-Phase Flow," *Chemical Engineering Progress,* July. pp. 38–46.

Jayanti, S., and Hewitt, G. F., 1994, "Hydrodynamics and Heat Transfer in Wavy Annular Gas-Liquid Flow: A CFD Study," Multiphase Flow Systems Programme Report MPS/59; accepted for publication in *International Journal of Heat and Mass Transfer.*

Jayanti, S., Tokarz, A., and Hewitt, G. F., 1994, "Gas Flow Over Large Waves. Part 2: Investigation of the Diameter Effect on Flooding in Counter-current Flow," Multiphase Flow Systems Programme, Imperial College, Report MPS/56; *Int. J. Multiphase Flow,* Vol. 22, pp. 307–324.

Jones, W. P., and Launder, B. E., 1972, "The Prediction of Laminarisation With a Two-Equation Model of Turbulence," *Int. J. Heat Mass Transfer,* Vol. 15, pp. 301–314.

Kokkonen, J., and Tuimisto, H., 1990, "Air/Water Countercurrent Flow Limitation Experiments With Full-Scale Fuel Bundle Structures," *Exp. Thermal Fluid Science,* Vol. 3, pp. 581–587.

Martin, C. J., and Azzopardi, B. J., 1985, "Waves in Vertical Annular Flow," *Physico-Chemical Hydrodynamics,* Vol. 6, pp. 257–266.

Martin, C. J., 1982, "Annular Two-Phase Flow," Ph.D. Thesis, Oxford University.

McQuillan, K. W., 1985, "Flooding in Annular Two-Phase Flow," Ph.D. Thesis, University of Oxford.

McQuillan, K. W., Whalley, P. B., and Hewitt, G. F., 1985, "Flooding in Vertical Two-Phase Flow," *Int. J. Multiphase Flow,* Vol. 11, pp. 741–760.

Pushkina, O. I., and Sorokin, Y. L., 1969, "Breakdown of Liquid Film Motion in Vertical Tubes," *Heat Transfer—Soviet Res.,* Vol. 1, pp. 56–68.

Shearer, C. J., and Davidson, J. F., 1965, "The Investigation of a Standing Wave Due to Gas Blowing Upwards Over a Liquid Film; Its Relation to Flooding in Wetted Wall Columns," *J. Fluid Mech.,* Vol. 22, pp. 321–335.

Shearer, C. J., and Nedderman, R. M., 1965, "Pressure Gradient and Liquid Film Thickness in Co-current Upwards Flow of Gas–Liquid Mixtures: Application to Film Cooler Design," *Chem. Eng. Sci.,* Vol. 20, pp. 671–683.

Sun, K. J., 1979, "Flooding Correlations for BWR Bundle Upper Tie Plates and Bottom Side-Entry Orifices," in: *Proc. Multiphase Flow and Heat Transfer Symposium Workshop,* T. N. Veziroglu, ed., Miami Beach, FL, pp. 1615–1635.

Wallis, G. B., 1961, "Flooding Velocities for Air and Water in Vertical Tubes," UKAEA Report No. AEEW-R123.

Wolf, A., 1995, "Film Structure of Vertical Annular Flow," Ph.D. Thesis, London University.

Zabaras, G. J., and Dukler, A. E., 1988, "Counter-current Gas–Liquid Annular Flow Including the Flooding State," *AIChE J.,* Vol. 34, pp. 389–396.

Downloaded 11 Dec 2010 to 193.140.21.150. Redistribution subject to ASME license or copyright; see http://www.asme.org/terms/Terms_Use.cfm

R. V. Davalos

B. Rubinsky[1]
email: rubinsky@euler.berkeley.edu

Department of Mechanical Engineering,
University of California at Berkeley,
Berkeley, CA 94720

An Evolutionary-Genetic Approach to Heat Transfer Analysis

Introduction

In this paper, ideas from the fields of evolution and genetics are incorporated in a new approach to solve heat transfer problems. Biological metaphors have been used as problem-solving strategies in the engineering sciences for well over fifty years (Denning, 1992). Early efforts include the work of Box (1957) and Friedman (1959). A rigorous mathematical formalism was introduced by Holland and his collaborators, and that formalism was first referred to as "genetic algorithms" by his student Bagley (1967). A comprehensive review of this field can be found in the book by Goldberg (1989). Genetic algorithms have been used primarily as search and optimization strategies in the areas of design, artificial intelligence, machine learning, and control.

The unquestionable ability of nature to produce solutions through an evolutionary-genetic approach and the success of "genetic algorithms" in engineering suggests that a similar approach could be also useful in analyzing situations governed by prescribed physical laws. The primary goal of this paper is to illustrate and demonstrate the feasibility of this conceptually new approach to solving problems in physics. Thus, this paper shows how concepts from evolution and genetics can be used to analyze a problem governed by the conservation of energy principle. First, the general principles will be discussed, followed by an illustration of the method through the solution of one and two-dimensional transient heat conduction problems.

Evolutionary-Genetic Methodology

In Darwinian evolution, only individuals most fit to withstand the rigors of their environment survive to reproduce and create future gene pools (while other, maladaptive individuals perish along the way). The properties of each individual are described using a chromosome, and reproduction between individuals occurs through the exchange of respective alleles within chromosomes. In this section we will establish a series of parallel concepts between Darwinian evolution and genetics with those of energy conservation and heat transfer.

Coding. In nature, the properties of an organism are described by a string of genes in the chromosome. In dealing with a problem of heat transfer, the most natural way to represent the solution is through the temperature distribution in the domain. The temperature distribution can be encoded as a string of normalized temperatures at discrete spatial and temporal locations. The trial solutions then become similar to chromosomes in form.

Every solution, or chromosome, is composed of a string of alleles. In nature, each allele represents a particular characteristic of the organism and is itself encoded in an alphabet composed of four letters. In problems that require the use of computers, the most natural way to encode the temperature is through a string of binary numbers. In this study we decided first to normalize the temperatures in the analyzed domain, and then represent the temperatures using a string of bits. For example, the use of six bits discretizes the temperature into 1/63 (0.015873). The discretization level can be halved by adding another bit to code the temperatures. In the methodology developed here, the solution (temperature chromosome) will be a string of binary numbers, such that the relation between their order in the string and the spatial location of the temperatures is maintained. Figure 1 is an example of a chromosome with five discrete temperatures each represented by six-bit alleles.

Fitness Criterion. In nature, organisms are exposed to environmental stresses, and the fitness of the organism corresponds to its ability to survive these stresses. In natural selection the "best" or "fittest" solution is selected for the mating process. But how do we determine what is "best" in a problem of heat transfer? We suggest that in a problem of physics, the fitness criterion should be related to how well a solution satisfies the fundamental physics of the problem, which in heat transfer is the principle of conservation of energy. To this end, we have formulated a fitness criterion based on the principle of conservation of energy which incorporates both local and global conservation. The local conservation of energy criterion is established by performing a local energy balance on a prescribed control volume, n:

$$Q_{\text{in}}(n) + Q_{\text{gen}}(n) + Q_{\text{strd}}(n) = Q_{\text{out}}(n) \tag{1}$$

Since this formulation is general, it can incorporate energy contributions by conduction, convection, or radiation.

Obviously, the ideal solution will satisfy the principle of conservation of energy precisely, both in a local and in a global sense. The relative fitness of a solution can be evaluated by its departure from the ideal behavior. That departure can be viewed as an error of the solution. We will list here a few types of errors that may be used to characterize the "fitness" of the solutions. The error associated with each local energy balance, in control volume n, is:

$$E_l(n) = Q_{\text{out}}(n) - (Q_{\text{in}}(n) + Q_{\text{gen}}(n) + Q_{\text{strd}}(n)) \tag{2}$$

From the local error we can define the absolute average local error, E_{lt}, as:

$$E_{lt} = \frac{1}{N}\sum_{n=1}^{N} |E_l(n)| \tag{3}$$

where N is the total number of control volumes, and the maximum local error, E_{lm}, as:

$$E_{lm} = \text{Max}|E_l(n)| \tag{4}$$

In addition, a global error, E_g, which represents the conservation of energy over the whole volume, is defined as:

[1] To whom the correspondence should be addressed.

Contributed by the Heat Transfer Division and based on a paper presented at the Symposium honoring Chancellor C. L. Tien, held at the International Mechanical Engineering Congress & Exposition, San Francisco, California, November 12–17, 1995. Manuscript received by the Heat Transfer Division September 7, 1995; revision received April 17, 1996. Keywords: Biotechnology, Numerical Methods, Thermodynamics & Second Law. Associate Technical Editor: B. W. Webb.

Copyright © 1996 by ASME

Downloaded 11 Dec 2010 to 193.140.21.150. Redistribution subject to ASME license or copyright; see http://www.asme.org/terms/Terms_Use.cfm

011110	111000	110111	010100	010001	111000

Fig. 1 A chromosome with five alleles each containing six bits

$$E_g = \frac{1}{N}\sum_{n=1}^{N} |E_l(n)| - \frac{1}{N}\left|\sum_{n=1}^{N} E_l(n)\right| \quad (5)$$

A boundary error term, E_b, which depends upon the particular formulation of the problem can also be created. This term can take two different forms, either related to an energy balance as in Eq. (2) or having a prescribed temperature.

In this paper we chose to relate the fitness of a solution to the compliment of the weighted sum of the errors. Specifically, the fitness, f, is related to the boundary, local, and global errors by the equation:

$$f = 1 - (w_b \cdot E_b + w_{lt} \cdot E_{lt} + w_{lm} \cdot E_{lm} + w_g \cdot E_g) \quad (6)$$

where w_b, w_{lt}, w_{lm}, and w_g are weights chosen by the user to emphasize the relative importance of the different errors. Here we chose the values of the weights based upon intuition and physical understanding of the problem. For instance, the global error was added to assess a higher penalty to those solutions with temperature profiles that have erroneous inflection points, or in effect conflict with the corollary of the second law of thermodynamics. Minimizing this criterion tends to smooth the temperature curve. The $1/N$ term in Eqs. (3) and (5) keeps the error between zero and one. The fitness value must always be positive; therefore the values of the weights were chosen so that the term in the parentheses is never greater than one. Studying the significance of the fitness function and of the weights is an important aspect for future research in this area.

Method of Solution. The general fitness criterion in Eq. (6) is expressed in terms of energy sources and the solution string is expressed in terms of local temperatures. One possible method to correlate between heat sources and temperature is by dividing the analyzed domain into finite difference like equal regions and performing a local energy balance for each region. In the energy balance the heat flux into the control volume can be approximated by a finite difference formulation of Fourier's equation and the energy storage term by an Euler forward approximation (Incropera and DeWitt, 1990). It is important to understand that the finite difference approximations were used here for their simplicity and convenience. However, the evolutionary genetic principle of analysis formulated here is much broader and fundamental and is not restricted to a finite difference formulation. In fact, we anticipate that many other formulations will be developed to incorporate the use of concepts from evolution and genetics to solve physical problems.

Using the finite difference approximations for a one-dimensional problem, the local error in each control volume (n) at a particular time step takes the form:

$$E_l(n) = \frac{1}{\Delta x^2}(T(n+1) - 2T(n) + T(n-1)) - \frac{1}{\alpha \Delta t}(T(n) - T_{\text{old}}(n)) \quad (7)$$

where Δx is the distance between the nodes, α is the thermal diffusivity, and Δt is the time step. Equation (7) can be used to evaluate the local errors for each temperature string. Then, the fitness criterion is established for each solution by evaluating Eq. (6) for that string. This fitness criterion, Eq. (6), is used to determine the probability of a solution becoming a parent and transferring its genetic content to the next generation.

Selection and Reproduction. In nature the probability that an organism will become a parent is related to its fitness. The process of reproduction in nature involves the exchange of genetic material between the two parents, i.e., exchange of parts of the chromosome between the parents. In the methodology developed here the selection and reproduction process emulates the process in nature and is typical of other genetic algorithms (Goldberg, 1989).

The selection process is similar to a roulette wheel in which the space allotted to each solution is proportional to its fitness (Denning, 1992). In choosing two parents, the roulette wheel is turned at random using a random number generator. Obviously, the fittest solution has a greater probability of becoming a parent. Thus, the probability of a particular chromosome being selected for reproduction is that chromosome's fitness divided by the total fitness of the population.

After selecting two chromosomes, the algorithm needs to exchange genetic information between the two parents. Mating is simply a random exchange of alleles between two fit solutions with an occasional mutation.

There are two methods the program alternately selects to exchange alleles. In the first, a random crossover point is selected. Up to the crossover point one parent is copied to one child and the other parent is copied to the second. After the crossover point the second parent is copied to the first child. For the second, every other allele in the chromosomes are switched.

To reduce the possibility of the degeneration of the solution, the best solution is kept from one generation to the next.

DNA mutations in biological genes occur when a random change of a base pair causes the structure of a gene to be permanently altered, creating new variability in the fitness of the individual. Here, mutations within individual solutions are also possible. When a solution mutates, a bit inside an allele changes from zero to one or vice versa. This creates new variability in the fitness of the individual solution.

In a typical procedure, a large population of solutions is generated randomly. The members of the solution are evaluated according to the fitness criterion, mated and caused to reproduce, with an occasional mutation. This continues from generation to generation until a final solution that satisfies a desirable prescribed fitness criterion is achieved.

Results and Discussion

The methodology described in this paper has been applied to a few simple cases of conduction heat transfer, for illustration of the method. The first problem solved is that of conduction heat transfer in a one-dimensional slab, with an original temperature of zero. One side is continuously kept at the temperature

Nomenclature

α = thermal diffusivity
E = error
f = fitness
Q = energy source
n = node n
N = total number of control volumes
t = time
T = temperature
w = weight
x = Cartesian coordinate
y = Cartesian coordinate

Subscripts

b = boundary
g = global
gen = generated
in = into control volume
l = local
lt = absolute local average
lm = local maximal
old = previous time step
out = out of control volume
strd = stored

Downloaded 11 Dec 2010 to 193.140.21.150. Redistribution subject to ASME license or copyright; see http://www.asme.org/terms/Terms_Use.cfm

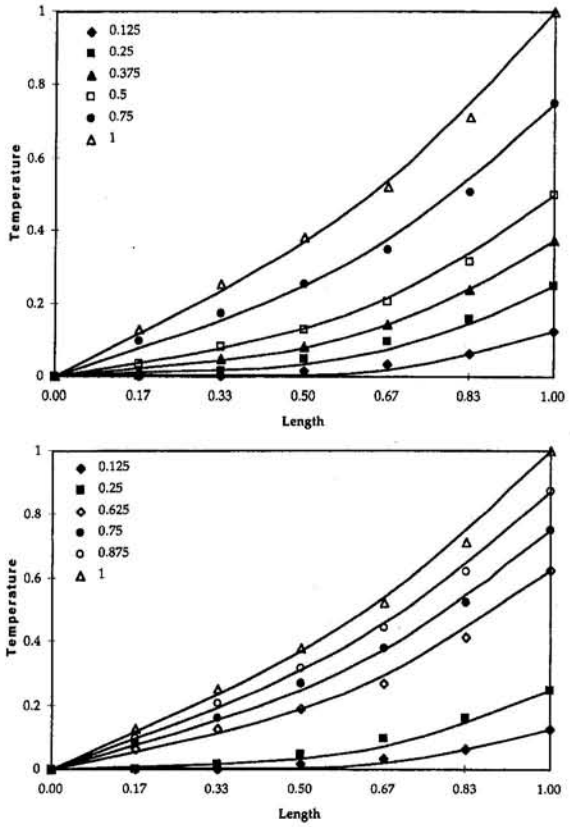


Fig. 2 Two solutions with different random original members of the population; comparison between exact solution (line) and evolutionary-genetic method (data points)

of zero while the other side temperature changes with a constant rate, H. This can be expressed mathematically through:

$$T(x, 0) = T(0, t) = 0, \quad T(1, t) = H^*t \tag{8}$$

The solution was developed using the methodology described above. The program was written in Pascal using a Macintosh Centris 650 computer with 16 MB of RAM. Different tests were employed varying time step, chromosome length, allele length, and random seed (original members of population).

Typical temperature profiles for different instances in time were obtained from the solution of the one-dimensional problem, Eq. (8), in which the values of H and α, the thermal diffusivity, are one. Figure 2 compares exact solutions (Myers, 1987) with results obtained by the method developed in this paper (marked points). The numbers in the legend correspond to the dimensionless time of the solution. The evolutionary-genetic solution has used a seven-node chromosome, containing six bits with a 0.125 nondimensional time step. The population consisted of 100 members, and each time step was carried out to a maximum of 150 generations. The two different figures were obtained from different randomly generated original members of the population.

It is obvious from Fig. 2 that the results obtained with this method inspired from evolution and genetics are accurate, and that the accuracy of the solution does not depend strongly on the original randomly generated members of the family of solutions.

Table 1 Number of iterations until convergence for different time steps

Time step	step 1	step 2	step 3	step 4
0.125	48(.9977)	24(.9925)	30(.9902)	66(.9939)
0.250	11(.9831)	45(.9851)	49(.9914)	61(.9936)

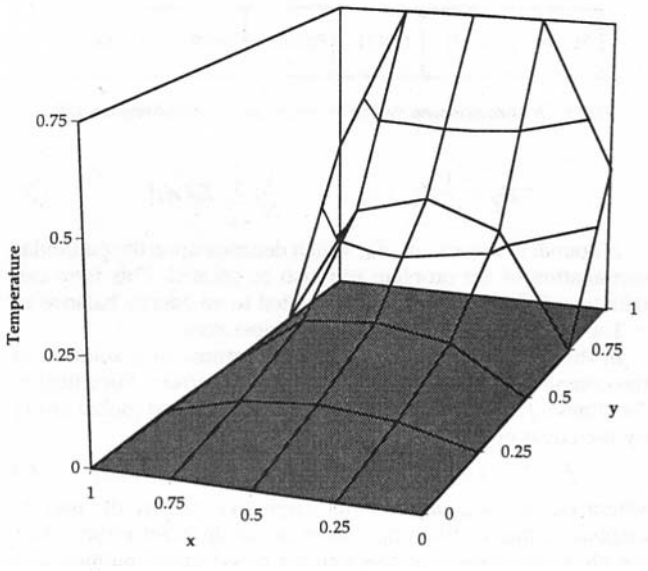


Fig. 3 Two-dimensional solution at time 0.75

Table 1 lists the number of generations, i.e., iterations, it takes for an original family of 100 members to converge to a solution of Eq. (8), with a fitness greater than 0.98, during each time step. The fitness that was achieved after these numbers of iteration is in parenthesis. (An ideal solution would have fitness of 1.00.)

To further verify the features of the method developed in this paper, it was tested against a two-dimensional square case in which the initial temperature was zero, the temperature of three sides of the square is zero, and the temperature on one of the sides changes with a constant rate H. These conditions are given below:

$$T(x, y, 0) = T(1, y, t) = T(x, 0, t) = T(0, y, t) = 0$$
$$T(x, 1, t) = H^*t \tag{9}$$

A typical two-dimensional temperature profile obtained for a 25-node solution with nine unknowns using a six-bit temperature chromosome is shown in Fig. 3. Figure 3 shows that this method can handle two-dimensional problems, which are not more difficult to solve than one-dimensional problems. It should be noted that the symmetry across the center line is remarkable,

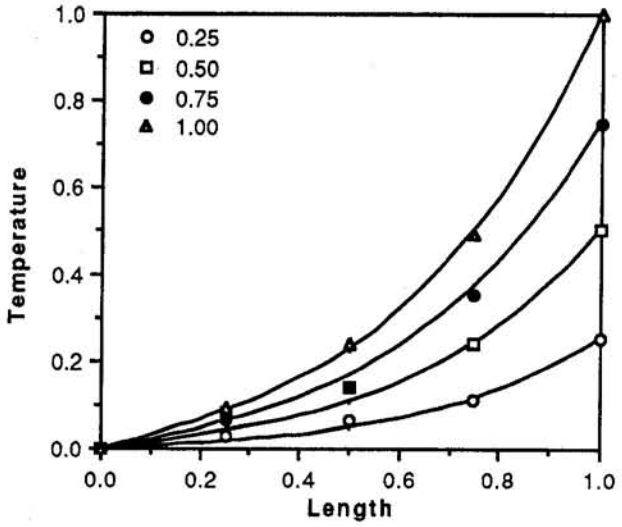


Fig. 4 Midsection two-dimensional solution; comparison between exact solution (line) and evolutionary-genetic method (data points)

Downloaded 11 Dec 2010 to 193.140.21.150. Redistribution subject to ASME license or copyright; see http://www.asme.org/terms/Terms_Use.cfm

considering that the method of solution begins with random temperature strings that do not have any symmetry.

Figure 4 shows how the midsection solution given by discrete data points compares with the exact solution given as a solid line. The accuracy of the solution is evident.

Conclusions

A new approach was developed for the solution of problems of heat transfer. The approach employs a biological metaphorical strategy to search for the fittest solution and incorporates laws of physics in establishing the fitness criterion for the solution. After developing the general methodology, two case studies were performed to illustrate and analyze the method.

It is obvious that much work needs to be done in expanding and improving the technique. Biological concepts such as dominance, expression, and diploidy would make the methodology more analogous to biological genetics. The results obtained so far nonetheless suggest that this method could become valuable in solving complex problems of heat transfer, in particular problems with highly irregular local behavior or material properties. Similar concepts can be developed for solving problems involving mass transfer, elasticity, fluid mechanics, and other problems involving the search for solutions that are governed by physical laws.

References

Bagley, J. D., 1967, "The Behavior of Adaptive Systems Which Employ Genetic and Correlation Algorithms," *Dissertation Abstracts International,* Vol. 28, No. 12.

Box, G. E. P., 1957, "Evolutionary Operation: A Method for Increasing Industrial Productivity," *Journal of the Royal Statistical Society,* C, pp. 81–101.

Denning, P. J., 1992, "The Science of Computing Genetic Algorithms," *American Scientist,* Vol. 80, pp. 12–14.

Friedman, G. J., 1959, "Digital Simulation of an Evolutionary Process," *General Systems Yearbook,* Vol. 4, pp. 171–184.

Goldberg, D. E., 1989, *Genetic Algorithms in Search Optimization and Machine Learning,* Addison-Wesley, MA.

Incropera, F. P., and DeWitt, D. P., 1990, *Fundamentals of Heat and Mass Transfer,* Wiley, New York.

Myers, G. E., 1987, *Analytical Methods in Conduction Heat Transfer,* Genium Publishing Corporation, New York.

Downloaded 11 Dec 2010 to 193.140.21.150. Redistribution subject to ASME license or copyright; see http://www.asme.org/terms/Terms_Use.cfm

A. F. Emery

T. D. Fadale

Department of Mechanical Engineering,
University of Washington,
Seattle, WA 98195

Design of Experiments Using Uncertainty Information

The process of parameter estimation and the estimated parameters are affected not only by measurement noise, which is present during any experiment, but also by uncertainties in the parameters of the model used to describe the system. This paper describes a method to optimize the design of an experiment to deduce the maximum information during the inverse problem of parameter estimation in the presence of uncertainties in the model parameters. It is shown that accounting for these uncertainties affects the optimal locations of the sensors.

Introduction

One of the most common procedures for parameter estimation is the least-squares technique in which the sum of the squares of the differences between the experimental measurements and the calculated responses of the system, using assumed parameters, is minimized. This approach is based on a deterministic view of the system. Procedures have been developed where the parameter estimation is based on a stochastic description of the experimental noise. The estimates obtained from this latter approach are referred to as the maximum likelihood estimates. A number of practical applications of parameter estimation, based on either of these approaches, have been in the fields of control and hydrology. A comprehensive review of these techniques is given by Polis (1982). Recent years have seen applications of parameter estimation techniques to heat and mass transfer process (Beck and Arnold, 1977; Alifanov, 1994; Taktak et al., 1993).

Although the maximum likelihood method considers the experimental noise to be stochastic, it does not take into account errors or uncertainties that might exist in the presumably known parameters of the system. The uncertainty information about the model parameters and the experimental constraints should be used in both the parameter estimation procedure, i.e., the inverse problem (Beck and Arnold, 1977), and in the design of the experiment. The aim of this paper is to describe a procedure by which information about the uncertain parameters and boundary conditions can be incorporated into the design of the experiment to reduce the uncertainty in the parameters estimated by solving the inverse problem. Examples are given of a one-dimensional heat transfer experiment developed to determine the thermal conductivity and specific heat capacity. The example shows how the optimal choice of sensor location and experiment duration can improve the accuracy of the experiment.

Theory

Consider a thermal system that can be modeled by a set of differential equations and model parameters. Of all the parameters involved in the model, let there be p unknown parameters represented by the vector $\mathbf{u}$, which are to be determined, while the q remaining parameters are *known* and are represented by the vector $\mathbf{b}$. In order to estimate the unknown parameters, $\mathbf{u}$, experimental observations of the response of the system are obtained at various locations (x_i, y_i) and times (t_k), none of which need be uniformly spaced.

Let N be the number of sensors used in the experiment and K be the number of readings in time taken at these sensor locations. Then the set of experimental observations can be represented by $\mathbf{z}_k$, where

$$\mathbf{z}_k^T = \{z_i(t_k),\ i = 1, 2, \ldots, N\} \quad k = 1, 2, \ldots, K \quad (1)$$

The predicted response of the system at these same locations and times can be represented by the vector $\mathbf{\Phi}_k$:

$$\mathbf{\Phi}_k^T = \{\phi(x_i, y_i, t_k),\ i = 1, 2, \ldots, N\} \quad k = 1, 2, \ldots, K \quad (2)$$

Each value $\phi(x_i, y_i, t_k)$ is a function of the known parameters and is determined by solving the field equations. As an example, consider a transient experiment to estimate the conductivity. ϕ could represent the temperature and the known parameters could be ρ, c, the sensor locations, and the boundary conditions. Let the difference between the predicted and measured responses be given as

$$\mathbf{\Psi}_k(u) = \mathbf{\Phi}_k - \mathbf{z}_k \quad (3)$$

where $\mathbf{z}_k$, the measured responses, have experimental errors and $\mathbf{\Phi}_k$, the predicted responses, vary due to uncertainties in $\mathbf{b}$. Both effects are considered to be additive, uncorrelated in time, with zero mean and a nonzero, spatial covariance. Bias errors, B_k, are assumed to be constant in time and space. If B_k are known, they are accounted for by defining a new variable $z_k - B_k$. If not, then minimizing the total error yields a relative minimum, which is the best that can be done (Moffat, 1988; Abernathy et al., 1985).

The aim of this paper is to describe a method to reduce the uncertainty in the estimated parameters. As shown in a previous paper (Fadale et al., 1995b), the best estimates of the unknown parameters $\mathbf{u}$ are those that maximize the likelihood of occurrence of the measurements relative to the estimated predictions, where the likelihood is given as

$$f_J(\mathbf{\Psi}|\mathbf{u}) = [(2\pi)^{NK} \prod_{k=1}^{K} \mathrm{Det}(\mathbf{V}_k)]^{-1/2} \times \exp[\sum_{k=1}^{K} -\tfrac{1}{2}\mathbf{\Psi}_k(\mathbf{u})^T \mathbf{V}_k^{-1} \mathbf{\Psi}_k(\mathbf{u})] \quad (4)$$

and where the covariance matrix $\mathbf{V}_k$ is defined as

$$\mathbf{V}_k = E[\{\mathbf{\Psi}_k - E[\mathbf{\Psi}_k]\}\{\mathbf{\Psi}_k - E[\mathbf{\Psi}_k]\}^T] = E[\delta\mathbf{\Phi}_k \delta\mathbf{\Phi}_k^T] + E[\delta\mathbf{z}_k \delta\mathbf{z}_k^T] = \mathbf{\Theta}_k \mathbf{G} \mathbf{\Theta}_k^T + \mathbf{S}_k \quad (5a)$$

The importance of using this extended theory based upon f_J can be shown by a simple example. Consider a slab with an initial temperature of zero, which is suddenly exposed to convective heating at time zero. Let us measure the temperature at a point in the interior of the slab and compare its measured temperature with that computed from a solution to the transient heat conduction equation. Let us assume that there is an uncertainty about the surface heat transfer coefficient h_f. That is, not knowing the

Contributed by the Heat Transfer Division for publication in the JOURNAL OF HEAT TRANSFER. Manuscript received by the Heat Transfer Division August 1995; revision received February 1996. Keywords: Instrumentation, Measurement Techniques, Modeling and Scaling. Associate Technical Editor: M. Sohal.

Copyright © 1996 by ASME

Downloaded 11 Dec 2010 to 193.140.21.150. Redistribution subject to ASME license or copyright; see http://www.asme.org/terms/Terms_Use.cfm

precise value of the convective coefficient, we will solve the heat conduction equation with an estimated value of h_f and choose the value of the thermal conductivity that gives the best agreement between the measured and predicted temperatures. What we would like is an estimating procedure that is not too sensitive to the assumed value of h_f. When the heat transfer coefficient is uncertain but this uncertainty is not accounted for in Eq. (4), i.e., $\mathbf{G} = 0$, all differences $\Phi_k - \mathbf{z}_k$ are weighted according to $\mathbf{S}_k$, irrespective of the effects of the uncertainty in h_f. The conductivity is then found by minimizing L,

$$L = \sum (\Phi_k - \mathbf{z}_k)^T \mathbf{S}_k^{-1} (\Phi_k - \mathbf{z}_k) \qquad (5b)$$

Figure 1(a) shows how L varies as a function of k. The minimum point in each curve defines the estimated conductivity. As expected, using different values of h_f yields different values of k, as shown in Fig. 1(b). When the weights are modified to account for the uncertainty in h_f such that the conductivity is defined by the minimum of J,

$$J = \sum (\Phi_k - \mathbf{z}_k)^T \mathbf{V}_k^{-1} (\Phi_k - \mathbf{z}_k) \qquad (5c)$$

the importance of the values of ϕ_k far from the central value are devalued and J is found to be less sensitive to variations in h (Figs. 1(a) and 1(b)). Of course there is a price to pay, namely that the minimum of J is less pronounced than that of L.

If there are no uncertainties in the *known* parameters $\mathbf{b}$, then $\mathbf{G}$ is identically zero, $\mathbf{V}_k \equiv \mathbf{S}_k$ and the likelihood reduces to the usual form which is dependent only upon the noise, i.e., $f_J(\Psi \mid \mathbf{u}) = f_L(\mathbf{z} \mid \mathbf{u})$.

Fisher Information Matrix (M). Even after the goal of the experiment has been decided upon, e.g., which unknown parameters are to be estimated, there are a number of variables that can be adjusted, subject to certain constraints, so that the information provided by the experiment is maximized. To form a basis for the comparison of different experiments, a measure of the *goodness* of the experiment is required. Almost all approaches used to define an optimal design are based upon minimizing the estimation errors. By the Cramer–Rao inequality the estimation error has a lower bound of $\mathbf{M}^{-1}$, where $\mathbf{M}$ is the Fisher Information matrix (Fedorov, 1972; Goodwin and Payne, 1977). This matrix can be expressed in terms of the probability distribution function $f_J(\Psi \mid \mathbf{u})$ by

$$\mathbf{M} = E\left\{\left[\frac{\partial}{\partial \mathbf{u}} (\ln f_J)\right]\left[\frac{\partial}{\partial \mathbf{u}} (\ln f_J)\right]^T\right\} \qquad (6)$$

Taking the derivative of the logarithm of the probability distribution function from Eq. (4) and making use of the identity (Fadale et al., 1995a)

$$\frac{\partial}{\partial \mathbf{u}} (\ln (\mathrm{Det}\ (\mathbf{V}))) = \mathrm{Tr}\left[\mathbf{V}^{-1} \frac{\partial \mathbf{V}}{\partial \mathbf{u}}\right] \qquad (7)$$

gives

$$\frac{\partial}{\partial \mathbf{u}} (\ln f_J) = -\frac{1}{2} \sum_{k=1}^{K} \mathrm{Tr}\left[V_k^{-1} \frac{\partial \mathbf{V}_k}{\partial \mathbf{u}}\right] - \frac{1}{2} \sum_{k=1}^{K} \Psi_k^T \frac{\partial \mathbf{V}_k^{-1}}{\partial \mathbf{u}} \Psi_k + \left\{\frac{\partial \Phi_k}{\partial \mathbf{u}}\right\}^T \mathbf{V}_k^{-1} \Psi_k \qquad (8)$$

Substituting Eq. (8) into Eq. (6) and using the identity

$$E[\Psi^T \mathbf{A} \Psi \Psi^T \mathbf{B} \Psi] = \mathrm{Tr}\ [\mathbf{AV}]\ \mathrm{Tr}\ [\mathbf{BV}] + \mathrm{Tr}\ [\mathbf{AVBV}] + \mathrm{Tr}\ [\mathbf{AVB}^T\mathbf{V}] \qquad (9)$$

the Fisher Information matrix for the likelihood functional $f_J(\Psi \mid \mathbf{u})$ is given by

$$(\mathbf{M})_{lm} = \sum_{k=1}^{K} \left[\left\{\frac{\partial \Phi_k}{\partial u_m}\right\}^T \mathbf{V}_k^{-1} \left\{\frac{\partial \Phi_k}{\partial u_l}\right\} + \frac{1}{2} \mathrm{Tr}\left[\mathbf{V}_k^{-1} \frac{\partial \mathbf{V}_k}{\partial u_l} \mathbf{V}_k^{-1} \frac{\partial \mathbf{V}_k}{\partial u_m}\right]\right] \quad l, m = 1, \ldots, p \qquad (10)$$

Measure of Goodness. The optimal experiment is one that maximizes the information gained, or conversely minimizes the estimation errors. This is done by choosing the best combination of the known parameters that can be adjusted, such as sensor types, sensor locations, sampling times, experiment duration time, and boundary conditions. Since the Cramer–Rao inequality states that the inverse of the Fisher Information matrix is the lower bound of the estimation errors or the confidence interval of the estimates, these adjustable parameters are chosen to minimize Ω, which is a measure of $\mathbf{M}^{-1}$, i.e.,

$$\Omega(\mathbf{M}^{-1}) \equiv \min_{X \in D} \{\mathrm{Measure}\ \mathbf{M}(\mathbf{X})\} \qquad (11)$$

where $\mathbf{X}$ represents all of the adjustable parameters over the domain $\mathbf{D}$ of all possible values. Various measures have been used (Walter and Pronzato, 1990; Seber and Wild, 1989; Kubrusly and Malebranche, 1982; Polis, 1982). Typically the measure for p unknown parameters is based upon

Nomenclature

$\mathbf{b}$ = known parameter vector
c = specific heat capacity
$E[\ ]$ = expected value operator
f = probability density function
Fo = Fourier number = $kt/\rho c$
$\mathbf{G}$ = covariance matrix of known parameters
k = thermal conductivity
J, L = objective functions to be minimized
K = number of observation times
$\mathbf{M}$ = Fisher Information Matrix
N = number of sensors
p, q = number of parameters
q_o = prescribed surface heat flux
q_x = heat flux
$\mathbf{S}$ = covariance matrix of measurements
t = time
T = temperature
$\mathbf{u}$ = unknown parameter vector
$\mathrm{Var}[\ ]$ = variance operator
$\mathbf{V}$ = covariance matrix of temperature
x, y = sensor position
$\mathbf{z}$ = measured temperature vector
δ_h = percentage variation in h
δ_n = percentage variation in measurements
σ_n = standard deviation of measurements
Θ = sensitivity matrix of temperature to $\mathbf{b}$
Φ = predicted temperature vector
Ψ = prediction minus measurement vector
Ω = scalar measure of $\mathbf{M}^{-1}$

Subscripts

i, j = sensors
k = time
l, m = parameters

Superscripts

T = transpose

Downloaded 11 Dec 2010 to 193.140.21.150. Redistribution subject to ASME license or copyright; see http://www.asme.org/terms/Terms_Use.cfm

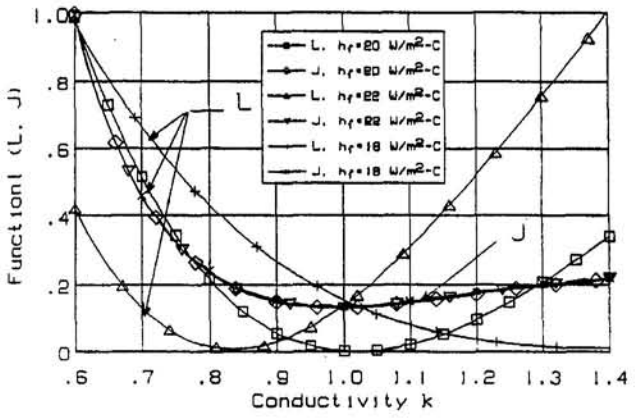


Fig. 1(*a*) Variation of the objective functions *L* and *J* with *k* for 1 percent noise and 30 percent uncertainty in h_f

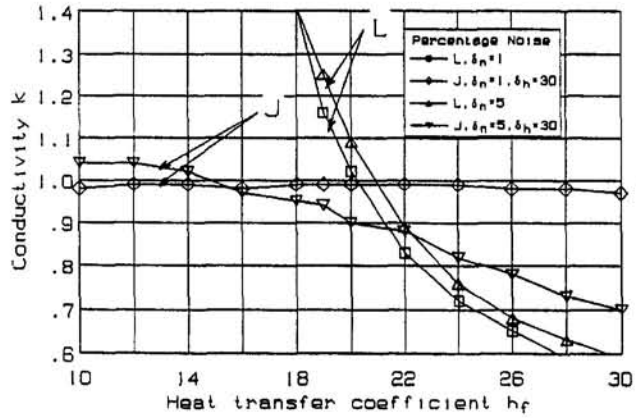


Fig. 1(*b*) Estimation of conductivity with 30 percent uncertainty h_f

$$\text{if } \det(\mathbf{M}) \neq 0, \quad \Omega = [p^{-1} \text{ trace } (\mathbf{H}\mathbf{M}^{-1}H^T)^k]^{1/k} \quad (12a)$$

$$\text{if } \det(\mathbf{M}) = 0, \quad \Omega = \infty \quad (12b)$$

where $\mathbf{H}$ is a nonsingular $p \times p$ matrix and where $k \geq 0$ (Walter and Pronzato, 1990). The most common optimality criterion, *D*-optimality, is defined by

$$\Omega(\mathbf{M}^{-1}) = [\det(\mathbf{M})]^{-1} \quad (13)$$

which is equivalent to $\mathbf{H} = \mathbf{I}$ and $k = 0$. The appeal of *D*-optimality is that it corresponds to minimizing the volume of the ellipsoids, which represent the confidence regions for the maximum likelihood estimate of the unknown parameters. Two other common optimality criteria are the *C*-optimality [$\mathbf{H} = \text{diag } (\mathbf{u}_i^{-1})$], which is related to the precision of the estimates of the unknown parameters and *E*-optimality [$\mathbf{H} = \mathbf{I}, k = \infty$], which minimizes the maximum diameter of the ellipsoidal confidence regions (i.e., the maximum eigenvalue of $\mathbf{M}$).

When only one parameter is sought, $\mathbf{M}$ is a scalar, and all of these criteria are equivalent. When more than one parameter is sought, the different criteria will differ in numerical value. Regardless of which optimality criterion is used, the minimum value of Ω can be found in two ways: first, by enumerating all of the values of Ω and visually searching for the minimum; second, by using a nonlinear minimizing program. We have used both methods, employing NPSOL (Gill et al., 1986) as the minimizing program. Although the problem of locating the minimum of Ω appears to be rather straightforward, we found that in a number of cases NPSOL was unable to determine the global minimum. Comments will be made in the following sections as to why this happened.

It is important to note that the use of $\mathbf{M}$ requires some knowledge about the noise of the readings, but requires no knowledge about the range of values of the known parameters. It must be emphasized that the elements of the information matrix $\mathbf{M}$ and, hence, the optimal values of the adjustable parameters depend upon the a priori estimates of the unknown parameters $\mathbf{u}$. This is because of the strongly nonlinear dependence of the temperature on the unknown parameters and is typical of measurement designs for the solution of inverse problem in thermal-structural problems. Accordingly, it is only meaningful to speak of locally optimal designs formulated with the use of a priori information about the unknown parameters.

As mentioned earlier, a number of variables can be adjusted, subject to certain conditions, so as to optimize the experiment. In this paper the response to be sensed, sensor locations, sampling rate, duration of the experiment, and the boundary conditions are considered to be the adjustable parameters being optimized. It must be emphasized that the minimum required number of sensors and the limits on their placement are completely determined by an analysis of the conditions for the existence and uniqueness of the solution of the corresponding inverse problem (Musylev, 1980). Requirements of this type on the measurements dictate the minimum experimental information that is required, in principle, for the solution of a specific inverse problem.

Example

Consider the case when the thermal properties k and c are to be determined. For simplicity we will examine a one-dimensional slab ($0 \leq x \leq L$) with $T(0, t) = 0$, $T(x, 0) = 0$. At steady state with prescribed surface temperatures, neither k nor c can be determined since the temperature distribution is independent of both properties. One approach would be to consider the transient case with prescribed surface temperatures, but in practice the imposition of a constant surface temperature is difficult. A simpler experiment is to impose a constant heat flux since this can be done fairly easily with an electric source of heat at $x = L$. At steady state, the temperature and heat flux are given by

$$T(x, \infty) = \frac{xq_o}{k} \quad \text{and} \quad q_x(x, \infty) = -q_o \quad (14)$$

and the uncertainty in k is related only to the uncertainty in q_o (assuming that the location, x, can be specified exactly). Thus the measurement of $T(x, \infty)$ and the specification of q_o are sufficient to determine k. To determine c requires that the transient history be measured. Although $q_x(x, \infty)$ is not a function of k, $q_x(x, t)$ is. Thus, in addition to information about c, a more precise definition of k can be determined by measuring $q_x(x, t)$—for example in a flash conductivity experiment.

All the sample calculations were carried out using $k = 10$ W/m-K, $c = 100$ J/kg-C, $\rho = 10{,}000$ kg/m^3, $L = 0.1$ m, $q_o = 10{,}000$ W/m^2, with a sensor noise of $\sigma_n = 0.1$ percent of T or q_x.

One Sensor. Figures 2(*a*, *b*) display the time history[1] of the sensitivity of T and q_x to k. When $\mathbf{S}_k$ is constant and diagonal, minimizing the value of Ω is equivalent to maximizing the sensitivity when using one sensor to estimate one property (Fadale et al., 1995b). Since at any time the value of $\partial T/\partial k$ is maximum at $x = L$, the estimation of k should always be done using the temperature measured at L. On the other hand, the sensitivity of q_x is initially greatest near L, but moves to $x = 0$ near a time of Fo = 0.2, reaching a maximum there at Fo =

[1] Henceforth, everything is expressed in nondimensional form; see Taktak et al. (1993).

Downloaded 11 Dec 2010 to 193.140.21.150. Redistribution subject to ASME license or copyright; see http://www.asme.org/terms/Terms_Use.cfm

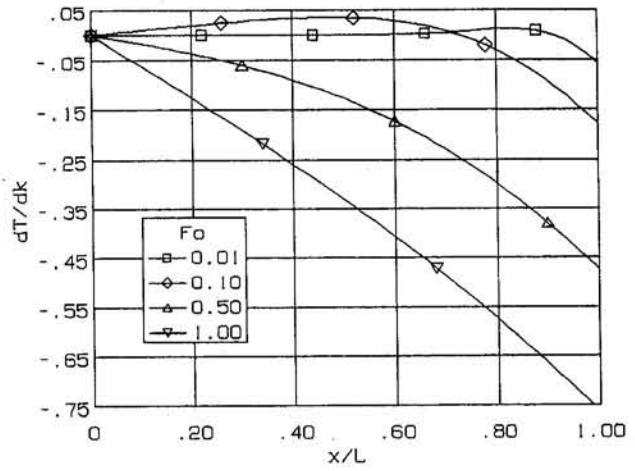


Fig. 2(*a*) Sensitivity of the temperature to the thermal conductivity as a function of position and time for a prescribed surface heat flux

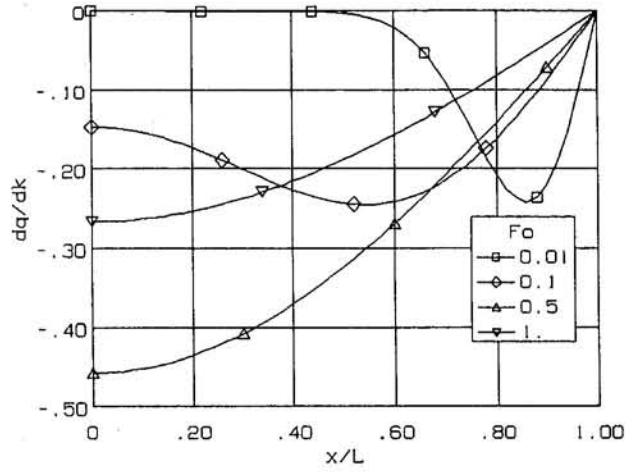


Fig. 2(*b*) Sensitivity of the heat flux to the thermal conductivity as a function of position and time for a prescribed surface heat flux

0.5 and then decreasing as steady state is approached. Thus the ideal location for the temperature sensor is always at $x = L$, while the optimal heat flux sensor position varies with time.

The optimal locations of the sensors and the values of Ω, which, as discussed in the previous section, is a measure of the precision of the estimated parameter, are listed in Table 1. With one temperature sensor, it is always placed at $x = L$ and as the duration of the experiment (henceforth referred to as *time*) increases, the value of Ω decreases, leading to the conclusion that long time values are to be preferred. Figure 3(*a*) shows the variation of Ω with time for one temperature sensor. Although the optimal location is always at $x = L$, as time increases the value of Ω becomes quite constant with respect to location. That is, as long as the sensor is not too close to $x = 0$, say $x/L > 0.5$, the precise location is not critical. Note how Ω tends to infinity at $x = 0$ and has a sharp peak near $x/L = 0.9$ at early times. The infinite value at $x = 0$ is because this temperature is fixed and is thus insensitive to k. The peak near $x = L$ is caused by the change in sign of the sensitivity of temperature to conductivity; see Fig. 2(*a*). Since Ω is proportional to the inverse of the sensitivity, but formed of samples at several times, it will have a local maximum near the point of zero sensitivity. It is this local maximum which we found caused NPSOL to miss finding the global minimum sometimes.

The information associated with q_x shows a strong variation with both time and position, Fig. 3(*b*). The minimum value of Ω changes only slightly with time, but is strongly dependent upon position, at least at early times. As steady state is approached, the optimal sensor location moves to $x = 0$, with a slightly reduced value of Ω. As the thermal wave progresses through the slab, the optimal sensor location follows it, but the value of Ω remains nearly constant at $\sim 2 \times 10^{-6}$. Then when the wave reaches $x = 0$, the optimal sensor location quickly jumps to $x = 0$ and the value of Ω reduces to $\sim 0.7 \times 10^{-6}$. Because **M** is made up of samples over the entire duration of the experiment, including values at early times when the sensitivity is relatively high, the value of Ω does not show an increase proportional to the inverse of the sensitivity.

Table 1 compares two experiments: (*a*) prescribed surface heat flux, (*b*) prescribed surface temperature, both with zero uncertainty of the boundary condition. It is clear that experiment (*a*) is to be preferred because: (1) The optimal location of the temperature sensor is fixed at $x = L$, (2) for reasonable dura-

Table 1 Optimal sensor location for determining *k*; zero uncertainty in boundary conditions

Prescribed Surface Heat Flux					Prescribed Surface Temperature				
	based on T		based on q_x			based on T		based on q_x	
Fo	x/L	Ωx10^7	x/L	Ωx10^7	Fo	x/L	Ωx10^7	x/L	Ωx10^7
0.010	1.00	892.4	0.90	0.21	0.001	0.96	589.7	0.98	1.31
0.050	1.00	192.5	0.78	0.23	0.002	0.96	562.6	0.98	1.94
0.100	1.00	97.2	0.70	0.23	0.005	0.94	583.5	0.98	2.85
0.500	1.00	16.2	0.00	0.08	0.010	0.90	582.6	0.98	3.38
0.750	1.00	9.1	0.00	0.07	0.020	0.86	585.0	0.98	3.72
1.000	1.00	6.2	0.00	0.08	0.050	0.78	586.5	0.98	3.96

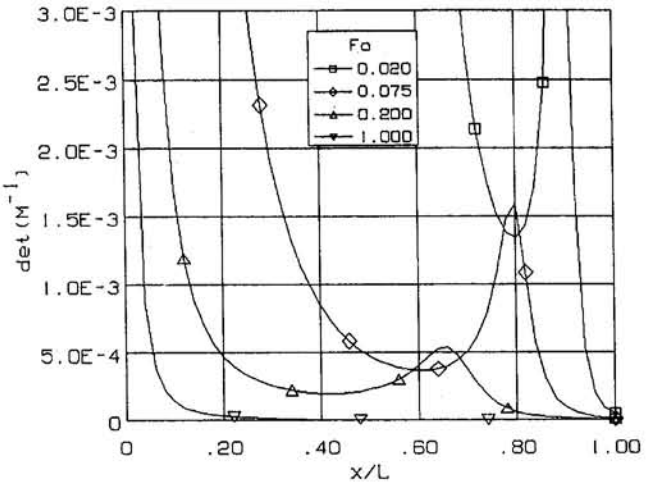


Fig. 3(*a*) Value of det($\mathbf{M}^{-1}$) when sensing temperature as a function of sensor location and duration of measurement

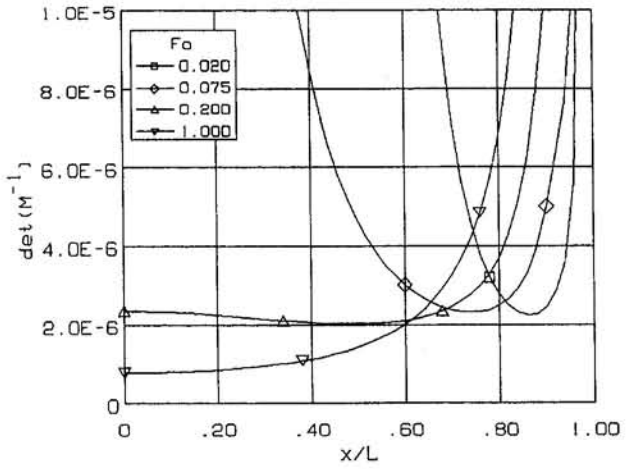


Fig. 3(*b*) Value of det($\mathbf{M}^{-1}$) when sensing heat flux as a function of sensor location and duration of measurement

Downloaded 11 Dec 2010 to 193.140.21.150. Redistribution subject to ASME license or copyright; see http://www.asme.org/terms/Terms_Use.cfm

tions, the magnitude of Ω is several orders of magnitude less than for experiment (b).

In all cases that we have examined, heat flux sensors are to be preferred when estimating k; the values of Ω are better by almost a factor of 100. However, it must be noted that measuring the heat flux at different positions calls for an invasive procedure and is not very practical (unless a sample is constructed of alternating layers of material and flux sensors). We have dwelt upon this contrived case to emphasize that sensing different responses may yield very different experimental designs.

Estimation of Thermal Capacitance, c. In the expression for q_x, k and c occur only in the thermal diffusivity, $k/\rho c$. The nondimensional values of $\partial q_x/\partial k$ and $\partial q_x/\partial c$ are identical and thus the history of the optimal heat flux sensor location for k and c are identical. On the other hand, k appears much differently than does c in the expression for $T(x, t)$; the sensitivity to c is greatest at $x = L$, but now reaches a maximum at $\sim$Fo $= 0.5$ and then diminishes. Thus although the optimal sensor location is always at $x = L$, there is a maximum time for the experiment, after which Ω increases and the precision with which c can be estimated diminishes.

Effect of Sampling Times and Variations of Noise Level. In most transient thermal problems, the maximum sensitivity changes with time. As a consequence the rate of sampling may affect the experiment's design. For the two cases considered here, no substantial difference was detected in the history of the optimal sensor location for sampling intervals which ranged from δFo $= 0.001$ to 10 percent of the experiment duration.

$\mathbf{S}_k$ represents imprecision in the sensor readings—both noise and inexactness in the measurements. Depending upon the data acquisition system used, the two limits for $\mathbf{S}_k$ are: (1) an upper bound proportional to the maximum capability of the sensor (e.g., least count of the instruments) and (2) a lower bound proportional to the actual reading or to the noise. Values of $\mathbf{S}_k$ ranging between these two bounds were not found to cause any difference in the calculated optimal location, but they did affect the magnitude of Ω and the efficiency of finding the optimal location. If $\mathbf{S}_k \propto \phi$, where ϕ is the sensor response, the components of Ω are $(\partial\phi/\partial u)^2/(\phi)^2$, where $u = k$ or c. For the thermal problems studied here ϕ approaches zero far from $x = L$. The value of Ω is then a competition between the rate at which $\partial\phi/\partial u$ and ϕ approach 0 and it proved necessary to restrict the calculation of Ω to regions where both $\partial\phi/\partial u$ and ϕ have reasonable values. In the example presented here, this means that the search region is restricted close to $x = L$, but the extent of this region varies with time. In general, this difficulty is overcome when N-dimensional maps of Ω, $\partial\phi/\partial u$, and ϕ can be scrutinized simultaneously. However, general optimizing computer programs, such as NPSOL, tend to run afoul of this problem. When $\mathbf{S}_k \propto \Phi$, a practical alternative is to define a minimum value of $\mathbf{S}_k$ in the order of 0.01 percent of $\phi(\max)$, i.e., either $T(\max)$ or $q_x(\max)$.

Estimation of k and c. When only one parameter is to be estimated, $\mathbf{M}$ is a scalar and all the optimality criteria are the same. When p parameters are to be determined, $\mathbf{M}$ is a $p \times p$ matrix and the choice of the best optimality criterion is open to question. For k and c, the contribution of each time sample to $\mathbf{M}$ (assuming that $\mathbf{S}_k$ is constant in time and $= \sigma^2\mathbf{I}$) is

$$\mathbf{M} = \frac{1}{\sigma^2}\sum_{k=1}^{K} M_k \quad \text{where}$$

$$M_k = \begin{bmatrix} \left(\frac{\partial\Phi}{\partial k}\right)^2 & \left(\frac{\partial\Phi}{\partial k}\right)\left(\frac{\partial\Phi}{\partial c}\right) \\ \left(\frac{\partial\Phi}{\partial k}\right)\left(\frac{\partial\Phi}{\partial c}\right) & \left(\frac{\partial\Phi}{\partial c}\right)^2 \end{bmatrix} \tag{15}$$

When $\Phi = q_x$, $\partial\Phi/\partial k = \partial\Phi/\partial c$ and $\det(\mathbf{M}) \equiv 0$. That is, it is impossible to use a single heat flux sensor to estimate both k and c. This is not the case for $T(x, y, t)$. Table 2 lists the optimal sensor positions and the values of Ω for determining k and c for D- and E-optimality criteria. At early times the optimal locations predicted by the two criteria are approximately the same, although the D-optimality values show erratic behavior. However, the optimal locations are substantially different.

We have found that the D-optimality criterion produces unacceptable results. It is reasonable to expect that the imprecision when using a single sensor to estimate two properties will be greater than the maximum imprecision found when using a single sensor to estimate either property singly. Comparing the values of Ω for D-optimality for determining both k and c with the values given in Table 1 for determining k alone, shows that not only is Ω less for two properties, it is less by several orders of magnitude at long times. We have observed this behavior frequently in thermal problems. The reason for this is the interaction of k and c in transient thermal problems. Generally, both $\partial T/\partial k$ and $\partial T/\partial c$ diminish with time and the problem does not occur. However, when the two sensitivities vary oppositely in time and with substantially different magnitudes, the off-diagonal terms in $\mathbf{M}$ become relatively unimportant and at long times the determinant tracks the product of the diagonal terms. Thus the value of Ω becomes less than the minimum value for a single parameter.

On the other hand, the E-optimality criterion produces nearly identical and consistent and understandable results as shown in Table 2. [Note that values of Ω computed using the different optimality criteria should not be compared with each other; only the optimal sensor locations can be compared.]

Figure 4 compares the D- and E-optimality profiles at Fo $= 0.1$. The E-optimality surface is smooth and posesses an easily identified and sharp minimum. By contrast, the D-optimal surface is nearly flat. As depicted, the optimal location is poorly defined by D-optimality as compared to E-optimality.

Multiple Sensors. When estimating only one parameter, only one sensor is needed and increasing the number of sensors simply reduces the value of Ω, i.e., increases the precision, but has no other effect. When the precision is weighted with respect to the number of sensors, the precision is constant for any number of sensors. However, when two parameters are to be estimated, the second sensor has a considerable effect. Table 3 lists the optimal locations and the values of Ω for two sensors when estimating both k and c. We see that one sensor always remains at $x = L$, basically to estimate k, and the other moves in accordance with the moving thermal wave, which is affected primarily by c. A comparison of Tables 2 and 3 shows that the addition of another sensor reduces the value of Ω calculated using the D-optimality criteria by over three orders of magnitude. This is totally unrealistic and is further evidence of the unsuitability of the D-optimality criteria. The E-optimality criteria shows reduction of a factor of approximately 2 at long times, which is more reasonable when doubling the number of sensors.

Imprecision in q_o. A general rule of thumb is that the optimal location of a sensor is where the sensitivity is high, but away from the location of errors. If the applied heat flux is not known accurately, i.e., $\sigma(q_o) \neq 0$, then the optimal location will change. Table 4 lists the optimal location of a temperature sensor for three different levels of uncertainty in q_o. For modest levels of uncertainty in q_o, the only effect is an increase in the imprecision, as expected. When the uncertainty is large ($\approx$5 percent), unreasonable and erroneous results are predicted, namely the precision at very short times is seen to improve. This leads to the important question is "how large can $\sigma(q_o)$ be" for the computed results to be valid? It is not possible to specify a priori the maximum uncertainty tolerable in q_o. However, a critical requirement for the application of the Fisher

Downloaded 11 Dec 2010 to 193.140.21.150. Redistribution subject to ASME license or copyright; see http://www.asme.org/terms/Terms_Use.cfm

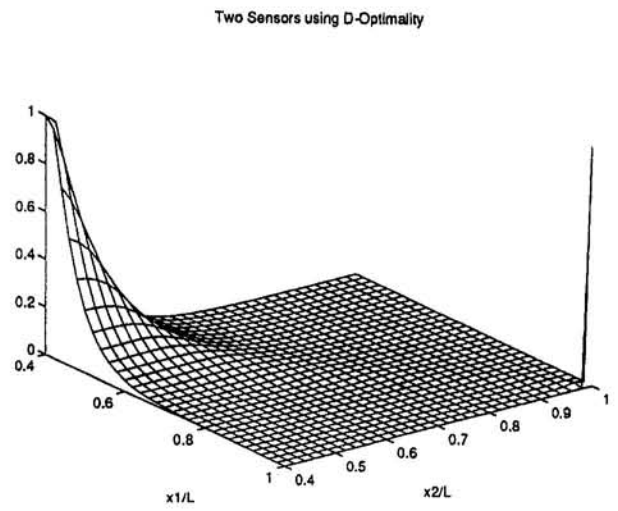


Fig. 4(*a*) Value of *D*-optimality measure of $\mathbf{M}^{-1}$ when sensing temperature at two locations for a duration of 100 seconds (values are clipped at 1.0)

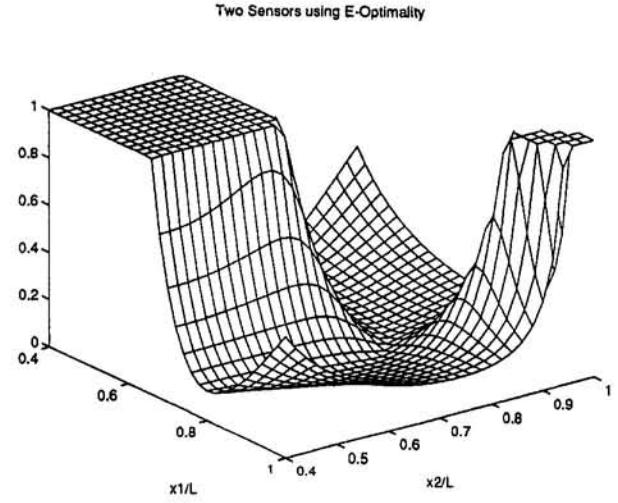


Fig. 4(*b*) Value of *E*-optimality measure of $\mathbf{M}^{-1}$ when sensing temperature at two locations for a duration of 100 seconds (values are clipped at 1.0)

Information matrix and the Cramer–Rao theorem is that, in addition to $\mathbf{S}_k$ being small, that

$$E\left[\frac{\partial^2 J}{\partial \mathbf{u}^2}\right] \approx \frac{\partial^2 J}{\partial \mathbf{u}^2} \tag{16}$$

Table 2 Optimal sensor location for determining *k* and *c* using one temperature sensor slab with a prescribed heat flux; zero uncertainty of q_o

	for k and c			
	D-optimality		E-optimality	
Fo	x/L	$\Omega \times 10^7$	x/L	$\Omega \times 10^3$
0.010	0.96	7.579	0.96	8.163
0.020	0.90	2.088	0.94	4.250
0.050	0.92	0.362	0.90	1.766
0.075	0.90	0.162	0.88	1.180
0.100	0.88	0.091	0.86	0.881
0.200	0.84	0.021	0.78	0.396
0.300	0.82	0.007	0.74	0.187
0.400	0.82	0.003	0.82	0.094
0.500	0.86	0.001	0.70	0.054
0.750	0.98	0.0002	0.72	0.021
1.000	1.00	0.0001	0.76	0.013

Table 3 Optimal sensor location for determining *k* and *c* using two temperature sensors; slab with a specified heat flux; zero uncertainty in q_o (one sensor is always located at $x = L$)

	D-optimality		E-optimality	
Fo	x_2/L	$\Omega \times 10^{10}$	x_2/L	$\Omega \times 10^3$
0.010	0.92	118.36	0.90	0.300
0.020	0.88	32.46	0.90	0.157
0.050	0.82	5.51	0.84	0.064
0.075	0.76	2.48	0.80	0.043
0.100	0.74	1.40	0.76	0.033
0.200	0.64	.37	0.66	0.017
0.300	0.62	.20	0.56	0.014
0.400	0.60	.13	0.50	0.013
0.500	0.62	.10	0.50	0.012
0.750	0.72	.05	0.62	0.009

Table 4 Estimation of *k* using one temperature sensor; slab with a specified heat flux and uncertainty in q_o

	$\sigma(q_o)/q_o$=0%		$\sigma(q_o)/q_o$=1.0%		$\sigma(q_o)/q_o$=5.0%	
Fo	x/L	$\Omega \times 10^5$	x/L	$\Omega \times 10^5$	x/L	$\Omega \times 10^5$
0.010	1.00	8.924	1.00	12.311	0.94	5.732
0.025	1.00	4.675	1.00	8.816	0.88	7.598
0.050	1.00	1.925	1.00	6.424	0.78	11.977
0.075	1.00	1.292	1.00	5.828	0.72	15.493
0.100	1.00	0.972	1.00	5.512	0.68	19.113
0.200	1.00	0.485	1.00	4.976	1.00	24.254
0.300	1.00	0.311	1.00	4.655	1.00	25.245
0.400	1.00	0.219	1.00	4.316	1.00	25.483
0.500	1.00	0.162	1.00	3.964	1.00	25.337
0.750	1.00	0.091	1.00	3.185	1.00	24.260
1.000	1.00	0.062	1.00	2.631	1.00	22.955

This requirement can be shown to be equivalent, when $\mathbf{S}_k \approx 0$, for a single sensor to

$$\Delta = \frac{1}{V^2}\left[\left(\frac{\partial V}{\partial \mathbf{u}}\right)^2 - \frac{1}{2}V\frac{\partial^2 V}{\partial \mathbf{u}^2}\right] \approx 0 \tag{17}$$

For the example considered here, when $\phi = q_x$, $\Delta \equiv 0$ at steady state and ≈ 0 at all other times, thus large uncertainties in q_o can be tolerated. When $\phi = T$, $\Delta \neq 0$ at all times and is largest at short times and for large values of $\sigma(q_o)$ and is of the order of 1–200 times S_k, explaining the behavior shown in Table 4.

Since multiple sensors have the effect of reducing the imprecision, it is instructive to see what effect they have when there is an uncertainty in q_o. Table 5 lists the optimal sensor locations. One temperature sensor always remains at $x = L$; the other stays at $x = L$ for short times and then moves toward $x = 0$. The second sensor is initially at $x = L$, even for relatively large uncertainties in q_o because of the very high sensitivities of T to k (Fig. 2*a*). Later, the imprecision due to variations in q_o causes the second sensor to follow the heat flux pulse.

Conclusions

When estimating a single parameter using error-free experimental conditions, either the sensitivity of the system re-

Table 5 Estimation of *k* using one or two temperature sensors ($\sigma(q_o) = 0.01\ q_o$)

Fo	x/L	$\Omega \times 10^6$	x_1/L	x_2/L	$\Omega \times 10^6$
0.010	1.00	12.311	1.00	1.00	77.373
0.025	1.00	8.816	1.00	1.00	62.683
0.050	1.00	6.424	1.00	0.76	46.156
0.075	1.00	5.828	1.00	0.72	37.465
0.100	1.00	5.512	1.00	0.68	32.026
0.200	1.00	4.976	1.00	0.60	21.815
0.300	1.00	4.655	1.00	0.56	18.635
0.400	1.00	4.316	1.00	0.54	17.574
0.500	1.00	3.964	1.00	0.54	17.199
0.750	1.00	3.185	1.00	0.54	16.922
1.000	1.00	2.631	1.00	0.52	16.526

Downloaded 11 Dec 2010 to 193.140.21.150. Redistribution subject to ASME license or copyright; see http://www.asme.org/terms/Terms_Use.cfm

sponse to the parameter or the Fisher Information Matrix may be used to determine the optimal sensor location. If the experimental conditions (boundary conditions, initial conditions, etc.) are imprecise, then it is necessary to use the extended form of the Fisher Information Matrix since the sensor location will be biased by the degree of imprecision relative to the signal noise.

When multiple parameters are to be estimated, the difference in sensitivities and their time variation renders their use alone inadequate. In this case, **M**, based on the extended principle, must be used. For most problems, any of the optimality criteria (*C*-, *D*-, *E*-) may be used. However, in thermal problems where the temporal histories of the sensitivities and their magnitudes differ substantially, we have found that *E*-optimality is to be preferred.

For imprecise boundary conditions, the question of the degree of acceptable imprecision relative to the signal noise is important. Although we have been able to provide such an estimate, its use is not straightforward. Empirically we have observed that as long as the imprecision is small enough so that the *trace* term in Eq. (10) is of the same order as the sensitivity term, the method is satisfactory.

For thermal problems in which some of the sensitivities change sign or for which both the sensitivity and signal approach zero such that the ratio is somewhat erratic, we have found that it is not possible to use an optimization program without limiting the range of variables to be considered. This range can normally only be found by examining n-dimensional maps of Ω, thus implying a limit on the number of parameters, n, that can be estimated.

References

Abernathy, R. B., Benedict, R. P., and Dowdell, R. B., 1985, "ASME Measurement Uncertainty," ASME *Journal Fluids Engineering*, Vol. 107, pp. 161–164.

Alifanov, O. M., 1994, *Inverse Heat Transfer Problems*, Springer-Verlag, New York.

Beck, J. V., and Arnold, K. J., 1977, *Parameter Estimation in Engineering and Science*, Wiley, New York.

Fadale, T. D., Nenarokomov, A. V., and Emery, A. F., 1995a, "Two Approaches to Optimal Sensor Locations," ASME JOURNAL OF HEAT TRANSFER, Vol. 117, pp. 373–379.

Fadale, T. D., Nenarokomov, A. V., and Emery, A. F., 1995b, "Uncertainties in Parameter Estimation: The Inverse Problem," *The International Journal of Heat and Mass Transfer*, Vol. 38, pp. 511–518.

Fedorov, V. V., 1972, *Theory of Optimal Experiment*, Academic Press, New York.

Gill, P. E., Murray, W., Saunders, M. A., and Wright, M. H., 1986, *User's Guide for NPSOL—A Fortran Package for Nonlinear Programming*, Technical Report SOL 86-2, Department of Operations Research, Stanford University, Stanford, CA, Jan.

Goodwin, G. E., and Payne, R. L., 1977, *Dynamic System Identification. Experiment Design and Data Analysis*, Academic Press, New York.

Kubrusly, C. S., and Malebranche, H., 1982, *Proc. 3rd IFAC Symposium on Control of Distributed Parameter Systems*, pp. 59–73.

Moffat, R. J., 1988, "Describing the Uncertainties in Experimental Results," *Experimental Thermal and Fluid Science*, Vol. 1, pp. 3–17.

Musylev, N. V., 1980, "Uniqueness Theorems for Certain Inverse Heat Conduction Problems," *Zh. Vychisl. Mat. Fiz.*, Vol. 20(2), pp. 388–400.

Polis, M. P., 1982, "The Distributed System Parameter Identification Problem: A Survey of Recent Results," *Proc. 3rd IFAC Symposium on Control of Distributed Parameter Systems*, pp. 45–58.

Seber, G. A. F., and Wild, C. J., 1989, *Nonlinear Regression*, Wiley Interscience, New York.

Taktak, R., Beck, J. V., and Scott, E. P., 1993, "Optimal Experimental Design for Estimating Thermal Properties of Composite Materials," *Int. J. Heat Mass Transfer*, Vol. 36(12), pp. 2977–2986.

Walter, E., and Pronzato, L., 1990, "Qualitative and Quantitative Experiment Design for Phenomenological Models—A Survey," *Automanca*, Vol. 26(3), pp. 195–213.

Downloaded 11 Dec 2010 to 193.140.21.150. Redistribution subject to ASME license or copyright; see http://www.asme.org/terms/Terms_Use.cfm

Nonlocal and Nonequilibrium Heat Conduction in the Vicinity of Nanoparticles

G. Chen
Assistant Professor,
Department of Mechanical Engineering
and Materials Science,
Duke University,
Durham, NC 27708
Mem. ASME

Heat transfer around nanometer-scale particles plays an important role in a number of contemporary technologies such as nanofabrication and diagnosis. The prevailing method for modeling thermal phenomena involving nanoparticles is based on the Fourier heat conduction theory. This work questions the applicability of the Fourier heat conduction theory to these cases and answers the question by solving the Boltzmann transport equation. The solution approaches the prediction of the Fourier law when the particle radius is much larger than the heat-carrier mean free path of the host medium. In the opposite limit, however, the heat transfer rate from the particle is significantly smaller, and thus the particle temperature rise is much larger than the prediction of the Fourier conduction theory. The differences are attributed to the nonlocal and nonequilibrium nature of the heat transfer processes around nanoparticles. This work also establishes a criterion to determine the applicability of the Fourier heat conduction theory and constructs a simple approximate expression for calculating the effective thermal conductivity of the host medium around a nanoparticle. Possible experimental evidence is discussed.

Introduction

The past few years have witnessed a significant increase of interests in micro- and nanometer scale thermal phenomena (Tien and Chen, 1994). Previous efforts have largely focused on the study of thin films for which boundary and interface effects are important. A wide range of micro- and nanoscale thermal problems, however, involves nonplanar geometries such as spherical particles. With the explosive growth of research and development in nanomaterials and quantum structures (Weisbuch and Vinter, 1991), understanding heat transfer processes around nanoparticles becomes increasingly important. Examples include the optical and electron beam probing of quantum dots (Rodrigues et al., 1995), micro- and nanoscale thermal conductivity profilers (Nonnenmacher and Wickramasinghe, 1992; Pylkii et al., 1994), high-density thermomagnetic recording (Nakamura et al., 1995), and nanofabrication (Li et al., 1989a).

Under the Fourier heat conduction theory, the temperature profile around a heated spherical region can be easily obtained. Solutions from the Fourier heat conduction theory have been applied to the modeling of a variety of heat conduction phenomena around nanometer scale heated regions, e.g., electron beam microscopy (Gryaznov et al., 1991), nanoscale thermal conductivity mapping (Nonnenmacher and Wickramasinghe, 1992; Pylkii et al., 1994), antifuse circuit (Zhang et al., 1995), and high-density thermomagnetic recording (Nakamura et al., 1995). The applicability of the Fourier theory for heat conduction around nanoparticles, however, needs to be examined. This is because the result of Fourier heat conduction theory is valid only when there are enough scattering events around the particle such that the heat carriers excited by the heat-generating particle can exchange energy with the surrounding medium. When the particle radius is much smaller than the heat-carrier (electrons or phonons) mean free path, however, very few scattering events occur around the heated sphere. In this region, the heat carrier transport is ballistic or nonlocal.

Contributed by the Heat Transfer Division for publication in the JOURNAL OF HEAT TRANSFER. Manuscript received by the Heat Transfer Division August 11, 1995; revision received March 28, 1996. Keywords: Conduction, Thermal Packaging, Thermophysical Properties. Associate Technical Editor: A. Lavine.

Ballistic heat transfer has been studied in planar geometries where boundary and interface scattering contributes significantly to the thermal resistance. Mahan and Claro (1988), and Claro and Mahan (1989) investigated the nonlocal heat transfer effects during transient heating of planar geometries based on the Boltzmann transport equation (BTE). Majumdar (1993) derived the equation of phonon radiative transfer from the BTE and employed it to study heat transfer across diamond thin films for both steady-state and transient cases (Joshi and Majumdar, 1993). Based on a similar approach, Chen and Tien (1993) studied thermal transport in quantum-well structures, and Goodson (1996) investigated heat conduction in nonhomogeneous diamond films. Monte-Carlo simulations of ballistic phonon transport in planar geometries have been carried out (Klitsner et al., 1988; Peterson, 1994).

The objectives of this work are to examine the applicability of the Fourier heat conduction theory to nonplanar nanostructures and to provide a general solution for the temperature rise of heat-generating nanometer and micrometer particles embedded in a host medium. Starting from the BTE and based on the established methods in radiation heat transfer, an integral equation governing the equivalent temperature distribution around nanoparticles is obtained and presented in the form of a universal function. This study shows that the effective temperature rise of a nanoparticle is significantly higher than the prediction of the Fourier law when its radius is smaller than the heat-carrier mean free path. The physical origin of the discrepancy between the two approaches is attributed to the nonlocal and nonequilibrium nature of the involved transport processes. This work also establishes a criterion to determine the applicability of the Fourier heat conduction theory and constructs a simple approximate expression for calculating the effective thermal conductivity of the host medium around a nanoparticle. Possible experimental evidence is discussed.

Mathematical Formulation

Consider a micrometer to nanometer scale particle with uniform heat generation embedded in a host medium as shown in Fig. 1. This work focuses on heat transfer around the particle rather than inside the particle because the final temperature rise at the boundary depends on heat conduction in the host medium.

Copyright © 1996 by ASME

Downloaded 11 Dec 2010 to 193.140.21.150. Redistribution subject to ASME license or copyright; see http://www.asme.org/terms/Terms_Use.cfm

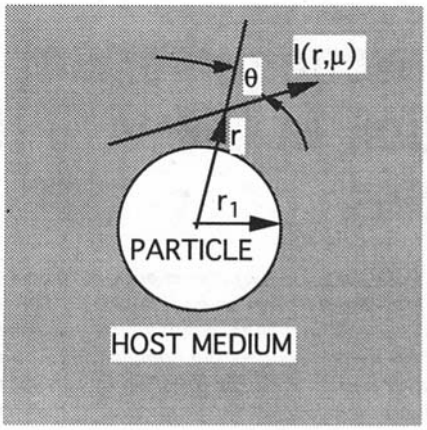


Fig. 1 Model and coordinate system

Due to heat generation inside the particle, heat carriers (electrons and/or phonons) will be excited in the host medium. In analogy to thermal radiation (Siegel and Howell, 1992), these excited heat carriers can be treated as emissions from the particle. The subsequent transport of the emitted heat carriers determines the heat transfer rate and the temperature rise of the particle. For reasons that will be explained later, results of this work apply mainly to dielectric host media in which the major heat carriers are phonons, although discussions on metallic media will be made whenever appropriate. To simplify the problem, the following assumptions are made: (1) diffuse heat carrier emission and reflection at the interface between the particle and the host medium; (2) relaxation time approximation for scattering in the host medium; and (3) frequency independent relaxation time (gray medium). A detailed discussion on the validity and limitations of these approximations will be presented in the next section.

Similar to the treatment of Majumdar (1993), a total carrier intensity is introduced[1]

$$I = \frac{1}{4\pi} \sum_p \int \nu_p f \hbar\omega D(\omega) d\omega \tag{1}$$

where D is the density of states, f the heat carrier distribution, v_p the heat carrier group velocity, and ω the angular frequency. The summation is over different polarizations of heat carriers and the integration spans all the allowable frequency of the heat carriers. Instead of the spectral heat-carrier intensity, the total intensity is employed because of the gray medium assumption. The BTE can be rewritten in terms of the heat-carrier intensity as

$$\mu \frac{\partial I}{\partial r} + \frac{1-\mu^2}{r} \frac{\partial I}{\partial \mu} = -\frac{I - I_o}{\Lambda} \tag{2}$$

where μ (=cos θ) is the directional cosine, I_o the equilibrium heat carrier intensity, and r the radial distance. As will become clear, this work addresses cases for which heat carriers deviate significantly from their thermal equilibrium distribution. Strictly speaking, a local temperature cannot be defined. The equilibrium distribution function employed here serves merely as a definition for the equivalent temperature corresponding to the average heat-carrier energy around each spatial point (Goodson and Flik, 1992; Chen and Tien, 1993). According to the assumption, the heat-carrier mean free path, Λ, is independent of frequency.

The diffuse boundary conditions for the problem can be written as

$$I(r_1, \mu \geq 0) = \epsilon I_e(T_e) + (1-\epsilon) I_-(r_1) = I_1$$
$$\text{and} \quad I(\infty, \mu) = I_\infty \tag{3}$$

where ϵ is the heat-carrier emissivity, which in principle can be calculated following a similar procedure as in the treatment of thermal boundary resistance (Swartz and Pohl, 1989). Again, ϵ is assumed to be independent of frequency. The temperature in Eq. (3), T_e, represents the equivalent temperature of the heat carriers excited in the host medium by the heat-generating particle at the particle and host medium interface, and I_e is the corresponding intensity of those carriers.

This formulation is a limiting case of the radiative transfer between two concentric spheres, for which a large amount of work has been done and will not be reviewed here (Viskanta and Crosbie, 1967; Siegel and Howell, 1992). Equation (2) can be transformed into an integral equation in terms of an universal function φ (Viskanta and Crosbie, 1967)

$$\varphi(\tau) = \frac{1}{2\tau} \int_{\tau_1}^{\infty} K(\tau, t) \varphi(t) dt \tag{4}$$

where

$$\varphi(\tau) = [e_o(\tau) - F_1]/(e_\infty - F_1) \tag{5}$$

$$K(\tau, t) = \{E_1(|\tau - t|) - E_1[(\tau^2 - \tau_1^2)^{1/2} + (t^2 - \tau_1^2)^{1/2}]\} t \tag{6}$$

E_n is the exponential integral function of nth order (Siegel and Howell, 1992), and τ (=r/Λ) is the nondimensional radial distance. The equilibrium heat-carrier emissive power $e_0 = \pi I_o$ and the heat-carrier radiosity $F_1 = \pi I_1$ have similar meanings as in thermal radiation. The heat flux at the interface between the particle and the host medium can be calculated from

[1] A factor of $1/4\pi$ is introduced (Chen and Tien, 1993) because $f \hbar\omega D$ represents the heat carrier energy density.

Nomenclature

C = volumetric specific heat, $Jm^{-3} K^{-1}$
D = density of states, m^{-3}
e = heat-carrier emissive power, Wm^{-2}
E = exponential function
f = heat-carrier distribution function
F = heat-carrier radiosity, Wm^{-2}
$\hbar$ = Planck's constant, Js
H = integration kernel
I = total heat-carrier intensity, Wm^{-2} sr^{-1}
k = thermal conductivity, $Wm^{-1}K^{-1}$
K = integration kernel
q = heat flux, Wm^{-2}
Q = nondimensional heat flux
r = radial distance, m
T = temperature, K
v = heat-carrier velocity, ms^{-1}
ϵ = heat-carrier emissivity
θ = angle between ray and radial direction
Λ = heat-carrier mean free path, m
μ = directional cosine
τ = nondimensional radius
φ = universal function
ω = angular frequency
Ω = solid angle

Subscripts

b = Boltzmann transport equation
e = excited carrier
eff = effective
f = Fourier heat conduction theory
o = equilibrium
p = heat-carrier polarization
1 = particle/host-medium interface
∞ = ambient

Downloaded 11 Dec 2010 to 193.140.21.150. Redistribution subject to ASME license or copyright; see http://www.asme.org/terms/Terms_Use.cfm

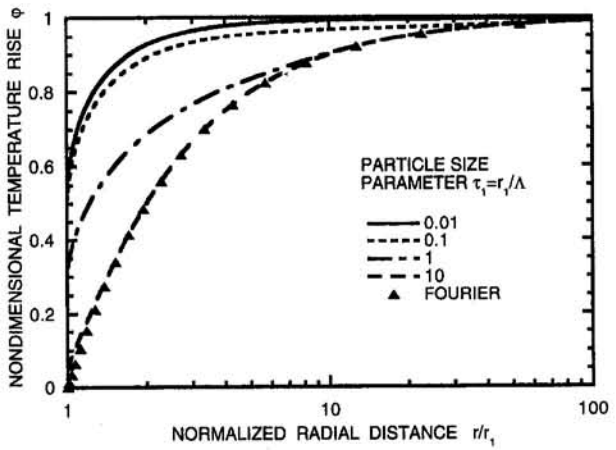


Fig. 2 Distribution of nondimensional equivalent temperature

$$q_{b1} = \frac{(e_e - e_\infty)Q(\tau_1)}{\tau_1^2 + (1/\epsilon_1 - 1)Q(\tau_1)} \tag{7}$$

where e_e [$=\pi I_e(T_e)$] is the emissive power of the excited heat carriers and $Q(\tau)$ the nondimensional heat flux defined as

$$Q(\tau) = \frac{\tau^2 q(\tau)}{F_1 - F_2} \tag{8}$$

with F_2 representing heat-carrier radiosity at infinite. At the particle-medium interface, $Q(\tau_1)$ can be expressed as (Viskanta and Crosbie, 1967)

$$Q(\tau_1) = -2\int_{\tau_1}^{\infty} H(\tau_1, t)\varphi(t)dt \tag{9}$$

$$H(\tau_1, t) = \{-\tau_1 E_2(t - \tau_1) + E_3(t - \tau_1) - E_3[(t^2 - \tau_1^2)^{1/2}]\}t \tag{10}$$

Before discussing the solution of Eq. (4), an examination of the relation between the BTE and the Fourier law will provide a foundation for comparison. Solution of the Fourier heat conduction equation yields the heat flux at the particle and host medium interface as

$$q_{f1} = \frac{k(T_e - T_\infty)}{r_1} = \frac{C\upsilon(T_e - T_\infty)}{3\tau_1} \tag{11}$$

where thermal conductivity has been replaced by $k = C\upsilon\Lambda/3$. Equation (11) implicitly assumes that thermal conductivity is independent of temperature. This assumption will be invoked for most of the work. To relate the equilibrium heat-carrier emissive power to the local temperature, the derivative of e_o with respect to temperature is taken:

$$\frac{de_o}{dT} = \frac{1}{4}\sum_p \upsilon_p \hbar\omega D(\omega)\frac{df_o}{dT} = \frac{\upsilon C}{4} \tag{12}$$

At low temperatures, the specific heat of phonons is proportional to the third power of temperature and approaches a constant at higher temperatures. The specific heat of electrons is linearly proportional to temperature (Ashcroft and Mermin, 1976). In this work, a temperature independent specific heat will be assumed. Integrating this equation and substituting e_e and e_∞ into Eq. (5) and Eq. (7) yields

$$\varphi(\tau) = \frac{T(\tau) - [\epsilon T_e + (1 - \epsilon)T(\tau = \tau_1)]}{T_\infty - [\epsilon T_e + (1 - \epsilon)T(\tau = \tau_1)]} \tag{13}$$

$$q_{b1} = \frac{C\upsilon(T_e - T_\infty)Q(\tau_1)/4}{\tau_1^2 + (1/\epsilon_1 - 1)Q(\tau_1)} \tag{14}$$

where $T(\tau = \tau_1)$ represents the host medium temperature at the interface. The ratio of heat flux at the interface predicted from the BTE and the Fourier law for a black emitting interface is then

$$\frac{q_{b1}}{q_{f1}} = \frac{3Q(\tau_1)}{4\tau_1} \tag{15}$$

As τ_1 becomes much larger than one, it is expected that the two heat fluxes given by Eq. (11) and Eq. (14) should approach each other, which means

$$\lim_{\tau_1 \to \infty} Q(\tau_1) = 4\tau_1/3 \tag{16}$$

Similar to Viskanta and Crosbie (1967), Eq. (4) is solved iteratively. The convergence criterion used for terminating the iteration is max $|\varphi_{n+1}(\tau) - \varphi_n(\tau)| < \Delta$. For most of the calculations, $\Delta = 10^{-6}$ is imposed. The value of $Q(\tau_1)$ calculated for $\tau = 0.1$ was 9.6×10^{-3}, slightly larger than the result of 9.28×10^{-3} obtained by Rhymings (1965) for a spherical shell with $\tau_1 = 0.1$ and $\tau_2 = 10$, which is probably due to the infinite outer shell radius for the current case. For $\tau_1 = 0.01$, the calculated value of $Q(\tau_1)$, 0.996×10^{-4}, is identical to the value obtained by Viskanta and Crosbie (1967) for a spherical shell with $\tau_1 = 0.01$ and $\tau_2 = 1$.

Results and Discussion

The solution of Eq. (4) for the nondimensional equivalent temperature distribution is shown in Fig. 2 as a function of the radial distance normalized to the particle radius for different particle size parameter τ_1. As expected, the temperature distribution calculated from the BTE approaches the prediction of the Fourier law when the particle radius is much larger than the heat-carrier mean free path. When the particle radius becomes comparable or even smaller than the heat-carrier mean free path, the temperature distribution deviates significantly from the prediction of the Fourier law. One major difference between the solution of the BTE and the Fourier heat conduction theory is that a temperature jump occurs at the boundary. The physical explanation for the observed difference will be given after an examination of the heat flux leaving the particle.

Figure 3 demonstrates the nondimensional heat flux $Q(\tau_1)$ predicted from the BTE and the Fourier law. Clearly, the actual heat transfer rate leaving the particle can be significantly smaller than the prediction of the Fourier law. For the application of the Fourier theory to a black particle with a 5 percent relative error, the required particle size parameter is

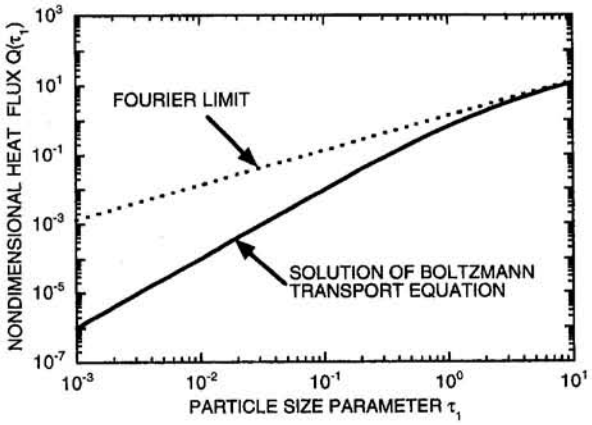


Fig. 3 Nondimensional heat flux as a function of particle size parameter

Downloaded 11 Dec 2010 to 193.140.21.150. Redistribution subject to ASME license or copyright; see http://www.asme.org/terms/Terms_Use.cfm

Table 1 Heat-carrier mean free path of representative materials at room temperature

Material	Thermal Conductivity $Wm^{-1}K^{-1}$	Specific Heat $10^6\ Jm^{-3}K^{-1}$	Carrier Velocity ms^{-1}	Mean-Free-Path nm
Diamond	2300	1.78	12288	315
Gold	315	0.021†	1460000	31
Gallium Arsenide	44	1.71	3324	23
Silicon Dioxide	1.4	1.79	4100	0.6
Sapphire	46	3.04	~11489	4.0
Silicon	153	1.64	6533	43

† electronic specific heat

$$\tau_1 > 21 \quad \text{for} \quad \left| \frac{q_{f1} - q_{b1}}{q_{f1}} \right| < 5 \text{ percent} \qquad (17)$$

The estimated values of the mean free path for several representative materials at room temperature are listed in Table 1.

Temperature Jump and Nonequilibrium Carrier Transport. According to Eq. (13), the value of φ at the interface is zero if $T(\tau = \tau_1)$ equals the temperature of the excited heat carriers. As shown in Fig. 2, this is indeed the case when the particle size parameter τ_1 is large. With decreasing particle size parameter value, however, the value of φ at the interface becomes nonzero, indicating a nonequal temperature between the excited heat carriers and the local temperature at the interface. Such a nonequal temperature, or temperature jump, was predicted by Klitsner et al. (1988) for radiative heat conduction across a bar and by Majumdar (1993) for heat conduction across a thin film. The temperature jump concept is routinely used in radiation calculations (Siegel and Howell, 1992), although it is often emphasized that such a discontinuity disappears in the presence of heat conduction. For heat conduction, there is no longer a similar explanation and the origin of such a temperature jump must be clearly understood.

The reason for the temperature jump lies in the nonequilibrium nature of the problem and the definition of the equivalent temperature. It has been carefully stated that T_e represents the temperature of heat carriers at the boundary of the host medium that are excited by the heat generating particle. The calculated temperature at $\tau = \tau_1$ is the equivalent temperature of the host medium at that point, which according to the definition, is an average of the energy of all heat carriers at that location. These include the heat carriers excited by the heat generating particle and the heat carriers coming from the region outside the particle. The nonzero value of φ suggests a nonequilibrium situation. Figures 4(*a*) and 4(*b*) illustrate the nonlocal and nonequilibrium nature of the transport processes in a one-dimensional bar (Klitsner et al., 1988) and around a spherical particle, respectively. In the limit of no internal scattering, two groups of heat carriers exist inside the medium. For the one-dimensional bar case, these are the carriers excited by the heater and the cooler,

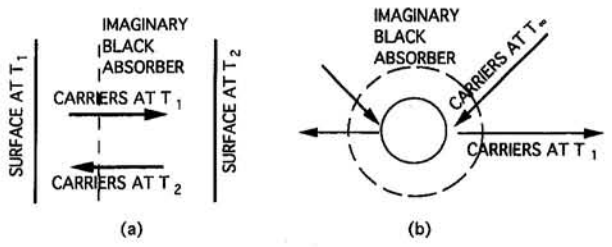


Fig. 4 Physical picture of the nonlocal and nonequilibrium heat transport processes (*a*) across a one-dimensional bar and (*b*) around a particle

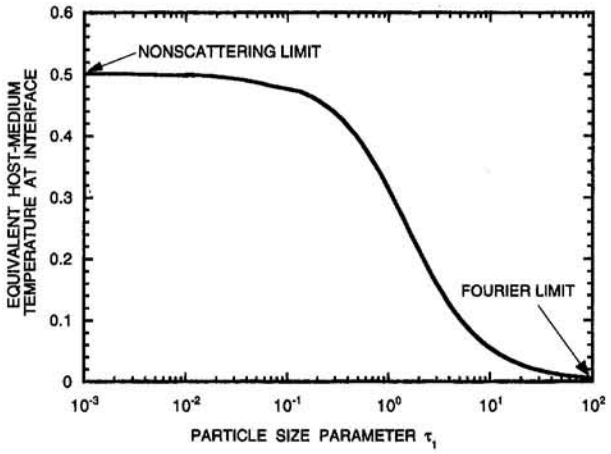


Fig. 5 Equivalent temperature of the host medium at the interface

respectively. Because of the absence of scattering, the heat-carriers excited by the heater and the cooler propagate in opposite directions without interacting with each other. The lack of interaction implies that the two groups of carriers will not reach a local equilibrium state with each other. Each group will have the same temperature as it is generated during the flight of these carriers across the bar. The temperature calculated in this work serves as a measure of the average energy of the two groups of energy carriers. This can be understood by imagining a black absorber inserted in the bar. Heat carriers reaching the absorber will be thermalized and the black absorber temperature will be some kind of average of the two. The exact relation of the average temperature to those of the two groups of heat carriers depends on the temperature dependence of the heat-carrier intensity. When the specific heat is independent of temperature, the average temperature is an arithmetic average of the temperatures of heat carriers emitted from the heater and the cooler, respectively. The same argument also holds for spherical geometries. Considering an imaginary black-absorbing concentric partition between the particle and the ambient, the heat carriers inside the partition come from the nanoparticle only and those outside the partition originate from the ambient energy input. The temperature of the partition can be estimated according to the standard radiation transfer method (Siegel and Howell, 1992). It can be shown that the partition temperature drops faster than the prediction of the Fourier law with increasing τ for small τ_1, as is evident in Fig. 2. It can also be anticipated that the average nondimensional temperature of the host medium at the interface approaches 0.5 as the nondimensional radius becomes much smaller than unity. This is indeed true, as demonstrated in Fig. 5. At $\tau_1 = 0.001$, the average nondimensional temperature of the medium at $\tau = \tau_1$ is 0.5.

Upon clarification of the nonequilibrium and the ballistic transport nature of heat carriers, it is straightforward to explain why the heat transfer rate predicted from the Fourier law is larger than that from the BTE. The temperature distribution obtained from the Fourier law implies that there is always enough scattering in a small volume around each point to establish the local thermal equilibrium condition. Clearly, this assumption breaks down in the limit of no scattering at all inside the medium. In this case, the solution obtained from the Fourier conduction theory still implies that scattering exists to cool down the hot carriers emitted from the particle. These nonexistent, imaginary scattering events implied in the Fourier theory for the temperature distribution have the false effect of cooling down the hot carriers emitted from the particle and thus causing the overprediction of the heat transfer rate between the particle and the host medium. At first glance, this explanation seems to be different from the prevailing understanding of size effects

Downloaded 11 Dec 2010 to 193.140.21.150. Redistribution subject to ASME license or copyright; see http://www.asme.org/terms/Terms_Use.cfm

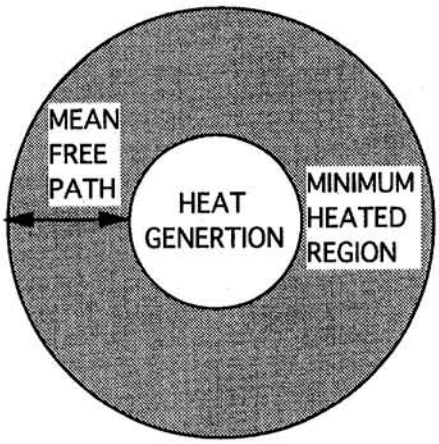


Fig. 6 Minimum heat affected region around a heat source

in thin film. For thin films, the boundaries as shown in Fig. 4(*a*) act as artificial scatterers; their presence shortens the heat-carrier mean free path. Such a difference, however, can be unified under the imaginary scattering picture discussed above. The linear temperature distribution in a thin film predicted from the Fourier heat conduction theory implies the existence of enough scattering events inside the film to transfer the energy of the hot carriers emitted from the hot wall to the low-energy carriers in the medium, which is impossible if there is no scattering inside the film. It is again the imaginary scattering events that cause the overprediction of heat flux by the Fourier heat conduction theory.

This discussion on the nonequilibrium nature of the carrier transport process leads to the following fundamental question: What is the size of the heat-affected region? The importance of this question can be appreciated by considering an extreme situation. Suppose that the interface temperature of a particle embedded in a superconducting material, such as in the case of scanning electron microscopy of superconductors (Flik and Tien, 1990), has reached the transition temperature of the host medium. Will the host medium lose its superconductivity? Superficially, the average temperature of the medium will be still lower than the transition temperature. Under the nonequilibrium carrier transport picture presented above, it should be realized that there are in fact two groups of lattice vibrations: one vibrating near the transition temperature and the other at a lower temperature. This picture suggests that the transition to normal state actually occurs although the equivalent temperature is lower than the transition temperature. For the more general question on the size of the heat affected region, this discussion indicates that in a region on the order of the heat-carrier mean free path, there will be two groups of phonons, one close to the temperature of the nanoparticle, the other close to the ambient temperature. This picture is consistent with the harmonic oscillator approach of phonons. The harmonic vibration of the atoms always extends into a region of the order of mean free path, nearly independent of the size of the excitation source. The concept of minimum heat-affected region is represented in Fig. 6.

So far, this work has intentionally avoided the case of a metallic host medium, in which the major heat carriers are electrons. The major resistance for the energy flow carried by the electrons, however, comes from the electron and phonon scattering, especially for pure metals (Ziman, 1960; Berman, 1975). Based on similar reasons discussed above, the electrons and phonons may not be at thermal equilibrium. The nonequilibrium energy exchange between electrons and phonons have been observed in ultrafast processes (Anisimov et al., 1974; Yajima et al., 1988; Qiu and Tien, 1993). In electronics, it is called hot electron effects and has been studied extensively (Reggiani, 1985). It is believed, however, that the thermally driven hot electron transfer mechanisms have not been proposed before this study.

Effective Thermal Conductivity. Although these discussions clearly indicate that the concept of thermal conductivity breaks down in the conventional sense, an effective thermal conductivity can nevertheless be defined such that the heat transfer rate at the interface formally obeys the result of the Fourier conduction theory, i.e., Eq. (11),

$$q_{b1} = \frac{k_{\text{eff}}(T_e - T_\infty)}{r_1} \tag{18}$$

Combining this definition with Eq. (15) gives

$$\frac{k_{\text{eff}}}{k} = \frac{3Q(\tau_1)}{4\tau_1} \tag{19}$$

Clearly, this effective thermal conductivity is particle size dependent. The solid line in Fig. 7 shows the normalized effective thermal conductivity of a medium surrounding a particle as a function of the particle size parameter calculated from the exact solution of the integral equation. For practical calculation, the following approximations are found to represent the exact solutions very well:

$$Q(\tau_1) = \frac{\tau_1^2}{3\tau_1/4 + 1} \tag{20}$$

$$\frac{k_{\text{eff}}}{k} = \frac{3\tau_1/4}{3\tau_1/4 + 1} \tag{21}$$

as shown by the dots in Fig. 7. The maximum relative error between the exact solution and the approximation for the effective thermal conductivity is 12 percent and occurs at $\tau_1 = 1$. Surprisingly, these expressions are closer to the solution of radiative transfer between two parallel plates than between two concentric spheres based on the P_1 method (Siegel and Howell, 1992). This is because this approximation approaches the correct limits for the cases of large and small particle size parameters. For small particle size parameter values, the scattering can be totally neglected and the heat flux can be calculated from the ray tracing method as used in radiative transfer (Siegel and Howell, 1992),

$$q_{b1} = e_e - e_\infty = Cv(T_e - T_\infty)/4 \quad \text{for} \quad \tau_1 \to 0 \tag{22}$$

Combining this equation with Eq. (11) yields

$$k_{\text{eff}}/k = 3\tau_1/4 \quad \text{for} \quad \tau_1 \to 0 \tag{23}$$

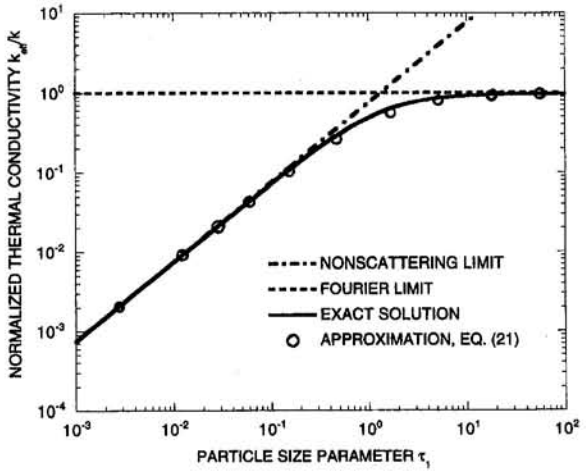


Fig. 7 Normalized effective thermal conductivity as a function of particle size parameter

Downloaded 11 Dec 2010 to 193.140.21.150. Redistribution subject to ASME license or copyright; see http://www.asme.org/terms/Terms_Use.cfm

which is consistent with the approximate expression, Eq. (21). This limiting solution is also plotted in Fig. 7.

Possible Experimental Evidence. Although the discussed problem is relevant to many contemporary technologies as exemplified in the introduction, there exist no definitive experimental data that can be cited to confirm the present model. Three experimentally observed phenomena, however, may be related to the present work. These experiments are in the quantum dots probing (Rodrigues et al., 1995), high density thermomagnetic recording (Nakamura et al., 1995), and nanofabrication (Li et al., 1989).

Quantum Dots. Quantum dots are very fine particles that demonstrate strong quantum size effects (Weisbuch and Vinter, 1991). These ultrasmall structures hold the promise of greatly improving the performance of electronic devices. Rodrigues et al. (1995) measured the temperature of CdSe quantum dots with an average radius of 3 nm embedded in a glass matrix under argon laser irradiation and observed an anomalous temperature rise of the particle. According to their calculation, which assumes the glass and quantum dots as a homogeneous medium with a measured absorption coefficient of 23 cm^{-1}, the theoretical temperature rise of the medium under a 2600 W/cm^2 irradiation should be 160 K. The measured temperature rise of the quantum dots, however, is about 480 K—a threefold increase compared to the predicted value. To estimate whether the observed anomalous temperature rise of the quantum dots is due to the absorption of the particle, the Rayleigh scattering theory is employed (Bohren and Huffman, 1983). Assuming that bulk optical constants of CdSe (Schaffner et al., 1992) are valid for the quantum dots, the calculated temperature rise of the quantum dots above its ambient, according to the Fourier theory, is of the order of 10^{-4} K. This temperature rise is much too low to explain the observed anomalous heating. According to Fig. 7 and Table 1, the effective thermal conductivity around a CdSe quantum dot should be 75 percent of the bulk glass (SiO_2) thermal conductivity. This value is still too low for the observed phenomena. Two additional factors should be combined to explain the observed phenomena. One is that the phonon quantization in the CdSe particle suggests that the transmissivity (or emissivity ϵ) is less than unit. The other is due to the gray body assumption (Chen and Tien, 1993). Among these two factors, the former is more likely to account for the observed large anomalous temperature rise.

High-Density Thermomagnetic Recording. Scanning tunneling electron microscope (STM) was used for high-density thermomagnetic recording by Nakamura et al. (1995). In this method, the tunneling current between the STM tip and the sample heats up a 5 nm region. The recording domain is determined by the Curie temperature of the recording medium. The recording domain diameter calculated according to the Fourier heat conduction theory is 180 nm, but the measured one is 230 nm (Nakamura et al., 1995). The larger observed recording domain diameter is consistent with the conclusion that the Fourier law overpredicts the heat transfer rate from the heated region.

Nanofabrication. Although previous discussion has suggested the possibility of a nonequilibrium state between electrons and phonons and cautioned against the application of the current study directly to metals, similar reduction in the effective thermal conductivity of metal can be expected. Strong experimental evidence exists on the reduction of the effective thermal conductivity in some nanofabrication experiments on metals. Li et al. (1989a) applied a voltage between the tip of a scanning electron microscope (STM) and a gold sample and observed nanoscale hillock formation. They attributed the observed phenomenon to a melting mechanism. This was questioned (Marella and Pease, 1989) because the calculated temperature rise under the tip from the Fourier heat conduction theory is only 0.2°C for a 10 Å heat generation region. Li et al. (1989b) pointed out the failure of the Fourier theory and the possibility of nonequilibrium states for their experimental conditions. This study provides quantitative proof for their argument. In a study of the energy dissipation processes in scanning tunneling microscope, Flores et al. (1986) argued that the effective thermal conductivity around a small heated region is proportional to τ_l, which is consistent with Eq. (23) at the small particle size parameter limit. Using the electron mean free path in gold and a 5 Å heat generation radius, the effective thermal conductivity of gold around the heated region is estimated to be 46.5 times smaller than its bulk value, and the calculated temperature rise under the same condition as used by Marella and Pease (1989) is approximately 10°C. This value, however, is still much lower than the proposed melting mechanism, probably due to the nonequilibrium processes that is not well accounted for in this model.

Limitations of the Model. The objectives of the current work are to demonstrate the failure of the Fourier law for a wide range of problems encountered in contemporary technologies and to present an alternative and more realistic approach. As can be seen in the discussions, this study raises many more interesting questions that should be addressed in future studies. One major limitation of the work is in the use of the temperature concept to represent nonequilibrium transport processes. The error caused by such an approximation is unknown and will be assessed in future studies. This work is based on the assumption that the mean free path can be represented by an average value, although it is straightforward to include the frequency dependence of the mean free path as has been carried out in planar geometries (Chen and Tien, 1993; Majumdar, 1993). The assumption made on diffuse emission can be relaxed to take into account specular reflection effects. From these discussions, it should be clear that this work captures the nonlocal nature of the heat conduction process and its consequence on heat transfer rate from the particle. The work can be readily extended to cylindrical geometry, which has important applications such as quantum wires, nanotubes, and electronic devices (Weisbuch and Vinter, 1991).

The discussion so far has not made any distinction on whether the heat generation region is made of the same material as the host medium, or is different. Both cases can arise in practice as is evident from the previously mentioned experiments. If the heat generation region is made of the same material as the host medium, no thermal boundary resistance exists between the "particle" and the host medium. Carriers inside the heat generation region are also in a nonequilibrium state, similar to the situation at the interface discussed before. The temperature T_e represents the temperature of those carriers excited by the energy input into the region. If the heat-generating region is a different material from the host medium, there will be a thermal boundary resistance at the particle and host–medium interface (Swartz and Pohl, 1989). In this case, the energy carriers inside the particle may still be at a nonequilibrium state, depending on the heat carrier mean-free-path inside the particle. The temperature of heat carriers excited inside the particle by the energy input can be estimated from the thermal boundary resistance, temperature T_e, and the energy input.

Another point that should be addressed is the lower particle diameter limit where this study is applicable. If the particle is made of a different material from the host medium, the allowable energy states of heat carriers inside the particle will change as its diameter becomes smaller and smaller (quantum size effects). The change of energy states inside the particle will affect the excitation of energy carriers and also the energy states of the host medium. If the energy states between the host medium and the particle are very different, very few energy carriers can be excited in the host medium as determined by the principle

Downloaded 11 Dec 2010 to 193.140.21.150. Redistribution subject to ASME license or copyright; see http://www.asme.org/terms/Terms_Use.cfm

of quantum mechanics. In a classical sense, this corresponds to a large thermal boundary resistance. A clearer picture can be obtained by considering an atomic impurity embedded in a host matrix, which is a topic treated extensively in physics (Baker and Sievers, 1975). The impurity atom may create a localized state, which has a very different energy level from those of the host atoms and is thus confined to a region around the impurity. If the particle is made of the same material as the host medium and the force constants between atoms are not affected by the methods of energy input, the previous analysis should be still applicable.

Conclusions

This work presents a theoretical study on the nonlocal and nonequilibrium heat transfer effects on the temperature rise of nanoscale particles embedded in a host medium. Based on the definition of the equivalent temperature, a general solution for the temperature rise of nanoscale particles embedded in a host medium is obtained by solving the Boltzmann transport equation. The results show that significant differences exist between the prediction of the BTE and the Fourier heat conduction theory when the particle radius approaches the heat-carrier mean free path. The physical origin for the difference between the two methods is explained based on the nonlocal and nonequilibrium nature of the heat carrier transport. A criterion is established to determine the applicability of the Fourier heat conduction theory. Possible experimental evidence is discussed.

Acknowledgments

The author is grateful to Professor T. Y. Tan for stimulating discussions on phonons, and particularly, on the heat-affected region of phonons. He would like to thank Dr. P. A. M. Rodrigues for sending him a preprint of their work and Dr. C. H. Goldman for pointing out an important reference. He is also grateful for the financial support of a National Science Foundation Young Investigator Award, the Lord Foundation of North Carolina, and the Duke university school of engineering start-up fund.

References

Anisimov, S. I., Kapeliovich, B. L., and Perel'man, T. L., 1974, "Electron Emission From Metal Surface Exposed to Ultrashort Laser Pulses," *Soviet Physics, JETP,* Vol. 39, pp. 375–377.

Ashcroft, N. W., and Mermin, N. D., 1976, *Solid State Physics,* Saunders, Philadelphia.

Baker, A. S., Jr., and Sievers, A. J., 1975, "Optical Studies of the Vibrational Properties of Disordered Solids," *Review of Modern Physics,* Vol. 47, Suppl. 2, pp. S1–S180.

Berman, R., 1976, *Thermal Conduction in Solids,* Clarendon, Oxford.

Bohren, C., and Huffman, D. R., 1983, *Absorption and Scattering of Light by Small Particles,* Wiley, New York.

Chen, G., and Tien, C. L., 1993, "Thermal Conductivity of Quantum Well Structures," AIAA *Journal of Thermophysics and Heat Transfer,* Vol. 7, pp. 311–318.

Claro, F., and Mahan, G. D., 1989, "Transient Heat Transport in Solids," *Journal of Applied Physics,* Vol. 66, pp. 4213–4217.

Flik, M. I., and Tien, C. L., 1990, "Intrinsic Thermal Stability for Scanning Electron Microscopy of Thin-Film Superconductors," *Journal of Applied Physics,* Vol. 67, pp. 362–370.

Flores, F., Echenique, P. M., and Ritchie, R. H., 1986, "Energy Dissipation Processes in Scanning Tunneling Microscopy," *Physics Review B,* Vol. 34, pp. 2899–2902.

Goodson, K. E., and Flik, M. I., 1992, "Microscale Phonon Transport in Dielectrics and Intrinsic Semiconductors," *Fundamental Issues in Small Scale Heat Transfer,* Y. Bayazitoglu, and G. P. Peterson, ed., ASME HTD-Vol. 227, pp. 29–37.

Goodson, K. E., 1996, "Thermal Conduction in Nonhomogeneous CVD Diamond Layers in Electronic Microstructures," ASME JOURNAL OF HEAT TRANSFER, Vol. 118, pp. 279–286.

Gryaznov, V. G., Kaprelov, A. M., and Belov, A. Y., 1991, "Real Temperature of Nanoparticles in Electron Microscope Beams," *Philosophical Magazine Letters,* Vol. 63, pp. 275–279.

Joshi, A. A., and Majumdar, A., 1993, "Transient Ballistic and Diffusive Heat Transfer in Thin Films," *Journal of Applied Physics,* Vol. 74, pp. 31–39.

Klitsner, T., VanCleve, J. E., Fisher, H. E., and Pohl, R. O., 1988, "Phonon Radiative Heat Transfer and Surface Scattering," *Physical Review B.,* Vol. 38, pp. 7576–7594.

Li, Y. Z., Vazquez, L., Piner, R., Andres, R. P., and Reifenberger, R., 1989a, "Writing Nanometer-Scale Symbols in Gold Using the Scanning Tunneling Microscope," *Applied Physics Letters,* Vol. 54, pp. 1424–1426.

Li, Y. Z., Andres, R. P., and Reifenberger, R., 1989b, "Reply to: Comment on 'Writing Nanometer-Scale Symbols in Gold Using the Scanning Tunneling Microscope'," *Applied Physics Letters,* Vol. 55, pp. 2366–2367.

Mahan, G. D., and Claro, F., 1988, "Nonlocal Theory of Thermal Conductivity," *Physical Review B,* Vol. 38, pp. 1963–1969.

Majumdar, A., 1993, "Microscale Heat Conduction in Dielectric Thin Films," ASME JOURNAL OF HEAT TRANSFER, Vol. 115, pp. 7–16.

Marella, P. F., and Pease, R. F., 1989, "Comment on 'Writing Nanometer-Scale Symbols in Gold Using the Scanning Tunneling Microscope'," *Applied Physics Letters,* Vol. 55, pp. 2366–2367.

Nakamura, J., Miyamoto, M., Hosaka, S., and Koyanagi, H., 1995, "High-Density Thermomagnetic Recording Method Using a Scanning Tunneling Microscope," *Journal of Applied Physics,* Vol. 77, pp. 779–781.

Nonnenmacher, M., and Wickramasinghe, H. K., 1992, "Scanning Probe Microscopy of Thermal Conductivity and Subsurface Properties," *Applied Physics Letters,* Vol. 61, pp. 168–170.

Peterson, R. B., 1994, "Direct Simulation of Phonon-Mediated Heat Transfer in a Debye Crystal," ASME JOURNAL OF HEAT TRANSFER, Vol. 116, pp. 815–822.

Pylkii, R. J., Moyer, P. J., and West, P., 1994, "Scanning Near-Field Optical Microscopy and Scanning Thermal Microscopy," *Japanese Journal of Applied Physics,* Vol. 33, pp. 3785–3790.

Qiu, T. Q., and Tien, C. L., 1993, "Heat Transfer Mechanisms During Short-Pulse Laser Heating of Metals," ASME JOURNAL OF HEAT TRANSFER, Vol. 115, pp. 835–841.

Reggiani, L., 1985, *Hot-Electron Transport in Semiconductors,* Spring-Verlag, Berlin.

Rhymings, I. L., 1965, "Radiative Transfer Between Two Concentric Spheres Separated by an Absorbing and Emitting Gas," *International Journal of Heat and Mass Transfer,* Vol. 9, pp. 315–324.

Rodrigues, P. A. M., Tamulaitis, G., Peter, Y., and Risbud, S. H., 1995, "Anomalously Efficient Laser-Induced Heating of Semiconductor Nanocrystals Embedded in Glass," submitted for publication.

Schaffner, M., Bao, X., and Penzkofer, A., 1992, "Principal Optical Constants Measurement of Uniaxial Crystal CdSe in the Wavelength Region Between 380 and 950 nm," *Applied Optics,* Vol. 31, pp. 4546–4551.

Siegel, R., and Howell, R., 1992, *Thermal Radiation Heat Transfer,* 3rd ed., Hemisphere, Washington, DC.

Swartz, E. T., and Pohl, R. O., 1989, "Thermal Boundary Resistance," *Review of Modern Physics,* Vol. 61, pp. 605–668.

Tien, C. L., and Chen, G., 1994, "Challenges in Microscale Radiative and Conductive Heat Transfer," ASME JOURNAL OF HEAT TRANSFER, Vol. 116, pp. 799–807.

Viskanta, R., and Crosbie, A., 1967, "Radiative Transfer Through a Spherical Shell of Absorbing-Emitting Gray Medium," *Journal of Quantitative Spectroscopy and Radiative Transfer,* Vol. 7, pp. 871–889.

Weisbuch, C., and Vinter, B., 1991, *Quantum Semiconductor Structures,* Academic Press, Boston.

Yajima, T., Yoshihara, K., Harris, C. B., and Shionoya, S., eds., 1988, *Ultrafast Phenomena VI,* Springer-Verlag, Berlin.

Zhang, G., Hu, C., Yu, P., Chiang, S., Eltoukhy, S., and Hamdy, E., 1995, "An Electro-Thermal Model for Metal-to-Metal Antifuse With Thin Insulation Oxide Layer," *IEEE Transactions on Electron Devices,* Vol. 42, pp. 1548–1558.

Ziman, J. M., 1960, *Electrons and Phonons,* Clarendon Press, Oxford.

Downloaded 11 Dec 2010 to 193.140.21.150. Redistribution subject to ASME license or copyright; see http://www.asme.org/terms/Terms_Use.cfm

Inverse Determination of Boundary Conditions and Sources in Steady Heat Conduction With Heat Generation

T. J. Martin

G. S. Dulikravich

Department of Aerospace Engineering,
Pennsylvania State University,
University Park, PA 16802

A Boundary Element Method (BEM) implementation for the solution of inverse or ill-posed two-dimensional Poisson problems of steady heat conduction with heat sources and sinks is proposed. The procedure is noniterative and cost effective, involving only a simple modification to any existing BEM algorithm. Thermal boundary conditions can be prescribed on only part of the boundary of the solid object while the heat sources can be partially or entirely unknown. Overspecified boundary conditions or internal temperature measurements are required in order to compensate for the unknown conditions. The weighted residual statement, inherent in the BEM formulation, replaces the more common iterative least-squares (L2) approach, which is typically used in this type of ill-posed problem. An ill-conditioned matrix results from the BEM formulation, which must be properly inverted to obtain the solution to the ill-posed steady heat conduction problem. A singular value decomposition (SVD) matrix solver was found to be more effective than Tikhonov regularization for inverting the matrix. Accurate results have been obtained for several steady two-dimensional heat conduction problems with arbitrary distributions of heat sources where the analytic solutions were available.

Introduction

The integrity of energy-producing or -consuming devices depends upon maintaining an acceptable operating temperature by the proper removal of generated heat. For example, Joule heating generated inside electronic components strongly depends on the frequency of the alternating electromagnetic field and the local material properties. Another example of such domain-distributed heat sources is the microwave heating of food and materials processing. In the case of buried nuclear or chemical toxic waste, the heat generated by ongoing reactions will vary throughout the burial site. In general, the internal heat generation may lead to local overheating, potentially serious equipment failures, and environmentally disastrous consequences. In order to understand the steady thermal field in these problems, a boundary value problem is often governed by the Poisson equation. A well-posed problem requires either temperature, heat flux, or convective heat transfer coefficients specified over the entire boundary of the solid region. Well-posed Poisson problems also require the specification of heat source intensities throughout the domain.

However, surface measurements and continuous monitoring of the heat sources throughout the solid are often impractical. This is because of the intrusive nature of a large number of sensors. In addition, using even a small number of sensors may be impossible to achieve in practice because of highly volatile environments (combustion chambers) or because of the prohibitively small space available for their placement (computer chips). Thus, in many cases we are forced to solve an ill-posed boundary value problem where no data are available on parts of the boundary or when the heat sources are partially or entirely unknown. It would be highly desirable to develop a nonintrusive monitoring technique capable of utilizing overdetermined thermal measurements where they are accessible to the designer. The overspecified boundary conditions would then be used to predict temperatures, heat fluxes, and convective heat transfer coefficients on the inaccessible boundaries. This objective is termed the steady inverse heat conduction problem (SIHCP).

We have developed a noniterative algorithm that can reliably and efficiently solve inverse (ill-posed) boundary condition problems governed by the Laplace equation in two-dimensional multiply connected domains including temperature-dependent material properties (Martin and Dulikravich, 1993, 1994; Dulikravich and Martin, 1994). An extended version of this method was also successfully used in solving ill-posed problems in two-dimensional elasticity (Martin et al., 1994). In the latter publication, no boundary conditions for traction and deformation were known on parts of the boundary while both traction and deformation vectors were specified on the remainder of the boundary of the multiply connected domain.

In this paper, the problem formulation is conceptually different from the more common unsteady inverse heat conduction problem (UIHCP) (Beck et al., 1984). The major concern when attempting to solve the UIHCP computationally has been with the automatic filtering of noisy data in the discrete thermocouple measurements. All measurement data errors, as well as numerical round-off errors, are amplified by the typical UIHCP algorithms. These numerical methods are usually formulated in the least-squares sense where the overall error between the computed and measured temperatures is minimized (Kagawa et al., 1995). Among others, the method of regulizers, discrete mollification (Murio, 1993) against a suitable averaging kernel and other filtering techniques have also been implemented in order to smooth the extrapolated boundary values. To date, many of the UIHCP solutions were performed for specific geometries and cannot be readily extended to complex geometries.

Contributed by the Heat Transfer Division for publication in the JOURNAL OF HEAT TRANSFER. Manuscript received by the Heat Transfer Division April 1995; revision received March 1996. Keywords: Computer Codes, Conduction, Numerical Methods. Associate Technical Editor: S. Ramadhyani.

Copyright © 1996 by ASME

Downloaded 11 Dec 2010 to 193.140.21.150. Redistribution subject to ASME license or copyright; see http://www.asme.org/terms/Terms_Use.cfm

In fact, most attention has been focused on the one-dimensional UIHCP. Another basic concern is that relatively few UIHCP techniques used in engineering provide a quantitative method for determining what effect their smoothing operations have on the accuracy of the estimates.

The theory behind our SIHCP method is based on the Green's function solution method, commonly referred to as the Boundary Element Method (BEM). It is an integral technique that generates a set of linear algebraic equations with unknowns confined only to the boundaries. For well-posed problems, the resulting solution matrix can be solved by Gaussian elimination or any other standard matrix inverter. When an ill-posed problem is encountered, the matrix becomes ill-conditioned. We have shown that the proper solution to this matrix provides accurate results to various SIHCPs. This method has been shown to suppress the amplification in measurement errors (Martin and Dulikravich, 1994) in the input data while both minimizing the variance in the output and preventing output bias. The approach is somewhat similar, at least in theory, to those delivered by Backus and Gilbert (1970) and Lanczos (1961). These authors have discussed techniques that allow one to selectively discard eigenvalues and eigenvectors of a particular system of equations that tend to magnify errors.

Numerical Formulation

This paper elaborates on a simple, robust, and fast numerical solution to the ill-posed two-dimensional Poisson equation using the BEM. The algorithm is applicable to complex, multiply connected, two and three-dimensional geometries. The BEM (Brebbia, 1978) is based upon a Green's function solution procedure. It has certain distinct advantages over other more common numerical methods. First, the analytic solution to the partial differential equation, in the form of the Green's function, is part of the BEM solution. Therefore, high accuracy is expected with the BEM because introducing the Green's functions does not introduce any error into the solution. In addition, the BEM does not, like the Finite Element Method (FEM), neglect the interelement continuity terms. Third, the degrees of freedom of the system are reduced such that unknowns are strictly confined to the boundaries of the domain. Most importantly, the noniterative nature of the BEM eliminates stability and convergence problems.

The governing partial differential equation for steady-state heat conduction in a two-dimensional solid with a constant coefficient of thermal conductivity, and arbitrarily distributed heat sources or sinks per unit area is

$$k\nabla^2 T(\mathbf{x}) + g(\mathbf{x}) = 0 \tag{1}$$

This equation can be nondimensionalized by introducing

$$u = \frac{T - T_{\min}}{(T_{\max} - T_{\min})} \quad b = \frac{gl^2}{k(T_{\max} - T_{\min})} \tag{2}$$

where l is a characteristic length. The nondimensional form of Eq. (1) then becomes

$$\nabla^2 u(\mathbf{x}) + b(\mathbf{x}) = 0 \tag{3}$$

This elliptic partial differential equation can be subject to the Dirichlet boundary conditions, $u = \bar{u}_1$, on the boundaries Γ_1, the Neumann boundary conditions, $\partial u/\partial n = \bar{q}_2$, on the boundaries Γ_2, and, when a boundary is exposed to a moving fluid, the Robin (convective heat transfer) boundary conditions, $-k(\partial u/\partial n) = h(\bar{u} - u_{\text{amb}})_3$, on the boundaries Γ_3. When an ill-posed boundary condition problem is encountered, the boundaries Γ_4 have both $u = \bar{u}_4$ and $q = \bar{q}_4$ specified, while nothing is known on boundaries Γ_5, that is, $\bar{u}_5$ = unknown and $\bar{q}_5$ = unknown.

Boundary Element Method. When a partial differential equation is formulated numerically, an approximate solution, which is, in general, not the exact solution, must be used. Therefore, error, often called the residual, is introduced into the problem. The weighted residual statement minimizes this error by

Nomenclature

$[\mathbf{A}]$ = coefficient matrix multiplying a vector of unknowns
A_{nm} = Fourier sine coefficients
b = nondimensional internal heat source function
$\{\mathbf{B}\}$ = vector of nodal nondimensional heat sources
B_{nm} = Fourier cosine coefficient
$[\mathbf{C}]$ = SVD matrix whose columns are an orthonormal basis that spans the range of $[\mathbf{A}]$
$[\mathbf{D}]$ = SVD matrix whose columns are an orthonormal basis for the null-space of $[\mathbf{A}]$
E = error
$\{\mathbf{F}\}$ = vector of known sources and boundary conditions
g = internal heat source per unit domain
$[\mathbf{G}]$ = BEM coefficient matrix multiplying nodal fluxes
h = convective heat transfer coefficient
$[\mathbf{H}]$ = BEM coefficient matrix multiplying nodal potentials
$[\mathbf{I}]$ = identity matrix
J_n = Bessel function of integer order n
k = coefficient of thermal conductivity
n = local outward unit normal direction
$\hat{n}$ = local outward unit normal vector
N = number of nodes
$[\mathbf{P}]$ = BEM coefficient matrix multiplying nodal sources
q = nondimensional flux
$\{\mathbf{Q}\}$ = vector of nodal nondimensional fluxes
R = random number with uniform distribution between 0.0 and 1.0
T = temperature
u = nondimensional temperature or potential
$\{\mathbf{U}\}$ = vector of nodal potentials
w = weighting function
$\mathbf{x}$ = real space coordinate (x_1, x_2)
$\mathbf{y}$ = coordinate of integration (y_1, y_2)
Y_n = Bessel function of integer order n
Γ = boundary contour
δ = Dirac delta function
θ = circumferential angle
λ = Tikhonov regularization parameter
μ_{nm} = roots of the characteristic equation
ρ = nondimensional radius
σ = standard deviation
σ^2 = variance
τ = singularity threshold
Ω = domain

Subscripts

a = inner circular boundary
amb = ambient fluid quantities
b = outer circular boundary
int = internal temperature measurement
j = column index of coefficient matrix A
max = maximum value of temperature
min = minimum value of temperature
opt = optimum value
T = temperature
vc = domain cells
1 = Dirichlet boundary condition
2 = Neumann boundary condition
3 = Robin boundary condition
4 = overspecified boundary conditions
5 = nonspecified boundary condition

Superscripts

$*$ = fundamental Green's function
T = transpose of a matrix
-1 = inverse of a matrix

Downloaded 11 Dec 2010 to 193.140.21.150. Redistribution subject to ASME license or copyright; see http://www.asme.org/terms/Terms_Use.cfm

setting the weighted sum of the residuals over the entire domain and in the boundary conditions to zero. For the Poisson equation, the weighted residual statement appears as

$$\int_\Omega (\nabla^2 u(\mathbf{y}) + b(\mathbf{y}))w(\mathbf{x}, \mathbf{y})d\Omega(\mathbf{y}) + \int_{\Gamma_1} (u(\mathbf{y}) - \bar{u}(\mathbf{y}))\frac{\partial w(\mathbf{x}, \mathbf{y})}{\partial n} d\Gamma(\mathbf{y}) - \int_{\Gamma_2} (q(\mathbf{y}) - \bar{q}(\mathbf{y}))w(\mathbf{x}, \mathbf{y})d\Gamma(\mathbf{y}) = 0 \quad (4)$$

This statement is the starting point of most numerical formulations. The difference among them lies in how the weighting function is formulated and what approximating function is used.

In the BEM, the fundamental Green's function solution, which will be represented by u^*, replaces the weighting function, w. It satisfies the following Green's function solution equation with a unit impulsive heat source and homogeneous boundary conditions:

$$\nabla^2 u^* + \delta(\mathbf{x} - \mathbf{y}) = 0 \quad (5)$$

The Dirac delta function, $\delta(\mathbf{x} - \mathbf{y})$, has the following property:

$$\int_\Omega f(\mathbf{y})\delta(\mathbf{x} - \mathbf{y})d\Omega = \begin{cases} 0 & \text{when } \mathbf{x} \text{ is outside } \Omega \\ f(\mathbf{x}) & \text{when } \mathbf{x} \text{ is inside } \Omega \end{cases} \quad (6)$$

The nondimensional steady heat conduction equation Eq. (3), enters into the first integral of Eq. (4). The nondimensional heat flux is defined as $q = \partial u/\partial n$. After integrating the weighted residual statement (4) by parts twice, retaining the Cauchy principal value of the boundary integrals, and using the properties of the Dirac delta function (Eqs. (5) and (6)), the following Boundary Integral Equation (BIE) is obtained (Brebbia and Dominguez, 1989):

$$c(\mathbf{x})u(\mathbf{x}) + \int_\Gamma q^*(\mathbf{x}, \mathbf{y})u(\mathbf{y})d\Gamma = \int_\Gamma u^*(\mathbf{x}, \mathbf{y})q(\mathbf{y})d\Gamma + \int_\Omega u^*(\mathbf{x}, \mathbf{y})b(\mathbf{y})d\Omega \quad (7)$$

The fundamental solution for the two-dimensional Poisson equation is

$$u^* = \frac{1}{2\pi} \ln\left(\frac{1}{|\mathbf{x} - \mathbf{y}|}\right) \quad (8)$$

The boundary integral is singular when the observation point, $\mathbf{x}$, is on the boundary. Therefore, these singular integrals must be evaluated in the sense of the Cauchy principal value. The integration over the boundary, Γ, is divided into an infinitesimal semicircular contour, Γ_ϵ, about the singular point plus the remaining contour, $\Gamma - \Gamma_\epsilon$. After taking the limit $\epsilon \to 0$, a free term, $c(\mathbf{x})u(\mathbf{x})$, results. For two-dimensional problems, $c(\mathbf{x}) = 0.0$ when $\mathbf{x}$ is outside the domain, $c(\mathbf{x}) = 1.0$ when $\mathbf{x}$ is inside the domain, and $c(\mathbf{x}) = \theta/2\pi$ when $\mathbf{x}$ is on the boundary, where θ is the internal angle at the corner between two neighboring boundary elements.

If the temperature gradient is known at some location in the domain, the following BIE can be derived:

$$\nabla u(\mathbf{x}) + \int_\Gamma \nabla q^*(\mathbf{x}, \mathbf{y})u(\mathbf{y})d\Gamma = \int_\Gamma \nabla u^*(\mathbf{x}, \mathbf{y})q(\mathbf{y})d\Gamma + \int_\Omega \nabla u^*(\mathbf{x}, \mathbf{y})b(\mathbf{y})d\Omega \quad (9)$$

The boundary was discretized into N linear, isoparametric, boundary elements connected at N boundary nodes. In addition, N_{int} internal points existed where temperature data were specified. Since the boundary elements were isoparametric, the functions u and q varied linearly between their values at the end-points (nodes) of each boundary element. Each boundary element, Γ_j, was integrated numerically using a standard Gaussian quadrature integration formula. Boundary elements containing a singularity at one end-point were integrated analytically. A set of $N + N_{\text{int}}$ boundary integral equations resulted, one for each boundary node plus one for every internal temperature measurement. In order to evaluate the field source integral, the domain, Ω, was discretized into N_{uc} quadrilateral, isoparametric bilinear cells, Ω_j, sharing both domain and boundary nodes at the vertices of these quadrilaterals.

The coefficients matrices $[\mathbf{H}]$, $[\mathbf{G}]$, and $[\mathbf{P}]$ were computed by integrating the fundamental solution over the linear boundary elements and over the bilinear domain elements. The resulting discretized form of the BIE can be represented in matrix form as follows (Dulikravich and Martin, 1995):

$$[\mathbf{H}]\{\mathbf{U}\} = [\mathbf{G}]\{\mathbf{Q}\} + [\mathbf{P}]\{\mathbf{B}\} \quad (10)$$

For a well-posed boundary value problem, every point on the boundary is given one Dirichlet, Neumann, or Robin-type boundary condition, no internal temperature measurements exist, and the heat source vector $\{\mathbf{B}\}$ is entirely known. These boundary conditions are then multiplied by their respective coefficient matrix, collected on the right-hand side and added to $[\mathbf{P}]\{\mathbf{B}\}$ to form a vector of knowns, $\{\mathbf{F}\}$. The left-hand side will remain in the standard form $[\mathbf{A}]\{\mathbf{X}\}$, with the matrix, $[\mathbf{A}]$, having N unknowns and N equations. This well-posed system of linear algebraic equations can be solved for the unknowns on the boundary by any standard matrix solver such as Gaussian elimination of LU factorization.

If the boundary conditions in the example above are partially unknown or not properly applied, if internal temperature measurements are included in the analysis, or if part or all of the heat source function is unknown, the problem becomes ill-posed. A solution may still be obtained by multiplying the known quantities in the vectors $\{\mathbf{U}\}$, $\{\mathbf{Q}\}$, and $\{\mathbf{B}\}$ by their respective coefficient matrix columns and collecting them into the vector of knowns. The unknowns form a single vector, $\{\mathbf{X}\}$, multiplied by a highly ill-conditioned coefficient matrix, $[\mathbf{A}]$, which is, in general, not square.

Singular Value Decomposition. Singular Value Decomposition (SVD) methods (Press et al., 1992; Throne and Olson, 1994; Sykulski, 1995) are widely used for dealing with sets of algebraic equations that are either singular or very close to singular. The goal of the SVD is to choose a solution vector $\{\mathbf{X}\}$ that minimizes the error function

$$E = \|\{\mathbf{F}\} - [\mathbf{A}]\{\mathbf{X}\}\| \quad (11)$$

which is the distance from the point $\{\mathbf{F}\}$ to the point $[\mathbf{A}]\{\mathbf{X}\}$ in the column space. Any $M \times N$ matrix $[\mathbf{A}]$ can be written as the product of an $M \times N$ column-orthogonal matrix, $[\mathbf{C}]$, an $N \times N$ diagonal matrix $[\mathbf{S}]$ with positive singular values, and the transpose of an $N \times N$ orthogonal matrix $[\mathbf{D}]$.

$$[\mathbf{A}] = [\mathbf{C}]\begin{bmatrix} s_1 & 0 & 0 \\ 0 & \vdots & 0 \\ 0 & 0 & s_N \end{bmatrix}[\mathbf{D}] \quad (12)$$

The singular values, $s_1, s_2, \ldots, s_N$, are the eigenvalues of a matrix $[\mathbf{A}]^T[\mathbf{A}]$. For a well-conditioned matrix, these values will be roughly of the same order of magnitude. As the matrix becomes more ill-conditioned, that is, more singular, these values become more dispersed. Formally, the condition number of a matrix is defined as the base 10 logarithm of the ratio between the largest of the s_j's to the smallest of the s_j's.

Downloaded 11 Dec 2010 to 193.140.21.150. Redistribution subject to ASME license or copyright; see http://www.asme.org/terms/Terms_Use.cfm

The SVD explicitly constructs orthonormal bases for the nullspace and range of a matrix [A]. If the matrix [A] is singular, then there is some subspace of {X}, called the nullspace, that is mapped to zero, that is, [A]{X} = {0}. The LU factorization and Gaussian elimination techniques may give a formal solution to an ill-conditioned set of equations, but the solution vector {X} will have highly oscillating components. When this solution vector, {X}, is multiplied by the matrix [A], a very poor approximation to the vector {F} will be the result.

Eliminating very small singular values has the effect of removing those algebraic terms that, because they are dominated by noise and round-off error, corrupt the solution. In order to determine which singular values are to be truncated, we must choose a parameter, τ, as a singularity threshold. Any singular value, whose ratio with the largest singular value is less than this singularity threshold, is zeroed out. This can be understood as follows: If $s_j/s_{\max} < \tau$, then $1/s_j = 0$.

Since [C] and [D] are each orthogonal in the sense that their columns are orthonormal, the solution vector can be easily found as

$$\{\mathbf{X}\} = [\mathbf{D}][\mathrm{diag}(1/s_j)]([\mathbf{C}]^T\{\mathbf{F}\}) \quad (13)$$

Tikhonov Regularization. Another type of single-parameter minimization where the solution vector {X} minimizes the weighted sum of the norm of the error vector plus a penalty term was defined by Tikhonov (1977) as

$$E = \|\{\mathbf{F}\} - [\mathbf{A}]\{\mathbf{X}\}\| + \lambda\|\{\mathbf{X}\}\| \quad (14)$$

We find a minimum error norm by differentiating this equation with respect to each component of the unknown vector, {X}, and setting the result equal to zero. After substituting the singular value decomposition and solving for the unknown vector {X}, the resulting formulation is as follows:

$$\{\mathbf{X}\} = [\mathbf{D}]([\mathbf{S}]^T[\mathbf{S}] + \lambda[\mathbf{I}])^{-1}[\mathbf{S}]^T\{\mathbf{C}\}\{\mathbf{F}\} \quad (15)$$

Tikhonov regularization is a generalization of least-squares truncation, but instead of simply eliminating terms associated with small singular values, they are weighted by a factor $(1 + \lambda/s^2)$. The Tikhonov regularization parameter, λ, plays an important role. A low value drives the residual term [A]{X} − {F} smaller, approaching the least-squares solution. Because of the destabilizing effect of the small singular values, the solution for an ill-conditioned matrix oscillates erratically. Larger Tikhonov regularization parameters act as a filter to gradually reduce the effect of the singular values because $s_j/s_{\max}$ are less than the regularization parameter, λ. Thus, the optimal choice of the regularization parameter provides a balance between the accuracy and the smoothness of the solution. Tikhonov suggested that this parameter can be found based upon knowledge of the input measurement errors (Beck et al., 1985). The optimum value of λ should be chosen so that the variance in the output vector is at its minimum.

Analytic Test Cases. The two-dimensional BEM algorithm was verified against the analytic solution for the heat conduction equation within an annular region. If the boundary conditions and the heat generation in the annular domain are axisymmetric, $b = b(\rho)$, then the temperature distribution is

$$u(\rho) = -\int\left[\frac{1}{\rho}\int b(\rho)\rho d\rho\right]d\rho + c_1 \ln \rho + c_2 \quad (16)$$

In case of a constant heat source function (b = constant) the analytic solution of Eq. (16) is

$$u = -b\frac{\rho^2}{4} + c_1 \ln \rho + c_2 \quad (17)$$

where the constants of integration c_1 and c_2 can be found after applying the boundary conditions.

The temperature distribution within an annular domain with an arbitrary heat source distribution, $b = b(\rho, \theta)$ was also needed as a test case. For this problem, the inner circular boundary of the annular domain had a Dirichlet boundary condition, $u(\rho_a) = 0$, while the outer circular boundary was adiabatic. We can obtain an eigenfunction set written in the form of the Helmholtz equation satisfying the homogeneous boundary conditions. After separation of variables and applying the single-valuedness condition, the analytic result for the temperature field in the annular domain is

$$u(\rho, \theta) = \sum_{n=0}^{\infty}\sum_{m=1}^{\infty}\left[J_n(\mu_{nm}\rho) - \frac{J_n(\mu_{nm}\rho_b)}{Y_n(\mu_{nm}\rho_b)}Y_n(\mu_{nm}\rho)\right] \times [A_{nm}\sin n\theta + B_{nm}\cos n\theta] \quad (18)$$

The Fourier coefficients, A_{nm} and B_{nm}, may be found knowing that the eigenfunctions form an orthogonal set. Here, J_n and Y_n are the Bessel functions of integer order n, and μ_{nm} are the roots of the characteristic equation (Dulikravich and Martin, 1995):

$$J_n\left(\mu_{nm}\frac{\rho_{\text{outer}}}{\rho_{\text{inner}}}\right)Y_n'(\mu_{nm}) - J_n'(\mu_{nm})Y_n\left(\mu_{nm}\frac{\rho_{\text{outer}}}{\rho_{\text{inner}}}\right) = 0 \quad (19)$$

Results

Our inverse BEM algorithm governing the Poisson equation was tested against the analytic solution for an annular, homogeneous, isotropic, planar region between two concentric circles with nondimensionalized radii $\rho_a = 0.5$ and $\rho_b = 1.2$ subject to axisymmetric nondimensional thermal boundary conditions (u_a and u_b) and constant nondimensional heat generation function, b.

Effects of Discretization. In the first test case no heat sources, ($b = 0$), were applied. Equation (17) gives an analytic solution for the well-posed problem, $u_a = 0.5$ and $u_b = 1$, that results in the analytic values of $q_a = -1.134$ and $q_b = 0.4976$. The outer boundary was then overspecified with both constant nondimensional temperature and flux boundary conditions ($u_b = 1$, $q_b = 0.4976$) taken from the analytic solution of the well-posed problem, while nothing was specified on the inner circular boundary. Each outer and inner circular boundary was discretized with a variable, $N_a = N_b = M/2$, isoparametric linear boundary elements connected between the same number of nodes. Various levels of discretization were employed such that $M/2 = 12$, 24, 36, 48, 72, 84 and 144. Each BEM solution matrix was square, ($M \times M$), all had very similar ranges of singular values and the condition number of each matrix was between 7 and 8. The variances in the output temperatures (computed on the inner boundary),

$$\sigma_T^2 = \sum_{j=1}^{M/2}(u_j - u_{\text{mean}})^2 \quad (20)$$

where u_{mean} is the mean value, were examined for a range of singularity thresholds, τ, and a range of Tikhonov regularization parameters, λ, varying between 1 and 10^{-16}. The idea is to find the optimum value, τ_{opt} or λ_{opt}, that simultaneously minimizes the output variance and the bias.

The computed nondimensional temperature and flux distributions on the inner circular boundary were very accurate, approaching the analytic solution with the increasing level of discretization. Figure 1 illustrates the effect of the user-specified singularity threshold, τ, on the computed nondimensional temperature variances on the inner circular boundary for a range of discretization levels. The bias (difference between computed u_{mean} and the analytic solution) in the results approached zero as the level of discretization increased while the output variance reached a minimum at about $M/2 = 36$ linear boundary ele-

Downloaded 11 Dec 2010 to 193.140.21.150. Redistribution subject to ASME license or copyright; see http://www.asme.org/terms/Terms_Use.cfm

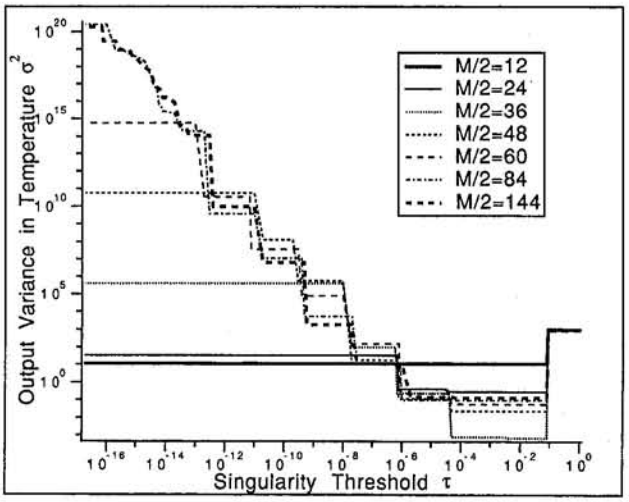


Fig. 1 Variances in the output (computed inner boundary) nondimensional temperatures as a function of the SVD singularity thresholds, τ. A range of M/2 boundary elements were used to discretize each circular boundary of the annular region.

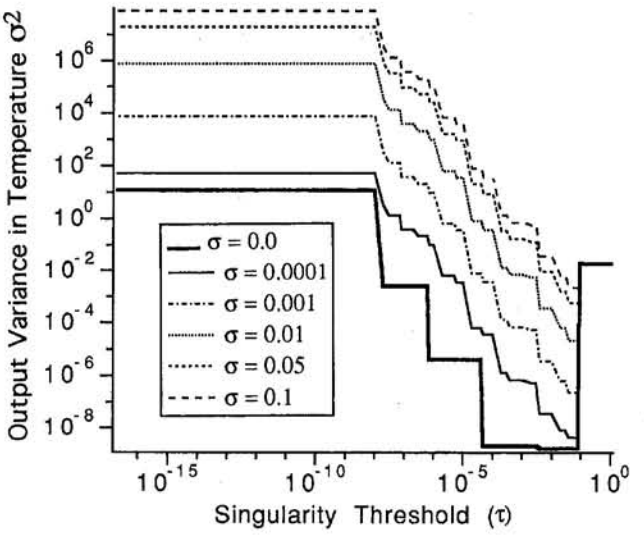


Fig. 2 Variances in the output (computed inner boundary) nondimensional temperatures and heat fluxes as a function of the SVD singularity threshold parameter, τ, for various levels of input standard deviation, σ

ments per circular boundary. This bias was, therefore, attributed to the fact that linear elements were used to model the circular geometry. The level of discretization was found to have no effect on τ_{opt}. The effective range of τ that produced the minimum variance and bias for all levels of discretization was $0.004 \leq \tau \leq 0.08$.

On the other hand, the level of discretization had some influence on Tikhonov's regularization scheme. After the BEM matrices were integrated and the singular value decomposition computed, an iterative quadratic optimization algorithm was employed in order to determine λ_{opt}. The value of λ was allowed to vary while the cost function

$$f(\lambda) = w_{var}\sigma_T^2 + w_{bias}(u_{mean} - u_{analytic})^2 \qquad (21)$$

was minimized. Here w_{var} and w_{bias} are user-specified weighting coefficients for the variance and the bias. With $w_{var} = w_{bias} = 1$, the optimum Tikhonov regularization parameter was usually found in 5 to 10 computationally inexpensive iterations.

Results With Input Data Noise. The major concern of researchers working on inverse problems is with the sensitivity of their algorithms to errors in the specified boundary conditions. In order to verify that our SIHCP technique did not amplify the input data errors, random Gaussian noise was introduced into the temperature function supplied to the outer circular boundary. The same annular geometry was used for this purpose and the heat generation was included as a constant, $b = 1$. For the temperature boundary condition on the outer boundary a uniform random real number, R, between 0 and 1, was generated using the RANF subroutine on the Cray C-90 computer. Using this value as the normalized probability density function, a noisy temperature boundary condition on the outer circular boundary was determined from the following equation:

$$u(\theta) = u_{bc} \pm \sqrt{-2\sigma^2 \ln [R(\theta)]} \qquad (22)$$

The sign was determined by generating another random number with a 50/50 chance of being +/−. Here, $u_{bc} = u_b = 0$, is the mean value of the temperature boundary condition on the outer circular boundary and σ^2 is the variance. With $u_b = u_a = 0$ and $b = 1$ the analytic solution of the well-posed problem was obtained from Eq. (17) with $c_1 = 0.3398$ and $c_2 = 0.298$ yielding a maximum nondimensional temperature, $u_{max} = 0.06248$, reached at the nondimensionalized radial distance $\rho = 0.8244$. The analytic solution also gives $q_a = 0.4296$ and $q_b = -0.3168$. For the inverse problem, no boundary conditions were specified on the inner circular boundary while specifying $u_b = 0$ and $q_b = -0.3168$ on the outer circular boundary. Each circular boundary was discretized with $M/2 = 36$ boundary elements. Ten rows of quadrilateral cells discretized the circular annular domain.

Our SIHCP BEM program was then tested with a variety of input nondimensional temperature standard deviations, σ, on the outer boundary. The ill-conditioned solution matrices were solved using the SVD algorithm and Tikhonov's regularization scheme. In order to determine τ_{opt} and and λ_{opt} for each case. Figs. 2 and 3 were generated to illustrate the behavior of these parameters. Each figure shows the output variance in temperature versus the range of possible τ's and λ's between 10^{-16} and 1. Notice that τ_{opt} is not a function of the input σ, but λ_{opt} is.

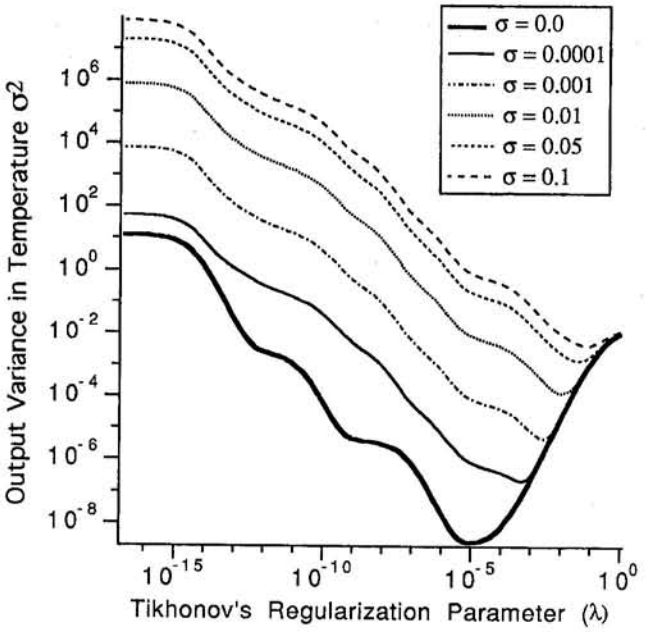


Fig. 3 Variances in the output (computed inner boundary) nondimensional temperatures and heat fluxes as a function of the Tikhonov's regularization parameter, λ. The curves are shown for various levels of input standard deviation, σ.

Downloaded 11 Dec 2010 to 193.140.21.150. Redistribution subject to ASME license or copyright; see http://www.asme.org/terms/Terms_Use.cfm

The optimum SVD threshold, τ_{opt}, which occurs when the variances in the output (inner circular boundary) nondimensional temperatures and heat fluxes are minimized, remained relatively constant and independent of all levels of input standard deviations. The input standard deviations, between $0 \leq \sigma \leq 0.1$, corresponding to errors from 0 up to 100 percent or more, yielded a minimum output variance when the singularity threshold, τ_{opt}, was $0.04 \leq \tau \leq 0.08$. The value of λ_{opt} was found by the iterative optimization process described earlier.

With the optimum SVD threshold and Tikhonov's regularization parameters known, Figs. 4, 5, and 6 were generated to depict the influence of the input percent errors supplied to the outer boundary conditions in temperature (solid lines) and the percent errors computed by the program as the inner boundary

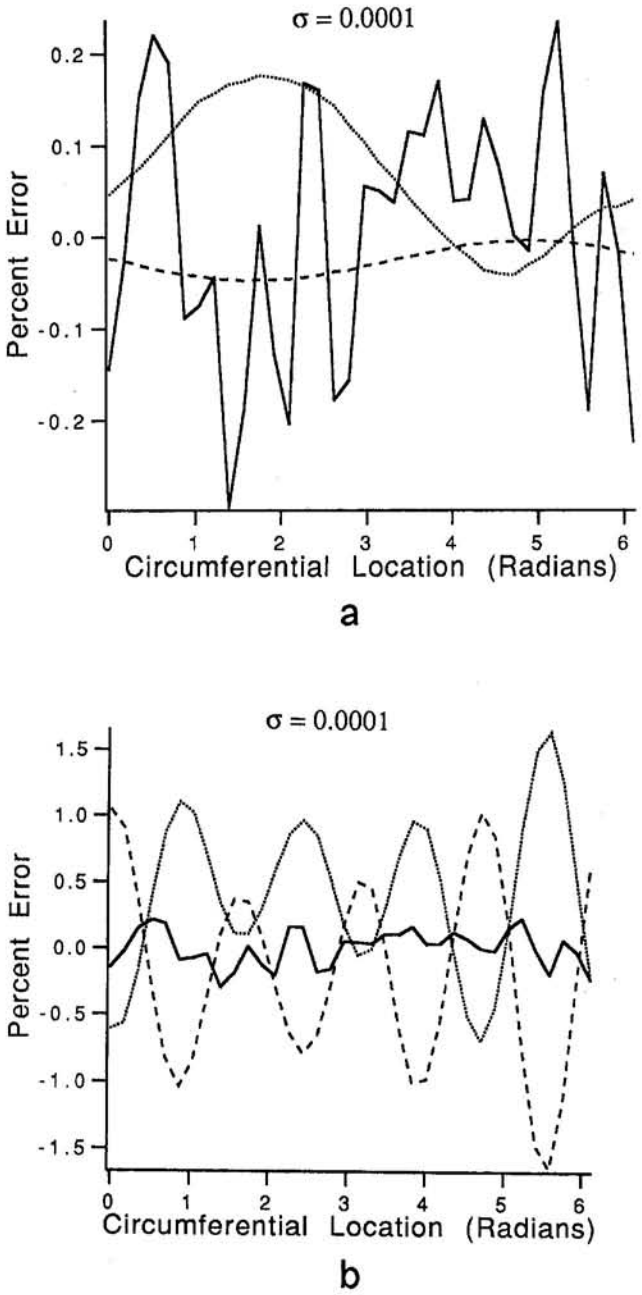


Fig. 4 Circumferential distribution of specified (input) percentage errors of nondimensional temperature on the outer circular boundary (full line) and computed (output) percentage errors in nondimensional temperature (dotted line) and heat flux (dashed line) on the inner circular boundary: (*a*) using the SVD algorithm, and (*b*) using Tikhonov's regularization. Input standard deviation was $\sigma = 0.0001$.

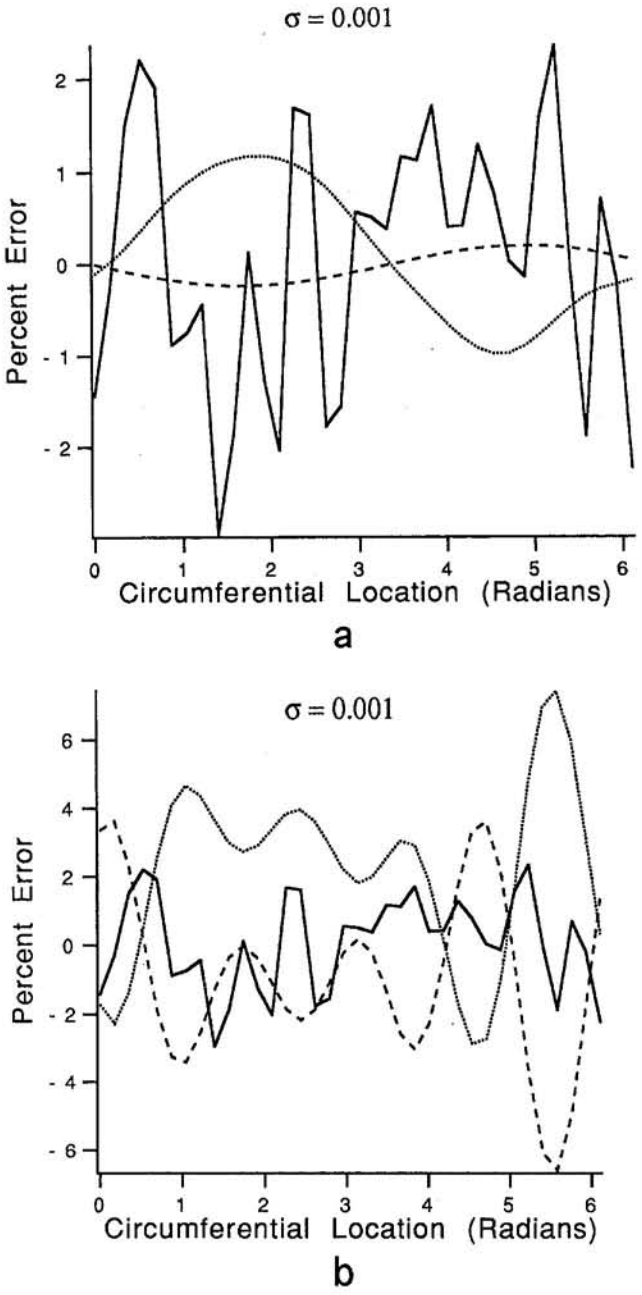
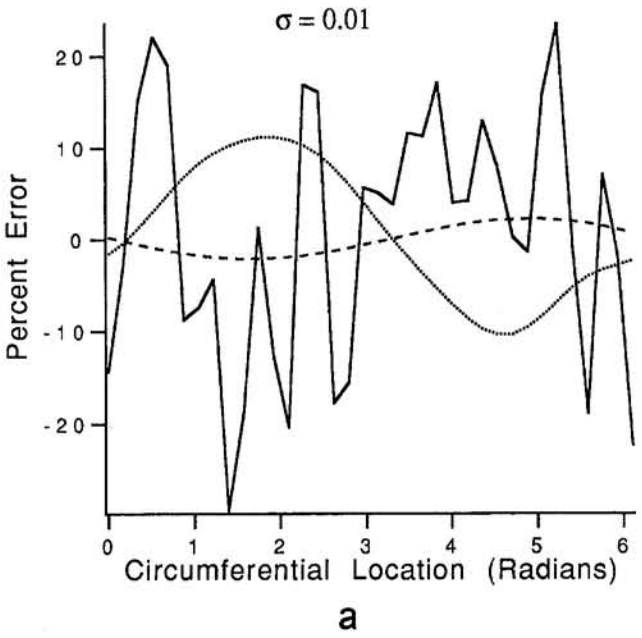


Fig. 5 Circumferential distribution of specified (input) percentage errors of nondimensional temperature on the outer circular boundary (full line) and computed (output) percentage errors in nondimensional temperature (dotted line) and heat flux (dashed line) on the inner circular boundary: (*a*) using the SVD algorithm, and (*b*) using Tikhonov's regularization. Input standard deviation was $\sigma = 0.001$.

temperatures (dotted lines) and fluxes (dashed lines). These figures, generated for different values of input σ, serve to prove that neither the SVD nor Tikhonov's methods amplified the noise supplied in the input measurement data. The SVD was less oscillatory and more accurate than Tikhonov's scheme. We repeated these tests by introducing input noise into the outer boundary heat flux data to see if there would be any difference, but similar results were found.

In addition, global energy conservation requires that the integrated heat flux through the unspecified boundaries equals the sum of all fluxes entering and leaving the domain through the specified and overspecified boundaries plus any heat generated inside the domain.

Downloaded 11 Dec 2010 to 193.140.21.150. Redistribution subject to ASME license or copyright; see http://www.asme.org/terms/Terms_Use.cfm



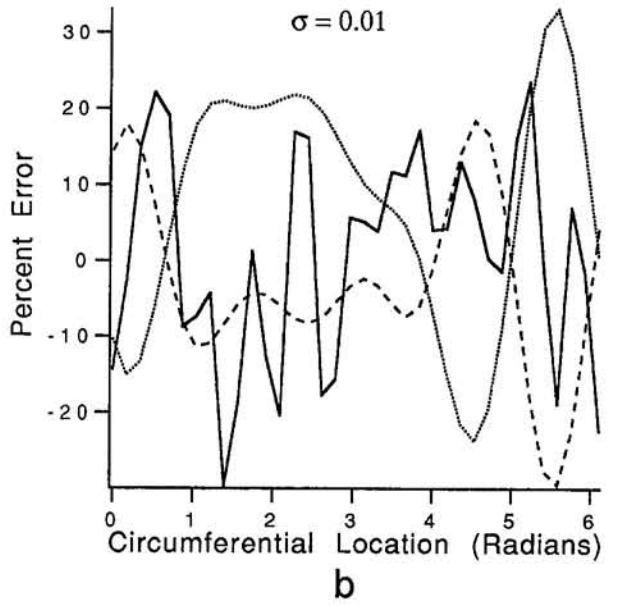


Fig. 6 Circumferential distribution of specified (input) percentage errors of nondimensional temperature on the outer circular boundary (full line) and computed (output) percentage errors in nondimensional temperature (dotted line) and heat flux (dashed line) on the inner circular boundary: (*a*) using the SVD algorithm, and (*b*) using Tikhonov's regularization. Input standard deviation was $\sigma = 0.01$.

$$Q_5 = \int_{\Gamma_5} (\nabla u_5 \cdot \hat{n}_5) d\Gamma$$

$$= -\left\{ \sum_{i=1}^{4} \left(\int_{\Gamma_i} (\nabla u_i \cdot \hat{n}_i) d\Gamma \right) + \int_{\Omega} b d\Omega \right\} \quad (23)$$

In our case, $b = 1$ and $Q_a = Q_5 = 2\pi\rho_a q_a = -\pi\{2\rho_b q_b + b(\rho_b^2 - \rho_a^2)\} = -1.35$. Again, a series of tests were performed for the same range of input standard deviations and the biases in the net heat fluxes on the unspecified boundary were computed with the SVD and Tikhonov methods.

The choice of Tikhonov's regularization parameter, λ, was found to affect Q_a strongly, although the amount of input standard deviation did not affect Q_a directly. Figure 7 readily shows that larger values of λ yielded a greater error in Q_a. Obviously, Tikhonov's regularization introduces artificial dissipation, which affects the physics of the problem by reducing the global amount of heat transfer. Since larger λ_{opt}'s are required for higher input variances, the results obtained with Tikhonov's regularization become increasingly biased as the input measurement data becomes more corrupted and noisy. A comparison between Figs. 3 and 7 indicates that this artificial dissipation of heat can become unacceptably large when using very noisy input data.

On the other hand, the SVD did not exhibit this behavior. Once the threshold parameter was small enough, the net heat flux, Q_a, became equal to the correct value and remained unchanged for all smaller values of τ.

We conclude from these observations that the SVD technique is more robust and reliable than Tikhonov's regularization since the latter can mislead the observer into thinking that a highly biased result is correct because it appears to be smooth. With the SVD, the user will immediately recognize if the chosen value of the threshold parameter, τ, is wrong since the computed temperatures and heat fluxes will be highly oscillatory. In addition, since the correct value of Q_5 is known in both well-posed and ill-posed problems, the value of τ_{opt} can be determined from this information after only 2–3 repetitive trials by starting with an initial guess $\tau < 0.1$. This is an easier procedure than with Tikhonov's method where λ_{opt} is found iteratively by simultaneously minimizing the variance and the bias. Even with this value of λ_{opt} Tikhonov's method will create results that have a nonzero bias, while the SVD approach offers a zero bias.

Results With an Arbitrary Heat Source Function. Our BEM algorithm was then tested against the complete analytic solution (Eq. (18)) for the same geometry, but with the nondimensional heat generation taken as a function of both the nondimensional radius, ρ, and azimuthal angle, θ. Specifically, we used the following expression:

$$b(\rho, \theta) = \sin\left[\frac{\rho - \rho_a}{\rho_b - \rho_a}\pi\right] \sin\theta \quad (24)$$

thus creating a variable heat source distribution on the upper

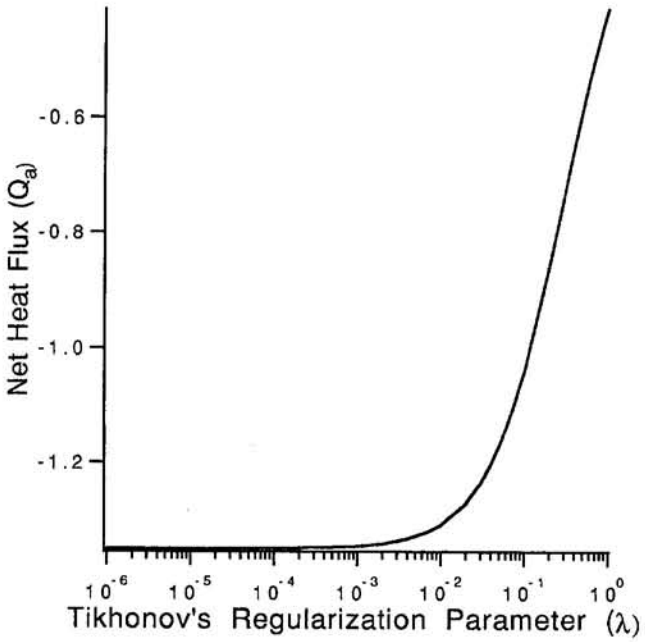


Fig. 7 Variation of the integrated net heat flux, Q_a, through the unspecified inner circular boundary as a function of Tikhonov's regularization parameters, λ. The nondimensional analytic result for the net heat flux is $Q_a = -1.35$.

Downloaded 11 Dec 2010 to 193.140.21.150. Redistribution subject to ASME license or copyright; see http://www.asme.org/terms/Terms_Use.cfm

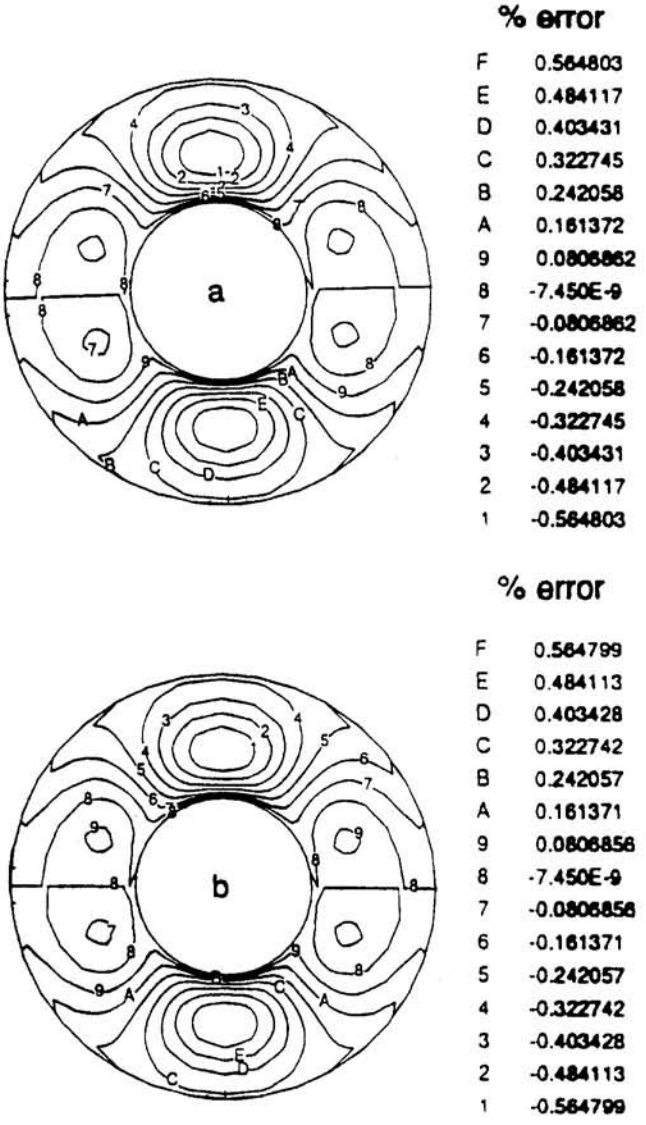


Fig. 8 Contours of constant error levels in computed nondimensional temperatures compared with the analytic results of the Poisson equation on an annular domain with $\rho_a = 0.5$, $\rho_b = 1.2$ and $b = \sin\{[(\rho - \rho_a)/(\rho_b - \rho_a)]\pi\}\sin\theta$: (a) error in numerical results obtained with the BEM for the direct problem ($u_a = 0.0$, $q_b = 0.0$); (b) error in numerical results obtained with the BEM for the inverse problem ($u_a = 0.0$, q_a = analytic, u_b = unknown, q_b = unknown)

half of the annular domain and an equal distribution of the heat sinks on the lower half of the annular domain. For the well-posed problem, the nondimensional temperature $u_a = 0$ was specified on the inner circular boundary while the outer circular boundary was kept adiabatic, $q_b = 0$. Both inner and outer boundaries were discretized with 36 linear isoparametric boundary elements and the annular domain was discretized with 36 $\times$ 10 quadrilateral cells. Accuracy of the numerical results obtained with our BEM analysis code for this well-posed test problem is very good (Fig. 8(a)). Next, the inner circular boundary heat fluxes were taken from the analytic solution (Eq. (18)) and supplied as overspecified boundary conditions together with nondimensional temperature on the inner circular boundary. No boundary conditions were specified on the outer circular boundary. This SIHCP was solved using our BEM code. The largest percentage errors found in the domain of the computed non-dimensional temperature field were less than 0.6 percent (Fig. 8(b)). Notice that the errors in both the direct (well-posed) and inverse (ill-posed) problems were nearly identical. The errors may seem to be somewhat larger near the boundaries because the singular fundamental solution is distributed over the boundary. A higher order integration scheme would alleviate this problem.

Results With Interior Temperature Measurements. The BEM approach to solving inverse (ill-posed) boundary condition problems is also capable of using internal temperature measurements at isolated interior points. To demonstrate this on the same annular geometry, only the temperature $u_a = 0$ was specified on the inner circular boundary. No boundary conditions were specified on the outer circular boundary. Instead, analytical values for temperatures at various locations within the domain were used as additional input data. Nondimensional temperatures ($u_{\text{int}} = 0.0496$), corresponding to the analytical values at $\rho = 1$ for Poisson's equation with the boundary conditions $u_a = 0$, $u_b = 0$, and $b = 1$, were specified at a finite number of circumferentially equidistantly spaced points in the annular domain. Each circular boundary was discretized with $M/2 = 36$ linear isoparametric boundary elements. A singularity threshold of $\tau = 0.06$ was used. Figure 9(a) illustrates the isotherms computed by the BEM algorithm when only four circumferentially and equidistantly spaced internal temperatures were utilized. The errors in the predicted temperature on the outer circular boundary are significant. This is understandable since the resulting BEM equation set contained 76 equations ($36 \times 2 + 4 = 76$) and 108 unknowns. The isotherms in Figs. 9(b) and 9(c) result from using 6 ($36 \times 2 + 6 = 78$ equations) and 9 ($36 \times 2 + 9 = 81$ equations) equidistantly spaced internal temperature input points, respectively. From these figures one notices that our algorithm produced very good results when at least 9 temperature measurements were used at equidistantly spaced locations within the annular domain while only temperature was given on one circular boundary.

Detection of the Heat Generation Inside an Annular Disk. In order to verify that the BEM is capable of finding the internal heat generation field given overspecified boundary data, we used the annular disk geometry described earlier with axisymmetric boundary conditions, $u_a = u_b = 0$ and $b = 1$. The resulting analytical values for the nondimensional heat fluxes on the outer and inner circular boundaries were $q_b = -0.3168$ and $q_a = -0.4296$, respectively.

These fluxes were then used as the overspecified boundary conditions on the outer and inner circular boundaries in order to predict the value of the heat generation field. The accuracy of the numerical solution was determined by how the internal region was discretized. The outer and inner circular boundaries were discretized with 36 linear isoparametric elements. When the annular domain (disk area) was discretized with 36 quadrilateral cells circumferentially, having only one cell between the outer and inner circular boundaries, the results were excellent. The heat generation field was predicted with an average error less than 0.01 percent. Similar results were found when the heat generation field was linearly varying, $b(\rho) = (\rho - \rho_a)/(\rho_b - \rho_a)$. But, when the domain was discretized with two or more radial rows of quadrilateral cells, the results produced errors that were, at worst, in error by about 30 percent. This is because the assembled BEM matrix had at least twice as many unknowns as it had equations. The results were significantly improved whenever internal temperature measurements were included in the analysis. For example, when the domain was discretized with two rows of quadrilateral cells, a single row of 9 known internal temperatures produced results that averaged an error of less than 0.1 percent.

Further results have shown that whenever the temperature field is entirely known everywhere in the domain, the resulting solution matrix, $[\mathbf{P}]$, is both square and well-conditioned. After inversion of this matrix, the unknown heat source vector $\{\mathbf{B}\}$ can be found with an accuracy comparable to the well-posed (forward) problem, where $\{\mathbf{B}\}$ is known and the temperature field is the objective of the computation.

Downloaded 11 Dec 2010 to 193.140.21.150. Redistribution subject to ASME license or copyright; see http://www.asme.org/terms/Terms_Use.cfm

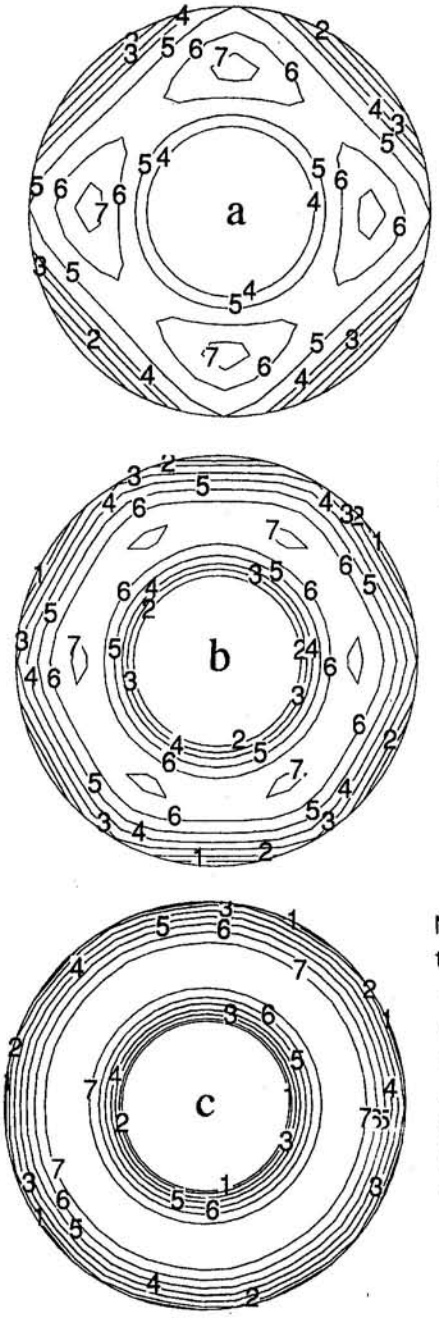


Fig. 9 Computed curves of constant nondimensional temperature in the annular region for the SIHCP with $b = 1.0$, $u_a = 0.0$, u_b = unknown, and local temperature measurements provided at: (*a*) four, (*b*) six, and (*c*) nine circumferentially equidistantly spaced points at $\rho = 1.0$

Conclusions

The BEM has been shown to provide stable and accurate solutions to several simple ill-posed problems of the Poisson equation where the boundary conditions or heat source functions were partially unknown and partially overspecified. Furthermore, this technique does not iterate to minimize a global function based upon the residual between the overspecified and computed boundary values. The magnification of errors in measurement data, the need for mollifiers to smooth the intermediate predictions, and the influence of regularizers on the physics of the problem have been eliminated. It was found that Singular Value Decomposition (SVD) technique is more reliable than Tikhonov's regularization for this class of ill-posed problems. This method can be readily extended to the solution of three-dimensional (Martin and Dulikravich, 1995) inverse (ill-posed) boundary condition problems governed by the Laplace and Poisson equations and to unsteady heat conduction problems involving the detection of unknown boundary conditions and initial conditions.

Acknowledgments

The authors are grateful for the remote access to NASA Ames Research Center (NAS) facility Cray C-90 computer granted by NASA Lewis Research Center. Postprocessing was performed on the equipment donated by Apple Computer. We also greatly appreciate Mr. Norman F. Foster's and Mr. Brian H. Dennis's help with the graphics and Mr. Sean R. Lynn's help with proofreading. The lead author is grateful for the NASA Graduate Traineeship received from the NASA-Pennsylvania State University Propulsion Engineering Research Center. This work was supported in part by NSF grant No. DMI-9522854 monitored by Dr. George Hazelrigg.

References

Backus, B., and Gilbert, F., 1970, "Uniqueness in the Inversion of Inaccurate Gross Earth Data," *Phil. Trans. Royal Soc. London,* Vol. 266, pp. 123–192.

Beck, J. V., Blackwell, B., and St. Clair, C. R., Jr., 1985, *Inverse Heat Conduction: Ill-Posed Problems,* Wiley-Interscience, New York.

Brebbia, C. A., 1978, *Boundary Elements in Engineering,* McGraw-Hill, New York.

Brebbia, C. A., and Dominquez, J., 1989, *Boundary Elements, An Introductory Course,* McGraw-Hill, New York.

Dulikravich, G. S., and Martin, T. J., 1994, "Inverse Problems and Design in Heat Conduction," *Proc. 2nd International Symposium on Inverse Problems in Engineering,* H. D. Bui, M. Tanaka, M. Bonnet, H. Maigre, E. Luzzato and M. Reynier, eds., Paris, France, Nov. 2–4, 1994; A. A. Balkema, Rotterdam, pp. 13–20.

Dulikravich, G. S., and Martin, T. J., 1995, "Inverse Shape and Boundary Condition Problems and Optimization in Heat Conduction," in: *Advances in Numerical Heat Transfer,* W. J. Minkowycz and E. M. Sparrow, eds., Taylor and Francis, Chap. 10.

Kagawa, Y., Sun, Y.-H., and Matsumoto, O., 1995, "Inverse Solution of Poisson Equation Using DRM Boundary Element Model—Identification of Space Charge Distribution," *Inverse Problems in Eng.,* Vol. 1, No. 3, pp. 247–266.

Lanczos, C., 1961, *Linear Differential Operators,* Van Nostrand, London.

Martin, T. J., and Dulikravich, G. S., 1993, "A Direct Approach to Finding Unknown Boundary Conditions in Steady Heat Conduction," *Proc. 5th Annual Thermal and Fluids Workshop,* Lewis Research Center, OH, Aug. 16–20, 1993, NASA CP-10122, pp. 137–149.

Martin, T. J., and Dulikravich, G. S., 1994, "Inverse Determination of Temperatures and Heat Fluxes on Inaccessible Surfaces," in: *Boundary Element Technology IX,* Computational Mechanics Publications, Southampton, C. A. Brebbia and A. Kassab, eds., pp. 69–76.

Martin, T. J., and Dulikravich, G. S., 1995, "Finding Temperatures and Heat Fluxes on Inaccessible Surfaces in 3-D Coated Rocket Nozzles," *Proc. 1994 JANNAF Propulsion and Subcommittee Joint Meeting,* Tampa, FL, Dec. 4–8.

Martin, T. J., Halderman, J., and Dulikravich, G. S., 1994, "An Inverse Method for Finding Unknown Surface Tractions and Deformations in Elastostatics," *Symposium on Inverse Problems in Mechanics,* S. Saigal and L. G. Olson, eds., ASME AMD-Vol. 186, pp. 57–66; also in *Computers and Structures,* Vol. 56, No. 5, Sept. 1995, pp. 825–836.

Murio, D. A., 1993, *The Mollification Method and the Numerical Solution of Ill-Posed Problems,* Wiley, New York.

Press, W. H., Teukolsky, S. A., Vetterling, W. T., and Flannery, B. P., 1992, *Numerical Recipes in FORTRAN,* 2nd ed., Cambridge University Press.

Sykulski, J. K., ed., 1995, *Computational Magnetics,* Chap. 5 (authored by K. Pawluk), Chapman & Hall, London.

Throne, R. D., and Olson, L. G., 1994, "A Generalized Eigensystem Approach to the Inverse Problem of Electrocardiography," *IEEE Transactions on Biomedical Engineering,* Vol. 41, No. 6, pp. 1–9.

Tikhonov, A. N., 1977, *Solutions of Ill-Posed Problems,* Halsted Press, Washington–Winston–New York.

Downloaded 11 Dec 2010 to 193.140.21.150. Redistribution subject to ASME license or copyright; see http://www.asme.org/terms/Terms_Use.cfm

Experimental Investigation of the Laminar Flow Heat Transfer Enhancement in a Small-Scale Square Duct With Aqueous Carbopol Solutions

Cheng-Xian Lin
Post-doctoral Research Fellow.

Shao-Yen Ko
Professor.
Mem. ASME

Institute of Engineering Thermophysics,
Chinese Academy of Sciences,
P.O. Box 2706,
Beijing 100080, People's Republic of China

F. K. Tsou
Professor,
Department of Mechanical Engineering and Mechanics,
Drexel University,
Philadelphia, PA 19104

This paper presents results of an experimental study on the heat transfer enhancement in laminar flow of non-Newtonian fluids, aqueous Carbopol-934 solutions through a small-scale square duct. The square duct is a top-wall heated configuration with a hydraulic diameter of 0.4 cm. The aqueous Carbopol solutions examined are those neutralized, and have a polymer concentration range of 1000–2000 wppm. It is shown that the enhanced heat transfer behavior of the Carbopol solutions within low Reynolds number range is different from that within relatively high Reynolds number range. There exists a limiting polymer concentration, C_{max}, at which the non-Newtonian fluid possesses the maximum ability to enhance heat transfer. If the polymer concentration becomes too high, the minimum Reynolds number required to enhance heat transfer increases with the increasing polymer concentration.

Introduction

The problem of laminar flow heat transfer enhancement associated with non-Newtonian fluids in rectangular or square ducts has received considerable attention in recent years. Studies on this topic are motivated mainly by the two facts: One is that non-Newtonian fluids are widely used in the chemical, pharmaceutical, and food industries, and recently in cooling of electronic equipments; another is that although many studies have been carried out with non-Newtonian fluids, the flow and heat transfer behavior of these fluids in rectangular or square ducts is not well understood.

Lawal and Majumdar (1987), Hartnett and Kostic (1989), Hartnett (1992), and Kostic (1994) have reviewed the current knowledge on fluid mechanics and heat transfer of non-Newtonian fluids in rectangular or square ducts. The most recent studies used mainly numerical methods, including those performed by Gingrich et al. (1992a, 1992b), Gao (1993), Kostic (1993), Shin and Cho (1994), and Payvar (1994). As the mathematical model that can capture the physics and predict the heat transfer is still not well developed, experiments are expected to be indispensable to the understanding of the heat transfer behavior of the non-Newtonian fluids.

Among the experimental studies, the laminar flow heat transfer in non-Newtonian flows through noncircular ducts was investigated by Oliver (1969) and Oliver and Karim (1971) with flattened tubes, by Kostic (1984) and Xie (1991) with a 2:1 rectangular duct, and by Rao (1988) with a 5:1 rectangular duct. As to the square ducts, Mena et al. (1978) studied the laminar flow heat transfer with Polyacrylamide (Separan) solutions in a duct heated by fluid flowing through a surrounding jacket, and Lawal (1985) used 1 percent unneutralized and 0.3 percent partially neutralized Polyacrylic Acid (Carbopol) solutions in a duct heated electrically. Hartnett et al. (1986) reported the experimental pressure drop measurements with Separan and Carbopol solutions in a square duct under isothermal conditions. The range of the hydraulic diameter, D_h, of the ducts used in all of the previous experiments is 1.0–3.75 cm. Almost all of the available experimental data on non-Newtonian fluid heat transfer in noncircular ducts have showed substantial laminar heat transfer enhancement, virtually without friction drag increase.

As discussed recently by Kostic (1994), the fluid elasticity may be the major cause for the laminar heat transfer enhancement in non-Newtonian fluids in noncircular duct flows. As non-Newtonian fluids withstand more elasticity in a small-scale duct than in a normal-scale duct from a point of view of rheology, the authors imagine here that non-Newtonian fluids may generate more enhanced heat transfer in a small-scale duct than in a normal-scale duct. The available analyses have indicated that the effects of the secondary flow resulting from the elasticity of non-Newtonian fluids are greatest in the square duct geometry, and their influence decreased as the aspect ratio of the ducts decreased (Dodson et al., 1974).

The goal of the present study is to investigate the laminar flow heat transfer enhancement in a relatively small-scale square duct with neutralized Carbopol solutions at various polymer concentrations. The duct with only one thermally active surface is selected, not only for its academic interest, but also for its particular application in the cooling of some electronic equipments. The limiting polymer concentration necessary for obtaining maximum heat transfer enhancement and the minimum Reynolds number required for the non-Newtonian fluids to start enhancing heat transfer will be explored and emphasized.

Experimental System

The designed test section is shown in Fig. 1. Five uniformly placed square ducts of the same hydraulic diameter (D_h = 0.4 mm) were employed to ensure the measuring accuracy. Only the middle duct was used for measurement. The top wall of the ducts was made from 0.9-mm-thick stainless steel. Outside the top wall is the 0.08 mm electrothermal band to provide the constant heat flux boundary conditions along the top wall, and the rubber belt pressed by the top cover. The base of the chan-

Contributed by the Heat Transfer Division for publication in the JOURNAL OF HEAT TRANSFER. Manuscript received by the Heat Transfer Division September 1994; revision received April 1995. Keywords: Augmentation and Enhancement, Forced Convection, Non-Newtonian Flows and Systems. Associate Technical Editor: T. J. Rabas.

Copyright © 1996 by ASME

Downloaded 11 Dec 2010 to 193.140.21.150. Redistribution subject to ASME license or copyright; see http://www.asme.org/terms/Terms_Use.cfm

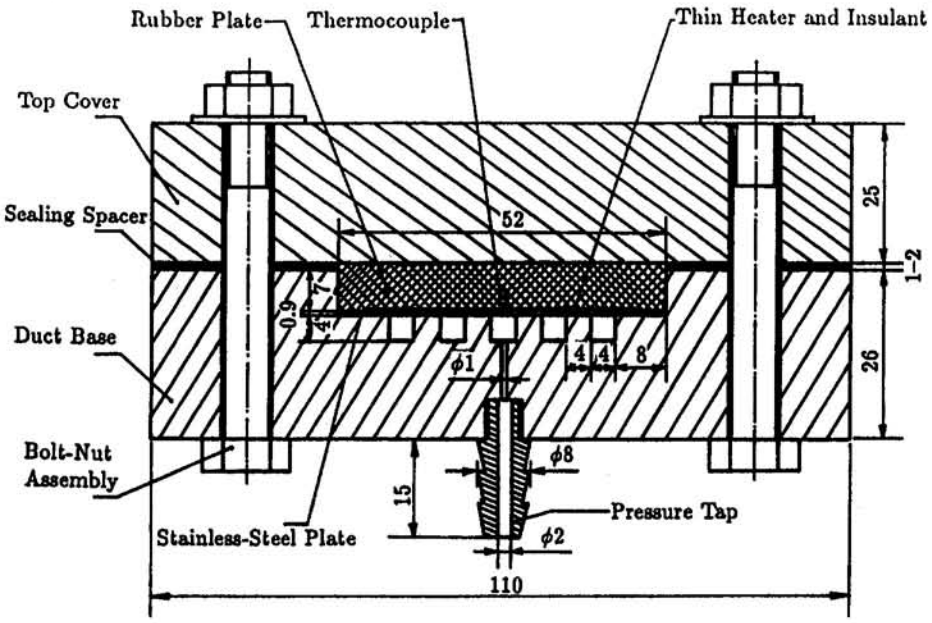


Fig. 1 Test section

nels is a transparent material, PMMA, with a low conductivity of about 0.14 W/(m·K).

Analysis has shown that the combined heat transfer that can occur due to the thickness of the duct wall is small. As only the top wall is heated, the buoyancy effects on the non-Newtonian flow should be weak. So, the heat transfer encountered in the square ducts would generally be the forced convection type. For each of the five square ducts, $L/D_h = 600$, and the fully developed flow and heat transfer were obtained. The entrance to the square ducts is sharp, so the thermal and hydrodynamic entrance lengths develop simultaneously.

The outside wall temperature distributions along the top wall were measured by 35 0.2 mm copper-constantan thermocouples located at different axial positions along the duct. The accuracy for the temperature measurement is 0.1°C with all the thermocouples carefully calibrated. The pressure taps of 1 mm inner diameter located at 16 positions along the bottom wall were used for measuring the pressure drops by a water-column manometer, the minimum graduation of which is 1 mm.

The experimental setup is shown in Fig. 2. The test fluids were prepared and stored in the bottom tank. A special G28-1 screw pump, which minimizes the mechanical rupture of the molecular structure of the aqueous Carbopol solutions, was used to transport the liquids from the bottom tank to the upper one. The liquids driven by the gravity then flow from the upper tank into the lower test section. A constant liquid head in the upper tank is maintained by using a funnel to direct the overflow down to the bottom tank. Before the test section, a calming chamber (calming section) was provided to reduce the disturbance and obtain a steady laminar flow. The valve before the calming chamber can be adjusted to give desired velocities in the test section. When exiting the test section, the test fluids were mixed in the mixing chamber (mixing section) to provide uniform bulk fluid temperature. After recovering the heat gain of the

Nomenclature

C = concentration of the polymer solution, wppm
C_{max} = polymer concentration at which maximum heat transfer enhancement can be obtained, wppm
C_p = specific heat of the fluid, J/kg·K
D_h = hydraulic diameter of the duct, m
f = fanning friction factor = $-D_h\Delta p/(2\Delta x\rho U^2)$
Gz = Graetz number = $\dot{m}C_p/kx$
h_x = local convective heat transfer coefficient = $q/(T_w - T_b)$, W/m²·K
$H1(1)$ = thermal boundary condition representing constant wall heat flux axially and constant temperature peripherally on one wall of the square duct
$H1(4)$ = thermal boundary condition representing constant wall heat flux axially and constant temperature peripherally on all four walls of the square duct
k = thermal conductivity, W/m·K
K = consistency index in power-law model, N·s^n/m²
L = length of the duct, m
$\dot{m}$ = mass flow rate, kg/s
n = power law index in power law model
Nu_{fd} = fully established Nusselt number
Nu_x = local Nusselt number = h_xD_h/k
Δp = pressure drop between pressure taps, N/m²
q = heat flux per unit heating area, W/m²
Re* = Kozicki generalized Reynolds number, defined in Eq. (3)
Re^*_{min} = minimum Reynolds number Re* required for polymer solution to start enhancing heat transfer
T_b = local bulk temperature of the fluid, °C
T_w = local wall temperature of the duct, °C
U = mean velocity in axial direction, m/s
wppm = weight parts per million
x = axial rectilinear coordinate, or axial location from the duct entrance, m
Δx = axial distance between pressure taps, m
$\dot{\gamma}$ = shear rate, 1/s
η = fluid apparent viscosity, N·s/m²
ρ = density of fluid, kg/m³

Downloaded 11 Dec 2010 to 193.140.21.150. Redistribution subject to ASME license or copyright; see http://www.asme.org/terms/Terms_Use.cfm

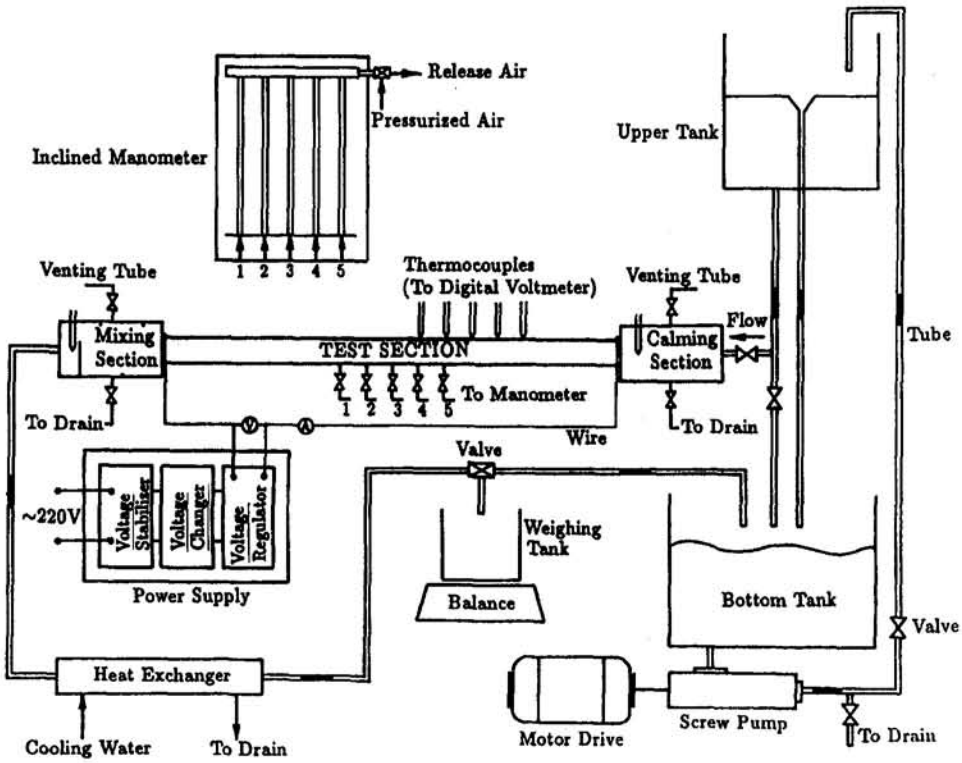


Fig. 2 Experimental setup

test fluids by a heat exchanger, the experimental setup either let the fluids go to the weighing tank or return to the bottom tank for recirculation.

An AC unit with maximum AC power output of 5 kW was used as the power supply. By measuring the electric current (by an amperometer) and voltage drop (by a voltmeter) across the electrothermal band, the heat flux, q, per unit heating area was determined. The uncertainty of the heat flux was calculated as ±2.6 percent. The liquid mass flow rate was measured by weighing collected fluid over a certain period of time with a stop watch. The minimum time interval taken should be 10 s to get an uncertainty of time of ± 1 percent. The calculated uncertainty of mass flow rate is about ±1.3 percent. Near the entrance in the calming section and close to the exit in the mixing section, the mean fluid temperature was measured. The temperature difference between inlet and outlet was kept not less than 2.5°C. The calming chamber, test section, and mixing chamber were wrapped by 100-mm-thick thermal insulation materials with an effective conductivity of 0.019 W/(m·K). During the experiments, the temperature distributions on the outside surfaces of the wrapped test section were monitored, and the heat loss to the environment was estimated to be considerably less than 1 percent.

An analysis was also performed to estimate the uncertainties in the reported dimensionless quantities. The friction factor, f, for water was found to have an uncertainty of ±19 percent, and that for aqueous Carbopol solutions ±8.5 percent. The uncertainties in Nusselt number, Nu_x, Reynolds number, Re*, and Graetz number, Gz, were estimated to be ±4.5, ±2, and ±2.8 percent, respectively.

Test Fluids

The investigated aqueous Carbopol solutions were prepared by adding the required amount of Carbopol-934 (from B.F. Goodrich Co.) into a certain amount of Beijing tap water. The polymer concentrations considered in the present study are 1000, 1250, 1500, 1725, and 2000 wppm. After a homogeneous solution was obtained, the aqueous Carbopol solution was neutralized to a pH value of 7 ± 0.2 by adding a 10 percent sodium hydroxide solution. As the Carbopol has a stable chemical structure, its solutions should be more suitable for heat transfer applications than other polymer solutions used in the literature.

Except viscosity, all the other thermophysical properties of the aqueous Carbopol solutions have been taken to be the same as those of water, on the basis of the previous studies (Cho and Hartnett, 1985). The NXS-11 rotational viscometer in the heat transfer laboratory, Institute of Engineering Thermophysics, Chinese Academy of Sciences, was used to measure the apparent viscosities of the non-Newtonian fluids in different shear-rate ranges before and after each heat transfer run, in order to clearly define the test fluids. The accuracy of the viscosity measurement is 1 percent.

Figure 3 provides the measured typical apparent viscosity, η, versus shear rate, γ, of the Carbopol solutions for the five polymer concentrations. Over the whole range of shear rate measured in the rotational viscometer, the apparent viscosity of the Carbopol solution for each examined polymer concentration increases with increasing concentration, and is fitted with good accuracy by the following power law:

$$\eta = K\dot{\gamma}^{n-1} \tag{1}$$

where K and n are the consistency index and power-law index, respectively, in the power-law model, and are dependent only on the polymer concentration for fixed value of temperature. In the present study, the range of the power-law index, n, for the non-Newtonian fluids extends from 0.48 to 0.89. For the Newtonian fluid, the Beijing tap water, n equals unity.

Results and Discussion

Friction Factor Measurements. The pressure drop data were measured simultaneously with heat transfer measurements. The fully developed Fanning friction factor f of the aqueous Carbopol solutions and Beijing tap water are shown in Fig. 4.

Downloaded 11 Dec 2010 to 193.140.21.150. Redistribution subject to ASME license or copyright; see http://www.asme.org/terms/Terms_Use.cfm

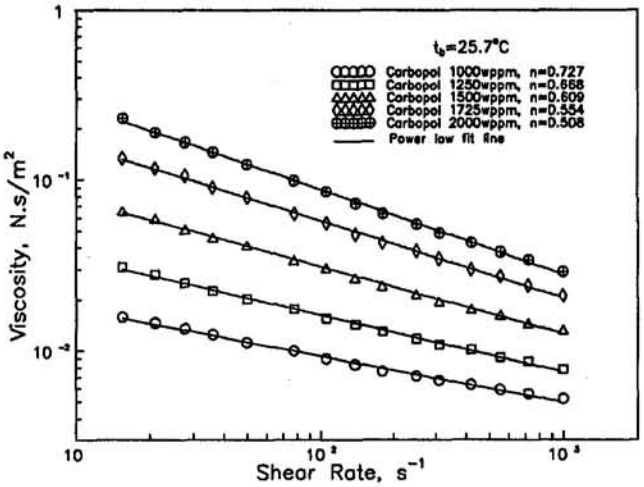


Fig. 3 Apparent viscosity versus shear rate of aqueous Carbopol solution, with polymer concentration as a parameter

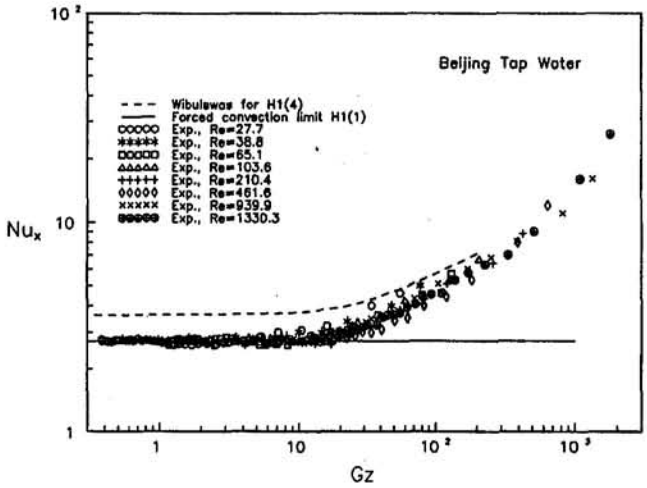


Fig. 5 Local Nusselt number versus Graetz number of Beijing tap water as a function of Reynolds number; Re = Re*

It is seen that the experimental results are in agreement with the power-law prediction of Kozicki et al. (1966) even at very low Reynolds numbers with the following relationship:

$$f = 16/\mathrm{Re}^* \tag{2}$$

where the Kozicki generalized Reynolds number, Re*, is dependent on the geometries of ducts. For a square duct, Re* can be written as

$$\mathrm{Re}^* = \rho U^{2-n} D_h^n \Big/ \left[8^{n-1} K \left(0.6766 + \frac{0.2121}{n} \right)^n \right] \tag{3}$$

There is a consistent trend in Fig. 4, that is, most of the data including those for tap water lie slightly above the theoretical line. The results of Seyer and Metzner (1967) with polymer solutions in a circular tube (D_h = 1.27 cm) behaved similarly, but the measurements of Hartnett et al. (1986) with polymer solutions in a square duct (D_h = 1.0 cm) did not show the trend. In the present study, the effects of the duct geometry, and the effects of the free convection that appeared due to nonadiabatic conditions, account for the occurrence of the trend in Fig. 4. Specifically, greater sensitivity of the friction factor of the Carbopol solutions to the duct geometry and free convection was found for $n \approx 0.65$. The maximum deviation of the experimental data from the power-law prediction is 40 percent.

For the investigated small-scale square duct, it was found from the experimental results that the aqueous Carbopol solutions did not generate significant apparent slip, which, as stated by Cohen and Metzner (1985) and Lu et al. (1991), may occur in laminar flows of polymer solutions through capillary tubes of very small diameters.

Heat Transfer Measurements. In the present study, the temperature range for heat transfer study was kept within 20–30°C. The bulk fluid temperature was used to characterize the values of the fluid properties.

Figures 5–7 shows the representative local Nusselt numbers, Nu_x, as a function of Graetz number, Gz, for Beijing tap water, 1250 wppm and 1750 wppm Carbopol solutions, respectively. Also shown is the Newtonian prediction of Wibulswas (1966) for the case where all four walls are heated under constant axial heat flux and constant local peripheral wall temperature, the $H1(4)$ boundary condition. Also, shown for reference is the fully developed limiting Nusselt value for Newtonian fluid when only one of the duct walls is heated, the $H1(1)$ boundary condition (Schmidt, 1978). As shown in Fig. 5, the Nusselt values for Beijing tap water in thermally developed flow are in good agreement with the Newtonian prediction of Schmidt (1978) within ±5 percent.

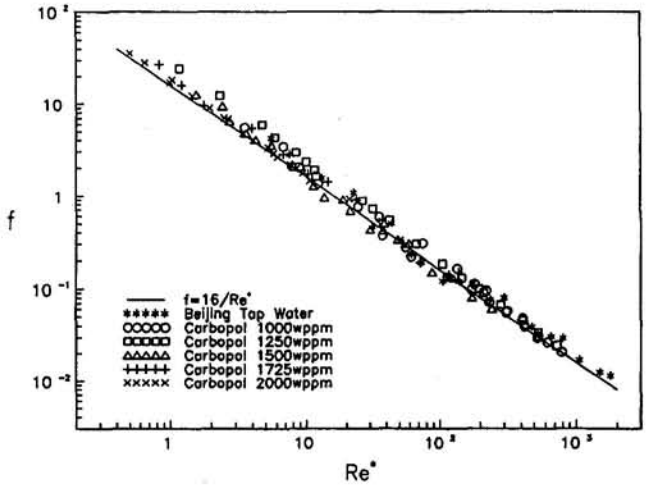


Fig. 4 Friction factor measurements for aqueous Carbopol solutions in fully established laminar flow through a square duct

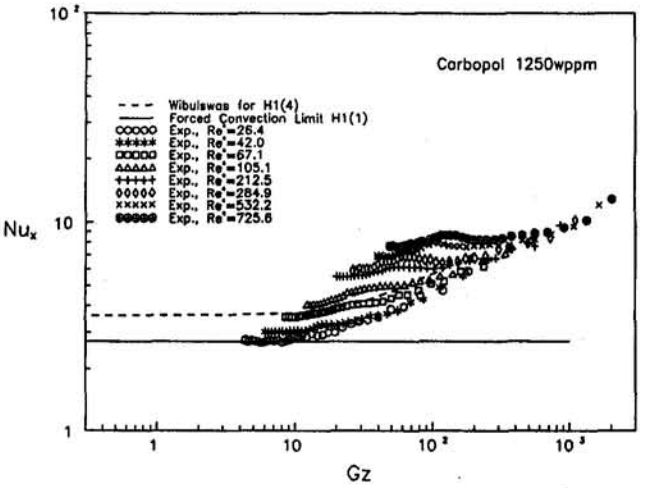


Fig. 6 Local Nusselt number versus Graetz number of 1250 wppm aqueous Carbopol solution as a function of Reynolds number

Downloaded 11 Dec 2010 to 193.140.21.150. Redistribution subject to ASME license or copyright; see http://www.asme.org/terms/Terms_Use.cfm

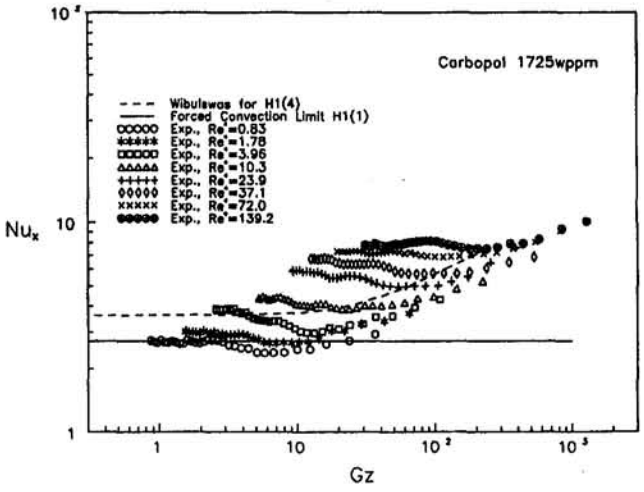


Fig. 7 Local Nusselt number versus Graetz number of 1725 wppm aqueous Carbopol solution as a function of Reynolds number

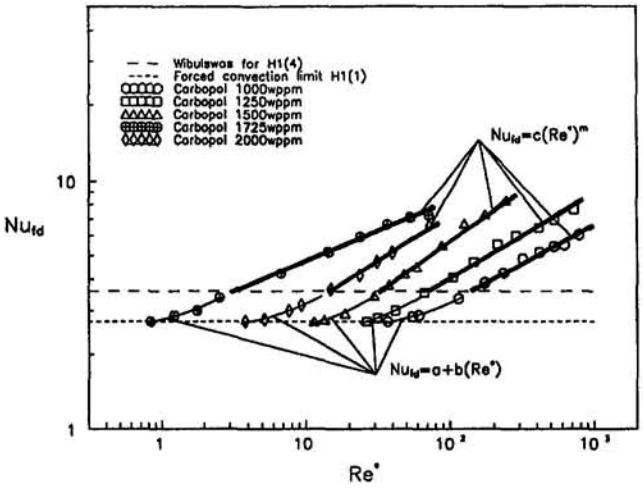


Fig. 8 Fully developed Nusselt numbers for aqueous Carbopol solutions as a function of Reynolds number with polymer concentration as a parameter

It is shown in Figs. 6 and 7 that for fixed polymer concentration, the Nu_x distributions for the Carbopol solutions at relatively low values of Re* are similar to that for water along the whole length of the duct. At relatively large values of Re*, the Carbopol solutions produce significant local heat transfer enhancement except close to the entrance. When polymer concentration is high, the heat transfer can be dramatically increased even at very low values of Re*. For example, results of 1725 wppm Carbopol solution shown in Fig. 7 give 42.3–60.8 percent increase in heat transfer even within a very low Re* range of 3.96–10.3.

The local Nusselt number, Nu_x, seems to be a very complex function of the polymer concentration, C, Reynolds number, Re*, and Graetz number, Gz:

$$Nu_x = F(C, Re^*, Gz) \tag{4}$$

C can be replaced by two or three elasticity parameters, which would be more reasonable for characterizing the investigated viscoelastic fluids than the polymer concentration.

Experimental heat transfer measurements have shown that the thermal entrance length of the duct decreases, in general, with the increase of polymer concentration. When both the polymer concentration and the Reynolds number are sufficiently high, the Nusselt number will become almost independent of the Graetz number.

It should be mentioned here that the reason that non-Newtonian fluids can substantially increase the heat transfer while not noticeably increasing friction in laminar noncircular duct flow is still not really understood. For the non-Newtonian flows through rectangular ducts, both computational studies using the viscoelastic fluid model of Reiner-Rivlin (Gao, 1993) and that using the inelastic fluid model of temperature-dependent viscosity (Shin and Cho, 1994) can produce results in good agreement with the experimental results of Xie and Hartnett (1992). Based on the present experimental results, the authors support the proposition of Kostic (1994) and others, that the fluid elasticity giving rise to secondary flows is responsible for the observed large increase in heat transfer in the noncircular duct flow.

The available previous heat transfer data closely related to the present study are scarce. As we knew, the experimental heat transfer results of Lawal (1985) with Carbopol solutions in a square duct (D_h = 1.575 cm) were about 50 percent higher than predicted. Compared with the results in circular tubes, Mena et al. (1978) announced 45 percent increase in heat transfer with Separan solutions in a square duct (D_h = 1.0 cm). For the present investigated square duct (D_h = 0.4 cm), the Carbopol solutions can produce up to 120–210 percent higher heat transfer than Newtonian fluid water. It seems that non-Newtonian fluids in a small-scale duct possess stronger heat transfer ability than in a normal-scale duct.

Figure 8 presents the fully developed Nusselt number, Nu_{fd}, versus Reynolds number, Re*, of the Carbopol solutions as a function of polymer concentration. Here, Nu_{fd} is determined from Nu_x within a corresponding low Gz range or a high x/D_h range ($x/D_h > 400$), where further development in Nu_x with Gz is within 5 percent. For each polymer concentration, the minimum heat transfer asymptote of each polymer solution is the line representing the forced convection heat transfer value of the Newtonian fluid. It was found that Nu_{fd} within a relatively low Re* range and that within a relatively high Re* range do not follow the same pattern, but can be well described by a linear and a power-law correlations, respectively:

$$Nu_{fd} = \begin{cases} c(Re^*)^m, & \text{if } Re^*/Re^*_{min} \geq 2.8 \\ a + b(Re^*), & \text{if } Re^*/Re^*_{min} < 2.8 \end{cases} \tag{5}$$

In the equation above, the use of the criterion, Re^*/Re^*_{min} = 2.8, is unique to the present experiments. Re^*_{min} is defined as the minimum Kozicki generalized Reynolds number required for the Carbopol solutions to start enhancing heat transfer. In other words, when the Reynolds number, Re*, becomes greater than Re^*_{min}, the heat transfer values of the Carbopol solutions will become greater than that of the Newtonian fluid water.

The values of c, m, a, and b in Eq. (5) depend on the concentration of the polymer solutions, and are given in Table 1. The power-law index, m, does not vary monotonously with an increase of polymer concentration, C, reflecting the nonlinear elasticity effects of the test fluids on the heat transfer enhancement with increasing C.

Table 1 Constants in heat transfer correlation

Concentration (wppm)	Constants			
	c	m	a	$b \times 100$
1000	0.93	0.28	2.38	0.83
1250	0.91	0.33	2.22	1.85
1500	0.97	0.39	2.21	4.03
1725	2.73	0.24	2.39	37.6
2000	1.65	0.31	2.37	8.13

Downloaded 11 Dec 2010 to 193.140.21.150. Redistribution subject to ASME license or copyright; see http://www.asme.org/terms/Terms_Use.cfm

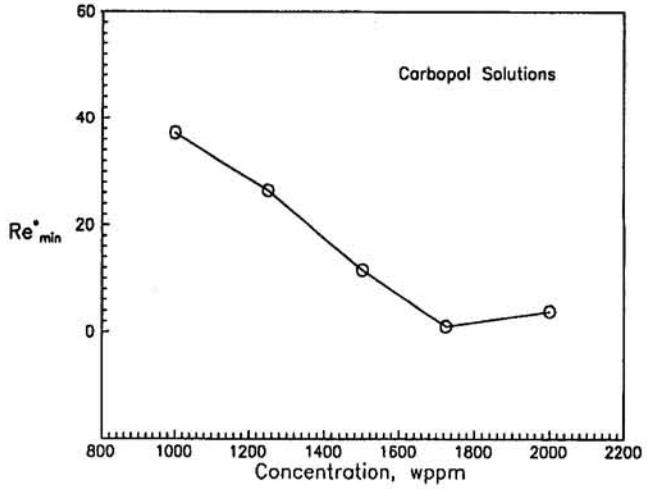


Fig. 9 Minimum Reynolds number required for aqueous Carbopol solutions to start heat transfer enhancement as a function of polymer concentration

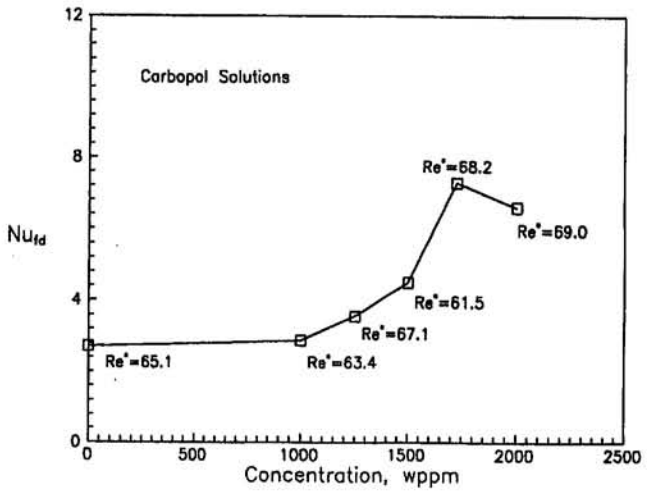


Fig. 11 Typical fully developed Nusselt number for aqueous Carbopol solutions as a function of polymer concentration at nearly constant Reynolds number

The Reynolds number, Re^*_{min}, as a function of polymer concentration, C, is shown in Fig. 9. For moderate concentration range ($C \leq 1725$ wppm), Re^*_{min} decreases with the increase of concentration. But within the higher concentration range ($C >$ 1725 wppm), Re^*_{min} displays the opposite behavior with the increasing concentration. The existence of the minimum value of Re^*_{min} is explained as follows. When concentration is high enough, further increase in it would cause reduction in the heat transfer ability of the test fluids. So, relatively larger value of Re^*_{min} of the flow is needed to generate stronger secondary flow to start the heat transfer enhancement.

Figures 10 and 11 show the typical results of developing and developed Nusselt numbers, respectively, at approximately the same Reynolds number, $Re^* = 65.23 \pm 3.75$. Within a polymer concentration range of less than 1725 wppm, the values of Nu_x in Fig. 10 increase with the increasing concentration. Though the Nu_x value of 2000 wppm is still somewhat larger than that of 1725 wppm within a large Gz range, it becomes lower than that of 1725 wppm within small Gz range, especially in the region of thermally developed flow.

It is clearly shown in Fig. 11 that under the condition of constant Re*, there exists a limiting polymer concentration, C_{max}, for the Carbopol solutions, at which the maximum heat transfer enhancement can be reached. When the polymer concentration becomes higher than the limiting values of C_{max}, further increase of concentration will give no further increase and even reduce the heat transfer. The reason for the limiting concentration, C_{max}, is similar to that for the minimum Reynolds number, Re^*_{min}, discussed above.

The results given in Figs. 9 and 11 suggest that there must be dependence between the minimum Reynolds number, Re^*_{min}, and the fully developed Nusselt number, Nu_{fd}, at certain Reynolds number. Over the investigated polymer concentration range, the minimum value of Re_{min} shown in Fig. 9 is in correspondence with the maximum value of Nu_{fd} shown in Fig. 11.

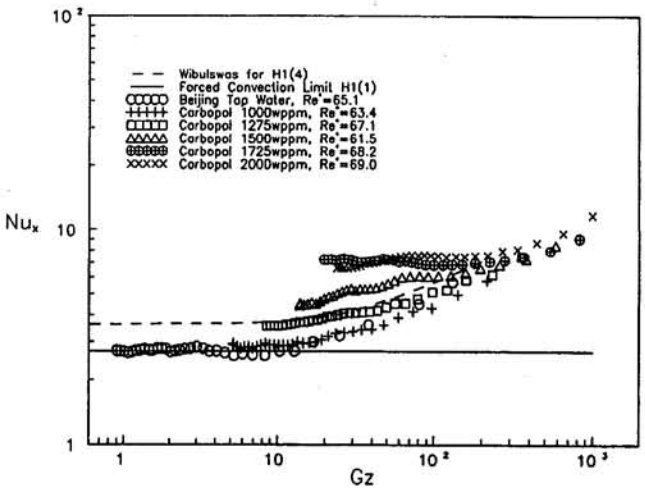


Fig. 10 Typical local Nusselt number for aqueous Carbopol solutions as a function of Graetz number at nearly constant Reynolds number

Conclusions

The heat transfer enhancement with different concentrations of neutralized aqueous Carbopol-934 solutions in a small-scale square duct has been investigated experimentally under the condition of laminar forced flow. Within the investigated parameter ranges, the following conclusions can be drawn:

- The local heat transfer of the Carbopol solutions depends on polymer concentration, Reynolds number, and Graetz number, and possesses more uniform patterns along the heated wall of the duct than that of Newtonian fluid.
- For the thermally developed flow of Carbopol solutions, the heat transfer behavior within a relatively low Reynolds number range ($Re^*/Re^*_{min} < 2.8$) is different from that within relatively high Reynolds number range ($Re^*/Re^*_{min} \geq 2.8$).
- The minimum Reynolds number Re^*_{min} required for heat transfer enhancement decreases with increasing polymer concentration until a high polymer concentration range is covered.
- Under constant Reynolds number conditions, aqueous Carbopol solutions can achieve maximum heat transfer at a limiting polymer concentration C_{max}. When the polymer concentration is higher than C_{max}, the ability of the fluids to enhance heat transfer becomes limited.

Acknowledgments

The authors gratefully acknowledge the financial support of the China Post-doctoral Science Funds (CPSF).

References

Cho, Y. Y., and Hartnett, J. P., 1985, "Non-Newtonian Fluids," in: *Handbook of Heat Transfer Applications*, W. M. Rohsenow, J. P. Hartnett, and E. N. Ganic, eds., 2nd ed., McGraw-Hill, New York.

Downloaded 11 Dec 2010 to 193.140.21.150. Redistribution subject to ASME license or copyright; see http://www.asme.org/terms/Terms_Use.cfm

Cohen, Y., and Metzner, A. B., 1985, "Apparent Slip Flow of Polymer Solutions," *J. Rheology,* Vol. 29, pp. 67–102.

Dodson, A. G., Townsend, P., and Walters, K., 1974, "Non-Newtonian Flow in Pipes of Non-circular Cross Section," *Computers & Fluids,* Vol. 2, pp. 317–338.

Gao, S., 1993, "Flow and Heat Transfer of Non-Newtonian Fluids in a Rectangular Duct," Ph.D. Thesis, University of Illinois at Chicago.

Gingrich, W. K., Cho, Y. I., and Shyy, W., 1992a, "Effects of Shear Thinning on Laminar Heat Transfer Behavior in Rectangular Ducts," *Int. J. Heat Mass Transfer,* Vol. 35, pp. 2823–2836.

Gingrich, W. K., Cho, Y. I., and Shyy, W., 1992b, "Effects of Aspect Ratio on Laminar Heat Transfer Behavior of a Non-Newtonian Fluid in an Electronics Coldplate," *Int. Comm. Heat Mass Transfer,* Vol. 19, pp. 311–3251.

Hartnett, J. P., Kwack, E. Y., and Rao, B. K., 1986, "Hydrodynamic Behavior of Non-Newtonian Fluids in a Square Duct," *J. Rheology,* Vol. 30(S), pp. 545–559.

Hartnett, J. P., and Kostic, M., 1989, "Heat Transfer to Newtonian and Non-Newtonian Fluids in Rectangular Ducts," *Adv. Heat Transfer,* Vol. 19, pp. 247–356.

Hartnett, J. P., 1992, "Viscoelastic Fluids: A New Challenge in Heat Transfer," ASME JOURNAL OF HEAT TRANSFER, Vol. 114, pp. 296–303.

Kostic, M., 1984, "Heat Transfer and Hydrodynamics of Water and Viscoelastic Fluid Flow in a Rectangular Duct," Ph.D. Thesis, University of Illinois at Chicago.

Kostic, M., 1993, "Influence of Viscosity Function Simplification on Non-Newtonian Velocity and Shear-Rate Profiles in Rectangular Ducts," *Int. Comm. Heat Mass Transfer,* Vol. 20, pp. 515–525.

Kostic, M., 1994, "On Turbulent Drag and Heat Transfer Reduction Phenomena and Laminar Heat Transfer Enhancement in Non-circular Duct Flow of Certain Non-Newtonian Fluids," *Int. J. Heat Mass Transfer,* Vol. 37, Suppl. 1, pp. 133–147.

Kozicki, W., Chou, C. H., and Tiu, C., 1966, "Non-Newtonian Flow in Ducts of Arbitrary Cross-Sectional Shape," *Chem. Eng. Sci.,* Vol. 21, pp. 665–679.

Lawal, A., 1985, "Laminar Flow and Heat Transfer to Variable Property Power Law Fluids in Arbitrary Cross-Sectional Ducts," Ph.D. thesis, McGill University, Canada.

Lawal, A., and Mujumdar, A. S., 1987, "Laminar Duct Flow and Heat Transfer to Purely Viscous Non-Newtonian Fluids," *Adv. Transp. Processes,* Vol. 5, pp. 352–443.

Lu, Z., Geng, Y., and Fan, C., 1991, "Analyses for Flow Enhancement of Polymer Solution Slip Flow by Using Laser Doppler Anemometry," *Proc. China–Japan Int. Conf. on Rheology,* Beijing, pp. 150–156.

Mena, B., Best, G., Bautista, P., and Sanchez, T., 1978, "Heat Transfer in Non-Newtonian Flow Through Pipes," *Rheol. Acta,* Vol. 17, pp. 454–457.

Oliver, D. R., 1969, "Non-Newtonian Heat Transfer: An Interesting Effect Observed in Non-circular Tubes," *Trans. Inst. Chem. Engrs.,* Vol. 47, pp. T18–T20.

Oliver, D. R., and Karim, R. B., 1971, "Laminar Flow Non-Newtonian Heat Transfer in Flattened Tubes," *Can. J. Chem. Eng.,* Vol. 49, pp. 236–240.

Payvar, P., 1994, "Heat Transfer Enhancement in Laminar Flow of Viscoelastic Fluids Through Rectangular Ducts," *Int. J. Heat Mass Transfer* (submitted).

Rao, B. K., 1988, "Heat Transfer to Viscoelastic Fluids in a 5:1 Rectangular Duct," Ph.D. Thesis, University of Illinois at Chicago.

Schmidt, F. W., 1978, presented in R. K. Shah and A. L. London, "Laminar Flow Forced Convection in Ducts," *Adv. Heat Transfer,* Suppl. 1, Academic Press.

Seyer, F. A., and Metzner, A. B., 1967, "Turbulent Flow Properties of Viscoelastic Fluids," *Can. J. Chem. Eng.,* Vol. 45, pp. 121–126.

Shin, S., and Cho, Y. I., 1994, "Laminar Heat Transfer in a Rectangular Duct With a Non-Newtonian Fluid With Temperature-Dependent Viscosity," *Int. J. Heat Mass Transfer,* Vol. 37, Suppl. 1, pp. 19–30.

Wibulswas, P., 1966, "Laminar Flow Heat Transfer in Non-circular Ducts," Ph.D. thesis, London University.

Xie, C. B., 1991, "Laminar Heat Transfer of Newtonian and Non-Newtonian Fluids in a 2:1 Rectangular Duct," Ph.D. Thesis, University of Illinois at Chicago.

Xie, C. B., and Hartnett, J. P., 1992, "Influence of Rheology on Laminar Heat Transfer to Viscoelastic Fluids," *Ind. Eng. Chem. Res.,* Vol. 31, pp. 727–732.

Downloaded 11 Dec 2010 to 193.140.21.150. Redistribution subject to ASME license or copyright; see http://www.asme.org/terms/Terms_Use.cfm

Prediction of Jet Impingement Heat Transfer Using a Hybrid Wall Treatment With Different Turbulent Prandtl Number Functions

G. K. Morris
Graduate Research Assistant.

S. V. Garimella
Cray-Research Associate Professor.
email: sureshg@csd.uwm.edu

R. S. Amano
Professor.

Department of Mechanical Engineering,
University of Wisconsin—Milwaukee,
P.O. Box 784,
Milwaukee, WI 53201

The local heat transfer coefficient distribution on a square heat source due to a normally impinging, axisymmetric, confined, and submerged liquid jet was computationally investigated. Numerical predictions were made for nozzle diameters of 3.18 and 6.35 mm at several nozzle-to-heat source spacings, with turbulent jet Reynolds numbers ranging from 8500 to 13,000. The commercial finite-volume code FLUENT was used to solve the thermal and flow fields using the standard high-Reynolds number $k-\epsilon$ turbulence model. The converged solution obtained from the code was refined using a post-processing program that incorporated several near-wall models. The role of four alternative turbulent Prandtl number functions on the predicted heat transfer coefficients was investigated. The predicted heat transfer coefficients were compared with previously obtained experimental measurements. The predicted stagnation and average heat transfer coefficients agree with experiments to within a maximum deviation of 16 and 20 percent, respectively. Reasons for the differences between the predicted and measured heat transfer coefficients are discussed.

Introduction

Impinging jet heat transfer has been studied extensively in the literature. Practical applications of impinging jets can be found in turbine-blade cooling, paper drying, steel mills, etc. Impinging air and liquid jets are also being examined as a tool for the thermal management of electronic components. Recent advances in electronic devices have led to power densities larger than 25 W/cm^2; this requirement exceeds the capabilities of traditional forced or natural convective cooling.

The jets investigated in this paper are axisymmetric, confined liquid jets that are *submerged,* that is, liquid from the jet issues into a region containing the same liquid at rest. The jet impinges on a solid surface and spreads out radially. The radial spread of the jet is *confined* on either side by the impingement surface and nozzle plate. This configuration has also been referred to as semi-confined in the literature (Obot et al., 1982). The jet and heat source dimensions in this paper are representative of electronics cooling applications. The fluid considered is FC-77, a perfluorinated dielectric liquid with a Prandtl number of 25.3 at 20°C.

Chang et al. (1993), Garimella and Rice (1994, 1995), Ma and Bergles (1990), Ma et al. (1990), and Sun et al. (1993) examined local heat transfer coefficient distributions using round, submerged liquid jets. Of these studies, only Chang et al. (1993) and Garimella and Rice (1994, 1995) considered a confining top wall such as that modeled in the present study. The local heat transfer coefficients were found to have a bell-shaped distribution where the maximum local value occurs at the stagnation point and symmetrically decreases with respect to the radial distance from the stagnation point. Experimental studies of submerged liquid jets in the literature have been reviewed by Garimella and Rice (1995) and Garimella and Nenaydykh (1996).

Theoretical and computational studies of jet impingement have also been presented in the literature. Wolfshtein (1969) used a one-equation turbulence model to solve the problem of a plane turbulent impinging jet and found good agreement with the experimental pressure and skin friction data. Bower et al. (1977) reported that the one-equation model did not compare favorably with experimental data at low nozzle-to-target plate spacings for a plane impinging jet. Agarwal and Bower (1982) used the low-Reynolds-number formulation of the $k-\epsilon$ model to compute the flow field of a compressible turbulent jet. They showed that the $k-\epsilon$ model was superior to the zero- and one-equation turbulence models. Two-dimensional, unconfined, axisymmetric jets were modeled by Amano and Jensen (1982), Amano and Brandt (1984), and Sugiyama and Amano (1983) using the high-Reynolds-number $k-\epsilon$ model of Launder and Spalding (1972); they reported good agreement with experimental data. The presence of a secondary peak in the skin friction profiles along the impingement surface was identified (Amano and Brandt, 1984); however, Amano and Jensen (1982) did not find secondary peaks in the heat transfer distribution using the same modeling approach. A comprehensive review of numerical studies related to impinging jets is available in Polat et al. (1989).

Several improvements to the Launder–Spalding $k-\epsilon$ model have been presented in the literature in the form of near-wall functions. Chieng and Launder (1980) assumed a two-layer turbulent kinetic energy profile near the wall and applied the treatment to the k equation. Amano and Jensen (1982) extended the physical model of the near-wall region proposed by Chieng and Launder (1980) to include the ϵ equation. The extended $k-\epsilon$ model was found to improve the prediction of the maximum heat transfer coefficient for a turbulent air jet impinging on a heated flat plate.

In this paper, two-layer models are applied to a converged solution obtained with FLUENT (Fluent, 1993) in a post-pro-

Contributed by the Heat Transfer Division for publication in the JOURNAL OF HEAT TRANSFER. Manuscript received by the Heat Transfer Division August 8, 1995; revision received April 17, 1996. Keywords: Electronic Equipment, Jets, Turbulence. Associate Technical Editor: V. K. Dhir.

Copyright © 1996 by ASME

Downloaded 11 Dec 2010 to 193.140.21.150. Redistribution subject to ASME license or copyright; see http://www.asme.org/terms/Terms_Use.cfm

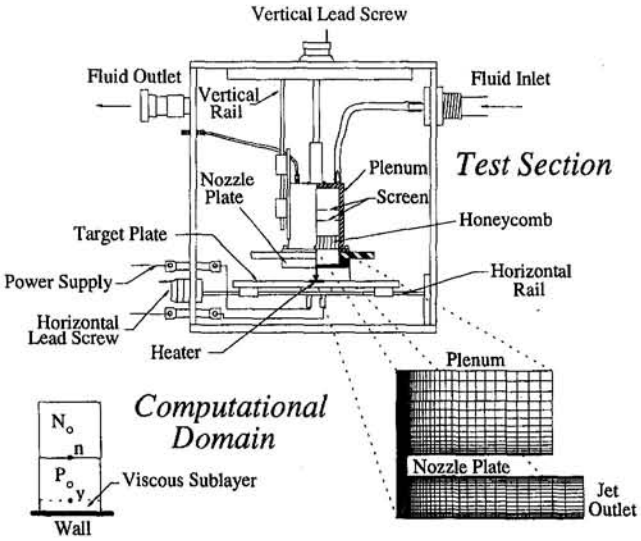


Fig. 1 Schematic of the test section and computational domain

cessing program to account better for the local variations of turbulence quantities near the wall. Four turbulent Prandtl number functions are used in the computations, and their performance evaluated with respect to agreement with experiment. One of the motivations for this study was to predict heat transfer coefficients computationally in a jet impingement configuration that was previously investigated experimentally as part of the same research program (Garimella and Rice, 1994, 1995; Garimella and Nenaydykh, 1996; Rice and Garimella, 1994). In keeping with the experiments, the local heat transfer distribution on a discrete heat source is predicted here for nozzle diameters of 3.18 and 6.35 mm, turbulent Reynolds numbers ($U_j d/\nu$) of 8500 to 13,000, and nozzle-to-target plate spacings (Z/d) of 1 to 4.

The Experiments

A description of the experiments against which the computational predictions of this study are compared is available from Garimella and Rice (1994, 1995). Some important aspects are included here. The technique for obtaining local heat transfer measurements was to move the heat source while holding the jet stationary. The heat source was an electrically heated foil with a thermocouple attached to the underside. Since lateral conduction along the foil thickness of 0.08 mm was negligible, the thermocouple read a local temperature. As the heat source was translated laterally, the heat transfer distribution on the heat source was mapped. The coolant used in the experiments was a perfluorinated dielectric liquid FC-77.

A schematic of the experimental test section is shown in Fig. 1. Located inside the plexiglass test section was a flow-conditioning plenum with a nozzle plate attached at one end. Facing the nozzle plate was a target plate containing the heat source. The fluid temperature was measured just prior to its exit from the nozzle. The plenum assembly was translated in the vertical direction to set the nozzle-to-target spacing (Z/d).

The stainless-steel foil heat source had an active area of 10 by 10 mm. A thermocouple affixed to the underside of the foil at the center of the heater provided local temperature measurements by horizontal traversal in fine increments relative to the jet. Details of the heat source assembly are available from Garimella and Rice (1995).

The local heat transfer coefficient was calculated from:

$$h = \frac{Q_{\text{out}} - Q_{\text{loss}}}{A_h(T_w - T_j)} = \frac{q''_w}{T_w - T_j} \tag{1}$$

where typical values for $T_w - T_j$ were in the range of 10–30°C for a heat flux of 25 W/cm^2, and Q_{loss}, which was the heat lost by conduction through the base, was always less than 2 percent. The jet exit temperature was maintained at 20°C for all the experiments. Uncertainties in the experimental heat transfer coefficients were found to be on the order of 5 percent (Garimella and Rice, 1995). The experiments were conducted for the same nozzle diameters, Reynolds numbers ($U_j d/\nu$), and nozzle-to-target spacings as considered in the present study.

Mathematical Modeling

The jet impingement heat transfer problem was numerically computed with the commercial finite-volume code FLUENT using the time-averaged Navier–Stokes and energy equations with the high-Reynolds-number $k-\epsilon$ turbulence model proposed by Launder and Spalding (1972). The Boussinesq viscosity

Nomenclature

A_h = area of heat source, m^2
C_μ = coefficient in turbulence model = 0.09
c_p = specific heat at constant pressure, J/(kg K)
d = nozzle diameter, m
E = log-law constant for smooth walls = 9.0
E^* = log-law constant for smooth walls = $EC_\mu^{1/4} \approx 5.0$
$\bar{G}$ = mean turbulence energy generation rate, m^2/s^3
h = local convective heat transfer coefficient, W/(m^2 K)
$\bar{h}$ = average convective heat transfer coefficient, W/(m^2 K)
h_0 = heat transfer coefficient at stagnation point, W/(m^2 K)
k = fluid thermal conductivity, W/(m K)
k = turbulent kinetic energy = $\overline{u_i^2}/2$, m^2/s^2
l = nozzle length, mm
Pr = fluid molecular Prandtl number
Pr_t = turbulent Prandtl number
Q = power dissipated by the heater, W
q''_w = heat flux dissipated by the heater, W/m^2
r = radial distance from the stagnation point, mm
Re = Reynolds number = $U_j d/\nu$
Re_{v0} = universal constant = 20
Re_v = turbulence Reynolds number, Eq. (7)
T = fluid temperature, °C
u = turbulent fluctuating velocity component, m/s
U = velocity of fluid, m/s
U^+ = dimensionless wall velocity = $\rho U k_v^{1/2}/\tau_w$
y = distance from wall, m
y^+ = dimensionless distance from the wall = $yk_v^{1/2}/\nu$
Z = distance between confining plates, mm
$\bar{\epsilon}$ = turbulence energy dissipation rate = $\nu\partial u_i^2/\partial x_j^2$, m^2/s^3
κ = von Karman constant, 0.42
κ^* = log-law constant; $\kappa C_\mu^{1/4} \approx 0.23$
ν = fluid kinematic viscosity, m^2/s
ρ = fluid density, kg/m^3
τ = shear stress, Pa

Subscripts

j = jet values
n = values at edge of the wall-adjacent cell (see Fig. 1)
N = values at node point N (see Fig. 1)
P = values at node P (see Fig. 1)
v = values at the edge of viscous sublayer (see Fig. 1)
w = wall values (see Fig. 1)

Downloaded 11 Dec 2010 to 193.140.21.150. Redistribution subject to ASME license or copyright; see http://www.asme.org/terms/Terms_Use.cfm

Table 1 Comparison of wall functions

Wall Functions	FLUENT	Present Model	Eq.
Logarithmic Law	$\frac{U_p}{\sqrt{\tau_w/\rho}} = \frac{1}{\kappa} ln\left(E^* \frac{y_p k_p^{1/2}}{\nu}\right)$	$\frac{U_p k_v^{1/2}}{\tau_w/\rho} = \frac{1}{\kappa^*} ln\left(E^* \frac{y_p k_v^{1/2}}{\nu}\right)$	(2)
Heat-Momentum Transfer Analogy	$\frac{k(T_w - T_p)/y_p}{q_w''} = \frac{1}{\kappa y_p^+} \frac{Pr_t}{Pr} ln(Ey_p^+) + \frac{1}{y_p^+}\left(\frac{Pr_t}{Pr}\right)^{\frac{5}{4}} \frac{\pi/4}{sin\,\pi/4}\left(\frac{26}{\kappa}\right)^{\frac{1}{4}}\left(\frac{Pr}{Pr_t} - 1\right)$	$\frac{(T_w - T_p)\rho c_p k_v^{1/2}}{q_w''} = Pr_t\left[\frac{1}{\kappa^*} ln\left(E^* \frac{y_p k_v^{1/2}}{\nu}\right) + \mathcal{P}\right]$	(3)
		$\mathcal{P} = 9.24\left[\left(\frac{Pr}{Pr_t}\right)^{0.75} - 1\right]\left[1 + 0.28\, exp\left(-0.007 \frac{Pr}{Pr_t}\right)\right]$	(4)
Average Generation Rate		$\rho\bar{G} = \frac{\tau_w(U_n - U_v)}{y_n} + \frac{\tau_w(\tau_n - \tau_w)}{\rho\kappa^* k_v^{1/2} y_n}\left(1 - \frac{y_v}{y_n}\right)$	(5)
Average Dissipation Rate		$\bar{\varepsilon} = \frac{2k_v^{3/2}}{y_v Re_v} + \frac{C_\mu^{3/4}}{y_n \kappa}\left[\frac{2}{3}\left(k_n^{3/2} - k_v^{3/2}\right) + 2a\left(k_n^{1/2} - k_v^{1/2}\right) + \lambda\right]$ $\lambda = \begin{cases} a^{3/2} ln\left[\frac{\left(k_n^{1/2} - a^{1/2}\right)\left(k_v^{1/2} + a^{1/2}\right)}{\left(k_n^{1/2} + a^{1/2}\right)\left(k_v^{1/2} - a^{1/2}\right)}\right] & if\ a > 0 \\ 2(-a)^{3/2}\left[tan^{-1}\left(\frac{k_n^{1/2}}{(-a)^{1/2}}\right) - tan^{-1}\left(\frac{k_v^{1/2}}{(-a)^{1/2}}\right)\right] & if\ a < 0 \end{cases}$ $a = k_p - \frac{k_p - k_N}{y_p - y_N} y_p$	(6)
Sublayer Thickness	$Re_v = 20$	$Re_v = \frac{y_v k_v^{1/2}}{\nu} = \frac{Re_{v0}}{1 + 3.1\left[(k_v - k_w)/k_v\right]}$	(7)
Turbulent Prandtl Number	$Pr_t = 1.2$	$Pr_t = \frac{e^g - 1 - g - (g)^2/2 - (g)^3/6 - (g)^4/24}{e^g - 1 - g - (g)^2/2 - (g)^3/6}$ $g = 0.4U_p^*$	(8)
		$Pr_t = 0.225\left(\frac{5.4 + \bar{G}/\bar{\varepsilon}}{12 + \bar{G}/\bar{\varepsilon}}\right)$	(9)
		$Pr_t = 1.01 - 0.09\, Pr^{0.36}$	(10)
		$Pr_t = 0.85$	(11)

model approximation was used with the $k-\epsilon$ turbulence model. The $k-\epsilon$ model was adopted since it has been in use for a long time with its merits and demerits well understood and documented. Also, it is more robust than newer models and better suited for solving application-oriented problems. However, several shortcomings of the $k-\epsilon$ model in solving the jet impingement problem (especially in the stagnation region) have been identified (Polat et al., 1989). This necessitates that the results obtained with FLUENT be appropriately modified by post-processing as discussed in the following.

Near-Wall Modeling. Wall functions (or near-wall models) account for the shortcomings of the high-Reynolds-number $k-\epsilon$ models in the region near walls, where molecular viscosity affects the generation, destruction, and transport of turbulence energy. Since viscous effects are related to nodes located immediately adjacent to the wall in the fully turbulent region (where viscous effects are negligible), near-wall functions have the advantage of reducing the number of nodes otherwise required in the wall region.

The wall functions of Chieng and Launder (1980) and Launder and Spalding (1972) assume that very close to the wall, two distinct fluid regions exist: a linear viscous sublayer ($y_v^+ \leq 11.0$) and a fully turbulent logarithmic region ($11 < y^+ < 400$). Chieng and Launder (1980) proposed the use of the near-wall turbulent kinetic energy $k_v^{1/2}$ (instead of $k_P^{1/2}$ used by Launder and Spalding, 1972), the turbulent energy at the edge of the viscous sublayer, as the velocity scale. This model has also been successfully applied by Amano and Brandt (1984) to impinging jet heat transfer problems, and it is used in the present work.

Table 1 compares the logarithmic laws used for velocity (Eq. (2)) and temperature (Eqs. (3) and (4); Jayatilleke, 1969) in the present model with those used in FLUENT (Launder and Spalding, 1973). The near-wall model of Chieng and Launder (1980) assumes that very close to the wall, the kinetic energy of turbulence has a parabolic variation in the viscous sublayer, which corresponds to a linear variation of velocity. In the fully turbulent region, the turbulent kinetic energy is taken to vary linearly and the turbulent length scale is based on the distance from the wall. The shear stress is taken to be purely viscous in origin. The mean generation rate of turbulence energy $\bar{G}$ and mean dissipation rate $\bar{\varepsilon}$ are given by Eqs. (5) and (6), respectively, in Table 1. The development of these equations and the assumptions therein are given by Chieng and Launder (1980). Johnson and Launder (1982) proposed an improved treatment of the dimensionless viscous sublayer thickness Re_v by allowing it to vary according to the near-wall values of the turbulent kinetic energy (see Eq. (7)). The "pseudo" kinetic energy of turbulence at the wall, k_w, was linearly extrapolated from k_P and k_v.

Turbulent Prandtl Number. The turbulent Prandtl number concept is used to evaluate the eddy diffusivity for heat in the $k-\epsilon$ model. Experiments have shown that Pr_t is primarily a function of the turbulent Peclet number ($\epsilon_M\, Pr/\nu$) in the logarithmic region (Kays, 1994), and many analytical and experimental solutions for Pr_t have been presented in the literature. Four turbulent Prandtl number functions were investigated in the present work: Wassel and Catton (1972); Gibson and Launder (1976); Malhotra and Kang (1984); and Kays (1994), corresponding to Eqs. (8)–(11) in Table 1, respectively. A constant turbulent Prandtl number of 1.2 is used in FLUENT.

Numerical Modeling

Since the geometric boundaries and physical conditions were symmetric about the axis of the jet, a two-dimensional axisymmetric model was constructed. In view of the short development length of the jet orifice ($l/d = 2$), the computational domain (see Fig. 1) included the lower portion of the jet plenum and the nozzle area itself, in addition to the jet outflow region, to simulate the experimental conditions. The assumptions and boundary conditions in the model are detailed below:

- *Inlet:* A constant pressure was imposed at the inlet since the exact flow pattern inside the plenum is unknown. The

Downloaded 11 Dec 2010 to 193.140.21.150. Redistribution subject to ASME license or copyright; see http://www.asme.org/terms/Terms_Use.cfm

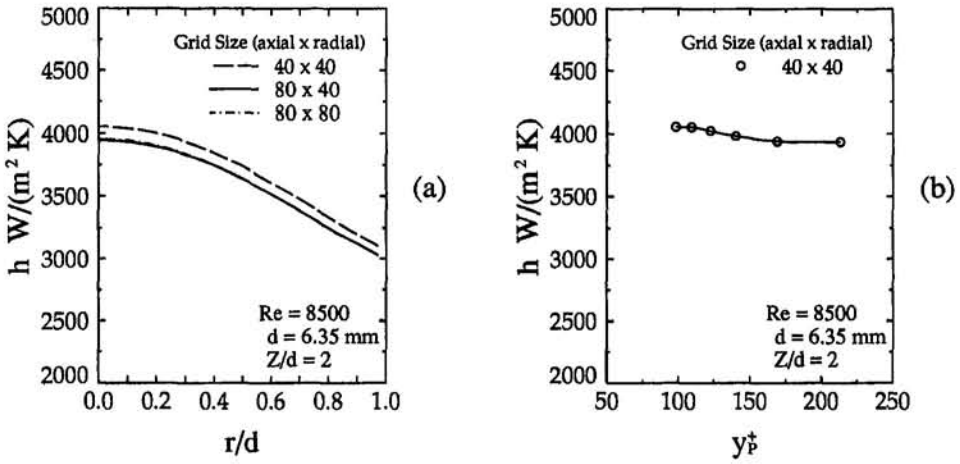


Fig. 2 Influence of grid size and dimensionless near-wall node distance y_P^+ on the heat transfer coefficient for the 6.35-mm-dia nozzle at $Z/d = 2$ and Re = 8500

value of the imposed pressure was adjusted until the volumetric flow rate at the nozzle exit agreed with the experimentally set value to within 1 percent. The jet diameter was chosen as the characteristic length. A constant inlet temperature was assigned to match experimental conditions. It must be noted that if the computational domain had started at the nozzle exit, the turbulence intensity imposed would affect the results; however, since the plenum is included in the domain in this work, and the flow is highly laminar at the model inlet, the turbulence intensity was found not to be a factor in calculating the stagnation heat transfer.

- *Nozzle Plate:* The temperature of the nozzle plate was set equal to that of the jet fluid and a no-slip boundary condition was imposed (all velocity components are zero).
- *Target Plate:* A no-slip boundary condition was also imposed along the impingement surface of the target plate. A constant heat flux was imposed over a circular area of diameter 2 cm, and the surrounding unheated portion of the target plate was assigned a zero heat flux. The applied heat flux was chosen to be equal to the experimental value for each configuration. The unheated portion of the target plate was considered to be insulated (zero heat flux).
- *Outlet:* Visualization of the flow (Garimella and Rice, 1994) revealed a toroidal recirculation zone at the radial edge of the computational domain. Thus the standard outlet boundary condition (zero diffusion flux for all variables) could not be used. Instead, a static pressure boundary condition was applied, as this allows the flow to enter or exit the domain. A pressure boundary condition at the outlet was recommended by Polat et al. (1989) for confined jet impingement. A constant temperature equal to the ambient fluid temperature was imposed at the boundary.

The thermophysical properties of FC-77 were entered as polynomial functions of temperature fitted to data supplied by the manufacturer.

All models presented in this paper were computed using FLUENT on a 40 × 40 grid. Exploratory computations with 80 × 40 and 80 × 80 grids suggest that the results are accurate to 3 percent (see Fig. 2(*a*)). Doubling the radial grid from 40 to 80 nodes was found to have a negligible effect on the predicted heat transfer coefficients. The sensitivity of the results to variations in the near-wall node distance y_P^+ in the range 90 to 220 was also explored and found to result in a maximum variation in the predicted heat transfer coefficient of 2 percent (see Fig. 2(*b*)); this is consistent with the recommendation of Guo and Maxwell (1984). In all the models, the radial grid size was varied so as to provide a finer grid along the axis of the jet. Similarly, a nonuniform grid in the axial direction was used to set a finer grid near the wall. A typical grid is illustrated in Fig. 1.

Numerical Solution Procedure. The momentum and energy equations were discretized in FLUENT using the third-order QUICK interpolation scheme. A second-order central/upwind differencing scheme was used with the turbulent kinetic energy and dissipation equations for stability. The discretized equations were solved using the SIMPLEC algorithm (Van Doormal and Raithby, 1984) with a nonstaggered grid system. The number of solver sweeps for the pressure term was increased from 5 to 20 to facilitate convergence. The solution was considered to be converged when the sum of the normalized residuals was on the order of 5×10^{-4}. The normalized velocity and enthalpy residuals were typically on the order of 5×10^{-5}. The numerical solutions presented in the paper took approximately 15 minutes on a Pentium personal computer (90 MHz).

Calculation of Heat Transfer Coefficient. Standard wall treatments incorporate the near-wall models directly into the numerical codes and apply them at each iteration step (Amano and Brandt, 1984; Ciofalo and Collins, 1989). In this paper, a hybrid wall treatment was used in a post-processing program in which the near-wall models were applied to a converged FLUENT solution. Ciofalo and Collins (1989) reported good agreement between standard treatments and a similar hybrid wall treatment procedure. The rationale that they offered for the use of a hybrid treatment was that the near-wall quantities, U_P, k_P, and T_P, would not be significantly affected if the wall functions were directly incorporated into the code, although the source terms in the governing equations may change. It was found that the only alteration due to the hybrid treatment was in the way in which U, k, and T were extrapolated to the wall.

A post-processing program was written to calculate the local heat transfer coefficients on the heat source for various turbulent Prandtl number functions using the near-wall models introduced earlier in this paper. The calculation procedure was as follows:

1 The velocity, turbulent kinetic energy, and temperature values (U, k, T) were obtained at the near-wall nodes P and N (see Fig. 1) from the converged FLUENT solution. The FC-77 fluid properties were evaluated at node P.
2 Using the Johnson and Launder (1982) recommendation and a "pseudo" kinetic energy profile, y_v, k_v, and k_w were evaluated using Eq. (7).

Downloaded 11 Dec 2010 to 193.140.21.150. Redistribution subject to ASME license or copyright; see http://www.asme.org/terms/Terms_Use.cfm

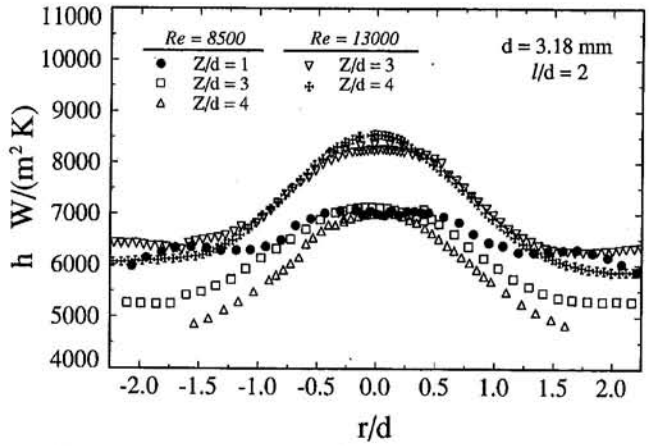


Fig. 3 Variation in the experimentally measured local heat transfer coefficient distribution with Z/d and Reynolds number for the 3.18-mm-dia nozzle

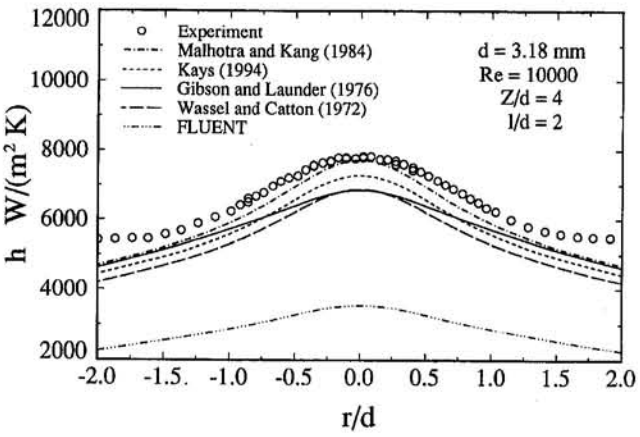


Fig. 4 Comparison of the local heat transfer predicted using various turbulent Prandtl number functions with experimental results for the 3.18-mm-dia nozzle at Z/d = 4 and Re = 10,000

3 The Chieng–Launder (1980) turbulent kinetic energy and shear stress profiles were assumed (U_v, U_n, τ_n, and k_n found). The quantity τ_w was calculated using Eq. (2) and $\bar{G}$ and $\bar{\epsilon}$ with Eqs. (5) and (6), respectively.
4 The turbulent Prandtl number Pr_t was calculated via Eqs. (8)–(11).
5 The wall temperature, T_w, was calculated from Eqs. (3) and (4).
6 The local heat transfer coefficient was calculated according to Eq. (1).

The average heat transfer coefficients $\bar{h}$ reported in this paper were calculated based on the area-averaged surface temperature, over the square area (1 cm by 1 cm) of the heat source, as described by Garimella and Rice (1995).

Experimental Results

The distribution of the local heat transfer on the heat source for the 3.18-mm-dia nozzle is presented in Fig. 3 as a function of the radial distance from the stagnation point. Three different nozzle-to-target plate spacings (Z/d) and two Reynolds numbers of 8500 and 13,000 are illustrated. All curves in Fig. 3 are bell shaped with the maximum value occurring near the stagnation point. At Re = 13,000, an increase in Z/d causes an increase in the stagnation heat transfer coefficient, h_0. Gardon and Akfirat (1965) and Baughn et al. (1991) reported similar trends at small Z/d. At Re = 8500, the magnitude of h_0 is relatively unchanged with increasing Z/d; however, the heat transfer coefficient away from the stagnation region decreases as Z/d increases.

Secondary peaks were recorded at Z/d = 1 for Re = 8500, and are located at $r/d \approx \pm 1.8$. As Z/d increases from 1 to 4, the magnitude of the secondary peaks decreases and moves radially outward (Garimella and Rice, 1994, 1995). The flat region around the stagnation point at Z/d = 1 for both Reynolds numbers may represent the radial extent of the potential core, which is on the order of one nozzle diameter.

Numerical Results and Discussion

Figure 4 shows the effect of the different turbulent Prandtl number functions used on the predicted heat transfer coefficient distribution. The results in Fig. 4 are for the 3.18-mm-dia nozzle at Re = 10,000 and Z/d = 4 and are representative of all the cases. The predicted h distributions are compared with the results measured experimentally and also with those calculated by FLUENT in Fig. 4. The curves with the four turbulent Prandtl number functions show a bell-shaped heat transfer distribution with the maximum value occurring at the stagnation point. The curves compare favorably with the experimental trend in the range $r/d \leq \pm 1.5$. Beyond this range, however, the predicted curves decrease in magnitude more sharply than the experimental results.

The primary effect of the turbulent Prandtl number appears in the magnitude of the local heat transfer coefficients in Fig. 4. The Pr_t function of Malhotra and Kang (1984) is dependent only on the local molecular Prandtl number (Eq. (10)), and consistently predicts the largest local heat transfer coefficients of the four functions investigated. Since the radial change in the molecular Prandtl number (due to temperature-dependent properties) is small, Eq. (10) gives a nearly constant Pr_t value of 0.73. The Pr_t functions proposed by Gibson and Launder (1976) and Wassel and Catton (1972) (Eqs. (9) and (8), respectively) yield nearly identical predictions of the stagnation heat transfer coefficient; however, the Gibson–Launder function decreases less rapidly with radial distance from the stagnation point. Since both functions are dependent on the local turbulent flow field, they would be expected to result in similar predictions. The Gibson–Launder and Wassel–Catton turbulent Prandtl numbers, however, decrease from unity in the stagnation region to about 0.7 and 0.9 at $r/d \approx \pm 2.0$, respectively. The decrease in Pr_t in the Gibson–Launder function to 0.7 makes

Table 2 Comparison of predicted and experimental stagnation heat transfer coefficients

d (mm)	Z/d	Re	Experiment	Gibson-Launder	Malhotra-Kang	Wassel-Catton	Kays	FLUENT
3.18	1	8500	7078	7096	8012	7136	7561	3959
	3	8500	7142	6104	6880	4733	6500	3250
		13000	8250	9533	10754	9559	10155	4866
	4	8500	7001	5870	6607	5883	6246	3036
		10000	7803	6846	7717	6863	7291	3540
		13000	8544	8793	9936	8812	9375	4537
6.35	2	8500	3827	4055	4563	4072	4313	1902
		13000	4744	5445	6138	4895	5797	2557

Downloaded 11 Dec 2010 to 193.140.21.150. Redistribution subject to ASME license or copyright; see http://www.asme.org/terms/Terms_Use.cfm

Table 3 Comparison of predicted and experimental average heat transfer coefficients

d (mm)	Z/d	Re	Experiment	Gibson-Launder	Malhotra-Kang	Wassel-Catton	Kays	FLUENT
3.18	1	8500	6607	5475	5577	5060	5278	2751
	3	8500	5972	4749	4800	4355	4550	2365
		13000	6528	7170	7285	6693	6898	3590
	4	8500	5304	4467	4548	4120	4309	2208
		10000	5793	5187	5307	4813	5023	2560
		13000	6342	6649	6816	6214	6442	3258
6.35	2	8500	3651	3542	3868	3320	3488	1707
		13000	4488	4694	4998	4507	4724	2224

the predicted heat transfer coefficient drop more gently with r/d, approaching the Malhotra–Kang prediction (which uses Pr_t of 0.73) at large r/d. Comparing the predictions for the Gibson–Launder and Wassel–Catton functions with the constant Pr_t values of 0.73 (Malhotra and Kang) and 0.85 (Kays), the constant Pr_t results differ from the former to a somewhat greater extent in the stagnation region than at points farther away. This concurs with the trend reported by Amano and Jensen (1982).

The stagnation and average heat transfer coefficients for the four turbulent Prandtl number functions as well as the FLUENT results are tabulated in Tables 2 and 3, for the eight jet configurations investigated. The experimentally recorded values of h_0 and $\bar{h}$ are also listed. The FLUENT results in Tables 2 and 3 (as well as in Figs. 4 and 7) are shown to underpredict the stagnation and average experimental heat transfer coefficients for every configuration with average deviations of 49 and 54 percent, respectively. This underprediction can be attributed to the formula used to calculate the heat transfer coefficients. The code calculates the local heat transfer using the heat–momentum transfer analogy suggested by Launder and Spalding (1973) with a constant Pr_t of 1.2 (see Table 1). Also, the code bases heat transfer coefficients on the bulk fluid temperature; the values shown in Table 2 have been corrected to be based on the jet inlet temperature, so that they can be compared with all the other calculations made according to Eq. (1). A possible source of error in the magnitude of the heat transfer coefficient may be that the wall function in FLUENT scales on the near-wall turbulent kinetic energy k_P instead of k_v, as is done in the Chieng–Launder model used in this work. Although the magnitude is underpredicted, the shape of the h distribution in the FLUENT curves illustrated in Figs. 4 and 7 agrees with experimental trends.

Of the four turbulent Prandtl number functions listed in Tables 2 and 3, the Gibson–Launder function has the lowest average deviations of 10 and 11 percent in h_0 and $\bar{h}$ compared to the experiment. Since this function takes the variation in the ratio of the local turbulence energy generation to dissipation into account, it would be expected to yield better predictions of heat transfer. Although results from the Wassel–Catton function differ from those with the Gibson–Launder function by only a few percent, the distribution resulting from the latter better matches the experiments.

Figures 5–7 compare the heat transfer coefficient distributions predicted with the Gibson–Launder function (GLF) and the experimental results for the 3.18-mm-dia nozzle. Figure 5 shows the local heat transfer coefficients at a spacing of $Z/d = 4$ for Re = 8500, 10,000, and 13,000. The heat transfer coefficient curves calculated with the GLF underpredict the experimental results at Re = 8500 and 10,000 and show good agreement at Re = 13,000. The average difference between the experimental results and those predicted by the GLF are 16 percent for h_0 and 10 percent for $\bar{h}$, for the range of Reynolds numbers investigated.

The predicted curves are again compared in Fig. 6 for a smaller spacing of $Z/d = 3$. The heat transfer is underpredicted at Re = 8500 and overpredicted at Re = 13,000. For this configuration, the stagnation heat transfer coefficient is also predicted to ±16 percent and the deviation in $\bar{h}$ is 20 percent and 10 percent for Re = 8500 and 13,000, respectively.

The predicted heat transfer curve at the smallest spacing of $Z/d = 1$ is shown in Fig. 7 for Re = 8500. In the region $r/d = \pm 1$, the curve shows good agreement with experimental values. Beyond this region, the predicted curve decreases more sharply. Maxima in h were predicted at $r/d = \pm 0.5$. Such maxima at $r/d \approx 0.5$ were also noted in the experiments of Huber and Viskanta (1994) and Lytle and Webb (1994) with unconfined and confined air jets, and were attributed to accelerated radial flow. The secondary peaks in heat transfer recorded at $r/d \approx 1.8$ in the experiments were not predicted by the model. Amano and Brandt (1984), however, predicted secondary peaks in the skin friction coefficient distributions for a similar jet configura-

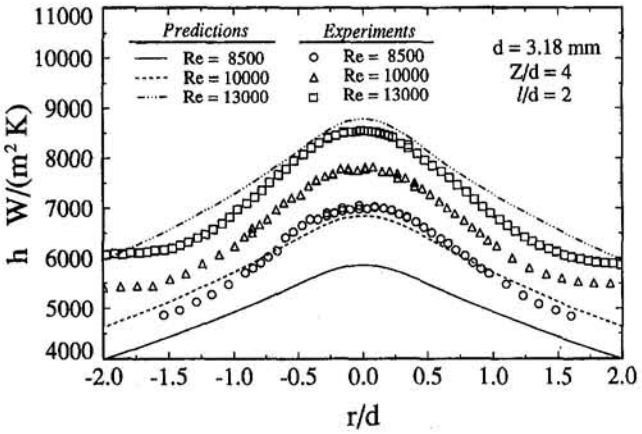


Fig. 5 Comparison with experimental results of predicted local heat transfer coefficients using the Gibson–Launder (1976) turbulent Prandtl number function for the 3.18-mm-diameter nozzle at $Z/d = 4$ and Re = 8500, 10,000, and 13,000

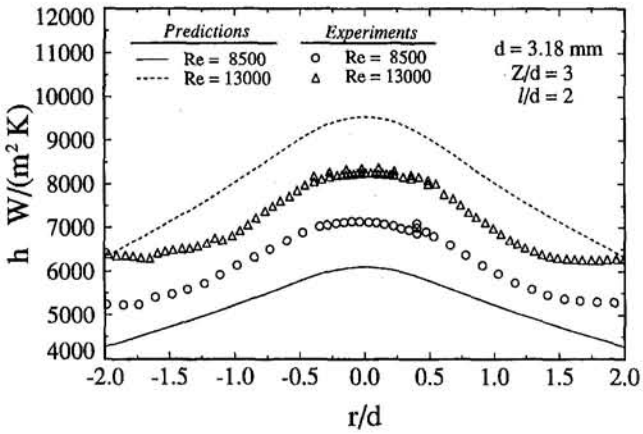


Fig. 6 Comparison with experimental results of predicted local heat transfer coefficients using the Gibson–Launder (1976) turbulent Prandtl number function for the 3.18 mm diameter nozzle at $Z/d = 3$ and Re = 8500 and 13,000

Downloaded 11 Dec 2010 to 193.140.21.150. Redistribution subject to ASME license or copyright; see http://www.asme.org/terms/Terms_Use.cfm

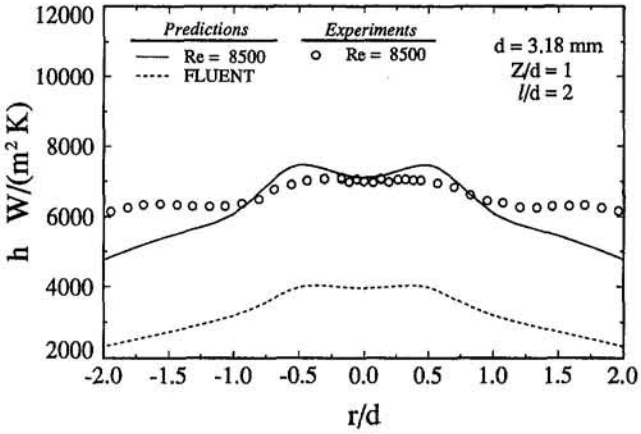


Fig. 7 Comparison with experimental results of predicted local heat transfer coefficients using the Gibson–Launder (1976) turbulent Prandtl number function for the 3.18 mm diameter nozzle at Z/d = 1 and Re = 8500

tion at $Z/d = 2$ using a standard high-Reynolds-number $k-\epsilon$ model. The FLUENT prediction shows good agreement with the experimental *trends,* although it again significantly underpredicts the magnitude of h. Local maxima were also predicted by FLUENT at $r/d = \pm 0.5$; however, they are less pronounced.

From flow visualizations, Garimella and Rice (1994) observed a toroidal recirculation zone extending to the top of the nozzle plate for $Z/d \leq 4$. As Z/d increased beyond 4, the behavior of the flow changed and quiescent fluid from the test section penetrated along the nozzle plate and was entrained into the mixing layer of the jet. It is possible that the high degree of recirculation outside the stagnation region at the smaller Z/d spacings may be better predicted with newer turbulence closure models such as the Reynolds Stress or RNG $k-\epsilon$ models.

Conclusions

Numerical predictions of the local heat transfer coefficient in submerged and confined liquid jet impingement were made using the commercial code FLUENT. In a hybrid wall-treatment approach, a post-processing program incorporating various near-wall models was applied to the numerical data obtained from the code to improve the calculated local heat transfer coefficients. The influence of four different turbulent Prandtl number functions on the heat transfer predictions was investigated. The main conclusions that emerge from this study are summarized as follows:

- The near-wall models of Chieng and Launder (1982) and Johnson and Launder (1982) give much better predictions of the local heat transfer distribution than the Launder and Spalding (1973) model used in FLUENT.
- The Gibson and Launder (1976) turbulent Prandtl number function predicts the stagnation h_0 and average $\bar{h}$ heat transfer coefficients to within 16 and 20 percent, respectively, for all cases investigated in this study.

Although the Gibson–Launder turbulent Prandtl number function [Eq. (9)] is recommended, the simplicity of the Wassel–Catton function [Eq. (8)] may justify the small increase in the deviation between the experimental and predicted heat transfer coefficients.

Acknowledgments

Partial funding for this work through a research grant from Cray Research, Inc., of Chippewa Falls, Wisconsin, is gratefully acknowledged.

References

Agarwal, R. K., and Bower, W. W., 1982, "Navier–Stokes Computations of Turbulent Compressible Two-Dimensional Impinging Jet Field," *AIAA Journal,* Vol. 20, No. 5, pp. 577–584.

Amano, R. S., 1984, "Development of a Turbulence Near-Wall Model and Its Application to Separated and Reattached Flows," *Numerical Heat Transfer,* Vol. 7, pp. 59–75.

Amano, R. S., and Jensen, M. K., 1982, "A Numerical and Experimental Investigation of Turbulent Heat Transport of an Axisymmetric Jet Impinging on a Flat Plate," ASME Paper No. 82-HT-55.

Amano, R. S., and Brandt, H., 1984, "Numerical Study of Turbulent Axisymmetric Jets Impinging on a Flat Plate and Flowing Into an Axisymmetric Cavity," ASME *Journal of Fluids Engineering,* Vol. 106, pp. 410–417.

Baughn, J. W., Hechanova, A. E., and Yan, X., 1991, "An Experimental Study of Entrainment Effects on Heat Transfer From a Flat Surface to a Heated Circular Impinging Jet," ASME JOURNAL OF HEAT TRANSFER, Vol. 113, pp. 143–149.

Bower, W. W., Kotansky, D. R., and Hoffman, G. H., 1977, "Computations and Measurements of Two-Dimensional Turbulent Jet Impingement Flow Fields," *Proc. Symposium on Turbulent Shear Flows,* Pennsylvania State University, Paper 3-1.

Chang, C. T., Kocamustafaogullari, G., Landis, F., and Downing, S., 1993, "Single and Multiple Liquid Jet Impingement Heat Transfer," *Proc. ASME National Heat Transfer Conference,* Atlanta, Georgia, ASME HTD-246, pp. 43–52.

Chieng, C. C., and Launder, B. E., 1980, "On the Calculation of Turbulent Heat Transport Downstream From an Abrupt Pipe Expansion," *Numerical Heat Transfer,* Vol. 3, pp. 189–207.

Ciofalo, M., and Collins, M. W., 1989, "$k-\epsilon$ Predictions of Heat Transfer in Turbulent Recirculating Flows Using an Improved Wall Treatment," *Numerical Heat Transfer,* Vol. 15, pp. 21–47.

Fluent, 1993, *FLUENT User's Manual—Vol. 1,* Version 4.23, Fluent, Inc.

Gardon, R., and Akfirat, J. C., 1965, "The Role of Turbulence in Determining the Heat Transfer Characteristics of Impinging Jets," *Int. J. Heat Mass Transfer,* Vol. 8, pp. 1261–1272.

Garimella, S. V., and Rice, R. A., 1994, "Heat Transfer in Submerged and Confined Jet Impingement," *Heat Transfer in High Heat Flux Systems,* ASME HTD-Vol. 301, pp. 59–68.

Garimella, S. V., and Rice, R. A., 1995, "Confined and Submerged Liquid Jet Impingement Heat Transfer," ASME JOURNAL OF HEAT TRANSFER, Vol. 117, pp. 871–877.

Garimella, S. V., and Nenaydykh, B., 1996, "Nozzle Geometry Effects in Liquid Jet Impingement Heat Transfer," *Int. J. Heat Mass Transfer,* Vol. 39, No. 14, pp. 2915–2923.

Gibson, M. M., and Launder, B. E., 1976, "On the Calculation of Horizontal, Turbulent, Free-Shear Flows Under Gravitational Influence," *Trans. ASME,* Vol. 98C, pp. 81–87.

Guo, C. Y., and Maxwell, W. H. C., 1984, "Numerical Modeling of Normal Turbulent Plane Jet Impingement on a Solid Wall," *J. Eng. Mech.,* Vol. 110, No. 10, pp. 1498–1509.

Huber, A. M., and Viskanta, R., 1994, "Convective Heat Transfer to a Confined Impinging Array of Air Jets With Spent Air Exits," ASME JOURNAL OF HEAT TRANSFER, Vol. 116, pp. 570–576.

Jayatilleke, C. L., 1969, "The Influence of Prandtl Number and Surface Roughness on the Resistance of the Laminar Sub-layer to Momentum and Heat Transfer," *Prog. Heat Mass Transfer,* Vol. 1, pp. 193–329.

Johnson, R. W., and Launder, B. E., 1982, "Discussion of 'On the Calculation of Turbulent Heat Transport Downstream From an Abrupt Pipe Expansion'," *Numerical Heat Transfer,* Vol. 5, pp. 493–496.

Kays, W. M., 1994, "Turbulent Prandtl Number—Where Are We?" ASME JOURNAL OF HEAT TRANSFER, Vol. 116, pp. 294–295.

Launder, B. E., and Spalding, D. B., 1972, *Lectures in Mathematical Models of Turbulence,* Academic Press, London, United Kingdom.

Launder, B. E., and Spalding, D. B., 1973, *The Numerical Computation of Turbulent Flows,* Imperial College of Science and Technology, London, United Kingdom, N74-12066.

Lytle, D., and Webb, B. W., 1994, "Air Jet Impingement Heat Transfer at Low Nozzle–Plate Spacings," *Int. J. Heat Mass Transfer,* Vol. 37, pp. 1687–1697.

Ma, C. F., and Bergles, A. E., 1990, "Convective Heat Transfer on a Small Vertical Heated Surface to an Impinging Circular Liquid Jet," *Heat Transfer Science and Technology,* B. X. Wang, ed., Hemisphere, Washington, DC, Vol. 2, pp. 193–200.

Ma, C. F., Sun, H., Auracher, H., and Gomi, T., 1990, "Local Convective Heat Transfer From Vertical Heated Surfaces to Impinging Circular Jets," *Proc. Ninth International Heat Transfer Conference,* Hemisphere, Washington, DC, Vol. 2, pp. 441–446.

Malhotra, A., and Kang, S. S., 1984, "Turbulent Prandtl Number in Circular Pipes," *Int. J. Heat Mass Transfer,* Vol. 27, pp. 2158–2161.

Obot, N. T., Douglas, W. J. M., and Mujumdar, A. S., 1982, "Effect of Semi-Confinement on Impingement Heat Transfer," *Proc. 7th International Heat Transfer Conf.,* Vol. 3, pp. 395–400.

Polat, S., Huang, B., Mujumdar, A. S., and Douglas, W. J. M., 1989, "Numerical Flow and Heat Transfer Under Impinging Jets: A Review," *Annual Review of Numerical Fluid Mechanics and Heat Transfer,* Vol. 2, pp. 157–197.

Rice, R. A., and Garimella, S. V., 1994, "Heat Transfer From Discrete Heat Sources Using an Axisymmetric, Submerged and Confined Liquid Jet," *Heat*

Downloaded 11 Dec 2010 to 193.140.21.150. Redistribution subject to ASME license or copyright; see http://www.asme.org/terms/Terms_Use.cfm

Transfer '94, Proc. 1994 International Heat Transfer Conference, Vol. 3, pp. 89–94.

Sugiyama, S., and Amano, R. S., 1983, "An Investigation on Turbulent Heat Transfer of an Axisymmetric Jet Impinging on a Flat Plate," *Trans. JSME,* Vol. 88, pp. 1–6.

Sun, H., Ma, C. F., and Nakayama, W., 1993, "Local Characteristics of Convective Heat Transfer From Simulated Microelectronic Chips to Impinging Submerged Round Water Jets," ASME *Journal of Electronic Packaging,* Vol. 115, pp. 71–77.

Van Doormal, J. P., and Raithby, G. D., 1984, "Enhancements of the SIMPLE Method for Predicting Incompressible Fluid Flows," *Numerical Heat Transfer,* Vol. 7, pp. 147–163.

Wassel, A. T., and Catton, I., 1972, "Calculation of Turbulent Boundary Layers Over Flat Plates With Different Phenomenological Theories of Turbulence and Variable Turbulent Prandtl Numbers," *Int. J. Heat Mass Transfer,* Vol. 15, pp. 1–17.

Wolfshtein, M., 1969, "Some Solutions of the Plane Turbulent Impinging Jet," ASME *Journal of Basic Engineering,* Vol. 38, No. 3, pp. 577–612.

Downloaded 11 Dec 2010 to 193.140.21.150. Redistribution subject to ASME license or copyright; see http://www.asme.org/terms/Terms_Use.cfm

Optimal Spacing Between Pin Fins With Impinging Flow

G. Ledezma

A. M. Morega

A. Bejan

Department of Mechanical Engineering
and Materials Science,
Duke University,
Box 90300,
Durham, NC 27708-0300

This is an experimental, numerical, and theoretical study of the heat transfer on a pin-finned plate exposed to an impinging air stream. The pin fins are aligned with the air approach velocity. The base plate and the fin cross section are square. It is demonstrated experimentally that the thermal conductance between the plate and the air stream can be maximized by selecting the fin-to-fin spacing S. Next, a simplified numerical model is used to generate a large number of optimal spacing and maximum heat transfer data for various configurations, which differ with respect to fin length (H), fin thickness (D), base plate size (L), fluid type (Pr), and air velocity (Re_L). Finally, the behavior of the optimal spacing data is explained and correlated theoretically based on the intersection of asymptotes method. The recommended correlations for optimal spacing, $S_{opt}/L \cong 0.81\, Pr^{-0.25}\, Re_L^{-0.32}$, and maximum thermal conductance, $(q/\Delta T)_{max}/k_a H \cong 1.57\, Pr^{0.45}\, Re_L^{0.69}\, (L/D)^{0.31}$, cover the range $D/L = 0.06 - 0.14$, $H/L = 0.28–0.56$, $Pr = 0.72–7$, $Re_D = 10–700$, and $Re_L = 90–6000$.

Introduction

The cooling of high-density electronics has generated considerable research, both fundamental and applied (e.g., Moffat and Ortega, 1988; Peterson and Ortega, 1990). Next to recently developed or improved techniques such as phase-change and jet impingement cooling, forced air cooling will continue to be used in the technology of the future because it is accessible, inexpensive, and robust. One air cooling configuration that has been considered for some time is the cooling of modules fitted with pin fin heat sinks oriented such that the air stream impinges on the surface of the module (Fig. 1).

The archival publications on this topic were reviewed most recently by Chu and Simons (1994), although considerable work has also been presented in conference proceedings. Sparrow and Larson (1982) and Larson and Sparrow (1982) reported experimental results for heat sinks with round pin fins, in which they tested arrays with two values of fin-to-fin spacing. In a subsequent study, Sparrow et al. (1984) tested arrays with several geometries including three different fin-to-fin spacings. A numerical simulation of the three-dimensional flow and temperature field was performed by Sathe et al. (1983) in a study of heat sinks with square pin fins, in which the spacing was fixed. The thermal performance of a complete sink and fan assembly was simulated using a commercial computational package by Mansuria and Kamath (1994) and Kamath (1994). Three geometries with fixed fin spacings were considered: square pin fins, straight fins, and radial fins.

Related advances were also made in the area of liquid jet impingement cooling. Sullivan et al. (1992a) conducted experiments with three heat sink geometries with square pin fins, in which two fin spacings were tested. Sullivan et al. (1992a) and Heindel et al. (1992) reported data for one heat sink with radial fins. Wadsworth and Mudawar (1992) enhanced the liquid jet cooling effect by using a surface with microstuds with square cross section (0.3 mm side) and fixed spacing (0.3 mm). A similar technique was described by Sullivan et al. (1992b), who used two types of artificially roughened surfaces: a dimpled surface, and a square-pattern sawcut surface.

The work described in this paper addresses the fundamentals of the cooling configuration of Fig. 1, fundamentals that can be summarized in two questions:

1 What are the heat transfer characteristics, i.e., what parameters influence the total heat transfer rate?
2 What geometric changes can be made in the design to maximize the overall thermal conductance between the module and the air stream?

The second question was inspired by the recent development of fundamental results for selecting the optimal spacing between parallel plates, in both natural convection (Bar-Cohen and Rohsenow, 1984; Bejan, 1984; Anand et al., 1992) and forced convection (Nakayama et al., 1988; Knight et al., 1991; Matsushima et al., 1992; Bejan and Sciubba, 1992). Indeed, we will show that the fin-to-fin spacing in Fig. 1 can be optimized, and that there is a theoretical scaling law that can be used to predict optimal spacings in this and other configurations. The importance of determining the optimal spacings between electronic components (e.g., boards) and fins in air-cooled heat sinks was emphasized in recent reviews (Chu and Simons, 1994; Nakayama, 1994). It is also worth noting that in the extensive work reviewed in the preceding paragraph the fin-to-fin spacing was not varied so that an optimal spacing could be determined.

The present study was conducted in three phases. In the first, we conducted wind tunnel experiments with several heat sinks with different fin-to-fin spacings. The objective was to demonstrate empirically the existence of an optimal spacing when the remaining dimensions of the array are fixed. In the second phase we conducted numerical simulations of the flow and heat transfer in a simplified model, which is not exactly the same as the devices tested in the wind tunnel. We chose a simplified numerical model because our objective was to study the performance of a large number of arrays, and to generate a large volume of information on optimal spacings. In the final phase we reexamined the collection of optimal spacing results in light of the theoretical scaling laws that have been reported for parallel plates and plate fins in forced convection.

Experiments

Five arrays of pin fins were milled out of identical solid blocks ($L \times L \times H$) of high-thermal-conductivity aluminum alloy. The overall dimensions were $L = 47.6$ mm and $H = 25.4$ mm, therefore each array occupied the same volume. Fixed were also the base thickness, $t = 2$ mm, and the side of the

Contributed by the Heat Transfer Division for publication in the JOURNAL OF HEAT TRANSFER. Manuscript received by the Heat Transfer Division August 11, 1995; revision received April 23, 1996. Keywords: Augmentation and Enhancement, Electronic Equipment, Finned Surfaces. Associate Technical Editor: T. J. Rabas.

Copyright © 1996 by ASME

Downloaded 11 Dec 2010 to 193.140.21.150. Redistribution subject to ASME license or copyright; see http://www.asme.org/terms/Terms_Use.cfm

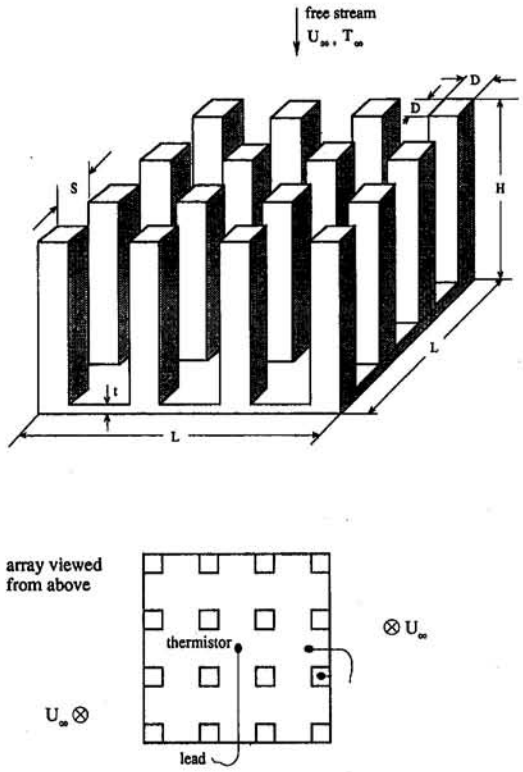


Fig. 1 Geometry and thermistor positions of the tested heat sinks ($n = 4$)

square cross section of the fins, $D = 4.8$ mm. The fin-to-fin spacing (S) varied as the number of fins (n) changes (Table 1). The limiting case of "zero spacing" was also tested by using a solid aluminum block of size $L \times L \times H$ without grooves (see also the left margin of Fig. 3).

Electric power was dissipated in the base of the fin array using a very thin thermofoil heater with a resistance of 5 Ω. The heater was sandwiched between the array base and a balsa wood insulation plate with a thickness of 5 mm. The sandwich was clamped together while heat sink compound was used to provide good thermal contact between the heater and the aluminum base.

The arrays were tested in a suction-type wind tunnel, which we built in the laboratory (Fig. 2). The test section had a cross section of 120 mm × 130 mm, and a length of 584 mm. The array base was oriented perpendicular to (and facing) the approaching air stream. The air speed (U_∞) was regulated using a variable autotransformer connected to a fan. The autotransformer provided voltages in the range 0–140 V. Five air speed settings were used (0.21, 0.34, 1.2, 1.7, and 2.2 m/s), which correspond to the Reynolds number $\mathrm{Re}_D = U_\infty D/\nu = 60$, 100, 350, 500, and 650.

Table 1 The fin numbers and spacings of the arrays used in the experiments

n×n	4×4	5×5	6×6	7×7	8×8	
S(mm)	9.53	5.95	3.81	2.39	1.36	0

The mean air speed was measured with a turbine (Taylor) anemometer, which is based on measuring the displacement of air over a certain time interval. To measure one velocity, the anemometer was placed inside the wind tunnel ten times, for periods of one hour each. In this way we estimated the fan power setting required to achieve a certain air speed in the test section of the tunnel. The standard deviation of the measured velocities was less than 2 percent: We accounted for this deviation by using a 5 percent uncertainty in the measured U_∞, instead of the 3 percent indicated by the anemometer manufacturer. During the actual runs (temperature measurements) the anemometer was not inside the tunnel.

The temperatures of the array and the free stream were measured with high-precision thermistors of type YSI44004. The thermistors were calibrated between 20 and 80°C with a bias limit of ±0.001 K. The bias limit was deduced from the temperature/resistance response of the thermistors, $dT/dR = -(1/14)$ K/Ω, and the 0.01 Ω resolution of the HP3468B used to read the thermistor resistance. The precision limit during temperature measurements was less than 0.4 K. Three thermistors were embedded in the aluminum surface: one in the middle of the base (or right next to the central fin when n is odd), another 7 mm away from the edge of the base (on one of the lines of symmetry of the base), and the third on the tip of a peripheral fin (Fig. 1). A fourth thermistor was used to monitor the free-stream temperature. In the case of the thermistors embedded in the aluminum surface, the contact gap between thermistor and aluminum was filled with highly conductive heat sink compound. The outer side of the thermistor was covered flush with a small strip of aluminum foil, which was glued (with heat-resistant plastic cement) to the aluminum surface.

Each run consisted of setting the air speed and heater power, reaching steady state, and taking 50 temperature readings with each of the four thermistors. These temperature values were averaged, and the precision limit was estimated as two times the standard deviation. The highest temperature reached by the base was 50°C, while the free stream was at room temperature (in the range 25–27°C). The difference between the temperatures indicated by the two thermistors embedded in the base was 1.7°C at the lowest air speed (0.21 m/s, $\mathrm{Re}_D = 60$), and 2.5°C at the highest (2.25 m/s, $\mathrm{Re}_D = 650$). The base temperature nonuniformity increases with the air speed, yet the nonuniformity is small (less than 10 percent) relative to the overall base stream temperature difference, even at velocities that are relatively high for air-cooling applications. The base temperature used in the calculation of the overall thermal conductance, $\bar{T}_b$, was the average of the two temperatures recorded with the

Nomenclature

A_b = area of base plate
B = bias limit
D = side of pin fin cross section
H = pin fin length
k_a = air thermal conductivity
L = side of square base plate
n = number of fins along L
Nu = Nusselt number, Eq. (1)
p = pressure
P = precision limit
Pe_D = Peclet number = $U_\infty D/\alpha$
Pr = Prandtl number
q = total heat transfer rate
Re_D, Re_L = Reynolds numbers = $U_\infty D/\nu$, $U_\infty L/\nu$
S = fin-to-fin spacing
T = temperature
$\bar{T}_b$ = average base temperature
T_S = surface temperature
T_∞ = air free-stream temperature
u, v, w = velocity components, Fig. 4
U = uncertainty limit
U_∞ = air free stream velocity
x, y, z = Cartesian coordinates, Fig. 4
α = air thermal diffusivity
ΔT = temperature difference = $\bar{T}_b - T_\infty$
ν = kinematic viscosity
ρ = air density
$(\tilde{\ })$ = dimensionless variables, Eqs. (8), (9)

Downloaded 11 Dec 2010 to 193.140.21.150. Redistribution subject to ASME license or copyright; see http://www.asme.org/terms/Terms_Use.cfm

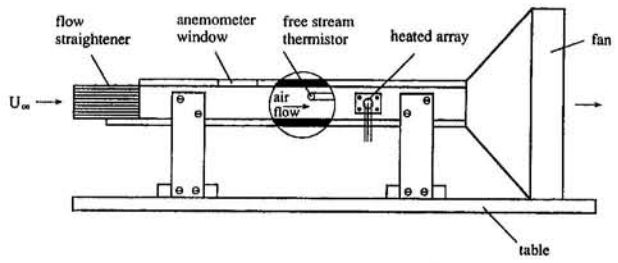


Fig. 2 Suction-type wind tunnel used for testing the heat sinks

base thermistors. The fin tip thermistor was used to monitor the fin efficiency, which was always greater than 0.9 because the temperature difference between the base and fin tip did not exceed 3°C. The overall thermal conductance was nondimensionalized as

$$\mathrm{Nu} = \frac{qD}{k_a A_b (\bar{T}_b - T_\infty)} \tag{1}$$

where $A_b = L \times L$, and q is the total heat generation rate. Air properties such as the thermal conductivity k_a were evaluated at the film temperature $(\bar{T}_b + T_\infty)/2$. We used D in the Nu definition (1) because D was held fixed during the experimental sequences of runs. Alternatively, we could have used L in place of D, because L was also fixed: In this case the Nu value would increase by a constant factor (L/D) relative to the Nu value of Eq. (1). Not eligible for use in Eq. (1) is the spacing S, because S varied from one tested array to the next.

The uncertainties in the quantities determined experimentally were estimated using the procedure recommended by Moffat (1988). Writing f for any such quantity, the uncertainty U_f has contributions due to the bias limit B_f (constant error) and the precision limit P_f (two times the standard deviation of measurements), namely

$$\frac{U_f}{f} = \left[\left(\frac{P_f}{f} \right)^2 + \left(\frac{B_f}{f} \right)^2 \right]^{1/2} \tag{2}$$

The bias limit of the temperature is negligible due to the use of high precision thermistors. The uncertainties associated with dimensions and properties (H, L, D, ν, k_a) are also negligible. The only sizeable contribution to the uncertainty in the Re_D calculation is due to the measurement of the air speed. The Nu uncertainty has two important contributions, the power dissipated in the base heater (bias and precision limits) and the precision limit of the temperature readings. The experimental uncertainties in Re_D and Nu are presented in Table 2.

The Nu results are summarized in Fig. 3, where the size of the error bars is equal to the maximum of the relative uncertainty $U_{\mathrm{Nu}}/\mathrm{Nu}$. The curves were drawn through the data only for the purpose of focusing the eye on the experiments with the same air velocity (Re_D). Marked on the left margin of the frame are the Nu values measured in the $S/L = 0$ limit, when no fins (grooves) were machined into the $L \times L \times H$ aluminum block. Note that in Fig. 3 the abcissa scale is linear. The measurements show conclusively that the overall thermal conductance Nu increases monotonically with the air speed, or Re_D. Figure 3 also shows that Nu has a maximum with respect to S (or n). The Nu maximum becomes sharper and moves toward smaller spacings as Re_D increases.

Figure 3 shows conclusively that the fin-to-fin spacing can be selected to maximize the overall thermal conductance of the assembly. At the same time the figure illustrates the limitations of the experimental method: There are just too few $n \times n$ arrays that can be machined on a given $L \times L$ base, to pinpoint S_{opt} accurately and discern its trend. Furthermore, the Re_D range is limited (dictated) by the construction of the wind tunnel. In order to expand the data base for S_{opt} as a function of Re_D and other design parameters, we conducted the numerical study described next.

Numerical Simulations

As shown in Fig. 4, the numerical model was three dimensional and limited to the space situated upstream of the base plane of the fin array. Furthermore, the fin surfaces were assumed isothermal so that we would have to perform calculations only in the spaces occupied by air. The unfinned portions of the base were isothermal. The size of the computational domain was finite, yet large enough so that it did not affect the final numerical results. The uniform free stream entered the computational domain by flowing in the negative z direction, turned, and exited by flowing in the x and y directions. The exiting flow, therefore, is unlike in the experimental setup, where the air flow spilled over the edges of the $L \times L$ base and continued on downstream.

These modeling simplifications make the "numerical heat sink" different from the devices tested in the wind tunnel. The numerical model matches closely the geometry of a module with built-in fan; it also facilitates the construction of a sufficiently fast and flexible program that generates the required information on the effect of changing the fin-to-fin spacing. We must emphasize that the numerical model was not designed to test or "reproduce" the situation studied in the laboratory.

The numerical model was designed from the very beginning with one objective in mind: to capture the effect of varying the spacing S in a model that is *sufficiently realistic*

Table 2 Experimental uncertainties for the Reynolds and Nusselt numbers

	$\mathrm{Re}_D = 60$		$\mathrm{Re}_D = 100$		$\mathrm{Re}_D = 350$		$\mathrm{Re}_D = 500$		$\mathrm{Re}_D = 650$	
Array (n × n)	$\frac{U_{\mathrm{Re}_D}}{\mathrm{Re}_D}$	$\frac{U_{\mathrm{Nu}}}{\mathrm{Nu}}$	$\frac{U_{\mathrm{Re}_D}}{\mathrm{Re}_D}$	$\frac{U_{\mathrm{Nu}}}{\mathrm{Nu}}$	$\frac{U_{\mathrm{Re}_D}}{\mathrm{Re}_D}$	$\frac{U_{\mathrm{Nu}}}{\mathrm{Nu}}$	$\frac{U_{\mathrm{Re}_D}}{\mathrm{Re}_D}$	$\frac{U_{\mathrm{Nu}}}{\mathrm{Nu}}$	$\frac{U_{\mathrm{Re}_D}}{\mathrm{Re}_D}$	$\frac{U_{\mathrm{Nu}}}{\mathrm{Nu}}$
4 × 4	0.050	0.021	0.050	0.016	0.048	0.048	0.049	0.046	0.049	0.039
5 × 5	0.050	0.041	0.050	0.013	0.048	0.023	0.049	0.076	0.049	0.033
6 × 6	0.050	0.017	0.050	0.024	0.048	0.030	0.049	0.030	0.049	0.061
7 × 7	0.050	0.047	0.050	0.026	0.048	0.013	0.049	0.019	0.049	0.016
8 × 8	0.050	0.021	0.050	0.022	0.048	0.019	0.049	0.067	0.049	0.015
S = 0	0.05	0.058	0.05	0.110	0.048	0.036	0.049	0.045	0.049	0.038

Downloaded 11 Dec 2010 to 193.140.21.150. Redistribution subject to ASME license or copyright; see http://www.asme.org/terms/Terms_Use.cfm

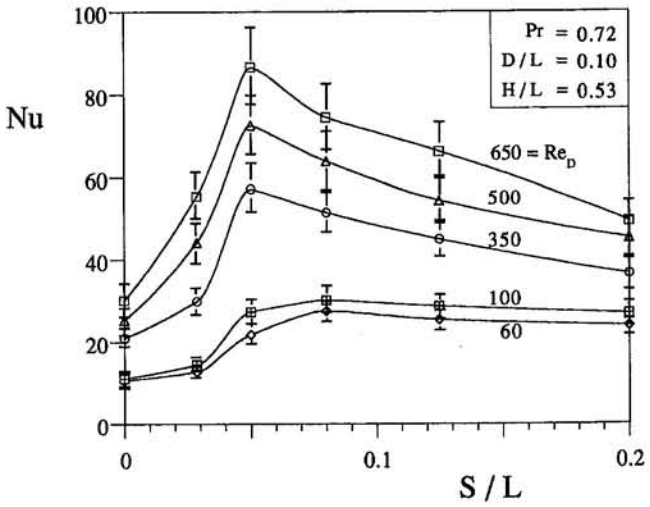


Fig. 3 Experimental results for the overall thermal conductance (Nu) as a function of fin-to-fin spacing (S) and air speed (Re_D)

and, at the same time, as simple and easy to implement as possible. This tradeoff is an essential aspect of our investigation, because we needed to generate numerical results for a very large number of (slightly different) geometries, which we then compared and optimized. The reader should take note of the fact that our numerical needs differ fundamentally from those of investigators who develop codes and produce "benchmark" results for one or a small number of configurations, which are expected to reproduce (mimic) available experimental measurements.

To judge whether our simplified numerical system is "sufficiently realistic," the reader should consider this while comparing the numerical results with experimental results: Our numerical results were finished one year before our first experiment started. We did not perform numerical work to mimic experimental results; on the contrary, based on our previous work (e.g., Bejan and Sciubba, 1992; Mereu et al., 1993; Morega and Bejan, 1994; Morega et al., 1995) we felt that our theoretical understanding of the S-optimization problem and our numerical "array system" were very good, so that we needed experiments only to convince the most skeptical members of the audience. Our interest was in calculating (expediently and accurately) the optimal spacing for a very complicated configuration, not the exact distribution of temperature over the complicated surface.

Symmetry allowed us to perform calculations in only one quarter of the computational domain. The conservation equations for mass, momentum, and energy

$$\frac{\partial \tilde{u}}{\partial \tilde{x}} + \frac{\partial \tilde{v}}{\partial \tilde{y}} + \frac{\partial \tilde{w}}{\partial \tilde{z}} = 0 \tag{3}$$

$$\tilde{u}\frac{\partial \tilde{u}}{\partial \tilde{x}} + \tilde{v}\frac{\partial \tilde{u}}{\partial \tilde{y}} + \tilde{w}\frac{\partial \tilde{u}}{\partial \tilde{z}} = -\frac{\partial \tilde{p}}{\partial \tilde{x}} + \frac{1}{\mathrm{Re}_D}\nabla^2\tilde{u} \tag{4}$$

$$\tilde{u}\frac{\partial \tilde{v}}{\partial \tilde{x}} + \tilde{v}\frac{\partial \tilde{v}}{\partial \tilde{y}} + \tilde{w}\frac{\partial \tilde{v}}{\partial \tilde{z}} = -\frac{\partial \tilde{p}}{\partial \tilde{y}} + \frac{1}{\mathrm{Re}_D}\nabla^2\tilde{v} \tag{5}$$

$$\tilde{u}\frac{\partial \tilde{w}}{\partial \tilde{x}} + \tilde{v}\frac{\partial \tilde{w}}{\partial \tilde{y}} + \tilde{w}\frac{\partial \tilde{w}}{\partial \tilde{z}} = -\frac{\partial \tilde{p}}{\partial \tilde{z}} + \frac{1}{\mathrm{Re}_D}\nabla^2\tilde{w} \tag{6}$$

$$\tilde{u}\frac{\partial \tilde{T}}{\partial \tilde{x}} + \tilde{v}\frac{\partial \tilde{T}}{\partial \tilde{y}} + \tilde{w}\frac{\partial \tilde{T}}{\partial \tilde{z}} = \frac{1}{\mathrm{Pe}_D}\nabla^2\tilde{T} \tag{7}$$

where $\nabla^2 = \partial^2/\partial\tilde{x}^2 + \partial^2/\partial\tilde{y}^2 + \partial^2/\partial\tilde{z}^2$, and the dimensionless variables are

$$(\tilde{x}, \tilde{y}, \tilde{z}) = \frac{(x, y, z)}{D} \quad (\tilde{u}, \tilde{v}, \tilde{w}) = \frac{(u, v, w)}{U_\infty} \tag{8}$$

$$\tilde{p} = \frac{p}{\rho U_\infty^2}, \quad \tilde{T} = \frac{T - T_\infty}{T_s - T_\infty}, \quad \mathrm{Pe}_D = \frac{U_\infty D}{\alpha} = \mathrm{Re}_D\,\mathrm{Pr} \tag{9}$$

The conditions on the larger boundaries of the computational domain are indicated directly on Fig. 4. The portions of the planes of symmetry ($x = 0$, $y = 0$) that cut through the fluid domain were zero-shear. The solid surfaces were modeled as no-slip.

The assumption that the fin surfaces are isothermal is clearly an approximation—a simplification without which we would have had to solve the conjugate convection and fin conduction problem. It is a good approximation, for two reasons. First, in air-cooled heat sinks tested in industry the fin efficiency is close to 100 percent (e.g., Nakayama et al., 1988; Matsushima et al., 1992). Second, we just completed a numerical study (Morega et al., 1995) in which we numerically optimized the spacing between straight fins in a parallel air stream, by modeling the fins as isothermal. We found that our numerical optimal spacing results and our theory-based correlation agree very well with the optimal spacings determined experimentally by Nakayama et al. (1988) and Matsushima et al. (1992).

Equations (3)–(7) were solved using a finite element code and a sufficiently fine nonuniform grid with brick elements and trilinear interpolation functions (FIDAP, 1993). Our group has considerable experience with the testing and accurate implementation of this code (Mereu et al., 1993; Morega and Bejan, 1994). The reason for using an existing and well-tested code in the present study is that we needed a fast and dependable tool for computer aided *optimization* (CAO), which is a process that requires the simulation of many (slightly different) heat and flow configurations.

Accuracy tests were performed in two parts. First, the grid fineness was increased until the relative change in the total heat transfer rate through the array became less than 1.5 percent when the number of elements was increased or decreased by 30 percent. Second, the overall dimensions of the fluid domain

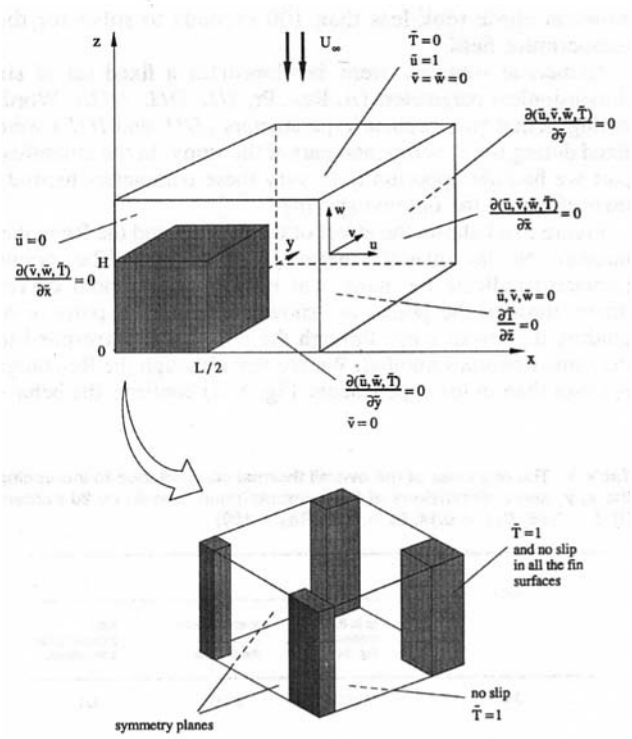


Fig. 4 Computational domain and boundary conditions

Downloaded 11 Dec 2010 to 193.140.21.150. Redistribution subject to ASME license or copyright; see http://www.asme.org/terms/Terms_Use.cfm

Table 3 The effect of grid density on the overall thermal conductance (H/L = 0.56, D/L = 0.14, Pr = 0.72, Re_D = 100)

Array	Number of elements / (Nu)	
2×2	5600 / (4.754)	8504 / (4.704)
3×3	7616 / (7.982)	11840 / (8.110)
4×4	7872 / (14.827)	10338 / (14.923)

were increased in steps of 20 percent in the x and y directions until the relative change in the overall heat transfer rate (Nu) became less than 1 percent. The domain was also increased in steps of 20 percent in the z direction until the change in the overall heat transfer rate became less than 6 percent. Samples of these accuracy tests are presented in Tables 3 and 4. The final (x, y, z) dimensions of the computational domain are drawn to scale in the upper half of Fig. 4. As shown in Table 5, the grid fineness tests recommended using grids with more elements as the geometry of the array became more complicated.

Since the flow and heat transfer parts of the numerical problem are uncoupled, we solved Eqs. (3)–(6) first and used the computed velocity field as input in Eq. (7). The pressure was eliminated using the penalty function approach with a compressibility factor of $\epsilon = 10^{-6}$. This consisted of introducing a small compressibility in the continuity equation, eliminating the pressure as an unknown,

$$\frac{\partial \tilde{u}}{\partial \tilde{x}} + \frac{\partial \tilde{v}}{\partial \tilde{y}} + \frac{\partial \tilde{w}}{\partial \tilde{z}} = -\epsilon \tilde{p} \tag{10}$$

An attenuation factor between 0.1 and 0.3 was applied to all the degrees of freedom to maintain the convergence under control. The velocity field solution for the most complicated problem (8 × 8), required roughly 6000 seconds of CPU time using a segregated solver on the CRAY Y-MP of the North Carolina Supercomputer Center. The energy equation, Eq. (7), was solved next: Since this problem is linear, the solution phase took less than 100 seconds to solve for the temperature field.

Numerical solutions were developed for a fixed set of six dimensionless parameters (n, Re_D, Pr, S/L, D/L, H/L). Worth noting is that two geometric parameters (D/L and H/L) were fixed during the experimental part of the study. In the numerical part we had the opportunity to vary these parameters to study their effect on the optimal spacing.

Figure 5(a) shows the effect of the spacing and the Reynolds number on the overall thermal conductance. The points (squares) indicate the numerical results. The smooth curves drawn through the points are shown only for the purpose of guiding the reader's eye through the points that correspond to the same Reynolds number. We see that although the Re_D range is lower than in the experiments, Fig. 5(a) confirms the behavior seen earlier in Fig. 3: Nu increases with Re_D, and the Nu peak shifts toward smaller spacings as Re_D increases.

Table 4 The response of the overall thermal conductance to increasing the x, y, and z dimensions of the computational domain by 20 percent (H/L = 0.56, D/L = 0.14, Pr = 0.72, Re_D = 100)

Array	Nu		
	as in the reported results, Fig. 5a	after increasing the x or y dimensions	after increasing the z dimension
3×3	7.982	8.025	7.531
4×4	14.827	14.852	13.963

Table 5 The fineness of the grids used in the numerical simulations

n×n	2×2	3×3	4×4	5×5	6×6	8×8
elements	5600	7616	7872	13152	13464	18883

The numerical and experimental results also agree quantitatively as can be seen by comparing the data for Re_D = 100. In this comparison, the experiments and numerical simulations refer to systems with the dimensions shown in Table 6. The maximum Nu determined numerically is 30 percent lower than the experimental Nu maximum: This makes sense, because in the experiments the spilling of the air flow over the edges of the base plate "pinches" the boundary layer, and augments the heat transfer. The optimal numbers of fins too agree fairly well, n_{opt} = 6 for the experiments versus n_{opt} = 5 for the numerical simulations. This level of agreement is remarkable in view of the simplifications adopted in the numerical model, and the fact that the geometric parameters of the numerical model (D/L, H/L) do not match exactly the geometry of the experiments.

The rest of Fig. 5 shows additional S-optimization results generated numerically by changing the pin height H [Fig. 5(b)], the pin side D [Figs. 5(c, d)], and the Prandtl number [Fig. 5(e)]. The behavior of Nu versus S/L is qualitatively the same as in Fig. 5(a). These additional S_{opt} data were necessary for testing the theoretical correlation described next. This, the generation of additional data, was the reason why we extended the Re_D range down to 10. Note that although in our experiments Re_D = 10 would correspond to a free-stream velocity of approximately 3 cm/s (too low to be of practical interest), the same Reynolds number corresponds to larger velocities in other (practical) heat sinks with smaller fins. The contribution of the Re_D = 10 results of Fig. 5 is to show that the Nu maximum decreases and becomes flatter as Re_D decreases.

Theoretical Considerations

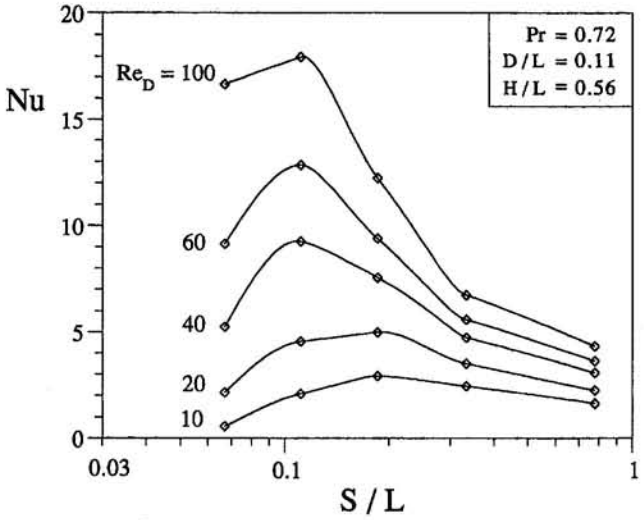
The behavior and order of magnitude of the optimal spacing can be anticipated and correlated on theoretical grounds. The flow pattern is complicated: It is initially aligned with the fins, later it stagnates into the center of the base, and, finally, it turns and flows across the fins. The crossflow direction is particularly evident in the planes situated close to the base. The key observation is that the order of magnitude of the pressure difference that drives the flow away from the center of the base is the excess pressure generated by the stagnation of the free stream,

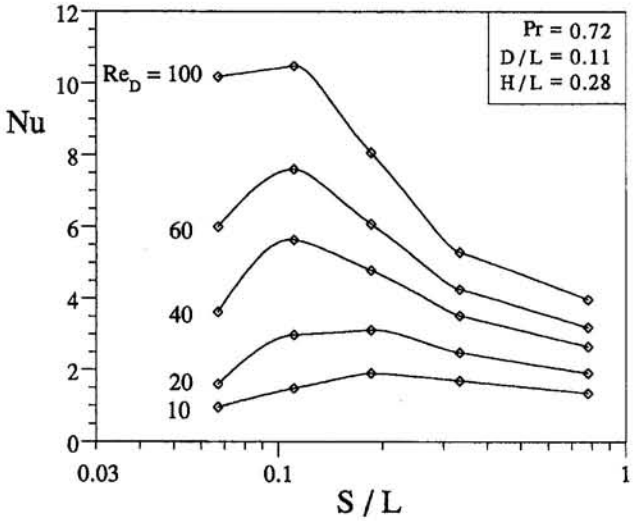
$$\Delta P \sim \tfrac{1}{2}\rho U_\infty^2 \tag{11}$$

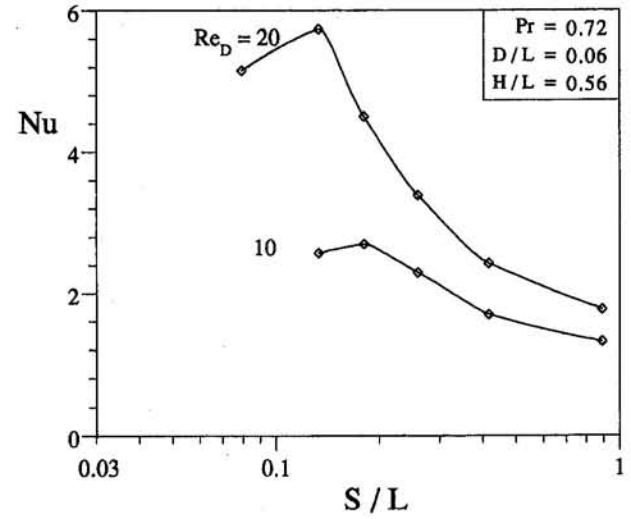
The literature contains several theoretical studies that predict the optimal spacing between heat-generating bodies in a given volume with specified pressure difference in the direction of flow. The physical basis for the existence of an optimal spacing S for maximum thermal conductance is as follows. The conductance decreases when $S \to 0$ because the fluid ceases to penetrate through the fins. The conductance also decreases in the opposite limit ($S \to \infty$) because the fin surfaces disappear. There exists an optimal, intermediate S for which the conductance is maximum. In simple geometries, this optimal value can be determined analytically by intersecting the known small-S and large-S asymptotes of the heat sink assembly. For example, in a stack of parallel plates of flow length L, the optimal plate to plate spacing in laminar flow is (Bejan and Sciubba, 1992)

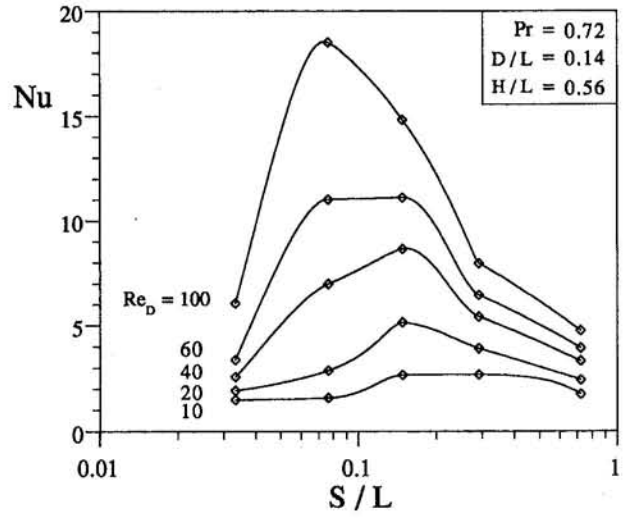
$$\frac{S_{opt}}{L} \cong 2.7\Pi_L^{-1/4} \tag{12}$$

Downloaded 11 Dec 2010 to 193.140.21.150. Redistribution subject to ASME license or copyright; see http://www.asme.org/terms/Terms_Use.cfm









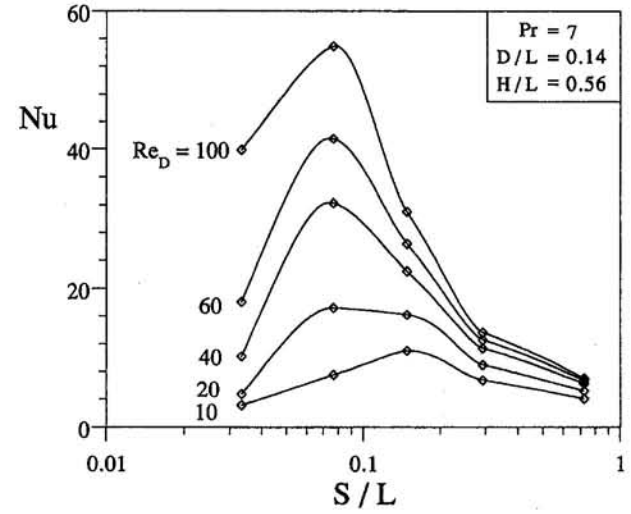


Fig. 5 Numerical results for the overall thermal conductance (Nu) as a function of fin-to-fin spacing (*S*) and air speed (Re_D), and geometry (*D/L*, *H/L*)

where Π_L is the "pressure drop number" (Bejan, 1995):

$$\Pi_L = \frac{\Delta P \cdot L^2}{\mu \alpha} \tag{13}$$

Equation (12) holds even when the plate thickness is not negligible with respect to S_{opt} (Mereu et al., 1993), and when the plate surfaces are covered with protuberances (Morega and Bejan, 1994). If, instead of specifying ΔP, we expose the stack of parallel plates to a free stream (U_∞) aligned with the plate surface length L, we may use Eq. (11) and rewrite Eq. (12) in terms of the length-based Reynolds number $Re_L = U_\infty L/\nu$ (Morega et al., 1995):

$$\frac{S_{opt}}{L} \sim 3.2\ \mathrm{Pr}^{-1/4}\ \mathrm{Re}_L^{-1/2} \tag{14}$$

The correctness of Eqs. (12) and (14) was documented extensively based on complete numerical simulations of the heat and fluid flow fields in and around parallel-plate packages (Bejan and Sciubba, 1992; Mereu et al., 1993; Morega et al., 1995).

Table 6 The dimensions (number of fins, spacing) of the compared experimental and numerical configurations

n × n	S/L	
	experimental (Re_D = 100)	numerical (Re_D = 100)
4 × 4	0.2	0.185
5 × 5	0.125	0.111
6 × 6	0.08	0.067

Downloaded 11 Dec 2010 to 193.140.21.150. Redistribution subject to ASME license or copyright; see http://www.asme.org/terms/Terms_Use.cfm

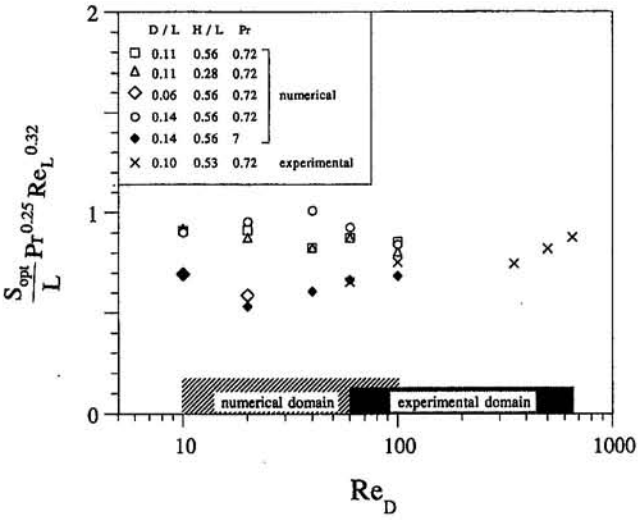


Fig. 6 Correlation of the optimal spacing results

It is worth emphasizing that Eqs. (12) and (14) are purely theoretical, as they were derived analytically by intersecting the known small-S and large-S asymptotes of the function for the total heat transfer rate of the package.

Another theoretical result that is relevant to predicting S_{opt} in the configuration of Fig. 1 is the optimal spacing between staggered cylinders of diameter D in a fixed volume of flow length L cooled by crossflow (Bejan, 1995)

$$\frac{S_{opt}}{D} \cong 1.7\ \Pr^{-0.24}\left(\frac{L}{D}\right)^{0.52}\mathrm{Re}_D^{-0.26} \tag{15}$$

This expression was derived by intersecting the small-S and large-S asymptotes based on available handbook data on banks of cylinders in crossflow (Zukauskas, 1987). Equation (15) is valid in the range $140 < \mathrm{Re}_D < 14{,}000$, $25 < L/D < 200$, and $0.72 < \Pr < 50$. Equation (15) can be rewritten in terms of S_{opt}/L versus Re_L,

$$\frac{S_{opt}}{L} \cong (1.7\ \mathrm{Re}_D^{0.22})\ \Pr^{-0.24}\ \mathrm{Re}_L^{-0.48} \tag{16}$$

to see that it is remarkably similar to the formula for parallel plates, Eq. (14). The agreement between Eqs. (16) and (14) is quantitative as well, because in the Re_D range of the present study $1.7\ \mathrm{Re}_D^{0.22}$ is of the same order as 3.2.

The square-fin array of Fig. 1 fits somewhere between the geometries covered by Eqs. (14) and (16). In fact, the small-S asymptote of the geometry of Fig. 1 is similar to the small-S asymptote of the stack of parallel plates for which Eq. (14) was derived. Note that when $S = 0^+$ the flow velocity profile is parabolic across the gap, and the flow channel is the same as that between two infinite parallel plates. The streamlines are curved, because the flow is three dimensional; however, the pressure difference scale that drives the flow through the vanishing gap is properly represented by Eq. (11). We seek, therefore, a correlation of type (14, 16) by plotting the group $(S_{opt}/L)\ \Pr^{1/4}\ \mathrm{Re}_L^{1/2}$ versus Re_D, and expect Re_D to have little or no effect on this group. This is indeed the case, however, as shown in Fig. 6, we find that somewhat less scatter occurs if we use $\mathrm{Re}_L^{0.32}$ in place of $\mathrm{Re}_L^{1/2}$ in the theoretical group. Projected onto Fig. 6 are all the optimal spacings determined numerically and experimentally (27 points in total). These data show that the group $(S_{opt}/L)\ \Pr^{1/4}\ \mathrm{Re}_L^{0.32}$ has the mean value 0.81 with a standard deviation of ± 16.3 percent. In other words, the optimal spacing correlation is

$$\frac{S_{opt}}{L} \cong 0.81\ \Pr^{-0.25}\ \mathrm{Re}_L^{-0.32} \tag{17}$$

The abscissa of Fig. 6 is a reminder that in spite of the mismatch between the respective D/L and H/L values, the experimental and numerical results overlap over the Re_D domain 60–100. In this domain the experimental and numerical trends mesh very well. In addition, it is worth noting that the usefulness of the S_{opt} correlation (17) is considerably better than the impression that might be given by the ± 16.3 percent standard deviation: The reason is that, for design optimization purposes, it is not absolutely necessary to pinpoint S_{opt} exactly. A "nearly optimal" geometry with a spacing that differs from S_{opt} (say, by 20 percent) has practically the same performance (overall thermal conductance) as the optimal design (e.g., Bejan et al., 1996, p. 4). This feature is due to the shallowness of the $q/\Delta T$ maximum with respect to S. This feature was also evident in our geometric optimization of the stack of parallel plates (Bejan and Sciubba, 1992), where we compared the results based on intersecting the S asymptotes with the results based on maximizing the function $q/\Delta T$ versus S numerically.

The maximum thermal conductance results (the peaks of the curves in Fig. 5) were correlated similarly, by using the analytical solution for staggered cylinders in crossflow (Bejan, 1995). The resulting expression

$$\frac{1}{k_a H}\left(\frac{q}{\bar{T}_b - T_\infty}\right)_{\max} \cong 1.57\ \Pr^{0.45}\ \mathrm{Re}_L^{0.69}\left(\frac{L}{D}\right)^{0.31} \tag{18}$$

fits the 22 numerical data (Fig. 7) within ± 20.7 percent. It is worth noting that the experimental data fall consistently above the numerical results. This is a reflection of the fact that the numerical configuration did not reproduce exactly the experimental configuration. One important difference that begins to be felt at $\mathrm{Re}_D \gtrsim 100$ is the presence of buckling flow (vortex shedding) behind and between the pin fins. This turbulence effect makes Eq. (18) a conservative estimate (an underprediction) of the maximum thermal conductance at Reynolds numbers higher than $O(10^2)$.

The two correlations, Eqs. (17), (18), cover the range $0.06 < D/L < 0.14$, $0.28 < H/L < 0.56$, $0.72 < \Pr < 7$, $10 < \mathrm{Re}_D < 700$, and $90 < \mathrm{Re}_L < 6000$.

Conclusion

In this paper we showed that the thermal conductance of a pin-finned surface with impinging air flow can be maximized

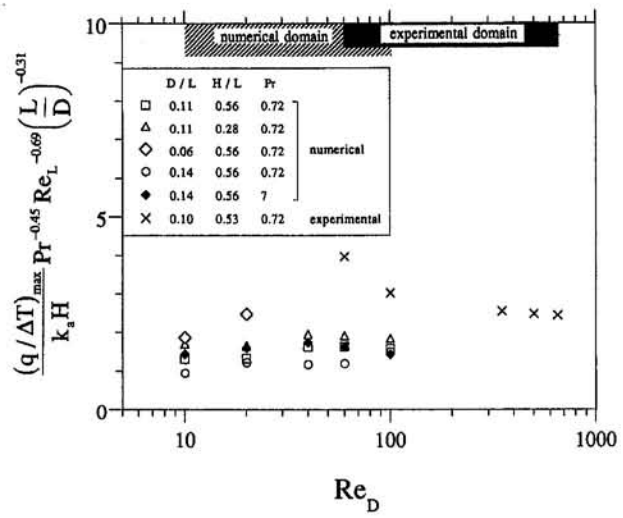


Fig. 7 Correlation of the results for maximum overall thermal conductance

Downloaded 11 Dec 2010 to 193.140.21.150. Redistribution subject to ASME license or copyright; see http://www.asme.org/terms/Terms_Use.cfm

by properly selecting the fin-to-fin spacing. We demonstrated this optimization principle experimentally by comparing several spacing designs in the same air stream in a wind tunnel. We also constructed a numerical model and generated a considerable volume of optimal-spacing and maximum heat transfer data, for various combinations of flow conditions (Re_L), pin dimensions (D/L, H/L), and fluid type (Pr).

Finally, we developed a theoretical approach to correlating the experimental and numerical data, Eqs. (17), (18). For example, the similarities between the recommended correlation (17) and the optimal spacings known for parallel plates (14) and parallel cylinders (15) strengthen the theoretical foundation for identifying and correlating optimal spacings in future, undocumented electronics cooling geometries.

Future studies may also provide more empirical data to strengthen or improve the correlations (17), (18). This is also a way of testing the theoretical argument on which the correlations were based [Eq. (11), and the intersection of the S asymptotes method]. An excellent example of how future studies may extend the line of inquiry started in this paper is provided by a recently published set of experiments on heat sinks with parallel plate fins and bypass air flow (Wirtz et al., 1994). The experimental geometry has the same "complications" as the configuration optimized in this paper, e.g., three-dimensional flow with bypass, fin conduction, and turbulence. Wirtz et al. (1994) reported in their Fig. 8 two cases (Re_L = 3000 and 10,000) in which the overall thermal resistance of the heat sink is shown to have a minimum with respect to a dimensionless "fin density" parameter. Their curves were drawn for a heat sink design with the fin flow length L = 50 mm and the plate fin thickness t = 1.5 mm.

The optimal spacing correlation that applies to the geometry of Wirtz et al. is Eq. (14): The derivation of Eq. (14) is based on the same simplifying assumptions as correlations (17), (18). Note that Eq. (14)—its development—inherits all the criticism that might be directed at the origin of Eq. (17) and the data on which Eq. (17) is based. It takes a very brief calculation to show that for the two cases of Wirtz et al. (Re_L = 3000 and 10,000) Eq. (14) predicts the optimal spacings: 3.17 mm and 1.74 mm, respectively. These spacings correspond to the "fin density" values 0.34 and 0.48 on the abscissa of Fig. 8 of Wirtz et al. and anticipate very well the positions of the thermal resistance minima.

Acknowledgments

This research was supported in part by IBM Corporation (Research Triangle Park), Duke University, and Fundayacucho Laspau, Venezuela. The numerical work was supported by a grant received from the North Carolina Supercomputing Center.

References

Anand, N. K., Kim, S. H., and Fletcher, L. S., 1992, "The Effect of Plate Spacing on Free Convection Between Heated Parallel Plates," ASME JOURNAL OF HEAT TRANSFER, Vol. 114, pp. 515–518.

Bar-Cohen, A., and Rohsenow, W. M., 1984, "Thermally Optimum Spacing of Vertical, Natural Convection Cooled, Parallel Plates," ASME JOURNAL OF HEAT TRANSFER, Vol. 106, pp. 116–123.

Bejan, A., 1984, *Convection Heat Transfer*, Wiley, New York, problem 11, p. 157; *Solutions Manual*, pp. 93–95.

Bejan, A., and Sciubba, E., 1992, "The Optimal Spacing of Parallel Plates Cooled by Forced Convection," *International Journal of Heat and Mass Transfer*, Vol. 35, pp. 3259–3264.

Bejan, A., 1995, *Convection Heat Transfer*, 2nd ed., Wiley, New York, pp. 154–155; *Solutions Manual*, pp. (3-36)–(3-40).

Bejan, A., Tsatsaronis, G., and Moran, M., 1996, *Thermal Design and Optimization*, Wiley, New York.

Chu, R. C., and Simons, R. E., 1994, "Cooling Technology for High Performance Computers: IBM Sponsored University Research," in: S. Kakac, H. Yüncü, and Hijikata, K., eds., *Cooling of Electronic Systems*, Kluwer Academic Publishers, Dordrecht, The Netherlands, pp. 97–122.

FIDAP, 1993, *Theory Manual*, Fluid Dynamics International, Evanston, IL, V.7.0.

Heindel, T. J., Ramadhyani, S., Incropera, F. P., and Campo, A., 1992, "Surface Enhancement of a Heat Source Exposed to a Circular Liquid Jet With Annular Collection of the Spent Fluid," ASME HTD-Vol. 206-2, pp. 111–118.

Kamath, V., 1994, "Air Injection and Convection Cooling of Multi-Chip Modules: A Computational Study," *Proc. InterSociety Conference on Thermal Phenomena in Electronic Systems (ITHERM IV)*, Washington, DC, May 4–7, pp. 83–90.

Knight, R. W., Goodling, J. S., and Hall, D. J., 1991, "Optimal Thermal Design of Forced Convection Heat Sinks—Analytical," *Journal of Electronic Packaging*, Vol. 113, pp. 313–321.

Larson, E. D., and Sparrow, E. M., 1982, "Performance Comparisons Among Geometrically Different Pin-Fin Arrays Situated in an Oncoming Longitudinal Flow," *International Journal of Heat and Mass Transfer*, Vol. 25, pp. 723–725.

Mansuria, M. S., and Kamath, V., 1994, "Design Optimization of a High-Performance Heat-Sink/Fan Assembly," ASME HTD-Vol. 292, pp. 95–103.

Matsushima, H., Yanagida, T., and Kondo, Y., 1992, "Algorithm for Predicting the Thermal Resistance of Finned LSI Packages Mounted on a Circuit Board," *Heat Transfer Japanese Research*, Vol. 21(5), pp. 504–517.

Mereu, S., Sciubba, E., and Bejan, A., 1993, "The Optimal Cooling of a Stack of Heat Generating Boards With Fixed Pressure Drop, Flowrate or Pumping Power," *International Journal of Heat and Mass Transfer*, Vol. 36, pp. 3677–3686.

Moffat, R. J., 1988, "Describing the Uncertainties in Experimental Results," *Thermal Fluid Sci.*, Vol. 1, pp. 3–17.

Moffat, R. J., and Ortega, A., 1988, "Direct Air Cooling of Electronic Components," in: *Advances in Thermal Modeling of Electronic Components and Systems Vol. I*, A. Bar-Cohen and A. D. Kraus, eds., Hemisphere, New York, pp. 129–282.

Morega, Al. M., and Bejan, A., 1994, "The Optimal Spacing of Parallel Boards With Discrete Heat Sources Cooled by Laminar Forced Convection," *Numerical Heat Transfer, Part A*, Vol. 25, pp. 373–392.

Morega, A. M., Bejan, A., and Lee, S. W., 1995, "Free Stream Cooling of a Stack of Parallel Plates," *International Journal of Heat and Mass Transfer*, Vol. 38, pp. 519–531.

Nakayama, W., Matsushima, H., and Goel, P., 1988, "Forced Convective Heat Transfer From Arrays of Finned Packages," in: *Cooling Technology for Electronic Equipment*, W. Aung, ed., pp. 195–210, Hemisphere, New York.

Nakayama, W., 1994, "Information Processing and Heat Transfer Engineering: Some Generic Views on Future Research Needs," in: S. Kakac, H. Yüncü, and K. Hijikata, eds., *Cooling of Electronic Systems*, Kluwer Academic Publishers, Dordrecht, The Netherlands, pp. 911–943.

Peterson, G. P., and Ortega, A., 1990, "Thermal Control of Electronic Equipment and Devices," *Advances in Heat Transfer*, Vol. 20, pp. 181–314.

Sathe, S., Kelkar, K. M., Karki, K. C., Tai, C., Lamb, C., and Patankar, S. V., 1983, "Numerical Prediction of Flow and Heat Transfer in an Impingement Heat Sink," ASME EEP-Vol. 4-2, pp. 893–898.

Sparrow, E. M., and Larson, E. D., 1982, "Heat Transfer From Pin-Fins Situated in an Oncoming Longitudinal Flow Which Turns to Crossflow," *International Journal of Heat and Mass Transfer*, Vol. 25, pp. 603–614.

Sparrow, E. M., Suopys, A. P., and Ansari, M. A., 1984, "Effect of Inlet, Exit, and Fin Geometry on Pin Fins Situated in a Turning Flow," *International Journal of Heat and Mass Transfer*, Vol. 27, pp. 1039–1054.

Sullivan, P. F., Ramadhyani, S., and Incropera, F. P., 1992a, "Extended Surfaces to Enhance Impingement Cooling With Single Circular Liquid Jets," *Advances in Electronic Packages*, ASME, New York, pp. 207–215.

Sullivan, P. F., Ramadhyani, S., and Incropera, F. P., 1992b, "Use of Smooth and Roughened Spreader Plates to Enhance Impingement Cooling of Small Heat Sources With Circular Liquid Jets," ASME HTD-Vol. 206-2, pp. 103–110.

Wadsworth, D. C., and Mudawar, I., 1992, "Enhancement of Single-Phase Heat Transfer and Critical Heat Flux from an Ultra-High-Flux Simulated Microelectronic Heat Source to a Rectangular Impinging Jet of Dielectric Liquid," ASME JOURNAL OF HEAT TRANSFER, Vol. 114, pp. 764–768.

Wirtz, R. A., Chen, W., and Zhou, R., 1994, "Effect of Flow Bypass on the Performance of Longitudinal Fin Heat Sinks," ASME *Journal of Electronic Packaging*, Vol. 116, pp. 206–211.

Zukauskas, A., 1987, "Convective Heat Transfer in Cross Flow," *Handbook of Single-Phase Convective Heat Transfer*, S. Kakac, R. K. Shah, and W. Aung, eds., Wiley, New York, Chap. 6.

Downloaded 11 Dec 2010 to 193.140.21.150. Redistribution subject to ASME license or copyright; see http://www.asme.org/terms/Terms_Use.cfm

Local Heat Transfer in Rotating Smooth and Ribbed Two-Pass Square Channels With Three Channel Orientations

S. Dutta
Department of Mechanical Engineering,
University of South Carolina,
Columbia, SC 29208

J.-C. Han
Department of Mechanical Engineering,
Texas A&M University,
College Station, TX 77843-3123

This paper presents experimental heat transfer results in a two-pass square channel with smooth and ribbed surfaces. The ribs are placed in a staggered half-V fashion with the rotation orthogonal to the channel axis. The channel orientation varies with respect to the rotation plane. A change in the channel orientation about the rotating frame causes a change in the secondary flow structure and associated flow and turbulence distribution. Consequently, the heat transfer coefficient from the individual surfaces of the two-pass square channel changes. The effects of rotation number on local Nusselt number ratio distributions are presented. Heat transfer coefficients with ribbed surfaces show different characteristics in rotation number dependency from those with smooth surfaces. Results show that staggered half-V ribs mostly have higher heat transfer coefficients than those with 90 and 60 deg continuous ribs.

Introduction

A two-pass rotating channel simulates the conditions of internal serpentine cooling passages in turbine rotor blades. Earlier studies on cooling passages were primarily based on stationary models, which are easier to build and work on. However, stationary models neglect the Coriolis and centrifugal buoyancy effects, which affect the velocity, turbulence, and temperature distributions. Johnston et al. (1972) experimentally observed that rotation causes unstabilization (enhancement of turbulence) on one side and stabilization (suppression of turbulence) of flow on the other. Location of the unstabilized and stabilized surfaces depends on the flow direction, rotation direction, and the channel orientation. Heat transfer from the unstabilized walls is superior to that from stabilized walls (Wagner et al., 1991a, b; Han et al., 1993, 1994). Investigation of the rotor blade coolant passage heat transfer characteristics in an actual rotating frame is better because many of the rotational features cannot be simulated in stationary tests. The channel orientation may significantly affect the heat transfer characteristics in rotation. The Coriolis-influenced flow distribution depends on the channel orientation with respect to the rotating frame and, consequently, the heat transfer from the individual surfaces changes with a change in the channel orientation.

Inclusion of angled ribs (placed at an angle to the bulk flow) enhances heat transfer coefficient due to increased turbulent mixing, secondary flow, and, to some extent, due to increased participating surface area. The turbulence enhancement by ribs and flow reversal in the separated region interacts with the rotational effects. Ribs and rotation combine to develop a new characteristic in the heat transfer coefficient distribution. Results obtained with angled ribs show some new characteristics not observed in the smooth channel.

Wagner et al. (1992), Taslim et al. (1991a, b), Fann et al. (1994), Johnson et al. (1994a, b), Parsons et al. (1994, 1995), and Zhang et al. (1995) studied the local heat transfer coefficient distribution in rotating ribbed channels. The effects of rotation on heat transfer coefficient in the ribbed square channels were mostly similar to the rotating smooth walled results in characteristics. Heat transfer increased on unstabilized walls (first pass trailing and second pass leading) and decreased on stabilized walls (first pass leading and second pass trailing) with an increase in the rotation number.

This paper presents heat transfer results from a rotating two-pass square channel. Both smooth and nonorthogonal staggered half-V ribbed wall results are presented. Our rib configuration is different from the previous reported works. Three different channel orientations, Models A, B, and C, are used. Results for four Reynolds numbers (Re = 2500 to 25,000) and corresponding four rotation numbers (Ro = 0.3 to 0.03) are included. Results show that staggered half-V ribs mostly have higher heat transfer coefficients than those with 90 and 60 deg continuous ribs. The heat transfer coefficient dependency on rotation number is mixed for staggered half-V ribs.

Summary of Experimental Details

This section includes a brief description of the experimental setup and data reduction procedure. The experimental rig is an improved version of the test facility of Han et al. (1993). The rotating arm length is extended to increase the R/D ratio from 30 to 55 in this modified test facility.

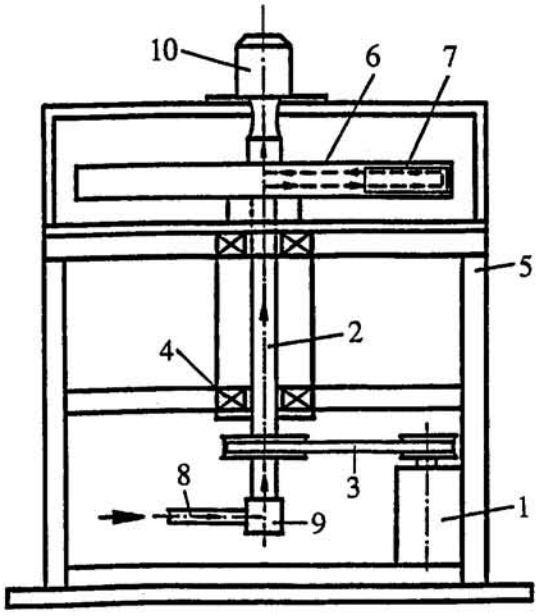
Experimental Facility. Figure 1 shows the schematic of the test rig. The working fluid is air at atmospheric pressure and room temperature. An orifice meter measures the mean flow rate. The test section rotates in a horizontal plane. The rotating and stationary parts of the setup communicate through rotary couplings and slip rings. A digital photo tachometer measures the rotation speed.

The hydraulic diameter of the square test section is 11.7 mm. The test section length to hydraulic diameter ratio is 26, while each pass is 13 hydraulic diameters long connected by a sharp 180 deg turn. The flow is radially outward in the first pass and radially inward in the second pass. The mean rotating radius is 55 hydraulic diameters. Figure 2 shows a schematic cut-away view of the two-pass test section. Like the test section of Han et al. (1993), each heat transfer surface uses six copper pieces (a total of 48 copper pieces in 8 heat transfer walls and 2 more copper pieces at the end cap of the turn region). A group of copper elements, laid on any of the eight surfaces, shares the

Contributed by the Heat Transfer Division for publication in the JOURNAL OF HEAT TRANSFER. Manuscript received by the Heat Transfer Division September 20, 1995; revision received March 1, 1996. Keywords: Forced Convection, Rotating Flows, Turbines. Associate Technical Editor: T. J. Rabas.

Copyright © 1996 by ASME

Downloaded 11 Dec 2010 to 193.140.21.150. Redistribution subject to ASME license or copyright; see http://www.asme.org/terms/Terms_Use.cfm



1. Frequency controlled electric motor
2. Rotating hollow shaft
3. Belt drive
4. Bearing
5. Chasis of the experimental rig
6. Horizontal rotating arm
7. Test section inside the rotating arm
8. Air supply
9. Rotary connector for air supply
10. Slip ring assembly

Fig. 1 Schematic of the rotating test facility (Han et al., 1993)

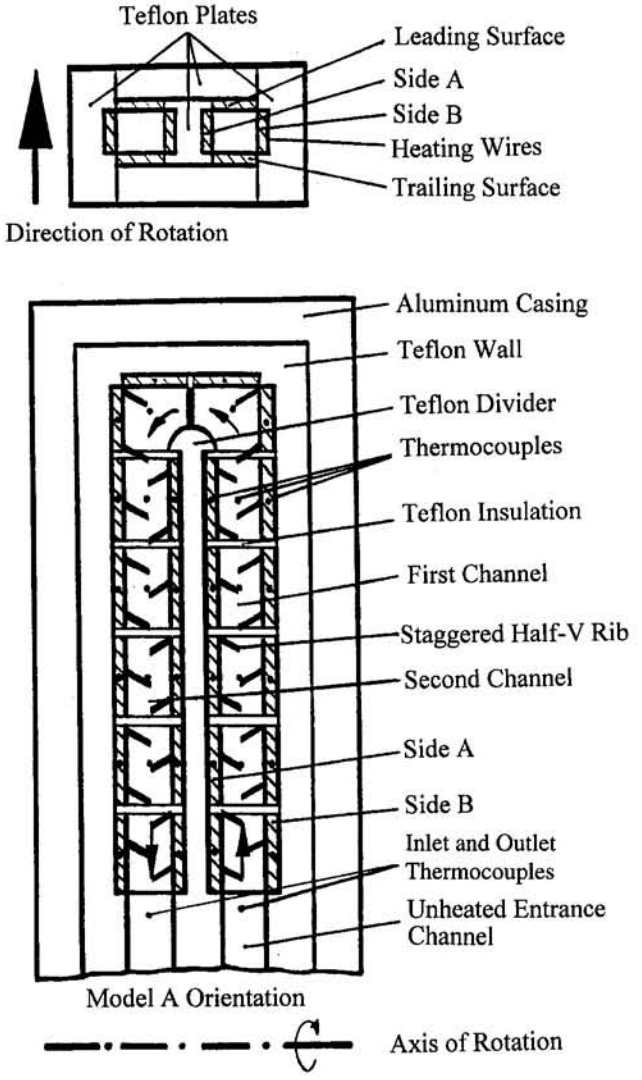


Fig. 2 Cross-sectional view of the test section for Model A orientation

same input power (i.e., one electrical heater is laid on the back side of a group of copper pieces) but each copper element is equipped with individual thermocouples to provide the local heat transfer coefficient. Each copper piece is 3.2 mm thick and its length-to-thickness ratio is 8. Therefore, one thermocouple can adequately measure the mean temperature of an individual copper piece. Since the resistance of the electrical heater is uniformly distributed along the length of the heater, each copper piece (covering the same length on the heater) will dissipate the same amount of thermal energy. Typical bulk and wall temperature profiles for this type of heating condition were shown by Han et al. (1993, 1994). Figure 2 shows the rib configuration. The ribs are oriented 60 deg to the bulk flow. Brass ribs of square cross section are glued to the heater surfaces. The high-temperature glue thickness is kept to less than 0.3 mm. The rib height to hydraulic diameter ratio is 0.125 and the pitch to height ratio is 10. The ribs on the opposing surfaces are aligned with each other and not staggered. Four Reynolds numbers (Re = 2500, 5000, 10,000, and 25,000) based on the hydraulic diameter of the channel are used. The channel rotates at 800 rpm, resulting in four rotation numbers (Ro = 0.3, 0.15, 0.075, 0.03). The heated walls are at 340 K giving a coolant-to-wall density ratio of 0.13.

Figure 3 shows three channel orientations with respect to the rotation plane. The channel orientations are called Models A, B, and C. Figure 3 shows the direction of rotation. The arrow represents the direction of the tangential velocity and not the rotation vector. Figure 3 shows the conceptual secondary flow structures developed in Models A, B, and C. The secondary flow by rotation is mostly on the bulk flow region, whereas the rib effect is expected to be more near the rib mounted surfaces. Note that the 180 deg turn influences the secondary flow in the second pass (II). For simplicity, secondary flows in Fig. 3 do not include the effects of the turn.

Nomenclature

D = hydraulic diameter, m
DR = coolant to wall density ratio = $(\rho_{bi} - \rho_w)/\rho_{bi} = (T_w - T_{bi})/T_w$
h = heat transfer coefficient, $W/m^2 \cdot °C$
Nu = Nusselt number = hD/k
Nu_o = Nusselt number in fully developed smooth-walled turbulent pipe flow
q''_{net} = net heat flux at wall, W/m^2
Re, Ro = Reynolds number = $\rho V D/\mu$; rotation number = $\Omega D/V$
T = temperature, K
V = average axial flow velocity, m/s
X = distance measured along the channel axis from the start of heating, m
μ = viscosity of air, $kg/m \cdot s$
Ω = rotational speed of the two-pass channel, rad/s
ρ = density of air, kg/m^3

Subscripts

b = bulk mean values
i = inlet values
w = wall values

Downloaded 11 Dec 2010 to 193.140.21.150. Redistribution subject to ASME license or copyright; see http://www.asme.org/terms/Terms_Use.cfm

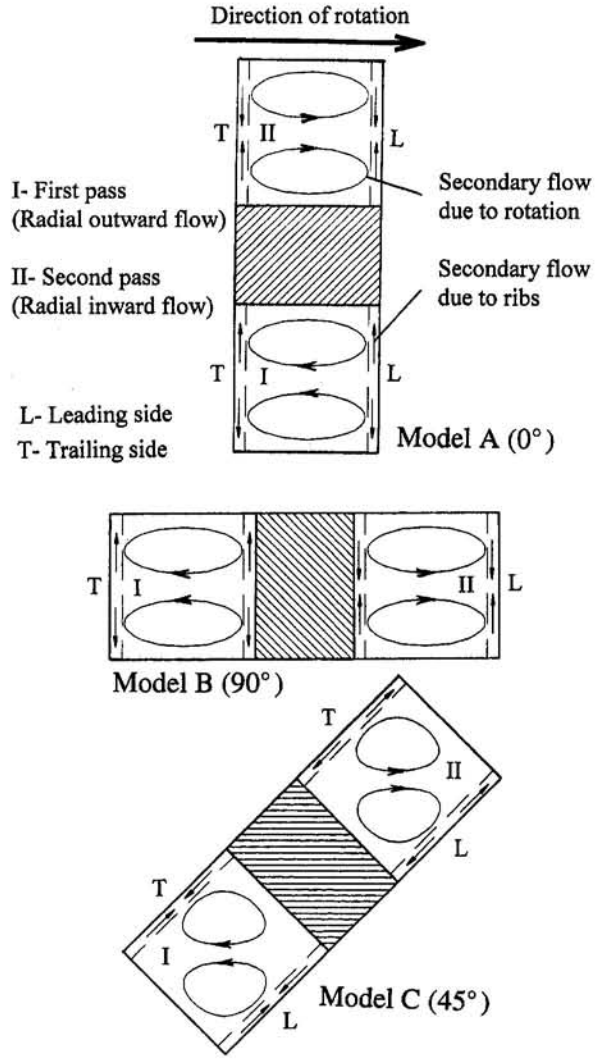


Fig. 3 Three channel orientations used

Data Reduction. The local heat transfer coefficient is calculated from the local net heat flux, the local wall temperature, and the local bulk mean air temperature difference as

$$h = \frac{q''_{\text{net}}}{T_w - T_b} \tag{1}$$

Local net heat flux (q''_{net}), based on the flat projected area, is obtained by subtracting the heat loss from the power supplied to the heaters. The side face areas of ribs are not included in our heat flux calculation. For information, the side face area of the rib used is about 23 percent (a 90 deg rib with similar features would have 20 percent) of the total ribbed surface projected area. Heat loss is estimated by running a separate test on the same test configuration but without air flow (no-flow condition) in the channel. Characteristic heat loss lines are obtained for each of the isolated rectangular copper pieces. The inlet and outlet openings for the rotating test section are located at more than 120 hydraulic diameters distance from the heated portion of the test channel and do not interfere with the heat loss test. This no-flow heat loss determination method was satisfactory when tested on a similar rotating test rig. The local wall temperature (T_w) is obtained from the thermocouple reading of the related heater section. The individual electrical resistive heaters give uniform heat flux heating conditions. Therefore, a linear interpolation between the measured inlet and outlet bulk temperatures gives the local bulk temperature (T_b). The calculated and thermocouple measured outlet bulk mean temperatures are within 3°C and show satisfactory heat balance in the measurements.

To reduce the influence of flow Reynolds number on the heat transfer coefficient, the local Nusselt number is normalized by the Nusselt number for fully developed turbulent flow in a smooth stationary pipe. This is correlated by Dittus–Boelter/McAdams (Rohsenow and Choi, 1961) as

$$\frac{\text{Nu}}{\text{Nu}_o} = \frac{hD}{k_{\text{air}}} \frac{1}{(0.023\ \text{Re}^{0.8}\ \text{Pr}^{0.4})} \tag{2}$$

The Prandtl number, Pr, for air is 0.72. Air properties are taken at the inlet condition (room temperature and pressure).

Uncertainty. The uncertainty of the local heat transfer coefficient depends on the uncertainties in the local wall and bulk air temperature difference and the net heat input for each test section, whereas the uncertainty of the local heat transfer coefficient increases with a decrease in either the local wall-to-air temperature difference or the net heat flux. The net heat flux is higher in a ribbed channel than in a smooth channel and, therefore, the uncertainty in ribbed channel results is less than that in the smooth channel results. Based on the method described by Kline and McClintock (1953), the typical uncertainty in the Nusselt number is estimated to be less than 8 and 5 percent for Reynolds numbers larger than 5000 for smooth and rib roughened test cases, respectively. However, the maximum uncertainty could be up to 20 percent for the lower heat transfer coefficient at the lowest Reynolds number tested (Re = 2500).

Results

Figures 4–6 show the regionally averaged Nusselt number ratios (Nu/Nu_o) at different channel locations. Nu/Nu_o is the

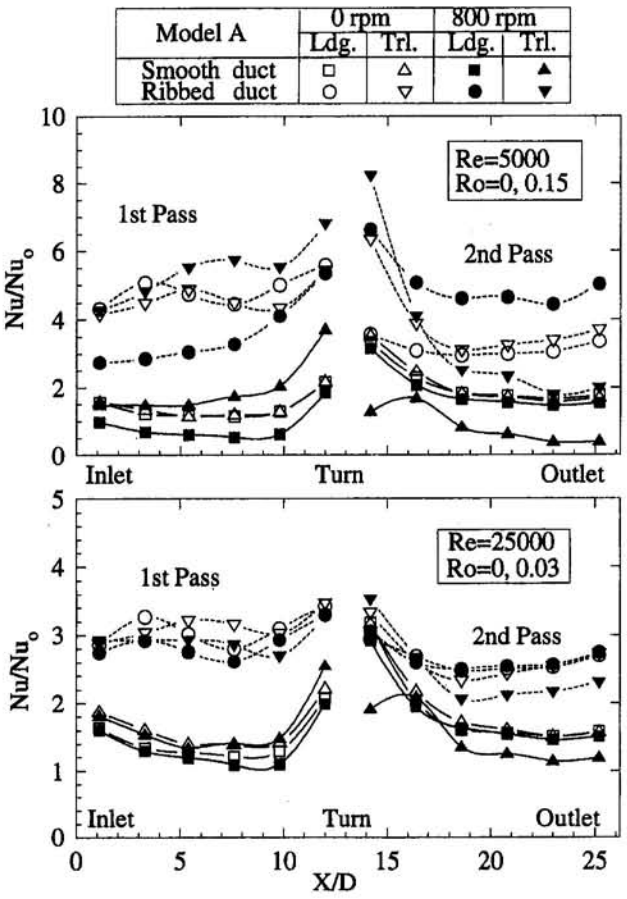


Fig. 4 Regionally averaged local Nusselt number ratios at different locations of the channel for Model A

Downloaded 11 Dec 2010 to 193.140.21.150. Redistribution subject to ASME license or copyright; see http://www.asme.org/terms/Terms_Use.cfm

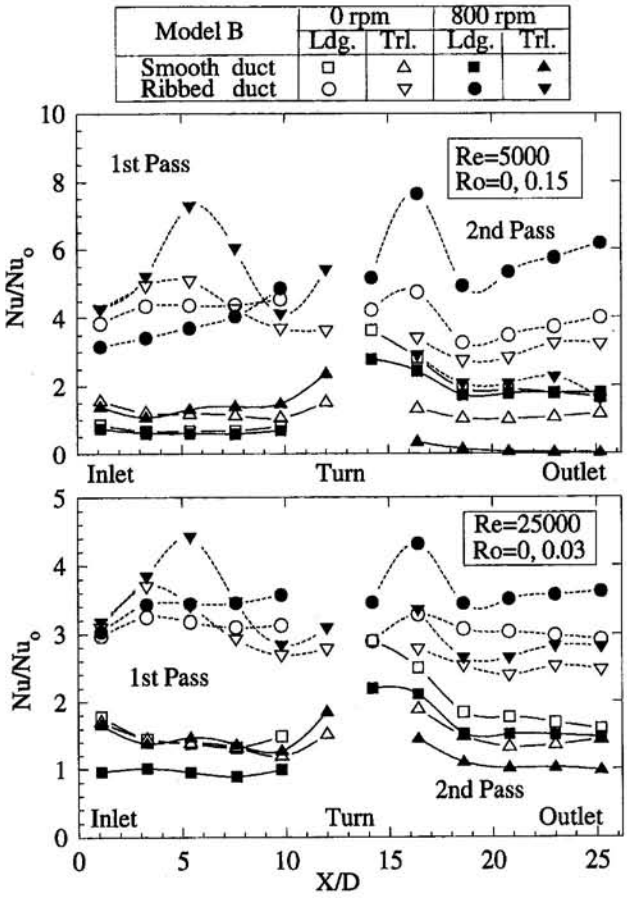


Fig. 5 Regionally averaged local Nusselt number ratios at different locations of the channel for Model B

ratio of heat transfer with rotation to the smooth-walled stationary fully developed circular tube data. Heat transfer results from the leading and trailing walls (as shown in Fig. 3) are presented. Figure 4 is for Model A, Fig. 5 is for Model B, and Fig. 6 is for Model C. Inclusion of ribs increase the heat transfer coefficient. Rotation enhances heat transfer from the first pass trailing and second pass leading surfaces. These are called *unstabilized* surfaces due to thin cooler boundary layers and enhancement of turbulence with rotation, whereas heat transfer decreases from the first pass leading and second pass trailing surfaces, which are *stabilized* surfaces due to thick warmer boundary layers in rotation. A higher rotation number mostly shows a larger difference between the trailing and leading surface heat transfer results than that for a lower rotation number.

Figure 4 shows the heat transfer results for smooth and ribbed walls with Model A. Rotating results are compared with nonrotating stationary heat transfer results. The results of Reynolds numbers (Re) 5000 and 25,000 with rotation number (Ro) of 0.15 and 0.03 are shown. The stationary and rotating results at lower Ro (Ro = 0.03) are not significantly different. The unstabilized surfaces show an increase in Nu/Nu_o over the stationary results at a higher Ro (Ro = 0.15). Heat transfer from the stabilized surfaces is lower with rotation than that at the stationary case. Note that the ribbed trailing surface of the second pass loses much of the rib-enhanced heat transfer capabilities at Ro = 0.15, and Nu/Nu_o from that surface is relatively low. However, the second pass leading side shows a significant improvement in heat transfer coefficient with rotation.

Figure 5 shows the effect of rotation on heat transfer for Model orientation B. Note that the effect of the 180 deg turn is not symmetric for leading and trailing walls for this channel orientation. The stationary results of Re = 5000 with smooth walls show that the stabilized surfaces (first pass leading and second pass trailing) have lower Nu/Nu_o compared to the unstabilized surfaces (first pass leading and second pass trailing) have lower Nu/Nu_o compared to the unstabilized surfaces (first pass trailing and second pass leading). Heat transfer from unstabilized surfaces increases and that from stabilized surfaces decreases with rotation. The nonorthogonal staggered half-V ribbed results show an increase and decrease in Nu/Nu_o with X/D on unstabilized surfaces. These nonuniform (increase and decrease) Nu/Nu_o distributions in the first pass are due to the interaction of the secondary flows by rotation and rib orientation, whereas the nonuniformities in the Nusselt number ratio profiles in the second pass are most likely the interaction of turn and rib generated secondary flows.

Figure 6 shows the effect of rotation on heat transfer for Model C. Figure 3 shows that the heat transfer surfaces are not orthogonal to the plane of rotation for this channel orientation. Therefore, the rotational effects are less significant for this channel orientation (Model C) compared to the other two channel orientations (Models A and B). At a higher rotation number (Ro = 0.15), the first pass of the smooth channel does not show much difference with rotation. However, in the second pass of the smooth channel, rotation decreases the heat transfer coefficient on the trailing (stabilized) surface. The second pass leading surface does not show any significant increase in the heat transfer coefficient in the rotating smooth square channel. The ribbed square channel at Ro = 0.15 shows that the decrease in heat transfer coefficient on the first-pass leading is more significant than the increase in the first-pass trailing surface heat transfer coefficient, whereas the second pass leading surface shows a significant increase in the heat transfer coefficient and the decrease in heat transfer coefficient on the second-pass trail-

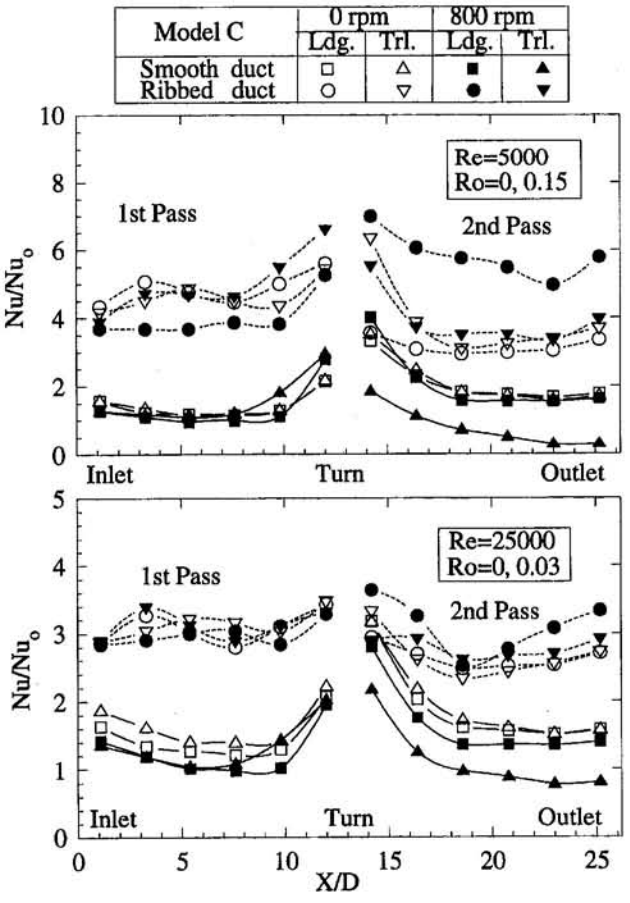


Fig. 6 Regionally averaged local Nusselt number ratios at different locations of the channel for Model C

Downloaded 11 Dec 2010 to 193.140.21.150. Redistribution subject to ASME license or copyright; see http://www.asme.org/terms/Terms_Use.cfm

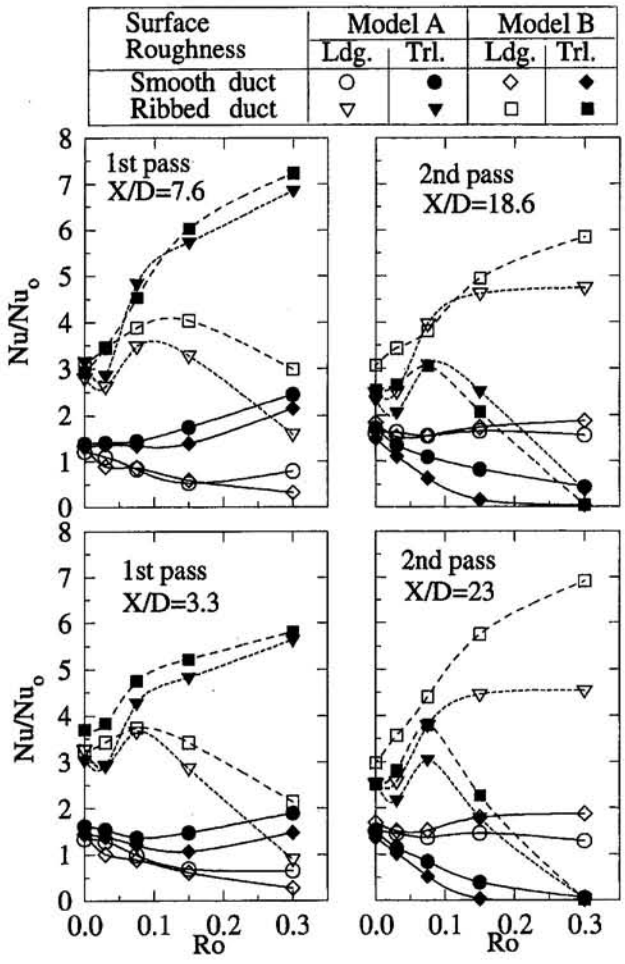


Fig. 7 Effect of rotation number on Nusselt number ratio at selected locations of the channel (comparison of Models A and B)

ing surface is comparatively less significant. At a lower rotation number (Ro = 0.03), the heat transfer coefficients in general decrease with rotation for both passes in this Model C smooth two-pass square channel. The rib-roughened heat transfer surfaces do not show much change in this low rotation number of Ro = 0.03, except the second-pass leading surface shows an increase in the heat transfer coefficient with rotation.

Effect of Rotation Number and Model Orientation. Figures 7 and 8 show the effects of rotation number and channel orientation on heat transfer. Channel orientation of Models A and B are compared in Fig. 7. The heat transfer coefficients on unstabilized surfaces (first pass trailing and second pass leading) increase and on stabilized surfaces (first pass leading and second pass trailing) decrease with increasing rotation number (Ro) for smooth surface results. Heat transfer from ribbed walls are, as expected, higher than the smooth wall results. Note that the dependence of heat transfer characteristics on Ro from the stabilized surfaces with ribs is different from those with smooth walls. Heat transfer from ribbed stabilized walls increases for smaller Ro and then decreases at higher Ro as opposed to a monotonic decrease in stabilized smooth surfaces. Perhaps interaction of rotation with secondary flow from ribs and flow separation near ribs are the cause of this beneficial increase in heat transfer coefficient from the stabilized surfaces at low Ro. Heat transfer from the unstabilized surfaces with ribs behaves similar to that for the smooth walls (but with higher Nu/Nu_o values). That is, Nusselt number ratio increases as Ro increases.

Figure 7 also shows that the ribbed unstabilized surfaces have a sharp increase in Nu/Nu_o with an increase in Ro, whereas the smooth wall results have a gradual increase in Nu/Nu_o with Ro. The difference in Nu/Nu_o between stabilized and unstabilized surfaces are more for ribbed walls than those with smooth walls at Ro > 0.1. At Ro = 0.3 the ribbed stabilized surfaces lose their heat transfer effectiveness significantly and become comparable to smooth walls, especially in the second pass. Note that lower Nu/Nu_o on the second-pass trailing surface has a high uncertainty (20 percent). It can be concluded from the results that the rotation enhances heat transfer performance from the unstabilized surfaces (first pass trailing and second pass leading) and decrease heat transfer from the stabilized surfaces (first pass leading and second pass trailing). Heat transfer enhancement (Nu/Nu_o) of ribbed surfaces is much higher in unstabilized regions than stationary ribbed or rotating smooth surfaces. However, the heat transfer enhancement of ribbed surfaces can be lower in rotation-induced stabilized regions than its nonrotating values at higher rotation conditions. Model B provides higher heat transfer enhancement (Nu/Nu_o) for unstabilized ribbed surfaces than that with Model A.

Figure 8 compares the effects of rotation number on the Nusselt number ratio for two channel orientations: Model A and Model C. Note that Model C orients the heat transfer surfaces at a nonorthogonal orientation to the plane of rotation and the effects of rotation are expected to be less. The smooth channel first-pass results show that the effects of rotation number on leading and trailing surfaces are much less in Model C compared with those in Model A. However, in the second pass the smooth surfaces show similar heat transfer characteristics in both the models. The ribbed surfaces with Model C show fewer variations in the heat transfer coefficients with rotation number than

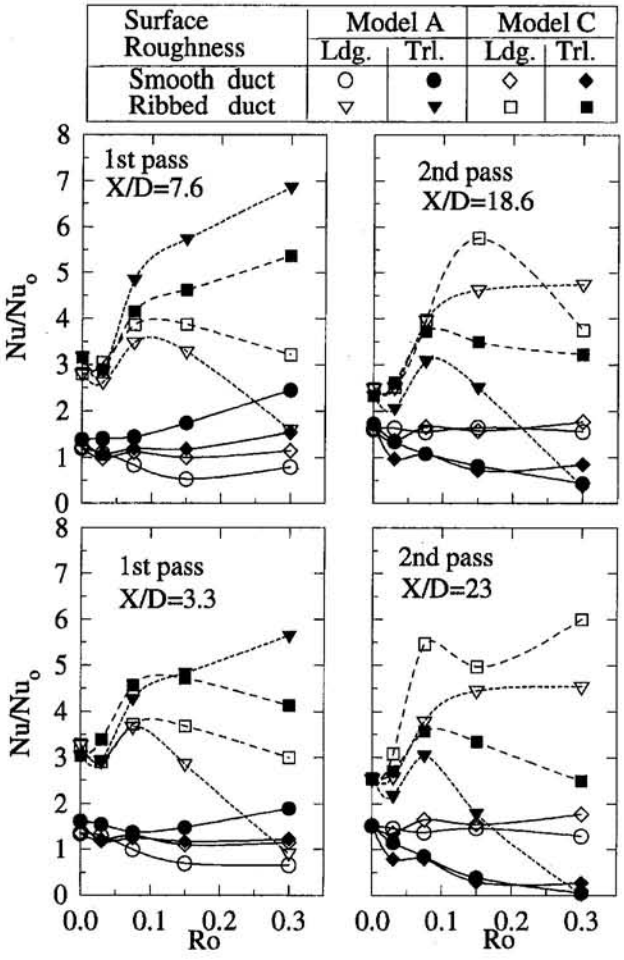


Fig. 8 Effect of rotation number on Nusselt number ratio at selected locations of the channel (comparison of Models A and C)

Downloaded 11 Dec 2010 to 193.140.21.150. Redistribution subject to ASME license or copyright; see http://www.asme.org/terms/Terms_Use.cfm

those observed for Model A. The first pass ribbed Nusselt number ratios of Model C are mostly contained within the upper and lower limits set by the Model A trailing and leading surface Nu/Nu_o ratios. In the second pass the Model C ribbed Nusselt number ratios are higher than the corresponding Model A Nusselt number ratios. It can be said that ribbed Model C has better heat transfer characteristics in the second pass.

Comparison With Previous Results (90 and 60 deg Ribs). Figures 9 and 10 compare the present staggered half-V results with the 90 and 60 deg continuous rib results of Parsons et al. (1995). The 90 and 60 deg results are for $X/D = 7$ and 17. Note that the test facility of Parsons et al. (1995) was similar to ours. Therefore, direct comparison can be made among these heat transfer results. Johnson et al. (1994b) presented model orientation effects on rotating smooth and ribbed channels. Their results on rotation number dependency are for near-turn regions and the results are believed to be affected by the turn regions. Moreover, their rib shape and orientation are also different from ours. Therefore, comparisons with their results are not attempted here.

Figure 9 compares staggered half-V rib results to the 90 deg ribs of Parsons et al. (1995). In general, staggered half-V ribs show higher heat transfer coefficients in Model A, except for the high rotation number (Ro = 0.3). At Ro = 0.3, the first pass leading and second pass trailing surface heat transfer coefficients with staggered half-V ribs are comparable or lower than those with 90 deg ribs. This is perhaps due to the interaction of the secondary flows of rotation and nonorthogonal ribs. Moreover, the R/D ratio of the present configuration is 55, which is higher than the $R/D = 30$ of Parsons et al. (1995). Therefore, buoyancy effects may be more significant in our results compared to those in Parsons et al. (1995). Staggered half-V ribs with Model C orientation show high heat transfer coefficients than those with 90 deg ribs.

Figure 10 compares Nu/Nu_o with staggered half-V ribs and 60 deg angled ribs. In general, heat transfer coefficients are higher with staggered half-V than that with 60 deg angled ribs. One important observation is that the characteristic changes in the Nu/Nu_o with channel orientation (e.g., from Model A to Model C) are similar for the two rib orientations. Figure 10 shows that both staggered half-V and 60 deg angled ribs have an increase in the second pass leading Nu/Nu_o with Model C

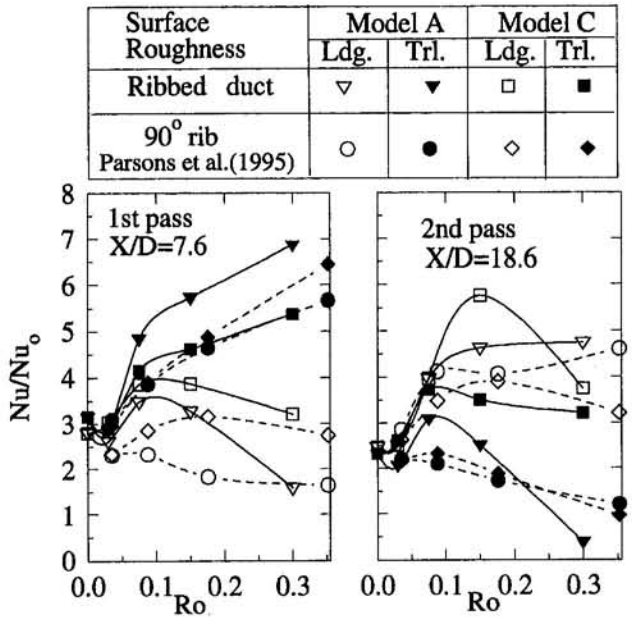


Fig. 9 Comparison of present data with 90 deg rib data of Parsons et al. (1995)

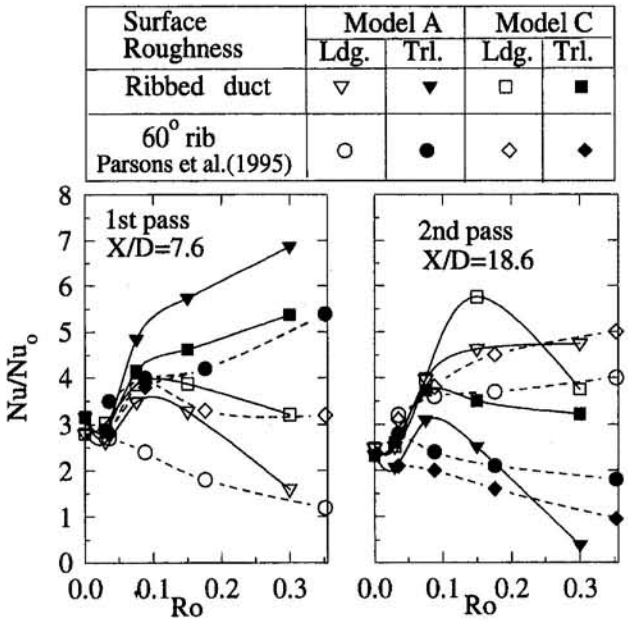


Fig. 10 Comparison of present data with 60 deg rib data of Parsons et al. (1995)

than those with Model A. This increase in Nusselt number ratio is not observed for 90 deg ribs (see Fig. 9), where Model C results are lower than Model A Nu/Nu_o for second pass leading surface.

Conclusion

An experimental heat transfer study is done on a two-pass square channel with rib-roughened walls. The channel rotates about an axis orthogonal to its own. The orientation of the two-pass channel is varied to influence the heat transfer characteristics from the individual surfaces. The experimental study shows that the characteristic dependence of the Nusselt number ratio on the rotation number is different for ribbed walls from that of all smooth walls in similar flow, rotation, and channel orientations. The Nusselt number ratios of stabilized ribbed sides show a mixed dependence on the rotation number. At lower rotation numbers, the Nusselt number ratios on the ribbed stabilized sides increase with an increase in the rotation number. This increase is followed by a decrease with a further increase in rotation number. Staggered half-V ribs perform better than orthogonal 90 deg and nonorthogonal 60 deg angled ribs. Effects of rotation are mostly reduced for nonorthogonal alignment of heat transfer surfaces with respect to the rotation plane (see Model C results).

Acknowledgments

This experimental work was sponsored by the U.S. Department of Energy, Morgantown Energy Technology Center, Cooperative Agreement No. DE-FC21-92 MC 9061. The technical team of Advanced Gas Turbine System Research at Clemson University is Dr. D. B. Fant and Dr. L. P. Golan. Their support is gratefully acknowledged.

References

Fann, S., Yang, W. J., and Zhang, N., 1994, "Local Heat Transfer in a Rotating Serpentine Passage With Rib-Roughened Surfaces," *International Journal of Heat and Mass Transfer*, Vol. 37, No. 2, pp. 217–228.

Han, J. C., Zhang, Y. M., and Kalkuehler, K., 1993, "Uneven Wall Temperature Effect on Local Heat Transfer in a Rotating Two-Pass Square Channel With Smooth Walls," ASME JOURNAL OF HEAT TRANSFER, Vol. 115, pp. 912–920.

Han, J. C., Zhang, Y. M., and Lee, C. P., 1994, "Influence of Surface Heating Condition on Local Heat Transfer in a Rotating Square Channel With Smooth

Downloaded 11 Dec 2010 to 193.140.21.150. Redistribution subject to ASME license or copyright; see http://www.asme.org/terms/Terms_Use.cfm

Walls and Radial Outward Flow," ASME *Journal of Turbomachinery,* Vol. 116, pp. 149–158.

Johnson, B. V., Wagner, J. H., Steuber, G. D., and Yeh, F. C., 1994a, "Heat Transfer in Rotating Serpentine Passages With Trips Skewed to the Flow," ASME *Journal of Turbomachinery,* Vol. 116, No. 1, pp. 113–123.

Johnson, B. V., Wagner, J. H., Steuber, G. D., and Yeh, F. C., 1994b, "Heat Transfer in Rotating Serpentine Passages With Selected Model Orientations for Smooth or Skewed Trip Walls," ASME *Journal of Turbomachinery,* Vol. 116, pp. 738–744.

Johnston, J. P., Halleen, R. M., and Lezius, D. K., 1972, "Effects of Spanwise Rotation on the Structure of Two-Dimensional Fully Developed Turbulent Channel Flow," *Journal of Fluid Mechanics,* Vol. 56, Part 3, Dec., 533–557.

Kline, S. J., and McClintock, F. A., 1953, "Describing Uncertainties in Single-Sample Experiments," *Mechanical Engineering,* Jan., pp. 3–8.

Parsons, J. A., Han, J. C., and Zhang, Y. M., 1994, "Wall Heating Effect on Local Heat Transfer in a Rotating Two-Pass Square Channel With 90° Rib Turbulators," *International Journal of Heat and Mass Transfer,* Vol. 37, No. 9, pp. 1411–1420.

Parsons, J. A., Han, J. C., and Zhang, Y. M., 1995, "Effects of Model Orientation and Wall Heating Condition on Local Heat Transfer in a Rotating Two-Pass Square Channel With Rib Turbulators," *International Journal of Heat and Mass Transfer,* Vol. 38, No. 7, pp. 1151–1159.

Rohsenow, W. M., and Choi, H., 1961, *Heat, Mass and Momentum Transfer,* Prentice-Hall, Inc., New Jersey, pp. 192–193.

Taslim, M. E., Bondi, L. A., and Kercher, D. M., 1991a, "An Experimental Investigation of Heat Transfer in an Orthogonally Rotating Channel Roughened With 45 Deg Criss-Cross Ribs on Two Opposite Walls," ASME *Journal of Turbomachinery,* Vol. 113, pp. 346–353.

Taslim, M. E., Rahman, A., and Spring, S. D., 1991b, "An Experimental Investigation of Heat Transfer Coefficients in a Spanwise Rotating Channel With Two Opposite Rib-Roughened Walls," ASME *Journal of Turbomachinery,* Vol. 113, pp. 74–82.

Wagner, J. H., Johnson, B. V., and Hajek, T. J., 1991a, "Heat Transfer in Rotating Passages With Smooth Walls and Radial Outward Flow," ASME *Journal of Turbomachinery,* Vol. 113, pp. 42–51.

Wagner, J. H., Johnson, B. V., and Kopper, F. C., 1991b, "Heat Transfer in Rotating Serpentine Passages With Smooth Walls," ASME *Journal of Turbomachinery,* Vol. 113, pp. 321–330.

Wagner, J. H., Johnson, B. V., Graziani, R. A., and Yeh, F. C., 1992, "Heat Transfer in Rotating Serpentine Passages With Trips Normal to the Flow," ASME *Journal of Turbomachinery,* Vol. 114, pp. 847–857.

Zhang, Y. M., Han, J. C., Parsons, J. A., and Lee, C. P., 1995, "Surface Heating Effect on Local Heat Transfer in a Rotating Two-Pass Square Channel With 60 Deg Angled Rib Turbulators," ASME *Journal of Turbomachinery,* Vol. 117, pp. 272–280.

Downloaded 11 Dec 2010 to 193.140.21.150. Redistribution subject to ASME license or copyright; see http://www.asme.org/terms/Terms_Use.cfm

G. Wang

K. Stone

S. P. Vanka

Department of Mechanical and Industrial Engineering, University of Illinois at Urbana–Champaign, Urbana, IL 61801

Unsteady Heat Transfer in Baffled Channels

In this paper, the enhancement of heat transfer due to unsteady flow in channels with in-line and staggered baffles is investigated through the numerical solution of the governing unsteady fluid flow and energy equations with periodicity in the streamwise direction. For the inline configuration, the flow becomes naturally unsteady at a critical Reynolds number (Q/ν) around 110. For the staggered case, this value is around 200. Significant increases in heat transfer rate are observed once the flow becomes unsteady. Results for several Reynolds numbers up to 500 are presented. The present results can be valuable to the design and operation of compact heat exchangers used in process industry.

1 Introduction

Many compact heat exchangers currently operate in the laminar flow regime. This is because the flow velocities and passage sizes are small and consequently the Reynolds numbers are low. Furthermore, the passage lengths are large, so the flow is fully developed over much of the channel. In order to enhance the heat transfer rates over the laminar fully developed values, devices that interrupt the growth of the boundary layers are commonly introduced. The periodic replenishment of the boundary layer fluid with the core fluid results in steeper gradients of temperature (and concentration) and consequently higher rates of heat (mass) transfer. A variety of such interruption devices have been proposed in the past. These have included placement of staggered and in-line baffles, vortex generators in the form of winglets on the channel surface, louvers, internal obstacles, etc. By deflecting the core fluid toward the channel walls, enhanced mixing of the core fluid and the boundary layers occurs. An extensive coverage of the various heat transfer augmentation devices is given by Webb (1994). The mixing between the core and boundary-layer fluids can be also increased by creating an unsteadiness in the flow either through natural transitioning or through external forcing of the inflow. Such self-sustained and forced oscillations are observed to increase considerably the rates of heat transfer in grooved channels (Ghaddar et al., 1986a, b), in corrugated passages (Greiner et al., 1991, 1995) and in wavy passages (Guzmán and Amon, 1994; Wang and Vanka, 1995a).

Placement of baffles or obstacles on walls of a channel interrupts the development of the laminar boundary layers and causes the flow to separate at the fixed edges, creating a recirculation zone downstream. The recirculating eddies carry the near-wall fluid to the edge of the core and then diffuse away the heat. Repeated placement of such obstructions prevents the development of the boundary layers, leading to enhanced heat transfer rates. Furthermore, the baffles provide additional surface area for heat transfer. Rowley and Patankar (1984) studied the effectiveness of circumferentially finned tubes by solving the governing steady-state equations. Periodic boundary conditions were used in the streamwise direction, simulating an infinite repetition of the geometry. It was observed that for fluids like air, such fins actually lower the heat transfer rates. In a subsequent study, Kelkar and Patankar (1987) analyzed a channel with staggered baffles, hoping that the staggered arrangement would increase the heat transfer. This was indeed observed at high Prandtl numbers and for long fins. For short fins and low Prandtl numbers there was a slight decrease in the heat transfer coefficient. Further, as the blockage ratio was progressively increased, the attractiveness of the baffled channel as an enhancement device decreased because of the significant increase in the pressure drop.

Berner et al. (1984) conducted experiments dealing with laminar and turbulent flow around segmented baffles in a channel. Reynolds numbers in the range of 600–10,500 and baffle cuts of 10–50 percent were considered. Data on the mean velocities and turbulence intensities were obtained using LDV. At Re = 600, the flow was visualized to be steady, although the appearance of small unsteady eddies is hinted at. Habib et al. (1988) used the standard $k-\epsilon$ turbulence model to compute the turbulent flow and heat transfer in a channel with segmented, staggered baffles. It was found that augmentation of heat transfer was obtained with increases in the Reynolds number and baffle height and with decreases in baffle spacing. Substantial increases in heat transfer were observed for high-Prandtl-number fluids. Recently Anand et al. (1995) analyzed the periodic fully developed flow and heat transfer in a rectangular channel with baffles placed in-line at the center of the channel. The flow was considered to be steady and periodic. Effects of blockage height, plate thickness ratio, pitch ratio, Reynolds number, and Prandtl number were studied. Based on pressure drop considerations, it was concluded that blockage ratios (height of baffle/channel height) greater than 0.6 are not desirable.

All of the above-mentioned numerical studies considered the flow to be steady. Thus, only the steady-state equations were solved. However, the assumption of steady flow in such periodically repeating channels appears to be questionable even at modest Reynolds numbers. Recently, several studies have been reported in different types of periodic channels, which demonstrate that self-sustained instabilities arise at relatively low Reynolds numbers. As the Reynolds number is increased progressively beyond this critical value the flow evolves into a chaotic state, eventually becoming turbulent. The self-sustained oscillatory flow is observed to increase significantly the heat transfer rate in wavy passages (Guzmán and Amon, 1994; Wang and Vanka, 1995a), corrugated passages (Greiner et al., 1991), grooved channels (Ghaddar et al., 1986a, b) and communicating channels (Amon et al., 1992). Howes et al. (1991) recently studied the effects of natural as well as forced oscillations in an in-line baffled channel. Both the mean and the oscillatory flow Reynolds numbers were varied, and the mixing process was studied through particle transport equations. The flow equations were numerically solved in the stream function–vorticity form with periodic boundary conditions in the streamwise direction. It was observed that the flow became naturally unsteady around a Reynolds number of 100, followed by increasingly

Contributed by the Heat Transfer Division for publication in the JOURNAL OF HEAT TRANSFER. Manuscript received by the Heat Transfer Division May 10, 1995; revision received April 22, 1996. Keywords: Flow Separation, Flow Transition, Forced Convection. Associate Technical Editor: S. Ramadhyani.

Copyright © 1996 by ASME

Downloaded 11 Dec 2010 to 193.140.21.150. Redistribution subject to ASME license or copyright; see http://www.asme.org/terms/Terms_Use.cfm

chaotic behavior when the Reynolds number was increased further. This led them to conclude that baffled channels can indeed be attractive as heat transfer enhancement devices, contrary to the conclusions of Rowley and Patankar (1984) and Kelkar and Patankar (1987). The effect of an external oscillation in the subcritical and supercritical regimes was also studied. Roberts (1994) followed up this investigation with a complimentary experiment in which the flow was visualized using neutral buoyant particles and sheet light illumination. It was observed that the flow became unsteady at a Reynolds number between 100 and 110. The experiments confirmed that the flow undergoes a supercritical Hopf bifurcation to a periodic state during which the velocities, heat transfer rate, and friction factor oscillate at a characteristic frequency. Upon further increase in the Reynolds number, the flow became very complex, with the formation of multiple eddies and the onset of spanwise variations. The numerical model produced an aperiodic behavior at a Reynolds number of 400. The instabilities are argued to be of the same kind as those in grooved channels and wavy passages (i.e., Tollmien-Schlichting waves), but the frequency was observed to be quite different from the *T-S* waves in a straight channel. This was attributed to the complexity of the mean flow due to the separated zones.

The effects of self-sustained oscillations in baffled channels are of interest to heat exchanger design because the critical Reynolds numbers at which these are manifested are quite low. Furthermore, if the blockage ratio is kept small, the increase in the pressure drop can also be kept small and there is not much penalty on the pumping power. The increased pressure drop can be afforded in many cases. In previous studies of Roberts (1994) and Howes et al. (1991), quantitative information on the benefits and penalties was not presented. Also, only the in-line configuration was considered. The present study was therefore undertaken to provide information on the unsteady flow and heat transfer processes in baffled channels and to quantify the beneficial effects of self-sustained oscillations. The time-dependent Navier–Stokes equations in primitive variable form are numerically integrated using a collocated grid finite-volume procedure. Both in-line and staggered baffle arrangements are considered. Calculations have been performed at a fixed value of the baffle height ratio for several flow Reynolds numbers (Q/ν) ranging from subcritical to supercritical values. The effects of the unsteady flow on the heat transfer and friction are presented together with representative time signals of the flow variables. The signals provide information on the dominant frequencies in the flow, and the manner in which they change as the Reynolds number is varied. Such information is important for resonant forcing of the flow, which may further increase the heat transfer rates.

In the present study, the flow is assumed to be two dimensional. This assumption is made primarily to keep the computational times manageable. Well-resolved three-dimensional computations will require considerably large CPU times to conduct parametric tests such as those conducted in this study. Thus, we have not taken into account the effects of three dimensionality that may arise due to either secondary instabilities or end walls. Also, flow and heat transfer in the entrance region are not considered, as the flow is assumed to be streamwise periodic. The instability considered here is simulated to be of absolute type, as any perturbation leaving the channel is recycled back to the entrance. Thus, the results are appropriate for an infinite array of baffles.

Section 2 presents the governing equations, numerical procedure, and the implementation of the periodicity conditions. The computational details and grid sensitivity tests are described in Section 3. The results for both staggered and in-line cases are next presented in Section 4, concluding the paper with a summary in Section 5.

2 Conservation Equations and Numerical Procedure

In the present study, the flow is considered to be two dimensional with no spanwise variation. The nondimensional governing equations for the flow and energy transport can be written as:

$$\nabla \cdot \mathbf{u} = 0 \tag{1}$$

$$\frac{\partial \mathbf{u}}{\partial t} + \nabla \cdot (\mathbf{uu}) = -\nabla p + \frac{1}{\mathrm{Re}} \nabla^2 \mathbf{u} \tag{2}$$

$$\frac{\partial \theta}{\partial t} + \theta \Lambda + \nabla \cdot (\mathbf{u}\theta) = \frac{1}{\mathrm{Re\ Pr}} \nabla^2 \theta \tag{3}$$

where $\theta = (T - T_w)/(T_{m1} - T_w)$, Re and Pr are the Reynolds number and Prandtl number, respectively. Here, T_w is the wall temperature, and T_{m1} is the mixed mean fluid temperature (mass-averaged temperature) evaluated at the inlet section of the computational domain. We have also assumed the density to be unity. The unknown function Λ in the energy equation is given by

Nomenclature

$\tilde{D}_h$ = hydraulic diameter, m
D_h = nondimensional hydraulic diameter
f = friction factor = $H/(2L) \times \Delta p/(\rho u_m^2)$; also frequency, 1/s
$G(f)$ = energy contained at a certain frequency
h = heat transfer coefficient, W/m^2 K
$\tilde{H}$ = interwall spacing, m
H = nondimensional interwall spacing = 1
k = thermal conductivity, W/m K
L = nondimensional interbaffle spacing on the same side
Nu = logarithmic mean Nusselt number = $h\tilde{D}_h/k$
Nu′ = standard deviation of the mean Nusselt number Nu
p = nondimensional pressure
Pr = Prandtl number = ν/α
Q = nondimensional volumetric flow rate
Re = Reynolds number = $\tilde{u}_{m1}\tilde{H}/\nu$
t = nondimensional time = $\tilde{t}\tilde{H}/\tilde{u}_{m1}$
T = temperature, K
$\tilde{u}$ = Cartesian velocity component in the x direction, m/s
u = nondimensional Cartesian velocity component
U = nondimensional volume flux perpendicular to the lines of constant x
$\tilde{v}$ = Cartesian velocity component in the y direction, m/s
v = nondimensional Cartesian velocity component
V = nondimensional volume flux perpendicular to the lines of constant y
x = nondimensional Cartesian coordinate
y = nondimensional Cartesian coordinate
α = thermal diffusivity, m^2/s
λ = length of the channel, m
ν = kinematic molecular viscosity, m^2/s
θ = nondimensional temperature = $(T - T_w)/(T_{m1} - T_w)$
ρ = nondimensional density = 1

Subscripts and Superscripts

in = quantities evaluated at the inlet
m = mean property evaluated at a line of constant y
$m1$ = mean property evaluated at the inlet
$m2$ = mean property evaluated at the outlet
n = time step
w = quantity evaluated at the wall

Downloaded 11 Dec 2010 to 193.140.21.150. Redistribution subject to ASME license or copyright; see http://www.asme.org/terms/Terms_Use.cfm

$$\Lambda = \frac{1}{T_{m1} - T_w} \frac{\partial}{\partial t} (T_{m1} - T_w) \tag{4}$$

This term results from the present normalization procedure as T_{m1} is a function of time when the flow is unsteady. This must be determined in an iterative fashion.

These conservation equations are solved on a Cartesian stretched grid. The equations are integrated using a two-stage fractional step with Adams–Bashforth differencing for the convection terms and a Crank–Nicolson scheme for the diffusion terms. The spatial discretization uses a collocated arrangement with the two Cartesian velocities and pressure situated at the centers of discrete finite volumes. The continuity equation is satisfied by the volume fluxes located at the cell faces. A Poisson equation is solved to determine the pressure field. The overall algorithm is second-order accurate in time and space. Complete details of the numerical procedure and the validation of the computer code can be found in Wang and Vanka (1995a).

The instantaneous pressure is decomposed into a mean part that is assumed to vary linearly in x, and a fluctuating part that varies in x and y (Ghaddar et al., 1986c). Thus

$$p(x, y, t) = \prod (t)x + p'(x, y, t) \tag{5}$$

where $\prod (t)$ is the mean pressure gradient. This gradient is adjusted every time step to satisfy the fixed mass flow condition. Boundary conditions are imposed on intermediate velocities and on the fluctuating part of the pressure.

The determination of the temperature distribution is complicated by the presence of the unknown function Λ in the energy equation. The coupling between θ and Λ can be solved iteratively. First, the energy equation is solved with periodic boundary conditions

$$\frac{\theta(0, y, t)}{\theta_{m1}} = \frac{\theta(L, y, t)}{\theta_{m2}} \tag{6}$$

and a guessed value of Λ. Then, the inlet temperature θ_{in} is adjusted to satisfy the constraint

$$\int_{in} \theta u dy = \int_{in} u dy \tag{7}$$

such that the mean temperature θ_{m1} is unity at the entrance. A new value of Λ is then computed by summing all the discrete finite difference equations at the inlet plane. This calculation procedure is repeated until a converged solution is obtained. The periodicity condition for the temperature field is imposed on the ratio of the local pointwise temperature to the local mean value.

The computer code was previously validated for a number of flow problems including the unsteady flow and heat transfer in a wavy channel. Good comparisons with known numerical solutions as well as experimental data were observed.

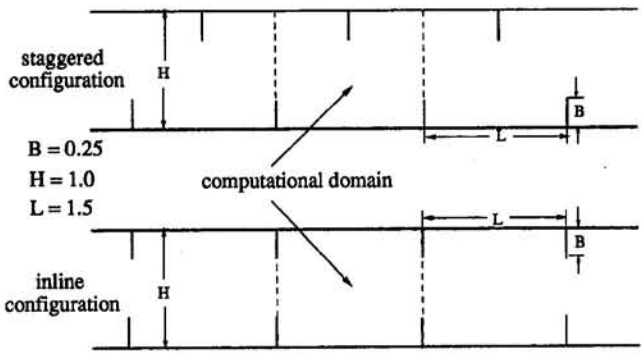


Fig. 1 Geometries of the staggered and in-line baffle channels

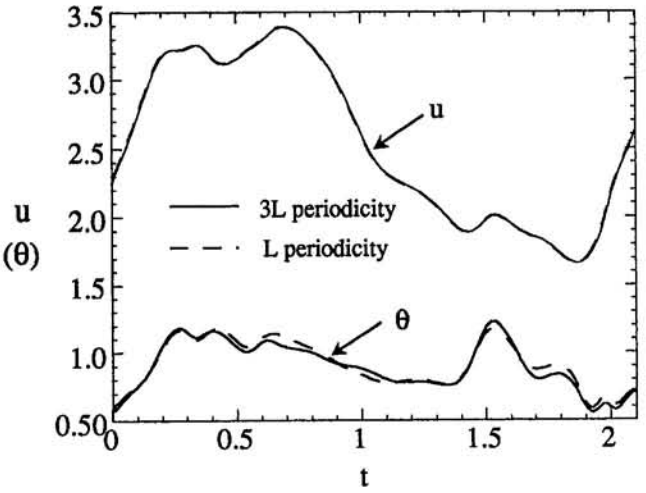


Fig. 2 Temporal signals of u velocity and temperature at the location ($L/4$, $H/2$). The calculations were performed for a domain of $3L$ and L for the staggered case.

3 Computational Details

The geometries considered for the present study are shown in Fig. 1, and the dimensions are identical to the experimental configuration of Roberts (1994). For the staggered arrangement, the top plate is moved to the right by half the interbaffle spacing. The computational domain and the grid size for both configurations, however, are the same. To ascertain the validity of the periodic boundary condition for a computational domain of length L, calculations were also performed for a computational domain of length $3L$ at a Reynolds number of 300 for the staggered case. At this Reynolds number, the flow is unsteady. Finite volume grids with 96×64 and 288×64 cells were used for the two calculations. Figure 2 shows the time-varying velocity and temperature at one representative location ($L/4$, $H/2$). It can be seen that the velocity signals match exactly with each other. The temperature signals differ slightly, but this is believed to be due to the interpolation practices at the boundaries and not due to the size of computational domain. Our observations are consistent with those of Amon and Mikic (1990) for a grooved channel and Wang and Vanka (1995a) for a wavy channel. All subsequent calculations were therefore performed for a computational domain of length L.

The computational domain was discretized by a stretched grid consisting of 192×128 control volumes. The adequacy of this fine grid was examined by performing calculations with a coarser grid containing half as many control volumes in each direction (that is, 96×64 cells). Figures 3 and 4 show comparisons of u-velocities and temperatures obtained on the two grids for the staggered baffle case. Figure 3 shows the u-velocity and temperature profiles at a Reynolds number of 150 for which the flow is steady. It can be seen that the two grids give identical results. Figure 4 shows the comparison in the unsteady regime at a Reynolds number of 300. Here the u velocity and the temperature at a point ($L/4$, $H/2$) are plotted in time. The two grids gave nearly the same variation, but small differences are seen in the regions of the valleys. Grids finer than 192×128 grid were not considered in this study due to associated computational costs; however, all calculations reported in this paper were performed with the 192×128 grid to minimize the errors. Because the scheme is second-order accurate in time and space, the differences between results from another finer (384×256) grid and those of the 192×128 grid should be four times smaller than the difference between results of the 192×128 and the 96×64 grids. This gives an indication of the possible errors in the present results. The time step for these calculations was 0.001 nondimensional units at low Reynolds numbers and

Downloaded 11 Dec 2010 to 193.140.21.150. Redistribution subject to ASME license or copyright; see http://www.asme.org/terms/Terms_Use.cfm

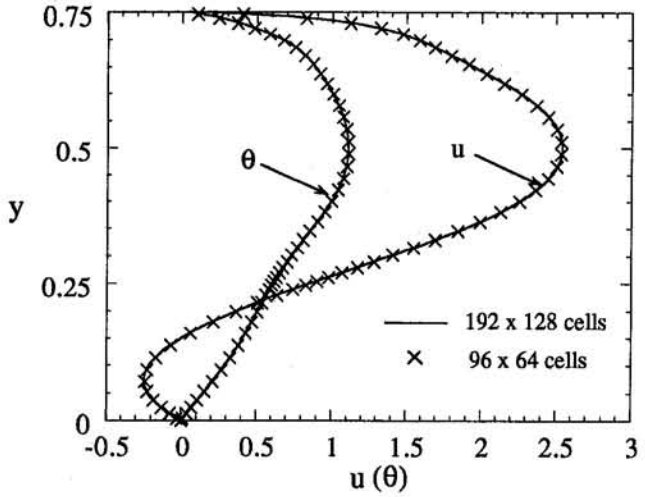


Fig. 3 The centerline u velocity and temperature profiles at $x/L = 0.5$ for Re = 150

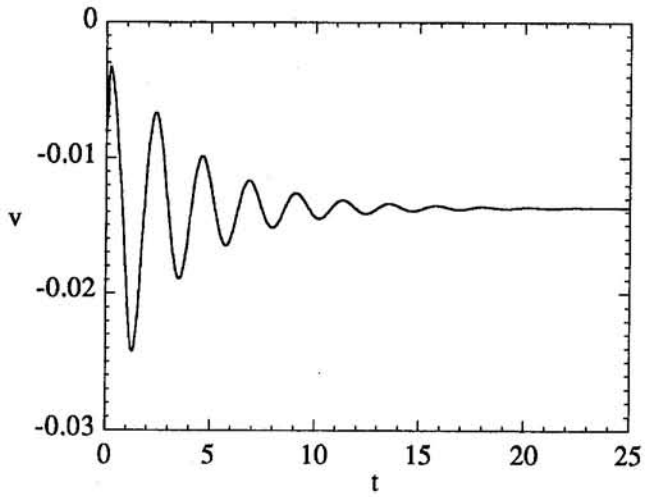


Fig. 5 Temporal variation of v velocity at a point ($L/4$, $H/2$) for Re = 150

0.0008 units at the higher Reynolds numbers, and the integrations were carried out for long times to infer the various frequencies in the time signals. The calculations were performed on an IBM RS6000 workstation.

4 Results and Discussion

As mentioned earlier, we have considered two configurations of the baffled channel. For both these configurations, the flow Reynolds number was systematically increased from a value at which the flow is thought to be steady to high values where the flow is known to be unsteady (Roberts, 1994). A steady flow was generated first at a low Reynolds number, and subsequent calculations at higher Reynolds numbers were started from solutions obtained at the adjacent low Reynolds number. To ascertain whether the flow was unsteady, a perturbation was introduced for one time step, and then removed. The flow was then computed for a long time to see if the oscillations in the time signal grew or decayed. This also provided information on the growth/decay rate of the least stable oscillatory mode. Results are first presented for the staggered configuration, followed by those for the in-line arrangement.

Staggered Configuration. For the staggered configuration, both the 96 × 64 and 192 × 128 grids predicted a steady solution up to a Reynolds number of 150. The calculated Nusselt number is nearly constant at a value of 7.9, which is not significantly larger than the value of 7.54 for a channel with no baffles. Figure 5 shows the plot of the v velocity oscillation decaying in time at the least stable oscillatory frequency. The frequency of this mode is observed to be 0.45, which matches reasonably well with the value of 0.467 computed by Roberts (1994) for the in-line configuration. As the Reynolds number increased to 200, the amplitude of the oscillatory mode grew with time and eventually reached a steady value. Calculation with the 96 × 64 grid showed a slow decay rather than growth. This difference is due to the numerical damping caused by the coarser grid. Thus, it is inferred that the transition Reynolds number is close to a value of 200. Although it is possible to obtain a more precise estimate through a number of runs with fine spacing in Re, the approximate value of 200 is adequate for characterizing the flow in the context of the present paper. All calculations reported in this paper were performed using the 192 × 128 grid.

Figure 6 shows the time variation of the Nusselt number for four selected Reynolds numbers (Re = 200, 300, 400, and 500). The Nusselt number is the logarithmic mean value defined[1] as:

$$\mathrm{Nu} = \frac{h\tilde{D}_h}{k} = -\mathrm{Re}\ \mathrm{Pr}\ \frac{D_h}{2L} \ln \theta_{m2} \tag{8}$$

At Re = 200, there is a single dominant frequency of periodic motion equal to 0.47 (Fig. 7(a)). The velocity signals display a similar behavior. The Nusselt number oscillates between 7.4 and 9.3 with a mean value of 8.4. Thus, there is a slight increase from the steady value of 7.9 (Re = 150). This increase is due to the exchange of the core fluid with the near-wall fluid through the oscillatory motion.

The flow remains oscillatory as the Reynolds number is increased further, and the Nusselt number is seen to increase with the Reynolds number. At Re = 500, the Nusselt number oscillates between 136 and −16, with a mean value of 34. The log-mean Nusselt number becomes negative at the valleys, but this does not mean that heat is locally transferred from the walls. The negative value is an artifact of the definition of the log-mean temperature difference. As the Reynolds number is increased, additional frequencies arise in the time signal (Fig. 7(b)), with the flow becoming chaotic and eventually turbulent. The scenario by which the flow becomes chaotic and transitions to turbulence is an interesting area of research in nonlinear

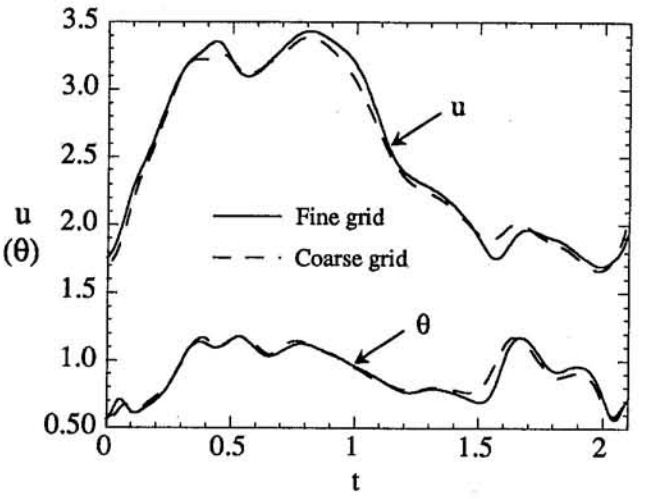


Fig. 4 Temporal variation of u velocity and temperature at a point ($L/4$, $H/2$) for the staggered case at Re = 300

[1] In the current formula for the Nusselt number, the surface area of the baffle is not included. If it is included the Nusselt numbers reported here should be multiplied by 0.75 for the present geometry.

Downloaded 11 Dec 2010 to 193.140.21.150. Redistribution subject to ASME license or copyright; see http://www.asme.org/terms/Terms_Use.cfm

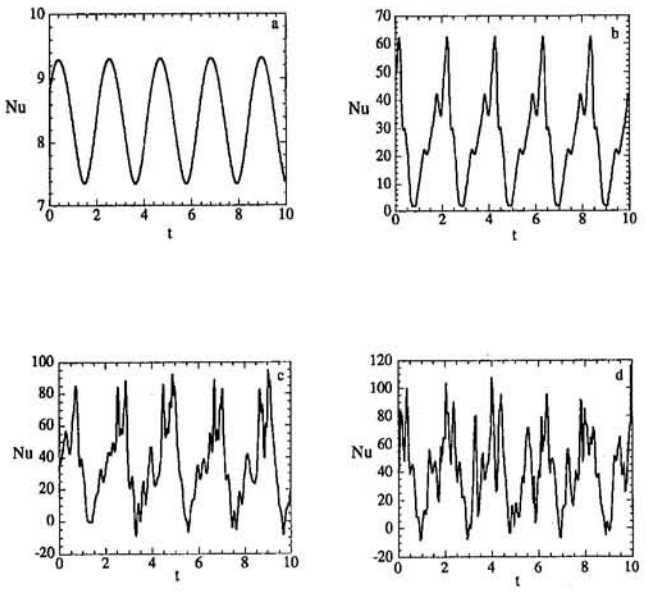


Fig. 6 Temporal variation of the Nusselt number for the staggered case: (*a*) Re = 200; (*b*) Re = 300; (*c*) Re = 400; (*d*) Re = 500

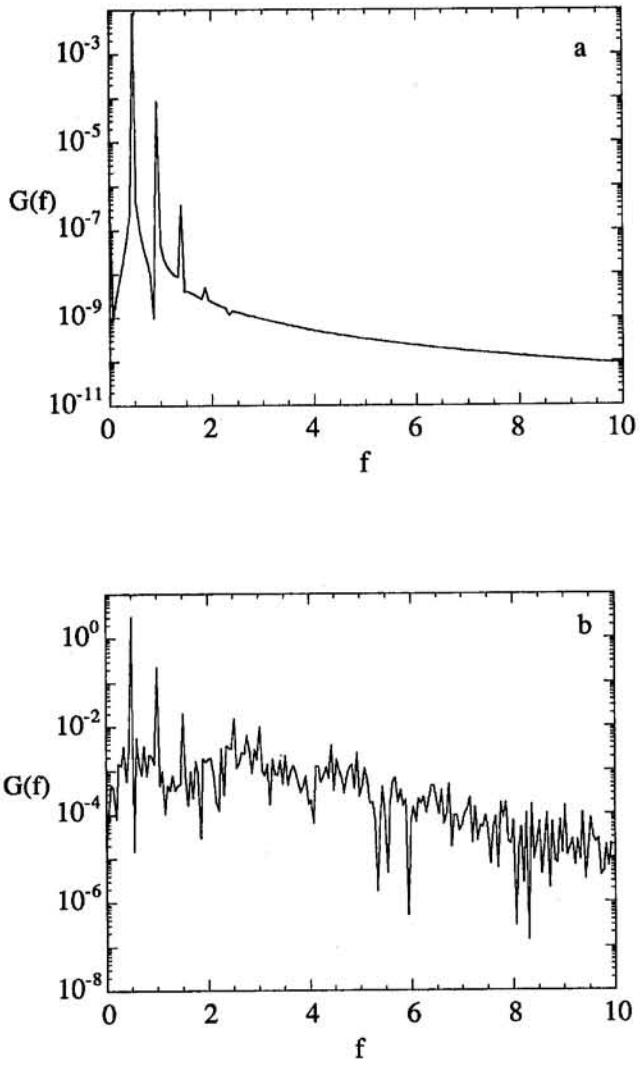
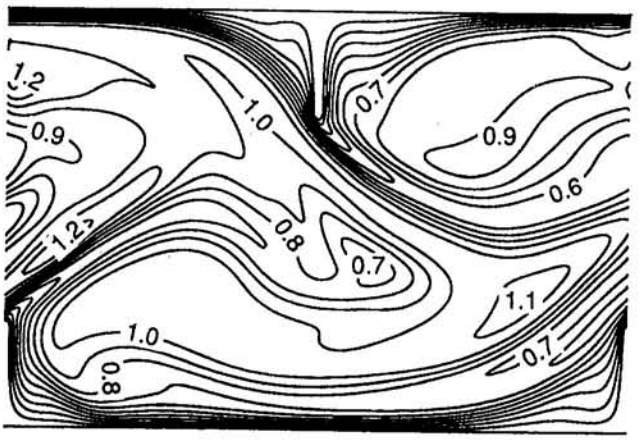
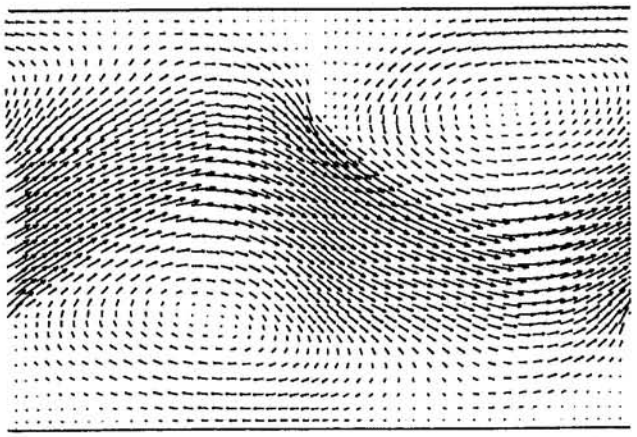


Fig. 7 Fourier spectrum of v velocity at the point ($L/4$, $H/2$) for the staggered case: (*a*) Re = 200; (*b*) Re = 500



(a)



(b)

Fig. 8 Instantaneous temperature distribution (*a*) and velocity vectors (*b*) for the staggered case at Re = 500

dynamics. In a recent study in wavy channels (Wang and Vanka, 1995b), we had observed that the flow becomes chaotic after the appearance of three incommensurate frequencies, following the Ruelle–Takens–Newhouse scenario. A similar scenario is postulated here, although a detailed analysis has not yet been conducted.

Figure 8 shows an instantaneous plot of the nondimensional temperature distribution and velocity vectors at Re = 500. At this Reynolds number, the flow has a complex dynamic structure, which cannot be described by one instantaneous picture. However, one can see the roll-up of the shear layer that forms at the baffle edge, forming vortices that re-enter the flow domain of the adjacent passage. In our computations, such a condition is simulated by imposing periodicity in the streamwise (x) direction. As expected, the gradients in the temperature are the largest in the near-wall region and in the shear layers. Details of the time evolution of the vortical structures in one period of oscillation have been illustrated in movies of the isotherms and are available on the research group's web site (http://www.mie.uiuc.edu/research-instruction/research/computational-fluid-dyn).

In-Line Configuration. Next, the in-line configuration is considered. The steady flow field for this configuration is different from that for the staggered arrangement. The flow field now contains a cavity region between adjacent baffles, with a central core flow. Depending on the baffle height, a strong or weak

Downloaded 11 Dec 2010 to 193.140.21.150. Redistribution subject to ASME license or copyright; see http://www.asme.org/terms/Terms_Use.cfm

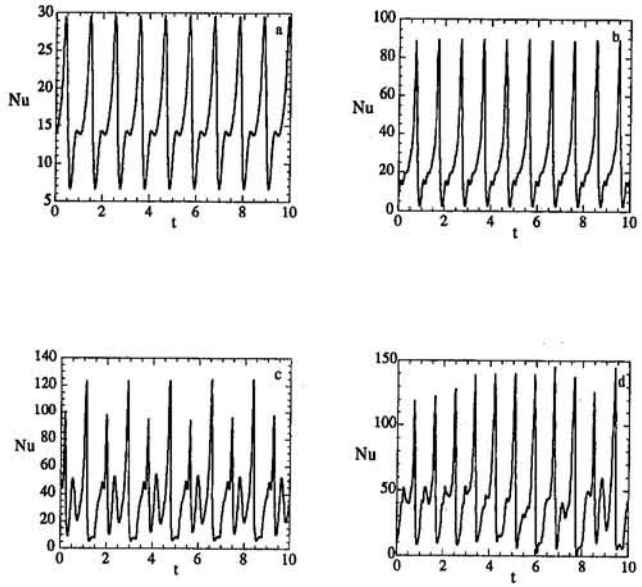
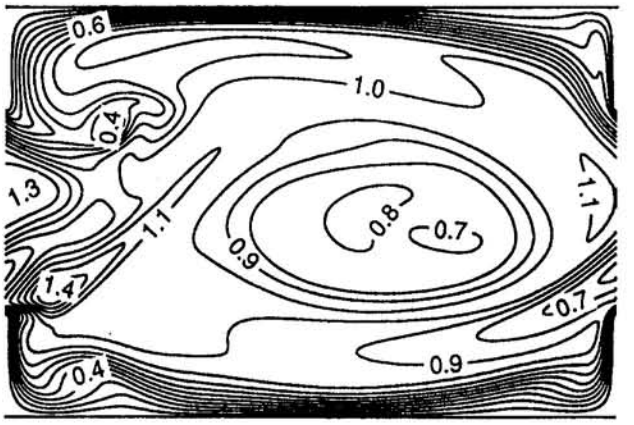


Fig. 9 Temporal variation of the Nusselt number for the in-line case: (*a*) Re = 200; (*b*) Re = 300; (*c*) Re = 400; (*d*) Re = 500

central jet is formed. In contrast with the staggered arrangement, there is no flow turning. For this configuration also, we first studied the decay of a perturbation in the steady regime. The frequency of the least stable mode was found to be 0.48. This compares with the value of 0.467 obtained by Roberts (1994), and the differences can be attributed to the different numerical procedures and the grids used. By successively increasing the Reynolds number and observing the growth rate as a function of the Reynolds number, we infer that for this geometry the first Hopf bifurcation occurs around Re = 110. This value is about the same as that obtained in Roberts' simulations and experiments. Since Roberts presented the fluid mechanics of this arrangement in detail, we shall concentrate here only on the heat transfer aspects. Figure 9 shows the time signal of the log-mean Nusselt number at four Reynolds numbers (Re = 200, 300, 400, and 500). Similar to the staggered case, the signals show the chaotic multiple frequencies at Reynolds numbers of 400 and 500. The signals again indicate a large variation in the Nusselt number around a mean that also increases with Reynolds number.

Figure 10 shows the instantaneous temperature profile and velocity vectors for this case, at Re = 500. One can notice the large recirculation of the flow in the cavity, which exchanges the core fluid with the near-wall fluid. As an in-depth discussion of the fluid mechanics was already given by Roberts (1994), we shall not dwell on this issue, but point to the different flow patterns between the inline and staggered arrangements. The time-averaged log-mean Nusselt numbers and friction factors $[H/(2L) \times \Delta p/(\rho u_m^2)]$ for various Reynolds numbers for both the staggered and in-line cases are shown in Fig. 11. The Nusselt number increases monotonically with Reynolds number, but the rate of growth decreases with increasing Reynolds number. The in-line baffle configuration appears to provide a slightly larger Nusselt number than the staggered case at the same Reynolds number. Also, the associated friction factors are nearly the same. The corresponding friction factor and Nusselt number for a straight channel are 6/Re and 7.54, respectively. Thus, it may be concluded that once the flow becomes unsteady, both configurations are attractive devices for heat/mass transfer enhancement. The time-averaged Nusselt numbers and their standard deviations are shown in Fig. 12 as a function of the pumping power ($f \times \mathrm{Re}^3$).



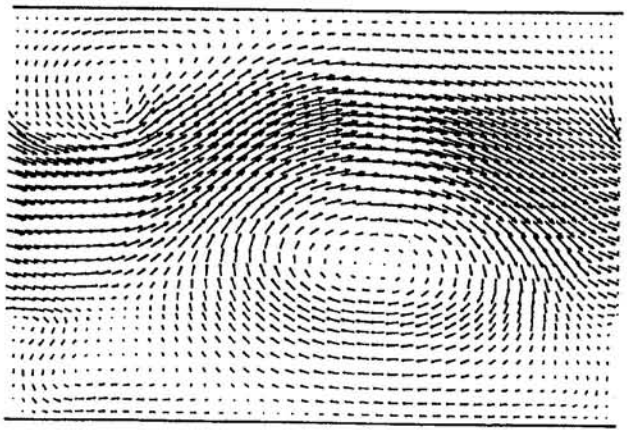


Fig. 10 Instantaneous temperature distribution (*a*) and velocity vectors (*b*) for the inline case at Re = 500

5 Summary

In the current paper, we have presented results from numerical calculations of the unsteady flow and heat transfer processes in channels with streamwise periodic baffles attached to the

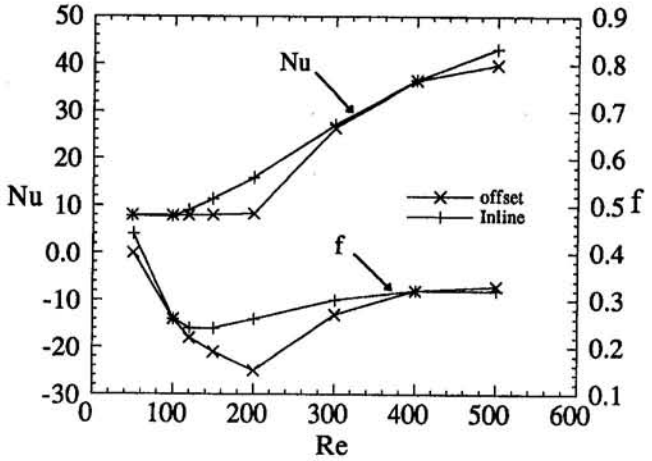


Fig. 11 Time-averaged Nusselt numbers and friction factors at various Reynolds numbers

Downloaded 11 Dec 2010 to 193.140.21.150. Redistribution subject to ASME license or copyright; see http://www.asme.org/terms/Terms_Use.cfm

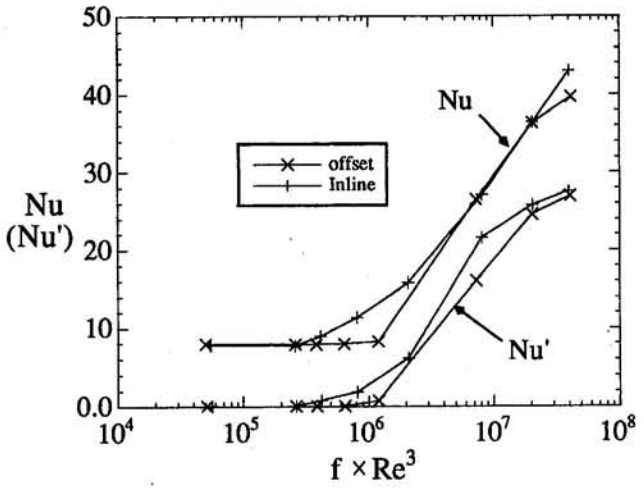


Fig. 12 Time-averaged Nusselt numbers and their standard deviations as a function of the pumping power

channel walls. Both in-line and staggered cases have been considered. The governing fluid flow equations are solved with a finite volume procedure using a fractional step temporal discretization. In both configurations, a Hopf bifurcation is seen to occur at the first critical Reynolds number (~110 for inline and ~200 for staggered), leading to an unsteady time-periodic flow. As a consequence of the self-sustained oscillations, there is enhanced mixing between the core fluid and the fluid near the walls. The rates of heat transfer are significantly enhanced, proving these passages to be attractive as compact heat exchangers. However, associated with the enhanced heat transfer is a higher friction factor, which also increases the required pumping power. Despite this increase in pumping power, the baffled channels are usefully employed in the regime where the flow is unsteady. Further work will examine the developing region and the effect of three dimensionality on the heat transfer and friction.

References

Amon, C. H., Majumdar, D., Herman, C. V., Mayinger, F., Mikic, B. B., and Sekulic, D. P., 1992, "Numerical and Experimental Studies of Self-Sustained Oscillatory Flows in Communicating Channels," *International Journal of Heat and Mass Transfer,* Vol. 35(11), pp. 3115–3129.

Amon, C. H., and Mikic, B. B., 1990, "Numerical Prediction of Convective Heat Transfer in Self-Sustained Oscillatory Flows," *Journal of Thermophysics,* Vol. 4, pp. 239–246.

Anand, N. K., Chin, C. D., and McMath, J. G., 1995, "Heat Transfer in Rectangular Channels With a Series of Normally In-Line Positioned Plates," *Numerical Heat Transfer,* Vol. 27, pp. 19–34.

Berner, C., Durst, F., and McEligot, D. M., 1984, "Flow Around Baffles," ASME JOURNAL OF HEAT TRANSFER, Vol. 106, pp. 743–749.

Brandt, A., 1977, "Multi-Level Adaptive Solutions to Boundary-Value Problems," *Mathematics of Computation,* Vol. 31(138), pp. 333–390.

Ghaddar, N. K., Karniadakis, G. E., and Patera, A. T., 1986a, "A Conservative Isoparametric Spectral Element Method for Forced Convection; Application to Fully Developed Flow in Periodic Geometries," *Numerical Heat Transfer,* Vol. 9, pp. 277–300.

Ghaddar, N., Magen, M., Mikic, B. B., and Patera, A. T., 1986b, "Numerical Investigation of Incompressible Flow in Grooved Channels. Part 2. Resonance and Oscillatory Heat Transfer Enhancement," *Journal of Fluid Mechanics,* Vol. 168, pp. 541–567.

Ghaddar, N. K., Korczak, K. Z., Mikic, B. B., and Patera, A. T., 1986c, "Numerical Investigation of Incompressible Flow in Grooved Channels. Part 1. Stability and Self-Sustained Oscillations," *Journal of Fluid Mechanics,* Vol. 163, pp. 99–127.

Greiner, M., Chen, R.-F., and Wirtz, R. A., 1991, "Enhanced Heat Transfer/Pressure Drop Measured From a Flat Surface in a Grooved Channel," ASME JOURNAL OF HEAT TRANSFER, Vol. 113, pp. 498–501.

Greiner, M., Chen, R.-F., and Wirtz, R. A., 1995, "Augmented Heat Transfer in a Recovery Passage Downstream From a Grooved Section: An Example of Uncoupled Heat/Momentum Transport," ASME JOURNAL OF HEAT TRANSFER, Vol. 117, pp. 303–308.

Guzmán, A. M., and Amon, C. H., 1994, "Transition to Chaos in Converging-Diverging Channel Flows: Ruelle–Takens–Newhouse Scenario," *Physics of Fluids,* Vol. 6(6), pp. 1994–2002.

Habib, M. A., Attaya, A. E., and McEligot, D. M., 1988, "Calculation of Turbulent Flow and Heat Transfer in Channels With Streamwise-Periodic Flow," ASME *Journal of Turbomachinery,* Vol. 110, pp. 405–411.

Howes, T., Mackley, M. R., and Roberts, E. P. L., 1991, "The Simulation of Chaotic Mixing and Dispersion for Periodic Flows in Baffled Channels," *Chemical Engineering Science,* Vol. 46(7), pp. 1669–1677.

Kelkar, K. M., and Patankar, S. V., 1987, "Numerical Prediction of Flow and Heat Transfer in a Parallel Plate Channel With Staggered Fins," ASME JOURNAL OF HEAT TRANSFER, Vol. 109, pp. 25–30.

Roberts, E. P. L., 1994, "A Numerical and Experimental Study of Transition Processes in an Obstructed Channel Flow," *Journal of Fluid Mechanics,* Vol. 260, pp. 185–209.

Rowley, G. J., and Patankar, S. V., 1984, "Analysis of Laminar Flow and Heat Transfer in Tubes With Internal Circumferential Fins," *International Journal of Heat and Mass Transfer,* Vol. 27, p. 553.

Wang, G., and Vanka, S. P., 1995a, "Convective Heat Transfer in Periodic Wavy Passages," *International Journal of Heat and Mass Transfer,* Vol. 17, pp. 3219–3230.

Wang, G., and Vanka, S. P., 1995b, "Self Sustained Unsteady Flow in Periodic Wavy Passages," *Forum on Unsteady Flows, ASME Fluid Engineering Division Summer Meeting,* Hilton Head, SC, Aug. 13–18.

Webb, R. L., 1994, *Principles of Enhanced Heat Transfer,* Wiley, New York.

Downloaded 11 Dec 2010 to 193.140.21.150. Redistribution subject to ASME license or copyright; see http://www.asme.org/terms/Terms_Use.cfm

Oscillatory Heat Transfer in a Pipe Subjected to a Laminar Reciprocating Flow

T. S. Zhao
Assistant Professor.

P. Cheng
Professor and Head
Fellow ASME.

Department of Mechanical Engineering,
The Hong Kong University of Science and Technology,
Clear Water Bay, Kowloon, Hong Kong

An experimental and numerical study has been carried out for laminar forced convection in a long pipe heated by uniform heat flux and subjected to a reciprocating flow of air. Transient fluid temperature variations in the two mixing chambers connected to both ends of the heated section were measured. These measurements were used as the thermal boundary conditions for the numerical simulation of the hydrodynamically and thermally developing reciprocating flow in the heated pipe. The coupled governing equations for time-dependent convective heat transfer in the fluid flow and conduction in the wall of the heated tube were solved numerically. The numerical results for time-resolved centerline fluid temperature, cycle-averaged wall temperature, and the space-cycle averaged Nusselt number are shown to be in good agreement with the experimental data. Based on the experimental data, a correlation equation is obtained for the cycle-space averaged Nusselt number in terms of appropriate dimensionless parameters for a laminar reciprocating flow of air in a long pipe with constant heat flux.

1 Introduction

Recently, the needs to improve the thermal performance of Stirling machines and cryocoolers have prompted researchers to pay increasing attention to the study of heat transfer and fluid flow characteristics in a reciprocating flow. In particular, the design of heat exchangers in these devices has been based on steady flow correlation equations, which are not applicable to a reciprocating flow. Simon and Seume (1988) presented an excellent survey of the literature on this subject, and pointed out important differences between steady and oscillatory flow and heat transfer. Iwabuchi and Kanzaka (1982) experimentally investigated heat transfer in an oscillatory flow in a test facility designed to obtain data for a specific prototype engine; they presented their heat transfer data in terms of rpm, mean pressure, and phase difference between the opposing pistons, but did not attempt to correlate their oscillatory heat transfer data in terms of dimensionless parameters. Therefore, their results cannot be of general use. Hwang and Dybbs (1983) presented their oscillatory heat transfer data graphically in terms of Nusselt number versus Reynolds number (defined based on the pipe diameter and the maximum cross-sectional mean velocity) at different oscillatory amplitudes. Wu et al. (1990) investigated oscillating flow resistance and heat transfer in a gap heat exchanger of a cryocooler. They found that the value of the cycle-averaged Nusselt number is constant at a value about 9, and is independent of the oscillatory frequency over a wide range of the cycle-averaged Reynolds numbers. Most recently, Zhao and Cheng (1994) show that the proper similarity parameters for the characterization of oscillatory convective heat transfer in a pipe subjected to a reciprocating flow are: the kinetic Reynolds number Re_ω, the dimensionless oscillation amplitude of fluid A_o, the length/diameter ratio of the pipe L/D_i, and the Prandtl number Pr. They found from their numerical solution that annular effects (similar to annular effects in velocity) also exist in the temperature profiles of a laminar flow near the entrance and exit of the heated pipe under certain conditions.

In this paper, an experimental and numerical study has been carried out for forced convection in a long pipe heated by uniform heat flux and subjected to a laminar reciprocating flow of air. Transient fluid temperature variations in the two mixing chambers adjacent to both ends of the heated test section were measured and used as the thermal boundary conditions for a numerical simulation. The finite difference scheme based on a control volume method by Patankar (1980) was used for the numerical solution of the conjugate heat transfer problem in the fluid flow and the heated wall of the pipe. The time-resolved centerline fluid temperature, cycle-averaged wall temperature, and the space-cycle averaged Nusselt number obtained from the numerical solution are presented and shown to be in good agreement with the experimental data. A correlation equation based on experimental data is obtained for the cycle-averaged Nusselt number (in terms of the kinetic Reynolds number Re_ω and the dimensionless oscillation amplitude of fluid A_o) for forced convection in a long pipe subjected to a laminar reciprocating flow of air.

2 Experimental Investigation

Figure 1 is a schematic diagram illustrating the major components of the experimental setup. A horizontal test rig, consisting of two velocity straighteners, two coolers, two mixing chambers, and a heated test section, was constructed for the present study. The test section was made of a long copper tube, with length $L = 60.5$ cm, inside diameter $D_i = 1.35$ cm, and outside diameter $D_o = 1.57$ cm. The test section was heated uniformly by a wrapped-around insulated flexible heater (manufactured by Omega), which was connected to a filtered DC power supply (Model PS-5, EPSCD). Each end of the heated tube was connected to two coolers of the same inside diameter. The two identical coolers, using tap water as coolant, were made of two concentric tubes. Two mixing chambers, made of a cylindrical tube (with length 3.5 cm and the same inside diameter as the test section) packed with a stack of plastic wire-screens (mesh 200), were inserted between the test section and the coolers. The reciprocating motion of the fluid in the test section was driven by a double-acting piston pump with a sinusoidal motion generator which, in turn, was driven by a 1 kW DC motor with an adjustable speed from 7 to 570 rpm. The sinusoidal motion

Contributed by the Heat Transfer Division for publication in the JOURNAL OF HEAT TRANSFER. Manuscript received by the Heat Transfer Division February 27, 1995; revision received March 6, 1996. Keywords: Forced Convection, Transient and Unsteady Heat Transfer. Associate Technical Editor: Y. Bayazitoglu.

Copyright © 1996 by ASME

Downloaded 11 Dec 2010 to 193.140.21.150. Redistribution subject to ASME license or copyright; see http://www.asme.org/terms/Terms_Use.cfm

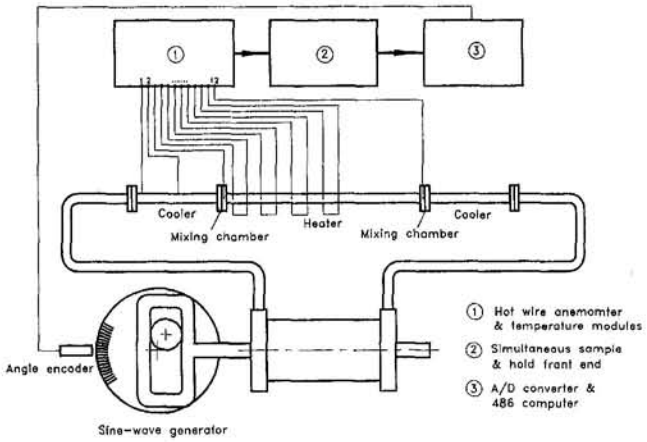


Fig. 1 Schematic of the apparatus

generator is designed such that the fluid displacement x_m varies according to

$$x_m = \frac{x_{\max}}{2}(1 - \cos \omega t) \tag{1}$$

where the fluid displacement x_m is defined by assuming that the fluid moves as a plug flow at a mean velocity u_m; $x_{\max}$ is the maximum fluid displacement, which is controlled by the stroke of the air pump; ω is the oscillation angular frequency and t is time. Differentiating Eq. (1) with respect to time gives the cross-sectional mean velocity:

$$u_m = u_{\max} \sin \phi \tag{2}$$

where $\phi = \omega t$ is the phase angle of the cross-sectional mean velocity, which ranges from 0 to 2π (or 0 deg $\leq \phi \leq$ 360 deg). The amplitude of the cross-sectional mean velocity $u_{\max}$ in Eq. (2) is related to the amplitude of the fluid displacement $x_{\max}$ by

$$u_{\max} = \frac{x_{\max}\omega}{2} \tag{3}$$

where $x_{\max}$ is adjustable. In a previous paper, Zhao and Cheng (1995) found that the measured temporal variations of the axial velocity in the mixing chamber at the inlet of the heated pipe during each half cycle were in good agreement with Eq. (2). For this reason, Eq. (2) will be used as the hydrodynamic boundary conditions for the numerical simulation of the heat transfer characteristics in the heated pipe, as will be presented the next section.

Because both the geometry and the imposed hydrodynamic and thermal boundary conditions were symmetric with respect to the midsection of the heated tube, the sensors were installed only in the left-hand side of the test rig. Six fine T-type thermocouples (manufactured by RdF) were used to measure wall temperatures, two on the outer surface of the cooler wall and the other four at the interior wall of the heater. Centerline fluid temperatures inside the heated tube were measured by four mini-needle T-type thermocouples (manufactured by Omega). To measure inlet and outlet fluid temperatures in the heated tube, two fine thermocouples (0.001 in. in diameter) were carefully installed inside the two mixing chambers. Analog-to-digital conversions were carried out by a MetraByte DAS-20 A/D board, giving 100,000 samples per second with 12-bit precision. A 4-channel simultaneous sample and hold front end for the A/D board (SSH-4) was employed, which was capable of allowing the 4-channel signals to be sampled simultaneously. An angle shaft encoder (Model LD 23, Lucas Ledex) was mounted on the crank shaft to provide the top dead center signal and angle positions for data acquisition purposes.

3 Mathematical Formulation for the Conjugate Heat Transfer Problem

A numerical simulation of the experiments will now be carried out. Consider an incompressible, laminar, viscous fluid oscillating in a copper pipe (with inner and outer diameters D_i and D_o) heated with uniform heat flux at the outer surface of the tube. We now define the dimensionless coordinates, time, velocity, pressure, and temperature as $(X, R) = (x/D_i, r/D_i)$, $\tau = \omega t$, $U = u/u_{\max}$, $P = p/\rho u_{\max}^2$, and $\theta = k_f T/qD_i$, where x, r, t, p, u, and T are the corresponding dimensional quantities, with ρ being the density of the fluid, k_f the thermal conductivity of the fluid, and q the prescribed uniform heat flux. Note that the dimensionless time τ is related to ϕ by $\tau = \omega t = 2\pi(i -$

Nomenclature

A_o = dimensionless oscillation amplitude of fluid = $X_{\max}/D_i$
D_i = inside diameter of pipe
D_o = outside diameter of pipe
k_f = thermal conductivity of fluid
k_s = thermal conductivity of solid
L = length of the pipe
$\overline{\mathrm{Nu}}$ = space-cycle averaged Nusselt number defined in Eq. (17)
p, P = dimensional and dimensionless pressure
Pr = Prandtl number
q = heat flux at the wall
r, R = dimensional and dimensionless radius of the pipe
Re_ω = kinetic Reynolds number = $\omega D_i^2/\upsilon$
t, τ = dimensional and dimensionless time
T, θ = dimensional and dimensionless temperature
T_c, θ_c = dimensional and dimensionless centerline temperature
$T_{m,l}$, $\theta_{m,l}$ = dimensional and dimensionless temperature of the fluid in the left mixing chamber
$T_{m,r}$, $\theta_{m,r}$ = dimensional and dimensionless temperature of the fluid in the right mixing chamber
T_s, θ_s = dimensional and dimensionless temperature of the solid wall
T_w, θ_w = dimensional and dimensionless interior wall temperature
$\overline{T}_w$, $\overline{\theta}_w$ = dimensional and dimensionless space-cycle averaged interior wall temperature
u, U = dimensional and dimensionless axial velocity
$u_{\max}$ = maximum cross-sectional mean velocity
u_m, U_m = dimensional and dimensionless cross-sectional mean velocity
$\vec{V}$ = dimensionless velocity vector
x, X = dimensional and dimensionless axial distance
$x_{\max}$ = dimensional maximum fluid displacement
α_f = thermal diffusivity of fluid
α_s = thermal diffusivity of solid
$\Gamma = \alpha_f/\alpha_s$
ϕ = phase angle
ν = kinematic viscosity of fluid
ρ = density of fluid
$\sigma = k_f/k_s$
ω = frequency of oscillation

Subscripts

c = centerline of the pipe
m = mixing chamber
max = maximum value
o = oscillation
w = wall of the pipe

Downloaded 11 Dec 2010 to 193.140.21.150. Redistribution subject to ASME license or copyright; see http://www.asme.org/terms/Terms_Use.cfm

1) + ϕ, with i being the number of cycles. The governing time-dependent dimensionless conservation equations of mass, momentum, and energy in the flow region ($0 \le R \le 0.5$) are given by Zhao and Cheng (1994) as

$$\nabla \cdot \vec{V} = 0 \tag{4}$$

$$\frac{\partial \vec{V}}{\partial \tau} + \frac{A_o}{2}[(\vec{V} \cdot \nabla)\vec{V} + \nabla P] = \frac{1}{\mathrm{Re}_\omega} \nabla^2 \vec{V} \tag{5}$$

$$\frac{\partial \theta}{\partial \tau} + \frac{A_o}{2}(\vec{V} \cdot \nabla)\theta = \frac{1}{\mathrm{Pr}\ \mathrm{Re}_\omega}(\nabla^2 \theta) \tag{6}$$

where $A_o = x_{\max}/D_i$ is the dimensionless oscillation amplitude of fluid, $\mathrm{Re}_\omega = \omega D_i^2/\nu$ is the kinetic Reynolds number with ν being the kinematic viscosity of the fluid, $\mathrm{Pr} = \nu/\alpha_f$ is the Prandtl number with α_f being the thermal diffusivity of the fluid. For heat conduction in the solid wall ($0.5 \le R \le (D_o/2)/D_i = 0.582$), the dimensionless time-dependent conservation equation of energy is given by

$$\frac{\partial \theta_s}{\partial \tau} = \frac{1}{\Gamma\ \mathrm{Pr}\ \mathrm{Re}_\omega}(\nabla^2 \theta_s) \tag{7}$$

where $\Gamma = \alpha_f/\alpha_s$, with α_s being the thermal diffusivity of the solid.

For the present problem, the hydrodynamic boundary conditions are the no-slip condition at the tube wall and continuous flow conditions at the outlet of the tube. If the fluid is assumed to be entering from the left during the first half cycle, the axial velocity at the inlet ($X = 0$) according to Eq. (2) in dimensionless form is

$$U(0, R, \tau) = U_m = \sin \phi \tag{8}$$

where $U_m = u_m/u_{\max}$. It is relevant to note that the inlet and outlet conditions change with each half-cycle as the fluid flow reverses its direction periodically. The thermal boundary conditions for the problem under consideration are

at $X = 0$,

$$0 \le R \le 0.5: \quad \theta(0, R, \tau) = \theta_{m,l} \tag{9}$$

$$0.5 \le R \le 0.582: \quad \frac{\partial \theta}{\partial X} = 0 \tag{10}$$

at $X = L/D_i$,

$$0 \le R \le 0.5: \quad \theta(L/D_i, R, \tau) = \theta_{m,r} \tag{11}$$

$$0.5 \le R \le 0.582: \quad \frac{\partial \theta}{\partial X} = 0 \tag{12}$$

at $R = 0$,

$$0 \le X \le L/D_i: \quad \frac{\partial \theta}{\partial R} = 0 \tag{13}$$

at $R = 0.58$,

$$0 \le X \le L/D_i: \quad \frac{\partial \theta_s}{\partial R} = \sigma \tag{14}$$

where $\theta_{m,l}$ and $\theta_{m,r}$ are the transient fluid temperatures measured in the left and right mixing chambers. At the solid–fluid interface ($R = 0.5$), the continuities in temperature and heat flux give:

$$0 \le X \le L/D_i: \quad \theta = \theta_s; \quad \sigma \frac{\partial \theta}{\partial R} = \frac{\partial \theta_s}{\partial R} \tag{15}$$

where $\sigma = k_f/k_s$, with k_s being the thermal conductivity of the solid. Thus, the parameters in the conjugate heat transfer problem are: Re_ω, A_o, Pr, L/D_i, D_o/D_i, Γ, and σ.

4 Mathematical Formulation for Negligible Heat Conduction in the Wall

For the case of a thin-walled tube made of copper, the effect of the heat conduction in the wall may be considered to be negligibly small. Under this situation, the governing equations for forced convection in the pipe are given by Eqs. (4)–(6) subject to boundary conditions given by Eqs. (8)–(13) with $D_i = D_o = D$. The parameters for this case are: Re_ω, A_o, Pr, and L/D_i.

5 Numerical Solutions

Computations were first carried out for the case of negligible heat conduction in the wall as discussed in Section 4. After the numerical results had been obtained, these values are used as the initial guess for the iterative solution of the conjugate heat transfer problem with $\Gamma = 0.709$ and $\sigma = 2.532 \times 10^{-5}$ as discussed in Section 3. For both cases, numerical solutions were obtained based on a control-volume method detailed by Patankar (1980). In this procedure, the domain is discretized by a series of control volumes, each containing a grid point. The differential equations are expressed in an integral manner over the control volume, and a power law variation is assumed in each coordinate direction, leading to a system of algebraic equations that can be solved in an iterative manner. Pressure-velocity inter linkages are handled by the SIMPLER formulation as described by Patankar (1980). The solution procedure starts with the initial estimates for velocities, temperatures, and pressure fields, along with the physical boundary conditions, and an iteration is performed until a converged solution is obtained. The convergence criterion used was

$$\frac{\max|(\psi_{ij}^{n+1} - \psi_{ij}^{n})|}{\max|\psi_{ij}^{n}|} < \epsilon \tag{16}$$

where ψ is either U, V, P, or θ; the superscript n is the nth iterative step; and $\epsilon(10^{-4})$ is the typical tolerance.

Because of the extremely thin boundary layer encountered at high kinetic Reynolds numbers and large velocity gradients in the inlet region of the tube, a nonuniform grid was deployed. Solutions were performed with different grid densities and grid numbers to ensure a grid-independent solution. The choice of 181 grid points in the axial direction and 51 points in the radial direction was found to be sufficient in providing a grid-independent solution. For the two mesh sizes 181×51 and 201×51, the maximum changes in the predicted centerline velocity and temperature at the midsection of the pipe were less than 2 and 1.5 percent, respectively. For each case, 360 time steps were used in one cycle and transient behaviors were recorded until a steady periodic state was reached.

6 Results and Discussion

For the present experiment with a thin-walled copper tube ($D_o/D_i = 1.16$), it was found that there are negligible differences between the numerical results for the cycle-space averaged Nusselt number and the cycle-averaged wall temperature based on Sections 3 and 4. In the following, we shall present experimental and numerical results (based on Section 3) for a laminar reciprocating flow of air ($\mathrm{Pr} = 0.71$) in a heated pipe (with $L/D_i = 44.8$) connected to two coolers at both ends. The frequency and the stroke of oscillations were varied such that the range of Re_ω was from 23 to 464 while the range of dimensionless oscillation amplitude of the fluid A_0 was from 8.5 to 34.9, which was less than the critical value of A_0 for the onset of turbulence according to Zhao and Cheng (1995).

Temperature Distributions. Figures 2(a) and 2(b) illustrate typical temporal temperature variations measured at the left and right mixing chambers during one cycle at the same oscillatory frequency ($\mathrm{Re}_\omega = 120.1$) for $A_o = 34.9$ and 15.3,

Downloaded 11 Dec 2010 to 193.140.21.150. Redistribution subject to ASME license or copyright; see http://www.asme.org/terms/Terms_Use.cfm

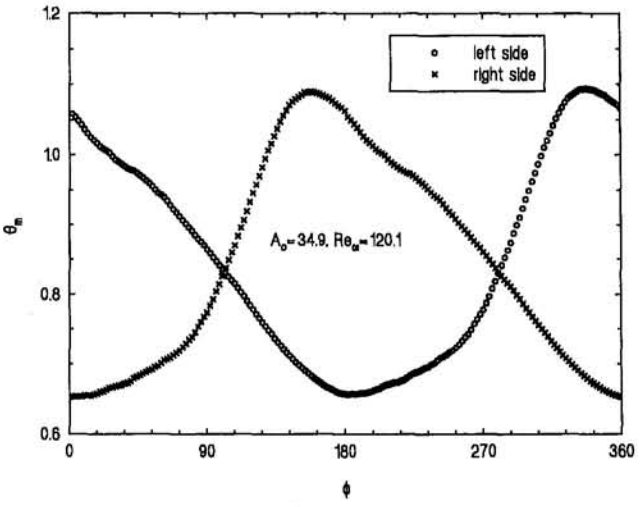


Fig. 2(*a*) Temporal fluid temperature variations in the left and right mixing chambers for A_o = 15.3, Re_ω = 120.1, and L/D_i = 44.8

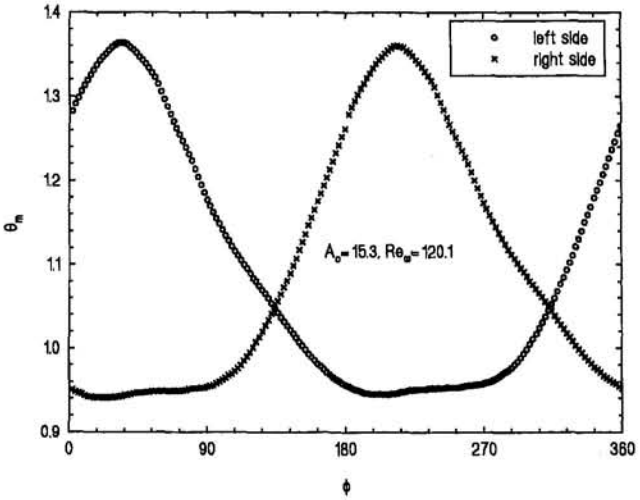


Fig. 2(*b*) Temporal fluid temperature variations in the left and right mixing chambers for A_o = 34.9, Re_ω = 120.1, and L/D_i = 44.8

respectively. These measurements were used as the thermal boundary conditions given by Eqs. (9) and (11), respectively. Generally, during the first half cycle (0 deg $\leq \phi \leq$ 180 deg) as the fluid flow moves from the left to right, the fluid temperature in the left mixing chamber drops due to the cooling effect from the left cooler while the temperature in the right mixing chamber goes up due to the heating effect from the heated test section. During the second half cycle (180 deg $\leq \phi \leq$ 360 deg) as the fluid flow reverses its direction, the reversed situation occurs. We now compare the temperature history (in the right mixing chamber, for example) for different values of A_o. For A_o = 34.9 (see Fig. 2(*a*), the fluid temperature in the right mixing chamber increases with the progress of phase angles and reaches a maximum value at about ϕ = 150 deg. For A_o = 15.3, however, the fluid temperature in the right mixing chamber increases at the beginning of the cycle, but much more slowly in comparison with the case of A_o = 34.9. The peak of the temperature is reached as late as at ϕ = 166 deg. The reason for the different behavior of temporal temperature variations for low and high values of A_o can be explained as follows. At a high value of A_o (A_o = 34.9 for example) where the maximum cross-sectional mean velocity is high (as can be deduced from Eq. (2)), a forced convection effect predominates. Therefore, the fluid temperature in the right mixing chamber rises immediately when the fluid reverses direction as hotter fluid enters. However, for A_o = 15.3 where the fluid velocity is small and axial heat conduction effect predominates at least initially, the fluid temperature in the right mixing chamber responds slower with respect to the velocity variations.

Typical variations of the centerline fluid temperature θ_c at different axial locations during one cycle for A_o = 15.3 and Re_ω = 150.6 are presented in Fig. 3. The triangle symbols represent the experimental data while the solid curves represent numerical solution. It is seen that the numerical solution is in fairly good agreement with the experimental data. Because both the geometry and imposed thermal boundary conditions are symmetric with respect to the midsection of the heated tube, only the temperature variations in the left-hand side of the test section ($X < 22.4$) are presented. As shown in this plot, during the first half-cycle the fluid temperature near the left mixing chamber (X = 1.4) begins to drop due to colder fluid entering from the cooler. The fluid temperature starts to rise near the end of the first half cycle due to warmer fluid exiting from the midsection of the heated pipe. The amplitude of the fluid temperature variations is maximum near the heater–cooler interface (X = 0) and progressingly smaller as the midsection of the heated tube (X = 22.4) is approached.

Next, the numerical results for temporal variations of the interior wall temperature at different dimensionless axial locations in the left-hand side of the pipe during one cycle (0 deg $\leq \phi \leq$ 360 deg) are presented in Fig. 4 for the following three cases: Case 1 with A_o = 32 and Re_ω = 50, Case 2 with A_o = 32 and Re_ω = 300, and Case 3 with A_o = 10 and Re_ω = 300. A comparison between Cases 1 and 2 is shown in Fig. 4(*a*) while a comparison between Cases 2 and 3 is presented in Fig. 4(*b*). From these figures, it can be seen that the temporal wall temperature variations are small. It is shown that colder fluid enters the heated section from the left during the first half cycle (0 deg $\leq \phi \leq$ 180 deg), and thus the temperatures at the left-hand side of the pipe drop with time until the phase angle is about 180 deg. Subsequently, during the second half cycle (180 deg $\leq \phi \leq$ 360 deg), the fluid reverses direction and the warmer fluid passes through the left-hand side of the pipe and consequently fluid temperatures at these locations increase with time until the beginning of the next cycle. From Figs. 4(*a*) and 4(*b*), it can be seen that the amplitudes of temperature variations decrease with the axial positions from the inlet to the midsection of the pipe (X = 22.4). Toward the midsection of the pipe, the temperature fluctuations become vanishingly small. A comparison of Case 1 (represented by the solid lines) and Case 2 (represented by the dash lines) in Fig. 4(*a*) shows that

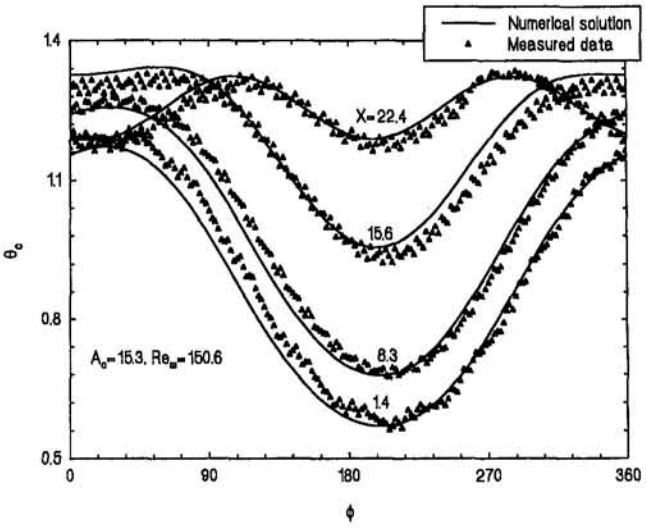


Fig. 3 Variations of the centerline temperature along the axial position at different phase angles for A_o = 15.3, Re_ω = 150.6, and L/D_i = 44.8

Downloaded 11 Dec 2010 to 193.140.21.150. Redistribution subject to ASME license or copyright; see http://www.asme.org/terms/Terms_Use.cfm

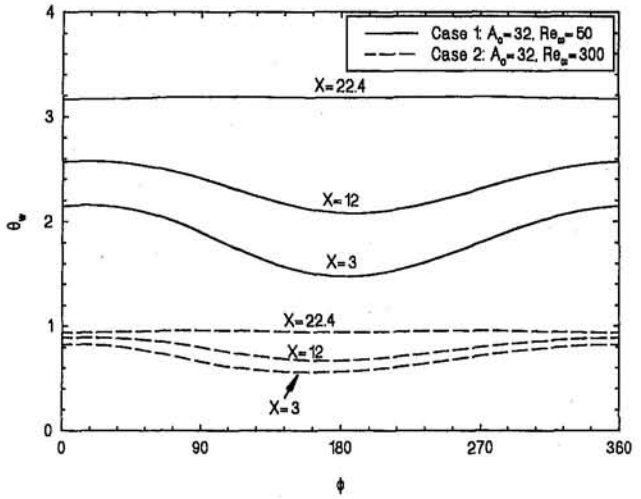


Fig. 4(*a*) Effects of the kinetic Reynolds number Re_ω on the interior wall temperature at the different locations for A_o = 15.3 and L/D_i = 44.8, generated from the numerical simulation

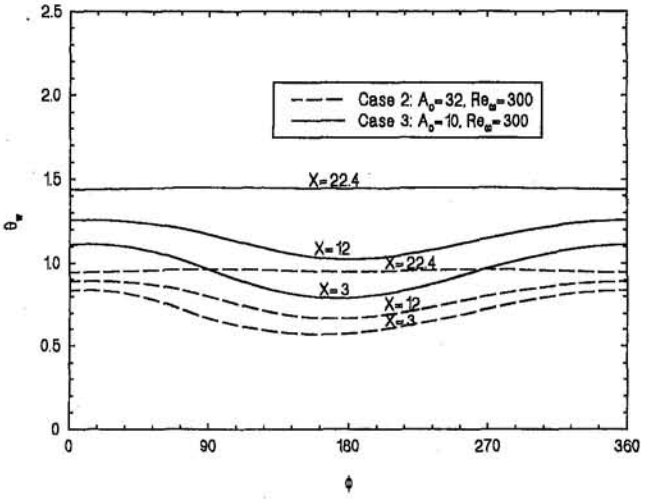


Fig. 4(*b*) Effects of the dimensionless oscillation amplitude of fluid A_o on the interior wall temperature at the different locations for Re_ω = 300 and L/D_i = 44.8, generated from the numerical simulation

the level of the wall temperatures decreases with the increase of Re_ω. This is because the thermal boundary layer becomes thinner with Re_ω. Therefore, the wall temperature decreases at the fixed value of heat flux. Similarly, a comparison of the Case 2 (represented by the dash lines) and Case 3 (represented by the solid lines) in Fig. 4(*b*) shows that the level of the wall temperature decreases with the increase of A_o at a fixed value of Re_ω. Physically, a higher value of A_o means a larger amount of colder fluid entering the heated test section and thus the wall temperature drops.

Figure 5 is a comparison of experimental and numerical results of the cycle-averaged wall temperature variation with axial location for the left-hand side of the test section ($X < 22.4$) for four different cases. The dashed lines represent the numerical solutions based on negligible heat conduction in the wall (i.e., the formulation of Section 4) while the solid lines represent the coupled conjugated heat transfer formulation. It is shown that there are slight differences in the numerical results based on the two formations, and that the numerical solutions are in good agreement with the experimental data. Generally, the cycle-averaged wall temperature increases progressively with the axial location, with the minimum value occurring at the left mixing chamber and maximum value at the midsection of the heated tube. It can also be observed that the cycle-averaged wall temperature decreases with the increase of either the kinetic Reynolds number Re_ω or the dimensionless oscillation amplitude of fluid A_o.

The Space-Cycle Averaged Nusselt Number. The space-cycle averaged Nusselt number is defined as

$$\overline{\mathrm{Nu}} = \frac{qD_i}{k_f(\bar{T}_w - \bar{T}_m)} = \frac{1}{\bar{\theta}_w - \bar{\theta}_m} \tag{17}$$

where $\bar{T}_w$ and $\bar{\theta}_w$ are the dimensional and dimensionless space-cycle averaged temperatures measured at the outer surface of the heated tube, with $\bar{\theta}_w$ being computed from

$$\bar{\theta}_w = \frac{1}{N}\sum_{i=1}^{N} \bar{\theta}_{w,i} \tag{18}$$

where $\bar{\theta}_{w,i}$ is the cycle-averaged local wall temperature and N is the number of positions in the test section at which the local wall temperatures were measured; $\bar{T}_m$ and $\bar{\theta}_m$ are the dimensional and dimensionless cycle-averaged temperatures of the fluid measured in the left or right mixing chambers with $\bar{\theta}_m$ computed from either

$$\bar{\theta}_m = \frac{1}{2\pi}\int_0^{2\pi} \theta_{m,l}\, d\tau \tag{19a}$$

or

$$\bar{\theta}_m = \frac{1}{2\pi}\int_0^{2\pi} \theta_{m,r}\, d\tau \tag{19b}$$

It was found that the difference between Eqs. (19*a*) and (19*b*) was within 2.1 percent for the experimental range.

The space-cycle averaged Nusselt number $\overline{\mathrm{Nu}}$ was computed according to Eqs. (17)–(19) based on the experimental data for A_o = 8.54 to 34.9 and Re_ω = 23 to 464 at L/D_i = 44.8. As mentioned earlier, since it was found that there are negligible differences between the numerical results for $\overline{\mathrm{Nu}}$ and $\bar{\theta}_w$ based on the formulation of Sections 3 and 4, we shall correlate the experimental results of $\overline{\mathrm{Nu}}$ based on the conjugate heat transfer problem. It follows that $\overline{\mathrm{Nu}}$ is a function of Re_ω, A_o, Pr, and L/D_i. The following correlation was obtained based on a least-squares fit of 53 experimental runs for a laminar reciprocating flow of air in a long tube with constant heat flux:

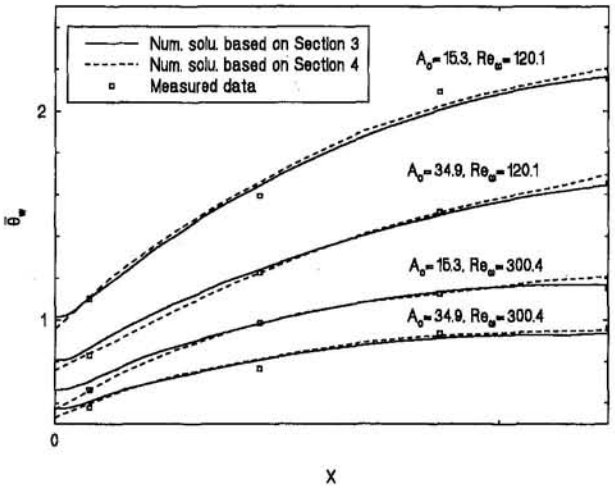


Fig. 5 Effects of the dimensionless oscillation amplitude of fluid A_o and the kinetic Reynolds number Re_ω on the cycle-averaged wall temperature at L/D_i = 44.8.

Downloaded 11 Dec 2010 to 193.140.21.150. Redistribution subject to ASME license or copyright; see http://www.asme.org/terms/Terms_Use.cfm

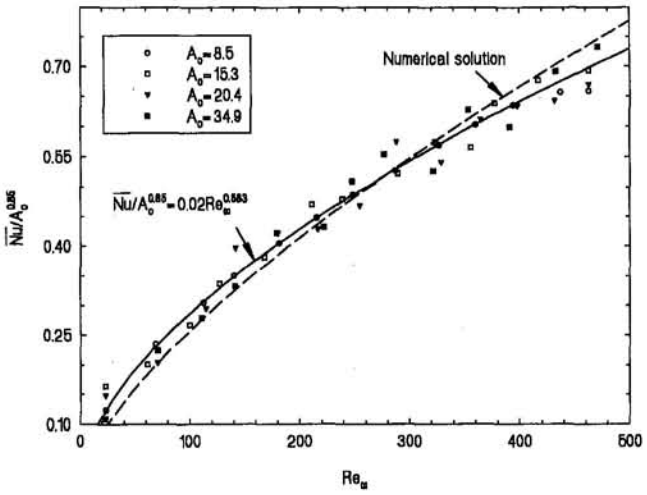


Fig. 6 A correlation equation based on the experimental data for the cycle-space averaged Nusselt number

$$\overline{\mathrm{Nu}} = 0.02\, A_o^{0.85}\, \mathrm{Re}_\omega^{0.58} \qquad (20)$$

Equation (20) with experimental data is presented in Fig. 6. The maximum relative error between Eq. (20) and the experimental data is about 12.8 percent. The space-cycle averaged Nusselt number $\overline{\mathrm{Nu}}$ generated from the numerical simulation was also presented in Fig. 6. It is shown that the numerical solution (represented by the dashed line) is slightly lower or higher than Eq. (19) depending on whether $\mathrm{Re}_\omega < 280$ or $\mathrm{Re}_\omega > 280$. The maximum relative deviation between the numerical solution and the data is about 7 percent. Note that Eq. (20) indicates that the heat transfer rate increases with both the dimensionless oscillation amplitude of fluid A_o and the kinetic Reynolds number Re_ω; the increase in heat transfer is more sensitive to A_o than to Re_ω because the exponent of A_o is greater than that of Re_ω. It is also relevant to note that Eq. (20) is valid for a long pipe with air as the working fluid medium. Thus Eq. (20) is a conservative estimate of heat transfer rate for a reciprocating flow in a pipe of finite length.

The uncertainty in the experimental data can be considered by identifying the main sources of errors in the measurements. Prior to the experiments, all thermocouples were calibrated in a constant temperature bath (CL 730, Omega) to ensure the accuracy of ±0.1°C. The voltage input to the electric heater was measured with a sensitivity of ±1 mV and an accuracy of 0.1 percent. Several runs were tested in which the voltage and the current for the circuit were measured, and the calculated power output was stable and its uncertainty was less than 3.5 percent. The energy losses in the heated test section were 5 percent of the total energy output of the electrical heating device. The maximum uncertainty in the measurements of oscillation frequency and stroke of the air pump were found to be 2 and 0.3 percent, respectively. The estimated uncertainties in the kinetic Reynolds number, the dimensionless oscillation amplitude of the fluid, and the space-cycle averaged Nusselt numbers are 2.1–2.3, 0.4–0.5, and 6.2–9.4 percent, respectively, using the uncertainty estimation method of Kline and McClintock (1953).

7 Concluding Remarks

An experimental and numerical study has been carried out for laminar oscillatory forced convection in a long circular tube heated by uniform heat flux and subjected to a laminar reciprocating flow of air. The numerical solutions for time-resolved centerline fluid temperature, cycle-averaged wall temperature, and the space-cycle averaged Nusselt number are shown to be in good agreement with the experimental data. Based on the experimental data, a correlation equation for the space-cycle averaged Nusselt number of an oscillatory laminar flow of air in a long tube in terms of appropriate similarity parameters is obtained. This correlation equation will be useful for the design of heat exchangers in a Stirling engine or a pulse-tube cryocooler.

References

Hwang, M. F., and Dybbs, A., 1983, "Heat Transfer in a Tube With Oscillatory Flow," ASME Paper No. 83-WA/HT-90.

Iwabuchi, M., and Kanzaka, M., 1982, "Experimental Investigation Into Heat Transfer Under the Periodically Reversing Flow Condition in a Heated Tube," *J. Mech. Engineers*, C24/82, pp. 135–139.

Kline, S. J., and McClintock, F. A., 1953, "Describing Uncertainties in Single-Sample Experiments," *Mechanical Engineering*, Jan., pp. 3–12.

Patankar, S. V., 1980, *Numerical Heat Transfer and Fluid Flow*, Hemisphere, Washington, DC.

Simon, T. W., and Seume, J. R., 1988, "A Survey of Oscillating Flow in Stirling Engine Heat Exchanger," NASA Contract Report 182108.

Wu, P., Lin, B., Zhu, S., He, Y., Ren, C., and Wang, F., 1990, "Investigation of Oscillating Flow Resistance and Heat Transfer in the Gap Used for Cryocoolers," *13th IECEC Proceedings*.

Zhao, T., and Cheng, P., 1995, "A Numerical Solution for Laminar Forced Convection in a Heated Pipe Subjected to a Periodically Reversing Flow," *Int. J. Heat Mass Transfer*, Vol. 38, No. 16, pp. 3011–3022.

Zhao, T. S., and Cheng, P., 1995, "Experimental Studies on the Onset of Turbulence and Frictional Losses in an Oscillatory Turbulent Pipe Flow," accepted for publication in *Int. J. Heat and Fluid Flow*.

Downloaded 11 Dec 2010 to 193.140.21.150. Redistribution subject to ASME license or copyright; see http://www.asme.org/terms/Terms_Use.cfm

Natural Convection Heat Transfer in Horizontal Rod-Bundle Enclosures

M. Keyhani

T. Dalton

Mech. & Aerospace Eng. and Engineering Science Department,
The University of Tennessee,
Knoxville, TN 37996-2210

Natural convection heat transfer in enclosed horizontal $N \times N$ arrays ($N = 3$, 5, and 7) of electrically heated rods with a pitch-to-diameter ratio (P/d) of 1.35 has been experimentally investigated. Each array was positioned in an isothermal square enclosure with a width-to-diameter ratio (W/d) of 20.6. Pressurized air or helium was used as the working fluid. It was observed that the bottom-row rods were relatively insensitive to increases in the array size, as they exhibit only slight temperature variations, but the top-row rods demonstrated substantial temperature increases. Natural convection correlations in the form of Nusselt number (Nu_d) as a function of modified Rayleigh number (Ra_d^*) were obtained for each rod in each array. The correlations cover three flow regimes of conduction, transition, and convection in the range of $6.45 < Ra_d^* < 3.08 \times 10^5$. A generalized enclosure Nusselt number was correlated as a function of enclosure modified Rayleigh number and the array size (N). Comparison of the data with previous numerical prediction showed that this correlation may be readily used to obtain a conservative estimate of the maximum temperature in the arrays with $N = 3$, 5, 7, and 9.

Introduction

Design of casks for transportation, storage, and permanent disposal of spent nuclear fuel assemblies requires tools for accurate prediction of the temperature field in such enclosures. Natural convection heat transfer is a major contributor to transfer of heat from the rods of a fuel assembly to the surfaces of the enclosing cask. The convective component of the heat transfer is a strong function of the orientation of the rod-bundle (i.e., vertical or horizontal), and depends on Grashof number (decay heat generation rate), Prandtl number (fill medium), and relevant geometric parameters.

Radiation heat transfer in rod-bundles has been studied by Cox (1976) and Reilly et al. (1978). In relation to nuclear reactors, free convection flow through vertical tube bundles has been investigated by Dutton and Welty (1975). Natural convection heat transfer within an enclosed rod-bundle has received very little attention from researchers. The only engineering correlations applicable to enclosed vertical rod arrays appears to be those reported by Keyhani and co-workers. Keyhani et al. (1983, 1985) conducted experiments with air and helium at various pressures, as well as under vacuum conditions for a single rod, 3×3, and 5×5 rod-bundles, each enclosed in a vertical canister. They reported convection correlations for Nusselt number of each rod in the 3×3 and 5×5 arrays, as well as a general correlation for the overall convection heat transfer from the bundle to the outer cylinder. Arya and Keyhani (1990) extended the work of Keyhani et al. to a non-square array rod-bundle with and without internal fins on the canister. The objective of their work was to model a sealed storage cask containing spent-fuel canister of the integral Monitored Retrievable Storage (MRS) facility.

For the horizontal orientation, correlations representing convection heat transfer from four to sixteen cylinders to cubical enclosures have been reported in the literature by Warrington and Weaver (1984). However, the heat transfer coefficients for the individual cylinders were not reported in that study. Large-scale experiments have been conducted by Fedorovitch (1989), Irino et al. (1986), and Vdovets et al. (1987). The qualitative analyses of the results of these studies provided evidence for the importance of natural convection heat transfer in these geometries.

Keyhani and Luo (1995) conducted a numerical study of natural convection heat transfer in enclosed horizontal $N \times N$ arrays of heated rods with a constant heat flux dissipation. For a fixed rod diameter (d), width of the isothermal outer enclosure (W), and a pitch-to-diameter ratio of $P/d = 1.33$, the number of rods was varied. They reported average Nusselt number of each rod (Nu_d) in $N = 3$, 5, 7, and 9 arrays for a modified Rayleigh number (Ra_d^*) range of 1 to 316 with $Pr = 0.7$. Also, pure conduction results for rod-bundles ranging from 3×3 to 13×13 were reported. They reported that at $Ra_d^* = 126$, more than 64 percent of the total power input was transferred to the top surface, while the bottom surface received less than 1 percent of the total. For each array the overall enclosure Nusselt number was correlated as a function of the enclosure modified Rayleigh number. The enclosure Nusselt number increased as the order of the array (N) was increased from 3 to 9.

The actual process of heat transfer from the heated rods of a bundle to the gas-filled enclosure takes place via free convection and radiation, and for the natural convection part the thermal boundary condition for the rods is neither isoflux nor isothermal. Therefore, the correlations reported by Keyhani and Luo may be used to obtain an approximate prediction, and the accuracy of the prediction depends on the fraction of total power transferred via radiation. A rigorous modeling of combined natural convection and radiation within an enclosed rod-bundle is extremely complicated and has not been attempted. Therefore, computer models to date have been based on gross approximations of the convective component of the heat transfer.

Engineering correlations pertaining to natural convection heat transfer in horizontal rod-bundle arrays are therefore needed to account fully for energy transfer in spent nuclear fuel assemblies. The objective of the present study is to provide an understanding of the natural convection heat transfer in horizontal enclosed rod-bundles along with correlations that may be used in conjunction with a radiation model, as described by Irino et al. (1983) and Dalton (1994), to predict the temperature field.

Contributed by the Heat Transfer Division and presented at the International Mechanical Engineering Congress & Exposition, San Francisco, California, November 12–17, 1995. Manuscript received by the Heat Transfer Division August 14, 1995; revision received April 2, 1996. Keywords: Enclosure Flows, Flow Visualization, Natural Convection. Associate Technical Editor: S. H. Chan.

Copyright © 1996 by ASME

Downloaded 11 Dec 2010 to 193.140.21.150. Redistribution subject to ASME license or copyright; see http://www.asme.org/terms/Terms_Use.cfm

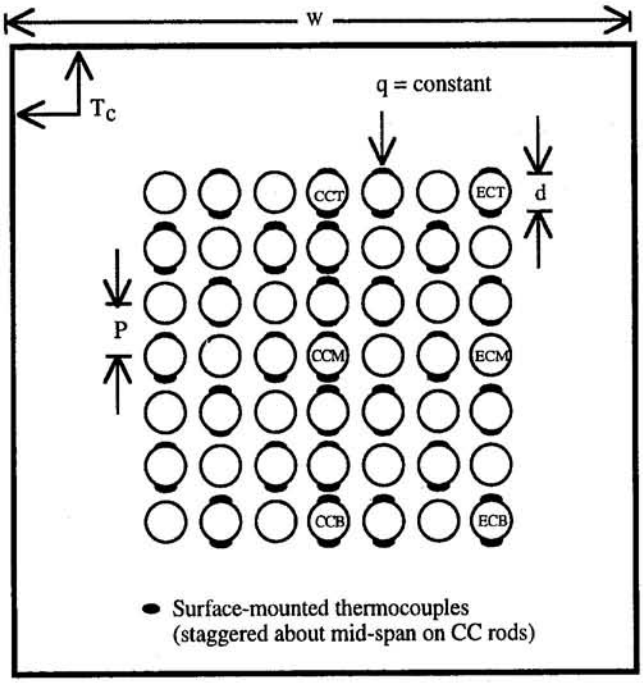


Fig. 1 Experimental model with rod designation (7 × 7 array, enclosure not to scale)

Experimental Apparatus and Procedure

Setup. The test facility had three main components: the rod-bundle assembly, the enclosing heat exchangers, and an outer cylinder. The experimental model and the side cross-sectional view of the experimental apparatus are presented in Figs. 1 and 2. Electric cartridge heaters with a diameter of 0.942 cm were used to simulate spent nuclear fuel rods. The rods had a nominal length of 61.0 cm and were designed to provide a constant power dissipation per unit length. They also had a 1.27 cm unheated length at each end for mounting purposes. Two guides made of phenolic material (19.2 cm square, 0.953 cm thick) were used to hold the array. Each guide had a 15 × 15 array of 0.942 cm holes, which were positioned with a 1.27 cm pitch (a 15 × 15 array of holes were drilled so that the system can be readily expanded). This assembly provided a pitch-to-diameter ratio of 1.35. All-thread rods were placed through the corner holes of the 15 × 15 array to support the phenolic guides and rod-bundle assembly, and the unused holes were plugged and covered with a thin phenolic plate.

The enclosure was constructed of four copper heat exchangers. Each heat exchanger was 61.0 cm long and 0.953 cm thick, and copper tubing (0.635-cm-dia) was soldered to its outer surface. When assembled, the heat exchangers formed a square duct with inner walls separated by 19.4 cm. An aluminum cylinder was used to contain the rod-bundle enclosure. The cylinder had an inner diameter of 30.5 cm, an outer diameter of 32.4 cm, and was 122 cm long. Eight pipe fittings were welded to the cylinder for inlet and exit ports of water supply to the heat exchanger. Flanges, gaskets, and end-plates were used to seal the cylinder during pressurized and vacuum experiments. The end-plates also served as inlet and exit ports for instrumentation. One end-plate was equipped with Conax compression fittings for thermocouple and heater leads, and the other end-plate had threaded ports for connection to vacuum pump, air or helium tank, vacuum gage, and pressure gage (Fig. 2).

Flow Visualization Setup. Limited flow visualization experiment were performed with the 3 × 3 array to investigate the flow pattern. The enclosure was built with Plexiglas with the same dimensions as the one used in the heat transfer experiment. To resemble closely the enclosure surface boundary condition found in the heat transfer experiments, the top wall was built from soldered copper plates with an engraved water channel and cooled by a constant-temperature bath. With thermocouple installations similar to the heat transfer experiments, first the system was calibrated, and then the thermocouples were removed for the flow field visualization experiments. A plane of light was projected transversely to the enclosure cell to illuminate a cross section of the enclosure. Incense smoke was injected into the enclosure through a small opening on the bottom surface of the enclosure. The smoke was injected in such a way that it caused the least disturbance to the flow field. A high-speed 35 mm film and short exposure time (≈1 second) was used to photograph the flow field.

Instrumentation. Considering the one-half symmetry of the bundle, copper-constantan thermocouples (30 AWG) were used to measure the temperatures at the top and bottom surfaces of the pertinent rods in each array, as shown in Fig. 1. The thermocouples were located at the midspan of the array, and were distributed in the right half and left half of the array. Also, in order to avoid overlapping of top and bottom surface-mounted thermocouples on the center-column rods, the thermocouples were staggered by 1.5 cm about the midspan of the array. The 3 × 3 array was equipped with additional thermocouples for axial conduction and symmetry check. All heater-rod thermocouples were secured with 34 AWG nickel–chromium wire and high-temperature cement. Each heat exchanger had

Nomenclature

A_d = heater-rod surface area, m^2
c_p = isobaric specific heat, J/kg-K
d = heater-rod diameter, m
g = acceleration due to gravity, m/s^2
h = average convection heat transfer coefficient = $q_c''/(T_d - T_c)$, W/m^2-K
k = thermal conductivity, W/m-K
Nu_d = Nusselt number of a given rod = $q_c'' d/(T_d - T_c)k$
Nu_W = enclosure Nusselt number = $Q_c'' W/(T_{CCT} - T_c)k$
p = containment pressure, atm
P = pitch distance between rods, m
Pr = Prandtl number
q = heater-rod power, W
q_{rad} = radiation heat transfer from a given rod, W
q_c'' = convected heat flux from a given rod = $(q - q_{rad})/A_d$, W/m^2
Q_c'' = average convective heat flux at the enclosure surface, W/m^2
Ra_d^* = modified Rayleigh number of a given rod = $g\beta q_c'' d^4/(k\alpha\nu)$
Ra_w^* = modified Rayleigh number for the enclosure = $g\beta Q_c'' W^4/(k\alpha\nu)$
T_c = enclosure temperature, K
T_{CCT} = average temperature of the center-column-top rod, K
T_{ECB} = average temperature of the edge-column-bottom rod, K
T_d = average temperature for a given rod, K
W = inside width of enclosure, m
α = thermal diffusivity = $k/(\rho c_p)$, m^2/s
β = isobaric coefficient of thermal expansion, K^{-1}
ϵ = emissivity
ν = kinematic viscosity, m^2/s
ρ = density, kg/m^3
σ = Stefan–Boltzmann constant, W/m^2-K^4

Downloaded 11 Dec 2010 to 193.140.21.150. Redistribution subject to ASME license or copyright; see http://www.asme.org/terms/Terms_Use.cfm

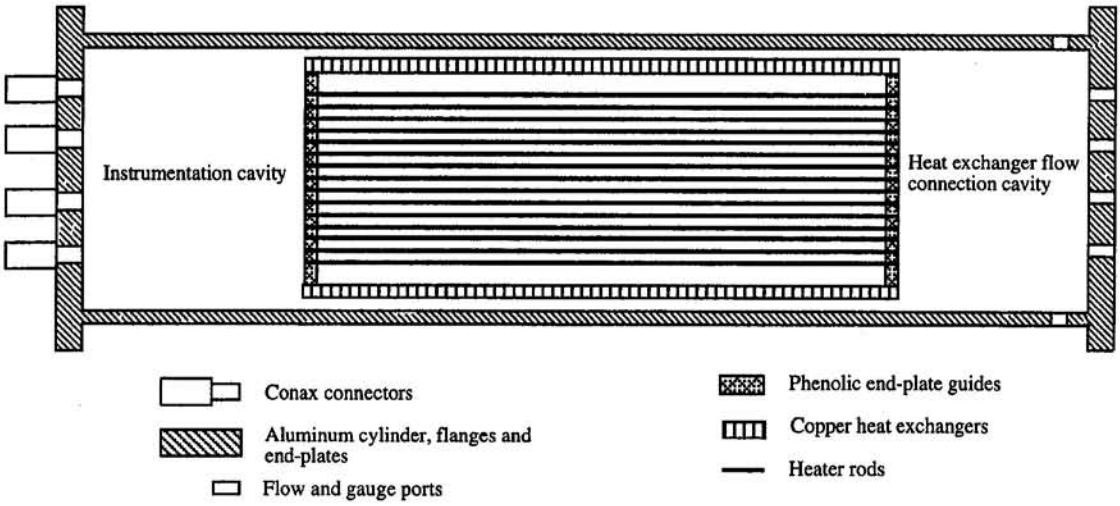


Fig. 2 Side cross-sectional view of the apparatus

six 30 AWG type-T thermocouples that were secured in 0.16-cm-deep groves with liquid solder; the groves faced the rod-bundle assembly. Thermocouple positioning was varied along the length and width of each plate to validate the extent of an isothermal enclosure. The temperature of each heat exchanger in the square duct was maintained by a constant-temperature bath. For all runs, the average deviation of the 24 thermocouples of the enclosure from the mean enclosure temperature was less than ±0.2°C.

Electrical leads exited the containment cylinder through the Conax connectors. Input voltages were regulated by an AC regulator, which supplied power, depending on the array size, to up to three power control panels. Each power control panel had variacs for controlling the rod voltages. Nine, fifteen, and twenty-eight variacs were used in the respective 3×3, 5×5, and 7×7 rod-bundle experiments. The panels had switching capabilities for measurements of the current and voltage of each circuit. A Fluke model 77 multimeter was used for current measurements. A Hewlett-Packard 3497A data acquisition/control unit was used to relay the voltages to a HP 3456A digital voltmeter. A Kay Instrument Unit provided an ice point temperature for reference thermocouples; it was precise to ±0.05°C from 0°C. Compressed breathing air and ultra-high-purity helium were used for pressurization, and the pressure was measured with an Omega Transducer Indicator. A mechanical vacuum pump and a diffusion pump were used to evacuate the cylinder during radiation experimentation, and a vacuum gage was used to measure the vacuum pressure.

Procedure. The procedure for a specific experiment with a medium (air or helium) involved pressurizing the containment cylinder, setting the voltage supply of each heater-rod to achieve uniform powers, adjusting the water baths to maintain isothermal condition on the enclosure surface, and waiting for steady-state conditions to occur. Heater-rod powers and temperatures were monitored periodically and adjusted when necessary. The system was allowed time to stabilize after each adjustment. It was considered steady state when rod temperatures agreed within 0.15 percent between consecutive readings taken every 30 minutes.

Radiation Correction. In order to determine the radiation contribution and report convective heat transfer coefficients, the procedure established by Keyhani et al. (1985) was followed. With air or helium as the test gas and a given power input per rod, the mean temperatures of rods in the array were measured. Then, the cylinder was evacuated. The power inputs to the rods were simultaneously adjusted until the mean measured temperature on each rod was the same as that obtained when the convection heat transfer was present. Furthermore, the enclosure surface was maintained at the same temperature as that when the gas was present. For example, in the 7×7 array air run at 1 atm with $q = 2$ W/rod, for the center-column-top rod we measured 374.85 K at the top of the rod and 375.35 K at the bottom of the rode (an average temperature of 375.1 K). In the vacuum experiment, for this rod we reproduced measured values of 373.45 K at the top of the rod and 376.15 K at the bottom of the rode (an average temperature of 374.8 K).

The mean free path of the molecules in the vacuum experiments were not sufficiently large to eliminate the transfer of energy from the rods to the enclosure via the conduction heat transfer mode. Therefore, in order to obtain an accurate estimate of the radiation effect, the rate of heat transferred by conduction in the vacuum experiments must be calculated and subtracted from the power inputs in the vacuum runs. The conduction Nusselt numbers reported by Keyhani and Luo (1995) were used to estimated the amount of energy conducted from each rod in the vacuum experiments. The power inputs under vacuum conditions (minus the calculated conduction heat transfer) were considered to be the radiation heat transfer contribution. It should be noted that by creating nearly the same temperatures in the vacuum run as those measured in the convection–radiation run, the radiation correction powers represent the radiation contribution as well as any axial conduction loss along the rods that may be present in the convection-radiation run.

Pressures ranging from 55 to 67 millitorr (7.23×10^{-5} to 8.82×10^{-5} atm) were maintained throughout the vacuum experiments. After selecting a run for correction, the average temperature of the enclosure was adjusted to within 1 percent of its corresponding value in the convection–radiation run. A two-dimensional model based on net-radiation method was employed to estimate the necessary power input to each rod (see Dalton, 1994 for further details). In this model all surfaces were assumed gray and diffuse with uniform radiosities, and view factors were adapted from Irino et al. (1986). Rod and enclosure emissivities were approximated as $\epsilon = 0.225$ and $\epsilon = 0.109$, respectively (Sandia National Laboratories measured these emissivities from rod and enclosure material samples). Next, the power inputs to the heater-rods were adjusted to the estimated values calculated by the radiation model. The resulting heater-rod temperatures were monitored and upon temperature stabilization periodic adjustments were made until the black-body emissive powers (σT^4) of the rods in the vacuum run matched the black-body emissive powers of the rods (to within 1 percent) in the convection–radiation run.

Downloaded 11 Dec 2010 to 193.140.21.150. Redistribution subject to ASME license or copyright; see http://www.asme.org/terms/Terms_Use.cfm

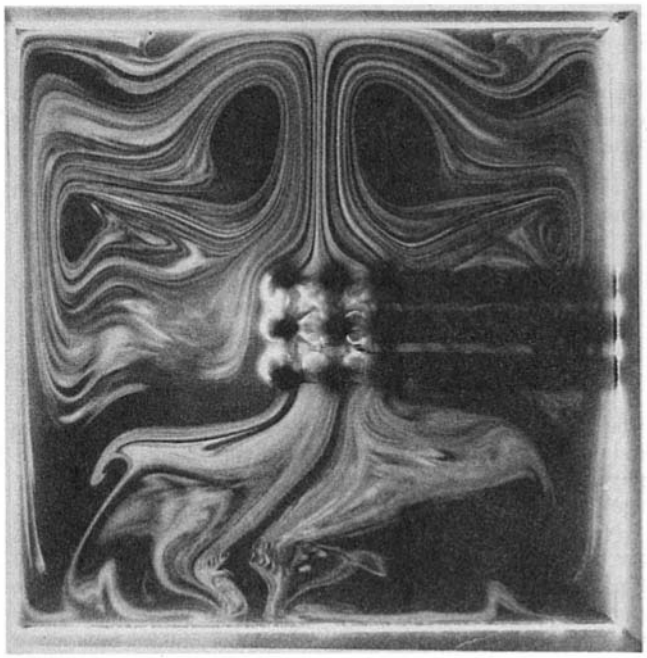


Fig. 3 Photograph of the flow field in the 3 × 3 array; power input = 0.2 W/rod; $Ra_d^* \approx 320$

Experimental Uncertainty. Uncertainty in the power input was within 3 percent for $0.5 < q < 2$ W and 2 percent for $q > 2$ W. Temperature measurements were accurate to within ±0.06°C for 24.8°C < T < 34.8°C and ±0.23°C for 34.8°C < T < 84.0°C. These values include uncertainties in thermocouple junctions (including the reference junction), voltmeter accuracy, and voltage-to-temperature conversion. These estimates were verified through a comparison with a precision thermometer calibrated by the National Bureau of Standards. Thermophysical properties of helium and air were assigned an assumed uncertainty of 1.5 percent. Containment pressure measurement had an uncertainty of 6.81×10^{-3} atm.

Using the procedure outlined by Kline and McClintock (1953), the calculated uncertainties in total modified Rayleigh numbers and total Nusselt numbers were 4.50 and 3.38 percent, respectively. Uncertainties in convective modified Rayleigh numbers and convective Nusselt numbers were functions of the aforementioned values as well as the uncertainty in the radiation correction. Uncertainties in convective modified Rayleigh numbers range between 5.27 and 9.85 percent, depending on array size, power input, fill media, and containment pressure. Similarly, convective Nusselt numbers have uncertainties between 4.36 and 9.30 percent.

Results and Discussion

Fifty-seven air and helium experiments were performed on the 3 × 3 array with pressures ranging from 1 to 7 atm and q = 2 to 16 W/rod. Nineteen vacuum experiments were conducted to correct nine helium runs and ten air runs. Twenty-seven air and helium experiments were performed on the 5 × 5 array with containment pressures ranging from 1 to 7 atm and q = 1 to 10 W/rod. Twenty vacuum experiments were conducted to correct ten helium runs and ten air runs. With the 7 × 7 array, fifteen air and helium tests were conducted with pressures ranging from 1 to 6 atm and q = 1 to 3 W/rod. Sixteen vacuum experiments, one of which was conducted with constant power input per rod, concluded the experimentation. Since the changes in the heat transfer coefficients of the bottom, middle, and top rods along the center-column (CCB, CCM, and CCT) and the edge-column (ECB, ECM, and ECT) will give a good representation of the global changes in the rod-bundle, the discussion of the results is focused on these rods (Fig. 1).

Flow Visualization Results. Limited flow visualization experiments were performed in the 3 × 3 array to investigate the flow pattern within the enclosure. The experiments were carried out with air at atmospheric pressure for six power levels in the range of q = 0.2 to 6 W/rod. Figure 3 shows the induced flow field due to 0.2 W/rod power input (a total of 1.8 W for the array), which corresponds to $Ra_d^* \approx 320$. As expected, a one-half symmetric flow field is observed with a strong plume rising at the centerline. The circulating flow pattern clearly shows the transport of energy by the rising air through the rods, and transferring a large fraction of that energy to the surface of the enclosure. A pair of large secondary flow cells occupy the top portion of the enclosure. Also a symmetric pair of smaller secondary flow cells are located above the midheight of the enclosure next to the side walls. The region next to the bottom surface of the enclosure is relatively inactive. The observed flow field is similar to the numerical prediction of Keyhani and Luo (1995).

Temperature Results. Average rod temperatures in the 3 × 3 and 7 × 7 arrays due to a power input of 2 W/rod with air at atmospheric pressure are presented in Fig. 4. Figure 4(a) shows the center column to left edge column rod temperatures in the 3 × 3 array, while Fig. 4(b) shows the center column to right edge column rod temperatures in the 7 × 7 array. The contribution of each heat transfer mode (convection and radiation) is indeterminable from the given temperature data. The temperatures do, however, demonstrate characteristics of natural convection heat transfer. The buoyancy-driven flow has created a substantial difference between the temperatures of the center-column-top (CCT) and the center-column-bottom (CCB) rods. Moreover, it can be seen that an increase in the size of the array has resulted in a substantial increase in the temperature of the CCT rod ($T_d - T_c$ increased from 33.8 to 77.0°C when N was increased from 3 to 7). For the CCB rod, however, a rather modest increase in its temperature was observed when the array size was increased ($T_d - T_c$ increased from 21.6 to 29.8°C when N was increased from 3 to 7). This should be expected since the bottom row is the location of the first contact between the cold (circulating) fluid and the rod-

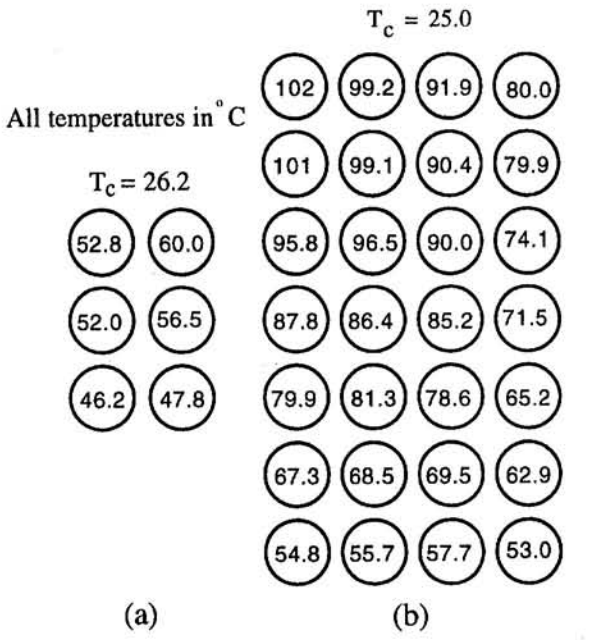


Fig. 4 Average rod temperatures for: (a) 3 × 3 array—air, 0.98 atm, 2.04 W/rod, center to left edge columns are shown; and (b) 7 × 7 array—air, 1.01 atm, 2.02 W/rod, center to right edge columns are shown

Downloaded 11 Dec 2010 to 193.140.21.150. Redistribution subject to ASME license or copyright; see http://www.asme.org/terms/Terms_Use.cfm

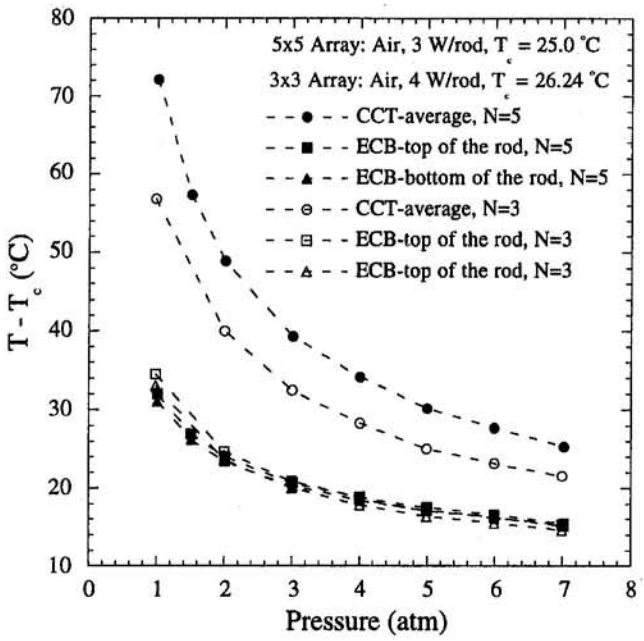


Fig. 5 Rod temperatures as a function of pressure

bundle. Thereafter, along a given column, the fluid is moving upward and is being heated by the rods. Thus, the convected part of the heat flux dissipated by a given rod must be transferred to the fluid at increasingly higher rod surface temperatures as the heated fluid moves to higher rows.

Figure 5 present the effect of gas pressure (air) on the rod temperatures in $N = 3$ and 5 arrays. Rods having the highest (CCT) and lowest (ECB) surface temperatures are represented. For rod ECB, the measured temperatures at its top and bottom surfaces are shown in Fig. 5. It must be noted that due to the small diameter of the rods (0.942 cm), $P/d = 1.35$, the moderating effect of radiation contribution, and the state of convection flow regime in the rod-bundle enclosure, the largest difference between the measured temperatures at the top surface and bottom surface of the rods in the arrays was less than 3.5°C. Also it may be noted that the heating condition at the surface of these rods as well as the rods in a spent nuclear fuel assembly is not a mathematical constant-flux case. This is due to the fact that internal conduction heat transfer through the thickness of the sheet covering the heating elements has a moderating effect on the temperature variation around the circumference of each rod. As shown, a substantial temperature decrease was observed when pressure was increased from 1 to 7 atm (for $N = 3$, the $T_d - T_c$ of the CCT rod decreased by 64 percent). Similar trends are apparent from the 5×5 data. Since Rayleigh number is proportional to ρ^2, the pressure increase means an increase in the Ra_d^*, which results in a higher Nusselt number, and hence lower temperatures. For example, out of 3 W dissipated by the CCT rod in the 5×5 bundle, at 1 atm air convection, approximately 52 percent of the input power is transferred by convection and 48 percent by radiation, whereas at 6 atm, approximately 87 percent is transferred by convection.

It is instructive to note differences between the resulting temperatures of a radiation-dominated rod-bundle and one where convection is the dominant mode of heat transfer. These two scenarios are shown in Fig. 6 for the 7×7 array with a power input of 1.0 W/rod. Figure 6(a) shows the center column to left edge column rod temperatures under vacuum, while Fig. 6(b) shows the center column to right edge column rod temperatures in a convection-dominated flow regime. Rod temperatures in the evacuated bundle are symmetric about the array's horizontal centerline, Fig. 6(a), but for the 1 atm air convection case, Fig. 6(b), there is substantial difference between the temperatures of the CCB and CCT rods. The magnitude, as well as position, of the highest temperature rod also varies. The highest temperature rod in the evacuated bundle, as may be expected, is the CCM rod, but the CCT rod has the highest temperature in the 1 atm air convection case.

Heat Transfer. The Nusselt number and modified Rayleigh number for a given rod in an array are calculated via,

$$\mathrm{Nu}_d = \frac{q_c'' d}{k(T_d - T_c)} \tag{1}$$

$$\mathrm{Ra}_d^* = \frac{g\beta d^4 q_c''}{k\alpha\nu} \tag{2}$$

where q_c'' is the convected heat flux from the rod, T_d the average rod temperature, and T_c the enclosure temperature. The thermophysical properties were evaluated at the film temperature (average value of T_d and T_c).

Nusselt numbers as functions of modified Rayleigh numbers for selected rods of $N = 3$, 5, and 7 arrays are presented in Figs. 7, 8, and 9, respectively. In general, the graphs have the same features. Namely, the data span a broad range of Ra_d^*; the magnitudes of Nu_d are highest for the bottom rods along any column and lowest for the top rods. Also, similar transitions of flow regimes are observed. Based on the observed changes in slope of Nusselt number dependence on Rayleigh number, three regions have been identified. These observations do not apply to all the rods in the three arrays investigated, and should be considered as a general attempt in classifying flow regimes in horizontal rod-bundle enclosures. At the lowest modified Rayleigh number investigated buoyancy-driven flow is beginning to develop and the flow is conduction dominated. Region (1) is considered to be a conduction flow regime. As Rayleigh number increases, convection begins to dominate the flow and rod Nusselt numbers exhibit the greatest sensitivity to changes in Ra_d^*. Region (2) is consider to be a conduction-convection transition flow regime. The final region of interest (3) is considered to be a convection dominated flow regime. It may be noted

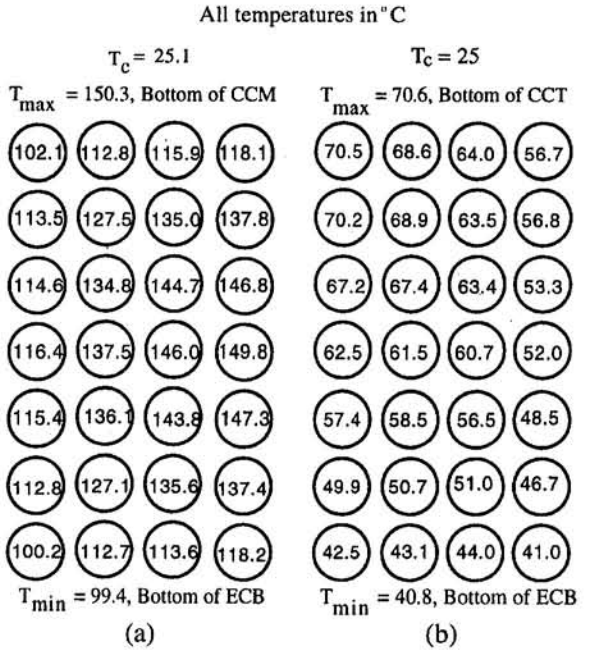


Fig. 6 Average rod temperatures in the 7×7 array: (a) under vacuum (1.07×10^{-4} atm), q = 1.00 W/rod, center to left edge columns are shown; (b) with air at 0.98 atm, q = 1.01 W/rod, center to right edge columns are shown

Downloaded 11 Dec 2010 to 193.140.21.150. Redistribution subject to ASME license or copyright; see http://www.asme.org/terms/Terms_Use.cfm

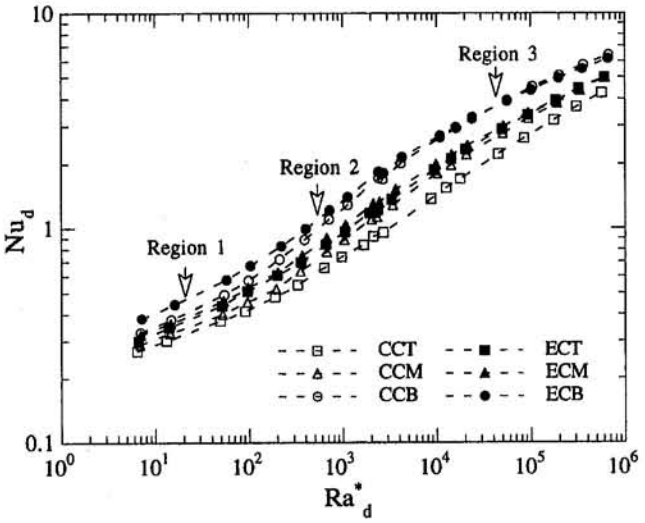


Fig. 7 Rod Nusselt numbers in the 3 × 3 array

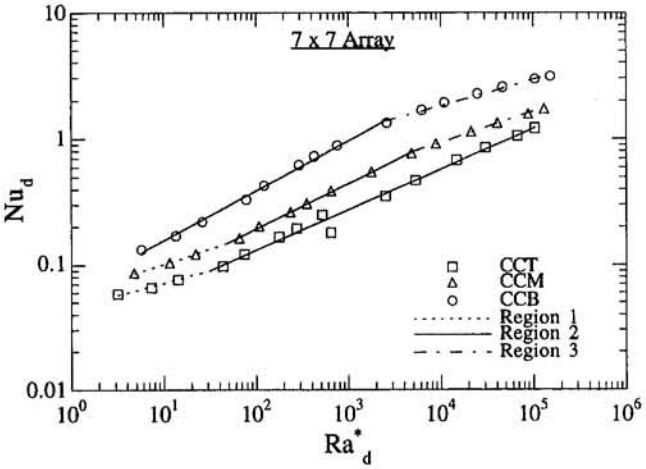


Fig. 9 Rod Nusselt numbers in the 7 × 7 array (center column rods)

that due to "plume" effect of the circulation flow pattern on the rods of a given array, the classical slopes of $m = 0.2$ for laminar flow and $m = 0.25$ for turbulent flow regime for the $\mathrm{Nu}_d = C(\mathrm{Ra}_d^*)^m$ correlation is not applicable here. The changes in the slope of the Nu_d dependence on Ra_d^* reveal that the individual rods in a given array may transfer their convected power to the fluid via different but coexisting flow regimes (consider $\mathrm{Ra}_d^* = 5 \times 10^4$ in Figs. 8 and 9). The numerical work of Keyhani and Luo (1995) revealed the same phenomenon for a rod boundary condition of constant heat flux.

The results for each rod in each array were correlated in terms of $\mathrm{Nu}_d = C(\mathrm{Ra}_d^*)^m$. Considering the half-symmetry of the phenomenon, the correlations are for 6 rods in the $N = 3$ array, 15 rods in the $N = 5$ array, and 28 rods in the $N = 7$ array. Due to page limitations these correlations are not reported here, and the interested reader is referred to Dalton (1994).

Comparison With Numerical Results. The numerical results of Keyhani and Luo (1995), which were based on the constant heat flux boundary condition at the surfaces of the rods, are valid only when all the energy dissipated by the rods is transferred to the enclosure surface through convection heat transfer. In the laboratory experiments the energy dissipated by the rods is transferred through convection and radiation heat transfer. Therefore, comparison of the numerical results with the experimental data may provide only qualitative information. In order to model the experimental conditions, one must specify the measured rod temperatures as the boundary condition for the rods in the array, and numerically determine the convected heat fluxes from the rods that correspond to those prescribed temperature boundary conditions. The comparison of the experimental and the numerical results in this case would mean that the numerically and experimentally determined convection heat fluxes (convection heat transfer coefficients) are being compared.

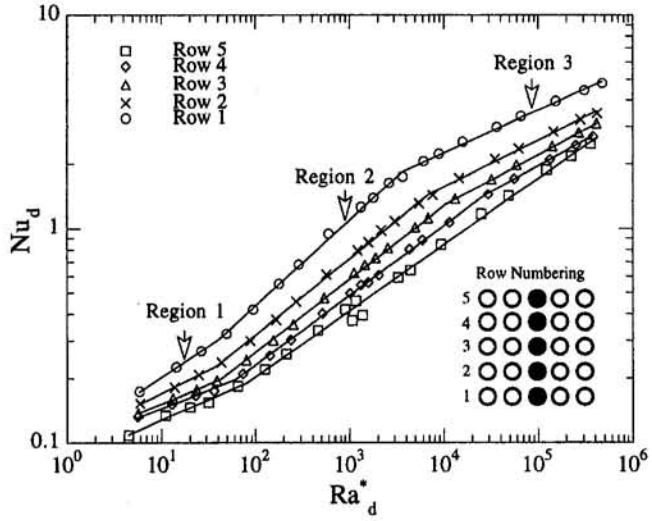


Fig. 8 Rod Nusselt numbers in the 5 × 5 array (center column rods)

Numerical simulations with prescribed temperature boundary condition at the rod surfaces for the 3 × 3 array have been performed using the finite element code FIDAP (Fluid Dynamics International, Inc.). Quadrilateral elements were used to construct a nonuniform mesh with smaller elements near the surfaces in order to achieve an accurate Nusselt number evaluation at rod surfaces while keeping the amount of calculation at a moderate level. The details of the computation, mesh size, and accuracy tests are given in Keyhani and Luo (1995) and will not be repeated here. For each experimental run the measured temperatures from the heat transfer experiments were used as input data. The measured temperatures were input for the top and the bottom surface of each rod, and the temperature distribution between the top point and the bottom point was assumed to vary linearly. The enclosure temperature was set at the average measured enclosure temperature. The medium (air or helium) thermophysical properties, evaluated at the mean of the array-average and enclosure temperatures, were used in the model. The mesh used in the constant heat flux rod surface boundary condition analysis was used in these simulations.

Nine simulation runs were performed with modified rod Rayleigh numbers ranging from 6 to 2×10^4. Figure 10 presents a comparison of results from experiment, FIDAP simulation with constant heat flux at rod surfaces, and FIDAP simulation with prescribed temperatures at rod surfaces. Conduction Nusselt numbers due to a constant heat flux boundary condition are also shown in Fig. 10. It can be seen that the simulations with prescribed temperature boundary condition are in a very good agreement with the experimental results. Also, it can be seen that at low Ra_d^* values (conduction dominated) there is a large difference between the specified temperature and constant heat flux boundary condition predictions. However, as Ra_d^* is increased (higher convection contribution) the difference between the two predictions decreases.

Generalized Correlations. The total heat removed by convection from all the rods in a given array is ultimately convected to the four enclosure surfaces, which are isothermally cooled.

Downloaded 11 Dec 2010 to 193.140.21.150. Redistribution subject to ASME license or copyright; see http://www.asme.org/terms/Terms_Use.cfm

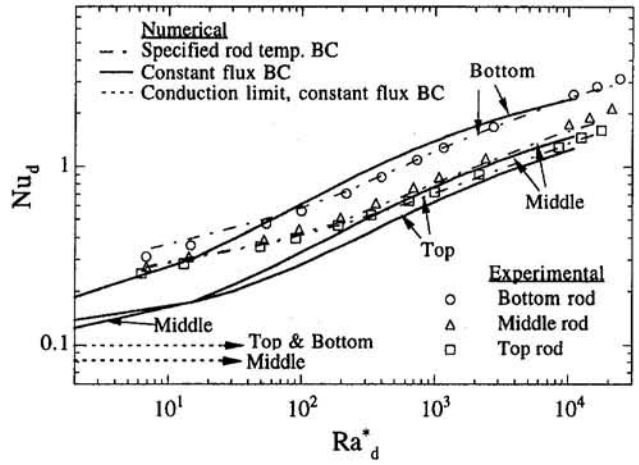


Fig. 10 Comparison of the experimental and numerical Nusselt numbers (center-column rods, 3 × 3 array)

In order to provide engineering correlations, the modified enclosure Rayleigh number and average enclosure Nusselt number have been defined as:

$$\mathrm{Ra}_W^* = \frac{g\beta W^4 Q_c''}{k\alpha\nu} \tag{3}$$

$$\mathrm{Nu}_W = \frac{Q_c'' W}{k(T_{CCT} - T_c)} \tag{4}$$

where Q_c'' is the average convected heat flux for the entire enclosure surface. Since among the average rod temperatures in the array rod CCT has the highest value, the enclosure heat transfer coefficient has been defined based on the temperature difference of $(T_{CCT} - T_c)$. The thermophysical properties were evaluated at the film temperature (average value of T_{CCT} and T_c).

Figure 11 shows a comparison of the enclosure Nusselt numbers of the arrays investigated. The enclosure Nusselt number increases as the order of the array (N) is increased from 3 to 7. The enclosure Nusselt numbers are correlated for each array, and the correlation coefficients are summarized in Table 1. The average deviation between the correlations and the data is less than 1.25 percent. The rod Nusselt number correlations (Nu_d) can be readily used to estimate the rod temperatures in the $N = 3$ to 7 arrays. However, the enclosure correlations (Nu_W) are expected to result in a more accurate estimate for the CCT

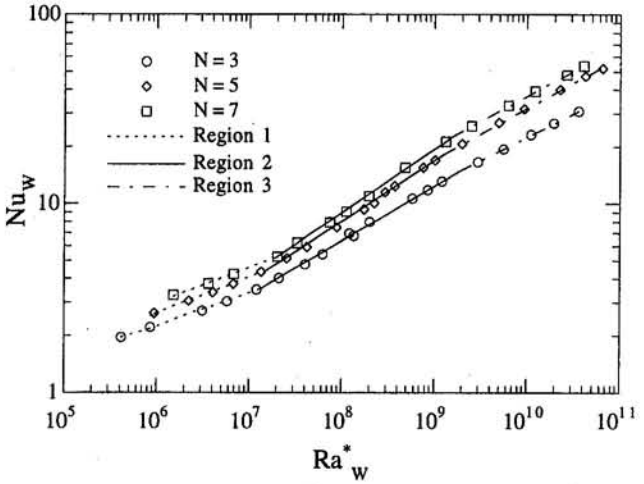


Fig. 11 Enclosure Nusselt numbers for the N = 3, 5, and 7 arrays

Table 1 Overall convection heat transfer correlations; $\mathrm{Nu}_W = C(\mathrm{Ra}_W^*)^m$

Enclosure	Region 1	Region 2	Region 3
3 x 3	$4.13\times10^5 < \mathrm{Ra}^*_W < 1.31\times10^7$ C=0.218; m=0.170	$1.31\times10^7 < \mathrm{Ra}^*_W < 1.88\times10^9$ C=0.0310; m=0.289	$1.88\times10^9 < \mathrm{Ra}^*_W < 3.57\times10^{10}$ C=0.0744; m=0.248
5 x 5	$9.47\times10^5 < \mathrm{Ra}^*_W < 1.53\times10^7$ C=0.190; m=0.190	$1.53\times10^7 < \mathrm{Ra}^*_W < 1.25\times10^9$ C=0.0214; m=0.322	$1.25\times10^9 < \mathrm{Ra}^*_W < 6.51\times10^{10}$ C=0.0636; m=0.270
7 x 7	$1.53\times10^6 < \mathrm{Ra}^*_W < 1.95\times10^7$ C=0.232; m=0.185	$1.95\times10^7 < \mathrm{Ra}^*_W < 1.53\times10^9$ C=0.0184; m=0.336	$1.53\times10^9 < \mathrm{Ra}^*_W < 4.05\times10^{10}$ C=0.0759; m=0.269

rod than the rod correlations (Nu_d) since they reduce the error involved in assuming that all the power inputs to the rods are transferred solely by natural convection. For example, in an atmospheric pressure air experiment with the $q = 2$ W/rod, the CCT rod in the $N = 5$ array dissipated approximately 52 percent of its power by natural convection. However, the bundle as a whole transferred about 81 percent of its total power input by natural convection. It may be noted that the estimated maximum temperature in the array (T_{CCT}) will be a conservative value since the simultaneous transfer of energy by radiation (a higher effective transfer coefficient) is neglected.

In order to determine the effect of array size (N) on enclosure Nusselt number, the present data for $N = 3$, 5, and 7 along with the constant heat flux predictions of Keyhani and Luo (1995) for $N = 3$, 5, 7, and 9 have been examined. The analysis shows that Nu_W dependence on N can be accurately represented by $N^{0.45}$ as illustrated in Fig. 12. Moreover, it can be seen that as Ra_W^* is increased, the difference between the experimental data and the constant heat flux predictions decreases. This is due to the fact that the high Ra_W^* data have been obtained with high gas pressures and low rod temperatures, such that the radiation contribution in the convection–radiation runs were often less than 10 percent. The enclosure Nusselt numbers are accurately presented by

$$\mathrm{Nu}_W = 0.0441(\mathrm{Ra}_W^*)^{0.316}(Nd/W)^{0.450} \tag{5}$$

This correlation is valid for $W/d = 20.6$, $P/d = 1.35$, $10^7 < \mathrm{Ra}_W^* < 10^{10}$, and $N = 3$, 5, 7, and 9. The array size effect is extended to $N = 9$ since $N^{0.45}$ accurately represents the numerical predictions for $N = 9$. The average deviation of this correlation from the data is less than 3.0 percent.

Conclusions

Natural convection heat transfer in enclosed horizontal $N \times N$ arrays with $N = 3$, 5 and 7 has been experimentally investi-

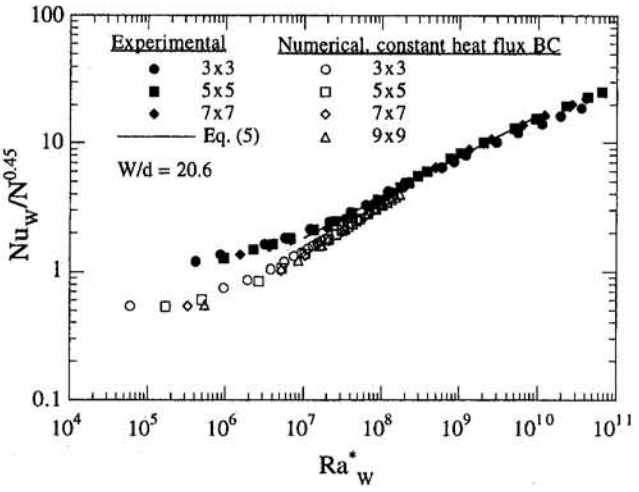


Fig. 12 Generalized enclosure Nusselt number as a function of array size N

Downloaded 11 Dec 2010 to 193.140.21.150. Redistribution subject to ASME license or copyright; see http://www.asme.org/terms/Terms_Use.cfm

gated for a wide range of Rayleigh number. Also for the 3 × 3 array numerical predictions are presented that are in very good agreement with the data. Natural convection correlations in the form of Nusselt number (Nu_d) as a function of modified Rayleigh number (Ra_d^*) are derived for each rod in each array. The correlations cover the three flow regimes of conduction, transition, and convection, which span a modified Rayleigh number range of $6.45 < Ra_d^* < 3.08 \times 10^5$. The correlations can be used to obtain conservative estimates of rod temperatures in $N = 3$, 5, and 7 arrays, or they may be combined with a radiation model to obtain accurate rod temperature predictions.

A generalized correlation for the enclosure Nusselt number as a function of the enclosure modified Rayleigh number and the array size (N) is presented. This correlation may be readily used to obtain a conservative estimate of maximum temperature (T_{CCT}) in $N = 3$, 5, 7 and 9 arrays. The array size effect is extended to $N = 9$ since $N^{0.45}$ accurately represents the numerical predictions for $N = 9$. The operating range of a 15 × 15 PWR (Pressurized Water Reactor) spent-fuel assembly stored in a cask at atmospheric pressure air is about $5 \times 10^7 < Ra_W^* < 2 \times 10^8$. Extrapolation of the generalized correlation from $N = 9$ to $N = 15$ results in a 26 percent higher average heat transfer coefficient for the enclosure surface. Based on our experience with natural convection in rod-bundle enclosures, this extrapolation seems to be a very reasonable approximation.

Acknowledgments

This work was supported by Sandia National Laboratories under contract No. AF9344.

References

Arya, M. S., and Keyhani, M., 1990, "Convective Heat Transfer in a Sealed Storage Cask Containing Spent-Fuel Canisters," *Journal of Nuclear Science and Engineering*, Vol. 105, pp. 391–403.

Cox, R. L., 1976, "Radiative Heat Transfer in Arrays of Parallel Cylinders," Ph.D. dissertation, University of Tennessee, Knoxville, TN.

Dalton, T. E., 1994, "An Experimental Study of Heat Transfer in Horizontal Enclosed Rod-Bundles," MS Thesis, University of Tennessee, Knoxville, TN.

Dutton, J. C., and Welty, J. R., 1975, "An Experimental Study of Low Prandtl Number Natural Convection in an Array of Uniformly Heated Vertical Cylinders," ASME JOURNAL OF HEAT TRANSFER, Vol. 97, pp. 372–377.

Fedorovitch, E. D., 1989, "The Thermal Conditions and the Strength of a Spent Fuel Package: Analysis and Test," *Proc. 9th International Symposium on the Packaging and Transportation of Radioactive Materials*, CONF-890631-Vol. 3, pp. 1647–1668.

Fry, E. J., Livesay, S., Spiller, G. T., and MacGregor, B. R., 1983, "Heat Transfer in a Dry, Horizontal LWR Spent Fuel Assembly," *Proc. 7th International Symposium on Packaging and Transportation of Radioactive Materials*, New Orleans, LA, pp. 1087–1094.

Irino, M., Oohashi, M., Irie, T., and Nishikawa, T., 1986, "Study on Surface Temperatures of Fuel Pins in Spent Nuclear Fuel Dry Shipping/Storage Casks," *Proc. International Symposium on the Packaging and Transportation of Radioactive Materials*, Davos, Vol. 2, pp. 585–589.

Keyhani, M., Kulacki, F. A., and Christensen, R. N., 1983, "Estimates of Maximum Temperatures in Spent Fuel Waste Packages via Generalized Correlations for Convective Heat Transfer," *Transaction, American Nuclear Society*, Vol. 45, pp. 138–140.

Keyhani, M., Kulacki, F. A., and Christensen, R. N., 1985, "Experimental Investigation of Free Convection in a Vertical Rod-Bundle—A General Correlation for Nusselt Numbers," ASME JOURNAL OF HEAT TRANSFER, Vol. 107, pp. 611–623.

Keyhani, M., and Luo, L., 1995, "A Numerical Study of Convection Heat Transfer Within Enclosed Horizontal Rod-Bundles," *Journal of Nuclear Science and Engineering*, Vol. 119, No. 2, pp. 116–127.

Kline, S. J., and McClintock, F. A., 1953, "Describing Uncertainties in Single-Sample Experiments," *Mechanical Engineering*, Jan., pp. 3–8.

Reilly, J. T., Chan, C. K., Edwards, D. K., and Kastenberg, W. E., 1978, "The Effects of Thermal Radiation on the Temperature Distribution in Fuel Rod Arrays," *Nuclear Engineering and Design*, Vol. 48, pp. 340–351.

Vdovets, N. V., Grivnin, A. I., Gotovskii, M. A., Pervitskaya, T. A., Fromzel, V. N., Fedorovitch, E. D., and Shleifer, V. A., 1987, "Natural-Convection Heat Transfer in Horizontal Bundles of Fuel Rods," *High Temperature, A Translation of Teplofizika Vysokikh Temperatur*, Vol. 24, No. 4, pp. 545–552.

Warrington, R. O., and Weaver, R. A., 1984, "Natural Convection Heat Transfer Between Arrays of Horizontal Cylinders and Their Enclosures," *Heat Transfer in Enclosures*, R. W. Douglass and A. F. Emery, eds., ASME HTD-Vol. 39.

Downloaded 11 Dec 2010 to 193.140.21.150. Redistribution subject to ASME license or copyright; see http://www.asme.org/terms/Terms_Use.cfm

Flow and Mixed Convection Heat Transfer in a Divergent Heated Vertical Channel

C. Gau
Professor.

T. M. Huang
Graduate Student.

Institute of Aeronautics and Astronautics,
National Cheng Kung University,
Tainan, Taiwan

W. Aung[1]
Adjunct Professor,
College of Engineering,
Southern Illinois University,
Carbondale, IL

This paper concerns an experimental study of the mixed convection flow and heat transfer inside a divergent channel formed by two plane walls. One of the side walls is oriented vertically and is heated uniformly, and the opposite wall is tilted at an angle of 3 deg with respect to the vertical position and is insulated. The ratio of the height to wall spacing at the flow inlet, which is at the smaller opening of the channel, is 15. The Reynolds number of the main forced flow ranges from 100 to 4000 and the buoyancy parameter, Gr/Re^2, varies from 0.3 to 907. Flow reversal is found to occur for both assisted and opposed convection. The effect of channel divergence on the occurrence and structure of the reversed flow and the heat transfer is presented and discussed. It is found that the divergence of the channel decelerates the mainstream such that flow reversal is initiated at a much lower buoyancy parameter. The adverse pressure gradient tends to push the reversed flow upstream and leads to a deeper penetration of the reversed flow into the channel. The destabilization effect of the divergent channel can lead to breakdown of vortices and to transition to turbulent flow. This can significantly enhance the heat transfer. Temperature fluctuation measurements at different locations are used to indicate oscillations and fluctuations of the reversed flow. The effect of the buoyancy parameter on the Nusselt number and the reversed flow structure is discussed. The average Nusselt number is determined and correlated in terms of relevant nondimensional parameters for pure forced and mixed convection, respectively.

Introduction

Combined free and forced convection in a symmetrically or asymmetrically heated vertical passage has received considerable attention for its practical application in various modern systems such as electronic equipment. Under certain circumstances the circuit boards may be slightly tilted, thereby turning the flow passage into a divergent or convergent channel. The divergence of the channel can decelerate the upward-flowing mainstream while the convergence can accelerate the flow. The divergence or convergence of the channel can have a significant effect on the occurrence and the structure of the reversed flow, and can change the heat transfer characteristics inside the channel.

Relevant studies of mixed convection in a heated vertical divergent (that is, one with a smaller opening at the entrance) or convergent (smaller opening at the exit) channel are nonexistent. Prior studies on the flow and heat transfer in a divergent or a convergent channel are mostly concerned with pure forced convection (Sparrow and Starr, 1965; Shiina, 1987). For developing flow, Su and Lin (1991a, b) obtained numerical results for both convergent and divergent ducts and concluded that both the pressure drop and the Nusselt number increase with the divergent or the convergent angle. Experimental work has been conducted for turbulent flow in a divergent channel with a fully developed inlet velocity profile (Komori et al., 1985; Kajiuchi et al., 1986). However, only the velocity and the pressure drop across the divergent section have been measured.

Other work dealing with a divergent or convergent channel includes the natural convection experiments performed by Sparrow et al. (1988), and Sparrow and Ruiz (1988) and Kihm et al. (1993) who considered symmetric, constant wall temperature conditions. Flow recirculation is found in the center portion of the divergent channel, which does not play an important role to affect the heat transfer.

For the mixed convection in a vertical channel, almost all the work completed thus far is dedicated to parallel-walled passages such as vertical or inclined tubes, annuli, and parallel-plate ducts. Comprehensive reviews of mixed convection in a vertical pipe or channel have been presented by Aung (1987) and Jackson et al. (1989). Yao and Rogers (1989) have recently analyzed the linear instability of assisted convection in an annulus with aspect ratio of 100 and found that the flow is unstable in the ranges of practical interest. Transition to turbulent flow and the enhancement in the heat transfer have been noticed by Scheele and Hanratty (1963). Wirtz and McKinley (1985) performed LDV measurements and holographic flow visualization for opposed convection in a parallel-plate channel. A slight enhancement in the heat transfer is observed and is attributed to the destabilization by the opposing buoyancy of the viscous flow adjacent to the heated wall leading to high turbulence intensity at the exit.

Gau et al. (1992a, b) have experimentally studied the reversed flow structure and heat transfer in a finite asymmetrically heated parallel-plate channel. Flow reversal can occur at relatively low values of the buoyancy parameter, Gr/Re^2, for opposed convection and at large Gr/Re^2 for assisted convection. The reversed flow is observed to induce the oscillation of flow. The Nusselt numbers based on the inlet temperature of the flow for both assisted and opposed convection are measured. A penetration model of the reversed flow is developed, and the prediction agrees with the data for small Reynolds numbers and large buoyancy parameters. Recently, mixed convection in a vertical heated convergent channel has been studied (Huang et al., 1995). The results indicate that the flow structure and the

[1] Permanent address: National Science Foundation, Arlington, VA 22230.

Contributed by the Heat Transfer Division for publication in the JOURNAL OF HEAT TRANSFER. Manuscript received by the Heat Transfer Division February 24, 1995; revision received March 29, 1996. Keywords: Flow Visualization, Mixed Convection, Thermal Packaging. Associate Technical Editor: Y. Jaluria.

Copyright © 1996 by ASME

Downloaded 11 Dec 2010 to 193.140.21.150. Redistribution subject to ASME license or copyright; see http://www.asme.org/terms/Terms_Use.cfm

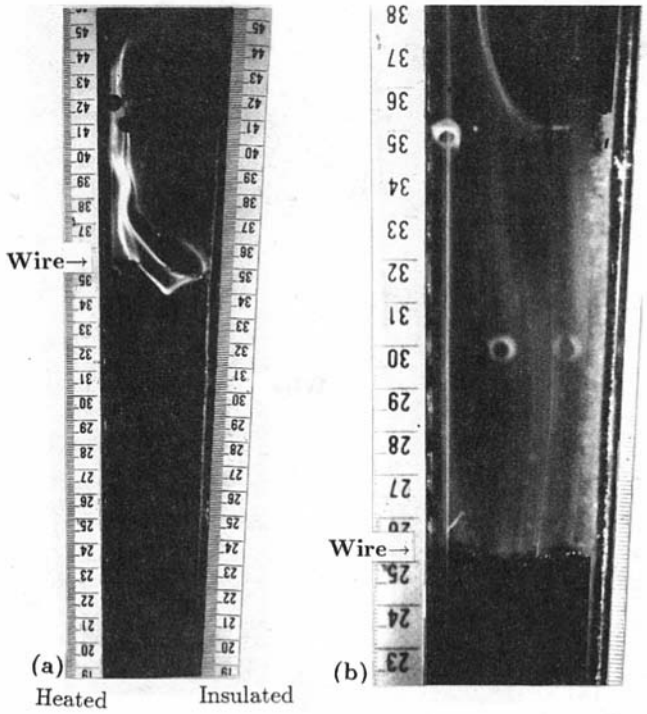


Fig. 1 Reversed flow structure for assisted convection in a divergent channel with $Gr/Re^2 = 20$ and $Re = 700$

heat transfer characteristics are significantly affected by even a slight convergence of the channel. It appears that the results in the parallel-plate channel cannot be used to predict the complicated mixed convection flow and heat transfer in a convergent channel.

The present paper describes an experimental study of mixed convection in a heated divergent channel with one wall held in the vertical position. The vertical wall is heated uniformly, while the opposite wall, which has a divergence angle of 3 deg, is tilted away from the heated wall and is well insulated. The objective of this work is to study the mixed convection, especially the occurrence and structure of the reversed flow and the heat transfer, in a heated vertical divergent channel. For the purpose of comparison, results for the parallel-plate channel are also presented and discussed.

Experimental Apparatus and Procedures

The experimental apparatus is a modification of the one used by Huang et al. (1995). The Plexiglas channel is 45 cm in length, 20 cm deep (perpendicular to the plane of the paper in Fig. 1) inside, and 3 cm wide at the entrance. One of the vertical walls is tilted slightly to form a 3 deg divergent angle, so that the channel is wider at the exit than at the entrance. This angle of divergence can be adjusted as desired. For the parallel-plate channel, the tilted wall is adjusted to be parallel to the opposite wall. This opposite wall is vertical and made of 2-cm-thick balsa wood on which 0.015-cm-thick stainless steel foil heating strips are glued. DC power is used to provide the desired heat flux, determined by the electric voltage across and the current passing through the foil. For better insulation, 12-cm-thick foam rubber is glued on the back of the heated wall to provide additional insulation, and the opposite wall is wrapped with 3-cm-thick foam rubber. The temperature of the heated wall is measured with 89 chromel-alumel thermocouples epoxied on the back at 5-mm intervals along the centerline. Spanwise wall temperature variations are monitored by 11 thermocouples positioned 5 cm away from the centerline and the maximum variation is shown to be less than 3.4 percent with respect to the temperature difference between the wall and the fluid at the inlet of the channel. This indicates that a two-dimensional boundary condition can be maintained when flow reversal is absent. Five additional thermocouples embedded along the surface of the insulated wall provide information needed for estimating the radiation loss from the heated wall. The temperature data are taken when the entire system reaches steady state, usually in 3–4 hours.

Flow visualization by smoke generation is facilitated by a thin, electrically heated wire coated with oil. To provide smoke of good quality, fine iron powders are added into the oil, as suggested by Fukamachi et al. (1991). The smoke wire is inserted through various small holes located on the insulated wall. A vertical sheet of light oriented perpendicular to the insulated wall is used for illumination.

The components of the wind tunnel, including the test section (i.e., the divergent channel), the diffuser, the settling chamber and the contraction section, are bolted together and placed on a rotatable frame. Thus, for assisted convection, air enters the channel from the bottom at the smaller opening, while for opposed convection, the divergent channel is turned upside down, and air enters the channel from the top. For pure forced convection experiments, the buoyancy force inside the channel is minimized by situating the channel in a horizontal position with the heated wall on top. The fluid velocity in the channel is measured with a TSI hot-wire anemometer using an improved calibration system originally designed by Chen and Miau (1987). The turbulence intensity measured at the entrance of the channel is 2.1 percent for an entrance velocity of 0.27 m/s and 0.7 percent for 1.59 m/s.

The convection heat transfer from the heating strips is determined by the voltage drop and the current passing through the strips, less conduction and radiation losses. The local heat transfer coefficient is evaluated by the equation:

$$h_r = (q_t - q_{\text{rad}} - q_{\text{cond}})/(T_w - T_r) \qquad (1)$$

where r refers to the bulk mean condition or the inlet condition. The conduction loss from the heated wall is estimated by solving the one-dimensional conduction equation for a composite wall. The radiation heat loss from the heated wall is calculated using a method very similar to that described by Webb and Hill (1989). The local Nusselt number is computed based on the

Nomenclature

A = cross-sectional area of channel
b = channel gap at the inlet of the channel
D_h = hydraulic diameter of the channel $= 2b$
g = gravitational acceleration
Gr = Grashof number $= g\beta q D_h^4/k\nu^2$
h = convective heat transfer coefficient
$\bar{h}$ = average heat transfer coefficient
k = thermal conductivity of air
Nu = local Nusselt number $= hD_h/k$
$\overline{\text{Nu}}$ = average Nusselt number $= \bar{h}D_h/k$
Pr = Prandtl number $= \nu/\alpha$
q = heat flux
Re = Reynolds number defined at the inlet of the channel $= u_0 D_h/\nu$
T = temperature
u_0 = inlet velocity
x, y = coordinate parallel, and normal to the heated wall
β = coefficient of expansion
ν = kinematic viscosity

Subscripts

b = refers to bulk mean value
0 = refers to inlet condition
i = refers to inlet condition

Downloaded 11 Dec 2010 to 193.140.21.150. Redistribution subject to ASME license or copyright; see http://www.asme.org/terms/Terms_Use.cfm

thermophysical properties evaluated at the bulk mean temperature of the flow. Properties in the Reynolds and Grashof numbers are evaluated at inlet conditions. Since the heat loss is relatively large near the channel exit, the last three heating strips are used only as guard heaters to prevent the heat loss. Further details on the experimental setup and procedures are given by Huang et al. (1995). The uncertainty of the experimental data obtained in the present system is determined according to the procedure outlined by Kline and McClintock (1953). It is found that the maximum uncertainty in the local Nusselt number is 5.6 percent, while it is 6.2 and 7.8 percent, respectively, for the Reynolds and Grashof numbers.

Results and Discussion

Buoyancy-Assisted Convection

Flow Visualization. For assisted convection in the divergent channel, the fluid near the heated wall accelerates with increasing Gr/Re^2, while the fluid adjacent to the insulated wall decelerates. When $Gr/Re^2 = 10$ and $Re = 700$, the flow in the entire channel is still very steady, and no flow reversal is found. As the heat flux increases so that $Gr/Re^2 = 20$ and $Re = 700$, the fluid downstream near the heated wall moves so rapidly that the fluid velocity near the insulated wall becomes zero at a certain channel height. Farther downstream, flow reversal occurs as shown in Fig. 1. The heated wall is on the left and insulated wall is on the right. The reversed flow enters the channel from the outside at the top (i.e., the exit opening for the mainflow) and moves along the insulated wall in a downward direction (i.e., opposed to the mainstream) and after traversing some distance down the channel, it turns upward under the combined influence of the mainstream and the buoyancy. This process of flow reversal occurs when the buoyancy force becomes so large that natural convection begins to dominate the transport process. Under this circumstance, the total mass flow rate supplied by the blower is less than the buoyant flow induced by natural convection flow along the heated wall. At the same time, a negative pressure is created inside the channel that induces the cold air from the outside into the channel along the insulated wall. A V-shaped circulation flow is created. Due to the divergence, the bottom region of the V-shaped recirculation flow region is not as narrow or sharp as in the parallel-plate channel (Gau et al., 1992b) but is very blunt as shown in Figs. 1(a) and 1(b). The reversed flow is situated in the dark area near the insulated wall after $x = 33$ cm. The smooth smoke pattern upstream of the reversed flow region may be noted in Fig. 1(b). Since the reversed flow opposes the mainstream, the entire flow becomes unstable due to Kelvin–Helmholtz instability. The downward penetration of the reversed flow moves up and down along the insulated wall as is also observed in the parallel-plate channel (Gau et al., 1992b). In the region upstream of (i.e., below) the reversed flow, however, the mainstream is laminar and is not appreciably affected by the presence of flow reversal as shown in Fig. 1(b). It has been observed that some of the heated buoyant flow exiting from the channel can be sucked back into the channel and mixed with the cold reversed flow; hence, the temperature of the reversed flow is higher than the ambient air, as indicated by the temperature fluctuation measurements in the next section.

Note that the divergence of the channel can decelerate the mainstream such that natural convection is more likely to dominate the transport process in the downstream region, thereby initiating the reversed flow. With divergence of the channel flow reversal can be initiated at a much smaller buoyancy parameter than in the parallel-plate channel. For example, in a parallel-plate channel with $Re = 700$, flow reversal is initiated at Gr/Re^2 greater than 80 (Gau et al., 1992b), whereas for the divergent channel, flow reversal is initiated at $Gr/Re^2 \geq 15$.

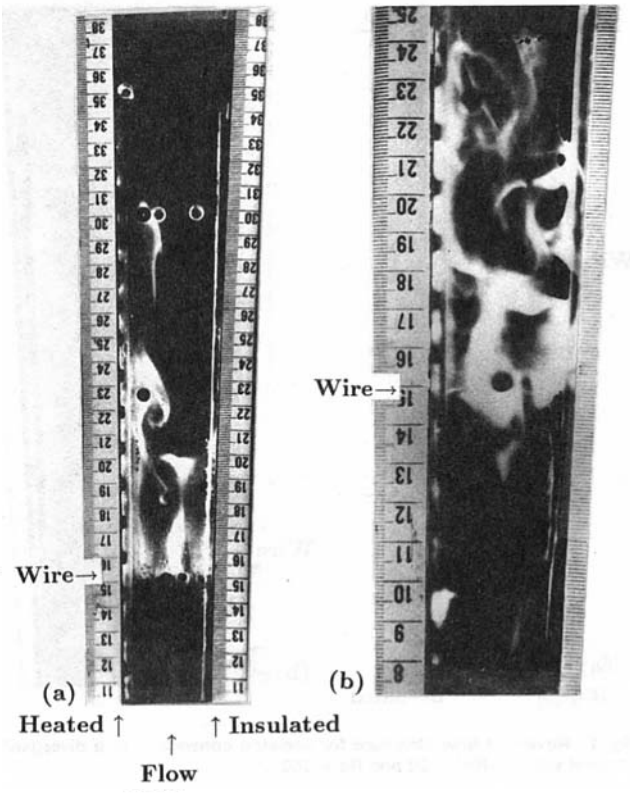


Fig. 2 Reversed flow structure for assisted convection in a divergent channel with (a) $Gr/Re^2 = 100$ and $Re = 316$ and (b) $Gr/Re^2 = 907$ and $Re = 105$

As Gr/Re^2 increases, the buoyant flow near the heated wall moves more rapidly. There is a deeper penetration of the reversed flow down the channel and a wider recirculation region. Due to the strong counter-rotating motion and the adverse pressure gradient, the mainstream/buoyant flow interface may become wavy and distorted, eventually generating a number of vortices as shown in Fig. 2(a) for $Gr/Re^2 = 100$ and $Re = 316$. This leads to a strong mixing of the mainstream and the reversed flow. This reversed flow structure is somewhat different from that for a parallel-plate channel. For the same experimental conditions, a very steady V-shaped recirculation flow occurs near the exit for the parallel-plate channel (Gau et al., 1992b). For the divergent channel, the presence of the adverse pressure gradient causes a deeper penetration of the reversed flow. In addition, due to the destabilization effects the flow is less stable and conducive to generation of vortices. When Gr/Re^2 is higher, the destabilization effect of the adverse pressure gradient can lead to transition to turbulent flow. In the parallel-plate channel, transition to turbulent flow is not observed, except in the case of extremely high Gr/Re^2.

For $Gr/Re^2 = 907$ and $Re = 105$, the reversed flow penetrates down to approximately $x = 8$ cm (the deepest penetration is at $x = 3$ cm), as may be inferred in Fig. 2(b), a location very close to the entrance. Thus, the penetration of the reversed flow in a divergent channel is significantly deeper than in the parallel-plate channel where the penetration depth is only up to about half the channel height (Gau et al., 1992b). The mixing of heated, buoyant flow with the reversed flow becomes intense so that, in the region where the interaction is most pronounced, it is difficult to differentiate the reversed flow from the main flow, as shown in the top part of Fig. 2(b). A very wide recirculation region is seen in the downstream region (Huang, 1994) such that the heated surface can be impacted by the cooler reversed flow. In addition, both large and small scale eddies can be seen, especially at the downstream region located in the

Downloaded 11 Dec 2010 to 193.140.21.150. Redistribution subject to ASME license or copyright; see http://www.asme.org/terms/Terms_Use.cfm

upper portions of the figures. This is a result of the transition to turbulence. In the region close to the point of flow reversal, the mixing of the heated buoyant flow with the reversed flow is not as intense as in the regions further downstream. Therefore, the fluctuation intensity there is much smaller.

Temperature Fluctuations. A very thin thermocouple probe having a wire diameter of 0.1 mm is inserted into the channel 15 mm away from the heated wall at different streamwise locations to measure the temperature fluctuations of the flow. No temperature fluctuations are found in the channel for $Gr/Re^2 \leq 10$ and $Re = 700$. For $Gr/Re^2 = 20$ and $Re = 700$, small temperature fluctuations occur only in the downstream region, that is, at $x > 36$ cm. Upstream of the reverse flow, no oscillations of temperature are found. Note that the complete results of temperature fluctuation measurements are available in Huang's (1994) thesis. With the increase of Gr/Re^2, temperature fluctuations become significant especially in downstream locations. For $Gr/Re^2 = 907$ and $Re = 105$, temperature fluctuations at $x = 5$ cm and $x = 15$ cm are small even though reversed flow is present in this region. The small amplitude of the temperature fluctuations is characteristic of the oscillation of the reversed flow. In the downstream region where vortices are generated, an intense fluctuation of temperature can be observed. The breakdown of vortices and the transition to turbulent flow, which are observed in the flow visualization experiment, lead to large amplitudes as well as high frequencies of temperature fluctuations. In addition, the temperature fluctuations propagate downstream, and are amplified downstream due to the destabilizing effect of a divergent channel. Due to mixing of the existing heated buoyant flow with the cold reversed flow, the average temperature near the exit, which is 41°C, is very close to that in the middle region of the channel.

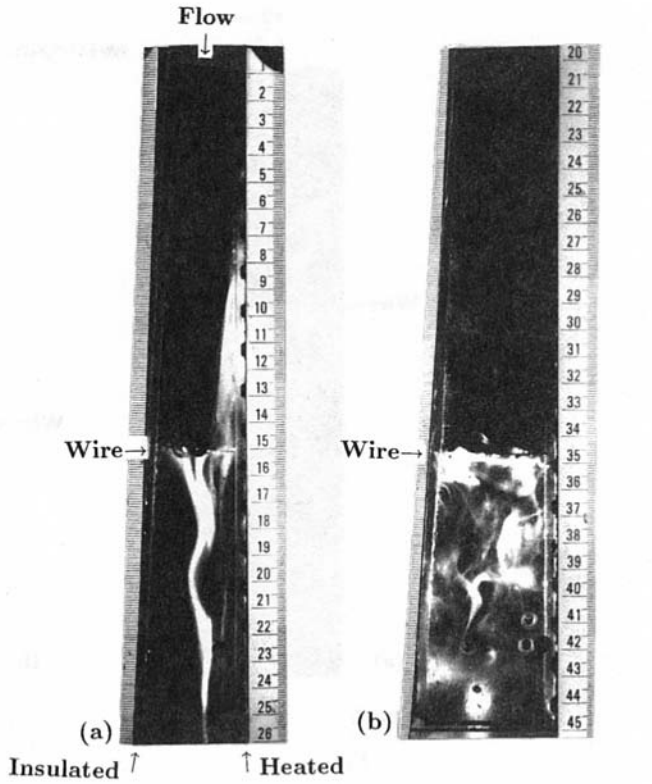


Fig. 3 Reversed flow structure for opposed convection in a divergent channel with $Gr/Re^2 = 1.1$ and $Re = 3000$

Buoyancy-Opposed Convection

Flow Visualization. For opposed convection in a divergent channel, flow reversals can occur at a very small Gr/Re^2. Figure 3 shows the occurrence of flow reversal for $Gr/Re^2 = 1.1$ with $Re = 3000$. The right wall of the channel is heated uniformly and the left wall is insulated. The mainstream enters the channel from the top and moves downstream (downward) while the reversed flow is initiated in the downstream region and moves upstream, as shown in Fig. 3(a), where the reversed flow, represented by the light area, has reached its highest point. The highest point that the reversed flow can reach is determined by the buoyancy force propelling the reversed flow and the inertia and the viscous forces imposed by the mainstream. The increase of Gr/Re^2 moves the reversed flow upstream while the increase of Re pushes the reversed flow downstream. However, the reversed flow accumulates fluid mass and becomes thicker, eventually detaching from the heated wall and merging with the mainstream. The merger is periodic and is preceded by the appearance of vortices caused by instabilities resulting from the counter-rotating flow and initiating at its interface. This is shown in Fig. 3(b). The initiation, upstream movement, and merger of the reversed flow occurs in a periodic manner. The periodicity is about 1.5 seconds. The vortices generated exhibit more chaotic characteristics as they move downstream, as is clear from a comparison of Figs. 3(a) and 3(b). The primary cause for this is the adverse pressure gradient, which decelerates and destabilizes the flow with the attendant breakdown of the large vortices (Gostelow and Blunden, 1989; Walker and Gostelow, 1990).

Using Fig. 3(a), one can estimate the time from the initiation of the reversed flow to the time when the latter reaches the highest point. This can be done by dividing the distance, from the highest point reached by the reversed flow (about at $x = 5$ cm) to the location of the vortex generated in the last period (at about $x = 15$ cm), by the velocity of the mainstream (0.8 m/s). The time required for initiation and growth of the reversed flow is 0.13 s which is only a small fraction of the entire period. The cause of the short time fraction is the adverse pressure gradient, which pushes and accelerates the reversed flow upstream. In a parallel-plate or convergent channel (Huang et al., 1995), however, the time required for initiation and growth of the reversed flow is much longer.

In order to make a more detailed comparison, the flow structure for both the parallel-plate and the divergent channel at $Re = 2000$ has been photographed and shown in Fig. 4. For the parallel-plate channel, flow reversal does not occur for $Gr/Re^2 = 2$, as shown in Fig. 4(a), but occurs at a significantly higher value of $Gr/Re^2 = 3.75$ as shown in Fig. 4(b). Thus, the threshold value for the initiation of flow reversal in the divergent channel is significantly lower than in the parallel-plate or convergent channel (Huang et al., 1995). The initiation of flow reversal in the divergent channel occurs at a downstream region where the mainstream has been greatly decelerated, and natural convection becomes relatively more significant.

Further comparison of the reversed flow structure indicates that the vortices generated in the divergent channel are relatively small. In addition, the destabilization effect and the resultant vortex breakdown make the bulk motion of the mainstream highly unstable, and it oscillates intensely as it flows downstream. These effects lead to the turbulent motion in the downstream. The turbulent motion of the fluid is evident from the dispersive smoke pattern. This is also confirmed in the temperature fluctuation measurements to be discussed later. It is expected that the turbulent flow structure will significantly enhance the heat transfer along the wall. In the parallel-plate channel, however, vortex breakdown, oscillation of the mainstream, and transition to turbulent flow in the downstream region are not observed, except in the very high buoyancy range (Gau et al., 1992b).

Although the reversed flow structure with $Gr/Re^2 = 1.1$ in a divergent channel at $Re = 3000$ (Fig. 3) and at $Re = 2000$

Downloaded 11 Dec 2010 to 193.140.21.150. Redistribution subject to ASME license or copyright; see http://www.asme.org/terms/Terms_Use.cfm

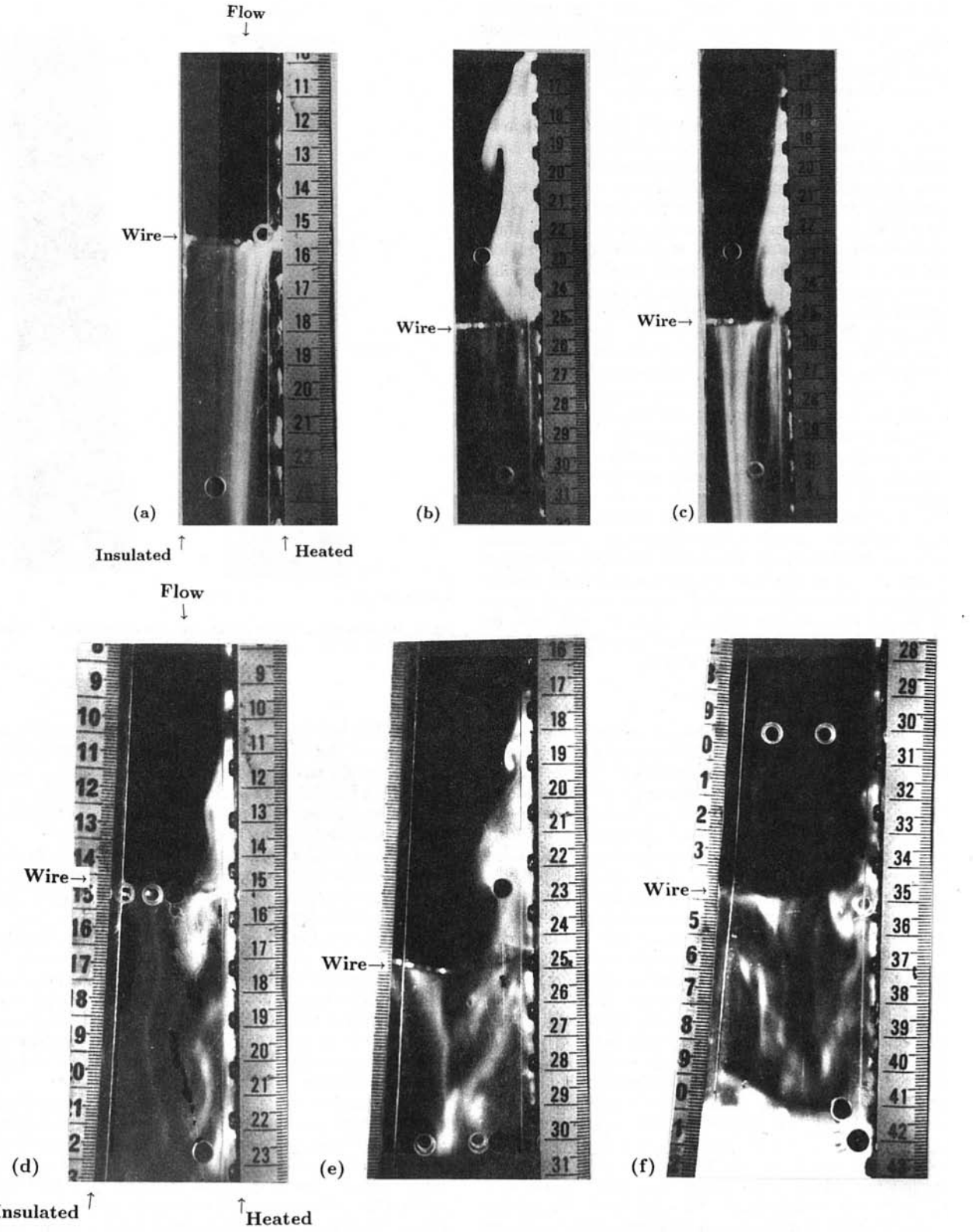


Fig. 4 Comparison of flow structure for opposed convection at Re = 2000 for (*a*) parallel-plate channel with $Gr/Re^2 = 2$, (*b*) and (*c*) parallel-plate channel with $Gr/Re^2 = 3.75$, (*d*), (*e*), and (*f*) divergent channel with $Gr/Re^2 = 1.1$

(Fig. 4) are somewhat similar, it might be argued that the higher Reynolds number in the mainstream would have a higher inertia force to push the reversed flow downstream. This, however, is not the case, since the buoyancy parameter Gr/Re^2 is constant. The increase of Re at a fixed Gr/Re^2 leads to a much larger increase of Gr. The enhanced natural convection pushes the reversed flow further upstream. The highest point attained by the reversed flow for Re = 3000 is higher than that for Re = 2000, when $Gr/Re^2 = 1.1$.

With an increase of Gr/Re^2, the reversed flow layer becomes thicker, and reaches farther upstream, as shown in Fig. 5 ($Gr/Re^2 = 20$ and Re = 700). The mixing of the reversed flow

Downloaded 11 Dec 2010 to 193.140.21.150. Redistribution subject to ASME license or copyright; see http://www.asme.org/terms/Terms_Use.cfm

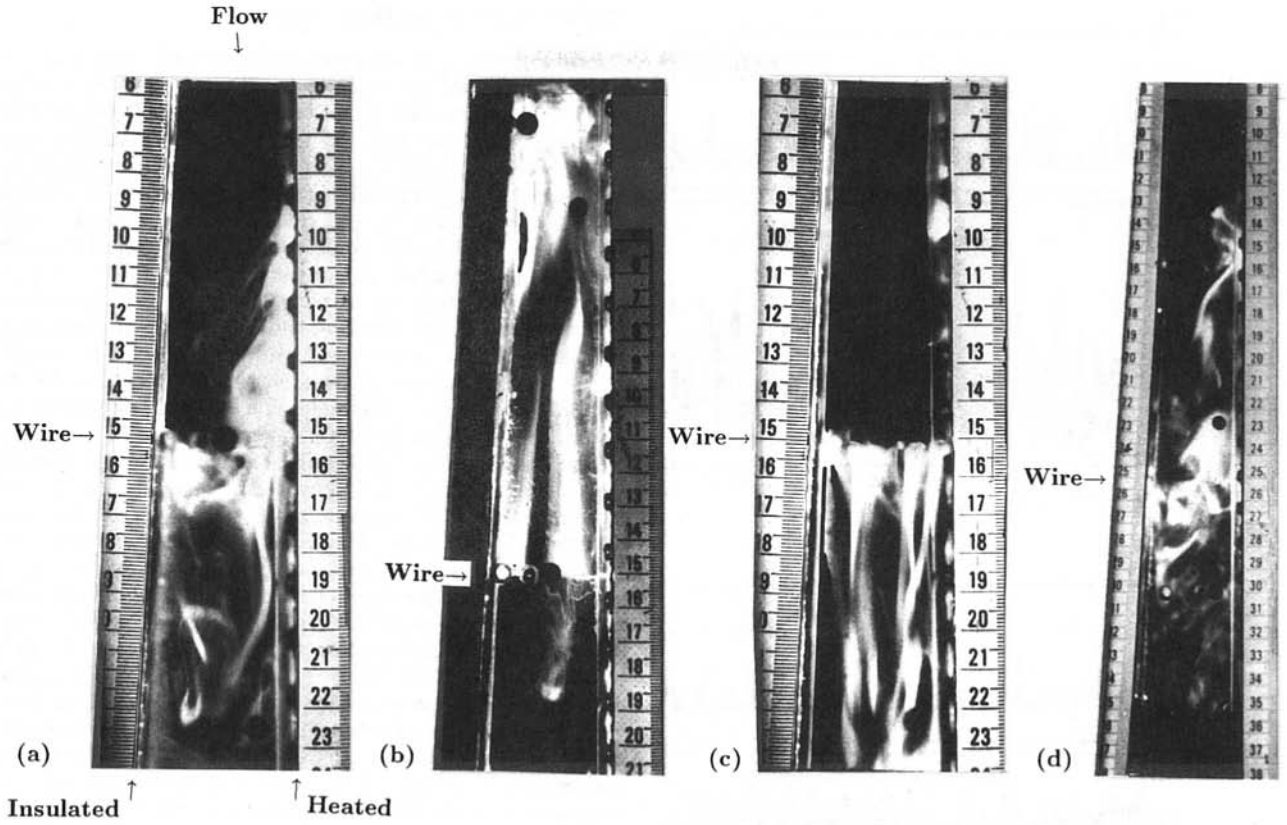


Fig. 5 Reversed flow structure for opposed convection in a divergent channel with $Gr/Re^2 = 20$ and $Re = 700$

with the mainstream becomes so intense that the reversed flow becomes highly unsteady and somewhat three dimensional, as shown in Figs. 5(*a*) and 5(*b*). Although the reversed flow is initiated and washed away in a periodic manner, as shown in Figs. 5(*b*) and 5(*c*), the time period varies slightly from one period to another. The highest point reached by the reversed flow oscillates up and down, and can extend as far as the entrance (i.e., the top) of the channel, as shown in Fig. 5(*b*). This intense mixing of the reversed flow with the mainstream results in transition to turbulent flow occurring much further upstream, as may be seen by comparing Fig. 5(*d*) with Fig. 4(*d*).

Temperature Fluctuations. The thermocouple probe is placed again along a vertical line, which is 15 mm away from the heated wall, at different streamwise locations. The temperature starts to oscillate in the region where flow reversal and vortex generation occur. In the middle region of the channel where active generation of vortices occurs, large amplitude and high frequency temperature fluctuations are triggered as shown in Fig. 6(*a*) for the parallel-plate channel and in Fig. 6(*b*) for the divergent channel. More complete information for temperature fluctuations can be found in Huang (1994). The buoyancy parameters in both the parallel plate and the divergent channel are selected such that the penetration depth of the reversed flow in both channels is approximately the same. The large spikes in temperature are caused by the mixing of the heated reversed flow with the cooler mainstream. It appears that both the amplitude and the frequency of the temperature fluctuations in the parallel plate channel are much higher than in the divergent channel. This is attributed to the higher wall heat flux imposed along the wall of the parallel plate channel, which causes intense mixing of the reversed flow with the mainstream. As the flow moves downstream, more vortices are generated, which leads to additional spikes in temperature, as shown in Figs. 6(*a*) and 6(*b*). In addition, the oscillations and fluctuations of the flow propagate downstream, giving rise to significantly higher frequency and larger amplitude temperature fluctuations. For the parallel-plate channel, however, the intense fluctuations of temperature do not imply the occurrence of turbulence since the flow visualization experiments do not indicate a turbulent mixing of smoke. In addition, the heat transfer measured in the downstream region (Gau et al., 1992a) does not exhibit a significant enhancement. It appears that the downstream flow is not turbulent, but is highly unstable and filled with large vortices.

For the divergent channel, the amplitude of the temperature fluctuation is relatively small due to the lower wall heat flux. A significant reduction in the amplitude of temperature fluctuation is noted in the downstream region (Huang, 1994). This is caused by the turbulent transport in the core, which makes the temperature more uniform. The previous flow visualization experiments have demonstrated that the destabilization effect of the divergent channel leads to the breakdown of vortices and results in a transition from laminar to turbulent flow. The transition to turbulent flow can also be inferred at a later section from the significant enhancement of the heat transfer in the downstream region.

As the buoyancy parameter increases, a similar kind of temperature fluctuation can be observed except that both its amplitude and frequency increase, as shown in Fig. 6(*c*). Large amplitude and high frequency of temperature fluctuation start far upstream. The intense mixing of the main flow with the reversed flow causes the breakdown of vortices and transition to turbulent flow to occur at an earlier stage (i.e., at a location further upstream). This can be inferred from the temperature fluctuations, the amplitude of which decreases significantly at an earlier stage as shown in Fig. 6(*c*) and the figures of Huang (1994). The mean temperature of the flow decreases significantly in the downstream direction, caused by the presence of

Downloaded 11 Dec 2010 to 193.140.21.150. Redistribution subject to ASME license or copyright; see http://www.asme.org/terms/Terms_Use.cfm

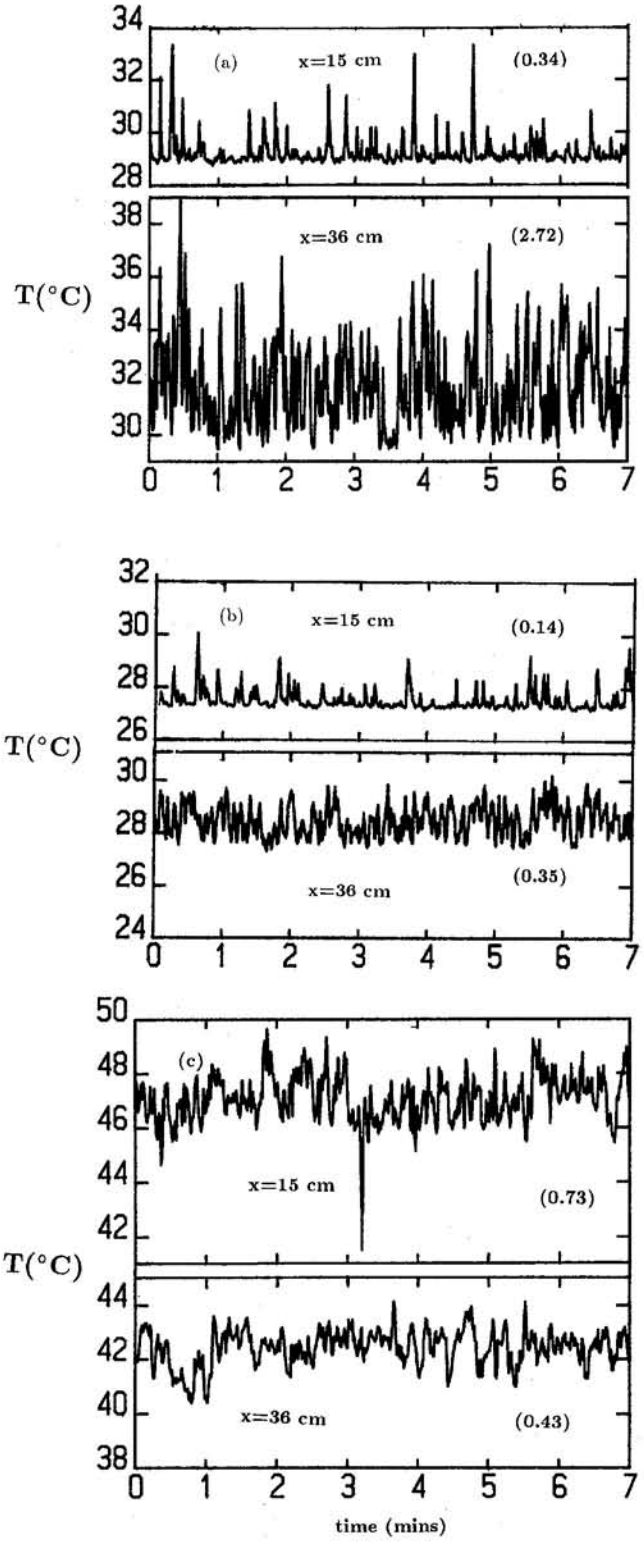


Fig. 6 Temperature fluctuations for opposed convection in a (*a*) parallel-plate channel with $Gr/Re^2 = 3.75$ and Re = 2000, (*b*) divergent channel with $Gr/Re^2 = 1.1$ and Re = 2000 and (*c*) divergent channel with $Gr/Re^2 = 20$ and Re = 700 at $x = 15$ cm and $x = 36$ cm

the cooler reversed flow drawn in from the outside. Turbulent mixing of the main flow with the colder reversed flow leads to a significant decrease in the mean temperature of the downstream flow. The phenomenon of decreasing temperatures in the downstream direction is not found in the parallel-plate channel (Gau et al., 1992a).

Forced Convection Heat Transfer

Pure forced convection experiments are performed in a horizontal channel and the results are used for comparison with the mixed convection data. In this case, in order to eliminate the buoyancy effect, the top wall is heated and maintained horizontal, while the bottom wall is insulated and divergent. It has been shown (Gau et al., 1992a) that for a parallel-plate channel when the Nusselt number is divided by $Re^{0.4}$ the result is independent of the Reynolds number. In Fig. 7, the present results are plotted with the Nusselt number divided by $Re^{0.4}$. Comparisons of the experimental data with the theoretical predictions (Naito, 1975) for the parallel-plate channel are also presented and the agreement is very good. However, the Nusselt number results for the divergent channel are smaller than those for the parallel-plate channel. The higher the Reynolds number is, the lower the normalized Nusselt number becomes. This is caused by the deceleration of flow, which reduces the heat transfer. Downstream of $x/D_h = 4$, however, the normalized Nusselt number at Re = 6000 increases rapidly. This is due to transition to turbulent flow. Flow visualization using a smoke wire indicates that the flow in the far downstream region is not laminar and a very small separation zone is observed near the exit along the tilted insulated wall. The rapid increase of Nusselt number in downstream locations does not occur in the parallel-plate channel for Re = 6000. This is further evidence that the adverse pressure gradient promotes the occurrence of turbulent flow. Note that the Nusselt number is based on the bulk mean temperature. When the Nusselt number is defined based on the air temperature at the inlet of the channel, all the normalized Nusselt numbers for the divergent channel will collapse into a single line. An attempt is made to correlate all the forced convection heat transfer data for the parallel-plate, the convergent (Huang et al., 1995) and the divergent channel with the dimensionless parameters $(r/D_h)/\mathrm{Re\ Pr}$ and A/A_o. The ratio A/A_o accounts for the variation of the cross section of the divergent (or the convergent) channel. It is found the Nusselt number can be correlated as follows:

$$\mathrm{Nu}_0 = 1.092\left(\frac{x}{D_h}\Big/\mathrm{Re\ Pr}\right)^{-0.4}(A/A_o)^{-0.5} \qquad (2)$$

Upon rearranging terms, the following equation results:

$$\mathrm{Nu}_0/\mathrm{Re}^{0.4} = 0.947(x/D_h)^{-0.4}(A/A_o)^{-0.5}. \qquad (3)$$

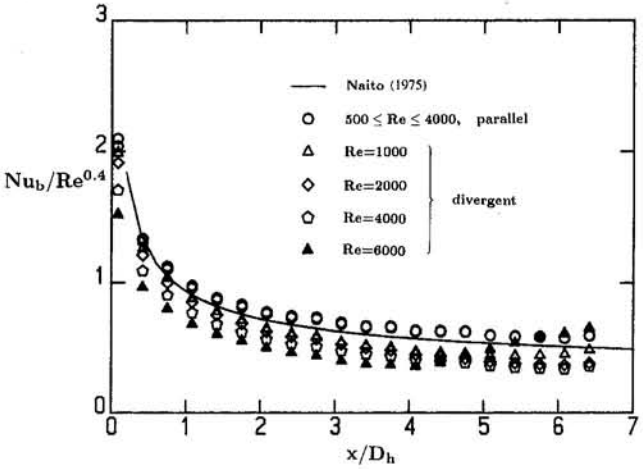


Fig. 7 Comparisons of the normalized Nusselt number for pure forced convection in the divergent and the parallel-plate channel

Downloaded 11 Dec 2010 to 193.140.21.150. Redistribution subject to ASME license or copyright; see http://www.asme.org/terms/Terms_Use.cfm

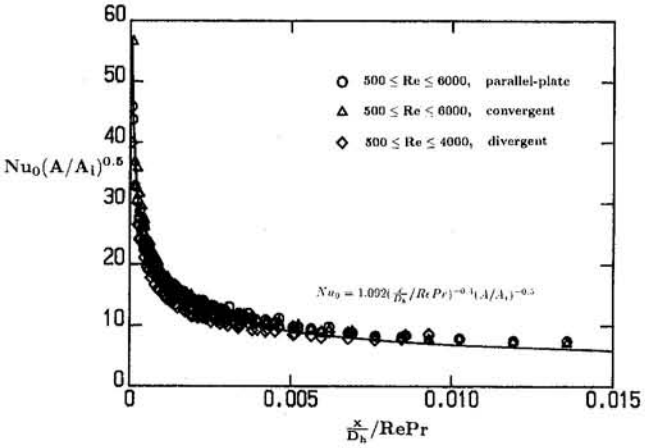


Fig. 8 Correlation of the heat transfer results for pure forced convection in the divergent, parallel-plate, and convergent channels

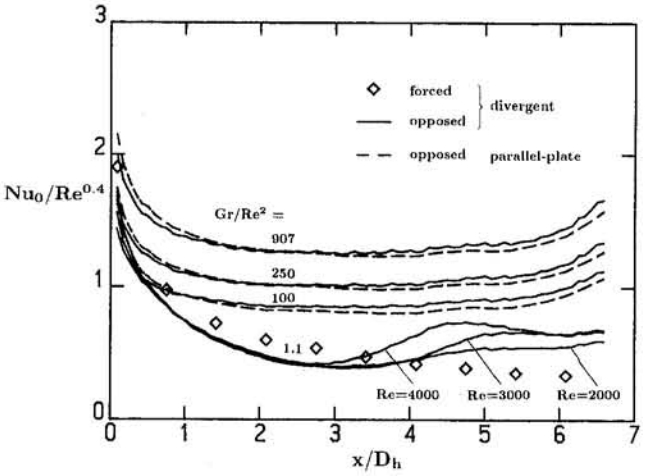


Fig. 10 $Nu/Re^{0.4}$ distributions at different Gr/Re^2 for opposed convection in a divergent channel

Comparison of the heat transfer data with Eq. (2) is shown in Fig. 8. The standard deviation of the experimental data from the results calculated using the equation is 2.56.

Mixed Convection Heat Transfer

For assisted convection, the heated plate is maintained in the vertical position while the opposite wall is divergent, and the Reynolds numbers range from 105 to 4000. For convenience, the Nusselt number results are normalized by $Re^{0.4}$ and the normalized Nusselt number is found to be independent of Reynolds number. This is also true for the parallel-plate and the convergent channel (Huang et al., 1995). The normalized Nusselt number distributions for the divergent channel at different values of the buoyancy parameter, including the pure forced convection results, are shown in Fig. 9. The results indicate that the Nusselt number increases with increasing buoyancy parameter. In general, for a divergent channel, the deceleration of the mainstream decreases the Nusselt number, but the destabilization effect, which can break down the large vortices and lead to a transition to turbulent flow, can enhance the heat transfer. When the buoyancy parameter Gr/Re^2 is small and flow reversal is absent, the destabilization effect can be neglected. Therefore, for small Gr/Re^2, the Nusselt number in a divergent channel is lower than in the parallel-plate channel, as shown in Fig. 9 for $Gr/Re^2 = 2.5$. When the buoyancy parameter is large, i.e., $Gr/Re^2 \geq 100$, the destabilization effect becomes significant, giving a larger heat transfer in the divergent channel than in the parallel-plate channel, especially in the downstream region where intense mixing of the reversed flow with the mainstream takes place. In the upstream area where the mixing is less intense, the Nusselt number in the divergent channel is lower, a result of the deceleration of the mainstream. For $40 < Gr/Re^2 < 100$, this is also the case in the upstream region of the channel. In the downstream region, however, the opposing effects of deceleration of the mainstream and the destabilization due to the adverse pressure gradient are of the same order of magnitude and they cancel each other. This makes the heat transfer almost identical in the divergent and the parallel-plate channels. In addition, in the absence of transition to turbulent flow, neither the Nusselt number nor the heated wall temperature is significantly influenced by the presence of flow reversal. This has also been found in the parallel-plate channel (Gau et al., 1992b).

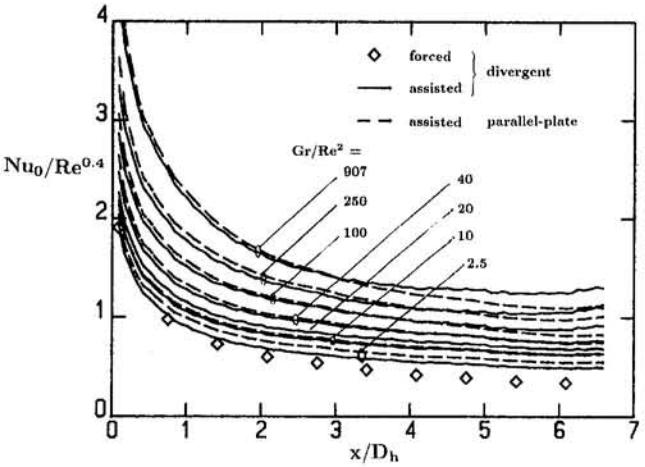


Fig. 9 $Nu/Re^{0.4}$ distributions at different Gr/Re^2 for assisted convection in a divergent channel

For opposed convection in the divergent channel, the Nusselt number is normalized by $Re^{0.4}$ for $Gr/Re^2 \geq 100$ and the results are shown in Fig. 10. This covers the regimes where natural convection is dominant and flow reversal extends over the entire channel. These trends are similar to those in the parallel-plate and convergent channels (Huang et al., 1995). For $Gr/Re^2 < 100$, however, the normalized Nusselt number distributions at different Reynolds numbers do not collapse into a single line. As shown in Fig. 10, the Nusselt number distributions for $Gr/Re^2 = 1.1$ at different Reynolds numbers differ significantly. The reason for the difference is the occurrence of flow reversal in the downstream region. This reversed flow propagates upstream and enhances the heat transfer as the Reynolds number increases while the buoyancy parameter is maintained at a constant value. The propagation of the flow reversal toward the upstream region, as the Reynolds number increases, has been observed and discussed previously. Once flow reversal occurs, the destabilization effect of the divergent channel may result in a transition to turbulent flow. This leads to a significantly higher heat transfer in the downstream region than in the parallel-plate channel. In the upstream region where mixing of the reversed flow with the mainstream is not so intense, the deceleration effect of the mainstream becomes significant, giving a lower heat transfer in the divergent channel.

Figure 11 shows the variation of $\overline{Nu}/Re^{0.4}$ with Gr/Re^2 in the divergent channel. Note that $\overline{Nu}/Re^{0.4}$ is the average over the entire heated wall, and $\bar{h} = \bar{q}/(\overline{T_w} - T_b)$. The Nusselt number results for pure forced convection in the divergent chan-

Downloaded 11 Dec 2010 to 193.140.21.150. Redistribution subject to ASME license or copyright; see http://www.asme.org/terms/Terms_Use.cfm

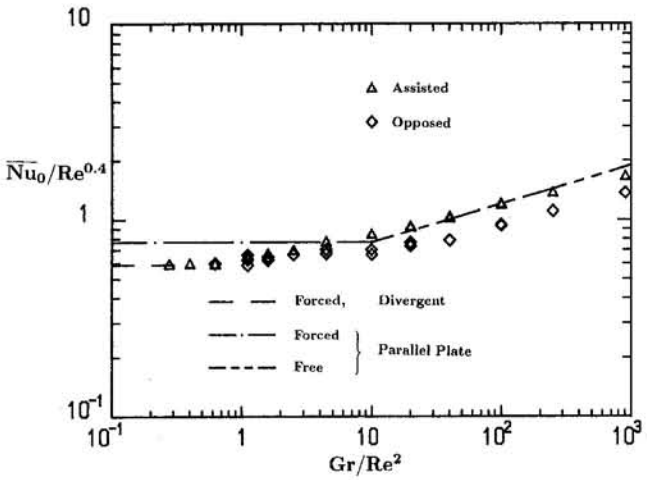


Fig. 11 Variations of $\overline{Nu}/Re^{0.4}$ with Gr/Re^2 for assisted and opposed convection in a divergent channel

nel are also presented; they are 28 percent lower than those for the parallel-plate channel due to the deceleration of flow. For both assisted and opposed convection, the average Nusselt number approaches the pure forced convection results for small Gr/Re^2 and increases with increasing Gr/Re^2. When the value of Gr/Re^2 is close to or greater than 10, natural convection becomes significant or even dominant, the average Nusselt numbers for both assisted and opposed convection deviate slightly and become close to those in the parallel-plate channel. It appears that the divergence of the channel has a negligible effect on the average heat transfer when the buoyancy parameter is large. However, the local variation of the Nusselt numbers for both assisted and opposed convection are significantly different as indicated previously.

The parameter $\overline{Nu}/Re^{0.4}$ for the divergent channel is correlated in terms of Gr/Re^2, and the results are written as follows:

For assisted convection and $Gr/Re^2 \leq 907$,

$$100 \log (\overline{Nu}/Re^{0.4}) = -17.75 + 8.6675 \log (Gr/Re^2) + 1.5805[\log (Gr/Re^2)]^2 \quad (5)$$

with a standard deviation of 0.013.

For opposed convection and $Gr/Re^2 \leq 907$,

$$100 \log (\overline{Nu}/Re^{0.4}) = -20.982 + 6.4672 \log (Gr/Re^2) + 1.1992[\log (Gr/Re^2)]^2 \quad (6)$$

with a standard deviation of 0.023.

Conclusions

Pure forced and mixed convection flow and heat transfer in a divergent channel have been studied experimentally. Flow reversal occurs for both assisted and opposed convection. Due to the counterflow motion with the mainstream, the reversed flow is not stable and may degenerate into vortices. Channel divergence decelerates the mainstream such that in the downstream regions natural convection becomes dominant and flow reversal is initiated at a much lower buoyancy parameter. In addition, the adverse pressure gradient has both an effect of pushing the reversed flow upstream resulting in a deeper penetration, and a destabilizing effect enabling the breakdown of vortices and transition to turbulent flow. The result is a significantly enhanced heat transfer in the downstream reaches of a divergent channel. In the upstream region, when the buoyancy parameter is relatively low such that flow reversal is still absent or relatively weak, the heat transfer in the divergent channel is lower than that in the parallel-plate channel due to the deceleration of the mainstream. Temperature fluctuation measurements have been shown to be useful in providing new information, in addition to confirming the flow visualization results.

Pure forced convection heat transfer in the divergent channel has been measured and the results have been successfully correlated together with the parallel-plate and the convergent channel. For assisted and opposed convection, both the local and average Nusselt numbers when divided by $Re^{0.4}$ are found to be functions only of the buoyancy parameter. This is not true, however, for $Gr/Re^2 < 100$ in opposed convection. For assisted convection, the Nusselt number increases with the buoyancy parameter, as is expected. For opposed convection, the increase of the Nusselt number with the buoyancy parameter is related to the occurrence of the reversed flow which interacts strongly with the mainstream. The correlations of the average Nusselt number in terms of the buoyancy parameter should be useful for practical application.

Acknowledgments

This research was sponsored by the National Science Council of Taipei, Taiwan, under contract No. NSC 80-041-E006-38.

References

Aung, W., 1987, "Mixed Convection in Internal Flow," in: *Handbook of Single-Phase Convective Heat Transfer*, S. Kakac, R. K. Shah, and W. Aung, eds., Chap. 15, Wiley, New York.

Chen, T. L., and Miau, J. J., 1987, "The Making and Application for Hot-Film Calibration," *Proc. 4th National Conference on Mechanical Engineering*, CSME, pp. 147–152.

Fukamachi, N., Ohya, Y., and Nakamura, Y., 1991, "An Improvement of Smoke-Wire Method of Flow Visualization," *Fluid Dynamics Research*, Vol. 169, pp. 23–29.

Gau, C., Yih, K. A., and Aung, W., 1992a, "Measurements of Heat Transfer and Flow Structure in Heated Vertical Channels," *AIAA Journal Thermophysics and Heat Transfer*, Vol. 6, pp. 707–712.

Gau, C., Yih, K. A., and Aung, W., 1992b, "Reversed Flow Structure and Heat Transfer Measurements for Buoyancy-Assisted Convection in a Heated Vertical Duct," ASME JOURNAL OF HEAT TRANSFER, Vol. 114, pp. 928–935.

Gostelow, J. P., and Blunden, A. R., 1989, "Investigations of Boundary Layer Transition in an Adverse Pressure Gradient," ASME *Journal of Turbomachinery*, Vol. 111, pp. 366–375.

Huang, T. M., 1994, "Mixed Convection Flow and Heat Transfer in a Heated Convergent or Divergent Channel," Ph.D. Thesis, National Cheng Kung University, Taiwan.

Huang, T. M., Gau, C., and Aung, W., 1995, "Mixed Convection Flow and Heat Transfer in a Vertical Convergent Channel," *International Journal of Heat and Mass Transfer*, Vol. 38, No. 13, pp. 2445–2456.

Jackson, J. D., Cotton, M. A., and Axcell, B. P., 1989, "Studies of Mixed Convection in Vertical Tubes," *International Journal of Heat and Fluid Flow*, Vol. 10, pp. 2–15.

Kajiuchi, T., Shiragami, N., and Miyagawa, I., 1986, "Pressure Drop in Divergent Flow Through a Tapered Tube," *International Chemical Engineering*, Vol. 26, pp. 499–505.

Kihm, K. D., Kim, J. H., and Fletcher, L. S., 1993, "Investigation of Natural Convection Heat Transfer in Converging Channel Flows Using Specklegram Technique," ASME JOURNAL OF HEAT TRANSFER, Vol. 115, pp. 140–148.

Kline, S. J., and McClintock, F. A., 1953, "Describing Uncertainties in Single-Sample Experiments," *Mechanical Engineering*, Vol. 75, Jan., pp. 3–12.

Komori, K., Iguchi, A., and Izumi, R., 1985, "Characteristics of Turbulent Flow in Divergent Channels of Rectangular Cross Section," *International Chemical Engineering*, Vol. 25, pp. 97–104.

Mori, Y., and Ohbuchi, M., 1989, "A Fundamental Study of Flow and Heat Transfer Performances of Downward Water at Low Reynolds Numbers in a Vertical Heated Straight Tube," *International Journal of Heat Mass Transfer*, Vol. 32, pp. 1231–1238.

Naito, E., 1975, "Laminar Heat Transfer in the Entrance Region Between Parallel-Plates—the Case of Uniform Heat Flux," *Heat Transfer—Japanese Research*, Vol. 4, No. 2, pp. 63–74.

Scheele, G. F., and Hanratty, T. J., 1960, "Effect of Natural Convection on Transition to Turbulence in Vertical Pipes," *The Canadian Journal of Chemical Engineering*, Vol. 38, pp. 67–73.

Scheele, G. F., and Hanratty, T. J., 1962, "Effect of Natural Convection on Stability of Flow in a Vertical Pipe," *Journal of Fluid Mechanics*, Vol. 14, pp. 244–256.

Scheele, G. F., and Hanratty, T. J., 1963, "Effect of Natural Convection Instabilities on Rates of Heat Transfer at Low Reynolds Number," *AIChE Journal*, Vol. 9, pp. 183–185.

Downloaded 11 Dec 2010 to 193.140.21.150. Redistribution subject to ASME license or copyright; see http://www.asme.org/terms/Terms_Use.cfm

Shiina, Y., 1987, "Heat Transfer in a Tapered Passage," *International Journal of Heat and Fluid Flow,* Vol. 8, pp. 64–71.

Sparrow, E. M., and Starr, J. B., 1965, "Heat Transfer to Laminar Flow in Tapered Passages," ASME *Journal of Applied Mechanics,* Vol. 32, pp. 684–689.

Sparrow, E. M., Ruiz, R., and Azevedo, L. F. A., 1988, "Experimental and Numerical Investigation of Natural Convection in Convergent Vertical Channels," *International Journal of Heat and Mass Transfer,* Vol. 31, pp. 907–915.

Sparrow, E. M., and Ruiz, R., 1988, "Experiments on Natural Convection in Divergent Vertical Channels and Correlation of Divergent, Convergent, and Parallel-Channel Nusselt Numbers," *International Journal of Heat and Mass Transfer,* Vol. 31, pp. 2197–2205.

Su, C. C., and Lin, H., 1991a, "Forced Convection in Convergent and Divergent Ducts of Rectangular Cross Section," *Numerical Heat Transfer, Part A,* Vol. 20, pp. 445–458.

Su, C. C., and Lin, H., 1991b, "Forced Convection in the Entrance Region of Convergent and Divergent Ducts of Rectangular Cross Section," *Journal of Chinese Society of Mechanical Engineering,* Vol. 12, No. 3, pp. 314–319.

Walker, G. J., and Gostelow, J. P., 1990, "Effect of Adverse Pressure Gradients on the Nature and Length of Boundary Layer Transition," ASME *Journal of Turbomachinery,* Vol. 112, pp. 196–205.

Webb, B. W., and Hill, D. P., 1989, "High Rayleigh Number Laminar Natural Convection in an Asymmetrically Heated Vertical Channel," ASME JOURNAL OF HEAT TRANSFER, Vol. 111, pp. 649–656.

Wirtz, R. A., and McKinley, P., 1985, "Buoyancy Effects on Downward Laminar Convection Between Parallel-Plates," in: *Fundamentals of Forced and Mixed Convection,* ASME HTD-Vol. 42, pp. 105–112.

Yao, L. S., and Rogers, B. B., 1989, "Mixed Convection in an Annulus of Large Aspect Ratio," ASME JOURNAL OF HEAT TRANSFER, Vol. 111, pp. 683–689.

Downloaded 11 Dec 2010 to 193.140.21.150. Redistribution subject to ASME license or copyright; see http://www.asme.org/terms/Terms_Use.cfm

X. Hu[1]

A. M. Jacobi
Assistant Professor of Mechanical Engineering. Assoc. Mem. ASME

Department of Mechanical and Industrial Engineering, University of Illinois at Urbana–Champaign, 1206 W. Green Street, Urbana, IL 61801

The Intertube Falling Film: Part 1—Flow Characteristics, Mode Transitions, and Hysteresis

When a liquid film falls from one horizontal tube to another below it, the flow may take the form of discrete droplets, jets, or a continuous sheet; the mode plays an important role in the wetting and heat transfer characteristics of the film. Experiments are reported that explore viscous, surface tension, inertial, and gravitational effects on the falling-film mode transitions. New flow classifications, a novel flow regime map, and unambiguous transition criteria for each of the mode transitions are provided. This research is part of an overall study of horizontal-tube, falling-film flow and heat transfer, and the results may have important implications on the design and operation of falling-film heat exchangers.

Introduction

Horizontal-tube, falling-film heat exchangers are used in the chemical, refrigeration, petroleum refining, desalination, and food industries because they provide higher heat transfer coefficients and operate with smaller liquid inventories than flooded heat exchangers. They also offer advantages in dealing with liquid distribution, noncondensable gases, fouling, and other problems (Yundt and Rhinesmith, 1981). In the past, the design of falling-film heat exchangers was based largely on experience; however, recent energy and environment concerns have encouraged the use of this technology in new applications, making a heuristic design approach difficult. A particular challenge is that there is no general method for predicting the flow pattern of the falling film.

When a falling liquid film flows from one horizontal tube to another below it, the flow may take the form of discrete droplets, jets, or a continuous sheet, as shown in Fig. 1. The pattern is referred to as the falling-film mode. When the flow rate is low, the liquid leaves the tube in the droplet mode. If the flow rate is increased, the flow pattern changes to continuous circular jets that fall from fixed sites on the bottom of the tube. With a further increase in the flow rate, the jets merge and form a continuous liquid sheet. If the flow rate is then reduced, the sheet becomes unstable and the flow pattern will eventually return to the jet mode. A further reduction in the flow rate finally results in a return to the droplet mode.

The flow behavior has a significant impact on the sensible and latent heat transfer to a liquid flowing over a horizontal circular tube (see Kutateladze et al., 1985; Mitrovic, 1986; Marto, 1986; Honda et al., 1991; Rogers et al., 1995). There have been a number of attempts to model the so-called inundation effect on heat transfer (e.g., Kern, 1958; Chen, 1961; Fujii, 1983; Nicol and Abdelghaffar, 1988), but these models assume knowledge of the flow pattern. An ability to predict the falling film mode would allow better data correlation and improve the modeling and analysis of heat transfer and fluid flow.

The flow mode transitions have been studied. Yung et al. (1980) correlated the liquid mass flow rate for a transition from the droplet mode to the jet mode by setting the droplet production frequency equal to the capillary wave oscillation frequency. The flow rate per unit length of the tube at the transition was given by

$$\Gamma = 0.81 \frac{\rho}{\lambda} \frac{\pi d_p^3}{6} \left(\frac{2\pi\sigma}{\rho\lambda^3} \right)^{1/2} \tag{1}$$

where

$$\lambda = \xi\sqrt{4\pi^2 n}. \tag{2}$$

In Eqs. (1) and (2), $n = 2$ and d_p is the diameter of primary drops, experimentally determined for water and alcohol to be

$$d_p = 3\xi. \tag{3}$$

Yung and co-workers found their transitional flow rate prediction to be within about 10 percent of the experimental data for the two fluids tested. However, the experimental geometry was very much simplified; it consisted of a single tube with a single site undergoing a droplet to jet mode transition in a quiescent vapor.

Dhir and Taghavi-Tafreshi (1981) studied falling-film transitions using glycerol, ethylene glycol, and silicone oil. They found the transitions to be independent of fluid thermophysical properties and solely dependent on the liquid volume flow rate. Transitions between the droplet and jet modes occurred at about the same volume flow rate for increasing or decreasing flow rates. However, the flow rate at a transition from the jet mode to the sheet mode was about twice the flow rate for a transition from the sheet to the jet mode. Their results indicated the existence of hysteresis for transitions between the jet and sheet modes. These results were obtained for a simplified single-tube geometry in a quiescent vapor.

Experimental observations by Maron-Moalem et al. (1978), Ganic and Roppo (1980), and Mitrovic (1986) indicated that transition from the droplet mode to the jet mode occurred at Reynolds numbers between about 150 and 200, whereas transition from the jet mode to the sheet mode occurred at Reynolds numbers between 315 and 600. Contrary to earlier work, marked hysteresis was observed for transitions between the jet and droplet modes. The study of Maron-Moalem et al. (1978) involved several working media; however, it focused on dripping characteristics and not mode transitions. The other two studies used

[1] Current address: Research Engineer, AlliedSignal, Phoenix, AZ.

Contributed by the Heat Transfer Division for publication in the JOURNAL OF HEAT TRANSFER. Manuscript received by the Heat Transfer Division September 1, 1995; revision received April 26, 1996. Keywords: Flow Instability, Forced Convection, Multiphase Flows. Associate Technical Editor: V. K. Dhir.

Copyright © 1996 by ASME

Downloaded 11 Dec 2010 to 193.140.21.150. Redistribution subject to ASME license or copyright; see http://www.asme.org/terms/Terms_Use.cfm

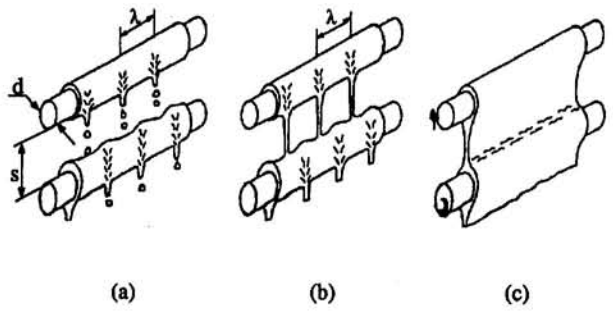


Fig. 1 The idealized intertube falling-film modes (per Mitrovic, 1986): (*a*) the droplet mode, with liquid leaving the tube intermittently; (*b*) the jet mode, where discrete jets continuously flow from the upper to the lower tubes; and (*c*) the sheet mode, in which the liquid film forms an unbroken sheet between the horizontal circular tubes

only water as a working fluid, and thus it was impossible to address liquid property effects on the transitions.

In a study of film condensation from stationary vapors onto horizontal tube banks, Kutateladze et al. (1985) suggested that the transition from one flow mode to another was governed by the Archimedes number based on the capillary constant:

$$\mathrm{Re} = f(\mathrm{Ar}^*). \tag{4}$$

Although a functional dependence was suggested, they did not provide the form of this relation for any transition, nor were transition data presented. Their studies were focused on condensation heat transfer for R-12 and R-21. The Archimedes number is closely related to the modified Galileo number defined later.

Honda et al. (1987) investigated the flow characteristics of condensate on a vertical column of horizontal low-finned tubes using R-113, methanol, and normal propanol. A dimensionless parameter, K, was predicted to govern the mode transitions:

$$K = \frac{\Gamma(g/\rho)^{1/4}}{\sigma^{3/4}} \tag{5}$$

The value of K at the transition from the droplet to the jet mode ranged from 0.12 for normal propanol to 0.26 for R-113. The sheet mode began (with simultaneous jet and sheet modes) at $K = 0.64$, and a complete sheet mode was observed when K reached 0.74 to about 0.94 for the three liquids studied. Two tube spacings were considered, but Honda et al. did not explore the effects of tube diameter or transition hysteresis.

In a similar report, Honda et al. (1991) found that for R-113 on finned tubes, transitions from the sheet mode to the jet mode were significantly influenced by a downward flowing vapor. A sheet mode was observed at liquid Reynolds numbers greater than 400 under stagnant vapor conditions, but a complete sheet mode was not observed even when the Reynolds number was increased to 1800 if a vapor velocity of 3.4 m/s was present. Their research focused on condensing heat transfer to low-finned horizontal tubes, and no attempt was undertaken to isolate property effects on mode transitions or to quantify hysteresis.

More recently, Armbruster and Mitrovic (1994, 1995) modeled the mode transitions between the droplet, jet and sheet modes using $\mathrm{Re} = \mathrm{A}\,\mathrm{Ga}^{1/4}$; where the constant A was experimentally determined. Armbruster and Mitrovic (1994) give values of A for flows of water and isopropyl alcohol. Only one tube diameter was considered, but a range of tube spacing was studied.

Clearly the falling-film Reynolds number (flow rate) plays an important role in the mode transitions; however, geometric and thermophysical property effects are not well understood, and there are contradictory reports as to whether the transitions exhibit hysteresis. The purpose of this article is to report research that will clarify the physical parameters governing the transitions and explore their influence. The flow modes will be carefully classified and new observations of the patterns will be presented. Unambiguous transition criteria, based on experimental data, will be proposed for the falling-film behavior on plain horizontal tubes, and a novel flow regime map will be presented. The utility of these results in correlating, modeling, and analyzing the performance of falling-film heat exchangers will be discussed.

Method

Apparatus. The test facility shown in Fig. 2 consisted of a closed-circuit, forced-circulation loop of the test liquid and an open-loop wind tunnel. The purpose of the liquid loop was to supply the working medium to the test section, and the purpose of the wind tunnel was to allow experimentation with a gas flow. Thus, this apparatus allowed the study of falling-film modes with or without an imposed flow of air from the laboratory.

The wind tunnel inlet provided a 9:1 area contraction with pull-out grids and honeycomb flow straighteners. The test section was made of transparent acrylic plastic and had a cross section 203.2 mm by 304.8 mm. The front cover of the test section was removable, allowing instrumentation and other adjustments within the wind tunnel. Two sides of the test section were used to support the test tubes and provide easy adjustment to the tube spacing. The transition section between the fan and expansion was made of a flexible rubber belt to prevent transferring vibrations from the blower to the test section. For the same purpose, gaskets were used at each interface between wind-tunnel sections. The wind tunnel provided air velocities from less than 1 m/s up to 15 m/s at the test section inlet, and the approach velocity profiles were flat to within 2.7 percent at the maximum blower speed.

The liquid circulation loop consisted of a head tank with a drain and overflow, a thermally controlled reservoir, a liquid pump, a filter, a needle valve, and flow meters. The test liquid in the reservoir was delivered by the pump to the adjustable

Nomenclature

Ar* = modified Archimedes number of Kutateladze et al., (1985) = $(\sigma^3/\nu^4\rho^2 g(\rho - \rho_\nu))^{1/2}$
d = tube diameter
d_p = diameter of primary drops
F_g = gravitational force
F_ν = viscous force
F_σ = surface tension force
Ga = modified Galileo number = $\rho\sigma^3/\mu^4 g$
g = gravitational acceleration
L = a characteristic length
n = constant appearing in Eq. (2)
Oh = Ohnesorge number = $\rho\sigma d/\mu^2$
q = heat flux
Re = Reynolds number = $2\Gamma/\mu$
s = tube spacing
V = characteristic velocity of the liquid
V_{air} = free-stream air velocity
We = Weber number = $\rho_{\mathrm{air}} V_{\mathrm{air}}^2 d/\sigma$
Γ = liquid mass flow rate per unit length of tube
λ = instability wavelength, spacing between neighboring jets or droplets
μ = dynamic viscosity of the liquid
ν = kinematic viscosity of the liquid
ρ = mass density of the liquid
ρ_{air} = mass density of the air
ρ_ν = mass density of the surrounding pure vapor
σ = surface tension at gas/liquid interface
ξ = capillary constant = $\sqrt{\sigma/\rho g}$

Downloaded 11 Dec 2010 to 193.140.21.150. Redistribution subject to ASME license or copyright; see http://www.asme.org/terms/Terms_Use.cfm

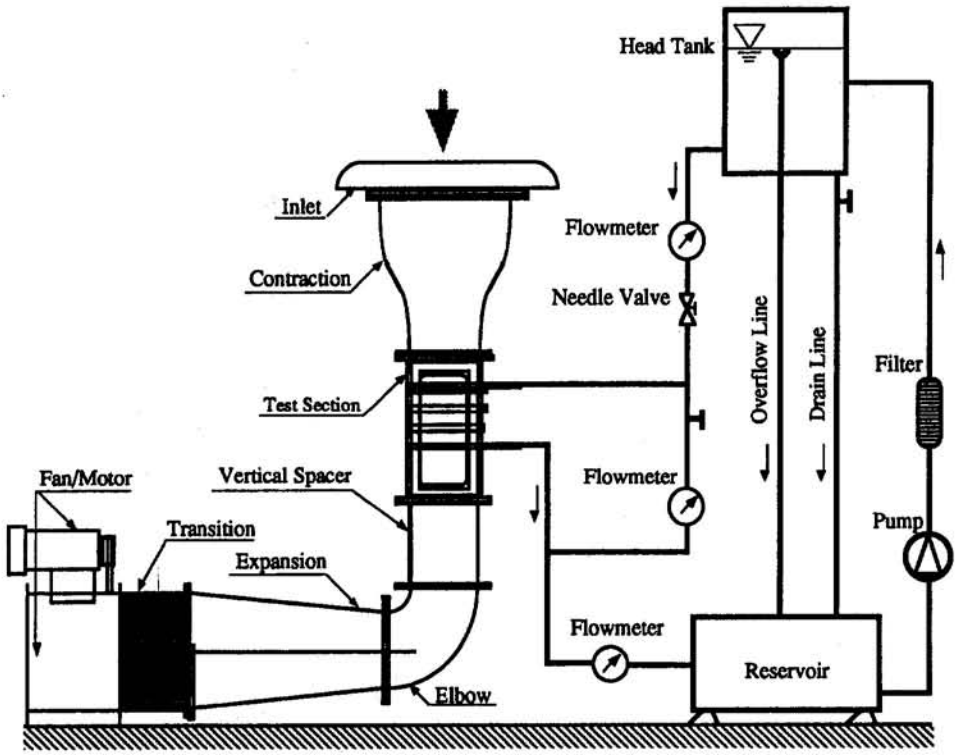


Fig. 2 A schematic of the experimental apparatus used to study the intertube falling film modes. An air flow is provided by the open-loop wind tunnel, and the test liquid is circulated in the thermally controlled closed-loop system.

constant-head tank. From the head tank, the liquid flowed through the first flow meter and needle valve to the upper feed tube in the test section. In the test section, as shown in Fig. 3, liquid issued from the upper feed tube, flowed around the lower feed tube where it was distributed into a uniform sheet, and then fell from the feeding tubes and impinged on the test tube. The liquid film flowed around the test tube, then fell to the dummy tube and eventually to the catching tube. The flow passed from the test section through a second flow meter and finally returned to the thermally controlled reservoir.

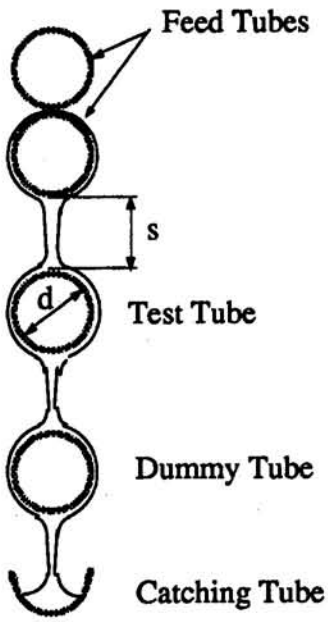


Fig. 3 A schematic of the tubes within the test section. Liquid issues from the upper feeding tube, flows around a lower feeding tube that helps ensure flow uniformity, and then falls through the test section to the catching tube.

The feeding tubes for the liquid film supply were designed after considering several schemes described in the literature. Fletcher et al. (1975) used a perforated plate, whereas Parken (1975) drilled holes along the bottom surface of a round tube and milled a shallow axial groove to connect the holes and provide flow distribution. Dhir and Taghavi-Tafreshi (1981) cut a thin slot in the feeding tube, and Honda et al. (1987) used a concentric-tube feeding arrangement. Mitrovic (1986) used a row of small holes along the bottom of the feeding tube and placed a second tube directly underneath it to help distribute the flow. We found Mitrovic's method consistently provided a uniform flow, and so it was adopted for this study. The top feed tube had inside and outside diameters of 15.86 mm and 22.22 mm, respectively. Along a 229 mm length on the bottom of this tube, 1.0-mm-dia holes were drilled 1.5 mm apart, center to center (yielding 152 holes). The gap between the bottom of the first feed tube and the top of the second feed tube was 1.4 mm. While the experimental program included a range of tube diameters for study, during a particular experiment the lower feeding tube and all dummy tubes had diameters equal to the test tube. Therefore, the liquid film always fell between tubes of identical diameter in the test section (see Fig. 3). The tubes were held in the test section by nonintrusive fasteners that attached their ends to the wind tunnel walls, and tube position could be adjusted by moving these fasteners (a more complete description is provided by Hu, 1995).

Instrumentation. The liquid flow rate and approach air flow velocity (if any) were measured during the experiments, as were the liquid temperatures. Images documenting the flow patterns and providing data on jet and droplet spacing and flow modes were also recorded during experiments. Before and after each experimental run, the liquid surface tension (in air), and the laboratory temperature, pressure, and relative humidity were

Downloaded 11 Dec 2010 to 193.140.21.150. Redistribution subject to ASME license or copyright; see http://www.asme.org/terms/Terms_Use.cfm

Table 1 The experimental range of the relevant physical variables

Physical Parameter,	Symbol	Experimental Range	Units
Mass flow rate per unit length,	Γ	up to 0.22	kg/m-s
Liquid dynamic viscosity,	μ	7.9 (10^{-4}) to 4.4 (10^{-2})	N-s/m^2
Mass density of the liquid,	ρ	780 to 1140	kg/m^3
Gas/liquid surface tension,	σ	2.2 (10^{-2}) to 6.8 (10^{-2})	N/m
Tube diameter,	d	9.5, 12.7, 15.9, 19.0, 22.2	mm
Tube spacing,	s	about 5 to 50	mm
Gravitational acceleration,	g	fixed at 9.8	m/s^2
Air velocity,	V_{air}	up to 15	m/s

recorded. The tube spacing and diameter were measured for each experimental configuration. The other thermophysical properties of the test liquids were determined using the measurements outlined above and property correlations from the literature (discussed later).

At high liquid flow rates, the oscillating-piston flow meter on the liquid line upstream of the test section was used to record the flow rate into the feeding tube, and the flow meter on the discharge line provided a redundant check. These flow meters had an operating range up to 252 ml/s and an uncertainty of ±0.5 percent of the flow rate reading. However, due to concerns with flow unsteadiness and their nonlinear response at low flow rates, the oscillating-piston flow meters were not used for flow rates below 36 ml/s. For these low flow rates, the liquid issuing from the catching tube was collected and weighed; this method had a maximum uncertainty of 2 percent for the experiments reported. The oscillating-piston flow meter was superior for high flow rates, because it avoided the problems associated with collecting a sample at high flow rates. The flow rates measured by the oscillating-piston meter and the collection method agreed to within the experimental uncertainty for flow rates where both methods could be reliably applied (from 36 ml/s to about 60 ml/s).

The surface tension of the fluids was measured using a Du Nouy ring tensiometer, and the associated uncertainty of this device was approximately 0.5 percent. Air velocity at the inlet of the test section was measured using a standard Pitot-static tube and an electronic manometer (±0.12 Pa). Air density was inferred from ideal gas behavior and the laboratory temperature (±0.1°C), relative humidity (±2 percent), and pressure (±0.5 mm Hg). A CCD digital camera and a 35 mm single-lens-reflex camera were used to record images of the falling films; the images were analyzed using standard methods to characterize the flow.

Experimental Scope. The experimental program was guided by the physical ranges appropriate for falling-film heat exchanger applications, but in some cases it was restricted by equipment limitations. Intermediate results also served to guide the experiments; therefore, it is difficult to explain a priori why particular fluids, geometries, or flow rates were selected. A discussion will be presented with the results.

For a falling film in quiescent surroundings,[2] the mode can depend on seven physical parameters: the liquid flow rate per unit length of tube, Γ; the dynamic viscosity of the liquid, μ; the mass density of the liquid, ρ; the gas/liquid surface tension, σ; the tube diameter, d; the intertube spacing, s; and the gravitational acceleration, g. If an air flow (at fixed conditions) was imposed during the experiments, the air velocity may also be important. The nominal range of the physical variables obtained in our experiments is given in Table 1.

[2] Assuming negligible shear at the gas/liquid interface, a tube length $\gg \lambda$, and $\rho \gg \rho_{air}$.

Table 2 Relevant dimensionless parameters, the experimental range, and typical uncertainties associated with propagated measurement uncertainty

Dimensionless Group	Physical Interpretation	Experimental Range	Estimated Uncertainty
Reynolds No. $Re = 2\Gamma/\mu$	(inertial force/viscous force) —based on film thickness length scale	up to 580	±2%
Modified Galileo No. $Ga = \rho\sigma^3/g\mu^4$	(gravitational force/viscous force)^4 —based on capillary length scale	7(10^2) to 8(10^{10})	±4%
Ohnesorge No. $Oh = \rho\sigma d/\mu^2$	reveals tube diameter effects	1.3(10^2) to 2.4(10^6)	±2%
s/d	reveals tube spacing effects	0.25 to 5.2	±1%
Weber No. $We = \rho_{air}V_{air}^2 d/\sigma$	(inertia force/surface tension force) —for gas flow, based on tube diameter	up to 200	±10%

A wide range in the important thermophysical properties was achieved by conducting experiments with five different working fluids. For the purposes of this paper, these liquids will be designated as water, ethylene glycol, water/glycol, oil, and alcohol. A description of these fluids is provided in the appendix, along with the correlations used to evaluate the relevant thermophysical properties.

Using a dimensional analysis, the physical variables discussed above can be rearranged to yield four dimensionless groups for a falling film in quiescent surroundings (see Hu, 1995, for details). These four dimensionless groups may be written in the following form: the Reynolds number Re, the modified Galileo number[3] Ga, the Ohnesorge number Oh, and the dimensionless tube spacing s/d. If an air flow was imposed during the experiment, the Weber number (We) also becomes relevant. The nominal experimental range, physical interpretation, and experimental uncertainty for each of these dimensionless groups are reported in Table 2.

Experimental Procedure. Before starting a test, tubes with the desired diameter were aligned in the test section at a prescribed tube spacing. Since the falling film flow is gravity driven, a tube inclination would cause a nonuniform distribution of the flow. Therefore, the tubes were carefully leveled before a test, and leveling was checked again after the liquid started circulating in the system. The liquid flow rate was adjusted to obtain a jet mode, and the tubes were considered level if the jets fell at fixed sites without drifting toward either end of the test tube. To make sure that the liquid flow rates on both sides of the tube were equal, the feeding tube was rotated until the liquid jets fell on the top dead center of each tube below the feeding tubes (except for the catching tube).

The test liquid was circulated through the system for 3 to 4 hours to ensure that the tubes were fully wetted and the piping system was free of air. The data acquisition system was set up, including the devices for measuring the liquid and air temperatures, liquid flow rate, and surface tension. Electronic devices were subjected to a warm-up period of at least one hour. For experiments that involved an air flow, the wind tunnel motor controller was set to provide the desired air velocity. For studies of mode characteristics such as flow pattern and spacing between the jets or droplets, photographic equipment was employed. A scale was photographed to provide a dimensional reference for each experiment.

For mode transition experiments, the needle valve shown in Fig. 2 was used to provide a fine adjustment of the flow rate.

[3] Ga may be interpreted as the fourth power of the ratio of gravity to viscous forces: $Ga = (F_g/F_\nu)^4$; where the gravity force scales according to $F_g \sim \rho L^3 g$, and the viscous force scales as $F_\nu \sim \mu VL$. The velocity scale is $V \sim \sqrt{gL}$, and the length scale is $L \sim \xi$. Because of this interpretation, we refer to the group as a modified Galileo number.

Downloaded 11 Dec 2010 to 193.140.21.150. Redistribution subject to ASME license or copyright; see http://www.asme.org/terms/Terms_Use.cfm

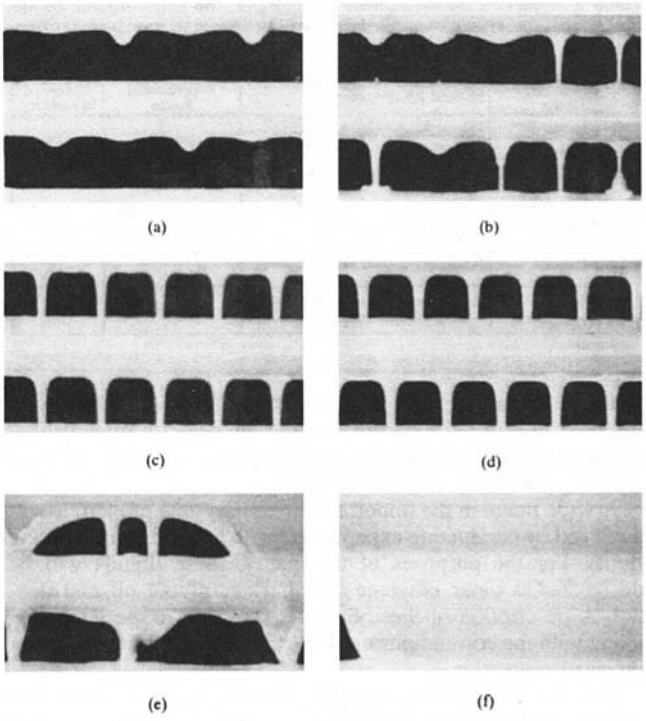


Fig. 4 The observed falling-film modes for ethylene glycol, $Ga^{1/4} \approx 36$. The modes are (*a*) droplet, Re = 1.3; (*b*) droplet-jet, Re = 8; (*c*) in-line jet, Re = 21; (*d*) staggered jet, Re = 41; (*e*) jet-sheet, Re = 57; and (*f*) sheet mode, Re = 64.

The valve was opened until the flow displayed a sheet mode; then it was slowly closed and the flow went through several mode transitions, eventually going to the droplet mode. The transitions are described in detail along with the results. At each transition, the flow rate and experimental conditions were recorded. The liquid flow rate was then increased and the flow went from the droplet to the sheet mode. Again, the flow rate and experimental conditions were recorded at each transition.

All the experiments being reported were conducted with adiabatic tubes; however, experiments with sensible heat transfer from the tube to the liquid show that the transitions are insensitive to heat flux (for $q \leq 115$ kW/m^2; see Hu, 1995).

Results and Discussion

Introductory Remarks. For each of the working fluids, the three idealized modes illustrated in Fig. 1 were observed. Mixed modes, representing combinations of two idealized modes[4] were also observed: the droplet-jet and jet-sheet modes. Furthermore, three distinct jet mode patterns were manifested—a distinction very rarely found in the literature. Because of these observations, and for other related reasons, a careful classification of the falling-film flow patterns was undertaken. The stable falling-film modes observed during the experiments are presented in Fig. 4, and the experimental path to each of the modes is discussed below to clarify their classification.

At low flow rates, liquid dripped from regularly spaced sites along the bottom of the horizontal tubes, exhibiting the so-called *droplet mode.* The sites were not simultaneously active; droplets alternately fell from neighboring sites. The dripping frequency increased with an increase in flow rate, and all the sites became active simultaneously at a certain flow rate. A further increase in the flow rate eventually resulted in liquid departing from at least one site as a continuous jet. A flow with droplets and jets is called a *droplet-jet mode,* and such a transition is a *droplet/droplet-jet transition* (cf. Fig. 4(*a*, *b*)); in the reverse direction these conditions represent a *droplet-jet/droplet transition* (all backward transitions will be denoted in this way).

From the droplet-jet mode, a sufficient increase in liquid flow rate caused liquid to fall continuously from every departure site on the bottom of the tube. The complete establishment of this flow pattern represents a *droplet-jet/jet transition.* Under some conditions, the jet mode was established with departure sites directly beneath impingement sites; this pattern is the *inline jet mode* (see Fig. 4(*c*)). For other conditions, the liquid departure sites were staggered with respect to the impingement sites ($\lambda/2$ out of phase), and this flow is the *staggered jet mode* (see Fig. 4(*d*)). For our experimental conditions, some liquids exhibited only staggered jets, some only inline jets, and some exhibited both patterns.

The diameter of the liquid jets increased with the flow rate and, eventually, the jets moved closer together and another discrete jet was added to the quasi-steady jet pattern. For some test conditions, a further increase in flow rate resulted in unsteadiness in the location of the jet departure sites. When the jet departure sites exhibited unsteady behavior, the flow was classified as an *unsteady jet mode.* All fluids did not exhibit unsteady jet behavior, and this transition was sometimes difficult to discern (see also Dhir and Taghavi-Tafreshi, 1981).

From inline jets, staggered jets, or unsteady jets, a sufficient increase in the flow rate eventually resulted in jets merging to form a partial sheet (see Fig. 4(*e*)). This flow pattern is called a *jet-sheet mode,* and the transition with an increasing flow rate is denoted as a *jet/jet-sheet transition.* Finally, the flow exhibited a *jet-sheet/sheet transition* when the final discrete jet merged to form a complete sheet of liquid (see Fig. 4(*f*))—the flow was said to be in the *sheet mode* under these conditions.

The flow classifications and transitions are summarized in Fig. 5, where the three manifestations of the jet mode are also noted. While some flow patterns were easy to discern, others were relatively difficult to classify. For example, the transition between inline and staggered jet modes was sharp; it occurred quickly and was easy to observe. The transition between steady and unsteady jets required more judgment and was more diffi-



Fig. 5 A schematic summary of the falling-film modes and transitions. The transitions associated with increasing and decreasing flow rates (Re) may be read from the chart. Three distinct jet patterns are indicated; however, all three were not observed for every fluid.

[4] Within the current experimental range, all three patterns never occurred simultaneously.

Downloaded 11 Dec 2010 to 193.140.21.150. Redistribution subject to ASME license or copyright; see http://www.asme.org/terms/Terms_Use.cfm

cult to ascertain. Therefore, the deviation in observed conditions at the transitions was usually greater than the estimated uncertainty in the experimental parameters, as presented later. It should be noted that a free edge condition (or end condition) for the falling film was always used in this study; i.e., no flow stabilizers were used.

Mode Transitions in Quiescent Surroundings. The transitional Reynolds numbers for water are plotted against the tube spacing at fixed diameter in Fig. 6. From Figs. 5 and 6, it is clear that the transitions for increasing and decreasing flow rate shown in Fig. 6 are not identical; therefore, the difference in transitional Reynolds numbers (at a fixed tube spacing) does not represent transition hysteresis. As discussed later, hysteresis is manifest when identical transitions occur at differing Reynolds numbers for increasing and decreasing flow rates. In Fig. 7, the transitions for water and for ethylene glycol are shown at two different tube diameters at a fixed tube spacing. In the range of the current experiments, the transitions were not significantly affected by the tube diameter or spacing. This behavior was exhibited for all tube spacings and diameters for each fluid tested. Since s/d and Oh have little effect, only the role of Re and Ga must be addressed. Figures 6 and 7 clearly demonstrate that both of these parameters are important.

The analytical approach described by Yung et al. (1980) resulted in a semi-empirical model for predicting transitions from the droplet to the jet mode. Rearranging Eqs. (1)–(3), they can be cast into a form consistent with our dimensional analysis:

$$\mathrm{Re} = 0.244\ \mathrm{Ga}^{1/4} \tag{6}$$

The form of Eq. (6) is in agreement with that suggested by Armbruster and Mitrovic (1995); furthermore, Kutateladze et al. (1985) suggested that sheet/jet transitions depend on the Archimedes number; an Archimedes number dependence may be cast into a Ga dependence.

Motivated by Eq. (6) and a hypothesis that similar relations could be developed for all transitions, we assumed a power-law relation between the Re and Ga for each falling-film mode transition. Then, using a least-squared-error criterion, correlations for the transitional Reynolds numbers as a function of Ga were developed. These correlations are presented below with the associated root-mean-squared (rms) deviations of the data. Approximately 400 observations of mode transitions were used to develop these correlations. Roughly 75 percent of the data were for $\mathrm{Ga}^{1/4} > 300$. Each correlation is based on approximately the same number of observations (about 50). When all mode data are included (see also Hu and Jacobi, 1996), a total of nearly 1000 flow observations were recorded during this study.

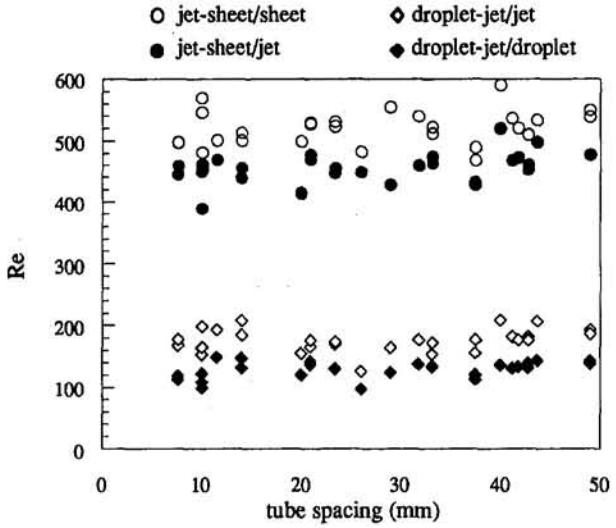


Fig. 6 Typical transition Reynolds number data for water ($\mathrm{Ga}^{1/4} \approx 530$) falling between two tubes with $d = 22.2$ mm ($\mathrm{Oh} = 2.4 \times 10^{6}$) at various values of the tube spacing ($0.3 < s/d < 2.2$). The transitional Reynolds numbers show no dependence on tube spacing in the experimental range.

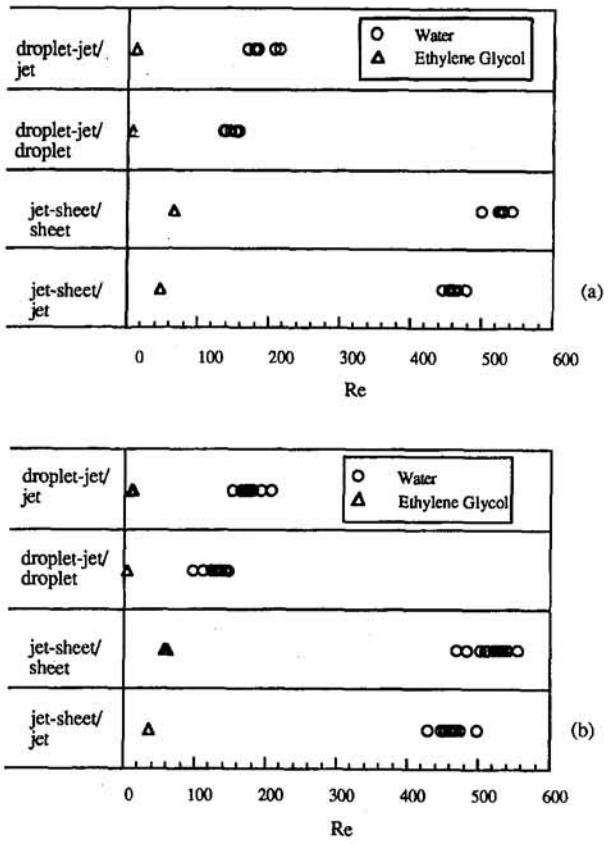


Fig. 7 Typical Reynolds number data for the various mode transitions of two fluids. The tube spacing is fixed at $s = 15$ mm, and the tube diameters are (*a*) $d = 15.9$ mm, and (*b*) $d = 22.2$ mm. The tube diameter has little effect on the mode transitions; however, the liquid properties have a profound effect (note the differences in transitional Reynolds numbers for water, $\mathrm{Ga}^{1/4} \approx 530$, and ethylene glycol, $\mathrm{Ga}^{1/4} \approx 36$).

Transition	Correlation	RMS deviation, percent	
Droplet/droplet-jet	$\mathrm{Re} = 0.121\ \mathrm{Ga}^{0.284}$	8.5	(7)
Droplet-jet/jet	$\mathrm{Re} = 0.159\ \mathrm{Ga}^{0.282}$	6.6	(8)
Jet/jet-sheet	$\mathrm{Re} = 1.880\ \mathrm{Ga}^{0.222}$	4.3	(9)
Jet-sheet/sheet	$\mathrm{Re} = 2.088\ \mathrm{Ga}^{0.220}$	4.2	(10)
Sheet/jet-sheet	$\mathrm{Re} = 1.004\ \mathrm{Ga}^{0.250}$	3.9	(11)
Jet-sheet/jet	$\mathrm{Re} = 1.064\ \mathrm{Ga}^{0.244}$	3.8	(12)
Jet/droplet-jet	$\mathrm{Re} = 0.057\ \mathrm{Ga}^{0.321}$	8.4	(13)
Droplet-jet/droplet	$\mathrm{Re} = 0.045\ \mathrm{Ga}^{0.321}$	6.2	(14)

Recall that the jet mode was observed to be in-line or staggered, and steady or unsteady. A modified power-law relation was assumed, and least-squared-error fits to the data were developed for each of these transitions. The power on Ga was fixed at 0.25, and two constants were determined. The correlations for transition between stable and unstable jets are based on 41 observations, but only 12 experiments were available for developing the correlation for inline and staggered jet transi-

Downloaded 11 Dec 2010 to 193.140.21.150. Redistribution subject to ASME license or copyright; see http://www.asme.org/terms/Terms_Use.cfm

tions. The correlations are presented below with the rms deviations of the data[5]:

Transition(s)	Correlation	RMS deviation, percent	
In-line/staggered	$Re = 23.08 + 0.277\ Ga^{1/4}$	8.8	(15)
Staggered/in-line	$Re = 17.91 + 0.243\ Ga^{1/4}$	8.7	(16)
In-line/staggered or staggered/in-line	$Re = 20.53 + 0.256\ Ga^{1/4}$	12.5	(17)
Staggered/unsteady or unsteady/staggered	$Re = 47.42 + 0.600\ Ga^{1/4}$	8.3	(18)

The difference between Eq. (17) and Eqs. (15) and (16) is that the former neglects hysteresis between the in-line and staggered jet modes. Equations (7)–(14) demonstrate that the other transitions also exhibit hysteresis. To clarify the magnitude of the transition hysteresis, the transitional Reynolds numbers for increasing and decreasing flow rates are plotted against each other in Fig. 8. In this figure, each point represents a particular experiment (a particular fluid, tube diameter, and tube spacing), and the transitional Reynolds numbers for each mode transition may be compared for increasing or decreasing flow rates. The figures show that the transitions exhibit a bias toward delayed transition with increasing flow rates. In other words, the transitional Reynolds numbers are higher for droplet-jet/jet transitions than for jet/droplet-jet transitions; likewise, jet-sheet/sheet transitions occur at higher Reynolds numbers than do sheet/jet-sheet transitions.

By neglecting hysteresis, a simplified map for the falling-film modes was developed and is presented in Fig. 9. Similar maps including the effects of hysteresis were presented by Hu (1995). The essential features of the map are not changed by hysteresis. The transition criteria for this simplified map are given in Eqs. (19)–(22) along with the rms deviations of the data. Each correlation is based on about 100 measurements. The rms errors associated with this map are larger than those for the transition criteria that account for hysteresis, but they are tenable for many engineering purposes (in the experimental range given in Table 2).

Transitions	Correlation	RMS deviation, percent	
Droplet/droplet-jet or droplet-jet/droplet	$Re = 0.074\ Ga^{0.302}$	11.0	(19)
Droplet-jet/jet or jet/droplet-jet	$Re = 0.096\ Ga^{0.301}$	11.2	(20)
Jet/jet-sheet or jet-sheet/jet	$Re = 1.414\ Ga^{0.233}$	5.8	(21)
Jet-sheet/sheet or sheet/jet-sheet	$Re = 1.448\ Ga^{0.236}$	6.6	(22)

Only two transition criteria are needed if the flow classifications are reduced to the droplet, jet, and sheet modes, as usually adopted in the literature. This further simplification may be useful under some circumstances. No mixed modes are considered, and once again transition hysteresis is neglected. Interpreting the data in this manner, the following transition criteria were developed:

[5] Due to limited low-Ga data and the inherent difficulties in determining the stable/unstable jet transitions, we recommend restricting the use of Eq. (18) to $Ga > 100$.

Transitions	Correlations	RMS deviation, percent	
Droplet/jet or jet/droplet	$Re = 0.084\ Ga^{0.302}$	15	(23)
Jet/sheet or sheet/jet	$Re = 1.431\ Ga^{0.234}$	7.7	(24)

The rms deviations associated with Eqs. (23) and (24) are approximately twice those of the more detailed criteria given by Eqs. (7)–(14).

Mode Transitions With a Concurrent Gas Flow. Limited experiments with an imposed concurrent air flow were conducted. In these experiments, the Weber number based on tube diameter reached as high as 200 (V_{air} = 15 m/s). In contrast to the counterflow results of Honda et al. (1991) for finned tubes, the Reynolds numbers for the sheet/jet-sheet and jet-sheet/sheet transitions were not significantly affected by the concurrent flow of air at any We or $Ga^{1/4}$ in the current experimental range. The same result was found for all transitions at $Ga^{1/4} < 100$; however, high-Ga transitions involving the droplet mode were affected. The transitional Reynolds numbers were about 25 percent higher for droplet-jet/jet transitions and 14 percent higher for droplet-jet/droplet transitions at $Ga^{1/4} = 550$. These results were essentially the same for any $We > 1$, and since the experiments were limited, we do not feel as if sufficient data exist to develop a correlation reflecting a We dependence of the mode transitions.

Discussion of the Results. Potential differences in flow-pattern interpretation notwithstanding, a comparison to earlier work is useful. The results of Yung et al. (1980) are in very good agreement with the current study for $Ga^{1/4} < 300$ (cf. Eqs. (6) and (7)); however, at $Ga^{1/4} = 500$ their prediction of the transitional Reynolds number is about 14 percent lower than ours. Comparing the droplet/jet transitions of Honda et al. (1987) to Eqs. (7) and (8), it is clear that while the magnitudes and trends agree, their data had more scatter than the current results. For transitions between the jet and sheet modes, Honda et al. predict transitional Reynolds numbers about 30 percent higher than we measured, and their data show more scatter. Since transition to the sheet mode is accompanied by axial spreading of the flow, and since fins inhibit spreading, it is sensible to expect that fins would affect transitions involving the sheet mode. The transitional Reynolds numbers given by Armbruster and Mitrovic (1994) are 30 to 60 percent below those measured in the current study, but the uncertainty and scatter in their data are not reported, and their data were obtained over a more limited experimental range. In summary, correlations based on our data are in reasonable agreement with related experimental work from the literature, supporting the reliability of the current data.

Axial spreading of the flow is also related to the in-line/staggered jet transitions, but the influence of jet spreading depends on the flow geometry. Consider two limiting cases: (*a*) The half-spacing of the jets is very small compared to the circumferential travel of the flow (or $\lambda \ll \pi d$); and (*b*) the half-spacing of the jets is very large compared to the circumferential travel of flow (or $\lambda \gg \pi d$). For case (*a*), neighboring jets have a strong momentum interaction in a complicated stagnation region between impingement sites. An "interaction ring" is formed, similar to the interaction fountain described by Slayzak et al. (1994), and jets depart from the bottom of the interaction ring to give the staggered pattern. For case (*b*), the flow reaches the bottom of the tube without significant interactions with neighboring jets, and jet departure sites are beneath the impingement sites in the inline pattern. For these reasons, we expected Oh (or another parameter including the tube diameter) to be important in characterizing the inline/staggered jet transitions.

Downloaded 11 Dec 2010 to 193.140.21.150. Redistribution subject to ASME license or copyright; see http://www.asme.org/terms/Terms_Use.cfm

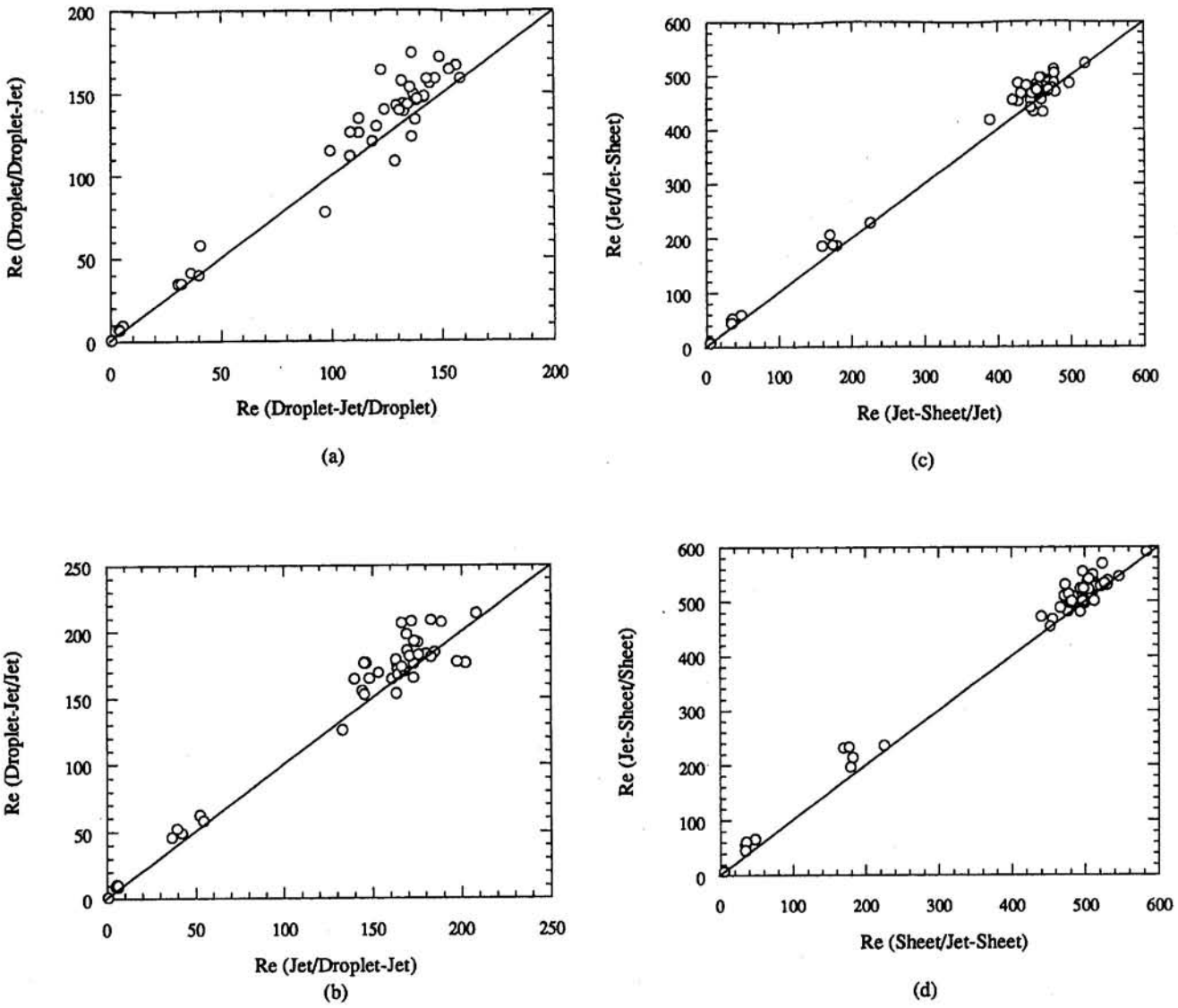


Fig. 8 Hysteresis in the mode transitions is demonstrated by considering the transitional Reynolds numbers for increasing and decreasing flow rates: (*a*) droplet/droplet-jet versus droplet-jet/droplet; (*b*) droplet-jet/jet versus jet/droplet-jet; (*c*) jet/jet-sheet versus jet-sheet/jet; (*d*) jet-sheet/sheet versus sheet/jet-sheet transitions

Nevertheless, within the current experimental range, an inline/staggered criterion based solely on Re and Ga is successful, and the complication of a third parameter can be avoided. The use of Eqs. (15)–(17) should be carefully restricted to the current experimental range.

Along with tube diameter restrictions, the tube spacing restrictions are important. It is easy to imagine a limiting tube-spacing case where the flow regime map will be invalid. For example, consider a tube spacing smaller than the characteristic diameter of a pendant drop. It is impossible to reach the droplet mode for such a geometry.

Although the parameter space is complicated, the experiments indicate that the mode transitions are properly scaled by Re and Ga. Consider the water/glycol mixture and alcohol: These two test liquids have surface tensions that differ by about 59 percent and viscosities that differ by roughly 55 percent at 30°C. Their Ohnesorge numbers (for a fixed tube diameter) differ by more than 50 percent, but their $Ga^{1/4}$ values differ by only 6.7 percent. The transitional Reynolds numbers are very close (within 7 percent for sheet/jet-sheet transitions), and they are accurately modeled by the simple relations given in Eqs. (7)–(14). The fact that the correlations are successful for fluids with widely varying properties supports the Re and Ga scaling.

Since Re represents a ratio of inertial to viscous forces, a high-Reynolds-number flow is inertially dominated. The flow map provides a clear interpretation of the physics: Inertia-dominated flows ($Re \to \infty$) will take the sheet mode. As explained earlier, $Ga^{1/4}$ can be interpreted as a ratio of gravitational to viscous forces. The flow map demonstrates that gravity-dominated flows ($Ga^{1/4} \to \infty$) will take the droplet mode. Equation (11) provides remarkable support to this interpretation; this fit to the data demonstrates that sheet breakup is related to competition between inertial and gravitational effects ($1 \sim Re/Ga^{1/4}$).

These experiments were conducted under constant gravity, and our inability to control this parameter allows another interpretation of the modified Galileo number. The surface tension force is $F_\sigma \sim \sigma\xi$, and the viscous force is $F_\nu = \mu V \xi$, where the length scale is the capillary constant. Setting the viscous length equal to the capillary constant yields a velocity scale, $V \sim \nu/\xi$. Finally, a little rearrangement will show that Ga can be interpreted as $(F_\sigma/F_\nu)^{1/2}$. With this alternate interpretation, the flow map implies that the droplet mode occurs when surface tension effects dominate. The modified Galileo number reflects both gravitational and surface tension effects; both of these interpretations are intuitive, and there is more than one valid interpretation of the physics reflected by the flow regime map.

Downloaded 11 Dec 2010 to 193.140.21.150. Redistribution subject to ASME license or copyright; see http://www.asme.org/terms/Terms_Use.cfm

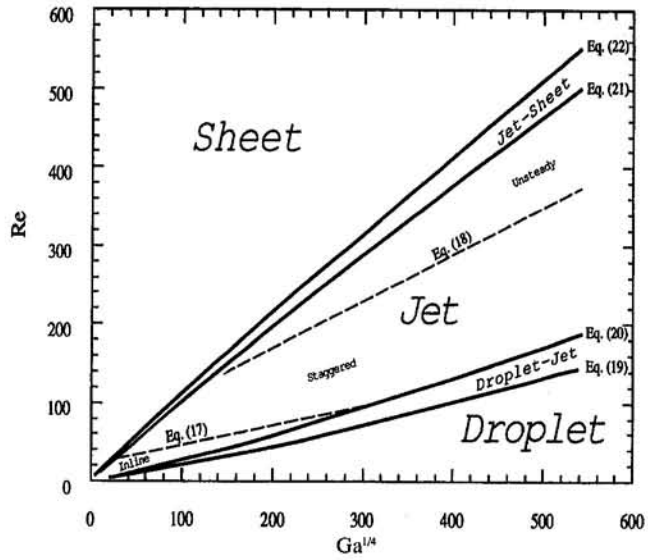


Fig. 9 A simplified flow regime map for the falling-film mode transitions. This map is based on Eqs. (17)–(22); it neglects transition hysteresis. The rms deviations of the Reynolds number data range from about 6 to 11 percent for this transition map.

Although the regime map is geometrically restricted, it covers a range important for application—the experimental parameters were selected with attention to refrigeration systems. The geometric and flow complications of every application have not been addressed. Work exploring the effects of nonuniform feeding and blow by may be especially important. Nevertheless, this generalized approach can serve as a powerful tool in the operation, design, and analysis of falling-film heat exchangers. For example, it is well known that intermittence (the droplet mode) is associated with potential dry-out problems during the operation of spray evaporators. Using the regime map of Fig. 9, one could determine the lowest acceptable mass flow rate for a tube bundle (and thus the required overfeed rate). Furthermore, since the nature of the flow differs significantly for each of the modes, heat transfer models developed without regard for flow pattern are of dubious value. Experimental results should be classified by flow mode, and the data for each mode should be correlated separately—this approach is easier with established transition criteria.

Conclusions

A liquid film falling between horizontal tubes may exhibit the following flow patterns: droplets, a mixture of droplets and jets, in-line jets, staggered jets, unsteady jets, a mixture of jets and sheets, or a continuous liquid sheet. In the range of the current experiments, the mode was found to be relatively insensitive to geometric effects, but gravitational, inertial, viscous, and surface tension forces are important. These effects are captured in the film Reynolds number and a modified Galileo number.

With a careful classification of the flow patterns, unambiguous transition criteria were developed (see Eqs. (7)–(18)). Transition hysteresis was observed for all the modes, but the effect on transitional Reynolds numbers was small. By neglecting transition hysteresis, simplified criteria were developed, and a graphic interpretation of these criteria was presented using a flow regime map (see Fig. 9). In adopting simplified transition criteria, the rms deviations of the data went from about 4 to 6 percent for jet/sheet transitions, and from about 8 to 11 percent for droplet/jet transitions. Limited data with a concurrent air flow indicate that a flow in the surrounding gas destabilizes the formation of jets from droplets, shifting the mode transition to Reynolds numbers that are 15–25 percent higher for $Ga > 300$.

The flow map indicates that when inertia effects dominate, the flow will take the sheet mode. Gravity or surface-tension-dominated flows result in a droplet pattern. The formation of jets is apparently related to a complicated competition between these effects and viscous forces. The transition between in-line and staggered jets is related to jet spreading and the flow geometry (jet spacing and tube diameter), but transitional Reynolds numbers can be correlated to modified Galileo numbers with reasonable accuracy in the current experimental range for all the transitions. These results provide a deeper understanding of the falling-film mode transitions and a useful tool for designing, operating, and modeling heat exchangers.

Acknowledgments

We gratefully acknowledge the National Science Foundation for support of this research (Grant No. NSF CTS-9396194).

References

Armbruster, R., and Mitrovic, J., 1994, "Patterns of Falling-Film Flow Over Horizontal Smooth Tubes," *Proc. Tenth International Heat Transfer Conference,* Vol. 3, pp. 275–280.

Armbruster, R., and Mitrovic, J., 1995, "Heat Transfer in Falling Film on a Horizontal Tube," *Proc. 1995 National Heat Transfer Conference—Vol. 12,* ASME HTD-Vol. 314, pp. 13–21.

Beaton, C. F., and Hewitt, G. F., 1988, *Physical Property Data for the Design Engineer,* Hemisphere, Washington, DC.

Bejan, A., 1994, *Convective Heat Transfer,* Wiley-Interscience, New York.

Chen, M. M., 1961, "An Analytical Study of Laminar Film Condensation: Part II—Single and Multiple Horizontal Tubes," ASME JOURNAL OF HEAT TRANSFER, Vol. 83, pp. 55–60.

Dhir, V. K., and Taghavi-Tafreshi, K., 1981, "Hydrodynamic Transition During Dripping of a Liquid From Underside of a Horizontal Tube," ASME Paper No. 81-WA/HT-12.

Fletcher, L. S., Sernas, V., and Parken, W. H., 1975, "Evaporation Heat Transfer Coefficients for Thin Sea Water Films on Horizontal Tubes," *Industrial Engineering Chemistry, Progress Des. Dev.,* Vol. 14, pp. 411–416.

Fujii, T., 1983, "Condensation in Tube Banks," *The Institute of Chemical Engineers Symposium Series,* Vol. 75, pp. 3–23.

Ganic, E. N., and Roppo, M. N., 1980, "An Experimental Study of Falling Liquid Film Breakdown on a Horizontal Cylinder During Heat Transfer," ASME JOURNAL OF HEAT TRANSFER, Vol. 102, pp. 342–346.

Honda, H., Nozu, S., and Takeda, Y., 1987, "Flow Characteristics of Condensate on a Vertical Column of Horizontal Tubes," *Proc. 1987 ASME–JSME Thermal Engineering Joint Conference,* Honolulu, HI, Vol. 1, pp. 517–524.

Honda, H., Uchima, B., Nozu, S., Nakata, H., and Torigoe, E., 1991, "Film Condensation of R-113 on In-Line Bundles of Horizontal Finned Tubes," ASME JOURNAL OF HEAT TRANSFER, Vol. 113, pp. 479–486.

Hu, X., 1995, "The Intertube Falling-Film Modes: Transition, Hysteresis, and Effect on Heat Transfer," Ph.D. Thesis, University of Illinois at Urbana–Champaign, Urbana, IL.

Kern, D. Q., 1958, "Mathematical Development of Tube Loading in Horizontal Condensers," *AIChE Journal,* Vol. 4, pp. 157–160.

Kutateladze, S. S., Gogonin, I. I., and Sosunov, V. I., 1985, "The Influence of Condensate Flow Rate on Heat Transfer in Film Condensation of Stationary Vapour on Horizontal Tube Banks," *International Journal of Heat and Mass Transfer,* Vol. 28, pp. 1011–1018.

Maron-Moalem, D., Sideman, S., and Dukler, A. E., 1978, "Dripping Characteristics in a Horizontal Tube Film Evaporator," *Desalination,* Vol. 27, pp. 117–127.

Marto, P. J., 1986, "Recent Progress in Enhancing Film Condensation Heat Transfer on Horizontal Tubes," *Heat Transfer Engineering,* Vol. 7, pp. 53–63.

Mitrovic, J., 1986, "Influence of Tube Spacing and Flow Rate on Heat Transfer From a Horizontal Tube to a Falling Liquid Film," *Proc. 8th International Heat Transfer Conference,* San Francisco, Vol. 4, pp. 1949–1956.

Nicol, A. A., and Abdelghaffar, M., 1988, "A Theory for Condensation with Drainage," *Proc. 2nd UK National Conference of Heat Transfer,* Glasgow, Vol. 1, pp. 639–651.

Parken, W. H., 1975, "Heat Transfer to Thin Water Films on Horizontal Tubes," Ph.D. Dissertation, Rutgers University, NJ.

Rogers, J. T., Goindi, S. S., and Lamari, M., 1995, "Turbulent Falling Film Flow and Heat Transfer on Horizontal Tubes," *Proc. 1995 National Heat Transfer Conference—Vol. 12,* ASME HTD-Vol. 314, pp. 3–12.

Slayzak, S. J., Viskanta, R., and Incropera, F. P., 1994, "Effects of Interactions Between Adjoining Rows of Circular, Free-Surface Jets on Local Heat Transfer From the Impingement Surface," ASME JOURNAL OF HEAT TRANSFER, Vol. 116, pp. 88–95.

Yundt, B., and Rhinesmith, R., 1981, "Horizontal Spray-Film Evaporation," *Chemical Engineering Proceedings,* Vol. 77, pp. 69–73.

Yung, D., Lorentz, J. J., and Ganic, E. N., 1980, "Vapor/Liquid Interaction and Entrainment in Falling Film Evaporators," ASME JOURNAL OF HEAT TRANSFER, Vol. 102, pp. 20–25.

Downloaded 11 Dec 2010 to 193.140.21.150. Redistribution subject to ASME license or copyright; see http://www.asme.org/terms/Terms_Use.cfm

APPENDIX

Test Liquids

Table 3 Correlations for thermophysical properties of the test liquids

Working Fluid	Property Correlations*	Source
Water: Filtered, deionized water	$\rho = 1004.4 \exp(-0.0002974T)$ $\mu = 0.00251 - 0.001159 \log(T)$	Bejan, 1984
Ethylene Glycol: DowTherm® 4000, 92.4% ethylene glycol and 7.6% water and inhibitors (by weight).	$\rho = 1154.24 \exp(-0.0006064T)$ $\mu = 0.04306 - 0.02281 \log(T)$	Dow Chem. Co, (product specs)
Water/Glycol: 55% water and 45% DowTherm® 4000 by weight.	$\rho = 1080.88 \exp(-0.000523T)$ $\mu = 0.007834 - 0.003818 \log(T)$	Dow Chem. Co, (product specs)
Oil: Chevron industrial hydraulic oil, AW ISO 32	$\rho = 886.32 \exp(-0.001183T)$ $\mu = 0.2518 - 0.141 \log(T)$	Chevron Research & Technology Co, (product specs)
Alcohol: Absolute ethyl alcohol	$\rho = 806.58 \exp(-0.0011T)$ $\mu = 0.002831 - 0.001254 \log(T)$	Beaton and Hewitt, 1988

* Surface tension was measured as described in the text. The temperature range of these experiments was 25–40°C.

Table 4 Approximate values of $Ga^{1/4}$ for each test liquid at standard conditions

Liquid	$Ga^{1/4}$
Water	530.2
Ethylene Glycol	35.7
Water/Glycol	165.0
Oil	5.2
Alcohol	176.1

Downloaded 11 Dec 2010 to 193.140.21.150. Redistribution subject to ASME license or copyright; see http://www.asme.org/terms/Terms_Use.cfm

X. Hu

A. M. Jacobi
Assistant Professor of Mechanical Engineering. Assoc. Mem. ASME

Department of Mechanical and Industrial Engineering, University of Illinois at Urbana–Champaign, 1206 W. Green Street, Urbana, IL 61801

The Intertube Falling Film: Part 2—Mode Effects on Sensible Heat Transfer to a Falling Liquid Film

When a liquid film falls from one horizontal tube to another below it, the flow may take the form of discrete droplets, jets, or a continuous sheet; the mode plays an important role in the heat transfer. Experiments are reported that explore the local heat transfer behavior for each of these flow patterns, and the results are related to the important features of the flow. Spatially averaged Nusselt numbers are presented and discussed, and new mode-specific design correlations are provided. This research is part of an overall study of horizontal-tube, falling-film flow and heat transfer.

Introduction

Recent environmental, safety, and cost concerns related to particular heat transfer fluids make low working inventories an engineering priority in some applications. For these situations, falling-film heat exchangers are attractive because they provide good heat transfer performance and low working-fluid inventories. The design of falling-film heat exchangers has been largely based on empirical data; however, to develop efficient new designs and minimize charge in existing systems, a thorough understanding of the falling-film flow and heat transfer interactions is important.

The most common geometry for falling-film heat exchangers is probably the horizontal tube bundle. When a liquid film falls from tube to tube in the bundle, the flow may take the droplet, droplet-jet, in-line jet, staggered jet, jet-sheet, or sheet modes. In a companion paper (Part 1; Hu and Jacobi, 1996), detailed observations of these modes and methods for predicting their occurrence were presented. The flow pattern is important for heat exchangers in condensing, evaporating, or sensible heat transfer applications.

Condensing heat transfer to a falling liquid sheet has been widely studied and is relatively well understood. Most investigations of this topic are related to Nusselt's early analysis of condensation, and they can be viewed as extensions or corrections to account for subcooling, advection, or inundation effects. While the flow pattern of the falling condensate film is known to affect condensing heat transfer (Kern, 1958; Shklover and Semenov, 1981; Kutateladze et al., 1985; Honda et al., 1991), this so-called inundation effect is one aspect of bundle condensation that remains somewhat unclear, and it may be responsible for the type of measurement and interpretation inconsistencies cited by Marto (1986). Understanding falling-film mode effects in sensible heat transfer may help in understanding condensate inundation effects.

The situation is more problematic for falling film evaporation, due to additional confusion over the effect of subcooling, heat flux, liquid flow rate and other parameters. For example, Fletcher et al. (1975) found that the Nusselt number increased with flow rate and heat flux, but Conti (1978) reported that over a wide range it was insensitive to flow rate, and Parken et al. (1990) reported that it was insensitive to heat flux. Such inconsistencies may be due to the complex media used in some applications, e.g., sea water with biological material. Nevertheless, it is difficult to isolate the effect of the falling film mode on evaporation heat transfer, and the problem can be exacerbated by the complexity of the flow in the jet and droplet modes. Understanding the role of falling-film mode in sensible heat transfer may help in isolating these effects on evaporation heat transfer.

Sensible Heat Transfer to Liquid Films on Horizontal Tubes. Sensible heat transfer to a falling film in the sheet mode has been studied by a number of investigators. Sernas (1979) correlated Parken's (1975) experimental data for the heating of subcooled water with $47 < q''_o < 79$ kW/m^2 and $1150 < \mathrm{Re} < 6000$, and the following relation was developed:

$$\mathrm{Nu} = C\,\mathrm{Re}^{0.24}\,\mathrm{Pr}^{0.66} \tag{1}$$

C was 0.01925 for a 25-mm-dia tube and 0.01729 for a 50-mm-dia tube.

A correlation developed by Gimbutis (1975) for heat transfer to a subcooled film in a vertical bank of horizontal tubes was recommended by Rohsenow (1985). For Reynolds numbers from 30 to 5000, the correlation takes the following form:

$$\mathrm{Nu} = 0.39\,\mathrm{Re}^{0.21}\,\mathrm{Pr}^{0.36}\,\mathrm{Ar}^{-0.12}(\mathrm{Pr}/\mathrm{Pr}_o)^{0.25} \tag{2}$$

Mitrovic (1986) studied heat transfer to a subcooled film on horizontal tubes, with a focus on the effects of tube spacing. Heat transfer coefficients were found to depend on not only the Reynolds number but also on the tube spacing and flow pattern. Tube spacing was found to have an insignificant effect on the heat transfer coefficients for Reynolds numbers greater than 160. A consistent increase of heat transfer coefficient was reported for an increase of liquid flow rate. An empirical relation for the heat transfer coefficient was given for water with $160 \le \mathrm{Re} < 560$.

$$\mathrm{Nu} = 1.374(10^{-2})\,\mathrm{Re}^{0.349}\,\mathrm{Pr}^{0.5}\beta \tag{3}$$

where

$$\beta = (1 + s/d)^{0.158}/[1 + \exp(-3.2(10^{-3})\,\mathrm{Re}^{1.32})] \tag{4}$$

Rogers and Goindi (1989) performed an experimental study with a large tube (d = 132 mm) and concluded that laminar flow occurred for film Reynolds numbers up to about 2000. Local measurements showed that the heat transfer coefficient was initially high, decreased to a minimum for angles between

[1] Current address: Research Engineer, Allied Signal, Phoenix, AZ.

Contributed by the Heat Transfer Division for publication in the JOURNAL OF HEAT TRANSFER. Manuscript received by the Heat Transfer Division September 20, 1995; revision received April 26, 1996. Keywords: Forced Convection, Heat Exchangers, Multiphase Flows. Associate Technical Editor: V. K. Dhir.

Copyright © 1996 by ASME

Downloaded 11 Dec 2010 to 193.140.21.150. Redistribution subject to ASME license or copyright; see http://www.asme.org/terms/Terms_Use.cfm

30 and 60 deg, increased to a maximum at around 90 deg, decreased to another local minimum around 150 deg, and finally increased near the bottom of the tube.

Several investigators have used integral methods to solve the governing laminar boundary layer equations. Solan and Zfati (1974) divided the flow into an initial region, in which the thermal boundary layer was thinner than the liquid film, and a main region, in which the whole film constituted a thermal boundary layer thickness. They numerically solved the governing equations and found the tube diameter to have a significant effect, with larger heat transfer coefficients for smaller tubes. They also predicted that the heat transfer coefficient would increase with Reynolds number at small Reynolds numbers and decrease slightly at high Reynolds numbers. In a similar analysis, Rogers (1981) divided the flow into a developing thermal boundary layer region and a fully developed thermal boundary layer region. The developing region began at the upper stagnation point and extended to the angular position at which the thermal boundary layer reached the surface of the film; the developed region covered the rest of the tube. The expression given for the local heat transfer coefficient in the developing region can be written as

$$\mathrm{Nu} = 0.831\ \mathrm{Re}^{1/9}\ \mathrm{Ar}^{-1/9}\ \mathrm{Pr}^{1/3}(\sin\phi/P(\phi))^{1/3} \quad (5)$$

where

$$P(\phi) = \int_0^{\phi} (\sin\phi)^{1/3} d\phi \quad (6)$$

The extent of thermal boundary layer development region, ϕ_d, was given by the following expression:

$$P(\phi_d) = 0.0606\ \mathrm{Re}^{4/3}\ \mathrm{Ar}^{-1/3}\ \mathrm{Pr} \quad (7)$$

For the fully developed thermal boundary layer region, the model of Rogers can be written in the following form:

$$\mathrm{Nu} = 2.167\ \mathrm{Re}^{-1/3}(\sin\phi)^{1/3} \quad (8)$$

Recently, Armbruster and Mitrovic (1995) provided a review of the related literature and measurements of local tube surface temperature distributions for several flow conditions, and Rogers et al. (1995) provided a correlation applicable for turbulent flow in the sheet mode (for $\mathrm{Re} > 2000$).

Objectives. In a companion paper we described a detailed study of the falling-film flow patterns and their transitions (Part 1). Understanding the hydrodynamics represents a necessary first step toward a complete understanding of falling-film heat exchangers. With this tool in hand, a clear grasp of the mode effects on sensible heat transfer is the next logical step. Therefore, the objective of this study is to provide a deeper understanding of sensible heat transfer to a falling liquid film on horizontal tubes. Such an understanding will provide a basis for modeling sensible heat exchangers and will contribute toward understanding falling-film evaporators, condensers, and absorbers. To meet this objective, new local and average sensible heat transfer data will be presented for each falling-film mode. These data will be compared to earlier work, and new design correlations will be provided.

Method

Apparatus. The test facility (see Fig. 2 of Part 1) consisted of a closed-circuit, forced-circulation loop of the test liquid and an open-loop wind tunnel. The liquid loop provided fluid to the test section, and the wind tunnel allowed experiments to be conducted with a gas flow (mainly for related hydrodynamic experiments). A detailed description of the wind tunnel apparatus and liquid circulation loop was given in Part 1.

Liquid was delivered to the feeding tube at the top of the test section at a controlled rate and temperature using the head tank and thermal reservoir. The flow issued from the upper tube, flowed around the lower feeding tube, and fell to the test tube. Tubes with outside diameters of 22.22 mm, 19.05 mm, and 15.88 mm were used in the heat transfer experiments. The tubes were mounted in the test section on bakelite fasteners to minimize heat conduction end-losses (see Part 1 and Hu, 1995, for details). All specimens were brass tubes with a 3.18 mm wall thickness. A uniform surface finish was obtained by polishing the tubes with emery cloth; the final polish used a 215F emery (surface roughness estimated to be less than 0.1 μm). An electric-resistance heater was pressed into the test tube after applying a thermal grease. As a rough check for flux uniformity, one specimen was coated with thermochromic liquid crystals and heated in still air. The resulting color pattern, representing the temperature distribution, was highly symmetric. As a further check, some experiments were repeated after rotating the heater within the test tube; no difference in the results was found. The thick-walled specimen design helped mitigate potential problems with flux nonuniformity; however, it complicated data interpretation by requiring an analysis to account for heat conduction within the specimen (discussed in detail later).

Instrumentation. During heat transfer experiments, the liquid mass flow rate ($\pm$0.5 to 2 percent), surface tension ($\pm$0.5 percent), air Pitot-static pressure ($\pm$0.12 Pa), air temperature ($\pm$0.1°C), relative humidity ($\pm$2 percent), and barometric pressure ($\pm$0.5 mm Hg) were measured as described in the companion article on falling-film mode observations (Hu and Jacobi, 1996). The heat transfer experiments required additional mea-

Nomenclature

Ar = Archimedes number based on tube diameter = d^3g/ν^2
c_p = constant-pressure specific heat
d = tube diameter
Ga = modified Galileo number = $\rho\sigma^3/\mu^4 g$
g = gravitational acceleration
h = heat transfer coefficient
k = thermal conductivity
L = tube length
L_{eff} = active length on the test specimen surface
Nu = Nusselt number = $(\nu^2/g)^{1/3}h/k$
Pr = Prandtl number = $c_p\mu/k$
q'' = heat flux
r = radial coordinate
Re = film Reynolds number = $2\Gamma/\mu$
s = tube spacing (see Fig. 3, Part 1)
T = temperature
V = velocity
We = Weber number = $\rho_{\mathrm{air}}V_{\mathrm{air}}^2 d/\sigma$
z = axial coordinate
Γ = liquid mass flow rate per unit length of tube
μ = dynamic viscosity
ν = kinematic viscosity
ρ = mass density
σ = surface tension at gas/liquid interface
ϕ = angular coordinate

Subscripts

air = of the surrounding air
f = at the liquid inlet temperature
i = at the inside of the tube
o = at the outside of the tube
Q = under an isoflux condition (see Eq. (13))
t = of the test tube

Note: Unsubscripted properties refer to the liquid film.

Downloaded 11 Dec 2010 to 193.140.21.150. Redistribution subject to ASME license or copyright; see http://www.asme.org/terms/Terms_Use.cfm

surements of the tube surface temperatures and electrical power to the resistance heater.

Specimen surface temperatures were measured using 36-gage, copper-constantan thermocouples. On each test tube, 24 thermocouples were embedded in axial grooves at 30 deg circumferential increments as shown in Fig. 1(*a*). Each groove was 0.51 mm deep for a length of 2.54 mm from the measuring end, and the rest of the groove was 0.76 mm deep and 0.81 mm wide. Using a thermally conductive epoxy, each thermocouple junction was fixed to the specimen surface at the end of a groove such that the bead was barely visible at the surface (see Fig. 1(*b*)). The thermocouple wires were placed in the axial groove, and the groove was filled with epoxy. About 50 percent of the groove volume was occupied by the thermocouples, and the rest was epoxy (the thermal conductivity of the epoxy was $1 \sim 2$ W/m·K). Approximately 6 percent of the test surface area was occupied by the instrument grooves. After the epoxy cured, the tubes were polished with fine emery cloth to remove the excess epoxy and the exposed portions of thermocouple junctions. The resulting specimen was smooth, with the surface thermocouples symmetrically located on each test tube. The thermocouple junctions spanned an axial length of 46 mm at 2-mm intervals on the largest test tube and an axial length of 34.5 mm at 1.5-mm intervals on the other two specimens. An in-situ calibration using an isothermal bath and a NIST-traceable reference ensured accurate surface temperature measurements (±0.15°C) over the entire experimental range.

During the course of a steady-state experiment, the specimen was rotated to obtain a total of 288 surface temperature measurements per test. This procedure provided surface temperature data on a grid with one temperature measurement for roughly every 6 to 11 mm^2 of surface area, depending on the tube diameter.

Liquid temperatures were measured in the feeding and catching tubes with calibrated type-T thermocouples. At steady state, each thermocouple was sampled about 4000 times and the results were averaged; these data were recorded over a period of roughly one minute (depending on the test). The heater input was measured using a digital multimeter (±0.1 V, ±0.001 A), and these data were used to infer the inside surface heat flux to the test specimen (see Hu, 1995, for details).

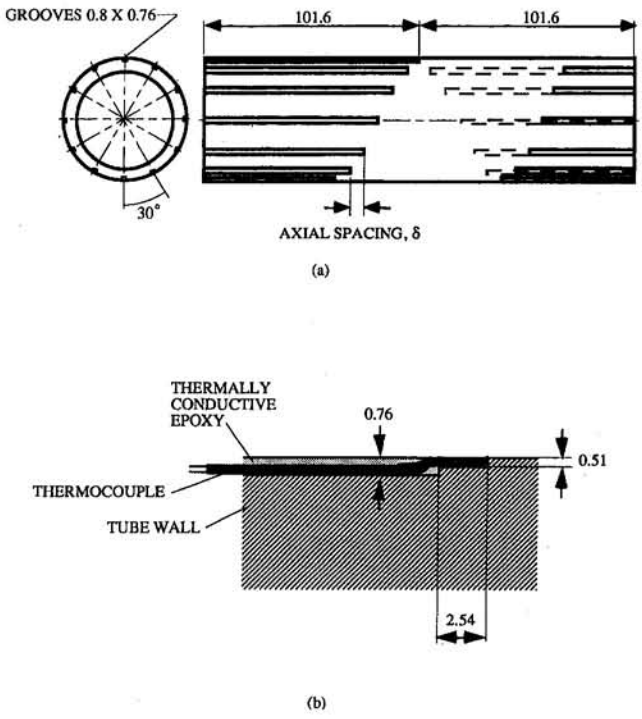


Fig. 1 Thermocouple placement on the test specimen tube (all dimensions in mm): (*a*) location on the tube surface; and (*b*) location in the tube wall. The axial spacing between thermocouples, δ, was 2 mm on the 22.22-mm-dia tube and 1.5 mm on the other two smaller tubes. Thermocouple wires were placed in the axial grooves and covered with a thermally conductive epoxy.

Experimental Scope and Procedure. The scope of the heat transfer experiments was similar to that described in Part 1; however, due to flammability concerns, only three of the test liquids were used: water, ethylene glycol, and the mixture of water and ethylene glycol. Property data were obtained using the sources given in Part 1, and these fluids provided a wide variation in thermophysical properties. The heat transfer coefficient for convection from the tube to the liquid could depend on the falling-film mode, flow rate, liquid temperature, surface heat flux, tube diameter and spacing, and the thermophysical properties of the liquid. These parameters were prescribed during the experiments, and their nominal ranges are summarized in Table 1.

Before conducting a heat transfer experiment, the equipment was subjected to the same set-up and warm-up procedures described for the hydrodynamic experiments (Hu and Jacobi, 1996). However, after the flow was established, the heat transfer experiments involved additional measurements. The approach temperature was set using electrical heaters within the thermal reservoir (see Fig. 2 of Part 1), and the heat flux was set using the in-tube heater. An experimental regimen consisted of setting the flow conditions and recording the measurements discussed above under varying thermal conditions. This procedure was repeated for wide ranging flow conditions (to include each possible mode for each test liquid and geometry).

Data Interpretation. On the basis of a dimensional analysis (see Hu and Jacobi, 1996; Hu, 1995), the Nusselt number is expected to depend on the falling-film mode and the following dimensionless parameters: the film Reynolds number, a modified Galileo number, the Archimedes number, the Prandtl number, and the dimensionless tube spacing. If an air flow is present, the Weber number could also become relevant. All of these parameters were determined directly from the measurements of physical properties discussed earlier; however, an indirect approach was needed to infer the Nusselt number from the local surface temperature measurements. In calculating the Nusselt number, it was necessary to determine the local heat transfer coefficient using

$$h(\phi, z) = \frac{q''_o(\phi, z)}{T_o(\phi, z) - T_f} \tag{9}$$

where q''_o is the local heat flux at the outer tube surface, and T_o and T_f represent the local temperature at the outer surface of the tube and the bulk fluid inlet temperature, respectively. The bulk fluid inlet temperature was used for several reasons: (1) T_f is commonly adopted as a reference temperature in the related literature (see Rogers and Giondi, 1989; Sernas, 1979), so comparisons to extant work are easier; (2) in the impingement region where the heat transfer behavior is interesting, the local mixing-cup and bulk inlet temperatures are identical; at film departure, where the heat transfer behavior is relatively uninteresting, the mixing-cup temperature typically had changed by less than 10 percent of the total driving potential, so its use does not affect our interpretation of the important physics; and finally, (3) the local velocity and temperature data needed to evaluate a true local mixing-cup temperature within the film were not available for the complicated three-dimensional flows of this study.

As noted earlier, due to the variation of the local heat transfer coefficient and the conductivity of the specimen, the heat flux at the outer surface of the tube may have been nonuniform. To account for these possible variations, the flux was inferred by

Downloaded 11 Dec 2010 to 193.140.21.150. Redistribution subject to ASME license or copyright; see http://www.asme.org/terms/Terms_Use.cfm

Table 1 The experimental range of the prescribed physical variables

Physical Parameter,	Symbol	Experimental Range	Units
Mass flow rate per unit length,	Γ	up to 0.72	kg/m-s
Liquid thermal conductivity,	k	0.27 to 0.61	W/m-K
Liquid specific heat,	c_p	2390 to 4180	J/kg-K
Liquid dynamic viscosity,	μ	7.9 (10^{-4}) to 9.4 (10^{-3})	N-s/m^2
Mass density of the liquid,	ρ	995 to 1140	kg/m^3
Gas/liquid surface tension,	σ	4.8 (10^{-2}) to 6.8 (10^{-2})	N/m
Tube diameter,	d	15.88, 19.05, 22.22	mm
Tube spacing,	s	about 5 to 50	mm
Heat flux,	q"	up to about 1.15 (10^5)	W/m^2
Inlet liquid temperature,	T_f	20 to 40	C

solving the steady-state heat equation for the specimen (assuming isotropic properties and no internal generation):

$$\frac{\partial}{r\partial r}\left(k_t r \frac{\partial T_t}{\partial r}\right) + \frac{\partial}{r^2 \partial \phi}\left(k_t \frac{\partial T_t}{\partial \phi}\right) + \frac{\partial}{\partial z}\left(k_t \frac{\partial T_t}{\partial z}\right) = 0 \quad (10)$$

The experimentally imposed flux at the inside tube surface provided one boundary condition:

$$-k_t \left.\frac{\partial T_t}{\partial r}\right|_{r=r_i} = q_i'' \quad (11)$$

and a convective condition was applied to the outside surface,

$$-k_t\left(\frac{\partial T_t}{\partial r}\right)_{r_o} = h(\phi, z)(T_o(\phi, z) - T_f). \quad (12)$$

The specimen was modeled as circumferentially periodic and, using the experimental data, the ends were selected such that they were adiabatic. With these additional conditions, Eqs. (10)–(12) were solved using standard, second-order finite difference techniques and a computational grid that was $10 \times 24 \times 20$ or finer in (r, ϕ, z). The numerical uncertainties associated with this solution of the heat equation were much less than the measurement uncertainties in the surface temperature. This scheme required iteration. As an initial guess, $h(\phi, z)$ was taken as uniform at a value that satisfied Eq. (9), where the flux at the outside tube wall was assumed uniform and consistent with the prescribed flux at the inside wall. Then an iterative scheme was used to determine a distribution of $h(\phi, z)$ (and thus $q_o''(\phi, z)$) that yielded calculated surface temperatures that agreed with the measured data to within the experimental uncertainty (all predicted surface temperatures were within 0.15°C of the measured values).

To develop correlations of general value that could be compared to data from the literature, the average Nusselt number was computed with a constant flux assumption applied at the outside tube wall. Thus, the local heat transfer coefficient could be integrated directly to find the average heat transfer coefficient:

$$\bar{h}_Q \equiv \frac{1}{2\pi r_o L_{\text{eff}}} \iint_A h(\phi, z) dA. \quad (13)$$

Equation (13) should be regarded as a definition of $\bar{h}_Q$, where the subscript "Q" is used to indicate the isoflux assumption. The corresponding average Nusselt number is then

$$\overline{\text{Nu}}_Q = \frac{\bar{h}_Q}{k}\left(\frac{\nu^2}{g}\right)^{1/3}. \quad (14)$$

This approach is identical to the common interpretation of average results (see Armbruster and Mitrovic, 1995), and it makes a direct comparison to the literature easy. The generality of this approach will be discussed along with the rest of the results later. The experimental range and estimated uncertainty of the experimental parameters is summarized in Table 2.

The local and average Nusselt numbers, as determined by the measurements and methods described earlier, had experimental uncertainties that depended on the experimental conditions and spatial location of interest. For example, very high uncertainties in local Nusselt numbers (roughly ±100 percent) were estimated for a few measurements in the jet impingement region (where small surface-to-liquid temperature differences occurred). However, outside these localized areas of high uncertainty, the local Nusselt number uncertainties over most of the tube surface were typically ±5 percent for an assumed uniform flux on the inside tube surface.[2] The average estimated uncertainty in the measured $\overline{\text{Nu}}_Q$ was ±7 percent for the entire experimental regimen of 291 experiments in the ranges summarized in Tables 1 and 2. The experimental uncertainty will be discussed further with the presentation of the results.

Results and Discussion

The flow and heat transfer interactions are fundamentally different for each of the falling-film modes; therefore, their local heat transfer characteristics will be presented separately. Following a discussion of local Nusselt number behavior, spatially averaged data will be presented and discussed for each mode. Finally, new design correlations will be presented and compared to previous results from the literature.

Local Heat Transfer Behavior

The Sheet Mode. For a falling film in the sheet mode, the local Nusselt number distribution exhibits small axial nonuniformities along the top of the tube ($\varphi = 0$). These variations may have been due to flow imperfections or to waviness of the falling sheet. Unfortunately, the experimental uncertainties were highest in this region, approaching the magnitude of the axial variations (see Hu, 1995, for details). In contrast, the local Nusselt numbers exhibited significant circumferential variations, with nearly an order of magnitude change from $\phi = 0$ to 180 deg. Typical circumferential distributions of the local heat transfer coefficient are shown in Fig. 2. The figure shows that circumferential variations become more pronounced at higher Reynolds numbers, and there is an increase in heat transfer with Reynolds number. Local coefficients at the top of the tube are more sensitive to the Reynolds number; this behavior may be anticipated since impingement heat transfer may be expected to scale with Re, whereas heat transfer in the boundary layer (away from the impingement region) may be expected to scale with $\text{Re}^{1/2}$. Along the bottom of the tube there appears to be a small increase in the heat transfer coefficient.

When a sheet falls onto a tube, the liquid is rapidly decelerated in the surface-normal direction and accelerated in the circumferential direction. Downstream of the impingement region, the flow around the tube is accelerated by gravity and opposed by viscous shear. A viscous boundary layer develops and eventually extends to the free surface. For liquids with Prandtl num-

[2] Chyu and Bergles (1988) give a thorough analysis of flux nonuniformity effects for cartridge heaters. We applied their analysis to our specimen design. If the flux on the inside surface varied by 50 percent (sinusoidally), then the local Nusselt numbers could be affected by roughly 12 percent. Given the measures described earlier to mitigate these effects and the symmetry of the final data, we feel as if this variation represents an upper limit on the local Nusselt number uncertainty due to flux variations.

Downloaded 11 Dec 2010 to 193.140.21.150. Redistribution subject to ASME license or copyright; see http://www.asme.org/terms/Terms_Use.cfm

Table 2 Relevant dimensionless parameters, the experimental range, and typical uncertainties associated with propagated measurement uncertainty

Dimensionless Group	Experimental Range	Estimated Uncertainty
$Ar = d^3g / \nu^2$	5.7(10^5) to 1.7(10^8)	±1.5%
$Ga = \rho\sigma^3 / g\mu^4$	7(10^2) to 8(10^{10})	±4%
$Pr = \nu / \alpha$	5.5 to 18	±0.7%
$Re = 2\Gamma / \mu$	up to 1900	±2%
s/d	0.25 to 5.2	±1%
$We = \rho_{air} V_{air}^2 d / \sigma$	up to 200	±10%

bers greater than one (the case for these experiments), a thermal boundary layer develops within the viscous boundary layer. The flow is thermally developed when the thermal boundary layer extends to the free surface. At the bottom of the tube, flows from both sides of the tube meet to form a stagnation and detachment region.

With these flow features in mind, the local heat transfer behavior shown in Fig. 2 can be explained. Heat transfer is high in the impingement region due to the surface-normal velocities and changing flow direction. The Nusselt number decreases in the circumferential direction as the thermal boundary layer grows. Eventually, the Nusselt number attains a relatively constant value in the region where the flow is fully developed. Near the bottom of the tube, the stagnation and detachment region exhibits a slight increase in Nusselt number, probably due to the surface-normal flow in this region. It seems sensible to further speculate that the detachment region could exhibit secondary flows associated with boundary layer separation in the adverse pressure gradient; however, we have no direct measurements to confirm this behavior.

The Jet Mode. A typical distribution of the local heat transfer coefficient in the staggered jet pattern is given in Fig. 3. In contrast to the sheet mode, heat transfer in the jet mode exhibits significant axial and circumferential variations. Figure 3 allows a direct comparison of the Nusselt number distribution to the location of impinging jets, and clearly heat transfer is high in the jet impingement regions along the top of the tube. Furthermore, there are regions of high heat transfer between the jet impingement sites. The Nusselt number is relatively low elsewhere and decreases with distance from the impingement sites.

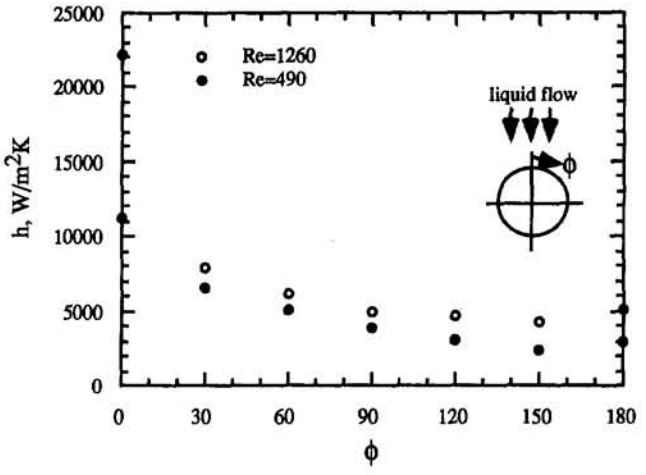


Fig. 2 Typical circumferential distribution of the local convective heat transfer coefficient for a falling liquid film in the sheet mode. Data are presented at two Reynolds numbers for d = 22 mm and s = 15 mm.

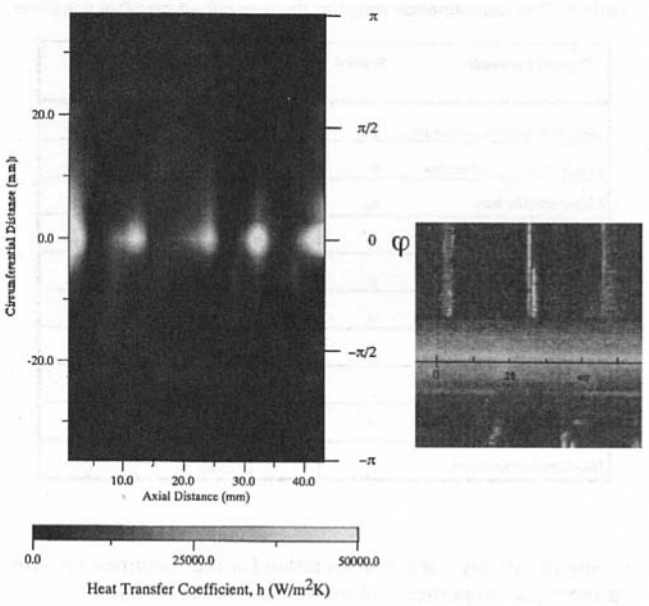


Fig. 3 A typical local heat transfer coefficient distribution for the staggered jet mode. The data shown are for water at Re = 236, with d = 22.22 mm and s = 32.5 mm.

The enhanced heat transfer of the impingement region is due to the surface-normal velocities and velocity gradients associated with jet stagnation. In the staggered jet configuration, there are important momentum interactions between neighboring jets that cause the formation of an "interaction ring" (see Part 1). This interaction ring is similar to the interaction fountain observed for jets impinging on a flat surface (Slayzak et al., 1994a, b). In this region between impingement sites, the surface-normal velocities and gradients associated with turning the flow from an axial to a circumferential direction increase the local heat transfer. The degree to which the local heat transfer is affected depends on the strength of the jet interaction.

When momentum interactions between jets are relatively unimportant, no interaction ring forms and an in-line jet pattern results. In that case, the local heat transfer enhancement associated with the interaction ring becomes less pronounced, as demonstrated by the typical distribution of the local heat transfer coefficient for the inline jet mode given in Fig. 4.

The Droplet Mode. A time-averaged local heat transfer coefficient distribution for the droplet mode is shown for typical conditions in Fig. 5. The heat transfer coefficient varies significantly in both the axial and circumferential directions on the tube surface. The droplet impingement zone, which is relatively larger than the jet or sheet impingement zones, exhibits higher Nusselt numbers than the rest of the tube.

The size of the droplet impingement region may be related to the size of the droplets. As correlated by Yung et al. (1980), the primary droplet diameter for the experimental conditions of Fig. 5 was about 8.1 mm. From a photographic study of the jets in this geometry, we found their diameter to be about 3 mm after a transition to the jet mode. Thus, the droplet diameters were nearly three times the jet diameters, and their spatial effect may have been larger due to their larger size. Because drop impingement is a transient phenomenon, the tube material may affect the heat transfer performance. Only time-averaged results have been reported, and since a single tube material was used for the current study, these effects remain unclear.

The absence of local maxima between dripping sites is due to the intermittent nature of the droplet mode. At low Reynolds

Downloaded 11 Dec 2010 to 193.140.21.150. Redistribution subject to ASME license or copyright; see http://www.asme.org/terms/Terms_Use.cfm

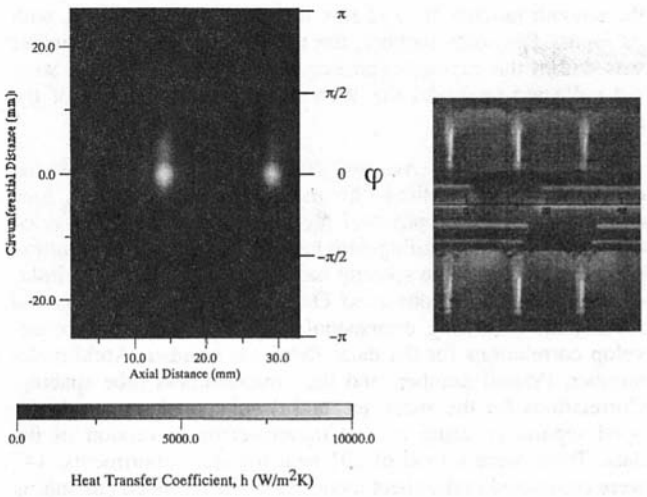


Fig. 4 A typical local heat transfer coefficient distribution for the inline jet mode. The data are for ethylene glycol at Re = 16, with d = 15.88 mm and s = 15 mm.

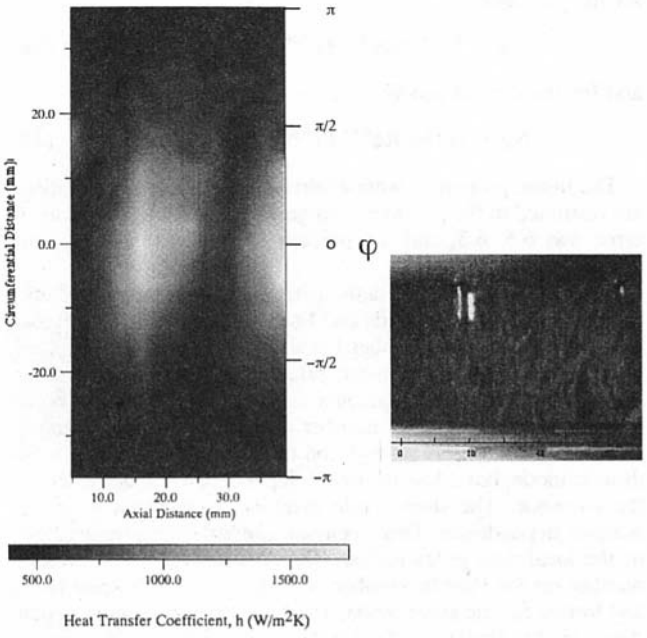


Fig. 5 A typical local heat transfer coefficient distribution for the droplet mode. The data shown are for water at a Re = 29, with d = 22.22 mm and s = 32.7 mm.

numbers, the droplet impingement sites are alternatively active, and momentum interactions among neighboring droplet sites apparently have little heat transfer effect. At higher Reynolds numbers (approaching a transition to jet mode), two neighboring droplet sites become active simultaneously and an interaction ring can form. In this case, local maxima between impingement sites will result; otherwise the distributions are qualitatively identical to Fig. 5.

Average Heat Transfer Behavior

Flow and Property Effects. Average Nusselt numbers for each test liquid in a fixed geometry are shown as a function of Reynolds number in Fig. 6. At low Reynolds numbers, the liquid falls in the droplet mode, and the average heat transfer coefficient shows a strong dependence on the Reynolds number. At moderate Reynolds numbers, in the jet mode, the average heat transfer coefficient increases with the Reynolds number, but the dependence is less pronounced than for the droplet mode. At high Reynolds numbers, the liquid falls in the sheet mode, and for water the Nusselt number still exhibits a Reynolds number dependence, but for the other liquids the Nusselt number becomes relatively insensitive to Reynolds number in the sheet mode.

The Reynolds number dependence in the droplet mode is related to the dripping frequency. Although no systematic measurements of dripping frequencies were conducted in the present study, a few measurements during the course of the experiments showed that when the Reynolds number increased from 30 to 100, the dripping frequency increased from about 1.4 to 2.9 Hz.

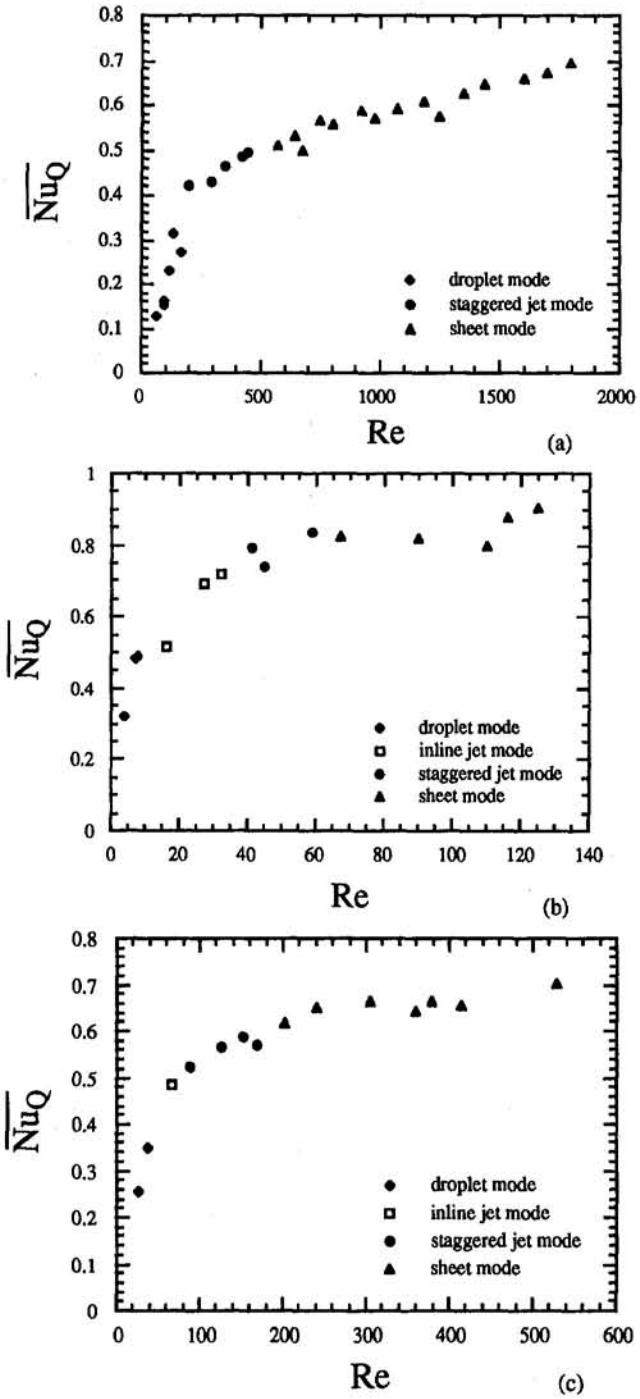


Fig. 6 Average Nusselt number behavior with Reynolds number d = 15.88 mm and s = 15 mm for: (a) water; (b) ethylene glycol; and (c) a mixture of water and ethylene glycol.

Downloaded 11 Dec 2010 to 193.140.21.150. Redistribution subject to ASME license or copyright; see http://www.asme.org/terms/Terms_Use.cfm

According to the data by Maron-Moalem et al. (1978), the dripping frequency increases almost linearly with Reynolds number; for water, they reported dripping frequencies of about 1.6 Hz at Re = 30 and 2.8 Hz at Re = 100. Because of the discrete nature of this flow, we expect a linear increase in dripping frequency to be accompanied by a similar increase in Nusselt number, and the data clearly support this expectation.

In the jet mode, average heat transfer behavior is dominated by the behavior in the impingement region. An increased Reynolds number implies increased momentum changes in the impingement zone and, as discussed by Hu and Jacobi (1996), is accompanied by closer jet spacing. Increased velocities in the impingement region and decreased jet spacing both act to increase heat transfer. Therefore, we expect the heat transfer to increase with Reynolds number in the jet mode, and the data confirm this expectation.

In the sheet mode, the Nusselt number is much less sensitive to the Reynolds number than in the other modes; however, the water data show more dependence than the other liquids. The sheet mode for water occurs for Re > 520, and most of the water heat transfer data are at much higher Reynolds numbers. Ethylene glycol and the water/glycol mixture flow in the sheet mode for Re > 50 and Re > 187, respectively; furthermore, most of their heat transfer data are at Re < 520. According to Seban (1978), Fujita and Ueda (1976), and Rogers (1981), transition from laminar to turbulent flow can be expected at Re $\approx$ 1000–3000, and waviness effects become important at lower Reynolds numbers (see Kutateladze, 1963). Therefore, water in the sheet mode is much more likely to exhibit turbulence and waviness effects than the other two liquids. For the sheet mode, the data show that the Nusselt number is sensitive to the Reynolds number only at high Reynolds numbers, suggesting that turbulence or waviness effects in the sheet are responsible for this dependence.

Geometry Effects. The tube diameter significantly affected the Nusselt number. The heat transfer coefficient was larger for smaller tubes over the entire experimental range of Reynolds numbers. For small tubes, the developing boundary layer occupies a larger fraction of the total heat transfer area; therefore, the average Nusselt number is higher. Tube spacing had no impact in the droplet or sheet modes; however, the Nusselt number did show a weak dependence on tube spacing in the jet mode. In the current experimental range, the increase in average Nusselt number with tube spacing in the jet mode was accompanied by a heat transfer increase in the region of the interaction ring. The increased jet momentum due to a longer free fall was apparently manifested in slightly higher heat transfer due to jet interaction (see Hu, 1995, for details).

Heat Flux Effects. The tube surface heat flux apparently has no impact on the heat transfer coefficient over the range of the current experiments (from 14 to 115 kW/m^2). No heat flux effect was found for any geometry, for any liquid, at any flow rate or in any falling film mode. The surface temperatures varied significantly, but there was no significant change in the heat transfer coefficient. This result supports the use of $\overline{\mathrm{Nu}}_Q$ as a generalization, because it provides evidence of weak coupling between the average heat transfer and the details of tube surface heat flux distribution, q''_o.

Air Flow Effects. Unfortunately, air flow effects on falling film heat transfer remain somewhat unclear. Limited data were recorded for We < 200, and the main effect of an air flow appears to be through its influence on falling film mode (see Hu and Jacobi, 1996). For a prescribed mode, an increase in the Weber number consistently resulted in an increased Nusselt number, but the changes were almost always within the estimated experimental uncertainty. It is interesting to note that the largest effect on the Nusselt number was for ethylene glycol in the sheet mode, suggesting that the air flow acted by disturbing the smooth laminar flow of this liquid. For a water flow, with its higher Reynolds number, the effect on the Nusselt number was within the experimental uncertainty. Sufficient data were not collected to model the Weber number dependence of the Nusselt number.

Correlation of the Average Heat Transfer Data. As discussed above, the falling-film mode, Reynolds number, tube diameter, and thermophysical properties significantly affected the horizontal-tube, falling-film heat transfer. In the current experimental range, tube spacing has a weak effect, and no influence of heat flux was observed. On the basis of the experimental results, the following dimensionless groups were used to develop correlations for the data: Reynolds number, Archimedes number, Prandtl number, and the dimensionless tube spacing. Correlations for the sheet, jet, and droplet modes were developed separately using a least-squares-error regression of the data. There were a total of 291 heat transfer experiments; 147 were conducted in the sheet mode, 89 in the jet mode (including both staggered and inline jets), and 55 in the droplet mode. The following equations resulted for the sheet mode:

$$\mathrm{Nu} = 2.194\ \mathrm{Re}^{0.28}\ \mathrm{Pr}^{0.14}\ \mathrm{Ar}^{-0.20}(s/d)^{0.07} \qquad (15)$$

for the jet mode,

$$\mathrm{Nu} = 1.378\ \mathrm{Re}^{0.42}\ \mathrm{Pr}^{0.26}\ \mathrm{Ar}^{-0.23}(s/d)^{0.08} \qquad (16)$$

and for the droplet mode:

$$\mathrm{Nu} = 0.113\ \mathrm{Re}^{0.85}\ \mathrm{Pr}^{0.85}\ \mathrm{Ar}^{-0.27}(s/d)^{0.04} \qquad (17)$$

The liquid properties were evaluated at T_f. These correlations are restricted to the parameter range given in Table 2. The mean error was 6.5, 6.3, and 6.1 percent for Eqs. (15), (16), and (17), respectively.

Equations (15)–(17) demonstrate that the Nusselt number increases with the Reynolds and Prandtl numbers and decreases with the Archimedes number for all three modes. As expected, the tube spacing has a weak effect on the Nusselt number. The Nusselt number dependence on Reynolds number, Prandtl number, and Archimedes number differs from mode to mode. Heat transfer depends strongly on the Reynolds number for the droplet mode, but a less profound dependence is manifested for the jet mode. The sheet mode exhibits the weakest Reynolds number dependence. This behavior supports the interpretation of the local data given earlier. The dependence of the Nusselt number on the Prandtl number is highest for the droplet mode and lowest for the sheet mode. The high Prandtl number dependence in the droplet mode may be because flow in the droplet mode significantly departs from the boundary-layer-type flow of the other modes.

A Comparison to the Literature. Predictions from Eqs. (15)–(17) were compared to experimental data for the droplet and jet modes reported by Ganic and Roppo (1980), and to data for the jet and sheet modes reported by Mitrovic (1986). In the study of Ganic and Roppo, heat transfer measurements were performed by embedding four thermocouples at 90 deg intervals around the circumference of a tube. The thermocouples were located at a single axial location on the 25.4-mm-dia tube, and distilled water was used as the working medium. Their data were slightly overpredicted by the new correlation, with a mean deviation of 11 percent for the droplet mode and 16 percent for the jet mode. To make this comparison possible, the modes associated with their data were determined using the method given in Part 1. The differences may be due to the larger tube of their study: The maximum Archimedes number for the data of Ganic and Roppo was Ar = 5.23(10^8); thus, some of their data are out of the range of the current study. However, the disagreement may be due to the finer spatial resolution of the current work.

Downloaded 11 Dec 2010 to 193.140.21.150. Redistribution subject to ASME license or copyright; see http://www.asme.org/terms/Terms_Use.cfm

In Mitrovic's study, heat transfer data were obtained within the current range for an 18-mm-dia tube with an intertube spacing from 12 to 87 mm. Mitrovic's data were consistently overpredicted by about 20 percent when Eqs. (15) and (16) were applied. Mitrovic used two embedded thermocouples axially located at a jet impingement and jet departure site. At steady state, the tube was rotated through 19 angular positions. The thermocouples in Mitrovic's experiment were embedded 0.8 mm below the surface of a copper tube with a wall thickness of 2.65 mm; a cartridge heater provided an inside flux, and the flux at the outer tube surface was assumed to be uniform. It is unclear whether differences in data interpretation or spatial resolution of the experiments could account for the discrepancy.

Summary and Conclusions

Typical local heat transfer coefficient distributions were presented for the sheet, staggered jet, in-line jet, and the droplet modes. In the sheet mode, the heat transfer coefficient exhibits large circumferential variations related to flow features such as sheet impingement, boundary-layer development, and liquid detachment. For the jet and droplet modes, the local Nusselt number distributions are highly two dimensional, with large axial and circumferential variations. This dependence is related to features of the flow, with local maxima in the impingement region and the interaction ring.

Spatially averaged Nusselt numbers were presented for each of the falling film modes for Reynolds numbers up to about 1900 (a wider range than was explored in the flow regime studies of Part 1). The average Nusselt numbers depend on the Reynolds, Archimedes, and Prandtl numbers, and on the dimensionless tube spacing. In the droplet mode, the Nusselt number increases sharply with increasing Reynolds number. A less pronounced dependence occurs in the jet mode, and in the sheet mode a Reynolds-number dependence is evident only at high Reynolds numbers, indicating that perhaps turbulence or waviness effects become important at these high Reynolds numbers. The average Nusselt number increases with a decrease in tube diameter, and the local data suggest that this behavior is caused by flow impingement and development affecting a relatively larger fraction of the tube area. The dependence on tube spacing is weak in the current experimental range. The Prandtl number dependence is most pronounced for the droplet mode, perhaps because of the intermittent nature of this falling-film mode.

The local data provide a clearer understanding of the important flow and heat transfer interactions for each mode, and the average data, in conjunction with the hydrodynamic study of Hu and Jacobi (1996), provide improved correlations for sensible heat transfer to a falling liquid film. Collectively, the hydrodynamic results and the local and average heat transfer data describe in detail the flow and heat transfer behavior important for some falling-film heat exchanger applications.

Acknowledgments

We gratefully acknowledge the National Science Foundation's support of this research through Grant No. NSF CTS-9396194.

References

Armbruster, R., and Mitrovic, J., 1995, "Heat Transfer in Falling-Film on a Horizontal Tube," *Proc. 1995 National Heat Transfer Conference—Vol. 12,* ASME HTD-Vol. 314, pp. 13–21.

Chyu, M. C., and Bergles, A. E., 1988, "Thermal Analysis of the Electrically Heated Cylindrical Test Section for Heat Transfer Experiments," *Experimental Thermal and Fluid Science,* Vol. 1, pp. 19–27.

Conti, R. J., 1978, "Experimental Investigation of Horizontal-Tube Ammonia Film Evaporators With Small Temperature Differentials," *Proc. 5th Ocean Thermal Energy Conversion Conference,* Miami Beach, FL, Vol. 6, pp. 161–180.

Fletcher, L. S., Sernas, V., and Parken, W. H., 1975, "Evaporation Heat Transfer Coefficients for Thin Sea Water Films on Horizontal Tubes," *Industrial Engineering Chemistry, Progress Des. Dev.,* Vol. 14, pp. 411–416.

Fujita, T., and Ueda, T., 1976, "Heat Transfer to Falling Liquid Films and Film Breakdown—I," *International Journal of Heat and Mass Transfer,* Vol. 21, pp. 97–108.

Ganic, E. N., and Roppo, M. N., 1980, "An Experimental Study of Falling Liquid Film Breakdown on a Horizontal Cylinder During Heat Transfer," ASME JOURNAL OF HEAT TRANSFER, Vol. 102, pp. 342–346.

Gimbutis, G., 1975, "Heat Transfer in Film Heat Exchangers," *Proc. 14th International Congress of Refrigeration,* Paper B1.49, Moscow, Vol. 2, pp. 1–7.

Honda, H., Uchima, B., Nozu, S., Nakata, H., and Torigoe, E., 1991, "Film Condensation of R-113 on In-Line Bundles of Horizontal Finned Tubes," ASME JOURNAL OF HEAT TRANSFER, Vol. 113, pp. 479–486.

Hu, X., 1995, "The Intertube Falling-Film Modes: Transition, Hysteresis, and Effect on Heat Transfer," Ph.D. Thesis, University of Illinois at Urbana–Champaign, Urbana, IL.

Hu, X., and Jacobi, A. M., 1996, "The Intertube Falling Film: Part 1—Flow Characteristics, Mode Transitions, and Hysteresis," ASME JOURNAL OF HEAT TRANSFER, Vol. 118, this issue, pp. 616–625.

Kern, D. Q., 1958, "Mathematical Development of Tube Loading in Horizontal Condensers," *AIChE Journal,* Vol. 4, pp. 157–160.

Kutateladze, S. S., 1963, *Fundamentals of Heat Transfer,* Academic Press, New York.

Kutateladze, S. S., Gogonin, I. I., and Sosunov, V. I., 1985, "The Influence of Condensate Flow Rate on Heat Transfer in Film Condensation of Stationary Vapour on Horizontal Tube Banks," *International Journal of Heat and Mass Transfer,* Vol. 28, pp. 1011–1018.

Maron-Moalem, D., Sideman, S., and Dukler, A. E., 1978, "Dripping Characteristics in a Horizontal Tube Film Evaporator," *Desalination,* Vol. 27, pp. 117–127.

Marto, P. J., 1986, "Recent Progress in Enhancing Film Condensation Heat Transfer on Horizontal Tubes," *Heat Transfer Engineering,* Vol. 7, pp. 53–63.

Mitrovic, J., 1986, "Influence of Tube Spacing and Flow Rate on Heat Transfer From a Horizontal Tube to a Falling Liquid Film," *Proc. 8th International Heat Transfer Conference,* San Francisco, Vol. 4, pp. 1949–1956.

Parken, W. H., 1975, "Heat Transfer to Thin Water Films on Horizontal Tubes," Ph.D. Dissertation, Rutgers University, NJ.

Parken, W. H., Fletcher, L. S., Sernas, V., and Han, J. C., 1990, "Heat Transfer Through Falling Film Evaporation and Boiling on Horizontal Tubes," ASME JOURNAL OF HEAT TRANSFER, Vol. 112, pp. 744–750.

Rogers, J. T., 1981, "Laminar Falling Film Flow and Heat Transfer Characteristics on Horizontal Tubes," *The Canadian Journal of Chemical Engineering,* Vol. 59, pp. 213–222.

Rogers, J. T., and Goindi, S. S., 1989, "Experimental Laminar Falling Film Heat Transfer Coefficients on a Large Diameter Horizontal Tube," *The Canadian Journal of Chemical Engineering,* Vol. 67, pp. 560–568.

Rogers, J. T., Goindi, S. S., and Lamari, M., 1995, "Turbulent Falling Film Flow and Heat Transfer on Horizontal Tubes," *Proc. 1995 National Heat Transfer Conference—Vol. 12,* ASME HTD-Vol. 314, pp. 3–12.

Rohsenow, W., 1985, "Boiling," in: *Handbook of Heat Transfer Fundamentals,* 2nd ed., Rohsenow, Hartnett, and Ganic, eds., McGraw-Hill, New York, pp. 12–78.

Seban, R. A., 1978, "Transport to Falling Films," *Proc. Sixth International Heat Transfer Conference,* Keynote Paper KS-30, Toronto.

Sernas, V., 1979, "Heat Transfer Correlation for Subcooled Water Films on Horizontal Tubes," ASME JOURNAL OF HEAT TRANSFER, Vol. 101, pp. 176–180.

Shklover, G. G., and Semenov, V. P., 1981, "The Flow Mode of Condensate in a Multirow Horizontal Tube Bundle," *Heat Transfer—Soviet Research,* Vol. 13, No. 3, pp. 127–133.

Slayzak, S. J., Viskanta, R., and Incropera, F. P., 1994a, "Effects of Interaction Between Adjacent Free Surface Planar Jets on Local Heat Transfer From the Impingement Surface," *International Journal of Heat and Mass Transfer,* Vol. 37, pp. 269–282.

Slayzak, S. J., Viskanta, R., and Incropera, F. P., 1994b, "Effects of Interactions Between Adjoining Rows of Circular, Free-Surface Jets on Local Heat Transfer From the Impingement Surface," ASME JOURNAL OF HEAT TRANSFER, Vol. 116, pp. 88–95.

Solan, A., and Zfati, A., 1974, "Heat Transfer in Laminar Flow of a Liquid Film on a Horizontal Cylinder," *Proc. 5th International Heat Transfer Conference,* Tokyo, Sept. 3–7, Vol. 2, pp. 90–93.

Yung, D., Lorentz, J. J., and Ganic, E. N., 1980, "Vapor/Liquid Interaction and Entrainment in Falling Film Evaporators," ASME JOURNAL OF HEAT TRANSFER, Vol. 102, pp. 20–25.

Downloaded 11 Dec 2010 to 193.140.21.150. Redistribution subject to ASME license or copyright; see http://www.asme.org/terms/Terms_Use.cfm

Correlations for Film Regeneration and Air Dehumidification for a Falling Desiccant Film With Air in Crossflow

M. Park

J. R. Howell

G. C. Vliet
email:gvliet@mail.utexas.edu

Department of Mechanical Engineering, and Center for Energy Studies, The University of Texas at Austin, Austin, TX 78712-1063

The coupled heat and mass transfer between a falling triethylene glycol (TEG) desiccant film and air in crossflow have previously been presented and solved numerically for the cases of regeneration and dehumidification. Here, correlations for the effects of independent variables on the rate of regeneration in the regenerator and on the rate of dehumidification and sensible cooling in the absorber are developed by statistical analysis of the numerical results. The functional correlations developed should be useful in the design of regenerators and absorbers having falling liquid desiccant films and air in crossflow.

Introduction

Recently, studies of hybrid air conditioners that use liquid desiccant dehumidification and regeneration in conjunction with vapor-compression cooling have shown potential for energy savings in hot and humid climates (Peterson and Howell, 1990). Liquid desiccant films improve heat and mass transfer for dehumidification and cooling of moist air in the evaporator coil and can be regenerated from the heat rejected from the condenser of the vapor-compression refrigerating cycle. This paper deals with the performance of the two critical heat and mass transfer components of the hybrid system, the desiccant regenerator (condenser) and evaporator (dehumidifier).

For efficient regeneration of weak TEG solution and dehumidification of air, a large contact area and extended contact time between the moving air and desiccant is necessary. For the configuration considered herein the liquid desiccant (aqueous TEG solution) is pumped to an overhead distributor from which it then flows downward in a thin film over the vertical surfaces of the regenerator and absorber. The regenerator and absorber are finned-tube exchangers. The desiccant film falls downward over the fins (plates), air is in crossflow over the liquid film, and refrigerant in the tubes of the exchanger heats or cools the contact surface. In the regenerator, water is evaporated from the heated liquid desiccant into the moist air. In the dehumidifier, vapor is absorbed from the moist air into the cooled liquid desiccant.

Although some work has been done for counterflow liquid desiccant regeneration/absorption, for example Ertas et al. (1993), other than the current work, no other work was found for the crossflow configuration.

A schematic of the physical model is shown in Fig. 1. This analytical study considers a vertical plate of height H and width L onto which aqueous TEG solution is introduced uniformly at the top and across which air flows horizontally through a clear passage of gap $2S_h$ between plates. This neglects the refrigerant coolant tubes present in the experimental tests (Park et al., 1994a). The TEG mass flow rates per unit of fin width, temperature, and concentration are G, $T_{t,i}$, and $C_{t,i}$, respectively. The crossflow air stream has a mass flux M_a, inlet temperature $T_{a,i}$, and inlet humidity ratio ω_i.

The coordinates in the TEG solution flow direction and in the air flow direction are x and z, respectively. The coordinates normal to the wall in the TEG solution film and from the symmetric plane in the air are y_1 and y_2, respectively.

The governing equations describing the heat and mass transfer and the method of solution (numerical) for this two-phase crossflow exchanger are presented by Park et al. (1994a). The outputs of the numerical analysis include three-dimensional temperature and concentration profiles of the TEG solution and air, as well as various heat and mass transfer rates. Comparison of the numerical predictions with experiment showed good agreement, lending credence to the correlation results presented here.

Statistical Analysis of Numerical Results

Numerical solution of the finite difference equations for this coupled heat and mass transfer problem requires extensive computer time. To aid the designer, numerical computations have been performed for both regeneration and dehumidification over a wide range of operating and design variables and these have been used as a basis for developing correlations for performance of these components. Design parameters and operating conditions for either an absorber or regenerator include: fin width, height, and spacing; air and TEG inlet solution flow rates and temperatures; air inlet humidity ratio; TEG solution inlet concentration; and the refrigerant temperature. Numerical results were obtained for regeneration over the ranges of variables shown in Table 1, and for dehumidification over the ranges of variables shown in Table 2. In general these results were obtained using a nominal condition for each process and then the individual parameters were varied while the others were kept at their nominal values. In a few cases two or more variables were changed simultaneously. Multivariable linear regression analysis software (Barnes, 1988) was used to find correlations for regeneration and dehumidification performances as functions of their respective design and operating variables.

Regeneration. Some of the results for regeneration are presented in a separate publication (Park et al., 1995), but the results herein are more extensive. The primary measure of re-

Contributed by the Heat Transfer Division and presented at the International Solar Energy Conference, Maui, Hawaii, March 1995. Manuscript received by the Heat Transfer Division November 22, 1995; revision received May 10, 1996. Keywords: Heat Exchangers, Mass Transfer, Refrigeration. Associate Technical Editor: K. Vafai.

Copyright © 1996 by ASME

Downloaded 11 Dec 2010 to 193.140.21.150. Redistribution subject to ASME license or copyright; see http://www.asme.org/terms/Terms_Use.cfm

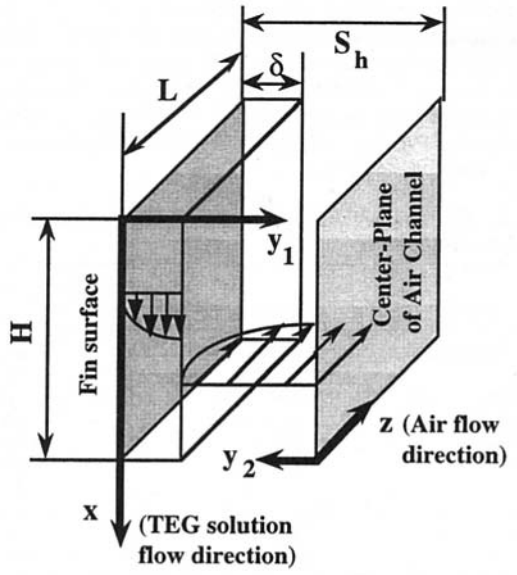


Fig. 1 Schematic for numerical simulation

generator performance is the ability to drive refrigerant from the solution, and the correlation obtained for the rate of regeneration is:

$$m_R = 0.46(e^{-0.52\overline{C_{t,i}}^{1.5}})(\overline{T_{t,i}}^{3.3})(\overline{\Gamma}^{0.083})(e^{-0.66\overline{\omega}_i^{4.4}})(\overline{T_{a,i}}^{1.3}) \times (e^{-0.55\overline{M}_a^{-0.7}})(\bar{H}^{0.98})(e^{-0.42\bar{L}^{-0.76}})(e^{-0.36\overline{S}_h^{-1.6}})(\overline{T}_r^{1.85}) \quad (1)$$

where m_R is the regeneration rate in kilograms water per hour for one surface of the plate. The forms of individual terms in the correlation were chosen to provide good fits to the observed trends in the numerical results. Each independent variable in this equation is normalized as follows:

$$\overline{C_{t,i}} = \frac{C_{t,i}}{0.78}, \quad \overline{T_{t,i}} = \frac{T_{t,i}}{37}, \quad \overline{\Gamma} = \frac{\Gamma}{0.007},$$

$$\overline{\omega_i} = \frac{\omega_i}{20}, \quad \overline{T_{a,i}} = \frac{T_{a,i}}{32}, \quad \overline{M_a} = \frac{M_a}{2.0},$$

$$\bar{H} = \frac{H}{50}, \quad \bar{L} = \frac{L}{20}, \quad \overline{S_h} = \frac{S_h}{0.2}, \quad \overline{T_r} = \frac{T_r}{44}$$

The normalizing value for each variable is typical of that variable and falls in the range examined. The normalizing values used and the range of variables treated are shown in Table 1 and have the dimensions listed in the nomenclature. Note that the normalizing values used in Eq. (1) are not the same as the nominal values around which parametric variations were made. The accuracy of Eq. (1) in representing the 148 numerical data sets is given by: multiple correlation coefficient squared (R^2) = 0.97, and standard deviation of error = 7.35×10^{-2}.

Table 1 Ranges, normalizing values, and nominal values for regeneration

Variable	Range	Normalizing Value	Nominal Value
$C_{t,i}$ (kg TEG/kg sol'n)	0.72 ~ 0.84	0.78	0.78
$T_{t,i}$ (°C)	27~ 40	37	37.3
Γ(kg TEG sol'n/m-s)	0.0012 ~ 0.015	0.007	0.0074
ω_i (g vap./kg dry air)	12 ~ 25	20	18.2
$T_{a,i}$ (°C)	29 ~ 37	32	32.2
M_a (kg/m^2 s)	0.9 ~ 3.0	2.0	1.09
T_r (°C)	40 ~ 50	44	44.4
S_h (cm)	0.13 ~ 0.28	0.2	0.184
H (cm)	19 ~ 115	50	38.2
L (cm)	5.5 ~ 44	20	11.1

Dehumidification. Some of the results for dehumidification were presented in an earlier publication (Park et al., 1994b), but the results herein are more extensive. Among the important performance measures of the dehumidifier (absorber) are the dehumidification rate and outlet air humidity and temperature. The correlation obtained for the rate of dehumidification in the absorber is:

$$m_D = 6.814(\overline{C_{t,i}}^{1.80})(e^{-0.50\overline{T_{t,i}}})(\overline{\Gamma}^{0.053})(e^{-1.89/\overline{\omega_i}}) \times (e^{-0.353\overline{T_{a,i}}})(e^{-1.24\overline{M}_a^{-0.435}})(\bar{H}^{1.04})(e^{-0.259/\bar{L}}) \times [e^{-1.818(0.18/\overline{S_h}-0.132)^{1.423}}](e^{-0.361\overline{T}_r^{1.05}}) \quad (2)$$

where m_D is the dehumidification rate in kilograms per hour on one surface. Equation (2) exhibits the following accuracy in correlating the data set: R^2 = 0.98, and standard deviation = 9.46×10^{-2}.

The correlation for the sensible cooling of the air in the absorber is:

$$Q_s = 26.36(\overline{C_{t,i}}^{0.25})(e^{-0.56\overline{T_{t,i}}})(e^{-0.02\Gamma})(\overline{\omega_i}^{0.02})(e^{2.28\overline{T_{a,i}}}) \times (e^{-0.98\overline{M}_a^{0.4}})(\bar{H}^{1.02})(e^{-0.21\bar{L}})(e^{-0.4\overline{S}_h^{1.42}})(e^{-0.65\overline{T}_r}) \quad (3)$$

Nomenclature

C = mass concentration of TEG in aqueous solution, kg TEG/kg solution
$\bar{C}$ = normalized mass concentration of TEG in aqueous solution
Eff_D = dehumidification efficiency (see Eq. (8))
Eff_R = regeneration efficiency (see Eq. (6))
H = plate height, cm
$\bar{H}$ = normalized plate height
L = plate width, cm
$\bar{L}$ = normalized plate width
m = mass flow rate, kg/h
M = mass flux, kg/(m^2-s)
$\bar{M}$ = normalized mass flux
Q = heat transfer rate, W
S_h = one half the plate spacing, cm
$\bar{S}$ = normalized plate spacing
SHR = ratio of sensible to total heat transfer
T = temperature, °C
$\bar{T}$ = normalized temperature
x = coordinate in direction of solution flow, cm
y_1 = coordinate from wall into liquid film, cm
y_2 = coordinate from air midplane toward interface, cm
z = coordinate in direction of air flow, cm
δ = liquid film thickness, cm
Γ = solution flow rate per unit width, kg solution/(m-s)
$\bar{\Gamma}$ = normalized solution flow rate per unit width
ω = humidity ratio, kg water vapor/kg dry air
$\bar{\omega}$ = normalized humidity ratio

Subscripts

a = air
comp = computed value
D = dehumidification
i = inlet
l = latent
o = outlet
r = refrigerant
R = regeneration
regr = regression value
s = sensible
t = TEG solution

Downloaded 11 Dec 2010 to 193.140.21.150. Redistribution subject to ASME license or copyright; see http://www.asme.org/terms/Terms_Use.cfm

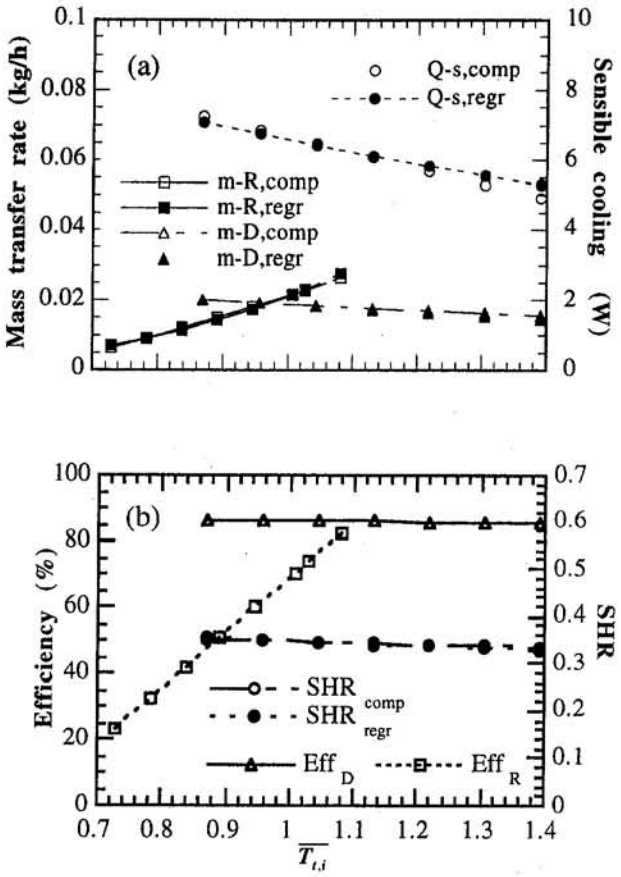


Fig. 2 Effect of TEG inlet temperature on: (*a*) the mass transfer rates and sensible cooling, and (*b*) the efficiencies and sensible heat ratio

where Q_s represents the sensible cooling in Watts based on one surface of the plate. Equation (3) has the following statistical accuracy: $R^2 = 0.99$, and standard deviation = 5.18×10^{-2}.

The correlation for the sensible to total heat ratio is:

$$\text{SHR} = \frac{Q_s}{Q_s + Q_l} = 0.0518(\overline{C_{t,i}}^{-1.32})(e^{-0.16\overline{T_{t,i}}})(\overline{\omega_i}^{1.34})(e^{2.02\overline{T_{a,i}}}) \times (e^{0.12\overline{M_a}^{0.4}})(\overline{H}^{0.02})(e^{-0.01\overline{L}})(e^{-0.22\overline{T_r}}) \quad (4)$$

The SHR is a measure of how well the absorber provides sensible cooling relative to total cooling. The numerical results indicated that the TEG flow rate and the plate spacing resulted in essentially no effect on the sensible heat ratio, so these two parameters do not appear in the correlation. Equation (4) has the following statistical accuracy: $R^2 = 0.98$, and standard deviation = 2.87×10^{-2}.

The ten independent variables examined for dehumidification are normalized as follows:

$$\overline{C_{t,i}} = \frac{C_{t,i}}{0.8}, \quad \overline{T_{t,i}} = \frac{T_{t,i}}{23}, \quad \overline{\Gamma} = \frac{\Gamma}{0.007},$$

$$\overline{\omega_i} = \frac{\omega_i}{20}, \quad \overline{T_{a,i}} = \frac{T_{a,i}}{32}, \quad \overline{M_a} = \frac{M_a}{2.0},$$

$$\overline{H} = \frac{H}{50}, \quad \overline{L} = \frac{L}{20}, \quad \overline{S_h} = \frac{S_h}{0.2}, \quad \overline{T_r} = \frac{T_r}{13}$$

The numerical value normalizing each variable is typical of that variable and has the dimensions listed in the nomenclature. These correlations were obtained for the ranges of design and operational variables given in Table 2.

Again, the normalizing values used in Eqs. (2), (3), and (4) are not the same as the nominal values used as the basis for the parametric study that is presented in the following section. For example, the normalizing value for air mass flux, M_a, used in the dehumidification correlations is 2.0 kg/m^2-s, while the nominal value for this variable as used in the parametric study that follows is 0.918 kg/m^2-s.

Table 2 Ranges, normalizing values, and nominal values for dehumidification

Variable	Range	Normalizing value	Nominal value
$C_{t,i}$ (kg TEG/kg sol'n)	0.74~0.86	0.8	0.8
$T_{t,i}$ (°C)	20~32	23	24
Γ (kg TEG sol'n/m-s)	0.0012~0.015	0.007	0.0025
ω_i (g vap./kg dry air)	12~25	20	18.2
$T_{a,i}$ (°C)	29~37	32	32.2
M_a (kg/m^2 s)	0.9~3.0	2.0	0.918
T_r (°C)	7~17	13	13.8
S_h (cm)	0.13~0.28	0.2	0.184
H (cm)	19~115	50	38.2
L (cm)	5.5~44	20	11.1

Parametric Performance Analyses of Regeneration and Dehumidification

Some graphic (parametric) results are presented and discussed below to show the influences of the several design and operating variables on regenerator and dehumidifier performances. The variables considered are those included in the regression analyses discussed above.

Regeneration. Two regeneration performance measures are discussed below: the regeneration rate and the regeneration efficiency. Regeneration rate (amount of water evaporated from the solution into the air) is calculated as:

$$m_R = m_a(\omega_o - \omega_i) \quad (5)$$

Regeneration efficiency is defined as the ratio of the latent heat transfer to the supplied wall heat transfer.

$$\text{Eff}_R = \frac{Q_{\text{latent}}}{Q_{\text{wall}}} \quad (6)$$

In the following discussion the regeneration and dehumidification results are discussed separately, even though the results for both are on the several figures. Also, the influences of some variables are interrelated, and they are discussed together. For example, the effects of TEG concentration, refrigerant temperature, and air inlet humidity are interdependent and discussed together. The regression results for some of the parameters are compared to the numerical predictions. In general the agreement between regression and computational predictions is seen to be quite good, and comparisons are only noted where there is a significant discrepancy.

Effect of TEG Solution Flow Rate. The effect of TEG flow rate on regeneration performance is found to be weak, and is not shown. Solution flow rate must be kept at a level sufficient to insure wetting of the exchanger surfaces, but high solution flow rates should be avoided to reduce parasitic pumping power. In general, the solution flow rate should be just sufficient to insure wetting. Wetting is not a very predictable phenomenon, and the flow rate necessary to insure wetting must be determined experimentally. In the numerical modeling reported here, the transfer surface is assumed to be fully wetted by the TEG solution film.

Effect of TEG Inlet Temperature. Figure 2 shows the effect of TEG inlet temperature on regeneration performance. For regeneration to take place, the TEG temperature must be raised

Downloaded 11 Dec 2010 to 193.140.21.150. Redistribution subject to ASME license or copyright; see http://www.asme.org/terms/Terms_Use.cfm

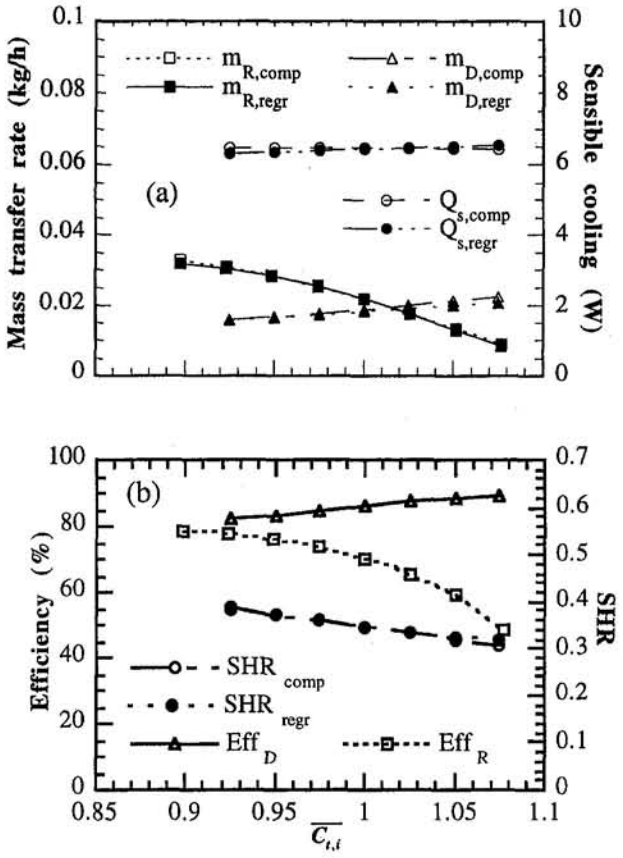


Fig. 3 Effect of inlet TEG concentration on: (*a*) the mass transfer rates and sensible cooling, and (*b*) the efficiencies and sensible heat ratio

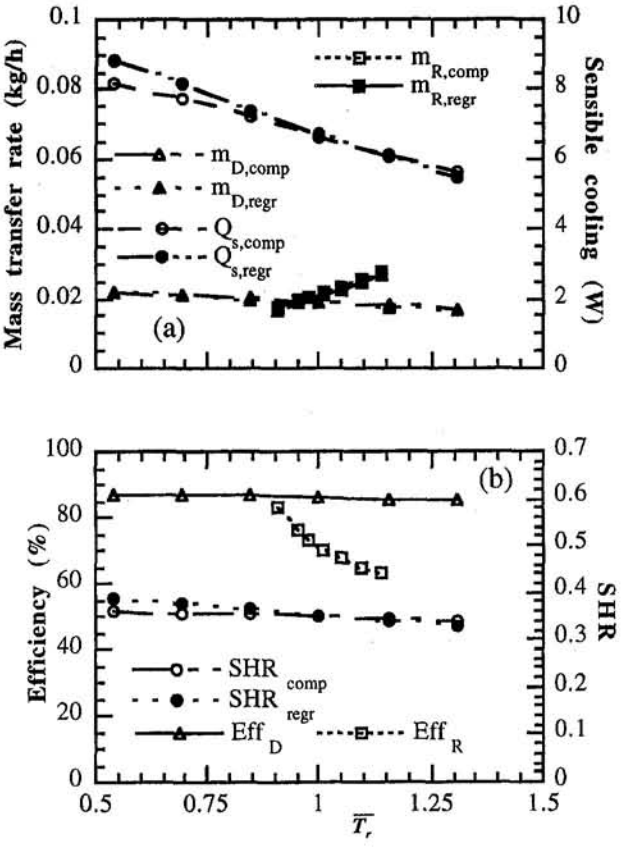


Fig. 4 Effect of refrigerant temperature on: (*a*) the mass transfer rates and sensible cooling, and (*b*) the efficiencies and sensible heat ratio

to a point where the water vapor pressure of the TEG solution exceeds the vapor partial pressure in the air.

The regeneration rate in Fig. 2(*a*) is seen to accelerate with TEG solution inlet temperature, the reason being that the solution vapor pressure increases nonlinearly with temperature. The regeneration efficiency (Fig. 2(*b*)) is also seen to increase strongly with TEG inlet temperature. At low TEG inlet temperatures, a significant portion of the input heat is used for sensible heating of the TEG solution, resulting in lower regeneration efficiency. It would appear from Fig. 2(*b*) that the efficiency may exceed 1.0 near a dimensionless inlet temperature of about 1.2. If the inlet temperature exceeds the equilibrium solution temperature for the given inlet TEG concentration and air inlet humidity, regeneration will occur without any heating from the refrigerant. This would result in the efficiency exceeding 1.0, considering how efficiency is defined here.

Thus, preheating of the solution is desirable. There is such preheat capability, since the fluid leaving the regenerator is normally warmer than the solution entering the regenerator from the absorber. Therefore, a solution heat exchanger between the regenerator and absorber can be used to increase the TEG solution temperature entering the regenerator. There is a secondary benefit to this, in that the solution entering the absorber (dehumidifier) will be cooler, thus improving the performance of the dehumidifier.

Effects of TEG Inlet Concentration, Refrigerant Temperature, and Inlet Air Humidity. The effects of these three parameters are strongly interrelated. The effects on regeneration rate and efficiency of TEG inlet concentration, refrigerant temperature and inlet air humidity are shown in Figs. 3, 4, and 5, respectively.

One would expect that decreasing solution concentration (higher fraction of water), increasing refrigerant temperature,

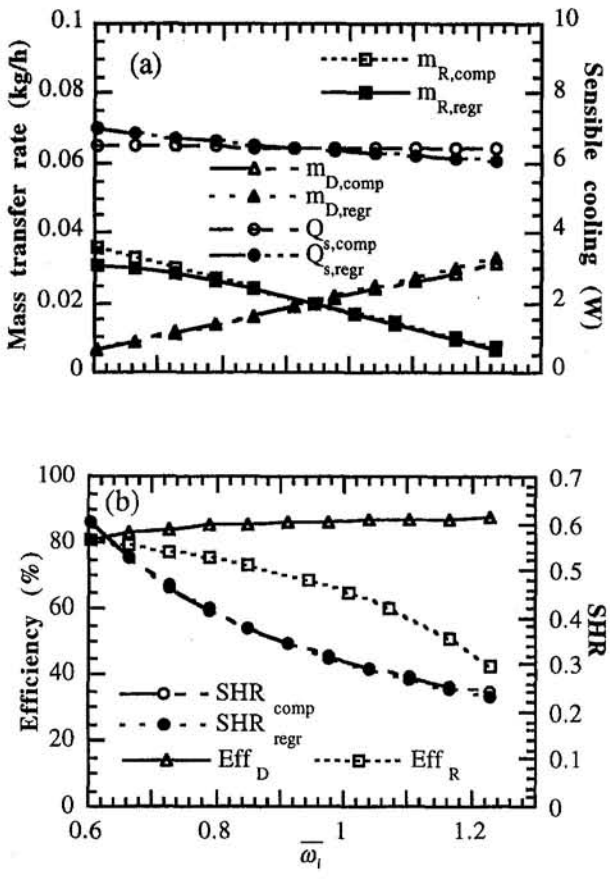


Fig. 5 Effect of air inlet humidity ratio on: (*a*) the mass transfer rates and sensible cooling, and (*b*) the efficiencies and sensible heat ratio

Downloaded 11 Dec 2010 to 193.140.21.150. Redistribution subject to ASME license or copyright; see http://www.asme.org/terms/Terms_Use.cfm

and decreasing air inlet humidity ratio would each result in increasing regeneration rate, and Figs. 3(*a*), 4(*a*), and 5(*a*) show this to be the case. On the other hand, while inlet TEG concentration and inlet air humidity ratio exhibit the same trends with respect to regeneration efficiency as they do for regeneration rate, the effects of refrigerant temperature on these two regeneration performance parameters are reversed. Even though the amount of water evaporated increases with increasing refrigerant temperature, the regeneration efficiency decreases as shown in Fig. 4(*b*), because the supplied regeneration energy is increasingly used in sensible heating of the solution.

The regression correlation results are seen to agree well with the numerical results, except that at low inlet air humidity the regeneration rate shows about a 10 percent difference, as seen in Fig. 5(*a*).

Effect of Air Inlet Temperature and Air Flow Rate. Increases in air inlet temperature or flow rate result in increased regeneration rate, as seen in Figs. 6(*a*) and 7(*a*). While the effect of air temperature is fairly linear, the trend with air flow rate is asymptotic.

The effects of these two parameters on regeneration efficiency are modest (Figs. 6(*b*) and 7(*b*)), with the effect of air flow rate being minimal (asymptotic) above a normalized air flow rate of about 1.0. Since the parasitic power for liquid desiccant systems results largely from the requirements for air circulation, it would be advisable to keep air flow rate as low as feasible, since its effect on regeneration performance is generally small. Since increased air temperature results in a modest increase in performance, an air preheater between the entering and exhausting hot air streams would improve the regenerator performance, provided the additional parasitic power was small.

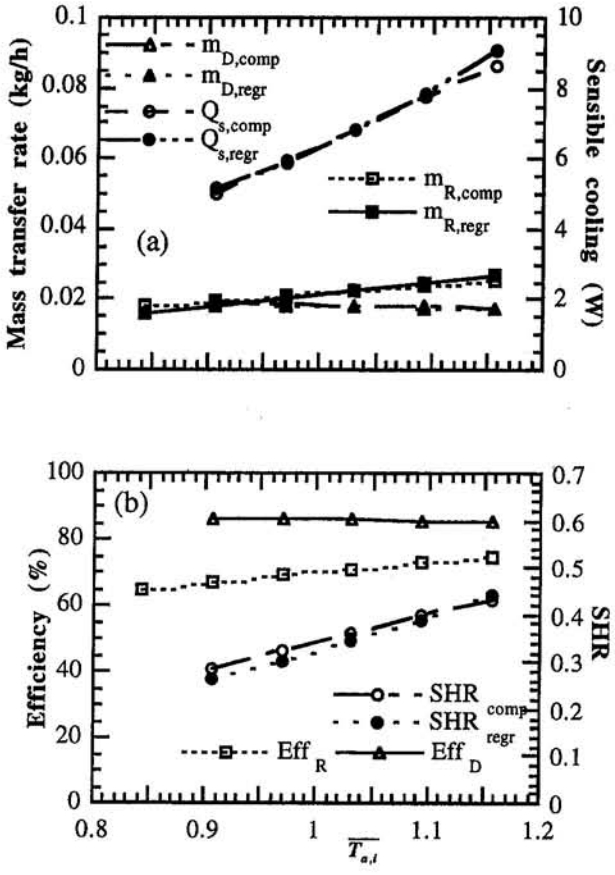


Fig. 6 Effect of air inlet temperature on: (*a*) the mass transfer rates and sensible cooling, and (*b*) the efficiencies and sensible heat ratio

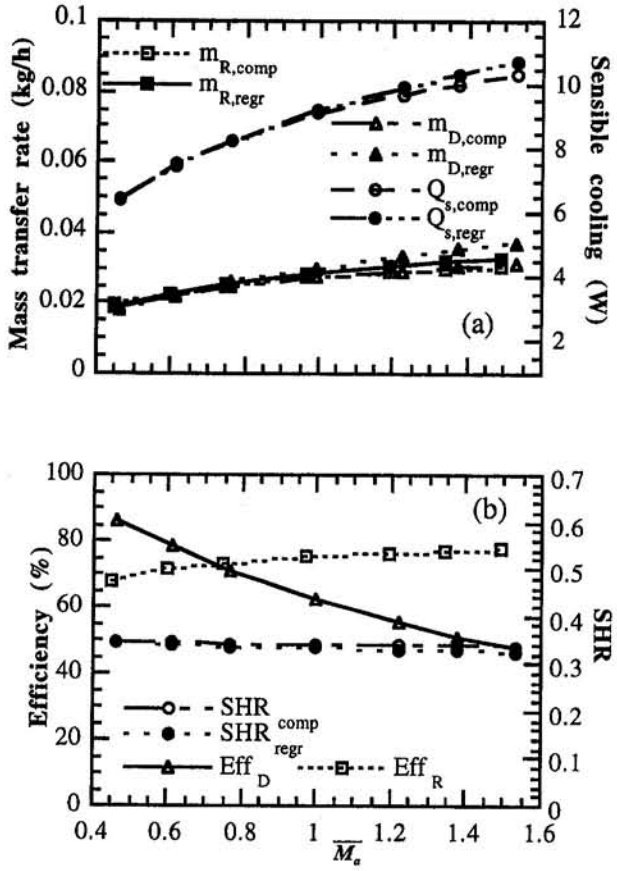


Fig. 7 Effect of air mass flux on: (*a*) the mass transfer rates and sensible cooling, and (*b*) the efficiencies and sensible heat ratio

Effect of Exchanger Geometry: Plate Spacing, Height, and Width. In the sensitivity results presented for geometry effects, it is assumed that air "mass flux" is constant as either plate spacing, $2S_h$, or plate height, H, is varied, and that the solution flow rate per unit of plate width is constant as plate width, L, is varied. Thus, total air mass flow rate varies linearly with either plate spacing or plate height. Also, as plate width is increased the total solution flow rate is increased linearly. Therefore, in assessing the effects of these three geometry variables, one should be aware of these secondary influences of the variations in total air flow rate or total solution flow rate. Also, increasing each of these three geometry variables results in increased exchanger volume.

Figure 8 shows the effect of plate spacing on the regeneration performance. The regeneration rate exhibits a fairly substantial increase with plate spacing (about 60 percent for the approximate twofold increase in spacing), but there was little increase beyond a normalized plate spacing of 1.0. Since total air flow also increases with plate spacing, the exit humidity is lower, resulting in an increased driving potential for regeneration. The regeneration efficiency exhibits a very slight decrease with plate spacing. Again, recall that air flow rate increases linearly with plate spacing, because of the way this sensitivity analysis was conducted, so the cost of parasitic power must be carefully considered in arriving at an optimal design. The range of plate spacing was limited to that for which the air flow was laminar.

Figure 9 shows that the regeneration rate is nearly linear with plate height. Plate area is proportional to plate height, and because there is not much change in TEG concentration from inlet to outlet for the range of variables examined, the driving potential for regeneration from inlet to outlet is not markedly changed. The regeneration efficiency exhibits a modest increase initially, but reaches an asymptote near a normalized height of

Downloaded 11 Dec 2010 to 193.140.21.150. Redistribution subject to ASME license or copyright; see http://www.asme.org/terms/Terms_Use.cfm

1.0. Again, it is to be noted that as plate height is increased, the total exchanger area and the total air mass flow rate increase proportionally.

The effects of plate width on regeneration performance are shown in Figs. 10. The regeneration rate is seen in Fig. 10(a) to become asymptotic with increasing plate width beyond a normalized value of about 1.0. The regeneration efficiency shows a fairly linear and modest decrease with plate width. These seemingly contradictory variations are a result of the TEG flow rate per unit width being held constant as plate width is varied. Predicted values by the correlation show good agreement below the nominal value of 1.0, but a large discrepancy (20–25 percent) is evident for large plate width. In particular, Figs. 10(a, b) suggest that an increase of plate width beyond about 10 to 12 cm (normalized value of 1.0) results in little improvement in regenerator performance.

Dehumidification. The dehumidification rate for the absorber (amount of water absorbed from the air into the solution) is calculated from:

$$m_D = m_a(\omega_i - \omega_o) \tag{7}$$

where m_a represents the dry air flow rate and ω_i and ω_o are air inlet and outlet humidity ratios, respectively. For a given set of operating and design conditions, there is a lower limit to which the air can be dehumidified. This limit depends on the entering TEG solution concentration and the refrigerant temperature, and a dehumidification efficiency can be defined as the quotient of the actual change in air humidity ratio to the maximum possible change:

$$\mathrm{Eff}_D = \frac{\omega_i - \omega_o}{\omega_i - \omega_e} \tag{8}$$

where ω_e represents the equilibrium humidity ratio at the inlet

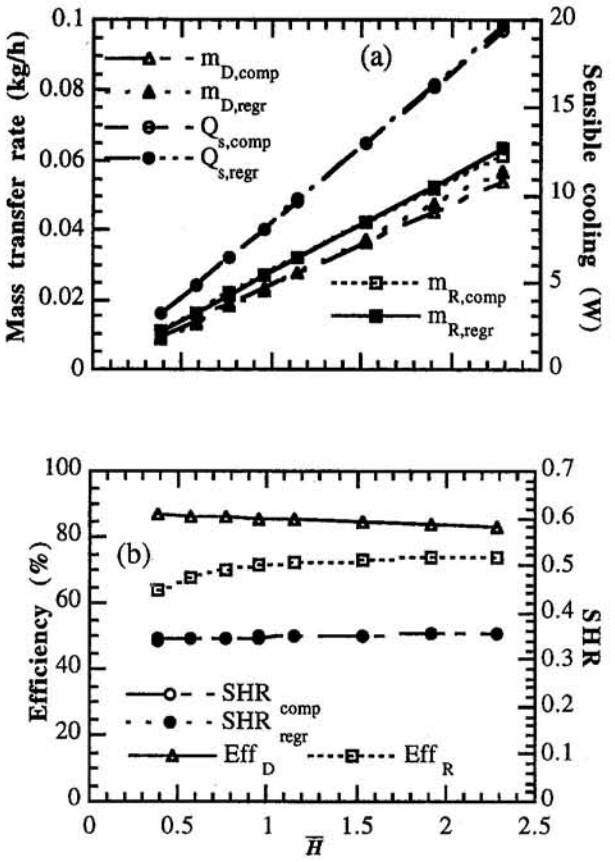


Fig. 9 Effect of plate height on: (a) the mass transfer rates and sensible cooling, and (b) the efficiencies and sensible heat ratio

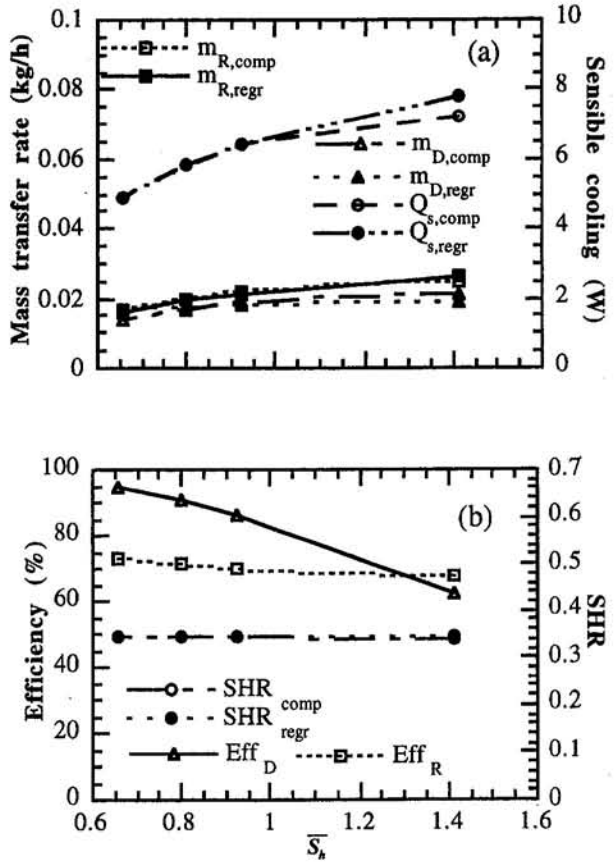


Fig. 8 Effect of plate spacing on: (a) the mass transfer rates and sensible cooling, and (b) the efficiencies and sensible heat ratio

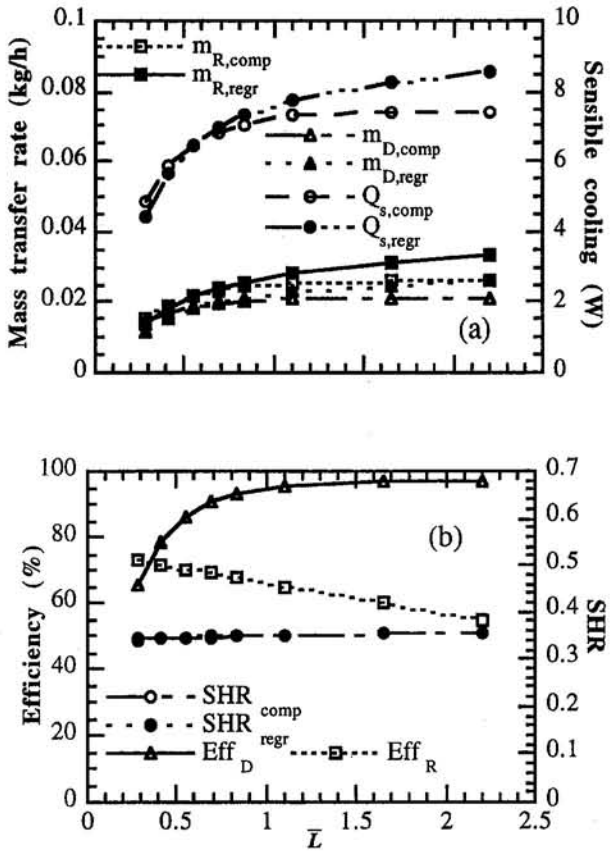


Fig. 10 Effect of plate width on: (a) the mass transfer rates and sensible cooling, and (b) the efficiencies and sensible heat ratio

Downloaded 11 Dec 2010 to 193.140.21.150. Redistribution subject to ASME license or copyright; see http://www.asme.org/terms/Terms_Use.cfm

TEG concentration $C_{t,i}$ and the lowest possible temperature of the TEG solution, which is the refrigerant temperature, T_r. This is the humidity ratio that would be reached if thermodynamic equilibrium could be achieved without change in TEG concentration at the minimum possible TEG solution temperature in the absorber.

In addition to the dehumidification rate and efficiency, the sensible cooling of the air and the sensible to total heat ratio, as defined earlier, are presented and discussed in the following sections.

Except for the one variable being examined, all other variables are maintained at their "nominal" conditions shown in the last column of Table 2. In a few cases, numerical results were obtained for the combined effect of several variables on the dehumidification rate (Park et al., 1994b), but are not shown here.

Effect of TEG Solution Flow Rate. Except for very low flow rates, solution flow rate has very little effect on any of the dehumidification parameters. In the regression correlations (Eqs. (2) and (3)) for two of the dehumidification parameters, the influences of solution flow rate were very small and this variable was omitted entirely from the SHR correlation (Eq. (4)).

Effect of TEG Inlet Temperature. Decreasing TEG inlet temperature results in a modest increase in dehumidification rate, Fig. 2(a). Thermally, the liquid film responds quite quickly, and therefore lowering the solution inlet temperature does not greatly increase the dehumidification rate. The sensible heat transfer (Q_s) also increases by about 25 percent with decreasing inlet TEG temperature. Figure 2(b) shows the dehumidification efficiency to be essentially constant and the sensible heat ratio (SHR) to increase very slightly with decreasing TEG inlet temperature. Since lowering the TEG inlet temperature is beneficial, precooling of the TEG upstream of the absorber is recommended. It was shown earlier that preheating the TEG prior to entry into the regenerator is also desirable, and therefore incorporation of an efficient heat exchanger between these two TEG streams benefits both regenerator and dehumidifier operation.

Effects of TEG Inlet Concentration, Refrigerant Temperature, and Inlet Air Humidity. These three parameters are discussed together since their effects are strongly interrelated, and their effects on the dehumidification performance parameters are shown in Figs. 3, 4 and 5.

One would expect that increasing solution concentration (lower fraction of water), decreasing refrigerant temperature, and increasing air inlet humidity ratio would each result in increasing dehumidification rate, and Figs. 3(a), 4(a), and 5(a) show this to be the case. Figure 3 shows the effect of TEG solution inlet concentration on the other dehumidification performance parameters. The sensible to total heat ratio decreases with TEG concentration, because increased concentration enhances absorption; however, sensible heat transfer is essentially unaffected. The efficiency is quite high overall and increases somewhat with concentration.

The sensible heat transfer drops markedly with increasing refrigerant temperature, but dehumidification efficiency and sensible to total heat ratio are essentially unaffected (Fig. 4).

In Fig. 5 the effect of increasing inlet air humidity ratio is to decrease sensible heat transfer slightly and increase efficiency slightly, but there is a major reduction in the sensible heat ratio. The reason for the latter is that latent transfer (absorption) increases strongly with increasing air humidity.

The regression correlation results show good agreement in terms of varying TEG concentration, but for varying refrigerant temperature or inlet air humidity, deviations from the numerical results are apparent for values significantly displaced from the nominal conditions.

Effect of Air Inlet Temperature. The air inlet temperature has very little influence on dehumidification rate or on dehumidification efficiency, as seen from Figs. 6(a, b), respectively. The sensible heat transfer does increase with air inlet temperature (linearly), as would be expected, and as a result the sensible heat ratio is also almost a linearly increasing function.

Effect of Air Flow Rate. The effect of increasing air mass flow rate (Fig. 7) is to increase the dehumidification rate, but not linearly. The outlet air humidity is thus increased, as indicated by the strong falloff in dehumidification efficiency seen in Fig. 7(b). The sensible to total heat ratio is seen to be almost constant, but the sensible heat transfer increases (not quite linearly). Thus, both outlet air temperature and absolute humidity increase with increasing air flow.

The regression analysis results generally show good agreement, but exhibit increasing deviation over the upper half of the air mass flux range.

Effect of Geometry: Plate Spacing, Height, and Width. As noted above in discussing the regeneration results, as plate spacing and height vary, the air mass flow varies proportionally and in varying plate width the solution flow rate varies proportionally. For changes in geometry the air mass flux and the solution flow per unit width were maintained constant, causing this behavior. The range of plate spacing is limited to values that maintain laminar air flow. The effects of spacing, height and width are shown in Figs. 8, 9, and 10, respectively.

As spacing increases, the dehumidification rate increases (less than linearly) and efficiency decreases, so outlet air humidity increases. The sensible cooling rate almost mirrors the dehumidification rate, so the sensible heat ratio is nearly constant. This is also similar to the air mass flux effect on absorber performance, as shown in Fig. 7(b). Thus, larger plate spacing adversely affects the air outlet conditions if air mass flux is held constant. As spacing increases, the total exchanger size must be increased to maintain the same contact area, and a correspondingly greater air flow is needed.

The effect of increasing plate height is to almost linearly increase the dehumidification rate and the sensible heat transfer (Fig. 9(a)), resulting in the sensible heat ratio being almost constant (Fig. 9(b)). Dehumidification efficiency falls off very little. Thus, increasing plate height has little effect on air outlet conditions.

The effects of plate width (in air flow direction) on dehumidification performance are shown in Figs. 10. As the plate width increases, the air contacts the TEG solution for a longer period of time, and as a result the dehumidification rate, sensible cooling, and efficiency all increase. The sensible heat ratio remains nearly constant. It appears that the nominal plate width used is nearly optimum for the other nominal conditions considered. Thus, the dehumidifier performance improves with increasing plate width, but an asymptote is approached near the normalized width of about 1.0 (L = 20–30 cm). In a system design the plate width will likely be short of the 20–30 cm for a number of reasons: to limit solution flow, reduce air pressure drop, and have a smaller system overall.

The regression results generally show good agreement, but the dehumidification rate and sensible cooling results deviate at large plate height. The correlation generally predicts well in terms of varying plate height. For varying plate width the correlations exhibit significant deviations in dehumidification rate and sensible cooling when the width deviates from the nominal, particularly for large width.

Summary

The effects of several design and operational variables on the performance of crossflow falling film absorbers and regenerators have been investigated. Based on numerical modeling results and a sensitivity analysis about a nominal set of conditions, correlations are presented for the effects of several of the inde-

Downloaded 11 Dec 2010 to 193.140.21.150. Redistribution subject to ASME license or copyright; see http://www.asme.org/terms/Terms_Use.cfm

pendent variables on dehumidification rate, sensible cooling and the sensible heat ratio when in the dehumidification mode, and on regeneration rate for operation in the regeneration mode. Predicted values by these correlations are generally in good agreement with the numerical results, and should be useful for design purposes.

Results are also presented graphically to provide insight into the influences of the several parameters on exchanger performance when operated in either mode.

Acknowledgments

The authors wish to acknowledge support for this work from the State of Texas Higher Education Coordinating Board under the Energy Research Applications Program Grant ERAP #086.

References

Barnes, W. J., 1988, *Statistical Analysis for Engineers—A Computer-Based Approach,* Prentice Hall, Englewood Cliffs, NJ.

Ertas, A., Gandhidasan, P., Kiris, I., and Anderson, E. E., 1994, "Experimental Study on the Performance of a Regeneration Tower for Various Climatic Conditions," *Solar Energy,* Vol. 53, No. 1, pp. 125–130.

Park, M. S., Howell, J. R., Vliet, G. C., and Peterson, J. L., 1994a, "Numerical and Experimental Results for Coupled Heat and Mass Transfer Between a Desiccant Film and Air in Cross-Flow," *Int. J. Heat Mass Transfer,* Vol. 37, Suppl., pp. 395–402.

Park, M. S., Howell, J. R., and Vliet, G. C., 1994b, "Correlation of Dehumidification by a Falling Film Desiccant With Air in Cross Flow," presented at the ASME Winter Annual Meeting, Chicago, Nov.

Park, M. S., Howell, J. R., and Vliet, G. C., 1995, "Correlation of Regeneration of a Falling Desiccant Film by Air in Cross Flow," ASME/JSME International Solar Energy Conference, Maui, HI, Mar.

Peterson, J. L., and Howell, J. R., 1990, "Hybrid Vapor-Compression/Liquid Desiccant Air Conditioner," U.S. Patent No. 4,941,324.

Downloaded 11 Dec 2010 to 193.140.21.150. Redistribution subject to ASME license or copyright; see http://www.asme.org/terms/Terms_Use.cfm

B. T. F. Chung
F. Theodore Harrington Professor and Chair.
Fellow ASME

B. X. Zhang[1]
Postdoctoral Fellow.

Department of Mechanical Engineering,
The University of Akron,
Akron, OH 44325-3903

E. T. Lee
President,
L and P Culture and Technology, Inc.,
5345 Toscana Way, Suite 517,
San Diego, CA 92122

A Multi-objective Optimization of Radiative Fin Array Systems in a Fuzzy Environment

This study analyzes and optimizes a new design for a four-fin radiating fin array system in a multi-objective fuzzy optimization environment. The conflicting objectives of minimizing both weight and horizontal size are considered simultaneously in the fuzzy optimization logic. A fuzzy feasible domain is constructed by considering all of the fuzzy sets individually defined by the fuzzy objectives and constraints. The system is optimized by maximizing the fuzzy decision function. A systematic procedure of the fuzzy optimization is discussed in detail.

1 Introduction

Radiating fin arrays play an important role in the thermal control of space vehicles and space stations. The weight and the size of a fin array are major design considerations. Conventionally, the radiating fin array has the structure as shown in Fig. 1(*a*), which is referred to as a "two-fin system" (only two fins extended from each pipe). To avoid radiative interaction, the fins are arranged in such a manner that the fins cannot "see" one another. The height and thickness of the fins can be optimized so that a minimum mass is required to dissipate a given amount of heat. A new "four-fin system" (four fins extended from each pipe in a multipipe system) was proposed by Chung and Zhang (1993a), which reveals that despite radiative interaction, the four-fin system requires less mass or weight while dissipating the same amount of heat.

An equally important design consideration is that, if more material than the minimum mass is allowed to be used in the fin array system, it is highly desirable to minimize the horizontal dimension, thereby reducing the total horizontal space occupied by the fin array system. Recently, Chung and Zhang (1993b) have demonstrated that the above-described four-fin system can be considerably shorter in the horizontal dimension than a two-fin system in the horizontal dimension. This type of minimization is impossible for the two-fin system because fewer design parameters can be manipulated. In four-fin systems additional variables are available, which allows the horizontal area of the whole array to be minimized for a given heat dissipation and total fin mass. The advantage of the proposed four-fin system is that it can be either lighter or smaller (with less total horizontal area) than the conventional two-fin system while transferring the same amount of heat.

A critical question is "how to design a fin array that is not only light but also short in horizontal dimension and still able to dissipate a given amount of heat." The two goals (light and short) mentioned above are conflicting, because the minimum mass design always yields a fairly long horizontal fin height, as reflected from many previous investigations, e.g., Wilkins (1960), Schnurr et al. (1976), and Chung and Zhang (1993a). To achieve a shorter horizontal fin height, one has to pay the penalty of using more fin mass (Chung and Zhang, 1993b). In other words, no unique solution exists that would accomplish the optimization for both of the two individual objective functions. In many cases, only linguistic statements are used to describe the goals. For example, the aforementioned problem may be stated as: The fin array is preferred to be designed reasonably short horizontally and also fairly light in weight. It is extremely difficult to solve the aforementioned problem using a conventional mathematical approach because of the lack of a precise definition of the objective functions. Note that the terms "fairly light" and "reasonably short" are fuzzily defined. Furthermore, the fuzzy information is often contained in the constraints in the real cases, instead of the "hard" or "crisp" constraint boundaries. For example, consider a system required to dissipate 1000 W of energy. If the amount of heat dissipated is 999 W, the system will be rejected; on the other hand, a system dissipating 1001 W would be acceptable. In practice, there is not much difference between the two values 999 W and 1001 W since many other inherent variations are always expected, e.g., heat transfer coefficient, conductivity, etc. In the real world, more likely the requirement may be fuzzily expressed as: "the heat transfer should be about 1000 W or more." Indeed, the closer one looks at a real world problem, the fuzzier its descriptions become. The management of uncertainty becomes an intrinsic issue in the design of a fin array system, because much of the available information may be imprecise or not completely reliable. A preliminary study by Zhang and Chung (1994) has demonstrated the usefulness of fuzzy sets theory in the solution of optimization of a simple convective fin.

The fuzzy sets theory was first proposed by Zadeh (1965) as a mathematical theory of vagueness. Since then the research on fuzzy sets has increased steadily and the theory has been applied to different practical systems. Kandel and Lee (1979) described the theory and applications of fuzzy switching and automata. Using the fuzzy sets concept, Lee (1980) dealt with image problems and Schmucker (1984) applied the theory to risk analysis. Bellman and Zadeh (1970) proposed an approach by which the multi-objective functions and constraints are represented by a "max-min" formulation. Rao (1987) successfully applied the "max-min" fuzzy optimization to a structure problem. Sakawa (1993) systematically presented the theories of the fuzzy multi-objective optimization.

The purpose of this work is to optimize a four-fin radiating fin array system using a fuzzy approach, in which both total weight and horizontal dimension of the fin system are minimized as much as possible. Note that the objective functions,

[1] Current address: Senior Engineer, Lintern Corporation, Mentor, OH.

Contributed by the Heat Transfer Division for publication in the JOURNAL OF HEAT TRANSFER. Manuscript received by the Heat Transfer Division October 9, 1995; revision received April 22, 1996. Keywords: Finned Surfaces, Numerical Methods, Radiation Interactions. Associate Technical Editor: S. H. Chan.

Copyright © 1996 by ASME

Downloaded 11 Dec 2010 to 193.140.21.150. Redistribution subject to ASME license or copyright; see http://www.asme.org/terms/Terms_Use.cfm

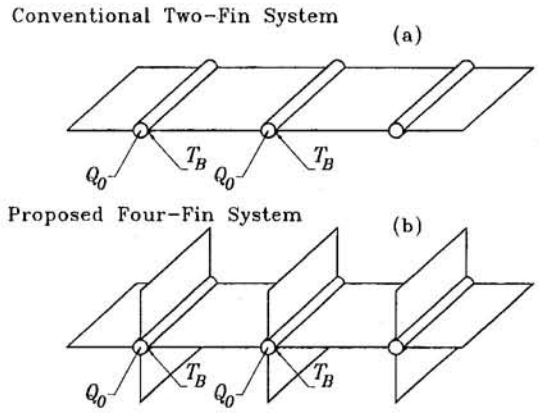


Fig. 1 Sketch of radiating fin arrays of two-fin system (*a*) and four-fin system (*b*)

i.e., the minimization of the profile area of the fin and the minimization of fin horizontal height, are two conflicting goals from the heat transfer point of view. The fuzzy formulation is therefore employed in order to achieve an optimal compromise between these two objectives so that the final design of the fin array system is both fairly light and reasonably short. In the present study, the horizontal fins are restricted to rectangular profile. As pointed out earlier (Chung and Zhang, 1993a, b), for the vertical fins, the triangular profile is the best in the family of trapezoidal fins for both material saving and horizontal dimension reduction. On the other hand, the rectangular vertical fin is preferred from the manufacturability point of view. Therefore, both triangular and rectangular vertical fins will be considered in this work. It should be pointed out that the present optimal design is purely from the heat transfer point of view. Other considerations such as stress analysis and choice of material are not included.

2 Fuzzy Optimum Formulation

In this section the multi-objective fuzzy optimization approach will be briefly described first. Then the detailed fuzzy optimization of the radiating fin array systems will be presented.

2.1 Multi-objective Fuzzy Optimization Approach. In fuzzy multi-objective optimization problems, objectives and constraints are specified by first using various membership functions, μ's (Lee and Zadeh, 1969; Bellman and Zadeh, 1970). μ represents the degree of satisfaction by a value between zero and unity. A value of one indicates a complete satisfaction, and zero stands for an entire rejection. A fuzzy decision function is constructed through the use of the defined membership functions. An optimum vector is determined so that the decision function is maximized using that vector. Mathematically, a fuzzy decision function with k objectives and m constraints is defined as (Sakawa, 1993)

$$\mu_D(X) = \min_{i,j} \{\mu_{f_i}(X), \mu_{g_j}(X)\} \quad \begin{matrix} i = 1, 2, \ldots, k \\ j = 1, 2, \ldots, m \end{matrix} \tag{1}$$

where the vector X is the design vector in an n-dimensional space. μ_{f_i} and μ_{g_j} are the membership functions for the ith objective f_i and jth constraint g_j, respectively. In addition, the overall membership function, μ_D, specifies a fuzzy design domain, D, in which $\mu_D(X) > 0$ for all X. More specifically, this means that a solution may be found for every vector X in domain D. According to the fuzzy optimization theory, the optimum vector, X^*, is obtained if $\mu_D(X^*)$ is the maximum, or

$$\begin{aligned} \mu_D(X^*) &= \max \{\mu_D(X)\} \\ &= \max \{\min_{i,j} \{\mu_{f_i}(X), \mu_{g_j}(X)\}\} \end{aligned} \tag{2}$$

Expression (2) is referred to as the optimum decision function. This concept was illustrated by Zhang and Chung (1994) in a simple convective fin optimization problem.

2.2 Determination of Membership Function. The determination of membership functions μ_{f_i} and μ_{g_j} is based on the designer's physical insights into the problem. One has to determine the target values, beyond which (or at which) the goals would be considered completely satisfied, and the least acceptable values, beyond which the design would be considered completely rejected. Rao (1987) presented a method to determine the target values and least acceptable values for the objective membership functions. Basically, this method first optimizes the problem with respect to each single-objective goal. Then, the best and the worst solutions possible for each of the objective functions are determined. These solutions are used as the target and the least acceptable values, both of which are necessary for the construction of the objective membership functions. Symbolically, the target values and the least acceptable values can be expressed in term of the matrix $[P]$,

Nomenclature

A_T = total profile area of fin array, m^2
$\bar{A}_T = A_T/(k/\sigma T_B^3)^2$ = dimensionless A_T
b = height of fin, m
$\bar{b} = b/(k/\sigma T_B^3)$ = dimensionless b
dF_{1-2} = view factor from dx_1 to dx_2
D = fuzzy decision domain
f_i = objective function
g_j = constraint function
G = irradiation of fin, W/m^2
H = dissipation function of fin, W/m^2
$\bar{H} = H/\sigma T_B^4$ = dimensionless H
J = radiosity of fin, W/m^2
k = conductivity of fin, W/m·K
$[P]$ = fuzzy membership boundary matrix
q_i = local heat transfer rate on the fin, W/m
$\bar{q}_i = q_i/kT_B$ = dimensionless q_i
Q = actual total heat transfer, W/m
Q_0 = required total heat transfer, W/m
ΔQ_0 = allowable heat transfer variance, W/m
$\bar{Q} = Q/kT_B$ = dimensionless Q
$\bar{Q}_0 = Q_0/kT_B$
t = half of thickness of fin tip, m
$\bar{t} = t/(k/\sigma T_B^3)$ = dimensionless t
T = local temperature of fin, K
T_B = temperature of fin base, K
x = coordinate of fin along its axis, m
$\bar{x} = x/(k/\sigma T_B^3)$ = dimensionless x
X = design vector; $X^T = (x_1, x_2 \ldots x_n)$
δ_i = half of thickness of radiating fin root, m
$\bar{\delta}_i = \delta_i/(k/\sigma T_B^3)$ = dimensionless δ_i
ϵ = emissivity
μ_D = membership function of the fuzzy set D
$\xi = T/T_B$ = dimensionless T
σ = Stefan–Boltzmann constant, W/m^2-K^4
$\phi = J/(\sigma T_B^4)$ = dimensionless J

Subscripts

1 = variable of the horizontal fin
1′ = variable of the conjugate horizontal fin
2 = variable of the vertical fin
2′ = variable of the conjugate vertical fin

Superscript

* = optimum value

Downloaded 11 Dec 2010 to 193.140.21.150. Redistribution subject to ASME license or copyright; see http://www.asme.org/terms/Terms_Use.cfm

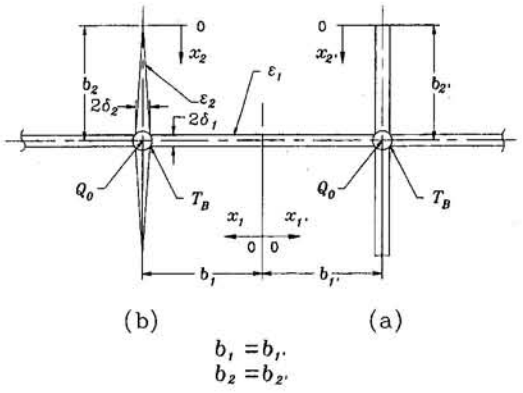


Fig. 2 Sketch of a portion of four-fin system with rectangular vertical fins (*a*) or triangular vertical fins (*b*)

$$[P] = \begin{bmatrix} f_1(X_1^*) & f_2(X_1^*) & \cdots & f_k(X_1^*) \\ f_1(X_2^*) & f_2(X_2^*) & \cdots & f_k(X_2^*) \\ \vdots & & & \\ f_1(X_k^*) & f_2(X_k^*) & \cdots & f_k(X_k^*) \end{bmatrix} \tag{3}$$

where X_i^* is the optimum solution for the single objective function $f_i(X)$. The diagonal elements in the matrix $[P]$ are the minima of the corresponding columns. The target and least acceptable values for the ith objective goal are identified as
Target value:

$$f_{i_{\min}} = f_i(X_i^*) \tag{4}$$

Least acceptable value:

$$f_{i_{\max}} = \max_{l=1}^{k} \{f_i(X_l^*)\} \tag{5}$$

It is recognized that in many cases the optimum solutions for the single objective functions do not exist, i.e., no extremum exists, such as a monotonically decreasing or increasing function. In such cases, the related boundaries are determined by the designer's judgment and the needs of design. Although this approach is not a rule, however, Rao's method still provides a reasonable guideline to determine the boundaries of the membership functions in the cases that the optimum solutions for the single objective functions do exist.

2.3 Fuzzy Optimization of the Radiating Fin Array. A system of radiating fin array as illustrated in Fig. 1(*b*) is now considered. One unit of array includes fin surfaces bounded by two vertical center lines, as indicated in Fig. 2. It is expected that this unit dissipates an amount of heat Q_0 by radiation with a maximum allowable variance ΔQ_0. The base temperature is maintained at T_B and the environment temperature is at absolute zero in space. It is intended to determine the optimum values of the horizontal fin height, b_1, the vertical fin height, b_2, the horizontal fin half thickness, δ_1, and the vertical fin half root thickness, δ_2, which minimize both of the total fin mass for one unit of fin array and the horizontal fin height of b_1.

The following simplifying assumptions are made in this study:

1 Steady state holds;
2 Only radiation heat transfer exists for the array to dissipate the heat to the environment of which the temperature is assumed to be absolute zero;
3 The base-fin radiation interaction can be neglected;
4 The heat conduction along the fin height is one dimensional, i.e., the thin fin assumption is valid and the length of the array in the direction of pipe axis is much larger than any of the other length dimensions of the system;
5 There is no heat transfer at the tip of the vertical fins due to the thin fin assumption;
6 Gray body assumption holds for all surfaces;
7 All the fins have the same properties, which are assumed to be temperature independent;
8 The upward and downward vertical fins have the same shape and are equally spaced;
9 The horizontal fins are restricted to the rectangular profile and the vertical fins can be either triangular or rectangular.

Additionally, the total mass of the fin array is not allowed to exceed a specified maximum amount. As mentioned before, both triangular and rectangular vertical fins will be included in the analysis, because they are easy to manufacture.

We first consider equally weighted objective goals to reduce the mass and to reduce the horizontal dimension. Then, a case of objective goals with different weights will also be illustrated. As pointed out earlier, these two objective goals are conflicting.

The aforementioned problem can be restated as follows:

Find b_1^*, b_2^*, δ_1^* and δ_2^*, which minimize the objective functions A_T and B. The objective A_T is the total profile area of the system, i.e.,

$$A_T(b_1, b_2, \delta_1, \delta_2) = 4b_1\delta_1 + 2b_2(\delta_2 + t_2) \tag{6}$$

in which the half fin tip thickness of vertical fin, t_2, takes the value of either zero or δ_2, respectively, for the case of triangular or rectangular vertical fin. The objective B is the horizontal fin dimension,

$$B(b_1, b_2, \delta_1, \delta_2) = b_1 \tag{7}$$

The system is subjected to

$$Q \geq Q_0 - \Delta Q_0 \tag{8}$$

Let μ_{A_T}, μ_B, and μ_Q be the objective and constraint membership functions. From Eq. (1), the overall membership function is thus given by

$$\mu_D(b_1, b_2, \delta_1, \delta_2) = \min \{\mu_{A_T}(b_1, b_2, \delta_1, \delta_2), \mu_B(b_1, b_2, \delta_1, \delta_2), \mu_Q(b_1, b_2, \delta_1, \delta_2)\} \tag{9}$$

According to Eq. (2), the problem is now expressed in terms of fuzzy sets terminology:

Determine b_1^*, b_2^*, δ_1^* and δ_2^*, such that

$$\mu_D(b_1^*, b_2^*, \delta_1^*, \delta_2^*) = \max \{\mu_D(b_1, b_2, \delta_1, \delta_2)\} \tag{10}$$

Before setting up the membership functions, we need to determine the best and the worst cases for all of the membership functions. To this end, we optimize the system individually with respect to the two single objectives (the mass and the horizontal height) based on Eq. (3) in which the matrix $[P]$ is constructed under the constraint $Q \geq Q_0$. The possible minimum value for the objective A_T is determined by minimizing the system mass without any other restrictions, denoted as $A_{T_{\min}}$. The worst value for A_T is specified by the problem, or by the designer, designated by $A_{T_{\max}}$. The dimension $b_{1_{\min}}$ is found by minimizing b_1 subjected to $A_T = A_{T_{\max}}$, *and is the possible minimum horizontal height for any combination of the system* (b_1 can be minimized only when A_T is specified. Note that b_1 and A_T are two conflicting objectives). The worst value $b_{1_{\max}}$ is identified by the value of b_1 corresponding to that of obtained from the minimization of $A_{T_{\min}}$. Among them, $A_{T_{\max}}$ is specified by the designer, while the other boundaries of objective membership functions are determined by referring to Eqs. (3)–(5). The worst value of heat transfer is determined from $Q_{\min} = Q_0 - \Delta Q_0$. If the heat transfer is greater than Q_0, it would be considered totally satisfied.

With the determined boundaries, the following sinusoid-based membership functions (Gupta et al., 1988) are employed:

Downloaded 11 Dec 2010 to 193.140.21.150. Redistribution subject to ASME license or copyright; see http://www.asme.org/terms/Terms_Use.cfm

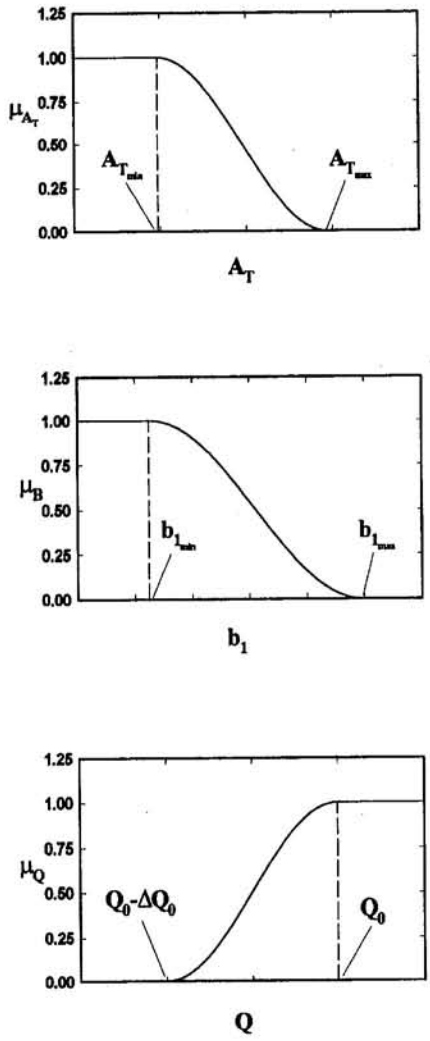


Fig. 3 Membership functions of μ_{A_T}, μ_B, and μ_Q

$$\mu_{A_T} = \begin{cases} 1 & \text{when} \quad A_T \le A_{T_{\min}} \\ \sin^2 \dfrac{\pi}{2}\left(\dfrac{A_{T_{\max}} - A_T}{A_{T_{\max}} - A_{T_{\min}}}\right) & \text{when} \quad A_{T_{\min}} < A_T \le A_{T_{\max}} \\ 0 & \text{when} \quad A_T > A_{T_{\max}} \end{cases} \tag{11}$$

$$\mu_B = \begin{cases} 1 & \text{when} \quad b_1 \le b_{1_{\min}} \\ \sin^2 \dfrac{\pi}{2}\left(\dfrac{b_{1_{\max}} - b_1}{b_{1_{\max}} - b_{1_{\min}}}\right) & \text{when} \quad b_{1_{\min}} < b_1 \le b_{1_{\max}} \\ 0 & \text{when} \quad b_1 > b_{1_{\max}} \end{cases} \tag{12}$$

and

$$\mu_Q = \begin{cases} 1 & \text{when} \quad Q > Q_0 \\ \sin^2 \dfrac{\pi}{2}\left(\dfrac{Q - Q_{\min}}{\Delta Q_0}\right) & \text{when} \quad Q_{\min} < Q \le Q_0 \\ 0 & \text{when} \quad Q \le Q_{\min} \end{cases} \tag{13}$$

The distributions of the three membership functions are shown in Fig. 3. It should be pointed out that if, according to a theorem of invariance of fuzzy optimum solutions (Zhang et al., 1996), these three membership functions were changed to linear functions, the final optimum solution would still be the same.

The values of $A_{T_{\min}}$, $b_{1_{\min}}$, and $b_{1_{\max}}$ involved in the formulation of the objective membership functions may be directly obtained from the authors' previous works (Chung and Zhang, 1993a, b). In the interest of saving space, no detailed description will be presented here and the reader is referred to the aforementioned references for further information. The determination of total heat transfer, Q in Eq. (13), will be presented in Section 3.

In many situations, the fuzzy goals are unequally desirable and fuzzily described. The fuzzy sets theory enables us to treat linguistic descriptions such as "very," "slightly," etc., mathematically by applying certain operations on the corresponding membership functions, as suggested by Zadeh (1975a–c). The operation concentration, **CON** has the effect of putting a weighting factor like "very," "strongly" on the fuzzy set; and the operation dilation, **DIL** reflects the concepts described by "slightly," "somewhat." They can be written as $\mathbf{CON}(\mu_F(X)) = \mu_F^2(X)$ and $\mathbf{DIL}(\mu_F(X)) = \mu_F^{0.5}(X)$.

3 Heat Transfer Formulation

As a fundamental step, the heat transfer of the system must be evaluated for any given dimensions of the horizontal fin and vertical fin, in order to obtain the solution of optimum decision function, i.e., Eq. (10). In this section, the governing equations and dissipation functions describing the heat transfer of the fin array will be formulated.

Consideration hereby is given to a system of radiating fin array as illustrated in Fig. 1(*b*). We wish to determine the heat transfer from one unit of array including fin surfaces bounded by two vertical centerlines, as indicated in Fig. 2. The base temperature is at T_B, while the environment temperature is at absolute zero. The assumptions made in Section 2 hold in this analysis.

For the system illustrated in Fig. 2 with one unit length along the direction of the pipe axis, the equation describing the heat transfer is

$$\frac{dq_i}{dx_i} = 2H_i \quad i = 1, 2 \tag{14}$$

where the subscript "1" designates the variables for the horizontal fin and subscript "2" for the vertical fin, q is the local heat flow rate on the fin, and H is the dissipation function. Letting $f_i(x)$ be the profile of the fin, we can also write

$$q_i = 2kf_i \frac{dT_i}{dx_i} \tag{15}$$

In the present problem, the fin profile has the form of

$$f_i(x_i) = t_i + \frac{(\delta_i - t_i)}{b_i} x_i \tag{16}$$

Combining Eqs. (14)–(16) yields the governing equation

$$\frac{d^2T_i}{dx_i^2} = \left[\frac{1}{k} H_i - \frac{(\delta_i - t_i)}{b_i}\frac{dT_i}{dx_i}\right] \frac{b_i}{t_i b_i + (\delta_i - t_i)x_i} \tag{17}$$

The associated boundary conditions are

$$\begin{aligned} T_i &= T_B \quad @x_i = b_i \\ q_i &= 0 \quad @x_i = 0 \end{aligned} \qquad i = 1, 2 \tag{18}$$

In Eq. (18), the half fin tip thickness, t_i, has the value δ_i or zero, as the case may be. The dissipation functions, H_1 and H_2, are the net heat dissipated from the fins, which depend on the heat transfer mode. They are required in order to solve for temperature profiles from Eqs. (17) and (18).

Downloaded 11 Dec 2010 to 193.140.21.150. Redistribution subject to ASME license or copyright; see http://www.asme.org/terms/Terms_Use.cfm

In their dimensionless forms, Eqs. (17) and (18) are expressed as

$$\frac{d^2\xi_i}{d\bar{x}_i^2} = \left[\bar{H}_i - \frac{(\bar{\delta}_i - \bar{t}_i)}{\bar{b}_i}\frac{d\xi_i}{d\bar{x}_i}\right]\frac{\bar{b}_i}{\bar{t}_i\bar{b}_i + (\bar{\delta}_i - \bar{t}_i)\bar{x}_i} \quad (19)$$

$$\begin{aligned} \xi_i &= 1 \quad @\bar{x}_i = \bar{b}_i \\ \bar{q}_i &= 0 \quad @\bar{x}_i = 0 \end{aligned} \qquad i = 1, 2 \quad (20)$$

The radiative heat transfer balance on the surfaces of the fins yields

$$H_1 = J_1 - G_1 \quad (21)$$

$$H_2 = J_2 - G_2 \quad (22)$$

where G and J represent irradiation and radiosity, respectively, and further

$$G_1 = \int_0^{b_2} J_2 dF_{1-2} + \int_0^{b_{2'}} J_{2'} dF_{1-2'} = \int_0^{b_2} J_2(dF_{1-2} + dF_{1-2'}) \quad (23)$$

$$G_2 = \int_0^{b_1} J_1 dF_{2-1} + \int_0^{b_{1'}} J_{1'} dF_{2-1'} + \int_0^{b_{2'}} J_{2'} dF_{2-2'} = \int_0^{b_1} J_1(dF_{2-1} + dF_{2-1'}) + \int_0^{b_{2'}} J_{2'} dF_{2-2'} \quad (24)$$

$$J_1 = \epsilon_1\sigma T_1^4 + (1 - \epsilon_1)G_1 \quad (25)$$

$$J_2 = \epsilon_2\sigma T_2^4 + (1 - \epsilon_2)G_2 \quad (26)$$

Eliminating G_1 and G_2 from Eqs. (21)–(26), a system of nonlinear integral equations in terms of J_1, J_2, H_1 and H_2, or in their dimensionless forms ϕ_1, ϕ_2, $\bar{H}_1$ and $\bar{H}_2$, respectively, is obtained:

$$\phi_1 = \epsilon_1\xi_1^4 + (1 - \epsilon_1)\int_0^{\bar{b}_2} \phi_2(dF_{1-2} + dF_{1-2'}) \quad (27)$$

$$\phi_2 = \epsilon_2\xi_2^4 + (1 - \epsilon_2)\left(\left\{\int_0^{\bar{b}_1}\left[\epsilon_1\xi_1^4 + (1 - \epsilon_1) \times \int_0^{\bar{b}_2} \phi_2(dF_{1-2} + dF_{1-2'})\right](dF_{2-1} + dF_{2-1'})\right\} + \left(\int_0^{\bar{b}_{2'}} \phi_{2'} dF_{2-2'}\right)\right) \quad (28)$$

$$\bar{H}_1 = \epsilon_1\xi_1^4 - \epsilon_1\int_0^{\bar{b}_2} \phi_2(dF_{1-2} + dF_{1-2'}) \quad (29)$$

$$\bar{H}_2 = \epsilon_2\xi_2^4 - \epsilon_2\left[\int_0^{\bar{b}_1} \phi_1(dF_{2-1} + dF_{2-1'}) + \int_0^{\bar{b}_{2'}} \phi_{2'} dF_{2-2'}\right] \quad (30)$$

The temperature distributions of horizontal and vertical fins ξ_1 and ξ_2 as well as the dissipation functions $\bar{H}_1$ and $\bar{H}_2$ are solved iteratively and numerically from Eqs. (19), (20), and (27)–(30).

Once the temperature profiles for the two fins are solved, the total dimensionless heat transfer for one unit array (i.e., the heat dissipated from one pipe) is evaluated by

$$\bar{Q} = 4\left(\bar{\delta}_1\frac{d\xi_1(\bar{b}_1)}{d\bar{x}_1} + \bar{\delta}_2\frac{d\xi_2(\bar{b}_2)}{d\bar{x}_2}\right) \quad (31)$$

The solutions of ξ_i and $\bar{H}_i$ are intensively invoked in the optimization process to evaluate the membership function μ_Q given by Eq. (13).

The optimum fuzzy decision function, Eq. (10), is solved numerically by a Simplex search (Walsh, 1975) combined with a Lattice search (Stoecker, 1989) in this study.

Table 1 Case study of fuzzy optimized fin arrays

Case No.	$\bar{Q}_0$	$\bar{A}_{T_{max}}$	Shape of vertical fins	Design Preference of Weighting Factor		$\bar{A}_{T_{min}}$, $\bar{b}_{1_{min}}$, $\bar{b}_{1_{max}}$ determined from
				$\bar{A}_T$	$\bar{b}_1$	
1	0.03	$(\bar{A}_{T_{max}})_{2\text{-}fin}$	Triangular	Balanced	Balanced	Triangular case
2	0.03	$(\bar{A}_{T_{max}})_{2\text{-}fin}$	Rectangular	Balanced	Balanced	Rectangular case
3	0.03	$(\bar{A}_{T_{max}})_{2\text{-}fin}$	Rectangular	Balanced	Balanced	Triangular case
4	0.01	$(\bar{A}_{T_{max}})_{2\text{-}fin}$	Rectangular	Balanced	Balanced	Rectangular case
5	0.03	$2(\bar{A}_{T_{max}})_{4\text{-}fin}$	Triangular	Balanced	Balanced	Triangular case
6	0.03	$2(\bar{A}_{T_{max}})_{4\text{-}fin}$	Triangular	Weak	Strong	Triangular case
7	0.03	$2(\bar{A}_{T_{max}})_{4\text{-}fin}$	Triangular	Strong	Weak	Triangular case

4 Results and Discussion

Seven different cases are studied based on the fuzzy optimization analysis. They are summarized in Table 1. For comparison purposes, the maximum allowable mass for the first four cases was chosen specifically to be the same as the minimum mass for two-fin system, or in other words, the worst total mass for the four-fin system is the best value for a two-fin system. The profile of vertical fins in Cases 1 and 5–7 is triangular, and in Cases 2–4 it is rectangular. The boundaries of membership functions for Case 2 are obtained from the corresponding optimizations for the arrays with rectangular vertical fins. For Case 3, the same boundaries as those of Case 1 are employed. Case 4 has the same situations as Case 2, except for a different heat transfer rate. In Cases 5–7, different preferences are assigned to the objectives. The vertical fins are triangular, and the maximum allowable mass is specified as twice the corresponding minimum mass in cases 5–7. Emissivities of the fin surfaces are set equal to 0.9 in all cases.

Referring to the earlier results by Chung and Zhang (1993a, b), the boundaries of membership function for each case are established. They are listed in Table 2. The allowable variance of heat transfer is specified as $\Delta\bar{Q}_0 = 0.02\,\bar{Q}_0$ in all cases.

In Table 3, the fuzzy optimum results for Cases 1–3 are presented together with the non-fuzzy optimum results from the corresponding single-objective optimizations. This table also includes the results from the optimization of a two-fin system. To ensure that the comparison has a common base, the maximum allowable fin mass is specifically selected the same as the minimum mass of the two-fin system (see Table 2). Table 3 indicates that the fin array with triangular vertical fin (Case 1) has the smallest values for both total fin mass and horizontal fin dimension. It has the highest overall degree of satisfaction $\mu_{D_{max}}$. This implies that, physically, the fin with triangular profile is more efficient for dissipating heat. Case 2 is the fin array with rectangular vertical fins. The boundaries of membership functions are determined from the single-objective optimizations for the case of a rectangular vertical fin. These boundaries are different from those in Case 1. Case 3 has exactly the same membership functions as those of Case 1; therefore, the differences in the corresponding optimum results are entirely due to the shape effect of the vertical fin. If one of the objectives

Downloaded 11 Dec 2010 to 193.140.21.150. Redistribution subject to ASME license or copyright; see http://www.asme.org/terms/Terms_Use.cfm

Table 2 Boundaries of membership functions for the seven cases in Table 1

Case No.	$\bar{Q}_0$	$\bar{Q}_0$-$\Delta\bar{Q}_0$	$\bar{A}_{T_{max}}$	$\bar{A}_{T_{min}}$	$\bar{b}_{1_{max}}$	$\bar{b}_{1_{min}}$
1, 3	0.03	0.0294	1.3625×10^{-5}	9.1115×10^{-6}	1.6323×10^{-2}	9.9406×10^{-3}
2	0.03	0.0294	1.3625×10^{-5}	9.8983×10^{-6}	1.5502×10^{-2}	1.0239×10^{-2}
4	0.01	0.0098	5.0463×10^{-7}	3.6661×10^{-7}	5.1675×10^{-3}	3.4131×10^{-3}
5, 6, 7	0.03	0.0294	1.8223×10^{-5}	9.1115×10^{-6}	1.6323×10^{-2}	9.1827×10^{-3}

is removed, the fuzzy optimum results of Cases 1 and 2 will reduce to the corresponding non-fuzzy optimum solution with respect to the remaining objective. That is, if we remove the objective on the horizontal dimension, the fuzzy results will reduce to the minimum mass solutions, and if we remove the objective on fin mass, they will be identical to the solutions based on the minimum horizontal fin height condition. In such cases, μ_Q always equals unity, and one of μ_{A_T} and μ_B will also be unity, depending on the objective being removed. However, this is not true for Case 3, simply because the boundaries of its membership functions are not based on its own corresponding non-fuzzy optimum solutions. That the overall degree of satisfaction, $\mu_{D_{max}}$, of Case 3 is somewhat smaller than that of Case 2 reflects that the objectives described by the membership functions in Case 1 are somewhat too stringent for Case 3. Both Cases 2 and 3 indicate that the four-fin array with the rectangular profile on vertical fins also has considerably smaller fin mass and horizontal dimension than those of two-fin system but is not as efficient as the array with triangular vertical fins. Cases 1, 2, and 3 save respectively 24.49, 19.91, and 22.33 percent in material as compared to the two-fin system. Furthermore, their horizontal dimensions are 21.24, 20.79, and 18.39 percent, respectively, shorter as compared to the two-fin system.

Table 3 also shows that the four-fin system would yield 5.2 percent (rectangular) and 10.8 percent (triangular) longer horizontal dimension than two-fin system if only minimization of fin mass were considered.

Table 3 Comparison of fuzzy optimum results with two-fin system and non-fuzzy optimum results

Optimum Parameters	Fuzzy optimization			Non-fuzzy optimization				
	Case 1	Case 2	Case 3	Min. A_T two-fin system	Min. A_T triangular case	Min. A_T rectangular case	Min. b_1 triangular case	Min. b_1 rectangular case
$\bar{Q}_0^*\times10^2$	2.9844	2.9837	2.9804	$\bar{Q}_0$=0.03	$\bar{Q}_0$=0.03	$\bar{Q}_0$=0.03	$\bar{Q}_0$=0.03	$\bar{Q}_0$=0.03
$\bar{A}_T^*\times10^5$	1.0288	1.0912	1.0583	1.3625	0.91115	0.98983	$\bar{A}_T\times10^5$ =1.3625	$\bar{A}_T\times10^5$ =1.3625
$\bar{b}_1^*\times10^2$	1.1604	1.1670	1.2023	1.4733	1.6323	1.5502	0.99406	1.0239
$\bar{b}_2^*\times10^3$	7.0563	6.0684	6.1096	---	8.5392	6.8612	6.7603	5.9894
$\bar{\delta}_1^*\times10^4$	1.7031	1.8741	1.7582	2.3120	1.0060	1.2413	2.6143	2.5879
$\bar{\delta}_2^*\times10^4$	1.6715	0.89109	0.87075	---	1.4899	0.80190	2.3890	1.2631
$\mu_{D_{max}}$	0.8415	0.8284	0.7596	---	0	0	0	0
μ_Q	0.8415	0.8284	0.7596	---	1	1	1	1
μ_{A_T}	0.8415	0.8284	0.7596	---	1	1	0	0
μ_B	0.8415	0.8284	0.7596	---	0	0	1	1

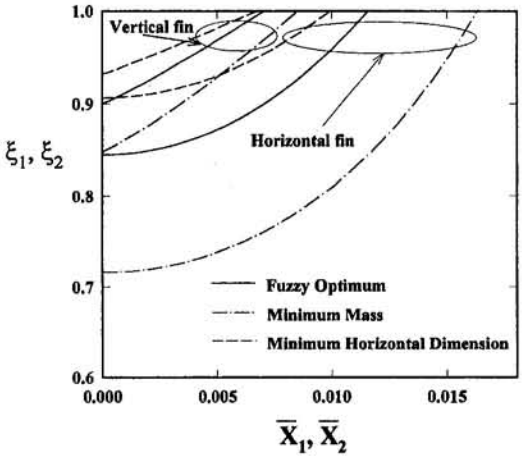


Fig. 4 Temperature profiles along the fuzzy optimized and non-fuzzy optimized fin arrays with triangular vertical fins (case 1)

Typical temperature distributions on fuzzy optimum fin array along with the corresponding arrays of minimum mass and minimum horizontal fin height for Case 1 and Case 2 are depicted in Figs. 4 and 5, respectively. The temperature distributions are found to be quite different due to different optimum goals. To utilize the maximum potential of fin material, the minimum mass solution has a much larger temperature drop than the minimum fin height solution. In Case 1, for example, the dimensionless temperature on the tip of horizontal fin for the minimum mass solution is 0.7162, while it is 0.9066 for the minimum fin height solution. The compromise between them is the fuzzy optimum solution. In Case 1 the tip temperature is 0.8451.

As pointed out by Chung and Zhang (1993a, b), the optimum fin height is proportional to $\bar{Q}_0$, while the optimum fin thickness is proportional to $\bar{Q}_0^2$. Thus the optimum aspect ratio b_2^*/δ_2^* varies with different requirement of heat rejection. In Case 1, this ratio is 42.2. The triangular vertical fin shape should be considered as the first choice if this ratio is acceptable from the manufacturing point of view. However, as $\bar{Q}_0$ decreases (either lower value of heat transfer, and/or higher values of base temperature and conductivity of the fin), the vertical fin may become too thin to be manufactured in triangular shape. In such a case the rectangular shape is preferred. Cases 4 and 2 are identical except that the required heat dissipation in Case 2 is three times larger. Since the expected optimum vertical fin would be very thin, the rectangular profile is selected for vertical

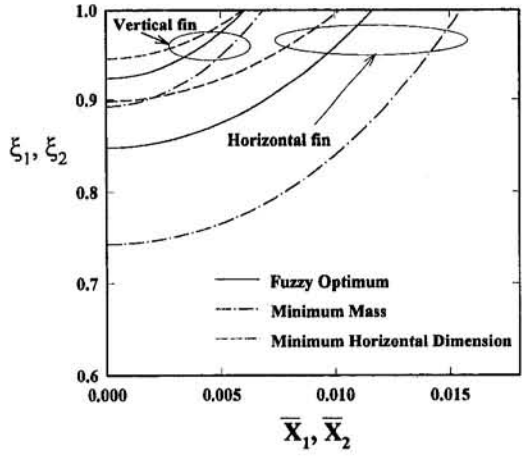


Fig. 5 Temperature profiles along the fuzzy optimized and non-fuzzy optimized fin arrays with rectangular vertical fins (case 2)

Downloaded 11 Dec 2010 to 193.140.21.150. Redistribution subject to ASME license or copyright; see http://www.asme.org/terms/Terms_Use.cfm

fins. The optimum results are given in Table 4. As expected, the heights of fins, including both horizontal and vertical fins, are one-third of those of Case 2 (see Table 3), and the thicknesses are one-ninth of those of Case 2. The optimum aspect ratio of vertical fin, b_2^*/δ_2^*, is 204.3, which is three times that of Case 2. Similar to Case 2, the design of Case 4 saves 19.91 percent in material and 20.79 percent in horizontal space compared to the two-fin system.

Table 5 shows the results of optimization with different preference on the objectives. In Case 6, the fin array is preferred to be designed very short horizontally and slightly light in weight. On the other hand, in Case 7, a strong preference is given to saving material, and less emphasis is placed on shortening horizontal fin height. Both cases are compared to Case 5, which has a balanced preference on the objectives. The maximum allowable fin mass is specified as double the corresponding minimum mass for all three cases.

5 Conclusions

A novel four-fin radiative fin array system is developed and optimized by employing the fuzzy optimization approach in this research. The objectives of minimizing fin mass and horizontal fin dimension are considered simultaneously. Two kinds of configuration are considered in this work: fin arrays with vertical rectangular fin profile, and with vertical triangular profile and horizontal fins restricted to the rectangular fin shape. The optimum results indicate that the four-fin array system we have developed considerably reduces the fin material and is much more compact compared to the traditional two-fin fin array system.

Comparisons are given to the optimum results from the fuzzy optimization and the non-fuzzy optimization. It is found that for a surface emissivity of 0.9 and with triangular vertical fins, by performing non-fuzzy optimization to fin mass, the four-fin system is 33.1 percent lighter in weight but 10.8 percent longer in horizontal dimension than the two-fin system; if only the minimization to system horizontal dimension is considered, the four-fin system is 32.5 percent shorter than the two-fin system while using the same amount of mass. Applying fuzzy optimization logic with a balanced preference on the objectives, the four-fin system saves 24.5 percent in material and reduces 21.2 percent in horizontal dimension simultaneously, as compared to the conventional two-fin system. For a fin array with rectangular profile vertical fins, the corresponding last two figures are 19.9 and 20.8 percent, respectively.

It has been further demonstrated that the fuzzily expressed preference can be in terms of fuzzy membership functions via the membership operations **CON** and **DIL**. With the modified membership functions, the optimum results change their emphasis between the fin mass and the fin horizontal dimension. The ability to use fuzzy linguistic descriptions makes fuzzy optimization very flexible and powerful for real-world engineering problems.

Table 4 Fuzzy optimum results for case 4

Optimum Parameters	Fuzzy optimization	Non-fuzzy optimization		
	Case 4	Min. A_T, two-fin system	Min. A_T, rectangular case	Min. b_1, rectangular case
$\bar{Q}_0^*\times10^3$	9.9456	$\bar{Q}_0$=0.01	$\bar{Q}_0$=0.01	$\bar{Q}_0$=0.01
$\bar{A}_T^*\times10^7$	4.0413	5.0463	3.6661	$\bar{A}_T\times10^5$ =5.0463
$\bar{b}_1^*\times10^3$	3.8900	4.9111	5.1675	3.4131
$\bar{b}_2^*\times10^3$	2.0228	---	2.2871	1.9965
$\bar{\delta}_1^*\times10^5$	2.0824	2.5688	1.3792	2.8755
$\bar{\delta}_2^*\times10^5$	0.99010	---	0.89100	1.4033
$\mu_{D_{max}}$	0.8284	---	0	0
μ_Q	0.8284	---	1	1
μ_{A_T}	0.8284	---	1	0
μ_B	0.8284	---	0	1

Table 5 Comparisons of results of fuzzy optimization with different weighting preference and non-fuzzy optimization

Optimum Parameters	Fuzzy optimization			Non-fuzzy optimization	
	Case 5	Case 6	Case 7	Min. A_T triangular case	Min. b_1 triangular case
$\bar{Q}_0^*\times10^2$	2.9860	2.9857	2.9868	$\bar{Q}_0$=0.03	$\bar{Q}_0$=0.03
$\bar{A}_T^*\times10^5$	1.1239	1.2137	1.0540	0.91115	$\bar{A}_T\times10^5$ =1.8223
$\bar{b}_1^*\times10^2$	1.0850	1.0390	1.1387	1.6323	0.91827
$\bar{b}_2^*\times10^3$	6.8184	6.8005	6.9860	8.5392	6.9284
$\bar{\delta}_1^*\times10^4$	2.0096	2.2484	1.7808	1.0060	3.6817
$\bar{\delta}_2^*\times10^4$	1.8272	2.0327	1.7210	1.4899	3.3917
$\mu_{D_{max}}$	0.8714	0.8670	0.8847	0	0
μ_Q	0.8714	0.8670	0.8847	1	1
μ_{A_T}	0.8714	DIL(μ_{A_T}) 0.8670	CON(μ_{A_T}) 0.8847	1	0
μ_B	0.8714	CON(μ_B) 0.8670	DIL(μ_B) 0.8847	0	1

Acknowledgments

This research is being supported by the National Science Foundation under grant No. CTS-9312024.

References

Bellman, R. E., and Zadeh, L. A., 1970, "Decision Making in a Fuzzy Environment," *Management Science,* Vol. 17, pp. 141–164.

Chung, B. T. F., and Zhang, B. X., 1993a, "A Novel Design for a Radiative Fin Array System," *J. Franklin Institute,* Vol. 330, No. 3, pp. 465–478.

Chung, B. T. F., and Zhang, B. X., 1993b, "Optimum Design for a Radiative Fin Array System With Least Horizontal Dimension," *J. Franklin Institute,* Vol. 330, No. 5, pp. 869–884.

Gupta, M. M., Knopf, G. K., and Nikforuk, P. N., 1988, "Sinusiodal-Based Cognitive Mapping Functions," *Fuzzy Logic in Knowledge-Based Systems, Decision and Control,* Elsevier Science Publishers, North-Holland.

Kandel, A., and Lee, S. C., 1979, *Fuzzy Switching and Automata: Theory and Applications,* Crane, Russak & Company, Inc., New York.

Lee, E. T., and Zadeh, L. A., 1969, "Note on Fuzzy Languages," *Information Sciences,* Vol. 1, pp. 421–434.

Lee, E. T., 1980, "Applications of Fuzzy Set Theory to Image Sciences," *J. Cybernetics,* Vol. 10, pp. 127–136.

Rao, S. S., 1987, "Multi-objective Optimization of Fuzzy Structural Systems," *Int. J. Numerical Methods in Engineering,* Vol. 24, pp. 1157–1171.

Sakawa, M., 1993, *Fuzzy Sets and Interactive Multiobjective Optimization,* Plenum Press, New York.

Schmucker, K. J., 1984, *Fuzzy Sets, Natural Language Computations, and Risk Analysis,* Computer Science Press, Rockville, MD.

Schnurr, N. M., Shapiro, A. B., and Townsend, M. A., 1976, "Optimization of Radiating Fin Arrays With Respect to Weight," ASME JOURNAL OF HEAT TRANSFER, Vol. 98, pp. 643–648.

Stoecker, W. F., 1989, *Design of Thermal Systems,* 3rd ed., McGraw-Hill, New York.

Downloaded 11 Dec 2010 to 193.140.21.150. Redistribution subject to ASME license or copyright; see http://www.asme.org/terms/Terms_Use.cfm

Walsh, G. R., 1975, *Methods of Optimization,* Wiley, London.

Wilkins, J. E., 1960, "Minimum Mass Thin Fins for Space Radiators," *Proc. 1960 Heat Transfer and Fluid Mechanics Inst.,* D. M. Mason et al., eds., Stanford Univ. Press, Stanford, CA, pp. 229–243.

Zadeh, L. A., 1965, "Fuzzy Sets," *Information and Control,* Vol. 8, pp. 338–353.

Zadeh, L. A., 1975a, "The Concept of a Linguistic Variable and Its Application to Approximate Reasoning—I," *Information Sciences,* Vol. 8, pp. 199–249.

Zadeh, L. A., 1975b, "The Concept of a Linguistic Variable and Its Application to Approximate Reasoning—II," *Information Sciences,* Vol. 8, pp. 301–375.

Zadeh, L. A., 1975c, "The Concept of a Linguistic Variable and Its Application to Approximate Reasoning—III," *Information Sciences,* Vol. 9, pp. 43–80.

Zhang, B. X., and Chung, B. T. F., 1994, "A Multi-objective Fuzzy Optimization for a Convective Fin," *The 10th International Heat Transfer Conference Proceedings,* Brighton, United Kingdom, Vol. 2, pp. 485–490.

Zhang, B. X., Chung, B. T. F., and Lee, E. T., 1996, "The Invariance of Optimum Solution in a Multi-objective Fuzzy Environment," *Kybernetes, Int. J. of Systems and Cybernetics,* Vol. 25, pp. 17–32.

Downloaded 11 Dec 2010 to 193.140.21.150. Redistribution subject to ASME license or copyright; see http://www.asme.org/terms/Terms_Use.cfm

A. B. De Miranda
Doctoral Student.

J. F. Sacadura
Professor.

CETHIL/GMC,
INSA de Lyon,
69621 Villeurbanne Cedex, France

An Alternative Formulation of the S-N Discrete Ordinates for Predicting Radiative Transfer in Nongray Gases

Introduction

In many industrial applications, such as furnaces, combustion chambers, and nuclear reactors, radiative transfer interacts with natural, forced, or mixed convection in gaseous atmospheres. Difficulties in modeling radiation in molecular gases are related to the fact that radiative properties and intensity are strongly wavelength dependent. Simple spectral averaging procedures like gray gas or gray band approximations may lead to unsatisfactory results. On the other hand, line-by-line approaches require large computing time. However, even though they provide the most accurate results (Taine, 1983; Hartmann et al., 1984) these methods may be inappropriate for some engineering applications. To reduce heavy calculations, band models were developed, using averaged radiative properties over spectral bands 25 cm^{-1} to 100 cm^{-1} wide for narrow-band models (Hartmann et al., 1984; Soufiani and Taine, 1987), and 1000 cm^{-1} for wide-band models (Edwards, 1976; Buckius, 1982; Edwards and Menard, 1964).

When the radiative transfer equation is averaged over a given wavenumber interval, spectral gas transmissivity radiative intensity correlation must be accounted for, no matter what band model is used. When the boundary walls are reflective, a finite number of reflections must be explicitly treated for accurate solutions.

Another difficulty arises when considering a nonhomogeneous and/or nonisothermal gas where a path-averaging procedure is needed; many authors use the Curtis–Godson approximation (Godson, 1953), which consists in approaching the length of an absorption path line through the medium by the corresponding length through an equivalent homogeneous and isothermal medium. The first work combining the SN discrete ordinates method with a narrow-band gas radiation model is reported by Kim et al. (1991), for a one-dimensional geometry with black walls; Menart and Lee (1991) studied diffusely reflecting walls. This technique was extended by Menart et al. (1993). It can be noted that both methods require a supercomputer of CRAY YMP size.

The purpose of this work is to find a good compromise between a certain required accuracy for realistic industrial applications, and moderate computing efforts. We introduce an integral formulation of the radiative transfer equation, derived from El-Wakil and Sacadura's previous SN model for gray media (El-Wakil and Sacadura, 1992; El-Wakil, 1991), extended here to nongray gas. This SN method combined with an exponential narrow-band model provides a numerical code that can be run on a workstation type computer. Then for some engineering applications this formulation may be more suitable than ones previously presented.

To test the accuracy of this integral approach, results in terms of radiative source distribution are compared to those obtained by Lee and coworkers in a one-dimensional water vapor slab.

Formulation

The differential form of the wavenumber-averaged radiative transfer equation is:

$$\frac{\partial \overline{I_\nu}(s,\Omega)}{\partial s} + \overline{\kappa_\nu(s)\, I_\nu(s,\Omega)} = \overline{\kappa_\nu(s)}\,.\,\overline{I_{b\nu}(s)} \qquad (1)$$

where terms below the same overbar must be averaged as a unit for a correlated solution. Integrating Eq. (1) along a path s in the Ω direction with a formal boundary condition leads to the integral form of the averaged radiative transfer equation:

$$\overline{I_\nu(s,\Omega)} = \overline{I_{w\nu}(s_w,\Omega)\,\tau_\nu(s_w \to s)} + \int_{s_w}^{s} \overline{\frac{\partial \tau_\nu(s' \to s)}{\partial s'}}\;\overline{I_{b\nu}(s')}\, ds' \qquad (2)$$

In Eqs. (1) and (2), the emission term $I_{b\nu}(s)$ can be separately averaged since the Planck function does not present dramatic variations over the spectrum.

Following is the intensity on the opaque diffuse gray boundary walls:

$$\overline{I_{w\nu}(s_w,\Omega)} = \epsilon_w\,\overline{I_{bw\nu}(s_w)} + \frac{\rho_w}{\pi}\int_{\hat{n}.\Omega'<0} |\hat{n}.\Omega'|\,\overline{I_{w\nu}(s_w,\Omega')}\, d\Omega' \quad \text{for} \quad \hat{n}.\Omega' > 0 \qquad (3)$$

$\overline{I_{bw\nu}(s_w)}$ is the in-going intensity at the wall while $\hat{n}$ is the inward normal vector.

The discretized form of Eq. (2) provides the following expression of intensity at the control volume face i:

$$\overline{I_{\nu,n,i}} = \overline{I_{w\nu,n,1}\tau_{\nu,1\to i}} + \sum_{k=1}^{i-1}\left[\overline{I_{b\nu,n,k+1/2}}\,(\overline{\tau_{\nu,k+1\to i}} - \overline{\tau_{\nu,k\to i}})\right] \qquad (4)$$

where the subscripts ν, n, and i stand for the wavenumber, direction of angular discretization and spatial discretization, respectively; $i = 1$ corresponds to the wall.

At this point, using the following noncorrelated expressions: $\overline{\tau_{\nu,1\to i}} = \prod_{k=1}^{i-1}\overline{\tau_{\nu,k\to k+1}}$ and $\overline{I_{w\nu,n,1}\tau_{\nu,1\to i+1}} = \overline{I_{w\nu,n,1}\tau_{\nu,1\to i}}\;\overline{\tau_{\nu,i\to i+1}}$, one obtains the recursive form of the integrated equation for the intensity for noncorrelated narrow-band SN calculations:

$$\overline{I_{\nu,n,i+1}} = \overline{I_{\nu,n,i}}\;\overline{\tau_{\nu,i\to i+1}} + \overline{I_{b\nu,i+(1/2)}}\,(1 - \overline{\tau_{\nu,i\to i+1}}). \qquad (5)$$

Equations similar to Eq. (5) are obtained for each direction of the angular discretization. One interest of this technique is to use transmissivities between adjacent control volumes, so there is no need to introduce an approximation such as the Curtis–

Contributed by the Heat Transfer Division for publication in the JOURNAL OF HEAT TRANSFER. Manuscript received by the Heat Transfer Division May 22, 1995; revision received March 11, 1996. Keywords: Modeling and Scaling, Numerical Methods, Radiation. Associate Technical Editor: B. W. Webb.

Copyright © 1996 by ASME

Downloaded 11 Dec 2010 to 193.140.21.150. Redistribution subject to ASME license or copyright; see http://www.asme.org/terms/Terms_Use.cfm

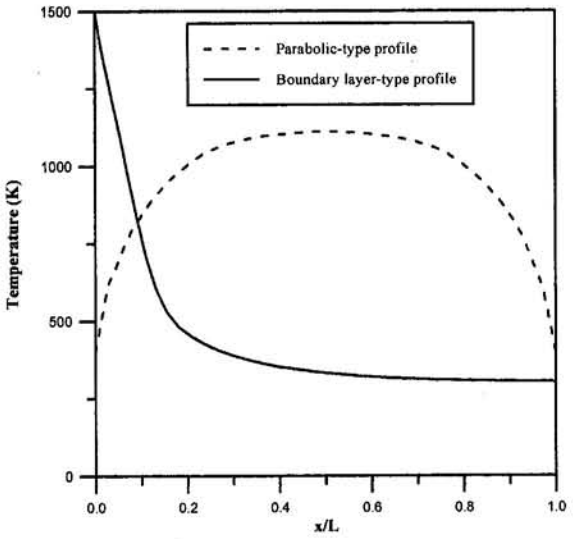


Fig. 1 Temperature profiles: parabolic and boundary layer type

Godson formal method, which is often used for nonhomogenous and nonisothermal media.

Averaged transmissivities over a narrow spectral interval are estimated for each control volume from the statistical narrow-band model with an exponential-tailed-inverse line-strength distribution (Malkmus, 1967; Young, 1977); the expression for the transmissivity for a given molar fraction of absorbing species f, through an isothermal and homogeneous path length $(s' \rightarrow s)$ under a total pressure p is:

$$\overline{\tau_\nu(s' \rightarrow s)} = \exp\left[-\frac{\overline{\beta_\nu}}{\pi}\left(\sqrt{1 + \frac{2\pi u \overline{k_\nu}}{\overline{\beta_\nu}}} - 1\right)\right] \quad \text{where}$$

$$u = fp.(s' \rightarrow s) \quad \text{and} \quad \overline{\beta_\nu} = 2\pi \frac{\overline{\gamma_\nu}}{\overline{\delta_\nu}} \quad (6)$$

$\overline{k_\nu}$ and $\overline{\delta_\nu}$ are spectral parameters for H_2O obtained by Soufiani and Taine (1985) and Hartmann et al. (1984), from line-by-line calculations.

The mean half-width $\overline{\gamma_\nu}$ is obtained from the general expression given by Zhang et al. (1988). For pure water ($f_{H_2O} = 1$), $\overline{\gamma_\nu}$ can be expressed as:

$$\gamma_{\nu H_2O} = 0.066 \frac{P}{P_S}\sqrt{\frac{T_S}{T}}\left\{7.0\sqrt{\frac{T_S}{T}} + 1.2\right\} \quad (7)$$

All parameters are averaged over a 25 cm^{-1} interval. The spectral range considered lies between 150 and 5675 cm^{-1}. P_s and T_S are respectively standard pressure and temperature (1 atm, 296 K), while the pressure P is set to 1 atm for our calculations.

Results and Discussion

Radiative Source Distributions. The volumetric radiative source distribution $(-dq/dx)$ is calculated for two temperature profiles, presented in Fig. 1. The parabolic temperature profile is taken from Zhang et al. (1988), and the second one corresponds to a combined radiation-convection boundary layer solution from Kim's doctoral dissertation (1990). These specific temperature distributions, as well as the gray wall reflectivities ($\rho_1 = 0.9$, $\rho_2 = 0.1$), and the slab thickness ($L = 0.5$ m), are selected to run calculations in similar configurations to those studied by Menart et al. (1993).

Narrow-band calculations are carried out in the three spectral intervals where the water vapor absorption is more intense: ν = 150 cm^{-1} to 2325 cm^{-1}, 2900 cm^{-1} to 4275 cm^{-1}, and 4900 cm^{-1} to 5675 cm^{-1}. For the angular discretization a Gaussian quadrature with 20 directions is used. The slab is divided into 20 sublayers.

In Fig. 2 are presented radiative source distributions obtained with the integral approach. Results are compared with the Menart and Lee (1991) calculations with what the authors call the "first-degree closure" formulation in which spectral correlations are accounted for and wall reflection explicitly treated.

Figure 2(a) corresponds to the parabolic temperature profile. For this case the error close to the highly reflecting wall is negligible. The largest error is in the center of the cavity where the integral approach underestimates the radiative source of about 11 percent. Close to the low reflecting wall, the integral approach overestimates $(-dq/dx)$ by about 5 percent.

Changes in the gas behavior from net emitter in the center of the slab to net absorber near walls are perfectly accounted for with our integral approach as well as with the first-degree closure. Similar calculations are presented in Fig. 2(b), for the boundary-layer type temperature profile. Here the gas behavior changes from a net emitter at the hot reflecting wall ($x = 0$) in the thermal boundary layer to a net absorber at the cold, almost black, wall ($x = L$). Outside the boundary layer ($x/L > 0.2$), $-(dq/dx)$ decreases slowly toward zero following the variation

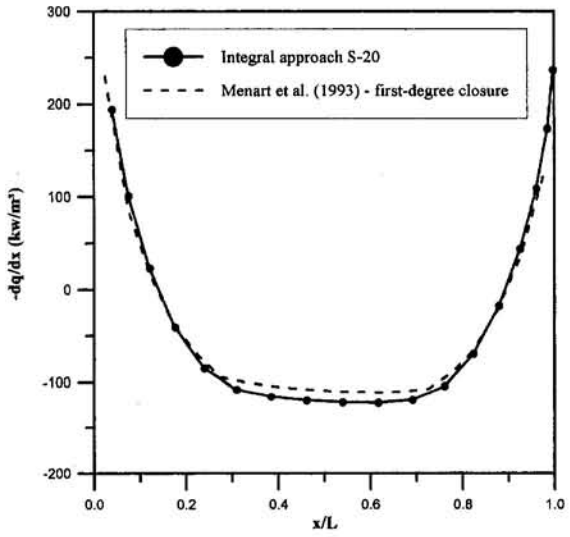


Fig. 2(a) Parabolic type temperature profile

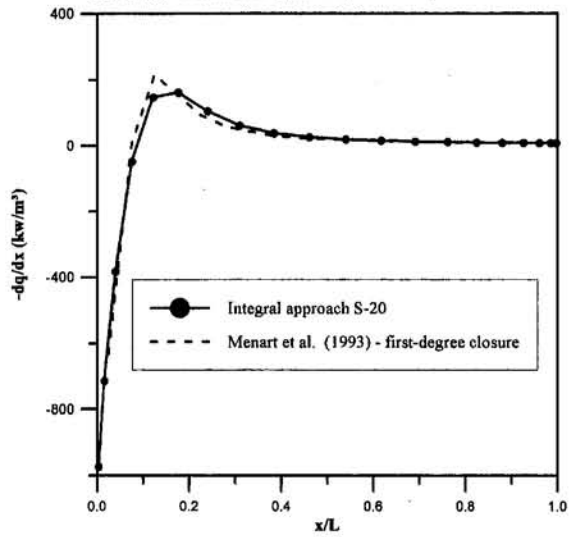


Fig. 2(b) Boundary-layer type temperature profile

Fig. 2 Radiative source distribution: L = 0.5 m, ρ_1 = 0.9, ρ_2 = 0.1

Downloaded 11 Dec 2010 to 193.140.21.150. Redistribution subject to ASME license or copyright; see http://www.asme.org/terms/Terms_Use.cfm

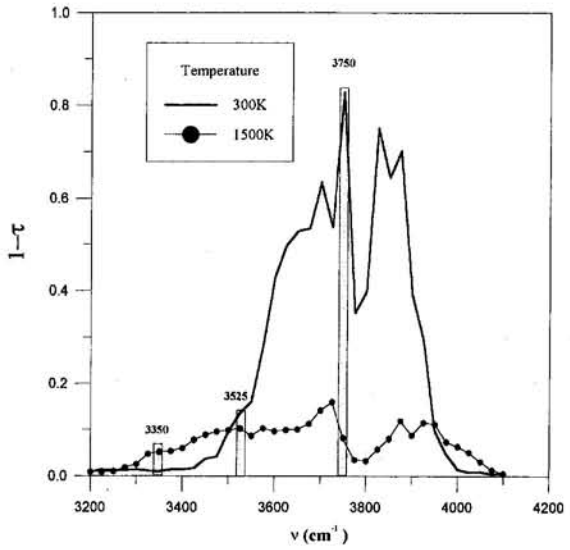


Fig. 3 Low resolution absorption spectra for water vapor, for a 8.33 cm sublayer

of the temperature gradient. The integral formulation shows no discrepancies close to the walls. It must be noted that the maximum difference of about 30 percent that can be observed at the limit of the boundary layer can be reduced to 14 percent by using a 45-point grid. These calculations are not presented here. An attempt to reduce the error by increasing the grid size showed that the solution was no longer grid dependent when the number of points was larger than 45. These calculations also allow us to conclude that more points are needed in areas where the temperature gradient is important.

These calculations, performed on an Apollo HP 425 workstation, require only 150 s for 20 points (300 s for 45 points); the convergence criterion on the intensity calculations is 0.1 percent. A second step consists in approaching the impact of no correlations on the integral approach itself, for a given temperature profile in the cavity filled with water vapor.

Single Beam Intensity. The radiative intensity is calculated along a single path in a specific direction Ω, starting from a black wall ($x = 0$, $\rho_1 = 0$), crossing a gas water vapor slab, and coming back after a specular reflection on the other wall ($x = L$, $\rho_2 = 1$). Calculations are performed with a boundary-layer type temperature profile. These intensities are obtained from Eqs. (4) and (5) for the correlated and noncorrelated results, respectively. For the correlated solutions, the nonuniform temperature is handled by using the Curtis–Godson approximation. The gas slab is divided into six control volumes. Figure 3 represents the water vapor absorption band centered on 3700 cm^{-1}, for the temperature inside the boundary layer ($T = 1500$ K), and for the cold gas temperature ($T = 300$ K) that occupies most of the cavity. Three typical narrow bands ($\Delta\nu = 25$ cm^{-1}) located at 3750 cm^{-1}, 3525 cm^{-1}, and 3350 cm^{-1} are considered for calculations of correlated and noncorrelated intensities. Integrated intensities over $\Delta\nu$ in the three intervals, and over the range 150–5675 cm^{-1}, are presented in Fig. 4. A comparison between transmissivities (τ) obtained from the correlated and noncorrelated methods shows that correlation effects are more noticeable on small transmissivities.

In the narrow band centered on 3750 cm^{-1} the slab is optically thick because of the high absorption of the cold gas areas that occupy most of the layer.

As a consequence, the radiative energy emitted by the hot boundary layer region is blocked and as the beam receives low energy from the cold layers, the integrated intensity decreases rapidly toward zero. Then even if the difference between correlated and noncorrelated intensities reaches 17 percent, their contribution to the integrated intensity over the whole spectrum is very small. The narrow band centered on 3350 cm^{-1} is characterized by high transmissivities in most of the gas slab, making the no-correlation effects less noticeable as said above; the error on the integrated intensities is about 8 percent.

In the last band centered on 3525 cm^{-1}, mean values of transmissivities are obtained in the hot gas layers as well as in the cold ones. Thus errors between correlated and noncorrelated intensities are greater than in the two previous bands. Here an important fraction of the radiative energy coming from the hot gas layer is transmitted by the cold gas layer and correlations are very significant. Calculations performed in the two other absorbing bands encountered between 150 cm^{-1} and 5675 cm^{-1} showed similar behavior.

When considering the intensity integrated over the whole spectrum, also presented in Fig. 4, errors between correlated and noncorrelated calculations stay lower than 10 percent. For the considered temperature profile, the contribution of intensities in the center of the absorbing band appears less significant than contribution of intensities in transparent bands.

Conclusion

The purpose of this work was to develop a model for solving the radiative transfer equation in nongray gases. The algorithm should combine a reasonable level of accuracy to a moderate computational effort in order to be adapted to industrial applications.

A noncorrelated integral approach combining a SN method with a statistical narrow-band gas model is introduced. Preliminary tests were carried out for a one-dimensional rectangular gas slab, with two temperature profiles and a uniform water vapor concentration. Results are compared with the ones obtained by a previous correlated model requiring much more computing efforts. These tests indicate that in spite of neglecting spectral correlations, the resulting intensity field stays fairly accurate and the calculations are compatible, in terms of computing cost, with engineering applications.

In this model, as only transmissivities between adjacent gas columns are involved in calculations, nonhomogeneous and nonisothermal aspects of the medium are implicitly accounted

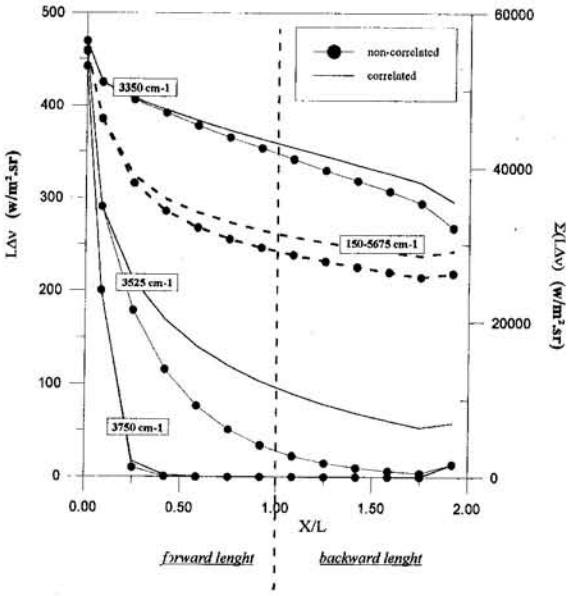


Fig. 4 Integrated normal intensity over $\Delta\nu = 25$ cm^{-1} versus X/L, for three narrow bands centered on $\nu = 3750$ cm^{-1}, 3525 cm^{-1}, 3350 cm^{-1}. Integrated intensity over the whole spectrum versus X/L. $L = 2 \times 0.5$ m; $\rho_1 = 0$, $\rho_2 = 1$. Boundary-layer type temperature profile.

Downloaded 11 Dec 2010 to 193.140.21.150. Redistribution subject to ASME license or copyright; see http://www.asme.org/terms/Terms_Use.cfm

for. As a consequence, the computing time is significantly reduced.

This algorithm offers possibilities for modeling radiative transfers in gases in a more complex geometry. In addition the coupling between radiation and other heat transfer modes, such as conduction or convection, commonly found in most engineering applications, can be considered.

Acknowledgments

The authors are grateful to Dr. A. Soufiani, from Ecole Centrale de Paris, EM2C, who provided the data files on spectral radiative properties for the narrow band calculations.

References

Buckius, R. O., 1982, "The Effect of Molecular Gas Absorption on Radiative Heat Transfer With Scattering," ASME JOURNAL OF HEAT TRANSFER, Vol. 104, pp. 580–586.

Edwards, D. K., and Menard, W. A., 1964, "Comparison of Models for Correlation of Total Absorption," *Applied Optics,* Vol. 3, pp. 621–625.

Edwards, D. K., 1976, "Molecular Gas Band Radiation," *Advances in Heat Transfer,* Vol. 12, Academic Press, New York, pp. 115–193.

El-Wakil, N., 1991, "Etude de Transferts de Chaleur par Conduction, Convection et Rayonnement Couplés dans des Milieux Semi-Transparents Fluides ou Poreux. Elaboration de Modèles de Simulation en Géométrie Bidimensionnelle," Thèse de Doctorat, INSA de Lyon, France: Order No. 91 ISAL 0050.

El-Wakil, N., and Sacadura, J. F., 1992, "Some Improvements of the Discrete Ordinates Method for the Solution of the Radiative Transport Equation in Multidimensional Anisotropically Scattering Media," *Developments in Radiative Heat Transfer,* S. T. Thynell, M. F. Modest, and L. C. Burmeister, eds., ASME HTD-Vol. 203, pp. 119–128.

Godson, W. L., 1953, "The Evaluation of Infrared Radiation Fluxes Due to Atmospheric Water Vapor," *Quarterly Journal of the Royal Meteorological Society,* Vol. 79, pp. 367–379.

Hartmann, J. M., Levi, D., Leon, R., and Taine, J., 1984, "Line-by-Line and Narrow-Band Statistical Model Calculations for H_2O," *J. Quant. Spectrosc. Radiat. Transfer,* Vol. 32, pp. 119–127.

Kim, T. K., 1990, "Radiation and Combined Mode Heat Transfer Analyses in Absorbing, Emitting and Mie-Anisotropically Scattering Media using the S-N Discrete Ordinates Method," Ph. D. dissertation, University of Minnesota, Minneapolis, MN.

Kim, T. K., Menart, J. A., and Lee, H. S., 1991, "Nongray Radiative Gas Analyses Using the S-N Discrete Ordinates Method," ASME JOURNAL OF HEAT TRANSFER, Vol. 113, pp. 946–952.

Menart, J. A., and Lee, H. S., 1991, "S-N Discrete Ordinates Solutions of Non gray Radiative Transfer with Diffusely Reflecting Walls," *Fundamentals of Radiation Heat Transfer,* W. A. Fiveland, A. L. Crosbie, A. M. Smith, and T. F. S. Smith, eds., ASME HTD-Vol. 160, pp. 79–87.

Malkmus, W., 1967, "Random Lorentz Band Model With Exponential-Tailed S-1 Line-Intensity Distribution Function," *Journal of the Optical Society of America,* Vol. 57, No. 3, pp. 323–329.

Menart, J. A., Lee, H. S., and Kim, T. K., 1993, "Discrete Ordinates Solutions of Nongray Radiative Transfer With Diffusely Reflecting Walls," ASME JOURNAL OF HEAT TRANSFER, Vol. 115, pp. 184–193.

Soufiani, A., and Taine, J., 1987, "Application of Statistical Narrow-Band Model to Coupled Radiation and Convection at High Temperature," *International Journal of Heat and Mass Transfer,* Vol. 30, No. 3, pp. 437–447.

Taine, J., 1983, "A Line-by-Line Calculation of Low-Resolution Radiative Properties of CO_2-CO-Transparent Nonisothermal Gas Mixtures Up to 3000 K," *J. Quant. Spectrosc. Radiat. Transfer,* Vol. 90, pp. 371–379.

Young, S. J., 1977, "Nonisothermal Band Model Theory," *J. Quant. Spectrosc. Radiat. Transfer,* Vol. 18, pp. 1–28.

Zhang, L., Soufiani, A., and Taine, J., 1988, "Spectral Correlated and Noncorrelated Radiative Transfer in Finite Axisymetric System Containing an Absorbing and Emitting Real Gas-Particle Mixture," *International Journal of Heat and Mass Transfer,* Vol. 18, pp. 2261–2272.

Downloaded 11 Dec 2010 to 193.140.21.150. Redistribution subject to ASME license or copyright; see http://www.asme.org/terms/Terms_Use.cfm

Transition Boiling Curves in Saturated Pool Boiling From Horizontal Cylinders

E. K. Ungar
Senior Thermal Analyst,
Crew and Thermal Systems Division,
NASA, Johnson Space Center,
Houston, TX 77058
Mem. ASME

R. Eichhorn
Professor of Mechanical Engineering and Dean,
Cullen College of Engineering,
University of Houston,
Houston, TX 77204
Fellow ASME

Pool boiling heat flux versus wall superheat boiling curves were obtained for horizontal 3.18-mm-dia thin-walled brass tubes heated by an internal high-speed flow of ethylene glycol. The boiling liquids were saturated n-pentane, R-113, acetone, methanol, ethanol, benzene, and isopropanol. Boiling results include nucleate and transition boiling in all the test liquids, but film boiling was achieved only with methanol. The measured peak heat fluxes are well correlated by available predictions. The methanol experiments clearly display two transition boiling curves, one obtained on increasing the cylinder temperature from nucleate boiling, the other on decreasing the cylinder temperature from film boiling. For the cases in which the highest cylinder temperature reached only into the transition regime, a single transition boiling curve resulted.

Introduction

Over the last fifty years, many studies have been performed to examine the heat flux versus wall superheat boiling curve and the peak heat flux in saturated pool boiling. This research has led to a broad understanding of the nucleate and film boiling regimes and to accurate methods of predicting the pool boiling peak heat flux from heaters in saturated liquids. In contrast, the nature of the boiling curve in the transition regime is not yet well understood, owing mainly to the difficulty of designing a steady-state experiment to operate in this regime. In this paper, we report a study of the boiling curve and the peak heat flux in saturated pool boiling from temperature controlled horizontal cylinders. Steady-state peak heat flux measurements were made in *n*-pentane, R-113, acetone, methanol, ethanol, benzene, and isopropanol. Detailed steady-state observations of at least part of the transition boiling regime were made in all liquids. The full transition boiling regime was studied for methanol.

Background

The Nature of the Boiling Curve. The transition boiling regime has conventionally been represented as a unique line on the heat flux versus wall superheat boiling curve. However, Witte and Lienhard (1982) proposed that the transition regime should not be considered as a third boiling regime, but as extensions of nucleate and film boiling, as shown in Fig. 1. This implies that the boiling curve is dual valued in the transition regime and thus, at a given heater temperature, there are two possible transition boiling heat fluxes. The higher heat fluxes of nucleate transition boiling occur as the heater surface temperature increases from nucleate boiling and the lower heat fluxes of film transition boiling occur as the temperature decreases from film boiling. Witte and Lienhard based their argument on quenching results from various sources and on previously discounted data from Berenson's (1960) steady-state horizontal flat plate boiling experiments. Other steady-state measurements of the full boiling curve had shown no indication that there were two possible states in the transition regime. Hesse (1973) and Yilmaz and Westwater (1980) obtained transition boiling heat flux and surface temperature data for temperature controlled horizontal cylinders boiling saturated Freons. However, these experiments were performed only in the direction of increasing cylinder temperature and thus would have disclosed only nucleate transition boiling. Other experiments (e.g., Sakurai and Shiotsu, 1974) purporting to show steady-state transition boiling results were actually examples of co-existing nucleate and film boiling in different longitudinal locations on the same heater surface.

Some of the experiments performed after Witte and Lienhard proposed the existence of two boiling curves supported their conclusions, while others showed no evidence of two states in the transition boiling regime. Broussard and Westwater's (1985) steady-state boiling experiments on temperature-controlled horizontal cylinders in saturated R-113 showed no indication of two boiling curves. However, their experiments were performed only in the direction of increasing cylinder temperature and thus would not have disclosed film transition boiling.

Bui and Dhir (1985) and Liaw and Dhir (1986) performed transient quenching and steady-state boiling experiments on a 103.4-mm-tall vertical electrically heated copper plate in saturated water and R-113. Their experiment was designed to allow steady-state heating in nucleate boiling, in film boiling, and in a small region of transition boiling near the minimum heat flux. It also allowed transient heating from nucleate boiling and slow quenching from film boiling. They found that, for fluid/surface combinations with poor wettability (contact angle of 108 deg for a water/fluorosilicone sealant combination) the peak heat fluxes during their slow quenches were as much as 60 percent lower than those measured during heating from nucleate boiling. Their experiments where the surface wettability was high (an oxidized copper surface with water and a polished copper surface with R-113) showed little difference between the peak heat fluxes in the two cases. However, in these cases there was some evidence of different transition boiling curves being followed upon heating from nucleate boiling and upon cooling from film boiling.

Ramilison and Lienhard (1987) used condensing steam to heat wetting and nonwetting horizontal flat plates in R-113 and various organic liquids. Their steady-state heat flux versus wall superheat data showed that, at a given heater temperature, the measured transition boiling heat flux varied with the wettability of the surface. Ramilison and Lienhard proposed that the transition boiling process is governed by the contact angle of the liquid with the heater surface. When the surface temperature increases from nucleate boiling, the surface becomes increasingly dry and the process should be governed by the receding contact angle. Thus the nucleate transition boiling curve is fol-

Contributed by the Heat Transfer Division for publication in the JOURNAL OF HEAT TRANSFER. Manuscript received by the Heat Transfer Division February 18, 1995; revision received May 17, 1996. Keywords: Boiling, Phase-change phenomena. Associate Technical Editor: V. K. Dhir.

Copyright © 1996 by ASME

Downloaded 11 Dec 2010 to 193.140.21.150. Redistribution subject to ASME license or copyright; see http://www.asme.org/terms/Terms_Use.cfm

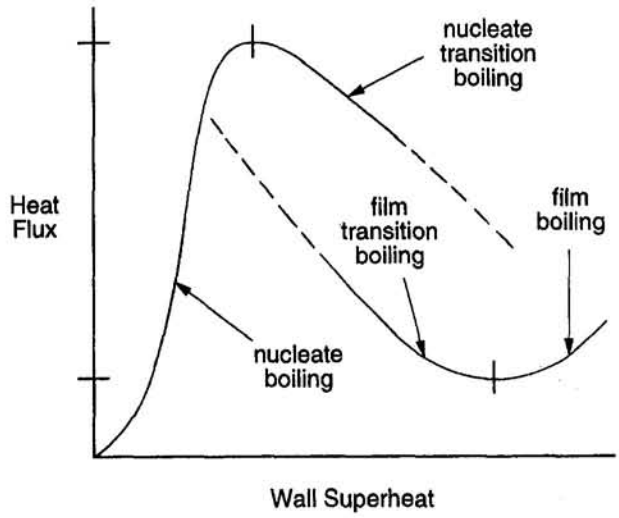


Fig. 1 Two transition boiling curves, from Witte and Lienhard (1982)

lowed. If the surface temperature decreases from film boiling, the surface progressively wets. In this case, the advancing contact angle governs the process and the boiling process follows the lower heat flux film transition boiling curve.

Haramura (1991) redesigned Ramilison and Lienhard's apparatus to enhance the film coefficient of the condensing steam. He obtained incomplete heat flux versus wall superheat curves for R-113 boiling above a 63.5-mm-dia 15.2-mm-thick copper plate. Three plate finishes were used, ranging from rough to mirror finish. Boiling curves were obtained in both the direction of increasing surface temperature from nucleate to film boiling and the direction of decreasing surface temperature from film to nucleate boiling. The measurements obtained in the transition regime showed no hysteresis. However, experiment limitations prevented Haramura from obtaining measurements throughout the transition region for any of the surfaces. His results show large gaps in the transition boiling regime from approximately 50 percent of q_{max} to near q_{max}.

Auracher (1992) performed steady-state boiling experiments for R-113 boiling on the upper end of an 11.3-mm-dia 30-mm-thick, electrically heated vertical copper cylinder. The boiling surface was mounted flush and concentric with an insulating surface 40 mm in diameter. The entire unit was mounted in the center of a much larger tank of R-113. By using a feedback heater controller to maintain the boiling surface temperature, Auracher was able to obtain complete steady-state boiling heat flux versus wall superheat curves in both the increasing and decreasing surface temperature directions. He too found no hysteresis in the transition boiling regime.

The hypothesis of the two transition boiling curves has been supported by the results of transient experiments (Bui and Dhir, 1985; Liaw and Dhir, 1986) and in steady-state experiments using heater surfaces with varying wettability (Berenson, 1960; Ramilison and Lienhard, 1987). The steady-state experiments that have more completely mapped the transition regime (Haramura, 1991; Auracher, 1992) have shown no hysteresis.

Steady-State Experimental Techniques. Investigations of steady-state boiling from cylindrical heaters have used three basic experimental techniques. Cylindrical resistance heaters can be heated by simple variable voltage sources, as in Nukiyama (1937). In this case, the heat flux is prescribed and only nucleate and film boiling can be studied. Alternately, a feedback controller can be used with an electric power source to control the temperature of the heater, as in Sakurai and Shiotsu (1974). Typically, the net resistance of the heater is used to provide the temperature measurement to the feedback circuit. This type of experimental technique can be successfully used to study nucleate and film boiling. However, when the average heater temperature is between ΔT_{max} and ΔT_{min}, the wire temperature can have extreme variation along its length. This allows nucleate and film boiling to coexist on the wire. Thus, no true transition boiling is obtained. In the third technique, the cylinder is heated from within by condensing steam (Yilmaz and Westwater, 1980; Broussard and Westwater, 1985) or a hot flowing liquid (Hesse, 1973). This technique prescribes the surface temperature and, if the net thermal resistance of the heater and the heating fluid film is small enough, allows operation at any point on the boiling curve.

Flat plate boiling experiments have been performed using two techniques. The heater surface can be heated from beneath by condensing steam (Berenson, 1960; Ramilison and Lienhard, 1987; Haramura, 1991). Here, as for cylindrical heaters, all regions of the boiling curve are accessible if the net thermal resistance of the heater and the heating fluid film is small enough. Alternately, a feedback controller can be used on a massive heater block (Auracher, 1992). According to Auracher, with good control this technique gives access to all regions of the boiling curve.

We have constructed an apparatus that uses a high-speed flow of ethylene glycol to heat thin wall brass tubes. Ethylene glycol has a high boiling point, which allows us to study boiling in multiple liquids. The cylindrical heater operates at steady state or in increasing or decreasing heater temperature modes.

Nomenclature

A_{tube} = outside surface area of tube, m^2
c_p = heat capacity, kJ/kg K
D = diameter of heater, m
D_i = inside diameter of tube, m
EG = ethylene glycol
g = gravitational acceleration = 9.81 m/s^2
h = convective heat transfer coefficient, kW/m^2K
k_t = correction factor
k_s = thermal conductivity of a solid, kW/m K
$\dot{m}$ = mass flow rate, kg/s
Pr = Prandtl number
q = heat flux, kW/m^2
q_{max} = peak nucleate boiling heat flux, kW/m^2
q_{min} = minimum film boiling heat flux, kW/m^2
R_{int} = thermal resistance of convective layer = $D/(hD_i)$, m^2K/kW
R_{tube} = wall thermal resistance = $D \ln (D/D_i)/(2k_s)$, m^2K/kW
T = temperature, K
Re_{D_i} = Reynolds number = $\rho_f V_t D_i/\mu_f$
T_i = inlet temperature measured by RTD, K
T_o = outlet temperature measured by RTD, K
T_{sat} = saturation temperature of liquid, K
T_{wall} = wall temperature of heater, K
ΔT = wall superheat temperature = $(T_{wall} - T_{sat})$, K
ΔT_{max} = wall superheat temperature at q_{max}, K
ΔT_{min} = wall superheat temperature at q_{min}, K
V_t = velocity of flow in tube, m/s
x = length along the tube, m
λ_d = Taylor wavelength = $2\pi\sqrt{3}\sqrt{\sigma/[g(\rho_f - \rho_g)]}$, m
μ_f = liquid viscosity, N s/m^2
ρ_f = liquid density, kg/m^3
ρ_g = vapor density, kg/m^3
σ = surface tension, N/m

Downloaded 11 Dec 2010 to 193.140.21.150. Redistribution subject to ASME license or copyright; see http://www.asme.org/terms/Terms_Use.cfm

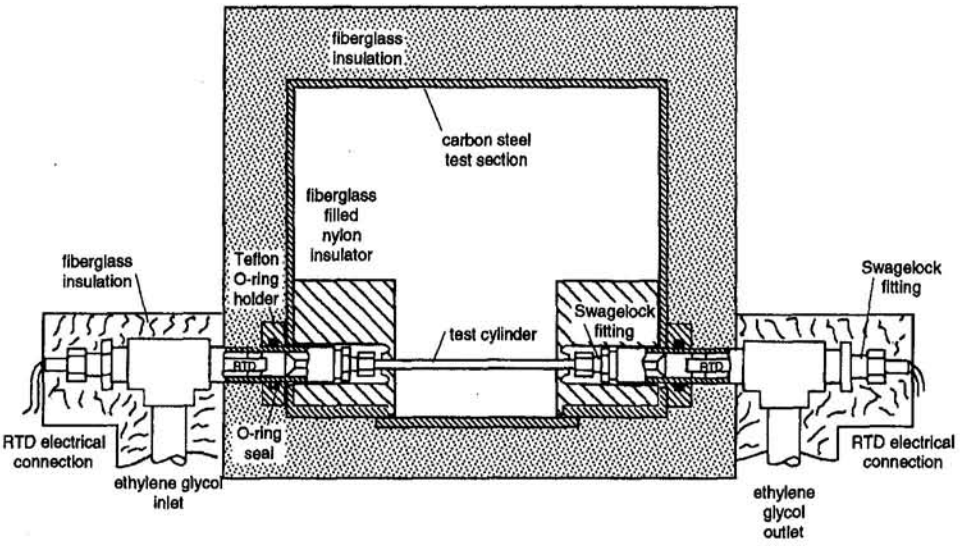


Fig. 2 Test section with EG heated cylinder

Peak Heat Flux in Pool Boiling. In the present work, the experimental procedure yields the peak heat flux as well as nucleate, transition, and film boiling results. We therefore report peak heat flux and wall superheat measurements for saturated pool boiling from a 3.18-mm-dia cylinder in multiple test liquids, and compare the peak heat flux results to the results and predictions available in the literature.

Experiment

Apparatus. The experimental study of pool boiling from horizontal cylinders was performed in the insulated test section shown in Fig. 2. The test section consisted of a galvanized steel box with two plate glass viewing windows. An electric immersion heater maintained the desired bulk liquid temperature. The vapor generated during the experiment was condensed by a water-cooled condenser above the test section. The condenser was open to the atmosphere and, thus, the liquid at the test heater was at a pressure slightly higher than the atmosphere owing to the static liquid head. A precision mercury thermometer and a bronze diaphragm pressure gage mounted in the test section were used to measure the temperature and gage pressure near the test cylinder. The local atmospheric pressure was measured by a mercury barometer.

A 3.18-mm-OD circular brass tube with 0.36-mm-thick walls was held rigidly 30 mm above the bottom of the test section. The active length of this test cylinder (the length between the insulating blocks) was 101.6 mm. The test cylinder was heated internally by Dowtherm SR-1 inhibited ethylene glycol (EG) (95.5 percent EG, 4.5 percent inhibitors by weight) flowing at an average velocity of approximately 40 m/s. The EG was stored in a reservoir that could be heated or cooled to maintain its temperature at any desired point between 300 and 425 K. A triplex positive displacement pump circulated the EG between the reservoir and the test cylinder. The EG mass flow rate was measured by a calibrated ASME (1959) standard orifice.

The temperature of the EG at the inlet and outlet of the test cylinder was measured by resistance temperature detectors (RTDs) installed on the test cylinder centerline within 20 mm of the inlet and outlet of the test tube. The RTDs were commercial platinum wire wound resistance thermometers mounted inside 4.76 mm stainless steel sheaths. The RTDs were connected electrically to a metal film resistor bridge to allow measurement of the temperature at the inlet of the test cylinder and extremely accurate measurement of the temperature difference across the test cylinder.

Calibration. The RTDs were calibrated individually against a ±0.1 K mercury thermometer and as a pair in an insulated well-stirred EG bath. The bath was heated to 425 K and allowed to cool slowly to room temperature.

Hydraulic losses and temperature recovery factors affect the temperatures measured by the RTDs mounted at the ends of the test cylinder. To account for this effect, we define a correction factor,

$$k_t = \frac{2c_p}{V_t^2}(T_o - T_i) \tag{1}$$

where V_t is the average liquid velocity in the tube, c_p is the specific heat of the EG, and T_o and T_i are the outlet and inlet temperatures measured by the RTDs if the tube is adiabatic.

An in situ calibration of the correction factor was performed after every five test runs. The test section was drained and the test cylinder was heavily insulated. The EG loop was then run at the test conditions over the entire operating temperature range. During the calibration, the temperature indicated by the outlet RTD was 0.4 to 1.0 K higher than that measured by the inlet RTD.

The correction factor k_t is a function of both the Reynolds number in the tube and the Prandtl number of the liquid (Eckert and Drake, 1972). However, because the calibration was performed at the same EG flow rate as was used in the experiments, it was sufficient to determine k_t only as a function of the ethylene glycol temperature measured by the inlet RTD.

Experimental Technique. Pool boiling experiments were performed in reagent grade n-pentane, R-113, acetone, methanol, ethanol, benzene, and isopropanol. Before each experiment, the test cylinder was cleaned with 0000 steel wool and polished with Brasso brass polish. The tube was then rinsed with acetone and wiped dry. The test section was filled with the test liquid (approximately 12 liters), heated to saturation, and boiled vigorously for at least 15 minutes to allow degassing. While the liquid was degassing, the EG reservoir was heated to a temperature near that of the test liquid. After the experiment was begun, the test section immersion heater was manually adjusted to maintain the liquid temperature within 0.2 K of saturation.

During an experiment, the temperature of the EG reservoir was increased by approximately 0.008 K/s to its maximum operating temperature of 425 K. The test liquid temperature, the EG orifice pressure drop, and the bridge voltages were recorded manually at EG temperature intervals of 3K or less. Each test

Downloaded 11 Dec 2010 to 193.140.21.150. Redistribution subject to ASME license or copyright; see http://www.asme.org/terms/Terms_Use.cfm

run took approximately three hours to traverse the boiling curve from the test liquid saturation temperature to 425 K.

In addition to these normal test runs, experiments were performed in n-pentane, acetone, methanol, and ethanol by cooling the EG reservoir from 425 K to the saturation temperature of the test liquid. The EG temperature decreased at a rate of approximately 0.008 K/s during these tests. Other experiments involved heating and cooling at approximately 0.008 K/s between the temperature limits several times in succession.

The boiling process was recorded at 1000 frames per second by a Kodak SP-2000 high-speed video system. The video system simultaneously records both the image and the elapsed time. Experiments in each test liquid were filmed over the entire range of EG temperatures.

Analysis. The heat flux from the temperature-controlled cylinders was determined from an energy balance on the ethylene glycol flow. The EG mass flow rate, $\dot{m}$, was determined from the pressure drop across the flow metering orifice. The liquid temperature was taken as the temperature measured by the inlet RTD. The heat flux from the tube was then calculated from

$$q = \frac{\dot{m}c_p}{A_{\text{tube}}}\left(T_i - T_o + k_t\frac{V_t^2}{2c_p}\right) \tag{2}$$

where A_{tube} is the outside surface area of the test cylinder. The quantity $[T_i - T_o + k_t V_t^2/(2c_p)]$ had a maximum value of 2.1 K in the experiments.

The average temperature of the heater surface was inferred from thermal resistance principles, taking the EG temperature to be the measured inlet temperature. The internal convection coefficient was calculated from Petukhov's (1970) correlation for fully developed turbulent flow in a tube. In the calculation, internal convection was 90–95 percent of the total resistance, with the tube wall accounting for the remainder.

The physical properties of the ethylene glycol as a function of temperature were determined from the data of Dow (1982). These variable properties were used in the calibration, in the data reduction, and in the analysis. The physical properties of the test liquids were taken from Vargaftik (1975) and Spalding and Taborek (1983).

A more detailed description of the construction, calibration, and operation of the experimental apparatus is given by Ungar (1987) and Ungar and Eichhorn (1988).

Uncertainty. The uncertainty in the calculated average heater surface temperature is caused by instrumentation, or bias error. The uncertainty in the average tube surface temperature has two components, the EG temperature measurement uncertainty and the uncertainty in the calculation of the temperature difference between the EG and the tube surface. The maximum calculated average temperature difference between the EG and the tube surface is 12.5 K with an uncertainty of ±6 percent (calculated from the EG flow rate and property uncertainty). The EG temperature varies through the tube by as much as 1 K and is measured at the tube entrance to within ±0.6 K. Thus the average surface temperature is known to within an uncertainty of ±2 K.

The uncertainty in the calculated tube heat flux has two components, the instrumentation or bias error and the calibration to calibration uncertainty. The components are:

- instrumentation uncertainty in measuring the EG mass flow rate (±2.4 percent) from the EG temperature and the pressure difference across the orifice plate.
- uncertainty in measuring the inlet temperature at the test section (±0.6 K) which causes an uncertainty of ±0.1 percent in the value of the EG specific heat.
- uncertainty in measuring the temperature difference across the test section (±0.01 K from the EG bath calibration), which yields an uncertainty of ±5.4 kW/m^2, independent of the heat flux.
- uncertainty in the correction factor, which was determined from the variation from calibration to calibration. This component yields a total uncertainty in the value of the tube heat flux of ±30 kW/m^2, independent of the absolute value of the heat flux.

Combining the four components at the largest measured value of heat flux yields a total uncertainty of ±33 kW/m^2. The uncertainty at lower values of the heat flux is only slightly smaller, so we take the uncertainty in the heat flux to be ±33 kW/m^2 independent of the absolute value of the heat flux.

Entrance Effects in the Test Cylinder. The Prandtl number, Pr, of the EG in the cylinder ranged from 100 at the lowest temperature of 315 K to 10 at the maximum temperature of 425 K. The Reynolds number, Re_{D_i}, ranged from 10,500 at the lowest temperature to 120,000 at the highest temperature. The test cylinder has an adiabatic length of 20 diameters upstream of the boiling section. This entrance length is sufficient to allow the flow to be hydrodynamically fully developed for the range of operation (Lienhard, 1987). Using the work of Sleicher and Tribus (1956), Kays and Crawford (1980) calculated the constants required to analyze the thermal entry length for a hydrodynamically fully developed turbulent flow with constant heat flux at various values of the Reynolds number and Prandtl number. A calculation using these constants shows that, for constant Reynolds number, the entry length decreases as the Prandtl number increases. Also, for constant values of the Prandtl number, the entry length decreases as the Reynolds number decreases. Therefore, using our minimum value of Pr = 10 and a value of Re_{D_i} = 100,000 to calculate the thermal entry length is generally conservative for this apparatus. For this case, the Nusselt number is less than 110 percent of its asymptotic value at $x/D_i = 1$, where x is the length along the tube and D_i is the tube inner diameter. This is small compared to the 41 diameters of active length. The high-speed films of all the boiling regimes show that the vapor wake is visually identical at both ends of the test cylinder. This confirms that any thermal boundary layer effects present near the inlet end of the boiling surface were minimal and had little effect on the boiling process.

Accessibility of the Transition Boiling Regime. The ability of an apparatus to operate stably in the transition boiling regime can be determined using the stability criterion developed by Adiutori (1964) and Stephan (1965). The criterion states that transition boiling is stable only if

$$-\frac{dq}{dT} < \frac{1}{R_{\text{int}} + R_{\text{tube}}} \tag{3}$$

i.e., if the slope of the measured transition boiling curve is less steep than that of the characteristic heat transfer curve, which is calculated from the thermal resistances of the convective boundary layer, R_{int}, and the test cylinder, R_{tube},

$$-\frac{dq}{dT} = \frac{1}{R_{\text{int}} + R_{\text{tube}}} \tag{4}$$

The slope of the characteristic curves ranged from −25 to −50 kW/m^{2}K in our experiments. The absolute value of the slope increases with increasing ethylene glycol temperature owing to the variation of the EG physical properties. In the transition boiling regime for the methanol experiments, it was never larger than −35 kW/m^{2}K.

Steady-State Boiling. It is reasonable to expect that quasi-steady-state boiling is achieved when the characteristic relaxation time of an apparatus is small compared to the period of a significant temperature change. Expressed another way, if the temperature change over the characteristic time of the apparatus

Downloaded 11 Dec 2010 to 193.140.21.150. Redistribution subject to ASME license or copyright; see http://www.asme.org/terms/Terms_Use.cfm

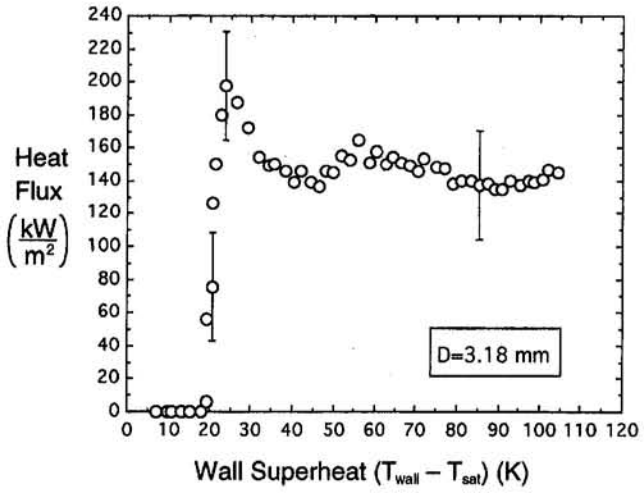


Fig. 3 R-113 saturated pool boiling curve: test sequence is in direction of increasing ΔT

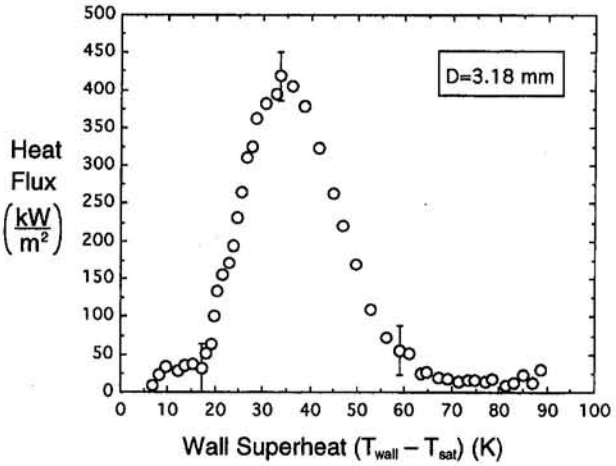


Fig. 4 Methanol saturated pool boiling curve: test sequence is in direction of increasing ΔT

is very small, then quasi-steady-state boiling should be obtained. If this is the case, the apparatus is able to adjust to small changes in the surface temperature.

For the present apparatus, there are three characteristic times: the transport time of the EG through the tube (0.003 s), the conduction time of the brass tube (0.004 s), and the conduction time through the EG viscous sublayer and the transition layer (0.144 s). The last time is the only one of significance. At the system temperature change rate of 0.008 K/s used in the experiment, this time translates to a temperature change of 0.001 K. Clearly, this is quasi-steady-state boiling.

Results and Discussion

Experimental Results. Figure 3 shows a typical saturated pool boiling curve for a horizontal 3.18 mm cylinder in R-113. This boiling curve was obtained with an initially polished brass tube by slowly increasing the temperature of the EG reservoir over a period of several hours. The heat flux measurement uncertainty is indicated in the figure. Similar boiling curves were obtained in *n*-pentane, acetone, ethanol, benzene, and isopropanol (these curves are available from Ungar, 1987, and Ungar and Eichhorn, 1993). None of the high-speed films taken near the maximum EG temperature of 425 K for *n*-pentane, R-113, acetone, ethanol, benzene, or isopropanol show a wake with the periodic bubble breakoff characteristic of film boiling. All the films show the random and more vigorous transition boiling regime at the EG upper temperature limit. Thus we conclude that only nucleate and transition boiling were obtained in these fluids.

We also obtained decreasing temperature saturated pool boiling curves in *n*-pentane, acetone, and ethanol. These experiments were performed by slowly decreasing the EG reservoir temperature from 425 K to the liquid saturation temperature. The decreasing temperature experiments in all these liquids began in a regime visually identifiable as transition boiling. Within the experimental uncertainty, the boiling curves in these liquids were indistinguishable from the increasing temperature boiling curves.

The fact that film boiling did not occur in our R-113 experiments, even at wall superheat temperatures as high as 105 K, is at odds with other data for R-113 in the literature. Broussard and Westwater reported q_{min} at a wall superheat of 45 K in their pool boiling experiments using a 3.18 mm tube. The minimum heat flux occurred at wall superheat temperatures ranging from 75 to greater than 110 K for the other tube sizes used in their R-113 experiments (1.59, 2.38, 4.75, 6.35, and 7.94 mm). Although the slope of the characteristic curve for their apparatus was not given in the paper, the unobtainable regions of the transition regime for the 7.94 mm tube (the only pointwise data in the paper) suggest a heat transfer characteristic no smaller than -10 kW/m^{2}K. Because this is the value of the characteristic for the largest tube used in their experiments, it is probably the steepest characteristic obtained in any of their experiments. The value of -10 kW/m^{2}K is only 30 percent of the value of the heat transfer characteristic of the present system. The tube in our experiment would tend to have significantly less temperature variation in the circumferential direction than would Broussard and Westwaters'. Thus it would more closely approach the ideal case of uniform tube wall temperature. This is the likely cause of the different behavior in the transition region found in our experiments.

Figures 4 and 5 show typical pool boiling curves for methanol, which has a small positive contact angle with the brass surface used in our experiments. Figure 4 was obtained in the direction of increasing wall superheat. Here the boiling curve extends into the film boiling regime. The high-speed films taken at the higher EG temperatures show a wake with the periodic bubble breakoff characteristic of film boiling. Figure 5 was obtained in a separate experiment by decreasing the cylinder temperature from the film boiling regime. Here a second transition boiling curve distinct from that in Fig. 4 was found.

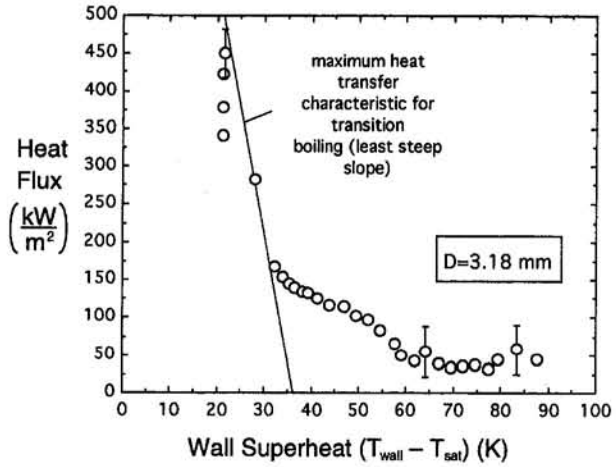


Fig. 5 Methanol saturated pool boiling curve: test sequence is in direction of decreasing ΔT

Downloaded 11 Dec 2010 to 193.140.21.150. Redistribution subject to ASME license or copyright; see http://www.asme.org/terms/Terms_Use.cfm

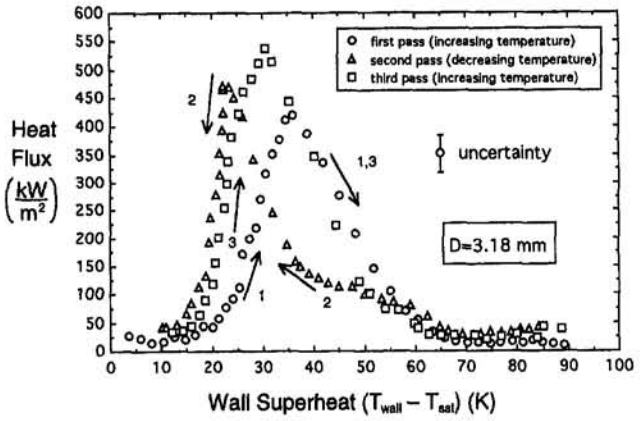


Fig. 6 Two transition boiling curves: pool boiling in saturated methanol

Figure 6 shows the methanol pool boiling curves obtained during an experiment in which the EG reservoir was successively heated, cooled, and heated again between the natural convection and film boiling regimes. The nucleate boiling results and the measured values of q_{max} differ between the passes owing to the buildup of a thin black powdery coating on the tube during the eight-hour experiment. The peak heat fluxes increase from pass to pass. This behavior is consistent with what would be expected from the increasing level of surface contamination that occurred in the test. However, the figure demonstrates the existence of two transition boiling curves, as was inferred from other experiments by Witte and Lienhard. The boiling curve followed in the transition regime during the third pass (increasing temperature) is clearly much more similar to the first pass (increasing temperature) than it is to the very different second pass (decreasing temperature). As Witte and Lienhard predicted, the higher heat flux nucleate transition boiling curve is followed as the cylinder temperature is increased from nucleate boiling and the lower heat flux film transition boiling curve is followed when the cylinder temperature is decreased from film boiling. This result does not agree with the transition boiling results of Haramura (1991) and Auracher (1992), who found only a single transition boiling curve in their experiments. This discrepancy is discussed below.

A careful comparison of Figs. 4, 5, and 6 shows that the transition boiling curve in Fig. 4 is virtually identical to the increasing temperature curves in Fig. 6 and that the transition boiling in Fig. 5 is virtually identical to the decreasing temperature curve in Fig. 6. The increasing and decreasing temperature experiments in methanol were performed several times and were found to be qualitatively repeatable. The nucleate transition boiling curve was followed in all the increasing temperature experiments and the film transition boiling curve was followed in all the experiments where the temperature was decreased from film boiling.

The high-speed films of transition boiling show that the vapor wake is uniform along the cylinder at each heater temperature. Therefore, we conclude that there is no longitudinal variation in the boiling process. If different modes of boiling do coexist on the cylinder, they must do so in the circumferential direction, which our visual techniques would be unable to resolve.

The peak heat fluxes in methanol measured as the surface temperature increased from nucleate boiling were similar to those measured as the surface temperature decreased from film transition boiling, as is shown in Figs. 4, 5, and 6. This agrees with the results obtained by Liaw and Dhir in their pool boiling experiments on a vertical copper plate in saturated water and R-113.

Comparison With Other Transition Boiling Experiments. Ramilison and Lienhard reported jumps between the film transition and nucleate transition boiling curves in their flat plate experiments. However, we did not observe any jumps between the two transition boiling curves during our experiments. The ethylene glycol temperature difference measured by the RTDs always changed smoothly, without the sudden changes that would occur during an abrupt change in the surface heat flux. The characteristic heat transfer curves in our experiments were four to six times as steep as in the experiments of Berenson (1960) and Ramilison and Lienhard (1987). This indicates that a local perturbation in the boiling process that could have caused the heat flux in their experiments to jump between the transition boiling curves would not have caused the same effect in our experiments. It appears that jumps between film transition boiling and nucleate transition boiling are not inevitable, although they certainly are possible.

Haramura (1991) and Auracher's (1992) experiments in pool boiling from flat plates showed no hysteresis in the transition boiling regime. There are notable differences between our experiment and theirs:

- Auracher's flat plate had a diameter of 11.3 mm because it had been originally designed to study boiling from electronic components. This is only slightly larger than the most dangerous Taylor wavelength of R-113 (λ_d = 10.9 mm). Because of the small diameter, classical film boiling would not occur on the plate. There is insufficient area for the standing waves and periodic bubble breakoff characteristic of film boiling on a large plate to occur. Therefore, Auracher's results are specific to small heaters. In the present experiments, the cylinder length of 101.6 mm is much greater than the most dangerous Taylor wavelength of the fluids (16.9 mm in *n*-pentane, 10.9 mm in R-113, 17.2 mm in acetone, 17.4 mm in methanol, 16.8 mm in ethanol, 17.7 mm in benzene, and 17.5 mm in isopropanol). Hence, the data of the present work are representative of a cylinder of infinite length.
- Haramura's flat plate was 63.5 mm in diameter, which is large enough to approximate an infinite flat plate. But, because of the characteristic heat transfer curve of -18 kW/m^{2}K for his experiment, there were large gaps in his transition boiling regime data from approximately 50 percent of q_{max} to near q_{max}. Figure 6 shows that, in our experiments, a common transition boiling curve was followed near ΔT_{min}. Most of Haramura's transition boiling data were near q_{min} and thus were likely to have been outside of the region of the two distinct transition curves.

The differences between the apparatuses used in Haramura and Auracher's studies and in our study are significant. Although Haramura and Auracher found no hysteresis in the transition boiling regime, our experiments using a long heater that is able to operate stably throughout the transition boiling regime clearly show the existence of the two transition boiling curves postulated by Witte and Lienhard.

The Nature of the Pool Boiling Curve. Allowing for variations in surface contamination, the saturated methanol pool boiling curves obtained in our increasing and decreasing temperature experiments (Figs. 4, 5, and 6) indicate the following:

- The nucleate boiling curves obtained in the increasing and decreasing temperature experiments were similar.
- A common transition boiling curve was followed over a small range of wall superheat lower than ΔT_{min}.
- The largest heat flux measured in the decreasing temperature experiments was similar to the nucleate boiling peak heat flux, q_{max}.

The general shape of the boiling curve indicated by the aggregate of all the methanol experiments is shown in Fig. 7.

Peak Heat Flux Results. The saturated pool boiling peak heat flux data obtained in the present study are summarized in Table 1, which includes all the q_{max} and ΔT_{max} data obtained in

Downloaded 11 Dec 2010 to 193.140.21.150. Redistribution subject to ASME license or copyright; see http://www.asme.org/terms/Terms_Use.cfm

the experiments. Our R-113 peak heat flux data can be compared directly with that of Broussard and Westwater for the same size tubes in R-113. They report peak heat flux values of 190 kW/m^2 at 28 K of wall superheat. Our values of 197 and 235 kW/m^2 at 23.7 and 28.8 K, respectively, are comparable.

Table 1 also contains the values of q_{max} predicted by Lienhard and Dhir's (1973) hydrodynamic theory of the peak heat flux and by Haramura and Katto's (1983) surface-controlled theory of the peak heat flux. Lienhard and Dhir's theory and Haramura and Katto's theory predict the q_{max} data of the present study to within rms errors of 21 and 25 percent, respectively. A large portion of this error results from the uncertainty of the q_{max} data obtained in the present work. As stated previously, the uncertainty in these measurements is ± 33 kW/m^2, which is higher than that in most controlled heating pool boiling experiments.

The peak heat flux data show approximately the same scatter as would be expected from the experimental uncertainty alone. For example, the six methanol peak heat flux data have an average of 420 kW/m^2 at an average surface superheat temperature of 32.5 K. These measurements have a standard deviation of 21 kW/m^2, which is comparable to the uncertainty of ± 33 kW/m^2. The superheat calculated at the peak heat flux for the five data points that were obtained with increasing temperature has a standard deviation of 2.3 K, which is comparable to the uncertainty of ± 2 K.

Conclusions

We have obtained saturated pool boiling curves that include q_{max} for horizontal cylinders in R-113 and various organic liquids. The results of these experiments are:

- The peak heat flux data of the present study are correlated by both the hydrodynamic and the surface-controlled predictions of the peak heat flux in saturated pool boiling from horizontal cylinders.
- Our temperature-controlled pool boiling experiments confirm the existence of two transition boiling curves for the case of horizontal cylinders in saturated methanol. When the heater temperature increases from nucleate boiling, the boiling process follows the higher heat flux curve of nucleate transition boiling. The lower heat flux curve of film transition boiling is followed when the heater temperature decreases from film boiling.
- Decreasing surface temperature experiments that began in the transition regime, as opposed to the film boiling regime, followed the nucleate transition boiling curve.
- The peak heat fluxes measured during the increasing heater temperature and decreasing heater temperature experiments were similar. This was the case even in the decreasing temperature experiments that followed the film transition boiling curve.

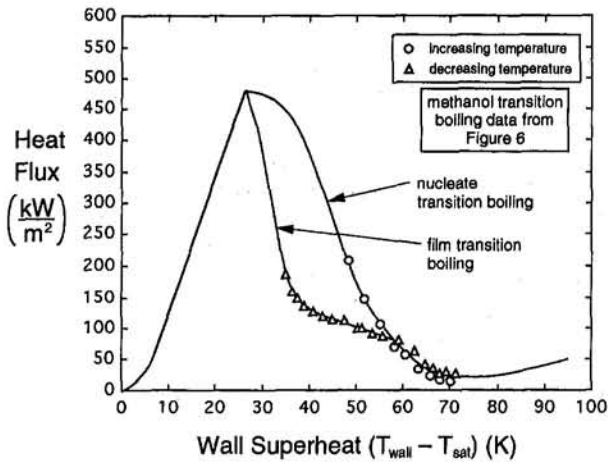


Fig. 7 Nature of the two transition boiling curves in saturated pool boiling as indicated by the methanol experiments of the present study

Table 1 Summary of saturated pool boiling peak heat flux data for 3.18-mm-dia horizontal cylinders (present study)

q_{max} (kW/m^2) (meas.)	ΔT_{max} (K)	up or down in T	q_{max} (kW/m^2) (pred. 1)	q_{max} (kW/m^2) (pred. 2)
n-pentane (T_{sat} = 309 K)				
243	31.6	up	231	258
283	16.1	down	231	258
R-113 (T_{sat} = 321 K)				
197	23.7	up	178	200
235	28.8	up	178	200
acetone (T_{sat} = 329 K)				
417	31.2	up	317	353
409	33.1	up	317	353
398	30.8	down	317	353
methanol (T_{sat} = 338 K)				
445	30.1	up	514	572
417	34.1	up	514	572
418	33.7	up	514	572
421	36.0	up	514	572
392	31.2	up	514	572
450	21.6	down	514	572
ethanol (T_{sat} = 352 K)				
345	36.0	up	477	534
367	31.9	down	477	534
benzene (T_{sat} = 353 K)				
339	32.9	up	294	326
isopropanol (T_{sat} = 356 K)				
361	17.6	up	409	454
362	18.7	up	409	454
347	18.6	up	409	454
341	25.9	up	409	454

prediction 1: Lienhard and Dhir (1973)
prediction 2: Haramura and Katto (1983)

Acknowledgments

The work was performed at the University of Houston. The Dowtherm SR-1 was donated by the Dow Chemical Company. We are grateful for partial support from the Shell Company Foundation, the University of Houston Energy Laboratory, the National Science Foundation, and the National Aeronautics and Space Administration. We also acknowledge helpful discussions with J. H. Lienhard and L. C. Witte of the University of Houston.

References

American Society of Mechanical Engineers, 1959, *Fluid Meters. Their Theory and Application,* New York.

Adiutori, E. F., 1964, "New Theory of Thermal Stability in Boiling Systems," *Nucleonics,* Vol. 22, No. 5, pp. 92–101.

Auracher, H., 1992, "Transition Boiling in Natural Convection Systems," *Proc. The Engineering Foundation Conference on Pool and External Flow Boiling,* Santa Barbara, CA, pp. 219–236.

Berenson, P. J., 1960, "Transition Boiling Heat Transfer From a Horizontal Surface," Heat Transfer Laboratory T. R. No. 17, MIT, Cambridge, MA.

Broussard, R. A., and Westwater, J. W., 1985, "Diameter and Velocity Effects for Cross-Flow Boiling," *AIAA Journal,* Vol. 23, No. 10, pp. 1615–1620.

Bui, T. D., and Dhir, V. K., 1985, "Transient Boiling Heat Transfer on a Vertical Surface," ASME JOURNAL OF HEAT TRANSFER, Vol. 107, pp. 756–763.

Dow Chemical Company, 1982, "Engineering and Operating Guide for Dowfrost and Dowtherm SR-1 Heat Transfer Fluids," Dow Form No. 173-1190-82, Midland, MI.

Eckert, E. R. G., and Drake, R. M., Jr., 1972, *Analysis of Heat and Mass Transfer,* McGraw-Hill, New York.

Haramura, Y., and Katto, Y., 1983, "A New Hydrodynamic Model of Critical Heat Flux, Applicable Widely to Both Pool and Forced Convection Boiling on

Downloaded 11 Dec 2010 to 193.140.21.150. Redistribution subject to ASME license or copyright; see http://www.asme.org/terms/Terms_Use.cfm

Submerged Bodies in Saturated Liquids," *Int. J. Heat Mass Transfer,* Vol. 26, No. 3, pp. 389–399.

Haramura, Y., 1991, "Steady-State Pool Transition Boiling Heated With Condensing Steam," *Proc. ASME/JSME Thermal Engineering Joint Conf.,* Reno, NV, Vol. 2, pp. 59–64.

Hesse, G., 1973, "Heat Transfer in Nucleate Boiling, Maximum Heat Flux and Transition Boiling," *Int. J. Heat Mass Transfer,* Vol. 16, pp. 1611–1627.

Kays, W. M., and Crawford, M. E., 1980, *Convective Heat and Mass Transfer,* McGraw-Hill, New York.

Liaw, S. P., and Dhir, V. K., 1986, "Effect of Surface Wettability on Transition Boiling Heat Transfer From a Vertical Surface," *Proc. 8th Int. Heat Trans. Conf.,* San Francisco, CA, Vol. 4, pp. 2031–2036.

Lienhard, J. H., and Dhir, V. K., 1973, "Hydrodynamic Prediction of Peak Pool-Boiling Heat Fluxes From Finite Bodies," ASME JOURNAL OF HEAT TRANSFER, Vol. 95, pp. 152–158.

Lienhard, J. H., 1987, *A Heat Transfer Textbook,* 2nd ed., Prentice-Hall, Englewood Cliffs, NJ.

Nukiyama, S., 1937, "The Maximum and Minimum Values of the Heat Q Transmitted From Metal to Boiling Water Under Atmospheric Pressure," *J. JSME,* Vol. 37, pp. 367–374 (translation: *Int. J. Heat Mass Transfer,* Vol. 9, 1966, pp. 1419–1423).

Petukhov, B. S., 1970, "Heat Transfer and Friction in Turbulent Pipe Flow With Variable Physical Properties," *Advances in Heat Transfer,* T. F. Irvine, Jr., and J. P. Hartnett, eds., Academic Press, New York, pp. 504–564 (as cited in Lienhard, 1987).

Ramilison, J. M., and Lienhard, J. H., 1987, "Transition Boiling Heat Transfer and the Film Transition Regime," ASME JOURNAL OF HEAT TRANSFER, Vol. 109, pp. 746–752.

Sakurai, A., and Shiotsu, M., 1974, "Temperature-Controlled Pool-Boiling Heat Transfer," *Proc. 5th Int. Heat Transfer Conf.,* Vol. 4, No. B3.1, pp. 81–82.

Sleicher, C. A., and Tribus, M., 1956, in: *Heat Transfer Fluid Mechanics Institute,* Stanford, Stanford, CA, p. 59 (as cited in Kays and Crawford, 1980).

Spalding, B. D., and Taborek, J., 1983, *Heat Exchanger Design Handbook, Heat Exchanger Theory,* Hemisphere Publishing Corp., Washington, DC.

Stephan, K., 1965, "Stabilitat Beim Sieden," *Brennst.-Warme-Kraft,* Vol. 17, No. 12, pp. 571–578 (as cited in Hesse, 1973).

Ungar, E. K., 1987, "Saturated Pool and Flow Boiling From Horizontal Cylinders," Ph. D. Dissertation, University of Houston, Houston, TX.

Ungar, E. K., and Eichhorn, R., 1988, "A New Hydrodynamic Prediction of the Peak Heat Flux From Horizontal Cylinders in Low Speed Upflow," *Proc. 25th National Heat Transfer Conf.,* Houston, TX, Vol. 2, pp. 643–657.

Ungar, E. K., and Eichhorn, R., 1993, "Transition Boiling Curves in Saturated Pool Boiling From Horizontal Cylinders," ASME Paper No. 93-HT-3.

Vargaftik, N. B., 1975, *Tables on the Thermophysical Properties of Liquids and Gases,* Wiley, New York.

Witte, L. C., and Lienhard, J. H., 1982, "On the Existence of Two Boiling Curves," *Int. J. Heat Mass Transfer,* Vol. 21, No. 6, pp. 771–779.

Yilmaz, S., and Westwater, J. W., 1980, "Effect of Velocity on Heat Transfer to Boiling Freon-113," ASME JOURNAL OF HEAT TRANSFER, Vol. 102, pp. 26–31.

Downloaded 11 Dec 2010 to 193.140.21.150. Redistribution subject to ASME license or copyright; see http://www.asme.org/terms/Terms_Use.cfm

J. P. O'Connor
Systems Group,
Texas Instruments,
Plano, TX 75086

S. M. You

J. Y. Chang

Department of Mechanical
and Aerospace Engineering,
University of Texas at Arlington,
Arlington, TX 76019-0023

Gas-Saturated Pool Boiling Heat Transfer From Smooth and Microporous Surfaces in FC-72

The effects of surface treatments and "gassy-subcooling" on pool boiling heat transfer are quantified by testing both smooth and treated surfaces at gassy-subcooling levels from 0°C to 40°C (1 atm) and 40°C to 85°C (3 atm). Incipient and nucleate boiling wall superheats decrease over this range of gassy-subcooling. At gassy-subcooling levels greater than 20°C, the boiling curves for the smooth surface indicate two distinct regions governed by different heat transfer mechanisms, one in which the boiling process is influenced by the presence of dissolved gas, the other by boiling of the pure liquid. The critical heat flux (CHF) for each surface continually increases with increased levels of gassy-subcooling and the CHF sensitivity to gassy-subcooling is higher for the treated surface. The CHF increase due to combined surface treatment and gassy-subcooling (85°C) is ~400 percent (78 W/cm²).

Introduction

Thermal management of future micro-electronic systems must provide adequate heat transfer coefficients for dissipation of the projected heat flux levels and control component Life Cycle Costs (LCC) by maintaining junction temperatures below 85°C. Boiling heat transfer via direct component immersion in a dielectric liquid is a possible means of meeting these requirements. Investigations of boiling heat transfer enhancement via surface treatment and subcooling have indicated the dissipation of high heat flux levels is realistic.

Gas-Saturated and "Gassy"-Subcooling. The terms "gas-saturated" and "gassy-subcooling" will be used throughout this paper and their definition is necessary.

Under gas-saturated conditions, the current test system is composed of two components: FC-72 and air. The solubility of air in FC-72 is high, 48 percent by volume at standard atmospheric conditions (1 atm and 25°C) where its saturation temperature is 56°C. The liquid phase of this system is at a pressure equivalent to the system total pressure (P_t). The vapor/gas phase of the system also exists at the total pressure, which is the sum of the partial vapor and gas pressures ($P_t = P_v + P_g$). The vapor pressure is equal to the saturation pressure at the bulk liquid temperature [$P_v = P_{sat}(T_{bulk})$]. The amount by which the bulk liquid temperature is reduced below the saturation temperature corresponding to the total pressure is the level of "gassy-subcooling":

$$\Delta T_{sub,gassy} = T_{sat}(P_t) - T_{bulk} = T_{sat}(P_t) - T_{sat}(P_v) \quad (1)$$

The dissolved gas content (C_g = ratio of moles gas to moles liquid) in the liquid phase under gas-saturated conditions can be related to the partial gas pressure (P_g) in the gas/vapor phase using Henry's law:

$$C_g = H(T_{bulk})\, P_g \quad (2)$$

Henry's proportionality constant $H(T_{bulk})$ is a function of temperature only. You (1990) measured Henry's constant for air in FC-72 and found values of 5.4×10^{-5} and 5.5×10^{-5} (moles/mole-kPa) at 31.5 and 59.5°C, respectively. Dissolved gas contents for the current investigation are calculated using a value of 5.5×10^{-5} moles/mole-kPa.

Under equilibrium conditions, the liquid is fully gas-saturated and the dissolved gas content (C_g) is uniform throughout. Therefore the liquid is not subcooled but is saturated at the vapor pressure, which is lower than the total pressure. If a surface is immersed in this system and heated until nucleate boiling occurs, the liquid near the heated surface is degassed, the local vapor pressure approaches the total pressure, and subcooled conditions at the gassy-subcooling level prevail (see You et al., 1995).

Summary of Previous Work. O'Connor and You (1995) and O'Connor et al. (1995) developed benign surface treatments that could enhance boiling heat transfer. The authors developed paint solutions composed of a solvent (isopropyl alcohol), an epoxy, and microsized structures (3-to-10 μm silver flakes and 8-to-12 μm diamond particles). These enhancement paints provided up to an 85 percent decrease in incipient and nucleate boiling wall superheats, increased the nucleate boiling heat transfer coefficient by a factor of four, and increased the Critical Heat Flux (CHF) by ~100 percent beyond those of an untreated surface. The abilities of the surfaces to provide these enhancement levels were attributed to the increase of active nucleation site densities and the generation of microporous cavities, which initiate the boiling process at low superheats. Single-phase natural convection data for the painted and untreated surfaces differed by less than the measurement uncertainty, indicating that the painted surfaces did not increase heat transfer surface area.

Kutateladze (1951) conducted the initial subcooling investigation, which focused on burnout heat flux. He developed a correlation that suggested that the subcooled CHF increases proportionally by an amount relative with the level of subcooling. Based on pool boiling data from horizontal wires immersed in water, Ivey and Morris (1962) modified Kutateladze's correlation:

$$\frac{q_{max,sub}}{q_{max,sat}} = 1 + C_{sub}\left(\frac{\rho_g}{\rho_f}\right)^{1/4} \mathrm{Ja};$$

where:

$$C_{sub} = 0.1 \quad \text{and} \quad \mathrm{Ja} = \frac{\rho_f C_p \Delta T_{sub}}{\rho_g h_{fg}} \quad (3)$$

Elkassabgi and Lienhard (1988) conducted subcooled boiling

Contributed by the Heat Transfer Division for publication in the JOURNAL OF HEAT TRANSFER. Manuscript received by the Heat Transfer Division July 14, 1995; revision received May 14, 1996. Keywords: Augmentation and Enhancement, Boiling, Phase-Change Phenomena. Associate Technical Editor: S. Ramadhyani.

Copyright © 1996 by ASME

Downloaded 11 Dec 2010 to 193.140.21.150. Redistribution subject to ASME license or copyright; see http://www.asme.org/terms/Terms_Use.cfm

(0 to 130°C) experiments using wire heaters (0.8 to 1.54 mm in diameter) in four different liquids: acetone, methanol, isopropyl, and R-113. They identified three burnout mechanisms depending on the level of subcooling and the particular liquid used. Generally speaking, they found the CHF to be linearly dependent on the level of subcooling (as indicated in Eq. (3)) over the low subcooled region (0 to 20°C for isopropanol, methanol, and R-113, and 0 to 40°C for acetone), and to vary with $\sim\Delta T_{sub}^{3/8}$ in the moderate subcooled region (20 to 60°C for isopropanol and methanol, and 20 to 35°C for R-113). At higher levels of subcooling (>60°C) they found the CHF to be independent of ΔT_{sub}.

Mudawar and Anderson (1989) investigated the effects of subcooling and pressure on square (12.7 mm × 12.7 mm) vapor-blasted heaters mounted vertically in FC-72. They identified a moderate CHF increase (26 percent) by increasing system pressure from 1 to 3 atm. They also found a 108 percent increase in CHF by increasing the level of subcooling from 0 to 35°C in FC-72 at 1 atm. They were able to correlate CHF data using Eq. (3) and a C_{sub} of 0.0643. Carvalho and Bergles (1990) investigated the effects of subcooling over a ΔT_{sub} range of 0 to 31°C using square (5 mm × 5 mm) heaters mounted vertically in FC-72. At lower heat flux conditions they reported significant reductions in surface temperature with increasing levels of subcooling; however, the surface temperatures converged at higher heat flux conditions regardless of the amount of subcooling. They correlated their CHF data using Eq. (3) and a C_{sub} of 0.065. Additional investigations have been conducted using highly wetting liquids. For vertical square (4.57 mm) heaters, Hwang and Moran (1981) correlated subcooled CHF data with C_{sub} values of 0.05 and 0.061 for FC-72 and FC-86, respectively. More recently, Bar-Cohen and McNiel (1992) tested square (10 mm × 10 mm) horizontally oriented heaters in FC-72 over a ΔT_{sub} range from 0 to 20°C. Again, they used similar C_{sub} values to correlate their data.

The effects of dissolved gas content on incipient and nucleate boiling superheats and on CHF from a 0.51-mm-dia wire boiling in FC-72 have been investigated by You et al. (1995). These authors indicated the dissolved gas effect on boiling incipience is small when the dissolved gas concentration of the bulk liquid is below ~0.0025 moles air/mole FC-72 liquid. They identified an increased CHF with increased gassy-subcooling at a fixed total pressure and suggested a nonuniform dissolved gas content within the liquid, with the gas concentration decreasing near the heated surface. This increasing CHF trend was correlated using Eq. (3) and a C_{sub} value of 0.077.

Objective. The current investigation will employ the 8-to-12 μm diamond painted surface from O'Connor et al. (1995) in conjunction with gassy-subcooling to enhance pool boiling heat transfer further. The primary objective is to attain the highest CHF possible. In addition, the effects of gassy-subcooling and dissolved gas content on nucleate boiling and its incipience will be identified.

Experimental Apparatus and Test Procedure

Pressurized Pool Boiling Test Facility. To achieve gassy-subcooling levels up to 85°C, elevated pressure (3 atm) test conditions are required. A stainless-steel pressure vessel (Eggelhof Series 105: 0–65 psig) is immersed in a thermal water bath (bath #1) and serves as the pressurized test chamber (Fig. 1(*a*)). A 1000 W immersion heater and an evaporator coil control the thermal water bath temperature. Two stainless steel $\frac{1}{2}$ in. NPT pressure sealed electrical harness plugs (Douglas Engineering Company, Rockaway, NJ) provide electrical access into the test chamber. Two thermocouples monitor heater temperature and two test liquid temperature. Filtered compressed air provides pressurization of the test chamber. Additional test liquid temperature control is provided by an internal condenser through which water is circulated from thermal bath #2. The test chamber is ventilated through an external condenser, which is used to replenish escaping vapor.

Details of the data acquisition system and instrumentation are provided by O'Connor and You (1995). A pressure control valve and a pressure transducer (Validyne-DP15-44-N-1-S-4-A) are used to control and monitor total pressure. The pressure transducer was calibrated prior to use as described by O'Connor (1994).

Test Heaters. One heater design is illustrated in Fig. 1(*b*). Corning microsheet glass (~130 μm thick and 0.5 cm × 1.8 cm) served as a substrate to sputter a thin film (~1000 Å) of platinum (heating element). A 1 mm platinum strip at each end of the glass allowed electrical leads to be attached. To provide a heater in which the CHF is not influenced by thermal conductance/capacitance effects, a 1.5-mm-thick piece of copper (0.5 cm × 1.6 cm) was bonded on top of the platinum heating element using Omegabond 200 epoxy (see O'Connor, 1994). Two holes (1 mm in diameter and ~2.5 mm in depth) were drilled into the copper and housed type-T thermocouples to provide surface temperature measurements. The glass was mounted to a Teflon substrate using Omegabond 200 epoxy.

An alternate heater design was required for test conditions where the heat flux exceeded 60 W/cm^2. This design (Fig. 1(*c*)) employs the same heater used by O'Connor and You (1995). Two thin films, ~200 Å of nichrome base and ~900 Å of platinum, were bonded on a 1-mm-thick piece of aluminum nitride (0.5 cm × 1.65 cm). Electrical leads were soldered across each end of the thin film. A type-T thermocouple was mounted in the middle of the thin film and the heater was flush mounted to a Teflon substrate.

Entire boiling curves from each heater treated with the diamond paint were compared at saturated conditions (1 atm). The

Nomenclature

C_g = dissolved gas concentration, moles gas/moles liquid
C_p = specific heat, kJ/kg-°C
C_{sub} = subcooling correlating coefficient (Eqs. (3) and (5))
CHF = Critical Heat Flux, W/cm^2
H(T) = Henry's constant, moles gas/moles liquid, kPa
h_{fg} = heat of vaporization, kJ/kg
Ja = volumetric Jacob number
P_f = bulk liquid pressure
P_g = gas pressure in gas-vapor phase above flat surface
P_{gb} = bubble partial gas pressure
P_{sat} = saturation pressure
P_t = total pressure
P_v = vapor pressure in gas-vapor phase above flat surface
P_{vb} = bubble partial vapor pressure
q = heat flux, W/cm^2
q_{max} = Critical Heat Flux, W/cm^2
$q_{max,sat}$ = saturated CHF
$q_{max,sub}$ = subcooled CHF
$q_{max\ z,p}$ = Zuber's CHF at indicated pressure
r_b = embryonic bubble radius
S = surface treatment coefficient (Eq. (5))
T_{bulk} = bulk liquid temperature
T_{sat} = saturation temperature
T_w = surface temperature
$\Delta T_{sub} = T_{sat} - T_{bulk}$, °C
ΔT_{sat} = wall superheat $= T_w - T_{sat}$
$\Delta T_{sub,gassy}$ = gassy-subcooling level, °C
ρ_g = vapor density, kg/m^3
ρ_f = liquid density, kg/m^3
σ = surface tension, N/m

Downloaded 11 Dec 2010 to 193.140.21.150. Redistribution subject to ASME license or copyright; see http://www.asme.org/terms/Terms_Use.cfm

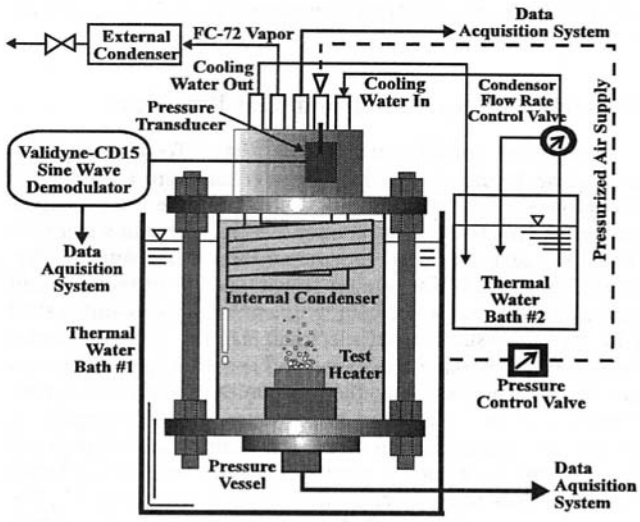


Fig. 1(*a*) Experimental apparatus

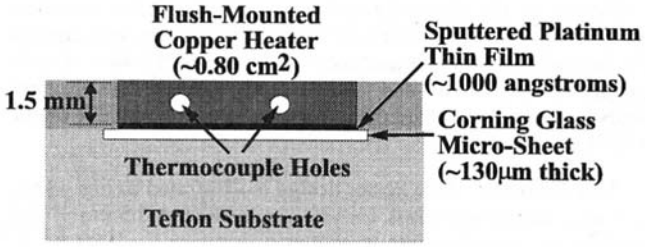


Fig. 1(*b*) Heater design #1

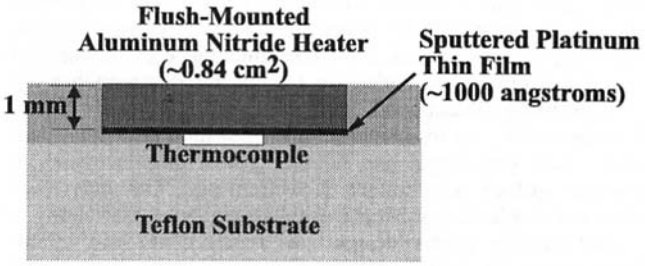


Fig. 1(*c*) Heater design #2

two data sets differed by less than the data uncertainty band, indicating data generated from each heater design could be compared directly.

Test Procedure. To achieve a degassed condition, the liquid (FC-72) is heated to its saturation temperature (~56.5°C, 1 atm) where it is maintained for approximately 12 hours. To achieve a gas-saturated condition, the ventilation line is closed and the test liquid is brought to the desired temperature and pressure by adjusting the temperature of thermal bath #1 and pressurizing the test vessel with compressed air. After gas-saturated bulk liquid conditions are verified (for more than 30 minutes) an experimental sequence is initiated. For each test condition three boiling curves were generated with increasing heat flux increments. In general, near boiling incipience and CHF, the heat flux was increased in increments less than 1 W/cm^2. Between these two conditions increments varied between 1.5 and 2.5 W/cm^2, depending upon the level of subcooling.

For heat flux values less than ~80 percent CHF, steady-state heater conditions were verified by assuring that the heater temperature was time invariant (less than 0.014°C/second). After steady-state conditions prevail, a ten second delay is encountered and the heat flux and steady-state surface temperature are measured and averaged, 200 samples over a four second time interval. After the measurements are made the heat flux is incremented and the process is repeated.

For heat flux conditions greater than ~80 percent CHF, after incrementing the heat flux, the heater surface temperature is immediately monitored for a 75-second time interval. The CHF is defined as the highest nucleate boiling heat flux prior to the onset of film boiling. This condition is visually identifiable and is easily detected by the data acquisition system through an excursion in heater surface temperature. If the heater surface temperature increase between two subsequent measurements for a 0.07-second time interval is larger than 12°C (171°C/second), CHF conditions are assumed to exist and the power supply is immediately disabled, preventing heater burnout. If CHF is not detected, the heat flux and surface temperature parameters are calculated (averaged) over the last 15-second time interval (out of 75 seconds). After the data are measured, the power supply is incremented to the next heat flux. If CHF conditions are met the process for one run is complete. Before another run is initiated the heater temperature must decrease to within 1°C of the bulk liquid temperature.

Uncertainty Estimates. Using the method of Kline and McClintock (1953), uncertainty estimates (20:1 odds; 95 percent confidence level) were made for the heat flux and temperature measurements. The indicated uncertainties account for measurement resolution, instrumentation variance, geometric uncertainty, substrate conduction loss, and calibration error. Substrate conduction losses were estimated at different heat flux conditions by solving three-dimensional conduction problems using a finite difference solver (FLUENT, 1991). These losses ranged from 15 percent (single-phase natural convection, 0.5 W/cm^2) to 0.5 percent (nucleate boiling regime, 19 W/cm^2) of the total heat flux. There were no discernible differences in substrate conduction heat transfer between the two heater designs. Accounting for all these contributions, the uncertainty estimates in heat flux were 15.5 and 5.0 percent for single-phase and nucleate-boiling conditions, respectively. The estimated uncertainty in superheat measurements is ±0.5°C. O'Connor and You (1995) give a more complete discussion of the uncertainty analysis including substrate conduction.

Discussion of Results

Gassy-subcooling levels between 0 and 85°C are investigated, 0, 20, 40°C, and 40, 60, 85°C, at 1 and 3 atm, respectively, resulting in six experimental conditions for each surface (Table 1). Each experiment is identified by a run number, which indicates the surface, total pressure, and level of gassy-subcooling. For example, run R10 indicates the reference surface (R) was tested at 1 atm (1) and 0°C subcooling (0), whereas run D36 indicates the diamond-treated surface (D) was tested at 3 atm

Table 1 System properties for each test condition

Run #	T_{bulk} (C)	$\Delta T_{sub,gassy}$ (C)	$P_v = P_{sat}(T_{bulk})$ (kPa)	P_t (kPa)	P_g (kPa)	C_g moles gas / moles liquid
R10	56.2	0.0	100.3	101.3	1.0	<0.0002
R12	35.6	20.4	47.3	100.9	53.6	0.0029
R14	15.4	40.6	19.4	101.0	81.6	0.0043
R34	51.4	42.6	84.9	303.5	218.5	0.0119
R36	36.3	57.7	48.5	302.7	254.1	0.0137
R39	8.8	85.2	13.9	302.8	288.9	0.0154
D10	56.6	0.0	100.5	101.9	1.4	<0.0002
D12	35.3	20.6	46.6	101.8	55.1	0.0029
D14	15.3	40.6	19.3	101.8	82.5	0.0044
D34	53.8	40.2	92.4	303.5	211.0	0.0116
D36	34.1	60.6	44.4	302.4	258.0	0.0139
D39	9.1	84.9	14.2	302.4	288.2	0.0153

Downloaded 11 Dec 2010 to 193.140.21.150. Redistribution subject to ASME license or copyright; see http://www.asme.org/terms/Terms_Use.cfm

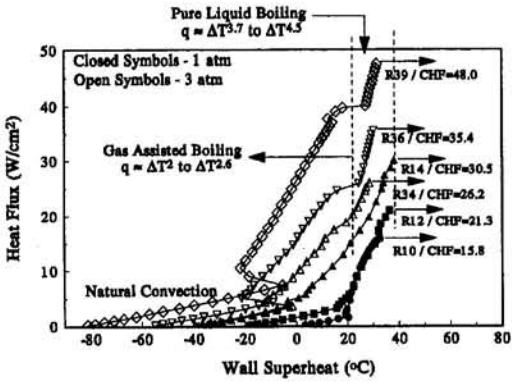


Fig. 2 Reference (copper) surface boiling curves

(3) and approximately 60°C gassy-subcooling (6). Three complete boiling curve data sets were generated at each condition. Table 1 identifies the run number, average bulk liquid temperature (for three data sets), level of gassy-subcooling, partial FC-72 vapor pressure at the bulk liquid temperature ($P_v = P_{sat}(T_{bulk})$), average total pressure (P_t, for three data sets), partial gas pressure ($P_g = P_t - P_v$), and the dissolved gas content (C_g, Eq. (2)) for each test condition.

The smooth (reference) surface is polished copper, which has surface cavity feature sizes ranging from 0.1 to 0.2 μm. The treated surface in the current study was made from the diamond paint developed by O'Connor et al. (1995), which has surface cavity feature sizes between 1 and 10 μm. Feature size was quantified using a Scanning Electron Microscope (SEM) as discussed by O'Connor et al. (1995) and O'Connor (1994).

For each experiment the bulk liquid temperature and total pressure were monitored and controlled throughout the duration of the three runs. The control was sufficient to assure a constant dissolved gas content in the bulk liquid throughout the duration of an experiment (±5 kPa and ±2°C).

Reference Surface Data. The effects of dissolved gas content on the reference surface boiling curve are illustrated in Fig. 2. The indicated wall superheats are the difference between the surface temperature and the saturation temperature ($\Delta T_{sat} = T_w - T_{sat}$) where T_{sat} is 56 and 94°C at 1 and 3 atm, respectively. Saturated data (R10) along with data representing gassy-subcooling levels up to 85°C are shown (third data set for each surface). All the boiling data (three data sets) at each test condition were repeatable (within the uncertainty band). The data indicate that if the dissolved gas content (C_g) is higher than 0.004 moles air/moles liquid (runs R14, R34, R36, and R39, see Table 1), incipience at a negative wall superheat occurs.

To understand the heterogeneous nucleation mechanism for gassy-subcooled conditions, consider mechanical equilibrium of the liquid–vapor/gas interface of a bubble resting in a conical cavity on a heated surface:

$$P_{vb} + P_{gb} - P_f = \frac{2\sigma}{r_b} \tag{4}$$

The pressure inside the bubble is the sum of the bubble partial vapor pressure [$P_{vb} = P_{sat}(T_w)$] and the bubble partial gas pressure (P_{gb}), which is influenced by the dissolved gas content near the heated surface. The pressure outside the bubble (liquid pressure) is equal to the total pressure ($P_f = P_t$). To initiate bubble growth, the pressure drop across the bubble interface must reach a certain value depending upon the size of the embryonic radii (r_b). Therefore, Eq. (4) indicates that if the bubble partial gas pressure (P_{gb}) increases, nucleation can occur at reduced wall superheats.

The reference surface data representative of dissolved gas contents higher than 0.004 moles air/moles liquid indicate that the bubble partial gas pressure (P_{gb}) is not zero and produces reduced incipient and nucleate boiling wall superheats. At low dissolved gas contents ($C_g < 0.004$ moles air/moles liquid: runs R10 and R12), the wall superheat values vary negligibly, indicating the bubble partial gas pressure is small.

These observations are similar to those of You et al. (1995), who suggested that the dissolved gas effect (P_{gb} in Eq. (4)) decreases if the gas concentration in the liquid near the surface is depleted. At gassy-subcooling levels greater than 20°C ($C_g >$ 0.004 moles air/moles liquid) nucleate boiling wall superheats decrease significantly (for a fixed heat flux) across the entire heat flux range. This enhancement is attributed to the ability of the dissolved gas in the FC-72 liquid to effectively penetrate the superheated liquid layer and produce increased bubble partial gas pressures (P_{gb}). This increased pressure promotes and expedites the nucleation process. The negative wall superheats at incipience and during nucleate boiling confirm the penetration of dissolved gas into the nucleation process. You et al. (1995) made similar observations.

The gas-saturated boiling curves at 3 atm all contain significant slope changes at ~20°C superheat. Two boiling regions are separated by an "inflection" point occurring at this wall superheat (~20°C), similar to the incipient superheat of the saturated run (R10). The heat flux values at the point of inflection depend on the bulk-liquid dissolved gas content. The first heat transfer region exists between the incipience point and the point of inflection ($\Delta T_{sat} < 20$°C), and the heat flux is proportional to the wall superheat raised to a power between ~2 and ~2.6, with the slope increasing with increasing dissolved gas content. At higher wall superheats ($\Delta T_{sat} > 20$°C) beyond the inflection point, the nucleate boiling curve slope at all three levels of subcooling increases significantly and the heat flux is proportional to the wall superheat raised to a power between ~3.7 and ~4.5.

It is proposed that two different heat transfer mechanisms exist: gas assisted boiling and pure liquid boiling. In the lower heat flux region the bubble partial gas pressure (P_{gb}) promotes bubble nucleation. In this region significant superheat reductions are realized with increasing dissolved gas concentrations. At the higher heat flux values, the wall superheats are not significantly influenced by dissolved gas concentrations. Although the bulk liquid is gas-saturated, the data indicate that significant degassing of the liquid near the heated surface has occurred and the bubble partial gas pressure (P_{gb}) available for nucleation is small. Boiling curves (3 atm) indicating the same two distinct heat transfer mechanisms were generated using a different heater and confirm the repeatability of this phenomenon. Additionally, Murphy and Bergles (1972) conducted gassy-subcooled flow boiling experiments using R-113 and identified two similar regions.

Photographs illustrate differences in bubble departure characteristics between these two mechanisms. Figure 3 illustrates reference surface boiling phenomena at ~50 percent CHF (Fig. 3(*a*)), and ~90 percent CHF (Fig. 3(*b*)) for run R36. The image at ~50 percent CHF is representative of the first heat transfer mechanism (gas assisted), and the image at ~90 percent CHF represents a condition more indicative of pure liquid boiling. The bubble size is significantly larger at the higher heat flux condition, where the near-surface liquid temperature increases due to a decrease in the local gas concentration.

Treated Surface Data. The effects of dissolved gas content on the treated surface (O'Connor et al., 1995) boiling curves are illustrated in Fig. 4. Saturated data (run D10) along with data representing gassy-subcooling levels up to 85°C are shown. Comparison with smooth surface data (Fig. 2) indicates significant heat transfer enhancement due to surface treatment at saturation and all levels of gassy-subcooling. At saturation the

Downloaded 11 Dec 2010 to 193.140.21.150. Redistribution subject to ASME license or copyright; see http://www.asme.org/terms/Terms_Use.cfm

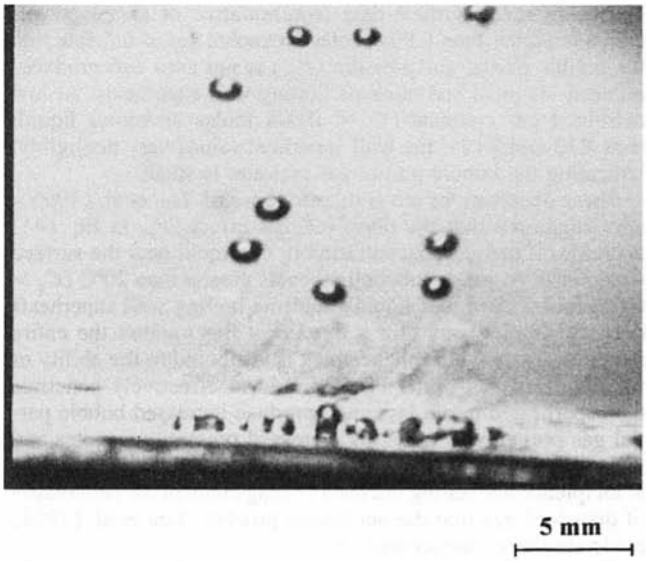


Fig. 3(*a*) Run R36 ($q \sim 19.5$ W/cm^2; q/CHF ~ 50 percent)

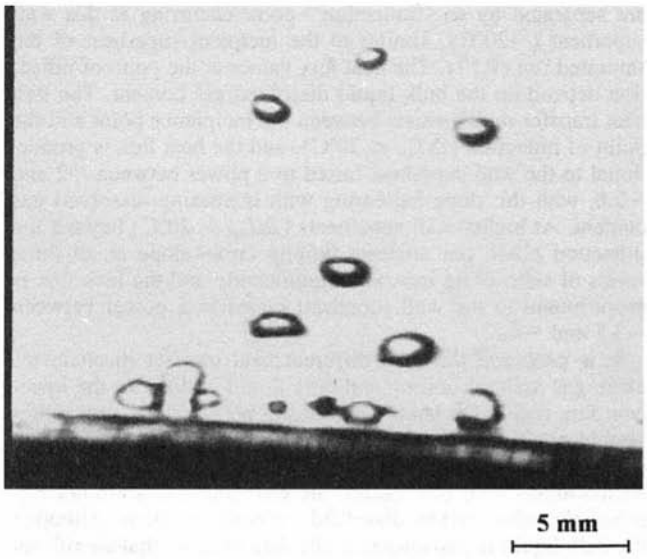


Fig. 3(*b*) Run R36 ($q \sim 32$ W/cm^2; q/CHF ~ 90 percent)

Fig. 3 Reference surface boiling phenomenon

incipient and nucleate boiling wall superheats are decreased between 70 and 85 percent and the CHF is increased by 72 percent, similar to the enhancement reported by O'Connor et al. (1995). The lower superheats can be attributed to improved heat transfer via increases in the nucleation site density provided by the surface treatment.

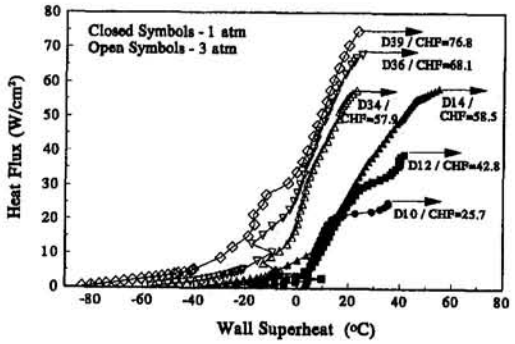


Fig. 4 Treated (diamond) surface boiling curves

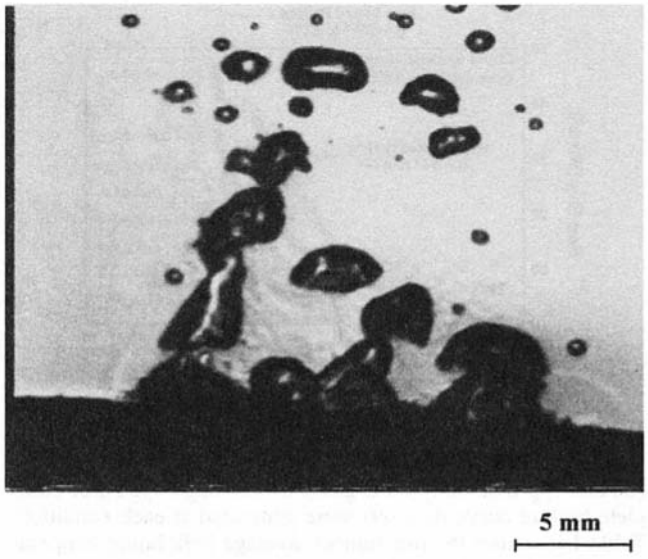


Fig. 5 Treated surface boiling phenomenon (Run D36, $q \sim 54$ W/cm^2, q/CHF ~ 90 percent)

The treated surface data in Fig. 4 indicate a significant decrease in wall superheat as the pressure is increased from 1 to 3 atm. Additionally, for a given total pressure, the treated surface superheats are lower and less sensitive to dissolved gas content than those from the smooth surface. The insensitivity to dissolved gas concentration at a given pressure possibly indicates that significant degassing of the liquid has occurred near the treated surface.

Figure 5 illustrates boiling conditions above the treated surface (D36) at a heat flux of ~90 percent CHF. Comparison with Fig. 3(*b*) illustrates that the treated surface provides significant increases in the vapor generation rate. The increase in vapor departing the surface expedites the degassing process, as illustrated by the data (Fig. 4). A photographic comparison between the surfaces at all other bulk liquid conditions is similar.

CHF Sensitivity to Gassy-Subcooling. The data illustrated in Figs. 2 and 4 indicate the CHF increases with increased gassy-subcooling levels. You et al. (1995) found similar trends with horizontal wires in gas-saturated FC-72. This may be attributed to local degassing near the heated surface. As the near liquid is degassed, the local vapor pressure approaches the total pressure, the net effect being to increase the subcooling level ($T_{sat}(P_v) - T_{bulk}$). To illustrate this, the Ivey and Morris (1962) CHF correlation (Eq. (3)), which accounts for subcooling, is used. The experimental CHF (q_{max}) is nondimensionalized using Zuber's (1959) saturated CHF correlation, which accounts for pressure via liquid property variations. Zuber's correlation predicts CHF values of 14.1 and 20.9 W/cm^2 at 1 and 3 atm, respectively. Substitution of the experimental CHF values for $q_{max,sub}$ and the respective gassy-subcooling levels for ΔT_{sub} in Eq. (3) allow the data to be plotted against the product of the volumetric Jacob number (Ja) and density ratio $(\rho_g/\rho_f)^{1/4}$ (Fig. 6). Reference surface data are indicated by circles and treated surface data by diamonds. The closed and open symbols represent CHF values (average of three runs) at 1 and 3 atm, respectively. The beneficial effect of surface treatment on the CHF is evident at all gassy-subcooling levels.

For a given surface (smooth or treated) the data at 1 and 3 atm can be correlated by a single expression, the result being a CHF correlation that accounts for surface treatment and subcooling:

Downloaded 11 Dec 2010 to 193.140.21.150. Redistribution subject to ASME license or copyright; see http://www.asme.org/terms/Terms_Use.cfm

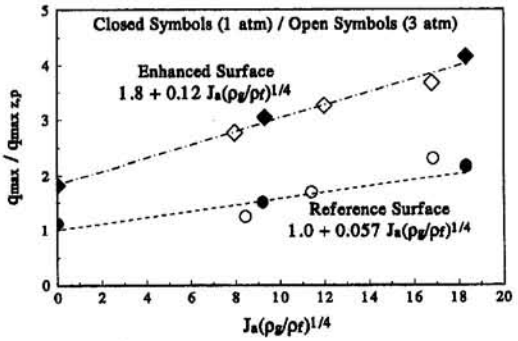


Fig. 6 Nondimensional CHF versus subcooling levels

$$\frac{q_{\max}}{q_{\max z,p}} = S + C_{\text{sub}}\left(\text{Ja}\left(\frac{\rho_g}{\rho_f}\right)^{1/4}\right) \tag{5}$$

The coefficient S in Eq. (5) accounts for the CHF enhancement at saturation due to surface treatment. For the smooth surface $S = 1$, whereas for the current treated surface $S = 1.8$ indicating an increase in the CHF at saturation due to surface treatments alone. The CHF sensitivity to gassy-subcooling is higher for the treated surface, as indicated by the increased slope of the data (Fig. 6). The subcooling coefficient in Eq. (5) (C_{sub}) is 0.057 for the reference surface and increases ~100 percent for the treated surface (0.12). Because of the increased number of active nucleation sites on the treated surface, the benefits of gassy-subcooling are pronounced, as seen by the CHF data. The overall CHF enhancement using surface treatment and subcooling was ~400 percent, from 15.8 W/cm^2 (R10) to 76.8 W/cm^2 (D39).

Conclusions

A benign surface treatment developed by O'Connor et al. (1995) that provides significant pool boiling heat transfer enhancement was combined with gassy-subcooling levels up to 85°C. Additional heat transfer enhancements beyond those due to the surface treatment alone were provided with increasing gassy-subcooling levels. The effects of gassy-subcooling and dissolved gas content on wall superheats and CHF are identified.

1 Reductions in incipient and nucleate boiling (up to ~40°C) wall superheats are observed with increased dissolved gas content for the reference surface. These reductions are attributed to increased bubble partial gas pressures, which promote nucleation.

2 Reductions in incipient and nucleate boiling (up to ~40°C) wall superheats are observed with increased total system pressure for the treated surface. For a given total pressure the wall superheats are independent of the dissolved gas content due to localized degassing of the liquid.

3 At high levels of gassy-subcooling (>40°C), two "boiling" regions governed by different heat transfer mechanisms are observed for the smooth surface. The lower heat flux region is influenced by dissolved gas, and the higher heat flux region is governed by pure subcooled liquid boiling.

4 The CHF continually increases with increased levels of gassy-subcooling, with the sensitivity increasing by ~100 percent for the treated surface. This increased sensitivity for the treated surface is attributed to additional degassing of the liquid near the surface. The overall CHF increase due to both surface treatment and subcooling is ~400 percent.

Acknowledgments

This study was supported by the Texas Higher Education Coordinating Board: Advanced Research/Technology Program grant number 003656-001. In addition, the donation of FC-72 from the 3M Industrial Chemical Products Division is greatly appreciated.

References

Bar-Cohen, A., 1993, "Thermal Management of Electronic Components With Dielectric Liquids," *JSME International Journal*, Series B, Vol. 36, No. 1.

Bar-Cohen, A., and McNeil, A., 1992, "Parametric Effects on Pool Boiling Critical Heat Flux in Dielectric Liquids," *Proc. Eng. Foundation Conf., Pool and External Flow Boiling*, Santa Barbara, CA, pp. 171–175.

Carvalho, R. D., and Bergles, A. E., 1990, "The Influence of Subcooling on the Pool Nucleate Boiling and Critical Heat Flux of Simulated Electronic Chips," *Proc. 9th International Heat Transfer Conf.*, Jerusalem, Israel, pp. 289–294.

Elkassabgi, Y., and Lienhard, J. H., 1988, "Influences of Subcooling on Burnout of Horizontal Cylindrical Heaters," ASME JOURNAL OF HEAT TRANSFER, Vol. 110, pp. 479–486.

FLUENT, Inc., 1991, "Users Manual," Version 4.1.

Hwang, U. P., and Moran, K. P., 1981, "Boiling Heat Transfer of Silicon Integrated Circuits Chip Mounted on a Substrate," ASME HTD Vol. 20, pp. 53–59.

Ivey, H. J., and Morris, D. J., 1962, "On the Relevance of the Vapor–Liquid Exchange Mechanism for Subcooled Boiling Heat Transfer at High Pressure," UK Report AEEW-R-137, Winfrith, United Kingdom.

Kline, S. J., and McClintock, F. A., 1953, "Describing Uncertainties in Single-Sample Experiments," *Mechanical Engineering*, Vol. 75, Jan., p. 3–8.

Kutateladze, S. S., 1951, "Hydrodynamic Theory of Changes in the Boiling Process Under Free Convection Conditions," *Izv. Akad. Nauk. USSR, Otd. Tekh. Nauk.*, No. 4, p. 529.

Mudawar, I., and Anderson, T. M., 1989, "High Flux Electronic Cooling by Means of Pool Boiling—Part I: Parametric Investigation of the Effects of Coolant Variation, Pressurization, Subcooling, and Surface Augmentation," ASME HTD-Vol. 111, pp. 25–34.

Murphy, R. W., and Bergles, A. E., 1972, "Subcooled Flow Boiling of Fluorocarbons—Hysteresis and Dissolved Gas Effect on Heat Transfer," *Proc. 1972 Heat Transfer and Fluid Mechanics Institute*, Stanford University, pp. 400–416.

O'Connor, J. P., 1994, "Enhancement of Pool Boiling Heat Transfer in Highly-Wetting Dielectric Liquids," Ph.D. Thesis, University of Texas at Arlington, Arlington, TX.

O'Connor, J. P., and You, S. M., 1995, "A Painting Technique to Enhance Pool Boiling Heat Transfer in Saturated FC-72," ASME JOURNAL OF HEAT TRANSFER, Vol. 117, pp. 387–393.

O'Connor, J. P., You, S. M., and Price, D. C., 1995, "A Dielectric Coating Technique to Enhance Boiling Heat Transfer From High Power Microelectronics," *IEEE Trans. CHMT*, Part A, Vol. 18, No. 3, pp. 656–663.

You, S. M., 1990, "Pool Boiling Heat Transfer With Highly-Wetting Dielectric Fluids," Ph.D. Thesis, University of Minnesota, Minneapolis, MN.

You, S. M., Simon, T. W., Bar-Cohen, A., and Hong, Y. S., 1995, "Effects of Dissolved Gas Content on Pool Boiling of a Highly-Wetting Fluid," ASME JOURNAL OF HEAT TRANSFER, Vol. 117, pp. 687–692.

Zuber, N., 1959, "Hydrodynamic Aspects of Boiling Heat Transfer," AEC Report No. AECU-4439, Physics and Mathematics.

Downloaded 11 Dec 2010 to 193.140.21.150. Redistribution subject to ASME license or copyright; see http://www.asme.org/terms/Terms_Use.cfm

J. Yang
Doctoral Student.

L. C. Chow
Professor.

M. R. Pais
Associate Research Professor.

Department of Mechanical Engineering,
University of Kentucky,
Lexington, KY 40506

Nucleate Boiling Heat Transfer in Spray Cooling

An experimental study to determine the effect of liquid and secondary gas flow in droplet impingement cooling is presented. The nucleate boiling regime in particular is analyzed. A correlation to predict the Nusselt number based on the liquid film thickness is derived and compared with the experimental data.

Introduction

The need for enhanced heat dissipation with temperature mitigation is critically observed in power electronics, optics, and aerospace applications. Not only are the predicted heat fluxes high, but the systems also demand low and uniform temperatures with minimum transients. The ability of liquids to change phase at a constant temperature and at the same time remove large amounts of heat in the form of latent heat makes phase-change cooling very attractive.

Spray cooling with phase change has been demonstrated to be a viable method to remove high heat fluxes (greater than 1000 W/cm^2) from surfaces with low superheat (surface temperature minus fluid saturation temperature) (Chow et al., 1989; Tilton, 1989; Yang, 1993). The ability of spray cooling to enhance heat transfer rates greatly while maintaining superheats low is largely attributed to the phenomena occurring within the thin film of liquid deposited on the surface. The thickness of the liquid film in conjunction with the droplet, surface, and film fluid interaction governs the intensities of bubble generation and stirring action. The secondary atomizing gas stagnation flow field strongly controls the droplet impact, liquid film thickness, and liquid film motion (Yang et al., 1992, 1996). The physics of boiling taking place within a thin film of liquid deposited on a hot surface by an air atomizing nozzle is detailed in reference (Chow et al., 1995). The air jet impinging on the surface forms a stagnation point flow field (Yang et al., 1996). The drops impinge on the hot surface to form flat disks, whose thickness is much lower than the diameter of the drop (Chandra and Avedisian, 1991). Simultaneously, the stagnation flow field spreads the droplets/disks further, through shear forces, to form a thin film on the surface.

The typical trend of spray cooling heat flux versus the heater surface temperature is shown in Fig. 1. Three distinct regions exist. In the first region A, forced convection and evaporation are the modes of heat transfer. In the second region B, nucleation plays the major role. Because of the greater magnitude of the latent heat as compared to the sensible heat (in forced convection) the heat transfer increases steeply. When the surface is totally saturated with nucleation sites, a point will be reached (the third region C) when any further increase in surface temperature causes only a marginal increase in the heat flux leading to the critical heat flux.

A close study of the second region B shows that for moderate changes in surface superheat, large changes in heat transfer can be realized. Conversely, this implies that a system can operate over a large power dissipation range and experience only moderate changes in its operating temperature. Hence, the second region is perhaps the most important region from the standpoint of a safe operating region for devices. Most of the studies in spray cooling have been experimental and the models have attempted to predict the maximum heat flux that occurs in the CHF regime (Yang et al., 1993; Chow et al., 1996). So far no model has been proposed to explain the high heat flux in the nucleate boiling region B of spray cooling. This paper attempts to explain the mechanism for high heat transfer in the nucleate boiling region of spray cooling and arrive at a model to predict the heat dissipation.

Experimental Setup

The experimental setup consists of a nozzle-spray system, test surface, phase-Doppler particle analyzer (PDPA) spray characteristics measurement system, and a temperature measurement system (Yang, 1993).

In the nozzle-spray system, an air atomizing nozzle is used to generate droplets over small areas (approximately 12 mm diameter). A thin annular liquid stream of distilled water is injected into the path of an accelerating jet of air. Through surface shear forces, the air jet atomizes the liquid into small droplets. The droplet size and velocity distribution depends on the liquid flow rate and the air pressure. Using the PDPA the spray characteristics were measured (Tilton, 1989; Yang, 1993). The measuring probe, i.e., the intersection of the two laser beams, was located at a distance of 2 mm above the heater surface. With the aid of a translation stage, the spray could be maneuvered to allow the measurement of droplet size and velocity distribution over the entire surface.

The test surface was constructed of a lightweight copper block of pyramidal construction heated by two cylindrical quartz radiation lamps (capable of providing a total of 2000 W). The design (Yang, 1993) allowed a low thermal mass permitting finer control and measurement of the thermal behavior during the spray cooling process. Four K-type thermocouples (0.2 mm diameter) imbedded below the surface provided the temperature gradient and temperature profile below the crown of the surface. Knowing the temperature difference between the thermocouples and the distance between them, it was possible to predict the heat flux using Fourier's law of heat conduction. Then the surface temperature was determined by extrapolation. Two thermocouples were positioned below the center and the other two were positioned halfway between the center and the edge of the surface to determine uniformity in the surface temperature. The whole heater block was insulated to reduce heat loses. The heater surface was of square geometry (11 mm × 11 mm) and was completely covered by the spray cone.

Each experiment was run at a predetermined liquid flow rate and air pressure. Spray droplet size and velocity distributions

Contributed by the Heat Transfer Division and presented at the National Heat Transfer Conference, Atlanta, Georgia, August 8–11, 1993. Manuscript received by the Heat Transfer Division November 17, 1995; revision received May 6, 1996. Keywords: Boiling, Sprays/Droplets, Thin Film Flow. Associate Technical Editor: R. A. Nelson.

Copyright © 1996 by ASME

Downloaded 11 Dec 2010 to 193.140.21.150. Redistribution subject to ASME license or copyright; see http://www.asme.org/terms/Terms_Use.cfm

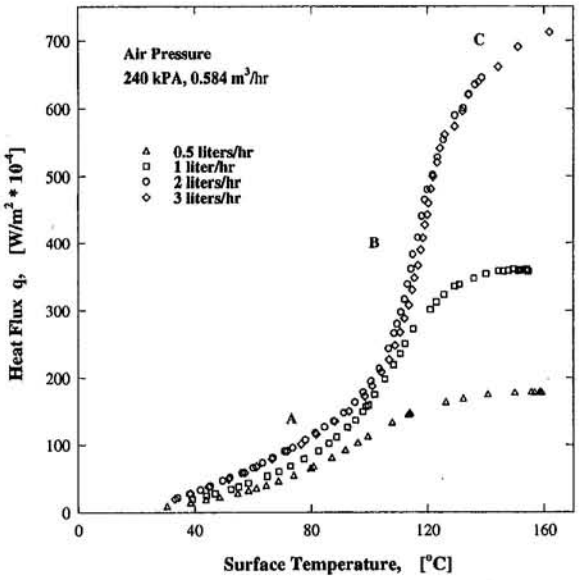


Fig. 1 Effect of liquid flow rate on heat transfer

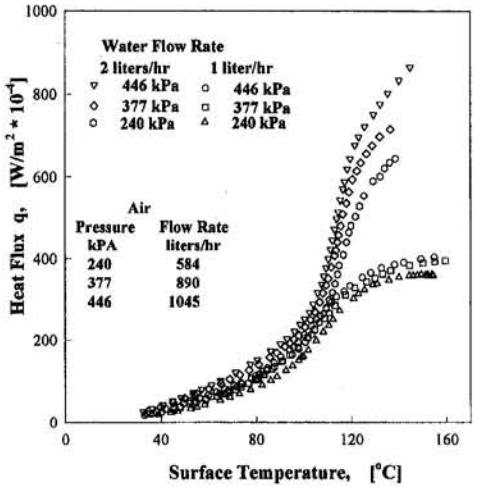


Fig. 2 Effect of air flow rate on heat transfer

were measured using the PDPA system without any heat input. The heater block was then gradually heated to higher temperatures until the CHF conditions were reached. The change in heat flux with surface temperature was continuously monitored. The spray characteristics (droplet size and velocity) for different liquid flow rates and air pressure are given by Yang (1993). For water flow rates between 0.5 to 3 liters per hour and air atomizing pressures between 240 to 446 kPa, the droplet size ranged from 10 μm $< d <$ 18 μm and the droplet velocities were within 25 m/s $< v <$ 58 m/s.

Experiment Results and Discussion

Distilled water at 20°C was sprayed onto the heater surface at varying air pressure and water flow rates. The heat flux and surface temperature were determined simultaneously as the surface was gradually heated.

The flow boiling phenomenon in the liquid film deposited on the top of the heater was monitored by a long-distance microscope. It was found that the bubbles appeared first on the edge of the surface. This is because as the liquid film flows from the center toward the edge of the heater surface, it is continuously absorbing heat through forced convection or nucleate boiling. Hence, saturation conditions within the liquid are first reached at the edge of the surface. In the heat transfer curve of Fig. 1, the heat flux at this point corresponds to the region where the curve tends to change to the nucleate boiling part B. As the heat flux is increased further, the region of nucleation widens in the form of an annular ring closing in toward the center of the surface. The heat transfer correspondingly increases steeply. The heat transfer in the nucleate boiling region B is a combination of forced convection and nucleate boiling; however, nucleation plays the major role. Once the nucleation region has spread over the entire surface, any further increase of heat flux is met with a dearth of liquid on the edge of the surface, i.e., no liquid reaches the edge other than through the direct spray, and nucleation is not visible (region C is reached). Details of spray cooling heat transfer phenomena are given by Chow et al. (1995, 1996).

Effects of Water Flow Rate and Air Pressure

Figure 1 also illustrates the effect of increasing the liquid flow rate at a constant air flow rate. The data indicate that for the nucleate boiling region B, the heat transfer capability increases as the flow rate is increased to 3 liters/h. Any further increase in water flow rate does not increase the heat flux any further. Region C, however, is extended with increase in flow rate.

Figure 2 illustrates the effect of increasing air pressure on the heat transfer at water flow rates of 1.0 liter/h and 2.0 liters/h, respectively. With an increase in air flow there is an increasing trend in the heat transfer and also a reduction in the superheat required. With increasing air flow the liquid film deposited on the surface is thinner and the heat transfer is increased significantly (Yang et al., 1996).

Mechanism of Heat Transfer in Spray Cooling

The heat transfer coefficient in the nucleate boiling region of spray cooling, for a water flow rate of 2 liters/h and an air pressure of 240 kPa, is about 200,000 W/m^2·K. The corresponding heat transfer coefficient for saturated pool boiling is only 40,000 W/m^2·K. This large difference in the heat transfer coefficient is not due to the mechanism of flow convection but rather more due to mechanisms that enhance heat dissipation through phase change. This is because at the low flow rates

Nomenclature

a, b = constants
c = specific heat, J·kg^{-1}·K^{-1}
d = droplet diameter, μm
g = gravity, m·s^{-2}
h = heat transfer coefficient, W·m^{-2}·K^{-1}
H = film thickness, m
k = thermal conductivity, W·m^{-1}·K^{-1}
L = latent heat of vaporization, J·kg^{-1}
Nu = Nusselt number
v = velocity, m·s^{-1}
w = liquid volume flux, m^3·m^{-2}·s^{-1}
X = parameters
μ = dynamic viscosity, Pa·s
ρ = density, kg·m^{-3}
σ = surface tension, N·m^{-1}

Superscripts

n = exponent

Subscripts

g = gas
H = liquid film thickness
l = liquid

Downloaded 11 Dec 2010 to 193.140.21.150. Redistribution subject to ASME license or copyright; see http://www.asme.org/terms/Terms_Use.cfm

used (1 to 3 liters/h) the sensible heat capacity of the flow is almost an order of magnitude less than the latent heat capacity.

Effect of Liquid Film Thickness

In spray impingement the droplets impinge on the surface to form flat disks. If the number of droplets falling on the surface is large enough, then these thin disks combine to form a uniform continuous film on the surface (of the order of 140 μm @ 2 liters/h and 240 kPa, Yang et al., 1992, 1996). The liquid film and its thickness play an important role in the nucleate boiling heat transfer contribution of spray cooling (Yang, 1993). The liquid level or liquid film thickness controls the boiling behavior and hence the heat transfer coefficient. As in pool boiling (Mesler, 1992), the population of nucleation sites increases in thin liquid films, with increase in the heat flux. Nishikawa et al. (1967) also noted that the population of nucleation sites increases as the liquid level is lowered. Hence, depending on the heat flux, the heat transfer coefficient can increase by as much as 50 percent as the liquid level is reduced, until dryout finally occurs (Nishikawa et al., 1967; Nishikawa and Fidgety, 1990; Marto et al., 1977). However, the mechanism that increases the heat transfer coefficient with decreasing liquid level is still not clear. Marto et al. (1977) claimed that such an increase is caused either by induced Marangoni flow (McGrew and Bamford, 1966) around each nucleation site, or by additional microlayer vaporization at the base of each growing bubble as assumed by Grigorev and Dudkevich (1970). Mesler (1976) indicates that the increase in the number of nucleation sites is partly caused by the bursting bubbles inducing the formation of secondary nucleation sites.

Nishikawa and Fidgety (1990) successfully found a correlation that can correlate the experimental data of thin film nucleate boiling within ±20 percent deviation. The correlation is of the form

$$\mathrm{Nu}_H = \frac{hH}{k_l} = bX^n \tag{1}$$

where

$$X = wH\left(\frac{c_l\mu_l}{k_l}\right)^{0.5}\frac{\rho_l g^{0.25}}{L\sigma^{0.75}\rho_g^{1.25}} \tag{2}$$

In spray cooling the liquid film thickness is of the order of 140 μm (@ 2 liters/h and 240 kPa, Yang et al., 1996) and nucleation does exist. Hence, this correlation can be applied by using the liquid film thickness H given in the form (Yang et al., 1996),

$$w = \frac{2}{3}\frac{\rho_g}{\mu_l}a^2H^3 + 1.312\sqrt{\frac{a^3\mu_g\rho_g}{\mu_l^2}}H^2 \tag{3}$$

Here, the constant a is dependent on the geometry, placement, and flow conditions in the nozzle (Martin, 1977; Yang et al., 1996).

Figure 2 shows the effect of air pressure on the heat flux. Since the liquid film is about 140 μm thick and the droplets are about 10 μm in diameter, the ratio of film thickness and droplet diameter is 14 to 1 (Yang, 1993). Experiments using a holographic technique (Yang et al., 1992) indicate that the liquid film produced by an air atomizing nozzle is superficially very flat and that the change in flatness is less than 1 μm (shutter speed 0.1 ms). Here, the term flatness is associated with the topography of the top of the liquid film. This implies that the effects of droplet impingement on the film are felt at the instant and in the vicinity of contact, and are immediately quenched (time < 0.1 ms), at least superficially. Equation (2) was correlated to the heat transfer data in the nucleate boiling region B for three air pressures (240, 377, 446 kPa) and a water flow rate of 1 liter/h. The best fit to Eq. (1) is obtained for b = 1.031 and n = 0.655. Figure 3 illustrates that the correlation effectively combines all the data at the different air pressures into a narrow band within a ±4 percent deviation.

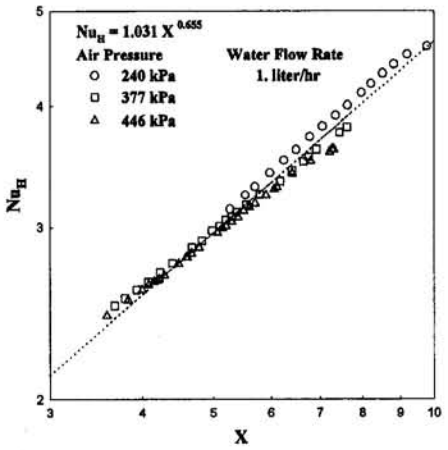


Fig. 3 Correlation for nucleate boiling in spray cooling

Although the nucleate boiling heat transfer coefficient for falling thin liquid films is high, the maximum heat flux that can be attained is low. This is because the adjacent bubbles coalesce to form a vapor blanket over the entire heating surface, thus causing premature dryout. In the spray cooling process, however, the liquid droplets penetrate the vapor blanket to maintain contact between the thin liquid film and the heated surface so that much higher heat fluxes can be reached.

Secondary Nucleation

With reference to Figs. 1 and 2, the heat transfer rate (and hence, also h) increases at any surface temperature as the liquid flow rate is increased. However, it is known that liquid film thickness increases with increase of liquid flow rate (Yang et al., 1996). Hence, in addition to heterogeneous nucleation on the surface, secondary nucleation (proposed by Mesler, 1976) and evaporation also contribute to the enhancement in the heat flux. Evaporation is evident because the enhancement in the value of the heat transfer coefficient from region A to region B occurs prior to 100°C, the boiling point of water under normal atmospheric conditions. Mesler (1992) noted that when droplets impinge on a liquid surface, they entrain vapor as bubbles into the liquid, which serve as nuclei for additional bubbles to grow. The droplet has adsorbed on its surface a layer of gas molecules. When a droplet impinges and penetrates into the liquid-covered surface, this layer of gas molecules is forcibly released to form a tiny gas nucleus which can act as a secondary homogeneous nucleation site. Hence, the number of secondary nucleation sites generated will be proportional to the number flux of droplets. The size and number of the nucleation sites will also depend on the surface area of the droplets. An analysis of the spray characteristics for different water flow rates and air pressures is given by Yang (1993). Figure 4 shows the product of the number flux and surface area of the droplets versus water flow rate. It is evident that the product increases as water flow rate increases. This implies that the number of secondary nucleation sites would increases with flow rate. However, Fig. 4 also indicates that the product of droplet number flux and surface area does not change significantly with increase in air pressure. This implies that air pressure effects the nucleate boiling of spray cooling through control of liquid film thickness.

To judge the effect of water flow rate on nucleate boiling heat transfer in spray cooling, it can be seen that increase of water flow rate, on one hand, increases the number of secondary nucleation sites and hence the heat transfer. On the other hand, it increases the liquid film thickness, resulting in a decrease in

Downloaded 11 Dec 2010 to 193.140.21.150. Redistribution subject to ASME license or copyright; see http://www.asme.org/terms/Terms_Use.cfm

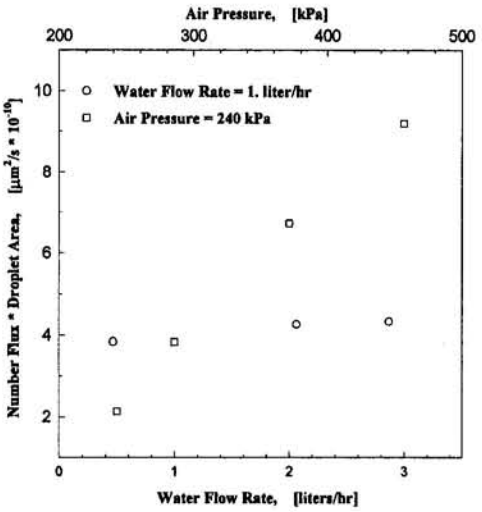


Fig. 4 Variation of droplet flux * area versus air and liquid flow rate

the heat transfer. This decrease in the heat transfer can be attributed to the thermal resistance within the liquid film to heat transfer. For even though secondary nucleation sites exist, the heat must still be conducted from the hot surface through the liquid to the nucleation site (Mesler et al., 1993). The combination of these two effects may lead to little change in the heat transfer at higher liquid flow rates as shown in Fig. 1.

Uncertainty Analysis

The uncertainty in the liquid film thickness or depth (Fresnel diffraction technique, Yang, 1992) from experimental measurements is ± 15 μm, in the pressure is ± 13 kPa, in the air flow rate is ± 0.001 m^3/h, in the water flow rate is 0.1 liters/h, in the temperature is ± 8 percent, and in the heat flux ± 10 percent. The correlation Eq. (1) predicts the experimental data within ± 4 percent.

Conclusions

An experiment was set up to study the heat transfer phenomena in the nucleate boiling regime of spray cooling using air-driven spray nozzles and water as the coolant. Experiments were run for a range of air and water flow rates. Flow field parameters such as liquid film thickness (derived from knowledge of nozzle size and flow geometry) and flow rate are used to arrive at a correlation for the Nusselt number in the nucleate boiling regime, which predicts the experimental data within ± 4 percent.

Acknowledgments

This work was funded by the Aero Propulsion and Power Directorate, Wright Laboratory, Wright-Patterson Air Force Base, Ohio.

References

Chandra, S., and Avedisian, C. T., 1991, "On the Collision of a Droplet With a Solid Surface," *Proc. R. Soc. Lond.*, Vol. 432, No. A, pp. 13–41.

Chow, L. C., Tilton, D. E., and Pais, M. R., 1989, "High Power Density Spray Cooling," WRDC-TR-89-2082, Wright Laboratory, OH.

Chow, L. C., Sehmbey, M. S., and Pais, M. R., 1995, "Critical Heat Flux in High Heat Flux Spray Cooling," *Symposium on Thermal Science and Engineering in Honor of Chancellor Chang-Lin Tien,* Berkeley, CA, Nov, pp. 407–413.

Chow, L. C., Sehmbey, M. S., and Pais, M. R., 1996, "High Heat Flux Spray Cooling," *Annual Review of Heat Transfer,* CRC Press, Inc., Boca Raton, FL, in press.

Grigorev, V. A., and Dudkevich, A. S., 1970, "Boiling Cryogenic Liquid in a Thin Film," *Thermal Engr.*, Vol. 17, p. 74.

Martin, H., 1977, "Heat and Mass Transfer Between Impinging Gas Jets and Solid Surfaces," *Advances in Heat Transfer,* Vol. 13, pp. 1–60.

Marto, P. J., Mackenzie, D. K., and Rivers, A. D., 1977, "Nucleate Boiling in Thin Liquid Films," *AIChE Symp. Ser.*, Vol. 73, No. 164, pp. 228–235.

McGrew, J. L., and Bamford, F. L., 1966, "Marangoni Flow: An Additional Mechanism in Boiling Heat Transfer," *Science,* Vol. 153, Sept., pp. 1106–1107.

Mesler, R., 1976, "A Mechanism Supported by Extensive Experimental Evidence to Explain High Heat Fluxes Observed During Nucleate Boiling," *AIChE J.*, Vol. 22, No. 2, pp. 246–252.

Mesler, R., 1992, "Improving Nucleate Boiling Using Secondary Nucleation," *Pool and External Flow Boiling Heat Transfer,* Engg. Foundation Conf., Santa Barbara, CA, pp. 43–47.

Mesler, R., Pais, M. R., Chow, L. C., and Mahefkey, E. T., 1993, "Discussions on Surface Roughness: Its Effects on the Heat Transfer Mechanism of Spray Cooling," ASME JOURNAL OF HEAT TRANSFER, Vol. 115, pp. 1083–1085.

Nishikawa, K., Kusuda, H., Yamasaki, K., and Tanaka, K., 1967, "Nucleate Boiling at Low Levels," *Bulletin of JSME,* Vol. 10, No. 38, pp. 328–338.

Nishikawa, K., and Fidgety, Y., 1990, "Nucleate Boiling Heat Transfer and Its Augmentation," *Advances in Heat Transfer,* Vol. 20, pp. 1–82.

Tilton, D. E., 1989, "Spray Cooling," PhD Dissertation, Dept. of Mechanical Engineering, University of Kentucky, Lexington, KY.

Yang, J., Chow, L. C., and Pais, M. R., 1992, "Liquid Film Thickness and Topography Determination Using Fresnel Diffraction and Holography," *Experimental Heat Transfer,* Vol. 5, pp. 239–252.

Yang, J., 1993, "Spray Cooling With an Air Atomizing Nozzle," PhD Dissertation, Dept. of Mechanical Engineering, University of Kentucky, Lexington, KY.

Yang, J., Pais, M. R., and Chow, L. C., 1993, "Critical Heat-Flux Limits in Secondary Gas Atomized Liquid Spray Cooling," *Experimental Heat Transfer,* Vol. 6, pp. 55–67.

Yang, J. D., Chow, L. C., and Pais, M. R., 1996, "An Analytical Method to Determine the Liquid Film Thickness Produced by Gas Atomized Sprays," ASME JOURNAL OF HEAT TRANSFER, Vol. 118, pp. 255–258.

Downloaded 11 Dec 2010 to 193.140.21.150. Redistribution subject to ASME license or copyright; see http://www.asme.org/terms/Terms_Use.cfm

Optimizing and Predicting CHF in Spray Cooling of a Square Surface

I. Mudawar
Professor and Director.

K. A. Estes
Graduate Student.

Boiling and Two-Phase Flow Laboratory,
School of Mechanical Engineering,
Purdue University,
West Lafayette, IN 47907

Spray cooling of a hot surface was investigated to ascertain the effect of nozzle-to-surface distance on critical heat flux (CHF). Full cone sprays of Fluorinert FC-72 and FC-87 were used to cool a 12.7 × 12.7 mm² surface. A theoretical model was constructed that accurately predicts the spray's volumetric flux (liquid volume per unit area per unit time) distribution across the heater surface. Several experimental spray sampling techniques were devised to validate this model. The impact of volumetric flux distribution on CHF was investigated experimentally. By measuring CHF for the same nozzle flow rate at different nozzle-to-surface distances, it was determined CHF can be maximized when the spray is configured such that the spray impact area just inscribes the square surface of the heater. Using this optimum configuration, CHF data were measured over broad ranges of flow rate and subcooling, resulting in a new correlation for spray cooling of small surfaces.

1 Introduction

Sprays can be formed either by supplying liquid at high pressure through a small orifice (pressure spray) or by breaking the liquid with the aid of a high-pressure supply of air (atomized spray). The present study is concerned with pressure sprays that simplify cooling by requiring a single (pure) working fluid.

Spray cooling has long been employed in the quenching of metals upon exit from a high-temperature furnace, and many studies exist in the literature for predicting spray heat transfer for those situations (e.g., Watchers et al., 1966; Bolle and Moureau, 1976; Moriyama et al., 1987). Since furnace temperatures typically correspond to the film boiling regime, these studies are not applicable to situations involving removal of high heat fluxes at relatively low surface temperatures such as cooling of supercomputer electronics, avionics, x-ray medical devices, and lasers—devices for which the findings of the present study are intended.

Spray and jet cooling are often considered competing options in these types of application. A major disadvantage to jet cooling is that the large concentration of heat removal within the impingement zone causes relatively large temperature gradients within the cooled surface, which can result in catastrophic failure of certain temperature sensitive devices. This problem can be partially alleviated by employing an array of jets to cool a single device; however, interference between neighboring wall jets emanating from the impingement zones of the individual impinging jets greatly complicates coolant flow. Two-phase jet cooling is further complicated by an inability to sustain much phase change in the wall jet. To release the vapor produced at the surface, wall jets tend to separate from the surface due to the vapor momentum perpendicular to the surface. In fact, CHF in jets is often encountered even with an abundance of liquid in the wall jet (Monde et al., 1980).

Sprays, on the other hand, utilize the momentum of liquid entering the spray nozzle to induce breakup into fine drops, which impinge individually upon the heated surface. Not only does the breakup increase the surface area to volume ratio of the liquid, but it also helps produce a more uniform spatial distribution of heat removal both in the single-phase and nucleate boiling regimes. Another key feature of spray cooling is delaying liquid separation from the surface during vigorous boiling. By bombarding the entire surface with drops, the momentum of the individual drops is more effective at resisting the momentum of vapor perpendicular to the surface than a wall jet. Simply stated, the liquid film deposited upon the heater surface in the case of jet cooling is "anchored" to the surface only at the impingement zone and is, therefore, susceptible to breakdown and separation over much of the heater surface; the liquid film in the case of spray cooling in anchored to the entire surface.

Despite these advantages, spray cooling remains less popular for cooling of low-temperature, high heat flux devices for several reasons. Breakup of the liquid flow to fine drops demands relatively high pressures, which may not be desirable in certain situations, and the small size of the spray orifice increases the likelihood of clogging, which could lead to eventual surface burnout. Furthermore, seemingly identical nozzles machined with close tolerances often fail to produce identical spray patterns; careful testing of nozzle patterns is essential where predictable and repeatable cooling performance is a must (Hall and Mudawar, 1995). But the single most important reason for the limited use of spray cooling in low-temperature, high heat flux situations is undoubtedly the lack of understanding of the mechanisms of boiling, especially CHF, and the absence of useful heat transfer correlations that can be employed over broad ranges of spray parameters.

Spatial Variations in Spray Cooling. The pressure (liquid-only) sprays commonly used in cooling applications are categorized as either full-cone sprays or flat sprays, which possess circular and oval spray impact areas, respectively. Mudawar and Deiters (1994) investigated the spatial variation of the heat transfer coefficient across the impact area in both full-cone and flat water sprays. They also measured the spatial variations of the key hydrodynamic parameters of the spray just prior to impact. These include volumetric flux, Q'', mean drop velocity, U_m, and Sauter mean diameter, d_{32}. Both Q'' and U_m are measured in units of velocity, the former being the volume flow rate of liquid impacting an infinitesimal portion of the impact area divided by the area of the same portion. Mudawar and Deiters observed that while U_m was virtually constant for the entire spray impact area, the heat transfer coefficient peaked at the center of the impact area and decayed gradually away from the center, becoming negligible just outside of the impact

Contributed by the Heat Transfer Division for publication in the JOURNAL OF HEAT TRANSFER. Manuscript received by the Heat Transfer Division January 10, 1995; revision received April 2, 1995. Keywords: Boiling, Electronic Equipment, Sprays/Droplets. Associate Technical Editor: T. W. Simon.

Copyright © 1996 by ASME

Downloaded 11 Dec 2010 to 193.140.21.150. Redistribution subject to ASME license or copyright; see http://www.asme.org/terms/Terms_Use.cfm

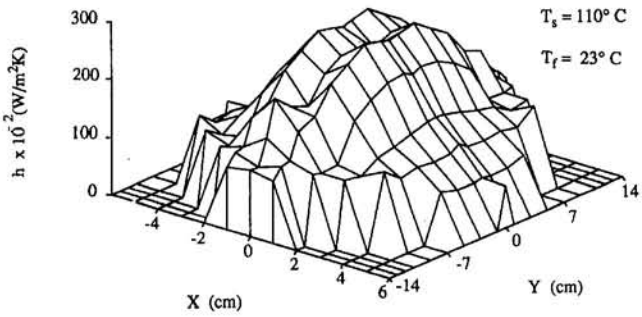


Fig. 1 Variation of heat transfer coefficient across spray impact area

area as shown in Fig. 1. This spatial distribution followed essentially the distribution of volumetric flux, Q'', across the impact area.

In fact, the dimensionless correlations developed by Mudawar and Valentine (1989) reveal what was suggested earlier by Toda (1972): The proper scaling velocity for heat transfer correlations near CHF is Q'' not U_m, and the scaling length is d_{32}. Increasing Q'' for water sprays ameliorated heat transfer, while increasing drop diameter adversely affected CHF; smaller drops yielded better cooling.

A key reason why Q'' and not U_m is the appropriate scaling velocity in correlating CHF data is that the latter fails to account for the commutative effect of multiple drop impact; i.e., its magnitude has no bearing on the number of drops impacting the surface per unit area per unit time. In fact, different sprays can possess equal drop velocities but vastly different volumetric fluxes.

Unlike the studies by Mudawar and Valentine and by Mudawar and Deiters, which resulted in correlations for a small heater positioned in a much larger spray impact area, the present study is concerned with spray boiling and CHF from a square heater almost entirely impacted by the spray. Key objectives of the present study are to

1 develop a better understanding of how volumetric flux influences cooling performance for the full cone sprays commonly employed in low-temperature, high heat flux applications;
2 optimize nozzle-to-surface distance in order to maximize CHF; and
3 develop a CHF correlation that precludes having to perform costly spray drop sizing experiments.

2 Experimental Facility

Flow Loop and Test Chamber. The working fluid (FC-72 or FC-87) was deaerated and conditioned to the desired operating pressure and temperature using the flow loop shown in Fig. 2(*a*). The spray was formed within the test chamber of the loop. A magnetically coupled centrifugal pump transferred the fluid from a reservoir situated beneath the test chamber through the loop components, which included three flat plate heat exchangers, a carbon filter, a flow-through electrical heater, and one of two rotameters. Two of the flat plate heat exchangers removed essentially the heat added by the pump, while fine tuning of the liquid temperature upstream of the test chamber was accomplished by heat addition in the flow-through electrical heater and additional heating or cooling via the third heat exchanger inside which water was circulated through a constant temperature bath.

A pressure gage was situated just upstream of the spray nozzle and another connected directly to the test chamber. Pressure difference across the nozzle was used to correlate Sauter mean diameter data, while the test chamber pressure was the reference for determining the saturation temperature and associated properties used in correlating CHF data. Uncertainties in the pressure measurements were determined from the pressure gage manufacturer specifications to be less than 0.5 percent, which was also confirmed by calibration. Uncertainties in the spray flow rate measurement resulting from fabrication tolerances, effects of temperature changes on the density and viscosity of the fluid, as well as the expansion and contraction of the rotameter parts, were estimated from the manufacturer specifications at 1.6 percent; this value was also confirmed by calibration.

Inside the chamber, liquid exiting the nozzle impinged upon the test heater and drained directly into the loop reservoir, as shown in Fig. 2(*b*). Any vapor produced within the chamber was recovered by a condensing coil situated within the chamber itself. A micrometer translation platform mounted atop the test chamber enabled precise positioning of the spray nozzle relative the test heater's surface. As shown in Fig. 3(*a*), the impingement surface, which measured 12.7 × 12.7 mm^2, was fabricated from oxygen-free copper. Heat was dissipated to the impingement surface by a thick film electrical resistor, which was soldered to the underside of the copper block as shown in Fig.

Nomenclature

A = area defined along the heater's surface
A' = area defined along a spherical surface
c_p = specific heat at constant pressure
d_i = middle diameter of ith class of drops
d_0 = nozzle orifice diameter
d_{32} = Sauter mean diameter (SMD)
H = nozzle-to-surface distance
h_{fg} = latent heat of vaporization
L = heater length (12.7 mm)
n_i = number of drops in ith class
P = test chamber pressure
ΔP = pressure drop across spray nozzle
q = electrical power input to heater
q'' = heat flux based on entire square heater area = q/L^2
q''_m = critical heat flux based on entire square heater area = q/L^2 (at CHF)
$q''_{m,p}$ = local critical heat flux at outer edge of impact area
$q''*$ = dimensionless CHF
Q = total volumetric flow rate of spray
Q'' = local volumetric flux (liquid volume per unit area per unit time)
$\overline{Q''}$ = average volumetric flux over spray impact area = $Q/(\pi R^2)$ (or $Q/(\pi L^2/4)$ for an optimized spray)
Q_i = flow rate incident at target (insert)
Q_s = flow rate incident on heater surface
Q''_{sp} = uniform volumetric flux along a spherical surface
r = radial coordinate
R = radius of spray impact area
R_i = target (insert) radius
T = temperature
T_f = spray inlet temperature
ΔT_{sub} = liquid subcooling at nozzle inlet = $T_{sat} - T_f$
ΔT_w = surface-to-liquid temperature difference = $T_w - T_f$
U_m = mean drop velocity
We = spray Weber number
γ = integration angle in volumetric flux distribution model
θ = spray cone angle
μ = viscosity
ρ = density
σ = surface tension

Subscripts

f = liquid
g = vapor
sat = saturation
sub = subcooling
w = heater surface condition

Downloaded 11 Dec 2010 to 193.140.21.150. Redistribution subject to ASME license or copyright; see http://www.asme.org/terms/Terms_Use.cfm

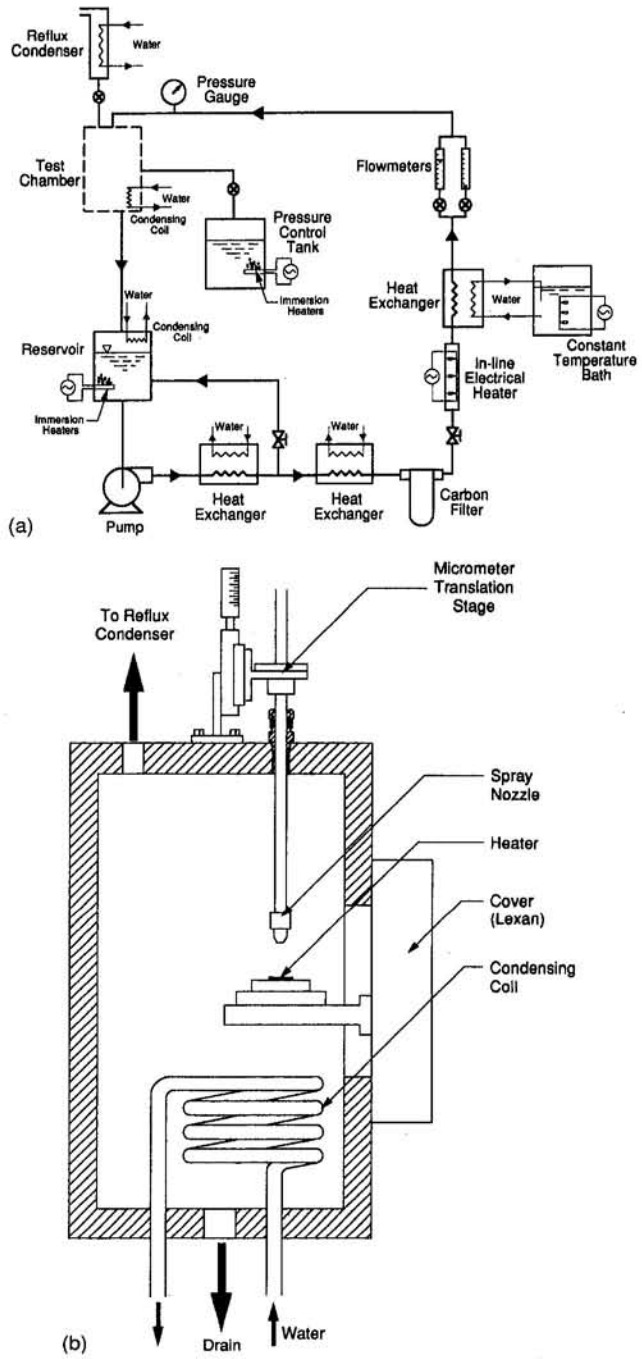


Fig. 2 Schematic of (*a*) flow loop and (*b*) test chamber

3(*b*). The heater assembly was insulated on all surfaces save the impingement surface with G-7 fiberglass plastic.

Uncertainties in the measurement of electrical power input to the thick film resistor due to the Watt transducer and the resistance of the thick film resistor's lead wires was estimated at 1.0 percent. Another source of uncertainty in the measurement of heat flux was the heat loss from boundaries other than the sprayed surface. A numerical scheme provided a conservative estimate for this heat loss. This scheme is based on the assumption that the heat transfer coefficient on the plastic surface surrounding the sprayed heater surface equals the heat transfer coefficient on the sprayed surface itself. To calculate this heat transfer coefficient, perfect contact was assumed between the heater and all surrounding plastic material. A two-dimensional finite element model was developed, assuming the heat transfer coefficient was equal to the electrical power divided by the product of measured temperature difference and sprayed area. The model was then refined by subtracting from the electrical power the heat loss estimated from the first calculation. Further iteration resulted in a heat loss estimate for a given electrical power input. This heat loss was adjusted for heat loss through the two transverse planes to account more accurately for three-dimensional heat loss. This numerical technique was employed for power input levels corresponding to the single-phase and nucleate boiling regimes, resulting in values smaller than 4.5 and 1.0 percent, respectively.

Operating Procedure. Prior to each test, the heater module was removed from the test chamber and the heater surface was polished using Happich Simichrome polishing paste. A cotton applicator dipped in methanol was then used to remove any residue left on the surface by the polish.

The fluid was carefully deaerated after the heater module was mounted inside the test chamber. Immersion heaters located in

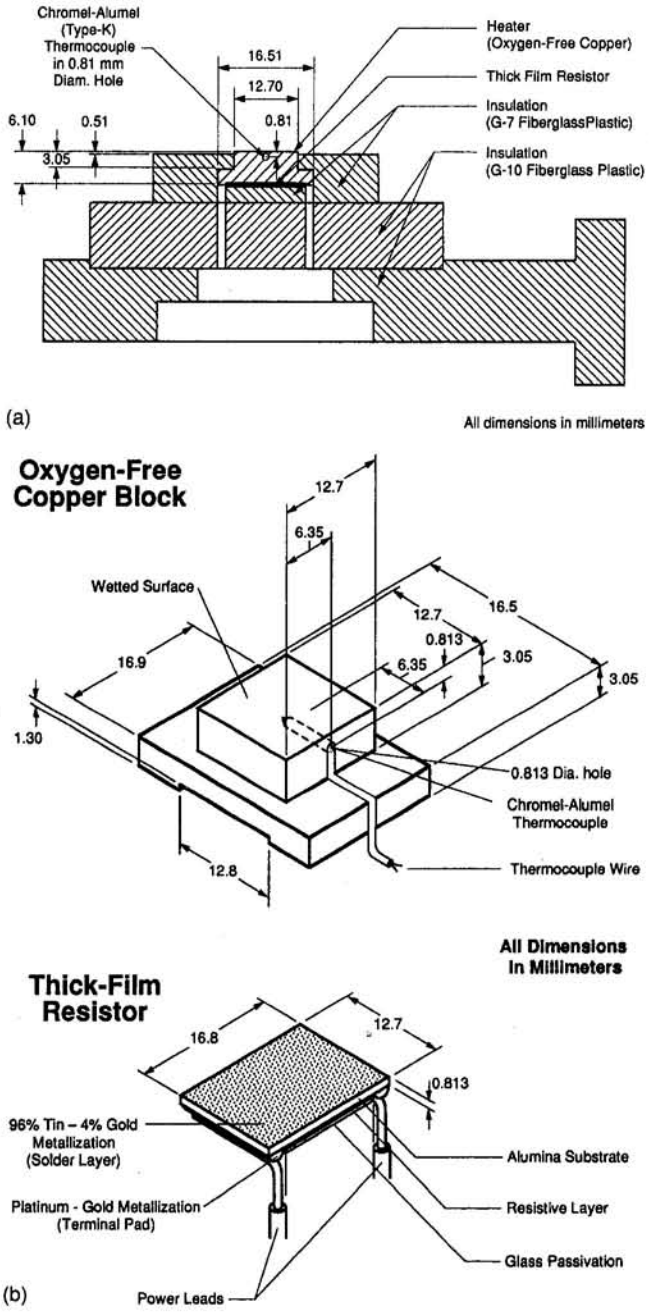


Fig. 3 Construction of (*a*) heater module and (*b*) test heater

Downloaded 11 Dec 2010 to 193.140.21.150. Redistribution subject to ASME license or copyright; see http://www.asme.org/terms/Terms_Use.cfm

the reservoir were used to boil the liquid, forcing the vapor produced and any dissolved noncondensible gases to exit through a reflux condenser connected to the top of the test chamber. Cold water circulating through the reflux condenser recovered the pure vapor while the noncondensible gases escaped freely to the ambient. After about 15 minutes of vigorous boiling in the reservoir, the pump was started and the deaeration proceeded for an additional 15 minutes as the fluid circulated through the loop.

Upon completion of the deaeration, the line connecting the test chamber to the reflux condenser was closed off to seal the loop completely. Pressure in the chamber was then adjusted to, and maintained at 1.03 bar (15 psia), by controlling vapor production inside the test chamber. The vapor production could be increased by increasing electrical power to immersion heaters inside a pressure control tank connected to the test chamber, or decreased by increasing the flow of water through the condensing coil inside the test chamber itself.

Boiling curves were obtained by raising the voltage across the heater's thick film resistor in small increments, using an autotransformer, and recording both the heat flux at the heater surface and the surface temperature. A Keithley 500 data acquisition system monitored and recorded both the power supplied to the heater, via a watt transducer, and temperatures throughout the loop, including the heater and nozzle inlet. The boiling data were recorded only after the heater temperature reached steady state. The power increments were reduced to less than 1.0 W/cm^2 as CHF was approached in order to both preclude premature occurrence of CHF and ensure accurate CHF measurement.

CHF was identified when the heater thermocouple detected a sudden unsteady rise in the heater temperature. Repeatability of CHF data throughout the study was ensured by running tests under identical conditions weeks and often months apart. No two such data points departed from one another by more than 5 percent. This repeatability was the result of the consistent operating procedure and the careful surface preparation, including the use of the polishing paste to help prevent the formation of an oxide layer during a given test.

3 Spray Sampling Techniques

As indicated earlier, two types of spray are commonly used in industry: air-assist (atomized) sprays and pressure (liquid-only) sprays. It is extremely difficult to publish generic fundamental studies on atomized sprays because their nozzles are available in a large variety of complex designs. With the exception of a few specialized nozzles (e.g., spiral-shaped, acoustically controlled), pressure sprays are generally available in a simple basic design. The applications for which the findings of the present study are intended (e.g., cooling of electronic and laser devices) preclude mixing of air with the liquid coolant, which explains why only pressure sprays were employed. To the authors' knowledge, Spraying Systems' full cone series nozzles are the industry's standard for sprays intended to provide full coverage over a circular impact area. The basic and generic design of these nozzles, and their popularity are all reasons behind their use in the present study. The full cone spray is produced by a simple stationary vane inside the nozzle, which induces turbulence in the liquid prior to exiting the orifice in order to promote liquid break-up.

Hall and Mudawar (1995) demonstrated experimentally that repeatability in spray impact pattern and cooling performance requires adherence to specific operation guidelines. These guidelines were strictly followed in the present study. They include: (*a*) avoiding brass nozzles and using nozzles made from erosion and corrosion resistant materials (only stainless steel nozzles were used in the present study); (*b*) testing nozzles periodically to make sure flow rate and spray angle are repeatable; (*c*) visually examining the spray pattern during operation for any irregularities (unsymmetric spray pattern, deflected spray, dented orifice); and (*d*) using a high-purity fluid and installing a small particle filter upstream of the nozzle. As an added precaution, the same nozzles used for drop diameter measurements were also used in the heat transfer measurements.

The spray heat transfer data measured in the present study were correlated with respect to the spray Weber number as proposed by Mudawar and Valentine (1989), the ratio of spray momentum to the surface tension forces exerted upon the spray drops:

$$\mathrm{We} = \frac{\rho_f Q''^2 d_{32}}{\sigma} . \tag{1}$$

The Weber number can be based on either local or average values of volumetric flux. The local volumetric flux, Q'', is the volumetric flow rate for an infinitesimal portion of the impact surface divided by the area of the same portion. Another convenient measure of spray flux is the average volumetric flux, $\overline{Q''}$, which can be readily determined by dividing the total volumetric flow rate of the spray by the portion of the surface directly impacted by the spray, the so called spray impact area. Of course, sprays with the same values of $\overline{Q''}$ can yield different cooling performances, depending upon the spatial distribution of Q''. This important issue will be discussed in detail in the next section.

The Sauter mean diameter (SMD), d_{32}, used to calculate the spray Weber number, Eq. (1), is defined as the diameter of the drop with a volume-to-surface area ratio that equals the volume to surface area ratio of the entire spray:

$$d_{32} = \frac{\Sigma\, n_i d_i^3}{\Sigma\, n_i d_i^2} , \tag{2}$$

where n_i represents the number of drops in a size class i and d_i is the middle diameter of this ith class. Estes (1994) measured drop diameters for the full cone spray nozzles employed in the present study using FC-72 and water using a Phase Doppler Particle Analyzer (PDPA). Adopting a correlation form recommended by Lefebvre (1989) for liquid breakup, Estes reduced his own full cone spray data according to the equation

$$\frac{d_{32}}{d_0} = 3.07 \left[\frac{\rho_g^{1/2} \Delta P d_0^{3/2}}{\sigma^{1/2} \mu_f} \right]^{-0.259} \tag{3}$$

with a mean absolute error of 12.4 percent, where d_0 and ΔP are the diameter of the nozzle orifice and the nozzle pressure drop, respectively.

As shown in Fig. 4, when the nozzle is remote from the heater surface, the fraction of liquid leaving the nozzle that impacts the surface is a function of spray angle, θ, nozzle-to-surface distance, H, and heater length, L. To measure this fraction experimentally, a spray sampler fitted with a graduated cylinder (collector) was fabricated. As shown in Fig. 5(*a*), the sampler possessed a knife-edged inlet with a sampling area equal to the heater surface area, 12.7 × 12.7 mm^2. The sampler was mounted in the heater flange itself with its inlet positioned at the exact location of the heater. Mounted above the sampler was a quick-release shading plate, which deflected the flow from the collector until the spray became fully developed and the operator was ready to commence sampling. An O-ring glued to the underside of the shading plate proved effective at preventing liquid that accumulated on the plate's underside from dripping into the collector. During the measurement, the shading plate was quickly pulled back, allowing liquid to accumulate in the collector to a preset volume, and then quickly repositioned to shelter the sampling area. The volumetric flow rate incident upon the heated surface was estimated as the volume collected divided by the product of sampling area (heater area) and fill time.

Since the spray's volumetric flux is not uniform across the heated surface area, the spray sampler shown in Fig. 5(*a*) could

Downloaded 11 Dec 2010 to 193.140.21.150. Redistribution subject to ASME license or copyright; see http://www.asme.org/terms/Terms_Use.cfm

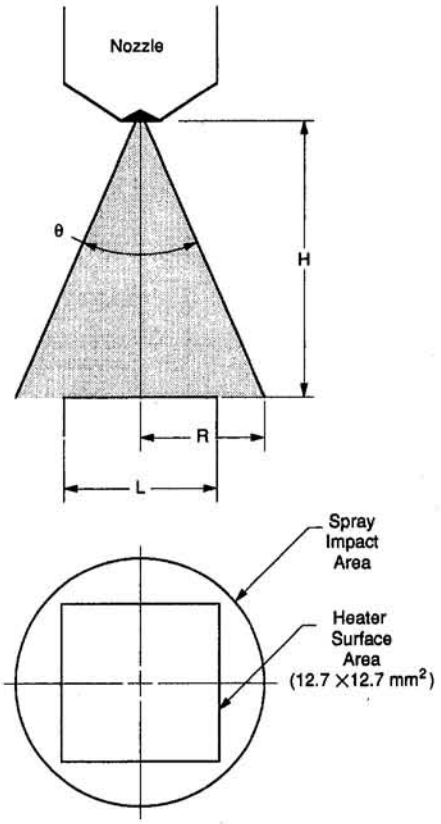


Fig. 4 Nozzle-heater configuration

not measure the spatial distribution of volumetric flux. This distribution was inferred with the aid of inserts, shown in Fig. 5(*b*), which were slid into the square opening of the original sampler as illustrated in Fig. 5(*c*). The three different sized circular openings of these inserts enabled measurement of flow rate over sampling areas smaller than the heater surface area.

4 Volumetric Flux Distribution Model

As indicated by Mudawar and Deiters (1994), volumetric flux is not uniform across the spray impact area. A model is, therefore, developed to predict how the spray flow rate is distributed across the heated surface. The model, which is intended for the full breakup region of the spray away from the orifice, is based on the assumption that the total spray flow rate, Q, is uniformly distributed over any spherical surface centered at the spray orifice (i.e., the orifice represents a uniform point source for the sprayed liquid) and bound by the spray cone angle, θ. The validity of this assumption will become apparent from the experimental results discussed later.

As the spray impacts a flat surface located a distance H from the orifice, the uniform volumetric spray flux along the spherical surface of radius H produces a volumetric flux on the impact surface, which decreases radially from the center of the impact surface. As shown in Fig. 6, a differential area, dA', along the spherical surface is given by

$$dA' = 2\pi H^2 \sin \gamma d\gamma. \tag{4}$$

Integrating γ between 0 and $\theta/2$ yields the area of the spherical surface bound by the spray angle,

$$A' = 2\pi H^2[1 - \cos(\theta/2)]. \tag{5}$$

Since a uniform volumetric spray flux is assumed over the spherical surface area A', this flux can be defined as

$$Q''_{sp} = \frac{Q}{2\pi H^2[1 - \cos(\theta/2)]}. \tag{6}$$

The projection of dA' upon the flat impact surface is another differential area, dA, which can be defined as

$$dA = \pi(H \tan(\gamma + d\gamma))^2 - \pi(H \tan \gamma)^2$$

$$= 2\pi H^2 \frac{\sin \gamma}{\cos^3 \gamma} d\gamma. \tag{7}$$

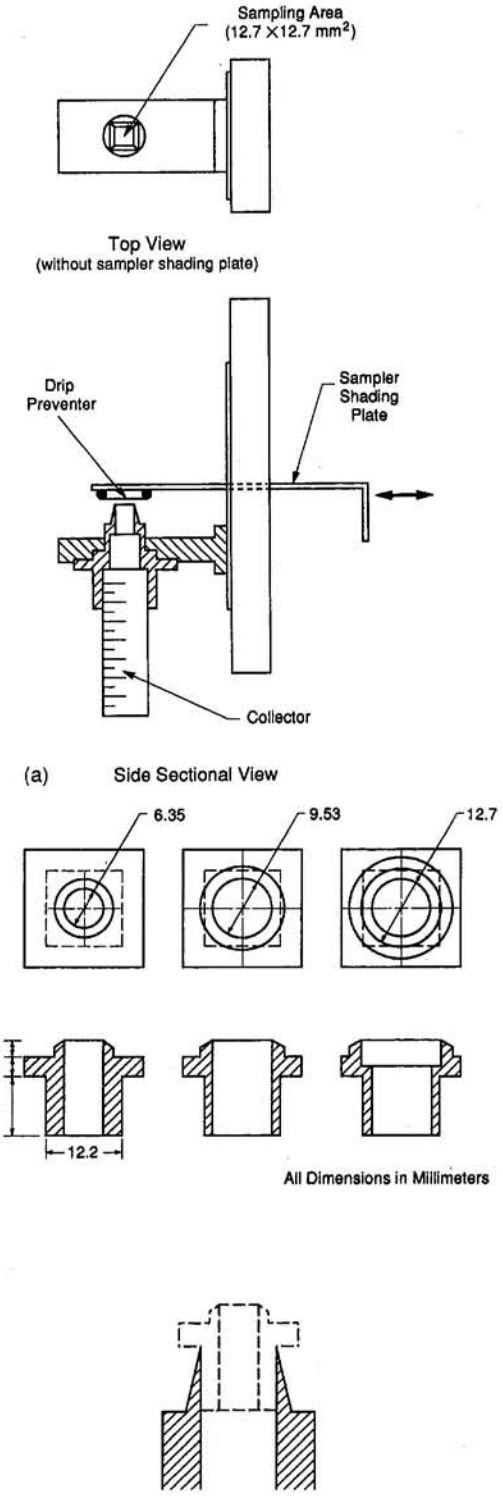


Fig. 5 Construction of (*a*) spray sampler and (*b*) inserts used for determination of volumetric flux distribution, and (*c*) placement of inserts in sampler

Downloaded 11 Dec 2010 to 193.140.21.150. Redistribution subject to ASME license or copyright; see http://www.asme.org/terms/Terms_Use.cfm

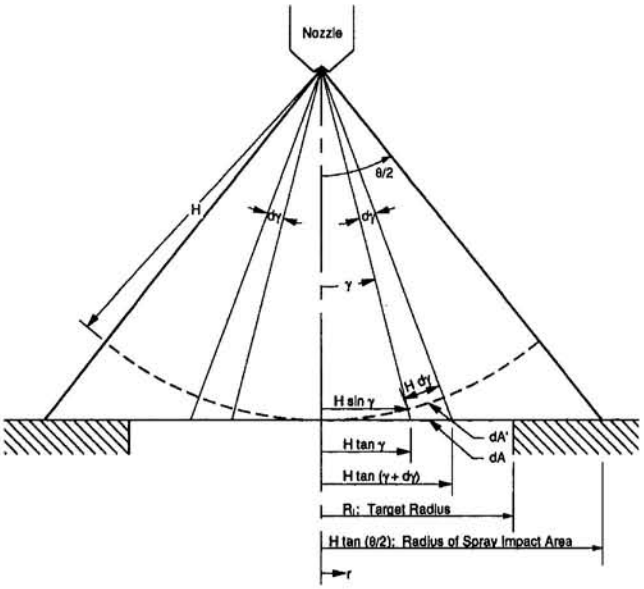


Fig. 6 Geometry used in development of volumetric flux distribution model

Thus, the spray volumetric flux along the impact surface is given by

$$Q'' = Q''_{sp}\frac{dA'}{dA} = \frac{Q}{[1-\cos(\theta/2)]}\cdot\frac{1}{2\pi H^2\cos^3\gamma}$$

$$= \frac{1}{2}\left[\frac{Q}{\pi(H\tan(\theta/2))^2}\right]\left[\frac{\tan^2(\theta/2)}{1-\cos(\theta/2)}\right]$$

$$\times\frac{1}{\left[1+\left(\frac{r}{H}\right)^2\right]^{3/2}}. \quad (8)$$

A small circular target of radius R_i centered on the impact surface will receive a flow rate

$$Q_i = \int_0^{R_i} Q''2\pi r dr. \quad (9)$$

Dividing Q_i by the total spray flow rate, Q, gives the fraction of the flow rate impacting the target.

$$\frac{Q_i}{Q} = \frac{1}{1-\cos(\theta/2)}\left[1-\frac{1}{\sqrt{1+\left(\frac{R_i}{H}\right)^2}}\right]$$

$$\text{for} \quad R_i < H\tan(\theta/2). \quad (10)$$

Targets with $R_i > H\tan(\theta/2)$, on the other hand, will capture the entire flow rate.

The flow rate captured by any of the inserts shown in Fig. 5(*b*) should then equal Q_i as defined in Eqs. (9) and (10). Figure 7 shows that the volumetric flux predicted by Eq. (8) decreases from a maximum along the spray axis to roughly one half of the maximum toward the outer edge of the impact area. Figure 8 illustrates, for Fluorinert FC-87 (only FC-87 was used in verifying the volumetric flux distribution model), the favorable agreement between measured and predicted ratios of flow rate captured by the insert to total spray flow rate, Eq. (10).

These results prove the fraction of the spray flow rate received by a target can be determined purely from geometric arguments. This fraction equals unity for $H \le R_i/\tan(\theta/2)$. This conclusion is crucial to the optimization of heat transfer from spray-cooled targets, especially near CHF. Maximum utilization of the spray flow rate is achieved when $H \le R_i/\tan(\theta/2)$. On the other hand, a very small nozzle-to-surface distance would concentrate the spray impact area over only a small central portion of the heated surface, depriving the surrounding surface from direct impact by the spray drops. It is, therefore, of paramount importance to determine the nozzle-to-surface distance that would yield the highest CHF. This issue is further complicated with square targets that possess corner regions that are less adequately cooled than the center. The next section will examine the problem of optimizing the nozzle-to-surface distance for a square target.

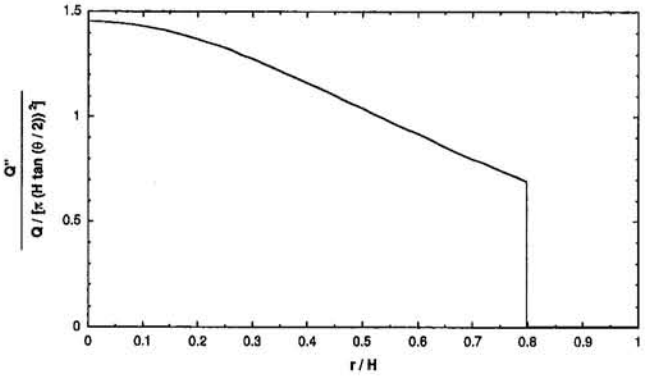


Fig. 7 Predicted distribution of volumetric flux

5 Optimization of Nozzle-to-Surface Distance and Correlation of CHF Data

CHF measurements were repeated at different nozzle-to-surface distances while maintaining the same flow rate. Figure 9 shows the ratio of CHF measured at a given nozzle-to-surface distance to the maximum CHF measured over the entire range of distances, plotted against $H\tan(\theta/2)/(L/2)$. Also shown in the same figure is the ratio of flow rate captured by the sampler without an insert (i.e., with a sampling area equal to the heater surface area) to the total spray flow rate. The largest critical heat flux seems to occur near the point where the spray just inscribes the square heated area, i.e., $H = (L/2)/\tan(\theta/2)$.

These results reveal that when the spray impact area is small (i.e., for small nozzle-to-surface distances), only a small fraction of the heated area is directly impacted by the spray drops, yielding small CHF values. CHF also decreases when the nozzle-to-surface distance is increased past the point of heated area inscription by the spray because a fraction of the liquid leaving

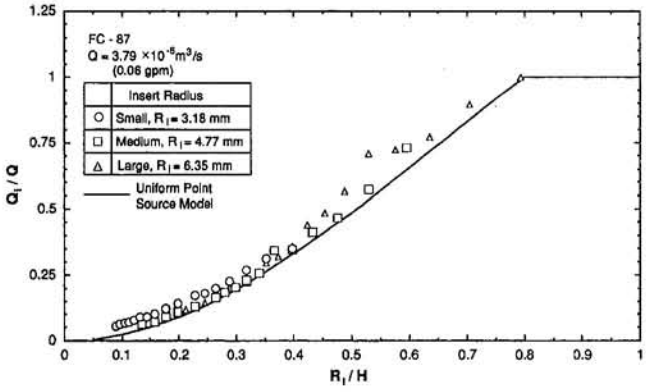


Fig. 8 Comparison of the model predictions of flow rate collected using the inserts with experimental data

Downloaded 11 Dec 2010 to 193.140.21.150. Redistribution subject to ASME license or copyright; see http://www.asme.org/terms/Terms_Use.cfm

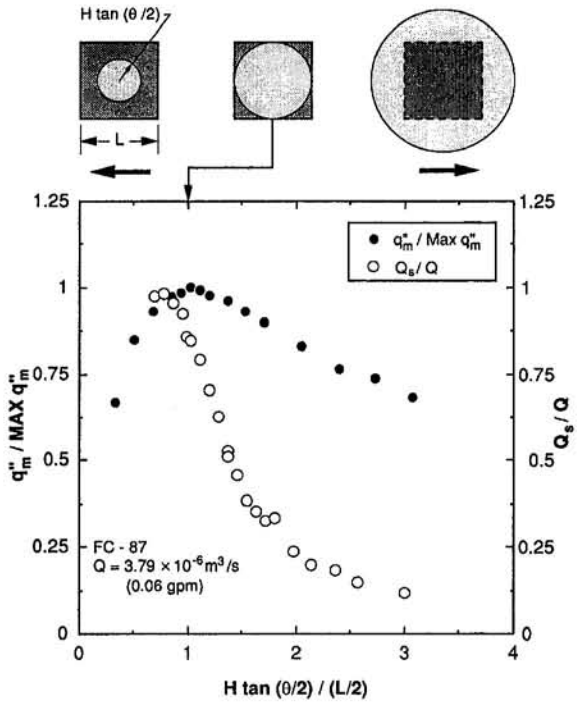


Fig. 9 Optimization of nozzle-to-surface distance for maximum CHF

the nozzle would be wasted. It is, therefore, recommended that a spray intended to cool a square heated surface be configured such that its impact area just inscribes the heater surface. Not only does this configuration maximize CHF, but it is also very simple to accomplish since it requires knowledge of only spray angle and heater size. This configuration was, therefore, utilized and maintained throughout the data base used to develop the CHF correlation.

Katto and co-workers (see Monde et al., 1980) proved that CHF data for most external flow boiling systems can be correlated according to a single dimensionless equation in terms of density ratio, Weber number, and Jacob number, using empirical coefficients and exponents. Mudawar and Valentine (1989) replaced the characteristic velocity and characteristic length in the general Katto equation by volumetric flux and Sauter mean diameter for spray cooling systems. They correlated CHF for a small circular heater situated in a large impact area according to the equation

$$\frac{q''_{m,p}}{\rho_g Q'' h_{fg}} = f\left[\frac{\rho_f}{\rho_g}, \frac{\rho_f Q''^2 d_{32}}{\sigma}, \frac{\rho_f c_{p,f}\Delta T_{sub}}{\rho_g h_{fg}}\right], \qquad (11)$$

where $q''_{m,p}$, Q'', and d_{32} are all based on local conditions within the spray impact area. The lowest CHF values were attained at the outer edge of the impact area, where Q'' is lowest; CHF was negligible outside the impact area.

Subcooling played an important role in the present study. Figure 10 shows that CHF increased monotonically with increasing subcooling in accordance with trends observed with most flow boiling systems. The subcooling was defined as the saturation temperature corresponding to the measured test chamber pressure minus the liquid temperature just upstream of the nozzle. Neglecting any significant temperature drop across the nozzle itself, this definition clearly depicts the state of liquid within the spray prior to impact, and is consistent with the definition of subcooling for all spray and jet studies. This is also a convenient definition for the user of a spray CHF correlation who has no means of determining a priori the temperature of liquid elsewhere in the system. In any case, the present study concerns cooling via a nozzle in close proximity

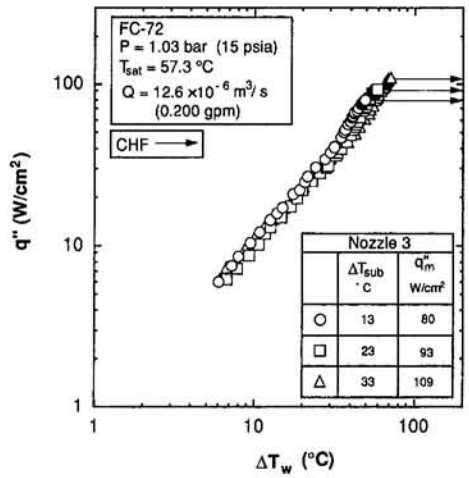


Fig. 10 Effect of subcooling on nozzle 3 boiling curve

to the surface, so any temperature changes in the liquid are expected to be quite small.

Unlike the water data of Mudawar and Valentine, the present study is concerned with intense cooling of a small square heater. It is postulated that CHF would commence at the outer edge of the spray impact area (which just inscribes the square heater), where volumetric flux is a minimum, and propagate inward in an unstable manner. Thus, critical heat flux at the outer edge, $q''_{m,p}$, can be related to the standard definition of CHF for the entire surface (i.e., q''_m) by the relation

$$q''_{m,p} = \frac{L^2}{\frac{\pi}{4}L^2} q''_m. \qquad (12)$$

The volumetric flux at the outer edge of the impact area can be related to the impact area's mean volumetric flux ($\overline{Q''} = Q/(\pi L^2/4)$) by setting $H = (L/2)/\tan(\theta/2)$ and $r = L/2$ in Eq. (8),

$$\frac{Q''}{\overline{Q''}} = \tfrac{1}{2}(1 + \cos(\theta/2))\cos(\theta/2). \qquad (13)$$

Figure 11 shows CHF data for FC-72 and FC-87 and the three full cone spray nozzles can be fitted over broad ranges of flow rate and subcooling according to the equation

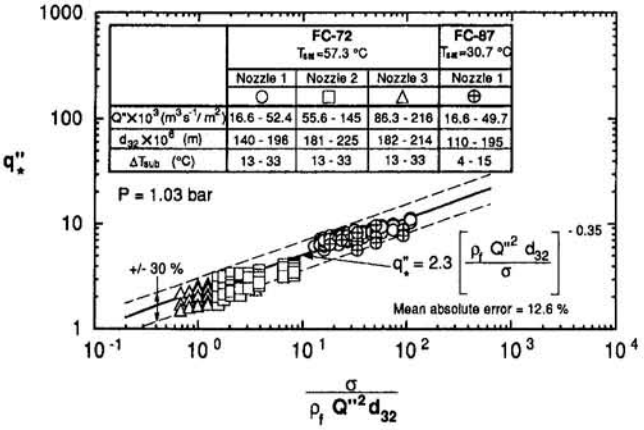


Fig. 11 Correlation of CHF data

Downloaded 11 Dec 2010 to 193.140.21.150. Redistribution subject to ASME license or copyright; see http://www.asme.org/terms/Terms_Use.cfm

$$q''_* \equiv \frac{\dfrac{q''_{m,p}}{\rho_g h_{fg} Q''}}{\left(\dfrac{\rho_f}{\rho_g}\right)^{0.3}\left[1 + 0.0019\,\dfrac{\rho_f c_{p,f}\Delta T_{sub}}{\rho_g h_{fg}}\right]}$$

$$= 2.3\left[\frac{\rho_f Q''^2 d_{32}}{\sigma}\right]^{-0.35} \qquad (14)$$

with a mean absolute error of 11.5 percent.

As indicated earlier, CHF was measured experimentally when the heater thermocouple detected a sudden unsteady rise in the heater temperature. This is a true measure for CHF considering the small size of the heater used in the present study. The hypothesis of a CHF commencing from the outer edge and propagating inward is a description of the trigger point for CHF and the subsequent process of attainment of burnout over the entire heater surface. It is important to emphasize all these events occur at the same electrical power input. Thus, while the central thermocouple detects the temperature rise as it occurs at the center, it does so at the same power setting responsible for the onset of CHF along the outer edge, delayed very briefly by a combination of heat diffusion resistance within the heater block and the propagation speed of the dryout front. Because of their construction and high-conductivity materials, the applications for which the present study is intended (e.g., electronic and laser devices), tend to respond essentially as a lumped mass once the conditions for CHF have been attained.

Combining Eqs. (12)–(14) yields another more convenient form of the CHF correlation relating q''_m to $\overline{Q''}$:

$$\frac{q''_m}{\rho_g h_{fg} \overline{Q''}} = 1.467[(1 + \cos(\theta/2))\cos(\theta/2)]^{0.3} \times \left(\frac{\rho_f}{\rho_g}\right)^{0.3}\left[\frac{\rho_f \overline{Q''}^2 d_{32}}{\sigma}\right]^{-0.35}\left[1 + 0.0019\,\frac{\rho_f c_{p,f}\Delta T_{sub}}{\rho_g h_{fg}}\right]. \qquad (15)$$

To predict CHF using Eq. (15), each nozzle has to be first tested to determine its flow characteristics (ΔP, Q, d_0, θ). These characteristics influence mean volumetric flux ($\overline{Q''}$), Sauter mean diameter (d_{32}), and optimum nozzle-to-surface distance (H) for a given heater length (L). Using Eq. (3) precludes having to perform any costly drop sizing experiments for each spray nozzle and operating pressure.

6 Conclusions

This study focused on optimizing CHF for spray cooling of a small heated surface. The key findings are as follows:

1 Volumetric flux is fairly uniform along any spherical surface centered at the spray orifice and confined by the spray angle. A theoretical model based on this assumption was developed that projects the uniform flux of the spherical surface onto the flat surface of the heater. This model shows volumetric flux is greatest at the center of the spray and decays radially toward the outer edge of the impact area.

2 New sampling techniques were developed to investigate the volumetric flux distribution across a flat surface. These techniques verified the accuracy of the theoretical volumetric flux distribution model.

3 Unlike jets, sprays produce drastically different cooling performances for the same nozzle and same flow rate depending upon the nozzle-to-surface distance. Therefore, this distance should be carefully selected to ensure both repeatability and predictability of cooling performance, especially near CHF.

4 Experiments revealed that when the nozzle-to-surface distance is very small, only a small fraction of the heater surface is directly impacted by the spray and the corresponding CHF is relatively small. Small CHF values are also encountered when the nozzle-to-surface distance is too large because a fraction of the spray liquid would fail to impact the heater surface and is, therefore, wasted. CHF is a maximum when the spray impact area just inscribes the square surface of the heater. Thus, the appropriate nozzle-to-surface distance can be easily determined knowing only the size of the heater and the spray angle.

5 A new correlation was developed for full cone sprays that accurately predicts CHF for different nozzles over broad ranges of flow rate and subcooling.

Acknowledgments

Financial support for this work by IBM is greatly appreciated. The authors also thank 3M Company for donating Fluorinert samples, and Spraying Systems Company for both donating spray nozzles and assisting with the spray droplet sizing.

References

Bolle, L., and Moureau, J. C., 1976, "Spray Cooling of Hot Surfaces: A Description of the Dispersed Phase and a Parametric Study of Heat Transfer Results," *Two Phase Flow Heat Transfer, Proceedings of NATO Advanced Study Institute*, Vol. 3, Washington, DC, pp. 1327–1346.

Estes, K. A., 1994, "Critical Heat Flux in Spray Cooling and Jet Impingement Cooling of Small Targets," Master's Thesis, School of Mechanical Engineering, Purdue University, West Lafayette, IN.

Hall, D. D., and Mudawar, I., 1995, "Experimental and Numerical Study of Quenching Complex-Shaped Metallic Alloys With Multiple, Overlapping Sprays," *International Journal of Heat and Mass Transfer*, Vol. 38, pp. 1201–1216.

Lefebvre, A. H., 1989, *Atomization and Sprays*, Hemisphere Publishing Corporation, New York.

Monde, M., Kusuda, H., and Uehara, H., 1980, "Burnout Heat Flux in Saturated Forced Convection Boiling With Two or More Impinging Jets," *Transactions of JSME*, Vol. 46, pp. 1834–1843.

Moriyama, A., Araki, K., Yamagami, M., and Mase, K., 1987, "Local Heat Transfer Coefficient in Spray Cooling a Hot Surface," *Proc. 15th Japanese Conference on Liquid Atomization and Spray Systems*, Vol. 28, Tokyo, Japan, pp. 104–109.

Mudawar, I., and Valentine, W. S., 1989, "Determination of the Local Quench Curve for Spray-Cooled Metallic Surfaces," *Journal of Heat Treating*, Vol. 7, pp. 107–121.

Mudawar, I., and Deiters, T. A., 1994, "A Universal Approach to Predicting Temperature Response of Metallic Parts to Spray Quenching," *International Journal of Heat and Mass Transfer*, Vol. 37, pp. 347–362.

Toda, S., 1972, "A Study in Mist Cooling," *Transactions of JSME*, Vol. 38, pp. 581–588.

Watchers, L. H. J., Smulders, L., Vermeulen, J. R., and Kleiweg, H. C., 1966, "The Heat Transfer From a Hot Wall to Impinging Mist Droplets in the Spheroidal State," *Chemical Engineering Science*, Vol. 21, pp. 1231–1238.

Downloaded 11 Dec 2010 to 193.140.21.150. Redistribution subject to ASME license or copyright; see http://www.asme.org/terms/Terms_Use.cfm

Study on Critical Heat Flux in Rectangular Channels Heated From One or Both Sides at Pressures Ranging From 0.1 to 14 MPa

Y. Sudo
Deputy Director, Department of High Temperature Engineering, Tokai Research Establishment, Japan Atomic Energy Research Institute (JAERI), 2-4 Shirakata-Shirane, Tokai-mura, Naka-gun, Ibaraki-ken 319-11 Japan

In this study, a quantitative analysis of critical heat flux (CHF) in rectangular heated channels was carried out based on new flow models and the analytical results were compared with existing experimental results at pressures of about 0.1 to 14 MPa with a water mass flux of 3.9 to 28,000 kg/m²s and inlet water subcooling ranging from 0 to 328 K. The flow models proposed for CHF were a completely separated two-phase flow model with a macroliquid sublayer under conditions of comparatively low velocity and zero water subcooling at outlet of the channel and a subcooled boiling flow model with a macroliquid sublayer under the conditions of high water subcooling and high velocity, respectively. It could be shown that the analytical CHF results gave good predictions for over 800 existing experimental results, identifying the effects of predominant parameters as regards CHF.

Introduction

It is very important to understand the characteristics of critical heat flux (CHF) in narrow rectangular channels heated from one or both sides regarding design and a safety evaluation of research nuclear reactors and beam target stations of the accelerator with high neutron flux because plate-type fuel and a beam target with rectangular cooling channels are so often used so as to attain a much higher neutron flux than before. Therefore, many experimental and analytical studies have been carried out until now to find a solution to these problems. As typical examples, the studies by Debortoli et al. (1958) at 3.5 to 14 MPa and El-Genk et al. (1988) at near atmospheric pressure might be pointed out as experiments covering a wide pressure range from 0.1 to 14 MPa.

In particular, for the core thermalhydraulic design and safety evaluation of research nuclear reactors such as JRR-3M, the author and others have proposed a set of empirical CHF correlations, illustrated in Fig. 1, corresponding to the characteristics of flows, that is, upward, downward, and countercurrent flows, respectively, for the vertical rectangular heated channels, showing errors, based on these and previous experiments (Sudo and Kaminaga, 1993). One of the important features that they obtained from the experimental results is that CHF in the downward flow is smaller than that in the upward flow for low mass flux (Region II of Fig. 1). On the other hand, there are no significant differences in CHF between upward and downward flows under the conditions of very small mass flux and stagnant flow (Region I of Fig. 1) and under the conditions of a mass flux higher than a certain value with outlet water subcooling being dominant to CHF (Region III of Fig. 1) at pressures lower than 4 MPa with a mass flux less than 6,250 kg/m²s.

With respect to CHF for downward flow in Regions I and II of Fig. 1, Sudo et al. (1989) proposed an analytical model that could give good predictions for their experimental results and those of Mishima (1984). They applied the criterion in which CHF should occur in the downward flow when water subcooling becomes zero at the outlet of channel and used an empirical correlation they derived for countercurrent flow limitation in the vertical rectangular channels. However, CHF in other regions of Fig. 1 had not been made clear analytically, especially for the upward flow for low to high-velocity conditions.

Haramura and Katto (1983) succeeded in explaining the CHF characteristics in saturated pool boiling and external forced convection boiling, proposing the existance of a macroliquid sublayer on the heated surface. In addition, Katto (1992) obtained very good analytical predictions to the experimental CHF data of subcooled forced convection boiling at pressures ranging from 0.1 to 20 MPa with high mass flux. He determined from the experimental data the ratios of water velocity to vapor blanket velocity at a distance of the macroliquid sublayer apart from the heated wall. However, analytical investigations have not been sufficiently made regarding CHF for the saturated to highly subcooled flow conditions of stagnant flow to high mass flux, especially in rectangular heated channels.

Based on the situation described above, this study analytically aims to help in getting a better systematic understanding of the CHF mechanism, identifying effects of dominant parameters regarding CHF at pressures ranging from 0.1 to 14 MPa under the conditions of low to high mass flux in rectangular channels heated from one or both sides.

Previous Studies

For reference, the major previous CHF correlations are described or listed in the following, which are closely related or are considered to be applied to the flow conditions investigated in this study.

Macbeth (1963) proposed CHF correlations for rectangular channels, identifying the difference in the CHF characteristics between low-velocity and high-velocity conditions as well as the effect of pressure, based on the experiments up to about 14 MPa.

Contributed by the Heat Transfer Division for publication in the JOURNAL OF HEAT TRANSFER. Manuscript received by the Heat Transfer Division November 7, 1995; revision received May 15, 1996. Keywords: Boiling, Forced Convection. Associate Technical Editor: A. Faghri.

Copyright © 1996 by ASME

Downloaded 11 Dec 2010 to 193.140.21.150. Redistribution subject to ASME license or copyright; see http://www.asme.org/terms/Terms_Use.cfm

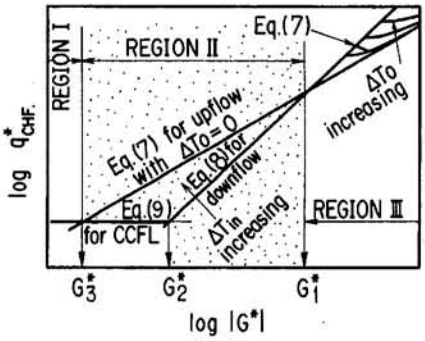


Fig. 1 An illustration of the characteristics of critical heat flux for upward and downward flows in the vertical, rectangular heated channel ranging from 0.1 to 4 MPa and −25,800 to 6,250 kg/m²s (Sudo et al., 1993)

Zenkevich (1959) also proposed an experimental CHF correlation for an upflow, including the effects of pressure, outlet subcooling and mass flux.

Katto (1981) proposed a rather simple set of CHF correlations having dominant dimensionless parameters, which are shown below:

$$q^*_{CHF} = 0.25\left(\frac{D_h}{L}\right)(1 + \Delta T^*_{in})G^* \qquad (1)$$

$$q^*_{CHF} = 0.15\left(\frac{\rho_l}{\rho_g}\right)^{0.133}\frac{\left\{\frac{1}{L}\left(\frac{\sigma}{\rho_g g}\right)^{1/2}\left(\frac{\rho_l}{\rho_g}\right)^{1/2}\frac{1}{G^{*2}}\right\}^{1/3}}{1 + 0.0077\frac{L}{D_h}} \times\left[1 + \frac{5}{9}\frac{\left(0.0308 + \frac{D_h}{L}\right)\cdot\Delta T^*_{in}}{\left\{\frac{1}{L}\left(\frac{\sigma}{\rho_g g}\right)^{1/2}\left(\frac{\rho_l}{\rho_g}\right)\frac{1}{G^{*2}}\right\}^{1/3}\left(\frac{\rho_g}{\rho_l}\right)^{0.133}}\right]G^* \qquad (3)$$

These correlations are used in order of smaller dimensionless mass flux of G^*. These can be applied for upflows in rectangular channels at the saturated to highly subcooled forced convection boiling flow at high pressures.

Mishima (1984) proposed the following CHF correlation for relatively low mass flux flow in vertical rectangular channels as the condition of transition to churn-annular flow,

$$q^*_{CHF} = \frac{A}{A_H}\left[\Delta T^*_{in}G^* + \left\{\frac{1}{1.35 - 0.35\sqrt{\rho_g/\rho_l}} - 0.11\right\}\left(\frac{D_e}{\lambda}\right)^{1/2}\right]. \qquad (4)$$

Sudo and Kaminaga (1989) investigated the characteristics

$$q^*_{CHF} = \left\{0.25 + 0.0009\left(\frac{L}{D_h} - 50\right)\right\}\left(\frac{D_h}{L}\right)\left\{\frac{1}{L}\left(\frac{\sigma}{\rho_l g}\right)^{1/2}\left(\frac{\rho_l}{\rho_g}\right)\frac{1}{G^{*2}}\right\}^{0.043} \times\left[1 + \frac{1.043\Delta T^*_{in}}{4\left\{0.25 + 0.0009\left(\frac{L}{D_h} - 50\right)\right\}\left\{\frac{1}{L}\left(\frac{\sigma}{\rho_l g}\right)^{1/2}\left(\frac{\rho_l}{\rho_g}\right)\frac{1}{G^{*2}}\right\}^{0.043}}\right]G^*. \qquad (2)$$

Nomenclature

A = constant in Eq. (11) or flow area of channel, m²
A_o = constant (= 0.00536) in Eq. (10)
A_H = heated area, m²
B = constant in Eq. (12)
Bo = dimensionless number = $W \cdot S(\rho_l - \rho_g)\cdot g/\sigma$
C = constant in Eq. (13)
C_{pl} = specific heat of water at constant pressure, kJ/kg·K
D_e = equivalent hydraulic diameter, m
D_h = equivalent heated diameter, m
f_w = wall friction factor
G = mass flux, kg/m²·s
G^* = dimensionless mass flux = $G/\{\lambda(\rho_l - \rho_g)\cdot\rho_g\cdot g\}^{1/2}$
g = acceleration of gravity, m/s²
h_c = forced convection heat transfer coefficient, kW/m²·K
h_{fg} = latent heat of evaporation of water, kJ/kg
k = thermal conductivity, kW/mK
L = channel length, m
m = constant in Eq. (11)
n = constant in Eq. (12)
Pr = Prandtl number
Re = Reynolds number
Re_f = Reynolds number of water film flow
S = channel gap size of rectangular channel, m
T = water temperature, K
T_s = saturation temperature, K
ΔT = subcooling of water = $T_s - T$, K
ΔT^* = dimensionless subcooling of water = $C_{pl}\cdot\Delta T/h_{fg}$
t = constant in Eq. (13)
u = velocity, m/s
u^+ = dimensionless velocity = $u/(\tau_w/\rho_l)^{1/2}$
W = channel width, m
W_h = heated circumference, m
y = distance from heated wall, m
y_i = water film thickness in completely separated two-phase flow, m
y^+ = dimensionless distance from heated wall = $y(\tau_w/\rho_l)^{1/2}/\nu_l$
δ = macroliquid sublayer thickness, m
λ = critical wavelength = $\{\sigma/(\rho_l - \rho_g)g\}^{1/2}$, m
ν = kinematic viscosity, m²/s
ρ = density, kg/m³
σ = surface tension, N/m
τ_w = wall shear stress, N/m²

Subscripts

B = boiling
CHF = critical heat flux
g = gas phase
i = interface between water and gas phases
in = inlet
l = water
o = outlet
w = wall
δ = macroliquid sublayer
$\bar{}$ = average

Downloaded 11 Dec 2010 to 193.140.21.150. Redistribution subject to ASME license or copyright; see http://www.asme.org/terms/Terms_Use.cfm

of CHF in downward flows with rather low to zero velocity, that is, in the stagnant flow or under countercurrent flow limitation (CCFL), and then proposed the following CHF correlation for downward flow including CCFL conditions, based on the empirical correlation for CCFL they derived:

$$q^*_{CHF} = \left(\frac{A}{A_H}\right)\left[\Delta T^*_{in} G^* + \left(\frac{1}{1.52}\right)^2 \left(\frac{W}{\lambda}\right)^{0.5} F^{2.875}\right], \quad (5)$$

where

$$F = 1.3^{0.7} - \left[1.52\left(\frac{\lambda}{W}\frac{\rho_g}{\rho_l}\right)^{0.25}(0.5 + 0.0015\,\mathrm{Bo}^{1.3})G^{*0.5}\right]^{0.7}. \quad (6)$$

Furthermore, the present author (Sudo and Kaminaga, 1993) investigated the characteristics of CHF in both upward and downward flows based on the existing CHF experiments. They proposed the following set of correlations, which are already shown in Fig. 1, for upward and downward flows in vertical rectangular channels at pressures ranging from 0.1 to 4 MPa and mass fluxes from −25,800 to +6,250 kg/m^{2}s, identifying the precision of the correlation:

$$q^*_{CHF} = 0.005 \cdot |G^*|^{0.611}\left(1 + \frac{5000}{|G^*|}\cdot \Delta T^*_0\right) \quad (7)$$

for upward and downward flows,

$$q^*_{CHF} = \frac{A}{A_H}\cdot \Delta T^*_{in} \cdot |G^*| \quad (8)$$

for downward flow, and

$$q^*_{CHF} = 0.7\,\frac{A}{A_H}\cdot\frac{\sqrt{W/\lambda}}{\{1 + (\rho_g/\rho_l)^{1/4}\}^2} \quad (9)$$

as lower limits common to both upward and downward flows.

As shown in Fig. 1, CHF for the downward flow is given by Eq. (8) for $G^*_2 < G^* < G^*_1$, by Eq. (7) for $G^* > G^*_1$ and by Eq. (9) for $G^* < G^*_2$, respectively. Here, G^*_1, G^*_2 and G^*_3 are determined as intersecting points of Eqs. (7), (8), and (9), respectively.

Analytical Models and Discussions

In the following, the analytical models regarding CHF are proposed and discussed, which are different from each other, corresponding to two different categories of flow. One is for CHF in the upward flow under a relatively low mass flux and saturated two-phase flow condition at the outlet of channel, which is shown as Region II in Fig. 1. The other is for CHF in the upward flow under the high mass flux and high subcooled condition at the outlet of channel, which is shown as Region III in Fig. 1.

1 CHF Under Relatively Low Mass Flux and Saturated Two-Phase Flow. Figure 2(*a*) illustrates the flow model where CHF occurs, that is, at the exit of the rectangular heated channel with a narrow gap S. This is a completely separated and saturated two-phase flow in which there are a vapor blanket with length L_B in the flow of the liquid phase with thickness y_i of completely separated two-phase flow and a macroliquid sublayer with thickness δ given as below under the vapor blanket, which has been proposed by Haramura and Katto (1983),

$$\delta = A_o \cdot \left(\frac{\rho_g}{\rho_l}\right)^{0.4} \cdot \left(1 + \frac{\rho_g}{\rho_l}\right) \cdot \sigma \cdot \rho_g \cdot \left(\frac{h_{fg}}{q_B}\right)^2 \quad (10)$$

where q_B is the heat flux due only to the nucleate boiling heat transfer without any effect from the forced convection heat transfer. Equation (10) has been proposed by Haramura and Katto (1983).

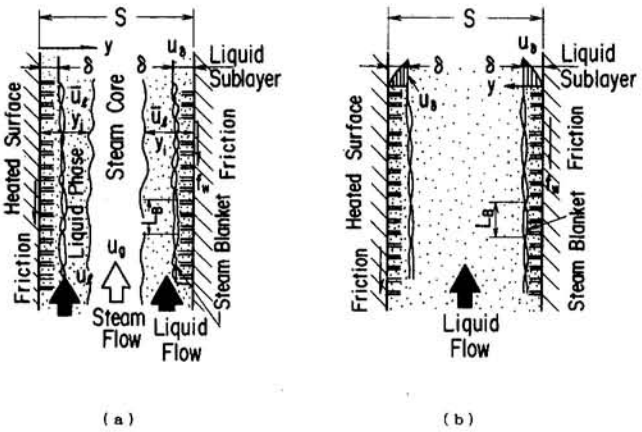


Fig. 2 Analytical flow model of CHF in the vertical rectangular heated channel: (*a*) completely separated two-phase flow model of upward saturated two-phase flow at CHF; (*b*) high subcooling and high velocity flow model at CHF

Water velocity at a distance of δ apart from the heated wall is expressed as follows in the dimensionless form:

$$u^+_\delta = A y^{+m}_\delta \quad (11)$$

where

$$u^+_\delta = u_\delta(\rho_l/\tau_w)^{1/2}, \quad y^+_\delta = \delta\left(\frac{\tau_w}{\rho_l}\right)^{1/2}\Big/\nu_l,$$

$$\tau_w = (f_w/2)\rho_l \bar{u}_l^2, \quad f_w = B(\bar{u}_l D_e/\nu_l)^n. \quad (12)$$

The averaged velocity of water phase flow is expressed as follows, with wall shear stress τ_w and thickness of water phase flow y_i after Ueda (1981),

$$\mathrm{Re}_f = 4\rho_l \bar{u}_l y_i/(\nu_l \rho_l) = C(y^+_i)^t \quad \text{or}$$

$$4\bar{u}_l y_i/\nu_l = C(y_i/\nu_l)^t(\tau_w/\rho_l)^{t/2} \quad (13)$$

The following correlation is introduced among the inlet water subcooling $T_s - T_{in}$, y_i, and $\bar{u}_l$, based on the assumption of completely separated two-phase flow:

$$2y_i\rho_l\bar{u}_l = GS\left\{1 + \frac{C_{pl}(T_s - T_{in})}{h_{fg}} - \frac{q_{CHF}LW_h}{Gh_{fg}SW}\right\}. \quad (14)$$

On the other hand, Shah (1977) proposed the following empirical correlations for total heat flux q, which consist of heat flux q_B of nucleate boiling heat transfer and heat flux $h_c(T_w - T_l)$ of forced convection single-phase flow heat transfer:

$$q = q_B + h_c(T_w - T_l), \quad (15)$$

$$T_w - T_o = \frac{\dfrac{q}{h_c} + \left\{230\left(\dfrac{q}{Gh_{fg}}\right)^{0.5} - 1\right\}(T_s - T_l)}{230\left(\dfrac{q}{Gh_{fg}}\right)^{0.5}}. \quad (16)$$

Under the saturated condition of $T_l = T_s$, these correlations are reduced to the correlation

Downloaded 11 Dec 2010 to 193.140.21.150. Redistribution subject to ASME license or copyright; see http://www.asme.org/terms/Terms_Use.cfm

$$q_B = \left\{1 - \frac{1}{230}\left(\frac{Gh_{fg}}{q}\right)^{0.5}\right\} \cdot q$$

Equation (10) is thus rewritten in the following way, using this correlation of q_B versus q for forced convection boiling heat transfer under the saturated two-phase flow condition,

$$\frac{\delta\rho_g}{\sigma} = A_o(\rho_g/\rho_l)^{0.4}\left(1 + \frac{\rho_g}{\rho_l}\right)(\rho_g h_{fg})^2 \Big/ q_{\mathrm{CHF}}^2 \times \left\{1 - \frac{1}{230}\left(\frac{Gh_{fg}}{q_{\mathrm{CHF}}}\right)^{0.5}\right\}^2. \quad (17)$$

The following correlation can be introduced for vapor blanket length L_B, assuming that L_B is equal to the length of Helmholtz's critical wavelength and that the velocity of vapor blanket is equal to water velocity u_δ at a distance δ apart from the heated wall:

$$L_B = \frac{2\pi\sigma}{\rho_g u_\delta^2} \quad (18)$$

Thus, CHF is expressed using Eq. (18) as follows, assuming that CHF is the heat flux with which all of the macroliquid sublayers are evaporated during the time that a vapor blanket passed the CHF point, as previous analyses such as that of Katto (1992) have assumed,

$$q_{\mathrm{CHF}} = \frac{\rho_l \delta h_{fg}}{(L_B/u_\delta)} = \frac{\rho_l \rho_g h_{fg} \delta u_\delta^3}{2\pi\sigma}. \quad (19)$$

From Eqs. (11) and (12) and from Eqs. (12) and (13), the following expressions can be reduced, respectively:

$$u_\delta/\bar{u}_l = A \cdot \left(\frac{B}{2}\right)^{(m+1)/2} \cdot \left(\frac{\delta}{D_e}\right)^m \cdot \left(\frac{\bar{u}_l D_e}{\nu_l}\right)^{m+n(1+m)/2}, \quad (20)$$

$$\left(\frac{\bar{u}_l y_i}{\nu_l}\right)^{1-t} = \frac{C}{4}\left(\frac{B}{2}\right)^{t/2}\left(\frac{\bar{u}_l D_e}{\nu_l}\right)^{nt/2}. \quad (21)$$

Furthermore, by using Eq. (14), the following expression can be reduced,

$$\frac{u_\delta D_e}{\nu_l} = A \cdot \left(\frac{B}{2}\right)^{(1+m)/2} \cdot \left(\frac{\delta}{D_e}\right)^m \cdot \left[\frac{4}{C}\left(\frac{2}{B}\right)^{t/2} \times \left\{\frac{GS}{2\rho_l \nu_t}\left(1 + \Delta T_{in}^* - \frac{LW_h q_{\mathrm{CHF}}}{SWGh_{fg}}\right)\right\}^{1-t}\right]^{(1+m)(2+n)/nt}. \quad (22)$$

From Eq. (17), the following expression is found:

$$\delta/D_e = \left(\frac{A_o\sigma}{\rho_g D_e}\right)\left(\frac{\rho_g h_{fg}}{q_{\mathrm{CHF}}}\right)^2\left(\frac{\rho_g}{\rho_l}\right)^{0.4} \times \left(1 + \frac{\rho_g}{\rho_l}\right) \Big/ \left\{1 - \frac{1}{230}\left(\frac{Gh_{fg}}{q_{\mathrm{CHF}}}\right)^{0.5}\right\}^2 \quad (23)$$

Thus, from Eqs. (19), (22) and (23), the expression for CHF is obtained as follows:

$$q_{\mathrm{CHF}}^{*K1}\left\{1 - \frac{1}{230}\left(\frac{G^*}{q_{\mathrm{CHF}}^*}\right)^{0.5}\right\}^{K2} = \left\{\frac{A^3}{2\pi}\left(\frac{B}{2}\right)^{-3(1+m)(2+n/2)/n} \times \left(\frac{C}{4}\right)^{-6(1+m)(1+n/2)/nt} \cdot Ao^{(1+3m)}\right\}^{K3} \cdot \left[\left(1 + \frac{\rho_g}{\rho_l}\right)^{1+3m}\left(\frac{\rho_g}{\rho_l}\right)^{1.2m-0.6} \times \frac{(\sigma D_e/\rho_g \nu_l^2)^{3m}}{\{De\sqrt{\lambda(\rho_l/\rho_g - 1)g}/\nu_l\}^{3(1+2m)}}\right]^{K3} \times \{(S/2)\sqrt{\lambda(1 - \rho_g/\rho_l)\rho_g g/\rho_l}/\nu_l\} \times \left\{(1 + \Delta T_{in}^*)G^* - \left(\frac{LW_h}{SW}\right)q_{\mathrm{CHF}}^*\right\} \quad (24)$$

where

$$K1 = \frac{-nt(1+2m)}{2(t-1)(1+m)\left(1+\frac{n}{2}\right)}, \quad K2 = \frac{-nt(1+3m)}{3(t-1)(1+m)\left(1+\frac{n}{2}\right)}, \quad K3 = \frac{-nt}{6(t-1)(1+m)\left(1+\frac{n}{2}\right)}. \quad (25)$$

As the case is considered here that G^* is rather small, as illustrated in Fig. 1, the flow could be treated as laminar flow with

$$m = 1, \quad A = 1, \quad t = 2, \quad C = 2 \quad \text{(Ueda, 1981)}, \quad n = -1, \quad B = 24 \quad (26)$$

giving

$$q_{\mathrm{CHF}}^{*3}\left\{1 - \frac{1}{230}\left(\frac{G^*}{q_{\mathrm{CHF}}^*}\right)^{0.5}\right\}^{8/3} = K \cdot \left(1 + \frac{\rho_g}{\rho_l}\right)^{4/3}\left(\frac{\rho_g}{\rho_l}\right)^{1.2}\left(\frac{S \cdot \lambda}{2D_e^2}\right) \times \left\{(1 + \Delta T_{in}^*)G^* - \left(\frac{LW_h}{SW}\right)q_{\mathrm{CHF}}^*\right\} \quad (27)$$

where $K = 0.44$.

One of the features as a result of this analytical model is that q_{CHF}^* is determined by mass flux, pressure, inlet water subcooling, and dimensions of flow channel such as L, W, W_h, and S, by assuming the performance characteristics of the flow to be investigated are similar to the laminar flow.

2 CHF Under High Mass Flux and High Subcooling Conditions. As the flow model of CHF under the conditions of high mass flux and high subcooling, a flow model shown in Fig. 2(*b*) is assumed at the exit of the heated channel, in which there is a vapor blanket with each length L_B in the flow of liquid phase and a macroliquid sublayer with thickness δ whose magnitude is also given by Eq. (10). In this analytical model, there is no flow of steam core, which was assumed in the flow model for relatively low mass flux and saturated two-phase flow.

In this analytical model, Eqs. (10), (11), (12), and (18) are also applied to the thickness of the macroliquid sublayer, water velocity at a distance of δ apart from the heated wall and vapor blanket length, respectively.

CHF is expressed as follows, again assuming that CHF is the heat flux with which all of the macroliquid sublayers are evaporated during the time that a vapor blanket passed the CHF point as before, based on Eqs. (11) and (12):

Downloaded 11 Dec 2010 to 193.140.21.150. Redistribution subject to ASME license or copyright; see http://www.asme.org/terms/Terms_Use.cfm

$$q_{CHF}L_B = \rho_l h_{fg}\int_0^{\delta} u dy = \rho_l h_{fg}\nu_l \int_0^{\delta(\tau_w/\rho_l)^{1/2}/\nu_l} Ay^{+m}dy^+$$

$$= \frac{A}{1+m}\nu_l\rho_l h_{fg}\left[\delta\left(\frac{\tau_w}{\rho_l}\right)^{1/2}/\nu_l\right]^{1+m} \quad (28)$$

The expression for q_{CHF} is then rewritten using Eq. (18) as below:

$$q_{CHF} = \frac{A}{1+m}\frac{\nu_l\rho_g\rho_l h_{fg}}{2\pi\sigma}u_\delta^2\left\{\delta\left(\frac{\tau_w}{\rho_l}\right)^{1/2}/\nu_l\right\}^{1+m}$$

Therefore, the CHF can be reduced as follows, using again Eqs. (11) and (12):

$$q_{CHF} = \frac{A^3B}{1+m}(B/2)^{(1+3m)/2}\cdot\left\{\frac{\rho_l\rho_g h_{fg}\bar{u}_l^2\nu_l}{4\pi\sigma}\right\}$$

$$\times(\bar{u}_l D_e/\nu_l)^{3n(1+m)/2}\cdot(\bar{u}_l\delta/\nu_l)^{1+3m} \quad (29)$$

On the other hand, Eqs. (15) and (16) are also applied to this model and the following is reduced because there is water subcooling at the outlet of the channel:

$$q_B = \left\{1 - \frac{1}{230}\left(\frac{Gh_{fg}}{q}\right)^{0.5}\right\}$$

$$\times\left[q + \left(\frac{h_{fg}}{C_{pl}}\right)h_c\left\{\frac{A_H q}{AGh_{fg}} - \frac{C_{pl}\Delta T_{in}}{h_{fg}}\right\}\right]. \quad (30)$$

From Eqs. (10) and (30), the following expression can be obtained, by applying Dittus–Boelter's correlation to h_c in Eq. (30):

$$\frac{\delta\rho_g}{\sigma} = A_o(\rho_g/\rho_l)^{0.4}\left(1+\frac{\rho_g}{\rho_l}\right)(\rho_g h_{fg})^2\Big/$$

$$\left\{1 - \frac{1}{230}\left(\frac{Gh_{fg}}{q_{CHF}}\right)^{0.5}\right\}^2\Big/\left[q_{CHF} - 0.023\cdot\mathrm{Re}_l^{0.8}\right.$$

$$\left.\times\,\mathrm{Pr}_l^{0.4}\left(\frac{h_{fg}}{C_{pl}}\right)\left(\frac{k_l}{D_e}\right)\left(\Delta T_{in}^* - \frac{A_H}{A}\frac{q_{CHF}^*}{G^*}\right)\right]. \quad (31)$$

Here, the flow is assumed to be comparatively developed, assuming that,

$$A = 2.06, \quad m = 0.55,$$

$$B = 0.12, \quad n = -0.25.$$

Then, the dimensionless CHF is expressed as below, eliminating the term δ from Eqs. (29) and (31):

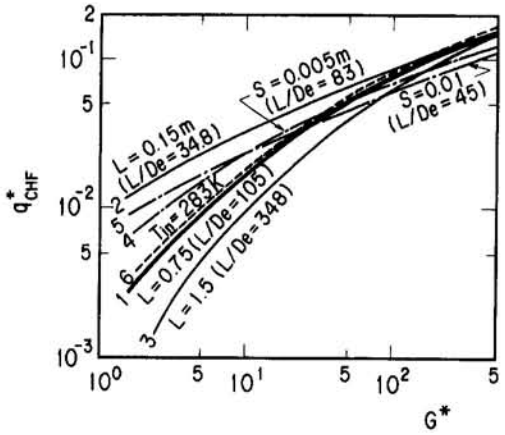


Fig. 3 An illustration of the analytical results on the effects of the dominant parameters regarding CHF based on the completely separated two-phase flow model

As one of features in Eq. (32), it is pointed out that CHF is determined only by the thermal properties, configuration of the channel, inlet water subcooling, and mass flux, which are easily understood to be the dominant parameters regarding CHF.

Table 1 shows the major run conditions of previous experiments investigated in this study.

Comparisons Between Analytical Results and Experimental Results

1 CHF Under Relatively Low Mass Flux and Saturated Two-Phase Flow. Figure 3 illustrates the overall characteristics of CHF given by Eq. (27) to investigate the effects of the dominant parameters, mass flux, inlet water subcooling, channel length, and gap size at atmospheric pressure. In this figure, Curve 1 shows analytical results of Eq. (27) for the case of channel length L = 0.75 m, channel gap size S = 0.0025 m with saturated condition T_{in} = 373 K at the inlet of channel. Curves 2 and 3 show the analytical results for cases of L = 0.15 and 1.5 m, respectively, and Curves 4 and 5 do so for cases of S = 0.005 and 0.01 m, respectively, without any change in the other parameters. In addition, Curve 6 shows the analytical results for inlet water subcooling, ΔT_{in} = 90 K. For G^* of 5 to 500, the slopes of Curves 1, 2, 4, 5, and 6 range from about 0.5 to 0.8, showing that q^*_{CHF} is proportional to $G^{*0.5}$ to $G^{*0.8}$, which shows the validity of Eq. (7), in which q^*_{CHF} is proportional to $G^{*0.6}$, proposed by Sudo et al. (1993) for the experimental conditions investigated. It is also understood in Fig. 3 that the effect of inlet water subcooling is not significant

$$q_{CHF}^{*0.1887}\left\{1 - \frac{1}{230}\left(\frac{G^*}{q^*_{CHF}}\right)^{0.5}\right\}\left\{q^*_{CHF} - F_1 G^{*0.8}\left(\Delta T^*_{in} - \frac{A_H\cdot q^*_{CHF}}{A\cdot G^*}\right)\right\} = 0.0158\cdot F_2^{0.1887}\cdot G^{*0.7677}$$

where

$$F_1 = 0.023\left(\frac{k_l\mathrm{Pr}_l^{0.4}}{D_e\rho_l C_{pl}}\right)\left\{D_e\sqrt{\lambda\left(1-\frac{\rho_g}{\rho_l}\right)\frac{\rho_g}{\rho_l}}\Big/\nu_l\right\}^{0.8}\Big/\sqrt{\lambda\left(1-\frac{\rho_g}{\rho_l}\right)\frac{\rho_g}{\rho_l}g},$$

$$F_2 = \left\{A_o\left(\frac{\sigma}{\rho_l\nu_l}\right)\left(\frac{\rho_g}{\rho_l}\right)^{1.4}\cdot\left(1+\frac{\rho_g}{\rho_l}\right)\Big/\sqrt{\lambda\left(1-\frac{\rho_g}{\rho_l}\right)\frac{\rho_g}{\rho_l}g}\right\}^{2.65}\cdot\left\{\frac{\rho_g\nu_l\sqrt{\lambda\left(1-\frac{\rho_g}{\rho_l}\right)\frac{\rho_g}{\rho_l}g}}{4\pi\sigma}\right\}\times\left\{\frac{D_e}{\nu_l}\sqrt{\lambda\left(1-\frac{\rho_g}{\rho_l}\right)\frac{\rho_g}{\rho_l}g}\right\}^{-0.581}. \quad (32)$$

Downloaded 11 Dec 2010 to 193.140.21.150. Redistribution subject to ASME license or copyright; see http://www.asme.org/terms/Terms_Use.cfm

Table 1 Major test conditions of previous experiments investigated in this study

Pressure P (MPa)	Channel length L (m)	Width W (mm)	Gap S (mm)	Heated by one or both sides	Inlet subcooling ΔT (K)	Mass flux G (kg/m^{2}s)	Critical heat flux q_{CHF} (MW/m^2)	Data number	Author(s)
0.085	0.61	50.8	1.98	one	25~70	32~78	0.17~0.35	19	Oh et al.
0.1	0.37~0.75	50	2.25~5	one/both	20~80	5.6~474	0.077~0.8	124	Sudo et al.
0.1	0.36	40	1.03	one	80	11~1240	0.11~0.58	33	Motomura et al.
0.1	0.35	40	2.4	one/both	15~70	3.9~353	0.065~1.16	44	Mishima
1.69~2.0	0.507	12.7	1.27	both	180	2870~28120	1.9~17.9	34	Siman-Tov et al.
0.5~3.1	0.15	4	3.5	one	13~166	3250~27000	8.0~62.1	124	Zeigarnik et al.
4.1	0.31~0.69	25.4	1.3~2.5	both	23~214	1050~3480	3.0~6.3	22	DeBortoli et al.
5.5	0.15~0.69	25.4	1.5~2.5	both	9~234	240~4920	0.44~7.11	41	DeBortoli et al.
6.9	0.94	53	6.4~12.7	both	7~93	244~1940	1.8~3.61	50	Tippets
8.4	0.15~0.69	25.4	1.5~2.6	both	5~264	235~5420	0.45~6.73	53	DeBortoli et al.
13.8	0.15~0.69	25.4	1.3~2.6	both	4~328	34~6490	0.15~7.77	336	DeBortoli et al.

at atmospheric pressure, but on the other hand, the effects of L and S are significant, giving a smaller CHF with a larger L and smaller S.

Based on the preliminary investigations described above, comparisons were enthusiastically made between the results of Eq. (27) and CHF data of previous experiments at 0.1 to 13.8 MPa, which are listed in Table 1. As a result, it was found that Eq. (27) could predict CHF characteristics of the experiments at about 0.1 MPa with respect to dominant parameters such as mass flux, inlet water subcooling, and channel dimensions, but the predictions became worse and worse as the pressure went over atmospheric pressure. So, the effect of pressure was investigated in detail and it was found that the following K:

$$K = 0.0033\left(\frac{\rho_g}{\rho_l}\right)^{-0.555} \tag{33}$$

could give good predictions for the experimental results with respect to mass flux, pressure, inlet water subcooling and channel dimensions at pressures ranging from 0.1 to 13.8 MPa. Then, q^*_{CHF} is given as follows,

$$q^{*3}_{CHF}\left\{1 - \frac{1}{230}\left(\frac{G^*}{q^*_{CHF}}\right)^{0.5}\right\}^{8/3} = 0.0033 \cdot \left(1 + \frac{\rho_g}{\rho_l}\right)^{4/3}\left(\frac{\rho_g}{\rho_l}\right)^{0.645}\left(\frac{S \cdot \lambda}{2D_e^2}\right) \times \left\{(1 + \Delta T^*_{in})G^* - \left(\frac{LW_h}{SW}\right)q^*_{CHF}\right\}. \tag{34}$$

In the following, the results of Eq. (34) are compared with the previous CHF experimental data.

Figures 4(a) and 4(b) show comparisons among the analyses of this study given by Eq. (34), correlations of Mishima (1984), Sudo et al. (1993), Katto (1981), Macbeth (1963), and Zenkevich (1959), and experimental results at atmospheric pressure by Sudo et al. (1994) and at 13.8 MPa by DeBortoli et al. (1958), respectively. It could be clearly observed that only the results of Eq. (34) gave good predictions common to the experimental results at 0.1 and 13.8 MPa.

Figures 5(a) and 5(b) show comparisons of CHF among the analyses of this study, previous correlations proposed and experimental results under saturated conditions at the outlet of the channel, showing the effect of inlet water subcooling in Fig. 5(a) and the effects of pressure and aspect ratio of the channel in Fig. 5(b), respectively. It is easily understood that Eq. (34) gives very good predictions to the previous experimental results by DeBortoli et al. (1958) with respect to the effects of inlet subcooling, pressure and aspect ratio of the channel, which had not been clarified at all systematically.

Figures 6(a) and 6(b) show comparisons among the analyses of this study, previous correlations proposed and experimental results at 13.8 MPa for saturated conditions at the inlet of the channel with respect to effects of channel length and channel gap size. It is also clearly observed that Eq. (34) can give good predictions for the experimental results with respect to the effects of L and S, showing the same tendency as the experiments that smaller L and larger S gives a larger q^*_{CHF} for the same G^*.

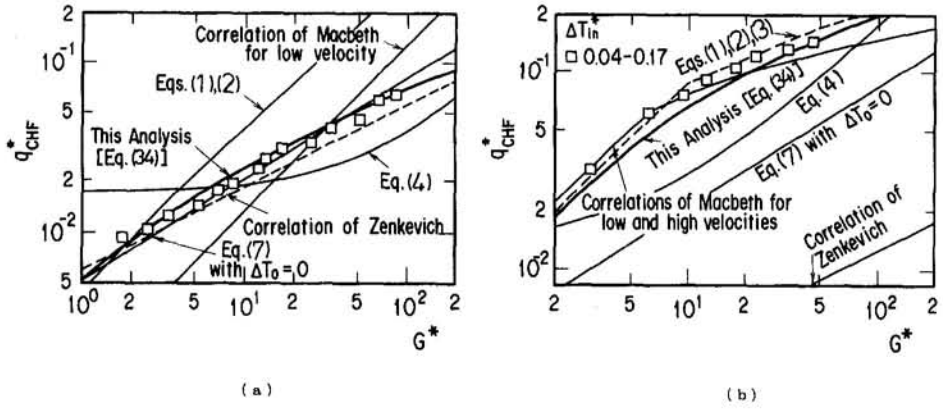


Fig. 4 Comparison of CHF regarding the analytical results of this study, previous correlations proposed by Zenkevich (1959), Macbeth (1963), Katto (1981), Mishima (1984), and Sudo et al. (1993) and the previous experimental results: (a) case of saturated flow condition at the inlet of the channel for channels of L = 0.75 m and S = 5 mm at 0.1 MPa (Sudo et al., 1993); (b) case of subcooled flow condition at inlet but saturated flow condition at the outlet of the channel for channels of L = 0.15 m and S = 2.56 mm at 13.8 MPa (DeBortoli et al., 1958)

Downloaded 11 Dec 2010 to 193.140.21.150. Redistribution subject to ASME license or copyright; see http://www.asme.org/terms/Terms_Use.cfm

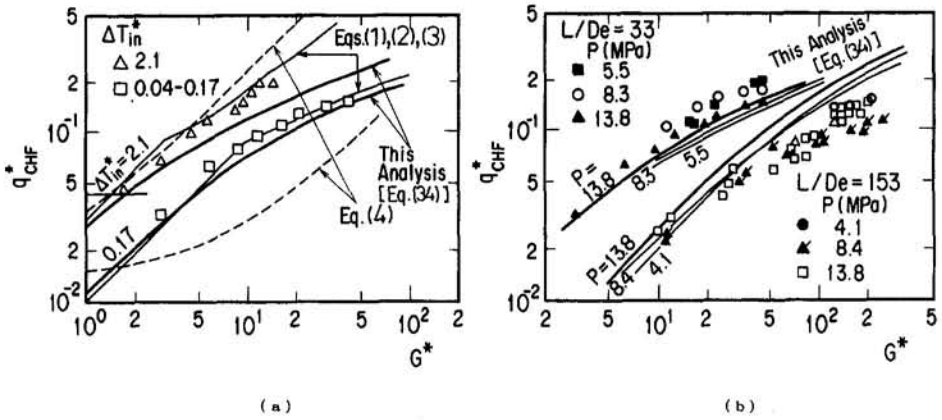


Fig. 5 Comparison of CHF regarding analytical results of this study, previous correlations proposed and experimental results for saturated flow conditions at outlet of the channel: (*a*) effect of inlet water subcooling for the experiment with channels of $L = 0.15$ m and $S = 2.56$ mm at 13.8 MPa by DeBortoli et al. (1958); (*b*) effects of pressure and aspect ratio L/D_e for the experiment by DeBortoli et al. (1958)

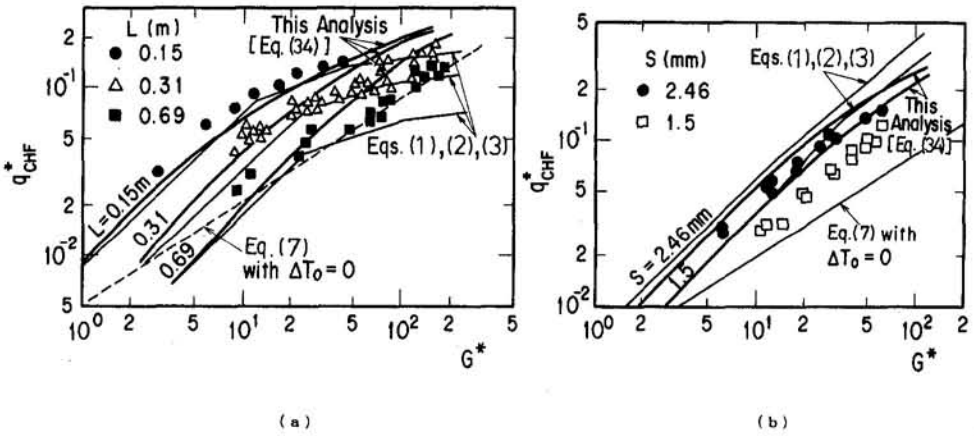


Fig. 6 Comparison of CHF regarding the analytical results of this study, previous correlations proposed, and experimental results for saturated flow conditions at the inlet of the channel with $G^* < 200$ at 13.8 MPa: (*a*) effect of channel length L with $S = 2.5$ mm; (*b*) effect of gap size S with $L = 0.69$ m

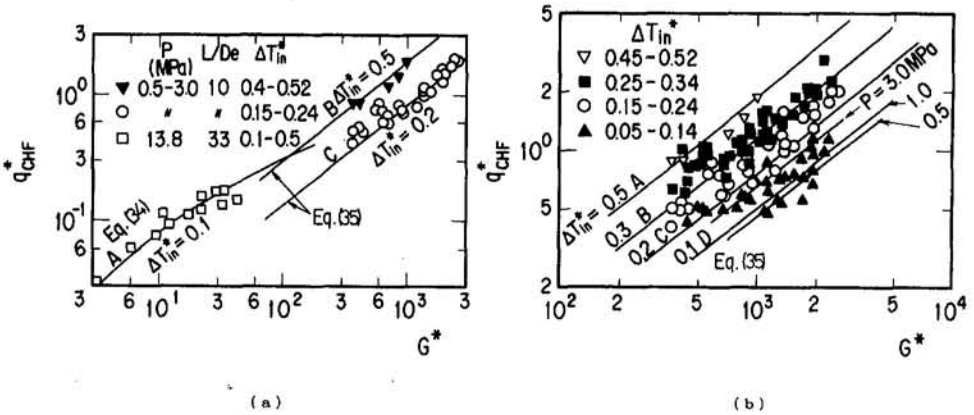


Fig. 7 Comparison of CHF between the analytical results of this study and previous experimental results for the conditions of high subcooling at the outlet of the channel and high velocity: (*a*) comparison between the flow of saturated and comparatively low velocity (experiment by DeBortoli et al., 1958) and the flow of the subcooled and high velocity (experiment by Zeigarnik et al., 1981); (*b*) effects of inlet water subcooling and pressure for experiments by Zeigarnik et al. (1981)

Downloaded 11 Dec 2010 to 193.140.21.150. Redistribution subject to ASME license or copyright; see http://www.asme.org/terms/Terms_Use.cfm

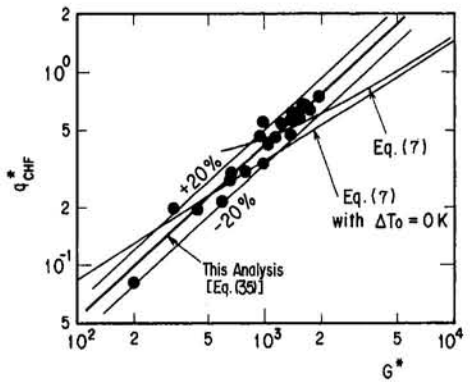


Fig. 8 Comparisons between analytical results of this study and previous experimental results (Siman-Tov et al., 1995) for the high-subcooling and high-velocity conditions

2 CHF Under High Mass Flux and High Subcooling Conditions. From the preliminary investigation on the effects of predominant parameters appearing in Eq. (32), a comparison with the experimental results revealed that the effect of pressure on CHF was not properly predicted by Eq. (32), as experienced already in Eq. (27), and it was found that the following change in pressure:

$$A_1 = 0.066(\rho_g/\rho_l)^{-0.4}$$

to F_2 in Eq. (32) could give a good prediction for the experimental results with respect to the effects of mass flux, pressure, inlet water subcooling, and channel dimensions at 0.3 to 3.1 MPa.

Thus, dimensionless CHF is given by the following expressions:

$$q^{*0.1887}_{CHF}\left\{1-\frac{1}{230}\left(\frac{G^*}{q^*_{CHF}}\right)^{0.5}\right\}\left\{q^*_{CHF}-F_1G^{*0.8}\left(\Delta T^*_{in}-\frac{A_H\cdot q^*_{CHF}}{A\cdot G^*}\right)\right\}=0.0158\cdot F_2^{0.1887}\cdot G^{*0.7677}$$

where

$$F_1 = 0.023\left(\frac{k_l\,\mathrm{Pr}_l^{0.4}}{D_e\rho_l C_{pl}}\right)\left\{D_e\sqrt{\lambda\left(1-\frac{\rho_g}{\rho_l}\right)\frac{\rho_g}{\rho_l}}\Big/\nu_l\right\}^{0.8}\Big/\sqrt{\lambda\left(1-\frac{\rho_g}{\rho_l}\right)\frac{\rho_g}{\rho_l}\,g},$$

$$F_2 = \left\{A_oA_1\left(\frac{\sigma}{\rho_l\nu_l}\right)\left(\frac{\rho_g}{\rho_l}\right)^{1.4}\cdot\left(1+\frac{\rho_g}{\rho_l}\right)\Big/\sqrt{\lambda\left(1-\frac{\rho_g}{\rho_l}\right)\frac{\rho_g}{\rho_l}\,g}\right\}^{2.65}\cdot\left\{\frac{\rho_g\nu_l\sqrt{\lambda\left(1-\frac{\rho_g}{\rho_l}\right)\frac{\rho_g}{\rho_l}\,g}}{4\pi\sigma}\right\}\left\{\frac{D_e}{\nu_l}\sqrt{\lambda\left(1-\frac{\rho_g}{\rho_l}\right)\frac{\rho_g}{\rho_l}\,g}\right\}^{-0.581},$$

$$A_1 = 0.066(\rho_g/\rho_l)^{-0.4}. \qquad (35)$$

Figure 7(a) and 7(b) shows comparisons of CHF between analytical results given by Eq. (35) and previous experimental results under the conditions of high mass flux and high subcooling at the outlet of channel, focusing on the effect of inlet water subcooling. In Fig. 7(a), as a reference, the comparisons between analytical results of Eq. (34) and previous experiments of relatively low mass flux and saturated conditions at the outlet of channel, which are shown by □-marks. On the other hand, in Fig. 7(b) the analytical results are shown at 0.5, 1.0, and 3.0 MPa as the effect of pressure given by Eq. (35), along with comparisons regarding the effect of inlet water subcooling at 1.0 MPa between analytical and experimental results.

Figure 8 shows the comparison among the analytical results of Eq. (35), the empirical correlation proposed by Sudo et al. (1993), and the previous experiments conducted by Siman-Tov et al. (1995).

Figures 7 and 8 clearly show that Eq. (35) gives very good predictions as regards the experimental results, featuring that the effect of inlet water subcooling is significant but the effect of pressure is rather small with respect to the relationship of q^*_{CHF} versus G^*.

3 Predicting Errors of Eqs. (34) and (35). Figures 9(a) and 9(b) show comparisons between the analytical results obtained by Eqs. (34) and (35) and all available CHF data of the previous experiments shown in Table 1. From the figures, it is seen that the analytical results can predict the experimental results within errors of about ±30 percent at 0.1 to 13.8 MPa. In Fig. 9(a), which is for relatively low mass flux and saturated conditions at the outlet of the channel, the average value of the experimental result/analytical results and their standard deviation are 0.92 and 0.26, respectively, and in Fig. 9(b), which is for high mass flux and subcooled condition at the outlet of the channel, the average value of experimental results/analytical results and their standard deviation are 1.17 and 0.29, respectively.

Concluding Remarks

The characteristics of CHF in both comparatively low-velocity saturated two-phase flows and high-velocity and high-subcooling flows in rectangular heated channels were investigated through quantitative comparisons of analyses based on the flow model with macroliquid sublayer with over 800 data of previous experiments at 0.1 to 13.8 MPa with inlet water subcooling of 0 to 328 K.

As a result, the following important knowledge was obtained:

1 Analytical results given by Eq. (34), which was based on the completely separated two-phase flow model with the macroliquid sublayer, could predict the existing results of experiments conducted under comparatively low-velocity and saturated conditions at the outlet of the rectangular heated channel.
2 Analytical results given by Eq. (35), which was based on the subcooled and forced convective boiling flow model with the macroliquid sublayer, could predict the existing results of experiments conducted under high-velocity and subcooled conditions at the outlet of the rectangular heated channel.

Downloaded 11 Dec 2010 to 193.140.21.150. Redistribution subject to ASME license or copyright; see http://www.asme.org/terms/Terms_Use.cfm

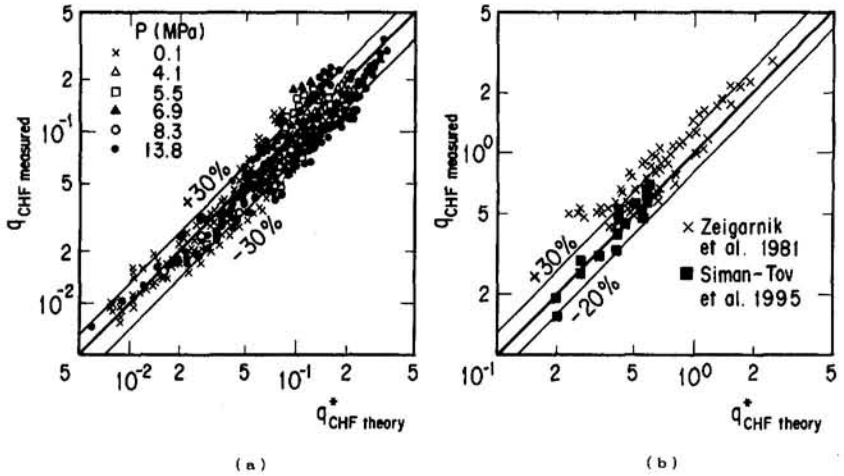


Fig. 9 Comparisons between the analytical results of this study and previous experimental results: (*a*) The case of $G^* < 200$ for saturated flow condition at the outlet of the channel (experiments by DeBortoli et al., 1958, Tippets, 1964, Mishima, 1984, Sudo et al., 1993, Motomura et al., 1993, and Oh et al., 1993); (*b*) a case of a high-subcooling and high-velocity flow condition (experiments by Zeigarnik et al., 1981, and Siman-Tov et al., 1995)

References

Bharathan, D., Wallis, G. B., and Richter, H. J., 1979, "Air-Water Countercurrent Two-Phase Flow," EPRI Rep., NP-1165.

DeBortoli, R. A., Green, S. J., LeTourneau, B. W., Troy, M., and Weiss, A., 1958, "Forced-Convection Heat Transfer Burnout Studies for Water in Rectangular Channels and Round Tubes at Pressures Above 500 psia," WAPD-188.

El-Genk, M. S., Haynes, S. J., and Kim, S.-H., 1988, "Experimental Study of Critical Heat Flux for Low Flow of Water in Vertical Annuli at Near Atmospheric Pressure," *Int. J. Heat Mass Transfer,* Vol. 31, pp. 2291–2304.

Haramura, Y., and Katto, Y., 1983, "A New Hydrodynamic Model of Critical Heat Flux, Applicable Widely to Both Pool and Forced Convection Boiling on Submerged Bodies in Saturated Liquids," *Int. J. Heat Mass Transfer,* Vol. 26, pp. 389–399.

Katto, Y., 1981, *Trans. JSME,* Vol. 47-424 B, pp. 2351–2357 [in Japanese].

Katto, Y., 1992, "A Prediction Model of Subcooled Water Flow Boiling CHF for Pressure in the Range 0.1 ~ 20 MPa," *Int. J. Heat Mass Transfer,* Vol. 26, pp. 1115–1123.

Kusuda, H., and Imura, H., 1974, "Stability of a Liquid Film in a Countercurrent Annular Two-Phase Flow," *Bulletin of JSME,* Vol. 17-114, pp. 1613–1618.

Macbeth, R. V., 1963, "Burnout Analysis. Part 4: Application of a Local Conditions Hypothesis to World Data for Uniformly Heated Round Tubes and Rectangular Channels," AEEW-R267.

Mishima, K., 1984, "Boiling Burnout at Low Flow Rates and Low Pressure Conditions," Dissertation Thesis, Kyoto Univ. Japan.

Motomura, T., Kurosawa, A., Otsuji, T., Mishima, K., Hibiki, T., and Nishihara, H., 1993, "Critical Heat Flux Experiment in a Narrow Vertical Rectangular Channel Heated From One-Side at Atmospheric Pressure," presented at the 1993 Fall Mtg. of the AES of Japan, A26 [in Japanese].

Oh, C. H., and Englert, S. B., 1993, "Critical Heat Flux for Low Flow Boiling in Vertical Uniformly Heated Thin Rectangular Channels," *Int. J. Heat Mass Transfer,* Vol. 36, pp. 325–335.

Shah, M. M., 1977, "A General Correlation for Heat Transfer During Subcooled Boiling in Pipes and Annuli," *ASHRAE Trans.,* Vol. 83, pp. 202–217.

Siman-Tov, M., Felde, D. K., Mcduffee, J. L., and Yoder, G. L. Jr., 1995, "Static Flow Instability in Subcooled Flow Boiling in Parallel Channels," *Proc. 2nd Int. Conf. Multiphase Flow '95-Kyoto,* Vol. 3, P4–77.

Sudo, Y., Miyata, K., Ikawa, H., Kaminaga, M., and Ohkawara, M., 1985, "Experimental Study of Differences in DNB Heat Flux Between Upflow and Downflow in Vertical Rectangular Channel," *J. Nucl. Sci. Technol.,* Vol. 22–7, pp. 604–618.

Sudo, Y., and Kaminaga, M., 1989, "A CHF Characteristics for Downward Flow in a Narrow Vertical Rectangular Channel Heated From Both Sides," *Int. J. Multiphase Flow,* Vol. 15–5, pp. 755–766.

Sudo, Y., Usui, T., and Kaminaga, M., 1990, "Experimental Study of Falling Water Limitation Under a Countercurrent Flow in a Vertical Rectangular Channel (1st Report, Effect of Flow Channel Configuration and Introduction of CCFL Correlation)," *JSME Int. J.,* Ser. II, Vol. 34–2, pp. 169–174.

Sudo, Y., and Kaminaga, M., 1993, "A New CHF Correlation Scheme Proposed for Vertical Rectangular Channels Heated From Both Sides in Nuclear Research Reactors," ASME JOURNAL OF HEAT TRANSFER, Vol. 115, pp. 426–434.

Tippets, F. E., 1964, "Critical Heat Fluxes and Flow Patterns in High-Pressure Boiling Water Flows," ASME JOURNAL OF HEAT TRANSFER, Vol. 86, pp. 12–22.

Ueda, T., 1981, "Kieki nisouryu—Nagare to netsu denntatsu," *Yokendo,* Tokyo, pp. 114–136 [in Japanese].

Wallis, G. B., 1969, *One-Dimensional Two-Phase Flow,* McGraw-Hill, New York, pp. 336–339.

Weisman, J., and Pei, B. S., 1983, "Prediction of Critical Heat Flux in Flow Boiling at Low Qualities," *Int. J. Heat Mass Transfer,* Vol. 26–10, pp. 1463–1477.

Zeigarnik, Yu. A., Privalov, N. P., and Klimov, A. I., 1981, "Critical Heat Flux With Boiling of Subcooled Water in Rectangular Channels With One-Sided Supply of Heat," *Thermal Engineering,* Vol. 28–1, pp. 40–43.

Zenkevich, B. A., 1959, "The Generalization of Experimental Data on Critical Heat Fluxes in Forced Convection of Subcooled Water," *J. Nuclear Energy, Part B: Reactor Technology,* Vol. 1–2, pp. 130–133.

Downloaded 11 Dec 2010 to 193.140.21.150. Redistribution subject to ASME license or copyright; see http://www.asme.org/terms/Terms_Use.cfm

A. Cavallini

L. Doretti

G. A. Longo

L. Rossetto

Istituto di Fisica Tecnica,
Università di Padova,
Padova, Italy

A New Model for Forced-Convection Condensation on Integral-Fin Tubes

This work investigates the effects of vapor shear during pure vapor external condensation on horizontal integral-fin tubes. More than 220 experimental data points in a wide range of operative conditions and enhanced surface geometries are reported together with the visual observation of the condensate flow patterns. The effects of vapor shear are relevant only for vapor Reynolds numbers greater than 70,000–100,000, while heat transfer enhancement is linked to the geometry of the extended surface. A simple semi-empirical equation was developed to account for the shear stress contribution in forced-convection condensation: this equation, applied in conjunction with the model by Briggs and Rose (1994) for stationary vapor condensation, displays a good ability in reproducing all the available data with relevant vapor velocities.

Introduction

Integral-fin tubes are extensively used in shell-and-tube condensers for refrigeration. Research data on this topic, both theoretical and experimental, are readily available in technical and scientific literature. The heat transfer coefficients during filmwise condensation on integral-fin tubes are determined by the thickness and the flow pattern of the condensate film. The condensate under stationary vapor conditions is drained along the finned surface by both gravity and surface tension. The surface tension induces a pressure gradient in the liquid film along the fin profile from the tip to the base of each fin. So the condensate is drained by the surface tension along the fin flanks and then runs down the interfin valley under the influence of gravity. The surface tension also causes liquid retention in the interfin spaces in the lower part of the tube, thus decreasing the effective heat transfer surface area.

Several research workers have developed correlations for the prediction of heat transfer coefficients that could account for the effects of surface tension and gravity under stationary vapor conditions: the early Nusselt-type model by Beatty and Katz (1948), the quite complex analyses by Honda et al. (1987a, b), Adamek and Webb (1990), Murata and Hashizume (1992) and a recent correlation formulated by Briggs and Rose (1994). A great deal of experimental work involving almost stagnant pure vapors condensing on integral-fin tubes has also been presented. Experimental work conducted in the past recognized the effects of vapor shear stress in increasing heat transfer when pure vapor condenses on horizontal integral-fin tubes. Honda et al. (1989, 1991, 1993) condensed R113 (at near atmospheric pressure) on finned tube bundles and achieved a heat transfer enhancement of 30 percent at vapor velocity $u_{max} = 18 - 20$ m/s (referred to the minimum cross-sectional area). Chu and McNaught (1992, 1994) and McNaught and Chu (1993) condensed pure R113 on four finned tube bundles with different tube geometries and achieved a 40 percent maximum increase in the heat transfer coefficient, in the vapor velocity range $1 < u_{max} < 9$ m/s with a vapor pressure range of 0.07 – 0.24 MPa. Michael et al. (1989) condensed pure R113 (at near atmospheric pressure) and pure saturated steam (at 11.6 kPa) on three single horizontal copper tubes with rectangular-shaped fins. Regarding data collected with R113, the velocities involved were not very high ($1.5 < u_{max} < 5.66$ m/s) and the maximum increase in the heat transfer coefficient with vapor velocity was within experimental error. With steam, a 50 percent maximum increase was measured ($14 < u_{max} < 93.6$ m/s). Bella et al. (1992, 1993) and Cavallini et al. (1994a, b, c) tested three different integral-fin tubes and one commercial finned tube with R113 (P = 109–125 kPa) and R11 (P = 109–198 kPa) vapor flowing at velocities referred to the minimum cross-sectional area of up to 30 m/s.

Different heat transfer enhancement values were achieved for the various tubes, reaching values of up to 80 percent at the maximum velocities.

As already mentioned, most of the theoretical equations and models that quantify the heat transfer coefficient realized during condensation of a pure vapor on a single integral-fin tube do not take into account the effects of vapor shear stress at the liquid-gas interface. Attempts to quantify the effects of shear stress were made by Ishihara and Palen (1983), Honda et al. (1992), Chu and McNaught (1994), Honda et al. as reported by Fujii (1993). Ishihara and Palen (1983) first modified the Beatty and Katz correlation (1948) with an empirical equation to account for vapor shear effect. Then, in the same paper, they also proposed a more sound model for shear-controlled flow based on a Dittus–Boelter type convective equation corrected by a two-phase flow multiplier. Unfortunately this second method is proprietary. Chu and McNaught (1994) modified the Rose (1993) correlation for stationary conditions but again the value of a constant in their model was not specified. Fujii (1993) presented results of two prediction methods by Honda et al.; the first is not available because it is unpublished, while the second uses an empirical equation for smooth tube bundles, accounting for the surface area increase due to finning. Since neither of the two methods was able to estimate data by Bella et al. (1992) with sufficient accuracy, Fujii suggested using the greater of the two predictions.

In this work, the authors analyze their data obtained by condensing pure R11 and R113 on three integral-fin tubes in a wide range of vapor velocities and driving temperature differences, and develop a specific model for predicting the heat transfer coefficient in the region where vapor shear effects are significant.

Experimental Data

The experimental apparatus, which is described in detail in previous papers (Bella et al., 1992, 1993; Cavallini et al.,

Contributed by the Heat Transfer Division for publication in the JOURNAL OF HEAT TRANSFER. Manuscript received by the Heat Transfer Division October 2, 1995; revision received March 19, 1996. Keywords: Condensation, Finned Surfaces, Forced Convection. Associate Technical Editor: T. H. Rabas.

Copyright © 1996 by ASME

Downloaded 11 Dec 2010 to 193.140.21.150. Redistribution subject to ASME license or copyright; see http://www.asme.org/terms/Terms_Use.cfm

Table 1 Geometric characteristics of the test tubes

Test tube	2000 fpm		1333 fpm
Tube length [mm]	150.0	145.0	150.0
Outside diameter at the fin tip [mm]	15.80	15.80	16.40
Fin thickness at the fin tip [mm]	0.20	0.20	0.10
Fin thickness at the fin root [mm]	0.20	0.20	0.35
Fin pitch [mm]	0.50	0.50	0.75
Fin height [mm]	1.50	0.60	0.70
Effective / Nominal surface area	6.31	3.26	2.40

Table 2 Operative conditions during experimental runs

Test tube	2000 fpm h= 1.5 mm	2000 fpm h= 0.6 mm	1333 fpm h= 0.7 mm
Number of experimental runs	63	83	74
Fluid	R11 - R113	R11-R113	R11-R113
Vapour inlet pressure [kPa]	114-187	111-193	109-198
Temperature difference ΔT_{ln} [°C]	4.0-13.3	4.4-18.5	4.4-16.8
Maximum vapour velocity [m/s]	0.6-24.9	0.8-23.3	1.9-29.5
Vapour Reynolds number $Re_G \cdot 10^{-5}$	0.13-3.00	0.11-2.92	0.3-3.55

1994a), consisted of a refrigerant loop in which dry, saturated vapor was made to condense partially in the test section on a single horizontal extended tube. This tube was cooled by a water flow kept at a constant inlet temperature. Two different test sections were used: The first was designed to measure heat transfer coefficients and consisted of a test tube instrumented with wall thermocouples; the second had two transparent sidewalls, which made it possible to observe directly the condensation of vapor and to take photographs and record the events on videotape. Three different enhanced copper tubes were tested: an integral-fin tube having 1333 fins per meter (fpm) and two integral-fin tubes with 2000 fpm with different fin heights. Table 1 lists their main geometric characteristics.

The experimental heat transfer coefficient measured in the first test section is defined by:

$$\alpha = Q/(A \cdot \Delta T_{ln}) \quad (1)$$

where Q is the heat flow rate exchanged in the test tube and calculated from the temperature gain and the mass flow rate of the cooling water, A is the envelope surface area of the tube at the fin tip, and:

$$\Delta T_{ln} = (T_{WO} - T_{WI})/\ln\left[(T_S - T_{WI})/(T_S - T_{WO})\right] \quad (2)$$

is the average logarithmic temperature difference between the vapor and the tube wall. T_S is the average vapor saturation temperature derived from the pressure profile, T_{WI} and T_{WO} are the average surface temperatures detected by the thermocouples embedded in the tube wall. The maximum uncertainty of experimental data is estimated to be ±5 percent. Table 2 reports the operative conditions during the experimental runs. More than 220 experimental runs were performed with two different fluids at vapor velocities ranging from 0.6 to 30 m/s, together with around 100 video-taped and photographic sessions of condensate flow.

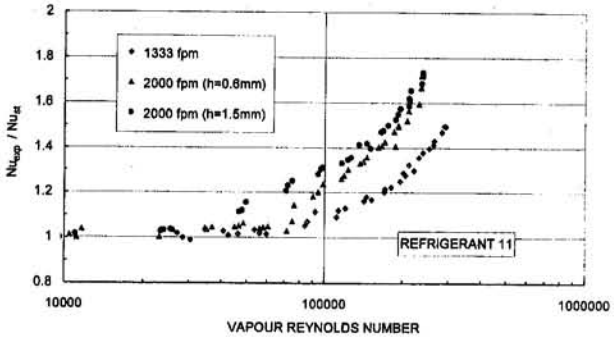


Fig. 1 Present data plotted on the coordinates Nu_{exp}/Nu_{st} versus Re_G; fluid R11

Analysis of these data shows that the effects of vapor shear become relevant only for vapor Reynolds numbers Re_G greater than 70,000–100,000, while a heat transfer enhancement is linked to the geometry of the extended surface. Figures 1 and 2 plot the ratio Nu_{exp}/Nu_{st} between the experimental Nusselt number measured at different vapor velocities and that measured under stationary conditions at the same ΔT_{ln} versus vapor Reynolds number Re_G. Vapor velocity effects for the 1333 fpm tube are appreciable only at vapor Reynolds numbers Re_G greater than 100,000 with a 50–60 percent maximum enhancement, while for both the 2000 fpm tubes they appear at Re_G greater than 70,000–80,000 giving a maximum increase of 70–80 percent at the highest vapor velocity tested. This heat transfer enhancement with vapor velocity is linked to the specific changes in condensate flow pattern observed in the transparent test section. At very low vapor velocities, the condensate leaves the tube forming equally spaced columns and flooding the lower portion of the tube completely. When vapor velocity increases, the columns break into

Nomenclature

A = envelope surface area
C = parameter in Eq. (8)
c_p = specific heat capacity
d = tube diameter
$E1 = \sum_{1}^{N} [(Nu_{cal} - Nu_{exp})/Nu_{exp}]/N$
$E2 = \sum_{1}^{N} |(Nu_{cal} - Nu_{exp})/Nu_{exp}|/N$
fpm = fins per meter
g = gravitational acceleration
h = fin height
n = exponent in Eq. (3)
Nu = Nusselt number = $\alpha d_o/\lambda_L$
p = fin pitch
P = pressure
Pr = Prandtl number
Q = heat flow rate
Re_{eq} = equivalent Reynolds number, Eq. (6)
Re_f = film Reynolds number = $2\Gamma/\mu_L$
Re_G = vapor Reynolds number = $\rho_G u_{max} d_o/\mu_G$
t = fin thickness
T_S = saturation temperature
T_{WI} = wall temperature at the tube inlet
T_{WO} = wall temperature at the tube outlet
u = vapor velocity
α = film heat transfer coefficient
Γ = specific condensate flow rate
ΔT_{ln} = logarithmic average temperature difference, Eq. (2)
λ = thermal conductivity
μ = dynamic viscosity
ρ = density

Subscripts

cal = calculated
eq = equivalent
exp = experimental
fc = forced convection
G = vapor phase
L = condensate
ln = logarithmic
max = maximum value
o = outside of finned tube at the fin tip
st = stationary vapor

Downloaded 11 Dec 2010 to 193.140.21.150. Redistribution subject to ASME license or copyright; see http://www.asme.org/terms/Terms_Use.cfm

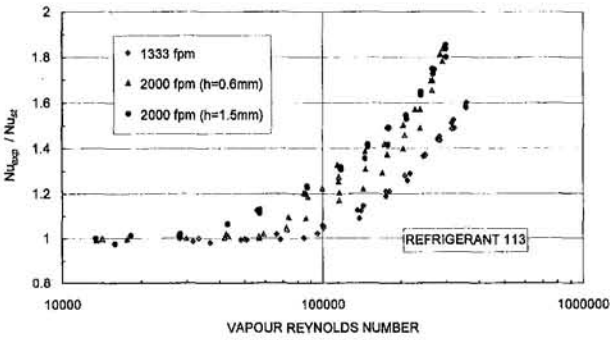


Fig. 2 Present data plotted on the coordinates Nu_{exp}/Nu_{st} versus Re_G; fluid R113

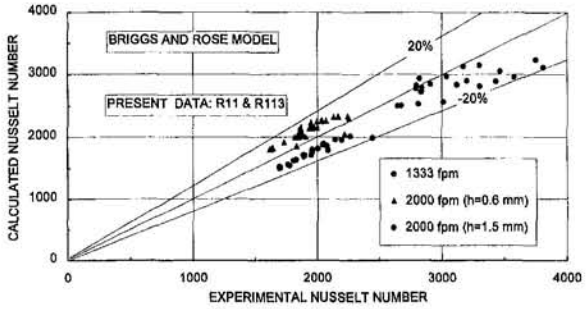


Fig. 3 Present data versus the Briggs and Rose (1994) model for stationary vapor conditions

droplets and a dispersed flow takes place. Vapor shear reduces the thickness and promotes turbulence in the liquid film, while the extension of the flooded portion of the tube does not seem to be influenced by vapor shear, as described in detail in previous papers (Cavallini et al., 1994b–c).

In the region where vapor shear stress effects are negligible ($Re_G < 70{,}000–80{,}000$ for the 2000 fpm tubes and $Re_G < 100{,}000$ for the 1333 fpm tube) the experimental heat transfer coefficients can be fairly well predicted by the available models for stationary vapor condensation on integral-fin tubes. With reference to the models by Beatty and Katz (1948), Honda et al. (1987a, b), Adamek and Webb (1990), Murata and Hashizume (1992), and Briggs and Rose (1994), Table 3 gives the mean percentage deviation E1 and the mean absolute percentage deviation E2 in reproducing the present data for stagnant vapor conditions. The Adamek and Webb (1990) analysis was applied utilizing a conventional value for the radius of the fin-tip edge, equal to 0.05 t_o (t_o being the fin tip thickness), as suggested by the authors (Adamek and Webb, 1996).

Best results are achieved by the recent Briggs and Rose (1994) model, which takes into account the contributions of gravity and surface forces on the fin tips, fin flanks, and interfin tube space, as well as the effects of condensate retention and conduction in the fins. This model, which features a fairly simple structure, was favorably tested by its authors on a vast data bank.

Figure 3 shows a comparison between the experimental Nusselt numbers and the Nusselt numbers calculated by the Briggs and Rose (1994) model. In the region where forced convection effects are important, a new model needs to be developed.

A New Equation for Forced-Convection Condensation

The experimental data from this present work show that stationary vapor condensation on integral-fin tubes is controlled by gravity and surface tension, whereas when vapor velocity increases, the effects of vapor shear also become relevant. For vapor Reynolds numbers greater than 70,000–100,000, the vapor shear stress contribution to heat transfer is comparable to gravity and surface tension contributions, while at the highest vapor Reynolds number tested (300,000–350,000), vapor shear is the predominant active force governing condensate drainage. To reproduce this complex behavior, an asymptotic model was adopted to compute the heat transfer coefficient in the form:

$$\alpha = [\alpha_{st}^n + \alpha_{fc}^n]^{1/n} \tag{3}$$

where the first asymptote α_{st} is the heat transfer coefficient under stationary vapor conditions when shear stress effects are insignificant, and the second asymptote α_{fc} is the heat transfer coefficient when forced convection mechanisms are predominant and gravity and surface tension become negligible. The heat transfer coefficients α, α_{st}, and α_{fc} are referred to the surface of a smooth tube of diameter d_o. Since experimental data approaches the first asymptote α_{st} for vapor Reynolds numbers less than 70,000, this coefficient is experimentally attainable. It depends on fluid surface tension and other properties, temperature difference (saturation-tube wall temperature), tube geometry and fin material thermal conductivity. The second asymptote α_{fc} can be directly derived from the experimental heat transfer coefficients α_{exp}, measured by the authors at vapor Reynolds numbers greater than 70,000–100,000; $\alpha_{exp,fc}$ can be evaluated by the expression:

$$\alpha_{exp,fc} = [\alpha_{exp}^n - \alpha_{exp,st}^n]^{1/n} \tag{4}$$

The experimental forced-convection contribution derived from Eq. (4) with $n = 2$ is plotted in Fig. 4 on the coordinate $Nu_{fc}/Pr_L^{0.333}$ versus Re_{eq}, as suggested by Honda et al. (1986), with:

$$Nu_{fc} = (\alpha_{fc} \cdot d_o)/\lambda_L \tag{5}$$

$$Re_{eq} = Re_f + Re_G(\mu_G/\mu_L)(\rho_L/\rho_G)^{1/2} \approx [(\rho_G u_{max} d_o)/\mu_L](\rho_L/\rho_G)^{0.5} \tag{6}$$

$$Pr_L = (c_{pL} \cdot \mu_L)/\lambda_L \tag{7}$$

Table 3 Comparison between models and present data

Model	1333 fpm h= 0.7 mm		2000 fpm h= 0.6 mm		2000 fpm h=1.5 mm	
	E1	E2	E1	E2	E1	E2
Beatty and Katz (1948)	-24.2	24.2	3.8	5.1	10.7	11.3
Honda et al. (1987a and b)	6.3	6.3	9.4	9.6	-23.1	23.1
Adamek and Webb (1990)	-0.1	3.2	37.4	37.4	-6.4	7.2
Murata and Hashizume (1992)	9.1	9.1	14.5	14.5	-7.4	8.1
Briggs and Rose (1994)	-10.6	10.6	9.9	9.9	-7.4	7.9

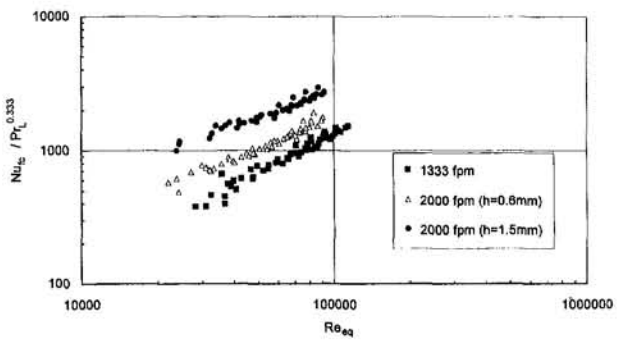


Fig. 4 Present data plotted on the coordinates $Nu_{fc}/Pr_L^{0.333}$ versus Re_{eq} ($Re_{eq} > 26{,}000$ for the 1333 fpm tube and $Re_{eq} > 22{,}000–24{,}000$ for the 2000 fpm tube)

Downloaded 11 Dec 2010 to 193.140.21.150. Redistribution subject to ASME license or copyright; see http://www.asme.org/terms/Terms_Use.cfm

Table 4 Data in the best-fit procedure

Test tube	2000 fpm h= 1.5 mm	2000 fpm h= 0.6 mm	1333 fpm h= 0.7 mm
Runs	45	55	51
Fluid	R11 - R113	R11-R113	R11-R113
$Re_G \cdot 10^{-5}$	0.80-3.00	0.70-2.92	1.00-3.55
$Re_{eq} \cdot 10^{-5}$	0.24-0.86	0.22-0.86	0.26-1.01
Pr_L	3-8	3-8	3-8

The data points for the three different tube geometries tend to stratify along three parallel lines. Figure 4 suggests an exponent for the equivalent Reynolds number Re_{eq} equal to 0.8, and a functional form for the forced-convection asymptote in Eq. (3):

$$Nu_{fc} = C \cdot Re_{eq}^{0.8} \cdot Pr_L^{1/3} \quad (8)$$

with the parameter C depending on fin geometry, or, as an approximation, fin pitch p, fin height h, and fin tip thickness t_o. Vapor shear stress certainly does not act in the same way on the different parts of the integral-fin tube heat transfer surface, affecting more the fin tips and the outer parts of the fin flanks. With this in mind the following expression was assumed for the constant C:

$$C = a + b(t_o/p) + c(h/p) \quad (9)$$

where a, b, and c are constants to be derived from a best-fit procedure. Equation (9) suggests a different weight attributed to the forced-convection contribution of the different parts of the finned surface. The constants a, b, and c in Eq. (9) and the optimum value for the exponent "n" in the asymptotic model (Eq. (3)) were determined by fitting the present data for vapor Reynolds numbers in excess of 70,000–100,000. This set of data includes more than 150 points, whose characteristics are reported in Table 4. The values obtained from the best-fit procedure are the following:

$$n = 2 \quad a = 0.03 \quad b = 0.166 \quad c = 0.07 \quad (10)$$

This model, with Eqs. (5)–(9) and the set of constants (10) is able to compute only the forced-convection contribution. A proper model for stationary vapor contribution is necessary to estimate the heat transfer coefficient with the asymptotic model (3): in this paper, the simple equation by Briggs and Rose (1994) is used for this purpose. The present model, together with the Briggs and Rose equation (1994), reproduces the present data at high vapor velocity with an absolute mean percentage deviation $E2 = 6.5$ percent. Figure 5 gives the relative comparison between all the experimental and calculated Nusselt numbers.

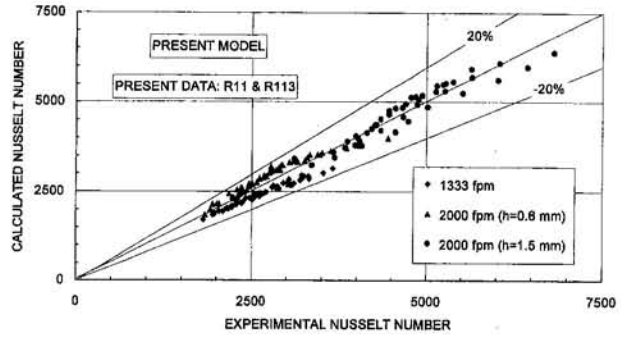


Fig. 5 Present data versus present model (Eqs. (5)–(10)): stationary vapor contribution by Briggs and Rose (1994) model

Table 5 Data by Honda et al. (1989, 1991)

Test tube	2000 fpm	1024 fpm
Runs	38	109
Fluid	R113	R113
Vapour Reynolds number $Re_G \cdot 10^{-5}$	0.39-2.40	0.37-2.15
Equivalent Reynolds number $Re_{eq} \cdot 10^{-5}$	0.11-0.69	0.10-0.63
Prandtl Number	7	7-8

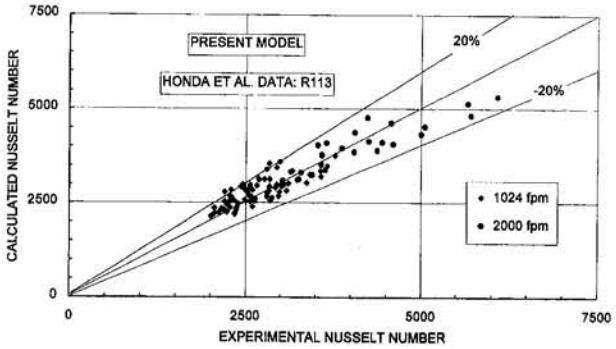


Fig. 6 Honda et al. data versus present model (Eqs. (5)–(10)): stationary vapor contribution by Briggs and Rose (1994) model

The only other experimental data sets for condensation on integral-fin tubes at sufficiently high vapor velocity available in the open literature are those by Honda et al. (1989, 1991, 1993) and those by Michael et al. (1989). The data by Honda et al. include condensation heat transfer coefficients of refrigerant 113 on 1024 fpm and 2000 fpm integral-fin tubes as the first row of a tube bundle or as a core tube in an otherwise uncooled bundle with vapor velocities up to 20 m/s. Table 5 gives the main distinctive characteristics of this data. The present model used together with the Briggs and Rose equation reproduces Honda et al. data with an absolute mean percentage deviation $E2 = 8.6$ percent. Figure 6 gives the relative comparison between experimental and calculated Nusselt numbers.

Michael et al. present condensation heat transfer coefficients of steam on 200, 400, and 800 fpm copper tubes, having machined, rectangular shape fins, mounted as a single tube in the test section. Steam flowed at 11.6 kPa, with maximum vapor velocity, referred to the minimum cross-sectional flow area, ranging from 14 to 94 m/s. Table 6 gives the main characteristics of this data.

The present model used together with the Briggs and Rose equation reproduces the Michael et al. data with an absolute mean percentage deviation $E2 = 18.05$ percent. Figure 7 gives the comparison between experimental and calculated Nusselt numbers. While for the 800 fpm tube absolute deviations are within 20 percent, for the other two tubes (400 and 200 fpm) they are within 30 percent. This is due to the Briggs and Rose correlation, which underestimates the heat transfer coefficients at the lowest vapor velocities.

Table 6 Data by Michael et al. (1989)

Test tube	800 fpm	400 fpm	200 fpm
Runs	47	47	38
Fluid	Steam	Steam	Steam
Vapour Reynolds number $Re_G 10^{-5}$	0.02-0.15	0.02-0.15	0.02-0.15
Equivalent Reynolds number $Re_{eq} 10^{-5}$	0.04-0.30	0.04-0.29	0.04-0.29
Prandtl Number	3.7	3.7	3.7

Downloaded 11 Dec 2010 to 193.140.21.150. Redistribution subject to ASME license or copyright; see http://www.asme.org/terms/Terms_Use.cfm

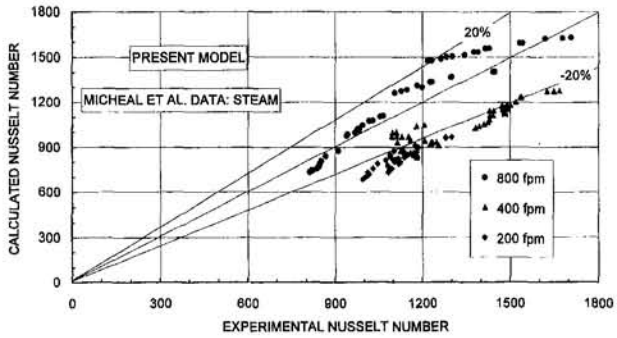


Fig. 7 Michael et al. data versus present model (Eqs. (5)–(10)): stationary vapor contribution by Briggs and Rose (1994) model

For the present data, at the highest vapor velocities the forced-convection contribution calculated by the present model is predominant over the stationary contribution computed by the Briggs and Rose (1994) model, reaching a value $\alpha_{fc,calc}/\alpha_{st,calc} = 1.7$; the same ratio for the Honda et al. (1989, 1991) data reaches the value of 1.3 at the highest vapor velocities, and for the Michael et al. (1989) data reaches the maximum value of 2.1. The forced-convection contribution to the heat transfer coefficient is well above the experimental errors and the Briggs and Rose correlation uncertainty.

At present, in the open literature there are no data concerning condensation of new alternative refrigerants (ozone-safe) at sufficiently high vapor velocity, but this model developed in terms of nondimensional groups can be confidently extended to them.

Conclusions

In technical literature, several models can be found (Honda et al., 1987a, b; Adamek and Webb, 1990; Murata and Hashizume, 1992; Briggs and Rose, 1994) to give a general good performance in reproducing experimental data for condensation of stagnant vapor on the outside of horizontal integral-fin tubes, whereas none of them takes into account the effects of vapor shear. This work presents a semi-empirical equation to account for the shear stress effects in forced-convection condensation.

This correlation, used together with the recent model by Briggs and Rose (1994) for stationary vapor condensation, shows a good ability in reproducing all the available data with relevant vapor velocities.

References

Adamek, T., and Webb, R., 1990, "Prediction of Film Condensation on a Horizontal Integral-Fin Tube," *Int. J. Heat Mass Transfer,* Vol. 33, pp. 1721–1735.

Adamek, T., and Webb, R., 1996, Private Communication.

Beatty, K. O., and Katz, D. L., 1948, "Condensation of Vapor on Outside of Finned Tubes," *Chem. Eng. Progr.,* Vol. 44, pp. 55–70.

Bella, B., Cavallini, A., Longo, G. A., and Rossetto, L., 1992, "Pure Refrigerant Condensation on a Single Integral Finned Tube: Vapour Velocity Effects," *Proc. 1992 Int. Refr. Conf.,* Purdue University, pp. 177–186.

Bella, B., Cavallini, A., Longo, G. A., and Rossetto, L., 1993, "Pure Vapour Condensation of Refrigerants 11 and 113 on a Horizontal Integral Finned Tube at High Vapour Velocity," *J. of Enhanced Heat Transfer,* Vol. 1, pp. 77–86.

Briggs, A., and Rose, J. W., 1994, "Effect of Fin Efficiency on a Model for Condensation Heat Transfer on a Horizontal Integral-Fin Tube," *Int. J. Heat Mass Transfer,* Vol. 37, pp. 457–463.

Cavallini, A., Doretti, L., Longo, G. A., and Rossetto, L., 1994a, "Experimental Heat Transfer Coefficients During External Condensation of Halogenated Refrigerants on Enhanced Tubes," *Proc. 10th Int. Heat Transfer Conf.,* Brighton, Vol. 6, pp. 7–12.

Cavallini, A., Doretti, L., Longo, G. A., and Rossetto, L., 1994b, "Flow Patterns During Condensation of Pure Refrigerants on Enhanced Tubes Under High Vapor Velocity," *Proc. Int. Refrig. Conf.,* Purdue University, p. 311–316.

Cavallini, A., Doretti, L., Longo, G. A., and Rossetto, L., 1994c, "Experimental Investigations on Condensate Flow Patterns on Enhanced Surfaces," *Proc. I. I. R. Conference "CFC, The Day After,"* Padova, Sept. 21–23, pp. 627–634.

Chu, C. M., and McNaught, J. M., 1992, "Condensation on Bundles of Plain and Low-Finned Tubes—Effects of Vapour Shear and Inundation," *I. Chem. E. Symp. Series,* No. 129, Vol. 1, pp. 225–232.

Chu, C. M., and McNaught, J. M., 1994, "Tube Bundle Effects in Crossflow Condensation on Low-Finned Tubes," *Proc. 10th Int. Heat Transfer Conf.,* Brighton, Vol. 3, pp. 293–298.

Fujii, T., 1993, "Enhancement to Condensing Heat Transfer. New Developments," *Proc. ICHMT Int. Symp,* Lisbon, Portugal, Sept. 6–9.

Honda, H., Uchima, B., Nozu, S., and Fujii, T., 1986, "Effect of Vapour Velocity on Film Condensation of R-113 on Horizontal Tubes in a Crossflow," *Int. J. Heat Mass Transfer,* Vol. 29, pp. 429–438.

Honda, H., Uchima, B., and Nozu, S., 1987a, "A Prediction Method for Heat Transfer During Film Condensation on a Horizontal Low Finned Tube," ASME JOURNAL OF HEAT TRANSFER, Vol. 109, p. 218–225.

Honda, H., Uchima, B., and Nozu, S., 1987b, "A Generalized Prediction Method for Heat Transfer During Film Condensation on a Horizontal Low Finned Tube," *Proc. ASME–JSME Joint Conf.,* Vol. 4, pp. 385–392.

Honda, H., Uchima, B., Nozu, S., Nakata, H., and Torigoe, E., 1989, "Film Condensation of Downward Flowing R-113 Vapour on In-Line Bundles of Horizontal Finned Tubes," ASME HTD-Vol. 108, pp. 117–125.

Honda, H., Uchima, B., Nozu, S., Torigoe, E., and Imai, S., 1991, "Film Condensation of Downward Flowing R-113 Vapour on Staggered Bundles of Horizontal Finned Tubes," *Proc. ASME/JSME Joint Conf.,* Vol. 2, pp. 487–494.

Honda, H., Kim, K., and Fukuda, T., 1992, "A Theoretical Model of Film Condensation in a Bundle of Horizontal Finned Tubes Considering the Effect of Vapour Velocity," *Proc. 29th Nat. Heat Transfer Symp. of Japan,* pp. 754–755.

Honda, H., 1993, Personal Communications.

Ishihara, K. I., and Palen, J. W., 1983, "Condensation of Pure Fluids on Horizontal Finned Tube Bundles," *Inst. Chem. Eng. Symp.,* No. 75, Manchester, p. 429–446.

McNaught, J. M., Chu, C. M., 1993, "Heat Transfer Measurements in Condensation on Bundles of Low-Finned Tubes—Effects on Fin Frequency," *Proc. Eng. Found. Conf.,* St. Augustine, FL, p. 367–376.

Michael, A. G., Marto, P. J., Wanniarachchi, A. S., and Rose, J. W., 1989, "Effect of Vapour Velocity During Condensation on Horizontal Smooth and Finned Tubes," ASME HTD-Vol. 114, pp. 1–10.

Murata, K., and Hashizume, K., 1992, "Prediction of Condensation Heat Transfer Coefficient in Horizontal Integral-Fin Tube Bundles," *Experimental Heat Transfer,* Vol. 5, pp. 115–130.

Rose, J. W., 1993, "Condensation on Low-Finned Tubes—an Equation for Vapor-Side Enhancement," *Proc. Eng. Found. Conf.,* St. Augustine, FL, pp. 317–334.

Downloaded 11 Dec 2010 to 193.140.21.150. Redistribution subject to ASME license or copyright; see http://www.asme.org/terms/Terms_Use.cfm

Study on Sublimation Phenomenon of Horizontal Frost Layer Exposed to Forced Convection Air Flow and Radiant Heat

H. Inaba
Professor.

S. Imai
Graduate Student.

Department of Mechanical Engineering,
Faculty of Engineering,
Okayama University,
Tsushimanaka, 3-1-1, 700 Japan

The present paper deals with a new defrosting method for application to a cold heat exchanger by means of a frost sublimation phenomenon. The frost sublimation phenomenon occurs under the condition of temperature below the triple point of water (0.01°C, 0.6105 kPa). The present experimental study has focused on the heat and mass transfer processes at a horizontal frost layer in a moist air flow. It is found that the mass flux from the frost layer increases with the increase of water vapor mass concentration difference between the frost and main moist air flow, main air flow velocity, and the infrared radiant heat intensity. Nondimensional correlations for mass transfer, heat transfer, and defrost completion time have been derived.

Introduction

When the cooling surface of the cold heat exchanger, whose temperature is below 0°C, is exposed to moist air, frost is deposited and accumulates on its surface. It is necessary for the heat exchanger to be defrosted because the frost layer decreases the heat transfer coefficient.

Previously, frost melting methods such as the use of hot gas in the reverse refrigerating cycle and the electric heater, etc., have been used for defrosting. These methods, however, result in curtailment of the cooling function, and a decrease in thermal efficiency due to an interruption of the refrigeration cycle. Furthermore, these methods bring an economic disadvantage owing to the small ratio of the energy consumed to melt the frost layer to total energy supplied during the defrosting process, and the cost of treating the melted water.

Frost exposed to the flowing air, whose temperature is below the triple point (0.01°C, 0.6105 kPa), sublimates. Defrosting by means of frost sublimation can solve the problem of melted water as seen in previous defrosting methods. Kochs et al. (1993) reported the influence of the various factors on ice sublimation time in a vacuum condition. However, few studies have dealt with sublimation characteristics of a frost layer in moist cold air. Defrosting by means of the sublimation phenomenon makes it possible to remove the frost layer under the condition of temperatures below the freezing point. That is, it is possible to defrost without the appearance of melted water. If defrosting by means of sublimation applies to the refrigeration equipment, it is possible to remove the frost layer on the heat exchanger without melting materials such as frozen food. It is necessary to provide heat energy under the condition of a temperature below the triple point of water in order to promote defrosting by means of frost sublimation. It is not an effective measure to provide heat energy from the heating surface under the frost layer since the frost layer provides a large thermal resistance due to a low thermal conductivity of a frost layer from 0.1 to 0.2 W/(m · K). Schmidt (1934) showed that the radiant absorptance of a frost layer in an infrared wavelength region was about 0.98. This high radiant absorptance suggests that frost sublimation may be accomplished with radiant heat. This paper deals with defrosting by means of frost sublimation with radiant heat in a forced convection air flow. The present fundamental experiments have been performed by defrosting the horizontal frost layer for some parameters of flowing air velocity and its temperature, water vapor mass concentration, and radiant heat intensity.

Experimental Apparatus and Procedure

The experimental apparatus is shown in Fig. 1. A cooling plate for frost formation is made of a copper sheet 100 mm in width × l = 300 mm in length × 1 mm in thickness. Before starting the defrosting experiments, a frost layer is formed on a test cooling plate to a certain thickness under various cooling conditions. The initial frost height is defined as the average value of vertical distances from the test cooling plate surface to the tips of an even frost layer. It is said that the initial frost layer height is almost uniform since the frost height difference from 20 measuring points is less than ±0.1 mm.

Frost sublimation experiments have been carried out using a rectangular wind tunnel set in an air-conditioned room. A test section is constructed of a rectangular channel 300 mm in width × 90 mm in height × 1300 mm in length. The frost layer formed on the test cooling plate is arranged horizontally in the test section. Two electronic balances (maximum value of mass measurement 620 g, minimum measuring range 0.1 mg) hang the thermal insulator/test cooling plate/frost composite layer with piano wires, and they measure the total mass of these materials (490 ~ 532 g). The sublimated mass of the frost layer is calculated from the time variation of the above-mentioned total mass. During the weighing, the main air flow is stopped. Therefore, it is possible to avoid the influence of the hydrodynamic force by air flow on the mass measurement. The uncertainty of the measured mass is ±0.50 mg. An electric plate heater (110 mm width × 310 mm length × 3 mm thickness), used as an infrared radiative heat source for frost sublimation promotion, is set horizontally 100 mm above the test cooling plate. When the temperature of the electric plate heater becomes constant at steady state, the experiment on frost sublimation starts by removing a thin aluminum plate cover above the frost

Contributed by the Heat Transfer Division for publication in the JOURNAL OF HEAT TRANSFER. Manuscript received by the Heat Transfer Division February 21, 1995; revision received April 15, 1996. Keywords: Double Diffusion Systems, Forced Convection, Radiation. Associate Technical Editor: B. W. Webb.

Copyright © 1996 by ASME

Downloaded 11 Dec 2010 to 193.140.21.150. Redistribution subject to ASME license or copyright; see http://www.asme.org/terms/Terms_Use.cfm

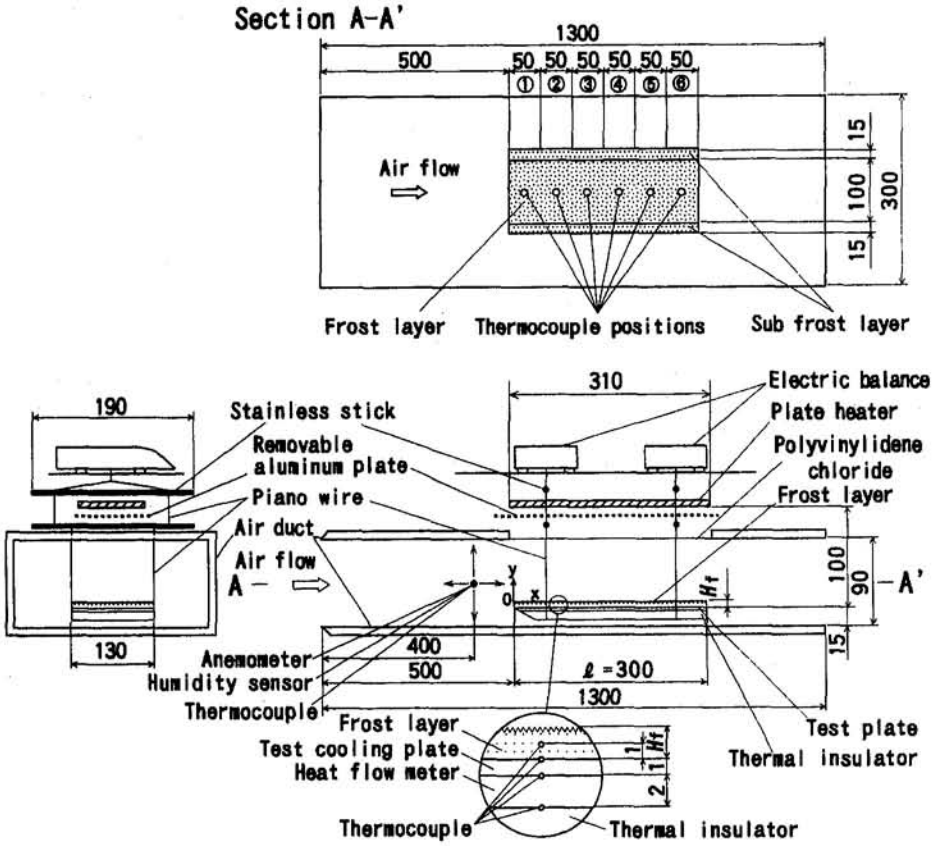


Fig. 1 Experimental apparatus

layer. The decrease of surface temperature of the plate heater receiving the reflected radiant heat from the thin aluminum plate cover is small when its cover is removed. The surface temperature of the electric plate heater ranges from 12.0°C to 212.0°C. The infrared radiative intensity E_λ and wavelength λ of the electric plate heater, which are calculated as a black body, are shown in Fig. 2 for reference. The electric plate heater and the test cooling plate are coated with a black paint (emissivity = 0.98) to minimize the reflection of incoming radiation. The air condition in an experimental room was carefully controlled to maintain temperature and humidity at a given value. The air velocity was measured by a micro-anemometer mounted in the test section. The hot-wire anemometer and the K-type thermocouple can be traversed in the vertical and horizontal directions as shown in Fig. 1. A heat flow meter of 2.0 mm thickness was installed below the cooling plate to measure the heat flow to the environment. A time variation of frost mass M_s, that is the amount of frost sublimation, was measured using the electronic balances. The frost mass measurement is performed by stopping the main air flow and overshadowing the radiant heat by an aluminum plate for a short time. Therefore the frost mass measurement is carried out without the hydrodynamic force and radiation effects.

Nomenclature

C_{TP} = water vapor mass concentration at triple point
C_∞ = water vapor mass concentration of main air flow
C_s = water vapor mass concentration at saturating condition of frost layer
C'_s = water vapor mass concentration at saturating condition of main air flow
C^* = ratio of humidity
C_{pf} = specific heat of frost layer
D = diffusion coefficient
Fo = Fourier number
h = overall heat transfer coefficient
h_D = overall mass transfer coefficient
h_D^* = modified mass transfer coefficient
H_f = frost height
H_{fin} = initial frost height
k_{cd} = thermal conductivity of air
L = sublimate latent heat
l = test cooling plate length
m_{Af} = mass flux
M_s = amount of frost sublimation
Nu = Nusselt number
Pr = Prandtl number
q_r = radiant heat intensity
q_r^* = nondimensional radiant heat
q_{cv} = convection heat flux
q_{cv}^* = nondimensional convection heat flux
Q_{cv} = quantity of convection heat
Q_s = quantity of latent heat for sublimation
R = surface roughness of frost layer
Re = Reynolds number
S = projectional sublimation area (cooling surface area)
Sc = Schmidt number
Sh* = modified Sherwood number
Ste = Stefan number
T_∞ = temperature of main air flow
T_w = surface temperature of test cooling plate
t_{cs} = defrost completion time
U_∞ = air velocity
ϕ_∞ = relative humidity of main air flow
ρ_f = frost density
ρ^* = ratio of density

Subscripts

f = frost layer
s = saturated
TP = triple point
∞ = main air flow

Downloaded 11 Dec 2010 to 193.140.21.150. Redistribution subject to ASME license or copyright; see http://www.asme.org/terms/Terms_Use.cfm

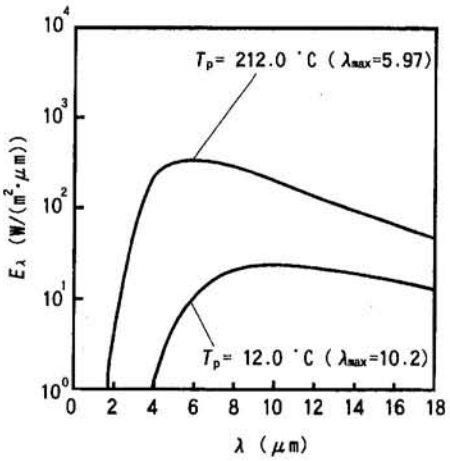


Fig. 2 Radiative characteristics of the electric heater

The range of experimental parameters is as follows:

- Initial frost height $H_{fin} = 2.0 \sim 7.0$ mm
- Frost density $\rho_f = 90 \sim 180$ kg/m^3
- Main air flow velocity $U_\infty = 0.3 \sim 12.0$ m/s
- Main flow air temperature $T_\infty = -20.0 \sim -2.0$°C
- Main flow relative humidity $\phi_\infty = 50 \sim 90\%$
- Radiant heat intensity $q_r = 0 \sim 900$ W/m^2

Uncertainty Estimates in Measurement

The uncertainty of the obtained data on temperature is ±0.05 K, which can be estimated by the thermocouple calibration and the temperature correction from the standard thermometer reading. The uncertainty of the water vapor mass concentration is estimated within $\pm 8.0 \times 10^{-6}$ kg/m^3.

The uncertainty of the heat flux obtained depends primarily on the heat loss from the frost layer to the environment and the uncertainty of the temperature measurement; it is estimated within ±0.8 W/m^2. The uncertainty of the radiant heat intensity q_r is estimated within ±1.0 W/m^2 from the measuring accuracy of the radiometer. The uncertainty of the convection heat flux q_{cv} is estimated by the uncertainty of the measuring accuracy of the latent heat for the sublimation Q_s, the radiant heat Q_r, the conduction heat Q_{cd}, and the sensible heat of the frost layer Q_{cpf}, test cooling plate Q_{cpt}, and heat flux sensor Q_{cpp}. As a result, the uncertainty of the convection heat flux q_{cv} is within ±1.8 W/m^2. The uncertainty of the mass flux for the sublimation depends mainly on the uncertainty of the frost mass and the time interval measurements. The uncertainty of the mass flux of the sublimation is within 5.6×10^{-8} kg/(m^2·s).

Sublimation Condition of the Frost Layer

Figures 3 and 4 show various sectional shapes of the frost layers obtained by photographs. These figures show the effect of radiant heat intensity q_r on the frost sublimation at the same time of $t = 10$ min. Figure 3 shows the initial shape of the frost layer, and this frost layer is obtained from the frost layer growth period reported by Inaba et al. (1992). The initial frost height H_{fin} is 2.0 mm and the surface roughness of the frost layer R is 0.5 mm. The surface roughness R of the frost layer is defined by a vertical distance between the top and bottom of the frost surface roughness. The surface roughness R is determined by the average value of 10 measuring points of R from the sectional enlarged photographs of the frost layer. Figure 4 shows sectional shapes of frost layers at the sublimation time $t = 10$ min, in the case where main air velocity $U_\infty = 8.0$ m/s, main flow air temperature $T_\infty = -5$°C, relative humidity $\phi_\infty = 60$ percent, frost density $\rho_f = 130$ kg/m^3, and radiant heat intensity q_r from 0 to 840 W/m^2.

Figure 4(*a*) shows the shape of the frost layer without radiant heat. A surface roughness R of the frost layer decreases from 0.5 mm at the initial condition to 0.2 mm, and the frost height decreases to 1.3 mm. The surface temperature of the cooling

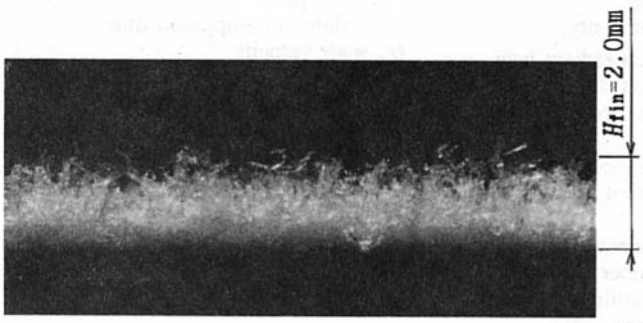


Fig. 3 Initial sectional shape of the frost layer

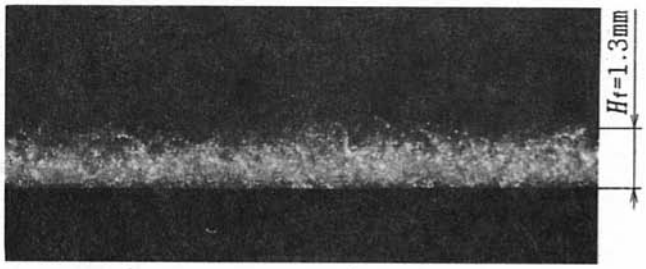


Fig. 4(*a*) $q_r = 0$ W/m^2, $R = 0.2$ mm

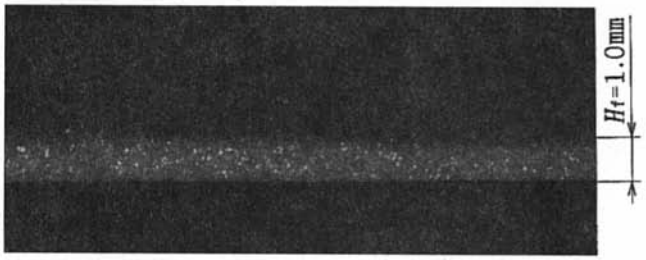


Fig. 4(*b*) $q_r = 280$ W/m^2, $R = 0.1$ mm

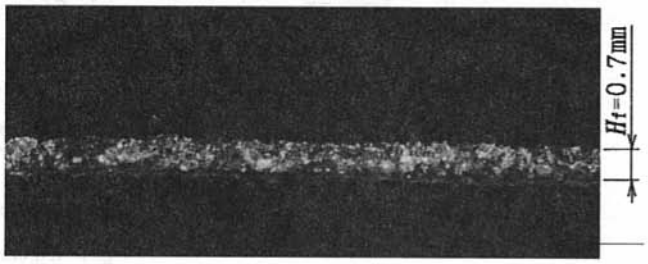


Fig. 4(*c*) $q_r = 560$ W/m^2, $R = 0.15$ mm

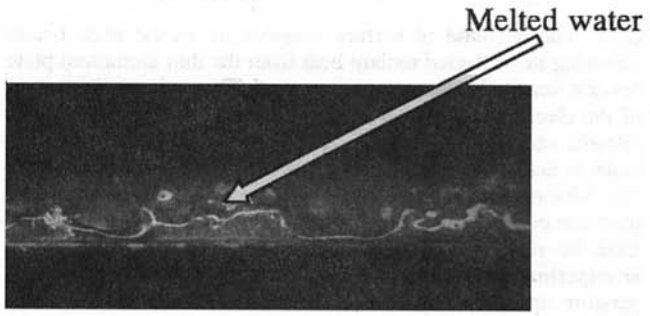


Fig. 4(*d*) $q_r = 840$ W/m^2

Fig. 4 Sectional shape of the frost layer ($u_\infty = 8$ m/s, $t = 10$ min)

Downloaded 11 Dec 2010 to 193.140.21.150. Redistribution subject to ASME license or copyright; see http://www.asme.org/terms/Terms_Use.cfm

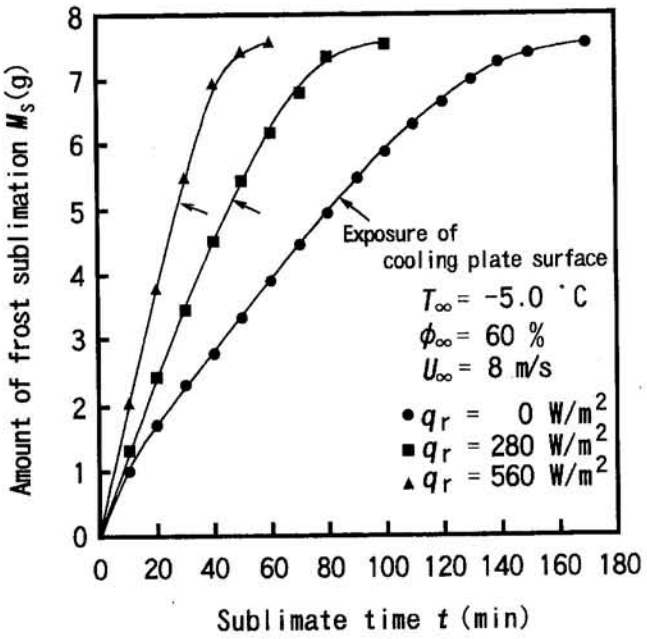


Fig. 5 Time history of amount of frost sublimation

plate T_w (−6.0°C) is lower than the main moist air flow temperature T_∞ because of the frost sublimation.

Figure 4(b) shows a shape of the frost layer in the case where radiant heat intensity q_r = 280 W/m^2. In this case, the surface roughness of the frost layer R decreases to 0.1 mm and the frost height H_f decreases to 1.0 mm due to sublimation promotion by radiant heat.

Furthermore, Fig. 4(c) shows a photograph of the frost layer in the case of radiant heat intensity q_r = 560 W/m^2. In this case, a surface roughness of the frost layer R is 0.05 mm and a frost height H_f is 0.7 mm. The temperature of the cooling plate T_w increases with an increase in radiant heat intensity q_r and it reaches about −1.8°C. However, the frost layer does not melt in this case. Finally, Fig. 4(d) shows the shape of the frost layer in the case of the q_r = 840 W/m^2. In this case, the frost layer starts to melt. The present data reduction for the frost sublimation is performed by using data without the frost melting in which the temperature of the frost layer is below 0°C during test run. The present study deals only with the defrost process by a frost sublimation.

Time History of the Frost Sublimation

Figure 5 shows the time history of the amount of frost sublimation M_s for various radiant heat intensities q_r under the experimental conditions of T_∞ = −5.0°C, ϕ_∞ = 60 percent, U_∞ = 8.0 m/s, H_{fin} = 2.0 mm, and ρ_f = 130 kg/m^3. The arrow symbols in Fig. 5 show defrost completion time when the length (X direction in Fig. 1) of the frost layer becomes 99 percent of the test cooling plate length (l = 300 mm) due to frost sublimation. The frost sublimation rate is large at the beginning of frost sublimation. This is explained by the fact that the surface roughness of the frost promotes air flow turbulent intensity over the increased sublimation surface area, since the surface roughness is larger at the beginning of frost sublimation. Also, the frost sublimation is promoted by an increase in the radiant heat intensity. However, the promotion rate by the radiant heat intensity is not so large since the convection heat loss from the frost surface, whose temperature rises with the radiant heat q_r, to the main air flow is increased with an increase in q_r as shown in Fig. 9. After the time shown in arrow symbols, the variation of the amount of frost sublimation with time decreases abruptly according to a decrease of a frost length.

Figure 6 indicates the time history of mass flux m_{Af} under the experimental conditions of q_r = 0, 280 W/m^2 and U_∞ = 2.0 and 8.0 m/s. The mass flux m_{Af} is defined as follows:

$$m_{Af} = \frac{\Delta M_s}{S \cdot \Delta t}$$

where S is the cooling surface area and ΔM_s is the amount of frost sublimation at time interval of Δt. The variation of mass flux m_{Af} with time is larger under the high air velocity condition of U_∞ = 8.0 m/s as compared with that under the low air velocity condition of U_∞ = 2.0 m/s. In particular, the mass flux m_{Af} increases abruptly at the beginning of frost sublimation under the condition of U_∞ = 8.0 m/s. As mentioned above, this abrupt increase of mass flux is caused by a large surface roughness of frost layer at the beginning of frost sublimation. This tendency cannot be seen under the low-velocity condition of U_∞ = 2.0 m/s. In the case of U_∞ = 2.0 m/s, the velocity and vapor concentration boundary layers developed at the vicinity of the frost surface are thicker than those in the case of U_∞ = 8.0 m/s. That is, the effect of surface roughness of frost layer in the case of U_∞ = 2.0 m/s is suppressed due to the thicker boundary layers.

Heat Balance of the Frost Layer

The heat consumed for a frost sublimation Q_s is supplied by the radiant heat Q_r from the plate heater, the convection heat Q_{cv} from the main air flow, and sensible heat composed of the frost layer, the test cooling plate, and the heat flux sensor. However, if the surface temperature of the frost layer is higher than the main flow air temperature T_∞ by radiant heat, the convection heat becomes the heat loss from the frost layer to the main air flow. The convection heat Q_{cv} is calculated as follows:

$$\begin{aligned} Q_{cv} &= \pm Q_r \mp Q_s - Q_{cd} - (Q_{cpf} + Q_{cpt} + Q_{cpp}) \\ &= \pm Q_r \mp Q_s - Q_{cd} - Q_p \end{aligned} \quad (1)$$

where the conduction heat $Q_{cd} = k_{cdp}(\partial T_p/\partial y)S$, the sensible heat $Q_{cpf} = M_f C_{pf} \Delta T_f$, $Q_{cpt} = M_t C_{pt} \Delta T_t$, $Q_{cpp} = M_p C_{pp} \Delta T_p$, and k_{cdp} is thermal conductivity of a heat flux sensor, ΔT_f, ΔT_t, ΔT_p are temperature variation of the frost layer, test cooling plate, and heat flux sensor per unit time, respectively, and C_{pf},

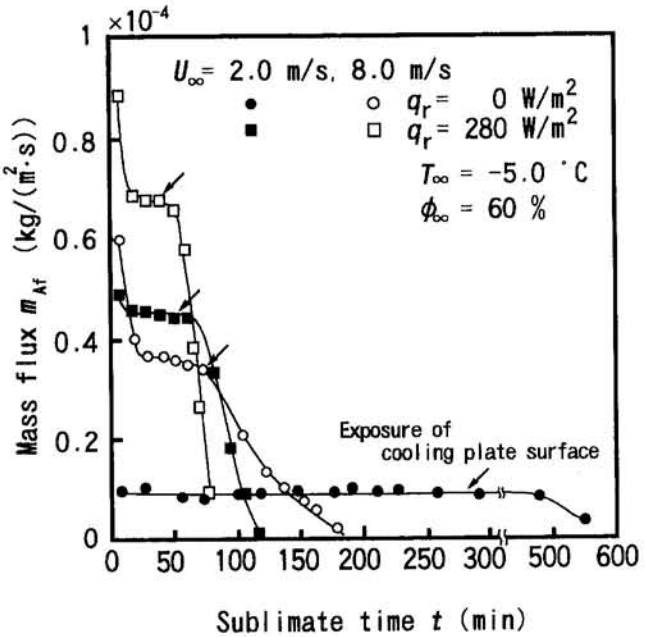


Fig. 6 Time history of the mass flux of frost sublimation

Downloaded 11 Dec 2010 to 193.140.21.150. Redistribution subject to ASME license or copyright; see http://www.asme.org/terms/Terms_Use.cfm

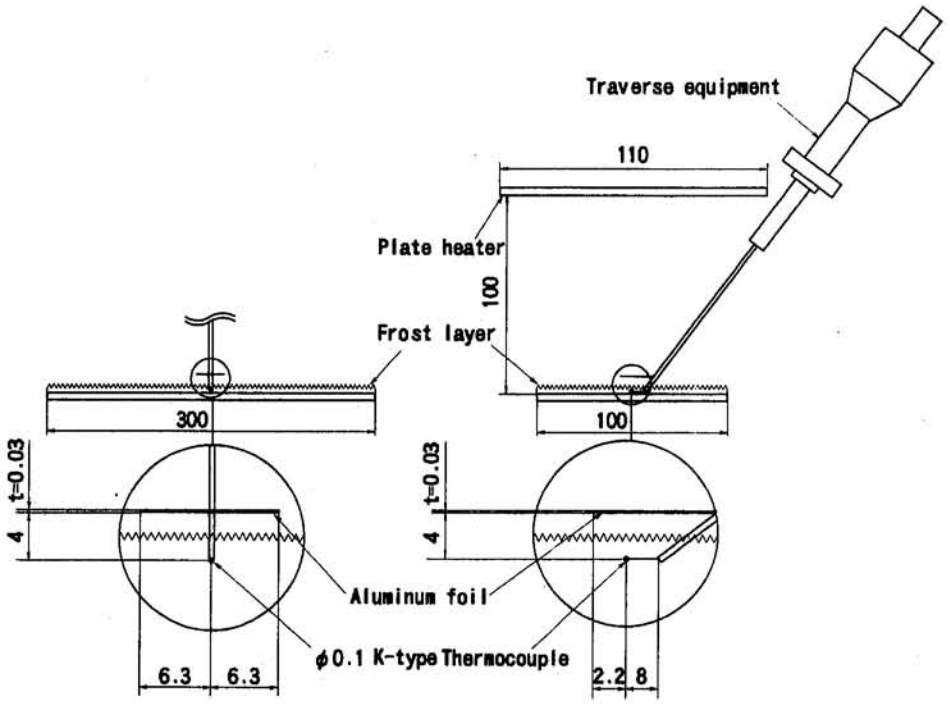


Fig. 7 Temperature measuring device in the frost layer

C_{pt}, C_{pp} are specific heats of frost layer, test cooling plate, and heat flux sensor, respectively. Q_p ($=Q_{cpf} + Q_{cpt} + Q_{cpp}$) is the amount of sensible heat. Q_s ($=m_{Af} \cdot L \cdot S$) is the sublimation latent heat defined by the mass flux m_{Af}, latent heat of sublimation L, and test cooling plate surface area S.

Figure 7 shows a temperature-measuring device in the frost layer. The K-type thermocouple is mounted on the traverse device constructed of a fine aluminum pipe and a micrometer. The traverse device can move the thermocouple in the right angle direction to the main moist air flow. The thermocouple has a small diameter of 0.1 mm in order to avoid the heat transmission of thermal conduction through the thermocouple and the turbulence of the air flow. The thermocouple is painted with aluminum paint and it is shaded with aluminum foil (reflectance 0.95) in order to avoid the direct radiant heat from the electric plate heater, as shown in Fig. 7.

Figure 8 shows the vertical temperature distribution of the frost layer under the experimental conditions of U_∞ = 2.0 and 8.0 m/s, radiant heat intensity q_r = 0, and 280 W/m^2. The y axis is defined as a vertical distance from the top of the frost layer as shown in Fig. 1. That is, the negative value of y means the frost layer, while the positive value of y refers to the main air flow region. Since the temperature of the frost layer T by a sublimation phenomenon in the case of q_r = 0 W/m^2 is lower than that of main flow air T_∞, the convection heat from the main air flow is transferred into the frost layer. On the other hand, in the case of q_r = 280 W/m^2, the temperature of the frost layer rises above the temperature of main flow air, since the radiant heat is absorbed into the frost surface layer, which has a rough dendritic ice structure. In this case, a part of heat absorbed into the frost is lost into the main flow air by convection.

Figure 9 shows the time history of heat balance of the frost layer under the experimental condition of q_r = 0, 280 W/m^2, and U_∞ = 8.0 m/s. In Fig. 9, the positive value of Q means the heat gain of the frost layer, while the negative value means the heat loss from the frost layer.

In Fig. 9, it is noticed that the conduction heat Q_{cd} and the amount of sensible heat emitted by the frost layer, the cooling plate, and the heat flux sensor Q_p are very small, and the latent heat for sublimation Q_s is mainly dependent on the convection heat by main air flow Q_{cv} and the radiant heat Q_r. By comparison of heat Q in Fig. 9(a) with q_r = 0 W/m^2 and in Fig. 9(b) with q_r = 280 W/m^2, it is understood that Q_s increases remarkably with an increase in radiant heat q_r. The broken line shows the time when the cooling surface appears at the leading edge (x = 0 mm) of the frost layer in progress of the frost sublimation. After this time, the value of Q_s for q_r = 280 W/m^2 decreases abruptly due to quick disappearance of the frost layer on the cooling surface due to radiant heat. With respect to the convection heat Q_{cv}, the Q_{cv} for q_r = 0 W/m^2 shows the positive value, which means the frost layer gains heat from the main

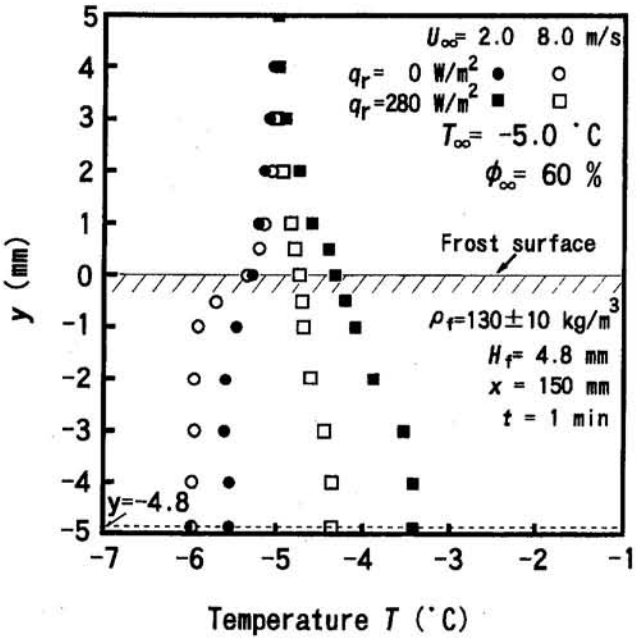


Fig. 8 Vertical temperature distribution of the frost layer

Downloaded 11 Dec 2010 to 193.140.21.150. Redistribution subject to ASME license or copyright; see http://www.asme.org/terms/Terms_Use.cfm

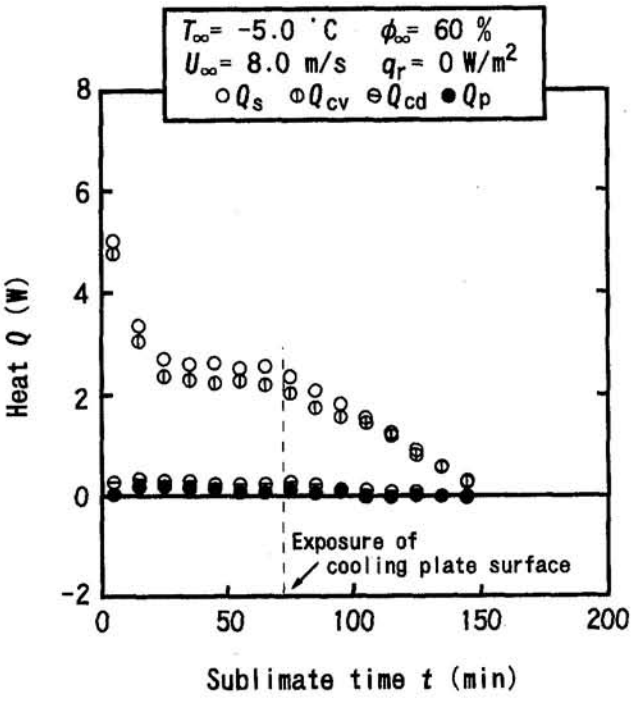


Fig. 9(a)

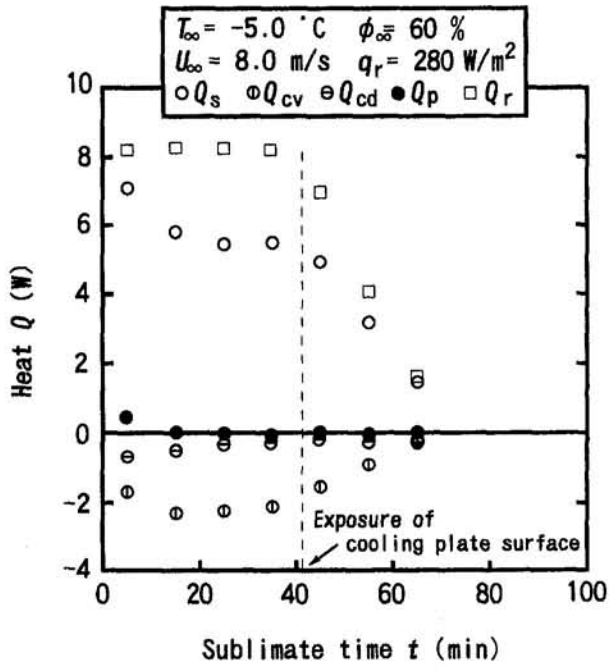


Fig. 9(b)

Fig. 9 Time history of the heat balance of the frost layer

flow air. Meanwhile, the Q_{cv} for $q_r = 280$ W/m^2 becomes negative, which means heat loss from the frost layer to the flow moist air, as shown in the temperature profiles of Fig. 8. The appearance of convection heat-loss brought by radiant heat results in a decrease of increasing rate of Q_s with time.

Data Reduction

It is necessary to define new nondimensional parameter of the radiant heat because it is impossible to measure the surface temperature of the frost layer supplied with the radiant heat. In the case that the frost layer is irradiated by the infrared rays and exposed to a main air flow, the amount of radiant heat and the convection heat are mainly determined by the heat balance of the frost surface layer. Therefore the nondimensionalized radiant heat q_r^* is expressed in terms of the convection heat parameter as follows:

$$q_r^* = \frac{q_r}{q_{cv}^+}, \quad q_{cv}^+ = h(T_\infty - T_w) \tag{2}$$

where h is the overall heat transfer coefficient without radiant heat, which is calculated by Eqs. (3)~(6), and T_w is the surface temperature of the test cooling plate without radiant heat. The h and the Nusselt number Nu are derived from experimental data without radiant heat as follows:

$$h = \frac{Q_{cv}}{(T_\infty - T_w) \cdot S} \tag{3}$$

$$\mathrm{Nu} = \frac{h \cdot l}{k_{cd}} \tag{4}$$

where k_{cd} is the thermal conductivity of main flow air. In this case the major part of the latent heat for the frost sublimation Q_s is supplied by the convection heat transfer from the main flow air. Nu is increased with an increase in Re. Nu varies from laminar heat transfer to turbulent heat transfer. Nu can be approximated from experimental data within the standard deviation of 5.0 percent as follows:

$$5 \times 10^3 \le \mathrm{Re} \le 9 \times 10^4$$

$$\mathrm{Nu} = 1.33\ \mathrm{Re}^{0.611} \left(\frac{H_{\mathrm{fin}}}{l}\right)^{0.242} \mathrm{Pr}^{1/3}\ \mathrm{Ste}^{0.00441} \tag{5}$$

$$9 \times 10^4 \le \mathrm{Re} \le 3 \times 10^5$$

$$\mathrm{Nu} = 3.52 \times 10^{-3}\ \mathrm{Re}^{1.13} \left(\frac{H_{\mathrm{fin}}}{l}\right)^{0.242} \mathrm{Pr}^{1/3}\ \mathrm{Ste}^{0.00441} \tag{6}$$

where $\mathrm{Ste} = C_{pf}(T_\infty - T_w)/L$; the applicable range is: $H_{\mathrm{fin}}/l = 0.667 \times 10^{-2} \sim 2.33 \times 10^{-2}$, $\mathrm{Ste} = 2.17 \times 10^{-4} \sim 1.66 \times 10^{-3}$. It is possible to define the nondimensional radiant heat q_r^* by the overall heat transfer coefficient h derived from Eqs. (5) and (6).

When the radiant heat irradiates into the frost layer in forced convection air flow, the latent heat for the frost sublimation is calculated by the heat balance Eq. (1). It is performed to derive the convection heat flux q_{cv} ($=Q_{cv}/S$) from Eq. (1) since the radiant heat flux q_r is approximated as the radiant heat intensity at the distance between the plate heater and the frost surface layer due to the high absorptance of the frost layer in an infrared rays region as mentioned above. The positive value of the q_{cv} means the heat gain of the frost layer. The nondimensional convection heat flux q_{cv}^* is defined as follows:

$$q_{cv}^* = \frac{q_{cv}}{q_{cv}^+} \tag{7}$$

Figure 10 shows the relationship between the q_{cv}^* and the q_r^*. The q_{cv}^* decreases with an increase in the q_r^*, and the q_{cv}^* becomes negative which means heat is lost from the frost layer with increasing q_r^*. The q_{cv}^* becomes negative in the range $q_r^* > 1.49$, and it decreases monotonously for each Re number. The q_{cv}^* can be approximated from experimental data within the standard deviation of 5.0 percent as follows:

$$q_{cv}^* = -0.668 q_r^* + 1.00 \tag{8}$$

The applicable range is: $q_r^* = 0 \sim 11.3$.

Figure 11 shows the relationship between the modified Sherwood number Sh* and the nondimensional radiant heat q_r^*. The

Downloaded 11 Dec 2010 to 193.140.21.150. Redistribution subject to ASME license or copyright; see http://www.asme.org/terms/Terms_Use.cfm

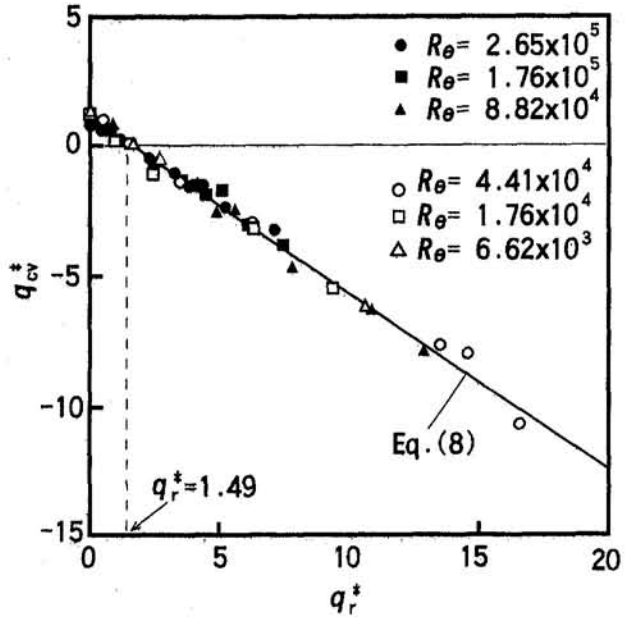


Fig. 10 Relationship between q_{cv}^* and q_r^*

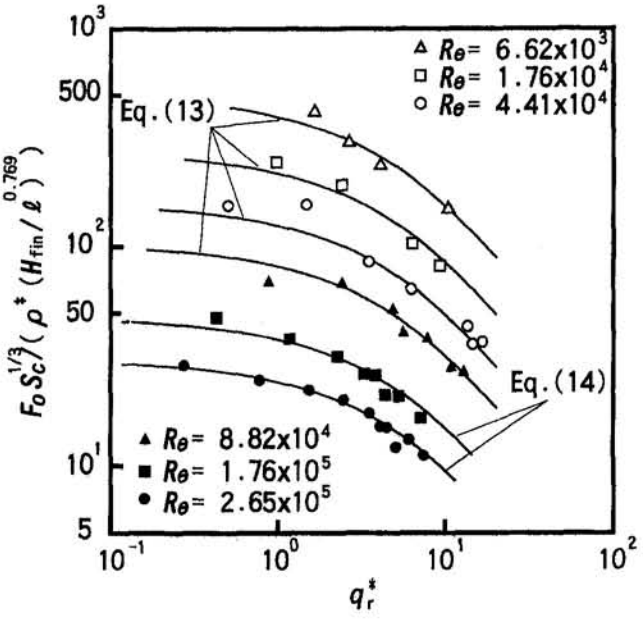


Fig. 12 Relationship between Fo $Sc^{1/3}/(\rho^*(H_{fin}/l)^{0.769})$ and q_r^*

modified Sherwood number Sh* concerning the mass transfer of the frost is defined as follows:

$$\mathrm{Sh}^* = \frac{h_D^* l}{D} = \frac{m_{Af} l}{(C_s' - C_\infty)D} \tag{9}$$

where C_s' is the water vapor mass concentration at the saturating condition, which is defined by the temperature of the main flow air T_∞, C_∞ is the water vapor mass concentration of the main flow air, D is the diffusion coefficient, and h_D^* is the modified mass transfer coefficient. In the same way as the data reduction of heat transfer mentioned above, the mass transfer before reaching the frost length of 99 percent of the cooling plate length is used for the data reduction. The Sh* is increased with an increase in q_r^*. In the case of small q_r^*, the increasing rate of Sh* with q_r^* becomes small. On the other hand, the rate of increase of Sh* with q_r^* in the case of large q_r^* becomes large. This is explained by the fact that since the surface temperature of the frost layer becomes higher than the main flow air temperature for large q_r^*, the difference of water vapor mass concentration between near the frost surface and main flow air increases with increasing of q_r^*.

The mass transfer coefficient for $q_r^* = 0$ W/m^2 shows higher values by 25 to 30 percent than that of the Colburn's analogy, which can apply to the mass transfer of the smooth surface. This result is explained by the fact that the surface roughness of the frost layer brings turbulence promotion of air flow in the boundary layer and the increase of sublimation surface area. The following equations of Sh* are derived from experimental data for the frost sublimation within the standard deviation of ±4.6 percent.

$$5 \times 10^3 \le \mathrm{Re} \le 9 \times 10^4$$

$$\mathrm{Sh}^* = 0.711\ \mathrm{Re}^{0.611}\left(\frac{H_{\mathrm{fin}}}{l}\right)^{0.242} \times \mathrm{Sc}^{1/3}\ \mathrm{Ste}^{0.00441}(2.26 \times 10^{-1} q_r^* + 1)^{1.05} \tag{10}$$

$$9 \times 10^4 \le \mathrm{Re} \le 3 \times 10^5$$

$$\mathrm{Sh}^* = 2.03 \times 10^{-3}\ \mathrm{Re}^{1.13}\left(\frac{H_{\mathrm{fin}}}{l}\right)^{0.242} \times \mathrm{Sc}^{1/3}\ \mathrm{Ste}^{0.00441}(2.26 \times 10^{-1} q_r^* + 1)^{1.05} \tag{11}$$

The applicable range is: $H_{\mathrm{fin}}/l = 0.667 \times 10^{-2} \sim 2.33 \times 10^{-2}$, $q_r^* = 0 \sim 1.13 \times 10^1$, $\mathrm{Ste} = 2.17 \times 10^{-4} \sim 1.66 \times 10^{-3}$.

Figure 12 shows the relationship between the nondimensional radiant heat q_r^* and the product of Fourier number, Schmidt number, the ratio of the density, and the ratio of the frost height. Each nondimensional parameter is defined as follows:

$$\mathrm{Fo} = \frac{a t_{cs}}{l^2}, \quad C^* = \frac{C_s' - C_\infty}{C_{TP}}, \quad \rho^* = \frac{\rho_f}{\rho_{\mathrm{ice}}} \tag{12}$$

where a is the thermal diffusivity, t_{cs} is the defrost completion time that the frost layer disappears completely, ρ_{ice} is the density of the ice. It is noticed that the Fourier number decreases with an increase in q_r^*. The following correlation equations of the

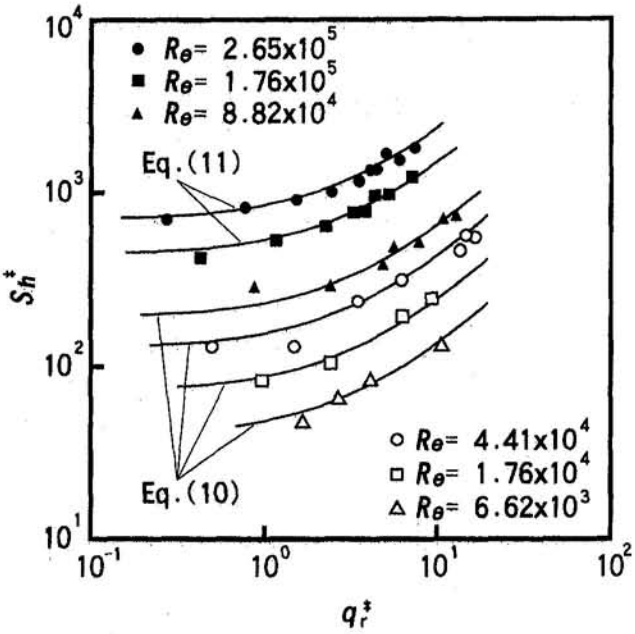


Fig. 11 Relationship between Sh* and q_r^*

Downloaded 11 Dec 2010 to 193.140.21.150. Redistribution subject to ASME license or copyright; see http://www.asme.org/terms/Terms_Use.cfm

nondimensional defrost completion time Fo are derived from experimental data within the standard deviation of ±5.2 percent:

$$5 \times 10^3 \leq \mathrm{Re} \leq 9 \times 10^4$$

$$\mathrm{Fo} = 2.86 \times 10^4\ \mathrm{Re}^{-0.611} \rho^* \left(\frac{H_{\mathrm{fin}}}{l}\right)^{0.769} C^{*-0.985} \times \mathrm{Sc}^{-1/3}\ \mathrm{Ste}^{-0.00441}(1 + 1.61 \times 10^{-1} q_r^*)^{-1.06} \quad (13)$$

$$9 \times 10^4 \leq \mathrm{Re} \leq 3 \times 10^5$$

$$\mathrm{Fo} = 1.08 \times 10^7\ \mathrm{Re}^{-1.13} \rho^* \left(\frac{H_{\mathrm{fin}}}{l}\right)^{0.769} C^{*-0.985} \times \mathrm{Sc}^{-1/3}\ \mathrm{Ste}^{-0.00441}(1 + 1.31 \times 10^{-1} q_r^*)^{-1.06} \quad (14)$$

The applicable range is: $H_{\mathrm{fin}}/l = 0.667 \times 10^{-2} \sim 2.33 \times 10^{-2}$, $q_r^* = 0 \sim 1.13 \times 10^1$, $\mathrm{Ste} = 2.17 \times 10^{-4} \sim 1.66 \times 10^{-3}$

Concluding Remarks

Frost sublimation characteristics of a horizontal frost layer in a forced convection air flow with radiant heat were experimentally investigated. The conclusions obtained are summarized as follows:

1 Frost sublimation characteristics of the frost layer with radiant heat are depend mainly on two heat supply patterns of convection heat from main flow air and radiant heat.
2 The mass transfer coefficient shows higher values by 25 to 30 percent than does Colburn's analogy. This result is explained by the fact that the surface roughness of the frost layer brings turbulence promotion of air flow in the boundary layer and the increase of sublimation surface area.
3 It is proposed that the nondimensional correlations for mass transfer, heat transfer, and defrost completion time are derived in terms of Reynolds number, humidity rate, density rate, Schmidt number, Stefan number, and nondimensional frost height.

References

Kochs, M., Körber, Ch., Heschel, I., and Nunner, B., 1993, "The Influence of the Freezing Process on Vapour Transport During Sublimation in Vacuum-Freeze-Drying of Macroscopic Samples," *Int. J. Heat Mass Transfer*, Vol. 36, No. 7, pp. 1727–1738.

Schmidt, E., 1934, "Die Warmestrahlung von Wasser und Eis, von bereiften und benetzten Oberflachen," *Forshung*, Vol. 5, No. 1, pp. 1–5.

Inaba, H., Otake, H., and Nozu, S., 1992, "Fundamental Study on a Horizontal Frost Layer Melted From Above by Radiative Heat," *Trans. JSME*, Vol. 58, No. 555, pp. 3373–3381.

Downloaded 11 Dec 2010 to 193.140.21.150. Redistribution subject to ASME license or copyright; see http://www.asme.org/terms/Terms_Use.cfm

H. K. Park

X. Zhang

C. P. Grigoropoulos[1]

Department of Mechanical Engineering,
University of California,
Berkeley, CA 94720

C. C. Poon

A. C. Tam

IBM Almaden Research Center,
San Jose, CA 95120-6099

Transient Temperature During the Vaporization of Liquid on a Pulsed Laser-Heated Solid Surface

The thermodynamics of the rapid vaporization of a liquid on a solid surface heated by an excimer laser pulse is studied experimentally. The transient temperature field is measured by monitoring the photothermal reflectance of an embedded thin film in nanosecond time resolution. The transient reflectivity is calibrated by considering a temperature gradient across the sample based on the static measurements of the thin film optical properties at elevated temperatures. The dynamics of bubble nucleation, growth, and collapse is detected by probing the optical specular reflectance. The metastability behavior of the liquid and the criterion for the onset of liquid–vapor phase transition in nanosecond time scale are obtained quantitatively for the first time.

1 Introduction

The accurate measurement of temperature of the short-pulsed laser irradiated target is essential for understanding laser beam interaction with materials and assessing the optimal operating parameters in many technical laser applications such as pulsed laser micromachining. There have been a significant number of endeavors to quantify the temperature development during laser irradiation processes. Earlier attempts include the temperature estimate by thermocouples (Dyer and Sindhu, 1985), pyroelectric crystals (Gorodetsky et al., 1985), probing the absorptance change of dye (Lee et al., 1992), and NiSi thermistors (Brunco et al., 1992). These studies aimed at resolving fundamental questions on the physical mechanism of the ultraviolet excimer laser ablation of polymers. The NiSi thermistor was successful in obtaining the time-resolved temperature profile in the polyimide film. The thermistors utilizing the temperature-dependent electrical resistance, however, have a significant drawback, which is the inapplicability to a metallic sample. It is necessary to deposit a layer of electrical insulator between the sample film and the thermistor, which in turn significantly lowers the temperature sensitivity.

The laser beam interaction with materials in a liquid environment exhibits unique characteristics in a variety of technical applications. The explosive vaporization of liquids induced by short-pulsed laser irradiation is utilized in laser cleaning of microcontaminants (Park et al., 1994) and medical laser surgery. The physical understanding of superheated liquids and phase transitions has been sought in order to achieve better control of such applications. The transient development of the bubble nucleation process and the onset of phase change in nanosecond time scale were monitored by simultaneous application of optical reflectance and scattering probes (Yavas et al., 1993). The numerical heat conduction calculation also shows that the solid surface achieves temperatures of tens of degrees of superheat (Yavas et al., 1994). However, no real-time measurement of the surface temperature development in the course of the laser-induced vaporization process has been made, although the surface temperature is one of the most important parameters in heterogeneous nucleation. Furthermore, thermodynamic considerations such as the degree of superheat in a liquid–vapor transition at the nanosecond time scale have never been addressed. Disturbances by bubbles near the solid surface and the relatively low temperature change have prohibited a precise detection of surface temperature. Recently, it has been demonstrated that probing the transient optical transmission or reflectivity is a fast and reliable method with nanosecond resolution to monitor the temperature field development (Jellison et al., 1986; Lowndes, 1982; Park et al., 1993; Xu et al., 1995). The photothermal reflectance technique is based on the detection of a change of surface reflectivity, i.e., the change of material optical properties, induced by temperature change. It works best for thin film semiconductors due to their large sensitivity of optical properties on temperature (Jellison and Burke, 1986). In this work, the metallic film that provides the laser-induced bubble nucleation sites is combined with a semiconductor film (a temperature sensor) to form a single sample. To this end, a thin semiconductor film is embedded between the metallic top layer and the substrate. The photothermal reflectance probe is thus applied from the backside to the semiconductor film. The backside reflectance probe is not affected by events occurring near the laser-irradiated surface. In addition, the temperature sensitivity can be greatly maximized so that it is successfully implemented for the first time to measure nonintrusively the temperature field development during the rapid vaporization.

2 Sample Structure and Fabrication

The solid sample has three layers as shown in Fig. 1(*a*). The top layer is an absorbing film (chromium). The intermediate layer is a thin film optical temperature sensor whose optical properties vary with temperature. The bottom layer is a transparent quartz substrate. Polycrystalline silicon (p-Si) is selected as the optical sensor. The heating source is an ultraviolet (UV) KrF excimer laser (λ = 248 nm, pulse width = 16 ns FWHM). Water and methanol are test liquids, which are both transparent to the KrF excimer laser beam. The thickness of the chromium layer is chosen to be greater than the optical penetration depth, 0.01 μm, for the excimer laser operating conditions to prevent direct heating of the p-Si layer by the excimer laser. The thickness of the temperature sensor layer has to be carefully designed

[1] To whom correspondence should be addressed; e-mail: cgrigoro@euler.berkley.edu.

Contributed by the Heat Transfer Division for publication in the JOURNAL OF HEAT TRANSFER. Manuscript received by the Heat Transfer Division September 1995; revision received February 1996. Keywords: Boiling, Laser Processing, Materials Processing and Manufacturing Process. Associate Technical Editor: M. F. Modest.

Copyright © 1996 by ASME

Downloaded 11 Dec 2010 to 193.140.21.150. Redistribution subject to ASME license or copyright; see http://www.asme.org/terms/Terms_Use.cfm

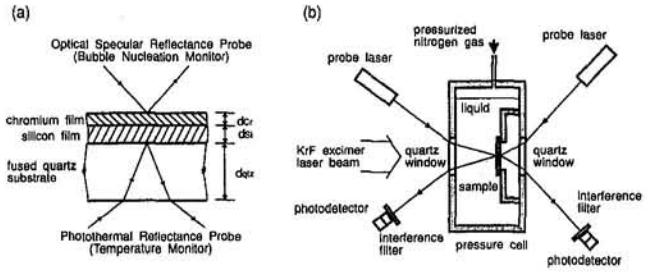


Fig. 1 Schematic of the experimental setup: (*a*) optical detection scheme and (*b*) overall view

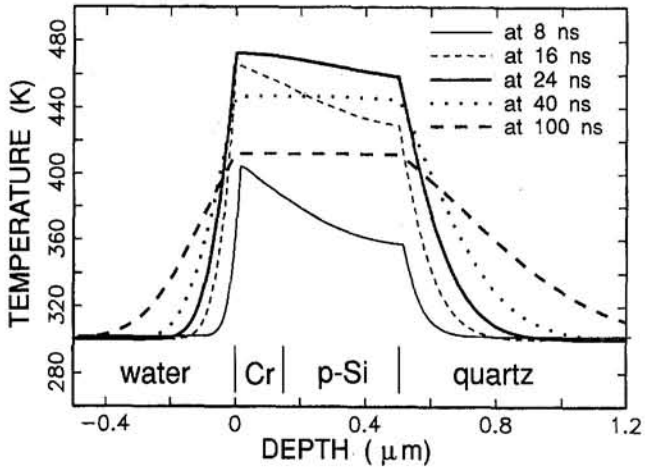


Fig. 2 Calculated spatial temperature profile at the nucleation threshold of water, F = 42.2 mJ/cm^2

for optimal temperature sensitivity. It is noted that the change of reflectivity due to the change of refractive index is maximum when the optical thickness nh is close to the wavelength (Born and Wolf, 1980). Thus, the sample is composed of a 0.15-μm-thick Cr film and 0.35-μm-thick p-Si film deposited on a 500-μm-thick fused quartz substrate. Figure 2 shows the calculated temperature profile in the sample that is irradiated with the excimer laser at a fluence of 42.2 mJ/cm^2.

The sample was prepared at the Microfabrication Laboratory of the University of California at Berkeley. The p-Si film was deposited on a fused quartz wafer at 878 K and 300 mTorr in a chemical vapor deposition furnace. Postdeposition annealing of the p-Si film was performed in a nitrogen environment at 1323 K for 30 minutes so as to make the film thermally and optically stable in transient heating experiments. A Nanospec interferometer was used to measure the thickness of the p-Si film. The metallization of chromium on the p-Si film was carried out by argon RF plasma sputtering at 300 W.

The optical properties of the top chromium layer were determined by ellipsometric measurements. It was found that the complex refractive index at λ = 248 nm is $\hat{n} = 1.026 - i\,1.754$, which is different from the bulk value, $\hat{n} = 0.85 - i\,2.01$ (Palik, 1991). Such a difference is consistent with previous results (Henderson and Weaver, 1966).

3 Static Temperature Calibration

The photothermal reflectivity from the backside of the sample is calibrated in a static experiment. In this paper, the backside refers to the quartz side. The front side refers to the chromium film side on which nucleation takes place. The sample is mounted on an aluminum block whose temperature is controlled within ±0.1 K. Figure 3 shows the results of the static reflectivity measurement from the backside of the sample. The backside reflectivity is the superposition of contributions from the change of the optical properties of both the p-Si film and the quartz substrate. The static reflectivity goes through a series of maxima and minima as temperature changes. Such fringe behavior is caused by changes in both the fused quartz refractive index and the p-Si refractive index. The reflectivity goes through a complete (one maximum and one minimum) cycle when the change of optical path length imparted by the temperature change ΔT is equal to half of the light wavelength:

$$n(T + \Delta T)h(T + \Delta T) - n(T)h(T) = \lambda/2 \qquad (1)$$

The change of the optical path length can be approximated as:

$$n(T + \Delta T)h(T + \Delta T) - n(T)h(T) \simeq \left(\frac{dn}{dT}\Delta T\right)h + n(\alpha_{th}h\Delta T) \qquad (2)$$

The temperature coefficient of refractive index dn/dT for the HeNe probing laser wavelength, λ = 632.8 nm, is found from literature to be approximately 10^{-5} for fused quartz (Matlison, 1965) and 3×10^{-4} for p-Si (Xu and Grigoropoulos, 1993). The thermal expansion coefficient α_{th} is 5×10^{-7} and 3×10^{-6} for fused quartz and silicon, respectively (Touloukian et al., 1975). It is noted that the contribution from the change of path length due to thermal expansion is negligible, i.e., $n\alpha_{th} \ll dn/dT$. Therefore, the temperature increment corresponding to one fringe spacing becomes:

Nomenclature

a = fitting parameter for the conversion of reflectivity to temperature
b = fitting parameter for the conversion of reflectivity to temperature
C = constant
C_p = specific heat at constant pressure
E = energy
f = vaporized mass fraction
F = excimer laser fluence
h = thickness
i = imaginary unit = $\sqrt{-1}$
k = imaginary part of material refractive index
K = thermal conductivity
L = latent heat of vaporization
m = vaporized mass
n = real part of material refractive index
$\hat{n}$ = complex refractive index = $n - ik$
N = bubble number density
p = pressure
Q_{ab} = laser energy absorption
r_c = critical bubble radius
R = bubble radius
$\Re$ = reflectivity
t = time
T = temperature
x = coordinate in the direction normal to the sample surface
α_{th} = linear thermal expansion coefficient
λ = laser light wavelength
ρ = density
σ = surface tension

Subscripts

fs = fringe spacing
l = liquid
p-Si = polycrystalline silicon
qtz = quartz
sat = saturation property
t = liquid–vapor phase transition
v = vapor
∞ = ambient

Downloaded 11 Dec 2010 to 193.140.21.150. Redistribution subject to ASME license or copyright; see http://www.asme.org/terms/Terms_Use.cfm

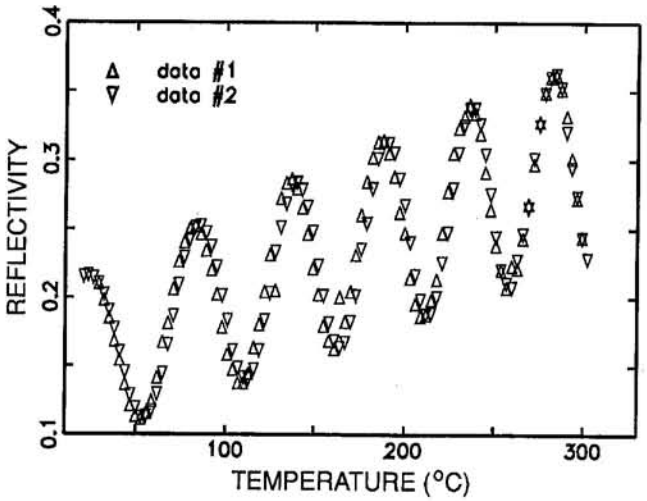


Fig. 3 Measured static reflectivity as a function of temperature; the probe is an unpolarized HeNe laser beam (λ = 632.8 nm) at an incident angle of 15 deg in air

$$(\Delta T)_{fs} = \frac{\lambda}{2(dn/dT)h} \tag{3}$$

The fringe spacings due to the quartz substrate and the p-Si layer are calculated to be approximately 60 K and 3000 K, respectively. The experimental data in Fig. 3 show good agreement. The heat-affected zone in the substrate during the transient process is confined within a depth of about 1 μm. The bulk of the substrate remains at ambient temperature due to low thermal conductivity of quartz. The ensuing change in the optical path length is negligible. Hence, the reflectivity response during transient heating exhibits a monotonic dependence on the temperature of the p-Si layer over a few hundred degree range.

A multiparameter fitting of the static calibration data coupled with thin-film optics (Born and Wolf, 1980; Heavens, 1965) has been utilized to determine the optical properties of the p-Si film and the fused quartz substrate. The following expressions are obtained from fitting measured static reflectivity changes with temperature for the quartz substrate and p-Si film:

$$n_{\text{qtz}} = 1.457 + 9.64 \times 10^{-6} \times (T - 293) + 6.1 \times 10^{-9} \times (T - 293)^2 \tag{4a}$$

$$n_{\text{p-Si}} = 4.01 + 3.31 \times 10^{-4} \times (T - 293) \tag{4b}$$

$$k_{\text{p-Si}} = 0.0355 \times \exp\left(\frac{T - 273}{590}\right) \tag{4c}$$

where the temperature T is in degrees Kelvin. It is noted that the determined optical properties are close to the literature values (Xu and Grigoropoulos, 1993). The accuracy of the fit is better than 1 percent.

4 Modeling of Temperature and Transient Reflectivity Response

The temperature profile penetration is of the order of 1 μm, whereas the laser beam spot area on the sample surface is about 1 cm^2. Accordingly, it may be assumed that the heat transfer at the center of the irradiated area is essentially one-dimensional. Hence, the temperature profile can be calculated using the one-dimensional heat diffusion equation:

$$\rho C_p \frac{\partial T}{\partial t} = \frac{\partial}{\partial x}\left(K \frac{\partial T}{\partial x}\right) + Q_{ab}(x, t) \tag{5}$$

The phase change in the liquid is not considered. The temperature-dependent thermal properties of bulk material are utilized. The error induced by the assumed bulk thermal properties is estimated to be of the order of 10 K. For instance, the peak surface temperature increases from 476 K to 488 K at F = 42.2 mJ/cm^2 when the thermal conductivities of both chromium film and silicon film are reduced to 50 percent of bulk values in the calculation. Further details of temperature modeling appear elsewhere (Park et al., 1993; Park, 1994).

At early times when a temperature gradient is present across the sample (see Fig. 2), the static calibration data cannot be used directly to convert reflectivity to temperature. This has been considered by Lompré et al. (1983) in the picosecond laser irradiation of thin c-Si films by assuming an average temperature for the fitting of the measured reflectivity. It can be dealt with more accurately by treating the sample as a stratified multilayer structure of varying complex refractive index (Jacobsson, 1965). Utilizing the formalism of the characteristic transmission matrix, the lumped structure reflectivity and transmissivity can be obtained (Born and Wolf, 1980; Heavens, 1965). The calculated temperature profile is utilized to compute the theoretical reflectivity response. This procedure is also applied in the inverse way to extract the experimental temperature profile $T(x, t)$ from the measured reflectivity, i.e., $T(x, t) = f(x, \Re(t))$. Figure 4 shows the relation between the surface temperature and normalized reflectivity at various times. Here, the reflectivity is normalized with its initial value, i.e., unity reflectivity at $t = 0^-$ (at room temperature). The use of normalized reflectivity eliminates the procedures for correcting losses at the cuvette windows and the interference filters. It is clearly seen in Fig. 4 that the dependence of the surface temperature on reflectivity differs with time due to the presence of a temperature gradient. The temperature is nearly a linear function of normalized reflectivity, $\Re(t)/\Re(0)$:

$$T(x, t) = a(x, t)\frac{\Re(t)}{\Re(0)} + b(x, t) \tag{6}$$

The fitting parameters a and b are dependent upon the time and the location where the temperature is to be determined.

5 Transient Temperature Measurement

The experimental setup is shown in Fig. 1(b). The liquid is contained in a pressure cell (maximum pressure ~ 100 atm). The pressure p_l of the liquid is varied by applying compressed nitrogen. The KrF excimer laser pulse is directed at normal

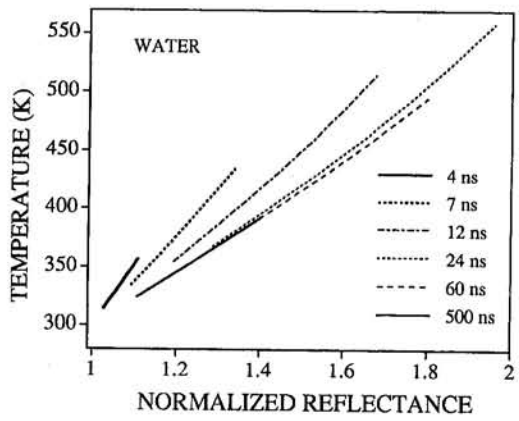


Fig. 4 Calculated relation of normalized reflectivity with surface temperature at various times; the sample is immersed in water

Downloaded 11 Dec 2010 to 193.140.21.150. Redistribution subject to ASME license or copyright; see http://www.asme.org/terms/Terms_Use.cfm

incidence onto the sample. The spatial uniformity of the excimer laser beam is achieved by the fly's eye-type beam homogenizer and found to be within ±5 percent. The laser energy is monitored by a calibrated pyroelectric energy meter. Since the UV-grade quartz window and the liquid (spectroscopic grade) are highly transparent to the excimer laser beam, the absorption and fluorescence losses are ignored.

The behavior of the front side of the sample, i.e., the liquid–chromium interface, is also monitored by specular reflectance from its surface. Since the Cr film has no intrinsic thermoreflectance effect within the temperature range used in this work (≤600 K), any change in the optical specular reflectance from the chromium surface is ascribed to the formation of bubbles on the probe beam path. On the other hand, due to the absence of bubbles in the backside, any change on the reflectance from the p-Si layer is caused by only the temperature change. Hence, the temperature and the bubble nucleation behavior can be obtained independently. Previous work utilizing the optical transmission probe (Leung et al., 1992) failed to resolve the temperature and the bubble growth in their optical transmission signal from the liquid film on the amorphous silicon surface. This is because the transient transmission signal carries information from the combined effects of bubble growth and the temperature-induced optical property change in the amorphous silicon film. The specular reflectance from a metallic surface, whose thermoreflectance effect is negligible, can distinguish the bubble growth behavior but does not produce temperature data (Yavas et al., 1993). In this work, a HeNe laser ($\lambda = 632.8$ nm, unpolarized, incident angle = 15 deg in air) and an Ar^+ laser ($\lambda = 488.0$ nm, s-polarized, incident angle = 10–32 deg in liquid) are used as the back-side and front-side reflectance probe, respectively.

Figure 5 shows the results from measurements of the transient temperature and bubble growth at atmospheric pressure for the water/chromium interface for two excimer laser fluences. The bubble growth behavior can be observed from the front-side reflectance signal. As bubbles form and grow on the surface, the specular reflectance shows distinct transient behavior, as seen in the top panels. The signal shown in the figure is an average of five shots of laser pulses. The reflectance increase following the excimer laser pulse is caused by the formation of a thin layer of small embryonic bubbles (Yavas et al., 1993).

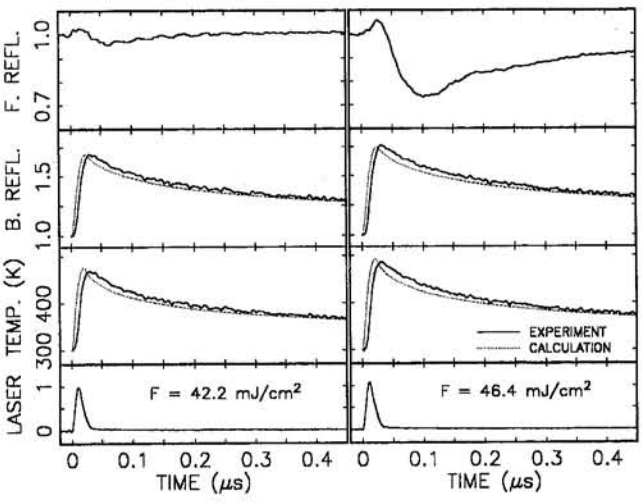


Fig. 5 Experimental reflectance curves (solid lines) for water are shown in both top panels for the front-side reflectance and both second panels for the back-side photothermal reflectance. The dotted lines in the second and third panels are calculated transient reflectivity response and surface temperature, respectively. Shown in solid lines in the third panels are resultant surface temperature traces from the measured reflectances. The bottom panels show the excimer laser pulses, $F = 42.2$ mJ/cm² (left) and 46.4 mJ/cm² (right).

The trailing decrease is due to scattering losses caused by enlarged bubbles. Finally, the slow recovery is due to unconcerted bubble collapse. At the lower excimer laser fluence, the initial increase in the front-side reflectance (top left panel) is rather moderate, indicating the water/chromium interface is barely above the nucleation threshold. The second row panels show the experimental photothermal reflectance curve (solid line) and the theoretical response (dotted line). It is seen that the modeling result closely follows the experimental curve. The measured and calculated evolutions of surface temperature are compared in the third row panels. The measured temperature traces are obtained by deconvoluting the measured reflectance signals following the steps described above. The precision of the temperature measurement can be demonstrated as follows. At the fluence $F = 42.2$ mJ/cm², the measured and calculated peak surface temperatures are 466 K and 476 K, respectively. The difference is within the experimental error. At this condition the measured degree of superheat is 93 K. The delay of the experimental trace as compared with the calculated trace is due in part to the time constants of the electronic data acquisition system. A similar measurement for methanol yields the peak temperature of 430 K at the threshold and hence the degree of superheat of 92 K (boiling point = 337.9 K). It is noted that the nucleation starts instantaneously as the surface temperature exceeds the boiling temperature. The onset of nucleation is manifested as an increase in the front-side reflectance. For instance, the first noticeable change in the front-side reflectance at $F = 46.4$ mJ/cm² is detected at $t = 13$ ns. At this moment, the measured surface temperature is 389 K, only 16 K above the boiling point. For all the conditions tested, this trend remains true. It is therefore concluded that the degree of superheat required for the nucleation of embryos is significantly lower than that for the formation of bubbles. This effect is observed only by simultaneously monitoring time-resolved bubble growth and surface temperature. On the basis of this observation, the dynamics of bubble growth can be understood as follows: Microscopic embryos are nucleated as soon as the surface reaches the boiling condition ("nucleation threshold"). Bubbles can grow in size if sufficient heat is supplied from the surface. When their radii exceed the limit $R \gg \lambda/2\pi n$, i.e., about 0.06 μm ($\lambda = 488$ nm and $n = 1.34$), scattering losses become much more appreciable and specular reflectance decreases. From the temperature measurements, bubble growth takes place only if the surface temperature is about 100 K above the boiling temperature for water and methanol at atmospheric pressure ("threshold for the onset of bubble growth").

The measured peak surface temperature at atmospheric pressure is plotted as a function of the excimer laser fluence in Fig. 6 for water. The temperature is approximately linear with fluence. The discrepancy between the measurement and calculation arises from the possible departure of thermal properties of thin films from bulk values and the existence of contact resistance between layers. Nevertheless, it can be stated that the technique used in this work can measure the surface temperature with accuracy of 30 K in nanosecond resolution. The different slope of the temperature rise versus fluence between experiment and calculation is in part due to the assumption in the computation that no phase change is taken into account. This is a reasonable assumption, however, because the amount of heat transferred to the solid is predominantly greater than that to the liquid. Therefore, the temperature field is not strongly affected by the occurrence of vaporization and the interface temperature can be well estimated by the simple conduction equation. It is, however, noted that the trend of lower measured temperature compared with the calculated values at higher laser fluence suggests an increasing amount of vaporization at higher temperatures.

6 Effect on the Ambient Liquid Pressure

Bubble growth monitoring and transient temperature measurement are also performed at various ambient liquid pressures.

Downloaded 11 Dec 2010 to 193.140.21.150. Redistribution subject to ASME license or copyright; see http://www.asme.org/terms/Terms_Use.cfm

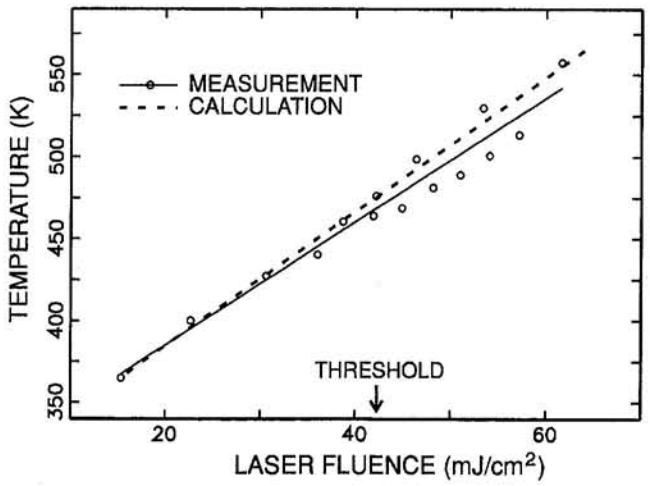


Fig. 6 The measured peak surface temperature is compared with the calculated surface temperature as a function of laser fluence for water. The nucleation threshold is indicated by arrow. Solid line is a linear fit of experimental data.

The dependences of the front-side reflectance signal and surface temperature on pressure at two fixed excimer laser fluences are shown in Fig. 7 for water. The initial rise of front-side reflectance, occurring during the nucleation of embryos and when the embryo radius $\ll \lambda/2\pi n$, i.e., when Rayleigh scattering is predominant, is nearly insensitive to the liquid pressure. This effect shows that surface tension force would dominate at this stage of nucleation. The surface tension σ of water is 0.059 N/m at boiling point and zero, by definition, at critical temperature (Carey, 1992). However, at pressures exceeding 3.3 MPa, the magnitude of the initial rise decreases, as can be seen from the case of water at $F = 48.2$ mJ/cm^2. As bubbles grow in size, scattering in the Mie regime becomes dominant and causes a subsequent drop in the front-side specular reflectance. The amplitude of the specular reflectance drop is proportional to the total scattering cross section of bubbles, which is a function of bubble radius and number density (Yavas et al., 1994). It is observed that the amplitude of the reflectance drop decreases with pressure increase, which indicates a smaller total volume of bubbles at a higher pressure. It is also noted that bubble growth and collapse rates are nearly independent of ambient pressure in the pressure range studied.

The fact that a smaller total volume of bubbles is produced at higher pressures is explained by the lower degrees of superheat. The measurements show that the maximum surface temperature is independent of pressure at a constant excimer laser fluence. For the case of water at $F = 54.1$ mJ/cm^2 (Fig. 7, right column), the peak surface temperatures are measured to be around 496 K while the boiling point increases from 373 K at 0.101 MPa to 492 K at 2.2 MPa. Hence the degrees of superheat reduce from 123 K at 0.101 MPa to 4 K at 2.2 MPa. There is, therefore, less superheat to drive bubble growth at higher pressures. Consequently, a smaller volume of bubbles is produced. This fact can be well illustrated by comparing the amplitude of reflectance drop with the maximum bubble radius, estimated on the basis of measured surface temperature, i.e., degree of superheat. The bubble growth speed at the liquid inertia-controlled limit can be estimated by equating the kinetic energy of the flow to the work performed by pressure forces, $dR/dt = ((2/3)(p_v - p_\infty)/\rho)^{1/2}$, where p_v is the vapor pressure inside the bubble, p_∞ the ambient pressure, and ρ the liquid density (Carey, 1992). It is noted that this estimate provides an upper bound for the growth velocity (Prosperetti and Plesset, 1978). The vapor pressure p_v is approximated by the saturation vapor pressure at the measured peak surface temperature so that the bubble growth speed can be calculated. The front-side reflectance curve provides the duration of bubble growth (excimer laser pulse to the reflectance minimum ~100 ns), which in turn yields the maximum bubble radius from the growth speed. A comparison between the amplitude of reflectance drop and the estimated maximum bubble radius is made in Fig. 8. It is seen that the reflectance drop can be correlated with the maximum bubble radius estimated from the measurements of surface temperature and ambient pressure. The scatter of the data is mainly attributed to the different number density of bubbles.

The pressure dependence of the "bubble-growth threshold" was also examined. This threshold is defined as the minimum fluence for the occurrence of the front-side reflectance signal to become smaller than its pre-laser pulse value, namely, the first appearance of bubbles causing Mie scattering. The peak surface temperature for water at the bubble-growth threshold for each ambient pressure is measured and plotted in Fig. 9. The solid line indicates the saturation curve and the dashed line the limit of superheat (Avedisian, 1985). The area between the saturation curve and the limit of superheat curve is the region of metastable states. The actual superheat in the experiment is the area between the saturation curve and the bubble growth threshold. The measured bubble-growth thresholds (p, T) are represented by symbols and connecting dotted lines. It is observed that the threshold temperature increases with pressure until it merges with the saturation curve at 2.2 MPa. Hence the

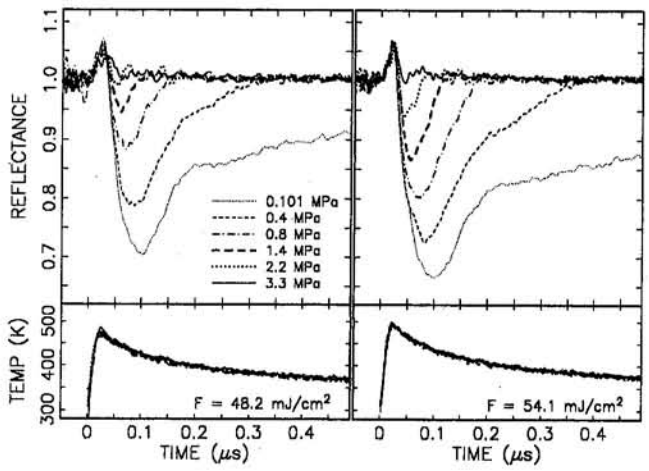


Fig. 7 Specular reflectance signals and measured surface temperature transients at various pressure at fixed excimer laser fluences; the probe beam is Ar$^+$ laser (λ = 488 nm, angle of incidence = 10.5 deg)

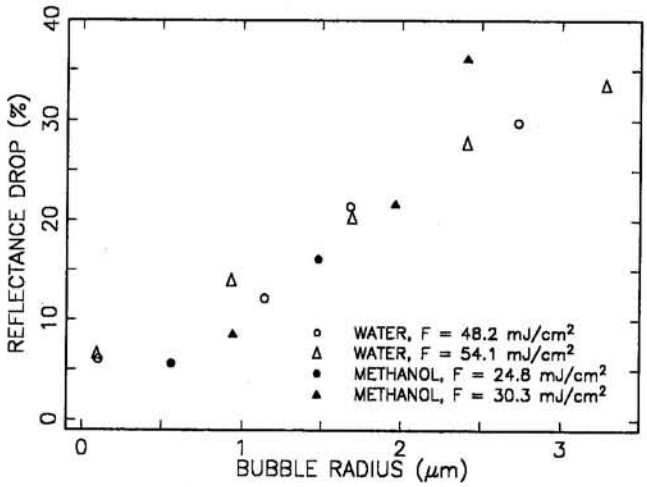


Fig. 8 Relationship between the amplitude of specular reflectance drop and the estimated maximum bubble radius

Downloaded 11 Dec 2010 to 193.140.21.150. Redistribution subject to ASME license or copyright; see http://www.asme.org/terms/Terms_Use.cfm

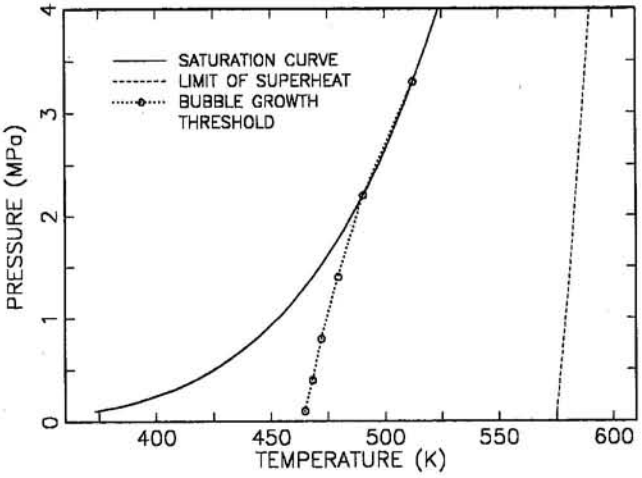


Fig. 9 The bubble-growth threshold temperatures and liquid pressures are identified as symbols ○ and connecting dotted lines in $p-T$ diagram

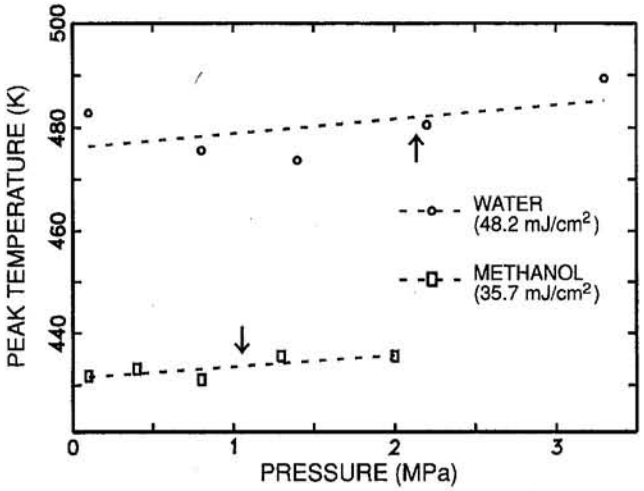


Fig. 11 Measured peak surface temperature as a function of liquid pressure at a fixed laser fluence; dotted lines are linear fits of experimental data

degree of superheat required for the bubble growth in nanosecond time scale decreases with pressure and becomes zero near 2.2 MPa. In the case of methanol, the decrease of degree of superheat with pressure is also observed. The spontaneous growth of bubbles is known to depend on the radius of embryonic nuclei ("critical bubble") and cavity centers on the solid surface. The critical bubble radii can be calculated (Carey, 1992) as a function of liquid temperature at various pressures, as shown in Fig. 10. The maximum thickness of superheated liquids (thermal boundary layer) determined from the heat transfer calculation is also shown as a function of peak surface temperature. The comparison between the critical radius and the thickness of superheated liquid indicates that the growth of bubble occurs when the thickness of superheated liquids exceeds the size of critical bubbles. Therefore, the condition for laser-induced vaporization of superheated liquid would be: $d_{sat} \geq r_c$, where d_{sat} is the thickness of superheated liquid layer. This condition implies that the heat transfer from the solid to liquid is a limiting factor for the onset of phase change. It is now clear that the degree of superheat for vaporization, i.e., the quantity $(T_t - T_{sat})$ in Fig. 10, decreases and approaches zero at high liquid pressures. By assuming that the formation of critical nuclei causes the transition from Rayleigh scattering to Mie scattering, the radius of nucleus can also be estimated by the scattering transition size, $R \equiv \lambda/2\pi n = 0.06$ μm. This estimate is comparable to the calculated radius at the bubble-growth threshold (see Fig. 10). It is noted that the critical radius concept is derived on the basis of the assumptions of chemical or mechanical equilibrium (Carey, 1992; Kagan, 1960) and may not be valid in the nanosecond time scale.

The temporal signatures of the photothermal reflectance show little difference upon the change of pressure as shown in the bottom of Fig. 7. The peak temperature, however, increases slightly with pressure as plotted in Fig. 11. The arrows in the figure indicate the bubble growth threshold, i.e., bubble growth does not takes place when $p > p_t$. The dotted line is a linear curve fit of experimental data illustrating the trend of a slight increase of peak surface temperature. This can be explained by the lower conversion of the absorbed energy to the latent heat of vaporization as bubble growth is suppressed at higher pressure. The total content of (thermal) energy in the system is:

$$E = \int_{-\infty}^{\infty} \int_{T_\infty}^{T_n(x)} (\rho C_p)_n dT dx \tag{7}$$

where the subscript n denotes liquid, chromium, p-Si, and quartz. The integral has to be evaluated for each material. When a mass of m kg of liquid is transformed to vapor, the total content of energy in the system is:

$$E' = \int_{-\infty}^{\infty} \int_{T_\infty}^{T_n'(x)} (\rho C_p)_n dT dx + mL + \sum^{N} 4\pi\sigma R^2 \tag{8}$$

where the first term gives the sensible heat, the second the latent heat of vaporization, and the third the energy of bubble surface formation. At the same excimer laser fluence, the contents of energy for two cases, with and without bubble formation, have to be the same as predicted by the energy conservation, i.e., $E = E'$, neglecting kinetic energy. It is assumed that the work for bubble surface formation is negligible since the radius of bubbles is very small. Then by knowing the temperature difference $T(x) - T'(x)$, the total mass of vapor can be obtained by:

$$m = \frac{1}{L} \int_{-\infty}^{\infty} (\rho C_p)_n \{T_n(x) - T_n'(x)\} dx \tag{9}$$

It is assumed that the temperature field is not grossly disturbed by the bubble formation. Thus, the spatial shape of the temperature is the same, i.e., $T'(x) - T_\infty = C(T(x) - T_\infty)$, where the constant C is a function of time and pressure. The experimen-

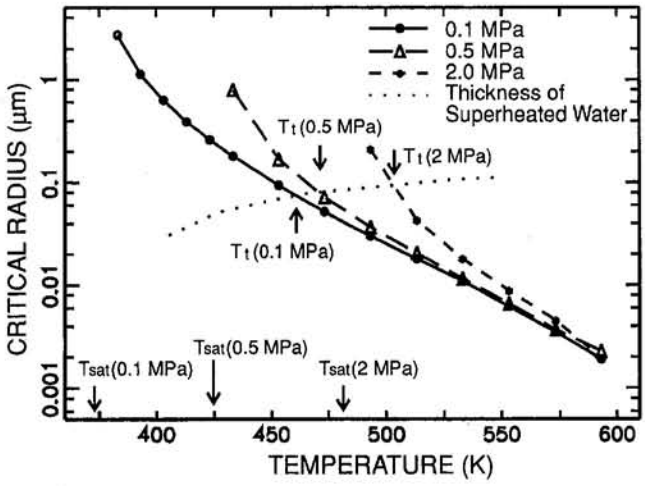


Fig. 10 The critical radius of bubble is plotted as a function of temperature at various liquid pressures (symbols with line) for water. The calculated maximum thickness of superheated water layer on a solid surface is also plotted. The boiling point T_{sat} and the phase transition temperature T_t are located by arrows.

Downloaded 11 Dec 2010 to 193.140.21.150. Redistribution subject to ASME license or copyright; see http://www.asme.org/terms/Terms_Use.cfm

tally determined C values are used to estimate the vaporized mass m:

$$m = \frac{1 - C}{L} E \tag{10}$$

The accuracy of the temperature measurement ($\sim$30 K) does not allow the exact evaluation of m. However, a typical value of temperature difference between the peak temperature at atmospheric pressure and that at elevated pressure where no vaporization is detected can be extracted from the fitting curves in Fig. 11. Thus $\Delta T = T - T'$ is estimated at 10 K for the case of water and consequently the vaporized mass is calculated to be 0.006 g/m^2. The total mass of superheated liquid per unit area is ρd_{sat} = 0.089 g/m^2. The vaporized mass fraction is therefore f = 0.067; only 6.7 percent of superheated liquid undergoes phase transition. It is noted that improvement in the accuracy of the temperature measurement is necessary for more precise estimate of vaporized mass.

7 Conclusion

The experiments described in this work investigate the thermodynamics of phase transformations of liquids on a solid surface heated by a short laser pulse at the nanosecond time scale. A novel photothermal reflectance probe is developed with specially fabricated samples. Static measurements of temperature-dependent reflectivity from the embedded optical sensor film have been performed. Transient conversion of reflectivity to temperature is achieved by accounting for the temperature gradient inside the sample on the basis of the calculated spatial temperature profiles. The time-dependent calibration of reflectivity enables measurement of temperature in nanosecond time resolution with 30 K accuracy. It has been found that embryonic nucleation begins as the surface reaches the boiling temperature (''nucleation threshold'') but bubble growth is not initiated until higher surface temperature is attained (''bubble growth threshold''). The bubble growth threshold requires surface temperatures up to 100 K higher than the boiling temperature. The total scattering cross section of bubbles, obtained optically from the front-side reflectance drop, correlates well with the maximum bubble radius, which is estimated using thermodynamic considerations and transient surface temperature measurement data. An investigation on the threshold temperature as a function of pressure reveals a criterion for the onset of bubble growth. The radius of the embryonic bubbles for the onset of bubble growth is found to scale with the thermal boundary layer thickness in the liquid. The comparison of surface temperature with and without bubble formation, i.e., at low and at high pressures, at the same laser energy results in an estimate of the vaporized mass, which is of the order of 1 percent.

Acknowledgments

Support to this work by the National Science Foundation under Grant CTS-9317708 is gratefully acknowledged. The authors thank Xianfan Xu at the University of California at Berkeley for the ellipsometric measurement of the sample optical properties.

References

Avedisian, C. T., 1985, ''The Homogeneous Nucleation Limits of Liquids,'' *Journal of Physical and Chemical Reference Data,* Vol. 14, pp. 695–729.

Born, M., and Wolf, E., 1980, *Principles of Optics,* 6th ed., Pergamon, Exeter, United Kingdom, pp. 51–70; 611–633.

Brunco, D. P., Thompson, M. O., Otis, C. E., and Goodwin, P. M., 1992, ''Temperature Measurements of Polyimide During KrF Excimer Laser Ablation,'' *Journal of Applied Physics,* Vol. 72, pp. 4344–4350.

Carey, V. P., 1992, *Liquid–Vapor Phase-Change Phenomena,* Hemisphere, Washington, DC.

Dyer, P. E., and Sidhu, J., 1985, ''Excimer Laser Ablation and Thermal Coupling Efficiency to Polymer Films,'' *Journal of Applied Physics,* Vol. 57, pp. 1420–1422.

Gorodetsky, G., Kazyaka, T. G., Melcher, R. L., and Srinivasan, R., 1985, ''Calorimetric and Acoustic Study of Ultraviolet Laser Ablation of Polymers,'' *Applied Physics Letters,* Vol. 46, pp. 828–830.

Heavens, O. S., 1965, *Optical Properties of Thin Solid Films,* Dover, New York.

Henderson, G., and Weaver, C., 1966, ''Optical Properties of Evaporated Films of Chromium and Copper,'' *Journal of the Optical Society of America,* Vol. 56, pp. 1551–1559.

Jacobsson, R., 1965, ''Light Reflection From Films of Continuously Varying Refractive Index,'' in: *Progress in Optics,* Vol. 5, E. Wolf, ed., North-Holland, Amsterdam, pp. 247–286.

Jellison, G. E., Jr., Lowndes, D. H., Mashburn, D. N., and Wood, R. F., 1986, ''Time-Resolved Reflectivity Measurements of Silicon and Germanium Using a Pulsed Excimer KrF Laser Heating Beam,'' *Physical Review B,* Vol. 34, No. 4, pp. 2407–2415.

Jellison, G. E., Jr., and Burke, H. H., 1986, ''The Temperature Dependence of the Refractive Index of Silicon at Elevated Temperatures at Several Laser Wavelengths,'' *Journal of Applied Physics,* Vol. 60, No. 2, pp. 841–843.

Kagan, Y., 1960, ''The Kinetics of Boiling of a Pure Liquid,'' *Russian Journal of Physical Chemistry,* Vol. 34, pp. 42–46.

Lee, I.-Y. S., Wen, X., Tolbert, W. A., Dlott, D., Doxtader, M., and Arnold, D. R., 1992, ''Direct Measurement of Polymer Temperature During Laser Ablation Using a Molecular Thermometer,'' *Journal of Applied Physics,* Vol. 72, pp. 2440–2448.

Leung, P. T., Do, N., Klees, L., Leung, W. P., Tong, F., Lam, L., Zapka, W., and Tam, A. C., 1992, ''Transmission Studies of Explosive Vaporization of a Transparent Liquid Film on an Opaque Solid Surface Induced by Excimer-Laser-Pulsed Irradiation,'' *Journal of Applied Physics,* Vol. 72, pp. 2256–2263.

Lompré, L. A., Liu, J. M., Kurz, H., and Bloembergen, N., 1983, ''Time-Resolved Temperature Measurement of Picosecond Laser Irradiated Silicon,'' *Applied Physics Letters,* Vol. 43, pp. 168–170.

Lowndes, D. H., 1982, ''Time-Resolved Optical Transmission and Reflectivity of Pulsed-Ruby-Laser Irradiated Crystalline Silicon,'' *Physical Review Letters,* Vol. 48, pp. 267–271.

Matlison, I. H., 1965, ''Interspecimen Comparison of the Refractive Index of Fused Silica,'' *Journal of the Optical Society of America,* Vol. 55, pp. 1205–1209.

Palik, E. D., 1991, *Handbook of Optical Constants of Solids II,* Academic, London.

Park, H. K., Xu, X., Grigoropoulos, C. P., Do, N., Klees, L., Leung, P. T., and Tam, A. C., 1993, ''Transient Optical Transmission Measurement in Excimer-Laser Irradiation of Amorphous Silicon Films,'' ASME JOURNAL OF HEAT TRANSFER, Vol. 115, pp. 178–183.

Park, H. K., 1994, ''Heat and Momentum Transfer on the Rapid Phase Change of Liquid Induced by Nanosecond-Pulsed Laser Irradiation,'' Ph.D. Dissertation, University of California at Berkeley.

Park, H. K., Grigoropoulos, C. P., Leung, W. P., and Tam, A. C., 1994, ''A Practical Excimer Laser-Based Cleaning Tool for Removal of Surface Contaminants,'' *IEEE Transactions on Components, Packaging, and Manufacturing Technology,* Vol. 17A, pp. 631–643.

Prosperetti, A., and Plesset, M. S., 1978, ''Vapour-Bubble Growth in a Superheated Liquid,'' *Journal of Fluid Mechanics,* Vol. 85, pp. 349–368.

Touloukian, Y. S., Kirby, R. K., Taylor, R. E., and Desai, P. D., 1975, *Thermophysical Properties of Matter—Thermal Expansion,* Vol. 12, IFI/Plenum, New York.

Xu, X., and Grigoropoulos, C. P., 1993, ''High Temperature Radiative Properties of Thin Polysilicon Films at the λ = 0.6328 μm Wavelength,'' *International Journal of Heat and Mass Transfer,* Vol. 36, pp. 4163–4172.

Xu, X., Grigoropoulos, C. P., and Russo, R. E., 1995, ''Transient Temperature Measurement During Pulsed Excimer Laser Heating of Thin Polysilicon Films Obtained by Optical Reflectivity Measurement,'' ASME JOURNAL OF HEAT TRANSFER, Vol. 117, pp. 17–24.

Yavas, O., Leiderer, P., Park, H. K., Grigoropoulos, C. P., Poon, C. C., Leung, W. P., Do, N., and Tam, A. C., 1993, ''Optical Reflectance and Scattering Studies of Nucleation and Growth of Bubbles at a Liquid–Solid Interface Induced by Pulsed Laser Heating,'' *Physical Review Letters,* Vol. 70, No. 12, pp. 1830–1833.

Yavas, O., Leiderer, P., Park, H. K., Grigoropoulos, C. P., Poon, C. C., Leung, W. P., Do, N., and Tam, A. C., 1994, ''Optical and Acoustic Study of Nucleation and Growth of Bubbles at a Liquid–Solid Interface Induced by Nanosecond-Pulsed Laser Heating,'' *Applied Physics A,* Vol. 58, pp. 407–415.

Downloaded 11 Dec 2010 to 193.140.21.150. Redistribution subject to ASME license or copyright; see http://www.asme.org/terms/Terms_Use.cfm

R. Stelling

E. V. McAssey, Jr.

Villanova University,
Villanova, PA 19085

T. Dougherty

B. W. Yang

Columbia University,
New York, NY 10027

The Onset of Flow Instability for Downward Flow in Vertical Channels

A simple analytical model to predict the onset of Ledinegg instability in vertical channels under downflow conditions has been developed and evaluated. The model divides the flow field into three regions based upon the fluid temperature. The pressure drop is then found by solving an appropriate set of equations for each region. The theoretical results are compared to an extensive set of experimental data covering a range of channel diameters and operating conditions. Agreement is excellent, and the prediction of the velocity at which the minimum point in the demand curve occurs is within 12 percent over the range of experimental results. A parameter, the ratio between the surface heat flux and the heat flux required to achieve saturation at the channel exit for a given flow rate, is found to be a very accurate indicator of the minimum point velocity.

Introduction

Flow instability is an important consideration in the design of nuclear reactors because of the possibility of flow excursion during a postulated accident. Generally, flow instability in a heated channel is classified as either dynamic or static. The present investigation addresses the latter type of instability. For the purposes of this paper, flow instability (static) is defined as the occurrence of a minimum in the demand curve (i.e., the channel pressure drop versus velocity curve). This is commonly referred to as a Ledinegg or excursive instability. The point at which this minimum occurs is defined as the onset of flow instability (OFI) point. Lahey and Moody (1977) present a complete discussion of flow instability in heated channels.

In an operational system with multiple flow paths, an increase in pressure drop in one flow channel can cause the flow to be diverted to an alternate channel. This flow reduction results in an even greater pressure drop and more flow diversion from the affected channel. Eventually, burnout can occur in the unstable channel. One operational approach to solving this problem is to identify the velocity at which the minimum point occurs and then to design the system so that this condition is not achieved during postulated accidents.

An analytical and experimental program has been conducted to investigate this type of flow instability in vertical channels under downflow conditions. Downflow was selected for this investigation because of the application to the Savannah River Reactors. The analytical phase involved the development of a pressure drop model that could predict the entire flow regime along a channel as it progresses from single phase flow through the fully developed nucleate boiling regime. Experimental data were obtained on circular tubes of varying diameter under a range of flow conditions and heat fluxes.

Background

Some of the earliest data for flow instability in downflow were obtained by Marshak (1958). Since that time, a number of investigators have examined this problem but generally for upflow. Dormer and Bergles (1964) investigated the pressure drop in small diameter tubes under subcooled boiling conditions. These experiments were conducted in horizontal channels under controlled flow so that data were obtained well beyond the minimum point. A large amount of data was correlated using the ratio of the channel pressure drop to the zero flux pressure drop versus the ratio of the surface heat flux to the heat flux required to raise the bulk fluid temperature to saturation at the channel exit. Using these parameters, it was shown that the only remaining effect was geometry. Maulbetsch and Griffith (1965) studied flow instability in small diameter, high L/D ratio channels. They determined that during parallel flow operation excursive flow instability occurred when the pressure drop versus mass flow reached a minimum.

Whittle and Forgan (1967) examined the pressure loss in rectangular and circular channels under subcooled boiling conditions. These investigators determined that for a given L/D ratio the minimum in the demand curve occurred at fixed values of the ratio of the channel temperature rise to the inlet subcooling $((T_{out} - T_i)/(T_{sat} - T_i))$. Whittle and Forgan also determined that flow direction, at least for their flow-rate regime, did not affect the velocity at which the minimum point (OFI) occurred.

Johnston (1989) conducted downflow experiments in an internally heated annulus. Because of apparatus limitations, data were limited to Peclet numbers below 50,000 and heat fluxes below 0.275 MW/m^2. The OSV Stanton number obtained was 0.0065, which was less than the value predicted by the Saha–Zuber (1974) correlation. However, the author recommended that for downflow an OSV Stanton number of 0.0065 be used provisionally for all Peclet numbers. The purpose of the test program described in this paper was to generate the required downflow data base.

Duffey and Hughes (1990) developed an analytical model to describe static flow instability (Ledinegg) in vertical channels. They showed that a linear relationship exists between the OFI point and the power density. In this paper, the authors developed a relationship for the flow rate at the minimum point based upon the frictional pressure drop and the buoyancy-induced pressure drop. In this development, the assumption was made that the friction factor including the two-phase multiplier was independent of flow rate.

Dougherty et al. (1989, 1990) presented experimental results for flow instability studies in a vertical tube for L/D ratios from 100 to 150. These authors showed that the results could be

Contributed by the Heat Transfer Division and presented at the ASME/JSME Thermal Engineering Joint Conference, Honolulu, Hawaii, March 1991, and the ASME National Heat Transfer Conference, Portland, Oregon, August 5–9, 1995. Manuscript received by the Heat Transfer Division December 4, 1995; revision received April 26, 1996. Keywords: Boiling, Flow Instability, Multiphase Flows. Associate Technical Editor: R. A. Nelson.

Copyright © 1996 by ASME

Downloaded 11 Dec 2010 to 193.140.21.150. Redistribution subject to ASME license or copyright; see http://www.asme.org/terms/Terms_Use.cfm

Table 1 Pressure drop model equations

Flow regime	Length of region	Pressure drop model
single phase	$\Delta Z_{sp} = \frac{(V_f \rho_f C_{pf} D)(T_{f,ONB} - T_{inlet})}{4\phi}$	$\frac{dP}{dZ} = \frac{2fV_f^2\rho_f}{D} - \rho g$
partially developed sub-cooled boiling	$\Delta Z_{nb} = \frac{(V_f \rho_f C_{pf} D)(T_{f,OSV} - T_{f,ONB})}{4\phi}$	$\frac{dP}{dZ} = \frac{2f_{tp}V_f^2\rho_f}{D} - \rho g$
fully developed sub-cooled boiling	$\Delta Z_{fnb} = L - \Delta Z_{sp} - \Delta Z_{nb}$	$\frac{dP}{dZ} = \frac{2f_{tp}V_f^2\rho_f}{D} + V_f^2\rho_f\left(\frac{\rho_f - \rho g}{\rho_g}\right)\frac{dx}{dZ} - \rho g$

correlated using a Q_{ratio} parameter defined by the following equation:

$$Q_{\text{ratio}} = \frac{\phi \pi D L}{m C_{pf}(T_{\text{sat}} - T_i)} \tag{1}$$

This ratio is the same as that developed by Dormer and Bergles (1964). In addition, it is also in agreement with the Whittle and Forgan (1967) R coefficient.

The Q_{ratio} can be appreciated if one considers that the pressure drop in the channel is composed of a single-phase component and a two-phase component. As the channel velocity decreases, the former component, which is proportional to the channel velocity, decreases. With decreasing channel flow rate, more voids are formed, and, therefore, the two-phase pressure drop component tends to increase. These competing effects cause a minimum in the pressure drop to occur. Under subcooled boiling conditions, the wall temperature exceeds saturation, and voids are formed in the fluid. As the fluid temperature approaches saturation, the number of subcooled voids increases. The corresponding increase in Q_{ratio} can be used as a measure of the void population increase. The ratio also contains all the test parameters such as the surface heat flux, the inlet temperature, the velocity, and the exit pressure, which determines the saturation temperature.

Lee et al. (1992) examined various models used to predict the onset of significant voids (OSV) under subcooled boiling conditions. Their results show that in vertical downflow the OFI point is almost coincident with OSV. These investigators also concluded that the Saha–Zuber (1974) correlation was the best predictor of OSV. In addition, it was shown that the model of Levy (1967) was best among analytical approaches.

Block et al. (1990) developed an analytical model to predict the pressure drop in a vertical channel under downflow conditions. This model considers four flow regimes: single phase, partial subcooled boiling, fully developed subcooled boiling, and saturated boiling. For each regime, a pressure drop correlation and transition criteria were applied. Comparisons with limited test data showed reasonable agreement. The present model is based upon the model proposed by Block et al. (1990).

This paper presents experimental results over an L/D ratio range from 90 to 270 for controlled flow conditions under downflow and uniform heating. Comparisons are made between these experimental data and a proposed analytical model.

Pressure Drop Model

In a heated tube of this nature, the fluid has four possible regions of flow: single-phase, partially developed subcooled boiling, fully developed subcooled boiling, and saturated boiling. Since the experimental data that will be used to evaluate the proposed model were obtained for conditions in which the fluid temperature did not reach saturation, the saturated boiling regime will not be included in the model.

The various regions can be identified by the vapor content and temperature of the fluid. The proposed analytical model divides the tube into the appropriate regions by fluid temperature only. The pressure drop for each region is then found by solving an appropriate set of equations for each region. The regional pressure drops are then summed to determine a total pressure drop across the tube.

The basic model used in this study was developed by Block et al. (1990). In this model, the total pressure drop is composed of several components including the frictional pressure drop, the acceleration pressure drop, and the gravitational pressure drop. The latter pressure drop is a function of the fluid temperature, which, under uniform heating conditions, is approximately linear up to saturation. The frictional pressure drop is a function of the particular flow conditions existing in the channel. The

Nomenclature

C_{fp} = fluid specific heat
D = tube inner diameter
f = Fanning friction factor
f_{tp} = two-phase friction factor
g = gravitational acceleration
h_{fg} = enthalpy of vaporization
h_{fo} = heat transfer coefficient for total flow assumed liquid
k = conductivity
L = length of heated channel
m = mass flow rate
Nu = Nusselt number
Pe = Peclet number = RePr
Pr = Prandtl number
Re = Reynolds number
St = Stanton number = $\phi/(\rho_f C_{pf} V_f)(T_{\text{sat}} - T_{ffdb})$
T = temperature
V = velocity
x = local quality
Y_b = bubble size parameter
z = distance from entrance of channel
dP = pressure drop
dZ = length of region
ϵ = channel roughness
ρ = density
σ = surface tension
ϕ = heat flux

Subscripts

f = liquid
fdb = fully developed subcooled boiling
g = vapor
i = inlet
nb = partially developed subcooled boiling
ONB = onset of nucleate boiling
OSV = onset of significant voiding
sat = saturation
sp = single phase
tp = two-phase

Downloaded 11 Dec 2010 to 193.140.21.150. Redistribution subject to ASME license or copyright; see http://www.asme.org/terms/Terms_Use.cfm

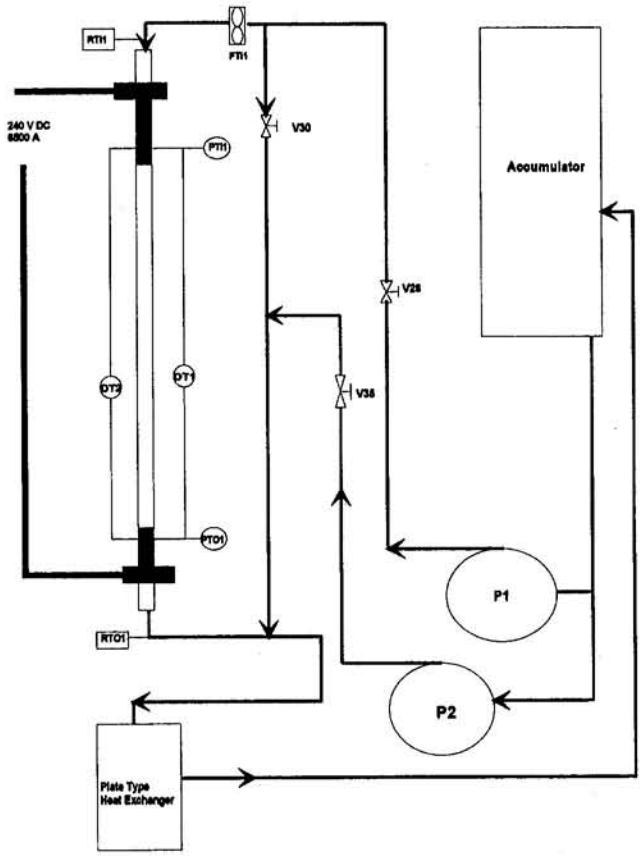


Fig. 1 Schematic of test loop

acceleration pressure becomes significant as voiding in the channel increases following OSV.

The pressure drop for each flow regime will be determined by the pressure gradient (dP/dz) and the length of the particular flow regimes. The extent of each region is based upon the fluid temperature at the onset of nucleate boiling, T_{ONB}, and the fluid temperature at OSV, T_{OSV}. Table 1 presents the equations used in the model for the various regions.

To establish the extent of each region, this model makes use of the fluid energy balance, which is linear with temperature in the single phase and partial subcooled boiling regions under steady-state conditions. It also uses the wall heat transfer coefficient equations by Dittus and Boelter (1930) and by Thom et al. (1965). Fluid temperatures at the ONB and OSV points are found by the Davis–Anderson (1966) and Saha–Zuber (1974) correlations, respectively. Equations (2) and (3) present these correlations:

$$T_{f,\mathrm{ONB}} = T_{\mathrm{sat}} + \sqrt{\frac{8\sigma\phi T_{\mathrm{sat}}}{h_{fg}k_f\rho_g}} - \frac{\phi D}{\mathrm{Nu}\,k_f} \tag{2}$$

$$T_{f,\mathrm{OSV}} = T_{\mathrm{sat}} - \frac{\phi}{\mathrm{St}_{\mathrm{OSV}}\rho_f C_{pf} V_f} \tag{3}$$

In Eq. (3), the high-Peclet-number form (Pe $\geq$ 70,000) of the Saha–Zuber correlation is given because the experimental data in the present paper were obtained at Peclet numbers above this limit. For this range of Peclet number, the Stanton number, $\mathrm{St}_{\mathrm{OSV}}$, is constant at 0.0065.

Finally, the friction factors that are included in the pressure drop equations were found using the Zigrang–Sylvester (1982) correlation:

$$f = 0.25\left(-2.0\log\left[\frac{\epsilon/D}{3.7} - \left(\frac{5.02}{\mathrm{Re}_f}\right)\times\log\left[\frac{\epsilon/D}{3.7} + \frac{13}{\mathrm{Re}_f}\right]\right]\right)^{-2} \tag{4}$$

Equation (4) is used in the single-phase liquid region of the flow. In the partially developed subcooled boiling region, a two-phase friction factor, f_{tp}, is obtained from Eq. (4) by replacing the roughness factor, ϵ, by the Levy (1967) bubble size parameter, Y_b.

In Table 1, the pressure drop expression for the fully developed subcooled boiling region contains a quality gradient. In the present model, the gradient is based upon a relationship presented by Collier (1972). This form of the quality gradient (see Eq. (5)) was used because it provided approximately a 50 percent improvement in prediction of pressure drop after OFI when compared to that used by Block et al. (1990).

$$\frac{dx}{dZ} = \frac{4}{DGh_{fg}}\,\frac{\phi - h_{fo}(T_{\mathrm{sat}} - T_f(z))}{1 + 3.2\left(\frac{\rho_f}{\rho_g}\right)\left(\frac{C_{pf}}{h_{fg}}\right)} \tag{5}$$

As noted earlier, the data that were used to evaluate the analytical predictions achieved the minimum in the demand curve before the fluid temperature reached saturation. For this reason, this model does not include a saturated boiling regime.

Experimental Apparatus

The test loop was designed to provide vertical downflow into test sections of various diameters with fixed length. Figure 1 presents a schematic of the test loop. Flow was supplied by either a centrifugal pump or a screw type pump. The latter pump was added to the loop in order to provide the capacity to test small-diameter tubes. With the centrifugal pump, the loop provided a maximum flow of 0.947 m^3/min at a head of 480 kPa. The screw pump provided a head of 5000 kPa at flows down to 0.05 m^3/min. All components in the flow loop were stainless steel or nickel plated. The water in the loop was maintained at a pH of slightly less than 7. As shown in Fig. 1, a 100 gallon accumulator supplied deionized water to the pump inlet. System pressure was maintained by adjusting the liquid level and helium blanket pressure in the accumulator. The test section inlet temperature was controlled by adjusting the loop external heat rejection rate.

Different diameter test sections were used; however, each test section had the same heated length (2.44 m). The test sections were constructed from either 300 series stainless steel or 600 series inconel. Upstream and downstream of the heated

Table 2 Test section description

Test section	Material	Inside diameter
ST-1	stainless steel 304	25.4 mm
ST-2	stainless steel 304	19 mm
ST-3	stainless steel 304	25.4 mm
ST-4	inconel 600	15.5 mm
ST-5	inconel 600	9.1 mm
ST-6	inconel 600	28 mm
ST-7	stainless steel 304	15.2 mm
ST-8	inconel 600	15.5 mm
ST-9	inconel 600	9.1 mm
ST-10	inconel 625	15.8 mm

Downloaded 11 Dec 2010 to 193.140.21.150. Redistribution subject to ASME license or copyright; see http://www.asme.org/terms/Terms_Use.cfm

Table 3 Uncertainty analysis

Measurement	Uncertainty	Range
Exit pressure	±0.323% of full scale	2.14 kPa
Differential pressure	±0.323% of full scale	(0.2067-0.483) kPa
Inlet temperature	±0.15°C	1°C
Flow-rate	±0.548% of full scale	$0.023*10^{-3}m^3/s$
Power	±0.441% of full scale	20.1 watts

portion of the test section, a 0.38 m calming length was provided. These sections were constructed from copper and had the same inside diameter as the heated length. The connection to the power system was accomplished through these copper sections. To insure that power dissipation was minimal in the calming regions, the wall thickness was approximately ten times the test section wall thickness. Table 2 provides a description of the various test sections used in the program.

The instrumentation for this program consisted of three categories, primary, secondary, and loop housekeeping. The primary instrumentation included parameters necessary to establish OFI. These were power, test section exit pressure, test section inlet temperature, flow rate, and test section pressure drop. Test section wall temperatures were measured at nine or ten axial locations; however, these were considered to be secondary measurements. Other secondary measurements included test section inlet pressure and outlet temperature. To insure proper loop operation, there were a number of flow-rate, pressure, and temperature measurements also made. For each test point, 60 to 70 items were recorded.

Test sections 1–9 were constructed from commercial grade tubing with wall thickness of 1.65 mm (±10 percent). Test section number 10 was a specially bored and ground tube with the same wall thickness but a tolerance approximately one half of commercial grade tubing. Table 2 contains several duplicate test sections that were required to replace burned out units. Heating was accomplished by passing a DC electric current directly along the test section wall. Each test section was designed to be capable of producing a maximum average surface heat flux of 3.16 MW/m^2. The entire exterior of the test section was insulated with approximately a 0.3 m thickness of fiberglass insulation. To minimize any circumferential flux variation, there were no penetrations in the heated length.

An uncertainty analysis was conducted for all instrumentation. This analysis included instrument error, line error, and digitizing error. Table 3 presents the results of this analysis for the primary instrumentation. In Table 3, the range represents the value of the uncertainty for a given range of instrument. As the required measurement range changed, the instrument was replaced so that the overall accuracy was maintained.

Test Procedure

Under controlled flow, sufficient pressure head was provided to assure that flow excursion did not occur. In this mode of operation, the test section inlet temperature, exit pressure, and surface heat flux were set to meet the test program requirements. Initial test conditions were established at a high enough flow rate to prevent local boiling. The test section flow rate was then gradually reduced in steps to insure that each data point was recorded at steady state. Whenever possible, several points were measured beyond the minimum point in test section pressure drop. The flow rate was then increased gradually. Data points were also measured as the flow rate increased. The number of points taken during a test varied depending upon test conditions. The physical limitations of the fluid temperature sensors (RTD's) restricted the maximum test section flow rate to approximately 0.19 m^3/min. For the largest diameter test sections, this limit was close to the minimum point. The data system scanned all the sensors in approximately 100 milliseconds. Forty scans were averaged to provide a single data point. Allowing for recording and unit conversions, the resulting test point represented approximately a five second average. The 40 scans were also used to compute standard deviations for the primary data. With the exception of the pressure drop data, the standard deviations were small over the entire test range. The standard deviation in test section pressure drop grew rapidly as the OFI point was reached. At this minimum point, the test section pressure drop oscillated violently due to the formation and collapse of bubbles. However, these oscillations did not affect the test section flow rate.

Table 4 Range of test conditions

Parameter	Range
L/D ratio	85.7 to 266.8
Surface heat flux	0 to 3.16 MW/m^2
Inlet temperature	25°C and 50°C
Exit pressure	241 kPa and 448 kPa

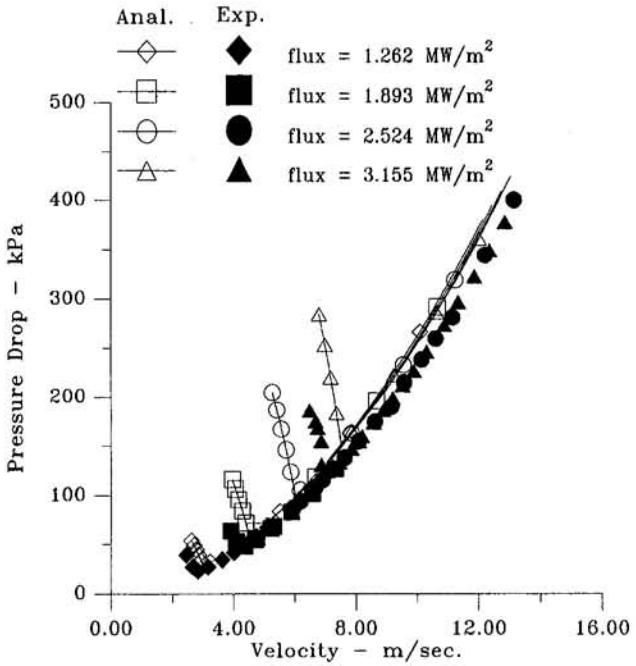


Fig. 2 Pressure drop versus velocity, P_{exit} = 448 kPa, T_{inlet} = 25°C, diameter = 9.14 mm

Discussion

Eighty-eight demand curves were generated during the experimental phase of this program. Table 4 presents the range of test conditions for which experimental data were obtained.

Figure 2 presents a comparison between the measured demand curve and the analytical demand curve for the 9.14 mm tube. Since the experimental pressure drop was obtained with a differential pressure transducer (for greater accuracy), a cold leg correction must be applied. This correction to the gravitational pressure gradient was applied to the analytical model by adding a constant term (equal to $\rho_i g$) to each of the pressure gradient expressions given in Table 1. The revised gravitational component of the pressure drop is therefore proportional to $(\rho_i - \rho)g$, which has a negligible contribution before OSV is reached. Figures 3 and 4 present similar results for the 15.6 mm and 25.3 mm tubes, respectively. All three figures show

Downloaded 11 Dec 2010 to 193.140.21.150. Redistribution subject to ASME license or copyright; see http://www.asme.org/terms/Terms_Use.cfm

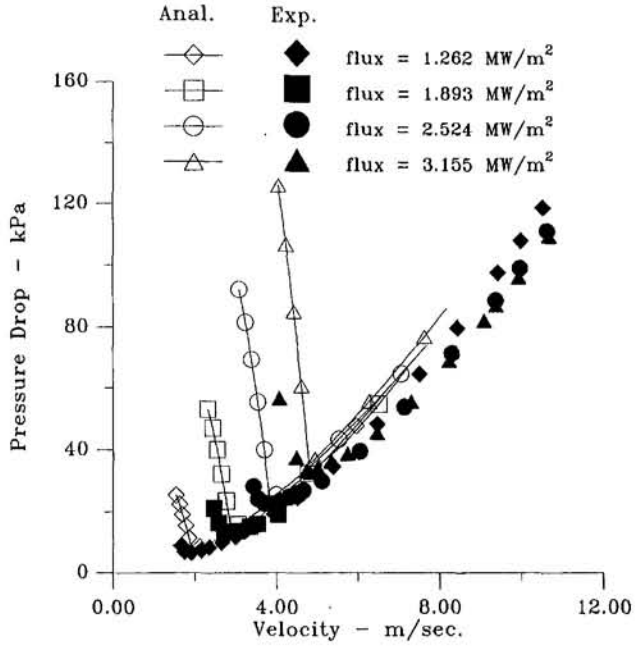


Fig. 3 Pressure drop versus velocity, P_{exit} = 448 kPa, T_{inlet} = 25°C, diameter = 15.62 mm

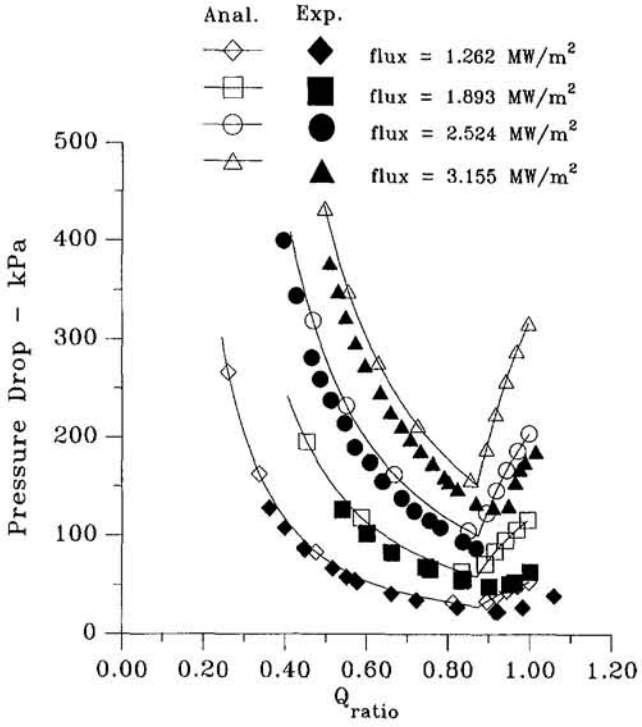


Fig. 5 Pressure drop versus Q_{ratio}, P_{exit} = 448 kPa, T_{inlet} = 25°C, diameter = 9.14 mm

very good agreement with respect to the prediction of the minimum point. The theoretical model tends to predict a larger pressure drop after the minimum point. Analysis shows that the pressure gradient in the fully developed subcooled boiling region is dominated by the quality gradient term. Equation (5) presents the model used for this gradient that was selected over the model used by Block et al. (1990). Considering the simplicity of the model, the results are very encouraging, particularly with respect to the accuracy of the minimum point velocity prediction, which was the objective of the present investigation.

As noted earlier, Dougherty et al. (1989, 1990) correlated the experimental results using the Q_{ratio} given by Eq. (1). Figures 5 and 6 present comparisons between measured pressure drop and calculated pressure drop as a function of Q_{ratio}. Again, the agreement is very good. From these figures, it can be seen that the minimum point in the pressure is correlated by the Q_{ratio} parameter. In the analytical model this parameter does not appear explicitly; however, it can be calculated for each point in the demand curve. Table 5 presents a comparison at OFI of the measured Q_{ratio} and the corresponding calculated Q_{ratio}. For each test section, the average, maximum, and minimum measured

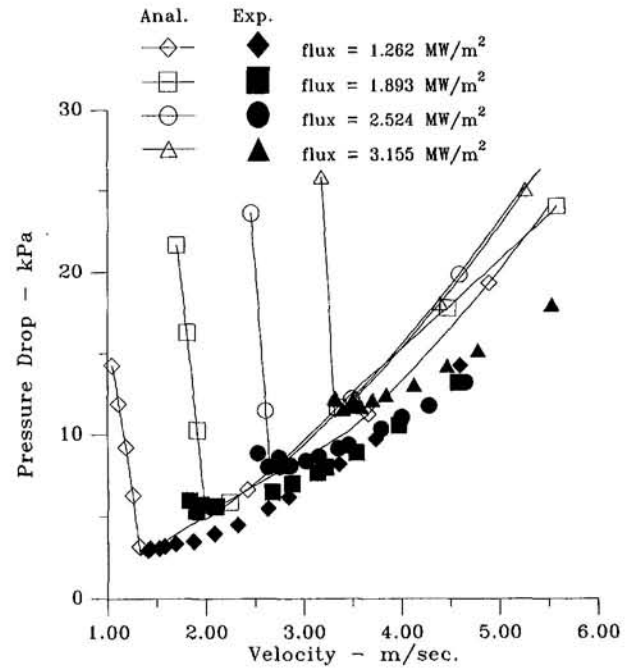


Fig. 4 Pressure drop versus velocity, P_{exit} = 448 kPa, T_{inlet} = 25°C, diameter = 25.27 mm

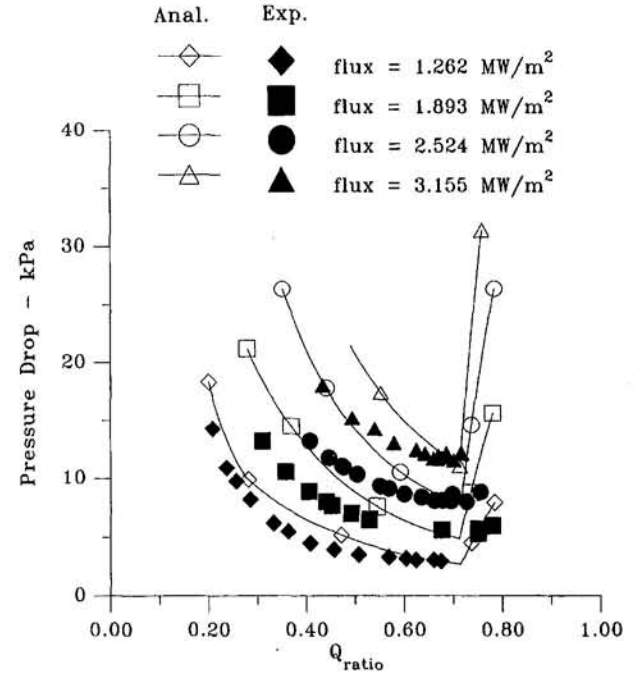


Fig. 6 Pressure drop versus Q_{ratio}, P_{exit} = 448 kPa, T_{inlet} = 25°C, diameter = 25.27 mm

Downloaded 11 Dec 2010 to 193.140.21.150. Redistribution subject to ASME license or copyright; see http://www.asme.org/terms/Terms_Use.cfm

Table 5 Comparison of Q_{ratio} at OFI

L/D	Q_{ratio} average	Q_{ratio} max.	Q_{ratio} min.	Q_{ratio} analytical
85.7	0.677	0.729	0.621	0.686
96.5	0.686	0.772	0.623	0.711
128.9	0.744	0.782	0.678	0.767
154.1	0.822	0.874	0.727	0.802
156.1	0.807	0.835	0.781	0.799
160	0.787	0.808	0.771	0.805
266.8	0.903	0.930	0.862	0.872

values of Q_{ratio} are given. In determining the measured Q_{ratio}, the flow rate corresponding to the lowest measured pressure drop was used. This procedure introduces some scatter in the results because the actual minimum point may lie between the selected data point and the next lower flow-rate point. However, this approach provides a conservative estimate of the OFI point.

The data in Table 5 represent a total of 88 demand curves. The agreement between the predicted velocities at the OFI is excellent. The maximum deviation between experimental and predicted velocity at OFI is 11.7 percent. The average deviation is only 4 percent.

Figure 7 shows the effect of the ratio L/D on the minimum point Q_{ratio}. The open symbols represent the experimental results for all 88 demand curves. The filled symbols present the theoretical predictions. As noted earlier, Lee et al. (1992) indicated that the Saha–Zuber correlation was a good predictor of OFI as well as OSV, at least under downflow conditions. The Saha–Zuber correlation is a local correlation and does not depend upon L/D. However, by combining this correlation with an overall energy balance, a global correlation in terms of Q_{ratio} can be obtained. Figure 7 presents the Q_{ratio} expressed in terms of the L/D ratio by means of the Saha–Zuber correlation, Eq. (3), and overall energy balance. Equation (6) presents the function used in Fig. 7:

$$Q_{ratio} = \frac{1}{(1 + 0.25[St_{OSV}(L/D)]^{-1})} \quad (6)$$

Equation (6) represents a very good tool for predicting the minimum point (OFI) at least for these downflow data.

Conclusions

The results from this investigation have shown that the analytical model presented can be used to obtain the pressure drop in a heated tube under downflow conditions. The model predicts flow conditions from single-phase flow through fully developed subcooled boiling. The model also provides a very accurate prediction of the velocity at which the minimum point in the demand curve occurs. This is an important reactor safety parameter.

The experimental data show that the occurrence of Ledinegg flow instability depends upon the L/D ratio of the channel, the inlet temperature, exit pressure, and surface heat flux. These parameters are combined in the Q_{ratio} defined in Eq. (1). The experimental results show that Q_{ratio} is an excellent predictor of the minimum point velocity (OFI). In addition, the Q_{ratio} calculated from the analytical results also exhibited very good agreement with the experimental data.

Finally, Eq. (6), which is based upon a combination of the Saha–Zuber correlation with an overall energy balance, has been shown to be a good predictor of the velocity at the minimum point in the demand curve. This equation contains all the significant parameters affecting the onset of flow instability.

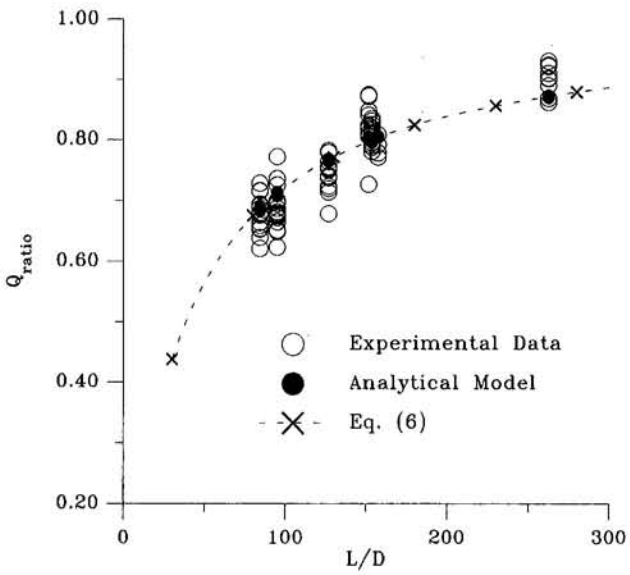


Fig. 7 Comparison of Q_{ratio} versus L/D for experimental and analytical results

References

Block, J. A., Crowley, C. J., Dolan, F. X., Sam, R. G., and Stoedefalke, B. H., 1990, "Nucleate Boiling Pressure Drop in an Annulus," CREARE TN 499, Oct.

Collier, J. G., 1972, *Convective Boiling and Condensation,* McGraw-Hill, New York.

Davis, E. J., and Anderson, G. H., 1966, "The Incipience of Nucleate Boiling in Forced Convection Flow," *AIChE J.,* Vol. 12, pp. 774–780.

Dittus, F. W., and Boelter, L. M. K., 1930, "Heat Transfer in Automobile Radiators of Tubular Type," Publ. in Engineering, University of California, Berkeley, p. 443.

Dormer, J., and Bergles, A. E., 1964, "Pressure Drop With Surface Boiling in Small Diameter Tubes," Report No. 8767-31, Department of Mechanical Engineering, MIT, Cambridge, MA.

Dougherty, T., Fighetti, C., McAssey, E., Reddy, G., Yang, B., Chen, K., and Qureshi, Z. C., 1989, "Flow Instability in Vertical Down-Flow at High Heat Fluxes," ASME HTD-Vol. 199, pp. 17–23.

Dougherty, T., Fighetti, C., Reddy, G., Yang, B., Jafri, T., McAssey, E., and Qureshi, Z., 1990, "Flow Boiling in Vertical Downflow," *Proc. Ninth International Heat Transfer Conference,* Vol. 2, Jerusalem, Israel.

Duffey, R. B., and Hughes, E. D., 1990, "Static Flow Instability in Tubes, Channels, Annuli, and Rod Bundles," ASME HTD-Vol. 150, pp. 145–159.

Johnston, B. S., 1989, "Subcooled Boiling of Downward Flow in a Vertical Annulus," ASME HTD-Vol. 109, pp. 149–156.

Lahey, R. T., and Moody, E. J., 1977, *The Thermal Hydraulics of a Boiling Water Nuclear Reactor,* American Nuclear Society.

Lee, S. C., Dorra, H., and Bankoff, S. G., 1992, "A Critical Review of Predictive Models for the Onset of Significant Void in Forced-Convection Subcooled Boiling, Fundamentals of Subcooled Flow Boiling," ASME HTD-Vol. 217, pp. 33–39.

Levy, S., 1967, "Forced Convection Subcooled Boiling Prediction of Vapor Volumetric Fraction," *Journal of Heat and Mass Transfer,* Vol. 10, pp. 951–965.

Marshek, S., 1958, "Transient Flow of Boiling Water in Heated Tubes," Savannah River Laboratory Report DP-301TL.

Maulbetsch, J. S., and Griffith, P., 1966, "A Study of System Induced Instabilities in Forced-Convective Flows With Sub-cooled Boiling," Report No. 5382-35, Department of Mechanical Engineering, MIT, Cambridge, MA.

Saha, P., and Zuber, N., 1974, "Point of Net Vapor Generation and Vapor Void Fraction Subcooled Boiling," *Proc. Fifth International Heat Transfer Conference,* B4.7, Tokyo, Japan.

Thom, J. R. S., Walker, W. M., Fallon, T. A., and Reising, G. F. S., 1965, "Boiling in Subcooled Water During Flow Up Heated Tube Annuli," presented at the Symposium on Boiling Heat Transfer in Steam Generating Units and Heat Exchangers, Inst. Mech. Engrs., Manchester, United Kingdom, Paper No. 6.

Whittle, R. H., and Forgan, R., 1967, "A Correlation for the Minima in Pressure Drop Versus Flow-Rate Curves for Sub-cooled Water Flowing in Narrow Heated Channels," *Nuclear Engineering and Design,* Vol. 6, pp. 88–89.

Zigrang, D. J., and Sylvester, N. D., 1982, "Explicit Approximations to the Solution of Colebrook's Friction Factor Equation," *AIChE Journal,* Vol. 28, No. 3, pp. 514–515.

Downloaded 11 Dec 2010 to 193.140.21.150. Redistribution subject to ASME license or copyright; see http://www.asme.org/terms/Terms_Use.cfm

Mechanism and Effects of Predominant Parameters Regarding Limitation of Falling Water in Vertical Countercurrent Two-Phase Flow

Y. Sudo
Deputy Director, Department of High Temperature Engineering, Tokai Research Establishment, Japan Atomic Energy Research Institute (JAERI), 2-4 Shirakata-Shirane, Tokai-mura, Naka-gun, Ibaraki-ken 319-11 Japan

In this study, an investigation was carried out to clarify the mechanism of countercurrent flow limitation (CCFL) or flooding, that is, limitations in the falling water mass flux in countercurrent two-phase flow in vertical channels, and to identify the effects of predominant parameters regarding CCFL, adopting the criterion that the CCFL condition be given by an envelope of momentum equation applied for the entire length of the channel with respect to any void fraction. As a result, it was found that the analytical model proposed could adequately predict all existing experimental results investigated in this study. In the channel configuration, circular, rectangular, and annular or planar channels, channel dimensions of diameter, gap size, width or circumference, and length, interfacial and wall friction, water injection mode, and inlet water subcooling were dominant parameters. Therefore, both the mechanism and the quantitative effects of CCFL have been identified.

Introduction

The countercurrent flow limitation (CCFL) is known as flooding (Wallis, 1969) in vertical channels and has been investigated, for circular tubes (Bharathan et al., 1979; Richter, 1981; Sudo and Ohnuki, 1984), rectangular channels (Osakabe and Kawasaki, 1989; Sudo et al., 1990; Cheng, 1990) and annular (Collier, 1978; Richter et al., 1979) or planar (Crowley and Block, 1975) channels. The CCFL is an important phenomenon because mass flux of water falling down is restricted due to the upward gas flow. The flow governs the capability to cool the core during a postulated accident of light-water reactors, determining the timing for emergency core cooling water so as to be effective for cooling of the core in the downcomer of a pressurized water reactor (PWR) or in the upper part of a PWR core (Sudo 1984).

In addition, a lot of attention has also been directed to the relationship between CCFL and critical heat flux (CHF) to predict the CHF under low water velocity or stagnant water conditions in vertical heated channels in a loss-of-flow accident in a research nuclear reactor. Thus, many experiments on CHF under CCFL conditions have been carried out, especially in circular tubes (Frea, 1970; Kusuda and Imura, 1974; Mishima, 1984; Chang et al., 1991), rectangular channels (Mishima, 1984; Sudo et al., 1985; Motomura et al., 1993), and annular channels (Kusuda and Imura, 1974; Mishima, 1984; El-Genk et al., 1988). Analytical studies were carried out by Kusuda and Imura (1974), Sudo and Kaminaga (1989), Katto and Hirao (1991), and others. Through investigations of the previous studies typically described above, it was found that the mechanism of CCFL in vertical channels was not yet understood systematically enough and the effects of dominant parameters on CCFL were not clear.

Therefore, the objective of this study is analytically to clarify the mechanism of CCFL in common in vertical channels of circular, rectangular, annular, or planar channels and to identify the predominant parameters along with the magnitude of their effects, by introducing a new analytical model for CCFL.

Discussion on Previous Studies

1 Circular Channels. The experimental results regarding the mass flux of water falling down toward upward gas flow in vertical circular tubes have been evaluated by the dimensionless superficial average velocities of gas and water, j_g^* and j_l^*, as shown below, using the correlation of Wallis (1969):

$$j_g^{*1/2} + m j_l^{*1/2} = C \tag{1}$$

In this correlation, m and C are not constant, but depend on the channel configuration and dimension. Many researchers have reported that constant m is ordinally unity and constant C is 0.725 to 0.75 for the sharp-edged end of channel and 0.875 for the round-edged end of channel.

On the other hand, Pushkina and Solokin (1969) introduced Ku as a governing parameter, proposing the following criterion as the condition that no water is falling into the circular tubes, that is, the condition of a complete bypass:

$$\mathrm{Ku}_g = 3.2 \tag{2}$$

Bharathan et al. (1979) came up with the relationship of j_g^* versus j_l^* in which the CCFL condition was given analytically by an envelope of curves given by the following correlation with respect to void fraction α:

$$\frac{2f_i}{\alpha^{5/2}} j_g^{*2} + \frac{2f_w}{(1-\alpha)^2} j_l^{*2} = 1 - \alpha \tag{3}$$

in which the friction factor f_i was used at the interface between water and gas obtained experimentally and the constant wall friction factor f_w (= 0.005) of water film flow falling down into the circular tube.

Contributed by the Heat Transfer Division for publication in the JOURNAL OF HEAT TRANSFER. Manuscript received by the Heat Transfer Division November 7, 1995; revision received May 15, 1996. Keywords: Multiphase Flows. Associate Technical Editor: A. Faghri.

Copyright © 1996 by ASME

Downloaded 11 Dec 2010 to 193.140.21.150. Redistribution subject to ASME license or copyright; see http://www.asme.org/terms/Terms_Use.cfm

Richter (1981) introduced an additional condition by which the thickness of the water film flow was determined by the momentum flux of gas flow as:

$$\delta = \sigma/2\rho_g u_g^2 \tag{4}$$

in the case of circular tubes, and also proposed the following relationship of j_g^* versus j_l^* in which were included the wall friction factor and the Bond number:

$$(f_W/4)\cdot \mathrm{Bo}^3\cdot j_g^{*6}\cdot j_l^{*2} + f_W\cdot \mathrm{Bo}\cdot j_g^{*4} + 150\cdot f_W\cdot j_g^{*2} = 1 \tag{5}$$

Sudo and Ohnuki (1984) reported the effect of tube length, for the first time, based on experiments and analyses, suggesting that the effect of length-to-diameter ratio (L/D) on CCFL was different for $L/D < 2$ and $L/D > 2$.

2 Rectangular Channels. Mishima (1984) and Osakabe and Kawasaki (1989) investigated the characteristics of CCFL in vertical rectangular channels and both pointed out that the channel width should be adopted as the representative length instead of the gap size. Sudo et al. (1990) reported that not all sides of a wall were uniformly wetted by water film flow; according to their observations, the shorter sides of the wall were primarily wetted. They proposed the following correlation including the effects of gap size and width:

$$X_0^{0.7} + Y_0^{0.7} = 1.3^{0.7} \tag{6}$$

where

$$X_0 = 1.52(b/a)^{0.25}(0.5 + 0.0015\cdot \mathrm{Bo}^{1.3})\, j_l^{*0.5},$$

$$Y_0 = 1.52(b/a)^{0.25} j_g^{*0.5}.$$

Here, the gap size b is adopted for the representative length in j_g^* and j_l^*.

Cheng (1990) analytically investigated the effect of gap size based on Eq. (4) proposed by Richter (1981), but did not give sufficient attention to the experimental results of Sudo et al. (1990) and Osakabe and Kawasaki (1989).

3 Annular and Planar Channels. Crowley and Block (1975) devised the correlation shown below for an annular channel, which was similar to Eq. (1), adopting a value of Ku in which no representative length of channel was used in the same way as by Pushkina and Solokin (1969):

$$\mathrm{Ku}_g^{0.5} + m'\cdot \mathrm{Ku}_l^{0.5} = C' \tag{7}$$

where m' and C' were the constants to be determined experimentally.

To investigate the effects of channel dimension, Crowley et al. (1976) compared two different models based on the gap size and circumferential length as the representative length in j_g^* and j_l^* to correlate the experimental data on PWR downcomer penetration of emergency core cooling water. They pointed out that the representative length should not be the gap size but the circumference. Furthermore, Richter (1981) proposed the following analytical correlation of j_g^* versus j_l^*, which included wall friction, Bond number, gap size, and circumference:

$$f_W\cdot \mathrm{Bo}^3\cdot j_g^{*6}\cdot (S/W)\cdot j_l^{*2} + f_W\cdot \mathrm{Bo}\cdot j_g^{*4} + 150\cdot f_W\cdot j_g^{*2}\cdot (S/W) = 1 \tag{8}$$

where the circumference was used as representative length.

The author (Sudo, 1984) reported that predominant parameters were circumference W, gap size S, and dimensionless superficial average velocity of water injected into the channel $j_{l,\mathrm{IN}}^*$ in the form of Eq. (1), by adopting S as the representative length in j_g^* and j_l^* and proposed the following expressions of m and C, based on the previous experiments of annular and planar channels:

$$m = [2.89 + 0.0267\cdot W/S]\exp(-5.78\cdot j_{l,\mathrm{IN}}^{*0.5}),$$

$$C = 0.7 + 0.00817\cdot W/S \tag{9}$$

4 Effects of D, b, a, S, W and Inlet Water Subcooling on CCFL. Referring to the experimental results and knowledge described above, the effects of channel dimensions of tube di-

Nomenclature

A = flow area of channel, m^2
A_i = flow area of water injection nozzle, m^2
A_1 = constant in Eq. (21)
a = channel width (longer side wall) of rectangular channel, m
Bo = Bond Number = $\{(\rho_l - \rho_g)\cdot g/\sigma\}^{1/2}\cdot D_e$
Bo_a = $\{(\rho_l - \rho_g)\cdot g/\sigma\}^{1/2}\cdot 2\cdot a$
Bo_b = $\{(\rho_l - \rho_g)\cdot g/\sigma\}^{1/2}\cdot 2\cdot b$
B_1 = constant in Eq. (21)
b = channel gap size (shorter side wall) of rectangular channel, m
C_{pl} = specific heat of water at constant pressure, kJ/kg·K
D = channel diameter, m
D_e = equivalent hydraulic diameter, m
f = friction loss factor
g = acceleration of gravity, m/s^2
H = accumulated water level in upper plenum, m
h_{fg} = latent heat of water, kJ/kg
j = superficial average velocity, m/s
j_i^* = dimensionless superficial average velocity = $\rho_i^{1/2} j_i/\{gD_e(\rho_l - \rho_g)\}^{1/2}$ ($i = l$ or g)
Ku_i = Kutateladze number = $\rho_i^{1/2}\cdot j_i/\{g\sigma(\rho_l - \rho_g)\}^{1/4}$ = $\mathrm{Bo}^{1/2}\cdot j_i^*$ ($i = l$ or g)
k = fraction of condensation
L = channel length, m
m = constant in Eq. (1)
m_1 = constant in Eq. (20)
n = constant in Eq. (20)
P = pressure, Pa
Re = Reynolds number
S = channel gap size of annular channel, m
T = water temperature, K
Ts = saturation temperature, K
ΔT = subcooling of water = $Ts - T$, K
ΔT^* = dimensionless subcooling of water = $C_{pl}\cdot \Delta T/h_{fg}$
u = velocity, m/s
X_0, X_1, X_2 = dimensionless parameters defined by Eqs. (6), (10), and (11), respectively
x = dimensionless water film thickness = $2\delta/S$
Y_0, Y_1, Y_2 = dimensionless parameters defined by Eqs. (6), (10) and (11), respectively
Z = aspect ratio of channel = b/a
W = circumferential length of channel, m
α = void fraction
δ = water film thickness, m
λ = contraction factor
ν = kinematic viscosity, m^2/s
ρ = density, kg/m^3
σ = surface tension, N/m

Subscripts

g = gas phase
i = interface of water and gas
IN = injected water
l = water phase
W = wall
0, 1, 2 = cross section of channel

Downloaded 11 Dec 2010 to 193.140.21.150. Redistribution subject to ASME license or copyright; see http://www.asme.org/terms/Terms_Use.cfm

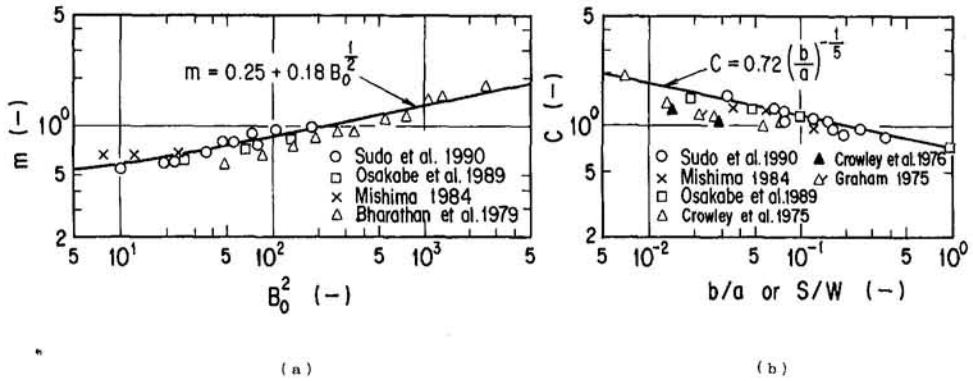


Fig. 1 Effects of channel dimensions, diameter of circular channel, gap and width of a rectangular channel, and the gap and circumferential length of an annular channel for constants *m* and *C* in Eq. (1)

ameter D, channel gap size b, and width a of rectangular channel, gap size S and circumference W of annular or planar channels, and inlet water subcooling were investigated again from the available CCFL data from previous experiments.

Figures 1(a) and 1(b) show the results of the effects of D, b, a, S, and W on m and C in Eq. (1), taking Bo $[=\{a \cdot b((\rho_l - \rho_g) \cdot g/\sigma\}^{0.5}]$ and b/a or S/W as the dominant parameters obtained from the experiments for circular tubes, rectangular channels, and annular channels conducted by Bharathan et al. (1979), Richter (1981), Mishima (1984), Osakabe and Kawasaki (1989), and Sudo et al. (1990). Figure 2 shows a comparison of the correlation newly proposed based on the results of Figs. 1(a) and 1(b) and the experimental results especially for rectangular channels conducted by Mishima (1984), Osakabe and Kawasaki (1989), and Sudo et al. (1990). The proposed correlation is expressed as follows:

$$X_1^{0.7} + Y_1^{0.7} = 1.3^{0.7} \tag{10}$$

where

$$X_1 = (1/0.72)(b/a)^{1/5} \cdot (0.25 + 0.18 \cdot \mathrm{Bo}^{1/2}) \cdot j_l^{*1/2},$$

$$Y_1 = (1/0.72)(b/a)^{1/5} \cdot j_g^{*1/2}.$$

Here, the gap size b is adopted for the representative length in j_g^* and j_l^*.

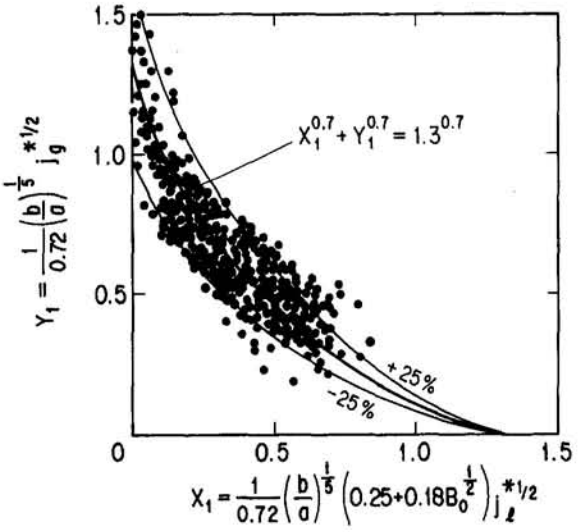


Fig. 2 New empirical correlation proposed with respect to the effects of the channel dimensions for rectangular channels based on the experiments by Mishima (1984), Osakabe and Kawasaki (1989), and Sudo et al. (1990)

Figure 2 shows, on the whole, that the new correlation is in good agreement with the tendency on the effects of channel dimensions within an error of about ±25 percent.

On the other hand, Fig. 3(a) shows the experimental results by Crowley and Block (1975), regarding the effects of inlet water subcooling and mass flux of injected water for a steam–water system in the planar channel. In this figure, Points A show the complete bypass conditions in which no water falls down toward upward steam flow at all, but on the other hand, Points B show the complete dumping conditions in which all water injected into the channel falls down even toward the upward steam flow. The curves CC', DD', and EE' indicate the loci of the complete dumping conditions for each given inlet water subcooling.

Figure 3(a) clearly shows that the higher inlet water subcooling and mass flux of injected water give a larger j_l^* compared with the same j_g^*. Figure 3(b) shows a comparison between experimental results and the following new correlation in which the effect of inlet water subcooling is included as well as the effect of $j_{l,\mathrm{IN}}^*$:

$$X_2 + Y_2 = 1 \tag{11}$$

where

$$X_2 = (m/C) j_l^{*1/2} / [1 + 0.5(\rho_g/\rho_l)^{1/4} \cdot \Delta T_{\mathrm{IN}}^*],$$

$$Y_2 = (1/C) j_g^{*1/2} / [1 + 0.5(\rho_g/\rho_l)^{1/4} \cdot \Delta T_{\mathrm{IN}}^*].$$

Here, the gap size S is adopted for the representative length in j_g^* and j_l^*, and Eq. (9) is used for m and C in X_2 and Y_2. Figure 3(b) shows that the new correlation is able to predict the experimental results within errors of about +30 to −15 percent.

It can be easily understood from Figs. 2 and 3 that the characteristics of CCFL, that is, the relationship of j_g^* versus j_l^* are strongly dependent on Bo, the aspect ratio of the channel (b/a or S/W), mass flux, and inlet subcooling of water injected into channel, which should be the predominant parameters for CCFL. However, the results of previous analyses could not give the systematic tendency of the experimental results obtained as described above to a sufficient degree. Therefore, the objective of this study is to introduce an analytical model that can give adequate and systematic predictions of the experimental results, especially regarding the predominant parameters for any type of channel investigated in this study. It should also be noted that the effect of the channel has not been sufficiently focused on in previous studies, but will be discussed as the key parameter in this study.

Analytical Model and Discussions

1 Circular Channels. A steady-state, completely separated two-phase flow is assumed for the air–water flow system

Downloaded 11 Dec 2010 to 193.140.21.150. Redistribution subject to ASME license or copyright; see http://www.asme.org/terms/Terms_Use.cfm

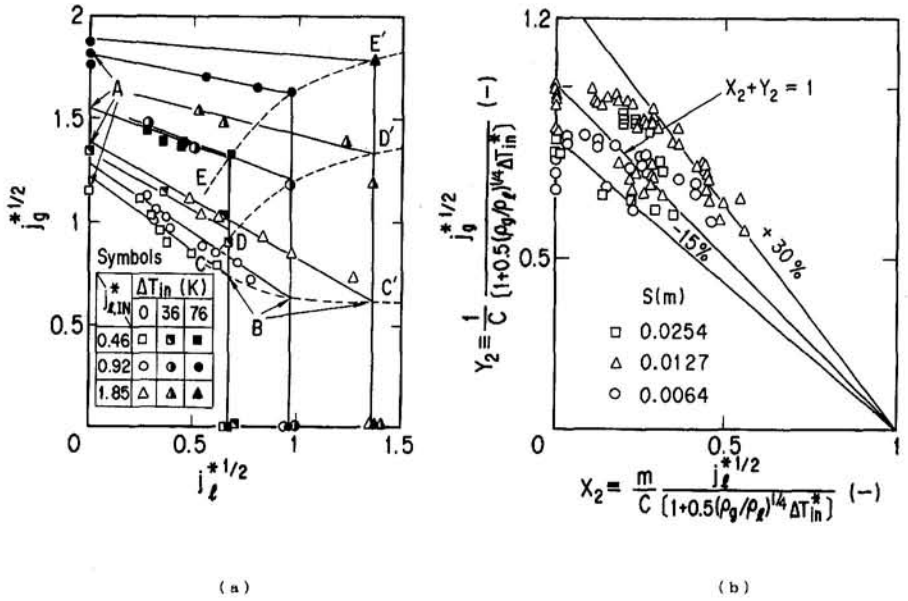


Fig. 3 Effects of water subcooling and mass flux of injected water on the CCFL for annular or planar channels: (*a*) results of typical experiments regarding the effects of ΔT_{iN}^* and $j_{i,IN}^*$; (*b*) new empirical correlation proposed on effects of ΔT_{iN}^* and $j_{i,IN}^*$

in the vertical circular tube shown in Fig. 4(*a*). The relationship of upward gas velocity u_{g1} versus downward water velocity u_{l1} in the tube could be obtained, allowing for the following momentum balance equations to be derived for the total and gas phase flows for the entire length of the channel, that is, between cross sections 0 and 2 in Fig. 4(*a*) with the terms of interfacial friction factor f_i between gas and water phases based on the relative velocity, wall friction factor f_W, enlargement, and contraction of passage at the exit and inlet of the channel:

Total flow

$$P_0 - P_2 = \rho_g g\alpha L + \rho_l g(1-\alpha)L + \{\rho_g g\alpha_2 + \rho_l g(1-\alpha_2)\}H - \frac{1}{2}\rho_l u_{l1}^2\left\{\left(\frac{u_{l0}}{u_{l1}}\right)^2 - \left(\frac{u_{l2}}{u_{l1}}\right)^2 + \lambda_l\right\}(1-\alpha) - \frac{\rho_l}{2} f_W u_{l1}^2 \frac{4L}{D} + \frac{1}{2}\rho_g u_{g1}^2\left\{\left(\frac{u_{g2}}{u_{g1}}\right)^2 - \left(\frac{u_{g0}}{u_{g1}}\right)^2 + \lambda_g\right\}\alpha \quad (12)$$

Flow of gas phase

$$P_0 - P_2 = \frac{1}{2}\rho_g u_{g1}^2\left\{\left(\frac{u_{g2}}{u_{g1}}\right)^2 - \left(\frac{u_{g0}}{u_{g1}}\right)^2 + \lambda_g\right\} + \frac{\rho_g}{2}\frac{4L}{D\sqrt{\alpha}} f_i(u_{g1}+u_{l1})^2 + \rho_g gL + \{\rho_g g\alpha_2 + \rho_l g(1-\alpha_2)\}H \quad (13)$$

Here, the following can be assumed from the incompressibility of gas and water at the outlet of the channel as:

$$\frac{u_{g2}}{u_{g1}} \fallingdotseq 1 \quad \text{and} \quad \frac{u_{l0}}{u_{l1}} \fallingdotseq 1.$$

On the other hand, the terms $(u_{g0}/u_{g1})^2$, $(u_{l2}/U_{l1})^2$, λ_g, and λ_l can be neglected by considering $D \ll D_0$ and $D \ll D_2$, because:

$$\left(\frac{u_{g0}}{u_{g1}}\right)^2 = \left(\frac{D}{D_0}\right)^4\alpha^2, \quad \left(\frac{u_{l2}}{u_{l1}}\right)^2 = \left(\frac{D}{D_2}\right)^4(1-\alpha)^2,$$

$$\lambda_g = (D/D_0)^2\alpha, \quad \lambda_l = (D/D_2)^2(1-\alpha)$$

By eliminating the terms of pressure difference, $P_2 - P_0$, and the water level in the upper plenum, H, from Eqs. (12) and (13), the following correlation can be reduced by the relationship of flow areas, void fraction α, etc.,

$$\frac{2}{\alpha^{5/2}}\left\{j_g^* + \frac{\alpha}{1-\alpha}\left(\frac{\rho_g}{\rho_l}\right)^{1/2} j_l^*\right\}^2 f_i + \frac{2}{(1-\alpha)^2} j_l^{*2} f_W + \frac{1}{2}\left(\frac{D}{L}\right)\frac{1-\alpha}{\alpha^2} j_g^{*2} + \frac{1}{2}\left(\frac{D}{L}\right)\frac{1}{1-\alpha} j_l^{*2} = 1-\alpha \quad (14)$$

including the effect of channel dimensions, L and D. Here, j_g^* and j_l^* are defined as follows:

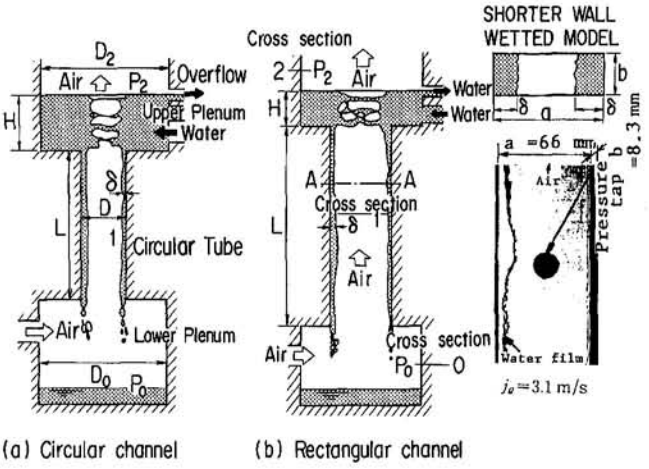


Fig. 4 Analytical flow models adopted in this study for circular and rectangular channels: (*a*) circular channel; (*b*) rectangular channel with observation results of the flow pattern

Downloaded 11 Dec 2010 to 193.140.21.150. Redistribution subject to ASME license or copyright; see http://www.asme.org/terms/Terms_Use.cfm

$$u_{g1} = \frac{j_g^*}{\alpha}\left(gD\frac{\rho_l - \rho_g}{\rho_g}\right)^{1/2},$$

$$u_{l1} = \frac{j_l^*}{1-\alpha}\left(gD\frac{\rho_l - \rho_g}{\rho_l}\right)^{1/2} \quad (15)$$

Here, when a situation is treated in which water is forcibly injected downward by a nozzle located at the top of circular tube as reported by Richter et al. (1979), a term expressing the effect of momentum of forcibly injected water downward into the tube is added as follows:

$$\frac{2f_i}{\alpha^{5/2}}\left\{j_g^* + \frac{\alpha}{1-\alpha}\left(\frac{\rho_g}{\rho_l}\right)^{1/2} j_l^*\right\}^2 + \frac{2f_w}{(1-\alpha)^2} j_l^{*2}$$

$$+ \frac{1}{2}\left(\frac{D}{L}\right)\frac{1-\alpha}{\alpha^2} j_g^{*2} + \frac{1}{2}\left(\frac{D}{L}\right)\frac{1}{1-\alpha} j_l^{*2}$$

$$= 1 - \alpha + \left(\frac{D}{L}\right)\frac{\pi}{4}\left(\frac{D^2}{A_i}\right) j_{l,\mathrm{IN}}^{*2} \quad (14')$$

where A_i is the flow area of water injection nozzle and $j_{l,\mathrm{IN}}^*$ is the dimensionless superficial average velocity of the injected water. It should be noted, in the case of water injection, that Eq. (14′) is valid only for $j_l^* \le j_{l,\mathrm{IN}}^*$ because more than the amount of injected water never falls down into the channel.

2 Rectangular Channel. Based on the flow patterns observed by Sudo et al. (1990), which are shown in Fig. 4(*b*), an analytical model for the air–water system could be developed in which only the shorter sides of wall become wet due to the falling water film flow in the vertical rectangular channel shown in Fig. 4(*b*). In the same way, as reduced in the case of circular tubes, the following correlation can be reduced by considering the momentum balances of two-phase flow across the entire length of the channel with interfacial friction factor f_i and wall friction factors f_{wg} and f_{wl} of air and water.

$$Zf_i\left\{j_g^* + \frac{1-X}{X}(\rho_g/\rho_l)^{1/2} j_l^*\right\}^2 \Big/ (1-X)^3$$

$$+ \frac{1}{2}\left(\frac{b}{L}\right) j_g^{*2} \Big/ (1-X)^2 + \frac{1}{2} Zf_{wl} j_l^{*2} \Big/ X^2$$

$$+ \frac{1}{2}\left(\frac{b}{L}\right) j_l^{*2} \Big/ X^2 + f_{wg} j_g^{*2} X/(1-X)^2 = X \quad (16)$$

where $X = 2\delta/a$ and $Z = b/a$, and j_g^* and j_l^* are defined as follows:

$$u_{g1} = \frac{ab}{b(a-2\delta)} j_g = \sqrt{gb}\{(\rho_l - \rho_g)/\rho_g\}^{1/2} j_g^*/(1-X)$$

$$U_{l1} = \frac{ab}{2b\delta} j_l = \sqrt{gb}\,\{(\rho_l - \rho_g)/\rho_l\}^{1/2} j_l^*/X \quad (17)$$

3 Annular Channel or Planar Channel. For the flow model of the saturated steam–water or air–water two-phase flow system in an annular or planar channel with water accumulation in the upper plenum or with simulation of cold leg injection of emergency core cooling water in PWR, as shown in Fig. 5, the following correlation could be reduced from the momentum balance across the entire length of the channel in the same way as in the case of the circular and rectangular channels:

$$\frac{f_i}{(1-x)^3}\left[j_g^* + \left(\frac{\rho_g}{\rho_l}\right)^{1/2}\cdot\frac{(1-x)}{x} j_l^*\right]^2 + \frac{f_{wl}}{x^2} j_l^{*2}$$

$$+ \frac{1}{2}\left(\frac{S}{L}\right)\frac{x}{(1-x)^2} j_g^{*2} + \frac{1}{2}\left(\frac{S}{L}\right)\frac{1}{x} j_l^{*2}$$

$$= x + \frac{S}{L}\left(\frac{WS}{A_i}\right) j_{l,\mathrm{IN}}^{*2} \quad (18)$$

where W is the circumference, S the gap size, $x = 2\delta/S$, A_i the flow area of the water injection nozzles, and j_g^* and j_l^* are defined as follows:

$$j_x^* = \frac{j_x}{\sqrt{gS(\rho_l - \rho_g)/\rho_x}} \quad (x = g, l) \quad (19)$$

In the case of water accumulation in the upper plenum, the second term in the right-hand side of Eq. (18) is neglected because the momentum flux of the injected water should be small enough. In addition, in case of subcooled water injection in the steam–water system, the effect of condensation of upward steam due to water subcooling can be estimated as follows regarding the average for the entire length of the channel:

$$\frac{f_i}{(1-x)^3}\left[\left\{j_g^* - k\cdot\Delta T_{\mathrm{IN}}^* j_l^*\left(\frac{\rho_l}{\rho_g}\right)^{1/2}\right\}\right.$$

$$\left. + \left(\frac{\rho_g}{\rho_l}\right)^{1/2}\frac{(1-x)}{x} j_l^*\right]^2 + \frac{f_{wl}}{x^2} j_l^{*2}(1 + k\cdot\Delta T_{\mathrm{IN}}^*)^2$$

$$+ \frac{1}{2}\left(\frac{S}{L}\right)\frac{x}{(1-x)^2}\left\{j_g^* - k\cdot\Delta T_{\mathrm{IN}}^* j_l^*\left(\frac{\rho_l}{\rho_g}\right)^{1/2}\right\}^2$$

$$+ \frac{1}{2}\left(\frac{S}{L}\right)\frac{1}{x} j_l^{*2}(1 + k\cdot\Delta T_{\mathrm{IN}}^*)^2$$

$$= x + \frac{S}{L}\left(\frac{WS}{A_i}\right) j_{l,\mathrm{IN}}^{*2} \quad (18')$$

where k is the condensation factor and ΔT_{IN}^* the dimensionless subcooling of injected water.

4 Friction Factors f_i, f_{wg}, f_{wl} Adopted. For the friction factor f_i of circular tubes, the following were used, referring and modifying the correlation proposed by Bharathan et al. (1979) based on their experiments:

$$\left.\begin{aligned} f_i &= 0.008\,\{1 + m_1(\delta/D_e)^n\} \\ m_1 &= 41.3\ \mathrm{Bo}^{(n+0.25)}\cdot 10^{9.07/\mathrm{Bo}} \\ n &= 1.63 + \frac{4.74}{\mathrm{Bo}} \\ \mathrm{Bo} &= \{(\rho_l - \rho_g)g/\sigma\}^{1/2}\cdot D_e \end{aligned}\right\} \quad (20)$$

Figure 6 shows the experimental results and correlation proposed by Bharathan et al. (1979), and Eq. (20) on m_1 versus δ/D. The correlation of Bharathan et al. predicts the experimental data for $\delta/D < 0.04$ well, but cannot predict well for $\delta/D > 0.04$, which is a major range of CCFL condition. So, Eq. (20) was newly introduced as an approximation for predicting the interfacial friction factor for $\delta/D > 0.04$ much better, as illustrated in Fig. 6. It should be mentioned here that the interfa-

Downloaded 11 Dec 2010 to 193.140.21.150. Redistribution subject to ASME license or copyright; see http://www.asme.org/terms/Terms_Use.cfm

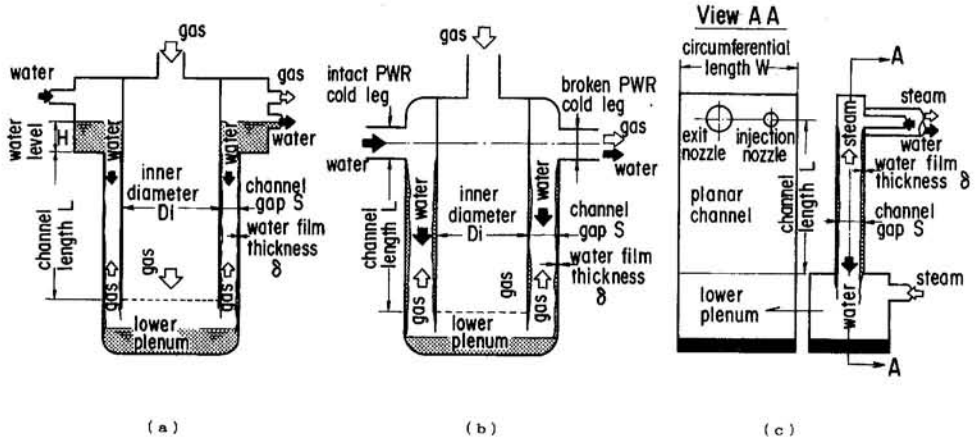


Fig. 5 Analytical flow model adopted in this study for annular and planar channels: (*a*) annular channel with water accumulation in upper plenum; (*b*) annular channel with top water injection; (c) planar channel with top water injection

cial shear stress at the steam–water interface might be different from that at the air–water interface, especially in the case of condensation, but in this study the correlation of shear stress at the air–water interface was applied to the steam–water interface in case of condensation for convenience.

For the wall friction factors of water film flow and gas flow along the wall, f_{wl} and f_{wg}, Eq. (21) was applied corresponding to each flow regime, that is, laminar, transition, and turbulent flows, respectively. The regime was determined by the value of Re for water or gas.

$$f_{wX} = A_1 \cdot \mathrm{Re}_{X^1}^{B} \ (X = g, l)$$

$$\mathrm{Re}_X < 2000 \text{ (laminar)} \quad A_1 = 16.0, \quad B_1 = -1.0$$

$$2000 \le \mathrm{Re}_X \le 4000 \text{ (transition)}$$

$$A_1 = 1.76 \times 10^{-10}, \quad B_1 = 2.32$$

$$\mathrm{Re}_X > 4000 \text{ (turbulent)} \quad A_1 = 0.314, \quad B_1 = -0.25 \quad (21)$$

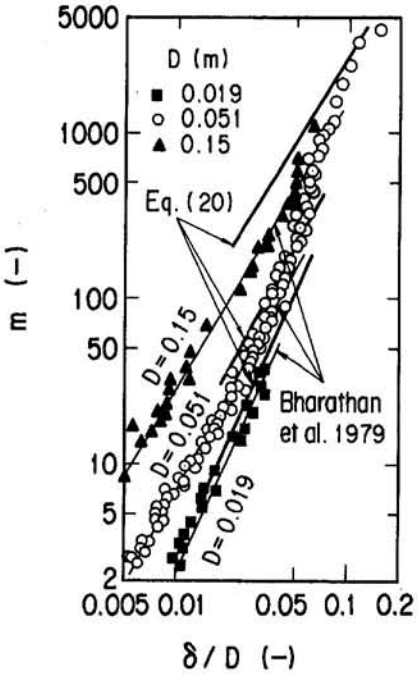


Fig. 6 Evaluation of the effects of the Bond number regarding the interfacial friction factor based on existing experimental results (Bharathan et al., 1979).

It should be noted here that in the rectangular channel, the friction factors f_{wl} and f_{wg} use $2a$ and $2b$, respectively, for representative lengths in Re, because flow patterns showed that the shorter sides were wet, as has been already described. Furthermore, equivalent hydraulic diameter $2a$ is used for D in f_i of Eq. (20) and the effect of gap size b is considered in m_1 of friction factor f_i as seen below, giving the tendency of experiment obtained by Sudo et al. (1990) that larger gap size b gives larger m_1:

$$m_1 = 44.38 \cdot \mathrm{Bo}_a^n \cdot \mathrm{Bo}_b^{0.55} \cdot 10^{9.07/\mathrm{Bo}_a} \quad (22)$$

where

$$\mathrm{Bo}_a = \{(\rho_l - \rho_g) \cdot g/\sigma\}^{0.5} \cdot 2a,$$

$$\mathrm{Bo}_b = \{(\rho_l - \rho_g) \cdot g/\sigma\}^{0.5} \cdot 2b.$$

In the case of an annular or planar channel, the equivalent hydraulic diameter $2S$ is used for De in f_i of Eq. (20) and in addition, m and Bo in Eq. (20) are evaluated as follows for estimating f_i, which is used in both Eqs. (18) and (18′):

$$m_1 = 41.3 \cdot \mathrm{Bo}^{(n+0.25)} \cdot 10^{9.07/\mathrm{Bo}},$$

$$\mathrm{Bo} = \{(\rho_l - \rho_g) \cdot g/\sigma\}^{0.5} \cdot 2S.$$

For evaluating thermal properties in the correlations already described for condensation, the saturation temperature was adopted for σ, ρ_g, and ν_g, and on the other hand, the averaged saturation temperature and temperature of water injected into the test channel for ρ_l and ν_l.

5 CCFL Condition and Feature of Analytical Model. In this study, it is assumed that the CCFL condition is given by an envelope of curves from Eqs. (14) or (14′), (16), (18) or (18′) with respect to void fraction α or dimensionless water film thickness x. It should be noticed that this criterion is equivalent to the CCFL condition that is given by maximizing j_l^* of Eq. (14) and so on with respect to α or x, with other parameters being constant, that is, $\partial j_l^*/\partial\alpha = 0$.

As the general feature of the model described above, the following are pointed out:

1 The larger f_i, f_{wg}, and f_{wl} give a smaller j_l^* for the same j_g^*.
2 The larger D/L, b/a, and b/L, or S/L give a smaller j_l^* for the same j_g^* when no water is injected forcibly into the channel.
3 When water is injected forcibly into the channel gives a much larger j_l^* for the same j_g^* than the case of water not being injected forcibly into the channel.

Downloaded 11 Dec 2010 to 193.140.21.150. Redistribution subject to ASME license or copyright; see http://www.asme.org/terms/Terms_Use.cfm

Table 1 Major test conditions of previous experiments investigated in this study

No.	Type of channel	Fluids	Channel length, L (m)	Diameter, D or D_i/D_o (m)	Channel width, W (m)	Gap, b or S (m)	Injection rate $j^*_{f,IN}$	Inlet water subcooling, ΔT_{in} (K)	Reference
1	Circular	Air–water	0.013–1.52	0.019–0.14	—	—	—	—	Richter (1981)
2	Circular	Air–water	1.22	0.254	—	—	0–0.096	—	Richter et al. (1979)
3	Rectangular	Air–water	0.36–0.78	—	0.033–0.066	0.0023–0.0123	—	—	Sudo et al. (1990)
4	Annular	Air–water	1.02	0.39/0.45	—	0.0254	—	—	Richter et al. (1979)
5	Annular	Air–water	1.02	0.34/0.45	—	0.0508	—	—	Richter et al. (1979)
6	Annular	Air–water	1.04	0.28/0.31	—	0.015	0.15–1.19	—	Collier et al. (1978)
7	Annular	Air–water	1.04	0.56/0.62	—	0.0312	0.47–1.25	—	Collier et al. (1978)
8	Planar	Steam–water	0.46	—	0.914	0.0064–0.0508	0.06–1.93	0–81	Crowley and Block (1975)

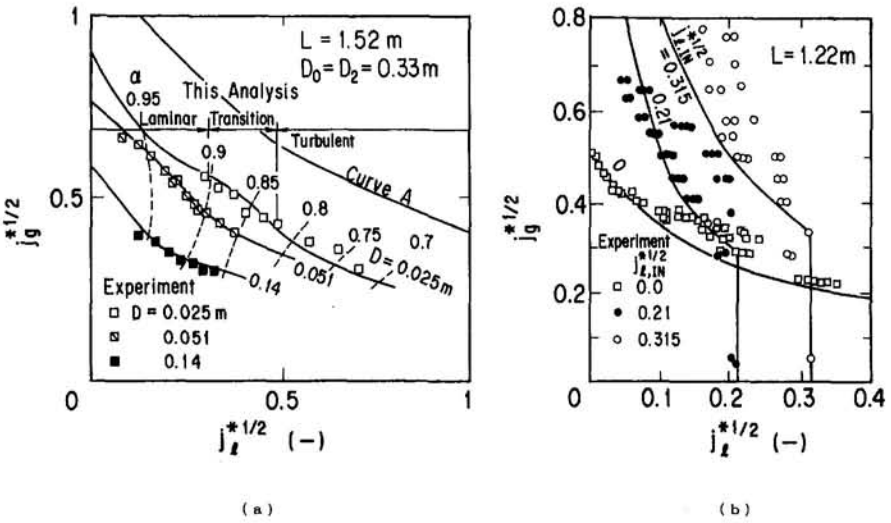


Fig. 7 Comparisons between analytical results of this study with the existing experimental results (Richter, 1981, Richter et al., 1979) for a circular channel: (*a*) effect of channel diameter under water accumulation in the upper plenum; (*b*) effect of mass flux of injected water under top water injection

4 The larger subcooling of injected water gives a much larger j_f^* for the same j_g^*.

Analytical Results and Discussion

Table 1 shows the major test conditions of the previous experiments at atmospheric pressure investigated in this study. In the following, the analytical results were compared with experimental ones after discussion.

1 Circular Tubes for Air–Water Systems. Figure 7(*a*) shows a comparison regarding $j_g^{*1/2}$ versus $j_f^{*1/2}$ between the results of this study by Eq. (14) and the experimental results of vertical circular tubes of $L = 1.52$ m and $D = 0.025$, 0.051, and 0.14 m by Richter (1981). In this figure, void fraction is shown as a parameter on the analytical results and the flow regime of water film flow is also shown due to the analytical results of $D = 0.025$ m. The analytical results and experiments are in good agreement, clearly identifying the effect of diameter in which a smaller diameter gives a larger j_f^* for the same j_g^*. As a reference, Curve A shows the analytical results of Eq. (14) with friction factors f_i and f_{wl} proposed by Bharathan et al. (1979), but the coincidence between the analytical and experimental results is not very good. Figure 7(*b*) shows the effect of mass flux of injected water for $j_g^{*1/2}$ versus $j_f^{*1/2}$, comparing the results of this study using Eq. (14′) and the experiments of $L = 1.22$ m and $D = 0.25$ m with water injection by a top nozzle having a diameter of 0.025 m (Richter et al., 1979). In this figure, $j_{f,IN}^{*1/2}$ is adopted as the parameter on mass flux of injected water. The case of $j_{f,IN}^{*1/2} = 0.0$ shows in this figure that no water is injected forcibly into the channel, but sufficient water is supplied to accumulate in the upper plenum of the channel. Also, in this case, the coincidence is very good between the analytical and experimental results, showing clearly the effect of mass flux of injected water: The larger mass flux of injected water gives a larger j_f^* for the same j_g^*. It should be noted here that j_f^* is less than or equal to $j_{f,IN}^*$ in case of

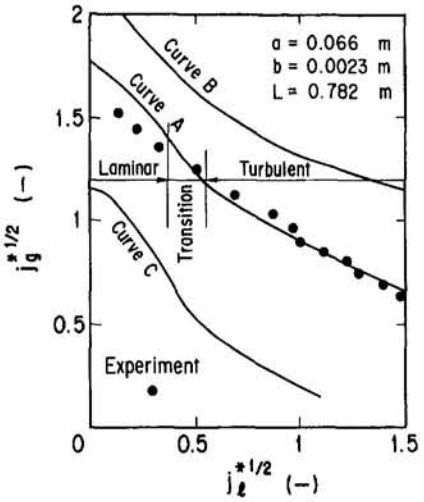


Fig. 8 Comparisons among analytical results of this study, those of previous models, and experimental results (Sudo et al., 1990) for a rectangular channel

Downloaded 11 Dec 2010 to 193.140.21.150. Redistribution subject to ASME license or copyright; see http://www.asme.org/terms/Terms_Use.cfm

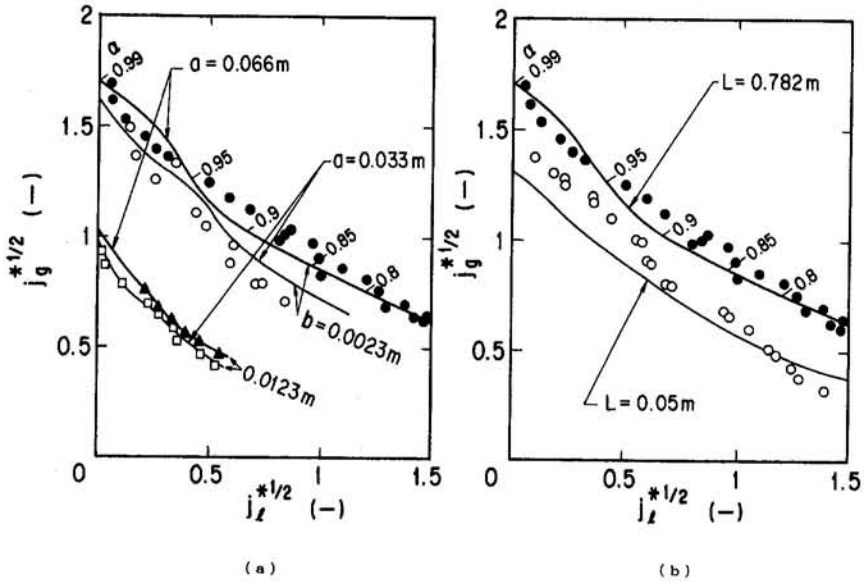


Fig. 9 Comparisons between the analytical results of this study and previous experimental results (Sudo et al., 1990) for rectangular channels: (*a*) effects of channel gap size and channel width for channel length of 0.782 m; (*b*) effect of channel length for a gap size of 0.0023 m and a width of 0.066 m

$j_{l,\mathrm{IN}}^{*1/2}$ = 0.21 and 0.315 because more than the amount of injected water does not fall, as has already been mentioned.

2 Rectangular Channels for Air–Water Systems. Figure 8 shows a comparison between the analytical results of this study and the experimental ones of Sudo et al. (1990) for the vertical rectangular channel with L = 0.782 m, a = 0.066 m and b = 0.0023 m. Curve A shows the results by Eq. (16), giving the flow regime of water film flow. For reference, Curve B shows the analytical results with f_i and f_{wl} (= 0.005) proposed by Bharathan et al. (1979) and Curve C shows the analytical results based on the flow model in which all walls of channel are uniformly wet due to falling water. It can be clearly understood that the analytical results of this study given by Eq. (16) give good predictions regarding the experimental results.

Figures 9(*a*) and 9(*b*) show the effects of the channel gap size, channel width, and the length of the rectangular channels by a comparison of the analytical results of this study with the experimental results of a = 0.033 and 0.066 m, b = 0.0023 and 0.0123 m, and L = 0.05 and 0.782 m found by Sudo et al. (1990). The analytical results are in good agreement with the experimental results, clearly showing the effects of the channel dimension in which the larger width a, smaller gap size b, and longer length L give a larger j_l^* for the same j_g^* in the rectangular channels.

Figures 10(*a*) and 10(*b*) show comparisons between the analytical results of this study and experimental ones by Richter (1981) for circular tubes and by Sudo et al. (1990) for the rectangular channel, respectively, on the complete bypass condition in which no water falls down at all toward the upward gas flow. In these figures, for reference, is shown the correlation of Ku_g = 3.2 proposed by Pushkina and Solokin (1969), while $\mathrm{Ku}_g = j_g^* \cdot \mathrm{Bo}^{1/2}$. The analytical results on complete bypass condition depend on channel length L, and in the test conditions investigated in this study the analytical results of this study as well as the correlation of Ku_g = 3.2 give good predictions as regards the experimental results both for circular and rectangular channels.

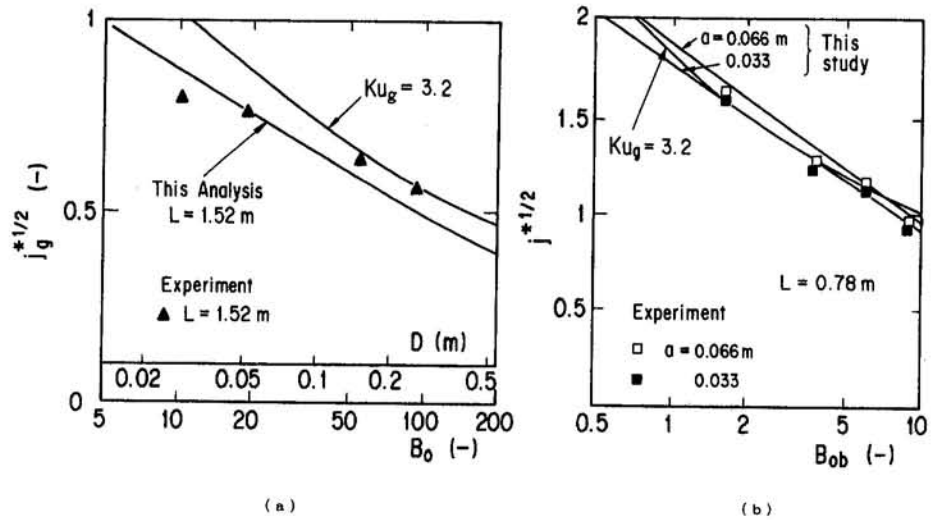


Fig. 10 Comparisons between analytical results of this study and previous experimental results (Richter, 1981, and Sudo et al., 1990) on the complete bypass conditions for circular and rectangular channels: (*a*) circular channel; (*b*) rectangular channel

Downloaded 11 Dec 2010 to 193.140.21.150. Redistribution subject to ASME license or copyright; see http://www.asme.org/terms/Terms_Use.cfm

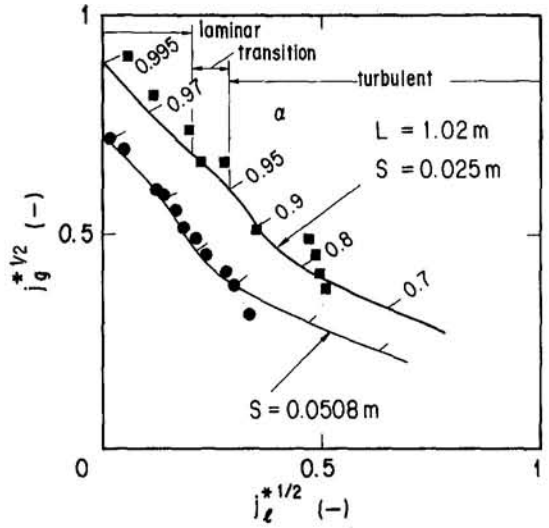


Fig. 11 Comparisons between analytical results of this study and previous experimental results (Richter et al., 1979) with respect to the effects of a channel gap for an annular channel with water accumulation in the upper plenumm

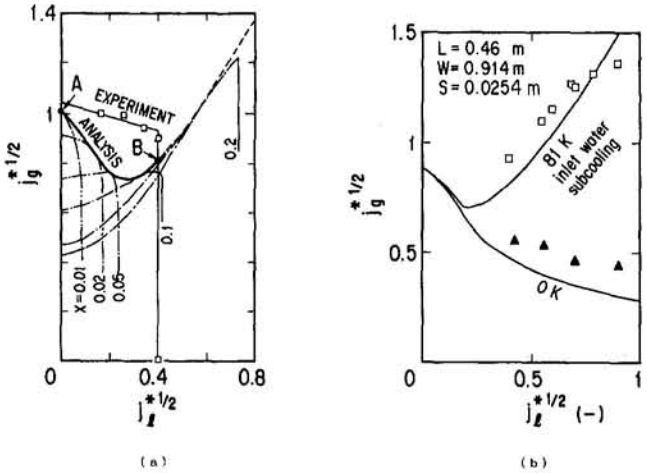


Fig. 13 Comparisons between the analytical results of this study and previous experimental results (Crowley and Block, 1975) with respect to the effects of an inlet water subcooling for planar channel: (*a*) $j_g^{*1/2}$ versus $j_l^{*1/2}$ for a planar channel with a gap of 0.0254 m, a width of 0.914 m, a length of 0.46 m, $j_{l,\text{IN}}^*$ of 0.16 and an inlet water subcooling of 81 K; (*b*) effects of inlet water subcooling and mass flux of injected water on the complete dumping conditions for a planar channel with a gap of 0.0254 m, a width of 0.914 m, and a length of 0.46 m

3 Annular or Planar Channel for Air– or Steam–Water System. Figure 11 shows a comparison between the analytical results of this study from Eq. (18) and the results of the experiments with annular channels of L = 1.02 m, S = 0.025, and 0.0508 m for air–water systems conducted by Richter et al. (1979). In this analysis, the second term on the right-hand side of Eq. (18) was neglected because the experiments were carried out without forced water injection. In this figure, the flow regime is indicated for the water film flow. The void fraction is shown for analysis of the channel whose gap size is 0.025 m for reference. The analytical results are in good agreement with the experimental ones, showing clearly the effect of gap size in which the smaller gap gives a larger j_l^* for the same j_g^*.

Figures 12(*a*) and 12(*b*) show comparisons regarding the effect of mass flux of injected water $j_{l,\text{IN}}^*$ between the analytical results of this study from Eq. (18) and the results of the experiments for the air–water system in an annular channel of L = 1.04 m and S = 0.015 m by Collier et al. (1978) and for saturated steam–water systems in a planar channel of L = 0.46 m, W = 0.914 m and S = 0.0254 m by Crowley and Block (1975), respectively. For both figures, Curves A give the analytical results of $j_{l,\text{IN}}^*$ = 0.0 as a reference. The analytical results agree fairly well with the experimental ones, showing the same tendency as the experiments in which a larger $j_{l,\text{IN}}^*$ gives a larger j_l^* for the same j_g^*.

With respect to the effect of inlet water subcooling, Fig. 13(*a*) shows a comparison of $j_g^{*1/2}$ versus $j_l^{*1/2}$ between the analytical results of this study from Eq. (18′) and the results of the experiments for a planar channel of L = 0.46 m, S = 0.0254 m, and W = 0.914 m with $j_{l,\text{IN}}^*$ = 0.16 conducted by Crowley and Block (1975). The analytical results are shown by a bold line, which is an envelope for the curves given by Eq. (18′) with respect to $x = 2\delta/S$. As the value for condensation factor k in Eq. (18′), 0.5 is adopted in this comparison. In Fig. 13(*a*), points A and B show the conditions of a complete

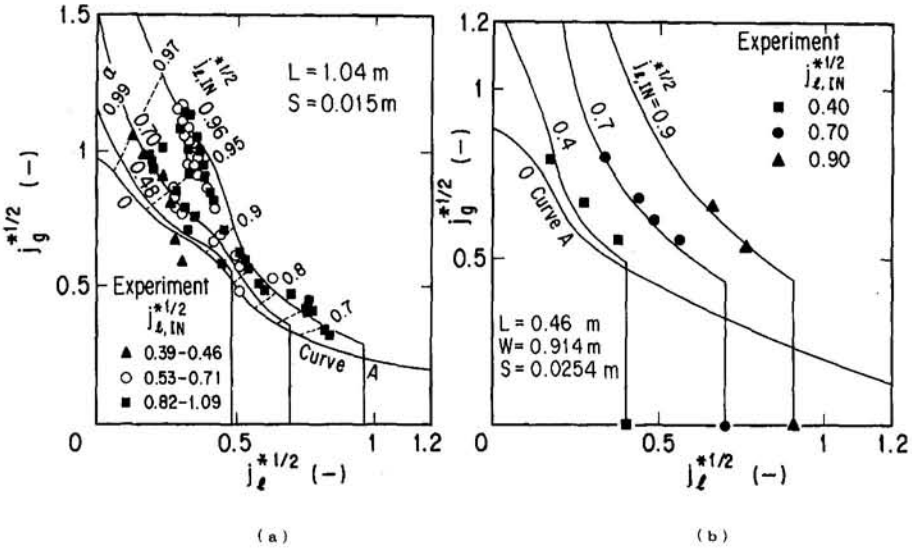


Fig. 12 Comparisons between analytical results of this study and previous experimental results (Collier et al., 1978, and Crowley and Block, 1975) with respect to the effects of mass flux of injected water for annular and planar channels: (*a*) annular channel with air–water two-phase flow; (*b*) planar channel with saturated steam–water two-phase flow

Downloaded 11 Dec 2010 to 193.140.21.150. Redistribution subject to ASME license or copyright; see http://www.asme.org/terms/Terms_Use.cfm

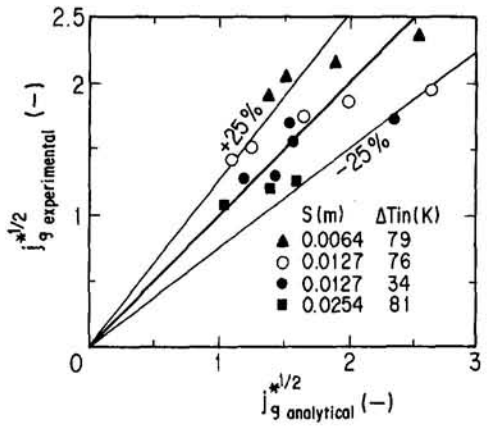


Fig. 14 Comparisons between analytical results of this study and previous experimental results (Crowley and Block, 1975) on the complete bypass condition for a planar channel

bypass in which no water falls down and complete dumping in which all the injected water falls down. The analytical results agree well with the conditions of a complete bypass and complete dumping, but there is a rather poor prediction between the two conditions. Figure 13(*b*) shows a comparison regarding the effect of inlet water subcooling to complete dumping conditions between analytical results and experimental ones for the same dimension of the channel. The analytical results also are in fairly good agreement with the experimental ones, showing clearly the same tendency as the experiment in which the larger subcooling gives a larger j_f^* for the same j_g^*.

With respect to the effect of inlet water subcooling regarding the complete bypass condition, however, Fig. 14 shows a comparison for j_g^* at the complete bypass between the analysis and experiments by Crowley and Block (1975). The analysis is in fairly good agreement with the experimental results for $j_g^{*1/2}$ with an error of about ±25 percent.

Conclusion

In this study, the mechanism of CCFL was investigated analytically and the conditions for CCFL were evaluated quantitatively. As a new analytical model common to any channel of circular, rectangular, annular, or planar channels, a completely separated two-phase flow model with water film flow along the wall was successfully proposed, based on the momentum balance equation applied for the entire length of the channels systematically, including the effects of interfacial and wall friction, channel configuration, channel dimensions of diameter, gap size, circumferential length, and entire channel length, water injection mode, and injected water mass flux.

As a result, it was found that the analytical results thus proposed could give good quantitative predictions regarding the existing CCFL experimental results of an air–water system for vertical circular tubes of 0.019 to 0.254 m in diameter and 0.0127 to 1.52 m in length and vertical rectangular channels of 0.033 and 0.066 m in width, 0.0023 to 0.0123 m in gap size, and 0.05 to 0.782 m in length as well as the experimental results of air–water and steam–water systems for annular and planar channels of 0.914 to 1.85 m in circumference, 0.0127 to 0.0508 m in gap size, 0.46 to 1.04 m in length, and inlet water subcooling of 0 to 81 K under atmospheric pressure, identifying clearly effects of predominant parameters in the CCFL condition in each type of channel.

It was also clarified that the analytical model applied for the entire length of the channel proposed in this study was the most effective for evaluating the effects of the channel length, mass flux, and inlet subcooling of water injected forcedly injected into the channel, which had not been considered sufficiently in the previous studies.

References

Bharathan, D., Wallis, G. B., and Richter, H. J., 1979, "Air–Water Countercurrent Two-Phase Flow," EPRI Rep. No. NP-1165.

Chang, S. H., Baek, W-P., and Bae, T. M., 1991, "A Study of Critical Heat Flux for Low Flow of Water in Vertical Round Tubes Under Low Pressure," *Nuclear Eng. & Design,* Vol. 132, pp. 225–237.

Cheng, L. Y., 1990, "Countercurrent Flow Limitation in Thin Rectangular Channels," *Proc. Int. Topical Mtg. on Safety Status and Future Non-commercial React. and Irradiat. Facilit.,* ANS, pp. 671–678.

Collier, R. P., et al., 1978, "Steam-Water Mixing and System Hydrodynamics Program," NUREG/CR-0526, BMI-2011.

Crowley, C. J., and Block, J. A., 1975, "ECC Delivery Study, Experimental Results and Discussion," Creare Technical Note, TN-217.

Crowley, C. J., Block, J. A., and Rothe, P. H., 1976, "An Evaluation of Scaling Parameters for ECC Penetration Data," Creare Technical Note, TN-217.

El-Genk, M. S., Haynes, S. J., and Kim, S-H., 1988, "Experimental Studies of Critical Heat Flux for Low Flow of Water in Vertical Annuli at Near Atmospheric Pressure," *Int. J. Heat Mass Transf.,* Vol. 31-11, pp. 2291–2304.

Frea, W. J., 1970, "Two-Phase Heat Transfer and Flooding in Countercurrent Flow," presented at the 4th Int. Heat Transfer Conf., Paris, Vol. B5, No. 10.

Graham, G., 1975, "Summary of Recent Thayer School Annulus Penetration Results, Memorandom," Thayer School of Engineering, Dartmouth College, Hanover, NH.

Katto, Y., and Hirao, T., 1991, "Critical Heat Flux of Counter-flow Boiling in a Uniformly Heated Vertical Tube With a Closed Bottom," *Int. J. Heat Mass Transf.,* Vol. 34-4/5, pp. 993–1001.

Kusuda, H., and Imura, H., 1974, "Stability of a Liquid Film in a Countercurrent Annular Two-Phase Flow," *Bulletin of the JSME,* Vol. 17-114, pp. 1613–1618.

Mishima, K., 1984, "Boiling Burnout at Low Flow Rate and Low Pressure Conditions," Ph.D. Thesis, Kyoto Univ., Japan.

Motomura, T., Kurosawa, A., Otsuji, T., Mishima, K., Hibiki, T., and Nishihara, H., 1993, "Critical Heat Flux Experiment in a Narrow Vertical Rectangular Channel Heated From One-Side at Atmospheric Pressure," presented at the 1993 Fall Mtg. of the AES of Japan, Paper No. A26.

Osakabe, M., and Kawasaki, Y., 1989, "Top Flooding in Thin Rectangular and Annular Passages," *Int. J. Multiphase Flow,* Vol. 15-5, pp. 747–754.

Pushkina, O. L., and Solokin, Y. L., 1969, "Breakdown of Liquid Film Motion in Vertical Tubes," *Heat Transf. Soviet Research,* Vol. 1–5, pp. 56–64.

Richter, H. J., Wallis, G. B., and Speers, M. S., 1979, "Effect of Scale on Two-Phase Countercurrent Flow Flooding," NUREG/CR-0312.

Richter, H. J., 1981, "Flooding in Tubes and Annuli," *Int. J. Multiphase Flow,* Vol. 7, pp. 647–658.

Sudo, Y., and Kaminaga, M., 1989, "A CHF Characteristics for Downward Flow in a Narrow Vertical Rectangular Channel Heated From Both Sides," *Int. J. Multiphase Flow,* Vol. 15-5, pp. 755–766.

Sudo, Y., 1984, "Parameter Effects of Downcomer Penetration of ECC Water in PWR-LOCA," *J. Nucl. Sci. Technol.,* Vol. 22-1, pp. 32–41.

Sudo, Y., and Ohnuki, A., 1984, "Mechanism of Falling Water Limitation Under Countercurrent Flow Through a Vertical Flow Path," *Bulletin of JSME,* Vol. 27-226, pp. 708–716.

Sudo, Y., Miyata, K., Ikawa, H., Kaminaga, M., and Ohkawara, M., 1985, "Experimental Study of Differences in DNB Heat Flux Between Upflow and Downflow in Vertical Rectangular Channel," *J. Nucl. Sci. Technol.,* Vol. 22-7, pp. 604–618.

Sudo, Y., Usui, T., and Kaminaga, M., 1990, "Experimental Study of Falling Water Limitation Under a Countercurrent Flow in a Vertical Rectangular Channel (1st Report, Effect of Flow Channel Configuration and Introduction of CCFL Correlation)," *JSME Int. J.,* Ser. II, Vol. 34-2, pp. 169–174.

Wallis, G. B., 1969, *One-Dimensional Two-Phase Flow,* McGraw-Hill, New York, pp. 336–339.

Downloaded 11 Dec 2010 to 193.140.21.150. Redistribution subject to ASME license or copyright; see http://www.asme.org/terms/Terms_Use.cfm

Fluid Flow Effects in Evaporation From Liquid–Vapor Meniscus

D. Khrustalev

A. Faghri

Department of Mechanical Engineering,
University of Connecticut,
Storrs, CT 06269

A mathematical model of the evaporating liquid–vapor meniscus in a capillary slot has been developed. The model includes two-dimensional steady-state momentum conservation and energy equations for both the vapor and liquid phases, and incorporates the existing simplified one-dimensional model of the evaporating microfilm. The numerical results, obtained for water, demonstrate the importance of accounting for the fluid flow in calculating the effective evaporative heat transfer coefficient and the superheat of the vapor over the liquid–vapor meniscus due to the heat transfer from the heated wall. With higher heat fluxes, a recirculation zone appears in the vapor near the heated wall due to extensive evaporation in the thin-film region of the liquid–vapor meniscus.

1 Introduction

Heat transfer during evaporation of liquid from the liquid–vapor meniscus attached to the heated solid wall has been considered by many investigators due to its importance in predicting the performance characteristics of various two-phase devices with capillary structures such as heat pipes, evaporators, heat sinks, and separators. Potash and Wayner (1972), Schneider et al. (1976), Holm and Goplen (1979), and Solov'ev and Kovalev (1984) demonstrated the importance of the thin-film region of a liquid–vapor meniscus in the overall heat transfer during evaporation. Heat transfer in evaporating microfilm and the influence of disjoining pressure was considered in various aspects by P. Wayner, Jr., and co-authors. The variation of heat transfer coefficients along the liquid microfilm was modeled by Wayner et al. (1976). Kamotani (1978), Stephan and Busse (1992), Stephan (1992), and Khrustalev and Faghri (1995) emphasized temperature variation at the liquid free surface of the microfilm while modeling evaporative heat transfer on capillary-grooved surfaces. The temperature of the saturated vapor over the liquid–vapor interface was assumed constant, which resulted in a constant temperature for the meniscus liquid–vapor interface, except in the microfilm region. The vapor was assumed saturated over the interface with constant pressure, p_v, and temperature, $T_v = T_{sat}(p_v)$. In fact, this assumption was made in all previous models of evaporating menisci in the absence of noncondensible gas. All of the above-mentioned works did not consider the flow and heat transfer in the vapor over the interface. Only heat transfer due to conduction in the liquid was considered. However, at high heat fluxes, fluid flow becomes important. The superheat of the vapor exiting the metal capillary structure of a heat pipe evaporator due to the heat transfer between the vapor and the heated structure should also be taken into account in heat pipe numerical simulation.

The objective of the present analysis is to investigate the influence of the liquid and vapor flows on the heat transfer in evaporation from the liquid–vapor meniscus and to evaluate the vapor flow patterns numerically in a narrow passage over the curved interface. Evaporation of liquids from capillary grooves, pores, and slots takes place due to the solid wall superheat. The temperature of the solid–liquid interface, T_w, is higher than that of the vapor–liquid interface. Since the solid wall thermal conductivity is significantly higher than that of liquid in many technical applications, constant wall temperature is assumed in the present analysis. The solid wall in the vicinity of the interline, which is an apparent liquid–vapor–solid boundary, can be dry or covered with nonevaporating liquid film; in both cases, the temperature of the solid wall or of the nonevaporating liquid free surface is T_w. Since the temperature of the vapor over the evaporating meniscus is lower than T_w, the vapor is affected by the superheated wall and/or liquid and becomes superheated itself. This means that the temperature of the vapor some distance from the liquid–vapor interface can be higher than $T_{sat}(p_v)$. Note that for comparatively thick liquid films ($\delta \geq 1$ μm) the liquid–vapor interface temperature is very close to the vapor temperature. This is due to the fact that the interfacial thermal resistance is small compared to that of the liquid films (Khrustalev and Faghri, 1995). Based on this consideration, the momentum conservation and energy equations for the evaporating liquid and vapor over the liquid–vapor interface are included in the present model of the evaporating extended meniscus.

2 Mathematical Model of Evaporating Meniscus in a Narrow Slot

The evaporation of the liquid from the liquid–vapor meniscus interface in a narrow slot considered in the present paper is illustrated by Fig. 1. Gravitational body forces are negligible compared to surface tension forces due to small size of the meniscus. It is assumed that the liquid–vapor interface curvature is constant: $K = 1/R_{men}$. This assumption can be justified by the results of Swanson and Peterson (1994) where one-sided formulation of the heat transfer and flow in liquid was used. Actually, the curvature of the liquid–vapor interface of the evaporating nonisothermal meniscus is not exactly constant, especially in the microfilm region. However, the assumption of constant curvature of the interface is sufficient to model the heat transfer and flow in the vapor phase over the evaporating meniscus. In the present paper, the evaporating microfilm is the thin-film part of the meniscus where the disjoining pressure is significant and the temperature of the liquid–vapor interface differs from that of the vapor phase over the given point of the interface. This microfilm is considered using the approach of Khrustalev and Faghri (1995), while the fluid flow and heat transfer in the major part of the domain shown in Fig. 1 is treated by two-dimensional analysis. A special control volume

Contributed by the Heat Transfer Division and presented at the National Heat Transfer Conference, Houston, Texas, August 3–5, 1996. Manuscript received by the Heat Transfer Division November 24, 1995; revision received May 1, 1996. Keywords: Evaporation, Heat Pipes and Thermosyphons, Phase-Change Phenomena. Associate Technical Editor: J. R. Howell.

Copyright © 1996 by ASME

Downloaded 11 Dec 2010 to 193.140.21.150. Redistribution subject to ASME license or copyright; see http://www.asme.org/terms/Terms_Use.cfm

for the microfilm part of the meniscus has been developed to include the characteristics of the microfilm in the two-dimensional analysis.

2.1 Governing Equations for the Two-Dimensional Analysis. For an incompressible fluid with constant vapor and liquid viscosities and temperature-dependent vapor density, the continuity and momentum equations for both the vapor and liquid are:

$$\frac{\partial u}{\partial x} + \frac{\partial v}{\partial y} = 0 \tag{1}$$

$$\rho\left(u\frac{\partial u}{\partial x} + v\frac{\partial u}{\partial y}\right) = -\frac{\partial p}{\partial x} + \mu\left(\frac{\partial^2 u}{\partial x^2} + \frac{\partial^2 u}{\partial y^2}\right) \tag{2}$$

$$\rho\left(u\frac{\partial v}{\partial x} + v\frac{\partial v}{\partial y}\right) = -\frac{\partial p}{\partial y} + \mu\left(\frac{\partial^2 v}{\partial x^2} + \frac{\partial^2 v}{\partial y^2}\right) \tag{3}$$

The energy equation for both the vapor and liquid is

$$\rho c_p\left(u\frac{\partial T}{\partial x} + v\frac{\partial T}{\partial y}\right) = k\left(\frac{\partial^2 T}{\partial x^2} + \frac{\partial^2 T}{\partial y^2}\right) \tag{4}$$

2.2 Boundary Conditions. The wall temperature is assumed constant (except for the control volume enclosing the microfilm):

$$T|_{x=0} = T_w \tag{5}$$

The inlet flow temperature is known:

$$T|_{y=0} = T_w \tag{6}$$

No-slip conditions at the wall are assumed:

$$u|_{x=0} = v|_{x=0} = 0 \tag{7}$$

At the inlet, the parabolic velocity profile is assumed given from the solution of the Stokes equation for viscous flows:

$$u|_{y=0} = 0 \tag{8}$$

$$v|_{y=0} = \frac{3\dot{m}_{l,in}}{2\rho_l}\frac{x}{X_L^3}(2X_L - x) \tag{9}$$

At the symmetry line, $x = X_L$, $u = 0$, $dv/dx = 0$, and $dT/dx = 0$.

2.3 Consideration of the Interface. The heat transported from the liquid to a vapor rectangular control volume at the interface by heat conduction and liquid flow in the neighboring liquid control volumes (from the left and/or from the bottom) is denoted as $\dot{Q}_{l,\text{int}}$. For the typical vapor control volume with adjacent left and bottom liquid control volumes shown in Fig. 1(*b*), $\dot{Q}_{l,\text{int}}$ can be expressed as follows:

$$\dot{Q}_{l,\text{int}} = -k_l\left[\left.\frac{\partial T_l}{\partial x}\right|_{(i^-)}\Delta y + \left.\frac{\partial T_l}{\partial y}\right|_{(j^-)}\Delta x\right] + \rho_l c_{p,l}(T_l v_l|_{(j^-)}\Delta x + T_l u_l|_{(i^-)}\Delta y) \tag{10}$$

The heat transported from the interfacial vapor control volume is denoted as $\dot{Q}_{v,\text{int}}$:

$$\dot{Q}_{v,\text{int}} = -k_v\left[\left.\frac{\partial T_v}{\partial x}\right|_{(i^+)}\Delta y + \left.\frac{\partial T_v}{\partial y}\right|_{(j^+)}\Delta x\right] + \rho_v c_{p,v}(T_v v_v|_{(j^+)}\Delta x + T_v u_v|_{(i^+)}\Delta y) + h_{fg}\rho_v(u_v|_{(i^-)}\Delta y + v_v|_{(j^-)}\Delta x) \tag{11}$$

Note that Eqs. (10) and (11) are written for a vapor control volume at the interface with respect to the numerical scheme used, similarly to Cao and Faghri (1990), and Voller et al. (1989). For steady state, $\dot{Q}_{v,\text{int}} = \dot{Q}_{l,\text{int}}$. Conservation of mass at the interface takes the form

$$\rho_v u_v|_{(i^-)} = \rho_l u_l|_{(i^-)}, \quad \rho_v v_v|_{(j^-)} = \rho_l v_l|_{(j^-)} \tag{12}$$

The vapor velocities at the liquid–vapor faces of the interfacial vapor control volumes due to the phase change are redefined at every step of the numerical procedure by taking into account the inclination of the liquid–vapor interface in a manner consistent with Eqs. (10)–(11):

$$u'_{v,\text{int}}(i,j) = \frac{[\dot{Q}_{l,\text{int}} - \dot{Q}_{v,\text{int}} + h_{fg}\rho_v(u_v|_{(i^-)}\Delta y + v_v|_{(j^-)}\Delta x)]}{h_{fg}\rho_v\Delta y} \times \frac{\sin\gamma}{\sin\gamma + \cos\gamma} \tag{13}$$

$$v'_{v,\text{int}}(i,j) = \frac{[\dot{Q}_{l,\text{int}} - \dot{Q}_{v,\text{int}} + h_{fg}\rho_v(u_v|_{(i^-)}\Delta y + v_v|_{(j^-)}\Delta x)]}{h_{fg}\rho_v\Delta x} \times \frac{\cos\gamma}{\sin\gamma + \cos\gamma} \tag{14}$$

Nomenclature

c_p = specific heat at constant pressure, J/(kg-K)
h_{fg} = latent heat of vaporization, J/kg
h = heat transfer coefficient, W/(m^2-K)
i, j = indices of a grid point
K = curvature, 1/m
k = thermal conductivity, W/(m-K)
$\dot{m}$ = mass flow rate, kg/(s-m)
p = pressure, Pa
p_d = disjoining pressure, Pa
$\dot{Q}$ = heat flow rate, W/m
R_g = gas constant, J/(kg-K)
R_{men} = radius of curvature of the meniscus, m
T = temperature, K
T_{sat} = saturated vapor temperature at the liquid–vapor interface, K
$\mathbf{V}$ = velocity vector, m/s
v = velocity in the y direction, m/s
u = velocity in the x direction, m/s
X_L = slot half-width, m
x, y = coordinates, m
$\Delta x, \Delta y$ = dimensions of a control volume, m
Y_L = length of the computational domain, m
Y_B = distance from the inlet to the meniscus bottom, m
Y_{mic} = distance from the inlet to the microfilm control volume, m
α = accommodation coefficient
γ = local interface characteristic angle
δ = film thickness, m
θ_{men} = arccos (X_L/R_{men}), meniscus contact angle
μ = dynamic viscosity, Pa-s
ρ = density, kg/m^3
σ = surface tension, N/m

Subscripts

a = adiabatic
e = evaporation
in = inlet
int = interface
l = liquid
men = meniscus
mic = microfilm
min = minimum
o = outlet
sat = saturation
v = vapor
w = wall
δ = liquid film free surface

Downloaded 11 Dec 2010 to 193.140.21.150. Redistribution subject to ASME license or copyright; see http://www.asme.org/terms/Terms_Use.cfm

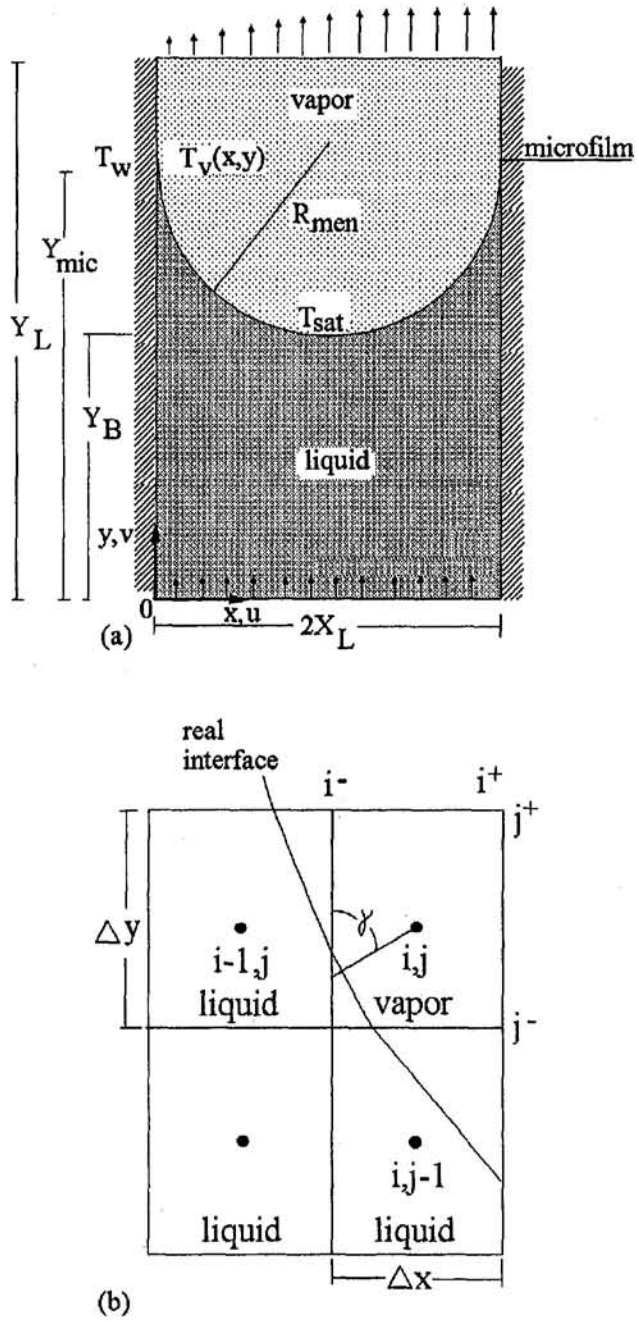


Fig. 1 Evaporating liquid–vapor meniscus: (*a*) computational domain conventions; (*b*) typical element of the liquid–vapor interface

The local inclination angle of the interface, γ, is calculated as $\gamma = \arcsin[(X_L - x)/R_{men}]$. For steady-state situation, the overall inlet and outlet mass flow rates should be equal to the mass flow rate of the evaporating fluid at the liquid–vapor interface:

$$\dot{m}_{l,in} = \dot{m}_{v,o} = \sum_{i,j} \rho_v [v_{v,int}(i,j)\Delta y + u_{v,int}(i,j)\Delta x] \quad (15)$$

While the conservation of normal and tangential momentum is satisfied for every control volume, including those at the interface, due to the conservative control-volume method used, the pressure jump conditions at the interface due to the surface tension should be addressed. For the case of the isothermal liquid–vapor meniscus with constant interface curvature, the pressure jump across the interface can be approximated by the Young–Laplace equation (Faghri, 1995):

$$(p_v - p_l)_{int} = \sigma / R_{men} \quad (16)$$

This pressure jump is not crucial for the present analysis because the pressure drops in the liquid and vapor in the present problem are infinitesimal compared to $(p_v - p_l)_{int}$. Therefore, taking the relative nature of pressure in fluid-flow problems into consideration, the liquid pressure can be simply adjusted by subtracting σ/R_{men} for all grid points in the liquid to satisfy Eq. (16).

The effective evaporative heat transfer coefficient characterizing the intensity of the evaporative heat transfer is defined as follows:

$$h_e = \frac{\dot{m}_{l,in} h_{fg}}{X_L (T_w - T_{sat})} \quad (17)$$

where T_{sat} is the vapor temperature over the liquid–vapor interface. In this study, the vapor temperature at the interface was assumed constant due to saturation conditions and because the curvature of the interface was constant.

The average vapor temperature over the liquid–vapor meniscus for a given y, $\bar{T}_v(y)$, increases along the y coordinate due to the heat transfer between the wall and the vapor. The intensity of the vapor–wall heat transfer can be depicted by the local Nusselt number calculated based on $\bar{T}_v(y)$ for $Y > Y_{mic}$:

$$\mathrm{Nu}_v(y) = \frac{\partial \bar{T}_v(y)}{\partial y} \frac{\dot{m}_{l,in} c_{pv}}{[T_w - \bar{T}_v(y)]} \frac{4X_L}{k_v} \quad (18)$$

$$\bar{T}_v(y) = \frac{1}{\dot{m}_{l,in}} \sum_i \rho_v T_v v_{v,i} \Delta x_i \quad (19)$$

3 Consideration of the Microfilm

The microfilm is considered using the approach of Khrustalev and Faghri (1995); therefore the model of the microfilm is not fully presented in this paper. The microfilm region where the temperature of the liquid–vapor interface changes along the interface from T_w at the interline to T_{sat} at the end of the microfilm has been enclosed into a special control volume with the dimensions $\Delta x \times \Delta y$ adjacent to the wall. This is a vapor control volume since the microfilm thickness, δ, is much smaller than Δx. This means that in the two-dimensional analysis the liquid microfilm is represented only by the vapor blowing velocity at the solid wall, $\mathbf{V}_{v,mic}$, and by the temperature of the wall, T_{mic} (this is the mean temperature of the microfilm free surface) in the special control volume. Note that for the liquid control volume located under the microfilm control volume (see Fig. 1) the velocity of the liquid is increased in the numerical procedure by $v_l = (\rho_v/\rho_l)|\mathbf{V}|_{v,mic}\Delta y/\Delta x$ in order to satisfy conservation of mass given by Eq. (15). However, the vapor velocity at the upper liquid–vapor face of this control volume is not changed since the vapor velocity due to evaporation from the microfilm is assigned to the solid–vapor face of the microfilm control volume. The values $\mathbf{V}_{v,mic}$ and T_{mic} are the microfilm characteristics averaged over Δy, that is along its length, which does not exceed Δy.

$$T_{mic} = \int_0^{\Delta y} q_\delta(y) T_\delta(y) dy \Big/ \int_0^{\Delta y} q_\delta(y) dy \quad (20)$$

$$|\mathbf{V}|_{v,mic} = \int_0^{\Delta y} q_\delta(y) dy / (\Delta y h_{fg} \rho_v) \quad (21)$$

where q_δ is the heat flux at the interface, which is equal to that due to heat conduction through the liquid film, and defined for the case of a comparatively small heat flux by the following expression (Carey, 1992; Faghri, 1995):

$$q_\delta = -\left(\frac{2\alpha}{2-\alpha}\right) \frac{h_{fg}}{\sqrt{2\pi R_g}} \left[\frac{p_v}{\sqrt{T_v}} - \frac{(p_{sat})_\delta}{\sqrt{T_\delta}}\right] \quad (22)$$

p_v and $(p_{sat})_\delta$ are the vapor pressures corresponding to the spe-

Downloaded 11 Dec 2010 to 193.140.21.150. Redistribution subject to ASME license or copyright; see http://www.asme.org/terms/Terms_Use.cfm

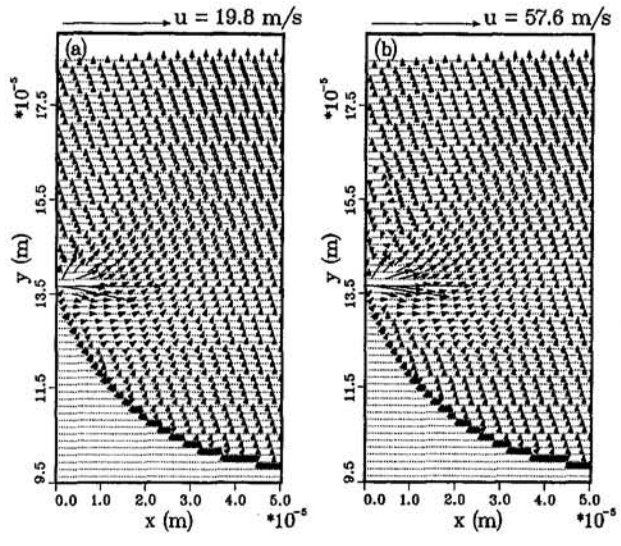


Fig. 2 Vapor flow over the evaporating meniscus: (*a*) $T_w - T_{sat} = 5$ K; (*b*) $T_w - T_{sat} = 10$ K

cial vapor control volume and at the thin liquid film interface, respectively. The extended Kelvin equation, which relates the disjoining pressure, p_d, normal saturation pressure, $p_{sat}(T_\delta)$, and $(p_{sat})_\delta$ affected by the disjoining and capillary pressures, was also used in the model to find T_δ (Khrustalev and Faghri, 1995). In the present model, T_v in Eq. (22) is set equal to the saturation temperature.

Note that the interfacial thermal resistance is very important for the microfilm and results in the difference between the interface temperature, T_δ, and that of the vapor over the interface, T_{sat}. For the rest of the meniscus, the interfacial thermal resistance is negligible in comparison to the thermal resistance of the liquid film and $T_\delta \approx T_{sat}$, which is justified by the calculations made at the end of the microfilm.

4 Numerical Procedure

The problem was solved using Patankar's (1980) SIMPLE algorithm employing the power law discretization scheme and line-by-line TDMA method. The numerical scheme was capable of handling nonuniform properties (Prakash, 1994). The solving procedure consisted of the following consecutive steps:

1 Prescribe the initial temperature field and interfacial velocities $u_{v,int}$ and $v_{v,int}$.
2 Solve the continuity and momentum conservation Eqs. (1), (2), and (3).
3 Solve the energy Eq. (4) for the calculated velocity field.
4 With the calculated temperature field, update the interfacial vapor velocities, $u_{v,int}$ and $v_{v,int}$, for the control volume liquid–vapor faces at the interface from Eqs. (13) and (14). Calculate T_{mic} and $|\mathbf{V}_{v,mic}|$ for the microfilm control volume from Eqs. (20) and (21), and the model by Khrustalev and Faghri (1995) where the microfilm curvature is set to $1/R_{men}$.
5 Go back to step 2 until a converged solution is obtained.

All control volumes in the computational domain were divided in two categories: "liquid" and "vapor," with corresponding thermophysical properties. The following nonequality was used to identify the vapor control volumes:

$$x \geq X_L - [R_{men}^2 - (y - Y_{men} - R_{men})^2] \qquad (23)$$

A uniform grid with rectangular control volumes was used with 98 grid points in the x direction and 270 grid points in the y direction. This grid size was found sufficient to approximate the curved liquid–vapor interface. The numerical solution was found to be essentially independent of the number of grid points used. For example, the value of the effective heat transfer coefficient, h_e, for the 98 × 360 grid was only 0.17 percent higher than that for the 98 × 270 grid for the same total number of iterations of 12,000 (500 iterations for each of the Steps 2 and 3 described above). The convergence of the solution was also verified. The heat transfer coefficients presented in the following figures were calculated with the numerical error of about 0.1 percent with the 98 × 270 grid. The overall mass flow rate balances, Eq. (15), were satisfied with an accuracy of at least 0.1 percent.

5 Results and Discussion

Numerical results were obtained for water at the saturation temperature of 373 K for $X_L = 50$ μm, $Y_L = 400$ μm, $Y_B = 100$ μm, and $\theta_{men} = 15$ deg. The accommodation coefficient, α, was set equal to unity. Typical vapor velocity fields over the evaporating meniscus are shown in Fig. 2 for comparatively small (a) and large (b) temperature drops ($\Delta T = T_w - T_{sat}$) between the wall and the saturation temperature. The vapor velocity in the microfilm control volume can be as high as 100 m/s for $\Delta T = 15$ K. Such a high blowing velocity results in a recirculation zone in the vapor near the wall over the interline, as shown in Fig. 2(b). Since the velocities in the liquid are much smaller than those in the vapor, they are not shown in Fig. 2. For small temperature drops, the vapor flows along the y coordinate near the heated wall over the interline. However, for larger temperature drops, the vapor flow changes its direction in the above-mentioned region due to appearance of the recirculation zone. This effect can be important for micro heat pipes and other applications.

The liquid flow is shown in Fig. 3. The liquid–vapor interface in Fig. 3 is represented by the velocity vectors at the vapor side of the interface. The liquid flow pattern did not change with temperature drop as can be seen from comparison of Figs. 3(a) and 3(b). The temperature contours are given in Fig. 4 for $\Delta T = 5$ K(a) and $\Delta T = 10$ K(b). For higher ΔT, the shape of the temperature contours changed compared to lower ΔT due to the fluid flow effect on the heat transfer.

The numerical results for the effective heat transfer coefficient, h_e, were compared to those obtained using the model by Khrustalev and Faghri (1995). In the model by Khrustalev and Faghri (1995), the fluid flow was neglected and the heat

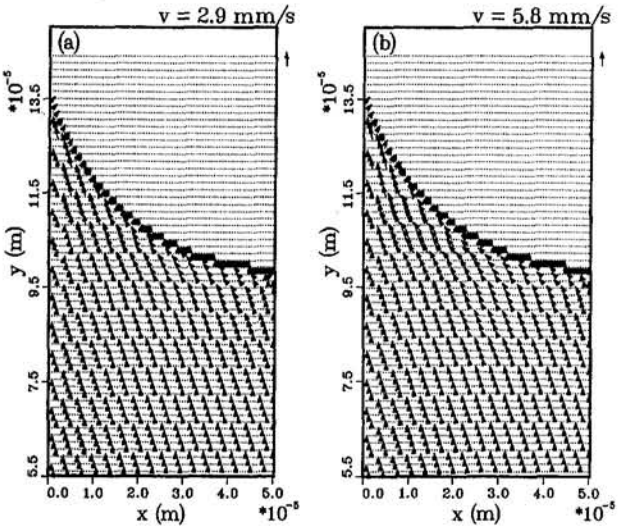


Fig. 3 Liquid flow in the evaporating meniscus: (*a*) $T_w - T_{sat} = 5$ K; (*b*) $T_w - T_{sat} = 10$ K

Downloaded 11 Dec 2010 to 193.140.21.150. Redistribution subject to ASME license or copyright; see http://www.asme.org/terms/Terms_Use.cfm

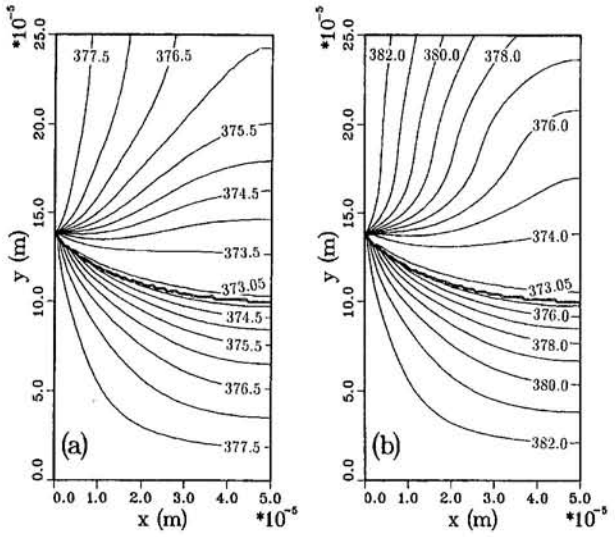


Fig. 4 Temperature contours in the liquid and vapor: (*a*) $T_w - T_{sat} = 5$ K; (*b*) $T_w - T_{sat} = 10$ K

conduction problem in the solid wall and meniscus liquid was reduced to one-dimension, allowing calculation of the overall heat flow rate per unit length of the liquid–vapor meniscus and the effective heat transfer coefficient. In the present paper, the overall heat flow rate per unit length of the meniscus was also calculated for the purpose of comparison in a similar manner but with a constant wall temperature. For small ΔT the agreement was very good: The simplified model underestimated the heat transfer coefficients by only about 3 percent as shown in Fig. 5. However, for larger temperature drops, the difference between the present (two-dimensional) and the simplified model became 30 percent (for $\Delta T = 10$ K) due to the convective heat transfer.

As the vapor moves in the y direction, its temperature increases due to heat transfer from the wall. Thus, it can be significantly superheated over the saturation temperature at the slot or pore exit. The local Nusselt numbers are larger some distance away from the microfilm control volume along the y coordinate than those near the interline or at the outlet of the computational domain, Fig. 6. For superheats of 9 K and 10 K, recirculation of vapor near the heated wall decreases the local Nusselt number due to the smaller vapor velocities near the wall in the recirculation zone.

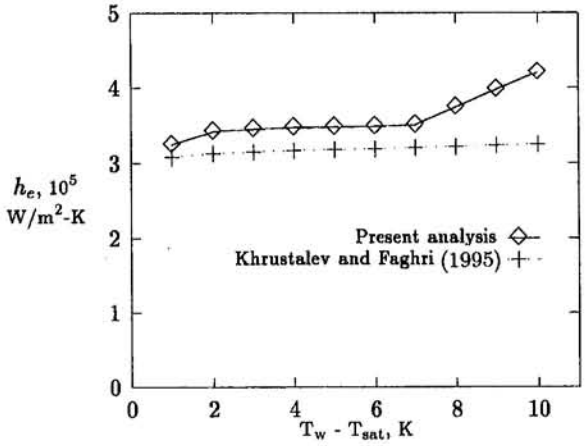


Fig. 5 Effective heat transfer coefficient versus superheat for water at atmospheric pressure

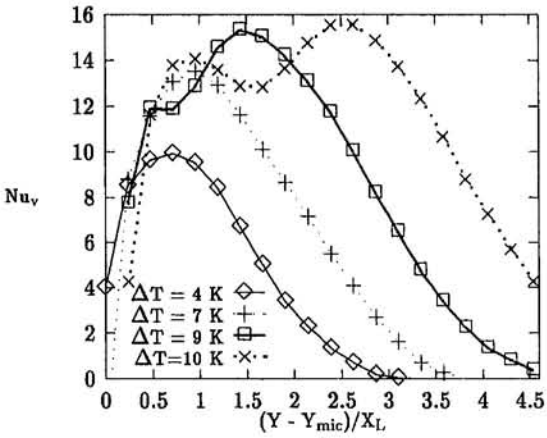


Fig. 6 Local Nusselt number for the vapor flow along the slot for water at atmospheric pressure

6 Conclusions

The following conclusions can be made based on the numerical results obtained:

1. For small temperature drops, the agreement between the present two-dimensional model and the model by Khrustalev and Faghri (1995) is good. This agreement allows the use of the simplified model of Khrustalev and Faghri (1995) for small temperature drops.
2. The fluid flow effect on the heat transfer during evaporation from the liquid–vapor meniscus results in the increase of the effective heat transfer coefficient by up to 30 percent.
3. For larger temperature drops, a recirculation zone appears in the vapor over the interline, which can be important for some applications including evaporation from capillary structures.
4. The vapor exiting a capillary slot or pore can be significantly superheated over the saturation temperature. The heat transfer between the vapor and the heated wall is the most extensive at a distance from the interline of about one slot width along the y coordinate.

Acknowledgments

Funding for this work was provided by the National Science Foundation Grant CTS-941458 and Thermal Energy Group of the Aero Propulsion Directorate of the U.S. Air Force under contract No. F33615-92-C-2276.

References

Cao, Y., and Faghri, A., 1990, "Transient Two-Dimensional Compressible Analysis for High-Temperature Heat Pipes With Pulsed Heat Input," *Numerical Heat Transfer*, Part A, Vol. 18, pp. 483–502.

Carey, V. P., 1992, *Liquid-Vapor Phase-Change Phenomena: An Introduction to the Thermophysics of Vaporization and Condensation Processes in Heat Transfer Equipment*, Hemisphere, New York.

Faghri, A., 1995, *Heat Pipe Science and Technology*, Taylor & Francis.

Holm, F. W., and Goplen, S. P., 1979, "Heat Transfer in the Meniscus Thin-Film Transition Region," ASME JOURNAL OF HEAT TRANSFER, Vol. 101, pp. 543–547.

Kamotani, Y., 1978, "Evaporator Film Coefficients of Grooved Heat Pipes," *Proc. 3rd Int. Heat Pipe Conf.*, Palo Alto, CA, pp. 128–130.

Khrustalev, D., and Faghri, A., 1995, "Heat Transfer During Evaporation on Capillary-Grooved Structures of Heat Pipes," ASME JOURNAL OF HEAT TRANSFER, Vol. 117, p. 740–747.

Patankar, S. V., 1980, *Numerical Heat Transfer and Fluid Flow*, McGraw-Hill, New York.

Downloaded 11 Dec 2010 to 193.140.21.150. Redistribution subject to ASME license or copyright; see http://www.asme.org/terms/Terms_Use.cfm

Potash, M., Jr., and Wayner, P. C., Jr., 1972, "Evaporation From a Two-Dimensional Extended Meniscus," *Int. J. Heat Mass Transfer,* Vol. 15, pp. 1851–1863.

Prakash, C., 1994, "Numerical Heat Transfer and Fluid Flow," Postgraduate Course, Wright State University, Dayton, OH.

Schneider, G. E., Yovanovich, M. M., and Wehrle, V. A., 1976, "Thermal Analysis of Trapezoidal Grooved Heat Pipe Evaporator Walls," AIAA Paper No. 76-481.

Solov'ev, S. L., and Kovalev, S. A., 1984, "Mechanism of Evaporation of a Liquid From a Porous Surface," *Proc. 5th Int. Heat Pipe Conf.,* Tsukuba, Japan, Preprints Vol. II, pp. 77–82.

Stephan, P., 1992, *Wärmedurchgang bei Verdampfung aus Kapillarrillen in Wärmerohren,* Fortschr.-Ber. VDI Reihe 19 No. 59, VDI-Verlag, Düsseldorf.

Stephan, P. C., and Busse, C. A., 1992, "Analysis of the Heat Transfer Coefficient of Grooved Heat Pipe Evaporator Walls," *Int. J. Heat Mass Transfer,* Vol. 35, No. 2, pp. 383–391.

Swanson, X. X., and Peterson, Y. Y., 1994, "Evaporating Extended Meniscus in a V-Shaped Channel," *J. Thermophysics and Heat Transfer,* Vol. 8, No. 1, pp. 172–180.

Voller, V. R., Brent, A. D., and Prakash, C., 1989, "The Modeling of Heat, Mass and Solute Transport in Solidification Systems," *Int. J. Heat Mass Transfer,* Vol. 32, No. 9, pp. 1719–1731.

Wayner, P. C., Jr., Kao, Y. K., and LaCroix, L. V., 1976, "The Interline Heat Transfer Coefficient of an Evaporating Wetting Film," *Int. J. Heat Mass Transfer,* Vol. 19, pp. 487–492.

Downloaded 11 Dec 2010 to 193.140.21.150. Redistribution subject to ASME license or copyright; see http://www.asme.org/terms/Terms_Use.cfm

Theoretical Analysis of the Maximum Heat Transport in Triangular Grooves: A Study of Idealized Micro Heat Pipes

G. P. Peterson
Tenneco Professor and Head.
email: gppeterson@mengr.tamu.edu
Fellow ASME

H. B. Ma
Graduate Research Assistant.

Department of Mechanical Engineering,
Texas A&M University,
College Station, TX 77843-3123

A mathematical model for predicting the minimum meniscus radius and the maximum heat transport in triangular grooves is presented. In this model, a method for determining the theoretical minimum meniscus radius was developed and used to calculate the capillary heat transport limit based on the physical characteristics and geometry of the capillary grooves. A control volume technique was employed to determine the flow characteristics of the micro heat pipe, in an effort to incorporate the size and shape of the grooves and the effects of the frictional liquid–vapor interaction. In order to compare the heat transport and flow characteristics, a hydraulic diameter, which incorporated these effects, was defined and the resulting model was solved numerically. The results indicate that the heat transport capacity of micro heat pipes is strongly dependent on the apex channel angle of the liquid arteries, the contact angle of the liquid flow, the length of the heat pipe, the vapor flow velocity and characteristics, and the tilt angle. The analysis presented here provides a mechanism whereby the groove geometry can be optimized with respect to these parameters in order to obtain the maximum heat transport capacity for micro heat pipes utilizing axial grooves as the capillary structure.

Introduction

Thermal management continues to be one of the most critical technologies in electronic product development, and directly influences the cost, reliability, and performance of electronic devices and the electronic wafers that comprise these devices. While the limitation on the maximum wafer temperature is significant, the level of temperature uniformity occurring across the wafer surface also plays an important role in both performance and reliability. Increasing heat fluxes, coupled with these temperature uniformity considerations, will require the development of new methods for distributing and removing heat from both current and new devices. Chip carriers utilizing single micro heat pipes, or arrays of micro heat pipes fabricated as an integral part of semiconductor wafers, present promising alternatives for the removal of high localized heat fluxes and the uniform distribution of heat fluxes in the wafers (Peterson, 1992, 1996).

One of the limiting factors in the transport processes occurring inside any heat pipe, and the most frequently encountered limit in micro heat pipes, is the capillary pumping capability. The upper limit of this capillary pumping is directly related to the minimum meniscus radius and plays a significant role in the determination of the maximum heat transport capacity for both conventional and micro heat pipes. This capillary pumping limit is reached when the capillary pumping pressure can no longer overcome the sum of all the pressure drops occurring in the liquid and vapor flow paths. Examination of the capillary pumping pressure, defined as

$$\Delta p_c = 2\sigma\left(\frac{1}{r_{c,e}} - \frac{1}{r_{c,c}}\right) \tag{1}$$

clearly indicates the importance of the meniscus radius in the evaporator, $r_{c,e}$, and the significance of understanding the conditions under which this radius reaches a minimum value.

Tien and Sun (1971) have previously developed a method for defining the minimum static meniscus radius in grooves of various shapes for classical heat pipe operating conditions. However, because this method yields a constant value, it cannot be used in situations where the meniscus shape varies significantly along the axial length of the pipe. While a number of other relationships have been developed for calculating the minimum meniscus radius of conventional heat pipes (Peterson, 1994; Chi, 1976), these methods are inappropriate for use in micro heat pipes because they do not consider either the radial meniscus variation or the interfacial frictional influences, both of which have been shown to be significant in micro heat pipes. Cotter (1984) initially attempted to overcome this problem by using the expression $A_l = \beta^2 r^2$, to estimate the meniscus radius where β is a constant dependent upon the wick structure. Later, Babin et al. (1990) used the expression, $r_{c,e} = \omega/\cos\phi\cos\alpha$, developed for conventional heat pipes, to estimate the meniscus radius, where ω is defined as the width of the groove. Here, problems were encountered in trying to determine how to define the width of the groove occurring in the sharp-angled corner regions of the micro heat pipe. In the model of Gerner et al. (1992), the capillary radius was simply defined as $r_{c,e} = D/2$, and more recently, Khrustalev and Faghri (1994) noted that the variation of the maximum heat transport due to a decreasing minimum radius was very small when $r_{c,e} < 0.1 D_{h,v}$. Finally, although Longtin et al. (1994) developed a method for determining the variation of the meniscus radius for a specific micro heat pipe, no generalized method for determining the precise minimum meniscus radius and hence, the actual maximum capillary pumping pressure, currently exists.

From the previous work, it is clear that in order to predict the maximum heat transport capacity accurately in a micro heat pipe, it is first necessary to find the correct minimum value for the radius of the capillary meniscus. Additionally, understanding the factors that affect this value, such as the effect of the

Contributed by the Heat Transfer Division and presented at the International Mechanical Engineering Congress & Exposition, San Francisco, California, November 12–17, 1995. Manuscript received by the Heat Transfer Division July 1, 1995; revision received May 10, 1996. Keywords: Heat Pipes and Thermosyphons, Phase-Change Phenomena, Thin Film Flow. Associate Technical Editor: A. Faghri.

Copyright © 1996 by ASME

Downloaded 11 Dec 2010 to 193.140.21.150. Redistribution subject to ASME license or copyright; see http://www.asme.org/terms/Terms_Use.cfm

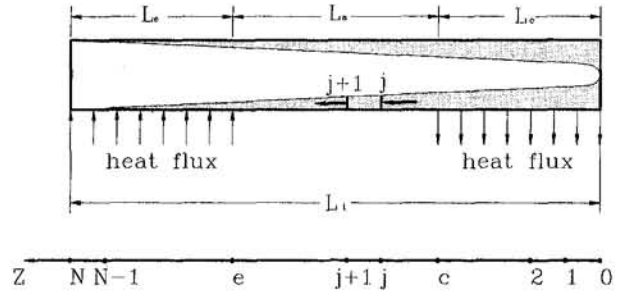


Fig. 1 Schematic of a micro heat pipe

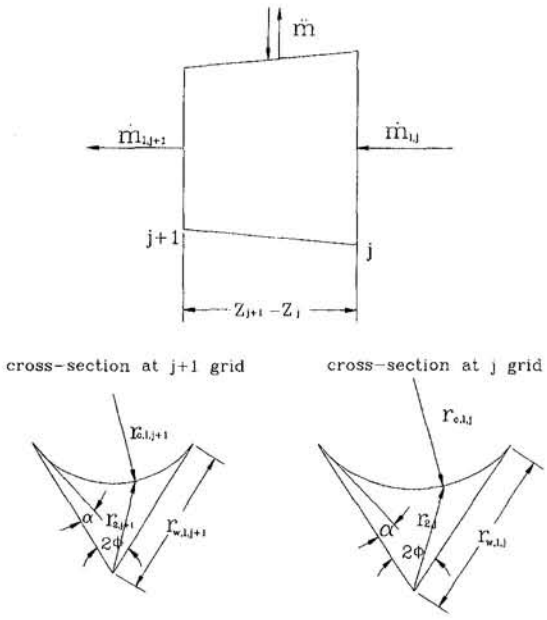


Fig. 2 Control volume

shear forces at the liquid–vapor interface, can lead to a better understanding of the parameters that influence the maximum heat transport capacity in micro heat pipes (Peterson et al., 1996).

Because the models presented by Cotter (1984), Babin et al. (1990), Gerner et al. (1992), and more recently, Khrustalev and Faghri (1994), Longtin et al. (1994), and Duncan and Peterson (1995) concentrated on the entire micro heat pipe and analyzed the heat transport characteristics with an "estimated" minimum meniscus radius, it is very difficult to expand any one of these models to determine what shape that will provide the maximum capillary heat transport capacity. In the current analysis, a theoretical expression for the minimum meniscus radius will be developed and used to calculate the maximum heat transport capacity as a function of the physical characteristics and geometry. To further refine the model, a control volume technique will be used to incorporate the effects of the frictional liquid–vapor interaction on the liquid flow based on a two-dimensional model. Unlike previous models, this analysis will consider variations in both the friction factor and the cross-sectional area of the liquid flow in the triangular grooves to determine the minimum meniscus radius and the maximum capillary heat transport capacity.

Theoretical Analysis

The capillary limit has been shown to be the limiting factor in almost all types of micro heat pipes. Cotter (1984), Babin et al. (1990), Gerner et al. (1990, 1992), and Duncan and Peterson (1995) developed pressure balance equations relating the capillary forces and frictional forces for the entire heat pipe or for a particular section (i.e., the evaporator section, the adiabatic section, and the condenser section). More recently, Longtin et al. (1994) developed a model that included the vapor flow effect based on a one-dimensional liquid flow model, the vapor pressure effect, and the dynamic pressure influences. Also, Khrustalev and Faghri (1994) developed a thermal model to determine the maximum heat transport capability for a specified geometry, and found that the vapor flow can have a significant effect on the liquid flow in the micro heat pipe. Based on the analysis of Longtin et al. (1994) and Khrustalev and Faghri (1994), the vapor pressure drop is very small compared with the liquid pressure drop, and the dynamic pressure changes the liquid pressure gradient by less than 0.1 percent. In the current investigation, the capillary flow in the triangular capillary grooves was assumed to be governed by the capillary force, the solid–liquid and liquid–water frictional force, and the gravitational force.

Maximum Capillary Heat Transport. If the evaporator and condenser sections of a micro heat pipe are assumed to have uniform heat flux and the triangular grooves are divided into N control volumes as shown in Fig. 1, the pressure drop produced by the shear forces at the solid–liquid and liquid–vapor interfaces for the jth control volume, shown in Fig. 2, and the gravity force must be overcome by the capillary pumping force. The net capillary pressure difference can be

Nomenclature

A = cross-sectional area, m^2
C = coefficient defined by Eq. (15)
D = diameter, m
f = friction factor
g = gravitational acceleration, m/s^2
h_{fg} = latent heat of vaporization, kJ/kg
L = length, m
L_v = dimensionless vapor–liquid interface number defined by Eq. (39)
$\dot{m}$ = mass flow rate, kg/s
p = pressure, N/m^2
P = perimeter, m
Q = heat transport, W
Q_{eff} = unit effective area heat transport, W/m^2
r = radius, coordinate, m
R = dimension of groove, m
Re = Reynolds number
u = velocity, m/s
$\bar{U}$ = average velocity, m/s
V = volume of liquid entering the control volume per unit time, m^3/s
z = coordinate, m
α = contact angle, deg
θ = coordinate, deg
μ = viscosity, Ns/m^2
ρ = density, kg/m^3
σ = surface tension, N/m
τ = shear stress, N/m^2
ϕ = half-channel angle, deg
ψ = tilt angle, deg
ω = groove width, m

Subscripts

0 = grid number
a = adiabatic
c = capillary, curvature, control volume, condenser
e = evaporator
g = geometric
h = hydraulic
j = grid number
l = liquid
N = grid number
t = total
v = vapor
w = wall

Downloaded 11 Dec 2010 to 193.140.21.150. Redistribution subject to ASME license or copyright; see http://www.asme.org/terms/Terms_Use.cfm

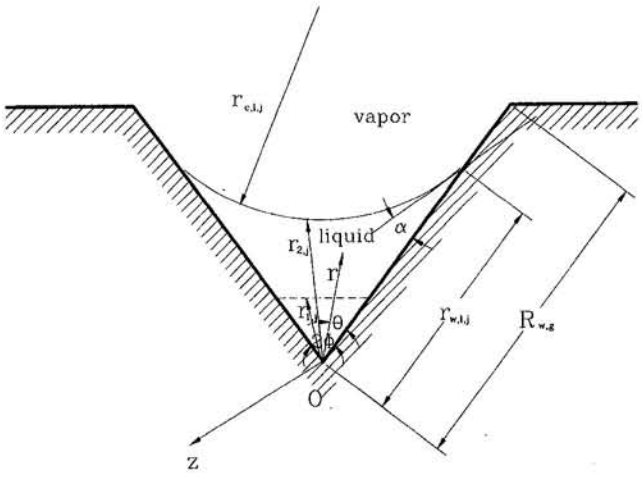


Fig. 3 Geometry of the triangular groove

found from the Laplace–Young equation for this control volume as

$$p_{c,j+1} - p_{c,j} = \sigma\left(\frac{1}{r_{c,l,j+1}} - \frac{1}{r_{c,l,j}}\right) \tag{2}$$

For capillary flows at very low Bond numbers, the surface of the liquid will have a nearly constant radius of curvature (Ayyaswamy et al., 1974), which is dependent upon the geometric shape of the liquid flow passage and the contact angle. Therefore, the equation for the surface curvature based on a constant radius of curvature can be written as

$$r_{2,j} = r_{w,l,j}\frac{\cos\alpha\cos(\phi-\theta) - [\sin^2\phi - \cos^2\alpha\sin^2(\phi-\theta)]^{0.5}}{\cos(\alpha+\phi)} \tag{3}$$

where $r_{2,j}$ is the distance between the apex (O) and the liquid surface as shown in Fig. 3.

The liquid pressure drop can be found by evaluating the shear forces at the solid–liquid and liquid–vapor interfaces. The frictional drag due to the shear stress can be written as

$$\left(\frac{dp_l}{dz}\right)_j = -\frac{2\tau_{l,j}}{r_{h,l,j}} \tag{4}$$

where $\tau_{l,j}$ is the frictional shear stress at the solid–liquid and liquid–vapor interface for the jth control volume and $r_{h,l,j}$ is the hydraulic radius, defined as twice the cross-sectional area divided by the wetted perimeter (Peterson, 1994). The shear stress can be expressed in terms of the friction factor, $f_{l,j}$, or

$$\tau_{l,j} = f_{l,j}\tfrac{1}{2}\rho_l\bar{U}_{l,j}^2 \tag{5}$$

where $\bar{U}_{l,j}$ is the local average liquid velocity, which is related to the local mass flow by

$$\bar{U}_{l,j} = \frac{\dot{m}_{l,j}}{A_{l,j}\rho_l} \tag{6}$$

In this expression, $A_{l,j}$ is the cross-sectional area of the liquid flow at the jth grid point. Combining Eqs. (5) and (6), and considering the Reynolds number, $\mathrm{Re}_{h,l,j}$,

$$\mathrm{Re}_{h,l,j} = \frac{2r_{h,l,j}\rho_l\bar{U}_{l,j}}{\mu_l} \tag{7}$$

Eq. (4) becomes,

$$\left(\frac{dp_l}{dz}\right)_j = -\frac{(f_{l,j}\,\mathrm{Re}_{h,l,j})\mu_l\dot{m}_{l,j}}{2r_{h,l,j}^2A_{l,j}\rho_l} \tag{8}$$

and given that

$$r_{h,l,j} = \frac{1}{2}D_{h,l,j} = \frac{2A_{l,j}}{P_{l,j}} \tag{9}$$

Eq. (8) can be written as

$$\left(\frac{dp_l}{dz}\right)_j = -\frac{(f_{l,f}\,\mathrm{Re}_{h,l,j})\mu_l\dot{m}_{l,j}P_{l,j}^2}{8A_{l,j}^3\rho_l} \tag{10}$$

Applying this expression to the control volume, j, the pressure drop can be expressed as

$$p_{l,j+1} - p_{l,j} = -\frac{(f_{l,f}\,\mathrm{Re}_{h,l,j})\mu_l\dot{m}_{l,j}(P_{l,j+1}+P_{l,j})^2}{(A_{l,j+1}+A_{l,j})^3\rho_l}(z_{j+1}-z_j) \tag{11}$$

where A_j and A_{j+1} are the cross-sectional areas of the liquid flow at the points j and $j+1$, respectively, and $P_{l,j}$ and $P_{l,j+1}$ are the corresponding wetted perimeters of the liquid flow. The cross-sectional area of the liquid flow at the jth grid point can be shown to be

$$A_{l,j} = \frac{1}{2}\int_0^{2\phi} r_{2,j}^2\,d\theta = \frac{1}{2}\int_0^{2\phi} r_{w,l,j}^2\left[\frac{\cos\alpha\cos(\phi-\theta) - [\sin^2\phi - \cos^2\alpha\sin^2(\phi-\theta)]^{0.5}}{\cos(\alpha+\phi)}\right]^2 d\theta \tag{12}$$

From the assumption of constant radius of surface curvature, the length of the wetted wall illustrated in Fig. 3 can be expressed in terms of the radius of curvature as

$$r_{w,l,j} = r_{c,l,j}\frac{\cos(\alpha+\phi)}{\sin\phi} \tag{13}$$

where α is the contact angle, which depends on the properties of liquid, the wall, and the heat flux. Although the value of the contact angle varies along the groove, the model presented here is still appropriate provided this contact angle variation is known. If the accurate contact angle variation along the groove is not known, a constant contact angle along the groove can be assumed.

Substituting Eq. (13) into Eq. (12) and rearranging, yields

$$A_{l,j} = Cr_{c,l,j}^2 \tag{14}$$

where

$$C = \frac{1}{2}\int_0^{2\phi}\left[\frac{\cos\alpha\cos(\phi-\theta) - [\sin^2\phi - \cos^2\alpha\sin^2(\phi-\theta)]^{0.5}}{\sin^2\phi}\right]^2 d\theta \tag{15}$$

Downloaded 11 Dec 2010 to 193.140.21.150. Redistribution subject to ASME license or copyright; see http://www.asme.org/terms/Terms_Use.cfm

Finally, for the control volume shown in Fig. 2 the pressure drop produced by the shear forces at the liquid–solid and liquid–vapor interfaces and the pressure drop caused by the gravitational body force must be overcome by the capillary pumping pressure, i.e.,

$$\sigma\left(\frac{1}{r_{c,l,j+1}} - \frac{1}{r_{c,l,j}}\right) \geq \frac{(f_{l,j}\,\mathrm{Re}_{h,l,j})\mu_l \dot{m}_{l,j}(P_{l,j+1} + P_{l,j})^2}{(A_{l,j+1} + A_{l,j})^3 \rho_l} \times (z_{j+1} - z_j) + \rho_l g(z_{j+1} - z_j)\sin\psi \quad (16)$$

where the wetted perimeter of the liquid flow is defined as

$$P_{l,j} = 2r_{w,l,j} = \frac{2r_{c,l,j}\cos(\alpha + \phi)}{\sin\phi} \quad (17)$$

Considering Eqs. (14) and (17), Eq. (16) can be written as

$$\sigma\left(\frac{1}{r_{c,l,j+1}} - \frac{1}{r_{c,l,j}}\right) \geq \rho_l g(z_{j+1} - z_j)\sin\psi + \frac{(f_{l,f}\,\mathrm{Re}_{h,l,j})\mu_l \dot{m}_{l,j}\cos^2(\alpha + \phi)(r_{c,l,j+1} + r_{c,l,j})^2}{C^3 \sin^2\phi\rho_l(r_{c,l,j+1}^2 + r_{c,l,j}^2)^3}(z_{j+1} - z_j) \quad (18)$$

This expression can then be independently applied to the evaporator, the adiabatic section, and the condenser, with the only difference being that the mass flow rate, $\dot{m}_{l,j}$, will have different values. For the condenser, the mass flow passing through the cross-sectional area can be expressed as

$$\dot{m}_{l,j} = \dot{m}_{c,l,j} = \frac{Q(jD_{h,g})}{h_{fg}A_{c,g}}(z_{j+1} - z_j) \quad (j = 0, 1, 2, 3 \ldots c, \ldots) \quad (19)$$

For the adiabatic section, no heat is transferred between the inside and outside of the heat pipe, hence the mass flow, $\dot{m}_{l,j}$, is constant. For the evaporator, the mass flow rate passing through any cross-sectional area can be expressed as

$$\dot{m}_{l,j} = \dot{m}_{e,l,j} = \frac{Q}{h_{fg}} - \frac{Q(j - e)D_{h,g}}{h_{fg}A_{e,g}}(z_{j+1} - z_j) \quad (j = e, e + 1, e + 2, \ldots N - 1, N) \quad (20)$$

If for the triangular groove illustrated in Fig. 3 the cross-sectional area of the channel perpendicular to the axial direction is assumed to be A_g, and the effective perimeter, P_g, which is equal to $2R_{w,g}$, the hydraulic diameter of triangular grooves can be expressed as

$$D_{h,g} = \frac{4A_g}{P_g} \quad (21)$$

The effective area for a single triangular groove is

$$A_{t,g} = D_{h,g}L_t = \frac{4AL_t}{P_g} \quad (22)$$

and the corresponding effective areas for the condenser and evaporator can be found as

$$A_{c,g} = D_{h,g}L_c \quad (23)$$

and

$$A_{e,g} = D_{h,g}L_e \quad (24)$$

respectively. These values for the hydraulic diameter and the effective area as defined by Eqs. (21), (23), and (24) will be used throughout the remaining discussion to define the characteristics of the channel geometry and to generalize the heat transport characteristics of the triangular grooves used in micro heat pipes.

Minimum Meniscus Radius—One of Boundary Conditions. Solution of Eq. (18) with Eqs. (19) and (20) requires two boundary conditions, i.e., the meniscus radius, $r_{c,l,0}$, at the first control volume and the meniscus radius, $r_{c,l,N}$, at the last control volume. Based on the geometry of the grooves and the contact angle, the meniscus radius, $r_{c,l,0}$, can be found as

$$r_{c,l,0} = \frac{r_{w,l,0}\sin\phi}{\cos(\alpha + \phi)} \quad (25)$$

where $r_{w,l,O}$ is equal to $R_{w,g}$, as shown in Fig. 3.

From Eq. (18), it can be seen that decreasing the capillary radius, $r_{c,l,N}$, will cause the capillary pressure to increase, while decreasing $r_{c,l,N}$ will cause the frictional pressure drop to increase. It is important to note, however, that the rate at which the frictional force increases is larger than the rate of increase for the capillary force. As a result, a lower bound on the capillary radius, i.e., a minimum capillary radius will exist.

As is the case for conventional heat pipes, when the heat input in the evaporator section of a micro heat pipe is larger than the maximum capillary heat transport, dryout will occur in the capillary grooves. Assuming the maximum heat transport added to the evaporator section is Q, the corresponding maximum heat flux (i.e., the unit effective area heat transport), is dependent upon the area of the evaporator, $A_{e,g}$, or

$$Q_{\mathrm{eff}} = \frac{Q}{A_{e,g}} \quad (26)$$

At the point just prior to dryout, the amount of liquid vaporized from the Nth control volume will be equal to the amount of liquid entering the control volume. Utilizing $V_{c,N}$ to represent the volume of liquid entering the last control volume per unit time, a mass balance yields

$$V_{c,N}\rho_l h_{fg} = Q_{\mathrm{eff}}D_{h,g}dz \quad (27)$$

and from the geometry, the volume of liquid entering per unit time can be obtained as

$$V_{c,N} = \bar{U}_{N-1}[r_* r_{w,l,N}\sin(\phi) - 0.5r_{c,l,N}^2(\pi - 2\alpha - 2\phi)] \quad (28)$$

where

$$r_* = \frac{r_{w,l,N}\cos(\alpha)}{\cos(\alpha + \phi)} \quad (29)$$

and

$$r_{w,l,N} = \frac{r_{c,l,N}\cos(\alpha + \phi)}{\sin(\phi)} \quad (30)$$

By definition, the maximum heat transport occurs when the liquid mass flow rate reaches a maximum value. Substituting Eqs. (28), (29), and (30) into Eq. (27), and rearranging, the minimum meniscus radius can be expressed as

$$r_{c,l,N} = \left(\frac{\dfrac{Q_{\mathrm{eff}}D_{h,g}dz}{\rho_l h_{fg}\bar{U}_{N-1}}}{\dfrac{\cos(\alpha + \phi)\cos(\alpha)}{\sin(\phi)} - \dfrac{1}{2}(\pi - 2\alpha - 2\phi)}\right)^{0.5} \quad (31)$$

Friction Factor. In previous studies, the vapor flow has been shown to have a significant influence on the liquid flow in micro heat pipes. Longtin et al. (1994) developed a one-dimensional model, which considered this effect using geometric coefficients. In reality, however, the capillary flow in a triangular groove should be treated as two-dimensional flow, particularly when trying to incorporate the effect of the liquid–vapor

Downloaded 11 Dec 2010 to 193.140.21.150. Redistribution subject to ASME license or copyright; see http://www.asme.org/terms/Terms_Use.cfm

shear interaction. In the model presented by Khrustalev and Faghri (1994), the vapor flow effect on the liquid flow in a micro heat pipe was based on a two-dimensional model; however, an approximate expression, $V(\alpha, F) = (a_0 + a_1\alpha + a_2\alpha^2)e^F$, was used to calculate the volume flux and a relatively small value of the dimensionless shear stress, F, was assumed. Clearly, this is not accurate, particularly for the case of micro heat pipes with high heat fluxes. In the current analysis, a two-dimensional model method for determining the liquid friction factor, which includes vapor flow effect, is developed.

If the capillary flow of an incompressible Newtonian fluid in the triangular groove with fully developed laminar vapor flow over the upper surface similar to that illustrated in Fig. 3 is considered, it is clear that the flow velocity and behavior of the liquid surface will be strongly influenced by the vapor flow direction and velocity. Utilizing a cylindrical coordinate system with the axis coincident with the apex (O), and assuming two-dimensional, fully developed flow of the liquid at the jth grid point, the pressure drop in the triangular grooves can be expressed as:

$$\frac{1}{r}\frac{\partial}{\partial r}\left(r\frac{\partial u_{l,j}}{\partial r}\right) + \frac{1}{r^2}\frac{\partial^2 u_{l,j}}{\partial \theta^2} = \frac{1}{\mu_l}\left(\frac{dp_l}{dz}\right)_j \tag{32}$$

The boundary conditions are defined as

$$u_{l,j} = 0 \quad \theta = 0$$

$$u_{l,j} = 0 \quad \theta = 2\phi$$

$$u_{l,j} = u_{l,r_2,j} \quad r = r_{2,j} \tag{33}$$

Using a coordinate transformation and the separation of variables method, the velocity, u_l, in the grooves can be found as

$$u_{l,j} = \frac{r_{1,j}^2}{4\mu_l}\left(-\frac{dp_l}{dz}\right)_j \left\{-\left(\frac{r}{r_{1,j}}\right)^2 + \sum_{n=1}^{\infty}\frac{2}{n\pi}[1-(-1)^n]\right.$$

$$\left.\times\left[\frac{\sinh\left[\frac{n\pi}{2\phi}(a-x)\right] + Hp\sinh\left(\frac{n\pi}{2\phi}x\right)}{\sinh\left(\frac{n\pi}{2\phi}a\right)}\right]\right.$$

$$\times\sin\left(\frac{n\pi}{2\phi}\theta\right) + \sum_{n=1}^{\infty}\frac{\frac{2}{n\pi}\left[1-\left(\frac{r_{2,j}}{r_{1,j}}\right)^2(-1)^n\right]}{1+\left(\frac{2a}{n\pi}\right)^2}$$

$$\left.\times\left[\frac{\sinh\left[\frac{n\pi}{a}(2\phi-\theta)\right] + \sinh\left(\frac{n\pi}{a}\theta\right)}{\sinh\left(\frac{n\pi}{a}2\phi\right)}\right]\sin\left(\frac{n\pi}{a}x\right)\right\} \tag{34}$$

where

$$a = \ln\frac{r_{2,j}}{r_{1,j}} \tag{35}$$

$$x = \ln\frac{r}{r_{1,j}} \tag{36}$$

and

$$Hp = \frac{\bar{u}_{l,r_2,j} + \frac{r_{2,j}^2}{4\mu_l}\left(-\frac{dp_l}{dz}\right)_j}{\frac{r_{1,j}^2}{4\mu_l}\left(-\frac{dp_l}{dz}\right)_j} \tag{37}$$

As $r_{1,j} \to 0$, the solution corresponds to that obtained for a triangular groove. In the numerical solution, $r_{1,j}$ was set equal to 10^{-10} m. Clearly, the surface velocity of the liquid flow with the vapor flow effect, $\bar{u}_{1,r2,j}$, will depend on the velocities, the density, and viscosity of both flows, which can be determined by

$$\bar{u}_{l,r_2,j} = \frac{K(1-L_v)}{2\phi}\int_0^{2\Phi}\left(-\frac{1}{4\mu_l}\frac{dp_l}{dz}\right)_j \times\left(\frac{r_{w,l,j}[\cos\alpha\cos(\phi-\theta) - [\sin^2\phi - \cos^2\alpha\sin^2(\phi-\theta)]^{0.5}]}{\cos(\alpha+\phi)}\right)^2[4\phi\theta - 2\theta^2]d\theta \tag{38}$$

where K is a modification coefficient. The L_v number in Eq. (38) was introduced by Ma et al. (1994) as

$$L_v = \frac{\Delta\bar{u}_{l,j}}{\bar{u}_{l,f,j}} \tag{39}$$

where

$$\Delta\bar{u}_{l,j} = \bar{u}_{l,f,j} - \bar{u}_{l,r_2,j} \tag{40}$$

The average velocity of the free liquid surface without any vapor flow effect, $\bar{u}_{l,f,j}$ in Eq. (39), can be found as

$$\bar{u}_{l,f,j} = \frac{K}{2\phi}\int_0^{2\Phi}\left(-\frac{1}{4\mu_l}\frac{dp_l}{dz}\right)_j[4\phi\theta - 2\theta^2]\cdot\left(\frac{r_{w,l,j}[\cos\alpha\cos(\phi-\theta) - [\sin^2\phi - \cos^2\alpha\sin^2(\phi-\theta)]^{0.5}]}{\cos(\alpha+\phi)}\right)^2 d\theta \tag{41}$$

Downloaded 11 Dec 2010 to 193.140.21.150. Redistribution subject to ASME license or copyright; see http://www.asme.org/terms/Terms_Use.cfm

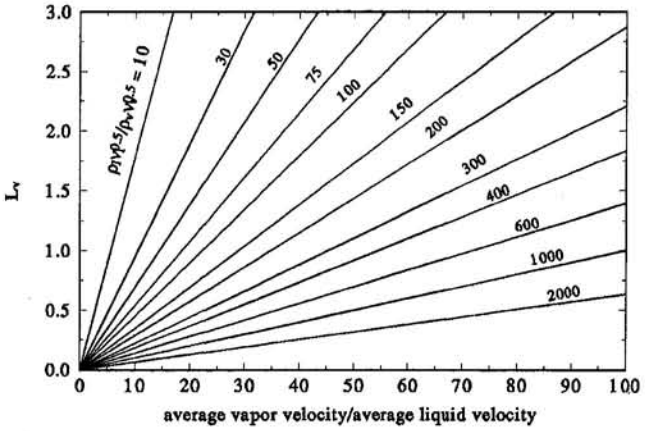


Fig. 4 Dimensionless vapor–liquid interface number

Table 1 Properties of methanol

Density	751.0 (kg/m^3)
Surface Tension	0.01875 (N/m)
Viscosity	3.26X10^{-4} (Ns/m^2)
Latent Heat	1101 (kJ/kg)

Ma and Peterson (1996) solved for the two-dimensional vapor flow and liquid flow fields previously and found that the value of L_v is related to the ratio of vapor velocity and liquid velocity, and the dimensionless term, $\rho_l\nu_l^{0.5}/\rho_v\nu_v^{0.5}$, as shown in Fig. 4.

The resulting friction factor of liquid flow in the triangular grooves with the vapor flow effect can be determined as follows:

$$f_{l,j}\cdot \mathrm{Re}_{h,l,j} = \left(\frac{-(dp_l/dz)_j D_{h,l,j}}{2\rho_l \bar{U}_{l,j}^2}\right)\left(\frac{\rho_l \bar{U}_{l,j} D_{h,l,j}}{\mu_l}\right) \quad (42)$$

where

$$\bar{U}_{l,j} = \frac{V_{l,j}}{A_{l,j}} \quad (43)$$

$$A_{l,j} = \tfrac{1}{2}\int_0^{2\phi} r_{2,j}^2\, d\theta \quad (44)$$

$$D_{h,l,j} = \frac{4A_{l,j}}{P_{l,j}} \quad (45)$$

$$P_{l,j} = 2r_{w,l,j} \quad (46)$$

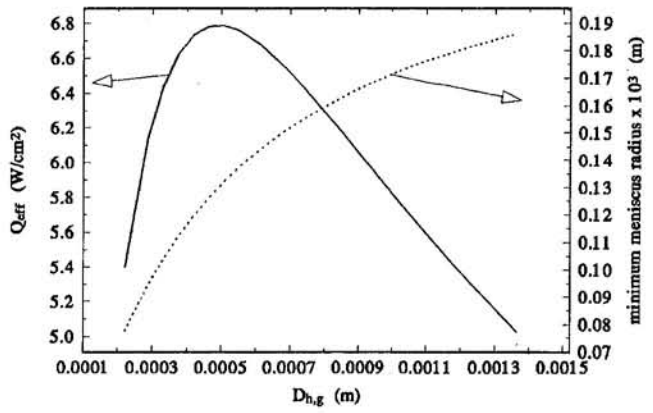


Fig. 5 Maximum unit effective area heat transport and minimum meniscus radius (α = 0 deg, 2ϕ = 60 deg, ψ = 10 deg, L_t = 0.06 m, L_v = 0)

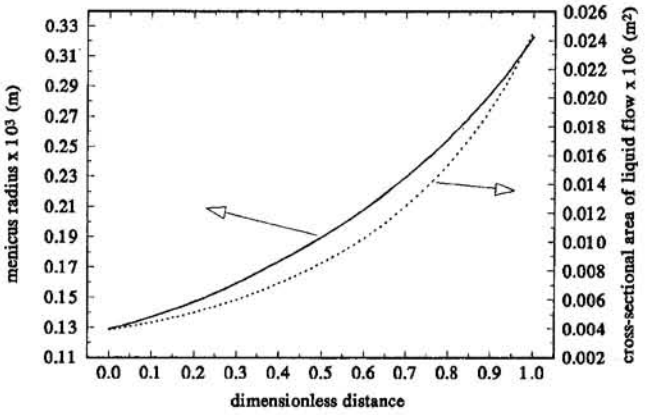


Fig. 6 Variations of meniscus radius and cross-sectional area of liquid flow (α = 0 deg, 2ϕ = 60 deg, ψ = 10 deg, L_t = 0.06 m, L_v = 0, $D_{h,g}$ = 0.000484 m)

and

$$V_{l,j} = \int_0^{2\phi}\int_0^{r_{2,j}} u_{l,j} r dr d\theta \quad (47)$$

For a specific micro heat pipe, the velocity distributions and properties of both the vapor flow and liquid flow can be found, and the values for L_v can be determined from Fig. 4. By solving Eqs. (42)–(47), the corresponding friction factor at any grid point can be calculated. This process yields a complete mathematical model for the maximum capillary heat transport in the triangular grooves, which includes the effect of the vapor flow

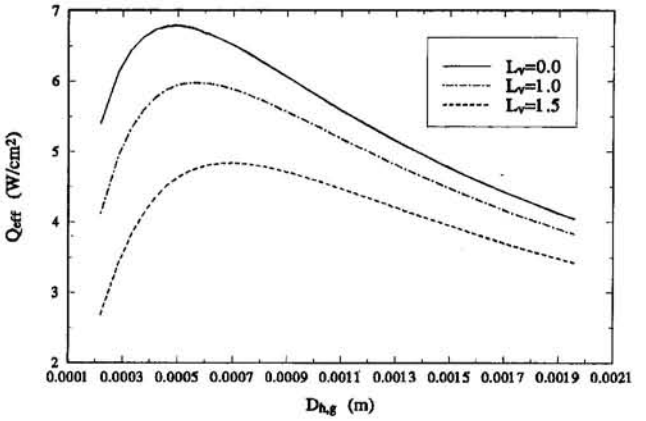


Fig. 7(a) The unit effective area heat transport with vapor flow influence (α = 0 deg, 2ϕ = 60 deg, ψ = 10 deg, L_t = 0.06 m)

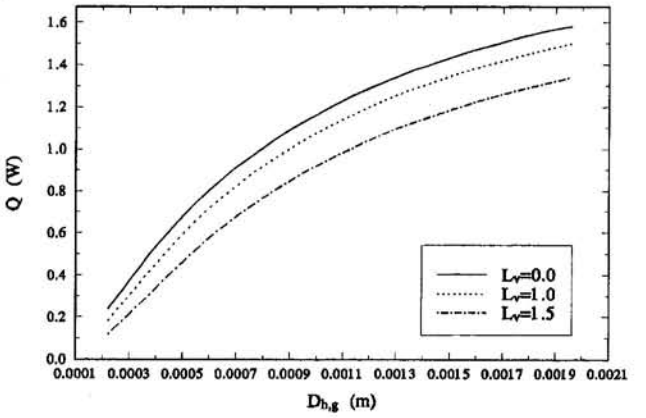


Fig. 7(b) The heat transport with vapor flow influence (α = 0 deg, 2ϕ = 60 deg, ψ = 10 deg, L_t = 0.06 m)

Downloaded 11 Dec 2010 to 193.140.21.150. Redistribution subject to ASME license or copyright; see http://www.asme.org/terms/Terms_Use.cfm

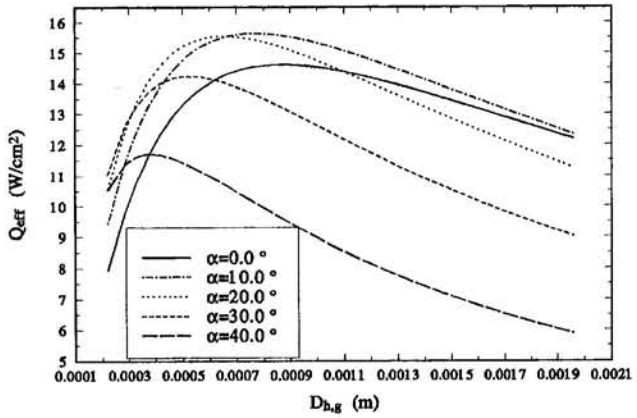


Fig. 8(*a*) The unit effective area heat transport with contact angles of $\psi = 5$ deg ($\alpha = 0$ deg, $2\phi = 60$ deg, $L_t = 0.06$ m, $L_v = 0$)

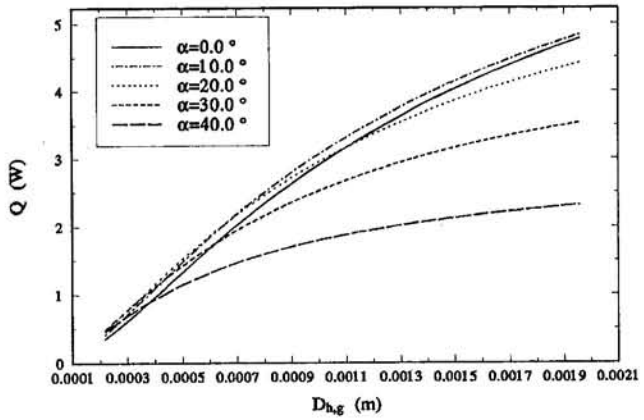


Fig. 8(*b*) The heat transport with contact angles of $\psi = 5$ deg ($\alpha = 0$ deg, $2\phi = 60$ deg, $L_t = 0.06$ m, $L_v = 0$)

and grooves geometry and provides a method for determining the minimum meniscus radius.

Results and Discussion

Many of the micro heat pipes successfully fabricated and tested to date consist of either three or four triangular grooves, i.e., a triangular heat pipe (Peterson et al., 1993) or a trapezoidal heat pipe (Peterson, 1992). For this reason, to generalize the current analysis, only one triangular liquid artery will be analyzed, as shown in Fig. 3. Because the amount of working fluid strongly affects the maximum capillary heat transport capability, the current analysis assumes that an optimum amount of working fluid always exists (practically this can be accomplished by a slight overcharge), and the effect of the condensing heat transfer coefficient is neglected. Based on these conditions, the maximum capillary heat transport in a triangular groove and the principal factors affecting the maximum capillary heat transport capability have been examined for one specific case.

Table 1 lists the physical properties of methanol used to obtain the calculated results that follow. These results are presented in terms of the unit effective area heat transport, Q_{eff}, and the heat transport, Q, occurring for a hydraulic diameter, $D_{h,g}$.

Based on the mathematical model presented previously, the maximum unit effective area heat transport and the minimum meniscus radius can be found as shown in Fig. 5. From Fig. 5, the hydraulic diameter of the triangular grooves is equal to 0.484 mm, and the groove reaches a maximum capillary heat transport capability of 6.79 W/cm^2. Figure 6 illustrates the variation of the meniscus radius and cross-sectional area of the liquid flow in the triangular groove for this situation.

Since the effect of the vapor flow on the liquid flow depends not only on the velocity, but also on the type of working fluid used, the dimensionless vapor–liquid interface flow number, L_v, was utilized to describe the vapor flow influence. From Fig. 7(a), it can be seen that as L_v increases, the heat transport capacity of the micro heat pipe becomes smaller, and the maximum effective area heat transport decreases rapidly. Figure 7(b) illustrates the relationship between the heat transfer and the effective hydraulic diameter for different values of the L_v number and shows a curvilinear increase in heat flux with increasing hydraulic diameter.

Figures 8(a) and 8(b) illustrate the effect of the contact angle, for a micro heat pipe with a tilt angle of 5 deg. As shown, when the contact angle increases, the heat transport capacity of the micro heat pipe initially increases, then reaches a maximum value, and finally decreases, significantly decreasing the maximum effective area heat transport. This implies that there is an optimum contact angle for a specific micro heat pipe that will result in a maximum unit effective area heat transport capacity, and that this value will vary somewhat as the tilt angle of the micro heat pipe changes. This dependence is further illustrated in Figs. 9(a) and 9(b).

Comparing the results shown in Figs. 8(a) and 9(a), it is apparent that the tilt angle has a significant influence on the capillary heat transport capacity. In addition, as the length of a micro heat pipe increases, the heat transport capacity decreases, as shown in Figs. 10(a) and 10(b) and not only does the unit effective area heat transport decrease, but so too does the total heat transport. Figures 11(a) and 11(b) illustrate the effect of variations in the channel angle. As shown, decreases in the channel apex angle result in increases in the heat transport

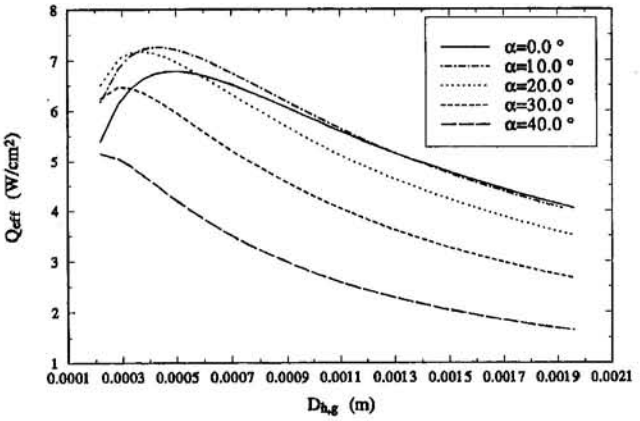


Fig. 9(*a*) The unit effective area heat transport with contact angles of $\psi = 10$ deg ($\alpha = 0$ deg, $2\phi = 60$ deg, $L_t = 0.06$ m, $L_v = 0$)

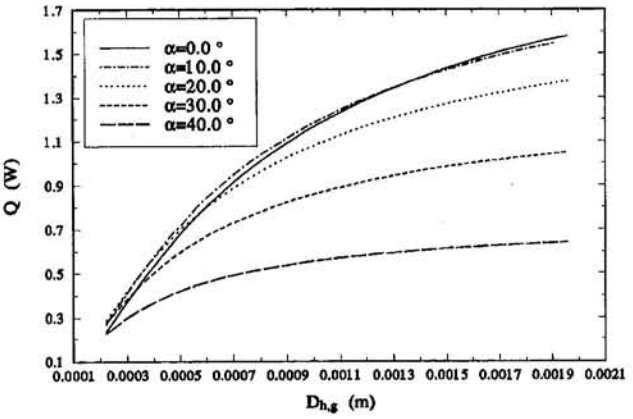


Fig. 9(*b*) The heat transport with contact angles of $\psi = 10$ deg ($\alpha = 0$ deg, $2\phi = 60$ deg, $L_t = 0.06$ m, $L_v = 0$)

Downloaded 11 Dec 2010 to 193.140.21.150. Redistribution subject to ASME license or copyright; see http://www.asme.org/terms/Terms_Use.cfm

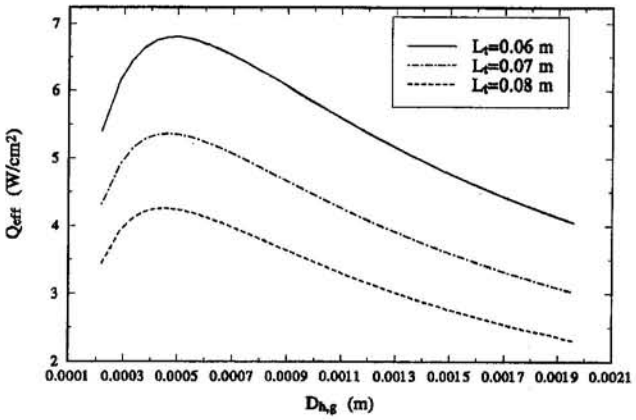


Fig. 10(*a*) The unit effective area heat transport as a function of the length of heat pipe (α = 0 deg, 2ϕ = 60 deg, ψ = 10 deg, L_v = 0)

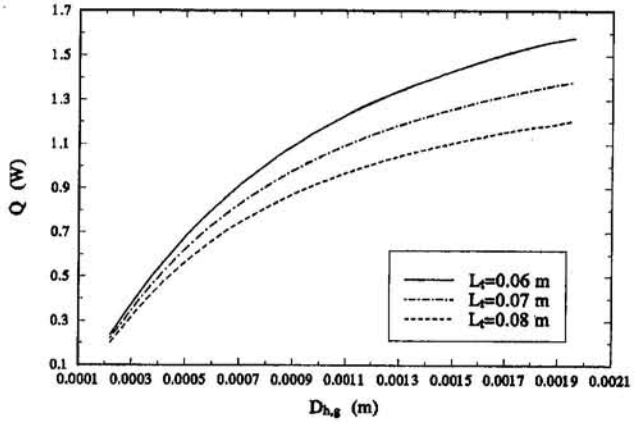


Fig. 10(*b*) The heat transport as a function of the length of heat pipe (α = 0 deg, 2ϕ = 60 deg, ψ = 10 deg, L_v = 0)

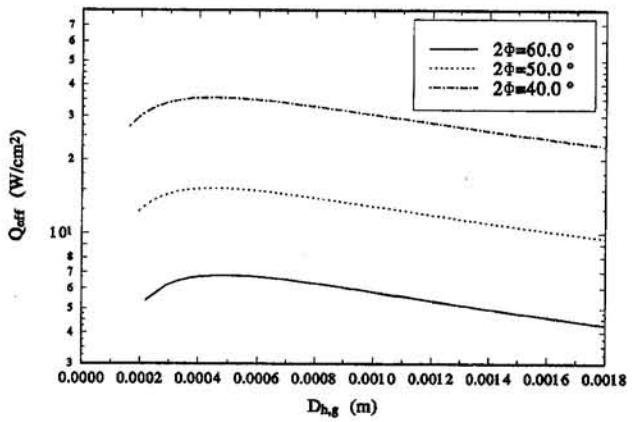


Fig. 11(*a*) The unit effective area heat transport as a function of the channel angle (α = 0 deg, ψ = 10 deg, L_t = 0.06 m, L_v = 0)

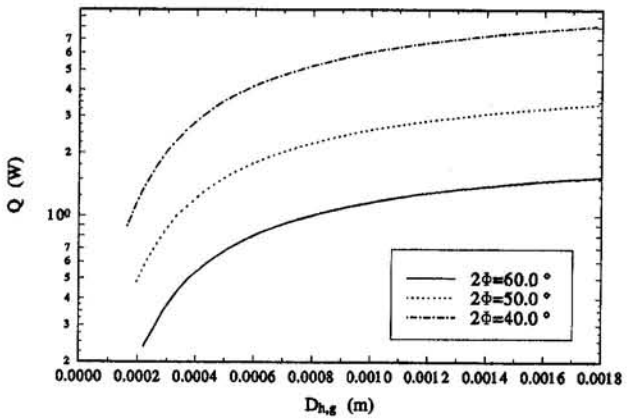


Fig. 11(*b*) The heat transport as a function of channel angle (α = 0 deg, ψ = 10 deg, L_t = 0.06 m, L_v = 0)

capacity. Utilizing the results illustrated in Figs. 7(*a*), 8(*a*), 9(*a*), 10(*a*), and 11(*a*), it is apparent that an optimum hydraulic diameter exists, such that a given micro heat pipe will have a single maximum heat transport capacity, which is also dependent upon the title angle. As a result, if the application environment is specified, the current analysis provides a method by which the optimum micro heat pipe geometry can be determined analytically.

In order to verify the theoretical analysis, a comparison of the numerical results and the experimental data obtained by Ma and Peterson (1996) for the maximum capillary heat transport in triangular grooves was made as shown in Fig. 12. This comparison only includes the evaporator and adiabatic sections, and effectively excludes the effect of any condensing heat transfer coefficient. As illustrated, the agreement between the experimental results is quite good, and not only verifies that there exists an optimum dimension for which the capillary grooves have the largest capillary heat transport capability, but also confirms the analytical approach. As a result, if the exact heat flux distribution is known, a better prediction can be obtained.

Conclusions

A mathematical model for predicting the maximum heat transport in micro heat pipes has been developed. The model is based on the capillary limit, which has been shown to be the principal operating limit for micro heat pipes. In this model, an expression for the theoretical minimum meniscus radius was used to calculate a capillary limit based on the geometric characteristics of the triangular grooves used in micro heat pipes. A control volume technique was employed to incorporate the flow characteristics of the grooves, and the frictional liquid–vapor interaction based on a two-dimensional model was included. The resulting model was solved numerically. The calculated results indicate that the heat transport capacity of a micro heat pipe is dependent on the channel angle of grooves, the contact angle of the liquid, the length of the micro heat pipe, the vapor flow characteristics, and the tilt angle, and that neglecting the effects of the frictional interaction between the liquid and vapor flow can result in significant errors in the predicted maximum heat transport capacity. The analytical technique presented here can be used effectively to direct the design of micro heat pipes with better performance characteristics and higher transport capacities.

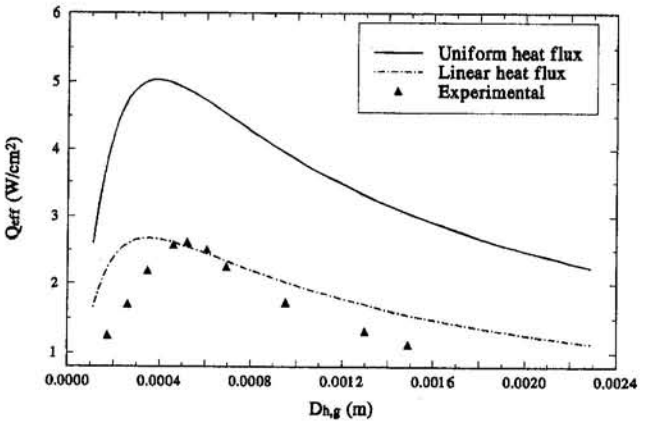


Fig. 12 Comparison with experimental data (α = 0 deg, 2ϕ = 60 deg, ψ = 16 deg, L_t = 0.05 m, L_v = 0, L_c = 0)

Downloaded 11 Dec 2010 to 193.140.21.150. Redistribution subject to ASME license or copyright; see http://www.asme.org/terms/Terms_Use.cfm

References

Ayyaswamy, P. S., Catton, I., and Edwards, D. K., 1974, "Capillary Flow in Triangular Grooves," ASME *Journal of Applied Mechanics,* Vol. 41, pp. 332–336.

Babin, B. R., Peterson, G. P., and Wu, D., 1990, "Steady-State Modeling and Testing of a Micro Heat Pipe," ASME JOURNAL OF HEAT TRANSFER, Vol. 112, pp. 595–601.

Chi, S. W., 1976, *Heat Pipe Theory and Practice,* McGraw-Hill, New York.

Cotter, T. P., 1984, "Principles and Prospects of Micro Heat Pipes," *Proc. 5th Int. Heat Pipe Conf.,* Tsukuba, Japan, pp. 328–335.

Duncan, A. B., and Peterson, G. P., 1995, "Charge Optimization for Triangular Shaped Etched Micro Heat Pipe," *AIAA Journal of Thermophysics and Heat Transfer,* Vol. 9, No. 2, pp. 365–367.

Gerner, F. M., 1990, *Micro Heat Pipes,* AFSOR Final Report No. S-210-10Mg-066, Wright-Patterson AFB, Dayton, OH.

Gerner, F. M., Longtin, J. P., Henderson, H. T., Hsieh, W. M., Ramadas, P., and Chang, W. S., 1992, "Flow and Heat Transfer Limitations in Micro Heat Pipes," *Proc. ASME Annual Meeting,* ASME HTD-Vol. 206-3, pp. 99–104.

Khrustalev, D., and Faghri, A., 1994, "Thermal Analysis of A Micro Heat Pipe," ASME JOURNAL OF HEAT TRANSFER, Vol. 116, No. 2, pp. 189–198.

Longtin, J. P., Badran, B., and Gerner, F. M., 1994, "A One-Dimensional Model of a Micro Heat Pipe During Steady-State Operation," ASME JOURNAL OF HEAT TRANSFER, Vol. 116, pp. 709–715.

Ma, H. B., Peterson, G. P., and Lu, X. J., 1994, "The Influence of Vapor–Liquid Interactions on the Liquid Pressure Drop in Triangular Microgrooves," *Int. J. Heat Mass Transfer,* Vol. 37, No. 15, pp. 2211–2219.

Ma, H. B., and Peterson, G. P., 1996, "Experimental Investigation of the Maximum Heat Transport in Triangular Grooves," ASME JOURNAL OF HEAT TRANSFER, Vol. 118, this issue, pp. 740–746.

Peterson, G. P., 1992, "Overview of Micro Heat Pipe Research and Development," *Appl. Mech. Rev.,* Vol. 45, No. 5, pp. 175–189.

Peterson, G. P., Duncan, A. B., and Weichold, M. H., 1993, "Experimental Investigation of Micro Heat Pipes Fabricated in Silicon Wafers," ASME JOURNAL OF HEAT TRANSFER, Vol. 115, pp. 751–756.

Peterson, G. P., 1994, *An Introduction to Heat Pipes: Modeling, Testing and Applications,* Wiley, New York.

Peterson, G. P., 1996, "Modeling, Testing, and Fabrication of Micro Heat Pipes: An Update," *Appl. Mech. Rev.,* in press.

Peterson, G. P., and Ma, H. B., 1996, "Analysis of Countercurrent Liquid–Vapor Interaction and the Effect on the Liquid Friction Factor," *Experimental Thermal and Fluid Sciences,* Vol. 12, No. 1, pp. 13–24.

Peterson, G. P., Swanson, L. W., and Gerner, F. M., 1996, "Micro Heat Pipes," in: *Microscale Energy Transport,* C. L. Tien, A. Majumdar, and F. M. Gerner, eds., Taylor-Francis Publishing Co., Washington DC, in press.

Tien, C. L., and Sun, K. H., 1971, "Minimum Meniscus Radius of Heat Pipe Wicking Materials," *Int. J. Heat Mass Transfer,* Vol. 14, pp. 1853–1855.

Downloaded 11 Dec 2010 to 193.140.21.150. Redistribution subject to ASME license or copyright; see http://www.asme.org/terms/Terms_Use.cfm

Experimental Investigation of the Maximum Heat Transport in Triangular Grooves

H. B. Ma
Graduate Research Assistant.

G. P. Peterson
Tenneco Professor and Head.
Fellow ASME

Department of Mechanical Engineering,
Texas A&M University,
College Station, TX 77843-3123

An experimental investigation was conducted and a test facility constructed to measure the capillary heat transport limit in small triangular grooves, similar to those used in micro heat pipes. Using methanol as the working fluid, the maximum heat transport and unit effective area heat transport were experimentally determined for ten grooved plates with varying groove widths, but identical apex angles. The experimental results indicate that there exists an optimum groove configuration, which maximizes the capillary pumping capacity while minimizing the combined effects of the capillary pumping pressure and the liquid viscous pressure losses. When compared with a previously developed analytical model, the experimental results indicate that the model can be used accurately to predict the heat transport capacity and maximum unit area heat transport when given the physical characteristics of the working fluid and the groove geometry, provided the proper heat flux distribution is known. The results of this investigation will assist in the development of micro heat pipes capable of operating at increased power levels with greater reliability.

Introduction

At present the limiting criteria in the microminiaturization of electronic components and devices are determined by the maximum acceptable junction temperature. This temperature limit is a function of several factors, including the temperature uniformity of the device and the heat rejection capability of the cooling system employed. Recently, a number of investigations have been performed to determine the feasibility of incorporating arrays of micro heat pipes as an integral part of silicon or gallium arsenide wafers (Peterson et al., 1993; Duncan and Peterson, 1995; Mallik and Peterson, 1995; Peterson and Mallik, 1995). These investigations have demonstrated that arrays of micro heat pipes can function as highly efficient heat spreaders with an effective thermal conductivity, several orders of magnitude greater than the bulk wafer material. What is not clear at this point, however, is what types of limitations will be encountered when these heat pipe arrays are incorporated into devices with localized heat fluxes on the order of 100 W/cm^2, similar to those reported by Cao et al. (1993).

Past research has shown that the most frequently encountered limitation in micro heat pipes results from the inability of the capillary wicking structure to effectively return the working fluid to the evaporator where it can be vaporized. In most of the recently developed models, the heat transport limit was determined using a pressure balance and the thermal analysis (Khrustalev and Faghri, 1994). However, more recent work indicates that for a typical micro heat pipe with sharp **V**-shaped corners, the maximum heat transport capacity cannot be determined by simply assuming the minimum capillary radius. Instead, a true capillary limit, which considers the combined effects of the capillary pumping pressure, the liquid viscous pressure losses, and the vapor/liquid interaction must be used (Peterson and Ma, 1995).

In a previous investigation, an analytical model was developed to predict the true capillary radius and the resulting maximum heat transport in micro heat pipes (Peterson and Ma, 1995). In this model, a theoretical minimum meniscus radius was determined and coupled with the combined effects of the capillary pumping pressure, the liquid viscous pressure losses, and the vapor/liquid interaction. A control volume technique was employed to determine the flow characteristics of micro heat pipes with no wicks, and to incorporate the effects of the frictional vapor–liquid interaction on the liquid flow. This model was then used to calculate the maximum heat transport limit based on the physical characteristics of the working fluid and the groove geometry.

This model for the first time considered the true characteristics of micro heat pipes to determine the minimum meniscus radius and the maximum heat transport capacity. The calculated results indicated that for wickless micro heat pipes, the heat transport capacity is strongly dependent on the channel angle of the liquid arteries, the contact angle of the liquid flow, the length of the heat pipe, the vapor flow, and the tilt angle. In addition, the model developed provided a mechanism that, for a given specified set of conditions, allowed the geometry to be optimized and a micro heat pipe with the maximum heat transport for a given cross-sectional area, designed. In an effort to determine the validity of this analytical approach, an experimental investigation was undertaken and the capillary limit of liquids in triangular grooved heat pipes was measured and evaluated.

Theoretical Model

The mathematical model presented by Peterson and Ma (1995) can be summarized and with minor modifications can be used to predict the capillary limit of liquid flows for a physical configuration that approximates that occurring in the micro heat pipe shown in Fig. 1. To simplify the problem under consideration, assume first that a uniform heat flux is applied to the evaporating section of a plate into which a series of **V**-shaped grooves has been machined. For this situation, each individual groove can be divided into N control volumes with the notation depicted in Fig. 2(a). Utilizing the control volume shown in Fig. 2(b), the pressure drop produced by the shear forces occurring at the liquid–solid interface, when added to the gravitational pressure drop, must be less than the pumping pressure produced

Contributed by the Heat Transfer Division for publication in the JOURNAL OF HEAT TRANSFER. Manuscript received by the Heat Transfer Division September 14, 1995; revision received April 29, 1996. Keywords: Boiling, Heat Pipes and Thermosyphons, Thermocapillary Flows. Associate Technical Editor: M. Modest.

Copyright © 1996 by ASME

Downloaded 11 Dec 2010 to 193.140.21.150. Redistribution subject to ASME license or copyright; see http://www.asme.org/terms/Terms_Use.cfm

by the small characteristic capillary radius (Peterson and Ma, 1995), i.e.,

$$\sigma\left(\frac{1}{r_{j+1}}-\frac{1}{r_j}\right) \geq \rho_l g(z_{j+1}-z_j)\sin\psi + \frac{(\mathrm{Re}\cdot f)\mu_l \dot{m}\cos^2(\alpha+\phi)(r_{j+1}+r_j)^2}{C_1^3\sin^2\phi\rho_l(r_{j+1}^2+r_j^2)^3}(z_{j+1}-z_j) \quad (1)$$

where

$$C_1=\frac{1}{2}\int_0^{2\phi}\left[\frac{\cos\alpha\cos(\phi-\theta)-(\sin^2\phi-\cos^2\alpha\sin^2(\phi-\theta))^{0.5}}{\sin^2\phi}\right]^2 d\theta$$

The r_j and r_{j+1} in Eq. (1) represent the meniscus radii of curvature at the j-th grid point and $j+1$-th grid point, respectively, as shown in Fig. 2(*b*). Assuming that the radius of curvature at the liquid surface is constant, which is true for low Bond numbers (Ayyaswamy et al., 1974), Eq. (1) can be applied to both the evaporating and adiabatic regions, with the primary difference being that the mass flow rate, $\dot{m}$, will have different values for the two sections, i.e.,

$$\dot{m}=\begin{pmatrix}\dfrac{Q}{h_{fg}}-\dfrac{Q(j-e)D_{\mathrm{eff}}}{h_{fg}A_{\mathrm{eff}}}(z_{j+1}-z_j) & \text{(evaporator section)}\\ \text{const} & \text{(adiabatic section)}\end{pmatrix} \quad (2)$$

Here Eq. (1) is written for the j-th control volume; however, since the groove is divided into N control volumes, there are N equations, one governing each control volume. While it is clear from Eq. (1) that finding the capillary radii is the key to solving these governing equations, it is also necessary to determine the boundary conditions. For the first control volume, the capillary radius can be found from the geometric shape by assuming a constant radius. For the last control volume, the capillary radius will depend on the heat flux and the balance between the shear stress and the capillary forces.

Experimental System and Methodology

In order to determine the maximum heat transport based on the true capillary limit, a physical model was designed and fabricated. In this physical model, which is illustrated in Fig. 3, one end of a plate was immersed in a liquid pool and held stationary at a specified tilt angle. The liquid was wicked up the grooves by the capillary pressure, against the gravitational force and the frictional pressure drop resulting from the continuous flow of liquid. To simulate a typical micro heat pipe in operation, an axial adiabatic region was included between the point of origin (where the plate emerges from the liquid pool) and the junction point (the start of the region where a uniform heat flux was applied). As shown in Fig. 3, the evaporating section extended from the junction point to the dryout point. No condensing section was included, thereby eliminating the influence of the condensation in the condenser region, on the measured maximum heat transport. In this way, it was possible to determine the true capillary limit of the liquid flowing in the V-shaped grooves, and approximate the conditions occurring in a typical micro heat pipe. In addition, data from these tests could be used to verify the model previously developed by Peterson and Ma (1995).

The experimental test facility, shown in Fig. 3, was comprised of a grooved plate, a liquid pool, a weight collecting unit, a power supply and measuring unit, a temperature data collection system, a liquid supply unit, and two constant temperature cooling baths. The working fluid utilized in this investigation was methanol, and the operating temperature was maintained at 60 ± 1°C, at a vapor pressure of one atmosphere, 742.5 mm Hg, which during the experiment was measured to be constant to within 0.05 mm Hg. The grooved plate was fabricated from pure copper, and care was taken to ensure that the bottom or apex angles of the grooves were very sharp, as shown in Fig. 4(*a*).

After machining the grooves, a photomicrograph of the cross-sectional shape and width of the grooves was taken. The dimensions, including the channel apex angle and width of the grooves, were obtained by measuring directly from the photomicrograph using a 10× measuring magnifier. The uncertainty of the measurement depends on the size of the grooves, with the relative error increasing as the grooves become smaller. The largest calculated uncertainties in the current investigation, were less than +3 deg for the channel angle, and ± 10 percent for the width of grooves. Table 1 presents the dimensions of the ten grooved plates used in the current investigation.

Prior to the start of the experiments, the grooved plates were first cleaned with acetone, then a solution containing 10 percent sulfuric acid by volume was used to remove copper oxides and tarnish. In this way, identical surface conditions could be obtained for all of the grooved plates (Taylor, 1967).

In order to obtain a constant operating temperature, four cooling passages were fabricated in each test article as shown in Fig. 3. These cooling passages were connected to cooling bath No. 1, where the temperature was held constant to within ±0.02°C by an ultrasensitive thermoregulator. These cooling passages allowed the temperature of the evaporator section of the grooved plates to be controlled and held constant to within ±0.5°C, while still allowing the input heat flux to be varied. Throughout all of the tests, the adiabatic section of the grooved

Nomenclature

A = cross-sectional area, m^2
B = Bond number
C_1 = coefficient
D_{eff} = hydraulic diameter, m
f = friction factor
g = gravity acceleration, m/s^2
h_{fg} = latent heat of vaporization, J/kg
$\dot{m}$ = mass flow rate, kg/s
N_g = number of grooves
p = perimeter, m
Q = heat transport, W
Q_{eff} = unit effective area heat transport, W/m^2
r = meniscus radius of curvature, m
Re = Reynolds number
z = distance, m
W_l = wight of liquid, kg
α = contact angle, deg
μ = viscosity, N·s/m^2
ρ = density, kg/m^3
σ = surface tension, N/m
τ = time, s
ϕ = half-channel angle, deg
ψ = tilt angle, deg

Subscripts

a = adiabatic
c = capillary
e = evaporator
eff = effective
l = liquid
t = total
w = wall

Downloaded 11 Dec 2010 to 193.140.21.150. Redistribution subject to ASME license or copyright; see http://www.asme.org/terms/Terms_Use.cfm

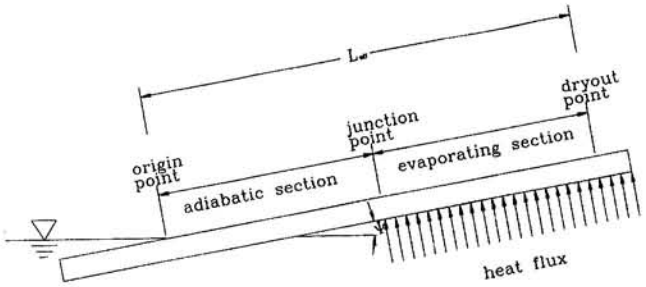


Fig. 1 Schematic of the physical model

plate was held constant at a temperature of 60 ± 1°C by adjusting the temperature and the flow rate of the coolant flowing through the cooling passages.

In order to monitor the temperature variation on the grooved plate, five thermocouples were embedded directly into the plate and monitored by a 3497A data acquisition system controlled by a personal computer. In addition, several thermocouples were used to measure and monitor the temperature of the cooling passages in the grooved plates, the room temperature, the liquid pool temperature, and the inlet and outlet temperatures of the micro heat exchanger. The liquid pool shown in Fig. 3 was fabricated from lexan and had a wall thickness of 12.7 mm. Because the thermal conductivity of the liquid container was low and well insulated, the experimental system achieved steady state relatively quickly.

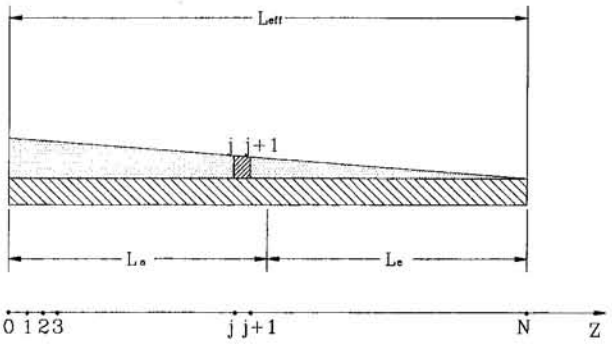


Fig. 2(*a*) Schematic of a triangular groove

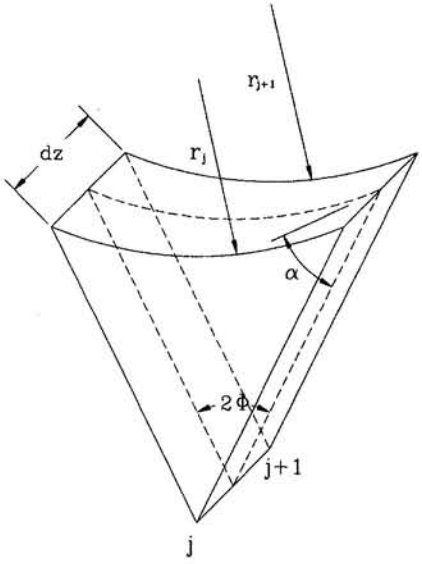
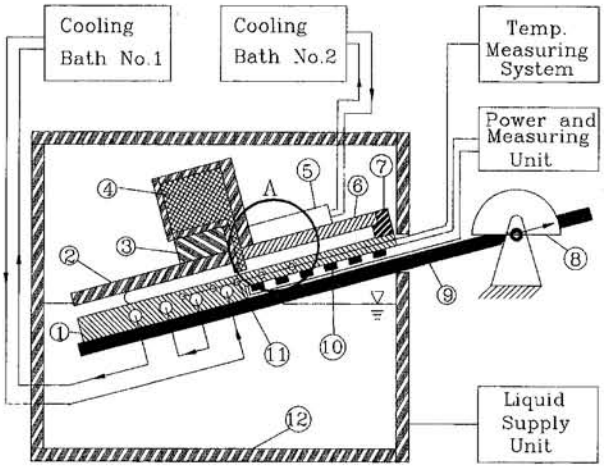
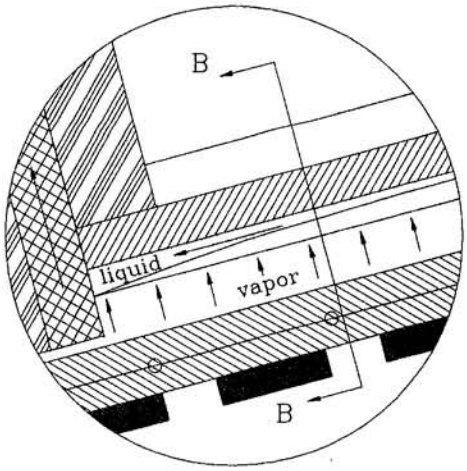


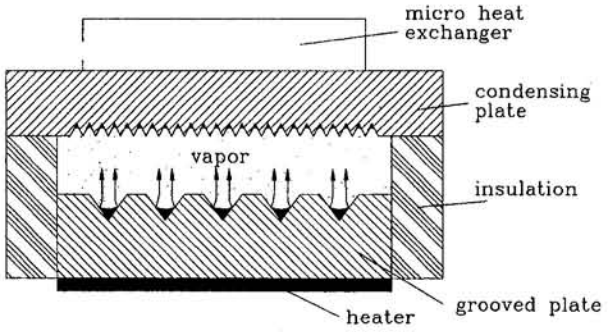
Fig. 2(*b*) Control volume



1	grooved plate	7	block
2	LEXAN sheet	8	protractor
3	slide	9	supporter
4	collector	10	heater
5	micro heat exchanger	11	thermocouple
6	condensing plate	12	liquid pool



Detail of A



Cross-section on B–B

Fig. 3 Schematic of experimental system

Downloaded 11 Dec 2010 to 193.140.21.150. Redistribution subject to ASME license or copyright; see http://www.asme.org/terms/Terms_Use.cfm

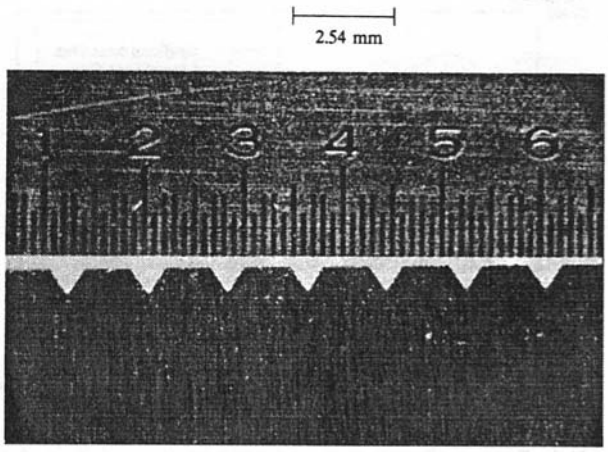


Fig. 4(*a*) Scanning micrograph of triangular grooves

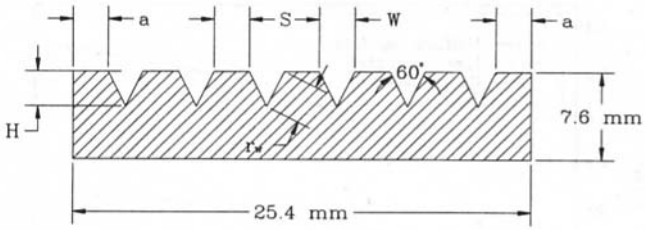


Fig. 4(*b*) The cross section of a grooved plate

To determine the actual heat transferred due to the vaporization and condensation of the working fluid, a weight collecting unit, composed of a slide, a collector, a micro heat exchanger, a condensing plate, and a vapor block was constructed. The purpose of this unit was to collect the vapor generated in the evaporating section of the grooved plate, condense it, and then by weighing it, provide an accurate measurement of the total energy transported through the vaporization process. In order to condense the vapor effectively, and transport the condensed liquid into the collector shown in Fig. 3, the condensing surface was constructed from aluminum, with a series of small triangular grooves to promote liquid flow. The liquid condensed on the condensing plate would then flow along these small grooves due to gravity and collect in the collection chamber, which was filled with highly absorbent material. The micro heat exchanger on the condensing plate was connected to a second cooling bath (No. 2). The temperature of the liquid from this bath was measured at the point where it entered the micro heat exchanger and was controlled to a temperature of 20 ± 1°C.

The heater was fabricated from stainless steel shim stock (0.025 mm). As discussed previously, the wetted length was divided into two distinct sections: an adiabatic section and an evaporating section. The heater was restricted to the evaporating section, as shown in Fig. 3 and power was supplied by a KEPCO power supply. In order to compare the results with the theoretical analysis and verify the model presented previously, the evaporating section length was held approximately equal to the length of the adiabatic section. Variable lengths of the adiabatic section and the evaporating section were achieved by adjusting the liquid level and the heat flux. The lexan sheet, which covered the adiabatic section shown in Fig. 3, provided clear observation of the origin line of the wetted length, and allowed the liquid between the grooved plate and the lexan sheet to be heated until it was approximately the same temperature as the adiabatic section of the grooved plate, prior to coming into contact with the grooves.

The liquid pool was 140 mm × 127 mm × 152 mm, and was designed in such a manner that the liquid level could be held constant throughout the experiment, regardless of the vaporization rate.

Prior to the start of the experiment, the system was allowed to equilibrate for approximately four hours until steady-state conditions had been reached and the temperature of the adiabatic section of the grooved plate had reached a temperature of 60 ± 1°C. Once the system obtained the required steady-state conditions, the length of the evaporating section and the corresponding heat flux were determined as follows:

1 The desired tilt angle of the grooved plate was fixed;
2 The length of the adiabatic section was fixed by adjusting the liquid supply unit or the distance between the lexan sheet and the grooved plate;
3 The heat flux was applied by the heat supply unit;
4 After reaching steady-state conditions, the temperature of the grooved plate was held constant, and the length of the evaporating section of the wetted length was measured.
5 A comparison was made between the fixed length of the adiabatic section, and the length of the evaporating section. If the length of the evaporating section was smaller than the fixed adiabatic section, the heat flux was decreased. If the length of the evaporating section was larger than the fixed adiabatic section, the heat flux was increased.

The procedure above was repeated until the heat flux was such that the length of the evaporating section was equal to the length of the adiabatic section.

Typically, the heat flux applied to the evaporating section of a heated plate can be measured directly by measuring the input power (Ha and Peterson, 1994; Stroes et al., 1992). In the current experimental investigation, however, a substantial fraction of the applied heat was conducted through the pure copper plate into which the grooves had been cut, to the cooling passages used to control the operating temperature. As a result, direct measurement of the thermal energy applied to the evaporator section could not provide an accurate estimation of the amount of energy transferred through the vaporization and condensation of the working fluid. Other losses, such as radiative and convective losses to the environment, also presented a problem. Hence, the development of a method for collecting and measuring the vapor generated in the evaporating sections was necessary. To accomplish this, a condensing plate with a micro heat exchanger was placed on the grooved plate as shown in Fig. 3, and the condensate collector put in place. When the system reached steady-state, i.e., a steady flow rate of the condensing liquid on the condensing plate had been achieved, a new condensate collector was weighed and was slid into place, forcing the first one aside. After a fixed period of time, typically 15 minutes, the condensate collector was removed and weighed on an Ainsworth AC-1200 scale. In this way, the weight of the liquid, W_i, that was vaporized from the grooved plate and collected in the condensate chamber, could be measured during the period of time, $\Delta\tau$, and using an energy balance

$$Q = \frac{W_i h_{fg}}{N_g \Delta\tau} \tag{3}$$

where h_{fg} is the latent heat of vaporization and N_g the number

Table 1 Dimensions of triangular grooves

W (mm)	0.20	0.30	0.40	0.53	0.60	0.70	0.80	1.10	1.50	1.65
D_m (mm)	0.17	0.26	0.35	0.46	0.52	0.61	0.69	0.95	1.30	1.43
H (mm)	0.17	0.26	0.35	0.46	0.52	0.61	0.69	0.95	1.30	1.43
S (mm)	1.27	1.27	1.27	1.27	1.27	1.27	1.27	1.27	1.27	1.27
a (mm)	0.11	0.78	0.81	0.74	1.18	0.53	0.92	1.49	2.26	1.66
No[1]	18	16	15	14	13	13	12	10	8	8

1. The number of triangular grooves on one grooved plate.

Downloaded 11 Dec 2010 to 193.140.21.150. Redistribution subject to ASME license or copyright; see http://www.asme.org/terms/Terms_Use.cfm

of grooves on the grooved plate, the heat transport resulting from the vaporization and condensation in one groove could be obtained. The procedure above was repeated until the measured results reached a constant value.

The uncertainty associated with this measurement technique was estimated to be approximately ±9.0 percent. Throughout the entire measurement procedure, the liquid level was held constant and the lengths of the evaporating and adiabatic sections were held equal, to ensure repeatable results.

The unit effective area heat transport, which is the focus of the current investigation, was defined as

$$Q_{\text{eff}} = \frac{Q}{A_{\text{eff}}} \tag{4}$$

where

$$A_{\text{eff}} = D_{\text{eff}} L_e = \frac{4AL_e}{p} \tag{5}$$

A is the cross-sectional area of the groove, L_e is equal to the length of the evaporating section of the grooved plate, and p is the perimeter of the groove, which is equal to $2r_w$.

Results and Discussion

Experimental measurements were made to determine the heat transport and the unit effective area heat transport in triangular grooves with apex angles of 60 deg as shown in Fig. 4(*a*) and 4(*b*). In order to determine the effect of variations of the groove size on the maximum unit effective area heat transport, ten grooved plates were fabricated. The experimental data for an effective length of 0.05 m and a tilt angle of 14 deg are plotted in Figs. 5(*a*) and 5(*b*). Figures 6(*a*) and 6(*b*) show the results

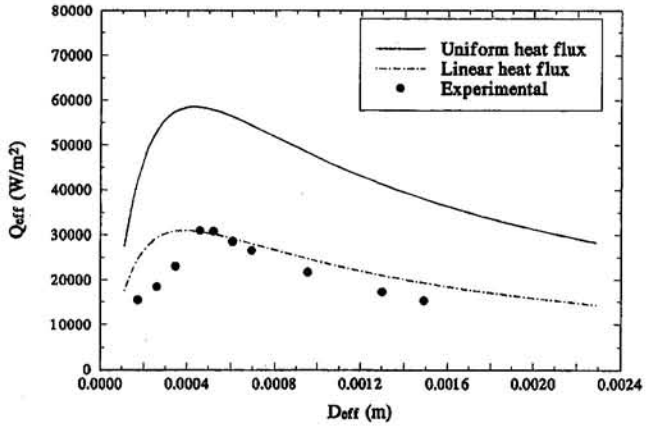


Fig. 5(*a*) The unit effective area heat transport (L_{eff} = 0.05 m, ψ = 14 deg)

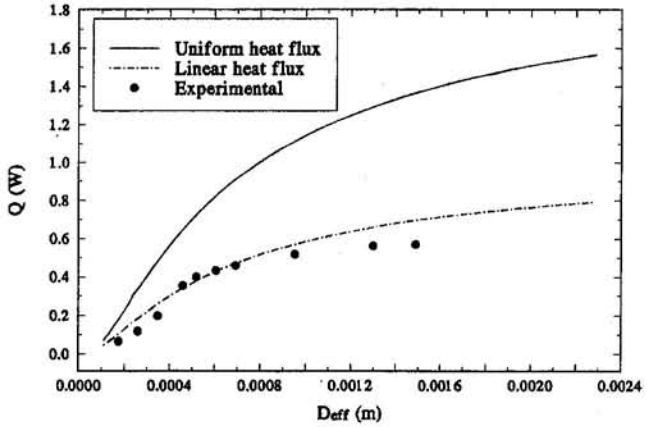


Fig. 5(*b*) The heat transport (L_{eff} = 0.05 m, ψ = 14 deg)

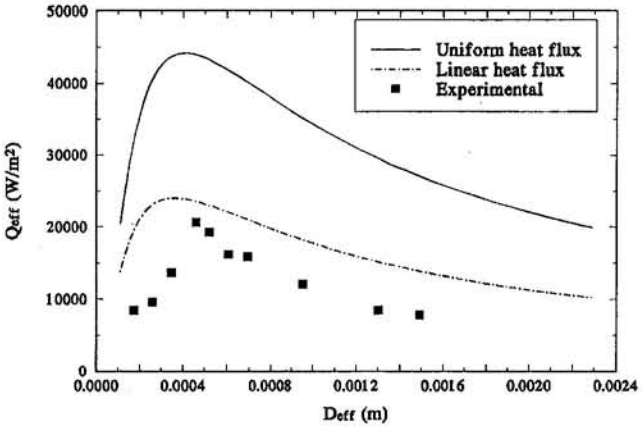


Fig. 6(*a*) The unit effective area heat transport (L_{eff} = 0.06 m, ψ = 14 deg)

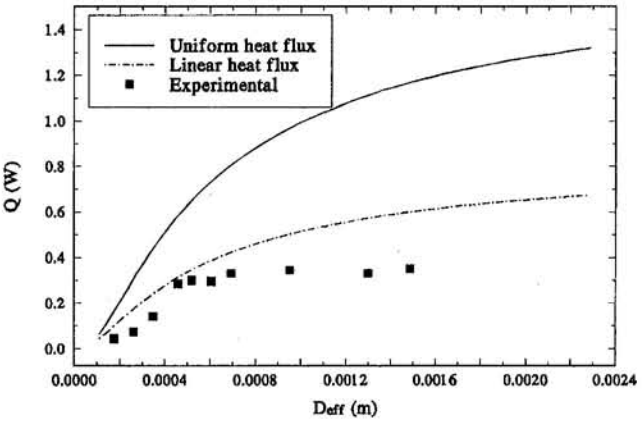


Fig. 6(*b*) The heat transport (L_{eff} = 0.06 m, ψ = 14 deg)

for an effective length of 0.06 m and a tilt angle of 14 deg, and Figs. 7(*a*) and 7(*b*) illustrate the results for an effective length of 0.05 m and a tilt angle of 16 deg. From Figs. 5(*a*), 6(*a*), and 7(*a*), it is clear that there exists an optimum geometry for which the unit effective area heat transport is at a maximum value, and that this unit effective area heat transfer depends on the tilt angle and the effective length. Decreasing the effective length of the groove and the tilt angle, increases the maximum unit effective area heat transport. From Figs. 5(*b*), 6(*b*), and 7(*b*), it is apparent that when the tilt angle and the effective length increase, the heat transport decreases. Although the heat transport continues to increase as the dimension of the groove increases, the heat transport soon reaches a constant value, and no optimum geometry for a maximum heat transport of one groove was found. This implies that increasing the dimensions of the individual grooves cannot improve the overall heat transport due to the decrease in the unit effective area heat transport.

In order to compare the results between the theoretical analysis and experimental data, the following assumptions were made for the theoretical model presented previously:

(*i*) The influence of the vapor flow was negligible;
(*ii*) The lengths of the evaporating and adiabatic sections were equal;
(*iii*) The properties of the working fluid were assumed to be α = 0 deg, ρ = 751.0 kg/m^3, σ = 0.01875 N/m, $\mu = 3.25 \times 10^{-4}$ N·s/m^2, and h_{fg} = 1101 kJ/kg; and
(*iv*) The disjoining pressure (Wayner, 1991) was assumed to be negligible.

As illustrated, for all three cases the theoretical predictions (shown as solid lines in Figs. 5–7) were all significantly higher

Downloaded 11 Dec 2010 to 193.140.21.150. Redistribution subject to ASME license or copyright; see http://www.asme.org/terms/Terms_Use.cfm

than the experimentally measured values. To resolve this disparity, the assumptions made in the model formulation were reexamined.

In 1990, Xu and Carey investigated the behavior of a thin liquid film, evaporating from a grooved plate. In this investigation, it was demonstrated that the heat transfer coefficient increased with decreasing average film thickness. These results were verified experimentally. Using a measured temperature difference, an approximate heat flux was found to have a nearly linear relationship with the plate length coordinate. For this reason, the linear heat flux distribution shown in Fig. 8 was assumed and incorporated into the previously developed model. The resulting correlation is in much better agreement with the experimental data, as shown in Figs. 5–7. Because the uncertainty in the thermocouple readings resulted in a high uncertainty for the experimentally determined values of the heat transfer coefficient in Xu and Carey's experimental investigation, and because some significant differences between their experiment and the current investigation exist, the correlation they used to obtain the heat flux on the evaporating section may not be completely appropriate for the current theoretical model. Extension of their work or alternative investigations designed to provide the exact heat flux distribution are necessary to make it possible to obtain better correlation with the experimental data.

It is apparent from Figs. 5–7 that increasing the hydraulic diameter increases the difference between the predictions and the experimental data. This may be due to the assumption of a constant radius of curvature, made previously. As stated, this assumption has a limit, i.e., the Bond number, defined as

$$B = \frac{\rho_l g D_{\text{eff}}^2}{4\sigma} \tag{6}$$

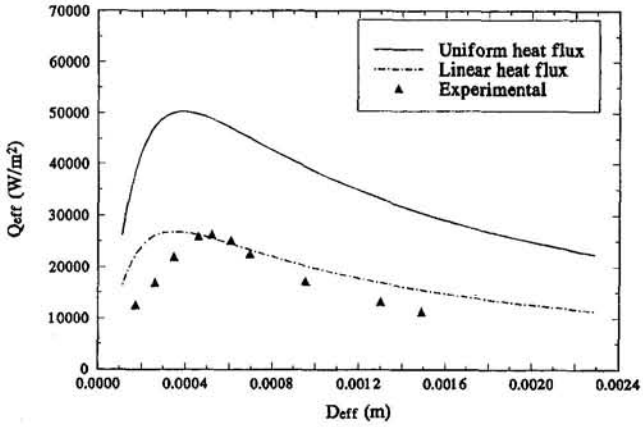


Fig. 7(*a*) The unit effective area heat transport (L_{eff} = 0.05 m, ψ = 16 deg)

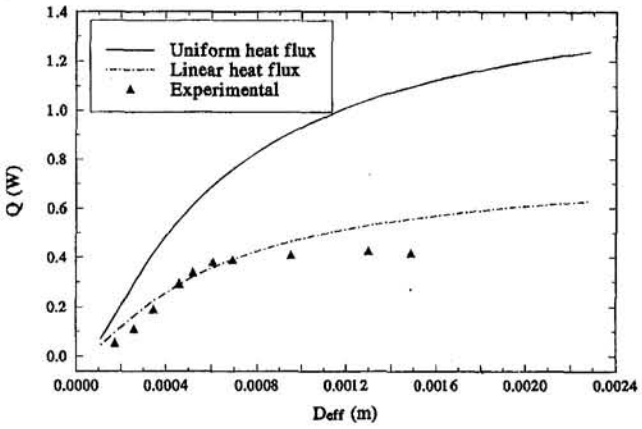


Fig. 7(*b*) The heat transport (L_{eff} = 0.05 m, ψ = 16 deg)

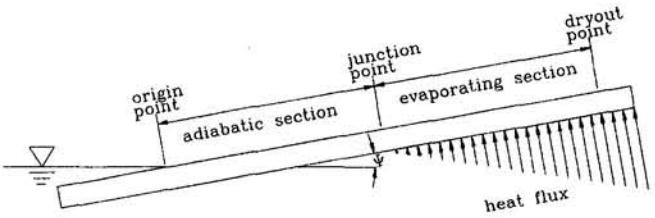


Fig. 8 The linear heat flux distribution

must be very small. From Figs. 5–7, it can be seen that when D_{eff} is larger than 0.00070 mm, i.e., the Bond number is larger than 0.05, the difference between the prediction and the experimental data becomes increasingly greater. This implies that when the Bond number is larger than 0.05, the assumption of constant meniscus radius of curvature may not be appropriate for the current configuration.

Conclusions

An experimental investigation was conducted to determine the heat transport and maximum unit effective area heat transport in triangular grooves, based on the pure capillary limit. Using methanol as the working fluid, the heat transport and unit effective area heat transport of ten different grooved plates with channel apex angles of 60 deg were measured and evaluated. As a result of this investigation, a physical model and the corresponding experimental system were developed and the maximum capillary heat transport capacity and pure capillary limit of liquid flowing in V-shaped grooves were measured.

The results of the experimental investigation verified that a maximum unit effective area heat transport does exist and indicated the accuracy of the previously developed theoretical model. The experimental results also indicated that increasing the tilt angle and the wetted length resulted in a significant decrease in the heat transport and the unit effective area heat transport. Finally, the experimental results indicated that the uniform heat flux assumption made previously may not be entirely correct, and that when the Bond number is much smaller than 1 (it was less than 0.05 for the current investigation), the assumption of constant radius of curvature is applicable.

The experimental results presented here, along with the previously developed and now modified theoretical analysis, will aid in the design of new micro heat pipes, capable of operating at increased power levels with greater reliability. Additional investigations, however, are necessary to provide the exact heat flux distribution in order to better correlate the experimental data with the analytical model.

References

Ayyaswamy, P. S., Catton, I., and Edwards, D. K., 1974, "Capillary Flow in Triangular Grooves," ASME *Journal of Applied Mechanics*, Vol. 41, pp. 332–336.

Cao, Y., Faghri, A., and Mahef key, E. T., 1993, "Micro/Miniature Heat Pipes and Operating Limitations," *Proc. ASME Annual Meeting*, ASME HTD-Vol. 236, pp. 55–62.

Duncan, A. B., and Peterson, G. P., 1995, "Charge Optimization of Triangular Shaped Micro Heat Pipes," *AIAA J. Thermophysics and Heat Transfer*, Vol. 9, No. 2, pp. 365–367.

Ha, J. M., and Peterson, G. P., 1994, "Analytical Prediction of the Axial Dryout Point for Evaporating Liquids in Triangular Microgrooves," ASME JOURNAL OF HEAT TRANSFER, Vol. 116, pp. 498–503.

Khrustalev, D., and Faghri, A., 1994, "Thermal Analysis of a Micro Heat Pipe," ASME JOURNAL OF HEAT TRANSFER, Vol. 116, pp. 189–198.

Mallik, A. K., and Peterson, G. P., 1995, "Steady-State Investigation of Vapor Deposited Micro Heat Pipe Arrays," ASME *Journal of Electronic Packaging*, Vol. 117, pp. 75–81.

Peterson, G. P., Duncan, A. B., and Weichold, M. H., 1993, "Experimental Investigation of Micro Heat Pipes Fabricated in Silicon Wafers," ASME JOURNAL OF HEAT TRANSFER, Vol. 115, No. 3, pp. 751–756.

Downloaded 11 Dec 2010 to 193.140.21.150. Redistribution subject to ASME license or copyright; see http://www.asme.org/terms/Terms_Use.cfm

Peterson, G. P., and Ma, H. B., 1996, "Theoretical Analysis of the Maximum Heat Transport in Triangular Grooves—A Study of Idealized Micro Heat Pipes," ASME JOURNAL OF HEAT TRANSFER, Vol. 118, this issue, pp. 731–739.

Peterson, G. P., and Mallik, A. K., 1995, "Transient Response Characteristics of Vapor Deposited Micro Heat Pipe Arrays," ASME *Journal of Electronic Packaging,* Vol. 117, pp. 82–87.

Stroes, G., Rohloff, T., and Catton, I., 1992, "An Experimental Study of the Capillary Forces in Rectangular Channels vs. Triangular Channels," *1992 ASME National Heat Transfer Conference,* ASME Vol. HTD-200, pp. 1–8.

Taylor, L., 1967, "Heat Treating Cleaning and Finishing," *Metals Handbook,* Vol. 2, 8th ed., American Society for Metals, Metals Park.

Wayner, P. C., 1991, *Effect of Interfacial Forces on Evaporative Heat Transfer in a Meniscus,* Final Report for Period Apr. 88–Jul. 91, Wright-Patterson AFB WL-TR-91-2061.

Xu, X., and Carey, V. P., 1990, "Film Evaporation From a Micro-Grooved Surface—An Approximate Heat Transfer Model and Its Comparison With Experimental Data," *AIAA Journal of Thermophysics and Heat Transfer,* Vol. 4, No. 4, pp. 512–520.

Downloaded 11 Dec 2010 to 193.140.21.150. Redistribution subject to ASME license or copyright; see http://www.asme.org/terms/Terms_Use.cfm

The Interline Heat Transfer of Evaporating Thin Films Along a Micro Grooved Surface

J. M. Ha
Graduate Research Assistant.

G. P. Peterson
Tenneco Professor and Head.
email: gppeterson@mengr.tamu.edu
Fellow ASME

Department of Mechanical Engineering,
Texas A&M University,
College Station, TX 77843-3123

An analytical investigation of the heat transfer characteristics for evaporating thin liquid films in V-shaped microgrooves with nonuniform input heat flux was conducted. This investigation assumed that the capillary pressure difference caused by the receding of the meniscus is responsible for the axial liquid flow along the groove, and that the disjoining pressure difference along the groove side wall provided the driving force for the flow up the groove wall. The combined heat transfer mechanisms of both liquid conduction and interfacial vaporization were used to describe the local interfacial mass flux in the interline region. Based on this approach, a local heat transfer coefficient was defined. The local and average heat transfer coefficients were both found to be sensitive to the characteristic thermal resistance ratio. In addition, when the film superheat was constant, the primary factor affecting the length of the evaporating interline region was found to be the heat flux supplied to the bottom plate, and for high heat flux conditions, the highest heat transfer coefficient did not necessarily exist at the axial dryout point. The expression developed for the evaporating film profile was shown to assume an exponential form if the heat flux distributed on the active interline region was assumed to be uniform.

Introduction

The use of phase-change techniques to enhance heat transfer coefficients is common in a number of applications, including conventional heat exchangers, chemical processing equipment, and nuclear reactors. More recently, increased interest in the use of phase-change heat transfer for the thermal control of spacecraft and electronic components, either through more traditional methods (Peterson, 1986; Peterson and Ortega, 1990) or for applications involving the use of micro heat pipe devices (Peterson, 1992) has resulted in the need for a better understanding of the liquid film behavior in these grooves.

As illustrated in Fig. 1, when a liquid contacts a flat surface, the extended meniscus is typically divided into three parts or regions: the intrinsic meniscus region, dominated by the capillary forces; the evaporating thin film region, which has the combined effects of both capillarity and disjoining pressure; and the adsorbed layer region, where the disjoining forces dominate, inhibiting vaporization (Peterson et al., 1992). The junction of the evaporating thin film region and the adsorbed layer is referred to as the interline region, and it is here that a majority of the heat transfer occurs due to the very thin film thickness.

While a number of investigations have been conducted on the extended meniscus, much of this research has focused on the mechanisms that govern the behavior of two-dimensional menisci formed on a flat plate. Schrage (1953) proposed a mass effusion model (i.e., the mass crossing the vapor–liquid interface) based on the kinetic theory of vapor. Applying this model to an evaporating wetting film where the disjoining pressure is dominant, Wayner et al. (1976) proposed an extended form of the mass flux model, which has been used extensively. Following this, Schonberg and Wayner (1992) developed an analytical model that introduced the concept of an integral heat sink. In this model, the amount of vaporization occurring in the portion of the film downstream of a certain position is assumed to be proportional to the integral heat sink of that position.

Future improvements in the heat transfer rate, along with additional advances in micro heat pipe technology (Peterson et al., 1993; Peterson and Mallik, 1995) will require a better understanding of the axial and cross-sectional flow characteristics. Xu and Carey (1990) conducted a combined analytical and experimental investigation of the liquid flow behavior in V-shaped microgrooves. Following this, Ha and Peterson (1994) conducted an analytical investigation of the axial intrinsic meniscus variation along V-shaped microgrooves. The axial dryout location was determined as a function of the input heat flux, the thermophysical properties of the system, and the geometric parameters of the grooves. In addition, the significance of the Bond number and the capillary number was demonstrated and several test cases were evaluated. While the results agreed reasonably well with the experimental data available in the literature, further study of the evaporating thin film region on grooved surfaces is necessary to fully understand the phenomena involved and optimize the groove design.

The objectives of the current investigation were to develop a method by which the vaporization occurring in the interline region on the groove wall could be better understood and to determine the average heat transfer coefficient and effective evaporating length of a given groove.

Analytical Model

Consider a thin liquid film flowing through V-shaped microgrooves, as illustrated in Figs. 2 and 3. One end of the grooved plate is immersed in a pool of liquid and held stationary at a predetermined inclination angle and a nonuniform heat flux is applied to the underside of the plate. For small grooves and small inclination angles, the liquid will wick up the groove against the gravitational body force and against the frictional pressure gradients caused by continuous flow. For this situation, the capillary behavior will determine the location of the end of the axially wetted length and above this point, the groove will be void of liquid or dried out.

For grooves relying primarily on capillary pumping for the flow of liquid, it is reasonable to assume that all the axial flow of liquid occurs in the groove (i.e., no flow occurs over the flat portion between the grooves). For a very small groove, the

Contributed by the Heat Transfer for publication in the JOURNAL OF HEAT TRANSFER. Manuscript received by the Heat Transfer Division July 14, 1995; revision received March 11, 1996. Keywords: Heat Pipes and Thermosyphons, Thermocapillary Flows, Thin Film Flow. Associate Technical Editor: V. K. Dhir.

Copyright © 1996 by ASME

Downloaded 11 Dec 2010 to 193.140.21.150. Redistribution subject to ASME license or copyright; see http://www.asme.org/terms/Terms_Use.cfm

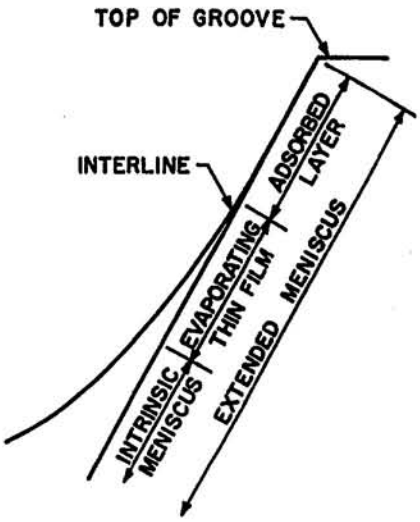


Fig. 1 Description of a meniscus

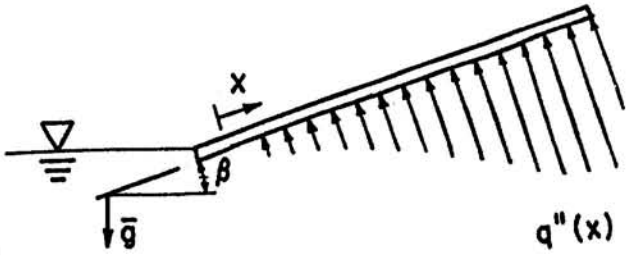


Fig. 2 Schematic of the modeled region

capillary radius of the intrinsic meniscus at a given cross section can be treated as a constant. When heat is added to the plate, the radius of curvature of the intrinsic meniscus decreases gradually in the groove along the axial or x direction. As the liquid recedes further and further toward the apex of the groove, the liquid film thins, finally reaching an ultrathin value. The wicking action or capillary pumping within these grooves is the result of the decrease in the radius of curvature caused by the intrinsic meniscus receding into the groove. In addition, the liquid meniscus at a given cross section is adsorbed on the groove wall, forming an extended thin film region above the intrinsic meniscus. The distribution of the thin film on the groove wall induces a large pressure gradient in the liquid. In this thin liquid region, the film behavior is dominated by the dispersion forces. Since the resistance to flow in the evaporating thin film and adsorbed layer regions of the extended thin film is much larger than in the intrinsic meniscus region, the majority of the axial flow will be confined to the intrinsic meniscus region. The heat transfer to the intrinsic meniscus can be neglected because it is small when compared to that occurring across the thin film, which has a much smaller thermal resistance.

Based on these arguments, several assumptions can be made to determine the end of the axial wetted length or the axial dryout point. These are:

(*i*) The axial flow along the groove in the x direction occurs primarily in the intrinsic meniscus region where the curvature is small;
(*ii*) The radius of curvature of the intrinsic meniscus across the groove width is constant at a given location, x, but the radius of curvature varies axially along the groove, and the capillary pressure gradient due to this decreasing radius drives the liquid flow in the x direction;
(*iii*) The disjoining pressure gradient due to the variation of the thin film thickness along the z direction drives the film flow up the groove wall;
(*iv*) Vaporization occurs primarily in the thin film region, particularly near the interline; and
(*v*) The vapor pressure is constant.

Axial Profile of the Intrinsic Meniscus. The general form of the force-momentum balance equation can be expressed as

$$\rho\left[\frac{\partial \vec{V}}{\partial t} + (\vec{\mathbf{V}} \cdot \nabla)\vec{\mathbf{V}}\right] = -\nabla P + \vec{\mathbf{F}} + \mu\nabla^2\vec{\mathbf{V}} \qquad (1)$$

from which the axial flow along the groove in the x direction

Nomenclature

$\bar{A}$ = constant in disjoining pressure term ($\bar{A} = A/6\pi$ where A is the Hamaker constant)
B, C = constants in Eq. (9)
a, b = coefficients in Eqs. (19) and (20)
c_1, c_2 = constants of nonuniform heat flux distribution in Eq. (7)
c_3 = constant in Eq. (5)
g = gravitational acceleration
h = heat transfer coefficient
h_{fg} = latent heat of vaporization
K = parameter in Eq. (4)
k = thermal conductivity
M = molecular weight
$\dot{m}''$ = local mass flux of vapor leaving the liquid–vapor interface
P = pressure
$q''(x)$ = heat flux normal to the primary surface at x
q_L'' = averaged uniform heat flux normal to the groove side wall
$\Re$ = universal gas constant
$r(x)$ = radius of curvature in the intrinsic meniscus at x
T = temperature
$\vec{\mathbf{V}}$ = velocity vector of fluid in Eq. (1)
V_l = molar volume of liquid
w = one-half of the top groove width
w_b = one-half of the bottom width
x = coordinate along the groove channel length
z = coordinate up the groove side wall
z_m = maximum length of the evaporating thin film on the groove side wall
α = half the vertex angle of the groove
β = slope of the plate with respect to gravity
Γ = mass flow rate in the z direction per unit width
Γ_c = mass flow rate in the x direction
γ_{loc} = dimensionless local heat transfer coefficient in Eq. (41)
$\bar{\gamma}$ = dimensionless average heat transfer coefficient in Eq. (43)
δ = thin film thickness in the interline region
η = dimensionless thin film thickness in the interline region
η_j = η at $z = 0$ where the maximum integral heat sink ends
λ = dimensionless parameter in Eq. (26)
ν = kinematic viscosity
ξ = dimensionless coordinate along the z direction
ρ = density
σ = surface tension

Superscript

id = ideal (i.e., neglecting adsorption forces)

Subscripts

j = junction of the intrinsic meniscus and interline region
l = liquid
loc = local
lv = liquid–vapor interface
m = maximum of axial groove side direction length
v = vapor
o = characteristic or reference
s = solid wall of the groove

Downloaded 11 Dec 2010 to 193.140.21.150. Redistribution subject to ASME license or copyright; see http://www.asme.org/terms/Terms_Use.cfm

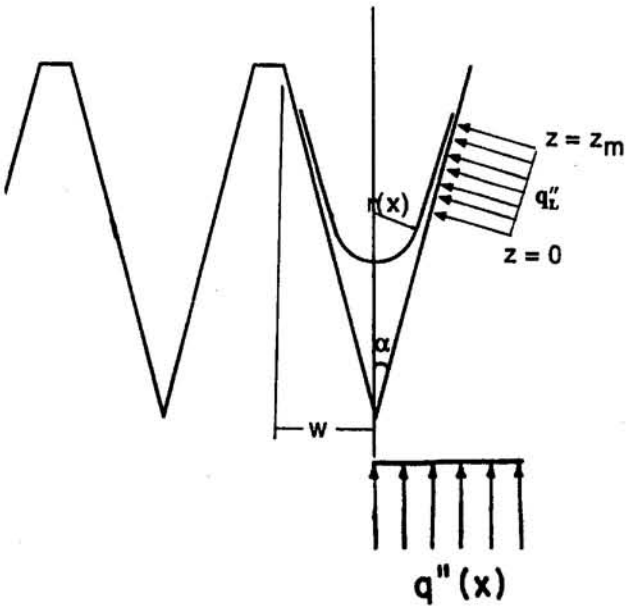


Fig. 3 Two heat fluxes q''_L and q'' with the profiles of intrinsic meniscus and the interline region

can be determined. Because the flow is very slow, the convective term in the governing equation can be neglected, and the viscous term can be related to the friction factor. For steady laminar flow, the force-momentum equation in the x direction can be simplified to be

$$\frac{dP_l}{dx} + \rho_l g \sin\beta + F_v = 0 \tag{2}$$

where β is the angle between the gravitational vector and a line normal to the grooved surface, and F_v is the viscous term related to the Fanning friction factor. Since the vapor pressure, P_v, is assumed to be constant, the liquid pressure gradient can be expressed in terms of the radius of curvature, or

$$\frac{dP_l}{dx} = -\frac{d}{dx}(P_v - P_l) = -\frac{d}{dx}\left(\frac{\sigma}{r(x)}\right) \tag{3}$$

Following the procedure originally proposed by Xu and Carey (1990), the form of Eq. (2) can be modified to

$$\frac{d}{dx}\left(\frac{\sigma}{r(x)}\right) = \frac{2K\nu_l}{c_3 r(x)^4}\Gamma_c + \rho_l g \sin\beta \tag{4}$$

where

$$c_3 = 4\tan^2\alpha\left(\frac{1}{\tan\alpha} + \alpha - \frac{\pi}{2}\right)^3 \tag{5}$$

In this expression, Γ_c is the mass flow rate through the groove and the parameter K, originally determined by Ayyaswamy et al. (1974), is a function of the groove half angle and the liquid contact angle.

Assuming the liquid in the evaporator region is saturated and the heat flux along the x direction is given by $q''(x)$, the mass flow rate at a given position x can be expressed as

$$\Gamma_c = \int_0^{\Gamma_c} d\Gamma_c = \frac{1}{h_{fg}}\int_{x_{\max}}^{x} q''(x)2w_b(-dx)$$

$$= \frac{2w_b}{h_{fg}}\int_x^{x_{\max}} q''(x)dx \tag{6}$$

where the value of $x_{\max}$ is the point farthest from the liquid pool at which the intrinsic meniscus could still be considered to exist. Note that the mass flow rate, Γ_c, is zero at the dryout point, $x_{\max}$. For the case of a heat flux distribution represented in terms of x by the expression $q''(x) = c_2x^2 + c_1x$, the mass flow rate, Γ_c, at a given position x can be expressed as

$$\Gamma_c = \frac{2w_b}{h_{fg}}\left\{\frac{c_2}{3}(x_{\max}^3 - x^3) + \frac{c_1}{2}(x_{\max}^2 - x^2)\right\} \tag{7}$$

Combining the governing equation, Eq. (4), with Eq. (7) yields

$$\frac{dr}{dx} = -C\left\{\frac{c_2}{3}(x_{\max}^3 - x^3) + \frac{c_1}{2}(x_{\max}^2 - x^2)\right\} \Big/ r^2 - Br^2 \tag{8}$$

where

$$B = \frac{\rho_l g \sin\beta}{\sigma} \quad \text{and} \quad C = \frac{4K\nu_l w_b}{c_3\sigma h_{fg}} \tag{9}$$

Assuming that the thin liquid film of the meniscus completely fills the V-groove at the origin results in a boundary condition of the form

$$r(x) = r_o = \frac{w}{\cos\alpha} \quad \text{at} \quad x = 0 \tag{10}$$

By solving Eq. (8) numerically with the boundary condition given in Eq. (10), the axial profile of the radius of curvature can be obtained.

Evaporating Thin Film Region on the Groove Wall. In Fig. 3, two heat fluxes q''_L and $q''(x)$ are defined with the profiles of the intrinsic meniscus and the evaporating thin film. The relations of mass and energy conservation result in an expression of the form

$$d(\Gamma h_{fg}) = h_{fg}d\Gamma = -q''_L dz \tag{11}$$

where Γ is the mass flow on the groove wall along the z direction. Whether the heat flux supplied from the bottom of the plate, $q''(x)$, is uniform or not along the x direction, it can be determined. However, the z variation of the heat flux, q''_L, is not known a priori. For simplicity, q''_L may be treated as an average uniform value along the portion of the groove wall covered by the evaporating thin film. From Fig. 3, the relationship between q''_L and $q''(x)$ must satisfy the energy balance requirement of

$$q''_L z_m = q'' w_b \tag{12}$$

where z_m is the maximum length of the evaporating thin film. Because $\Gamma = 0$ at the point where the evaporating thin film meets the non-evaporating adsorbed layer, the following function at z can be written:

$$\Gamma = \int_0^{\Gamma} d\Gamma = \int_{z_m}^{z} \frac{q''_L}{h_{fg}}(-dz) = \frac{q''w_b}{h_{fg}z_m}(z_m - z) \tag{13}$$

However, in this expression, z_m is still not known. Xu and Carey (1990) described z_m in terms of $r(x)$ by assuming that the evaporation ends at the top of the side wall. This approach may not be appropriate since the side wall above the interline is adiabatic, and the position of the interline does not necessarily coincide with the top of the side wall. Hence, determination of the value for z_m requires an alternative approach.

As stated previously, the driving force in the thin liquid film is assumed to be the result of the disjoining pressure gradient. The relationship between the disjoining pressure and the film thickness of nonpolar liquids can be represented by

$$P_v - P_l = \frac{\bar{A}}{\delta^3} \tag{14}$$

Downloaded 11 Dec 2010 to 193.140.21.150. Redistribution subject to ASME license or copyright; see http://www.asme.org/terms/Terms_Use.cfm

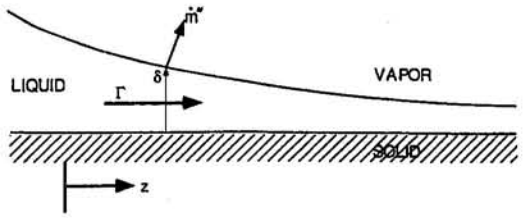


Fig. 4 Evaporating thin film and coordinate system

where $\bar{A}$ is a dispersion constant, treated here as a positive value. The z direction force–momentum balance equation using a boundary layer approximation can be expressed as

$$\frac{dP_l}{dz} = -\frac{3\Gamma\nu_l}{\delta^3} - \rho_l g \cos\beta\cos\alpha \approx -\frac{3\Gamma\nu_l}{\delta^3} \quad (15)$$

In this equation, the gravitational term $\rho_l g \cos\beta\cos\alpha$ is negligible with respect to the viscous term because the film thickness is quite small in this region. From this idealization, the lubrication approximation (laminar flow, inertial force and gravitational force, all negligible) can be adopted. The mass flow rate in the thin film region, Γ, is clearly related to the pressure gradient in the flow direction. Combining Eqs. (14) and (15) yields

$$\Gamma = -\frac{\delta^3}{3\nu_l}\frac{dP_l}{dz} = -\frac{\bar{A}}{\nu_l}\frac{1}{\delta}\frac{d\delta}{dz} \quad (16)$$

The local evaporating mass flux, $\dot{m}''$, can be related to Γ by a mass balance

$$\dot{m}'' = -\frac{d\Gamma}{dz} = \frac{\bar{A}}{\nu_l}\frac{d}{dz}\left(\frac{1}{\delta}\frac{d\delta}{dz}\right) \quad (17)$$

Note that the evaporating direction of $\dot{m}''$ is normal to the interface as shown in Fig. 4. Once the lubrication approximation has been assumed, the expression for $\dot{m}''$ established by Schonberg and Wayner (1992) can be applied.

Schonberg and Wayner's (1992) Model on a Flat Plate. The local mass flux of vapor leaving the liquid–vapor interface, $\dot{m}''$, at a given position z, can be expressed as

$$\dot{m}'' = a(T_{lv} - T_v) + b(P_l - P_v) \quad (18)$$

where the coefficients a and b are functions of the thermophysical properties

$$a = \frac{2\hat{\sigma}}{2 - \hat{\sigma}}\sqrt{\frac{M}{2\pi\Re T_{lv}}}\left(\frac{P_v M h_{fg}}{\Re T_v T_{lv}}\right) \quad (19)$$

and

$$b = \frac{2\hat{\sigma}}{2 - \hat{\sigma}}\sqrt{\frac{M}{2\pi\Re T_{lv}}}\left(\frac{V_l P_v}{\Re T_{lv}}\right) \quad (20)$$

Here, the functions a and b are not sensitive to small changes in T_{lv} and T_v. While the temperature of the vapor–liquid interface, T_{lv}, is hard to measure, it is related to the temperature of the substrate, T_s, by the one-dimensional conduction heat transfer equation through the liquid

$$\dot{m}'' = \frac{k_l}{\delta h_{fg}}(T_s - T_{lv}) \quad (21)$$

Combining Eq. (18) with Eq. (21) eliminates T_{lv} in favor of T_s:

$$\dot{m}'' = \left(1 + \frac{a\delta h_{fg}}{k_l}\right)^{-1}\{a(T_s - T_v) + b(P_l - P_v)\} \quad (22)$$

If δ is so small that the meniscus curvature becomes flat, no evaporation occurs. This value denoted by δ_o represents the reference thickness given by

$$\delta_o = \left(\frac{b}{a}\frac{\bar{A}}{\Delta T}\right)^{1/3} \quad (23)$$

The temperature difference, ΔT, is a constant causing the evaporation

$$\Delta T \equiv T_s - T_v \quad (24)$$

where T_s is the temperature of the wall and T_v is the vapor temperature. Substituting this reference thickness into Eq. (22) yields

$$\dot{m}'' = \frac{1}{1 + \lambda\delta/\delta_o}\left(a\Delta T - b\frac{\bar{A}}{\delta^3}\right) \quad (25)$$

where

$$\lambda \equiv \frac{a h_{fg}\delta_o}{k} \quad (26)$$

Combining Eq. (17) with Eq. (25) yields

$$\frac{\bar{A}}{\nu_l}\frac{d}{dz}\left(\frac{1}{\delta}\frac{d\delta}{dz}\right) = \frac{1}{1 + \lambda\delta/\delta_o}\left(a\Delta T - b\frac{\bar{A}}{\delta^3}\right) \quad (27)$$

The characteristic evaporative mass flux, $\dot{m}''^{id}$, is the ideal mass flux that would occur with $P_l = P_v$ in the absence of pressure effects and with $T_{lv} = T_s$:

$$\dot{m}''^{id} = a\Delta T = b\bar{A}\delta_o^{-3} \quad (28)$$

The dimensionless thickness and position are defined as

$$\eta = \frac{\delta}{\delta_o}, \quad \xi = \frac{z}{z_o} \quad \text{where} \quad z_o^2 \equiv \frac{\bar{A}}{\nu_l \dot{m}''^{id}} \quad (29)$$

By nondimensionalizing Eq. (27) with $\dot{m}''^{id}$, the local evaporative flux can be expressed for the thin film profile as

$$\frac{d}{d\xi}\left(\frac{1}{\eta}\frac{d\eta}{d\xi}\right) = \frac{1}{(1 + \lambda\eta)}\left(1 - \frac{1}{\eta^3}\right) \quad (30)$$

with two far field conditions imposed on the solution

$$\eta \to 1 \quad \text{as} \quad \xi \to \infty \quad (31)$$

$$\frac{d\eta}{d\xi} \to 0 \quad \text{as} \quad \xi \to \infty \quad (32)$$

Schonberg and Wayner (1992) established the solution of Eq. (30) in the form of a first-order differential equation:

$$-\frac{1}{\eta^3}\frac{d\eta^3}{d\xi} = \left(\begin{array}{c} 18(1 + \lambda^3)\ln\left(\dfrac{\eta(1 + \lambda)}{1 + \lambda\eta}\right) + 6(\eta^{-3} - 1) \\ -9\lambda(\eta^{-2} - 1) + 18\lambda^2(\eta^{-1} - 1) \end{array}\right)^{1/2} \quad (33)$$

and found that the evaporated integral heat amount in the interline region is directly related to this quantity as follows:

$$\Gamma h_{fg} = -\frac{\bar{A}h_{fg}}{3\nu_l z_o}\frac{1}{\eta^3}\frac{d\eta^3}{d\xi} \quad (34)$$

Here, the quantity $-\eta^{-3}d\eta^3/d\xi$ in Eq. (33), i.e., the total heat absorbed in the evaporating thin film, can be interpreted as the dimensionless maximum integral heat sink up to η.

Downloaded 11 Dec 2010 to 193.140.21.150. Redistribution subject to ASME license or copyright; see http://www.asme.org/terms/Terms_Use.cfm

Model for Channel Groove. A dimensionless plot of the integral heat sink as a function of η for various values of λ was shown by Schonberg and Wayner (1992). This graph indicated that the thinnest part of the meniscus experienced the greatest vaporization, especially for large values of λ. This fact is particularly important in the current investigation, in that for a given value of η, the total heat absorbed within this interline region from 1 to η can be determined.

Based on this argument, more attention should be paid to the fact that only a small portion of the interline region is responsible for most of the evaporation that occurs. Beyond this thin interline region, the combined effects of both the capillarity and disjoining pressure are present. However, because a majority of the heat transfer occurs within the interline region, which behaves as an evaporative heat sink, the present model will focus on that portion of the interline region where the disjoining pressure effect is dominant. For this reason, it will be assumed that along the z direction, the capillary pressure affects only the intrinsic meniscus, and that the disjoining pressure alone determines the behavior of the interline region, especially in that part responsible for most of the evaporation. Because the heat supplied from the bottom plate at each x location must be dissipated in the interline region on the groove wall, the requirement of $q''(x)w_b = \Gamma h_{fg}$ will be satisfied. As a result, Eq. (34) can be used to provide the relationship between the supplied heat at x and the thin film profile at a certain η value

$$q''(x)w_b = -\frac{\bar{A}h_{fg}}{3\nu_l z_o}\frac{1}{\eta^3}\frac{d\eta^3}{d\xi} \tag{35}$$

Henceforth, the origin of the z direction will be defined as the point where δ satisfies Eq. (35). That is, at a given x, Eq. (35) is satisfied at $z = 0$ for a certain η. This implies that the location of $z = 0$, or the junction of the intrinsic meniscus and the interline region, varies along the x direction as a function of the given heat input.

Using Eq. (35), it is necessary to specify the proper value of $\bar{A}$. To accomplish this, consider the axial dryout or region adjacent to x_{max} where the smallest radius of curvature causes the highest capillarity. Around the axial dryout point, the film thickness of the intrinsic meniscus is on the same order as that occurring near the interline. As a result, it is reasonable to assume that near x_{max}, the liquid pressure caused by capillarity will match the disjoining pressure at the junction of the intrinsic meniscus and the interline region. Using Eq. (8) for the radius of curvature of the intrinsic meniscus, the boundary condition at $z = 0$ adjacent to x_{max} can be specified by matching the liquid pressure to the disjoining pressure

$$P_v - P_l = \frac{\sigma}{r(x)} = \frac{\bar{A}}{\delta_j^3} \quad \text{at} \quad z = 0, \quad \text{near} \quad x_{max} \tag{36}$$

Note that this calculation cannot be carried out just at x_{max}, because the radius of curvature is zero at x_{max}. The film thickness at the junction can be expressed as

$$\delta = \delta_j(x) = \left(\frac{\bar{A}r(x)}{\sigma}\right)^{1/3} \quad \text{at} \quad z = 0, \quad \text{near} \quad x_{max} \tag{37}$$

This value of δ_j assists in the determination of the value of $\bar{A}$ because δ_j depends on $\bar{A}$ from Eq. (37) and is also responsible for the adsorbed amount of heat occurring at x_{max} given by Eq. (35). The value of $\bar{A}$ that satisfies both Eq. (37) and Eq. (35) can be determined by numerical iteration. Once $\bar{A}$ has been determined, Eq. (35) can be applied to any other x position, to produce the film thicknesses corresponding to $z = 0$, which is where the maximum integral heat sink exists.

With a constant ΔT value, the local heat transfer coefficient at a given position z can be introduced as

$$h_{loc} = \frac{h_{fg}\dot{m}''}{\Delta T} = \frac{h_{fg}}{1 + \lambda\delta/\delta_o}\left(a - b\frac{\bar{A}}{\delta^3\Delta T}\right) \tag{38}$$

The definition of h_{loc} can be interpreted as follows

$$q'' = h_{fg}\dot{m}'' = h_{loc}(T_s - T_v) = \frac{1}{\frac{\delta}{k} + \frac{1}{h_{evap}}}(T_s - T_v) \tag{39}$$

Because ΔT is the temperature difference between the wall and vapor, the thermal resistance or sum of the two heat transfer modes, i.e., conduction and interfacial evaporation, are used in the definition given above of h_{loc}. That is, h_{loc} is the local heat transfer coefficient that contains the combined effect of both conduction through the thin film and evaporation from the surface.

With the ideal mass flux from Eq. (28), the ideal heat transfer coefficient also can be introduced as

$$h^{id} = h_{fg}\dot{m}''^{id}/\Delta T = ah_{fg} \tag{40}$$

The ratio of the local to ideal heat transfer coefficient becomes

$$\gamma_{loc} = \frac{h_{loc}}{h^{id}} = \frac{1 - \eta^{-3}}{1 + \lambda\eta} \tag{41}$$

The dimensionless local heat transfer coefficient, γ_{loc}, is a function of only two variables, λ and η.

From $\eta = 1$ to a certain value of η, γ_{loc} can be averaged over the range of applicability of the thin film region, and the average heat transfer coefficient can be defined as

$$\bar{\gamma} = \frac{\int_1^\eta \gamma_{loc}\, d\eta}{\int_1^\eta d\eta} \tag{42}$$

Manipulation of this expression yields an expression for $\bar{\gamma}$ as a function of only two variables, λ and η, or

$$\bar{\gamma} = \frac{1}{\eta - 1}\left\{\frac{1}{\lambda}\ln\left(\frac{\lambda\eta + 1}{\lambda + 1}\right) - \lambda^2 \ln\frac{(\lambda + 1)\eta}{\lambda\eta + 1} - \frac{2\lambda\eta - 1}{2\eta^2} + \lambda - \frac{1}{2}\right\} \tag{43}$$

It should be noted that in the limit with $\lambda = 0$, $\gamma_{loc} = 1 - \eta^{-3}$ from Eq. (41) is used for $\bar{\gamma}$ in Eq. (42), and that the calculated $\bar{\gamma}$ has the same result obtained by Wayner et al. (1976). Because γ_{loc} represents only the local value at the given point η, it does not include the effects of the surrounding region. However, $\bar{\gamma}$ as a representative value indicates the averaged value over the whole range from $\eta = 1$ to the given η. By substituting the proper value for η at each x, the requirement given in Eq. (35) can be satisfied and $\bar{\gamma}$ can be used as a representative heat transfer coefficient for a given x position.

Using $\bar{\gamma}$, the effective length of evaporation in the interline region, the value of z_m, defined in Eq. (12), can be determined from the following expression:

$$q''w_b = ah_{fg}\bar{\gamma}\Delta T z_m = q_L'' z_m \tag{44}$$

The effective film profile in the interline region can then be obtained using the known value of z_m. Combining Eqs. (13) and (16) yields

$$\frac{q''w_b}{h_{fg}z_m}(z_m - z) = -\frac{\bar{A}}{\nu_l}\frac{1}{\delta}\frac{d\delta}{dz} \tag{45}$$

Downloaded 11 Dec 2010 to 193.140.21.150. Redistribution subject to ASME license or copyright; see http://www.asme.org/terms/Terms_Use.cfm

Table 1 Nonuniform heat flux distribution and measured x_{max} by Carey (1993)

working fluid	β	$q''(x)$ $x = 3.23$ mm	$q''(x)$ $x = 7.47$ mm	measured x_{max}	ΔT
Methanol	20°	6.32 W/m^2	12.14 W/m^2	9.6±1.5 mm	7.65°C

and the integrated result with the boundary condition $\delta = \delta_j$ at $z = 0$ results in a film profile of the form

$$\delta = \delta_j \exp\left(- \frac{q'' w_b \nu_l}{h_{fg} \bar{A}} z \left(1 - \frac{1}{2} \frac{z}{z_m} \right) \right) \tag{46}$$

This result indicates an exponential profile for the evaporating thin film if the heat flux profile along the active interline region is approximated as a uniform heat flux, q''_L.

In summary, the algorithm for determining the average heat transfer coefficient, and the corresponding effective length of the evaporating thin film is

(*i*) Determine the profile of the radius of curvature and the axial wetted length x_m from Eq. (8) and Eq. (10).
(*ii*) For a point near x_{max}, start by assuming a small value of $\bar{A}$, and calculate δ_j from Eq. (37) and check the equality of η from Eq. (35). Continue to increase $\bar{A}$ until the proper value of $\bar{A}$ satisfies both Eq. (37) and Eq. (35).
(*iii*) Calculate the remaining parameters such as δ_o, λ, and z_o with $\bar{A}$ and ΔT. At each x, determine the corresponding values of η that satisfies Eq. (35).
(*iv*) The dimensionless average heat transfer coefficient, $\bar{\gamma}$, can then be obtained from Eq. (43) at each x.
(*v*) With these, the effective length of the interline region, z_m, can be calculated from Eq. (44).
(*vi*) The thin film profile in the active interline region can then be represented by Eq. (46).

It is worth noting that the effect of resistance to conduction in the whole substrate is not included in the definition of the heat transfer coefficient because T_s represents the surface temperature of the substrate only in the interline region.

Results and Discussion

The purpose of this investigation was to study the features of the interline region that are responsible for vaporization. To determine the validity of this analysis, the case proposed by Xu and Carey (1990), given in Table 1, can be compared with the model developed here. The shape of the groove utilized in the experiment was triangular with the dimensions of $w = 32$ μm, $w_b = 45.45$ μm, and $\alpha = 9.35$ deg. The capillary performances of acetone and methanol were tested for varying tilt angles and heat fluxes. As explained in the original reference, the heat fluxes at two points, $x = 3.23$ mm and $x = 7.47$ mm, were calculated from the measured temperatures inside the grooved plate. The measured superheat $\Delta T = 7.65$°C was relatively high for film evaporation, but was nearly constant along the axial direction, at least within the uncertainty of the thermocouples used.

Because the heat flux is only known for two locations on the plate, a quadratic form of $q''(x) = c_2 x^2 + c_1 x$ was assumed by the authors. This profile assumes zero heat flux at $x = 0$. The possible presence of nucleate boiling at $x = 0$ was not included in the assumed heat flux distribution because the nucleate boiling applicable length in the x direction was very small. From the two known heat fluxes at the two known locations, the values of the constants c_2 and c_1 were found to be -7.818×10^8 and 2.209×10^7, respectively, and the distributed heat flux is equal to 85.649 W/m^2, i.e., the average heat flux integrated along the total x_{max}.

Equation (8) was solved numerically for x_{max} by Euler's method, and the calculated x_{max} value was found to be 10.2 mm. The profiles of the heat flux and the radius of curvature at each x location are shown in Fig. 5. Comparison of the case of equivalent uniform heat flux shows a longer x_{max} value than that for the nonuniform heat flux case because the cross-sectional mass flow is less. This makes the rate of change of the radius of curvature less, thus enhancing the capillary performance.

With the aid of the radius of curvature profile, the value of δ_j calculated near x_{max}, the value of $\bar{A}$ can be determined through iteration of Eqs. (35) and (37). (Note that this calculation can not be carried out at x_{max}, because at x_{max}, the radius of curvature is zero.) Although the assumption of equality in Eq. (37) needs to be refined, there is no obvious reason to discard it. From a small initial value of $\bar{A}$, a corresponding value of η that is dependent on $\bar{A}$ can be found from Eq. (35). Checking the equality of η_j, the value of $\bar{A}$ can be increased until η is equal to η_j. This iterative procedure finally determines the value of $\bar{A}$, which for this case is $\bar{A} = 7.145 \times 10^{-20}$. This value would appear to be more reasonable than the value of 1.0×10^{-11}, obtained by Xu and Carey, especially when compared to the values obtained by other investigators. One approach for estimating the composite Hamaker constant has been presented by Israelachvili (1985) as $A_{132} \approx (\sqrt{A_{11}} - \sqrt{A_{33}})(\sqrt{A_{22}} - \sqrt{A_{33}})$, where A_{ii} is the Hamaker constant for pure component i. Estimates of the individual Hamaker constants are tabulated in Israelachvili (1985). For a copper/methanol/vapor system, $A_{11} = (30 - 50) \times 10^{-20}$ J, $A_{22} = 0$, $A_{33} = 4.8 \times 10^{-20}$ J, and the disjoining pressure constant is estimated to be $3.8 \times 10^{-21} < \bar{A} < 5.71 \times 10^{-21}$, which is independent of temperature. Using a somewhat different method, Gregory (1969) proposed an expression for the calculation of A, using the macroscopic optical properties of the materials. Using this approach, A for carbon tetrachloride with several types of glass were calculated and the values on the order of 10^{-20}. And finally, Lopez et al. (1974) estimated the value of A for the same system as being on the order of 10^{-19}. Once $\bar{A}$ has been determined, Eq. (35) can be applied to all the other x positions, and can be used to find the film thickness at the point where the maximum integral heat sink exists. The calculated values of δ_o and λ are, respectively, $\delta_o = 1.5653 \times 10^{-3}$ μm, and $\lambda = 8.5873 \times 10^{-2}$.

For the given $q''(x)$ at each x, the corresponding value of η responsible for the given heat can be obtained from Eq. (35), to yield the dimensionless local heat transfer coefficient γ_{loc} and the dimensionless average heat transfer coefficient $\bar{\gamma}$. The graphs of γ_{loc} and $\bar{\gamma}$ with respect to η, constructed from Eqs. (41) and (43), respectively, are plotted in Fig. 6 for two values of λ, 0.0 and 0.1. As seen, γ_{loc} and $\bar{\gamma}$ are both smaller for the larger λ value. When compared to γ_{loc}, the graph of $\bar{\gamma}$ at a given λ moves slightly further to the right, because γ_{loc} represents the local heat transfer coefficient only at the given η,

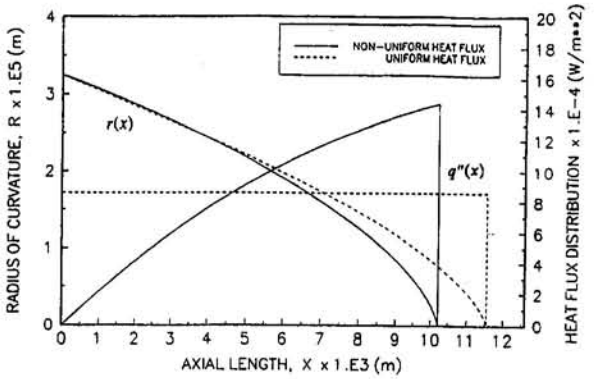


Fig. 5 Radius of curvature profile and heat flux distribution along the axial x direction

Downloaded 11 Dec 2010 to 193.140.21.150. Redistribution subject to ASME license or copyright; see http://www.asme.org/terms/Terms_Use.cfm

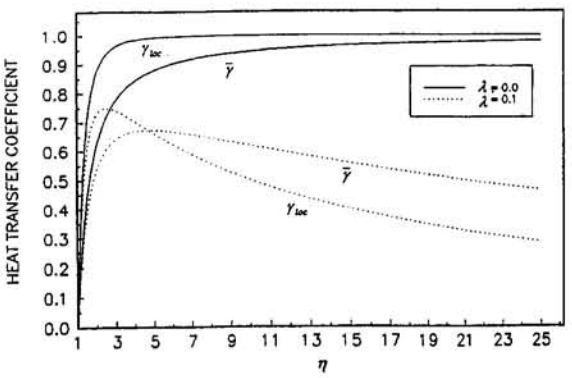


Fig. 6 Local and average heat transfer coefficient with respect to film thickness

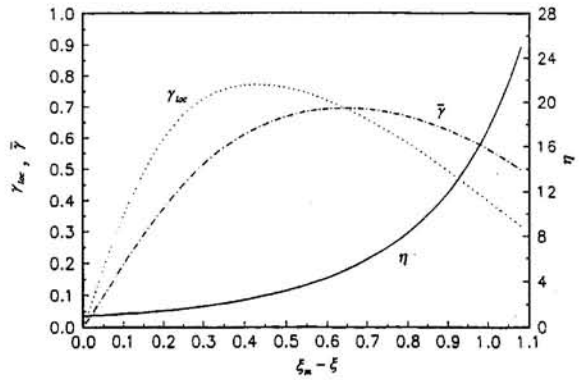


Fig. 8 γ_{loc}, $\bar{\gamma}$, and η with respect to ξ for $\lambda = 0.086$

whereas $\bar{\gamma}$ represents the average of the integrated value of γ_{loc} over the whole range from $\eta = 1$ to the given η. In the case of $\lambda = 0.1$, $\bar{\gamma}$ crosses over at some point, whereas the line of $\bar{\gamma}$ for $\lambda = 0.0$ is always under the line of γ_{loc}. This results from the fact that $\bar{\gamma}$ represents the average of the integrated value of γ_{loc} over the given η. For the case of $\lambda = 0.1$, the value of γ_{loc} starts from zero at $\eta = 1$ and reaches the highest value at approximately $\eta = 2.5$. Since the local heat transfer coefficient is proportional to the local mass flux of the vapor, the highest local evaporation mass flux occurs in the very thin region close to the interline.

If the dimensionless averaged heat transfer coefficient, $\bar{\gamma}$, is constructed from Eq. (43) with respect to η, and plotted as shown in Fig. 7 for five values of λ, some interesting features can be observed. First, as was the case for γ_{loc}, $\bar{\gamma}$ is very sensitive to the value of λ. By increasing λ, $\bar{\gamma}$ becomes smaller due to the increased conduction resistance. As defined in Eq. (26), λ can be interpreted as a characteristic dimensionless parameter of the ratio of thermal resistance of conduction through the reference film thickness to that of the ideal interfacial evaporation, or

$$\lambda = \frac{ah_{fg}\delta_o}{k} = \frac{\delta_o}{k} \Big/ \frac{1}{ah_{fg}} \quad \text{where} \quad \delta_o = \left(\frac{b}{a}\frac{\bar{A}}{\Delta T}\right)^{1/3} \tag{47}$$

The value of λ is dependent on the reference film thickness δ_o which is a strong function of ΔT. Hence, a larger ΔT makes δ_o, and thus the value of λ becomes smaller. In other words, a large temperature difference between the vapor and the wall results in a smaller conduction resistance compared to the interfacial evaporation resistance. For the ultimate case where the conduction resistance at the interline can be neglected due to the very thin reference film thickness, λ becomes zero, and as shown in Fig. 7, $\bar{\gamma}$ as well as γ_{loc} has the highest value for all ranges of η than any other λ. For the case of $\lambda = 0$, $\bar{\gamma}$ keeps on increasing and asymptotically approaches 1 after sharply increasing within a very small range of η. For every case except $\lambda = 0$, $\bar{\gamma}$ decreases after reaching the maximum value because of the effect of increasing conduction resistance caused by the increasing film thickness. For every case of λ, there exists a small range of η where a sharply increasing value of $\bar{\gamma}$ occurs. The length of this range gets smaller when λ increases. In this range, which is near the extremely thin nonevaporating film, the conduction heat transfer resistance is negligible, and the interfacial evaporation heat transfer is dominant, thus causing the sharply increasing heat transfer coefficients to achieve the maximum value. After reaching the peak of $\bar{\gamma}$, within a fairly small range, $\bar{\gamma}$ starts to decrease slowly. From these observations, it is clear that not only is the interfacial evaporation important, but the conduction heat transfer also plays an important role in the behavior at the interline region.

The dimensionless film profile η with respect to ξ can be calculated numerically from Eq. (33), and plotted for $\lambda = 0.086$ as shown in Fig. 8. The graphs of γ and $\bar{\gamma}$ with respect to ξ are also plotted in Fig. 8 with corresponding η. Note that $\eta = 1$ corresponds to $\xi = \xi_m$. In Fig. 7, the variation of $\bar{\gamma}$ in the range of η from 1 to 5 is very sharp, but in Fig. 8, the increase of $\bar{\gamma}$ with respect to the corresponding ξ is not nearly as rapid. This implies that the length of the active evaporating interline region is not nearly as short, because the slope of the heat transfer coefficient $d\bar{\gamma}/d\xi$ is not as steep as $d\bar{\gamma}/d\eta$. In other words, small values of η do not necessarily correspond to small values of $\xi = \xi_m$ as long as the film thickness continues to thin. For the case considered here, the applied heat flux, $q''(x)w_b$, and the corresponding value of η_j that satisfies Eq. (35), are plotted in Fig. 9 with respect to x. As the heat input is increased, η_j increases to compensate. This raises the question "at what axial location does the highest $\bar{\gamma}$ exist?"

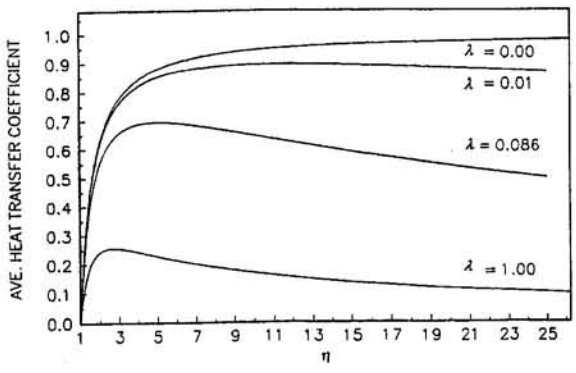


Fig. 7 Average heat transfer coefficient with respect to film thickness

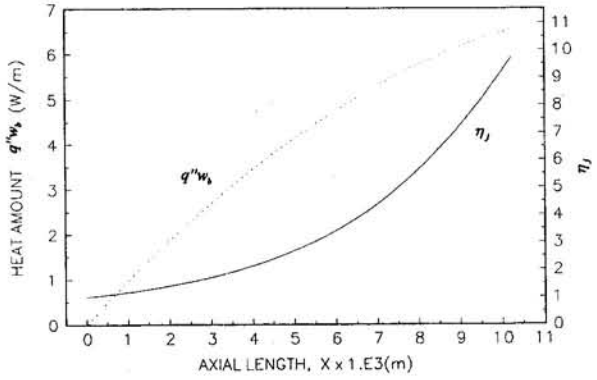


Fig. 9 Applied heat and corresponding film thickness along the x direction

Downloaded 11 Dec 2010 to 193.140.21.150. Redistribution subject to ASME license or copyright; see http://www.asme.org/terms/Terms_Use.cfm

The axial variation of $\bar{\gamma}$ calculated from the corresponding value of η_j is plotted in Fig. 10. In the region where a large heat flux is applied, large values of $\bar{\gamma}$ are shown, which is as expected, but the highest $\bar{\gamma}$ value does not exist around the axial dryout point at x_{max}. Instead, $\bar{\gamma}$ slowly decreases around the dryout region. This result can be explained by considering Fig. 8 where $\lambda = 0.086$. For this case, the highest value of $\bar{\gamma} = 0.695$ occurs at $\eta = 5.0$. The axial location corresponding to this value is $x = 7.52$ mm, as shown in Fig. 9. In the cross section at $x = 7.52$ mm, the thin film portion from $\eta = 1$ to 5.0 can absorb heat up to approximately 5.54 W/m as determined from Eq. (35). If the heat input is greater than this value, the region up to $\eta = 5$ is incapable of absorbing all of the heat, even though $\eta = 5$ corresponds to the maximum value of $\bar{\gamma}$. For this case, the length of the evaporating region must be extended in order for all the given heat to be completely vaporized. Due to the required expansion of the evaporating length, the film region expands and thins, decreasing the magnitude, and hence reducing the heat transfer coefficient.

If ΔT is constant, Eq. (44) implies that $\bar{\gamma}$ is proportional to the heat flux in the interline region, q''_L. Here the value of $\bar{\gamma}$ was defined to be integrally averaged along η not ξ. The length of the effective evaporating region, z_m, can be is calculated from Eq. (44). In Fig. 10, the axial variation of z_m keeps increasing up to the dryout point, which is not the largest $\bar{\gamma}$. The liquid profile along the z direction was found by assuming that the intrinsic meniscus meets the interline region at the point where δ_j satisfies Eq. (35). The x-directional flow of the intrinsic meniscus for $z < 0$ can be obtained using the radius of curvature and Eq. (8), and the interline region flow along the z direction can be found from Eq. (46). In this way it is possible to obtain a three-dimensional liquid profile along both the x and z directions. In Fig. 11, the film profiles at two points, $x = 3.23$ mm and $x = 7.47$ mm, are plotted using the exponential form of Eq. (46). The small integral heat sink at $x = 3.23$ mm has a short evaporating length and a small $\bar{\gamma}$ value.

Conclusion

A theoretical model has been developed for the heat transfer characteristics of the evaporating thin film on a V-shaped groove wall. This model can be used to understand the axial variation of the average heat transfer coefficient and the effective evaporating length for a given set of parameters, such as groove geometry, working fluid properties under a certain system vapor pressure, heat flux variation along the plate, and measured temperatures of vapor and groove wall. Unlike previous models, the current analysis considers the effect of superheat and interfacial resistance and can provide the z direction distribution of the liquid in the grooves. Because of the microscopic dimensions of the phenomena considered, quantitative experimental verification of the model developed here is not straightforward. In spite of this fact, comparison of the results of the current model with the experimental results of Xu and Carey provides insight and information about the qualitative features of the phenomena occurring in the interline region on the groove wall. Most important is that the average heat transfer coefficient, $\bar{\gamma}$, as well as local heat transfer coefficient γ_{loc}, are both sensitive to a characteristic thermal resistance ratio, λ; where a larger λ yields a $\bar{\gamma}$ and/or γ_{loc} that is smaller. Also, $\bar{\gamma}$ as well as γ_{loc} increases sharply in a very short range of η, and after reaching a maximum value, decreases slowly.

It is also apparent from this investigation that when the values of $\bar{A}$ and the superheat ΔT are constant, one of the main factors affecting the length of the evaporating interline region is the heat flux supplied to the bottom of the plate. Because the average heat transfer coefficient has a limit on the upper value, it requires that, for a large heat flux, the length of the evaporating region increase to absorb the entire amount of heat, decreasing the average heat transfer coefficient. Therefore, when a high heat flux is applied, it is possible that the highest heat transfer coefficient may not exist at the axial dryout point.

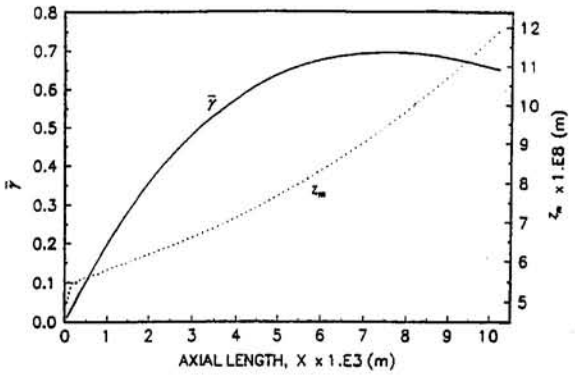


Fig. 10 $\bar{\gamma}$ and z_m along the x direction

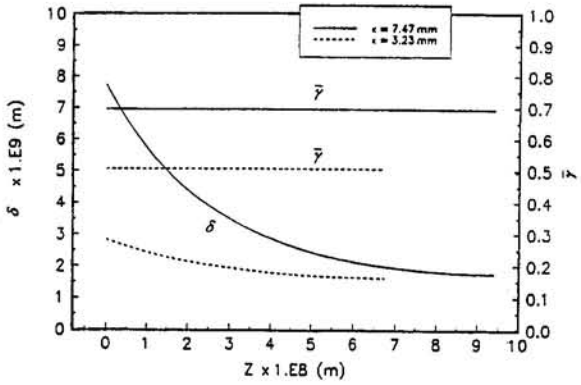


Fig. 11 Film profile and average heat transfer along the z direction

Acknowledgments

The authors would like to acknowledge the support of the Texas Higher Education Coordinating Board for the support provided through the Texas Advanced Technology Program.

References

Ayyaswamy, P. S., Catton, I., and Edwards, D. K., 1974, "Capillary Flow in Triangular Grooves," *J. Applied Mechanics,* Vol. 41, pp. 332–336.

Carey, V. P., 1993, personal communication to G. P. Peterson.

Gregory, J., 1969, "The Calculation of Hamaker Constants," *Adv. Colloid Interface Sci.,* Vol. 2, pp. 396–417.

Ha, J. M., and Peterson, G. P., 1994, "Analytical Prediction of the Axial Dryout Point for Evaporating Liquids in Triangular Microgrooves," ASME JOURNAL OF HEAT TRANSFER, Vol. 116, No., pp. 498–503.

Israelachvili, J. C., 1985, *Intermolecular and Surface Forces,* Academic Press, Washington, DC.

Lopez, J., Miller, C. A., and Ruckenstein, E., 1974, "Dynamics of Wetting Processes," *Proc. 48th National Colloid Symposium,* University of Texas, Austin, TX, pp. 65–70.

Peterson, G. P., 1986, "Thermal Control Systems for Spacecraft Instrumentation," *AIAA J. Spacecraft and Rockets,* Vol. 24, No. 1, pp. 7–14.

Peterson, G. P., and Ortega, A., 1990, "Thermal Control of Electronic Equipment and Devices," *Advances in Heat Transfer,* Vol. 20, J. P. Hartnett and T. F. Irvine, eds., Pergamon Press, New York, pp. 181–314.

Peterson, G. P., 1992, "An Overview of Micro Heat Pipe Research," Invited Review Article, *Applied Mechanics Review,* Vol. 45, No. 5, pp. 175–189.

Peterson, G. P., Lu, X. J., Peng, X. F., and Wang, B. X., 1992, "Analytical and Experimental Investigation of the Rewetting of Circular Channels With Internal V-Grooves," *Int. J. Heat Mass Transfer,* Vol. 35, No. 11, pp. 3085–3094.

Downloaded 11 Dec 2010 to 193.140.21.150. Redistribution subject to ASME license or copyright; see http://www.asme.org/terms/Terms_Use.cfm

Peterson, G. P., Duncan, A. B., and Weichold, M. H., 1993, "Experimental Investigation of Micro Heat Pipes Fabricated in Silicon Wafers," ASME JOURNAL OF HEAT TRANSFER, Vol. 115, pp. 751–756.

Peterson, G. P., and Mallik, A. K., 1995, "Transient Response Characteristics of Vapor Deposited Micro Heat Pipe Arrays," ASME *Journal of Electronic Packaging*, Vol. 117, pp. 82–87.

Schonberg, J. A., and Wayner, P. C., Jr., 1992, "Analytical Solution for the Integral Contact Line Evaporative Heat Sink," *AIAA J. of Thermophysics and Heat Transfer*, Vol. 6, No. 1, pp. 128–134.

Schrage, R. W., 1953, *A Theoretical Study of Interface Mass Transfer*, Columbia University Press, New York.

Wayner, P. C., Jr., Kao, Y. K., and LaCroix, L. V., 1976, "The Interline Heat-Transfer Coefficient of an Evaporating Wetting Film," *Int. J. Heat Mass Transfer*, Vol. 19, pp. 487–492.

Xu, X., and Carey, V. P., 1990, "Film Evaporation From a Micro-Grooved Surface—An Approximate Heat Transfer Model and Its Comparison With Experimental Data," *AIAA J. of Thermophysics and Heat Transfer*, Vol. 4, No. 4, pp. 512–520.

Downloaded 11 Dec 2010 to 193.140.21.150. Redistribution subject to ASME license or copyright; see http://www.asme.org/terms/Terms_Use.cfm

A Numerical Study of Thermal Dispersion in Porous Media

F. Kuwahara

A. Nakayama

H. Koyama

Department of Mechanical Engineering,
Shizuoka University,
3-5-1 Johoku, Hamamatsu, 432 Japan

Thermal dispersion in convective flow in porous media has been numerically investigated using a two-dimensional periodic model of porous structure. A macroscopically uniform flow is assumed to pass through a collection of square rods placed regularly in an infinite space, where a macroscopically linear temperature gradient is imposed perpendicularly to the flow direction. Due to the periodicity of the model, only one structural unit is taken for a calculation domain to resolve an entire domain of porous medium. Continuity, Navier–Stokes and energy equations are solved numerically to describe the microscopic velocity and temperature fields at a pore scale. The numerical results thus obtained are integrated over a unit structure to evaluate the thermal dispersion and the molecular diffusion due to tortuosity. The resulting correlation for a high-Peclet-number range agrees well with available experimental data.

Introduction

The complexity associated with the geometric structure of a porous medium does not allow us to treat the detailed velocity and temperature fields inside each individual porous structure. Thus, it has been a common practice to introduce volume-averaged quantities and concentrate on the overall aspects of mass, momentum, and energy conservation principles (e.g., Quintard and Whitaker, 1993). Accordingly, a number of heuristic and semi-heuristic models have been introduced to describe Darcy and non-Darcy flows and dispersion in heat and mass transfer through a porous medium. The model constants in these models are usually determined on the basis of exhaustive experimental data.

Detailed flow and temperature fields inside a microscopic structure may be investigated using a periodic structure (such as lattice structures) rather than treating complex porous media in reality. Eidsath et al. (1983), Coulaud et al. (1988), Sahraoui and Kaviany (1991), and Fowler and Bejan (1994) carried out two-dimensional numerical simulations for flows across banks of circular cylinders, whereas the authors (Kuwahara et al., 1994; Nakayama et al., 1995) investigated a collection of square rods to cover a wide range of porosity, virtually from zero to unity. Three-dimensional analyses were also conducted by Larson and Higdon (1989) for Stokes flows through lattice of spheres, and by the authors (1995) for fully elliptic flows through a lattice of cubes to study not only the Darcy contribution but also the porous inertial contribution to the macroscopic pressure drop.

Dispersion in porous media was studied by Koch and Brady (1985) and Koch et al. (1989) who obtained closed-form expressions for the dispersion tensor. However, in their analysis, an extremely dilute suspension of particles (i.e., high porosity) having the same thermal conductivity as the fluid was assumed using Stokes flow approximation along with the point force approximation. Thus, no Reynolds number and boundary layer effects were implemented, and the transverse dispersion coefficient was found to be independent of Peclet number and less than the thermal diffusivity of fluid. Full Navier–Stokes and energy equations were solved by Eidsath et al. (1983) and Edwards et al. (1991) for flows through a periodic structure of circular cylinders with in-line and staggered arrangements. In their models, the thermal conductivity of particles is assumed to be zero, such that no coupling of the energy equations for the fluid and solid phases was present. Kuwahara et al. (1994) proposed an idea to determine the transverse dispersion coefficient by fitting the numerical results against the similarity solution for forced convection from a line heat source in a porous medium, and conducted exhaustive numerical calculations for a large computational domain made of lattice of square rods. Arquis et al. (1991, 1993) extended the numerical model proposed by Coulaud et al. (1988) to the coupling of momentum and heat transfer to study both axial and transverse dispersion coefficients. The elegance of the work by Arquis and his group is that they imposed a macroscopic temperature gradient either normal or parallel to a macroscopically uniform flow such that the microscopic temperature field within only one structural unit is needed, as in the velocity field, to determine the corresponding dispersion coefficient. However, in these numerical studies, computations were carried out only for a limited number of sets of the parameters such as the porosity, macroscopic flow direction, and Peclet number. No general functional relationships for the dispersion coefficient as a function of these parameters were drawn from these studies due to a rather narrow porosity range.

In the present study, we follow the numerical approach proposed by Arquis et al. to determine the transverse dispersion coefficient purely from a theoretical basis. A macroscopically uniform flow is assumed to pass through a lattice of square rods placed regularly in an infinite space, where a macroscopically linear temperature gradient is imposed perpendicularly to the flow direction. The macroscopic flow angle is varied every 5 deg to investigate geometric effects on the dispersion coefficient. The present numerical model made of a lattice of square rods allows us to change the porosity virtually from zero to unity, and to establish a possible correlation for the dispersion coefficient. We strictly follow the mathematical definition of dispersion correlation in an exact form, appearing in the volume-averaged energy equation, and isolate it from the tortuosity contribution. (Note that Arquis et al. did not treat these apparent conductivities individually.)

Numerical Model and Boundary Conditions

We shall consider a macroscopically uniform flow with an angle θ meandering through an infinite number of square rods placed in a regular fashion, where a macroscopically linear temperature gradient is imposed perpendicularly to the flow direction, as illustrated in Fig. 1. Thus, the macroscopic velocity and temperature fields follow:

Contributed by the Heat Transfer Division for publication in the JOURNAL OF HEAT TRANSFER. Manuscript received by the Heat Transfer Division October 9, 1995; revision received March 29, 1996. Keywords: Forced Convection, Numerical Methods, Porous Media. Associate Technical Editor: K. Vafai.

Copyright © 1996 by ASME

Downloaded 11 Dec 2010 to 193.140.21.150. Redistribution subject to ASME license or copyright; see http://www.asme.org/terms/Terms_Use.cfm

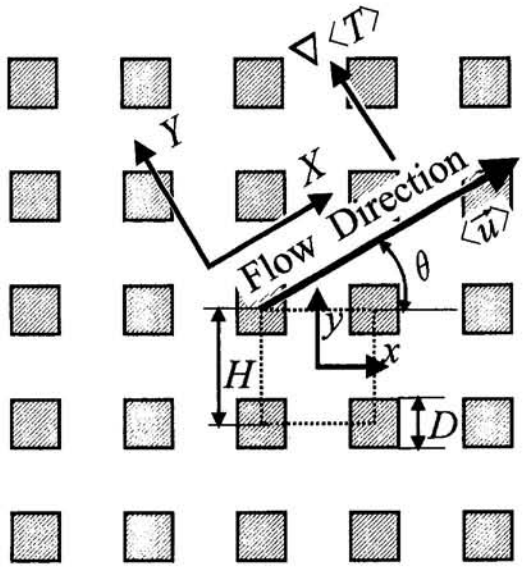


Fig. 1 Numerical model and its coordinates

$$\langle \vec{u} \rangle = |\langle \vec{u} \rangle|(\cos\theta \vec{i} + \sin\theta \vec{j}) \tag{1}$$

$$\nabla\langle T \rangle = \frac{\Delta T}{H}(-\sin\theta \vec{i} + \cos\theta \vec{j}) \tag{2}$$

where $\langle\ \rangle$ denotes volume average, namely,

$$\langle \phi \rangle = \frac{1}{V}\int_V \phi dV$$

The control volume V is much smaller than a macroscopic characteristic length and can be taken as H^2 for this periodic structure. Due to the periodicity of the model, only one structural unit as indicated by dashed lines may be taken as a calculation domain. The governing equations for the whole domain (i.e., fluid and solid phases) are given as follows:

$$\nabla \cdot \vec{u} = 0 \tag{3}$$

$$(\nabla \cdot \vec{u})\vec{u} = -\frac{1}{\rho}\nabla p + \nu\nabla^2\vec{u} \tag{4}$$

$$\rho_f C_{p_f} \nabla \cdot (\vec{u}T) = k_f \nabla^2 T: \quad \text{fluid phase} \tag{5}$$

$$k_s \nabla^2 T = 0: \quad \text{solid phase} \tag{6}$$

where the subscripts f and s denote fluid and solid phases, respectively. The boundary, compatibility, and periodic constraints are given by:

On the solid walls:

$$\vec{u} = \vec{0} \tag{7}$$

$$T_s = T_f \tag{8a}$$

$$k_s \left.\frac{\partial T}{\partial n}\right|_s = k_f \left.\frac{\partial T}{\partial n}\right|_f \tag{8b}$$

On the periodic boundaries:

$$\vec{u}|_{x=-H/2} = \vec{u}|_{x=H/2} \tag{9a}$$

$$\vec{u}|_{y=-H/2} = \vec{u}|_{y=H/2} \tag{9b}$$

$$\int_{-H/2}^{H/2} u dy\Big|_{x=-H/2} = \int_{-H/2}^{H/2} u dy\Big|_{x=H/2} = H|\langle \vec{u} \rangle| \cos\theta \tag{10a}$$

$$\int_{-H/2}^{H/2} v dx\Big|_{y=-H/2} = \int_{-H/2}^{H/2} v dx\Big|_{y=H/2} = H|\langle \vec{u} \rangle| \sin\theta \tag{10b}$$

$$T|_{x=-H/2} = T|_{x=H/2} + \Delta T \sin\theta \tag{11a}$$

$$T|_{y=-H/2} = T|_{y=H/2} - \Delta T \cos\theta \tag{11b}$$

We shall define the Reynolds number based on the Darcian velocity $|\langle \vec{u} \rangle|$ and length of structural unit H as $\mathrm{Re} = |\langle \vec{u} \rangle| H/\nu$.

Method of Computation

The governing equations are discretized by integrating them over a grid volume. The SIMPLE algorithm for the pressure-velocity coupling, as proposed by Patankar and Spalding (1972), is adopted to correct the pressure and velocity fields. Calculation starts with solving the two momentum equations, and subsequently, the estimated velocity field is corrected by solving the pressure correction equation reformulated from the discretized continuity and momentum equations, such that the velocity field fulfills the continuity principle. Then, the energy conservation equation is solved to find the corresponding temperature field. This iteration sequence is repeated until convergence is achieved. Convergence is measured in terms of the maximum change in each variable during an iteration. The maximum change allowed for the convergence check is set to 10^{-5}, as the variables are normalized by appropriate references. A fully implicit scheme is adopted with the hybrid differencing scheme for the advection terms. Further details on this numerical procedure can be found from Patankar (1980) and Nakayama (1995).

Nomenclature

$\vec{A}$ = surface area vector
A_{int} = total interface between the fluid and solid
b = Forchheimer constant
C_p = specific heat at constant pressure
C_s = specific heat of solid
D = size of square rod
H = size of structural unit
$\vec{i}, \vec{j}$ = unit vectors in the x and y directions
k = thermal conductivity
K = permeability
p = microscopic pressure
Pe = Peclet number based on H and the macroscopically uniform velocity
Re = Reynolds number based on H and the macroscopically uniform velocity
T = microscopic temperature
$\langle T'\vec{u}' \rangle$ = dispersion vector
ΔT = macroscopic temperature difference across a structural unit
u, v = microscopic velocity components in the x and y directions
V = control volume
x, y = Cartesian coordinates
X, Y = coordinates set along the macroscopic flow direction and its normal
ϵ = porosity
θ = macroscopic flow angle
ν = kinematic viscosity
ρ = density

Subscripts and Superscripts

dis = dispersion
e = effective
f = fluid
s = solid
tor = tortuosity

Special Symbols

$\langle\ \rangle$ = volume average
$\langle\ \rangle^{f,s}$ = intrinsic average

Downloaded 11 Dec 2010 to 193.140.21.150. Redistribution subject to ASME license or copyright; see http://www.asme.org/terms/Terms_Use.cfm

All computations have been carried out for a one structural unit $H \times H$ using nonuniform grid arrangements with 45×45. Sample calculations were also carried out using a finer grid system, 80×80, to ensure that the results are independent of the grid system. The Reynolds number was varied from 10^{-2} to 10^3 (assuming a typical range of $H = 1$ mm $\sim$ 1 cm); the ratio of the solid phase thermal conductivity to the fluid phase k_s/k_f, from 2 to 100; and the porosity ϵ, from 0.1 to 0.96, whereas the Prandtl number was fixed at 0.71. All computations were performed using the computer system CONVEX 220 at Shizuoka University Computer Center.

Volume-Averaged Energy Equation and Expressions for Tortuosity and Thermal Dispersion

Following Cheng (1978) and Nakayama (1995), we integrate the microscopic energy equation, Eq. (5), for the incompressible fluid over an elementary control, and obtain

$$\rho_f C_{p_f}\left[\frac{\partial \epsilon\langle T\rangle^f}{\partial t} + \langle \vec{u}\rangle \cdot \nabla\langle T\rangle^f\right] = \nabla \cdot \left[k_f \nabla \epsilon\langle T\rangle^f + \frac{1}{V}\int_{A_{\text{int}}} k_f T d\vec{A} - \rho_f C_{p_f}\langle T'\vec{u}'\rangle\right] + \frac{1}{V}\int_{A_{\text{int}}} k_f \nabla T \cdot d\vec{A} \quad (12)$$

Similarly, the microscopic energy equation for the solid, Eq. (6), may be integrated to give

$$\rho_s C_s \frac{\partial (1-\epsilon)\langle T\rangle^s}{\partial t} = \nabla \cdot \left[k_s \nabla (1-\epsilon)\langle T\rangle^s - \frac{1}{V}\int_{A_{\text{int}}} k_s T d\vec{A}\right] - \frac{1}{V}\int_{A_{\text{int}}} k_f \nabla T \cdot d\vec{A} \quad (13)$$

where A_{int} is the total interface between the fluid and solid, while $d\vec{A}$ is its vector element pointing outward from the fluid side to solid side. $\langle T\rangle^f$ and $\langle T\rangle^s$ are the intrinsic average of the fluid temperature and that of the solid phase, respectively. The continuity of heat flux at the interface is implemented in Eq. (13). We shall assume that thermal equilibrium exists between the fluid and solid matrix, namely, $\langle T\rangle^f = \langle T\rangle^s = \langle T\rangle$. For the present case of steady periodic flow, the thermal equilibrium condition proves to be exact. Adding up Eqs. (12) and (13), we have

$$[\epsilon \rho_f C_{p_f} + (1-\epsilon)\rho_s C_s]\frac{\partial \langle T\rangle}{\partial t} + \rho_f C_{p_f}\langle \vec{u}\rangle \cdot \nabla\langle T\rangle = \nabla \cdot \left\{[\epsilon k_f + (1-\epsilon)k_s]\nabla\langle T\rangle + \frac{1}{V}\int_{A_{\text{int}}} (k_f - k_s) T d\vec{A} - \rho_f C_{p_f}\langle T'\vec{u}'\rangle\right\} \quad (14)$$

For the case of steady flow, we rewrite Eq. (14) as

$$\rho_f C_{p_f}\langle \vec{u}\rangle \cdot \nabla\langle T\rangle = \nabla \cdot \{(k_e \bar{\bar{I}} + \bar{\bar{k}}_{\text{tor}} + \bar{\bar{k}}_{\text{dis}}) \cdot \nabla\langle T\rangle\} \quad (15)$$

where

$$k_e \equiv \epsilon k_f + (1-\epsilon)k_s \quad (16)$$

$$\frac{1}{V}\int_{A_{\text{int}}} (k_f - k_s) T d\vec{A} \equiv \bar{\bar{k}}_{\text{tor}} \cdot \nabla\langle T\rangle \quad (17)$$

$$-\rho_f C_{p_f}\langle T'\vec{u}'\rangle \equiv \bar{\bar{k}}_{\text{dis}} \cdot \nabla\langle T\rangle \quad (18)$$

The first two terms $-(k_e \bar{\bar{I}} + \bar{\bar{k}}_{\text{tor}}) \cdot \nabla\langle T\rangle$ on the right-hand side of Eq. (15) account for the molecular diffusion, whereas the third term $-\bar{\bar{k}}_{\text{dis}} \cdot \nabla\langle T\rangle$ accounts for contributions from thermal (mechanical) dispersion. k_e defined in Eq. (16) is the stagnant thermal conductivity. The apparent conductivity tensors $\bar{\bar{k}}_{\text{tor}}$ and $\bar{\bar{k}}_{\text{dis}}$ are introduced to model the tortuosity molecular diffusion term and the thermal dispersion term, respectively, by a gradient-type diffusion hypothesis. For the case of low-Peclet-number flow with the assumption of equal fluid and solid conductivities (Koch et al., 1989), both the tortuosity and dispersion terms may be dropped, and we have

$$\rho_f C_{p_f}\langle \vec{u}\rangle \cdot \nabla\langle T\rangle = \nabla \cdot (k_e \nabla\langle T\rangle) \quad (19)$$

In contrast, for the case of high-Peclet-number flow, the thermal dispersion predominates over the molecular diffusion such that

$$\rho_f C_{p_f}\langle \vec{u}\rangle \cdot \nabla\langle T\rangle = \nabla \cdot (\bar{\bar{k}}_{\text{dis}} \cdot \nabla\langle T\rangle) \quad (20)$$

For the case of high-Peclet-number flow, differences in the stagnant conductivity no longer affect macroscopic heat transfer in porous media. In this study, we shall determine both the tortuosity and thermal dispersion conductivities purely from a theoretical basis by substituting the microscopic numerical results into Eqs. (17) and (18).

When one coordinate is set along the macroscopic flow direction, only diagonal components of the tortuosity and dispersion conductivity tensors remain nonzero. Since the macroscopically linear temperature gradient is imposed along the Y direction normal to the X direction of macroscopic flow in the present model, the YY components of $\bar{\bar{k}}_{\text{tor}}$ and $\bar{\bar{k}}_{\text{dis}}$ can readily be determined from

$$(k_{\text{tor}})_{YY} = \frac{\left(\frac{k_s - k_f}{V}\int_{A_{\text{int}}} T d\vec{A}\right) \cdot (-\sin\theta \vec{i} + \cos\theta \vec{j})}{(\Delta T/H)} \quad (21)$$

$$(k_{\text{dis}})_{YY} = \frac{-\frac{\rho_f C_{p_f}}{H^2}}{(\Delta T/H)}\int_{-H/2}^{H/2}\int_{-H/2}^{H/2} (T - \langle T\rangle)(\vec{u} - \langle \vec{u}\rangle^f) dx dy \times (-\sin\theta \vec{i} + \cos\theta \vec{j}) \quad (22)$$

respectively.

Results and Discussion

Microscopic Velocity Field and Macroscopic Pressure Gradient. Two distinct velocity vector plots obtained at $\theta = 0$ and 45 deg for three different Reynolds numbers, namely, Re $= 10^{-1}$, 10, and 10^3, are compared in Fig. 2. When the Reynolds number is comparatively small, say Re $\leq$ 10, the velocity profiles for both $\theta = 0$ and 45 deg exhibit parabolic profiles as in a fully developed channel flow such that the viscous force contribution to the pressure drop predominates over the inertial contribution. As the Reynolds number increases, a distinct difference appears between the velocity field of $\theta = 0$ deg and that of $\theta = 45$ deg. Flow separation takes place for $\theta = 45$ deg, such that the inertial contribution to the pressure drop becomes significant, whereas the flow field for $\theta = 0$ deg remains of the channel flow type such that the inertial contribution is negligibly small. Accordingly, we may expect that the resulting macroscopic pressure drop for a fixed mass flow rate would be fairly insensitive to the macroscopic flow direction for low-Reynolds-number flows, while it becomes sensitive to the flow direction as the Reynolds number grows high.

The macroscopic pressure gradient (i.e., the gradient of the intrinsic average pressure measured along the macroscopic flow direction) of our primary interest may readily be evaluated using the microscopic numerical results as

Downloaded 11 Dec 2010 to 193.140.21.150. Redistribution subject to ASME license or copyright; see http://www.asme.org/terms/Terms_Use.cfm

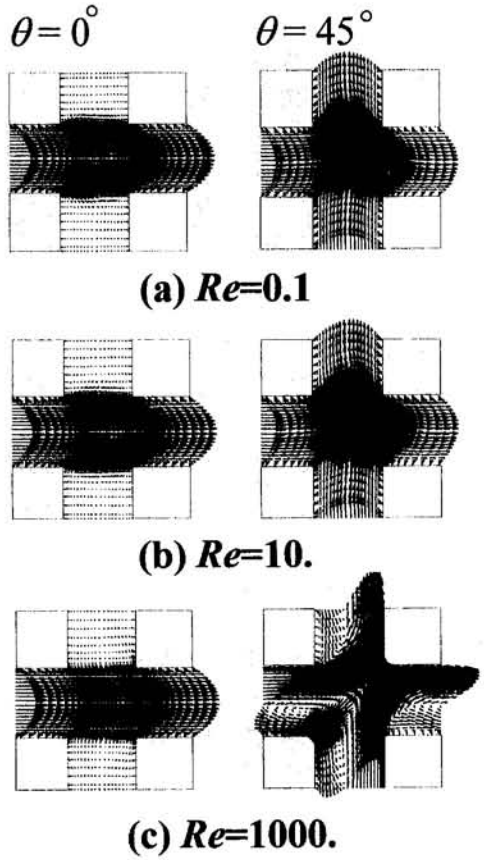


Fig. 2 Velocity vector plots

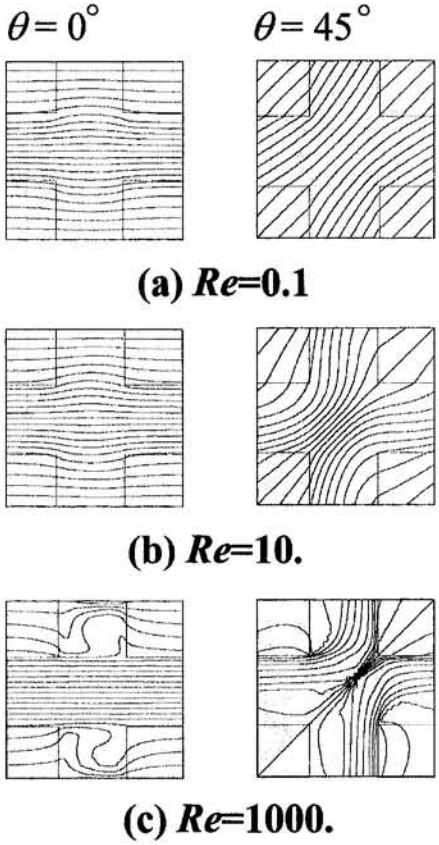


Fig. 4 Isotherms

$$-\frac{d\langle p\rangle^f}{dX} = \frac{\cos\theta}{H(H-D)}\int_{-(H-D)/2}^{(H-D)/2}(p|_{x=-(H-D)/2} - p|_{x=(H-D)/2})dy + \frac{\sin\theta}{H(H-D)} \times \int_{-(H-D)/2}^{(H-D)/2}(p|_{y=-(H-D)/2} - p|_{y=(H-D)/2})dx \quad (23)$$

The pressure gradient results, thus obtained with $\epsilon = 0.64$, changing the Reynolds number and macroscopic flow angle are assembled in Fig. 3, in terms of the dimensionless pressure gradient against the Reynolds number. All data show that the dimensionless pressure gradient stays constant for Re $\leq$ 10, irrespective of the flow angle, as we expected from the velocity vector plots in Fig. 2. The pressure gradient increases drastically as Re goes beyond 10 in which the porous inertial contribution becomes appreciable as compared with the viscous (Darcian) contribution.

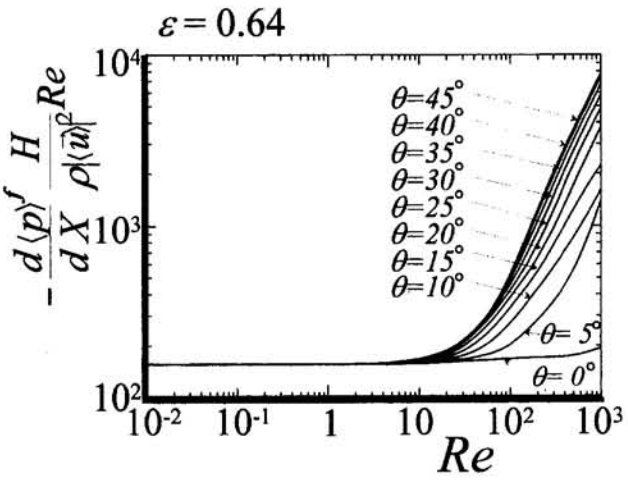


Fig. 3 Dimensionless pressure gradient

The Forchheimer–extended Darcy law may be written as

$$-\frac{d\langle p\rangle^f}{dX}\frac{H}{\rho|\langle\vec{u}\rangle|^2}\,\mathrm{Re} = \frac{H^2}{K} + bH\,\mathrm{Re} \quad (24)$$

Thus, the permeability K may readily be determined by reading the intercept of the ordinate variable in Fig. 3. The constancy of the dimensionless pressure gradient, irrespective of θ, substantiates the validity of the periodic numerical models to determine K from the first principles. The second term on the right-hand side of Eq. (24) represents the porous inertial contribution, which increases with Re. The coefficient b for the inertial contribution may be determined by fitting the numerical results obtained at high Reynolds numbers into Eq. (24). Such an attempt and its extension to a three-dimensional model have been recently reported by Nakayama et al. (1995).

Microscopic Temperature Field and Thermal Conductivity Due to Tortuosity. The microscopic temperature fields obtained at $\theta = 0$ and 45 deg with $\epsilon = 0.64$ are shown for Re = 10^{-1}, 10, and 10^3 in Fig. 4 in terms of isotherms. The isotherms obtained at low Reynolds numbers exhibit a typical pattern for the case of pure thermal conduction. For the case of high-Reynolds-number flows, the temperature pattern becomes very complex, as a result of thermal dispersion, as seen from Fig. 4(*c*), where comparatively uniform temperature regions exist

Downloaded 11 Dec 2010 to 193.140.21.150. Redistribution subject to ASME license or copyright; see http://www.asme.org/terms/Terms_Use.cfm

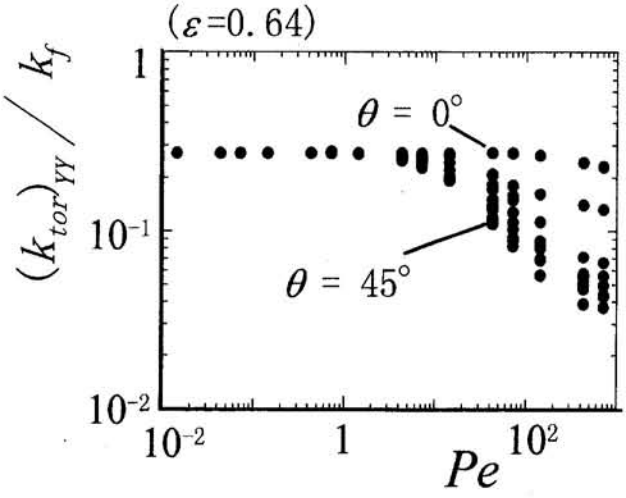


Fig. 5 Apparent thermal conductivity due to tortuosity

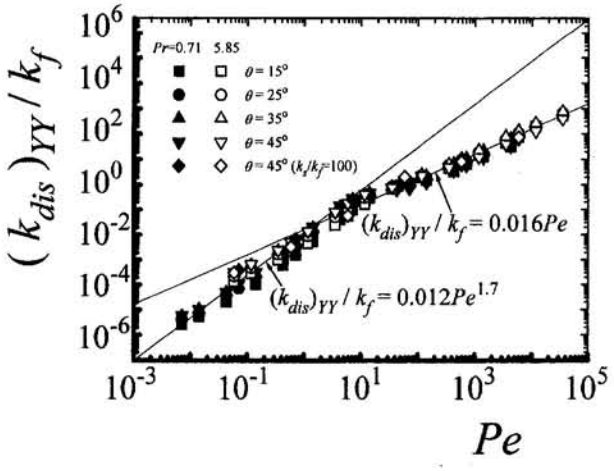


Fig. 7 Apparent thermal conductivity due to dispersion

within recirculation regions. In Fig. 5, the tortuosity conductivity $(k_{tor})_{YY}$ determined by feeding the microscopic numerical results into Eq. (21) is plotted against the Peclet number Pe for the case of $\epsilon = 0.64$. It is interesting to note that all data obtained for different macroscopic flow angles fall onto a horizontal asymptote as Pe decreases. An approximate analytical formula for this asymptotic value may be found by approximating the temperature distribution in a structural unit at low Peclet number (see Fig. 4(*a*)) by a piecewise linear temperature distribution within a one-dimensional composite slab, as

$$\frac{(k_{tor})_{YY}}{k_f} = \left(\frac{k_s}{k_f} - 1\right) \frac{(1-\epsilon)}{(1-\epsilon)^{1/2} + \frac{k_s}{k_f}(1-(1-\epsilon)^{1/2})} \quad (25)$$

The tortuosity conductivity results obtained for a low-Peclet-number range as the porosity is changed from 0.1 to 0.96, and thermal conductivity ratio from 2 to 100, are plotted with the curves generated by the foregoing approximate formula in Fig. 6 with the abscissa $(1 - \epsilon)$. An excellent agreement can be seen between the numerical results and the approximate formula for the entire range of porosity.

Figure 5 clearly shows that the tortuosity conductivity decreases as Pe increases. However, the contribution from thermal dispersion predominates over the tortuosity contribution as Pe increases, such that the tortuosity conductivity may no longer be important and may well be neglected in such a high-Peclet-number range.

Thermal Conductivity Due to Thermal Dispersion. The microscopic temperature results obtained for 15 deg $\leq \theta \leq$ 45 deg with Pr = 0.71, 5.85, and k_s/k_f = 2, 100, are processed using Eq. (22), and the resulting thermal conductivity $(k_{dis})_{YY}$ due to thermal dispersion is plotted for the case of $\epsilon = 0.64$ in Fig. 7. The figure suggests that the lower and higher Peclet number data follow two distinct limiting lines, respectively. The lower Peclet number data vary in proportion to $Pe^{1.7}$, whereas the high-Peclet-number data vary in proportion to Pe. The Peclet number dependency at low Pe, namely, $Pe^{1.7}$, which is the same as what Eidsath et al. (1983) observed numerically for the axial thermal dispersion conductivity, but different from Pe^2 suggested by Taylor (1953) and Aris (1956) in the classical study of solute in a fluid flowing in a tube. A further analytical and numerical investigation is needed to clarify this difference in the Peclet number dependency at low Pe. Exhaustive computations were conducted to extract functional relationships for the thermal dispersion conductivities at low and high Peclet number ranges, $0.01 < Pe < 10$ and $10 < Pe < 5000$, respectively. The thermal dispersion conductivities obtained for different ϵ are plotted in Fig. 8 with the abscissa variable $(1 - \epsilon)$ to investigate the porosity dependency. The resulting expressions for the low and high Peclet number ranges are given by

$$\frac{(k_{dis})_{YY}}{k_f} = 0.022 \frac{Pe_D^{1.7}}{(1-\epsilon)^{1/4}} \quad \text{for} \quad (Pe_D < 10) \quad (26a)$$

$$\frac{(k_{dis})_{YY}}{k_f} = 0.052(1-\epsilon)^{1/2} Pe_D \quad \text{for} \quad (Pe_D > 10) \quad (26b)$$

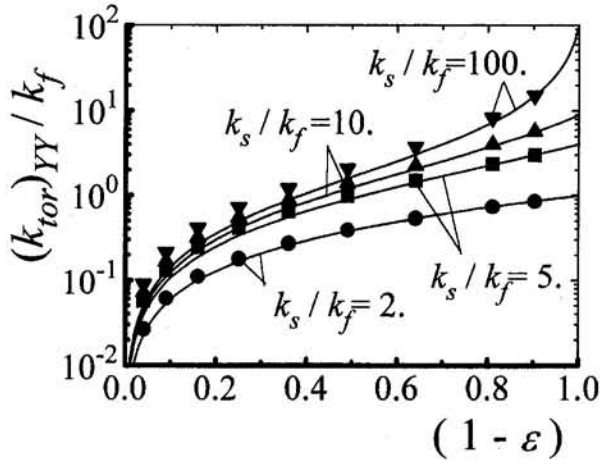


Fig. 6 Apparent thermal conductivity due to tortuosity as a function of porosity

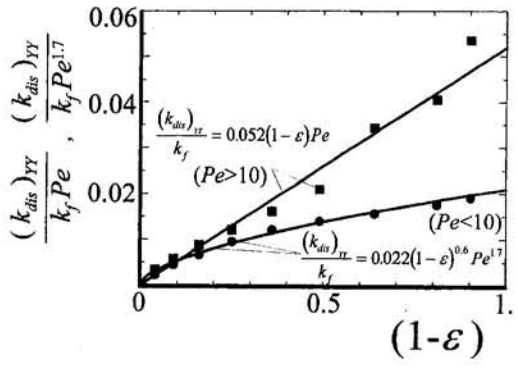


Fig. 8 Apparent thermal conductivity due to dispersion as a function of porosity

Downloaded 11 Dec 2010 to 193.140.21.150. Redistribution subject to ASME license or copyright; see http://www.asme.org/terms/Terms_Use.cfm

where the relationship $Pe_D = Pe(1 - \epsilon)^{1/2}$ is used.

The predicted total thermal conductivity $(k_e + (k_{tor})_{YY} + (k_{dis})_{YY})$ is compared against the experimental data of Fried and Combarnous (1971), Han et al. (1985), and Yagi et al. (1960) for packed beds in Fig. 9, where a fairly good agreement can be seen between the present correlation and the experimental data, in light of the simplicity of the present periodic model. In the same figure, Koch and Brady's (1985) Stokes flow analysis on dilute suspension of particles is shown for reference. Their analysis, however, should be compared with the experimental data with caution, since their analysis applies only for the case of high porosity, and their leading order analysis of Stokes flow of high-Prandtl-number fluid takes no account of the Reynolds number effects, which are definitely included in Fried and Combarnous' experimental data.

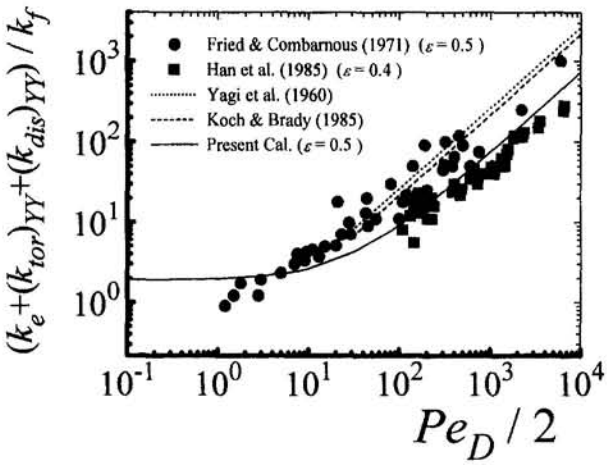


Fig. 9 Comparison of the prediction and experiment

Concluding Remarks

A successful attempt was made to investigate the apparent conductivities due to the tortuosity and thermal dispersion numerically, considering a macroscopically uniform flow through a periodic model of square rods. The transverse components of the conductivities were determined imposing a macroscopically linear temperature gradient normal to the macroscopic flow direction. The corresponding streamwise components of the conductivities may be determined similarly, by imposing a temperature gradient parallel to the flow direction. Such an attempt is under way.

Acknowledgments

One author (A.N.) wishes to thank Dr. E. Arquis for kindly sending copies of his papers and for the inspiring discussion held at Brighton in the summer of 1994.

References

Aris, R., 1956, "On the Dispersion of a Solute in a Fluid Flowing Through a Tube," *Proc. Roy. Soc. London,* Vol. A235, pp. 67–77.

Arquis, E., Caltagirone, J. P., and Le Breton, P., 1991, "Détermination des propriétés de dispersion d'un milieu périodique à partir de l'analyse locale des transferts," *C.R. Acad. Sci. Paris,* Vol. II, No. 313, pp. 1087–1092.

Arquis, E., Caltagirone, J. P., and Delmas, A., 1993, "Derivation in Thermal Conductivity of Porous Media Due to High Interstitial Flow Velocity," *Proc. 22nd Int. Thermal Conductivity Conf.,* Tempe, AZ, Nov.

Cheng, P., 1978, "Heat Transfer in Geothermal Systems," *Advances in Heat Transfer,* Vol. 14, pp. 1–105.

Coulaud, O., Morel, P., and Caltagirone, J. P., 1988, "Numerical Modeling of Nonlinear Effects in Laminar Flow Through a Porous Medium," *J. Fluid Mech.,* Vol. 190, pp. 393–407.

Edwards, D. A., Shapiro, M., Brenner, H., and Shapira, M., 1991, "Dispersion of Inert Solutes in Spatially Periodic Two-Dimensional Model Porous Media," *Transport in Porous Media,* Vol. 6, pp. 337–358.

Eidsath, A., Carbonell, R. G., Whitaker, S., and Herman, L. R., 1983, "Dispersion in Pulsed Systems: III. Comparison Between Theory and Experiment for Packed Beds," *Chem. Engng. Sci.,* Vol. 38, pp. 1803–1816.

Fowler, A. J., and Bejan, A., 1994, "Forced Convection in Banks of Inclined Cylinders at Low Reynolds Numbers," *Int. J. Heat Fluid Flow,* Vol. 15, pp. 90–99.

Fried, J. J., and Combarnous, M. A., 1971, "Dispersion in Porous Media," *Advances in Hydro. Science,* Vol. 7, pp. 169–282.

Han, N.-W., Bhakta, J., and Carbonell, R. G., 1985, "Longitudinal and Lateral Dispersion in Packed Beds: Effect of Column Length and Particle Size Distribution," *AIChE J.,* Vol. 31, pp. 277–288.

Katsuki, S., and Nakayama, A., 1990, *Numerical Simulation of Heat and Fluid Flow,* Morikita Shuppan, Tokyo.

Kawamura, Y., 1994, "Numerical Simulation of Microscopic Flow in a Porous Structure," M.S. Thesis, Shizuoka University, Japan.

Koch, D. L., and Brady, J. F., 1985, "Dispersion in Fixed Beds," *J. Fluid Mech.,* Vol. 154, pp. 399–427.

Koch, D. L., Cox, R. G., Brenner, H., and Brady, J. F., 1989, "The Effect of Order on Dispersion in Porous Media," *J. Fluid Mech.,* Vol. 200, pp. 173–188.

Kuwahara, F., Nakayama, A., and Koyama, H., 1994, "Numerical Modelling of Heat and Fluid Flow in a Porous Medium," *Proc. 10th Int. Heat Transfer Conf.,* Vol. 5, pp. 309–314.

Larson, R. E., and Higdon, J. J. L., 1989, "A Periodic Grain Consolidation Model of Porous Media," *Physics of Fluids,* Vol. A1, pp. 38–46.

Nakayama, A., 1995, *PC-Aided Numerical Heat Transfer and Convective Flow,* CRC Press, Boca Raton, FL.

Nakayama, A., Kuwahara, F., Kawamura, Y., and Koyama, H., 1995, "Three-Dimensional Numerical Simulation of Flow Through a Microscopic Porous Structure," *Proc. ASME/JSME Thermal Engineering Conf.,* Vol. 3, pp. 313–318.

Patankar, S. V., and Spalding, D. B., 1972, "A Calculation Procedure for Heat, Mass and Momentum Transfer in Three-Dimensional Parabolic Flows," *Int. J. Heat Mass Transfer,* Vol. 15, pp. 1787–1806.

Patankar, S. V., 1980, *Numerical Heat Transfer and Fluid Flow,* Hemisphere, Washington, DC.

Quintard, M., and Whitaker, S., 1993, "One- and Two-Equation Models for Transient Diffusion Processes in Two-Phase Systems," *Advances in Heat Transfer,* Vol. 23, pp. 369–464.

Sahraoui, M., and Kaviany, M., 1991, "Slip and No-Slip Boundary Condition at Interface of Porous, Plain Media," *Proc. ASME/JSME Thermal Engineering Proceedings,* Vol. 4, pp. 273–286.

Taylor, G. I., 1953, "Dispersion of Solute Matter in Solvent Flowing Slowly Through a Tube," *Proc. Roy. Soc. London,* Vol. A219, pp. 186–203.

Yagi, S., Kunii, D., and Wakao, N., 1960, "Studies on Axial Effective Thermal Conductivities in Packed Beds," *AIChE J.,* Vol. 6, pp. 543–546.

Downloaded 11 Dec 2010 to 193.140.21.150. Redistribution subject to ASME license or copyright; see http://www.asme.org/terms/Terms_Use.cfm

P. S. Wei
Professor.
Mem. ASME

S. C. Wang
Graduate Student.

M. S. Lin
Graduate Student.

Institute of Mechanical Engineering,
National Sun Yat-Sen University,
Kaohsiung, Taiwan

Transport Phenomena During Resistance Spot Welding

Unsteady, axisymmetric transport of mass, momentum, energy, species, and magnetic field intensity with a mushy-zone phase change in workpieces and temperature, and magnetic fields in electrodes during resistance spot welding, are systematically investigated. Electromagnetic force, joule heat, heat generation at the electrode–workpiece interface and faying surface between workpieces, different properties between phases, and geometries of electrodes are taken into account. The computed results show consistencies with observed nugget growth, electrical current, and temperature fields. The effects of the face radius and cone angle of the electrode, parameters governing welding current, electrical contact resistance, magnetic Prandtl number, electrical conductivity ratio, and workpiece thickness on transport phenomena are clearly provided.

Introduction

Resistance spot welding has been widely used in joining workpieces. The weldments are brought together under pressure by a pair of electrodes. During welding, high electric currents pass between electrodes and melt faying surfaces of workpieces. After power is off, heat is conducted through electrodes. Workpieces are thus joined via solidification of the molten nugget. In order to obtain consistent weld quality, the face of the electrode can be pointed, domed, flat, eccentric, or truncated (e.g., Dickinson, 1981). A coolant hole in the electrode is also required to enhance heat transfer during solidification.

Understanding the effects of the electrode geometry on resistance spot welding is crucial. Unfortunately, realistic investigation is still lacking. Idealized distributions of voltage in the electrode and workpiece were excellently reviewed by Holm (1958). Greenwood and Williamson (1958) provided closed-form solutions for temperature and electrical potential in arbitrary shapes of the electrode experienced by joule heat. By assuming constant temperatures and electrical potentials at the inlet and outlet and ignoring electric contact resistance, a current constriction was found to occur at the contact surface. In view of high current densities near the outer face edge, an annular molten zone were observed at the faying surface.

A more relevant simulation of the electrode geometry and steady voltage drop resulting from contact resistances at the electrode–workpiece interface and faying surface was provided by Cho and Cho (1989). The effects of the electrode shape on voltage and temperature, however, were not presented. Using a uniform welding current and an appropriate model for evaluating electric contact resistance, Wei and Ho (1990) quantitatively found that a smaller radius of the electrode face increases the nugget growth and reduces the width of the nugget. Fields of electrical current density in the electrode by varying cone angles of truncated cone and pimple-tip electrodes were predicted by Bowers et al. (1990). Constant voltages were specified at the cross section on the bottom surface of the coolant hole and electrode–workpiece interface, respectively. The result showed that a decrease in the cone angle increases the ratio of current density at the edge and axisymmetric axis. A uniform current density was found for a flat face electrode.

In reality, electric currents do not flow directly across workpieces. Most of the currents that spread into the workpiece enter near the electrode edge, as qualitatively mentioned by Greenwood (1961). Such a phenomenon aids in explaining observations of not only an annular molten zone at the periphery of a spot weld but also a magnetic stirring. Cunningham and Begeman (1965) observed projection welding from high-speed photography. It was found that there were generally two patterns observed shortly after the formation of the weld started. In one case the nugget started in the center and continued to progress into a large nugget, while in the other, molten areas started on each side gradually came together. It was also proposed that four cells flow in a direction toward the axisymmetric axis near the faying surface while two cells occurred for an asymmetric case. The interpretation was that the Lorentz force is proportional to the product of field strength and current density, which decreases from a maximum at the outside boundary of the workpiece to zero at the axis. It also decreases above and below the interface due to divergence of the current. Thus maximum force causes liquid to be pushed along the faying surface toward the axis where at this point it tends to flow either up or down, then out along the outer boundary of the nugget. Velocities were estimated to be at least 0.15–0.3 m/s. In order to understand resistance spot welding accounts for the divergence of electric currents as a function of electrode geometry, and transport of mass, momentum, and energy in the molten nugget are necessary. The latter has been investigated by Wei and Yeh (1991).

This study is to determine unsteady transport phenomena during resistance spot welding by using different shapes of electrodes. The model proposed by Wei and Yeh (1991) to predict unsteady axisymmetric mass, momentum, heat, and species transport in binary alloys during resistance spot welding were extended by including equations of magnetic intensity fields in electrodes and workpieces, and energy equation in electrodes in this work. Aside from confirmation of previous experimental observations, results also give more realistic and systematic understanding of resistance spot welding.

System Model and Analysis

Resistance spot welding, as illustrated in Fig. 1, is in a cylindrical coordinate system having the origin at the intersection of the axisymmetric axis and bottom electrode–workpiece surface. Workpieces are a binary alloy of radius r_b and total thickness l. The electrode has a truncated cone face of radius r_e, length l_1, outer radius r_s, and cone angle $\tan^{-1}[l_1/(1 - r_e)]$ while the outer radius of the coolant hole is r_c. The major assumptions made are the same as those proposed by Wei and Yeh (1991). Briefly speaking, they are:

Contributed by the Heat Transfer Division for publication in the JOURNAL OF HEAT TRANSFER. Manuscript received by the Heat Transfer Division March 22, 1995; revision received April 1, 1996. Keywords: Materials Processing and Manufacturing Processes, Phase-Change Phenomena, Transient and Unsteady Heat Transfer. Associate Technical Editor: A. Lavine.

Copyright © 1996 by ASME

Downloaded 11 Dec 2010 to 193.140.21.150. Redistribution subject to ASME license or copyright; see http://www.asme.org/terms/Terms_Use.cfm

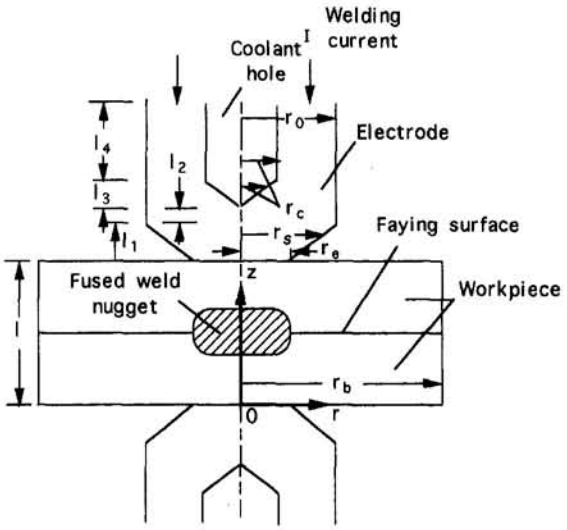


Fig. 1 Resistance spot welding and coordinate system

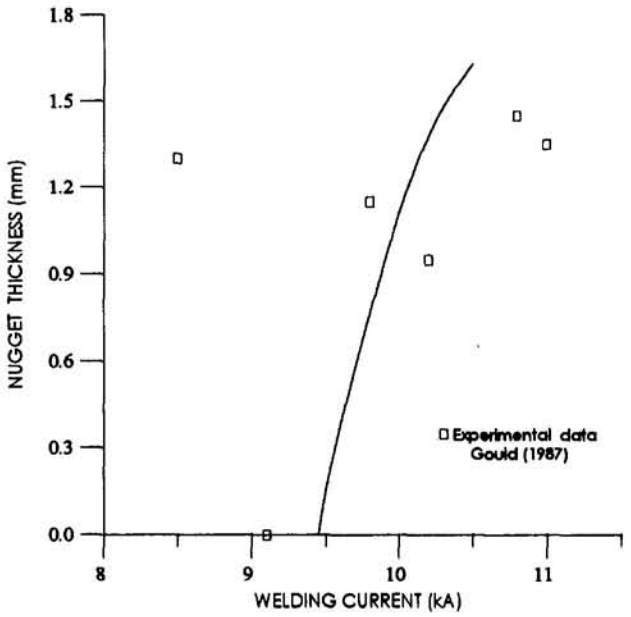


Fig. 2 Comparison between predicted and measured nugget thickness versus welding current at a dimensional time of 0.15 s for welding AISI 1008 steel

1 The faying surface and electrode–workpiece interface are considered to be thin volumetric heat sources (Wei and Ho, 1990; Wei and Yeh, 1991);
2 Electrical contact resistance decreases linearly with temperature (Dickinson et al., 1980; Gould, 1987; Wei and Ho, 1990) until the faying surface becomes fully liquid;
3 The mushy zone is a porous medium in a local thermal and phase equilibrium to a first approximation;
4 Mean values of properties within the temperature range considered are chosen and allowed to be distinct between phases.

Nomenclature

Bi_{0E} = Biot number = $\tilde{h}_0 r_0/\tilde{k}_E$
Bi_E = $\tilde{h}_E r_0/\tilde{k}_s$
Bi_w = $\tilde{h}_w r_0/\tilde{k}_E$
C = specific heat ratio, as defined in Eq. (6)
D = solute diffusivity
Da = Darcy number, as defined in Eq. (6)
E = dimensionless parameter, as defined in Eq. (6)
E_f = ϵ_f/r_0
f = mass fraction of liquid or solid
F_0 = dimensionless parameter, as defined in Eq. (6)
f^α = solute mass fraction = $\hat{f}^\alpha/\hat{f}^\alpha_{m,0}$
$\hat{f}^\alpha$ = solute mass fraction
$\hat{f}^\alpha_{m,0}$ = initial solute content
g = volume fraction or gravitational acceleration
Gr = Grashof number, as defined in Eq. (6)
h = enthalpy = $\tilde{h}/h_f$; or heat transfer coefficient
H = magnetic field intensity in θ direction = $\tilde{H}\pi r_0/I$
h_f = fusion latent heat at eutectic point, J/kg
h_l = $RCT + R(1 - C)T_e + 1$
h_s = RT
I, j = welding current, amp, electric current density, $j = \tilde{j}\pi r_0^2/I$
k = thermal conductivity
K = $g_l + g_s k_s$
k_E = thermal conductivity ratio = $\tilde{k}_E/\tilde{k}_s$
k_s = thermal conductivity ratio = $\tilde{k}_s/\tilde{k}_l$
k_p = equilibrium partition coefficient
K_0 = permeability constant, m^2
l = distance between electrodes
l_1, l_2, l_3, l_4 = length, as illustrated in Fig. 1
Lo = dimensionless parameter, as defined in Eq. (6)
M = $-(dr_c/d\zeta + \xi dN/d\zeta)/N$
M_{liq} = $\hat{f}_{l,e}/\hat{f}^\alpha_{m,o}$
M_{sol} = $\hat{f}_{s,e}/\hat{f}^\alpha_{m,o}$
N = $r_s(\zeta) - r_c(\zeta)$
Pr = Prandtl number, as defined in Eq. (6)
Pr_m = magnetic Prandtl number = $\tilde{\eta}_1/\tilde{\alpha}_1$
R = $\tilde{c}_s\tilde{T}_0/h_f$
R_E = $\tilde{c}_E\tilde{T}_0/h_f$
R_f = dimensionless temperature ratio, as defined in Eq. (6)
r_0 = maximum radius of electrode, as shown in Fig. 1
$\tilde{R}_0$ = electrical contact resistance at faying surface at $\tilde{T}_0$
R_{0E} = electrical contact resistance at electrode–workpiece interface at $\tilde{T}_0$; $R_{0E} = \tilde{R}_{0E}/\tilde{R}_0$
Sc = Schmidt number, as defined in Eq. (6)
t = time = $\tilde{t}\tilde{\alpha}_l/r_0^2$
T = temperature = $\tilde{T}/\tilde{T}_0$
T_c, T_e, T_m = Curie, eutectic, and melting temperatures
u, v = axial and radial velocity, $u = \tilde{u}r_0/\tilde{\alpha}_l$, $v = \tilde{v}r_0/\tilde{\alpha}_l$
$\mathbf{V}$ = velocity vector
α = thermal diffusivity
β_S, β_T = solutal and thermal expansion coefficient
ϵ_f = effective thickness of heat source at faying surface and electrode-workpiece interface, m
$\tilde{\eta}_l$ = magnetic diffusivity of liquid = $1/\tilde{\sigma}_l\mu_0\mu_{rl}$
η_E = $\tilde{\eta}_E/\tilde{\eta}_l$, where $\tilde{\eta}_E = 1/(\tilde{\sigma}_E\mu_0\mu_{rE})$
θ_0 = dimensionless temperature ratio, as defined in Eq. (6)
μ_r = relative magnetic permeability = $\mu_{rs}g_s/\mu_{rl} + g_l$
μ_0 = free magnetic permeability, $\mathrm{N/amp}^2$
ν = kinematic viscosity
ρ = density = $\tilde{\rho}/\tilde{\rho}_l$
ρ_E = $\tilde{\rho}_E/\tilde{\rho}_l$
σ = electrical conductivity = $\tilde{\sigma}/\tilde{\sigma}_l = g_s\tilde{\sigma}_s/\tilde{\sigma}_l + g_l$, mho/m
Σ = dimensionless parameter, as defined in Eq. (6)
σ_E = $\tilde{\sigma}_E/\tilde{\sigma}_l$
τ = dimensionless time = t

Downloaded 11 Dec 2010 to 193.140.21.150. Redistribution subject to ASME license or copyright; see http://www.asme.org/terms/Terms_Use.cfm

Table 1 Typical values of dimensionless parameters

Biot numbers, Bi_{oE}, Bi_E, Bi_w	0.0025, 0.72, 0.5
Darcy number, Da	6.17×10^{-6}
Electrical contact resistance, E	4.96×10^{-3}
Effective thickness of heat source at contact surface, E_f	10^{-3}
Electrode thermal conductivity, k_E	11.4
Solid-to-liquid thermal conductivity ratio, k_s	1.0
Welding current parameter, Lo	2×10^7
Lengths for electrode, l_2, l_3, l_4	0.5, 0.5, 1
Slope parameter of liquidus and solidus lines, m_{liq}, m_{sol}	4.0, 3.0
Magnetic Prandtl number, Pr_m	10^5
Maximum radius of coolant hole, r_c	0.5
Electrode enthalpy parameter, R_E	0.59
Electrical contact resistance at electrode-workpiece surface, R_{0E}	0.1
Curie temperature, T_c	3.5
Eutectic and melting temperatures, T_e, T_m	5.0, 6.0
Solid-to-liquid permeability ratio, μ_{rs}/μ_{rl}	3500
Electrode density, ρ_E	1.28
Thermal-to-electrical property parameter, Σ	3×10^{-5}
Electrical conductivity ratios, σ, σ_E	1.0, 10

Governing Equations in Workpiece. With these assumptions, the continuity, momentum, energy, and species equations (Bennon and Incropera, 1987; Wei and Yeh, 1991), respectively, become

$$\frac{\partial \rho}{\partial t} + \nabla.(\rho \mathbf{V}_m) = 0 \tag{1}$$

$$\frac{\partial \rho u_m}{\partial t} + \nabla.(\rho \mathbf{V}_m u_m) = \mathrm{Pr}\nabla.(\rho \nabla u_m) - \frac{\mathrm{Pr}\rho(1-g_l)^2}{\mathrm{Da}\, g_l^3} u_m - \frac{\partial p}{\partial z} + \mathrm{Pr}^2\,\mathrm{Gr}[\theta_0(T - T_{\mathrm{sol}}) + F_0(f_l^{\alpha} - f_{l,T=T_{\mathrm{sol}}}^{\alpha})] - \frac{Lo}{\pi^2}\mu_r H \frac{\partial H}{\partial z} \tag{2}$$

$$\frac{\partial \rho v_m}{\partial t} + \nabla.(\rho \mathbf{V}_m v_m) = \mathrm{Pr}\nabla.(\rho \nabla v_m) - \frac{\mathrm{Pr}\rho(1-g_l)^2}{\mathrm{Da}\, g_l^3} v_m - \frac{\partial p}{\partial r} - \frac{Lo}{\pi^2}\frac{\mu_r}{r} H \frac{\partial}{\partial r}(rH) \tag{3}$$

$$\frac{\partial \rho h_m}{\partial t} + \nabla.(\rho \mathbf{V}_m h_m) = C\nabla.(K\nabla h_m) + C\nabla.[K\nabla(h_s - h_m)] - \nabla.[\rho(h_l - h_m)\mathbf{V}_m] + Lo\left(\frac{Er_e^2}{\pi} R_f + \frac{\Sigma}{\sigma\pi^2}\right) \times \left[\left(\frac{1}{r}\frac{\partial rH}{\partial r}\right)^2 + \left(\frac{\partial H}{\partial z}\right)^2\right] \tag{4}$$

$$\frac{\partial \rho f_m^{\alpha}}{\partial t} + \nabla.(\rho \mathbf{V}_m f_m^{\alpha}) = \frac{\mathrm{Pr}}{\mathrm{Sc}}\nabla.(\rho f_l \nabla f_m^{\alpha}) + \frac{\mathrm{Pr}}{\mathrm{Sc}}\nabla.[\rho f_l \nabla(f_l^{\alpha} - f_m^{\alpha})] - \nabla.[\rho(f_l^{\alpha} - f_m^{\alpha})\mathbf{V}_m] \tag{5}$$

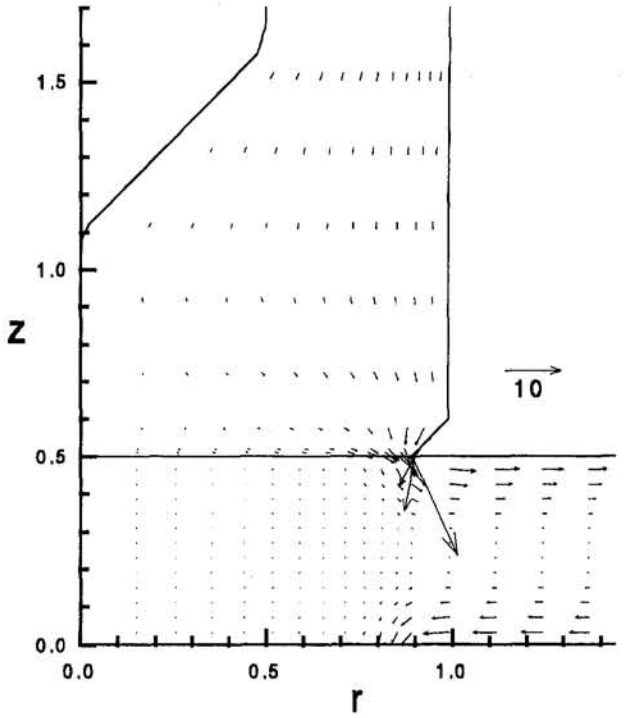


Fig. 3 Dimensionless electric current density field in a truncated cone electrode and workpieces at a dimensionless time of 10^{-4}; $j_{max} = 19$

where the dimensionless parameters are defined as

$$\mathrm{Pr} = \frac{\tilde{\nu}_l}{\tilde{\alpha}_l}, \quad \mathrm{Da} = \frac{K_0}{r_0^2}, \quad \mathrm{Gr} = \frac{g\beta_T(\tilde{T}_{\mathrm{sol}} - \tilde{T}_e)r_0^3}{\tilde{\nu}_l^2},$$

$$\theta_0 = \frac{\tilde{T}_0}{\tilde{T}_{\mathrm{sol}} - \tilde{T}_e}, \quad F_0 = \frac{\beta_s \hat{f}_{m,0}^{\alpha}}{\beta_T(\tilde{T}_{\mathrm{sol}} - \tilde{T}_e)}, \quad Lo = \frac{I^2\mu_0\mu_{rl}}{\tilde{\rho}_l\tilde{\alpha}_l^2},$$

$$C = \frac{\tilde{c}_l}{\tilde{c}_s}, \quad E = \frac{\tilde{R}_0\tilde{\sigma}_l\tilde{\alpha}_l\tilde{\eta}_l}{h_f\epsilon_f},$$

$$\Sigma = \frac{\tilde{\alpha}_l\tilde{\eta}_l}{r_0^2 h_f}, \quad R_f = \frac{T_{\mathrm{liq}} - T}{T_{\mathrm{liq}} - 1}, \quad \mathrm{Sc} = \frac{\tilde{\nu}_l}{D_l^{\alpha}}. \tag{6}$$

All the lengths in Eqs. (1)–(5) are nondimensionalized by the maximum radius of the electrode r_0. The second and last terms on the right-hand side of Eqs. (2) and (3) are referred to as Darcy's law and Lorentz force, respectively. The last term on the right-hand side of Eq. (4) is a combination of heat generation at the faying surface and joule heating in bulk workpieces (Wei and Yeh, 1991). The equation governing magnetic field intensity in workpieces is

$$\frac{\partial \mu_r H}{\partial t} + \nabla.(\mu_r \mathbf{V}_m H) = \mathrm{Pr}_m\nabla.\left(\frac{1}{\sigma}\nabla H\right) + \mathrm{Pr}_m\left[\frac{H}{r}\frac{\partial}{\partial r}\left(\frac{1}{\sigma}\right) - \frac{1}{\sigma}\frac{H}{r^2}\right] + \frac{\mu_r v_m H}{r} \tag{7}$$

Nomenclature (cont.)

Superscripts

α = solute
$\sim$ = dimensional quantity

Subscripts

e = eutectic
E = electrode
l, liq = liquid and liquidus
m = mixture
max = maximum
s, sol = solid or surface and solidus
w = water or coolant
0 = ambient

Downloaded 11 Dec 2010 to 193.140.21.150. Redistribution subject to ASME license or copyright; see http://www.asme.org/terms/Terms_Use.cfm

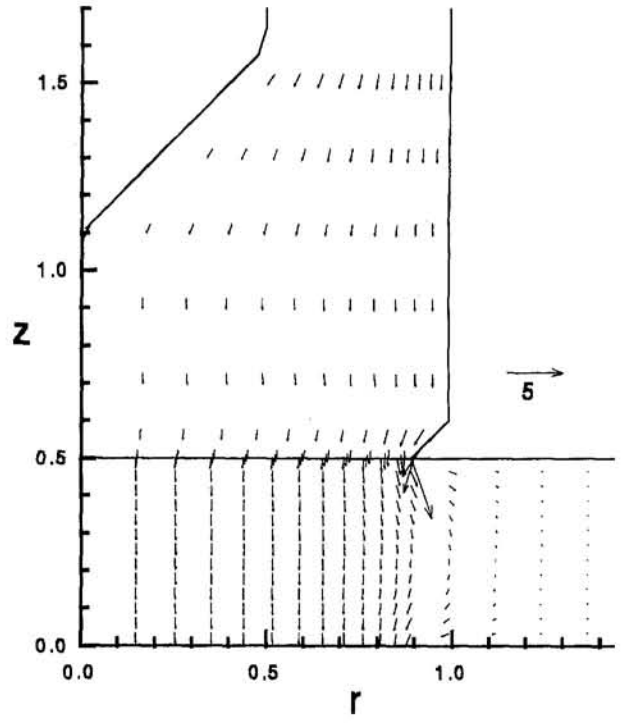


Fig. 4 Dimensionless electric current density field in a truncated cone electrode and workpieces at a dimensionless time of 0.0808; $j_{max} = 5.6$

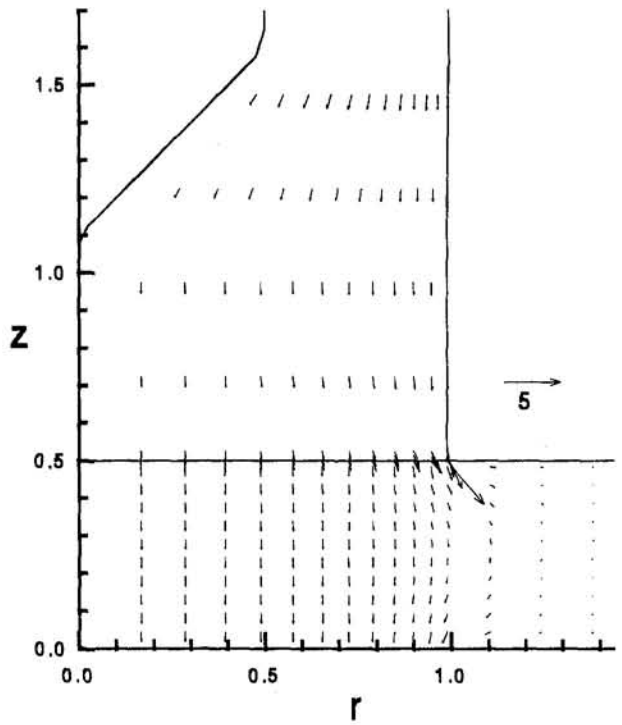


Fig. 6 Dimensionless electric current density field in a flat face electrode and workpieces at a dimensionless time of 0.028; $j_{max} = 5$

where electrical conductivity and relative magnetic permeability are allowed to be distinct between phases and across the Curie temperature.

Supplementary Relationships. In Eq. (5) the fraction of the solute α in the solid or liquid is found by

$$f_s^\alpha = \frac{k_p f_m^\alpha}{1 + f_s(k_p - 1)}, \quad f_l^\alpha = \frac{f_m^\alpha}{1 + f_s(k_p - 1)} \tag{8}$$

where the equilibrium partition coefficient k_p represents the ratio of solute contents in the solid and liquid at the same temperature. Determinations of distinct regions of the mushy zone, full liquid, and solid have been presented in detail by Bennon and Incropera (1987, 1988) and Wei and Yeh (1991).

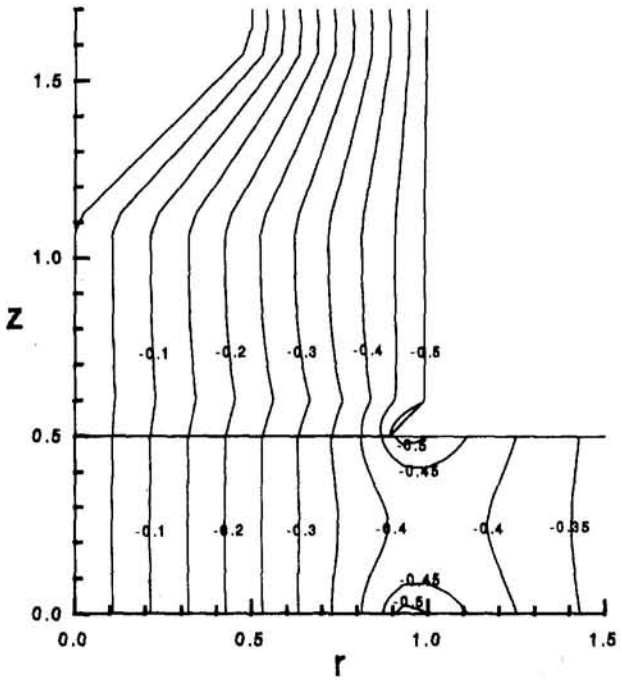


Fig. 5 Dimensionless magnetic field intensity field in a truncated cone electrode and workpieces at a dimensionless time of 0.0808

Boundary Conditions for Workpiece. Thermal boundary conditions of the electrode and workpiece at the electrode–workpiece interface ($z = l$, $0 \le r \le r_e$) are, respectively, required. One is an energy balance

$$K\frac{\partial T}{\partial z} = k_s k_E \frac{\partial T_E}{\partial z} + \frac{r_e^2}{\pi}\frac{LoE_f ER_{0E}}{RC} R_f\left[\left(\frac{1}{r}\frac{\partial rH}{\partial r}\right)^2 + \left(\frac{\partial H}{\partial z}\right)^2\right] \tag{9}$$

where the last term on the right-hand side denotes interfacial heat generation. The other condition is that temperatures can be discontinuous (Kim and Eagar, 1989) and modeled as

$$-K\frac{\partial T}{\partial z} = k_s \, \mathrm{Bi}_E(T - T_E) \tag{10}$$

Provided that the Biot number $\mathrm{Bi}_E \to \infty$ the temperature difference $T - T_E \to 0$. Tangential magnetic field intensity is continuous across the contact surface (e.g., Cramer and Pai, 1973)

$$H = H_E \tag{11}$$

Continuity of tangential electric field by substituting the Ohm's law yields

$$\frac{\sigma_E}{\sigma}\frac{\partial H}{\partial z} = \frac{\partial H_E}{\partial z} \tag{12}$$

At the workpiece surface ($z = l$, $r_e < r < r_b$ and $0 < z < l$, $r = r_b$) electric currents dissipated to the surroundings are zero. Conduction is removed by convection on the surface. Accounting for the molten region possibly occurring near the electrode–workpiece surface, boundary conditions are

Downloaded 11 Dec 2010 to 193.140.21.150. Redistribution subject to ASME license or copyright; see http://www.asme.org/terms/Terms_Use.cfm

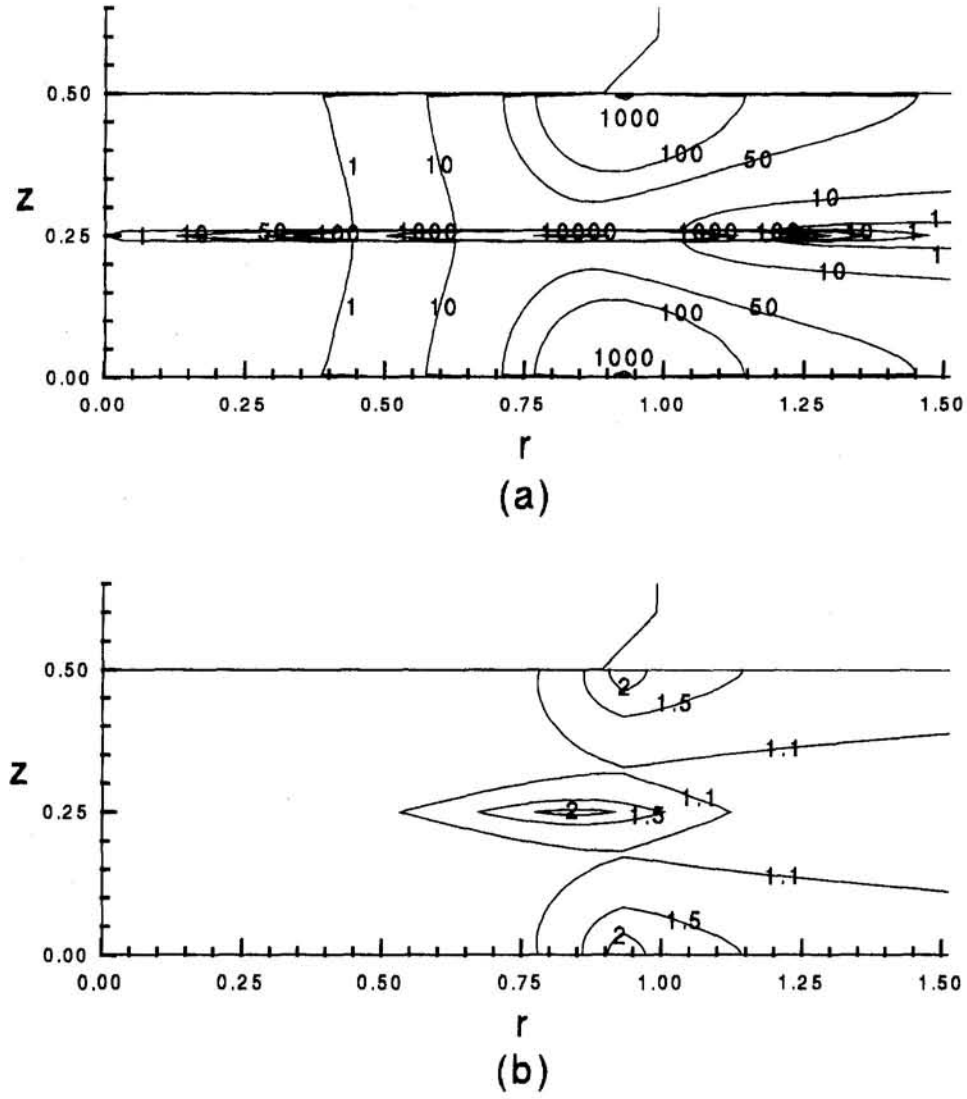


Fig. 7 Dimensionless fields of (*a*) heat generation and (*b*) temperature in workpieces for a truncated cone electrode at a dimensionless time of 0.001

$$u_m = v_m = \frac{\partial f_m^a}{\partial z} = 0 \quad 0 \le r \le r_e \quad \text{at} \quad z = l \tag{13}$$

$$u_m = \frac{\partial v_m}{\partial z} = \frac{\partial f_m^a}{\partial z} = 0 \quad r_e \le r \le r_b \quad \text{at} \quad z = l \tag{14}$$

The second relation in Eq. (14) is due to zero shear on the free surface of the molten region. Zero gradients are imposed at $r = 0$. Since Ampere's law $j_z = (\partial rH/\partial r)/r$, magnetic field intensity must vanish at the axisymmetric axis to avoid infinite electric currents. Initial conditions are $u_m = v_m = H = 0$, $f_m^a = 1$, $h_m = R$, $T_E = 1$.

Governing Equations and Boundary Conditions in Electrode. Since the electrode is irregular in shape, an immobilization transformation can be effectively used for facilitating a numerical computation. Independent variables are chosen to be

$$\xi = \frac{r - r_c(z)}{r_s(z) - r_c(z)}, \quad \zeta = z - l, \quad \tau = t \tag{15}$$

where $r_s = l$ for $z \ge l + l_1$, $r_c = 0$ for $l \le z \le l + l_1 + l_2$. Energy and magnetic field intensity equations for the top electrode become

$$\frac{\partial T_E}{\partial \tau} = \frac{k_E k_s RC}{\rho_E R_E}\left[\frac{\partial^2 T_E}{\partial \zeta^2} + \left(\frac{1}{N^2} + M^2\right)\frac{\partial^2 T_E}{\partial \xi^2} + 2M\frac{\partial^2 T_E}{\partial \xi \partial \zeta} + \left(\frac{1}{\xi N + r_c} - 2M\frac{dN}{d\zeta}\right)\frac{1}{N}\frac{\partial T_E}{\partial \xi}\right] + \frac{Lo\Sigma}{\pi^2 \rho_E R_E \sigma_E}\left[\left(M\frac{\partial H_E}{\partial \xi} + \frac{\partial H_E}{\partial \zeta}\right)^2 + \left(\frac{H_E}{\xi N + r_c} + \frac{1}{N}\frac{\partial H_E}{\partial \xi}\right)^2\right] \tag{16}$$

$$\frac{\partial H_E}{\partial \tau} = \mathrm{Pr}_m \eta_E\left[\frac{\partial^2 H_E}{\partial \zeta^2} + \left(\frac{1}{N^2} + M^2\right)\frac{\partial^2 H_E}{\partial \xi^2} + 2M\frac{\partial^2 H_E}{\partial \xi \partial \zeta} + \left(\frac{1}{\xi N + r_c} - 2M\frac{dN}{d\zeta}\right)\frac{1}{N}\frac{\partial H_E}{\partial \xi} - \frac{H_E}{(\xi N + r_c)^2}\right] \tag{17}$$

By using the Ampere law, a uniform welding current density at the top of the electrode leads to the distribution of magnetic field intensity:

Downloaded 11 Dec 2010 to 193.140.21.150. Redistribution subject to ASME license or copyright; see http://www.asme.org/terms/Terms_Use.cfm

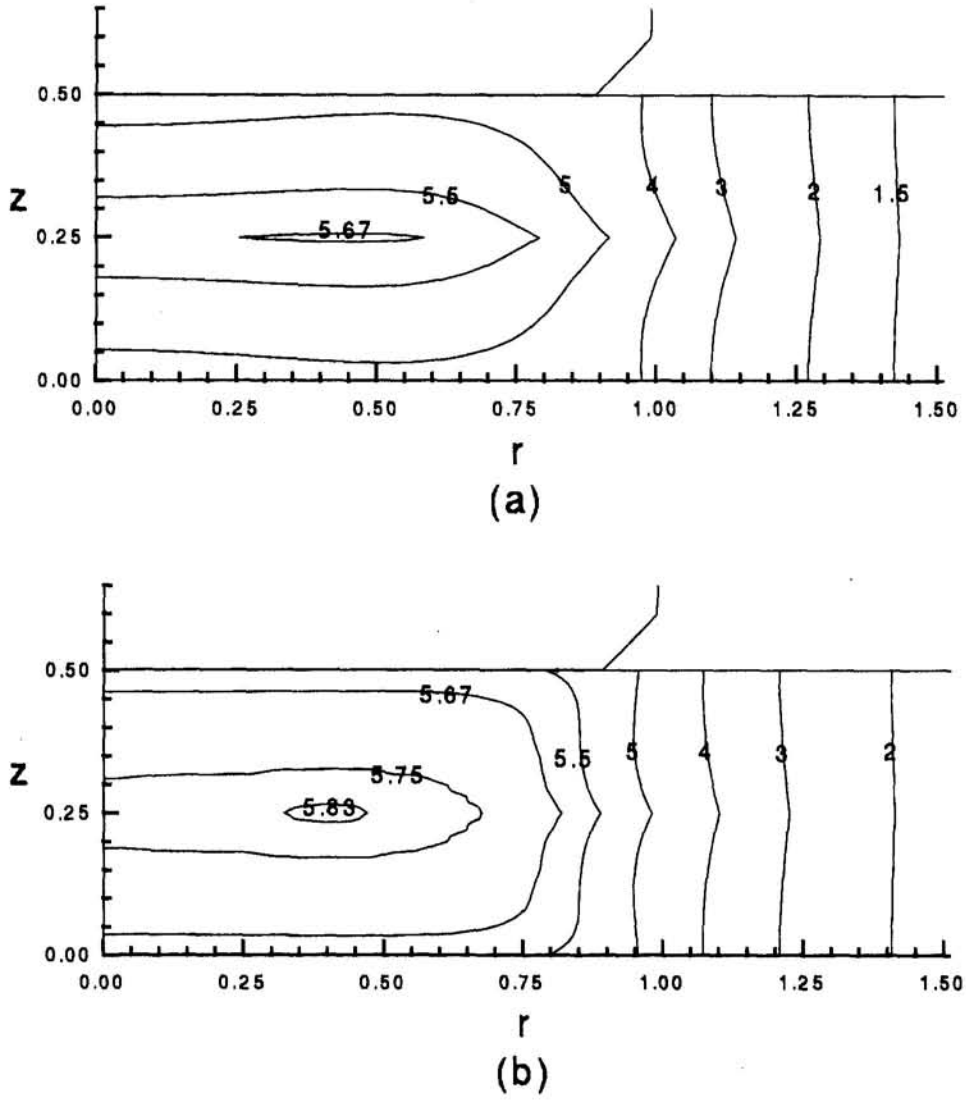


Fig. 8 Dimensionless temperature fields in workpieces for a truncated cone electrode at dimensionless times of (*a*) 0.04, (*b*) 0.071

$$H_E = \frac{-1}{2(1+r_c)} \frac{\xi^2(1-r_c)+2r_c\xi}{\xi(1-r_c)+r_c} \quad 0 \le \xi \le 1 \quad (18)$$

where magnetic field intensity $H_E = 0$ at $\xi = 0$ is satisfied because of negligible currents in the coolant hole. With the same reason, magnetic field intensities at the inner and outer surface of the electrode are zero and $-\frac{1}{2}$, respectively. Other boundary conditions associated with Eqs. (16) and (17) are described as follows:

1 The boundary $\zeta = l_1 + l_2 + l_3 + l_4$ and $0 \le \xi \le 1$. Energy dissipation in the electrode is removed by convection at the surface.

2 Boundaries $l_1 + l_2 + l_3 \le \zeta \le l_1 + l_2 + l_3 + l_4$. Energy across the coolant hole is

$$\frac{1}{N}\frac{\partial T_E}{\partial \xi} = \mathrm{Bi}_w(T_E - T_w) \quad \text{at} \quad \xi = 0 \quad (19)$$

Conduction is removed by convection at the outer surface of the electrode.

3 Boundaries $l_1 + l_2 \le \zeta \le l_1 + l_2 + l_3$. At the surface of the coolant hole energy balance yields

$$\frac{1}{N}\frac{\partial T_E}{\partial \xi}\cos\left(\tan^{-1}\frac{r_c}{l_3}\right) - \left(M\frac{\partial T_E}{\partial \xi} + \frac{\partial T_E}{\partial \zeta}\right)\sin\left(\tan^{-1}\frac{r_c}{l_3}\right)$$

$$= \mathrm{Bi}_w(T_E - T_w) \quad \text{at} \quad \xi = 0 \quad (20)$$

where r_c is evaluated at $\zeta = l_1 + l_2 + l_3$. Boundary conditions at the outer surface of the electrode are the same as those in case (2).

4 Boundaries $l_1 \le \zeta \le l_1 + l_2$. The temperature gradient is zero at the axisymmetric axis. Other conditions are the same as in case (2).

5 Boundaries $0 \le \zeta \le l_1$. Conditions at the axisymmetric axis are the same as in case (4). The energy balance at the outer surface of electrodes is

$$-\frac{1}{N}\frac{\partial T_E}{\partial \xi}\cos\left(\tan^{-1}\frac{1-r_e}{l_1}\right) + \left(M\frac{\partial T_E}{\partial \xi} + \frac{\partial T_E}{\partial \zeta}\right)\sin\left(\tan^{-1}\frac{1-r_e}{l_1}\right)$$

$$= \mathrm{Bi}_{0E}(T_E - 1) \quad \text{at} \quad \xi = 1 \quad (21)$$

Replacing 1 by r_s and $r_c = 0$ in Eq. (18) magnetic field intensity yields $H_E = -1/2r_s$ at $\xi = 1$.

Downloaded 11 Dec 2010 to 193.140.21.150. Redistribution subject to ASME license or copyright; see http://www.asme.org/terms/Terms_Use.cfm

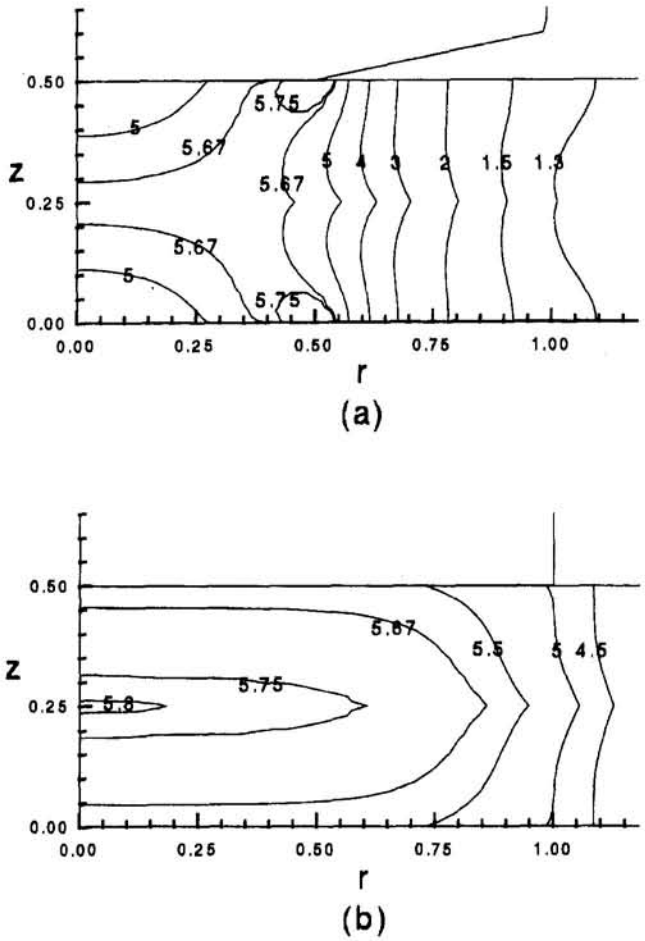


Fig. 9 Dimensionless temperature fields in workpieces for (*a*) a truncated cone electrode by reducing face radius (r_e = 0.5) at a dimensionless time of 0.009, (*b*) a flat face electrode at a dimensionless time of 0.0875

Solution Methodology. Each of conservation Eqs. (1)–(5), (7), (16), and (17) can be cast in the form

$$\frac{\partial \rho \phi}{\partial t} + \nabla.(\rho \mathbf{V}_m \phi) = \nabla.(\Gamma_\phi \nabla \phi) + S_\phi \qquad (22)$$

A control-volume, staggered grid, implicit finite-difference scheme (Patankar, 1980) was used. This work selects a 80 × 53 grid system in workpieces and 27 × 72 in the electrode. The axial direction is divided into uniform spaces while the spacing ratio in the radial direction is 0.95. A dimensionless uniform time step was 2.0×10^{-5}. The solution procedure is that temperature and magnetic field intensity in the electrode are determined from Eqs. (16) and (17) subject to boundary conditions (10) and (11), while the continuity, momentum, energy, species, and magnetic field intensity transport equations are solved by satisfying other boundary conditions. The convergence tolerances for global energy and velocity components and enthalpy, concentration, and magnetic intensity fields are 10^{-2} and 10^{-3}, respectively. Otherwise, equations in the electrode are solved again and the process is repeated. Computations then proceed to the next time. The number of iterations at each time is around 100. The global energy balance is that heat generation in workpieces and electrodes should equal to the total internal energy rise and heat convected to the electrodes, coolant hole, and surroundings.

Results and Discussion

The present work is confirmed by comparing experimental data provided by Gould (1987). The parameters chosen were $l = 0.715$, $r_e = 0.96$, $E = 4.0 \times 10^{-7}$, $\sigma = 1.198$ from estimations of an alloy AISI 1008, permeability $K_0 = 10^{-12}$ m^2 (Poirier, 1987) and $\bar{f}^{\alpha}_{m,0} = 0.32$ wt% of manganese in a Fe–Mn alloy (Gould, 1987). The predicted nugget thickness versus welding current agrees with available experimental data, as shown in Fig. 2. The deviations, unfortunately, are still unknown. One possible reason is that the evaluation of the electric contact resistance is not very accurate.

In this study, values of dimensionless parameters estimated from pure iron and manganese and its alloy are listed in Table 1. Distributions of dimensionless electric current density in workpieces and a truncated cone top electrode with an angle of 45 deg at a dimensionless time of 10^{-4} ($\approx 10^{-4}$ s for welding iron) are presented in Fig. 3. The faying surface is located at the coordinate $z = 0.25$. It can be seen that electric currents flow convergently toward the corner of the electrode and workpiece surface. On entering the workpiece electric currents spread strongly. Most of currents flow along the workpiece surface. The maximum dimensionless current is 19, which corresponds to 2.4×10^9 amp/m^2 for a welding current and electrode radius of 10^4 amp and 5×10^{-3} m, respectively.

At a longer time of 0.0808 the divergence and density of electric current are both reduced, as shown in Fig. 4. The currents flow downward with positive and negative radial components in the outer and inner regions of the top workpiece, respectively. The associated dimensionless magnetic field intensity is shown in Fig. 5. It is seen that the lines of isomagnetic field intensity are nearly parallel to the inner and outer surfaces of the electrode and the axisymmetric axis in workpieces. Magnetic field intensity is concentrated near the corner between the electrode and workpiece surface.

Fields of electric current density in workpieces and a flat face electrode are similar to those for the truncated cone electrode as shown in Fig. 6. However, no negative radial component of electric currents is seen in the top workpiece.

Dimensionless heat generation, which includes joule and interfacial heats prior to the formation of the molten nugget at a time of 0.001, is shown in Fig. 7(a). Heat generation exhibits a sudden jump at the faying surface. That is, the ratio of heat generations due to electric contact resistance and joule heat can be several hundreds (Wei and Ho, 1990). Two relative maxima of heat generation take place near the corner of the electrode and workpiece surface where electric current density is high and at approximately the same radius as the electrode face on the faying surface where electrical contact resistance exists. The corresponding temperature field is shown in Fig. 7(b). Evidently, relative maximum temperatures occur at locations where heat generation is high, as confirmed by the microstructure shown by Han et al. (1993). Heat flow exhibits a rather complicated pattern.

As time becomes large the molten nugget forms, as shown in Fig. 8(a). The dimensionless temperature of 5.67 delineate the solidus line. The faying surface begins to be melted at a dimensionless radius of 0.45. This is attributed to the relative maximum heat generation on the faying surface as presented in previous figure. High joule heat near the corner of the electrode and workpiece is unable to melt workpieces. In view of thermal diffusion and convection, as can be seen later, the maximum temperature moves inward by increasing time. Finally, the nugget becomes a rectangle, as shown in Fig. 8(b). The dimensionless temperature of 5.75 represents the liquidus line. It is seen that the maximum temperature is not at the axisymmetric axis.

Temperature fields affected by reducing the face radius of the electrode are shown in Fig. 9(a). In view of high current densities joule heat melts the workpiece near the corner of the electrode and workpiece. Combined with the subsequent formation of a molten region near the faying surface, the molten nugget becomes a triangle. The thickness of the molten nugget

Downloaded 11 Dec 2010 to 193.140.21.150. Redistribution subject to ASME license or copyright; see http://www.asme.org/terms/Terms_Use.cfm

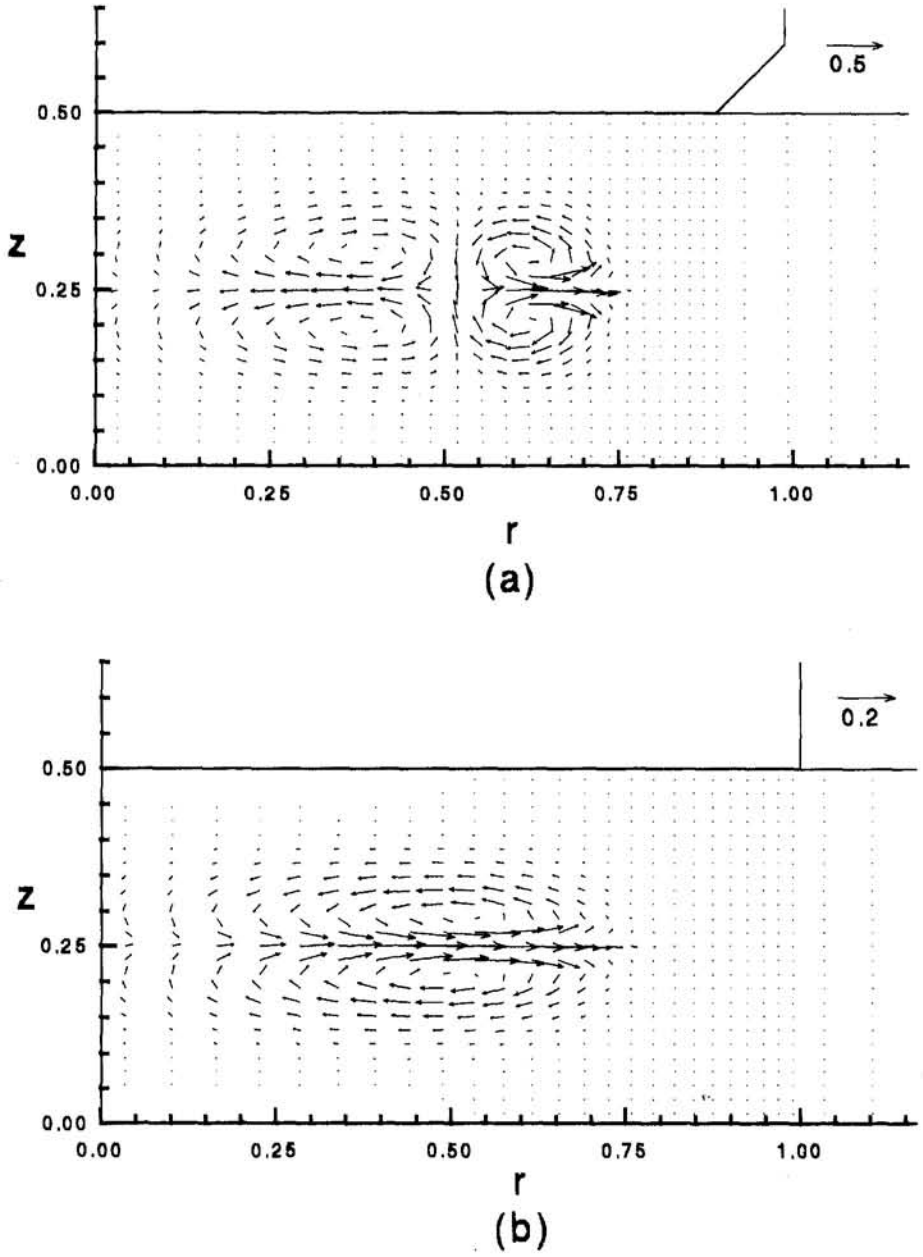


Fig. 10 Dimensionless velocity fields in molten nugget for (*a*) a truncated cone at a dimensionless time of 0.0699; $|V_{max}| = 0.5$, and (*b*) a flat face electrodes at a dimensionless time of 0.0875; $|V_{max}| = 0.23$

increases with radial distance from the axisymmetric axis. In this case, workpieces are broken into two pieces. On the other hand, for the flat face electrode, the mushy zone gradually decreases in thickness by increasing radial distance, as shown in Fig. 9(*b*). The maximum heat generation now occurs at the axisymmetric axis instead of at a location just near the face radius, thereby causing the molten nugget initiation at the axisymmetric axis where the maximum temperature exists.

The difference in flow patterns for truncated cone and flat face electrodes is revealed by comparing Figs. 10(*a*) and 10(*b*). In the first quadrant, two cells in the former and one cell for the latter are seen. The reason for this is that outward radial flows (see Fig. 4) of electric currents decrease magnitudes of downward vertical components. The pinch effect or inward Lorentz force thus decreases. The right cell therefore circulates in the counterclockwise direction. On the other hand, the clockwise direction of the left cell for the truncated cone electrode results from an increase of the inward Lorentz force in the downward direction. Increasing Lorentz force is attributed to an increase in magnitudes of downward vertical components of currents from inward currents. The maximum velocity of the cell can be 0.5, which is around 6×10^{-4} m/s for welding iron. The maximum velocity for the flat face electrode is 2.8×10^{-4} m/s. The cell in the counterclockwise direction is displaced more inward for the flat face electrode than for the truncated cone electrode.

As shown in Fig. 11(*a*), an increase of the dimensionless parameter governing welding current produces a molten region in a triangular shape. This defect is similar to the case where the face radius of the electrode is reduced as discussed previously. In Fig. 11(*b*), aside from the right cell is moved farther from the axisymmetric axis, the maximum velocity of 107.5 corresponding to 0.13 m/s is 200 times that for a low welding current (see Fig. 10(*a*)). Convection in the right cell is much stronger than that in the left cell. This is because of high electric current density near the corner of the electrode and workpiece.

Downloaded 11 Dec 2010 to 193.140.21.150. Redistribution subject to ASME license or copyright; see http://www.asme.org/terms/Terms_Use.cfm

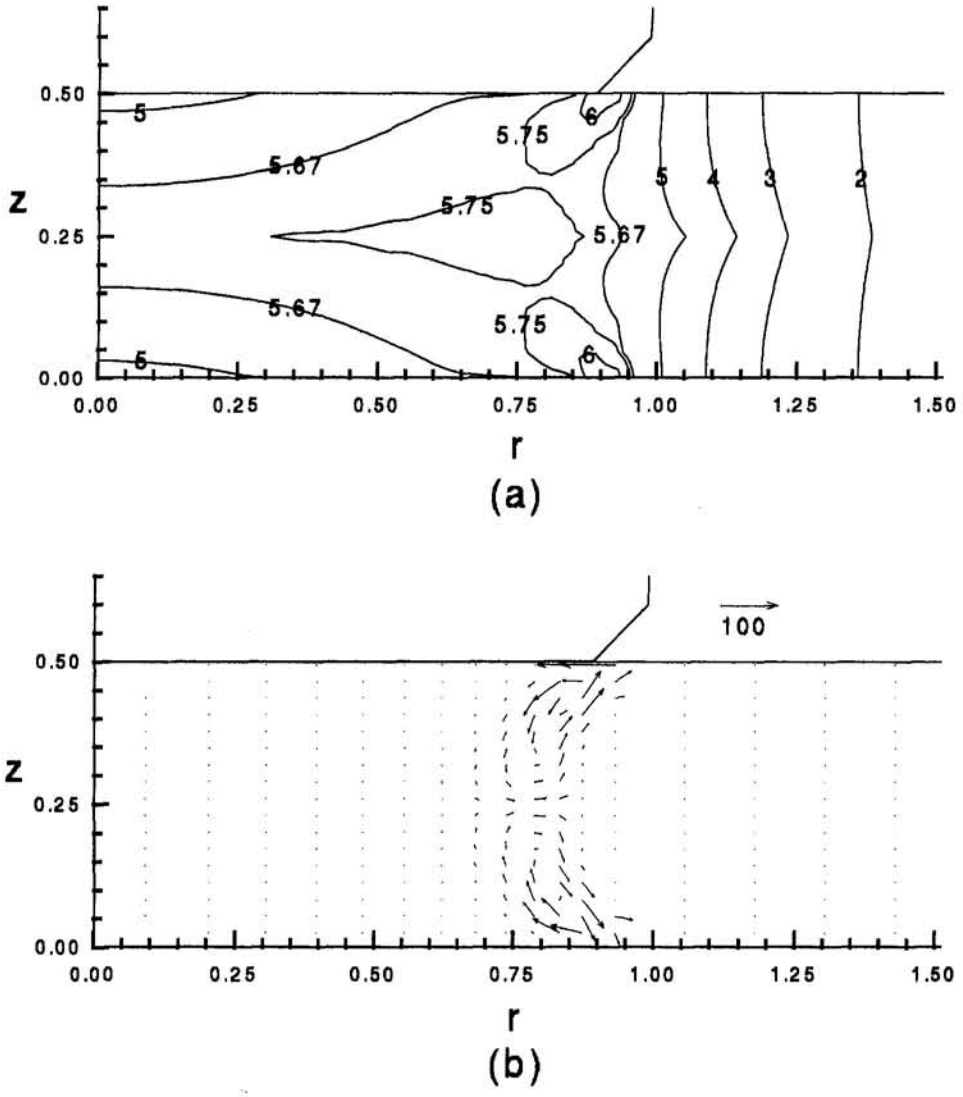


Fig. 11 Dimensionless fields of (*a*) temperature and (*b*) velocity in workpieces for a truncated cone electrode by increasing parameter governing welding current ($Lo = 8 \times 10^7$) at a dimensionless time of 0.018; $|V_{max}| = 107.5$

A decrease in the magnetic Prandtl number causes an increase in the thickness of the molten nugget with radial distance, as shown in Fig. 12(a). Strong vorticity is also produced in the right cell, as presented in Fig. 12(b). Decreasing the magnetic Prandtl number indicates that the gradient of magnetic field is high. As a result, the induced Lorentz force becomes strong. The velocity field therefore increases significantly near the corner of the electrode and workpiece surface. The right cell is displaced outward.

A decrease in the dimensionless electrical contact resistance reduces the width of the molten nugget, as shown in Fig. 13. The left cell is stronger than the right cell, which is within the mushy zone. The effect of the solid-to-liquid electrical conductivity ratio on the flow pattern is shown in Fig. 14. In view of high electrical resistance in the molten nugget divergence of electric currents is enhanced. The right cell therefore is stronger than the left cell. As shown in Fig. 15, vorticity in the left cell is stronger than that in the right cell as the thickness of the workpiece decreases. This is attributed to a low resistance, which reduces outward radial components of currents.

Conclusions

1 Unsteady transport phenomena during resistance spot welding for different values of the parameter governing welding current (Lo), dimensionless electric contact resistance (E), face radius (r_e) and cone angle ($\tan^{-1}[l_1/(1-r_e)]$) of the electrode, workpiece thickness (l), magnetic Prandtl number (Pr_m), and solid-to-liquid electrical conductivity ratio ($\tilde{\sigma}_s/\tilde{\sigma}_l$) are presented in details for the first time. The predicted nugget thickness versus welding current show good agreement with available experimental data.

2 Electric currents in the electrode convergently flow toward the corner of the electrode and workpiece surface irrespective of a truncated cone or flat face electrode. On entering the workpiece, electric currents spread strongly. Most of currents flow along the surface. The convergence and divergence of currents are both reduced as time increases. Negative radial currents occur for the truncated cone electrode while only positive radial currents are found for the flat face electrode.

3 Current densities near the corner of the electrode and workpiece are significantly enhanced by decreasing the face radius and cone angle of the electrode, magnetic Prandtl number, and increasing the dimensionless parameter governing welding current. Provided that current densities are sufficiently high, the molten nugget is initiated at this corner, followed by a molten region near the faying surface at approximately the same radius as the electrode face. Two molten regions develop and combine. The final shape of the molten nugget thus is

Downloaded 11 Dec 2010 to 193.140.21.150. Redistribution subject to ASME license or copyright; see http://www.asme.org/terms/Terms_Use.cfm

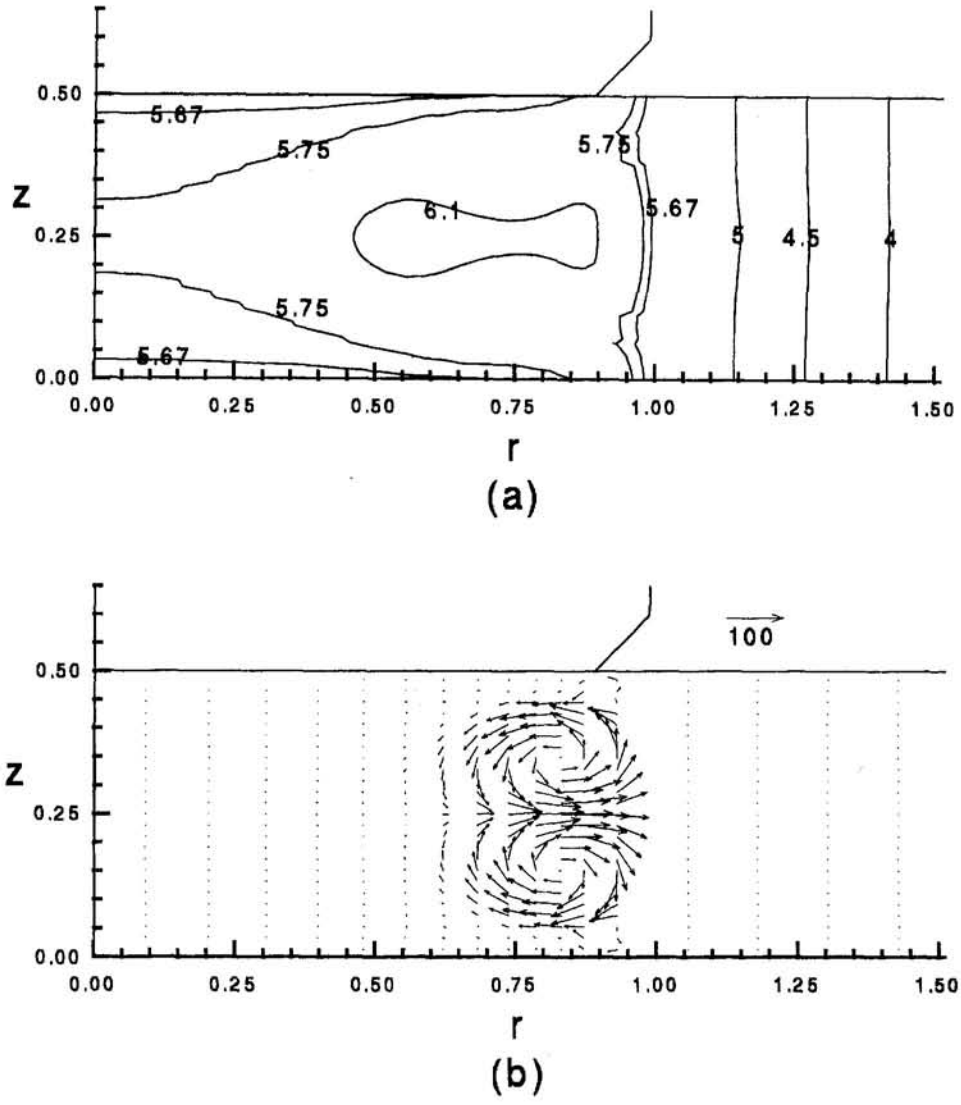


Fig. 12 Dimensionless fields of (*a*) temperature and (*b*) velocity in workpieces for a truncated cone electrode by reducing magnetic Prandtl number (Pr_m = 5000) at a dimensionless time of 0.0971; $|V_{max}|$ = 91.8

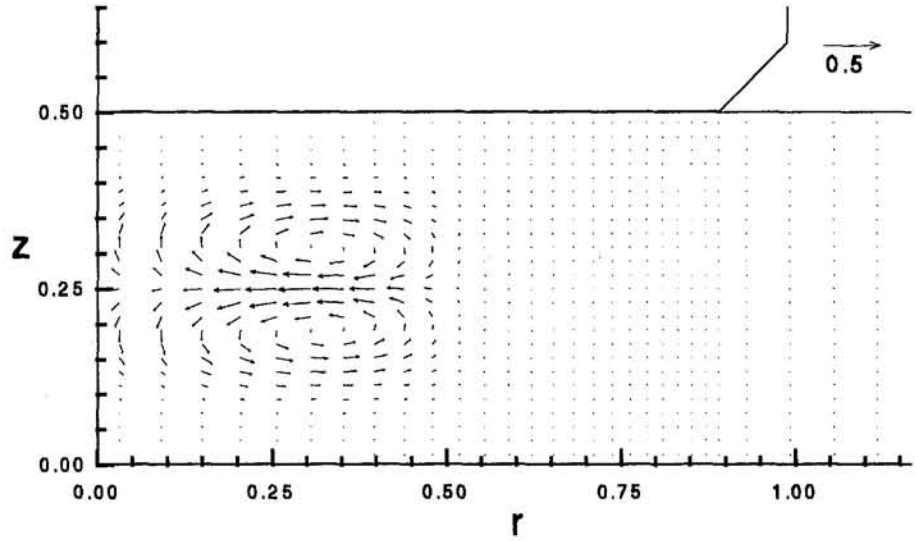


Fig. 13 Dimensionless velocity field in workpieces for a truncated cone electrode by reducing the dimensionless electrical contact resistance ($E = 4.96 \times 10^{-4}$) at dimensionless time of 0.103; $|V_{max}|$ = 0.3

Downloaded 11 Dec 2010 to 193.140.21.150. Redistribution subject to ASME license or copyright; see http://www.asme.org/terms/Terms_Use.cfm

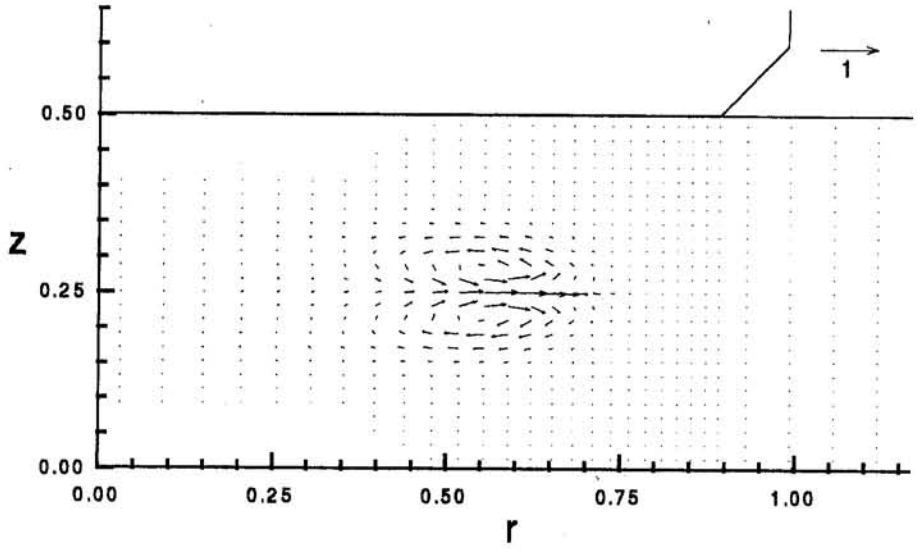


Fig. 14 Dimensionless velocity field in workpieces for a truncated cone electrode by increasing solid-to-liquid electrical conductivity ratio (σ_s = 2.0) at a dimensionless time of 0.1218; $|V_{max}|$ = 0.7

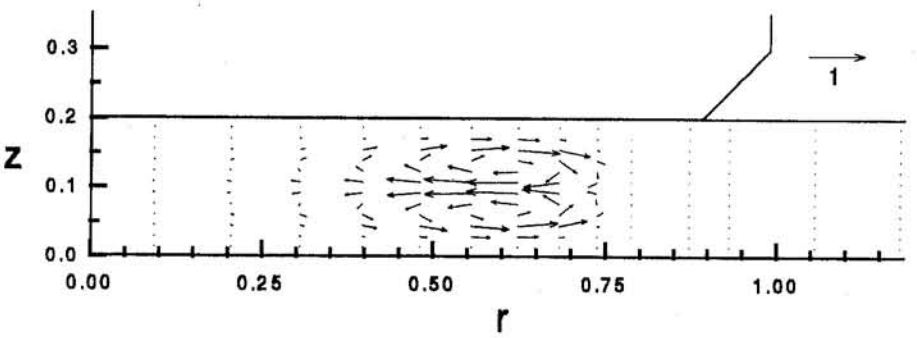


Fig. 15 Dimensionless velocity field in workpieces for a truncated cone electrode by decreasing total workpiece thickness (l = 0.2) at a dimensionless time of 0.0822; $|V_{max}|$ = 1

increased in thickness with radial distance until the workpiece surface is reached.

4 The molten nugget induced by the truncated cone electrode starts to grow on the faying surface at approximately the same radius as the electrode face, provided that current densities near the corner of the electrode and workpiece are not high enough. The molten nugget therefore is triangular. As time is large the nugget becomes a rectangle. A further decrease in current density especially for the flat face electrode the molten nugget is initiated on the faying surface near the axisymmetric axis. The molten nugget then decreases in thickness with radial distance.

5 The maximum temperature is located on the axisymmetric axis at the faying surface for the flat face electrode while it is near one-half of the electrode radius for the truncated cone electrode.

6 Two cells in the first quadrant of workpieces occur for the truncated cone electrode. The right and left cells are in the counterclockwise and clockwise directions, respectively. This is attributed to nonparallel electric currents. The only cell induced by the flat face electrode is in the counterclockwise direction.

7 The maximum velocity in the molten nugget can be as high as 0.3 m/s. The right cell is displaced outward, vorticity is enhanced significantly by reducing the face radius and cone angle of the electrode, and the magnetic Prandtl number, and increasing the parameter governing welding current. Velocities in the left cell can be stronger than those in the right cell by decreasing dimensionless electric contact resistance and thickness of workpieces.

Acknowledgments

The authors acknowledge the financial support from the National Science Council, Taiwan, China, under contract No. NSC84-2212-E-110-003.

References

Bennon, W. D., and Incropera, F. P., 1987, "A Continuum Model for Momentum, Heat and Species Transport in Binary Solid–Liquid Phase Change Systems—I. Model Formulation," *International Journal of Heat and Mass Transfer*, Vol. 30, pp. 2161–2170.

Bennon, W. D., and Incropera, F. P., 1988, "Numerical Analysis of Binary Solid–Liquid Phase Change Using a Continuum Model," *Numerical Heat Transfer*, Vol. 13, pp. 277–296.

Bowers, R. J., Sorensen, C. D., and Eagar, T. W., 1990, "Electrode Geometry in Resistance Spot Welding," *Welding Journal*, Vol. 69, pp. 45-s–51-s.

Cho, H. S., and Cho, Y. J., 1989, "A Study of the Thermal Behavior in Resistance Spot Welds," *Welding Journal*, Vol. 68, pp. 236-s–244-s.

Cramer, K. R., and Pai, S.-I., 1973, *Magnetofluid Dynamics for Engineers and Applied Physicists*, Scripta Publishing, Washington, DC, pp. 42–45.

Cunningham, A., and Begeman, M. L., 1965, "A Fundamental Study of Projection Welding Using High Speed Photography," *Welding Journal*, Vol. 44, pp. 381-s–384-s.

Dickinson, D. W., Franklin, J. E., and Stanya, A., 1980, "Characterization of Spot Welding Behavior by Dynamic Electrical Parameter Monitoring," *Welding Journal*, Vol. 59, pp. 170-s–176-s.

Dickinson, D. W., 1981, *Welding in the Automotive Industry*, Report SG 81-5, Aug. 1981, Committee of Sheet Steel Producers, American Iron and Steel Institute.

Downloaded 11 Dec 2010 to 193.140.21.150. Redistribution subject to ASME license or copyright; see http://www.asme.org/terms/Terms_Use.cfm

Gould, J. F., 1987, "An Examination of Nugget Development During Spot Welding, Using Both Experimental and Analytical Techniques," *Welding Journal,* Vol. 66, pp. 1-s–10-s.

Greenwood, J. A., 1961, "Temperatures in Spot Welding," *British Welding J.,* Vol. 8, pp. 316–322.

Greenwood, J. A., and Williamson, J. B. P., 1958, "Electrical Conduction in Solids. II. Theory of Temperature-Dependent Conductors," *Proc. Royal Soc. of London,* Vol. 246, pp. 13–31.

Han, Z., Indacochea, J. E., Chen, C. H., and Bhat, S., 1993, "Weld Nugget Development and Integrity in Resistance Spot Welding of High-Strength Cold-Rolled Sheet Steels," *Welding Journal,* Vol. 72, pp. 209-s–216-s.

Holm, R., 1958, *Electric Contacts Handbook,* Springer-Verlag, Berlin, Part I.

Kim, E. W., and Eagar, T. W., 1989, "Measurement of Transient Temperature Response during Resistance Spot Welding," *Welding J.,* Vol. 68, pp. 303-s–312-s.

Patankar, S. V., 1980, *Numerical Heat Transfer and Fluid Flow,* Hemisphere Publishing Corp., New York, Chaps. 5 and 6.

Poirier, D. R., 1987, "Permeability for Flow of Interdendritic Liquid in Columnar-Dendritic Alloys," *Metallurgical Transactions,* Vol. 18B, pp. 245–255.

Wei, P. S., and Ho, C. Y., 1990, "Axisymmetric Nugget Growth During Resistance Spot Welding," ASME JOURNAL OF HEAT TRANSFER, Vol. 112, pp. 309–316.

Wei, P. S., and Yeh, F. B., 1991, "Factors Affecting Nugget Growth With Mushy-Zone Phase Change During Resistance Spot Welding," ASME JOURNAL OF HEAT TRANSFER, Vol. 113, pp. 643–649.

Downloaded 11 Dec 2010 to 193.140.21.150. Redistribution subject to ASME license or copyright; see http://www.asme.org/terms/Terms_Use.cfm

Transient Model for CW and Pulsed Laser Machining of Ablating/Decomposing Materials—Approximate Analysis

M. F. Modest
Professor of Mechanical Engineering,
The Pennsylvania State University,
University Park, PA 16802
email: mfm@michelle.me.psu.edu
Fellow ASME

Approximate, quasi-one-dimensional conduction models have been developed to predict the changing shape of holes, single grooves, or overlapping grooves carved by ablation into a thick solid that is irradiated by a moving laser source. For CW or pulsed laser operation a simple integral method is presented, which predicts shapes and removal rates with an accuracy of a few percent, while requiring one order of magnitude less CPU time than a three-dimensional, numerical solution. For pulsed operation a "full-pulse" model is presented, computing the erosion from an entire pulse in a single step, and reducing computer time by another order of magnitude.

Introduction

Since their invention in 1960, lasers have found diverse applications in engineering and industry because of their ability to produce high-power beams. Laser applications include welding, drilling, cutting, scribing, machining, heat treatment, medical surgery, and others. One of the principal advantages of laser cutting is its ability to cut very hard materials easily. Ceramics are among the most difficult materials to machine by conventional machining techniques, since they are very hard and brittle. The cost of machining ceramics into complex shapes is often prohibitive if conventional machining is used. Lasers may provide a cheaper alternative to conventional machining and have found widespread use in industry.

Modeling of laser drilling, cutting, and scribing has been addressed by a number of investigators. Simple one-dimensional drilling models have been given by Dabby and Paek (1972) and Wagner (1974). Other approximate laser drilling models have been developed by von Allmen (1976), Petring et al. (1988), and others. Multiple reflections during laser drilling have been addressed by Anthony (1980), Bailey and Modak (1989), Vorreiter et al. (1991), and Ramanathan and Modest (1992b).

Simple cutting models have been developed by Bunting and Cornfield (1975), and by the group working with Schuöcker, e.g., Schuöcker and Müller (1987), and Ramanathan and Modest (1992a).

Laser scribing of ablating and/or decomposing materials has been investigated primarily by Modest and co-workers. They developed a number of simple models for quasi-steady CW laser scribing, e.g., Modest and Abakians (1986) and Ramanathan and Modest (1990), as well as sophisticated three-dimensional models for CW as well as pulsed lasers, e.g., Roy and Modest (1993), Bang et al. (1993), Modest (1995), and Modest et al. (1995).

Finally, simple modeling of three-dimensional machining with a dual beam has been presented by Chryssoloris (1991).

While sophisticated three-dimensional models describing the grooving process, such as Modest (1995), are able to predict groove shapes accurately, this accuracy is only as good as the knowledge of relevant material properties (which is generally poor). In addition, these models tend to demand vast amounts of computer time, due to their nonlinearity as well as their three dimensionality. Therefore, it would be highly desirable to have a simple, approximate model that can predict transient and pulsed shaping processes, similar to the approximate model of Modest and Abakians (1986) for quasi-steady CW laser grooving. In the following, two such approximate models are developed. Comparison with "exact" three-dimensional calculations will show that these models can reduce computer times by orders of magnitude, accompanied by only a minor loss in accuracy.

Theoretical Background

A sketch for the problem under consideration is given in Fig. 1. Simplifying assumptions for the present model are similar to the assumptions for the fully three-dimensional model of Modest (1995); for convenience and to clarify the applicability and limitations of the model, they are repeated here:

1. The solid moves with constant velocity u.
2. The solid is isotropic.
3. Property variations of the solid with temperature are negligible. Numerical experiments with two- and three-dimensional models have shown that, even for ceramics with thermal diffusivity variations close to a full order of magnitude, this assumption is adequate provided properties are evaluated at the ablation temperature (Ramanathan and Modest, 1990; Roy and Modest, 1993).
4. The material is opaque, i.e., the laser beam does not penetrate appreciably into the medium. This assumption is somewhat limiting since some ceramics and other nonmetals are relatively transparent at shorter wavelengths (i.e., at YAG and excimer laser wavelengths). Even the opaquest material becomes semitransparent during ultrashort pulses compared to thermal penetration by conduction, which may only be a fraction of a μm. Fortunately, for such cases conductive losses are negligible.
5. Change of phase from solid to vapor (or decomposition products) occurs in a single step with a rate governed by a simple Arrhenius relation. This assumption is relatively

Contributed by the Heat Transfer Division for publication in the JOURNAL OF HEAT TRANSFER. Manuscript received by the Heat Transfer Division September 1, 1995; revision received May 7, 1996. Keywords: Laser Processing, Materials Processing and Manufacturing Process, Modeling and Scaling. Associate Technical Editor: J. R. Howell.

Copyright © 1996 by ASME
Downloaded 11 Dec 2010 to 193.140.21.150. Redistribution subject to ASME license or copyright; see http://www.asme.org/terms/Terms_Use.cfm

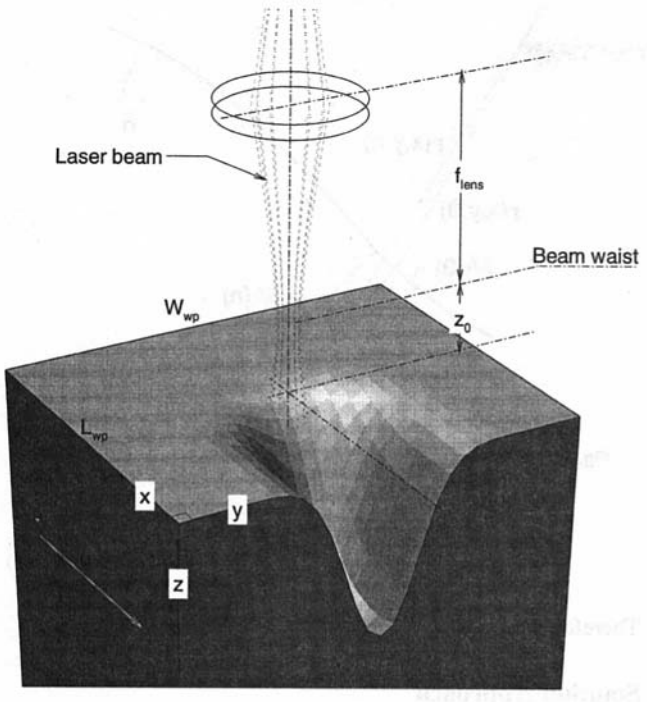


Fig. 1 Laser machining setup and coordinate system

good for a number of ceramics and other nonmetals, in particular since the exact removal process is not well understood for many materials to date. For example, graphite is expected to ablate, silicon carbide to decompose into various gases, and silicon nitride to decompose into nitrogen and liquid silicon (forming a very thin liquid layer, with droplets being expelled; Ramanathan and Modest, 1995). Alumina is known to melt, but the liquid layer may be thin enough due to alumina's low thermal diffusivity. On the other hand the present model is unsuitable for metals, which are expected to form thick liquid layers, possibly with strong convection.

6 The evaporated material does not interfere with the incoming laser beam and ionization of the gas does not occur. Most laser machining devices are outfitted with strong gas assists, which have the purpose of (*i*) protecting the lens, (*ii*) blowing debris out of the way, and (*iii*) suppressing or aiding chemical reactions on the material's surface. Thus, for nonmetals, this assumption is generally good. For metals plasma formation is commonly observed and beam interaction with free electrons is likely in spite of strong gas assist.

7 Heat losses by convection and radiation are negligible as compared to the intensity of the incident beam. Such losses could easily be included in the analysis. However, Modest and Abakians (1986) have shown these effects to be negligible for virtually all situations, including a sonic assist jet blowing across the surface.

8 Multiple reflections of laser radiation within the groove are neglected. This limits the present analysis to strongly absorbing media and/or shallow grooves. Multiple reflections effects have been studied by Bang and Modest (1991, 1992) and Bang et al. (1993). Their reflection models could be combined with the present analysis.

As a consequence of these assumptions it is clear that the present analysis is aimed at nonmelting ceramics and other nonmetals. For the present theory we will also assume, in addition to the above, that conduction losses are relatively minor, i.e., if conduction losses are less than, say, 25 percent of total absorbed laser energy and if these losses can be predicted with, say, 20 percent accuracy, the overall error would be below $0.25 \times 0.20 = 5$ percent.

Following Modest (1995) the transient heat conduction equation for a thick solid irradiated by a scanning Gaussian laser beam, and its auxiliary conditions, may be written in nondimensional form as

$$\frac{\partial \theta}{\partial t} = \nabla^2 \theta, \tag{1}$$

Initial condition:

$$t = 0: \quad \theta(x, y, z, 0) = 0$$
$$s(x, y, 0) = s_0(x, y), \tag{2}$$

Boundary conditions:

$$x \to \pm\infty, \quad y \to \pm\infty, \quad z \to +\infty: \quad \theta = 0;$$
$$z = s(x, y, t): \quad \alpha \mathbf{Q} \cdot \hat{\mathbf{n}} = -N_k[\hat{\mathbf{n}} \cdot \nabla\theta - V_n \mathrm{Ste}]; \tag{3}$$

Nomenclature

a = curvature parameter, Eq. (15)
c = specific heat
C_1, C_2, C_3 = constants in Arrhenius relation
dA = infinitesimal cross-sectional area
$\mathbf{F}$ = irradiation flux vector
F_0 = radiation flux density at center of beam at focal plane
Δh_{re} = "heat of removal"
$\hat{\mathbf{i}}, \hat{\mathbf{j}}, \hat{\mathbf{k}}$ = unit vector in x, y, and z directions
k = thermal conductivity
$\hat{\mathbf{n}}$ = unit surface normal
N_k = conduction-to-laser power parameter
$\mathbf{Q}$ = dimensionless irradiation flux vector at surface = $\mathbf{F}/F_0$
$\bar{s}(\bar{x}, \bar{y})$ = local groove depth
$s(x, y)$ = dimensionless groove depth
$\hat{\mathbf{s}}$ = unit direction vector
Ste = Stefan number (ablation energy-to-sensible heat parameter)
$\bar{t}$ = time
t = dimensionless time
T = temperature
u = laser scanning speed
U = laser speed-to-diffusion speed parameter
v_n = ablation velocity (of solid surface)
V_n = dimensionless ablation velocity
w, w_0 = $1/e^2$ radius of laser beam (at focal plane)
W = dimensionless radius of laser beam = w/w_0
$\bar{x}, \bar{y}, \bar{z}$ = Cartesian coordinates
x, y, z = dimensionless Cartesian coordinates
α_H = thermal diffusivity
α = local effective absorptivity at laser wavelength
β_∞ = far-field beam divergence
δ = temperature penetration depth
θ, θ_0 = dimensionless temperature (at the surface)
λ = wavelength of laser radiation
ρ = density of the medium

Subscripts

re = evaluated at evaporation (or decomposition) temperature
∞ = evaluated at ambient conditions, or located far away

Downloaded 11 Dec 2010 to 193.140.21.150. Redistribution subject to ASME license or copyright; see http://www.asme.org/terms/Terms_Use.cfm

Ablation condition:

$$z = s(x, y, t): \quad V_n = C_1 e^{C_2[1 - T_{re}/T(\theta)]}, \tag{4}$$

with

$$x = \bar{x}/w_0; \quad y = \bar{y}/w_0; \quad z = \bar{z}/w_0; \quad s = \bar{s}/w_0;$$

$$\tau = \frac{\alpha_H \bar{t}}{w_0^2}; \quad \theta = \frac{T - T_\infty}{T_{re} - T_\infty};$$

$$U = \frac{uw_0}{\alpha_H}; \quad V_n = \frac{v_n w_0}{\alpha_H};$$

$$N_k = \frac{k(T_{re} - T_\infty)}{F_0 w_0}; \quad \text{Ste} = \frac{\Delta h_{re}}{c(T_{re} - T_\infty)}. \tag{5}$$

Here $\bar{x}$, $\bar{y}$, $\bar{z}$, and $\bar{s}$ are dimensional coordinates and groove depth, which are then nondimensionalized with the beam radius at the focal point, w_0; $\alpha_H = k/\rho c$ is the thermal diffusivity of the material, T_{re} is the equilibrium ablation (or "removal" temperature), and Δh_{re} is the energy required to remove material ("heat of removal"). The parameters U and V_n are nondimensional laser scanning and (transient) surface recession velocities (by ablation), N_k approximates the ratio of conduction losses, for a surface normal to irradiation, and the absorbed laser flux; and Ste is the Stefan number that compares ablation energy with sensible heat.

The boundary condition at the top surface, $z = s(x, y, t)$, specifies that absorbed laser irradiation is used up by conduction losses and by the latent heat required to ablate material. The ablation velocity (normal to the surface) is governed by a simple reaction equation of the Arhennius type (Modest, 1995).

The energy intensity distribution, $\mathbf{F}$, for a focused Gaussian laser beam having a waist w_0 at the focal plane z_0 and a total average power of $P = (\pi/2)F_0 w_0^2$ is given by Kogelnik and Li (1956), and for a laser moving with constant velocity u into the positive $\bar{x}$ direction is:

$$\mathbf{Q} = \frac{\mathbf{F}}{F_0} = \frac{\phi(t)}{W^2} \exp\left[-2\frac{(x - Ut)^2 + y^2}{W^2}\right] \frac{\hat{\mathbf{s}}}{\hat{\mathbf{s}} \cdot \hat{\mathbf{k}}}, \tag{6}$$

where

$$W^2(z) = \frac{w^2(z)}{w_0^2} = 1 + \beta_\infty^2 (z - z_0), \tag{7}$$

defines the beam radius, w, away from focus, and

$$\beta_\infty = \frac{\lambda}{\pi w_0} \tag{8}$$

is the far-field beam divergence angle for the diffraction-limited case of a Gaussian beam. If the laser beam is visualized as consisting of a bundle of rays into the direction $\hat{\mathbf{s}}(x, y, z)$, perpendicular to the wave-front of propagation, then $\hat{\mathbf{s}}$ can be related to the radius of the wave-front (Luxon and Parker, 1985), $r_c(z)$, as:

$$\frac{\hat{\mathbf{s}}}{\hat{\mathbf{s}} \cdot \hat{\mathbf{k}}} = \frac{(x - Ut)\hat{\mathbf{i}} + y\hat{\mathbf{j}}}{\sqrt{r_c^2(z) - x^2 - y^2}} + \hat{\mathbf{k}}, \tag{9}$$

$$r_c(z) = (z - z_0)\left[1 + \frac{1}{\beta_\infty^2 (z - z_0)^2}\right]. \tag{10}$$

Results given in this paper are limited to the Gaussian laser described above to simplify their presentation; arbitrary spatial intensity profiles are readily incorporated.

Finally, $\phi(t)$ defines the temporal intensity variation during a laser pulse period of duration $t_p = t_{p,\text{on}} + t_{p,\text{off}}$, and is normalized such that

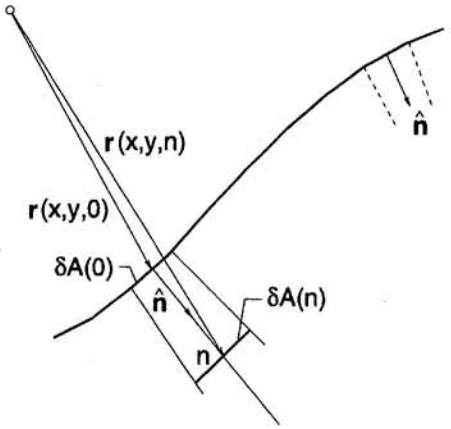


Fig. 2 Local coordinate system into direction of surface normal

$$\frac{1}{t_p}\int_t^{t+t_p} \phi(t)dt = 1. \tag{11}$$

Therefore, for a CW laser $\phi \equiv 1$.

Solution Approach

Equation (1) with its auxiliary conditions (2)–(4) forms a complete set of dimensionless equations in transient form to predict the forming groove shape $s(x, y, t)$ and temperature field $\theta(x, y, z, t)$. In order to find a simple, approximate solution for the conduction loss, Eq. (1), we will assume that conduction takes place only in the direction of the (local) surface normal, i.e., the loss is locally one dimensional. Transforming coordinates to n, a nondimensional distance from a surface location pointing into the medium along the local surface normal (see Fig. 2), the solid will move through the origin for n with the ablation velocity V_n into the negative n direction. Thus, Eq. (1) transforms to

$$\frac{\partial}{\partial t}(dA\theta) - V_n \frac{\partial}{\partial n}(dA\theta) = \frac{\partial}{\partial n}\left(dA \frac{\partial \theta}{\partial n}\right), \tag{12}$$

where $dA(n)$ is a local conduction cross section (Fig. 2). Inclusion of the factor $dA(n)$ allows one to estimate surface curvature effects, which enhance conduction losses (concave surface, as shown in Fig. 2) or impede them (convex surface, e.g., near the rim of the groove). If

$$\mathbf{r}(x, y, n) = \mathbf{r}(x, y, 0) + n\hat{\mathbf{n}} = x\hat{\mathbf{i}} + y\hat{\mathbf{j}} + s\hat{\mathbf{k}} + n\hat{\mathbf{n}} \tag{13}$$

is the vector to a point along n, then the cross-sectional area may be calculated from

$$dA(n) = \left|\frac{\partial \mathbf{r}}{\partial x}\right| \left|\frac{\partial \mathbf{r}}{\partial y}\right| dxdy. \tag{14}$$

Evaluating Eq. (14) up to $O(n)$ (since the heat-affected zone is expected to be thin), one finds

$$dA(n) = dA(0)[1 + an + O(n^2)],$$

$$a = -\frac{1}{\sqrt{1 + s_x^2 + s_y^2}}\left[\frac{s_{xx}}{1 + s_x^2} + \frac{s_{yy}}{1 + s_y^2}\right], \tag{15}$$

where the subscripts denote differentiation, i.e., $s_x = \partial s/\partial x$, etc. Equation (12) is readily solved approximately using an integral method with a chosen temperature profile

$$\theta \simeq \theta_0 e^{-n/\delta}, \tag{16}$$

Downloaded 11 Dec 2010 to 193.140.21.150. Redistribution subject to ASME license or copyright; see http://www.asme.org/terms/Terms_Use.cfm

where θ_0 is local surface temperature and δ is a measure of the local penetration depth. Using this profile to satisfy Eq. (12) in an integral sense (i.e., integrating the equation over all n from 0 to ∞), and again using Eq. (16) in boundary condition (3), leads to three simultaneous, nonlinear equations for the unknown values of θ_0, V_n, and δ, which are all functions of surface location and time:

$$\frac{d}{dt}\left[\theta_0\delta(1 + a\delta)\right] + V_n\theta_0 = \frac{\theta_0}{\delta}, \tag{17}$$

$$\frac{\theta_0}{\delta} = \frac{\mathbf{Q}\cdot\hat{\mathbf{n}}}{N_k} - V_n\text{Ste}, \tag{18}$$

$$V_n = C_1 \exp\left[C_2\frac{\theta_0 - 1}{\theta_0 + C_3}\right], \quad C_3 = \frac{T_\infty}{T_{re} - T_\infty}. \tag{19}$$

The last equation is simply the ablation condition, Eq. (4), which relates surface temperature to the ablation velocity, which in turn is related to the receding groove depth by

$$\frac{ds}{dt} = \frac{V_n}{\hat{\mathbf{n}}\cdot\hat{\mathbf{k}}} \tag{20}$$

Equations (17)–(20) must be solved simultaneously to obtain an expression for the surface topology, $s(x, y, t)$.

It is important to realize that Eq. (16) is a rather simplistic temperature profile and that the solution to Eqs. (17)–(20) is going to be satisfactory only as long as the temporal variation of $\mathbf{Q}\cdot\hat{\mathbf{n}}$ allows this profile to be acceptable. In particular, Eq. (16) cannot have an inflection point and is, therefore, unable to predict the trends after laser power has been turned off abruptly. Fortunately, extensive numerical experiments with the "exact" three-dimensional-code show that ablation ceases almost immediately after the laser is turned off, making a solution of Eqs. (17)–(20) unnecessary for those times.

Pulsed Lasers. Equations (17)–(20) are equally applicable to continuous-wave as well as pulsed lasers. However, for pulsed lasers, ablation takes place only during the laser-on periods, and conduction losses are generally very small. Therefore, it should be possible to simplify the governing equations even further, and still arrive at a reasonably accurate prediction for the forming surface topography. This may be achieved by breaking up each laser pulse into three separate, idealized stages: (1) a heat-up period of duration t_1, during which the underlying material is heated to ablation conditions, but during which no ablation occurs ($V_n = 0$), (2) ablation of duration $t_{p,\text{on}} - t_1$, during which a fully established heat-affected zone is pushed into the material along with the ablation front [i.e., the rate of change of heat stored in the substrate—the first term in Eq. (17)—is negligible as compared with ablation energy, $V_n(\theta_0 + \text{Ste})$], and (3) a cool-down period (the laser-off time $t_{p,\text{off}}$), during which the solid cools back to ambient conditions. It is this internally stored preheat energy at the end of the second period that constitutes the conductive loss. Thus, we have:

Heat-up period:

$$\frac{d}{dt}\left[\theta_0\delta(1 + a\delta)\right] = \frac{\mathbf{Q}\cdot\hat{\mathbf{n}}}{N_k}, \quad 0 < t < t_1, \tag{21}$$

or

$$\theta_0\delta(1 + a\delta)(t_1) = \int_0^{t_1}\frac{\mathbf{Q}\cdot\hat{\mathbf{n}}}{N_k}\,dt \tag{22}$$

Ablation period:

$$V_n\theta_0 = \frac{\theta_0}{\delta} = \frac{\mathbf{Q}\cdot\hat{\mathbf{n}}}{N_k} - V_n\,\text{Ste}, \quad t_1 \le t \le t_{p,\text{on}}, \tag{23}$$

or

$$V_n(t) = \frac{1}{\delta} = \frac{\mathbf{Q}\cdot\hat{\mathbf{n}}(t)}{N_k(\theta_0 + \text{Ste})}, \tag{24}$$

and the ablation temperature follows from Eq. (19). It is the nature of an Arrhenius rate equation that ablation temperature remains almost constant ($\theta_0 \simeq \text{const} = \overline{\theta}_0 \simeq 1$), even though the ablation rate may vary strongly with $\mathbf{Q}\cdot\hat{\mathbf{n}}(t)$. Thus, Eq. (24) may be further simplified replacing $\theta_0(t)$ by an average value $\overline{\theta}_0$, which may be determined by inverting Eq. (19) in terms of an average ablation velocity,

$$\overline{\theta}_0 = \frac{1 + C_3}{1 - \dfrac{1}{C_2}\ln\left(\dfrac{\overline{V}_n}{C_1}\right)} - C_3, \tag{25}$$

$$\overline{V}_n = \frac{1}{t_{p,\text{on}} - t_1}\int_{t_1}^{t_{p,\text{on}}} V_n\,dt = \frac{\displaystyle\int_{t_1}^{t_{p,\text{on}}}\mathbf{Q}\cdot\hat{\mathbf{n}}\,dt}{(t_{p,\text{on}} - t_1)N_k(\overline{\theta}_0 + \text{Ste})}. \tag{26}$$

The two solutions (heat-up and ablation) may be mated by specifying the heat-up period to have ended when θ_0 reaches the value $\overline{\theta}_0$ and $\delta(t_1)$ is assumed to have reached the value given by Eq. (24) at $t = t_1$: t_1 is determined from this condition. The solution proceeds as follows:

1 A t_1 is guessed [an accurate first guess is obtained from Eqs. (22) and (24) since it is known that $\overline{\theta}_0 \simeq 1$].
2 An average ablation velocity is obtained from Eq. (26) (again, starting with $\overline{\theta}_0 \simeq 1$).
3 A new value for $\overline{\theta}_0$ is obtained from Eq. (25).
4 Updated values for $\delta(t_1)$ and t_1 are found from Eqs. (24) and (22), respectively.

Converged values for $\overline{\theta}_0$ and t_1 are then found through iteration. The situation is particularly simple for a basic on-off pulse [$\phi(t) = t_p/t_{p,\text{on}} = \text{const}$ for $t < t_{p,\text{on}}$, $\phi(t) = 0$ otherwise]. In that case $\mathbf{Q}\cdot\hat{\mathbf{n}} = \text{const}$ during laser-on time, and ablation proceeds quasi-steady with V_n, δ, θ_0 all being constant. Then, for an on-off pulse,

$$\overline{V}_n = V_n = \frac{1}{\delta} = \frac{\mathbf{Q}\cdot\hat{\mathbf{n}}}{N_k(\theta_0 + \text{Ste})} = \text{const}, \tag{27}$$

$$t_1 = \frac{N_k}{\mathbf{Q}\cdot\hat{\mathbf{n}}}\,\theta_0\delta(1 + a\delta). \tag{28}$$

For any temporal pulse shape, the updated local groove depth after the ith pulse, s_i, follows then from Eq. (20) as

$$s_i(x, y) = s_{i-1}(x, y) + \frac{\overline{V}_n(t_{p,\text{on}} - t_1)}{(\hat{\mathbf{n}}\cdot\hat{\mathbf{k}})}, \tag{29}$$

where the values for $\overline{V}_n$ and $(\hat{\mathbf{n}}\cdot\hat{\mathbf{k}})$ can be calculated based on the topology after the $(i - 1)$th pulse, or some average value may be used by iteration.

Illustrative Examples

To demonstrate the strengths and limitations of the present models, a number of example calculations are shown in Figs. 3–7. For simplicity, all nondimensional parameters (except laser-on time $t_{p,\text{on}}$) were held constant at $N_k = 0.0427$, Ste = 2.16, $U = 3.185$, $\alpha = 0.9$, and $t_p = 0.14$. This corresponds to a laser with an average power of 600 W and a radius of $w_0 = 147\ \mu$m scanning over graphite at 6.5 cm/s, for which a comparison with experimental data was carried out in a previous paper (Modest et al., 1995). Most laser machining operations on nonmetals can be expected to have relatively similar sets of parameters. In all cases the laser is first turned on at $x_{\text{start}} = -1.5$, i.e., at a location $1.5w_0$ before the center of the laser reaches the

Downloaded 11 Dec 2010 to 193.140.21.150. Redistribution subject to ASME license or copyright; see http://www.asme.org/terms/Terms_Use.cfm

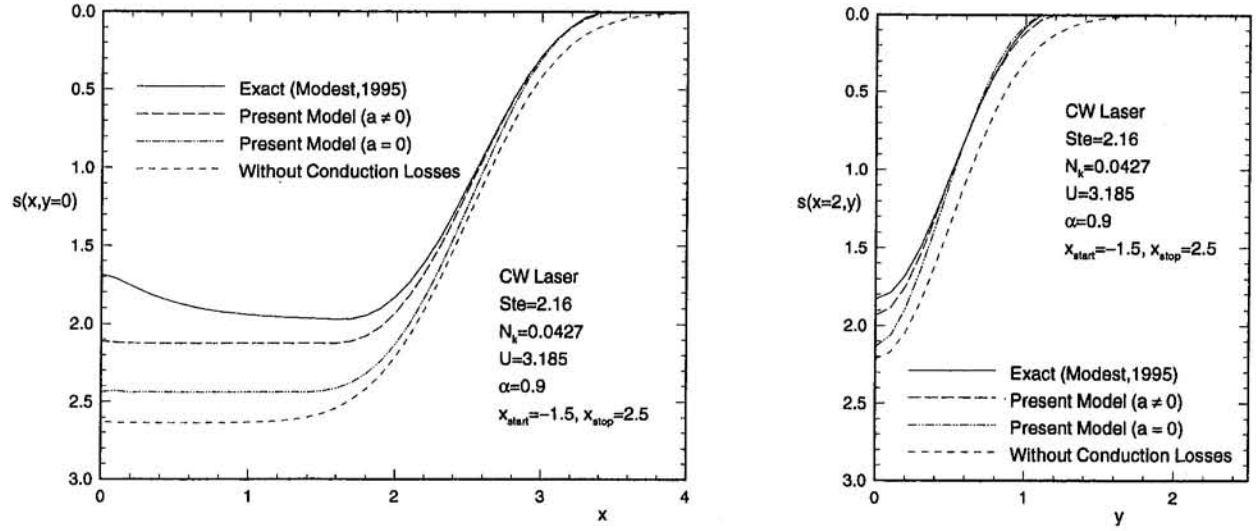


Fig. 3 Groove development along centerline (left) and groove cross section (right) for continuous-wave laser operation

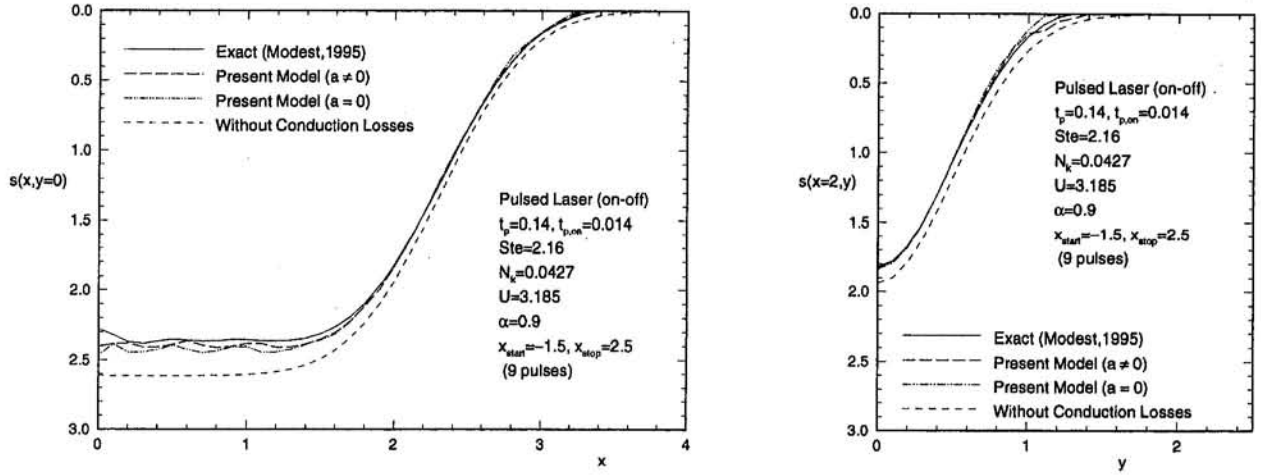


Fig. 4 Groove development along centerline (left) and groove cross section (right) for pulsed laser operation (on-off pulse shape)

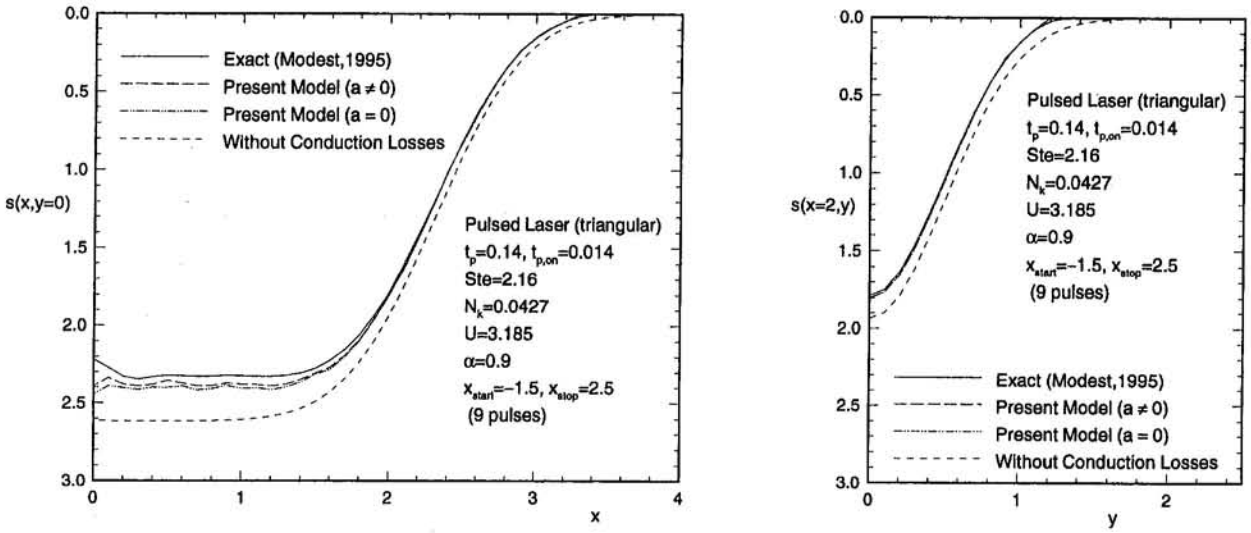


Fig. 5 Groove development along centerline (left) and groove cross section (right) for pulsed laser operation (triangular pulse shape)

Downloaded 11 Dec 2010 to 193.140.21.150. Redistribution subject to ASME license or copyright; see http://www.asme.org/terms/Terms_Use.cfm

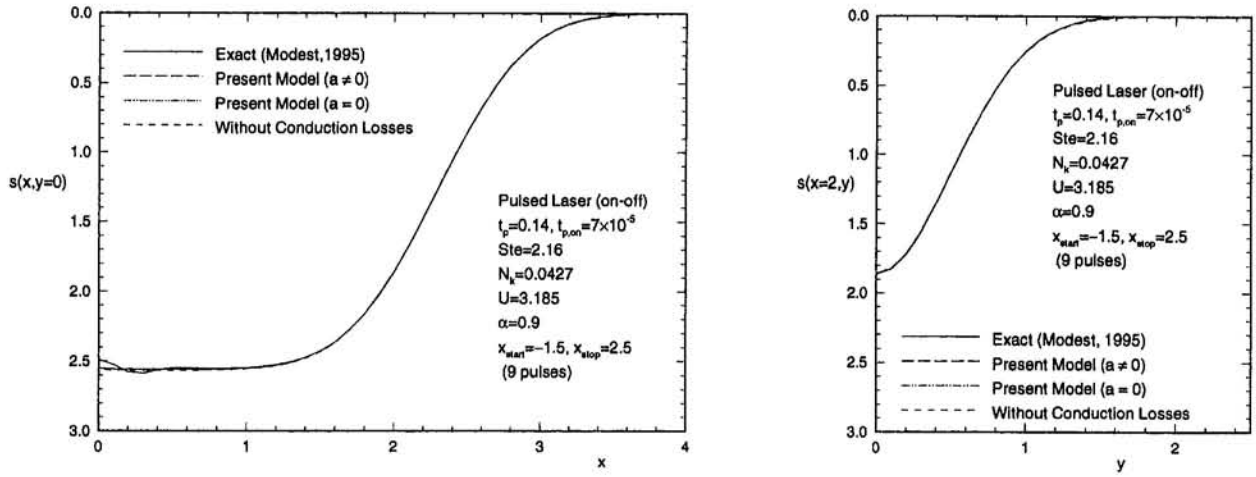


Fig. 6 Groove development along centerline (left) and groove cross section (right) for Q-switched laser operation

edge of the solid, and is turned off as soon as the laser center reaches $x_{stop} = 2.5$.

Figure 3 shows the case of a continuous wave laser. The exact solution shows distinct entry/start-up effects, apparently due to warming up of surrounding material (Modest, 1995), which is neglected by the approximate models. At quasi-steady operation the maximum groove depth is almost $2w_0$, at which time approximately 30 percent of absorbed laser energy is lost to conduction (not including preheating of material, which eventually ablates). If conduction losses are neglected, a maximum depth of $2.63w_0$ is obtained (with, of course, a 30 percent larger overall removal rate). The approximate model does rather well if the correction factor a in Eq. (15) is included, predicting maximum depth to about 5 percent and removal rate with about 3 percent accuracy. For CW operation the penetration depth can be appreciable, making curvature effects important, as seen from the $a = 0$ line in the figure.

To assess whether the present integral method provides acceptable accuracy, one may apply the integral method with and without conductive losses [with and without the *transient* preheating term in Eq. (17); in the latter case the θ_0/δ reflects preheating of material to be ablated]. A comparison gives an estimate of the conductive losses.

Figure 4 shows the same situation for a pulsed laser with a simple on-off pulse and a 10 percent duty cycle ($t_{p,on} = 0.1 \times t_p$, during which time the laser power is ten times the average power). Conductive losses during the quasi-steady part of each laser pulse are about 10 percent. The curves labeled "present model" use the full-pulse model, Eq. (29). While including curvature effects ($a \neq 0$) produces slightly better results, this improvement probably does not justify the considerable additional effort. Applying the full-pulse model is somewhat marginal in this case, producing groove bottom undulations much stronger than indicated by the exact solution. This is apparently due to the fact that the laser moves a distance of $U \times t_{p,on}$ or $0.045w_0$ during each laser-on time, which is neglected by the full-pulse model.

The simple full-pulse model of Eqs. (22), (24), (25), and (26) is expected to be most accurate for simple on-off pulses, for which quasi-steady ablation is reached during each pulse, Eqs. (27) and (28). To ensure the validity of the model for arbitrary temporal pulse shapes, a triangular pulse was also considered, i.e.,

$$\phi(t) = \begin{cases} \dfrac{4t_p t}{t_{p,on}^2}, & 0 < t < 0.5t_{p,on}, \\ \dfrac{4t_p}{t_{p,on}}\left(1 - \dfrac{t}{t_{p,on}}\right), & 0.5t_{p,on} < t < t_{p,on}, \\ 0, & t_{p,on} < t < t_p. \end{cases} \tag{30}$$

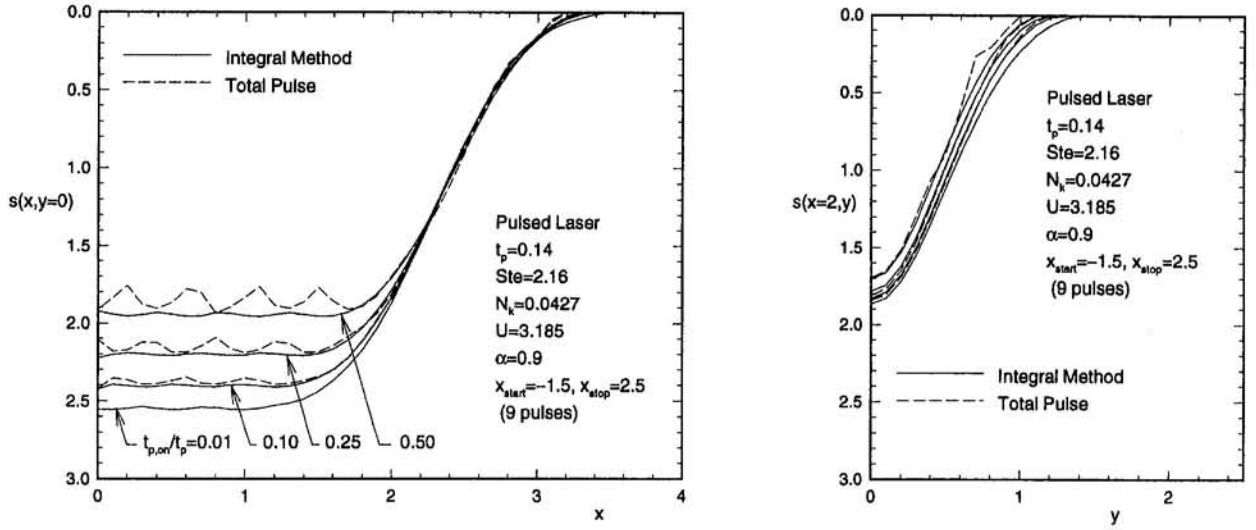


Fig. 7 Groove development along centerline (left) and groove cross section (right) for varying laser pulse lengths

Downloaded 11 Dec 2010 to 193.140.21.150. Redistribution subject to ASME license or copyright; see http://www.asme.org/terms/Terms_Use.cfm

As Fig. 5 shows, the results are very similar. Due to the more gradual ramp-up in laser power, the conduction losses are slightly larger, resulting in an about 1.5 percent lesser groove depth. Thus, the results suggest that, for short enough pulses (10 percent duty cycle or less), the actual temporal variation of pulse power $\phi(t)$ is unimportant and the pulse may be replaced by a (computationally simpler) on-off pulse.

If the laser has extremely short pulses, such as a Q-switched laser, then conduction losses become negligible, regardless of pulse profile $\phi(t)$, as seen from Fig. 6 for simple on-off pulses. The "exact" solution shows a slight oscillation at the entry, which is apparently due to numerical instability because of the fact that at the edge interior nodes cannot be orthogonal to the top surface during transient recession. All curves virtually collapse, implying that curvature effects and, indeed, all conduction losses may be neglected, and that the full-pulse model can be applied.

Finally, Fig. 7 shows a comparison between the two approximate models for different (on-off) pulsing conditions. For small duty cycles, $t_{p,\text{on}}/t_p \leq 0.01$, the results from Eqs. (17)–(20) (Integral Method) are indistinguishable from those obtained from Eqs. (27)–(29) (Full-Pulse Method). Small, but acceptable, differences become apparent for duty cycles of around 10 percent while the full pulse method should probably not be used for duty cycles >20 percent (or, rather, when $t_{p,\text{on}} \times U > 0.1$). In addition, for large values of $t_{p,\text{on}} \times U$ calculations with the curvature correction factor become rather unstable for $a < 0$ (as seen from the jaggedness of some of the dashed lines in Fig. 7).

Summary and Conclusions

Two simplified models have been introduced for the calculation of shapes produced by laser machining. The models are limited to opaque, strongly absorbing materials that ablate or decompose upon irradiation by a laser (such as most ceramics), and that do not generate significant amounts of liquid in the cutting zone (as would be expected for most metals, which melt and have large thermal diffusivities). It is further assumed that any laser-generated plume/plasma is blown away by strong gas-assist. The first of these models results in a time-dependent ordinary differential equation and is based on an integral method to determine conductive losses. This model is applicable to shaping with continuous-wave as well as pulsed lasers. The second model is valid only for pulsed laser operation, calculating ablation due to an entire pulse in one step. Depending on the problem at hand, spatial and temporal nodal sizes, CPU times (on a high-power workstation) are reduced from an hour or more (exact numerical) to minutes (integral method) and less than a second (full pulse method), respectively. The integral method may be applied whenever conduction losses are relatively small (less than, say, 30 percent). In order for the full-pulse method to be valid, the laser should also not move an appreciable amount across the surface during each laser pulse (less than $\simeq 0.1 \times$ laser radius).

References

Anthony, T. R., 1980, "The Random Walk of a Drilling Laser Beam," *Journal of Applied Physics,* Vol. 51, pp. 1170–1175.

Bailey, A. W., and Modak, A., 1989, "Numerical Simulation of Laser Ablation With Cavity Reflections," *Journal of Thermophysics and Heat Transfer,* Vol. 3, No. 1, pp. 42–45.

Bang, S. Y., and Modest, M. F., 1991, "Multiple Reflection Effects on Evaporative Cutting With a Moving CW Laser," ASME JOURNAL OF HEAT TRANSFER, Vol. 113, No. 3, pp. 663–669.

Bang, S. Y., and Modest, M. F., 1992, "Evaporative Scribing With a Moving CW Laser—Effects of Multiple Reflections and Beam Polarization," in: *Proc. ICALEO '91, Laser Materials Processing,* Vol. 74, San Jose, CA, pp. 288–304.

Bang, S. Y., Roy, S., and Modest, M. F., 1993, "CW Laser Machining of Hard Ceramics—Part II: Effects of Multiple Reflections," *International Journal of Heat and Mass Transfer,* Vol. 36, No. 14, pp. 3529–3540.

Bunting, K. A., and Cornfield, G., 1975, "Toward a General Theory of Cutting: A Relationship Between the Incident Power Density and the Cut Speed," ASME JOURNAL OF HEAT TRANSFER, Vol. 97, pp. 116–121.

Chryssolouris, G., 1991, *Laser Machining: Theory and Practice,* Springer-Verlag, New York.

Dabby, F. W., and Paek, U.-C., 1972, "High-Intensity Laser-Induced Vaporization and Explosion of Solid Material," *IEEE Journal of Quantum Electronics,* Vol. QE-8, pp. 106–111.

Kogelnik, H., and Li, T., 1956, "Laser Beams and Resonators," *Applied Optics,* Vol. 5, No. 10, pp. 1550–1565.

Luxon, J. T., and Parker, D. E., 1985, *Industrial Lasers and Their Applications,* Prentice-Hall, Englewood Cliffs, NJ.

Modest, M. F., and Abakians, H., 1986, "Evaporative Cutting of a Semi-infinite Body With a Moving CW Laser," ASME JOURNAL OF HEAT TRANSFER, Vol. 108, pp. 602–607.

Modest, M. F., Ramanathan, S., Raiber, A., and Angstenberger, B., 1995, "Laser Machining of Ablating Materials—Overlapped Grooves and Entrance/Exit Effects," *Journal of Laser Applications,* Vol. 7, pp. 210–218.

Modest, M. F., 1995, "Three-Dimensional, Transient Model for Laser Machining of Ablating Materials," *International Journal of Heat and Mass Transfer,* Vol. 39, No. 2, pp. 221–234.

Petring, D., Abels, P., and Beyer, E., 1988, "Absorption Distribution on Idealized Cutting Front Geometries and Its Significance for Laser Beam Cutting," in: *High Power CO_2 Laser Systems and Applications,* Bellingham, WA, SPIE, pp. 123–131.

Ramanathan, S., and Modest, M. F., 1990, "Effect of Variable Properties on Evaporative Cutting With a Moving CW Laser," in: *Heat Transfer in Space Systems,* ASME HTD-Vol. 135, pp. 101–108.

Ramanathan, S., and Modest, M. F., 1992a, "CW Laser Cutting of Composite Ceramics," in: *Laser Advanced Materials Processing—LAMP '92,* Vol. 2, Nagaoka, Japan, pp. 625–632.

Ramanathan, S., and Modest, M. F., 1992b, "CW Laser Drilling of Composite Ceramics," in: *Proc. ICALEO '91, Laser Materials Processing,* Vol. 74, San Jose, CA, pp. 305–326.

Ramanathan, S., and Modest, M. F., 1993, "Measurement of Temperatures and Absorptances for Laser Processing Applications," in: *ICALEO '93,* Orlando, FL.

Ramanathan, S., and Modest, M. F., 1995, "High-Speed Photographic Visualization of Laser Processing Phenomena," *Journal of Laser Application,* Vol. 7, pp. 75–82.

Roy, S., and Modest, M. F., 1993, "Evaporative Cutting With a Moving CW Laser—Part I: Effects of Three-Dimensional Conduction and Variable Properties," *International Journal of Heat and Mass Transfer,* Vol. 36, No. 14, pp. 3515–3528.

Schuöcker, D., and Müller, P., 1987, "Dynamic Effects in Laser Cutting and Formation of Periodic Striations," in: *Proc. SPIE,* Vol. 801, pp. 258–264.

von Allmen, M., 1976, "Laser Drilling Velocity in Metals," *Journal of Applied Physics,* Vol. 47, pp. 5460–5463.

Vorreiter, J. O., Kaminski, D. A., and Smith, R. N., 1991, "Monte Carlo Simulation of a Laser Drilling Process," ASME Paper No. 91-WA-HT-9.

Wagner, R. E., 1974, "Laser Drilling Mechanics," *Journal of Applied Physics,* Vol. 45, pp. 4631–4637.

Downloaded 11 Dec 2010 to 193.140.21.150. Redistribution subject to ASME license or copyright; see http://www.asme.org/terms/Terms_Use.cfm

Anomalous Diffusion in Short-Pulse Laser Interactions With Random Media

M. C. Hipwell
Graduate Student Researcher.
Student Mem. ASME

C.-L. Tien
A. Martin Berlin Professor.
Honorary Member ASME

Department of Mechanical Engineering,
University of California,
Berkeley, CA 94720

This work applies fractal percolation theory to examine the impact of anomalous diffusion in short time-scale applications of random media. It is shown that there exist three regimes of heat transport corresponding to transport over the basic percolation unit (particle), the fractal cluster, and the homogeneous medium. Scaling is performed to determine the characteristic time scales of anomalous diffusion. The dependence of these time scales on both material properties and structure is examined to assess the impact of the anomalous diffusion regime on short time-scale energy transport. Additional criteria that determine the importance of anomalous diffusion relative to other transport phenomena and properties, such as radiation and thermal boundary resistance, are established.

Introduction

Short-pulse lasers are finding increasingly widespread use in materials processing and diagnostics. Examples include annealing of radiation damage in ion-implanted semiconductors, recrystallization of amorphous and polycrystalline silicon, rapid thermal cleaning, deposition of thin films, creation of metastable alloys, and thin-film and atomic-level diagnostics (von der Linde, 1993). The increased temporal resolution of optical observations in diagnostics allows detailed "stop action" observations of previously inaccessible phenomena. In addition, the ultrashort laser-material interaction time permits highly localized observation and processing due to the short range of diffusion during the interaction time.

In these applications, laser interactions with random media such as amorphous (noncrystalline) materials, porous media, and composites are often required. Amorphous forms of materials such as silicon dioxide, silicon nitride, and silicon are widely used in microelectronics and microsensor/actuator fabrication. In addition, porous metal "black" coatings, polymers, and composites are becoming increasingly important in these applications. Nanoporous silicon has been shown to photoluminesce efficiently at visible wavelengths at room temperature, and therefore may revolutionize optoelectronics with the possibility of optical devices made of silicon.

In laser-assisted processes, temperature and process control are critical factors. Temperature control is also a major consideration in the design of the laser system itself, because thermal damage of optical components is currently one of the main barriers to increasing laser power. This means that accurate characterization and modeling of energy transport during laser-material interactions is extremely important. As the pulse width of lasers used in many of these applications has decreased into the picosecond and subpicosecond range, the applicability of conventional macroscopic models of energy transport is questionable (Qiu and Tien, 1993). In addition, on the microscopic scale, transport calculations for crystalline materials are possible only because of concepts and simplifications that are based on lattice periodicity and therefore do not apply to amorphous materials such as glasses (Kittel, 1986).

Contributed by the Heat Transfer Division and presented at the National Heat Transfer Conference, Portland, Oregon, August 5–9, 1995. Manuscript received by the Heat Transfer Division October 9, 1995; revision received May 6, 1996. Keywords: Laser Processing, Porous Media, Transient and Unsteady Heat Transfer. Associate Technical Editor: A. S. Lavine.

Fractals and percolation theory have been applied to model the structure, growth phenomena, and transport in a wide variety of random media (Weil et al., 1983; Zallen, 1983). A percolation network is characterized by its correlation length, a length scale below which the network exhibits anomalous behavior and above which it appears homogeneous. On short time scales, the thermal diffusion length is on the order of the correlation length in random media, carriers move only on anomalous length scales, and thus, anomalous diffusion is expected. This raises questions as to the range and impact of anomalous diffusion in short time-scale applications involving these materials. This work examines these questions and establishes conditions under which anomalous diffusion will have a significant impact on transient thermal transport.

Fractals, Percolation Theory, and Anomalous Diffusion

A fractal is a shape that is made up of parts similar to the whole in some way (Mandelbrot, 1977). A percolation network is a random fractal (self-similarity is considered as average) that can be understood as a periodic lattice of sites (or bonds) randomly occupied with probability p. For small values of p, a small portion of lattice sites are occupied, and only small, finite clusters of connected occupied sites exist. During dynamic phenomena, such as conduction, sites can interact only with nearest neighboring sites. Thus, for small occupation probabilities, there is no conduction path across the lattice. As the occupation probability, and hence the concentration of occupied sites, increases, the average cluster size increases. There is a sharp transition that occurs at the critical concentration, or percolation threshold, p_c, where an infinite cluster spanning the entire lattice appears for the first time. At and above this critical concentration, at least one continuous conduction path traverses the lattice, and energy can therefore percolate from one edge to the other (Bunde and Havlin, 1991).

In percolation theory, the correlation length, ξ, is the characteristic length (Havlin and Bunde, 1991). It refers to the average size of finite clusters or voids in an infinite cluster in the network. It is also used to identify the transition between fractal and Euclidean behavior. On length scales smaller than ξ, the system is self-similar, or fractal, characterized by a fractal dimension, D_f, and has properties that can be determined from percolation scaling theory (Bunde and Havlin, 1991). On length scales larger than ξ, the structure is viewed and behaves as a homogeneous system.

Copyright © 1996 by ASME

Downloaded 11 Dec 2010 to 193.140.21.150. Redistribution subject to ASME license or copyright; see http://www.asme.org/terms/Terms_Use.cfm

The dynamic properties of percolation networks are often described based on the theory of diffusion of "random walkers" on the network (de Gennes, 1976). In uniform (Euclidean) systems, the mean-square displacement of the random walker, $\langle R^2(t)\rangle$, is proportional to time, t,

$$\langle R^2(t)\rangle \propto t, \tag{1}$$

for any Euclidean dimension, d. In a percolation network, however, at length scales below the correlation length, ξ, Gefen et al. (1983) showed that diffusion is anomalous. The mean-square displacement in this case is

$$\langle R^2(t)\rangle \propto t^{2/(2+\theta)} \propto t^{2/d_w}, \tag{2}$$

where θ is the anomalous diffusion exponent and $d_w = 2 + \theta$ is the dimension of the random walk. Since $\theta > 0$, and hence $d_w > 2$, diffusion is slowed compared to that which occurs in a uniform medium. The diffusing particles are delayed due to the presence of bottlenecks, backbends, and dead ends in the fractal network into which a random walker may travel. It is also important to note that when anomalous diffusion occurs, the diffusion coefficient, D, is not constant since

$$D = \frac{1}{2}\frac{d\langle R^2(t)\rangle}{dt} \tag{3}$$

and therefore

$$D \propto t^{(2/d_w)-1}. \tag{4}$$

The random walk dimension can be related to the fractal dimension, D_f, through the spectral dimension, $d_f = 2D_f/d_w$ (also called the "fracton dimension," Alexander and Orbach, 1982). The spectral dimension characterizes anomalous diffusion and basic properties of vibration on the fractal network.

There are many random media that can be described or whose behavior can be qualitatively modeled by percolation theory. Anomalous diffusion is most likely to be significant in systems in which an infinite cluster exists. In these systems the correlation length will correspond to the average size of voids in the network. If a material is a metal-insulator composite, for example, this length may actually refer to the cluster size of the nonconducting material. Anomalous diffusion is also most likely to be significant in a material where the "percolating network" structure is the dominant conductor. In porous media, for example, both the solid and the fluid are intertwined percolating networks, so if either is a significantly better conductor, one would expect anomalous diffusion to be observed.

Anomalous Diffusion Regime

The presence of anomalous diffusion is an extremely important result, which must be considered when examining transport in random media. It will occur when carrier transport is limited to a fractal cluster in the network, or when the characteristic length scale of transport is less than the correlation length. In short time-scale applications, the thermal diffusion length will be less than the correlation length and carriers will travel only on anomalous length scales. Gefen et al. (1983) predicted that anomalous diffusion will have an important effect on the AC electrical conductivity of a percolating network in high frequency (short time-scale) applications. Similarly, Goldman et al. (1995) predicted that anomalous diffusion will have a significant effect on thermal transport in amorphous materials on short time scales, such as in short-pulse laser-material interactions.

The anomalous diffusion regime can be more easily understood by examining the temporal behavior of surface temperature of a random medium heated by an instantaneous plane source. For diffusion of energy from a source of dimension d_s into a Euclidean medium of dimension d the behavior is given by (Fournier and Boccara, 1989)

$$T(0, t) \propto t^{-(d-d_s)/2}, \tag{5}$$

which for a plane source, $d_s = 2$, diffusing into a three-dimensional Euclidean medium, $d = 3$, results in

$$T(0, t) \propto t^{-1/2}. \tag{6}$$

If, on the other hand, energy is diffusing into a fractal medium of fractal and spectral dimensions D_f and d_f, the behavior is given by (Fournier and Boccara, 1989)

$$T(0, t) \propto t^{-(d_f/2-d_s d_f/2D_f)}, \tag{7}$$

where d_s can be a fractal or Euclidean source dimension. For a plane source, $d_s = 2$, of energy diffusing into an ideal percolation network ($d_f = 1.31$ (Havlin and Bunde, 1991) and $D_f = 2.54$ (Bunde and Havlin, 1991)) immersed in three-dimensional space ($d = 3$), Eq. (7) gives

$$T(0, t) \propto t^{-0.14}. \tag{8}$$

As the behavior of random media can vary from the ideal percolation network, a range of exponent values near negative 0.14 will be found in real materials.

Nomenclature

A = constant in diffusivity expression
A_l = laser beam spot area, m^2
a = particle diameter, m
C = specific heat, J kg^{-1} K^{-1}
D = diffusion coefficient, m^2s^{-1}
D_f = fractal dimension
d = Euclidean dimension
d_f = spectral dimension
d_s = source dimension
d_w = dimension of the random walk
E = total laser pulse energy, J
h = film thickness, m
K_λ = spectral absorption coefficient, m^{-1}
k = absorption index
l_d = diffusion length, m
m = slope
p = occupation probability
p_c = percolation threshold
$\langle R^2\rangle$ = mean-square displacement of a random walker, m^2
R_b = thermal boundary resistance, m^2K W^{-1}
T = temperature, K
t = time, s
v = phonon velocity, m s^{-1}
x = spatial coordinate, m
α = thermal diffusivity, m^2s^{-1}
δ = optical penetration (skin) depth, m
Δt = time step, s
Δx = space step, m
θ = anomalous diffusion exponent
κ = thermal conductivity, W m^{-1} K^{-1}
λ = wavelength, m
ξ = correlation length, m
ρ = density, kg m^{-3}
σ_K = Kapitza conductance, W m^{-2} K^{-1}
τ = characteristic decay time, s
τ_{ph} = phonon relaxation time, s

Subscripts

bulk = of the bulk
eff = effective
f = film
i = initial
o = value in vacuum
p = particle
s = substrate
ξ = at the scale of the correlation length

Downloaded 11 Dec 2010 to 193.140.21.150. Redistribution subject to ASME license or copyright; see http://www.asme.org/terms/Terms_Use.cfm

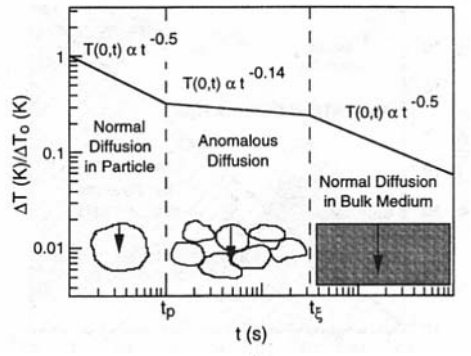


Fig. 1 Regimes of diffusion in random media

Regimes based on these surface temperature versus time results are shown in Fig. 1. Heat is first absorbed in the surface layer of percolation sites (often particles). The sites themselves are Euclidean, so in the first regime energy diffuses[1] over the length of the site and diffusion is normal, with temperature behavior as given in Eqs. (5) and (6). Next, the energy begins to be transmitted from one site to another in the fractal cluster and diffusion is anomalous, with temperature being given by Eqs. (7) and (8). Finally, the energy carriers have traveled a distance greater than the correlation length in the material, the material appears homogeneous, and diffusion is once again normal and given by Eqs. (5) and (6).

It is clear that the time scale and range of the anomalous diffusion regime will determine the impact of this phenomenon in random media. It is therefore important to examine the time scales of the phenomenon and establish criteria that determine its significance relative to other transport phenomena. The criteria are relevant to pulsed laser interactions with these materials, but are also generally applicable to any pulsed heating that occurs on a time scale less than the time range when anomalous diffusion occurs.

Scaling in Anomalous Diffusion

Criteria can be established to determine when anomalous diffusion is expected to be important by considering the characteristic time and length scales of heating and other transport mechanisms relative to the time and length scales of anomalous diffusion. Anomalous diffusion is expected to occur when the length scale of transport is on the order of the correlation length. As shown in Fig. 1, there are also characteristic times that determine when anomalous diffusion will occur. These characteristic times can be determined by examining the length over which a carrier has diffused after a certain amount of time, known as the thermal diffusion length, l_d, given by

$$l_d = (\alpha t)^{1/2}, \tag{9}$$

where α is the thermal diffusivity. The characteristic time that corresponds to transport over a length scale equal to the correlation length can be determined from Eq. (9) to be

$$t_\xi = \left(\frac{\xi^2}{\alpha_{\text{eff}}}\right), \tag{10}$$

where α_{eff} is the effective diffusivity of the random medium. This diffusivity value can be used because the material crosses over from fractal to bulk behavior at the correlation length. In other words, the time/size-dependent value at this point and the bulk constant value for the medium will be equal. Anomalous diffusion will occur for $t < t_\xi$. There is also the lower limit to the anomalous regime, which corresponds to transport across the basic unit of the percolating network. For example, in silica aerogels, the basic unit is a porous silica particle (Richter et al., 1994). Again using Eq. (9), the characteristic time for transport over the basic unit is given by

$$t_p = \left(\frac{a^2}{\alpha_p}\right), \tag{11}$$

where a is the diameter (or basic length scale) of the constituent particles (or basic units) and α_p is the diffusivity of these particles. Anomalous diffusion then occurs for times

$$t_p < t < t_\xi. \tag{12}$$

It is important to note that the lower limit is not relevant in dense amorphous materials since the correlation length is already very small (~2 nm (Jagannathan et al., 1989)), and not only would the time scale for transport across the basic percolation unit be very short, but also transport across a distance less than one lattice spacing is not physically meaningful.

These limits then determine the time scale and range of anomalous diffusion. A main factor to consider when predicting the impact of anomalous diffusion, therefore, is the relative position of the upper and lower bounds of the anomalous regime. The lower bound is fixed by the particle size, as can be seen in Fig. 2. The upper bound, and therefore the length of the anomalous diffusion regime, on the other hand, is dependent on the correlation length and effective diffusivity of the random material. This behavior is also shown in Fig. 2, where two limiting cases are demonstrated. First, as the correlation length and diffusivity of the effective medium approach that of the particle, the impact of the anomalous diffusion regime becomes small, until the continuous line of slope $m = -\frac{1}{2}$ is reached. The upper and lower limits of the anomalous region occur at the same point, and this behavior is essentially that of a continuous Euclidean medium where no anomalous behavior is observed. If, on the other hand, the correlation length (in most cases the pore size) is large compared to the particle size, the anomalous diffusion time range will be broad due to the a^2 and ξ^2 dependence of the crossover times in Eqs. (10) and (11), respectively. Further, if the effective diffusivity of the bulk random medium is less than that of the particle, the anomalous diffusion regime will extend to even longer times, resulting in a greater impact. This is the case for carbon aerogels (Lu et al., 1993) (provided the constituent particles are large enough to meet the condition $\delta < a$ discussed below), and significant impact is therefore expected in these materials.

As an example, this analysis can be applied to the experimental results of Fournier and Boccara (1989), shown in Fig. 3. The data are the measured transient surface temperature of an assembly of weakly bonded, copper spheres (~100 μm in diam-

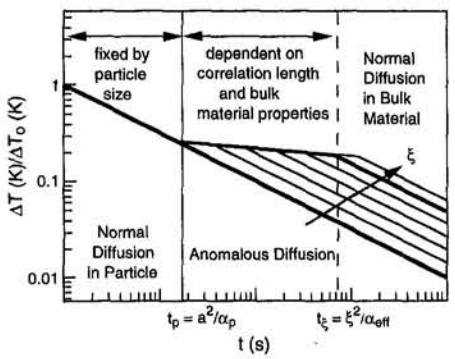


Fig. 2 Scaling of the anomalous diffusion regime

[1] It is important to note that this analysis assumes that diffusive transport is valid in the particles. If the particles are small enough (a few nanometers) thermal transport may be ballistic and/or lattice vibrations may be quantized.

Downloaded 11 Dec 2010 to 193.140.21.150. Redistribution subject to ASME license or copyright; see http://www.asme.org/terms/Terms_Use.cfm

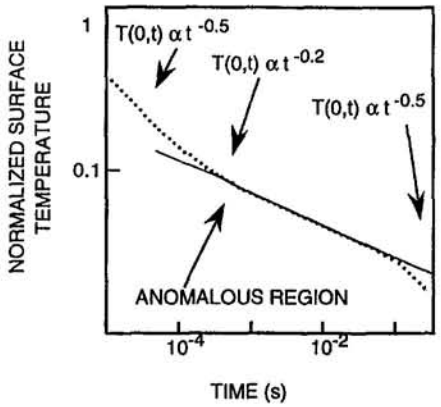


Fig. 3 Time-dependent surface temperature of an assembly of weakly bonded, copper spheres (Fournier and Boccara, 1989)

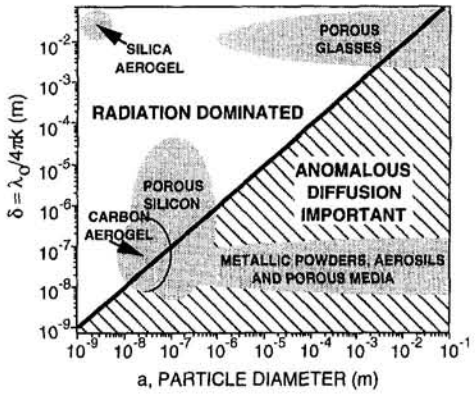


Fig. 4 Importance of anomalous diffusion versus radiation in examples of pulsed-laser heated random media

eter) heated by a short-pulse (~1 ns) laser. Below t_p, normal diffusion should occur in the first layer of irradiated spheres. Using the diffusivity of copper, $\alpha_p \sim 11 \times 10^{-5}$ m^2/s, and the 100 μm diameter of the spheres, the crossover time is calculated to be $t_p \sim 9 \times 10^{-5}$ s. This matches well with the beginning of the anomalous diffusion regime in the data. Between t_p and t_ξ, anomalous behavior is exhibited with a slope, $m = -0.2$, which is very close to the percolation value of $m = -0.14$ calculated in Eq. (8). The second crossover time, t_ξ, is at 0.15 s. This is about three orders of magnitude greater than t_p. Since the correlation length and effective diffusivity of this material are not given, the expected t_ξ cannot be calculated directly. This value is very reasonable, however, considering that it would only require a correlation length an order of magnitude larger than the particle size and a diffusivity an order of magnitude smaller than the copper spheres.

The time scale is not the only scale that must be considered when determining the impact of anomalous diffusion in various short-pulse heating situations. Anomalous diffusion is observed in this example because both the characteristic heating time and length scales are less than those of the upper and lower limits of the anomalous diffusion regime. For radiation heating by a short-pulse laser, the length scale of heating is the optical penetration, or skin, depth, δ, (the depth at which the intensity has decayed to $1/e$ times the original intensity), which is the inverse of the spectral absorption coefficient, K_λ, as given by

$$\delta = \frac{1}{K_\lambda} = \frac{\lambda_o}{4\pi k}, \qquad (13)$$

where λ_o is the wavelength of the radiation in vacuum and k is the absorption index. If this length is longer than the correlation length, then the deposited radiant energy will be carried further into the material by photons than by diffusive transport by electrons or phonons. Therefore, for anomalous diffusion to be important in the laser-pulse heating of random media, the optical penetration depth must be less than the correlation length, $\delta < \xi$. Both the upper and lower limits of the range will be observed for radiant energy of optical penetration depth less than the particle size, $\delta < a$. This condition is shown in Fig. 4 along with some examples of practical applications. As can be seen from this figure, anomalous diffusion can have an impact on a wide variety of random media during short-pulse laser processing or other short time-scale applications. It is also important to note that for radiant heating of dense glasses, whose correlation length is on the order of nanometers, anomalous diffusion will not be significant, considering the wavelengths of typical heating sources.

Anomalous Diffusion in Metallized Dielectric Layers

An important application of these criteria is to amorphous materials used as the dielectric layers of electronic devices. As pointed out by Goldman et al. (1995), the origin of anomalous diffusion is different in glasses from its origin in general random systems, such as porous media and composites. In the case of glasses, the glass transition is modeled as a percolation problem and the origin of anomalous diffusion is hypothesized to be liquid-like clusters frozen into the glass. As a result, for dense amorphous dielectrics (glasses) the correlation length, on the order of nanometers (Jagannathan et al., 1989), is smaller than it is for many random media. Considering the order of magnitude of diffusivity for dielectrics, $\alpha \sim O(10^{-7}$ m^2/s), anomalous diffusion is expected on the picosecond time scale in these materials (in other words, for $t < t_\xi = \xi^2/\alpha \sim O$ (10 ps)). Since the origin of application of percolation theory is different in these materials and on this time scale other factors may become significant, it is important to examine the impact of anomalous diffusion in amorphous dielectric layers.

A common situation is a metallized layer of silicon dioxide. In this case a thin metallic film is deposited onto the dielectric, and laser material processing of this film may be required. Since the transport of heat into the dielectric will significantly affect the processing temperature of the film, it is important to examine the effect of anomalous diffusion on energy transport into the dielectric. The relevant dimensions and material properties for this situation are shown in Fig. 5. If the spot size of the laser is large compared to the optical penetration depth of the film, as will generally be the case, the heat transfer problem can be considered to be one-dimensional in the direction perpendicular to the film.

If the metal film is relatively thick, heat transport in the picosecond range will be dominated by the transport of energy

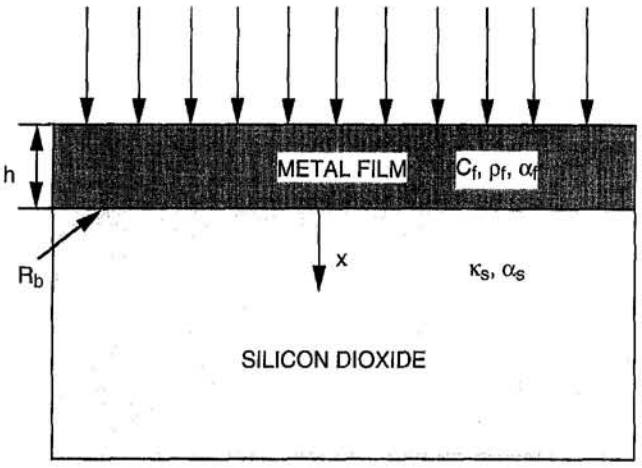


Fig. 5 Schematic of sample for calculations

Downloaded 11 Dec 2010 to 193.140.21.150. Redistribution subject to ASME license or copyright; see http://www.asme.org/terms/Terms_Use.cfm

through the film. If the film is thin, on the other hand, and quickly comes to thermal equilibrium after heating by a short pulse laser (assuming the film is at least as thick as the skin depth of the metal), this film may act as a short time-scale heating source for the dielectric.

This situation was examined experimentally by Young et al. (1986). A 16 nm gold film was evaporated onto silicon dioxide samples, which were pulse heated by a 0.1 nJ laser pulse of 0.2 ps duration. By observing the transient change in reflectivity of the gold film, they were able to determine the transient temperature behavior of the film on a picosecond time scale. The thin film, with its low heat capacity, was designed to serve as both a heat source and a thermometer for the silicon dioxide with picosecond resolution. Rather than obtaining a picosecond resolution temporal profile of the silicon dioxide surface temperature, however, they found that the cooling curve over the period up to a few hundred picoseconds was dominated by the thermal boundary resistance at the gold-silicon dioxide interface. By a curve fit to the data, the thermal boundary resistance was calculated to be 1.45×10^{-8} m^{2}K/W, which is larger than the acoustic mismatch theory (Little, 1959) value by more than two orders of magnitude. This value is close to the results observed experimentally by Swartz and Pohl (1987), however, and recently, Käding et al. (1994) showed that the thermal boundary resistance between silicon dioxide and a metal coating was comparable to the internal resistance of the dielectric film. These studies show that thermal boundary resistance should be considered when determining the impact of anomalous diffusion in metallized amorphous dielectric layers.

The following equations govern the cooling of a thin metal film, taking into consideration the thermal boundary resistance and the diffusivity of the underlying layer (Stoner and Maris, 1993):

$$\rho_f C_f h \frac{\partial T_f(t)}{\partial t} = -\sigma_K (T_f(t) - T_s(t, 0)) \tag{14}$$

$$\frac{\partial T_s(t, x)}{\partial t} = \alpha_s \frac{\partial^2 T_s(t, x)}{\partial x^2}, \tag{15}$$

where T_f and T_s are the temperature of the film and the substrate, respectively, α_s is the diffusivity of the substrate, C_f is the specific heat of the film, ρ_f is the density of the film, h is the thickness of the film, and σ_K is the Kapitza conductance, or the inverse, $1/R_b$, of the thermal boundary resistance between the film and the substrate. Hyperbolic non-Fourier effects are neglected in Eq. (15) since the time scale is well over an order of magnitude greater than the phonon relaxation time, $\tau_{ph} = 3\alpha/v^2 \sim 7 \times 10^{-14}$ s (Vedavarz et al., 1994). The initial and boundary conditions are

$$T_f(0) = \frac{E}{\rho_f C_f A_l h} \tag{16}$$

$$T_s(0, 0) = T_i = 300\ K \tag{17}$$

$$T_s(t, \infty) = T_i = 300\ K \tag{18}$$

$$-\kappa_s \left.\frac{\partial T}{\partial x}\right|_{x=0} = \sigma_K (T_f - T_s(x = 0)), \tag{19}$$

where E is the total laser pulse energy, κ_s is the thermal conductivity of the substrate, A_l is the beam spot area, and h is the thickness of the thin film that has obtained a uniform temperature.

If consideration of anomalous diffusion in the silicon dioxide substrate is taken, using Eq. (4) in the heat equation, the diffusivity is time dependent,

$$\alpha_s = D \propto t^{d_f/D_f - 1}, \tag{20}$$

for times $t \ll t_\xi$ and is constant for times $t \gg t_\xi$. The value for all times is achieved by use of a scaling function of time, correlation length, and cluster length that has been fitted to data and to asymptotically approach

$$\alpha_s = A t^{d_f/D_f - 1} \quad \text{for} \quad t \ll t_\xi \tag{21}$$

and

$$\alpha_s = \text{const} = \alpha_{\text{bulk}} \quad \text{for} \quad t \gg t_\xi. \tag{22}$$

For the calculations that follow, it was assumed that Eq. (21) applied for times $t \leq t_\xi$ and Eq. (22) applied for $t \geq t_\xi$. The constant A was first taken so that the two values would be equal at $t = t_\xi$, and then was varied substantially to determine that this assumption had little effect on the results. Since the diffusivity is time dependent, it is possible that both the specific heat and thermal conductivity are time dependent, thus affecting the boundary condition in Eq. (19). Calculations were performed by first assuming the thermal conductivity was constant and then assuming that it had the same time dependence as the diffusivity. The calculations proved to be very insensitive to both the value of A and the time dependence of κ_s.

Equations (14) and (15) were solved numerically by finite differences using the explicit scheme in time for Eq. (14) and the Crank–Nicholson scheme for Eq. (15). Both of the schemes are second order accurate, $O(\Delta x^2)$, in space. The explicit scheme is first-order accurate, $O(\Delta t)$, in time, while the Crank–Nicholson scheme is second-order accurate, $O(\Delta t^2)$, in time. A central difference, which is second-order accurate, $O(\Delta x^2)$, was used for the last boundary condition, given in Eq. (19). Grid sizes of $\Delta x = 1 \times 10^{-10}$ m and $\Delta t = 1 \times 10^{-12}$ s were used. When the grid size was doubled, the difference between the two solutions was less than 0.2 percent.

Calculations were performed for silicon dioxide with a 16 nm gold film using the value of thermal boundary resistance from the curve fit of Young et al. (1986), $R_b = 1.45 \times 10^{-8}$ m^2 K/W. The results including and not including anomalous diffusion are shown in Fig. 6, where it can be seen that the two profiles are essentially identical. For the anomalous diffusion case, a crossover time from anomalous to normal behavior of $t_\xi = \xi^2/\alpha = \sim 5$ ps was calculated using a 2 nm correlation length (Jagannathan et al., 1989) and a diffusivity $\alpha_s \sim 8 \times 10^{-7}$ m^2/s. Unlike the situation of an "instantaneous" source (Goldman et al., 1995), anomalous diffusion has essentially no impact on the transient surface temperature behavior. This is because the film temperature decay time due to the thermal boundary resistance alone is

$$\tau = \rho_f C_f h R_b = 580 \text{ ps}, \tag{23}$$

using the values $\rho_f = 19{,}320$ kg/m^3, $C_f = 129$ J/kg-K, and $h = 16$ nm for gold. In this case, the laser-heated gold is not an

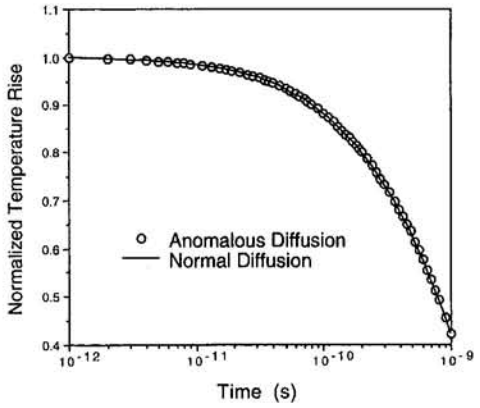


Fig. 6 Transient temperature of a gold thin film on silicon dioxide with and without anomalous diffusion effects

Downloaded 11 Dec 2010 to 193.140.21.150. Redistribution subject to ASME license or copyright; see http://www.asme.org/terms/Terms_Use.cfm

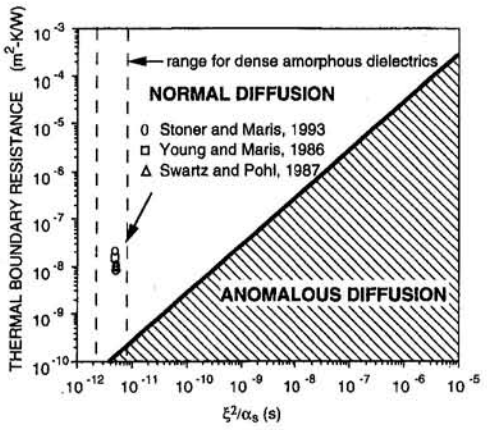


Fig. 7 Importance of anomalous diffusion versus thermal boundary resistance for metallized amorphous dielectrics

"instantaneous" source on the picosecond time scale, but a time-dependent source. The characteristic time of this heating is one to two orders of magnitude greater than the time scale on which anomalous diffusion occurs, so the transient heating dominates the problem.

For anomalous diffusion to be a factor, the thermal boundary resistance would have to be two orders of magnitude less than the value used above. That would require approaching the acoustic mismatch theory value. Swartz and Pohl (1987) have found that even crystalline materials deviate from values predicted by the acoustic mismatch theory by at least an order of magnitude at room temperature and have hypothesized that this is due to the presence of a thin amorphous layer formed at the interface that scatters phonons. It is therefore unlikely that this ideal value of thermal boundary resistance would be approached by a metal film on an amorphous substrate.

These results indicate that not only does the laser–material interaction time need to be small compared to the time range over which anomalous diffusion occurs, but also two further criteria must be met for anomalous diffusion to be significant in metallized dielectrics. The thermal response of the film and the film temperature decay time due to thermal boundary resistance, given in Eq. (23), must be less than the crossover time for anomalous diffusion, as given by

$$\frac{h^2}{\alpha_f} < t_\xi = \frac{\xi^2}{\alpha_s}, \tag{24}$$

and

$$\tau = \rho_f R_b C_f h < t_\xi = \frac{\xi^2}{\alpha_s}. \tag{25}$$

The second limit is plotted in Fig. 7 along with values of thermal boundary resistance from available data. It should be noted that most of these data are for metal films on crystalline dielectrics. As can be seen from the figure, anomalous diffusion will not be a significant factor for metallized dielectric layers for the interface conditions possible with current and near-future process technology. These limits apply to general random media as well, if a continuous, absorbing thin film can be formed on the surface and the thermal boundary resistance of the interface is determined.

Conclusions

Percolation theory has been applied to examine short-time-scale transport in random media. It is shown that there are three regimes of heat transport that correspond to transport over the basic percolation unit (particle), the fractal cluster, and the homogeneous medium. Time scaling shows that anomalous diffusion occurs at times between an upper and lower bound determined by both the material properties and structure. Anomalous diffusion is found to have a sizable effect in materials whose average void size is much larger than the average particle size or whose bulk diffusivity is less than that of the constituent particles, both of which occur in materials such as carbon aerogels. Characteristic time and length scales of anomalous diffusion were compared to those important in situations involving thermal radiation and thermal boundary resistance. Anomalous diffusion is predicted to be important in absorbing materials whose optical penetration depth is less than the correlation length, while both the upper and lower limits of the anomalous diffusion regime are observed in materials whose constituent particles' optical penetration depth is less than the average particle diameter. In dense amorphous materials, where anomalous diffusion is predicted on the picosecond time scale, it is shown that the impact of anomalous diffusion is expected to be small in situations where the thermal boundary resistance is important.

References

Alexander, S., and Orbach, R., 1982, "Density of States on Fractals: Fractons," *J. Phys. Lett.*, Vol. 43, pp. L625–631.

Bunde, A., and Havlin, S., 1991, "Percolation I," *Fractals and Disordered Systems*, A. Bunde and S. Havlin, eds., Springer-Verlag, New York, pp. 51–96.

de Gennes, P. G., 1976, "La Percolation: un Concept Unificateur," *La Recherché*, Vol. 7, pp. 919–927.

Fournier, D., and Boccara, A. C., 1989, "Heterogeneous Media and Rough Surfaces: A Fractal Approach for Heat Diffusion Studies," *Physica A*, Vol. 157, pp. 587–592.

Gefen, Y., Aharony, A., and Alexander, S., 1983, "Anomalous Diffusion on Percolating Clusters," *Phys. Rev. Lett.*, Vol. 50, pp. 77–80.

Goldman, C. H., Norris, P. M., and Tien, C. L., 1995, "Picosecond Energy Transport in Amorphous Materials," *Proc. 1995 ASME/JSME Thermal Engineering Joint Conference*, Vol. 1, pp. 467–473.

Havlin, S., and Bunde, A., 1991, "Percolation II," *Fractals and Disordered Systems*, A. Bunde and S. Havlin, eds., Springer-Verlag, New York, pp. 97–150.

Jagannathan, A., Orbach, R., and Entin-Wohlman, O., 1989, "Thermal Conductivity of Amorphous Materials Above the Plateau," *Phys. Rev. B*, Vol. 39, pp. 13465–13477.

Käding, O. W., Skurk, H., and K. E. Goodson, 1994, "Thermal Conduction in Metallized Silicon-Dioxide Layers on Silicon," *Appl. Phys. Lett.*, Vol. 65, pp. 1629–1631.

Kittel, C., 1986, *Introduction to Solid State Physics*, 6th ed., Wiley, New York, pp. 495–511.

Little, W. A., 1959, "The Transport of Heat Between Dissimilar Solids at Low Temperature," *Can. J. Phys.*, Vol. 37, pp. 334–349.

Lu, X., Nilsson, O., Fricke, J., and Pekala, R. W., 1993, "Thermal and Electrical Conductivity of Monolithic Carbon Aerogels," *J. Appl. Phys.*, Vol. 73, pp. 581–584.

Mandelbrot, B. B., 1977, *Fractals: Form, Chance, and Dimension*, Freeman, San Francisco.

Qiu, T. Q., and Tien, C. L., 1993, "Heat Transfer Mechanisms During Short-Pulse Laser Heating of Metals," ASME JOURNAL OF HEAT TRANSFER, Vol. 115, pp. 835–841.

Richter, K., Norris, P. M., and Tien, C. L., 1995, "Aerogels: Applications, Structure, and Heat Transfer Phenomena," *Annual Review of Heat Transfer*, Vol. VI, pp. 61–114.

Stoner, R. J., and Maris, H. J., 1993, "Kapitza Conductance and Heat Flow Between Solids at Temperatures From 50 to 300 K," *Phys. Rev. B*, Vol. 48, pp. 16373–16387.

Swartz, E. T., and Pohl, R. O., 1987, "Thermal Resistance at Interfaces," *Appl. Phys. Lett.*, Vol. 51, pp. 2200–2202.

Vedavarz, A., Kumar, S., and Moallemi, M. K., 1994, "Significance of Non-Fourier Heat Waves in Conduction," ASME JOURNAL OF HEAT TRANSFER, Vol. 116, pp. 221–224.

von der Linde, D., 1993, "Ultrashort Interactions in Solids," *Ultrashort Laser Pulses: Generation and Applications*, 2nd ed., W. Kaiser, ed., Springer-Verlag, New York, pp. 113–182.

Weil, R., Deutscher, G., Zallen, R., and Adler, J., eds., 1983, *Percolation Structures and Processes* (Annals of the Israel Physical Society: Vol. 5), Adam Hilger, Bristol, United Kingdom.

Young, D. A., Thomsen, C., Grahn, H. T., Maris, H. J., and Tauc, J., 1986, "Heat Flow in Glasses on a Picosecond Timescale," *Phonon Scattering in Condensed Matter V*, A. C. Anderson, and J. P. Wolfe, eds., Springer-Verlag, Berlin, pp. 49–51.

Zallen, R., 1983, *The Physics of Amorphous Solids*, Wiley, New York.

Downloaded 11 Dec 2010 to 193.140.21.150. Redistribution subject to ASME license or copyright; see http://www.asme.org/terms/Terms_Use.cfm

Journal of Heat Transfer

Technical Notes

This section contains shorter technical papers. These shorter papers will be subjected to the same review process as that for full papers.

Correlation for Opposing Flow, Mixed Convection Heat Transfer in a Vertical Tube With Constant Wall Temperature

D. D. Joye[1]

Nomenclature

- C_p = fluid heat capacity, kJ/(kg-K)
- D = tube diameter, m
- g = gravitational acceleration, m/s^2
- Gr_{bD} = Grashof number based on properties evaluated at the average bulk fluid temperature and tube diameter = $\rho^2 g D^3 \beta \Delta T/\mu^2$
- Gz = Graetz number = wC_p/kL
- h = film heat transfer coefficient, W/(m^2-K)
- k = fluid thermal conductivity, W/(m-K)
- L = heated length of tube, m
- Nu = Nusselt number = hD/k
- Pr = Prandtl number = $\mu C_p/k$
- Re = Reynolds number = $Dv\rho/\mu$
- T = temperature, K
- ΔT = temperature difference (K) average wall to average bulk fluid for Grashof number, unless otherwise noted
- v = average fluid velocity, m/s
- w = mass flow rate, kg/s
- β = volume expansivity, 1/K
- μ = viscosity, Pa·s
- ρ = density, kg/m^3
- ϕ_v = viscosity correction factor = μ/μ_w

Subscripts

- b = fluid properties evaluated at the bulk average temperature
- D = (Grashof number) evaluated with tube diameter as the characteristic length
- f = fluid properties evaluated at the average film temperature ((average wall temperature + bulk average fluid temperature)/2)
- w = fluid properties evaluated at the average wall temperature

[1] Department of Chemical Engineering, Villanova University, Villanova, PA 19085-1681.

Contributed by the Heat Transfer Division of THE AMERICAN SOCIETY OF MECHANICAL ENGINEERS. Manuscript received by the Heat Transfer Division September 14, 1995; revision received April 24, 1996. Keywords: Heat Exchangers, Mixed Convection, Modeling and Scaling. Associate Technical Editor: A. S. Lavine.

Introduction

The correlations of Jackson and Fewster (presented by Jackson et al., 1989) and Swanson and Catton (1987) have been shown to be useful in opposing flow, vertical mixed convection heat transfer in a tube with uniform heat flux (UHF) boundary conditions. In the Swanson and Catton theory, the UHF boundary condition is specific. The method of Churchill (1983) for "turbulent" mixed convection in the opposing flow case in a vertical tube is a close equivalent to the above-mentioned two more recent correlations. All three correlations can be used with confidence for constant wall temperature (CWT) boundary conditions only if the Reynolds number is above about 4000 (Joye, 1996a, b). This cut-off is Grashof number sensitive, but the dependence is not very strong. Below this Reynolds number the boundary condition becomes critical, and the data fall into the asymptote region discussed in some detail by Martinelli et al. (1942) and McAdams (1954).

One way to use the Jackson and Fewster or the Swanson and Catton correlation for process design situations, which are mostly CWT boundary conditions, is to use a critical Reynolds number to differentiate which equation to use. If Reynolds number is below critical, the asymptote equation should be used; if it is above, then the Jackson and Fewster or the Swanson and Catton correlation, or the Churchill method can be used. The critical Reynolds number is a function of Grashof number and Prandtl number (Joye, 1996b) as shown below:

$$Re_{crit} = 0.36\,(Gr_{bD}[L/D]^3)^{1/3}/Pr^{2/3} = 0.36\,Gr_{bL}^{1/3}/Pr^{2/3} \quad (1)$$

As an alternative one could try to combine an already existing correlation with the asymptote equation in an attempt to arrive at a generally valid equation for CWT boundary conditions under all flows and heating conditions. That is the goal of the present work.

Theory

The correlation of Jackson and Fewster is given below:

$$Nu/Nu(forced) = (1 + 4500\,Gr_{barD}/Re^{2.625}\,Pr^{0.5})_b^{0.31} \quad (2)$$

where the subscript "b" refers to properties evaluated at the bulk average temperature, and Gr_{barD} is defined by the integrated density term:

$$Gr_{barD} = \rho(\rho - \rho_{bar})gD^3/\mu^2 \quad (3)$$

Copyright © 1996 by ASME

Downloaded 11 Dec 2010 to 193.140.21.150. Redistribution subject to ASME license or copyright; see http://www.asme.org/terms/Terms_Use.cfm

and

$$\rho_{\text{bar}} = \left(\int_{T_w}^{T_b} \rho dT\right)/(T_w - T_b) \tag{4}$$

and the forced flow model is the Petukhov–Kirillov model given by the following:

$$\text{Nu(forced)} = \frac{\text{Re Pr}C_f/2}{12.7(\sqrt{C_f/2})(\text{Pr}^{2/3} - 1) + 1.07} \tag{5}$$

where

$$C_f = 1/(3.64 \log_{10} \text{Re} - 3.28)^2 \tag{6}$$

The correlation of Swanson and Catton (1987) for flow in vertical channels of rectangular cross section is shown below. This has an additional term and slightly different Prandtl number dependence. The Reynolds number formulation originally contained the well-known hydraulic diameter, thus this equation is also applicable to flow in tubes:

$$\text{Nu} = 0.0115\ \text{Re}^{0.8}\ \text{Pr}^{0.5}\{1 + [1 - (696/\text{Re}^{0.8}) + 8300\ \text{Gr}/\text{Re}^{2.6}(\text{Pr}^{0.5} + 1)]^{0.39}\} \tag{7}$$

These correlations use, as a base case, the turbulent forced-flow only correlation from which increases in heat transfer due to natural convection effects can be followed. The Sieder–Tate equation with viscosity correction (Holman, 1990) is often preferred as the base case,

$$\text{Nu}/\text{Pr}^{1/3}\phi_v^{0.14} = 0.023\ \text{Re}^{0.8} \tag{8}$$

For heating situations the viscosity correction factor, ϕ_v, is often folded into a slightly different power for Pr. The Swanson and Catton base case shows this preference; Jackson and Fewster choose the Petukhov–Kirillov relationship, which differs only slightly from the Sieder–Tate. Thus, the base cases are all comparable.

Martinelli et al. (1942) and McAdams (1954) both show an asymptotic relationship for constant wall temperature (CWT) conditions at low Reynolds numbers. This is a result of losing ΔT driving force at the exit, and consequently would not be expected to hold for uniform heat flux (UHF) experiments, which maintains ΔT driving force. The asymptote equation takes various forms, but fundamentally it is

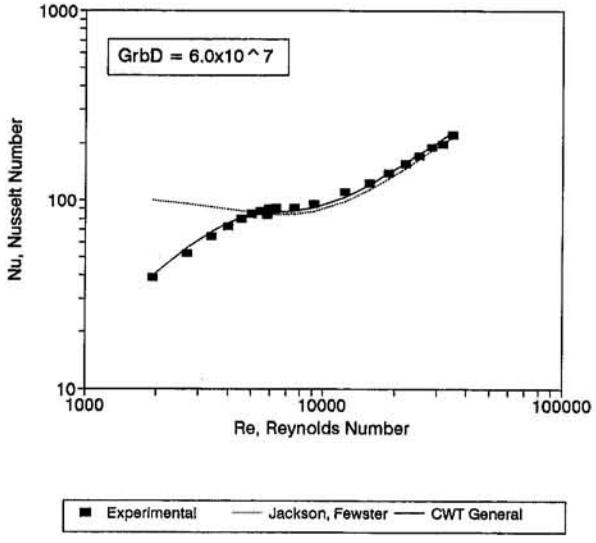


Fig. 1 Downflow heating data compared with correlation of Jackson and Fewster and the general correlation. Shell-side steam pressure = 345 kPa abs. ($Gr_{bD} = 6.0 \times 10^7$).

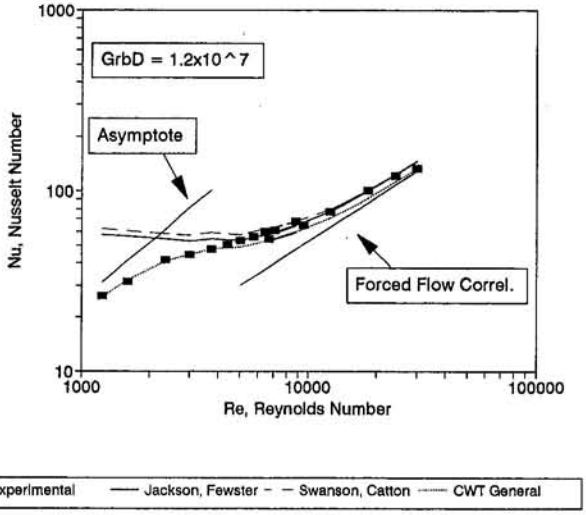


Fig. 2 Downflow heating data compared with correlations of Jackson and Fewster, Swanson and Catton, and the general correlation. Shell-side steam pressure = 67 kPa abs. ($Gr_{bD} = 1.2 \times 10^7$).

$$\text{Nu}_{\text{asymptote}} = (2/\pi)\text{Gz} \tag{9}$$

where Gz is the well-known Graetz number. When Re is used as an independent parameter as we prefer, the asymptote is also Prandtl-number dependent:

$$\text{Nu}_{\text{asymptote}} = 0.5\ \text{Re Pr}D/L \tag{10}$$

which translates to

$$\text{Nu}_{\text{asymptote}}/\text{Pr}^{1/3}\phi_v^{0.14} = 0.5\ \text{Re Pr}^{2/3}D/L \tag{11}$$

in the equivalent Sieder–Tate style formulation.

Alternatively, the Churchill method (1983) could be used in the same way, but because of its formulation, the algebra required to reduce the resulting expression to manageable form is very much more complicated, and the present formulation with this correlation would be more difficult to use.

General Correlation for CWT Boundary Condition

The Jackson and Fewster correlation appears somewhat simpler to use than the Swanson and Catton, because it has one less term, but the base case is much more complex, and the Grashof number calculation is not simple. The predictive ability of each equation under CWT boundary condition is shown in the figures and for other Grashof numbers by Joye (1996a, b) and Wojnovich (1995). Both correlations predict quite well for Reynolds numbers above about 4000.

In Fig. 1 the Jackson and Fewster line should bend into the asymptote along with the data, but it does not, because it was developed for UHF boundary condition, not CWT, and the low Reynolds number is the area where this makes a difference. The correlations take no notice of the asymptote, which does not exist for uniform heat flux conditions. Under such conditions, driving force temperature difference is always maintained, because the driving force temperature difference takes a value consistent with the heat flux, which is constant. In order to transfer heat to the fluid whose temperature is rising, the wall temperature must also rise; therefore, the outlet temperature can never approach the wall temperature under the UHF boundary condition.

The asymptote equation governs the low-Reynolds-number region for CWT boundary condition, but the data do not make a sharp transition. Thus, it might be preferred to have one equation that follows the data more closely. We found this by trying various combinations and testing for goodness of fit. The fol-

Downloaded 11 Dec 2010 to 193.140.21.150. Redistribution subject to ASME license or copyright; see http://www.asme.org/terms/Terms_Use.cfm

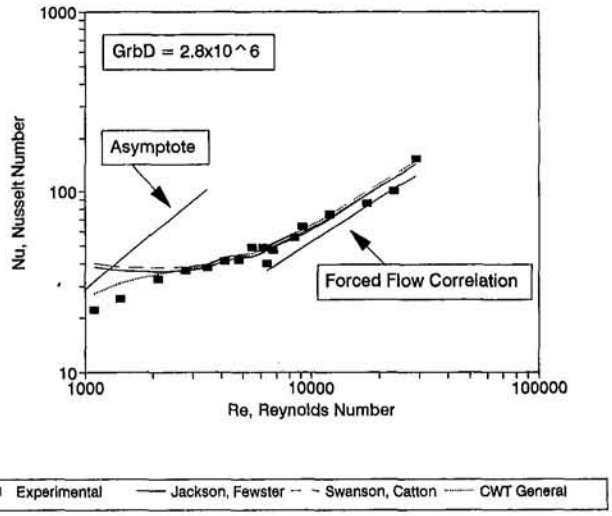


Fig. 3 Downflow heating data compared with correlations of Jackson and Fewster, Swanson and Catton, and the general correlation. Shell-side steam pressure = 30 kPa abs. ($Gr_{bD} = 2.8 \times 10^6$).

lowing is what finally seems to work best, as illustrated in Figs. 1–3:

$$Nu/Nu_{ff} = \{(1/(1 + 2984\ Gr/Re^{2.625}\ Pr^{0.5})^{0.31})^3 + (1/21.7\ Re^{0.2}Pr^{0.5})^3\}^{-1/3} \quad (12)$$

where

$$Nu_{ff} = 0.023\ Re^{0.8}\ Pr^{0.5} \quad (13)$$

Equation (12) was obtained by combining the enhancement factors for a modified Jackson and Fewster correlation and the asymptote. We used the enhancement factor from Jackson and Fewster and modified the constant multiplying the Grashof number, since the Grashof number was changed from Jackson's definition to one based on the bulk average fluid temperature. Thus, all dimensionless groups are calculated on the same temperature basis. In our data (Wojnovich, 1995) we calculated Grashof number both ways, so we were able to make the change easily. The asymptote equation also had to be reformulated as a multiple of the base case (Nu_{ff}), so that both enhancement factors were on the same basis.

Summing the enhancement factors to obtain a general formula cannot work, because, as Re is decreased, the Nusselt number data show a downward trend, rather than an increase. By plotting the inverses, however, one could see that the contributions should be additive. Various forms of adding the inverses were tried, until taking the cube root of the sum of the cubes of the inverses yielded an excellent fit, as seen in Figs. 1–3. The Grashof numbers in these figures are the two extreme values and one in the middle from our data (Wojnovich, 1995), which have experimental uncertainty of better than ±10 percent at the high Grashof numbers to ±25 percent at the lowest. The reasons are discussed in the references cited. The sum of the cubes principle has also been used successfully in external mixed convection flows (Churchill, 1977; Chen et al., 1986).

The identical method can be used for the enhancement factor of the Swanson and Catton correlation. In that case the first term under the cube root in the denominator of Eq. (12) becomes

$$\{2/(1 + [1 - (696/Re^{0.8}) + 8300\ Gr/Re^{2.6}(Pr^{0.5} + 1)]^{0.39})\}^3 \quad (14)$$

The "2" is needed in the numerator of Eq. (14), because the Swanson and Catton base case is $\frac{1}{2}$ of Nu_{ff} of Eq. (13).

Figures 1–3 show an excellent fit of Eq. (12) to the data. This was consistent with our data at still other Grashof numbers, although the data were sometimes a bit low, as in the two lowest points of Fig. 3. Equation (12) or its modification by substituting Eq. (14) for the Jackson and Fewster term should have good general application, since the range of Gr and Re is broad.

Although our data were obtained with water, the correlation of Swanson and Catton was obtained with refrigerant 113, and the correlation of Jackson and Fewster used data from several sources including data on air. Direct comparison of the data is not generally possible, because various investigators use different bases for calculating their correlating parameters. Thus, the correlations themselves were used (even these had to be modified) in the present method.

References

Chen, T. S., Armaly, B. F., and Ramachandran, N., 1986, "Correlations for Laminar Mixed Convection Flows on Vertical, Inclined, and Horizontal Flat Plates," ASME JOURNAL OF HEAT TRANSFER, Vol. 108, pp. 835–840.

Churchill, S. W., 1977, "A Comprehensive Correlating Equation for Laminar, Assisting, Forced and Free Convection," *AIChE J.*, Vol. 23, No. 1, pp. 10–16.

Churchill, S. W., 1983, "Combined Free and Forced Convection in Channels," *Heat Transfer Design Handbook*, E. Schlünder, ed., Section 2.5.10, Hemisphere, NY.

Holman, J. P., 1990, *Heat Transfer*, 7th ed., McGraw-Hill, New York.

Jackson, J. D., Cotton, M. A., and Axcell, B. P., 1989, "Studies of Mixed Convection in Vertical Tubes: A Review," *Int. J. Heat Fluid Flow*, Vol. 10, No. 1, pp. 2–15.

Joye, D. D., 1996a, "Comparison of Correlations and Experiment in Opposing Flow, Mixed Convection Heat Transfer in a Vertical Tube With Grashof Number Variation," *Int. J. Heat Mass Transfer*, Vol. 39, No. 5, pp. 1033–1038.

Joye, D. D., 1996b, "Design Criterion for Heat Transfer Coefficient in Opposing Flow, Mixed Convection Heat Transfer in a Vertical Tube," *Ind. Eng. Chem. Research*, July, in press.

Martinelli, R. C., Southwell, C. J., Alves, G., Craig, H. L., Weinberg, E. B., Lansing, N. F., and Boelter, L. M. K., 1942, "Heat Transfer and Pressure Drop for a Fluid Flowing in the Viscous Region Through a Vertical Pipe," *Trans. Am. Inst. Chem. Eng.*, Vol. 38, pp. 493–530.

McAdams, W. H., 1954, *Heat Transmission*, 3rd ed., McGraw-Hill, New York, pp. 229–235.

Swanson, L. W., and Catton, I., 1987, "Surface Renewal Theory for Turbulent Mixed Convection in Vertical Ducts," *Int. J. Heat Mass Transfer*, Vol. 30, No. 11, pp. 2271–2279.

Wojnovich, M. J., 1995, "Mixed Convection Heat Transfer in a Vertical Tube With Grashof Number Variation and Heated Inlet Fluid," M. S. Thesis, Department of Chemical Engineering, Villanova University, Villanova, PA.

Integrals Involving Bickley and Bessel Functions in Radiative Transfer, and Generalized Exponential Integral Functions

Z. Altaç[1]

1 Introduction

In order to solve radiative transfer problems, one has to deal with either Boltzmann's equation for radiation intensity or the integral equation for incident energy. In some cases it is attractive to work with the radiative integral equation since it deals

[1] Associate Professor, Osmangazi University, School of Engineering and Architecture, Mechanical Engineering Department, 26030 Bademlik, Eskişehir, Turkey.

Contributed by the Heat Transfer Division of THE AMERICAN SOCIETY OF MECHANICAL ENGINEERS. Manuscript received by the Heat Transfer Division August 2, 1995; revision received March 12, 1996. Keywords: Radiation. Associate Technical Editor: B. W. Webb.

Downloaded 11 Dec 2010 to 193.140.21.150. Redistribution subject to ASME license or copyright; see http://www.asme.org/terms/Terms_Use.cfm

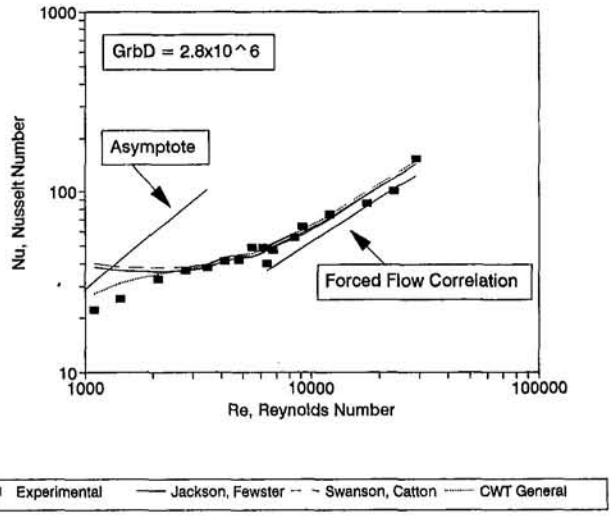


Fig. 3 Downflow heating data compared with correlations of Jackson and Fewster, Swanson and Catton, and the general correlation. Shell-side steam pressure = 30 kPa abs. ($Gr_{bD} = 2.8 \times 10^6$).

lowing is what finally seems to work best, as illustrated in Figs. 1–3:

$$Nu/Nu_{ff} = \{(1/(1 + 2984\ Gr/Re^{2.625}\ Pr^{0.5})^{0.31})^3 + (1/21.7\ Re^{0.2}Pr^{0.5})^3\}^{-1/3} \quad (12)$$

where

$$Nu_{ff} = 0.023\ Re^{0.8}\ Pr^{0.5} \quad (13)$$

Equation (12) was obtained by combining the enhancement factors for a modified Jackson and Fewster correlation and the asymptote. We used the enhancement factor from Jackson and Fewster and modified the constant multiplying the Grashof number, since the Grashof number was changed from Jackson's definition to one based on the bulk average fluid temperature. Thus, all dimensionless groups are calculated on the same temperature basis. In our data (Wojnovich, 1995) we calculated Grashof number both ways, so we were able to make the change easily. The asymptote equation also had to be reformulated as a multiple of the base case (Nu_{ff}), so that both enhancement factors were on the same basis.

Summing the enhancement factors to obtain a general formula cannot work, because, as Re is decreased, the Nusselt number data show a downward trend, rather than an increase. By plotting the inverses, however, one could see that the contributions should be additive. Various forms of adding the inverses were tried, until taking the cube root of the sum of the cubes of the inverses yielded an excellent fit, as seen in Figs. 1–3. The Grashof numbers in these figures are the two extreme values and one in the middle from our data (Wojnovich, 1995), which have experimental uncertainty of better than ±10 percent at the high Grashof numbers to ±25 percent at the lowest. The reasons are discussed in the references cited. The sum of the cubes principle has also been used successfully in external mixed convection flows (Churchill, 1977; Chen et al., 1986).

The identical method can be used for the enhancement factor of the Swanson and Catton correlation. In that case the first term under the cube root in the denominator of Eq. (12) becomes

$$\{2/(1 + [1 - (696/Re^{0.8}) + 8300\ Gr/Re^{2.6}(Pr^{0.5} + 1)]^{0.39})\}^3 \quad (14)$$

The "2" is needed in the numerator of Eq. (14), because the Swanson and Catton base case is $\frac{1}{2}$ of Nu_{ff} of Eq. (13).

Figures 1–3 show an excellent fit of Eq. (12) to the data. This was consistent with our data at still other Grashof numbers, although the data were sometimes a bit low, as in the two lowest points of Fig. 3. Equation (12) or its modification by substituting Eq. (14) for the Jackson and Fewster term should have good general application, since the range of Gr and Re is broad.

Although our data were obtained with water, the correlation of Swanson and Catton was obtained with refrigerant 113, and the correlation of Jackson and Fewster used data from several sources including data on air. Direct comparison of the data is not generally possible, because various investigators use different bases for calculating their correlating parameters. Thus, the correlations themselves were used (even these had to be modified) in the present method.

References

Chen, T. S., Armaly, B. F., and Ramachandran, N., 1986, "Correlations for Laminar Mixed Convection Flows on Vertical, Inclined, and Horizontal Flat Plates," ASME JOURNAL OF HEAT TRANSFER, Vol. 108, pp. 835–840.

Churchill, S. W., 1977, "A Comprehensive Correlating Equation for Laminar, Assisting, Forced and Free Convection," *AIChE J.*, Vol. 23, No. 1, pp. 10–16.

Churchill, S. W., 1983, "Combined Free and Forced Convection in Channels," *Heat Transfer Design Handbook*, E. Schlünder, ed., Section 2.5.10, Hemisphere, NY.

Holman, J. P., 1990, *Heat Transfer*, 7th ed., McGraw-Hill, New York.

Jackson, J. D., Cotton, M. A., and Axcell, B. P., 1989, "Studies of Mixed Convection in Vertical Tubes: A Review," *Int. J. Heat Fluid Flow*, Vol. 10, No. 1, pp. 2–15.

Joye, D. D., 1996a, "Comparison of Correlations and Experiment in Opposing Flow, Mixed Convection Heat Transfer in a Vertical Tube With Grashof Number Variation," *Int. J. Heat Mass Transfer*, Vol. 39, No. 5, pp. 1033–1038.

Joye, D. D., 1996b, "Design Criterion for Heat Transfer Coefficient in Opposing Flow, Mixed Convection Heat Transfer in a Vertical Tube," *Ind. Eng. Chem. Research*, July, in press.

Martinelli, R. C., Southwell, C. J., Alves, G., Craig, H. L., Weinberg, E. B., Lansing, N. F., and Boelter, L. M. K., 1942, "Heat Transfer and Pressure Drop for a Fluid Flowing in the Viscous Region Through a Vertical Pipe," *Trans. Am. Inst. Chem. Eng.*, Vol. 38, pp. 493–530.

McAdams, W. H., 1954, *Heat Transmission*, 3rd ed., McGraw-Hill, New York, pp. 229–235.

Swanson, L. W., and Catton, I., 1987, "Surface Renewal Theory for Turbulent Mixed Convection in Vertical Ducts," *Int. J. Heat Mass Transfer*, Vol. 30, No. 11, pp. 2271–2279.

Wojnovich, M. J., 1995, "Mixed Convection Heat Transfer in a Vertical Tube With Grashof Number Variation and Heated Inlet Fluid," M. S. Thesis, Department of Chemical Engineering, Villanova University, Villanova, PA.

Integrals Involving Bickley and Bessel Functions in Radiative Transfer, and Generalized Exponential Integral Functions

Z. Altaç[1]

1 Introduction

In order to solve radiative transfer problems, one has to deal with either Boltzmann's equation for radiation intensity or the integral equation for incident energy. In some cases it is attractive to work with the radiative integral equation since it deals

[1] Associate Professor, Osmangazi University, School of Engineering and Architecture, Mechanical Engineering Department, 26030 Bademlik, Eskişehir, Turkey.

Contributed by the Heat Transfer Division of THE AMERICAN SOCIETY OF MECHANICAL ENGINEERS. Manuscript received by the Heat Transfer Division August 2, 1995; revision received March 12, 1996. Keywords: Radiation. Associate Technical Editor: B. W. Webb.

Copyright © 1996 by ASME

Downloaded 11 Dec 2010 to 193.140.21.150. Redistribution subject to ASME license or copyright; see http://www.asme.org/terms/Terms_Use.cfm

with spatial variables only. The transport kernels are in the form of integrals of modified Bessel and Bickley functions (Razzaque et al., 1984; Heaslet and Warming, 1966; Crosbie and Koewing, 1977; Carlson and Lathrop, 1968; Echigo et al., 1972). On the other hand, solution of transport equation requires inversion of dense matrices. In establishing the matrix, depending on the spatial grids, many kernel evaluations might be required. This results in too many calls to subprograms that evaluate Bickley and/or Bessel functions, which may take significant run times.

Another method for evaluating the integrals, in addition to numerical integration, involves interpolation of already computed and stored values. For large values of arguments and orders computer memory requirements may be quite large.

Use of series expansions that yield exact integrals clearly will reduce the computation time in evaluating the integrals since only one or a few function calls will be needed. In addition, they can provide a form that can be used to compute the integrals to desired significant degree of accuracy.

It may be appropriate to point out here that there seems to be an oversight in previous papers that have used the radiative integral transfer approach; that is, functions in Cartesian x–y geometry (which are Bickley functions) have been referred to as S_n functions (Breig and Crosbie, 1974a; Yuen and Wong, 1983; Razzaque et al., 1984; Yuen and Takara, 1988; Wu and Ou, 1994). The S_n functions Breig and Crosbie (1974a, b), and Razzaque et al. (1984) correspond to Ki_{n+1}; on the other hand, Yuen and Takara (1988) and Wu and Ou's (1994) S_n definition correspond to $(2/\pi)Ki_n(x)$. Glatt and Olfe (1973) and Modest (1975) refer to a set of functions represented by f_n (or so-called exchange area integrals), which are also nth-order Bickley functions. Chung and Kim's (1984) geometric function can be expressed in terms of first-order Bickley function as $F_v(\tau) = 2Ki_1(\tau)/\tau$.

In literature, there is no agreement on the function's name either. Bickley (or so-called S_n) functions are referred to and misused as generalized exponential integral functions. There is another set of functions (ϵ_n), which are referred to as generalized exponential integral functions (Breig and Crosbie, 1974a, b; Crosbie and Koewing, 1977).

2 Integrals of Bickley Functions

In two-dimensional Cartesian geometries, the resulting integrals can be, in general, classified as:

$$Bis_n(x, \theta) = \int_0^\theta Ki_n(x \sec \alpha)(\cos \alpha)^{n-2} d\alpha, \quad (1)$$

and

$$Cis_n(x, \theta) = \int_0^\theta Ki_n(x \sec \alpha) \sin \alpha (\cos \alpha)^{n-3} d\alpha, \quad (2)$$

where Ki_n is the nth-order Bickley function. Properties and expansions can be found from Abramowitz and Stegun (1972), Milgram (1978), and Lewis and Miller (1984).

If we let f_n represent both Bis_n and Cis_n, f_n satisfies the following relations:

$$\frac{df_{n+1}}{dx} = -f_n(x) \quad \text{and} \quad f_{n+1} = \int_x^\infty f_n dx \quad (3)$$

For $0 < \theta < \pi/2$, the series expansions for Bis_3 is obtained as

$$Bis_3(x, \theta) = \frac{\pi}{4} \sin \theta - \theta\left(x - \frac{x^3}{6}\right) + \frac{\pi x^2}{4} \ln (\sec \theta + \tan \theta) + \frac{x^3 \tan \theta}{6}\left[\gamma - \frac{17}{6} + \ln\left(\frac{x}{2} \sec \theta\right)\right] + \left(\frac{x^3 \tan \theta}{2}\right)\left[\gamma + \ln\left(\frac{x}{2} \sec \theta\right)\right] \times \sum_{k=1}^{\infty} \frac{(x^2/4)^k A_k(\tan \theta)}{k!(k+1)!(2k+1)(2k+3)} - \left(\frac{x^3 \tan \theta}{4}\right) \times \sum_{k=1}^{\infty}\left[\frac{4k^2 + 2k - 1 + 2k(2k+1)(k+1)\Phi(k+1)}{k(k+1)!^2(2k+1)^2(2k+3)}\right] \times \left(\frac{x^2}{4}\right)^k A_k(\tan \theta) - \left(\frac{x^3 \tan \theta}{2}\right) \times \sum_{k=1}^{\infty} \frac{(x^2/4)^k A_k(\tan \theta)}{k!(k+1)!(2k+1)(2k+3)^2} - \left(\frac{x^3 \tan \theta}{4}\right) \times \sum_{k=1}^{\infty}\left[\frac{(\sec^2 \theta)^k + 4k^2 C_{k-1}(\tan \theta)}{kk!(k+1)!(2k+1)^2(2k+3)}\right]\left(\frac{x^2}{4}\right)^k, \quad (4)$$

where

$$\Phi(k+1) = 1 + \frac{1}{2} + \frac{1}{3} + \ldots + \frac{1}{k}, \quad (5)$$

and γ is the Euler constant. A_n and C_n in Eq. (4) satisfy the following recurrence relations:

$$(2n+1)A_n(x) = (1+x^2)^n + 2nA_{n-1}(x), \quad n \geq 1 \quad (6)$$

$$C_n(x) = \frac{1}{2n(2n+1)}[(1+x^2)^n - A_n(x) + 4n^2 C_{n-1}(x)], \quad n \geq 1 \quad (7)$$

with

$$A_0(x) = 1, \quad C_0(x) = 1 - \frac{\tan^{-1} x}{x}, \quad (8)$$

Here, expansion for only Bis_3 is given to save space, but lower and higher orders can be obtained by using the relations given in Eq. (3). As a special case, for $\theta = \pi/2$, Bis_n functions yield exponential integral functions (E_n); that is, $Bis_n(x, \pi/2) = (\pi/2)E_n(x)$.

Cis_n are found rather more simply, by integration of Eq. (2), in terms of Dis_n functions. Dis_n functions will be defined as

$$\frac{Dis_n(x)}{x^{n-1}} = \frac{1}{(n-1)!}\int_1^\infty (t-1)^{n-1} \frac{Ki_2(xt)}{t} dt, \quad n \geq 1 \quad (9)$$

where $Dis_0(x) = Ki_2(x)/x$. The series expansions for Dis_1 is found to be

$$Dis_1(x) = \frac{\pi}{2} x - \left[1 + \gamma + \ln\left(\frac{x}{2}\right)\right] + \left[\gamma + \ln\left(\frac{x}{2}\right)\right] \sum_{k=1}^{\infty} \frac{(x^2/4)^k}{(k!)^2(2k-1)} - \sum_{k=1}^{\infty}\left[\frac{1 + (2k-1)\Phi(k+1)}{(k!)^2(2k-1)^2}\right]\left(\frac{x^2}{4}\right)^k \quad (10)$$

This function also satisfies the relations given in Eq. (3).

Asymptotic expansions and recursive relation of Dis_n functions are found, respectively, to be

Downloaded 11 Dec 2010 to 193.140.21.150. Redistribution subject to ASME license or copyright; see http://www.asme.org/terms/Terms_Use.cfm

$$Dis_n(x) \approx \sqrt{\frac{\pi}{2x}}\frac{e^{-x}}{(x+n)} \times \left\{1 - \frac{(9+4n^2)}{8x} + \frac{4(111n^2 - 65n + 86)}{2!(8x)^2}\right\} \quad (11)$$

$$nDis_{n+1}(x) = Ki_{n+2}(x) - xDis_n(x), \quad n \geq 0 \quad (12)$$

In the light of these newly defined functions, Cis_n yield the following expression:

$$Cis_{n+1}(x, \theta) = Dis_n(x) - (\cos\theta)^{n-1} Dis_n(x \sec\theta) \quad (13)$$

3 Integrals of Bessel Functions

Kernels presented in this section are encountered in neutron and radiative transfer. Integrals of modified Bessel functions of interest (for $b > a$) can be defined as

$$\mathbf{K}_{n,m}(a, b) = \int_1^\infty I_n(ax)K_m(bx)\frac{dx}{x^{n+m}} \quad (14)$$

Series expansions are given as

$$\mathbf{K}_{0,0}(a, b) = \frac{\pi}{2}F\left(\frac{1}{2}, \frac{1}{2}; 1; \frac{a^2}{b^2}\right) + \left[\gamma + \ln\left(\frac{b}{2}\right)\right] \times \sum_{k=0}^{\infty}\frac{(b^2/4)^k}{(2k+1)}\sum_{m=0}^{k}\frac{(a^2/b^2)^m}{[m!(k-m)!]^2} - \sum_{k=0}^{\infty}\frac{(b^2/4)^k}{(2k+1)^2}\sum_{m=0}^{k}\frac{(a^2/b^2)^m}{[m!(k-m)!]^2} - \frac{b^2}{4}\sum_{k=0}^{\infty}\frac{(b^2/4)^k}{(2k+3)}\sum_{m=0}^{k}\frac{\Phi(m+2)(a^2/b^2)^{k-m}}{[(m+1)!(k-m)!]^2} \quad (15)$$

$$\mathbf{K}_{0,1}(a, b) = -\frac{\pi}{2}F\left(\frac{1}{2}, -\frac{1}{2}; 1; \frac{a^2}{b^2}\right) + \frac{1}{b} - \frac{b}{2}\left[\gamma + \ln\left(\frac{b}{2}\right)\right] \times \sum_{k=0}^{\infty}\frac{(b^2/4)^k}{(2k+1)}\sum_{m=0}^{k}\frac{(a^2/b^2)^m}{(m!)^2(k+1-m)!(k-m)!} + \frac{b}{2}\sum_{k=0}^{\infty}\frac{(b^2/4)^k}{(2k+1)^2}\sum_{m=0}^{k}\frac{(a^2/b^2)^m}{(m!)^2(k+1-m)!(k-m)!} - \frac{1}{b}\sum_{k=0}^{\infty}\frac{(a^2/4)^k}{(k!)^2(2k-1)} + \frac{b}{4}\sum_{k=0}^{\infty}\frac{(b^2/4)^k}{(2k+1)} \times \sum_{m=0}^{k}\frac{\{\Phi(k+1-m) + \Phi(k+2-m)\}(a^2/b^2)^m}{(m!)^2(k+1-m)!(k-m)!} \quad (16)$$

$$\mathbf{K}_{1,0}(a, b) = \frac{\pi a}{4b}F\left(\frac{1}{2}, \frac{1}{2}; 2; \frac{a^2}{b^2}\right) + \frac{a}{2}\left[\gamma + \ln\left(\frac{b}{2}\right)\right]\sum_{k=0}^{\infty}\frac{(b^2/4)^k}{(2k+1)} \times \sum_{m=0}^{k}\frac{(a^2/b^2)^m}{(k-m)!^2 m!(m+1)!} - \frac{a}{2}\sum_{k=0}^{\infty}\frac{(b^2/4)^k}{(2k+1)^2}\sum_{m=0}^{k}\frac{(a^2/b^2)^m}{(k-m)!^2 m!(m+1)!} - \frac{a}{2}\sum_{k=1}^{\infty}\frac{(b^2/4)^k}{(2k+1)}\sum_{m=1}^{k}\frac{\Phi(m+1)(a^2/b^2)^{k-m}}{(m!)^2(k+1-m)!(k-m)!} \quad (17)$$

$$\mathbf{K}_{1,1}(a, b) = \frac{a}{2b} - \frac{\pi a}{4}F\left(\frac{1}{2}, -\frac{1}{2}; 2; \frac{a^2}{b^2}\right) - \frac{ab}{4}\left[\gamma + \ln\left(\frac{b}{2}\right)\right] \times \sum_{k=0}^{\infty}\frac{(b^2/4)^k}{(2k+1)}\sum_{m=0}^{k}\frac{(a^2/b^2)^m}{m!(m+1)!(k-m)!(k+1-m)!} + \frac{ab}{4}\sum_{k=0}^{\infty}\frac{(b^2/4)^k}{(2k+1)^2} \times \sum_{m=0}^{k}\frac{(a^2/b^2)^m}{m!(m+1)!(k-m)!(k+1-m)!} - \frac{a}{2b}\sum_{k=1}^{\infty}\frac{(a^2/4)^k}{k!(k+1)!(2k-1)} + \frac{ab}{8}\sum_{k=0}^{\infty}\frac{(b^2/4)^k}{(2k+1)} \times \sum_{m=0}^{k}\frac{\{\Phi(k+1-m) + \Phi(k+2-m)\}(a^2/b^2)^m}{m!(m+1)!(k-m)!(k+1-m)!} \quad (18)$$

where F is the hypergeometric function.

Expansions for large arguments ($b > a > 1$) are obtained by using the asymptotic expansions of Bessel functions. Resulting expressions are given as follows:

$$\mathbf{K}_{0,0}(a, b) \approx \frac{1}{2\sqrt{ab}}\left\{E_1(b-a) + \frac{(b-a)}{8ab}E_2(b-a) + \frac{9(b-a)^2}{128a^2b^2}E_3(b-a)\right\} \quad (19)$$

The following expansions are valid for $b \geq a > 1$:

$$\mathbf{K}_{0,1}(a, b) \approx \frac{1}{2\sqrt{ab}}\left\{E_2(b-a) + \frac{(3a+b)}{8ab}E_3(b-a) + \frac{3(b-a)(5a+3b)}{128a^2b^2}E_4(b-a)\right\} \quad (20)$$

$$\mathbf{K}_{1,0}(a, b) \approx \frac{1}{2\sqrt{ab}}\left\{E_2(b-a) - \frac{(3b+a)}{8ab}E_3(b-a) - \frac{3(b-a)(3a+5b)}{128a^2b^2}E_4(b-a)\right\} \quad (21)$$

$$\mathbf{K}_{1,1}(a, b) \approx \frac{1}{2\sqrt{ab}}\left\{E_3(b-a) - \frac{3(b-a)}{8ab}E_4(b-a) + \frac{3(5a^2+6ab+5b^2)}{128a^2b^2}E_5(b-a)\right\} \quad (22)$$

4 Generalized Exponential Integral Functions

The nth-order generalized exponential integral function referred to by Breig and Crosbie (1974a) is indeed a generalized function. It has a general form

$$\epsilon_n(x, y) = \frac{1}{(n-1)!}\int_x^\infty (t-x)^{n-1} \times \frac{\exp(-\sqrt{t^2 + (xy)^2})}{\sqrt{t^2 + (xy)^2}}dt, \quad n \geq 1 \quad (23)$$

Downloaded 11 Dec 2010 to 193.140.21.150. Redistribution subject to ASME license or copyright; see http://www.asme.org/terms/Terms_Use.cfm

where $\epsilon_0(x, y) = \exp(-x\sqrt{1+y^2})/(x\sqrt{1+y^2})$. The tendency is to compute these integrals numerically as well (Breig and Crosbie, 1974b).

The series expansion for ϵ_1 is found to be

$$\epsilon_1(x, y) = (\ln 2 - \gamma) I_0(xy) + \sum_{k=1}^{\infty} \left(\frac{x^2y^2}{4}\right)^k \frac{\Phi(k+1)}{(k!)^2} + \sum_{k=0}^{\infty} \frac{D_k}{(2k+1)!} - \sum_{k=0}^{\infty} \frac{B_k}{(2k)!}, \quad (24)$$

where

$$B_n = \frac{1}{2n}\left[x^{2n}(\sqrt{1+y^2})^{2n-1} + (2n-1)x^2y^2B_{n-1}\right], \quad n \geq 1 \quad (25)$$

$$D_n = \frac{1}{2n+1}\left[x^{2n+1}(\sqrt{1+y^2})^{2n} + (2n)x^2y^2D_{n-1}\right], \quad n \geq 1 \quad (26)$$

with

$$D_0 = x, \quad B_0 = \ln(x + x\sqrt{1+y^2}) \quad (27)$$

Asymptotic expansion of ϵ_1 has been derived by Breig and Crosbie (1974b) and the recursive relation by Yuen and Wong (1983).

5 Discussion

Bis_n functions with small x and θ converge a solution with a few terms. Series expansions for Bis_n functions work well up to the value of $x \to 8$, which is adequate for most problems. Above this limit the number of terms that should be taken into account increases and thus the round-off errors. This becomes very important since Bis_n functions approach zero with increasing x. Above this limit double precision programming is recommended. A single asymptotic expansions that covers all angles could not be obtained and turn out to be a bit complicated.

In addition to series expansion for Dis_1 functions, asymptotic expansions have been provided and can be used for $x > 6$. Relative percent errors for $x = 5$ are about 1–3 percent; for $x = 6$ this range is reduced to less than 1 percent.

Series expansions for the Bessel integrals with large arguments yield accurate results even when a is small ($a \geq 1$). In this case relative errors are less then 1 percent. The exponential integrals are not replaced with their asymptotic expansions since a and b could be large enough and yet the difference may be small.

Series expansion of ϵ_1 contains forms of K_0 and E_1 and converges rapidly.

6 Conclusion

Series expansions for the integrals of Bickley functions and modified Bessel functions encountered in radiative transfer have been derived. The functions Bis_n and Dis_n, and generalized exponential integral functions, as well as their relations, have been further investigated and presented. In addition, Bickley functions and their properties have been discussed.

References

Abramowitz, M., and Stegun, I. A., 1972, *Handbook of Mathematical Functions,* Dover Publications, Inc., p. 483.

Breig, W. F., and Crosbie, A. L., 1974a, "Two Dimensional Radiative Equilibrium," *J. Math. Analy. Appl.,* Vol. 46, pp. 104–125.

Breig, W. F., and Crosbie, A. L., 1974b, "Numerical Computation of a Generalized Exponential Integral Functions," *Math. Comp.,* Vol. 28, pp. 575–579.

Carlson, B. G., and Lathrop, K. D., 1968, "Extensions of the Discrete Ordinates—The Integral Transport Theory," in: *Computing Methods in Reactor Physics,* H. Greenspan, C. N. Kelber, and D. Okrent, eds., Gordon and Breach, New York.

Chung, T. J., and Kim, J. Y., 1984, "Two-Dimensional, Combined-Mode Heat Transfer by Conduction, Convection, and Radiation in Emitting, Absorbing and Scattering Media—Solution by Finite Elements," ASME JOURNAL OF HEAT TRANSFER, Vol. 106, pp. 448–452.

Crosbie, A. L., and Koewing, J. W., 1977, "Two-Dimensional Isotropic Scattering," *J. Math. Anal. Appl.,* Vol. 57, pp. 91–109.

Echigo, R., Hasegawa, S., and Tamehiro, H., 1972, "Radiative Transfer by Flowing Multiphase Medium—Part II. An Analysis on Heat Transfer of Laminar Flow in an Entrance Region of Circular Tube," *Int. J. Heat Mass Transfer,* Vol. 15, pp. 2595–2610.

Glatt, L., and Olfe, D. B., 1973, "Radiative Equilibrium of a Gray Medium in a Rectangular Enclosure," *JQSRT,* Vol. 13, p. 452.

Heaslet, M. A., and Warming, R. F., 1966, "Theoretical Predictions of Radiative Transfer in a Homogeneous Cylindrical Medium," *JQSRT,* Vol. 6, pp. 751–774.

Lewis, E. E., and Miller, W. F., 1984, *Computational Methods of Neutron Transport,* Wiley, New York, pp. 208–252.

Milgram, M. S., 1978, "Analytic Method for the Numerical Solution of the Integral Transport Equation for a Homogeneous Cylinder," *Nucl. Sci. Eng.,* Vol. 68, pp. 249–269.

Modest, M. F., 1975, "Radiative Equilibrium in a Rectangular Enclosure Bounded by Gray Walls," *JQSRT,* Vol. 15, p. 888.

Razzaque, M. M., Howell, J. R., and Klein, D. E., 1984, "Coupled Radiative and Conductive Heat Transfer in a Two Dimensional Rectangular Enclosure With Gray Participating Media Using Finite Elements," ASME JOURNAL OF HEAT TRANSFER, Vol. 106, pp. 613–619.

Yuen, W. W., and Wong, L. W., 1983, "Numerical Computation of an Important Integral Function in Two-Dimensional Radiative Transfer," *JQSRT,* Vol. 29, pp. 145–149.

Yuen, W. W., and Takara, E. E., 1988, "Analysis of Combined Conductive Radiative Heat Transfer in a Two-Dimensional Rectangular Enclosure With a Gray Medium," ASME JOURNAL OF HEAT TRANSFER, Vol. 110, pp. 468–474.

Wu, C., and Ou, N., 1994, "Transient Two-Dimensional Radiative and Conductive Heat Transfer in Scattering Medium," *Int. J. Heat Mass Transfer,* Vol. 37, pp. 2675–2688.

Nucleate Pool Boiling on Micro Graphite–Copper Composite Surfaces

Gai-Wai Yang,[1] Hsing-Sheng Liang,[1] Wen-Jei Yang,[1] and Daniel Leroy Vrable[2]

Nomenclature

F_m = maximum temperature fluctuation point
h_{fg} = latent heat of evaporation, J/kg
k = thermal conductivity, W/mK
q'' = heat flux, W/m^2
r_o = embryonic bubble radius, m
T = temperature, °C
T_{amp} = amplitude of temperature fluctuation, °C
y = distance from heater surface, m
ΔT = wall superheat = $T_w - T_{sat}$, °C
δ = extrapolated thermal boundary thickness, μm
δ_L = thermal boundary thickness, μm
ρ = fluid density, kg/m^3
σ = surface tension, N/m
ϕ = graphite fiber concentration

[1] Department of Mechanical Engineering and Applied Mechanics, University of Michigan, Ann Arbor, MI 48109.

[2] Thermal & EM Components Technology, Sparta, Inc., San Diego, CA 92121.

Contributed by the Heat Transfer Division of THE AMERICAN SOCIETY OF MECHANICAL ENGINEERS. Manuscript received by the Heat Transfer Division March 3, 1995; revision received May 3, 1996. Keywords: Augmentation and Enhancement, Boiling Heat Transfer. Associate Technical Editor: V. K. Dhir.

Downloaded 11 Dec 2010 to 193.140.21.150. Redistribution subject to ASME license or copyright; see http://www.asme.org/terms/Terms_Use.cfm

where $\epsilon_0(x, y) = \exp(-x\sqrt{1+y^2})/(x\sqrt{1+y^2})$. The tendency is to compute these integrals numerically as well (Breig and Crosbie, 1974b).

The series expansion for ϵ_1 is found to be

$$\epsilon_1(x, y) = (\ln 2 - \gamma) I_0(xy) + \sum_{k=1}^{\infty} \left(\frac{x^2y^2}{4}\right)^k \frac{\Phi(k+1)}{(k!)^2} + \sum_{k=0}^{\infty} \frac{D_k}{(2k+1)!} - \sum_{k=0}^{\infty} \frac{B_k}{(2k)!}, \quad (24)$$

where

$$B_n = \frac{1}{2n}\left[x^{2n}(\sqrt{1+y^2})^{2n-1} + (2n-1)x^2y^2B_{n-1}\right], \quad n \geq 1 \quad (25)$$

$$D_n = \frac{1}{2n+1}\left[x^{2n+1}(\sqrt{1+y^2})^{2n} + (2n)x^2y^2D_{n-1}\right], \quad n \geq 1 \quad (26)$$

with

$$D_0 = x, \quad B_0 = \ln(x + x\sqrt{1+y^2}) \quad (27)$$

Asymptotic expansion of ϵ_1 has been derived by Breig and Crosbie (1974b) and the recursive relation by Yuen and Wong (1983).

5 Discussion

Bis_n functions with small x and θ converge a solution with a few terms. Series expansions for Bis_n functions work well up to the value of $x \to 8$, which is adequate for most problems. Above this limit the number of terms that should be taken into account increases and thus the round-off errors. This becomes very important since Bis_n functions approach zero with increasing x. Above this limit double precision programming is recommended. A single asymptotic expansions that covers all angles could not be obtained and turn out to be a bit complicated.

In addition to series expansion for Dis_1 functions, asymptotic expansions have been provided and can be used for $x > 6$. Relative percent errors for $x = 5$ are about 1–3 percent; for $x = 6$ this range is reduced to less than 1 percent.

Series expansions for the Bessel integrals with large arguments yield accurate results even when a is small ($a \geq 1$). In this case relative errors are less then 1 percent. The exponential integrals are not replaced with their asymptotic expansions since a and b could be large enough and yet the difference may be small.

Series expansion of ϵ_1 contains forms of K_0 and E_1 and converges rapidly.

6 Conclusion

Series expansions for the integrals of Bickley functions and modified Bessel functions encountered in radiative transfer have been derived. The functions Bis_n and Dis_n, and generalized exponential integral functions, as well as their relations, have been further investigated and presented. In addition, Bickley functions and their properties have been discussed.

References

Abramowitz, M., and Stegun, I. A., 1972, *Handbook of Mathematical Functions,* Dover Publications, Inc., p. 483.

Breig, W. F., and Crosbie, A. L., 1974a, "Two Dimensional Radiative Equilibrium," *J. Math. Analy. Appl.,* Vol. 46, pp. 104–125.

Breig, W. F., and Crosbie, A. L., 1974b, "Numerical Computation of a Generalized Exponential Integral Functions," *Math. Comp.,* Vol. 28, pp. 575–579.

Carlson, B. G., and Lathrop, K. D., 1968, "Extensions of the Discrete Ordinates—The Integral Transport Theory," in: *Computing Methods in Reactor Physics,* H. Greenspan, C. N. Kelber, and D. Okrent, eds., Gordon and Breach, New York.

Chung, T. J., and Kim, J. Y., 1984, "Two-Dimensional, Combined-Mode Heat Transfer by Conduction, Convection, and Radiation in Emitting, Absorbing and Scattering Media—Solution by Finite Elements," ASME JOURNAL OF HEAT TRANSFER, Vol. 106, pp. 448–452.

Crosbie, A. L., and Koewing, J. W., 1977, "Two-Dimensional Isotropic Scattering," *J. Math. Anal. Appl.,* Vol. 57, pp. 91–109.

Echigo, R., Hasegawa, S., and Tamehiro, H., 1972, "Radiative Transfer by Flowing Multiphase Medium—Part II. An Analysis on Heat Transfer of Laminar Flow in an Entrance Region of Circular Tube," *Int. J. Heat Mass Transfer,* Vol. 15, pp. 2595–2610.

Glatt, L., and Olfe, D. B., 1973, "Radiative Equilibrium of a Gray Medium in a Rectangular Enclosure," *JQSRT,* Vol. 13, p. 452.

Heaslet, M. A., and Warming, R. F., 1966, "Theoretical Predictions of Radiative Transfer in a Homogeneous Cylindrical Medium," *JQSRT,* Vol. 6, pp. 751–774.

Lewis, E. E., and Miller, W. F., 1984, *Computational Methods of Neutron Transport,* Wiley, New York, pp. 208–252.

Milgram, M. S., 1978, "Analytic Method for the Numerical Solution of the Integral Transport Equation for a Homogeneous Cylinder," *Nucl. Sci. Eng.,* Vol. 68, pp. 249–269.

Modest, M. F., 1975, "Radiative Equilibrium in a Rectangular Enclosure Bounded by Gray Walls," *JQSRT,* Vol. 15, p. 888.

Razzaque, M. M., Howell, J. R., and Klein, D. E., 1984, "Coupled Radiative and Conductive Heat Transfer in a Two Dimensional Rectangular Enclosure With Gray Participating Media Using Finite Elements," ASME JOURNAL OF HEAT TRANSFER, Vol. 106, pp. 613–619.

Yuen, W. W., and Wong, L. W., 1983, "Numerical Computation of an Important Integral Function in Two-Dimensional Radiative Transfer," *JQSRT,* Vol. 29, pp. 145–149.

Yuen, W. W., and Takara, E. E., 1988, "Analysis of Combined Conductive Radiative Heat Transfer in a Two-Dimensional Rectangular Enclosure With a Gray Medium," ASME JOURNAL OF HEAT TRANSFER, Vol. 110, pp. 468–474.

Wu, C., and Ou, N., 1994, "Transient Two-Dimensional Radiative and Conductive Heat Transfer in Scattering Medium," *Int. J. Heat Mass Transfer,* Vol. 37, pp. 2675–2688.

Nucleate Pool Boiling on Micro Graphite–Copper Composite Surfaces

Gai-Wai Yang,[1] Hsing-Sheng Liang,[1] Wen-Jei Yang,[1] and Daniel Leroy Vrable[2]

Nomenclature

F_m = maximum temperature fluctuation point
h_{fg} = latent heat of evaporation, J/kg
k = thermal conductivity, W/mK
q'' = heat flux, W/m^2
r_o = embryonic bubble radius, m
T = temperature, °C
T_{amp} = amplitude of temperature fluctuation, °C
y = distance from heater surface, m
ΔT = wall superheat = $T_w - T_{sat}$, °C
δ = extrapolated thermal boundary thickness, μm
δ_L = thermal boundary thickness, μm
ρ = fluid density, kg/m^3
σ = surface tension, N/m
ϕ = graphite fiber concentration

[1] Department of Mechanical Engineering and Applied Mechanics, University of Michigan, Ann Arbor, MI 48109.

[2] Thermal & EM Components Technology, Sparta, Inc., San Diego, CA 92121.

Contributed by the Heat Transfer Division of THE AMERICAN SOCIETY OF MECHANICAL ENGINEERS. Manuscript received by the Heat Transfer Division March 3, 1995; revision received May 3, 1996. Keywords: Augmentation and Enhancement, Boiling Heat Transfer. Associate Technical Editor: V. K. Dhir.

Copyright © 1996 by ASME

Downloaded 11 Dec 2010 to 193.140.21.150. Redistribution subject to ASME license or copyright; see http://www.asme.org/terms/Terms_Use.cfm

Subscripts

fg = liquid-to-vapor phase change
l = liquid
v = vapor

Introduction

The development of high-performance heat transfer surfaces continues to be an important mission in heat transfer research. Studies on nucleate pool boiling on the surface of pure substances are abundant and can be considered as a matter of record. Therefore, a survey of the literature pertinent to that subject is omitted here. In comparison, similar studies of nucleate pool boiling on composite surfaces are still in their infancy. Recently, an experimental study disclosed that the presence of 50 percent (by volume) of ultrahigh thermal conductivity graphite fibers in graphite–copper composite surfaces was found to cause an enhancement of pool boiling heat transfer in Freon 113 by three to six times over a pure copper surface (Yang et al., 1991). Yang and Zhang (1992) suggested an explanation for the enhancement of pool boiling heat transfer performance in nonisothermal surfaces based on the previous experimental results on composite materials (Yang et al., 1991; Blagojevic et al., 1990). Later, a two-tiered model (Yang et al., 1992a; Yang, 1995) was developed that divided the characteristics of nucleate pool boiling performance into two regions: low and high heat flux regions, that is, the discrete bubble region and the vapor mushroom region, respectively. The boiling phenomena in these two regions combined with the micro configured composite surface formed the two-tiered model to support the theory of Yang et al. (1992b) in explaining the mechanism of nucleate pool boiling on the composite materials.

Nucleate pool boiling on the composite material of 50 percent graphite-fiber composition (Yang et al., 1991) was repeated in this study, utilizing more sophisticated instruments in order to confirm previous findings. Experiments were performed to investigate micro- and macro-phenomena in nucleate pool boiling of Freon 113 on graphite–copper composite materials under atmospheric pressure. The composition of graphite fiber concentration, ϕ, in the composite materials was varied, near 0, 25, and 50 percent in volume, to determine its effects on the heat transfer performance. Details of the composite materials are available in Yang (1995). Temperature profiles in the boundary layer near the boiling surface were measured by a moving microthermocouple probe (50 μm junction diameter) with the aid of a three-dimensional micro positioner and a digital micro indicator. Superheated liquid layer thicknesses and temperature profiles were determined. The enhancement mechanisms of heat transfer for nucleate pool boiling on the micro configured surface are analyzed here.

This study has potential applications in electronic cooling, power generation, distillation processes, and others, with the great advantage of tailoring nonhomogeneous boiling heat fluxes to meet specific requirements by varying the local density of graphite fibers in the copper matrix.

Experimental Apparatus and Procedure

The experimental apparatus used in the study is schematically depicted in Fig. 1. Its major components include a heat source assembly, boiling vessel assembly, condenser assembly, data acquisition system, and microthermocouple probe assembly. Details of the heat source assembly are schematically shown in Fig. 2. The main heater was a 750 W cartridge type with its power supply controlled by an adjustable voltage controller. A copper rod, 2.54 cm in diameter and 11 cm in length, was used to conduct heat from the cartridge heater to the boiling surface. Thermocouples were appropriately located to monitor the rate of heat loss. On top of the heat source assembly sat a boiling

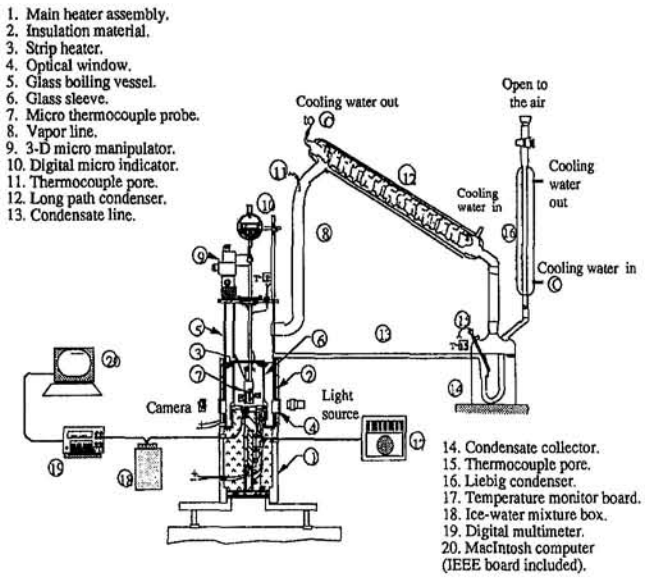


Fig. 1 Experimental setup

surface surrounded by a G11 glass fiber ring, and a stainless steel extension frame. The boiling surface, 2.54 cm in diameter and 1.0 cm in thickness, was aligned with the copper rod. The boiling surface dimensions chosen were assured to be free of thermal conductance/capacitance effects (Carvalho and Bergles, 1990). High-temperature/low-thermal-conductivity epoxy was applied to seal the gap (less than 0.0254 mm) between the boiling surface and the glass fiber ring to prevent leakage, lateral heat loss, and especially the unexpected air-cavity bubbling from the gap. An O-ring was press-fitted between the glass fiber ring and the stainless-steel frame to avoid leakage and conductive heat loss. Six chromel-alumel thermocouples were employed to measure temperatures along the heat transfer path. Heat fluxes and boiling surface temperatures were obtained from these thermocouple readings by Fourier conduction law and linear extrapolation, respectively. Insulation materials were applied around the heating rod.

The boiling vessel assembly, shown in Fig. 1, consisted of a glass boiling vessel (30.48 cm in length and 12.7 cm in diameter), strip heater, inner glass sleeve, and two optical windows for visualization. The strip heater, which closely contacts the glass boiling vessel, was used to maintain the test liquid, Freon 113, at the saturated condition, especially during the boiling process in the low heat flux regime. The inner glass sleeve that stood on the stainless extension plate isolated the convective wakes induced by the strip heater. The test liquid was constantly maintained at a depth of 8 cm above the boiling surface. Two thermocouples were placed at 1 cm and 4 cm above the boiling surface to measure the bulk temperature of the test liquid. A three-axis movable micro positioner along with a digital micro indicator was installed on top of the boiling vessel, which sensed movements as small as 2 μm. This device provided a precise movement control of the microthermocouple probe assembly (to be discussed later). The condenser assembly consisted of a vapor line and a long path condenser (No. 6012, ACE Glass Company), Liebig condenser (No. 5994), condensate collector, and condensate return line. Vapor generated during the boiling process escaped through the vapor line and condensed in the long path condenser by cooling water. Condensate was collected in the condensate collector and returned by gravity through the condensate return line to the boiling vessel. In order to maintain the boiling pressure at atmospheric, the top of the Liebig was open to air.

The microthermocouple probe, shown in Fig. 3, consisted of 25.4-μm-dia bare chromel and alumel wires (CHAL-001,

Downloaded 11 Dec 2010 to 193.140.21.150. Redistribution subject to ASME license or copyright; see http://www.asme.org/terms/Terms_Use.cfm

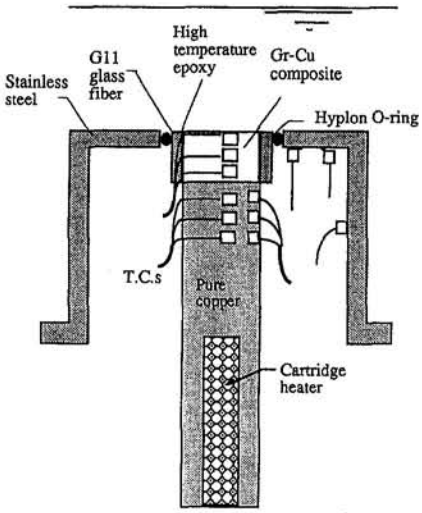


Fig. 2 Details of boiling heater assembly

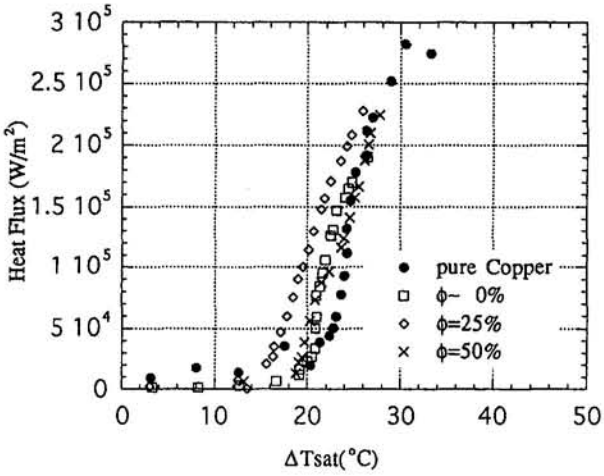


Fig. 4 Boiling curve for Freon 113 on pure copper and the composites

Omega Engineering Company) forming a junction of about 55 to 60 μm in diameter. The microthermocouple supporter was formed by two 2-mm capillary glass tubes fixed in place by a Teflon fixture. The spring in the probe served to adjust the tightness of the thermocouple wires. The probe was moved vertically to measure temperature profiles within the boundary layer over the boiling surface at various heat fluxes. A microscope was used to detect the movement of the thermocouple and to position the junction of the thermocouple at zero, the point of close contact with the boiling surface.

The data acquisition system included an ice–water mixture jar, a digital multimeter, an IEEE interface, and a Macintosh computer. The device used to detect the voltage outputs from thermocouples was a $6\frac{1}{2}$ digit multimeter (model 196, Keithley Instruments) with accuracy 0.005 percent for this pool boiling experiment application. An IEEE 488 interface (by National Instruments Company) was employed to transfer data to the Macintosh computer. A computer program was developed to control the data transfer and A/D conversion. All thermocouples were calibrated with a platinum resistance thermometer. The uncertainty of temperature measurements by calibration and instrumentation errors were estimated to be within 0.05°C (Kline and McClintock, 1953).

Three composites with various graphite fiber concentrations, $\phi \approx 0$, 25, and 50 percent, along with a pure copper reference surface, were tested. To ensure a repeatable surface condition, each surface was polished by an identical polishing procedure prior to each test. The details of surface preparation can be found in Yang (1995). After pouring Freon 113 into the boiling vessel, the strip heater was turned on, allowing the test liquid to boil vigorously for 20 minutes for degassing. The heater was then turned off, allowing the test liquid to cool down to room temperature. The subsequent boiling test was begun by heating the test liquid to its saturated temperature by means of a strip heater. Then the cartridge heater was gradually turned on to reach a preset voltage level. Recording began after both the composite test piece and the copper rod achieved steady state, which was verified by time invariance of thermocouple readings. Next, the voltage supply to the cartridge heater was raised by 2 V increments for a subsequent test. The process was repeated until the boiling heat flux reached or exceeded 60 percent of the critical heat flux, q_c (190 kW/m^2; Westwater et al., 1989). At this stage, the microthermocouple probe was put into operation to measure the temperature profile in the boundary layer over the boiling surface. More tests were performed at increments of 2 V until the boiling heat flux reached about 90 percent of q_c (limited by the maximum allowable temperature of the G11 glass fiber ring). The maximum boiling heat flux achieved here, 90 percent of q_c, was high enough to cover the entire vapor mushroom region in which the temperature profile was to be monitored.

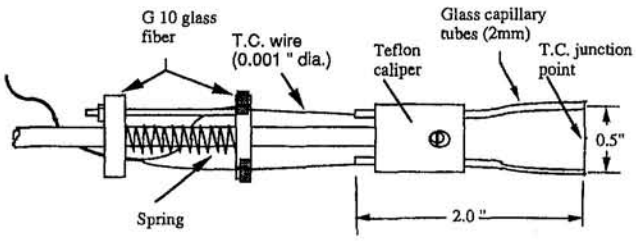


Fig. 3 Detail of the microthermocouple probe

Results and Discussion

Boiling Heat Transfer Performance. Figure 4 compares the boiling curves of Freon 113 on various composites and the pure copper reference surface. Although this plot is rather unconventional, it clearly reveals the effect of graphite fiber volume fraction on performance enhancement. It is seen that nucleate pool boiling performance is enhanced by three to six times on the composites as compared to the reference (copper) surface. This may be attributed to the much higher thermal conductivity (1200 W/m-K) of graphite fibers, compared with that of the copper matrix (401 W/m-K), which causes the formation of "hot spots" on the graphite fiber tips. The formation of hot spots on inserted composite material was confirmed by numerical simulation (Blagojevic et al., 1990) and later considered by Yang and Zhang (1992) as a feasible way to reduce the adverse temperature sensitivity on nucleate boiling performance. Each hot spot acts as a "nucleation activator" in promoting nucleation at a considerably lower surface-averaged temperature. In addition, the hot spot exerts an effect on strengthening an embryonic bubble during boiling incipience. The embryonic bubble radius was obtained through a static equilibrium analysis on the liquid–vapor interface of a bubble (Griffith and Wallis, 1960) as:

$$r_o = \frac{2\sigma T_{\text{sat}}}{h_{fg}(\rho_l - \rho_v)\Delta T_{\text{sat}}}$$

In the present study, boiling was initiated at a superheat of 14°C for $\phi = 25$ percent and at 21°C for pure copper ($\phi = 0$ percent), thus generating an embryonic bubble with a radius of 0.6 μm

Downloaded 11 Dec 2010 to 193.140.21.150. Redistribution subject to ASME license or copyright; see http://www.asme.org/terms/Terms_Use.cfm

and 0.4 μm for $\phi = 25$ and $\phi = 0$ percent, respectively. If the bubble volume is reduced by a quenching of its surrounding liquid, mutual interaction or thermal interference of nucleation sites (more discussion later), it would be unlikely for larger embryonic bubbles on the $\phi = 25$ percent surface to be deactivated. This serves as an explanation for an enhancement mechanism.

Another special feature exhibited in Fig. 4 is the existence of an optimum graphite fiber concentration, ϕ, in the composite materials, which yields the best boiling performance. The figure shows that as ϕ increases from near 0 to 25 percent, the boiling curve continues to shift leftward, indicating an enhancement in the nucleate boiling performance. However, as ϕ changes from 25 to 50 percent, the boiling curve shifts rightward, suggesting that an optimum graphite content exists between the two values. The main factors affecting nucleation on composite materials include (*i*) the amount of graphite fibers embedded in the copper matrix (through heat dissipation directly), (*ii*) the spacing between adjacent graphite fibers (through site interaction; Eddington and Kenning, 1978), and (*iii*) the boiling area fraction, A_{NB}/A_T, the rate of the area for nucleate boiling to the total boiling surface area (through thermal influence; Calka and Judd, 1985; Chekanov, 1977). A scanning electron microscope (SEM) was employed to observe and compare micro configurations (not shown here) of the 25 and 50 percent composite surfaces. It was disclosed that the average spacing between adjacent graphite fibers in the $\phi = 50$ percent case was about the same as its fiber diameter, but was larger than the diameter of graphite fibers in the $\phi = 25$ percent case. It is more likely that heat transfer performance on the $\phi = 25$ percent surface is better than that on the $\phi = 50$ percent because of the existence of more space for bubble nucleation without mutual interference. More composite materials of various graphite-fiber contents need to be tested to provide further information of the nucleation site interaction.

The $\phi \approx 0$ percent surface contains only 30 graphite fibers (identified by the SEM) in the copper matrix. Its thermal and mechanical properties were somehow altered by these less than 0.1 percent graphite fibers. It was revealed by SEM images that more grooves and stripes were formed on each graphite fiber tip and the nearby copper base than on the reference surface, and nucleation constantly began around the fiber tip areas as revealed by visualization, resulting in higher boiling heat fluxes.

One additional comment on Fig. 4 is that the boiling curves converge near the critical heat flux (CHF) region with the formation of a relatively high thermal resistance vapor film, which blankets the fiber tips, thus causing the function of the graphite fibers to deteriorate.

Boiling Boundary Layer. In order to understand the mechanism for inducing a substantial augmentation in pool boiling heat transfer performance on the composite materials, measurements were made on the temperature distribution and thickness of a superheated boundary layer at a vapor mushroom heat flux ranging from 127,000 to 182,000 W/m^2. Figure 5 compares temperature profiles at $q'' \approx 175{,}000$W/m^2 for pure copper, $\phi = 25$ and $\phi = 50$ percent. It is seen that the temperature profile for $\phi = 25$ percent lies closest to the boiling surface while that for pure copper lies farthest, with that of $\phi = 50$ percent in between. Table 1 shows that for $q'' \approx 175{,}000$ W/m^2 the "extrapolated superheated layer thickness" δ (defined as the height of the intersection between the tangent to the temperature profile and the constant liquid bulk temperature; Marcus and Dropkin, 1965), under vapor masses in the vapor mushroom region were 92, 73, and 83 μm for pure copper, $\phi = 25$ and $\phi = 50$ percent, respectively. This finding could be significant in analyzing the mechanisms of nucleation and bubble dynamics according to Han and Griffith (1965). The boiling heat transfer dissipation is the contribution of natural convection, latent heat, and microlayer evaporation (Judd and Hwang, 1976). More bubble dynamics data such as bubble departure frequency, terminal velocity, and size, are needed for a better understanding of the boiling mechanisms. Figure 6 is a plot of δ versus various boiling heat flux. It confirms the observation that δ is thinnest for the 25 percent graphite content, thickest for pure copper, and in between for the 50 percent graphite case.

Temperature profiles of the boiling boundary layer were also characterized by vigorous fluctuations with certain amplitudes whose magnitude varied with the location, boiling heat flux, and boiling surface. Figure 5 reveals the distribution of the maximum amplitude, T_{amp}, over the $\phi = 25$ percent surface. It is seen that T_{amp} increases gradually as the distance from the boiling surface, y, decreases, practically following the temperature profile. Inside the boiling boundary layer, T_{amp} rises steeply toward the boiling surface and reaches a maximum value at point F_m. It is of interest to note that as it approaches the boiling surface from point F_m, T_{amp} decreases, reaching a minimum value (not zero) at $y = 0$. Thermal fluctuations in the region close to the boiling surface were caused by rigorous agitations induced by the bubbles departing from the boiling surface. A similar phenomenon was reported by Marcus and Dropkin (1965), who defined the height of point F_m as the thickness of

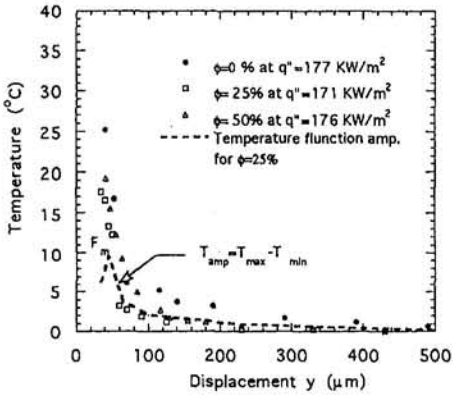


Fig. 5 Temperature profiles and fluctuations on various surfaces

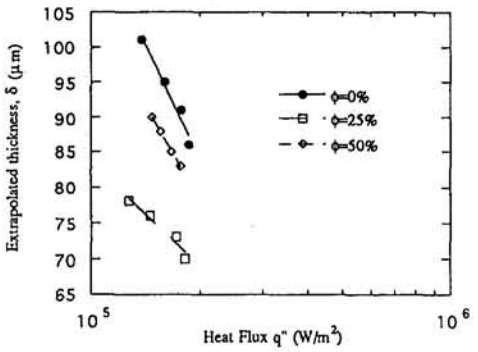


Fig. 6 Plot of extrapolated superheated layer thickness δ versus boiling heat flux

Table 1 Superheated thermal layer thickness

Material	Pure Copper	Graphite-Copper Composites	
Graphite Fiber Content	ϕ=0%	ϕ=25%	ϕ=50%
Heat Flux [KW/m^2]	177	172	176
δ [μm]	92	73	83
δ_L [μm]	58	47	57
δ / δ_L	0.63	0.64	0.69

Downloaded 11 Dec 2010 to 193.140.21.150. Redistribution subject to ASME license or copyright; see http://www.asme.org/terms/Terms_Use.cfm

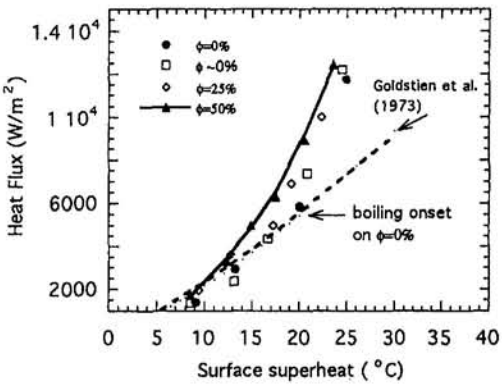


Fig. 7 Comparison of natural convection heat transfer performance

the "superheated thermal boundary layer," δ_L (to distinguish it from δ). Table 1 compares the magnitudes of δ and δ_L for pure copper and the composites. It is interesting to note that δ/δ_L for the three surfaces takes about the same value.

Natural Convection. An experiment was performed on natural convection in Freon 113 from the pure copper and composite surfaces. It is noted that the good consistency of measured data on the reference surface and those predicted by a previous correlation (Goldstein et al., 1973) confirmed the unique character of the composites. It can be calculated using the data in Fig. 7 that the average natural convective heat transfer coefficients for the 25 and 50 percent graphite contents were 1.22 to 1.33, and 1.33 to 1.39 times those for a pure copper surface, respectively. This enhancement in natural convective heat transfer performance with a change in ϕ from 25 to 50 percent is in sharp contrast to a deterioration in nucleate pool boiling heat transfer performance with the same change in ϕ from 25 to 50 percent. In the former case, the $\phi = 50$ percent surface has more graphite fibers, which have a much higher thermal conductivity than the $\phi = 25$ percent surface, thus transfer more heat to the liquid. On the other hand, nucleate pool boiling heat transfer performance depends on the formation of hot spots on the graphite fiber tips as previously mentioned.

Summary and Conclusion

Nucleate pool boiling of Freon 113 on the composite materials of different graphite fiber contents has been studied experimentally. The results reveal that graphite-fiber reinforced copper materials provide not only super-high heat transfer performance (compared with pure copper), but also distinctive features in their nucleate boiling curves. The mechanisms that cause these results are revealed by a scanning electron microscope. A microthermocouple probe measured temperature profiles inside the boiling boundary layer from which the thickness of the superheated thermal boundary layer and the maximum amplitude of temperature fluctuations were evaluated. A summary of the mechanisms involved follows:

1 A substantial enhancement in nucleate boiling heat transfer performance is achieved when graphite fibers are embedded in the copper matrix. A scanning electron microscope discloses a great number of micro stripes and cavities on the graphite fiber tips that serve as potential nucleation sites. These sites lead to the substantial enhancement in boiling heat transfer performance.
2 There exists a certain graphite fiber content that yields the optimum boiling performance on the composite materials, which can be explained as a result of thermal interaction and nucleation competition among the neighboring fibers.
3 A composite surface of higher boiling performance is characterized by a lower temperature profile, a thinner "superheated thermal boundary layer," and the maximum amplitude of temperature fluctuations being situated closer to the heating surface.
4 A natural convection experiment has revealed that the $\phi = 50$ percent surface has a better heat transfer performance than that of the $\phi = 25$ percent surface because of more hot spots forming on the $\phi = 50$ percent surface.

References

Blagojevic, B. D., Novakovic, M. N., and Ilic, G. S., 1990, "Pool Boiling Heat Transfer From Composite Solid Wall," *Proc. 9th Int. Heat Transfer Conf.*, Jerusalem, Israel, Vol. 4, pp. 307–310.

Carvalho, R. D., and Bergles, A. E., 1990, "The Effect of Heater Thermal Properties and Thickness on the Pool Boiling Critical Heat Flux," *Proc. Third Brazilian Thermal Sciences Meeting (III ENCIT)*, Itaperna, Brazil, Vol. 2, pp. 577–582.

Calka, A., and Judd, R. L., 1985, "Some Aspects of the Interaction Among Nucleation Sites During Saturation Nucleate Boiling," *Int. J. Heat Mass Transfer*, Vol. 28, pp. 2331–2342.

Chekanov, V. V., 1977, "Interaction of Centers in Nucleate Boiling," *Teplofizika Vysokikh Temperatur*, Vol. 15, pp. 121–128.

Eddington, R. I., and Kenning, D. B. R., 1978, "The Prediction of Low Boiling Bubble Populations From Gas Bubble Nucleation Experiments," *Proc. 6th Int. Heat Transfer Conference*, Toronto, Vol. 1, pp. 275–279.

Goldstein, R. L., Sparrow, E. M., and Jones, D. C., 1973, "Natural Convection Mass Transfer Adjacent to Horizontal Plates," *Int. J. Heat Mass Transfer*, Vol. 16, pp. 1025–1034.

Griffith, P., and Wallis, J. D., 1996, "The Role of Surface Conditions in Nucleate Boiling," *Chemical Engineering Progress Symposium Series*, No. 30, Vol. 56, pp. 49–63.

Han, C.-Y., and Griffith, P., 1965, "The Mechanism of Heat Transfer in Nucleate Pool Boiling—Part I," *Int. J. Heat Mass Transfer*, Vol. 8, pp. 887–904.

Judd, R. L., and Hwang, K. S., 1976, "A Comprehensive Model for Nucleate Pool Boiling Heat Transfer Including Microlayer Evaporation," ASME JOURNAL OF HEAT TRANSFER, Vol. 98, No. 1.

Kline, S. J., and McClintock, F. A., 1953, "Describing Uncertainties in Single-Sample Experiments," *Mechanical Engineering*, Vol. 75, Jan., pp. 882–886.

Marcus, B. D., and Dropkin, D., 1965, "Measured Temperature Profiles Within the Superheated Boundary Layer Above a Horizontal Surface in Saturated Nucleate Pool Boiling of Water," ASME JOURNAL OF HEAT TRANSFER, Vol. 87, pp. 333–341.

Nishikawa, K., Fujita, Y., Ohta, H., and Hidaka, S., 1979, "Heat Transfer in Nucleate Boiling of Freon," *Heat Transfer—Japanese Research*, Vol. 8, No. 3, pp. 16–36.

Rohsenow, W. M., 1952, "A Method of Correlating Heat-Transfer Data for Surface Boiling of Liquids," *Trans. ASME*, Vol. 74, pp. 969–976.

Westwater, J. W., Zinn, J. C., and Brodbeck, K. J., 1989, "Correlation of Pool Boiling Curves for the Homologous Groups: Freons," ASME JOURNAL OF HEAT TRANSFER, Vol. 111, pp. 204–207.

Yang, G. W., Yang, Wen-Jei, and Zhang, N., 1992a, "Two-Tier Model for Nucleate Pool Boiling on Micro Configured Composite Surfaces," *Int. Communications in Heat and Mass Transfer*, Vol. 19, pp. 767–779.

Yang, G. W., Yang, Wen-Jei, and Zhang, N., 1992b, "Mechanisms of Nucleate Pool Boiling on Composite Surfaces," *Int. Comm. Heat Mass Transfer*, Vol. 19, pp. 781–791.

Yang, G. W., 1995, "Micro- and Macro- Phenomena in Nucleate Pool Boiling on Graphite–Copper Composite Materials," Ph.D. Dissertation, Department of Mechanical Engineering and Applied Mechanics, University of Michigan, Ann Arbor, MI.

Yang, Wen-Jei, Takizawa, H., and Varable, D., 1991, "Augmented Boiling on Copper-Graphite Composite Surface," *Int. J. Heat Mass Transfer*, Vol. 34, No. 11, pp. 2751–2758.

Yang, Wen-Jei, and Zhang, N., 1992, "Boiling Performance on Nonisothermal Surfaces," *Proc. Engineering Foundation Conference on Pool and External Flow Boiling*, Santa Barbara, CA, pp. 119–124.

Downloaded 11 Dec 2010 to 193.140.21.150. Redistribution subject to ASME license or copyright; see http://www.asme.org/terms/Terms_Use.cfm

Laminar Film Condensation on a Horizontal Surface With Surface Tension Effect

J. S. Chiou,[1,3] T. B. Chang,[2,3] and C. K. Chen[1,3]

Introduction

The heat transfer problem associated with the film condensation on a horizontal plate is of practical interest in the design of evaporative condensers, distillation facilities, and other industrial applications.

Heat transfer rates in laminar film condensation on vertical or nearly vertical surfaces are adequately predicted by Nusselt's analysis (1916). For horizontal surfaces, the earliest attempt at predicting heat transfer rates was investigated experimentally by Popov (1967). Gerstmann and Griffith (1965) then investigated the condensation on the underside of a horizontal plate. The condensation on the upper side of the horizontal plate was first studied by Leppert and Nimmo (1968) and Nimmo and Leppert (1970). In their studies the nondimensional film thickness and the Nusselt number profiles along the plate were obtained both experimentally and theoretically.

Recently, Shigechi et al. (1990) studied the same problem, the heat transfer coefficient was then calculated and found to be about 28 percent higher than the experimental data of Nimmo and Leppert (1970). In Shigechi's study, the inclination angle of the vapor–liquid interface was used as the necessary boundary at the plate edge. The inclination angle, however, was continuously adjusted to minimize the thickness of condensate film.

In the previous theoretical studies, the thickness of condensate at plate edge (a necessary boundary condition) is either arbitrarily assumed or by means of "trial and error," and the effect of surface tension was never included in their analyses.

In this study, the controversial boundary condition (film thickness at plate edge) will be determined by the concept of minimum mechanical energy inherited in the condensated flow, and the effect due to surface tension will also be considered in the analysis.

Analysis

Consider a pure quiescent vapor at saturated state with temperature T_{sat} and pressure P_{sat} condensing on a horizontal isothermal plate with temperature at T_W, and the width of the plate is 2L as shown in Fig. 1. Under steady-state conditions, a laminar film condensation boundary layer will be established with maximum depth at the center of plate, gradually decreasing to a minimum depth at the plate edge. The condensate flow rate within the boundary layer increases from zero at $x = 0$ to a maximum value at the edge of plate. To analyze this problem, we assume the flow is steady and laminar, the inertia within the film is negligible (a creeping film flow is assumed), the wall temperature and vapor temperature are uniform and kept constant, the kinetic energy of the film flow is negligible, the properties of dry vapor and condensate are constant.

Under the aforementioned assumptions, the governing equations for the condensate film can be written as

Continuity:

$$\frac{\partial u}{\partial x} + \frac{\partial v}{\partial y} = 0 \tag{1}$$

Momentum:

$$0 = -\frac{\partial p}{\partial x} + \mu \frac{\partial^2 u}{\partial y^2} \tag{2}$$

In Eq. (2), the pressure (P) in the liquid film includes the static pressure, the hydraulic pressure, and that induced by the surface tension, i.e.,

$$P = P_s + \rho g(\delta - y) + \Delta P_{st} \tag{3}$$

In Eq. (3) P_s is equivalent to P_{sat} (saturation pressure) since the liquid temperature is near the saturation temperature, δ in the thickness of liquid film, and ΔP_{st} is the surface tension pressure, which can be expressed by

$$\Delta P_{st} = P|_{y=\delta} - P_{sat} = \frac{\sigma}{r} = \sigma \mathcal{R} \tag{4}$$

where r is the radius of curvature of liquid–vapor interface, which can be expressed as

$$r = -\frac{\left[1 + \left(\frac{d\delta}{dx}\right)^2\right]^{3/2}}{d^2\delta/dx^2}$$

and $\mathcal{R}$ is the curvature of liquid film. Equation (2) becomes

$$O = -\left[\sigma \frac{d\mathcal{R}}{dx} + \rho g \frac{d\delta}{dx}\right] + \mu \frac{\partial^2 u}{\partial y^2} \tag{5}$$

By using the boundary-layer conditions of liquid film, which are $u = 0$ at $y = 0$ and $\partial u/\partial y = 0$ at $y = \delta$, we obtain

$$u = \frac{1}{\mu}\left[\rho g \frac{d\delta}{dx} + \sigma \frac{d\mathcal{R}}{dx}\right]\left(\frac{y^2}{2} - y\delta\right) \tag{6}$$

The energy balance on a finite volume of liquid condensate at x can be written as

$$\left(k \frac{\partial T}{\partial y}\bigg|_{y=0}\right) dx = \frac{d}{dx}\left\{\int_0^\delta \rho u[h_{fg} + c_p(T_{sat} - T)]dy\right\} dx \tag{7}$$

The left-hand side is the energy transfer from liquid film to the solid plate, and the right-hand side is the net energy flux across the liquid film (from x to $x + dx$).

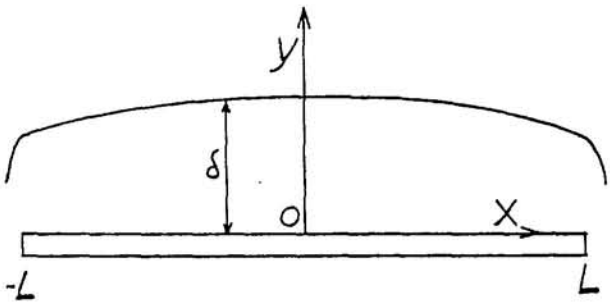


Fig. 1 Film condensation on a flat plate

[1]Professor.
[2]Graduate Student.
[3]Mechanical Engineering Department, National Cheng Kung University, Tainan, Taiwan.

Contributed by the Heat Transfer Division of THE AMERICAN SOCIETY OF MECHANICAL ENGINEERS. Manuscript received by the Heat Transfer Division February 24, 1995; revision received March 11, 1996. Keywords: Condensation, Thin Film Flow. Associate Technical Editor: V. K. Dhir.

Copyright © 1996 by ASME
Downloaded 11 Dec 2010 to 193.140.21.150. Redistribution subject to ASME license or copyright; see http://www.asme.org/terms/Terms_Use.cfm

Assuming a linear temperature profile through the condensate film, Eq. (7) yields

$$\delta \frac{d}{dx}\left\{\delta^3\left(\frac{d\delta}{dx}+\frac{\sigma}{\rho g}\frac{d\mathcal{R}}{dx}\right)\right\} = -\frac{3k\Delta T\mu}{\rho^2 g\lambda} \tag{8}$$

If we set $x^* = x/L$; $\delta^* = \delta/L$; $\mathcal{R}^* = \mathcal{R}L$, Eq. (8) can be expressed in a dimenssionless form as

$$\delta^* \frac{d}{dx^*}\left[\delta^{*3}\left(\frac{d\delta^*}{dx^*}+\frac{1}{\mathrm{Bo}}\frac{d\mathcal{R}^*}{dx^*}\right)\right] = -3\frac{\mathrm{Ja}}{\mathrm{Ra}} \tag{8a}$$

where L is the half-length of the plate, $\lambda = h_{fg} + (3/8)\,C_p\Delta T$, and the dimensionless parameters are $\mathrm{Ja} = (C_p\Delta T)/\lambda$ (Jakob number), $\mathrm{Ra} = (\rho^2 g \mathrm{Pr} L^3)/\mu^2$ (Rayleigh number), $\mathrm{Pr} = (\mu C_p)/k$ (Prandtl number), $\mathrm{Bo} = (\rho g L^2)/\sigma$ (Bond number).

Since $\mathcal{R}$ is a second-order differential form in terms of δ, Eq. (8a) is thus a fourth-order differential equation. However, there exist only three boundary conditions from the observation of the boundary layer of liquid film, which are

$$\frac{d\delta}{dx} = 0 \quad \text{at} \quad x = 0$$

(the thickness of liquid film is maximum at the plate center)

$$\frac{d\mathcal{R}}{dx} = 0 \quad \text{at} \quad x = 0$$

(the interfacial curvature is minimum at the plate center)

$$\frac{d\mathcal{R}}{dx} = 0 \quad \text{at} \quad x = L$$

(the interfacial curvature is maximum at the plate edge)

In this study, the fourth boundary condition is obtained from the concept of minimum energy, the concept applied in the hydraulics of an open channel (Bakhmeteff, 1966). The principle of the concept essentially implies that a fluid flowing across a horizontal plate under the influence of pressure gradient and flowing off the edge of the plate will adjust itself so that the rate of mechanical energy within the fluid will be minimum with respect to the boundary layer thickness at the plate, which is

$$\left[\frac{\partial}{\partial\delta}\int_0^\delta\left(\frac{u^2}{2}+gy+\frac{p}{\rho}\right)\rho u dy\right]\Bigg|_{\dot{m}_c} = 0 \tag{9}$$

where $\dot{m}_c$ is the critical value of mass flow rate flowing out of the plate edge, and

$$\dot{m}_c = \int_0^\delta \rho u dy\Big|_{x=L} = \frac{\rho^2 g}{\mu}\left(-\frac{\delta_{\min}^3}{3}\right)\left(\frac{d\delta}{dx}+\frac{L^2}{B_o}\frac{d\mathcal{R}}{dx}\right)\Bigg|_{x=L} \tag{10}$$

From Eqs. (3), (6), and (9), we have

$$-\frac{54}{35}\dot{m}_c^3\frac{1}{\rho^2\delta^3}+\dot{m}_c g = 0 \tag{11}$$

Equating Eqs. (10) and (11), and using the condition $d\mathcal{R}/dx\,|_L = 0$, yields

$$\left.\frac{d\delta}{dx}\right|_L = -\left(\frac{35}{6}\frac{\mathrm{Pr}}{\mathrm{Ra}}\frac{L^3}{\delta_{\min}^3}\right)^{1/2} \tag{12}$$

With this (the fourth) boundary condition, Eq. (8) can be solved by the finite difference method. Since the slope of film thickness is not flat at the plate edge, the progressive finer grid size toward the edge is used in the calculations.

The mean Nusselt number is also calculated by way of $\mathrm{Nu} = \bar{h}L/k$, where

$$\bar{h} = \frac{1}{L}\int_o^L h(x)dx = \frac{k}{L}\int_o^L\frac{1}{\delta(x)}dx = \frac{k}{L}\int_o^1\frac{1}{\delta^*}dx^* \tag{13}$$

Results and Discussion

In order to understand the effect of surface tension more clearly, the inverse Bond number $I_{\mathrm{Bo}} = 1/\mathrm{Bo} = \sigma/\rho g L^2$ is used in the plot; the I_{Bo} number becomes larger when the surface tension (σ) increases.

After the profile of film thickness is determined, Eq. (13) can be used to calculate the dimensionless heat transfer coefficient (Nu), which is a function of many parameters such as Ja, Pr, I_{Bo} (or Bo), and Ra. If we plot the calculated Nusselt number versus each parameter as a variable and setting other parameters as constants, and then switch every parameter as the variable one by one, we can derive the empirical correlation as

$$\mathrm{Nu} = 0.82[1 - I_{\mathrm{Bo}}^{0.25}\,\mathrm{Ja}^{-0.3}\,\mathrm{Pr}^{0.35}]\,(\mathrm{Ra/Ja})^{0.2} \tag{14}$$

In reducing Eq. (14), Ja is changed from 0.002 to 0.05, and the difference between the result of Eq. (14) and the result directly calculated from numerical method is ± 4 percent. Similarly, the ranges of Pr and I_{Bo} are from 1.0 to 10 and from 1.5×10^{-4} to 10^{-7}; the corresponding difference are ± 0.5 and ± 1 percent.

Figure 2 indicates that Nu increases as I_{Bo} decreases. This means a higher surface tension can hold up more condensate, so the film thickness will become thicker, and a thicker liquid film will result in a larger thermal resistance.

The experimental data on a finite-size horizontal plate by Nimmo and Leppert (1970) is fitted into the following form:

$$\mathrm{Nu} = 0.64\,(\mathrm{Ra/Ja})^{0.2} \tag{15}$$

If the test conditions conducted by Nimmo and Leppert (1970) (such as the half-width of plate L = 61 cm, and the physical properties of water at 100°C, etc.) were used in the simulation, the plotted curve, with $I_{\mathrm{Bo}} = 1.68 \times 10^{-5}$ in Fig. 2, is very close to the curve of Eq. (15). The calculated results are weekly functions of Jakob number, the range of Jakob number for $0.01 \le \mathrm{Ja} \le 0.05$ reflects the different plate temperature T_w, or different $\Delta T = T_w - T_{\mathrm{sat}}$, for $5.4°\mathrm{C} \le \Delta T \le 27.3°\mathrm{C}$. Since the actual temperature difference in the test was not speci-

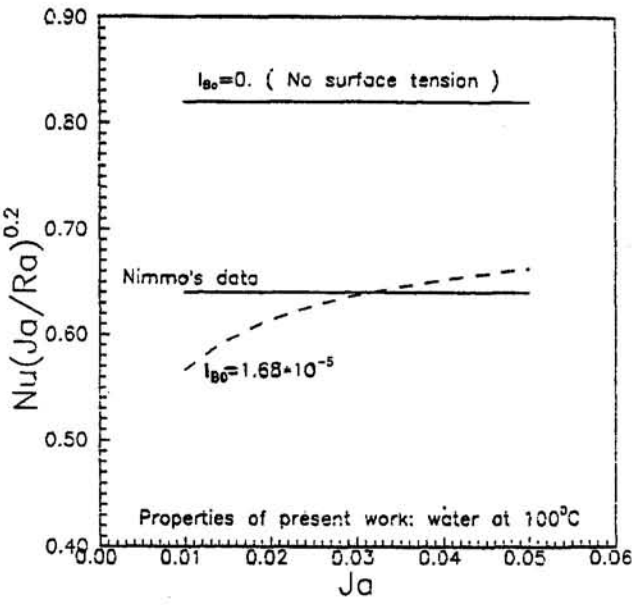


Fig. 2 Present work compared with Nimmo's data

Downloaded 11 Dec 2010 to 193.140.21.150. Redistribution subject to ASME license or copyright; see http://www.asme.org/terms/Terms_Use.cfm

fied, the average Nusselt number of Eq. (15) is very close to the calculated value when Ja = 0.015 (or $\Delta T \cong 8$°C).

In the absence of surface tension ($I_{Bo} = 0$), Eq. (14) becomes

$$\mathrm{Nu} = 0.82\ (\mathrm{Ra/Ja})^{0.2} \qquad (16)$$

with the maximum error of 4 percent. Equation (16) is the same as that theoretically obtained by Shigechi et al. (1990), where the effect due to surface tension was not considered in their analysis.

Conclusions

In solving the laminar film condensation on a horizontal plate, we have applied the concept of minimum energy inherited in the condensated flow to determine the boundary condition at the plate edge rather than arbitrarily assumed.

The surface tension effect of the liquid-film on a finite-size horizontal plate is not negligible. In fact, from this study, we find that the surface tension effect plays the role of contributing the difference of heat transfer coefficient between the theoretical result of Shigechi et al. (1990) and the experimental result of Nimmo and Leppert (1970).

References

Bakhmeteff, B. K., 1966, *Hydraulics of Open Channels*, McGraw-Hill, New York, pp. 39–41.

Gerstmann, J., and Griffith, P., 1965, "Laminar Film Condensation on the Underside of Horizontal and Inclined Surfaces," *Int. J. Heat Mass Transfer*, Vol. 10, pp. 567–580.

Leppert, G., and Nimmo, B., 1968, "Laminar Film Condensation on Surfaces Normal to Body or Inertial Forces," ASME JOURNAL OF HEAT TRANSFER, Vol. 80, pp. 178–179.

Nimmo, B., Leppert, G., 1970, "Laminar Film Condensation on a Finite Horizontal Surfaces," *Proc. 4th Int. Heat Transfer Conference*, pp. 402–403.

Nusselt, W., 1916, "Die Oberfächen-Kondensation des Wasserdampfer," *Zeitschrift des Vereines Deutscher Ingenieure*, Vol. 60, pp. 541–546.

Popov, V. D., 1967, "Heat Transfer During Vapor Condensation on a Horizontal Surface," *Trudy kiev. Teknol. Inst. Pishch*, Prom. 11, pp. 567–580.

Shigechi, T., Kawae, N., Tokita, Y., and Yamada, T., 1990, "Film Condensation Heat Transfer on a Finite-Size Horizontal Plate Facing Upward," *JSME Series B*, Vol. 56, pp. 205–210.

Fundamental Study on Latent Cold Heat Storage by Means of Direct-Contact-Freezing Between Oil Droplets and Cold Water Solution

H. Inaba[1,3] **and K. Sato**[2,3]

Nomenclature

$\bar{d}_p$ = mean diameter of dispersed phase particle
R = solidification rate of frozen oil particles
T_c = temperature of water solution
T_m = melting point of tetradecane = 5.8°C
T_n = injection temperature of tetradecane oil jet
U_c = velocity of water solution
U_n = injection velocity of tetradecane oil

Introduction

The latent cold energy storage system can store a large amount of cold heat energy in a relatively small vessel by using phase-change material (PCM). One of the most important elements in a latent cold storage system is the heat exchanger for freezing the PCM. Generally, the capsule-type heat exchanger is used for the latent cold energy storage system. The capsule type heat exchanger can maintain the PCM and the coolant fluid in a high purity by separating them with the capsule wall. However, the capsule-type heat exchanger has the drawback that it takes longer to complete the latent heat storage and the size of the heat storage vessel becomes larger because of the thermal resistance of the capsule wall. A direct-contact heat exchanger can overcome these problems.

The present study deals with a new kind of latent cold heat storage system using the direct-contact heat exchange between PCM and the coolant fluid. The spray tower is the most suitable configuration as the heat exchanger for freezing the liquid PCM by the direct-contact cooling with the cold medium. Therefore, this study deals with the spray tower in which the dispersed phase causes solidification.

Some studies have been reported about direct-contact heat exchange in which the dispersed phase causes a solidification (Umano, 1959; Mehrabian et al., 1978). For example, theoretical studies of solidification of a drop or a plane or spherical thin molten film have been carried out in the previous work (Siegel, 1978; Fetecău and Petrescu, 1992; Petrescu, 1992). In particular, Petrescu and Fetecău (1993) performed a theoretical study on the temperature profile and the cooling duration of a drop falling freely in a fluid. Some experimental studies have also been seen concerning peal granulation in a liquid or gaseous media (Filipescu, 1987; Onu et al., 1988). The previous researches have studied the fundamental heat transfer characteristics between dispersed phase and continuous phase under a certain condition.

The target of the present study is to investigate the overall performance of a direct-contact heat exchanger in which the dispersed phase droplets freeze, with a view to applying the direct-contact freezing to latent cold energy storage system. Little research has been done in this field.

Experimental Apparatus and Procedure

Tetradecane and 30 mass percent ethylene glycol water solution were used for the PCM and coolant fluid, respectively. The physical properties of tetradecane and 30 mass percent ethylene glycol water solution are indicated in Table 1 (Inaba and Morita, 1993).

As indicated in Fig. 1, the test section is made of transparent acrylic resin plate of 10 mm in thickness, and it has a 100 cm^2 cross section. The vertical distance between the outlet of the nozzle and the surface of the water solution layer is fixed at 1600 mm ± 3 mm. The cold water solution flows downward in the test section with very low velocity ($U_c = 0.7$ cm/s). The PCM oil is injected from the nozzle fixed at the lower part of the test section. The oil disperses to many tiny oil droplets. The

Table 1 Physical properties of tetradecane

Melting point	(°C)	:	5.8	
Latent heat	(kJ/kg)	:	229.1	
			(Liq: (6 °C))	(Sol. (5 °C))
Specific heat	(kJ/kgK)	:	2.0	1.8
Density	(kg/m^3)	:	770	810

[1]Professor.
[2]Graduate Student.
[3]Department of Mechanical Engineering, Faculty of Engineering, Okayama University, Tsushimanaka 3-1-1, Okayama 700, Japan.

Contributed by the Heat Transfer Division of THE AMERICAN SOCIETY OF MECHANICAL ENGINEERS. Manuscript received by the Heat Transfer Division February 28, 1996; revision received May 2, 1996. Keywords: Direct-Contact Heat Transfer, Heat Exchangers, Thermal Energy Storage. Associate Technical Editor: S. Ramadhyani.

Downloaded 11 Dec 2010 to 193.140.21.150. Redistribution subject to ASME license or copyright; see http://www.asme.org/terms/Terms_Use.cfm

fied, the average Nusselt number of Eq. (15) is very close to the calculated value when Ja = 0.015 (or $\Delta T \cong 8°C$).

In the absence of surface tension ($I_{Bo} = 0$), Eq. (14) becomes

$$Nu = 0.82\ (Ra/Ja)^{0.2} \qquad (16)$$

with the maximum error of 4 percent. Equation (16) is the same as that theoretically obtained by Shigechi et al. (1990), where the effect due to surface tension was not considered in their analysis.

Conclusions

In solving the laminar film condensation on a horizontal plate, we have applied the concept of minimum energy inherited in the condensated flow to determine the boundary condition at the plate edge rather than arbitrarily assumed.

The surface tension effect of the liquid-film on a finite-size horizontal plate is not negligible. In fact, from this study, we find that the surface tension effect plays the role of contributing the difference of heat transfer coefficient between the theoretical result of Shigechi et al. (1990) and the experimental result of Nimmo and Leppert (1970).

References

Bakhmeteff, B. K., 1966, *Hydraulics of Open Channels*, McGraw-Hill, New York, pp. 39–41.

Gerstmann, J., and Griffith, P., 1965, "Laminar Film Condensation on the Underside of Horizontal and Inclined Surfaces," *Int. J. Heat Mass Transfer*, Vol. 10, pp. 567–580.

Leppert, G., and Nimmo, B., 1968, "Laminar Film Condensation on Surfaces Normal to Body or Inertial Forces," ASME JOURNAL OF HEAT TRANSFER, Vol. 80, pp. 178–179.

Nimmo, B., Leppert, G., 1970, "Laminar Film Condensation on a Finite Horizontal Surfaces," *Proc. 4th Int. Heat Transfer Conference*, pp. 402–403.

Nusselt, W., 1916, "Die Oberfächen-Kondensation des Wasserdampfer," *Zeitschrift des Vereines Deutscher Ingenieure*, Vol. 60, pp. 541–546.

Popov, V. D., 1967, "Heat Transfer During Vapor Condensation on a Horizontal Surface," *Trudy kiev. Teknol. Inst. Pishch*, Prom. 11, pp. 567–580.

Shigechi, T., Kawae, N., Tokita, Y., and Yamada, T., 1990, "Film Condensation Heat Transfer on a Finite-Size Horizontal Plate Facing Upward," *JSME Series B*, Vol. 56, pp. 205–210.

Fundamental Study on Latent Cold Heat Storage by Means of Direct-Contact-Freezing Between Oil Droplets and Cold Water Solution

H. Inaba[1,3] **and K. Sato**[2,3]

Nomenclature

$\bar{d}_p$ = mean diameter of dispersed phase particle
R = solidification rate of frozen oil particles
T_c = temperature of water solution
T_m = melting point of tetradecane = 5.8°C
T_n = injection temperature of tetradecane oil jet
U_c = velocity of water solution
U_n = injection velocity of tetradecane oil

Introduction

The latent cold energy storage system can store a large amount of cold heat energy in a relatively small vessel by using phase-change material (PCM). One of the most important elements in a latent cold storage system is the heat exchanger for freezing the PCM. Generally, the capsule-type heat exchanger is used for the latent cold energy storage system. The capsule type heat exchanger can maintain the PCM and the coolant fluid in a high purity by separating them with the capsule wall. However, the capsule-type heat exchanger has the drawback that it takes longer to complete the latent heat storage and the size of the heat storage vessel becomes larger because of the thermal resistance of the capsule wall. A direct-contact heat exchanger can overcome these problems.

The present study deals with a new kind of latent cold heat storage system using the direct-contact heat exchange between PCM and the coolant fluid. The spray tower is the most suitable configuration as the heat exchanger for freezing the liquid PCM by the direct-contact cooling with the cold medium. Therefore, this study deals with the spray tower in which the dispersed phase causes solidification.

Some studies have been reported about direct-contact heat exchange in which the dispersed phase causes a solidification (Umano, 1959; Mehrabian et al., 1978). For example, theoretical studies of solidification of a drop or a plane or spherical thin molten film have been carried out in the previous work (Siegel, 1978; Fetecău and Petrescu, 1992; Petrescu, 1992). In particular, Petrescu and Fetecău (1993) performed a theoretical study on the temperature profile and the cooling duration of a drop falling freely in a fluid. Some experimental studies have also been seen concerning peal granulation in a liquid or gaseous media (Filipescu, 1987; Onu et al., 1988). The previous researches have studied the fundamental heat transfer characteristics between dispersed phase and continuous phase under a certain condition.

The target of the present study is to investigate the overall performance of a direct-contact heat exchanger in which the dispersed phase droplets freeze, with a view to applying the direct-contact freezing to latent cold energy storage system. Little research has been done in this field.

Experimental Apparatus and Procedure

Tetradecane and 30 mass percent ethylene glycol water solution were used for the PCM and coolant fluid, respectively. The physical properties of tetradecane and 30 mass percent ethylene glycol water solution are indicated in Table 1 (Inaba and Morita, 1993).

As indicated in Fig. 1, the test section is made of transparent acrylic resin plate of 10 mm in thickness, and it has a 100 cm^2 cross section. The vertical distance between the outlet of the nozzle and the surface of the water solution layer is fixed at 1600 mm ± 3 mm. The cold water solution flows downward in the test section with very low velocity (U_c = 0.7 cm/s). The PCM oil is injected from the nozzle fixed at the lower part of the test section. The oil disperses to many tiny oil droplets. The

Table 1 Physical properties of tetradecane

Melting point	(°C)	:	5.8	
Latent heat	(kJ/kg)	:	229.1	
			(Liq: (6 °C))	(Sol. (5 °C))
Specific heat	(kJ/kgK)	:	2.0	1.8
Density	(kg/m^3)	:	770	810

[1]Professor.
[2]Graduate Student.
[3]Department of Mechanical Engineering, Faculty of Engineering, Okayama University, Tsushimanaka 3-1-1, Okayama 700, Japan.

Contributed by the Heat Transfer Division of THE AMERICAN SOCIETY OF MECHANICAL ENGINEERS. Manuscript received by the Heat Transfer Division February 28, 1996; revision received May 2, 1996. Keywords: Direct-Contact Heat Transfer, Heat Exchangers, Thermal Energy Storage. Associate Technical Editor: S. Ramadhyani.

Copyright © 1996 by ASME

Downloaded 11 Dec 2010 to 193.140.21.150. Redistribution subject to ASME license or copyright; see http://www.asme.org/terms/Terms_Use.cfm

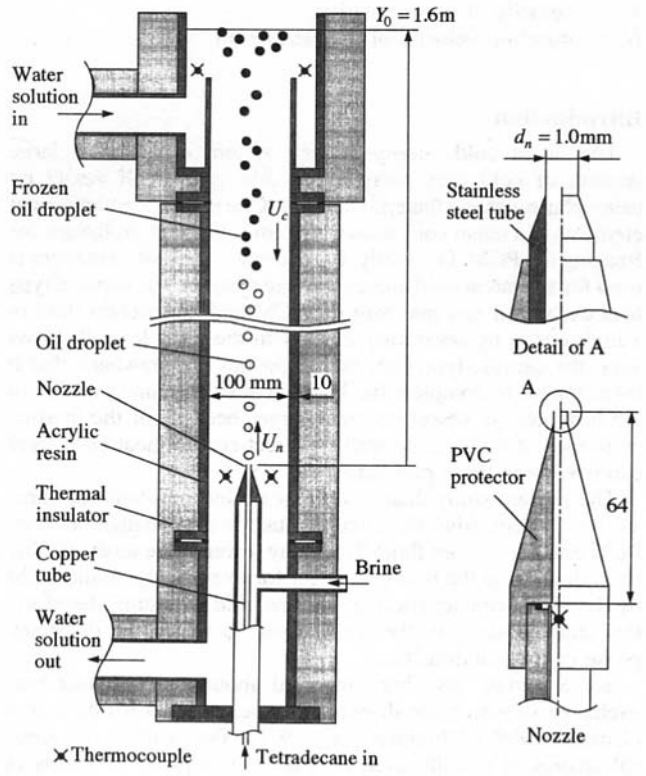


Fig. 1 Detail of test section

oil droplets ascend in the water solution layer by buoyancy. During their ascent, they start to solidify by direct-contact cooling in the cold water solution layer. The solidification progresses from the surface of the oil droplets toward the center of them. When they arrive at the surface of the water solution layer, they become frozen oil droplets composed of outer shells of solidified oil and central cores of unsolidified oil. In this study, the oil droplet that has not started to solidify is referred to as an "oil droplet," the one that has started to solidify as a "frozen oil droplet," and both as "dispersed phase droplets." The frozen oil droplets, arriving at the surface of the water solution layer, were sampled, and the solidification rate was measured using the volumeter. Details of the volumeter will be provided later. The four thermocouples are set in the test section to measure the water solution temperature. The nozzle is made of a stainless steel tube of 1.0 mm in inner diameter with a polyvinyl chloride (PVC) protector as illustrated in Fig. 1. The injecting oil temperature T_n is measured by the thermocouple fixed at the bottom of the nozzle tube. All of the thermocouples used in this experiment were T-type and 0.32 mm in diameter. They were calibrated by a standard thermometer with a minimum temperature scale of 0.05°C. The measuring precision of the temperature is within ± 0.1°C.

The specific volume of tetradecane increases about 5.2 percent during melting. Therefore, the solidified fraction among the frozen oil droplets can be determined by measuring the volume change in the droplets by completely melting them. Figure 2 illustrates the volumeter used to measure the volume change of the frozen oil droplets. As shown in Fig. 2, the volumeter is constructed of a PVC airtight vessel with inner volume of about 200 cm^3, wire-mesh sample container of 4 cm × 4 cm × 2 cm inside, and a glass tube with inner diameter of 5 mm ± 0.02 mm. The volume variation in the frozen oil droplets, packed in the vessel, can be measured by the liquid level displacement in the glass tube. The frozen oil droplets, arriving at the water solution layer, were successively transported to a water bath set at 5.8°C ± 0.1°C (melting point of tetradecane), and stored in the same condition as that when they were sampled. The storing time of the droplets in the water bath is about 2 or 3 minutes. It was confirmed that there was no variation in the solidification rate with the storage time within 2 to 3 minutes. When a sufficient number of sample frozen oil droplets (about 50 to 100 droplets) were accumulated in the water bath, they were packed in the wire-mesh sample container. Subsequently, the container is inserted into the volumeter with liquid phase tetradecane oil of 5.8°C ± 0.1°C. The wire-mesh sample container and the volumeter are set at 5.8°C ± 0.1°C in order to prevent an extra phase change in the sampled frozen oil droplets. Then, the volumeter is immersed into the water bath set at 5.8°C, and the liquid level in the glass tube h_1 is read immediately. Next, the volumeter is transferred to another water bath set at 7.0°C ± 0.1°C to melt the frozen oil droplets inside it. Then the liquid level in the glass tube h_2 is read when the temperature of the entire volumeter becomes stable. The solidified fraction of the frozen oil droplets R is defined as the mass fraction of the solidified parts to the whole of the droplets. It is obtained by using the following equation:

$$R = m_{tf}/m_t \times 100 = \Delta h/\Delta h_0 \times 100$$

where m_{tf} is the total mass of the solidified parts in all sampled droplets, m_t is the total mass of the sampled droplets, Δh is the liquid level displacement in the glass tube measured at the experiment ($=h_2 - h_1$), and Δh_0 is that when the solid phase tetradecane of mass m_t is melted. The value of Δh_0 was obtained from the preliminary experiment. The measurements were repeated two or three times under the same conditions, and the average of all runs were employed as the solidification rate. To check the measuring precision of this measuring device, some mixtures composed of liquid and solid phase tetradecanes with arbitrary mixing ratio were measured. Then the measuring precision of this measuring device was estimated ± 3.5 percent. In the actual experiment, the uncertainty of the entire measuring process of the solidification rate (from the sampling of the frozen oil droplets on the surface of the water solution layer to the end of the measurement with the volumeter) is estimated to be within ± 4.2 percent.

Results and Discussion

Flow and Solidification Characteristics of the Dispersed Phase Droplets. Figure 3(*a*) shows the dispersion characteristics of the tetradecane oil injected into the water solution layer for the three injection velocities: U_n = 30.7 cm/s, 68.6 cm/s,

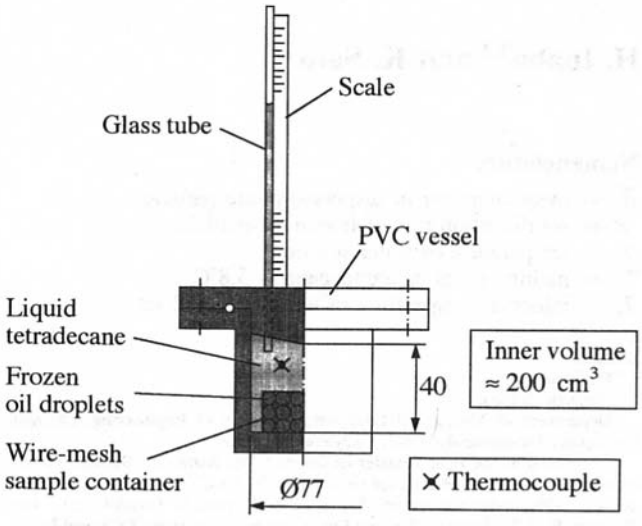


Fig. 2 Volumeter

Downloaded 11 Dec 2010 to 193.140.21.150. Redistribution subject to ASME license or copyright; see http://www.asme.org/terms/Terms_Use.cfm

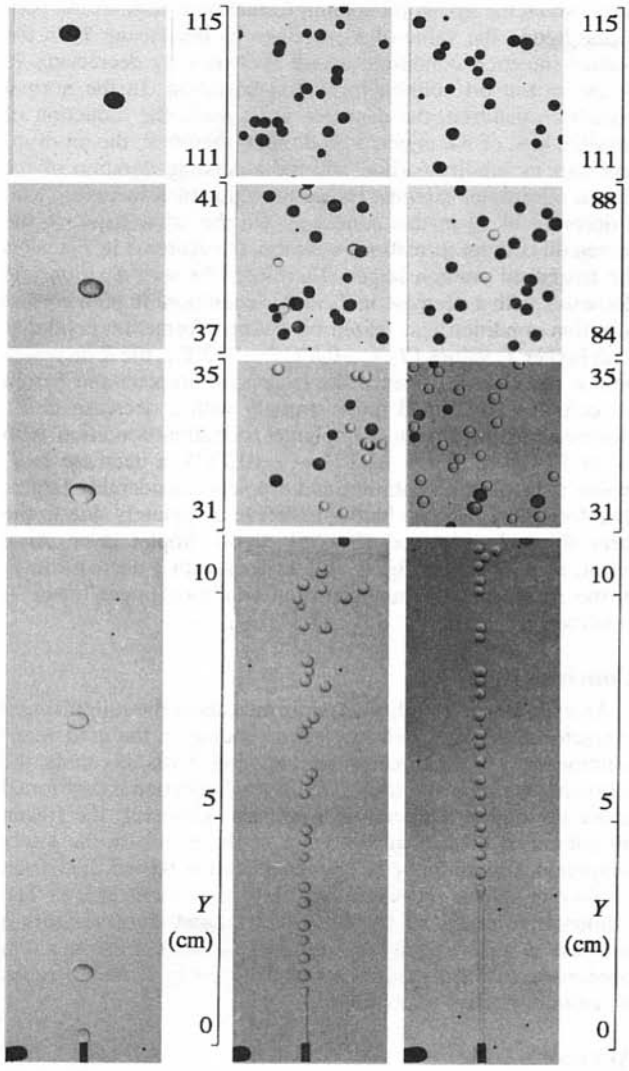


Fig. 3(*a*) Dispersion and solidification characteristics of tetradecane oil droplets

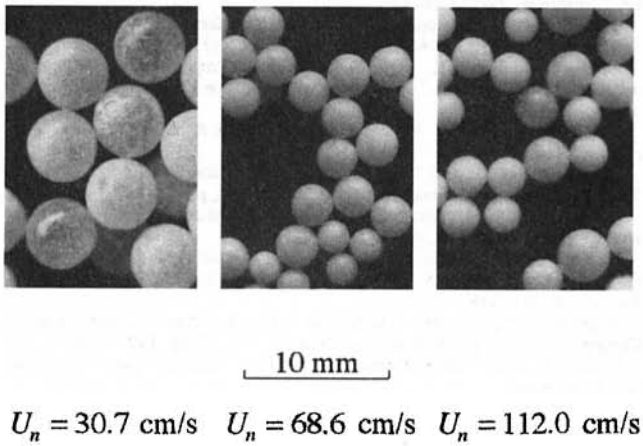


Fig. 3(*b*) Frozen oil droplets that have accumulated on the surface of the water solution layer

Fig. 3 Behavior of dispersed phase droplets in the water solution layer (T_n = 12°C, T_c = 0°C)

and 112.0 cm/s. In Fig. 3(*a*), the transparent objects are the oil droplets, and the black ones are the frozen oil droplets. The mean droplet diameter $\bar{d}_p$ is 5.40 mm at U_n = 30.7 cm/s, 2.76 mm at U_n = 68.6 cm/s, and 3.05 mm at U_n = 112.0 cm/s. From Fig. 3(*a*), it is seen that the tetradecane oil droplets start to solidify as they ascend and become frozen ones. It is noticed that there is a variation in the starting height where the oil droplets start to solidify in the case of U_n = 68.6 cm/s and 112.0 cm/s in Fig. 3(*a*). It is considered that this variation is due to the distributions of droplet diameter and local packing ratio of the oil droplet, temperature distribution of the water solution adjacent to the droplet, and the existence of a supercooling phenomenon in the oil droplets. As to the supercooling phenomenon, however, since the water solution is repeatedly used, there exist fine frozen oil droplets and impurities in the water solution layer (seen as fine black objects in the picture). Since these fine droplets and impurities act as a nucleus for solidification, the oil droplets start to solidify with very small

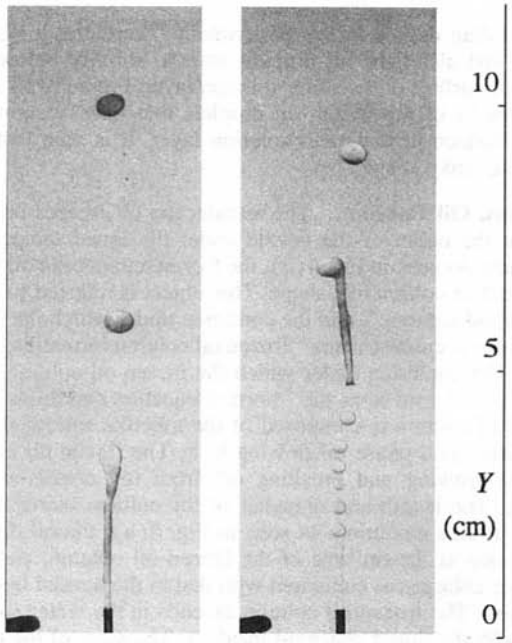


Fig. 4(*a*) Creation and breaking off of the frozen oil column

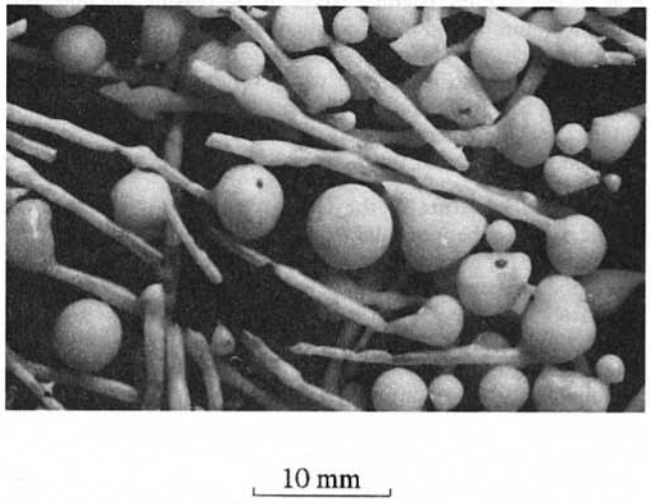


Fig. 4(*b*) Frozen oil column and diameter-enlarged frozen oil droplets accumulated on the surface of the water solution layer

Fig. 4 Behavior of frozen oil column (U_n = 68.6 cm/s, T_n = 19°C, T_c = −3°C)

Downloaded 11 Dec 2010 to 193.140.21.150. Redistribution subject to ASME license or copyright; see http://www.asme.org/terms/Terms_Use.cfm

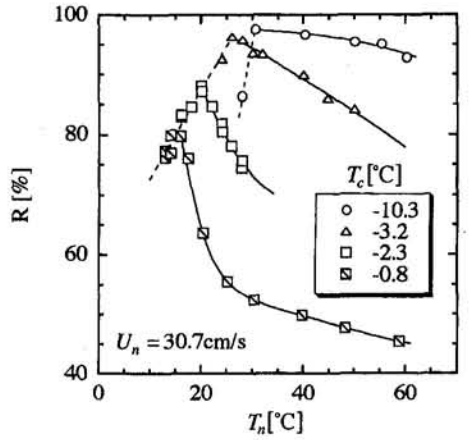


Fig. 5 Variation of solidification rate R for injecting tetradecane oil temperature T_n

supercooling degree in this experiment. Therefore, it was observed that all of the oil droplets start to solidify before they reach the surface of the water solution layer. Figure 3(b) shows photographs of the frozen oil droplets that have accumulated on the surface of the water solution layer. It is seen that they take spherelike shape.

Frozen Oil Column. The tetradecane oil freezes immediately at the outlet of the nozzle under the lower temperature condition. As seen in Fig. 4(a), the frozen tetradecane oil forms the object of columnlike shape. This object is referred to as the "frozen oil column," and the condition under which the frozen oil column is created as the "frozen oil column formation condition." The condition under which the frozen oil column is not created is referred to as the "normal injection condition." The frozen oil column is composed of the tubelike solidified outer shell and liquid phase oil flowing in it. The frozen oil column repeats, growing and breaking off from the nozzle as time elapses. The length and diameter of the column increase as it grows. In this condition, as seen in Fig. 4(a), the oil droplets are created at the tip hole of the frozen oil column, and their diameter enlarges as compared with that in the normal injection condition. The frozen oil column ascends in the water solution layer with the liquid phase oil inside it. The sizes of the frozen oil column ascending, and the oil droplet created from the tip hole of the column, become larger by decreasing the injecting oil temperature T_n and water solution temperature T_c. Therefore, the solidification rate of the frozen oil column and droplet, arriving at the surface of the water solution layer, decreases with decreases in T_n and T_c. Figure 4(b) shows the frozen oil column and diameter-enlarged oil droplets that have accumulated on the surface of the water solution layer.

Solidification Rate of the Oil Droplets. Figure 5 shows the relationship between the solidified fraction R of the frozen oil droplets that have arrived at the surface of the water solution layer and injection temperature of tetradecane oil T_n for the parameter of water solution temperature T_c. As seen in the figure, the R has the maximum point for each T_c condition. The right side regions of the maximum point (solid lines) show the normal injection condition and the left side regions (dotted lines) show the frozen oil column formation condition. As seen in the figure, the value of R increases by decreasing T_n in the normal injection condition, and R decreases by decreasing T_n in the frozen oil column formation condition. In the normal injection condition, the decrease in T_n leads the reduction of sensible heat of the injected oil droplet; therefore, the oil droplets start to solidify earlier, and the ascending duration of the frozen oil droplet extends. Hence the value of R increases with a decrease of T_n in this condition. On the other hand, in the frozen oil column formation condition, the decrease in T_n makes the frozen oil column larger. Therefore, the solidification rate decreases with a decrease in T_n in this condition. In both normal injection condition and frozen oil column formation condition with higher T_c values ($T_c = -0.8°C \sim -3.2°C$), the R increases with a decrease in T_c since the frozen oil droplets and frozen oil columns are cooled more strongly with a decrease in T_c. However, in the frozen oil column formation condition with lower T_c values ($T_c = -3.2°C \sim -10.3°C$), a decrease in T_c makes the frozen oil columns and droplets considerably larger; therefore, they become harder to freeze completely due to the large thermal resistance of solidified oil droplet layer. As a result, as seen in the Fig. 5, R decreases with a decrease in T_c in the frozen oil column formation condition under lower T_c condition.

Conclusion

An experimental study was performed about the solidification characteristics of the oil droplets ascending in the cold water solution layer by the direct-contact cooling. From this study, the following things are clarified: (1) Normal injection is performed under the higher temperature condition. However, the frozen oil column is created at the outlet of the nozzle in the lower temperature condition. (2) The solidification rate of the frozen oil droplet can be measured by using the volumeter. (3) The solidification rate R of the frozen oil droplet increases with a decrease in injection oil temperature T_n under normal injection conditions, and R decreases with a decrease in T_n under frozen oil column formation condition.

Acknowledgments

The authors would like to express their thanks to Mr. Yasuhiro Yoshida and Mr. Sou Tadatomo for their aid in the present experiment.

References

Filipescu, L., 1987, "Proprietăţile Fizico-Mecanice ale Ingrăşămintelor Granulate," Bucureşti, Editura M.I.Ch.

Fetecău, C., and Petrescu, S., 1992, "Heat Transfer at Spherical Thin Film Solidification," *ACTA Mechanica,* Vol. 91, pp. 107–111.

Inaba, H., and Morita, S., 1993, "Thermophysical Properties of Low Temperature Latent Heat Emulsion," *Proc. 14th Symposium on Thermophysical Properties,* pp. 307–310.

Mehrabian, R., Kear, B. H., and Coheu, M., 1978, *Rapid Solidification Processing,* Clasitor's Pub.

Onu, P., Ginju, D., and Luca, C., 1988, "Granularea Zeoliţilor," *Lucrările Sesiunii Jubiliare de Communicări Ştiinţifice,* Vol. 10, pp. 46–49.

Petrescu, S., 1992, "Transferul de Caldură la Cristalizarea din Topitură," *Revista de Chimie,* Vol. 1–2, pp. 44–49.

Petrescu, S., and Fetecău, C., 1993, "Liquid–Liquid Heat Transfer at Direct Contact, Accompanied by Solidification. The Cooling Stage," *ACTA Mechanica,* Vol. 99, pp. 213–218.

Siegel, R., 1978, "Analysis of Solidification Interface Shape During Continuous Casting of a Slab," *Int. J. Heat Mass Transfer,* Vol. 21, pp. 1421–1430.

Umano, S., 1959, "Direct-Contact Refrigeration," Japanese Gov. Chem. Ind. Res. Publication.

Downloaded 11 Dec 2010 to 193.140.21.150. Redistribution subject to ASME license or copyright; see http://www.asme.org/terms/Terms_Use.cfm

The Effect of Temperature-Dependent Viscosity on the Onset of Convection in a Saturated Porous Medium

D. A. Nield[1]

1 Introduction

The problem of determining the critical Rayleigh(–Darcy) number for the onset of convection in a homogeneous horizontal layer of a fluid-saturated porous medium, uniformly heated from below, is a classical problem associated with Horton and Rogers and Lapwood (see, for example, Section 6.1 of Nield and Bejan, 1992). When the Oberbeck–Boussinesq approximation is invoked, linear stability analysis shows that, for the case of impermeable, perfectly conducting upper and lower boundaries, the value of the critical Rayleigh number is $4\pi^2$ (approximately 39.48).

An analysis of the extension of the Horton–Rogers–Lapwood problem to the case where the variation of viscosity with temperature is accounted for was reported by Kassoy and Zebib (1975). They discussed the situation with water as the fluid and they reported their results in their Table 1, part of which is reproduced as Table 1. Here $\tau = (T_1 - T_0)/T_0$, where T_0 and T_1 are respectively the upper and lower surface temperatures, R is the critical Rayleigh number based on the viscosity at temperature T_0, and R_A is the critical Rayleigh number based on an arithmetic average for the viscosity. The reader will note the substantial reduction in R_A as τ increases from zero, and also the fact that this reduction is not uniform; there is a dramatic reduction as τ increases from 0 to 0.34 and a much smaller further reduction as τ increases from 0.34 to 0.84. Kassoy and Zebib did not comment on this phenomenon. The author is not aware of any physical effect that could account for this anomaly so he decided that a further investigation was warranted. The results of this investigation are reported below.

Referring to Wooding (1957), Kassoy and Zebib used a very complicated expression for the variation of dynamic viscosity of water with temperature. As a result, they were forced to employ a numerical procedure (a form of quasi-linearization), which must have been a complicated one. In fact, Wooding gives a simple expression for the kinematic viscosity υ and a complicated one for the density ρ. Within the temperature range treated by Kassoy and Zebib, ρ varies by less than 1 percent, and can be reasonably approximated by a constant. One is then left with an expression for the dynamic viscosity $\mu = \rho\upsilon$ such that $1/\mu$ is linear in the temperature. Because the basic temperature profile in the Horton–Rogers–Lapwood problem is linear in the vertical coordinate z, one has a situation where $1/\mu$ is linear in z. The ordinary differential equation that now arises is one whose coefficients are linear in z. This means that the equation can be solved using a comparatively simple series method, one employed by Sparrow et al. (1964), which was there demonstrated to be capable of yielding results of high accuracy.

2 Analysis

The linear stability analysis follows very closely that in Sections 6.1 and 6.2 of Nield and Bejan (1992). The axes are chosen so the lower and upper boundaries are at $z = 0$ and $z = H$, respectively, and the temperatures there are $T_0 + \Delta T$ and T_0, respectively. The permeability and thermal diffusivity of the porous medium are denoted by K and α_m, respectively. When the inertial term is neglected and scales for length, velocity, temperature, and pressure are chosen to be H, α_m/H, ΔT, and $\mu_0\alpha_m/K$, respectively, the perturbation equations take the form

$$\nabla \cdot \hat{\mathbf{v}} = 0, \tag{1}$$

$$0 = -\nabla \hat{P} - \hat{\mu}\hat{\mathbf{v}} + \mathrm{Ra}\,\hat{T}\mathbf{k}, \tag{2}$$

$$\frac{\partial \hat{T}}{\partial \hat{t}} - \hat{w} = \nabla^2 \hat{T}. \tag{3}$$

(The carets denote nondimensional quantities.) Here Ra is the Rayleigh number defined by

$$\mathrm{Ra} = \frac{\rho_0 g K H \Delta T}{\mu_0 \alpha_m} \tag{4}$$

and ρ_0 and μ_0 are the density and viscosity of the fluid at temperature T_0, g is the gravitational acceleration, while $\hat{\mu}$ denotes the ratio μ/μ_0.

In this problem it is well known that, without loss of generality, it is permissible to consider two-dimensional disturbances only, so that $\hat{\mathbf{v}} = (\hat{u}(\hat{x}, \hat{z}), 0, \hat{w}(\hat{x}, \hat{z}))$, and it is possible to introduce a stream function ψ such that $\hat{u} = \partial\psi/\partial\hat{z}$ and $\hat{w} = -\partial\psi/\partial\hat{x}$. It is also known that convection appears in a nonoscillatory form, and hence the time derivative in Eq. (3) can be replaced by zero. Then Eq. (1) is satisfied identically, and Eq. (3) becomes

$$\frac{\partial \psi}{\partial \hat{x}} = \nabla^2 \hat{T}, \tag{5}$$

and when $\hat{P}$ is eliminated from the components of Eq. (2) one has

$$\frac{\partial}{\partial \hat{x}}\left(\hat{\mu}\frac{\partial \psi}{\partial \hat{x}}\right) + \frac{\partial}{\partial \hat{z}}\left(\hat{\mu}\frac{\partial \psi}{\partial \hat{z}}\right) = -\mathrm{Ra}\,\frac{\partial \hat{T}}{\partial \hat{x}}. \tag{6}$$

We now suppose that $\mu = \mu(T_b)$, where the basic (rest state) temperature T_b is given by

$$T_b = T_0 + \Delta T(1 - \hat{z}). \tag{7}$$

Equation (6) then becomes

$$\frac{\partial^2 \psi}{\partial \hat{x}^2} + \frac{\partial^2 \psi}{\partial \hat{z}^2} - \eta\frac{\partial \psi}{\partial \hat{z}} = -\frac{\mathrm{Ra}}{\hat{\mu}}\frac{\partial \hat{T}}{\partial \hat{x}}, \tag{8}$$

Table 1 Calculated critical Rayleigh numbers (Kassoy and Zebib, 1975)

τ	R	R_A
0	$4\pi^2$	$4\pi^2$ (39.48)
0.34	17.25	24.3
0.50	13.35	23.9
0.67	10.76	22.9
0.84	8.68	21.8

[1] Associate Professor, Department of Engineering Science, University of Auckland, Private Bag 92019, Auckland, New Zealand.

Contributed by the Heat Transfer Division of THE AMERICAN SOCIETY OF MECHANICAL ENGINEERS. Manuscript received by the Heat Transfer Division November 26, 1995; revision received March 1, 1996. Keywords: Natural Convection, Porous Media. Associate Technical Editor: P. Simpkins.

Copyright © 1996 by ASME

Downloaded 11 Dec 2010 to 193.140.21.150. Redistribution subject to ASME license or copyright; see http://www.asme.org/terms/Terms_Use.cfm

where

$$\eta = \frac{\Delta T}{\mu}\frac{d\mu}{dT_b}. \tag{9}$$

Use has been made of the fact that $\partial\mu/\partial z = (d\mu/dT_b)(\partial T_b/\partial z)$.

Following Wooding (1957) and Kassoy and Zebib (1975), but making the modification explained above, the viscosity of water is taken to be given by

$$\mu = \frac{0.332}{13 + T}, \tag{10}$$

where μ is measured in g/cm·s and T in °C. From Eq. (7), it follows that, at the rest state, one has

$$\eta = \frac{1}{\hat{z} - A} \quad \text{and} \quad \hat{\mu} = \frac{1 - A}{\hat{z} - A} \tag{11}$$

where

$$A = 1 + (13 + T_0)/\Delta T. \tag{12}$$

Making the normal modes expansion

$$\psi = F(\hat{z})\exp(i\alpha\hat{x}), \quad \hat{T} = G(\hat{z})\exp(i\alpha\hat{x}) \tag{13}$$

and substituting in Eqs. (5) and (8), one gets

$$i\alpha F = G'' - \alpha^2 G \tag{14}$$

$$F'' - \alpha^2 F - \eta F' = -(\mathrm{Ra}/\hat{\mu})i\alpha G. \tag{15}$$

Elimination of F from Eqs. (14) and (15), and using Eq. (11) leads to

$$(\hat{z} - A)G'''' - G''' - 2\alpha^2(\hat{z} - A)G'' + \alpha^2 G' + [\alpha^4(\hat{z} - A) - \alpha^2\mathrm{Ra}\,(\hat{z} - A)^2/(1 - A)]G = 0. \tag{16}$$

For the case of impermeable, perfectly conducting boundaries the appropriate boundary conditions on the perturbation quantities are

$$\psi = 0, \hat{T} = 0 \quad \text{at} \quad \hat{z} = 0, 1, \tag{17}$$

which implies that

$$G = G'' = 0 \quad \text{at} \quad \hat{z} = 0, 1. \tag{18}$$

Four independent solutions of Eq. (16) are given by

$$f^{(i)}(\hat{z}) = \sum_{n=0}^{\infty} b_n^{(i)}\hat{z}^n, \quad (i = 0, 1, 2, 3) \tag{19}$$

where $b_n^{(i)} = \delta_{ni}$ for $n = 0, 1, 2, 3$,

$$b_{-2}^{(i)} = 0, b_{-1}^{(i)} = 0,$$

and, for $n \geq 4$,

$$b_n^{(i)} = \{(n - 5)(n - 1)!b_{n-1}^{(i)} + 2\alpha^2 A(n - 2)!b_{n-2}^{(i)} - \alpha^2(2n - 7)(n - 3)!b_{n-3}^{(i)} - [\alpha^4 A + \alpha^2\mathrm{Ra}\,A^2/(1 - A)](n - 4)!b_{n-4}^{(i)} + [\alpha^4 + 2\alpha^2\mathrm{Ra}\,A/(1 - A)](n - 4)!b_{n-5}^{(i)} - [\alpha^2\mathrm{Ra}/(1 - A)](n - 4)!b_{n-6}^{(i)}\}/An! \tag{20}$$

(Here δ_{ni} is the Kronecker delta, while $b_{-2}^{(i)}$ and $b_{-1}^{(i)}$ are specified so that Eq. (20) is meaningful and correct for the cases $n = 4$ and $n = 5$. The advantage of the method is its simplicity; there is no need to orthogonalize the polynomials in order to ensure satisfactory convergence. About 15 terms, with double precision arithmetic, were sufficient to determine Rayleigh number values accurate to five or six significant figures. The known exact result for the case $\tau = 0$ provided a check on the accuracy of the process.)

The general solution of Eq. (16) is then of the form

$$G(\hat{z}) = \sum_{i=0}^{3} c_i f^{(i)}(\hat{z}), \tag{21}$$

where the coefficients c_i are constants. The boundary conditions at $\hat{z} = 0$ imply that $c_0 = c_2 = 0$, and the other two boundary conditions lead to the eigenvalue equation

$$f^{(1)}(1)\frac{d^2 f^{(3)}}{d\hat{z}^2}(1) - f^{(3)}(1)\frac{d^2 f^{(1)}}{d\hat{z}^2}(1) = 0. \tag{22}$$

The left-hand side of this equation is a function of A, α, and Ra. For a given value of A, the equation gives Ra as a function of α, and the critical Rayleigh number is the minimum of Ra as α varies. For their calculations Kassoy and Zebib took $T_0 = 25$, and thus their quantity τ is related to A by

$$A = 1 + 1.52\tau^{-1}. \tag{23}$$

3 Results and Discussion

Calculations were carried out for the same values of τ as those used by Kassoy and Zebib (1975). The results are presented in Table 2. It is seen that although the critical value of the Rayleigh number R (based on the viscosity at the temperature of the cold boundary) decreases substantially as τ increases, the critical value of R_A (based on the viscosity at the average temperature) is almost constant and in fact increases slowly with τ. The corresponding value of the wavenumber α also increases very slowly as τ increases.

(The case $\tau = 0$ has to be interpreted in a limiting sense. Clearly, if the viscosity varies with temperature, then, strictly speaking, one cannot have simultaneously nonzero buoyancy and zero viscosity variation. For the case of deep layers (large H) a small ΔT is sufficient to cause convection, and the effect of viscosity variation will be small.)

The present results, which are dramatically different from those of Kassoy and Zebib (1975), are uniform and consistent with expectations based on the concept of an effective Rayleigh number introduced by Nield (1994). In the present problem the reciprocal of the viscosity is linear in the temperature, and hence linear in the vertical coordinate. The Rayleigh number based on properties at the average temperature (R_A) is thus identical with the effective Rayleigh number based on the harmonic mean viscosity (R_{eff}) and one would expect that R_{eff} would not differ much from $4\pi^2$.

The author is aware of just two other papers that explicitly discuss the effect of viscosity variation on the onset of convection in porous media. Patil and Vaidyanathan (1981) treated the case of a stratified fluid where the viscosity varies with depth in a cosinusoidal manner. Blythe and Simpkins (1981)

Table 2 Calculated critical Rayleigh numbers and critical wavenumbers (new results)

τ	R	R_A	α
0	39.48	39.48	3.14
0.34	35.60	39.58	3.14
0.50	34.00	39.59	3.15
0.67	32.50	39.67	3.15
0.84	31.14	39.74	3.16

Downloaded 11 Dec 2010 to 193.140.21.150. Redistribution subject to ASME license or copyright; see http://www.asme.org/terms/Terms_Use.cfm

considered convection at large Rayleigh numbers only, and for laterally heated cavities only. Thus neither paper is directly relevant to the present paper.

4 Conclusion

The onset of convection in a horizontal layer occupied by a water-saturated porous medium has been re-examined. It is shown that the results obtained by Kassoy and Zebib (1975) (indicating that the critical Rayleigh number can be substantially reduced, relative to the uniform viscosity value, when the variation of viscosity is included in the analysis) are anomalous. When the Rayleigh number is based on an appropriate mean viscosity, the critical Rayleigh number is increased slightly as a result of the variability.

Acknowledgments

The author is grateful to Mr. Shaneel S. Narayan for performing the computations.

References

Blythe, P. A., and Simpkins, P. G., 1981, "Convection in a Porous Layer for a Temperature Dependent Viscosity," *International Journal of Heat and Mass Transfer,* Vol. 24, pp. 497–506.

Kassoy, D. R., and Zebib, A., 1975, "Variable Viscosity Effects on the Onset of Convection in Porous Media," *Physics of Fluids,* Vol. 18, pp. 1649–1651.

Nield, D. A., and Bejan, A., 1992, *Convection in Porous Media,* Springer, New York.

Nield, D. A., 1994, "Estimation of an Effective Rayleigh Number for Convection in a Vertically Inhomogeneous Porous Medium or Clear Fluid," *International Journal of Heat and Fluid Flow,* Vol. 15, pp. 337–340.

Patil, P. R., and Vaidyanathan, G., 1981, "Effect of Variable Viscosity on the Setting Up of Convection Currents in a Porous Medium," *International Journal of Engineering Science,* Vol. 26, pp. 789–809.

Sparrow, E. M., Goldstein, R. J., and Jonsson, V. K., 1964, "Thermal Instability in a Horizontal Fluid Layer: Effect of Boundary Conditions and Non-linear Temperature Profile," *Journal of Fluid Mechanics,* Vol. 18, pp. 513–528.

Wooding, R. A., 1957, "Steady State Free Thermal Convection of Liquid in a Saturated Permeable Medium," *Journal of Fluid Mechanics,* Vol. 2, pp. 273–285.

A Thermodynamic Method for the Comparison of Plate-Fin Heat Exchanger Performance

L. Tagliafico[1] and G. Tanda[1]

Nomenclature

A = heat exchanger frontal area, m^2
A_c = minimum free flow area, m^2
A_s = total heat transfer surface area, m^2
B = heat transfer parameter (Eq. (12))
C_p = specific heat at constant pressure, J/(kgK)
D = hydraulic diameter, m
f = friction factor (Eq. (3))
H = heat exchanger plate spacing, m
j = Colburn number (Eq. (4))
k = thermal conductivity, W/(mK)
L = heat exchanger length, m
$\dot{m}$ = mass flow rate, kg/s
N = entropy generation number (Eq. (11))
Nu = Nusselt number (Eq. (6))
p = pressure, Pa
Pr = Prandtl number (Eq. (5))
Q = heat flux, W
Re = Reynolds number (Eq. (2))
$\dot{S}_{p,x}$ = entropy generation rate per unit exchanger length, W/(mK)
$\dot{S}_p$ = entropy generation rate, W/K
T = fluid bulk temperature, K
ΔT = mean wall-to-fluid temperature difference, K
V = total heat exchanger volume, m^3
W = heat exchanger width, m
x = coordinate along the main flow direction, m
δ = dimensionless plate spacing = H/D
μ = dynamic viscosity, kg/(ms)
ρ = density, kg/m^3
σ = minimum free flow to frontal area ratio

Subscripts

i = inlet section
0 = reference condition

Introduction

Compact heat exchangers are widely used for cooling electronic equipment, for environmental control systems, in aircraft vehicles, and in the automotive industry. Selection of the surface is an important step in the design of a compact heat exchanger. A wide range of surface-selection criteria has been proposed in the literature (see, for instance, Bergles et al., 1974). The following basic categories were identified by Shah (1978):

- direct comparison of Colburn number j and friction factor f values;
- comparison of heat transfer as a function of fluid pumping power;
- miscellaneous comparison methods;
- performance comparison with a reference surface.

A general method for the comparison of compact heat transfer surfaces has been recently proposed by Cowell (1990) and Cowell et al. (1993). The method provides compact statements of the relative merits of different heat transfer surfaces by comparing relative pumping powers and relative hydraulic diameters. These two parameters are scaled by the values for an ideal offset strip-fin surface (with zero strip thickness and strip width equal to strip pitch), selected as a reference surface, keeping frontal area, volume, and number of transfer units constant.

In these methods the influence of each parameter on performance (in particular heat transfer duty and required pumping power) is considered separately, while the other parameters remain fixed. A possibility to combine hydraulic and heat transfer characteristics is offered by the thermodynamic (second law) analysis developed by Bejan (1982, 1987). From this point of view, the entropy generation (irreversibilities) in the heat exchanger can be assumed to measure the "quality" of the performance (London, 1982; Paoletti et al., 1989; Sekulic, 1990; Schenone et al., 1991). Furthermore, irreversibility analysis can take into account the overall internal operating costs of the heat exchanger. Attempts to consider material and investment costs as a function of the component geometry and working life are reported in the literature (see, for instance, Gaggioli and El-Sayed, 1987; Aceves-Saborio et al., 1989), though links between this measure of quality and economic considerations remain to be studied. In this paper the entropy production of a given heat transfer surface geometry is evaluated and scaled by

[1] Dipartimento di Termoenergetica e Condizionamento Ambientale (DITEC), Università di Genova, via all'Opera Pia 15/a, I-16145 Genova, Italy.

Contributed by the Heat Transfer Division of THE AMERICAN SOCIETY OF MECHANICAL ENGINEERS. Manuscript received by the Heat Transfer Division November 15, 1995; revision received April 18, 1996. Keywords: Finned Surfaces, Heat Exchangers, Thermodynamics and Second Law. Associate Technical Editor: T. J. Rabas.

Downloaded 11 Dec 2010 to 193.140.21.150. Redistribution subject to ASME license or copyright; see http://www.asme.org/terms/Terms_Use.cfm

considered convection at large Rayleigh numbers only, and for laterally heated cavities only. Thus neither paper is directly relevant to the present paper.

4 Conclusion

The onset of convection in a horizontal layer occupied by a water-saturated porous medium has been re-examined. It is shown that the results obtained by Kassoy and Zebib (1975) (indicating that the critical Rayleigh number can be substantially reduced, relative to the uniform viscosity value, when the variation of viscosity is included in the analysis) are anomalous. When the Rayleigh number is based on an appropriate mean viscosity, the critical Rayleigh number is increased slightly as a result of the variability.

Acknowledgments

The author is grateful to Mr. Shaneel S. Narayan for performing the computations.

References

Blythe, P. A., and Simpkins, P. G., 1981, "Convection in a Porous Layer for a Temperature Dependent Viscosity," *International Journal of Heat and Mass Transfer*, Vol. 24, pp. 497–506.

Kassoy, D. R., and Zebib, A., 1975, "Variable Viscosity Effects on the Onset of Convection in Porous Media," *Physics of Fluids*, Vol. 18, pp. 1649–1651.

Nield, D. A., and Bejan, A., 1992, *Convection in Porous Media*, Springer, New York.

Nield, D. A., 1994, "Estimation of an Effective Rayleigh Number for Convection in a Vertically Inhomogeneous Porous Medium or Clear Fluid," *International Journal of Heat and Fluid Flow*, Vol. 15, pp. 337–340.

Patil, P. R., and Vaidyanathan, G., 1981, "Effect of Variable Viscosity on the Setting Up of Convection Currents in a Porous Medium," *International Journal of Engineering Science*, Vol. 26, pp. 789–809.

Sparrow, E. M., Goldstein, R. J., and Jonsson, V. K., 1964, "Thermal Instability in a Horizontal Fluid Layer: Effect of Boundary Conditions and Non-linear Temperature Profile," *Journal of Fluid Mechanics*, Vol. 18, pp. 513–528.

Wooding, R. A., 1957, "Steady State Free Thermal Convection of Liquid in a Saturated Permeable Medium," *Journal of Fluid Mechanics*, Vol. 2, pp. 273–285.

A Thermodynamic Method for the Comparison of Plate-Fin Heat Exchanger Performance

L. Tagliafico[1] and G. Tanda[1]

Nomenclature

A = heat exchanger frontal area, m^2
A_c = minimum free flow area, m^2
A_s = total heat transfer surface area, m^2
B = heat transfer parameter (Eq. (12))
C_p = specific heat at constant pressure, J/(kgK)
D = hydraulic diameter, m
f = friction factor (Eq. (3))
H = heat exchanger plate spacing, m
j = Colburn number (Eq. (4))
k = thermal conductivity, W/(mK)
L = heat exchanger length, m
$\dot{m}$ = mass flow rate, kg/s
N = entropy generation number (Eq. (11))
Nu = Nusselt number (Eq. (6))
p = pressure, Pa
Pr = Prandtl number (Eq. (5))
Q = heat flux, W
Re = Reynolds number (Eq. (2))
$\dot{S}_{p,x}$ = entropy generation rate per unit exchanger length, W/(mK)
$\dot{S}_p$ = entropy generation rate, W/K
T = fluid bulk temperature, K
ΔT = mean wall-to-fluid temperature difference, K
V = total heat exchanger volume, m^3
W = heat exchanger width, m
x = coordinate along the main flow direction, m
δ = dimensionless plate spacing = H/D
μ = dynamic viscosity, kg/(ms)
ρ = density, kg/m^3
σ = minimum free flow to frontal area ratio

Subscripts

i = inlet section
0 = reference condition

Introduction

Compact heat exchangers are widely used for cooling electronic equipment, for environmental control systems, in aircraft vehicles, and in the automotive industry. Selection of the surface is an important step in the design of a compact heat exchanger. A wide range of surface-selection criteria has been proposed in the literature (see, for instance, Bergles et al., 1974). The following basic categories were identified by Shah (1978):

- direct comparison of Colburn number j and friction factor f values;
- comparison of heat transfer as a function of fluid pumping power;
- miscellaneous comparison methods;
- performance comparison with a reference surface.

A general method for the comparison of compact heat transfer surfaces has been recently proposed by Cowell (1990) and Cowell et al. (1993). The method provides compact statements of the relative merits of different heat transfer surfaces by comparing relative pumping powers and relative hydraulic diameters. These two parameters are scaled by the values for an ideal offset strip-fin surface (with zero strip thickness and strip width equal to strip pitch), selected as a reference surface, keeping frontal area, volume, and number of transfer units constant.

In these methods the influence of each parameter on performance (in particular heat transfer duty and required pumping power) is considered separately, while the other parameters remain fixed. A possibility to combine hydraulic and heat transfer characteristics is offered by the thermodynamic (second law) analysis developed by Bejan (1982, 1987). From this point of view, the entropy generation (irreversibilities) in the heat exchanger can be assumed to measure the "quality" of the performance (London, 1982; Paoletti et al., 1989; Sekulic, 1990; Schenone et al., 1991). Furthermore, irreversibility analysis can take into account the overall internal operating costs of the heat exchanger. Attempts to consider material and investment costs as a function of the component geometry and working life are reported in the literature (see, for instance, Gaggioli and El-Sayed, 1987; Aceves-Saborio et al., 1989), though links between this measure of quality and economic considerations remain to be studied. In this paper the entropy production of a given heat transfer surface geometry is evaluated and scaled by

[1] Dipartimento di Termoenergetica e Condizionamento Ambientale (DITEC), Università di Genova, via all'Opera Pia 15/a, I-16145 Genova, Italy.

Contributed by the Heat Transfer Division of THE AMERICAN SOCIETY OF MECHANICAL ENGINEERS. Manuscript received by the Heat Transfer Division November 15, 1995; revision received April 18, 1996. Keywords: Finned Surfaces, Heat Exchangers, Thermodynamics and Second Law. Associate Technical Editor: T. J. Rabas.

Copyright © 1996 by ASME

Downloaded 11 Dec 2010 to 193.140.21.150. Redistribution subject to ASME license or copyright; see http://www.asme.org/terms/Terms_Use.cfm

that of a reference configuration (a parallel-plate channel) with the same frontal area, volume, heat transfer duty, and mass flow rate, in order to relate the relative merit of the surface geometry to the corresponding irreversibility level. The method has been applied to a number of plate-fin compact heat exchanger surfaces, whose performance data were taken from Kays and London (1984).

Analysis

A model of plate-fin heat exchanger geometry is schematically depicted in Fig. 1. The heat exchanger is required to transfer a given heat flux Q, uniform along the exchanger length L, between the fluid flow and the wall surface. The analysis only considers the behavior of one fluid in the heat exchanger. The thermal resistance between the other fluid and the exchanger surface is neglected. In real compact-surface heat exchangers with gases on the side under study and liquids on the other side this assumption can be closely approached. Other assumptions include: The flow is steady in time and hydraulically and thermally fully developed (i.e., the pressure gradient dp/dx along the main direction of flow and the mean wall-to-fluid temperature difference ΔT are constant along the heat exchanger length L), thermophysical properties are constant, fin efficiency effects and entry/exit pressure losses are ignored. Finally the method only considers the exergy losses associated with the operation of the heat exchanger (heat transfer and fluid friction) without considering the exergy or economic cost of the heat exchanger itself.

The geometry is defined by the following parameters:

- heat exchanger plate spacing H [m]
- heat exchanger frontal area $A = W \cdot H$ [m^2]
- total heat exchanger volume $V = A \cdot L$ [m^3]
- minimum free flow to frontal area ratio $\sigma = A_c/A$
- hydraulic diameter $D = 4 \cdot A_c \cdot L/A_s = 4 \cdot \sigma \cdot V/A_s$ [m]

where A_c is the minimum free flow area, A_s is the total heat transfer surface area and W and L are the exchanger width and length, respectively.

Under the aforementioned assumptions, the entropy generation rate per unit exchanger length is:

$$\dot{S}_{p,x} = \frac{Q\Delta T}{L \cdot T^2} + \frac{\dot{m}}{\rho T}\left(-\frac{dp}{dx}\right) \tag{1}$$

The first term represents the entropy generation rate due to the heat transfer between the wall and the fluid, assuming ΔT to be much smaller than the fluid bulk temperature T; the second term (in which $\dot{m}$ is the mass flow rate, ρ is the density) is due to the irreversibilities caused by fluid friction.

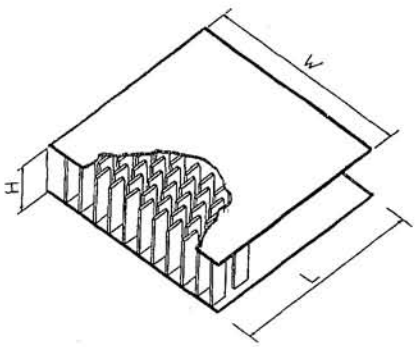


Fig. 1 Schematic view of a plate-fin heat exchanger geometry

The following dimensionless groups are introduced:

$$\mathrm{Re} = \frac{\dot{m}D}{\mu A_c} = \frac{\dot{m}D}{\sigma \mu A} \quad \text{Reynolds number} \tag{2}$$

$$f = \frac{D\rho A_c^2}{2\dot{m}^2}\left(-\frac{dp}{dx}\right) \quad \text{friction factor} \tag{3}$$

$$j = \frac{\mathrm{Nu}}{\mathrm{Re\ Pr}^{1/3}} \quad \text{Colburn number} \tag{4}$$

$$\mathrm{Pr} = \frac{\mu C_p}{k} \quad \text{Prandtl number} \tag{5}$$

$$\mathrm{Nu} = \frac{QD^2}{4k\Delta T A_c L} = \frac{QD^2}{4k\Delta T \sigma V} \quad \text{Nusselt number} \tag{6}$$

where μ, C_p, and k are the dynamic viscosity, the specific heat, and the thermal conductivity of the fluid, respectively.

Integrating Eq. (1) between $x = 0$ and $x = L$ with the assumption $T_i = T_{(x=0)} \gg |T_{(x=L)} - T_{(x=0)}|$ leads to

$$\dot{S}_p = \left(\frac{Q^2D^2}{4kT_i^2A_cL}\right)\frac{1}{j\ \mathrm{Re\ Pr}^{1/3}} + \left(\frac{2L\mu^3A_c}{T_i\rho^2D^4}\right) f\,\mathrm{Re}^3 \tag{7}$$

The j and f values as a function of Re and Pr depend on the particular configuration being studied; in the present work they have been deduced from the literature data reported by Kays and London (1984).

In the same way Eq. (7) can be rewritten for a reference configuration here assumed as a parallel-plate channel without fins, having the same frontal area A (same height H and width W), volume V, heat transfer duty Q, fluid, and mass flow rate $\dot{m}$ as the compact heat exchanger surface:

$$\dot{S}_{p_0} = \left(\frac{Q^2D_0^2}{4kT_i^2A_{c_0}L}\right)\frac{1}{j_0\ \mathrm{Re}_0\ \mathrm{Pr}^{1/3}} + \left(\frac{2L\mu^3A_{c_0}}{T_i\rho^2D_0^4}\right) f_0\ \mathrm{Re}_0^3 \tag{8}$$

the subscript 0 refers to the reference condition, and f_0 and $j_0 = \mathrm{Nu}_0/\mathrm{Re}_0\mathrm{Pr}^{1/3}$ are assumed according to the following relationships:

Laminar region. ($\mathrm{Re}_0 < 2000$)

$$f_0 = 24/\mathrm{Re}_0 \tag{9.a}$$

$$\mathrm{Nu}_0 = 8.25 \tag{9.b}$$

Turbulent region. ($\mathrm{Re}_0 > 10{,}000$)

$$f_0 = 0.046\ \mathrm{Re}_0^{-0.2} \tag{10.a}$$

$$\mathrm{Nu}_0 = 0.023\ \mathrm{Re}_0^{0.8}\ \mathrm{Pr}^{0.4} \tag{10.b}$$

with $\mathrm{Re}_0 = \dot{m}D_0/(\mu A_{c_0}) = \dot{m}D_0/(\mu A)$; $\sigma_0 = 1$, $A_{c_0} = A$

In the transitional region (Re_0 between 2000 and 10,000) f_0 and j_0 were fitted by a weighted average between laminar and turbulent values. Furthermore, the assumption $H \ll W$ implies $D_0 = 2H$ and $\mathrm{Re}_0 = 2\dot{m}H/(\mu A) = 2\dot{m}/(\mu W)$.

In order to quantify the thermodynamic impact of the compact geometry with respect to the reference geometry, the entropy generation number N is introduced:

$$N = \dot{S}_p/\dot{S}_{p_0} \tag{11}$$

on substituting Eqs. (7), (8) in Eq. (11), and introducing the dimensionless parameter

$$B = \frac{\mu^3 kT_i}{8\rho^2Q^2}\left(\frac{V^2}{H^6}\right) \tag{12}$$

Downloaded 11 Dec 2010 to 193.140.21.150. Redistribution subject to ASME license or copyright; see http://www.asme.org/terms/Terms_Use.cfm

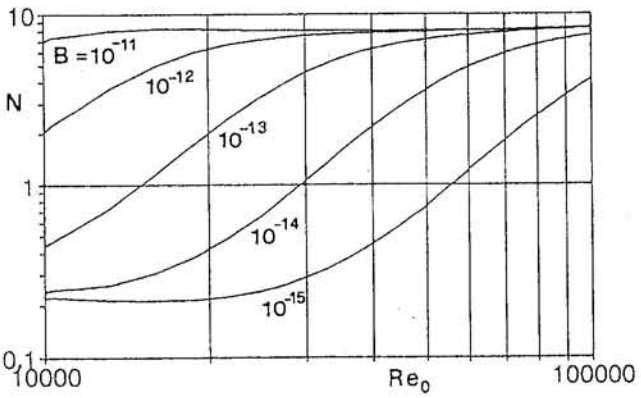


Fig. 2 Entropy generation number N for a plain plate-fin surface

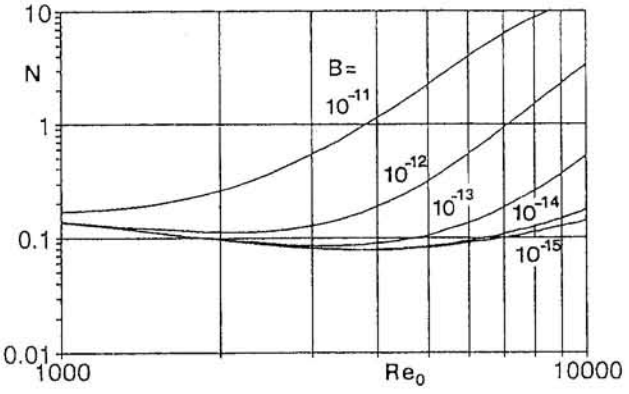


Fig. 3 Entropy generation number N for an offset strip-fin surface

Eq. (11) becomes:

$$N = \frac{\left(\frac{1}{4\delta^2\sigma}\right)\frac{1}{j\ \mathrm{Re}\ \mathrm{Pr}^{1/3}} + 16\sigma\delta^4 B f\ \mathrm{Re}^3}{\frac{1}{j_0\ \mathrm{Re}_0\ \mathrm{Pr}^{1/3}} + B f_0\ \mathrm{Re}_0^3} \tag{13}$$

where $\delta = H/D$.

The constraints here considered involve keeping the heat exchanger plate spacing H and volume V fixed and assuming the same mass flow rate $\dot{m}$ and heat transfer Q for both compact and reference configurations. The Reynolds numbers Re and Re_0 are linked through the relationship:

$$\mathrm{Re} = \mathrm{Re}_0/(2\delta\sigma) \tag{14}$$

Thus for any value of Re_0, Re is automatically fixed by the constraints.

If the dimensions (V and H), thermophysical properties (μ, k, ρ), and inlet temperature T_i are specified, the parameter B depends only on heat transfer duty Q. In conclusion, under the given constraints, N emerges as a function of the flow rate (Re_0), heat transfer duty (B), and working fluid (Pr). In the ranges of variation of the parameters Re_0, B, and Pr, the entropy generation number N is a measure of the thermodynamic quality of the compact surface geometry. Operating conditions for which N values are minimized are thermodynamically advantageous.

Results and Discussion

Calculations of N values have been performed considering air as the working fluid (Pr = 0.71), and varying the operational parameters B within a proper range ($B = 10^{-15} - 10^{-11}$) and Re_0 within the limits for which the performance data are available.

Performance Analysis for a Particular Surface. First, it is possible to determine the thermodynamically optimum operating regime of a given compact heat transfer surface, where the "optimum" corresponds to the working condition for which N is minimum (i.e., when the system destroys the least exergy, as compared with the reference system, while still performing its function). Figures 2 and 3 present N distributions for two plate-fin surfaces. The first one is a plain fin (surface 3.97, D = 8.59 mm, H = 19.05 mm, σ = 0.84) and the second one is an offset strip-fin (surface 19.86, D = 1.54 mm, H = 2.49 mm, σ = 0.87). The figures show the typical behaviors of N curves in two different ranges of Re_0 values.

For the highest Re_0 values in Fig. 2, N tends to the pure fluid-flow irreversibility limit ($N = 2\delta/\sigma^2 \cdot (f/f_0)$ for $\mathrm{Re}_0 \to \infty$). In this case friction effects are dominant and the improvement in heat transfer performance is of little value.

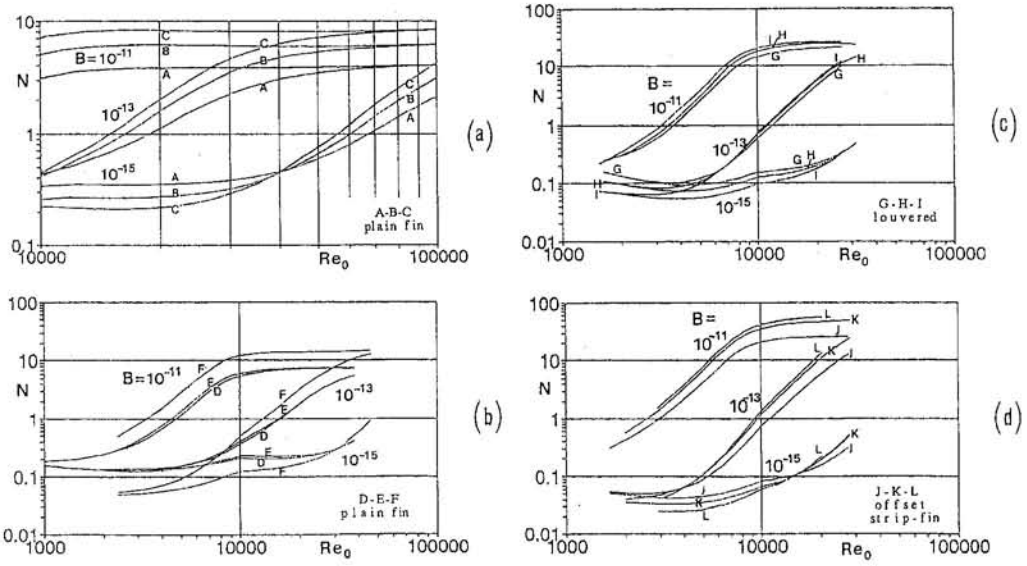


Fig. 4 Entropy generation number N for plain plate-fin surfaces (*a*), (*b*), louvered surfaces (*c*), and offset strip-fin surfaces (*d*)

Downloaded 11 Dec 2010 to 193.140.21.150. Redistribution subject to ASME license or copyright; see http://www.asme.org/terms/Terms_Use.cfm

As Re_0 is reduced, N values fall into a wide range ($N = 0.2 - 8$), depending on operating parameters Re_0 and B, because of the competition between flow and heat transfer irreversibilities. The higher the heat transfer duty Q (or the lower B), the greater the importance of entropy production by thermal effects.

Figure 3 refers to the opposite limiting case. As Re_0 is reduced, N approaches the pure heat transfer irreversibility limit ($N = 1/(2\delta)\cdot(j_0/j)$ for $Re_0 \to 0$); very low values of N can be achieved when the heat transfer performance of the surface under consideration is markedly higher than that of the reference system.

Comparison Among Surfaces With the Same Plate Spacing H. The computed N values for each particular geometry can be used to directly compare performance, under the constraint that mass flow rate (Re_0), heat transfer duty (B), and overall dimensions (W, L, and H) are fixed. In Fig. 4 the N values for a number of compact heat transfer surfaces are reported. Each figure refers to three plate-fin surfaces of the same type (plain, Figs. 4(a) and 4(b), louvered, Fig. 4(c), and offset strip-fin, Fig. 4(d)) having the same plate spacing H and different hydraulic diameters D. Surface designations and geometric parameters as reported by Kays and London (1984) are listed in Table 1.

N trends reflect the general considerations previously discussed for Figs. 2 and 3. Furthermore, decreasing the hydraulic diameter D is advantageous when Re_0 and B are low (region dominated by wall-fluid ΔT irreversibility) and is disadvantageous when Re_0 and B values are high (region dominated by fluid-friction irreversibility).

It can be noted that Figs. 4(b) and 4(c) refer to geometries of different kinds, but with the same plate spacing ($H = 6.35$ mm). Therefore, results can be directly compared in order to assess the relative merits of each configuration from the thermodynamic point of view.

Comparison Among Generic Types of Surface. In the previous sections, a thermodynamic comparison among different surfaces was performed, keeping mass flow rate, heat transfer duty, and sizes fixed. Comparisons among surfaces with different plate spacing H are also possible. A number of criteria can be considered for comparison purposes among surfaces with different H. For instance, the entropy generation rates (from Eq. (7)) of different surface configurations can be directly compared assuming the same mass flow rate per unit frontal area ($\dot{m}/A = \dot{m}/(WH) = \text{const}$) and the same heat transfer duty per unit volume ($Q/V = Q/(WHL) = \text{const}$).

A different constraint involves keeping the mass flow rate $\dot{m}$ and the heat transfer duty Q (as well as W and L dimensions) fixed. Under these conditions, the comparison can be developed on the basis of the entropy generation number N. Equation (12) shows that B parameter includes the heat transfer duty Q and a geometric factor $V^2/H^6 = (W\cdot L)^2/H^4$. Keeping W and L fixed, the comparison between surfaces with different H and same Q implies considering different B values according to the relationship:

Table 1 Geometric parameters of the surfaces considered in Fig. 4

LABEL	TYPE	SURFACE DESIGNATION	H(mm)	D(mm)	σ	Fig.
A	plain	2.0	19.05	14.45	0.902	
B	plain	3.01	19.05	10.82	0.872	4(a)
C	plain	3.97	19.05	8.59	0.841	
D	plain	11.11	6.35	3.08	0.927	
E	plain	12.00T	6.35	2.87	0.924	4(b)
F	plain	19.86	6.35	1.875	0.863	
G	louvered	1/2(a)-6.06	6.35	4.453	0.935	
H	louvered	3/8(a)-8.7	6.35	3.650	0.919	4(c)
I	louvered	3/16-11.1	6.35	3.084	0.928	
J	strip-fin	1/4-15.4 D	5.23	1.61	0.848	
K	strip-fin	1/8-16.12 D	5.23	1.55	0.839	4(d)
L	strip-fin	1/8-19.82 D	5.21	1.54	0.859	

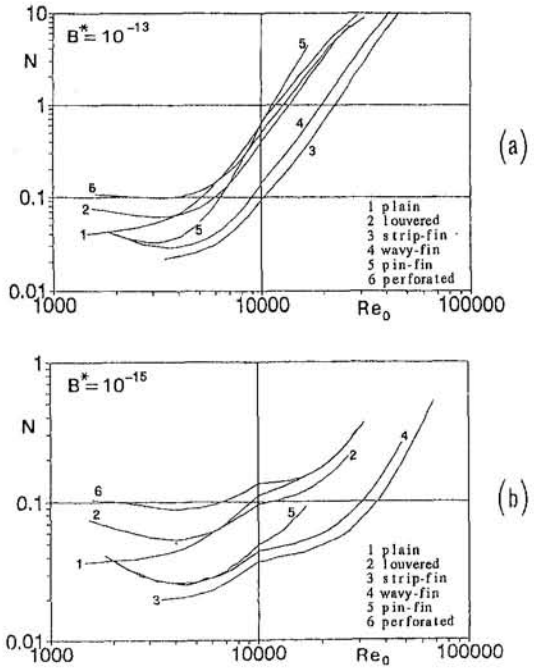


Fig. 5 Entropy generation number N for different types of plate-fin surfaces: $B^* = 10^{-13}$ (a), $B^* = 10^{-15}$ (b)

$$B = B^*\left(\frac{H^*}{H}\right)^4 \tag{15}$$

where (B^*, H^*) and (B, H) refer to the two surfaces to be compared.

N-curves for six different types of plate-fin surface are shown in Fig. 5. The selected surfaces, chosen among those reported by Kays and London (1984), are listed in Table 2. The values $B^* = 10^{-13}$ and $B^* = 10^{-15}$ are based on $H^* = 5.18$ mm (surface No. 1, Table 2). The corresponding values of B (at fixed heat transfer duty Q) for the other surfaces (No. 2–6) can be calculated from Eq. (15). The statement of the thermodynamic performance of surfaces is related to N values. For $B^* = 10^{-13}$ (Fig. 5(a)) and Re_0 less than 10,000, the best performance corresponds to surfaces No. 3, 4 (strip-fin and wavy-fin), with N values in the range 0.02–0.1. For Re_0 higher than 10,000, the use of surfaces No. 3, 4 remains advantageous, even though the degree of exergy destruction is higher ($N = 0.1-10$).

As the heat transfer duty Q is increased ($B^* = 10^{-15}$, Fig. 5(b)), the thermodynamic performance of the surfaces improves, especially for Re higher than 10,000 (N always less than unity).

It is apparent that the same heat transfer surface may do its job very close to its thermodynamic "optimum" for certain values of heat transfer and mass flow rates, but perform very far from the optimum when the operational parameters are changed. Therefore, the choice of a suitable surface from the thermodynamic standpoint should be addressed by heat transfer and mass flow rate considerations, under the given design constraint.

Table 2 Geometric parameters of the surfaces considered in Fig. 5

No.	TYPE	SURFACE DESIGNATION	H(mm)	D(mm)	σ	$(H^*/H)^4$
1	plain	25.79 T	5.18	1.151	0.808	1
2	louvered	3/16-11.1	6.35	3.084	0.928	0.443
3	strip-fin	3/32 12.22	12.3	3.41	0.951	0.0315
4	wavy-fin	11.44 -3/8W	10.49	3.23	0.930	0.0595
5	pin-fin	AP-2	10.1	3.58	0.599	0.0692
6	perforated	13.95(P)	5.08	2.50	0.781	1.081

Downloaded 11 Dec 2010 to 193.140.21.150. Redistribution subject to ASME license or copyright; see http://www.asme.org/terms/Terms_Use.cfm

Conclusions

A thermodynamic analysis for comparing the performance of a number of plate-fin heat transfer surfaces has been presented. The relative merit of each surface geometry has been linked to its irreversibility level, taking into account both heat transfer and fluid flow exergy destruction. Comparisons have been performed under the constraint that heat transfer duty, mass flow rate, heat exchanger length and width are fixed.

The thermodynamic performance of the most suitable surfaces, among those considered in the paper, turned out to be strongly related to the operating conditions (both heat transfer duty and mass flow rate).

Acknowledgments

The funding for this paper came from a MURST (Italian Government) grant.

References

Aceves-Saborio, S., Ranasinghe, J., and Reistad, G. M., 1989, "An Extension to the Irreversibility Minimization Analysis Applied to Heat Exchangers," ASME JOURNAL OF HEAT TRANSFER, Vol. 111, pp. 29–36.

Bejan, A., 1982, *Entropy Generation Through Heat and Fluid Flow*, Wiley, New York, pp. 119–134.

Bejan, A., 1987, "The Thermodynamic Design of Heat and Mass Transfer Processes and Devices," *Int. J. Heat Fluid Flow*, Vol. 8, pp. 258–276.

Bergles, A. E., Blumenkrantz, A. R., and Taborek, J., 1974, "Performance Evaluation Criteria for Selection of Enhanced Heat Transfer Surfaces," *Proc. V. Int. Heat Transfer Conf.*, Tokyo, Vol. II, pp. 239–243.

Cowell, T. A., 1990, "A General Method for the Comparison of Compact Heat Transfer Surfaces," ASME JOURNAL OF HEAT TRANSFER, Vol. 112, pp. 288–294.

Cowell, T. A., Heikal, M. R., and Achaichia, A., 1993, "Flow and Heat Transfer in Compact Louvred Fin Surfaces," in: *Aerospace Heat Exchanger Technology*, R. K. Shah and A. Hashemi, eds., Elsevier Science Publ., Amsterdam, pp. 549–560.

Gaggioli, R. A., and El-Sayed, Y. M., 1987, "A Critical Review of Second Law Costing Methods," *Proc. IV Int. Symp. on 2nd Law Analysis of Thermal Systems*, M. J. Moran and E. Sciubba, eds., ASME, New York, pp. 59–73.

Kays, W. M., and London, A. L., 1984, *Compact Heat Exchangers*, 3d ed., McGraw-Hill, New York.

London, A. L., 1982, "Economics and the Second Law: an Engineering View and Methodology," *Int. J. Heat Mass Transfer*, Vol. 25, pp. 743–751.

Paoletti, S., Rispoli, F., and Sciubba, E., 1989," Calculation of Exergetic Losses in Compact Heat Exchanger Passages," ASME AES-Vol. 10, No. 2, pp. 21–29.

Schenone, C., Tagliafico, L., and Tanda, G., 1991, "Second Law Performance Analysis for Offset Strip-Fin Heat Exchangers," *Heat Transfer Engineering*, Vol. 12, pp. 19–27.

Sekulic, D. P., 1990, "The Second Law Quality of Energy Transformation in a Heat Exchanger," ASME JOURNAL OF HEAT TRANSFER, Vol. 112, pp. 295–300.

Shah, R. K., 1978, "Compact Heat Exchanger Surface Selection Methods," *Proc. VI Int. Heat Transfer Conf.*, Toronto, Vol. 4, pp. 193–199.

Downloaded 11 Dec 2010 to 193.140.21.150. Redistribution subject to ASME license or copyright; see http://www.asme.org/terms/Terms_Use.cfm